COMPUTATIONAL METHODS IN NONLINEAR STRUCTURAL AND SOLID MECHANICS

Papers presented at the Symposium on Computational Methods in Nonlinear Structural and Solid Mechanics

Held 6–8 October 1980, Washington, D.C.

Editors

AHMED K. NOOR

Professor of Engineering and Applied Science, The George Washington University Center at NASA Langley Research Center, Hampton, Virginia, U.S.A.

and

HARVEY G. McCOMB, JR.

Assistant Chief, Structural Mechanics Division, NASA Langley Research Center, Hampton, Virginia, U.S.A.

Sponsored by the George Washington University and NASA Langley Research Center in cooperation with the American Society of Civil Engineers, the American Society of Mechanical Engineers, and the National Science Foundation.

PERGAMON PRESS

OXFORD · NEW YORK · TORONTO

PARIS · FRANKFURT · SYDNEY

U.K.	Pergamon Press Ltd., Headington Hill Hall, Oxford OX3 0BW, England
U.S.A.	Pergamon Press Inc., Maxwell House, Fairview Park, Elmsford, New York 10523, U.S.A.
CANADA	Pergamon Press Canada Ltd., Suite 104, 150 Consumers Road, Willowdale, Ontario M2J 1P9, Canada
AUSTRALIA	Pergamon Press (Aust.) Pty. Ltd., P.O. Box 544, Potts Point, N.S.W. 2011, Australia
FRANCE	Pergamon Press SARL, 24 rue des Ecoles, 75240 Paris, Cedex 05, France
FEDERAL REPUBLIC OF GERMANY	Pergamon Press GmBH, Hammerweg 6, Postfach 1305, 6242 Kronberg-Taunus, Federal Republic of Germany

ISBN 0 08 027299 1

Published as a special issue of the journal *Computers & Structures*, Volume 13, Number 1–3 and supplied to subscribers as part of their normal subscription. Also available to non-subscribers.

Printed in Great Britain by A. Wheaton & Co. Ltd., Exeter.

Computers & Structures Vol. 13, pp. v–vi, 1981.
Printed in Great Britain

0045–7949/81/01000v–02$02.00/0
Pergamon Press Ltd.

PREFACE

Significant and far-reaching advances have been made in the last decade in the development and application of computational methods to analyze nonlinear behavior of structures and solids. The increasing importance of nonlinear analysis is largely due to the emphasis placed by manufacturers, contractors and certifying agencies on realistic modeling and accurate analysis of critical structural components. This endeavor has prompted the development of efficient discretization procedures, numerical algorithms and programming techniques as well as versatile and powerful finite element software systems for nonlinear analysis. These developments have been greatly facilitated by extensive advances in computer hardware and software technology. Nonlinear analysis currently represents the new frontier and "cutting edge" of modern structures and solid mechanics technology. It is important for the future progress of this field that technical information be exchanged quickly and accurately among researchers, structural analysts and structural engineering software designers.

As a means of communicating recent advances and as a step towards stronger interaction among numerical analysts, computer scientists and structural engineers, a symposium entitled, "Computational Methods in Nonlinear Structural and Solid Mechanics," was held in Washington, D.C. on 6–8 October 1980. The organizing committee expected that by bringing together leading experts and active researchers in areas which could impact future developments in numerical analysis of nonlinear response of structures and solids, formal presentations and personal interaction would increase communications among the disciplines and foster effective development of the technology.

Most of the papers presented at the symposium which report completed research work are contained in this Proceedings volume. A companion NASA Conference Publication entitled, "Research in Nonlinear Structural and Solid Mechanics," contains primarily short papers reporting research in progress.

These papers document clearly recent developments in efficient discretization approaches, advanced numerical methods, improved programming techniques, and applications of these developments to nonlinear analysis of structures and solids. They also help identify directions of future developments in this field. The topic headings in the symposium are largely represented by the section headings of this volume, namely: (1) Nonlinear Mathematical Theories and Formulation Aspects, (2) Computational Strategies for Nonlinear Problems, (3) Time Integration Techniques and Numerical Solution of Nonlinear Algebraic Equations, (4) Material Characterization and Nonlinear Fracture Mechanics, (5) Nonlinear Interaction Problems, (6) Seismic Response and Nonlinear Analysis of Concrete Structures, (7) Nonlinear Problems for Nuclear Reactors, (8) Crash Dynamics and Impact Problems, (9) Nonlinear Problems of Fibrous Composites and Advanced Nonlinear Applications, and (10) Computerized Symbolic Manipulation and Nonlinear Analysis Software Systems. The papers contained in this volume will also appear in a special issue of the Journal of Computers and Structures.

The last paper in this volume was not presented at the symposium and is included in the volume because it gives an indication of the status of existing software for nonlinear analysis. The paper is a survey of current capabilities of thirty-six computer programs for solution of structural and solid mechanics problems. This spectrum of programs ranges from large, general purpose to small, special purpose codes. It is hoped that this survey will guide analysts and researchers in the initial selection of programs most suitable for selected applications.

The fields covered by the symposium are rapidly changing, and if new results and anticipated future directions are to have the maximum impact and use, it is imperative that they reach workers in the field as soon as possible. This consideration led to the decision to publish these proceedings prior to the symposium. Special thanks go to Pergamon Press for their cooperation in publishing this volume and to Dean Harold Liebowitz, School of Engineering and Applied Science of the George Washington University for making arrangements for the publication.

The editors express their sincere thanks to the many individuals who contributed to the planning of the symposium, in particular to the members of the technical program committee and to the symposium secretary, Mrs. Mary Torian. The assistance of the American Society of Civil Engineers, the American Society of Mechanical Engineers, and the National Science Foundation are especially appreciated.

The George Washington University Center
at NASA Langley Research Center
Hampton, Virginia, U.S.A.

AHMED K. NOOR
HARVEY G. MCCOMB, JR.

Computers & Structures, Vol. 13, pp. 3–9, 1981
Printed in Great Britain.

0045-7949/81/010003-07$02.00/0

A NONLINEAR THEORY OF GENERAL THIN-WALLED BEAMS

D. MEREDITH
Meredith Engineering, 33170 Glen Valley Drive, Farmington Hills, MI 48018, U.S.A.

and

E. A. WITMER
Department of Aeronautics and Astronautics, Massachusetts Institute of Technology, Cambridge, MA 02139, U.S.A.

(*Received* 18 *April* 1980)

Abstract—A complete and consistent theory is formulated to describe the large-deflection elastic–plastic behavior of thin-walled beams of arbitrary initial shape and subjected to arbitrary transient loadings. The nonlinear beam theory is derived from a well-documented nonlinear shell theory through an application of Hamilton's Principle. By interpreting classical beam theory displacement fields as the lower order terms in a more general series expansion of deformation modes which describe the behavior of the beam cross section, a higher order beam theory based on such an expansion can be developed. The theory can be sufficiently general so as to incorporate the effects of cross-sectional distortion and collapse in addition to the complete range of behavior normally associated with beam theory (translation, extension, bending, transverse shear deformation, torsion, and warping). The generalized equations of motion associated with this series or modal technique are shown to be of the same form as the generalized equations of shell theory from which they were derived. These nonlinear equations of motion for the beam are cast into an approximate form suitable for implementation on a digital computer. The resulting program, MENTOR-3 is applied to treat a nonlinear response and impact problem.

1. INTRODUCTION

In recent years the concern over nuclear power plant safety and vehicle crashworthiness has speeded the development of sophisticated analytical tools and computer codes required by the analyst to predict the nonlinear behavior of safety related structures during abnormal or upset conditions. It has been demonstrated that when sufficient care and attention is paid in developing the nonlinear analysis, the predictions can be shown to be reliable and accurate to within the order of accepted approximation. Therein, the engineer must determine the appropriate level of sophistication or precision which must be incorporated into the analysis in order for the predictions to be useful and meaningful.

The three basic theories of structural mechanics available to the engineering analyst include beam, shell and general 3-dimensional continuum theory. Each of these "macro-mechanics" type theories incorporates a particular level of approximation which is clearly evident in its derivation from the fundamental principles of physics. Traditional continuum theory involves the least amount of approximation and is normally considered to be a valid basis for the development of the more specialized theories of shells and beams.

A measure which forms a suitable basis for distinguishing between beam, shell, and solid structures lies in their relative physical dimensions (additional criteria concerned with material properties, and smoothness of geometry and loading may also be addressed). For instance, shells are distinguishable from solids by their having one physical dimension, their thickness, small in comparison with their other dimensions. Beams on the other hand have two dimensions (their cross section measurements) small in comparison with the remaining dimension (span). It is evident, therefore, that one should in principle be able to connect and derive the equations for beams, shells and 3-dimensional continuum (solids) by taking advantage of these basic factors which serve to distinguish each structure. Such a relationship is illustrated in Fig. 1 for smoothly contoured and loaded homogeneous structures.

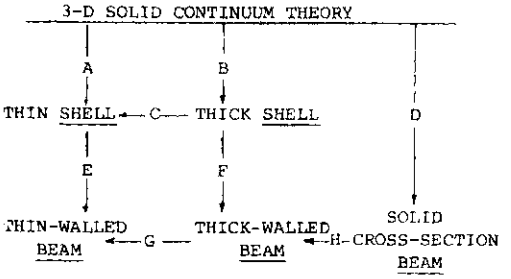

Fig. 1. Inter-relation between theories for solids, shells and beams.

Some of the paths discernable in Fig. 1 have already been developed. The theoretical developments associated with paths *A*, *B*, *C* and *D* are available in [1–4]. For instance, in [1] advantage is taken of the fact that the thickness of a shell is thin in comparison with its other dimensions to reduce a 3-dimensional continuum theory to one defined on a 2-dimensional subspace or reference surface. This is accomplished by assuming within the context of Hamilton's Principle that the deformation through the shell thickness is of a known functional form (truncated series of deformation modes) whose parameters are defined on the shell reference surface. Unfortunately, it is often prohibitively expensive to treat many problems of engineering interest by

employing a 3-dimensional continuum analysis or even the less-costly shell analysis. This is particularly true for structures in which at least one, and more likely two, of its physical dimensions is "thin" with respect to its other dimensions.

Many investigators [5–7] have studied the behavior of such doubly-thin structures and have contributed to the modern engineering theory of general beams. Most of these formulations were developed to treat the behavior of beams whose cross-sections deformed in accordance with classical beam theory assumptions (translation, bending and torsion) or incorporated the first order effects of warping and transverse shear deformation. Several attempts to incorporate higher order effects in beams have been reported [8]; however, most are restricted to elastic beam material behavior and specific types of deformation fields. Of specific interest in the present paper is the nonlinear response of general 3-dimensional thin-walled beams. This field has also received considerable attention [9–11]; however, again the published results are generally restricted to small strain elastic behavior or incorporate a multitude of kinematic assumptions or constraints. It is nevertheless important to note that in each of the above-mentioned shell and beam formulations, the displacement field of the structure along its thin dimension(s) is postulated in terms of generalized displacements defined along the remaining dimension(s). By reducing the infinite number of degrees of freedom along the thin dimension to a suitable and finite number (these normally are just the displacements of the structure at its reference surface or reference axis), great economies in expenditure and effort are derived while maintaining suitable engineering accuracy.

The present paper extends this basic concept to develop a thin-walled beam theory from shell theory by imposing an assumed displacement field along the shell reference surface coordinate (η) which lies within the cross sectional face of the beam (Fig. 2). This reduces the shell theory to a beam theory (path E in Fig. 1) wherein the parameters (displacement field coefficients) which describe the structural deformation are evaluated or defined on a reference line (the beam axis). Such a formulation for thin-walled beams has a number of distinct advantages, the most significant of which is the orderly overlapping of the domains of applicability of shell and beam theory. In addition, since no restriction is applied to the type or number of independent degrees of freedom incorporated in the description of the displacement field of the beam across its cross section, the analyst is no longer confined by the deformation restrictions of classical beam theory (which may be interpreted as the lower order terms in a more general series expansion). By the judicious insertion of additional independent degrees of freedom into the assumed displacement field of the cross section, effects such as cross-section distortion and collapse, normally associated with shell theory, may readily be incorporated into the "beam-type" analysis. It is perhaps worthwhile to note at this stage that because each deformation mode is treated as being independent (at least in an incremental sense), the present procedure may also be interpreted as a "generalized nonlinear incremental modal technique" as applied to a beam-type structure. Also note that in the limit, as an infinite number of independent degrees of freedom is employed in the beam cross section displacement field, the beam solution should converge to the shell-theory solution as the truncation error approaches zero.

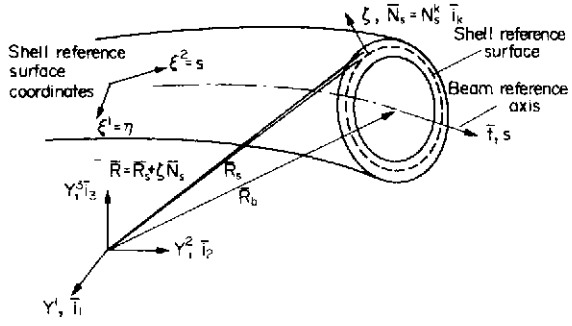

Fig. 2. Position vector to a 3-dimensional thin-walled beam.

†Standard tensor summation conventions are used throughout. Greek minuscules range over the values 1 and 2 whereas Latin minuscules range over the values 1, 2 and 3.

In the following sections, the generalized equations which describe the arbitrarily large-deflection elastic–plastic response of a thin-walled beam are derived from a thin-walled shell theory through an application of Hamilton's Principle into which the above-mentioned beam displacement field is introduced. It will be shown that the generalized equations of motion suitable for describing the behavior of a beam are similar in form to the equations which describe the behavior of a shell and of a 3-dimensional continuum; a similar analogy exists in any modal or generalized Ritz or finite-element analysis. The finite-difference method is employed to approximate the spatial derivatives along the span of the beam. The resulting approximate equations of equilibrium are then integrated in time by means of a central-difference procedure to obtain the transient response of the beam.

This analysis has been incorporated into the MENTOR-3 computer code which is available for treating structures such as shells, beams, or combinations thereof. This program has been employed to analyze a variety of problems wherein the effects of large-displacement elastic plastic behavior associated with the overall deformation of the structure are complicated by the presence of local cross sectional collapse.

2. THEORETICAL DEVELOPMENT

An outline of the general development leading to the formulation of the general modal equations of motion suitable for a thin-walled beam is presented in this section. A more comprehensive and detailed development may be found in [1, 3].

Geometry and position vector of the beam

A general 3-dimensional body can be described in terms of the position vector $\mathbf{R}$ to any point within the body. Each such point can be uniquely defined by its ξ^i intrinsic coordinates† (which, for each material point, are invariant in time). The position vector may be described in terms of its coordinates Y^j in Cartesian space as:

$$\mathbf{R} = Y^j \mathbf{i}_j = Y^j(\xi^i)\mathbf{i}_j.$$

In general, the positions Y^j are a function of the three intrinsic coordinates ξ^i used to identify the material point.

Consider now a beam whose cross section is comprised of thin-walled members. It is often advantageous

when treating thin structures to employ the concept of a reference surface which may, but need not be, the mid-surface of the structure. The reference surface of such a shell-type structure is defined by its position vector $\mathbf{R}_s$ which can be described in terms of the two intrinsic coordinates ξ^1, ξ^2 associated with material points on the reference surface (Fig. 2)

$$\mathbf{R}_S = Y_S^j \mathbf{i}_j. \tag{2}$$

Next, a third intrinsic coordinate ζ is introduced which is associated with the direction which is initially normal to the reference surface and is needed to describe the position of points located through the thickness of the structure. For thin structures, one employs the Kirchhoff hypothesis to describe the deformed shape through the thickness as:

$$\begin{aligned}\mathbf{R} = \mathbf{R}(\xi^i) &= \mathbf{R}(\xi^1, \xi^2, \zeta)\\ &= [Y_s^j + \zeta N_s^j(\xi^1, \xi^2)]\mathbf{i}_j\\ &= Y^j(\xi^1, \xi^2, \zeta)\mathbf{i}_j.\end{aligned} \tag{3}$$

When describing a thin-walled beam which is treated as a thin-shell constrained in some fashion to behave as a beam, it is advantageous to employ the coordinates s, η and ζ which are defined to exist along the beam reference axis, lateral cross section coordinate (on the reference surface), and through the shell thickness, respectively (Fig. 2).

The position vector to the beam reference axis, $\mathbf{R}_b$, can be described in terms of its axial coordinate s as:

$$\mathbf{R}_b = \mathbf{R}_b(s) = Y_b^j(s)\mathbf{i}_j. \tag{4}$$

In the present analysis, the reference axis has no particular significance other than being a convenient means of describing the position of the beam in space. Next, the position vector $\mathbf{R}_s$ to any point on the reference surface of the thin-walled beam may be described by

$$\mathbf{R}_s = Y_s^j(\eta, s)\mathbf{i}_j \tag{5a}$$

and since this same reference surface may be described in terms of the shell intrinsic coordinates as

$$\mathbf{R}_s = Y_s^j(\xi^1, \xi^2)\mathbf{i}_j \tag{5b}$$

it is convenient to set, without loss of any generality

$$\xi^1 = \eta \quad \xi^2 = s. \tag{6}$$

The position vector $\mathbf{R}_s$ to the deformed reference surface will now be related to the beam displacement field. First, the position vector to the deformed beam axis is given by

$$\begin{aligned}\mathbf{R}_b &= \mathbf{r}_b + \mathbf{u}_b\\ &= Y_b^j(\xi^2)\mathbf{i}_j\end{aligned} \tag{7}$$

where $\mathbf{r}_b$ is the position vector to the undeformed beam axis, and $\mathbf{u}_b$ is the displacement field vector of the beam reference axis. Consider now the position vector to points away from the beam axis. Since shell theory will be employed to describe the behavior of the beam through the wall thickness, it suffices to describe the position vector to the deformed reference surface in order to describe fully the geometry of the deformed beam. If $\mathbf{r}_s$ represents the position vector to the undeformed reference surface, then

$$\mathbf{R}_s = \mathbf{r}_s + \mathbf{u}_s. \tag{8}$$

The reference surface displacement vector $\mathbf{u}_s$ is represented by a series of generalized displacements (referred to Cartesian directions)

$$\mathbf{u}_s = \sum_{n=1}^{N} \psi_{s(n)} \Delta Y^{(n)k} \mathbf{i}_k. \tag{9}$$

Consequently, one can describe the position vector to any point through the beam thickness as

$$\begin{aligned}\mathbf{R} &= \mathbf{R}_s + \zeta \mathbf{N}_s\\ &= \mathbf{r}_s + \sum_{n=1}^{N} \psi_{s(n)} \Delta Y^{(n)k} \mathbf{i}_k + \zeta \mathbf{N}_s\\ &= [Y_s^k + \zeta N_s^k]\mathbf{i}_k.\end{aligned} \tag{10}$$

The base vectors to the deformed beam geometry are then given by

$$\begin{aligned}\mathbf{G}_1 &= \frac{\partial \mathbf{R}}{\partial \xi^1} = \left[\frac{\partial Y^k}{\partial \xi^1} + \zeta \frac{\partial N_s^k}{\partial \xi^1}\right]\mathbf{i}_k,\\ \mathbf{G}_2 &= \frac{\partial \mathbf{R}}{\partial \xi^2} = \left[\frac{\partial Y^k}{\partial \xi^2} + \zeta \frac{\partial N_s^k}{\partial \xi^2}\right]\mathbf{i}_k, \quad \mathbf{G}_3 = \mathbf{N}_s^k \mathbf{i}_k.\end{aligned} \tag{11}$$

Expressions for the changes in the base vectors and the associated incremental strain tensor are available in [3].

The equations of modal equilibrium and the associated boundary conditions

The equilibrium equations and boundary conditions for a thin-walled beam can be obtained from an application of Hamilton's Principle as applied to a shell upon whose reference surface a beam-type displacement field is imposed. Hamilton's Principle for a shell reads [1–3]

$$\int_t (\delta H_i + \delta H_l + \delta H_e)\, \mathrm{d}t = 0. \tag{12}$$

Neglecting transverse shear and rotary inertia terms through the shell thickness, the various terms in Hamilton's Principle read:

$$\begin{aligned}\delta H_i &= \delta T + \delta W_i - \delta U_i\\ &= \iint_{\substack{\xi^1\\ \xi^2}} \left(-\sqrt{a}\bar{\rho}_0 \ddot{Y}_s^k + \frac{\partial \tilde{N}^{\alpha k}}{\partial \xi^\alpha} + \tilde{E}^k\right) \delta Y_{s_k}\, \mathrm{d}\xi^1\, \mathrm{d}\xi^2\end{aligned} \tag{13}$$

$$\begin{aligned}\delta H_l &= (\delta W_l - \delta U_l)\big|_{\xi_1}\\ &= -\int_{\xi_2} \left\{(\bar{T}^{1k} - \tilde{T}_{(A)}^{1k})\delta Y_{s_k} + (\tilde{m}^{11} - \tilde{m}_{(A)}^{11}) \times \left(-N_{s_k} \frac{\partial \delta Y_s^k}{\partial \xi^1}\right)\right\} \mathrm{d}\xi^2\end{aligned} \tag{14}$$

$$\begin{aligned}\delta H_e &= (\delta W_e - \delta U_e)\big|_{\xi_2}\\ &= -\int_{\xi_1} \left\{(\bar{T}^{2k} - \tilde{T}_{(A)}^{2k})\delta Y_{s_k} + (\tilde{m}^{22} - \tilde{m}_{(A)}^{22}) \times \left(-N_{s_k} \frac{\partial \delta Y_s^k}{\partial \xi^2}\right)\right\} \mathrm{d}\xi^1.\end{aligned} \tag{15}$$

Consider now the satisfaction of Hamilton's Principle within the interior of the beam. Setting at each time instant

$$\delta H_i + \delta H_l = 0 \tag{16a}$$

one obtains the following interior condition:

$$\iint_{\xi_1\xi_2}\left(-\sqrt{a}\bar{\rho}_0\ddot{Y}_s^k+\frac{\partial\tilde{N}^{\alpha k}}{\partial\xi^\alpha}+\tilde{E}^k\right)\delta Y_{sk}\,d\xi^1\,d\xi^2$$
$$-\int_{\xi_2}\left\{(\tilde{T}^{1k}-\tilde{T}^{1k}_{(A)})\delta Y_{sk}+(\tilde{m}^{11}-\tilde{m}^{11}_{(A)})\times\left(-N_{sk}\frac{\partial\delta Y_s^k}{\partial\xi^1}\right)\right\}d\xi^2=0 \tag{16b}$$

where $(\sqrt{a}\bar{\rho}_0)$ is the mass per unit $d\xi^1\,d\xi^2$, $\tilde{E}^k$ is the internal loading, and (see [3])

$$\tilde{N}^{\alpha k}=\tilde{n}^{\alpha\beta}Y_\beta^k+\tilde{q}^\alpha N_s^k \tag{17a}$$

$$\tilde{T}^{\alpha k}=\tilde{N}^{\alpha k}+\frac{\partial(\tilde{m}^{\alpha\sigma}N_s^k)}{\partial\xi^\sigma} \tag{17b}$$

$$\tilde{q}^\alpha=\frac{\partial\tilde{m}^{\beta\alpha}}{\partial\xi^\beta}+\tilde{m}^{\beta\delta}\begin{Bmatrix}\alpha\\ \beta\quad\delta\end{Bmatrix} \tag{17c}$$

$$\tilde{n}^{\alpha\beta}=\int_\zeta\sqrt{G}\tau^{\alpha\sigma}(\delta_\sigma^\beta-\zeta B_\sigma^\beta)\,d\zeta \tag{17d}$$

$$\tilde{m}^{\alpha\beta}=\int\sqrt{G}\tau^{\alpha\sigma}(\delta_\sigma^\beta-\zeta B_\sigma^\beta)\zeta\,d\zeta. \tag{17e}$$

Note that the lateral edge terms have been included in the internal work contribution as is appropriate for a beam theory formulation. Next, the variation and the acceleration of the beam displacement field may be written as

$$\delta\bar{u}_s=\delta Y_s^k\mathbf{i}_k \tag{18a}$$

$$\delta Y_s^k=\sum_n\psi_{s(n)}\delta Y^{(n)k} \tag{18b}$$

$$\ddot{Y}_s^k=\sum_n\psi_{s(n)}\ddot{Y}^{(n)k}. \tag{18c}$$

Upon implementing eqns (18) into eqn (16b) and performing the appropriate integration by parts, the internal work contribution becomes

$$\delta H_i+\delta H_l=\int_{\xi_2}\left\{-M_{(m,n)}\ddot{Y}^{(m)k}+\frac{\partial N^{2k}_{(n)}}{\partial\xi^2}-p^k_{(n)}+F^k_{(n)}+R^k_{(n)}\right\}\delta Y_k^{(n)}\,d\xi^2 \tag{19}$$

where

$$N^{2k}_{(n)}=\int_{\xi_1}\tilde{N}^{2k}\psi_{s(n)}\,d\xi^1 \tag{20a}$$

$$p^k_{(n)}=\int_{\xi_1}\left(\tilde{N}^{1k}\frac{\partial\psi_{s(n)}}{\partial\xi^1}+\tilde{N}^{2k}\frac{\partial\psi_{s(n)}}{\partial\xi^2}\right)d\xi^1 \tag{20b}$$

$$F^k_{(n)}=\int_{\xi_1}\tilde{E}^k\psi_{s(n)}\,d\xi^1+\tilde{N}^{1k}_{(A)}\psi_{s(n)}\Big|_{\xi_1} \tag{20c}$$

$$M_{(m,n)}=\int_{\xi_1}\sqrt{a}\bar{\rho}_0\psi_{s(m)}\psi_{s(n)}\,d\xi^1 \tag{20d}$$

$$R^k_{(n)}=\frac{\partial}{\partial\xi^2}\{(\tilde{m}^{12}-\tilde{m}^{12}_{(A)})N_s^k\}\psi_{s(n)}+(\tilde{m}^{11}-\tilde{m}^{11}_{(A)})\left(-N_s^k\frac{\partial\psi_{s(n)}}{\partial\xi^1}\right)\Big|_{\xi_1}. \tag{20e}$$

For beams continuous in ξ^1 (closed cross section), the $R^k_{(n)}$ are zero. The $R^k_{(n)}$ are also zero if one imposes on the lateral beam boundary the condition that the shell-type moments $(\tilde{m}^{11})$ and twists $(\tilde{m}^{12})$ are equal to their applied values. Under either condition the equilibrium conditions associated with satisfying eqn (16) in the interior of the beam become (for arbitrary and independent $\delta Y^{(n)k}$)

$$M_{(m,n)}\ddot{Y}^{(m)k}=\frac{\partial N^{2k}_{(n)}}{\partial\xi^2}-p^k_{(n)}+F^k_{(n)} \tag{21}$$

which have the same form (but one less dimension) as the generalized equation of shell theory [1].

Attention will now be focused on the beam end-edge boundary conditions. Returning to Hamilton's Principle as applied to a thin structure, the beam edge work terms along the boundary $\xi^2=$ constant may be written as

$$\int_t\delta H_e\,dt=\int_t\int_{\xi_1}\left\{(\tilde{T}^{2k}_{(A)}-\tilde{T}^{2k})\delta Y_{sk}+(\tilde{m}^{22}_{(A)}-m^{22})\times\left(-N_s^k\frac{\partial\delta Y_{sk}}{\partial\xi^2}\right)\right\}d\xi^1\,dt=0 \tag{22}$$

Employing eqn (17b) and (18b) in eqn (22) leads to

$$\int_t\delta H_e\,dt=\int_t\int_{\xi_1}\left[\left\{\left(\tilde{N}^{2k}_{(A)}\psi_{s(n)}+\frac{\partial}{\partial\xi^1}(\tilde{m}^{21}_{(A)}N_s^k)\psi_{s(n)}-\tilde{m}^{22}_{(A)}N_s^k\frac{\partial\psi_{s(n)}}{\partial\xi^2}\right)-\left(\tilde{N}^{2k}\psi_{s(n)}+\frac{\partial}{\partial\xi^1}(\tilde{m}^{21}N_s^k)\psi_{s(n)}-\tilde{m}^{22}N_s^k\frac{\partial\psi_{s(n)}}{\partial\xi^2}\right)+(\tilde{m}^{22}N_s^k\psi_{s(n)}-\tilde{m}^{22}_{(A)}N_s^k\psi_{s(n)})\frac{\partial\delta Y_k^{(n)}}{\partial\xi^2}\right]d\xi^1\,dt=0. \tag{23}$$

Then, if one sets the shell-type moments $(\tilde{m}^{22})$ and twist $(\tilde{m}^{21})$ on the boundary edge to their prescribed values, the boundary edge work term becomes

$$\int_t\delta H_e\,dt=\int_t(N^{2k}_{(n)(A)}-N^{2k}_{(n)})\delta Y_k^{(n)}\,dt \tag{24}$$

which implies, at each time instant, the following conditions

$$N^{2k}_{(n)}=N^{2k}_{(n)(A)}\quad\text{or}\quad\delta Y_k^{(n)}=0. \tag{25}$$

Displacement field employed for the beam reference surface

The MENTOR-3 computer code employs a Fourier-type series expansion of deformation modes to describe the behavior of the beam reference surface cross-section as a function of the lateral reference surface coordinate ξ^1. This displacement field was chosen since it decouples the generalized mass term $M_{(m,n)}$ for many geometries.

$$\delta\bar{u}_s=\delta Y_s^k\bar{i}_k=\sum_m\psi_{s(m)}\delta Y^{(m)k}i_k$$

$$\left.\begin{aligned}\psi_{s(1)}&=1\ \text{(Translation)}\\ \psi_{s(2N)}&=L\cos\frac{n\pi\xi'}{(\xi'_{\max}-\xi'_{\min})}\\ \psi_{s(2N+1)}&=L\sin\frac{n\pi\xi'}{(\xi'_{\max}-\xi'_{\min})}\end{aligned}\right\}\begin{aligned}&\text{(Rotation, Distortion, etc)}\\ &n=1,2,\ldots,N\end{aligned} \tag{26}$$

where the "effective lateral moment arm" L is introduced as an aid in relating the generalized beam reac-

tions to the classical beam moment and torsion terms. The user may set L to unity if desired.

3. FINITE-DIFFERENCE FORMULATION

Approximate solutions to the variational statement of equilibrium (eqn 12) may be obtained by a variety of techniques (finite element, finite-difference, etc.). In the present formulation, the differential equations of equilibrium (eqn 21) are cast into finite-difference form, resulting in a set of algebraic equations suitable for numerical integration in time. In general, the central-difference formulae having truncation errors of the order Δ^2 are used to represent the spatial and the temporal derivatives. A method for joining structures which are modeled as finite-difference grids has also been devised. Details of the techniques are available in [3].

4. COMPARISON WITH EXPERIMENT OR INDEPENDENT PREDICTIONS

The analysis which has been described in the previous sections has been incorporated into the MENTOR-3 computer program. This program has been applied to various example problems to compare predictions with those from other computer codes and/or experimental results for large-deflection, elastic-plastic dynamic responses and to examine the impact interaction process involving colliding structures [3]. An example to demonstrate the feasibility of employing MENTOR-3 to treat problems of generic interest is included below.

Impact of an elbow with attached pipe against a rigid barrier

MENTOR-3 was employed to treat the pipe elbow impact example presented in [12]. Therein, the 3500 in./sec (8890 cm/sec) impact of a whipping pipe against a stationary rigid barrier was modeled as an elbow with straight lengths of pipe attached at each end to represent the additional effective piping length and mass which must be stopped via the local impact interaction. The differences in boundary conditions, fluid momentum change, and the effect of the changing elbow geometry on the forcing function was ignored. This model was intended to demonstrate the classical unrestrained pipe whip impact problem in a configuration which would be easier to model experimentally.

A 1.5 D 90° 24 in. SCH 80 elbow was employed in this example. The following material parameters were employed:

Mass density $= 0.738 \times 10^{-3}$ lb-sec^2/in.^{4}
$(0.8 \times 10^{-5}$ kg-sec^2/cm$^4)$

Poisson's ratio $= 0.3$

The stress–strain coordinates used to model the uniaxial stress–strain curve (reflecting conditions at typical operating temperature) were:

σ psi	σ kg/cm^2	ε in/in	$1/D$ sec	$1/P$
26,000	1828	0.001	0.316	0.3
42,500	2988	0.025	0.316	0.3
65,000	4570	0.15	0.316	0.3

Advantage was taken of symmetry along two axes, and the quarter section of the piped elbow was modeled. Both shell and beam predictions were obtained. For the shell and initial beam analysis, a 17×18 mesh was employed. The beam analysis incorporated 11 deformation modes across the pipe cross section. Due to the fine axial mesh size, the stable time increment for the higher order modes of the beam theory was considerably smaller than the shell theory stable time increment (the beam stable time increment typically diminishes faster with decreasing mesh size than the corresponding shell theory stable time increment). Consequently, the generalized masses of the higher order beam modes were artificially increased to permit the use of the same time increment as that employed in the shell analysis; this was not expected to have a significant influence on the lower frequency response which dominates the solution.

One benefit of employing a beam modal theory analysis is the ability to employ a coarse axial mesh in conjunction with a finer circumferential mesh and not have to be concerned with a circumferential time stability criterion. Therefore, a coarser mesh beam analysis was performed; this also permitted the use of a larger execution time increment.

Typical impact deformation patterns are illustrated in Fig. 3. The predictions display the local oil-canning indentation phenomena associated with typical elbow crush. As can be readily observed, under these impact

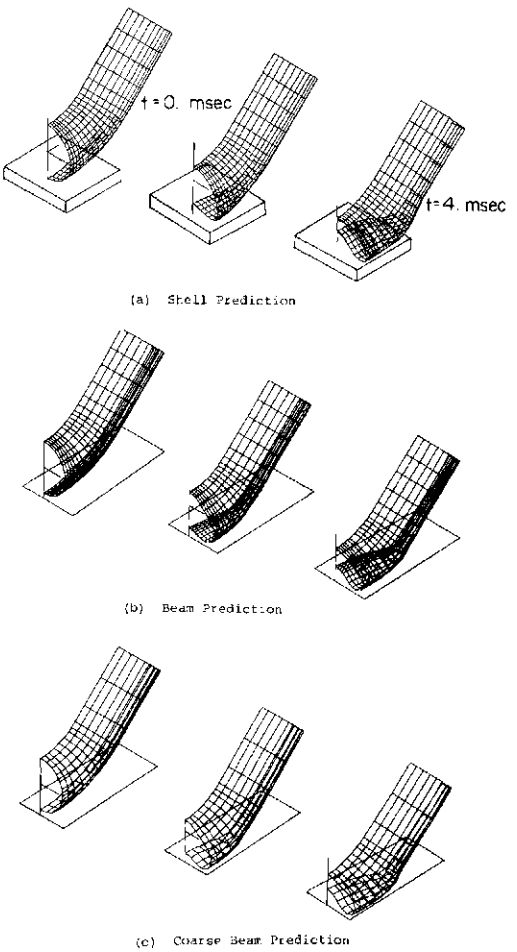

Fig. 3. Elbow deformations (one-quarter model).

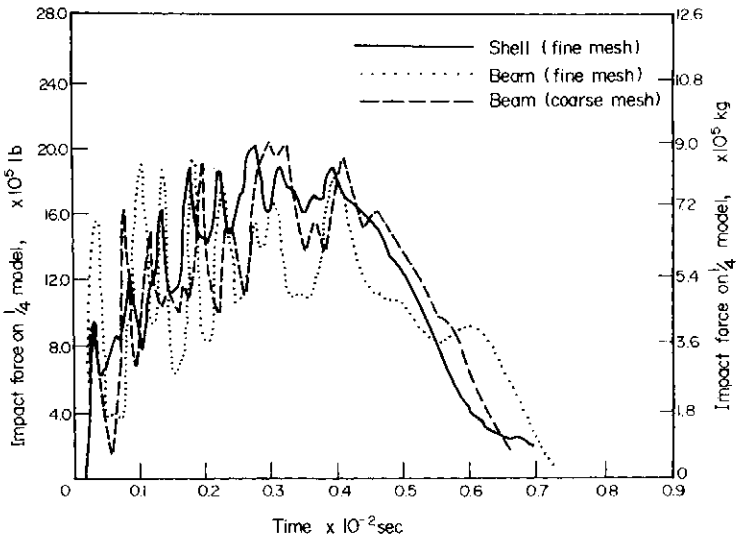

Fig. 4. Impact force time histories.

conditions, most of the deformation occurs locally around the region of impact. The two end pipes served to stiffen the elbow to some extent in the latter stages of crush and their deformations were relatively small compared to the severity of the local deformation and indentation of the elbow.

Both the fine and coarse mesh beam predictions for the present example compared favorably with the shell predictions. The 11 beam modes reasonably reproduced the severe axial and circumferential curvature changes experienced by the crushing elbow. The beam impact forces (Fig. 4) compared reasonably well with the shell theory prediction. The general amplitude, period, and characteristics of the impact forces were similar, although the beam theory predictions demonstrated a somewhat greater fluctuation in the smaller high frequency oscillations which were superimposed on the main loading cycle. Employing the coarser beam mesh with the larger time increment did not significantly degrade the prediction.

5. SUMMARY OF CURRENT RESULTS

The present beam formulation represents a general nonlinear dynamic incremental modal technique suitable for analyzing the transient response of thin-walled structures. The theoretical-experimental results showed generally good correlation for shells and beams subjected to prescribed transient forces, initial velocities and impacts [3]. Predictions for impacts of flexible structures with rigid missiles also show good correlation with experiment [3]. Predictions for impacts between flexible structures, as illustrated in Fig. 5, appear plausible. The present technique has been applied successfully to predict the static and dynamic crush of pipe elbows. MENTOR-3 also has been applied to predict the nonlinear response of piping systems incorporating elbows in which the inplanar and out-of-plane elbow rigidity dominates the structural response [3].

6. CONCLUSIONS AND COMMENTS

The present modal formulation unifies the concepts of shell and beam theories to form a hybrid theory capable of incorporating, to any desirable degree, the salient features of either theory. This general formulation provides the framework for a unified theory of structural mechanics (Fig. 1). Such a unified approach can serve as a valuable teaching aid for students first being exposed to structural mechanics since it places each of the basic theories of applied mechanics into clearer focus and proper perspective. The basic formulation presented herein has already been employed to develop a nonlinear theory for beams of solid cross section [4]. The concept of employing an incremental modal solution along one coordinate can be extended to employing an assumed modal solution along the remaining coordinates, resulting in a nonlinear incremental modal analysis theory for shells and solids.

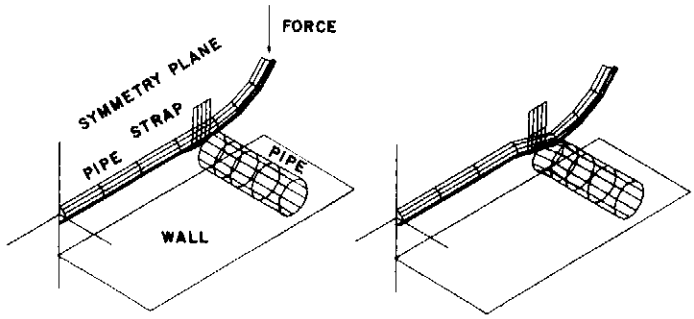

Fig. 5. MENTOR-3 general impact capability.

Similarly, alternate displacement fields may be investigated for use in the current thin-walled beam formulation.

The generalized beam theory incorporated herein offers several distinct computational advantages over traditional shell and beam formulations including:

—Elimination of stability requirements associated with coordinate directions other than the axial direction (an advantage somewhat offset by the need to consider the stability of the axial propagation of the higher order beam deformation modes).

—Ability to tailor the accuracy of the analysis to suit the problem by incorporating only those modes considered necessary for an adequate solution.

—Ease of joining beams to shells either axially or laterally.

—Ease of input, modeling, and interpretation of results.

Of major interest to the nuclear power industry is the interaction between pipes (pressure vessels) and contained or impinging fluids. The MENTOR-3 computer code is ideally suited for incorporating or interfacing with a fluid-dynamics program which would determine the response of the fluid.

Although conceived primarily to treat beams with crushable cross-sections, the technique introduced herein constitutes a new and attractive approach to nonlinear structural analysis.

Acknowledgement—This paper is dedicated to the memory of Dr. John Peech who provided the inspiration for the present investigation.

REFERENCES

1. S. D. Pirotin, L. Morino and J. W. Leech, Finite-difference analysis for predicting large elastic-plastic transient deformations of variable thickness Kirchhoff, soft-bonded thin and transverse shear deformable thicker shells. *BRL CR* 315 (*MIT ASRLTR* 152-3) (Sept. 1976).
2. MENTOR-1 Computer Program Manual. Meredith Engineering, 91 Sycamore Road, Melrose, Massachusetts.
3. MENTOR-3 Computer Program Manual. Meredith Engineering, 91 Sycamore Road, Melrose, Massachusetts.
4. D. Meredith, Development of a 3-dimensional solid cross section beam theory. Meredith Engineering Internal Document, Meredith Engineering, Melrose, Massachusetts.
5. V. Z. Vlasov, *Thin-Walled Elastic Beams*, 2nd Edn. Israel Program for Scientific Translations, Jerusalem, Israel (1961).
6. S. Timoshenko and J. N. Goodier, *Theory of Elasticity*, 2nd Edn. McGraw-Hill, New York (1951).
7. K. Washizu, Some considerations on a naturally curved and twisted slender beam. *J. Math. Phys.* **43**(2), 111–116 (1964).
8. J. T-S. Wang and J. N. Dickson, Elastic beams of various orders. *AIAA*, pp. 535–537 (May 1979).
9. A. Rosen and P. Friedman, The nonlinear behavior of elastic slender straight beams undergoing small strains and moderate rotations. *J. Appl. Mech.* **46**, 161–167 (1979).
10. S. D. Pirotin and G. H. East, Jr., Large-deflection, elastic–plastic response of piping: experiment, analysis and application. Paper F3/1, *4th SMiRT Conf.*, San Francisco (Aug. 1977).
11. E. A. Witmer, F. Merlis and R. L. Spilker, Experimental transient and permanent deformation studies of steel-sphere-impacted of impulsively-loaded aluminum beams with clamped ends. *NASA CR* 134922, *MIT ASRL TR* 154–11 (Oct. 1975).
12. D. Meredith and E. A. Witmer, Computer code for predicting the dynamic response of high energy piping, pressure vessels, and shell structures to transient loads and impacts. ASME Paper 78-PVP-33, Presented at *Joint ASME/CSME Pressure Vessels and Piping Conf.*, Montreal, Canada (June 1978).

Computers & Structures, Vol. 13, pp. 11–18, 1981
Printed in Great Britain.

0045-7949/81/010011-08$02.00/0

STABILITY ANALYSIS OF STRUCTURES VIA A NEW COMPLEMENTARY ENERGY METHOD

H. MURAKAWA†, K. W. REED‡, S. N. ATLURI§ and R. RUBENSTEIN¶
Center for the Advancement of Computational Mechanics School of Civil Engineering, Georgia Institute of Technology, Atlanta, GA 30332, U.S.A.

(*Received* 29 *May* 1980)

Abstract A new procedure for the analyses of finite deformations and stability of structures, based on a complementary energy principle and an associated hybrid-mixed finite element method, is presented. In this procedure, the description of kinematics is based on the polar-decomposition of the displacement gradient into pure stretch and rigid rotation. The details of the procedure are illustrated through the problems of (i) post-buckling of a column, (ii) the elastica, and (iii) finite-displacements of a transversely loaded beam.

INTRODUCTION

As discussed by Atluri and Murakawa [1], the most consistent and easily applicable development of a complementary energy principle for finite deformations is due to the late Fraeijs de Veubeke [2]. Such a principle, involving both the first Piola–Kirchhoff stress tensor as well as the point-wise rigid rotation tensor as variables, has been stated in [2] so as to govern the finite deformations of a compressible nonlinear elastic solid. Also discussed in [1] are contributions to the subject of complementary energy principles for finite elasticity due to Zubov, Koiter, Christoffersen, and others. Since the appearance of [1], the authors became aware of the work by Ogden [3] who discussed more critically the key element in the works of Zubov, and Koiter, namely, the invertibility of the relation between the first Piola–Kirchhoff stress tensor and the displacement-gradient tensor. Odgen [3] demonstrates clearly the non-unique nature of this inverse relation.

The concepts of discretizing the equations of angular momentum balance through a complementary energy principle involving rigid rotations also as variables has been exploited by the authors in their studies related to incremental (rate) analyses of finite strain problems involving nonlinear elastic solids (compressible as well as incompressible), as well as elastic-plastic solids [4–9]. All of the studies in [4–9] were limited to problems of solids in plane stress/plane strain or of axisymmetric strain. In this paper we explore the concepts outlined in [1, 4–9] as they may be applied in the analysis of finite deformations and stability of structural members such as beams, plates and shells wherein certain plausible deformation hypotheses of the well-known "Kirchhoff–Love" type are invoked.

The case for the possible advantages of using a complementary energy approach to structural stability problems has been succinctly presented by Masur and Popelar [10], and Koiter [11]. The analyses presented in [10, 11] are, however, limited to the cases of bifurcation instability of beams/columns with irrotational fundamental states (linear prebuckling states).

In the present paper we consider, as an example, the general problem of finite deformation of a "one-dimensional" structural member undergoing arbitrarily large rotations but only moderate stretching. The material is considered to be isotropic and semilinear, i.e. exhibiting a linear relation between the stretch (or engineering strain) tensor and the Jaumann stress (or equivalently, in the case of isotropy, the Lure of Biot stress) tensor. While the procedures presented herein may be directly extended to the cases of plates and shells, such extensions are not included here.

We present here detailed results, and their discussion, for the problems of (i) post-buckling of a column, (ii) the elastica, and (iii) large displacements of a transversely loaded beam.

In the following, we present, as a starting point, a general variational principle for finite elasticity, analogous to the well-known Hu–Washizu principle of linear elasticity, involving the displacements, stretches, rotations, and the first Piola–Kirchhoff stresses, as variables. By incorporating appropriate "plausible" assumptions for a structural member, such as a beam, the above principle is specialized to the case of the respective structural member. From this general principle an appropriate complementary energy principle, and an associated "hybrid-mixed" finite element method, are developed for the case of a beam.

1. PRELIMINARIES AND A GENERAL VARIATIONAL PRINCIPLE

We use a fixed rectangular Cartesian Coordinate system. We adopt the notation: Bold denotes a vector; bold italic denotes a second-order tensor; $\mathbf{a}=\boldsymbol{A}\cdot\mathbf{b}$ implies that $a_i=A_{ik}b_k$; $\boldsymbol{A}\cdot\mathbf{B}$ denotes a product such that $(\boldsymbol{A}\cdot\mathbf{B})_{ij}=A_{ik}B_{kj}$; $(\boldsymbol{A}:\mathbf{B})=A_{ij}B_{ij}$; and $\mathbf{u}\cdot\mathbf{t}=u_it_i$.

The position vector of a particle in the undeformed body is $\mathbf{x}=(x_\alpha\mathbf{e}_\alpha)$ where $\mathbf{e}_\alpha$ are unit Cartesian bases, and the gradient operator ∇ in the initial configuration is $\nabla=\mathbf{e}_\alpha\partial/\partial x_\alpha$. The position vector of the same particle in the deformed body is $\mathbf{y}$ and the corresponding gradient operator $\nabla^N=\mathbf{e}_i\partial/\partial y_i$. The deformation gradient tensor $\boldsymbol{F}$ is given by $\boldsymbol{F}=(\nabla\mathbf{y})^T$; $F_{i\alpha}=y_{i,\alpha}=\partial y_i/\partial x_\alpha$. For non-singular $\boldsymbol{F}$ the polar-decomposition, $\boldsymbol{F}=\boldsymbol{\alpha}.(\boldsymbol{I}+\boldsymbol{h})$ exists, where $(\boldsymbol{I}+\boldsymbol{h})$ is a symmetric positive definite tensor called the stretch tensor (with $\boldsymbol{h}$ often being called the en-

†Hitachi Co., Japan.
‡Graduate Student.
§Regents' Professor of Mechanics.
¶Research Scientist.

gineering strain tensor), $\boldsymbol{I}$ an identity tensor; and $\boldsymbol{\alpha}$ an orthogonal rotation tensor such that $\boldsymbol{\alpha}^T=\boldsymbol{\alpha}^{-1}$. The deformation tensor $\boldsymbol{G}$ is defined by $\boldsymbol{G}=\boldsymbol{F}^T\cdot\boldsymbol{F}=(\boldsymbol{I}+\boldsymbol{h})^2$. The Green Lagrange strain tensor is defined by $\boldsymbol{g}=1/2(\boldsymbol{G}-\boldsymbol{I})=\frac{1}{2}(\boldsymbol{h}^2+2\boldsymbol{h})=1/2(\boldsymbol{e}+\boldsymbol{e}^T+\boldsymbol{e}^T\cdot\boldsymbol{e})$ where $\boldsymbol{e}$ is the gradient of the displacement vector $\mathbf{u}(\equiv\mathbf{y}-\mathbf{x})$, i.e. $\boldsymbol{e}=(\nabla\mathbf{u})^T$ such that $e_{i\alpha}=u_{i,\alpha}$. For our present purposes we introduce the stress measures: (i) the true (Cauchy) stress tensor, $\boldsymbol{\tau}$, (ii) the Piola–Lagrange or the first Piola Kirchhoff stress tensor, $\mathbf{t}$; (iii) and the Jaumann stress tensor (or what is also at times referred to as the symmetrized Lure' stress tensor or the symmetrized Biot stress tensor) $\boldsymbol{r}$. As discussed in [1], and elsewhere, the relations between $\boldsymbol{\tau}$, $\boldsymbol{t}$ and $\boldsymbol{r}$ are:

$$\boldsymbol{t}=J(\boldsymbol{F}^{-1}\cdot\boldsymbol{\tau}) \tag{1}$$

$$\boldsymbol{r}=1/2(\boldsymbol{t}\cdot\boldsymbol{\alpha}+\boldsymbol{\alpha}^T\cdot\boldsymbol{t}^T) \tag{2}$$

where $\boldsymbol{F}^{-1}$ is the inverse of $\boldsymbol{F}$, and J is the determinant of the Jacobian $y_{i,\alpha}$. As also discussed in [1], and elsewhere, $\boldsymbol{\tau}$ and $\boldsymbol{r}$ are symmetric, while $\boldsymbol{t}$ is in general an unsymmetric tensor. In the case of isotropic elastic materials, $\boldsymbol{h}$, $\boldsymbol{g}$ and $\boldsymbol{r}$ become coaxial, and the relation (2) becomes:

$$\boldsymbol{r}=\boldsymbol{t}\cdot\boldsymbol{\alpha}. \tag{3}$$

As discussed in detail in [1], a functional $\Pi(\mathbf{u},\boldsymbol{h},\boldsymbol{\alpha},\boldsymbol{t})$ whose stationary conditions are the field equations governing the finite deformation of a nonlinear elastic body can be stated as:

$$\pi_{HW}(\mathbf{u},\boldsymbol{h},\boldsymbol{\alpha},\boldsymbol{t})=\int_{V_0}\{W(\boldsymbol{h})-\rho\mathbf{g}\cdot\mathbf{u}+\boldsymbol{t}^T:[(\boldsymbol{I}+\nabla\mathbf{u})^T-\boldsymbol{\alpha}\cdot(\boldsymbol{I}+\boldsymbol{h})]\,dv-\int_{S_{u_0}}\mathbf{t}\cdot(\mathbf{u}-\bar{\mathbf{u}})\,ds-\int_{S_{\sigma_0}}\mathbf{t}\cdot\mathbf{u}\,ds. \tag{4}$$

The stretch $\boldsymbol{h}$ is required to be symmetric a priori, the rotation $\boldsymbol{\alpha}$ is required to be orthogonal, *a priori*, and the first Piola Kirchhoff stresses $\boldsymbol{t}$ must be allowed to be unsymmetric, *a priori*. In eqn (3), V_0 is the volume of the space occupied by the undeformed body; S_{u_0} and S_{σ_0} are, respectively, the surfaces where displacements and traction are prescribed; $W(\boldsymbol{h})$ is the strain energy density, per unit initial volume, as a function of the symmetric engineering strain tensor $\boldsymbol{h}$; $\mathbf{g}$ are body forces/unit mass; ρ is the mass density/unit initial volume; $\mathbf{t}=\mathbf{n}\cdot\boldsymbol{t}$ are surface tractions, and superposed bar implies a prescribed quantity. The first variation of the functional in eqn (4) can be shown [1] to be:

$$\delta\pi_{HW}(\delta\mathbf{u};\delta\mathbf{h};\delta\boldsymbol{\alpha};\delta\boldsymbol{t})=\int_{V_0}\left\{\left[\frac{\partial W}{\partial h}-1/2(\boldsymbol{t}\cdot\boldsymbol{\alpha}+\boldsymbol{\alpha}^T\cdot\boldsymbol{t}^T)\right]:\delta\mathbf{h}-[\nabla\cdot\boldsymbol{t}+\rho\mathbf{g}]\cdot\delta\mathbf{u}-[(\mathbf{I}+\mathbf{h})\cdot\boldsymbol{t}\cdot\boldsymbol{\alpha}]:(\boldsymbol{\alpha}^T\cdot\delta\boldsymbol{\alpha})^T+[(\mathbf{I}+\nabla\mathbf{u})^T-\boldsymbol{\alpha}\cdot(\mathbf{I}+\mathbf{h})]:\delta\boldsymbol{t}^T\right\}dv-\int_{S_{\sigma_0}}(\bar{\mathbf{t}}-\mathbf{n}\cdot\boldsymbol{t})\cdot\delta\mathbf{u}\,ds-\int_{S_{u_0}}\delta\mathbf{t}\cdot(\mathbf{u}-\bar{\mathbf{u}})\,ds=0 \tag{5}$$

The vanishing of the above first variation leads to the following Euler–Lagrange equations from the usual arguments of calculus of variations: (i) the constitutive equation (corresponding to $\delta\mathbf{h}$); (ii) the linear momentum balance condition for $\boldsymbol{t}$ (corresponding to $\delta\mathbf{u}$); (iii) the angular momentum balance condition for $\boldsymbol{t}$, viz. that $(\boldsymbol{I}+\mathbf{h})\cdot\boldsymbol{t}\cdot\boldsymbol{\alpha}=$ symmetric (due to the skew-symmetric nature of $\boldsymbol{\alpha}^T\cdot\delta\boldsymbol{\alpha}$, since $\boldsymbol{\alpha}$ is required to be orthogonal *a priori*, such that $\boldsymbol{\alpha}^T\cdot\boldsymbol{\alpha}=\boldsymbol{I}$); (iv) the compatibility condition between $\mathbf{u}$, $\boldsymbol{\alpha}$ and $\mathbf{h}$ (corresponding to $\delta\boldsymbol{t}$); (v) the traction at S_{σ_0}, viz., $\bar{\mathbf{t}}=\mathbf{n}\cdot\boldsymbol{t}$ (corresponding to $\delta\mathbf{u}$ at S_{σ_0}); and (vi) the displacement boundary condition at S_{u_0} corresponding to $\delta\boldsymbol{t}$ at S_{u_0}.

In the technical theory of beams, or plates, and shells, certain "plausible" approximations are introduced to reduce these problems, respectively, to one or two dimensional in nature from what may rigorously be classified as three-dimensional problems. It is well-known that variational principles often provide a convenient way of deriving the field equations and consistent boundary conditions for these problems. One may systematically introduce "plausible" approximations for the field variables in a functional, then the stationary conditions of the functional yield the relevant field equations and boundary conditions for the considered structural member. Thus, the "modus operandi" of the present procedure is to introduce certain approximations to $\mathbf{u}$, $\boldsymbol{h}$, $\boldsymbol{\alpha}$ and $\boldsymbol{t}$ appearing in eqn (4) so that the relevant field equations for the structural problems of beams, plates, and shells may be derived from the stationary condition of the thus approximated functional π_{HW}. While this approach can be systematically extended to the cases of plates and shells along the same general lines as indicated here, we present in the following the details of only the case of arbitrarily large deformations (characterized by large rotations and perhaps moderate stretches) of a beam.

2. FINITE DEFORMATIONS OF A BEAM

We consider, without loss of generality, an initially straight rectangular beam (of a symmetrical cross section) as shown in Fig. 1, with material coordinates x_1, x_2. Coordinate x_1 is along the length of the beam, and x_2 is in the depth-direction of the beam ($x_2=0$ being the mid-plane). We consider the beam to be of a unit width and consider deformation of the beam only in the x_1x_2 plane.

The position vector of a particle on the mid-plane of the beam is denoted by $\mathbf{x}^*=x_1\mathbf{e}_1$. Upon deformation, the same particle is located by the position vector, $\mathbf{y}^*=\mathbf{x}^*+\mathbf{u}^*=(x_1+u_1^*)\mathbf{e}_1+u_2^*\mathbf{e}_2)$ (see Fig. 1). The position of an arbitrary point in the undeformed beam is denoted by the vector, $\mathbf{x}=\mathbf{x}^*+x_2\mathbf{e}_2$.

We invoke, in the present work, the Kirchhoff Love hypothesis for the deformation of the beam, viz. the x_2 lines of the undeformed beam remain normal to the deformed mid-plane and, moreover, remain unstretched. Thus, the position vector of an arbitrary particle in the deformed beam is given by,

$$\mathbf{y}=\mathbf{y}^*+x_2\mathbf{N} \tag{6}$$

where $\mathbf{N}$ (see Fig. 1) is normal to the deformed mid-plane. Thus, the displacement of an arbitrary particle from the undeformed to the deformed state of the beam is given by:

$$\mathbf{u}=\mathbf{y}-\mathbf{x}=\mathbf{u}^*+(\mathbf{N}-\mathbf{e}_2)x_2=(u_1^*\mathbf{e}_1+u_2^*\mathbf{e}_2)+(\mathbf{N}-e_2)x_2. \tag{7}$$

The base vectors at an arbitrary point in the deformed beam are given by:

$$\partial\mathbf{y}/\partial x_1\equiv\mathbf{y}_{,1}=\mathbf{G}_1=(\delta_{i1}+u_{i,1})\mathbf{e}_i+\mathbf{N}_{,1}x_2 \tag{8}$$

$$\partial\mathbf{y}/\partial\mathbf{x}_2\equiv\mathbf{y}_{,2}=\mathbf{G}_2=\mathbf{N}. \tag{9}$$

Thus, in eqn (8), and throughout the remainder of the paper, the notation, $(\,)_{,1} \equiv \partial(\,)/\partial x_1$ is used.

The deformation gradient tensor $\boldsymbol{F}$ can be represented as:

$$\boldsymbol{F} = (\nabla \mathbf{y})^{\mathrm{T}} = \mathbf{G}_1 \mathbf{e}_1 + \mathbf{N}\mathbf{e}_2. \tag{10}$$

We consider here a class of problems characterized by large rotation, but moderate stretches. For all deformations given by eqn (7) the material coordinates coincide with the principal axes of stretch, so the deformation of the beam may be decomposed into a pure stretch along the $\mathbf{e}_1$ direction, followed by a rigid rotation. The stretch tensor $\boldsymbol{h}$ is thus,

$$\boldsymbol{h} = h_{11}\mathbf{e}_1\mathbf{e}_1. \tag{11}$$

From eqns (10) and (11) it is seen that,

$$\mathbf{N} = \boldsymbol{F}\cdot\mathbf{e}_2 = [\boldsymbol{\alpha}\cdot(\boldsymbol{I}+\boldsymbol{h})]\cdot\mathbf{e}_2 \equiv \boldsymbol{\alpha}\cdot\mathbf{e}_2. \tag{12}$$

Using eqn (12), eqn (7) can be written as:

$$\mathbf{u} = (u_1^*\mathbf{e}_1 + u_2^*\mathbf{e}_2) + (\boldsymbol{\alpha}-\boldsymbol{I})\cdot\mathbf{e}_2 x_2 \tag{13a}$$

where

$$u_\alpha^* = u_\alpha^*(x_1)(\alpha = 1, 2). \tag{13b}$$

In the present case of moderate stretches, we assume that $h(x_1, x_2)$ can be represented as:

$$h_{11}(x_1, x_2) = (h + \chi x_2) \tag{14}$$

where $h = h(x_1)$ is the midplane stretch, and $\chi = \chi(x_1)$ is the curvature strain. These are the well-known engineering measures of strain. Further, we assume plane-stress conditions in the beam and assume the first Piole–Kirchhoff stress tensor (i.e. stress measured/unit area in the undeformed configuration) to be represented by:

$$\boldsymbol{t} = t_{\alpha\beta}\mathbf{e}_\alpha\mathbf{e}_\beta(\alpha, \beta = 1, 2) \tag{15}$$

where

$$t_{\alpha\beta} = t_{\alpha\beta}(x_1, x_2). \tag{16}$$

Likewise, we assume the rigid rotation tensor to be represented by:

$$\boldsymbol{\alpha} = \alpha_{\beta\gamma}\mathbf{e}_\beta\mathbf{e}_\gamma \tag{17}$$

where, under the present deformation assumptions,

$$\alpha_{\beta\gamma} = \alpha_{\beta\gamma}(x_1) \text{ only.} \tag{18}$$

The orthogonal tensor $\alpha_{\beta\gamma}$ is represented conveniently in terms of the angle θ (Fig. 1) as:

$$\alpha_{\beta\gamma} = \begin{bmatrix} \cos\theta; & \sin\theta \\ -\sin\theta; & \cos\theta \end{bmatrix}. \tag{19}$$

We assume the beam to be of a semi-linear isotropic material, such that the relation between the stretch h_{11} and its conjugate stress measure, the Jaumann stress r_{11}, is given by

$$r_{11} = Eh_{11}. \tag{20}$$

We assume the following system of external tractions on the beam in general:

$$\text{at } x_1 = 0 \text{ or } L\text{: } t_{11} = \bar{t}_{11}(x_2);\ t_{12} = \bar{t}_{12}(x_2). \tag{21}$$

The external forces distributed along the beam are assumed, without much loss of generality, to be specified per unit length x_1 along the midaxis of the beam to be $g_\alpha = g_\alpha(x_1)$. Finally, the specified displacements at the ends of the beam are assumed to be:

$$\text{at } x_1 = 0 \text{ or } L\text{: } u_1 = \bar{u}_1(x_2);\ u_2 = \bar{u}_2(x_2). \tag{22}$$

We assume that $\bar{u}_1$ and $\bar{u}_2$ are compatible with the presently invoked hypotheses, such that:

$$\text{at } x_1 = 0 \text{ or } L\text{: } \bar{u}_1(x_2) = \bar{u}_1^* + \bar{\alpha}_{12}x_2;$$
$$\bar{u}_2 = \bar{u}_2^* + (\bar{\alpha}_{22} - 1)x_2. \tag{23}$$

Even though the boundary conditions (21) and (23) are given in their general form, it is to be understood that at either end of the beam, either both the traction components $\bar{t}_{11}$ and $\bar{t}_{12}$, or both displacements $\bar{u}_1$ and $\bar{u}_2$, or one component of traction and a complementary component of displacement, such at t_{11} and $\bar{u}_2$, are assumed to be given.

Substituting eqns (13)–(18) into eqn (4), we obtain, after some straightforward manipulations, that for a beam under the above discussed assumptions,

$$\begin{aligned}
&\Pi_{HW}(u_\alpha^*, \alpha_{\gamma\beta}, h_{11}, t_{\alpha\beta}) \equiv \Pi_{HW}(u_1^*, u_2^*, h, \chi, \theta, t_{\alpha\beta}) \\
&= \int_{x_1,x_2} \{\tfrac{1}{2}E(h+\chi x_2)^2 + t_{11}[(1+u_1{}^*{}_{,1}) - (1+h)\cos\theta \\
&\qquad + x_2\cos\theta(\theta_{,1} - \chi)] \\
&\quad + t_{12}[u_{2,1}^* + (1+h)\sin\theta - x_2\sin\theta(\theta_{,1} - \chi)]\} \\
&\qquad \times \mathrm{d}x_1\mathrm{d}x_2 \\
&\quad + \int_{x_1} g_\alpha u_\alpha^*\,\mathrm{d}x_1 - \Big[\int_{x_2}\Big\{t_{11}[(u_1^* - \bar{\theta}) + x_2 \\
&\qquad \times(\sin\theta - \sin\bar{\theta})] + t_{12}(u_2^* - \bar{u}_2^*) + x_2 \\
&\qquad + x_2(\cos\theta - \cos\bar{\theta})\Big\}\mathrm{d}x_2\Big]_0^L \text{ (or)} \\
&- \Big[\int_{x_2}\{\bar{t}_{11}(u_1^* + x_2\sin\theta) \\
&\qquad + \bar{t}_{12}(u_2^* + x_2(\cos\theta - 1))\}\mathrm{d}x_2\Big]_0^L \text{ (or).}
\end{aligned} \tag{21}$$

It is of interest to note that only t_{11} and t_{12} enter the above energy expression, due to the nature of the presently assumed deformation pattern. We now define first Piola–Kirchhoff stress-resultants ($T_{\alpha\beta}$) and stress-couples ($M_{\alpha\beta}$) such that,

$$\begin{aligned}
T_{11} &= \int_{x_2} t_{11}\,\mathrm{d}x_2; \quad T_{12} = \int_{x_2} t_{12}\,\mathrm{d}x_2 \\
M_{11} &= \int_{x_2} t_{11}x_2\,\mathrm{d}x_2; \quad M_{12} = \int_{x_2} t_{12}x_2\,\mathrm{d}x_2.
\end{aligned} \tag{22}$$

Accordingly, we define the prescribed equivalent stress-resultants and stress couples, at $x_1 = 0$ or L, as

$$\begin{aligned}
\bar{T}_{11} &= \int_{x_2} \bar{t}_{11}\mathrm{d}x_2; \quad \bar{T}_{12} = \int_{x_2} \bar{t}_{12}\mathrm{d}x \\
\bar{M}_{11} &= \int_{x_2} \bar{t}_{11}x_2\mathrm{d}x_2; \quad \bar{M}_{12} = \int_{x_2} \bar{t}_{12}x_2\mathrm{d}x_2.
\end{aligned} \tag{23}$$

With the definitions of eqns (22) and (23), eqn (21) can be written as:

$$\begin{aligned}
&\pi_{HW}(u_1^*, u_2^*, h, \chi, \theta, T_{11}, T_{12}, M_{11}, M_{12}) \\
&= \int_0^L \{\tfrac{1}{2}EAh^2 + \tfrac{1}{2}EI\chi^2 - g_\alpha u_\alpha^* + \\
&\quad + T_{11}\langle 1 + u_{1,1}^* - (1+h)\cos\theta\rangle + \\
&\quad + T_{12}\langle u_{2,1}^* + (1+h)\sin\theta\rangle
\end{aligned}$$

$$+(M_{11}\cos\theta - M_{12}\sin\theta)(\theta_{,1}-\chi)\}\,dx_1$$
$$-[T_{11}(u_1^*-\bar{u}_1^*)+T_{12}(u_2^*-\bar{u}_2^*)+M_{11}(\sin\theta-\sin\bar{\theta})$$
$$+M_{12}(\cos\theta-\cos\bar{\theta})]_0^L(\text{or})$$
$$-[\bar{T}_{11}u_1^*+\bar{T}_{12}u_2^*+\bar{M}_{11}\sin\theta+\bar{M}_{12}(\cos\theta-1)]_0^L(\text{or}) \tag{24}$$

where

$$I=\int_{x_2} x_2^2\,dx_2.$$

For convenience, we define new variable M and W as:†

$$M=M_{11}\cos\theta-M_{12}\sin\theta$$
$$W=M_{11}\sin\theta+M_{12}\cos\theta. \tag{25}$$

The thus transformed functional can be written as:

$$\pi_{W}(u_1^*, u_2^*, h\chi, \theta, \mathbf{T}_{11}, T_{12}, \mathbf{M}, \mathbf{w})$$
$$=\int_0^L \{\tfrac{1}{2}EAh^2+\tfrac{1}{2}EI\chi^2-\bar{g}_v u_2^*$$
$$+T_{11}\langle 1+u_{1,1}^*-\cos\theta(1+h)\rangle$$
$$+T_{12}\langle u_{2,1}^*+\sin\theta(1+h)\rangle+M(\theta_{,1}-\chi)\}\,dx_1$$
$$-[T_{11}(u_1^*-\bar{u}_1^*)+T_{12}(u_2^*-\bar{u}_2^*)+M\sin(\theta-\bar{\theta})$$
$$+W(1-\cos(\theta-\bar{\theta}))]_0^L(\text{or})$$
$$-[\bar{T}_{11}u_1^*+\bar{T}_{12}u_2^*+\bar{M}_{11}\sin\theta+\bar{M}_{12}(\cos\theta-1)]_0^L(\text{or}). \tag{26}$$

With a view to simplify the boundary conditions on θ and M, we consider the variation of the term $(M\theta_{,1})$ in the integral and the corresponding terms at the boundaries, in eqn (26). Thus,

$$\delta\Big\{\int_0^L M\theta_{,1}\,dx_1-[M\sin(\theta-\bar{\theta})+W(1-\cos(\theta-\bar{\theta}))]_0^L(\text{or})$$
$$+\bar{W}(1-\cos(U-\bar{\theta}))]_0^L(\text{or})$$
$$-[\bar{M}_{11}\sin\theta+\bar{M}_{12}(\cos\theta-1)]_0^L(\text{or})\Big\}$$
$$=\int_0^L \delta M\theta_{,1}\,dx_1-\int_0^L M_{,1}\delta\theta\,dx_1+[M\delta\theta]_0^L(\text{and})$$
$$-(\delta M\sin(\theta-\bar{\theta})+M\cos(\theta-\bar{\theta})\delta\theta$$
$$+\delta W(1-\cos(\theta-\bar{\theta}))+W\sin(\theta-\bar{\theta})\delta\theta]_0^L(\text{or})$$
$$-[(\bar{M}_{11}\cos\theta-\bar{M}_{12}\sin\theta)\delta\theta]_0^L(\text{or}). \tag{27}$$

From the usual arguments of calculus of variations, the vanishing of the first variation in eqn (27) for arbitrary variations of allowable δM, ∂W and $\delta\theta$ at $x_1=0$ or L, leads simply to the boundary conditions,

$$\text{at } x_1=0 \text{ or } L:\quad \sin(\theta-\bar{\theta})=0 \text{ or } \cos(\theta-\bar{\theta})=1,$$
$$\text{i.e. } \theta=\bar{\theta} \tag{28a}$$

$$\text{and } M=\bar{M}_{11}\cos\theta-\bar{M}_{12}\sin\theta \text{ at } x_1=0 \text{ or } L \tag{28b}$$

From eqns (27) and (28a, b) it can be observed that precisely the same boundary conditions, as in eqns (28a, b) follow even if the boundary terms in eqn (26) are simplified as in the following redefined functional:

$$\pi_{HW}(u_1^*, u_2^*, h, \chi, \theta, T_{11}, T_{12}, M)$$
$$=\int_0^L \{\tfrac{1}{2}EAh^2+\tfrac{1}{2}EI\chi^2-g_a\bar{u}_2^*+$$
$$+T_{11}\langle 1+u_{1,1}^*-\cos\theta(1+h)\rangle$$
$$+T_{12}\langle u_{2,1}^*+\sin\theta(1+h)\rangle+M(\theta_{,1}-\chi)\}\,dx_1$$
$$-[T_{11}(u_1^*-\bar{u}_1^*)+T_{12}(u_2^*-\bar{u}_2^*)+M(\theta-\bar{\theta})]_0^L(\text{or})$$
$$-[\bar{T}_{11}u_1^*+\bar{T}_{12}u_2^*+\bar{M}_{11}\sin\theta+\bar{M}_{12}(\cos\theta-1)]_0^L(\text{or}). \tag{29}$$

It is of interest to note that the Jaumann stress-couple W does not appear in eqn (29), due, primarily, to the nature of the present deformation assumptions. The Euler–Lagrange equations and natural boundary-conditions from the stationarity of the functional in eqn (29) can be seen to be:

$$EAh=T_{11}\cos\theta-T_{12}\sin\theta\equiv R_{11} \tag{30a}$$
$$EI\chi=M \tag{30b}$$
$$1+u_{1,1}^*=(1+h)\cos\theta \tag{30c}$$
$$u_{2,1}^*=-(1+h)\sin\theta \tag{30d}$$
$$\theta_{,1}=\chi \tag{30e}$$
$$M_{,1}-(1+h)(T_{11}\sin\theta+T_{12}\cos\theta)$$
$$\equiv M_{,1}-(1+h)(R_{12})=0 \tag{30f}$$
$$T_{11,1}+g_1=0 \tag{30g}$$
$$T_{12,1}+g_2=0 \tag{30h}$$
$$u_1^*=\bar{u}_1^*;\ u_2^*=\bar{u}_2^*;\ \theta=\bar{\theta} \text{ at } x_1=0 \text{ or } L \tag{30i}$$
$$T_{11}=\bar{T}_{11};\ T_{12}=\bar{T}_{12};\ M=\bar{M}_{11}\cos\theta-\bar{M}_{12}\sin\theta$$
$$\text{at } x_1=0 \text{ or } L. \tag{30j}$$

Again, it is seen that R_{11} and R_{12} defined in eqns (30a) and (30f) respectively, can be identified as the Jaumann stress-resultants,

$$R_{11}=\int_{x_2} r_{11}\,dx_2;\quad R_{12}=\int_{x_2} r_{12}\,dx_1. \tag{31}$$

Equations (30a, b) are constitutive relations, (c–e) are compatibility conditions, (*f–h*) are equilibrium equations, and (*i, j*) are boundary conditions, in terms of the presently defined beam variables.

By satisfying, a priori, eqns (30a, b) one may eliminate h and χ as variables from eqn (29); and satisfying, *a priori*, eqns (30g, h) one may eliminate u_2^* as variables within the integral in eqn (29). Thus one derives a modified complementary energy functional, as:

$$\pi_c(\hat{u}_1^*, \hat{u}_2^*, \theta, T_{11}, T_{12}, M)$$
$$=\int_0^L \Big\{-\frac{1}{2EA}(T_{11}\cos\theta-T_{12}\sin\theta)^2-\frac{1}{2EI}M^2$$
$$+T_{11}(1-\cos\theta)+T_{12}\sin\theta-M_{,1}\theta\Big\}dx_1$$
$$+[T_{11}\bar{u}_1^*+T_{12}\bar{u}_2^*+M\bar{\theta}]_0^L(\text{or})$$
$$+[(T_{11}-\bar{T}_{11})\hat{u}_1^*+(T_{12}-\bar{T}_{12})\hat{u}_2^*$$
$$+\langle M\theta-\bar{M}_{11}\sin\theta-\bar{M}_{12}(\cos\theta-1)\rangle]_0^L(\text{or}). \tag{32}$$

It is noted that in the above complementary energy functional, only the variables θ, T_{11}, T_{12} and M occur in the interior of the beam, while $\hat{u}_1^*$ and $\hat{u}_2^*$ occur only at the boundaries of the beam. Thus the point-variables $\hat{u}_1^*$ and $\hat{u}_2^*$ may be viewed as point-Lagrange-multipliers to enforce the traction boundary conditions, $T_{11}=\bar{T}_{11}$ and $T_{12}=\bar{T}_{12}$, respectively, at $x_1=0$ or L.

The Euler–Lagrange equations and natural bound-

†From the definition of the Jaumann stress of Eq. (3), i.e. $r_{\alpha\beta}=t_{\alpha\gamma}x_{\gamma\beta}$, and eqn (22), it is immediately seen that M and W can be identified as "Jaumann stress-couples", defined by $M=\int_{x_2} r_{11}x_2\,dx_2$, and $W=\int_{x_2} r_{12}x_2\,dx_2$.

ary conditions corresponding to $\delta\pi_C=0$, with π_C as in eqn (32), can easily be seen to be: (i) the compatibility conditions, eqn (30c–e); (ii) the moment balance condition, eqn (30f), (iii) the displacement boundary conditions, eqn (30i); and (iv) the traction and moment boundary conditions, eqn (30j).

We now consider formulations for a piecewise linear incremental solution procedure. Thus, let C^N denote a known deformed configuration of the beam, and C^{N+1} be a further deformed state of the beam which is to be solved for. We assume that C^{N+1} is sufficiently close to C^N, such that $C^{N+1}=C^N+\Delta C$ where ΔC represents a "small" change in the variables, θ, T_{11}, T_{12} and M.

We will use a total Lagrangean (TL) formulation, the details for which are elaborated in Atluri and Murakawa [1], in the following. Using this (TL) formulation, we can write:

$$\begin{aligned}\Pi_C(C^{N+1}) &= \Pi_C[(\bar{u}_1^*)^{N+1}, (\bar{u}_2^*)^{N+1}, \theta^{N+1}, T_{11}^{N+1}, T_{12}^{N+1}, M^{N+1}]\\ &= \Pi_C[(\bar{u}_1^{*N}+\Delta\bar{u}_1^*), (\bar{u}_2^{*N}+\Delta\bar{u}_2^*), (\theta^N+\Delta\theta), (T_{11}^N+\Delta T_{11}), (T_{12}^N+\Delta T_{12}), (M^N+\Delta M)]\\ &= \Pi_C(C^N)+\Delta^1\Pi_C(C^N,\Delta C)+\Delta^2\Pi_C[C^N,(\Delta C)^2].\end{aligned} \tag{33}$$

Further, in the present complementary energy formulation, the incremental constitutive relations ~~eqns~~ (30a, b), ~~and the incremental linear momentum~~ balance conditions, eqns (30g, h) are assumed to be satisfied *a priori*, i.e.

$$EA\Delta h\equiv\Delta R_{11}=(\Delta T_{11}\cos\theta-\Delta T_{12}\sin\theta)-(T_{11}\sin\theta+T_{12}\cos\theta)\Delta\theta \tag{34}$$

$$EI\Delta\chi=\Delta M \tag{35}$$

$$\Delta T_{11,1}+\Delta g_1=0 \tag{36}$$

$$\text{and}\quad \Delta T_{12,1}+\Delta g_2=0. \tag{37}$$

Expanding $\Pi_C(C_L^{N+1})$, we find, through some straightforward algebra, that:

$$\begin{aligned}\Delta^1\Pi_C=\int_0^L\Big\{&-\frac{1}{EA}\langle T_{11}^N\cos\theta^N-T_{12}^N\sin\theta^N\rangle\\ &\times\langle\Delta T_{11}\cos\theta^N-\Delta T_{12}\sin\theta^N-(T_{11}^N\sin\theta^N+T_{12}^N\cos\theta^N)\Delta\theta\rangle\\ &-\frac{1}{EI}M^N\Delta M+\Delta T_{11}(1-\cos\theta^N)+T_{11}^N\sin\theta^N\Delta\theta\\ &+\Delta T_{12}\sin\theta^N+T_{12}^N\cos\theta^N\Delta\theta-M_{,1}^N\Delta\theta-\Delta M_{,1}\theta^N\Big\}\\ &\times dx_1+[\Delta T_{11}\bar{u}_1^{*N}+\Delta T_{12}\bar{u}_2^{*N}+\Delta M\overline{\theta}^N]_0^L(\text{or})\\ &+[\Delta T_{11}\bar{u}_1^{*N}+\Delta T_{12}\bar{u}_2^{*N}+(T_{11}-\overline{T}_{11})\Delta\bar{u}_1^*\\ &+(T_{12}-\overline{T}_{12})\Delta u_2^*+\langle\Delta M\theta^N+(M-(\overline{M}_{11}\cos\theta^N-\overline{M}_{12}\sin\theta^N))\Delta\theta\rangle_0^L(\text{or}).\end{aligned} \tag{38}$$

In view of the fact that the *a priori* conditions eqns (30a, b, g and h) hold at C^N, and the incremental variables ΔT_{11} and ΔT_{12} are required to satisfy eqns (36) and (37) it is seen that $\Delta^1\Pi_C$ must be identically zero if the solution obtained, from the present complementary energy approach, at C^N satisfies the conditions, eqns (30c–f, i–k) exactly. However due to the inherent errors of the present piecewise linear procedure, this may not be so, i.e. $\Delta^1\Pi_C\neq 0$. Thus, the term $\Delta^1\Pi_C$ is retained to devise an iterative corrective procedure to keep the solution path from straying from the true path, as discussed in detail in Atluri and Murakawa [1].

The incremental functional $\Delta^2\Pi_C$ is obtained to be:

$$\begin{aligned}\Delta^2\Pi_C(&\Delta\bar{u}_1^*,\Delta\bar{u}_2^*,\Delta\theta,\Delta T_{11},\Delta T_{12},\Delta M)\\ =\int_0^L\Big\{&-\frac{1}{2EA}\langle\Delta T_{11}\cos\theta^N-\Delta T_{12}\sin\theta^N-R_{12}^N\Delta\theta\rangle^2\\ &+\frac{1}{2EA}(R_{11}^N\Delta\theta)^2+\frac{1}{EA}R_{11}^N(\Delta T_{11}\sin\theta^N+\Delta T_{12}\cos\theta^N)\Delta\theta-\frac{1}{2EI}(\Delta M)^2\\ &+(\Delta T_{11}\sin\theta^N+\Delta T_{12}\cos\theta^N)\Delta\theta+\tfrac{1}{2}R_{11}^N(\Delta\theta)^2\\ &-(\Delta M)_{,1}\Delta\theta\Big\}dx_1\\ &+|\Delta T_{11}\Delta\bar{u}_1^*+\Delta T_{12}\Delta\bar{u}_2^*+\Delta M\Delta\overline{\theta}|_0^L(\text{or})\\ &+|(\Delta T_{11}-\Delta\overline{T}_{11})\Delta\bar{u}_1^*+(\Delta T_{12}-\Delta\overline{T}_{12})\Delta\bar{u}_2^*+<\\ &+<\Delta M\Delta\theta-(\Delta\overline{M}_{11}\cos\theta^N-\Delta\overline{M}_{12}\sin\theta^N)\Delta\theta\\ &+(\overline{M}_{11}\sin\theta^N)\\ &+(\overline{M}_{12}\cos\theta^N)(\Delta\theta)^2/2|_0^L(\text{or})\end{aligned} \tag{39}$$

where

$$R_{12}^N\equiv(T_{11}^N\sin\theta^N+T_{12}^N\cos\theta^N);\qquad R_{11}^N\equiv(T_{11}^N\cos\theta^N-T_{12}^N\sin\theta^N) \tag{40}$$

~~Recognizing~~ that ΔT_{11} ~~and~~ ΔT_{12} ~~are subject to the~~ constraints, eqns (36) and (37), *a priori*, it can be shown that the condition of stationarity of the functional in eqn (39) leads to the following Euler equations and n.b.c.:

$$\Delta u_{1,1}^*=\frac{1}{EA}\cos\theta^N(\Delta T_{11}\cos\theta^N-\Delta T_{12}\sin\theta^N-R_{12}^N\Delta\theta)-\sin\theta^N\Delta\theta\left(1+\frac{R_{11}^N}{EA}\right) \tag{41}$$

$$\Delta u_{2,1}^*=-\frac{1}{EA}\sin\theta^N(\Delta T_{11}\cos\theta^N-\Delta T_{12}\sin\theta^N-R_{12}^N\Delta\theta)-\cos\theta^N\Delta\theta\left(1+\frac{R_{11}^N}{EA}\right) \tag{42}$$

$$0=-(\Delta M)_{,1}+\frac{R_{12}^N}{EA}(\Delta T_{11}\cos\theta^N-\Delta T_{12}\sin\theta^N)+\frac{R_{11}^N}{EA}(\Delta T_{11}\sin\theta^N+\Delta T_{12}\cos\theta^N)+(\Delta T_{11}\sin\theta^N+\Delta T_{12}\cos\theta^N) \tag{43}$$

$$\frac{\Delta M}{EI}=(\Delta\theta)_{,1} \tag{44}$$

$$\Delta u_\alpha^*=\Delta\bar{u}_\alpha^*\ \text{at}\ x_1=0\ \text{or}\ L \tag{45}$$

$$\Delta T_{11}=\Delta\overline{T}_{11};\ \Delta T_{12}=\Delta\overline{T}_{12};\ \text{at}\ x_1=0\ \text{or}\ L \tag{46}$$

$$\Delta M=(\Delta\overline{M}_{11}\cos\theta^N-\Delta\overline{M}_{12}\sin\theta^N)-(\overline{M}_{11}^N\sin\theta^N+\overline{M}_{12}^N\cos\theta^N)\Delta\theta\ \text{at}\ x_1=0\ \text{or}\ L. \tag{47}$$

We now consider a finite element implementation of the complementary energy method represented by the stationarity of the functional in eqn (39). We segment the beam into M elements $i=0,1\ldots M$, each with end points denoted by $x_1=x_{1(i)}$ and $x_{1(i+1)}$, with $x_{1(0)}=0$ and $x_{1(M+1)}=L$. To satisfy eqns (36) and (37), *a priori*, we assume within each element:

$$\Delta T_{11}^i = -\int_{x_1} \Delta g_1 + \Delta a_1^i (i=0, \ldots M) \tag{48}$$

$$\Delta T_{12}^i = -\int_{x_1} \Delta g_2 + \Delta a_2^i (i=0, \ldots M) \tag{49}$$

wherein Δa_1^i and Δa_2^i are undetermined parameters which are taken, for simplicity, to be independent for each element, $i=0, \ldots M$. In view of this, the traction reciprocity conditions, at the node $x_1 = x_{1(i)}$ at which the $(i-1)$th and ith elements are connected, viz. $(\Delta T_{11})^+ = (\Delta T_{11})^-$ and $(\Delta T_{12})^+ = (\Delta T_{12})^-$ (where + and − denote, respectively, the left and right hand sides of $x_{1(i)}$ in the limit that $x_{1(i)}$ is approached), are enforced through a Lagrange-multiplier technique as described in Atluri and Murakawa [1].

Further, within each element, the moment ΔM is assumed as:

$$\Delta M^i = \Delta M_{(i)}(1-\xi) + \Delta M_{(i+1)}\xi (i=0, \ldots M) \tag{50a}$$

where

$$\xi = \frac{x_1 - x_{1(i)}}{x_{1(i+1)} - x_{1(i)}} \tag{50b}$$

where $\Delta M_{(i)}$ and $\Delta M_{(i+1)}$ are, respectively, the moments at $x_{1(i)}$ and $x_{1(i+1)}$. Thus, eqn (50) inherently satisfies the moment reciprocity condition. Finally, we assume the rigid rotation within each element to be a constant, i.e.

$$\Delta\theta^i = \Delta\beta^i;\ x_{1(i)} \quad x_1 \quad x_{1(i+h)} (i=0, \ldots M) \tag{51}$$

when the interelement traction-reciprocity conditions, viz $(\Delta T_{11})^+ = (\Delta T_{11})^-$ and $(\Delta T_{12})^+ = (\Delta T_{12})^-$ at $x_1 = x_{1(i)}$ are introduced as subsidiary conditions through Lagrange-multipliers $(\Delta \tilde{u}_\alpha^*)^i$ at $x_{1(i)}$, the functional for the finite element system, which is a modification to eqn (39) as described in Atluri and Murakawa [1], can be written as:

$$\Delta^2\Pi_C = \sum_{i=0}^{M} (\Delta^2\Pi_C)^i \tag{52}$$

where $(\Delta^2\Pi_C)^i$ is defined simply by chaing the limits of integrals occurring in eqn (39) as follows:

$$\int_0^L (\,)\,dx_+ \rightarrow (\text{change to}) \rightarrow \int_{x_{1(i)}}^{x_{1(i+1)}} (\,)\,dx_1 \tag{53a}$$

$$[\ ]_0^L (\text{or}) \rightarrow (\text{change to}) \rightarrow [\ ]_{x_{1(i)}}^{x_{1(i+1)}} \text{or.} \tag{54a}$$

When the assumptions in eqn (48)–(50) and (57) are introduced, the functional in eqn (52) can be written as

$$\Delta^2\Pi_C[(\Delta\tilde{u}_\alpha^*)^i, \Delta a_\alpha^i, \Delta M^i, \Delta\beta^i] = \sum_{i=0}^{N} \frac{1}{2} \begin{Bmatrix} \Delta a^i \\ \Delta M^i \\ \Delta\tilde{u}^{*i} \\ \Delta\beta^i \end{Bmatrix} \begin{bmatrix} K_{11} & K_{12} & 0 & K_{14} \\ K_{21} & K_{22} & K_{23} & 0 \\ & K_{32} & K_{33} & 0 \\ K_{41} & 0 & 0 & 0 \end{bmatrix} \begin{Bmatrix} \Delta a^i \\ \Delta M^i \\ \Delta\tilde{u}^{*i} \\ \Delta\beta^i \end{Bmatrix} + \begin{bmatrix} Q_1 \\ Q_2 \\ Q_3 \\ Q_4 \end{bmatrix} \begin{Bmatrix} \Delta a^i \\ \Delta M^i \\ \Delta\tilde{u}^{*i} \\ \Delta\beta^i \end{Bmatrix}. \tag{55}$$

In the above, the notations, $[\Delta a^i] = [\Delta a_1^i,\ \Delta a_2^i]$, $[\Delta M^i] = [\Delta M_{(i)},\ \Delta M_{(i+1)}]$, and $[\Delta\tilde{u}^{*i}] = [\Delta\tilde{u}_{1(i)}^*, \Delta\tilde{u}_{1(i+1)}^*, \Delta\tilde{u}_{2(i)}^*, \Delta\tilde{u}_{2(i+1)}^*]$ are used. Since Δa^i and $\Delta\beta^i$ are independent for each element, they may be eliminated as variables at the element level, from the conditions of stationarity of the functional in eqn (55) w.r.t. Δa^i and $\Delta\beta^i$. When this is done, it is seen that the functional $\Delta^2\Pi_C$ can be written as:

$$\Delta^2\Pi_C = \sum_{i=0}^{M} \frac{1}{2} \begin{Bmatrix} \Delta M^i \\ \alpha\tilde{u}^{*i} \end{Bmatrix} \begin{bmatrix} K_{33} & 0 \\ 0 & 0 \end{bmatrix} \begin{bmatrix} 0 & K_{32} \\ K_{41} & 0 \end{bmatrix} \begin{bmatrix} K_{11} & K_1{}^2 \\ K_{21} & K_{12} \end{bmatrix}^{-1} \begin{bmatrix} 0 & K_{14} \\ K_{27} & 0 \end{bmatrix} \begin{Bmatrix} \Delta M^i \\ \Delta\tilde{u}^{*i} \end{Bmatrix} + \begin{bmatrix} Q_3 \\ Q_4 \end{bmatrix} \begin{Bmatrix} \Delta M^i \\ \Delta\tilde{u}^{*i} \end{Bmatrix} - \begin{bmatrix} Q_1 \\ Q_2 \end{bmatrix} \begin{bmatrix} K_{11} & K_{12} \\ K_{21} & K_{22} \end{bmatrix}^{-1} \begin{Bmatrix} \Delta M^i \\ \Delta\tilde{u}^{*i} \end{Bmatrix}. \tag{56}$$

By carrying out the element assembly, eqn (56) can be reduced to:

$$\Delta^2\Pi_C = \frac{1}{2} \begin{Bmatrix} \Delta M \\ \Delta\tilde{u}^* \end{Bmatrix} \begin{bmatrix} A \end{bmatrix} \begin{Bmatrix} \Delta M \\ \Delta\tilde{u}^* \end{Bmatrix} - \begin{bmatrix} F_1 \\ F_2 \end{bmatrix} \begin{Bmatrix} \Delta M \\ \Delta\tilde{u} \end{Bmatrix} \tag{57}$$

where $\{\Delta M\}$ represents a column vector of moments at all nodes, and $\{\Delta u^*\}$ represents a column vector of displacements (in x_1 and x_2 directions) at all nodes. Finally, setting $\Delta^2\Pi_C = 0$ w.r.t. ΔM and Δu^*, we obtain the algebraic equation:

$$[A] \begin{Bmatrix} \Delta M \\ \Delta\tilde{u}^* \end{Bmatrix} = \begin{Bmatrix} F_1 \\ F_2 \end{Bmatrix}. \tag{58}$$

Thus, in the present method, the final algebraic equations can be solved for both the nodal moment resultants as well as the nodal displacements. For this reason, in accordance with the definitions given in Atluri [12] and Atluri and Murakawa [1], the present method can be classified as a mixed method. Moreover, since the reciprocity conditions for T_{11} and T_{12} at the nodes are satisfied through Lagrange-multiplier technique, the present method is also a hybrid method [1]. Thus, the present method is a "mixed-hybrid" method [1].

In the following we present three illustrative examples.

Examples

(i) *Post-buckling of a column.* The details of the problem are given in Fig. 2, which shows a cantilever beam subject to a compressive axial force P at the free end. Post buckling behavior was initiated by a small axial force $q = 10^{-5} P_E$, as shown in Fig. 2. The finite element solution is obtained by using 4 elements, each with (i) a constant rotation, (ii) linear displacement

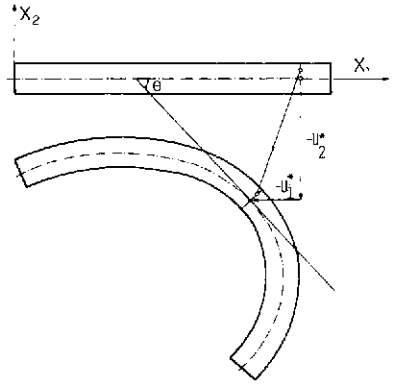

Fig. 1. Undeformed and deformed configurations of a beam.

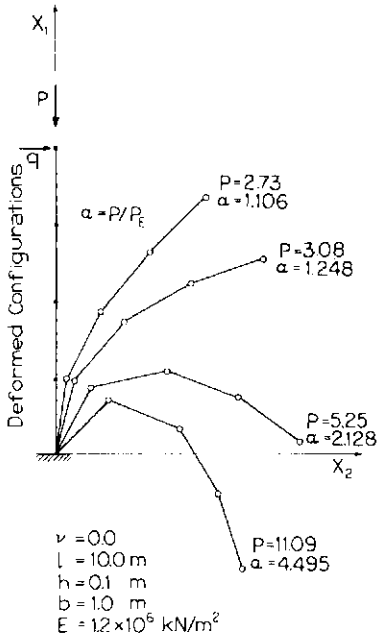

Fig. 2. Post-buckling deformation patterns of a beam column.

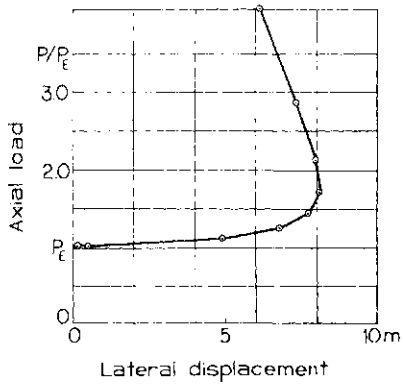

Fig. 3. Lateral displacement at the free end vs axial load in a centilever beam-column.

field of u_1^*, u_2^*, and (iii) a linear moment field. The deformed shapes of the column for axial load of αP_E, for various values of α, are shown in Fig. 2.

The transverse displacement of the free end of the centilever beam-column is shown in Fig. 3 as a function of the axial load αP_E. It has been verified that the solid line shown in Fig. 3 matches exactly the analytical solution given by Timoshenko and Gere [13]. It is noted that a finite element solution for this problem was also presented by Horrigome [14]. In [14] the beam-column was modeled as a 2-dimensional plate-strip. The solution [14], which is based on an incremental potential energy formulation, was obtained by using 14 triangular elements and was also noted [14] to correlate well with that of [13].

(ii) *Elastica:* The problem, depicted in Fig. 4, is that of a simply supported beam with an axially movable hinge, and subject to concentrated moments at the ends. The problem was analyzed by using 4 elements each with the previously mentioned field assumptions. The deformed shapes of the beam for various values of applied M are shown in Fig. 4. The

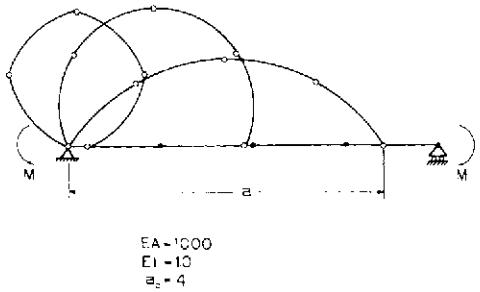

Fig. 4. Deformation patterns of a simply supported beam with a movable hinge, and subject to pure bending.

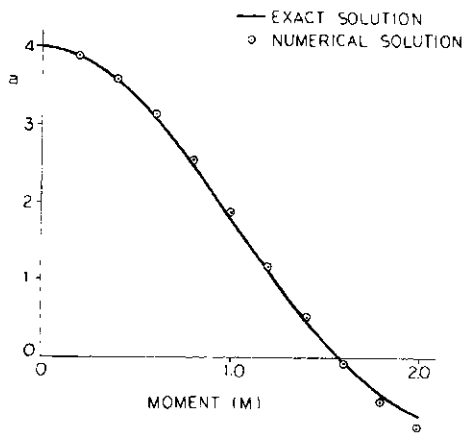

Fig. 5. Axial shortening vs applied moment of a simply supported beam subject to pure bending.

variation of "a" (the projection of the deformed axis of the beam on the axis of the undeformed beam as in Fig. 4) with M is shown in Fig. 5. This variation is seen to correlate excellently with the analytical solution [13].

(iii) *Transversely loaded simply-supported beam:* The problem, depicted in Fig. 6, is that of a transversely loaded simply-supported beam with axially-imovable hinges. The predominant nonlineality in the problem is due to the mid-plane stretching of the beam. The problem was analysed by using 4 elements in a half of the beam. The analytical solution for a rectangular plate-strip was given by Timoshenko and Woinowsky-Krieger [15]. The solution in [15] would thus have a Piosson-ratio effect, whereas the present beam solution does not have a similar effect. The solution of [15] was numerically evaluated in [14] for $\nu = 0.3$ and is reproduced here. It is seen from Fig. 6 that there is an excellent correlation between the present results and those of [15]. It is noted that numerical solution for the problem of a simply supported rectangular plate-strip, based on an incremental potential energy formulation, and using 15 elements (10 triangular and 5 rectangular) in a half of the plate, was also given in Horrigmoe [14].

The comparison of the present results with those of Horrigmore [14] for identical problems appears to indicate the relative merits of the presently proposed complementary energy method, in terms of accuracy as well as computational economy.

CLOSURE

A new complementary energy method for the stress and stability analyses of structures, which undergo

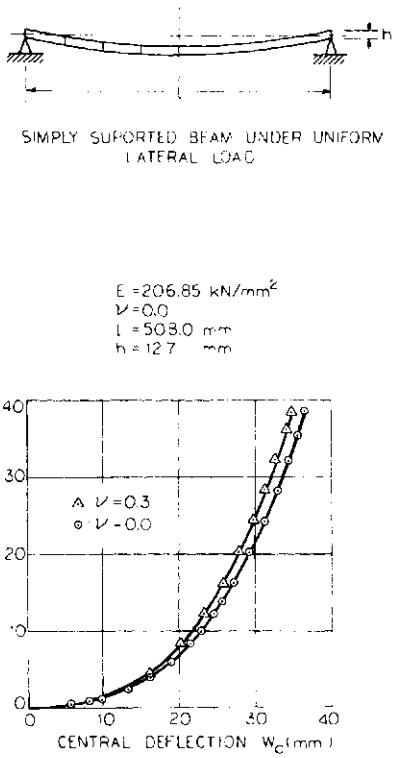

Fig. 6. Problem of a transversely loaded simply supported beam with immovable hinges.

large rotations but moderate stretches, has been indicated. The relative merits of the present procedure have been illustrated in some representative problems of beams. Further work along the present lines is underway and will be reported elsewhere.

Acknowledgements—The authors gratefully acknowledge the support for this work provided by U.S.A.F.O.S.R. under contract No. F49620-78-C-0085 with Dr. Don Ulrich as program director. Thanks are also expressed to Ms. M. Eiteman for her care in typing this manuscript.

REFERENCES

1. S. N. Atluri and H. Murakawa, On hybrid finite element models in nonlinear solid mechanics. In *Finite Elements in Nonlinear Mechanics* (Edited by P. G. Bergan *et al.*), Vol. 1. pp. 3–41. Tapir Press, Trondheim, Norway (1977).
2. B. Fraeijs de Veubeke, A new variational principle for finite elastic displacements. *Int. J. Engng Sci* **10**, 745–763 (1972).
3. R. W. Ogden, Inequalities associated with the inversion of elastic stress-deformation relations and their implications. *Math. Proc. Cambridge Phil. Soc.* Vol. 81, 1977, pp. 313–324.
4. H. Murakawa and S. N. Atluri, Finite elasticity solutions using hybrid finite elements based on a complimentary energy principle. *J. Appl. Mech., Trans. ASME*, **45**, 539–548 (1978).
5. H. Murakawa and S. N. Atluri, Finite elasticity solutions using hybrid finite elements based on a complementary energy principle—II. Incompressible materials. *J. Appl. Mech.* **46**, 71–78 (1979).
6. S. N. Atluri, On rate principles for finite strain analysis of elastic and inelastic nonlinear solids. In *Recent Research on Mechanical Behavior of Solids*, pp. 79–107. (Professor H. Miyamoto's Anniversary volume). University of Tokyo Press, Tokyo, Japan (1979).
7. S. N. Atluri, On some new general and complementary energy theorems for the rate problems of finite strain, classical elasto-plasticity. *J. Struct. Mech.* **8**(1) (1980) (In press), 54 pages.
8. S. N. Atluri, Rate complementary energy principles, finite strain plasticity problems; and finite elements. In *Proc. IUTAM Symp. on Variational Methods*, Northwestern Univ., Sept. 1978 (Edited by S. Nemat-Nasser and K. Washizu). Pergamon Press, Oxford (00–00).
9. H. Murakawa and S. N. Atluri, Finite element solutions of finite strain elastic plastic problems, based on a new complementary rate principle. In *Advances in Computer Methods for Partial Differential Equations* (Edited by R. Vishnevetsky and B. Stepleman), pp. 53–61. IMAS, Rutgers University Press (1979).
10. E. F. Masur and C. H. Popelar, On the use of the complementary energy in the solution of buckling problems. *Int. J. Solids Structures* **12**, 203 216 (1976).
11. W. T. Koiter, Complementary energy, neutral equilibrium and buckling. *Proc. Kon. Ned. Akad., Wetensch.*, Series B, 1977, pp. 183–200.
12. S. N. Atluri, On hybrid finite element models in solid mechanics. In *Advances in Computer Methods for Partial Differential Equations* (Edited by Vishnevetsky), pp. 346–356. AICA, Rutgers University Press (1975).
13. S. P. Timoshenko and J. M. Gere, *Theory of Elastic Stability*, pp. 76 82. McGraw-Hill, New York (1961).
14. G. Horrigmoe, Finite element instability analysis of free-form shells. *Rep.* 77-2, Institut For Statikk, University of Trondheim, 1977.
15. S. P. Timoshenko and S. Woinowsky-Krieger, *Theory of Plates and Shells*. McGraw-Hill, New York (1959).

Computers & Structures, Vol. 13, pp. 19–27, 1981
Printed in Great Britain.

0045-7949/81/010019-09$02.00/0

A LARGE DEFORMATION FORMULATION FOR SHELL ANALYSIS BY THE FINITE ELEMENT METHOD

WORSAK KANOK-NUKULCHAI†
Division of Structural Engineering and Construction, Asian Institute of Technology, Bangkok, Thailand

ROBERT L. TAYLOR‡
Division of Structural Engineering and Structural Mechanics, Department of Civil Engineering, University of California, Berkeley, CA 94721, U.S.A.

and

THOMAS J. R. HUGHES §
Division of Engineering and Applied Science, California Institute of Technology, Pasadena, CA 91109, U.S.A.

(*Received* 18 *April* 1980)

Abstract A total Lagrangian formulation for large deformation analysis of shells by the finite element method is presented. The development of the model is based upon the three dimensional field equations. To permit solution of shell problems without numerical difficulties, a special discretization in the thickness direction is employed. The displacement field of the shell element is represented by the displacement on the shell midsurface together with the relative displacement on the shell top surface, without resorting to the more complicating finite rotation parameters. Consistent linearization of the discretized balance equations is used to establish a Newton–Raphson solution scheme. The versatility and accuracy of the present shell element are demonstrated by solving several numerical examples.

INTRODUCTION

In recent years, a number of finite elements have been developed for shell analysis. Their applications span over a wide range of shell geometric forms, thicknesses and severities of shell deformation. Shortcomings inherent in many shell elements include the following: (a) the element application is limited, usually within the scope of an underlying shell theory; it could also be restricted by a number of numerical instabilities intrinsic to certain shell situations, (b) the element formulation is highly complicated, particularly in nonlinear analysis and, (c) the computational cost of element characteristics is too high for practical use.

The purpose of this paper is to develop a shell finite element for large-deformation applications which is free of the above shortcomings. Computational cost is usually a prime concern in nonlinear analysis. Frequent reformations of element tangent stiffness and generalized force often lead to an exorbitant computational expenditure. Besides, the uncertainty of many nonlinear characteristics often limits the confidence level of a nonlinear solution to a point that any accuracy improvement made by using a highly accurate element becomes merely an extravagence. Under such circumstances, an economic consideration usually entails the use of simple and efficient elements. For this reason, we focus our attention on a shell element which is simple, versatile and yet competitively accurate.

Special features characterizing this element can be highlighted as follows: (1) Bilinear functions are selected for the element geometry so that the element can serve as a convenient basis for unlimited forms of shell surfaces. (2) Relative displacement degrees-of-freedom are introduced to replace the cumbersome finite rotations. Special shape functions are devised to accommodate these degrees-of-freedom with no sacrifice of the element isoparametric property. (3) The formulation of the shell element, being a special case of continuum, employs rigorous three-dimensional field equations. The computation utilizes the reduced integration technique [1–3] which extends the element application to thin shells.

STRATEGIES OF SHELL ELEMENT DERIVATION

Shell finite elements are often derived from governing equations based on a classical shell theory; these are referred to as classical shell elements. Alternatively, one can obtain shell elements by modifying a continuum element to comply with shell assumptions without resorting to a shell theory. These are known as degenerate shell elements [2–6]. Both derivation concepts involve, at one stage or another, the process of reducing a shell-like continuum into a consistent surface patch of shell elements (Fig. 1). This process utilizes two classes of approximation: one results from the finite-element discretization and the other from enforcing certain shell approximations.

Formulation of a classical shell element is often complicated by the inherent complexities of the underlying shell theory and the global shell geometry. This prompts the shift from complex and restrictive classical shell elements towards the simpler and more versatile degenerate shell elements [2–5, 7].

The degeneration concept employs the two classes of approximation in the reverse order. A finite element discretization is performed first on the shell-like continuum before shell approximations are imposed. As a result, three-dimensional field equations are reduced to depend only on the element mid-surface coordinates.

†Assistant Professor of Structural Engineering.
‡Professor of Civil Engineering.
§Associate Professor of Structural Mechanics.

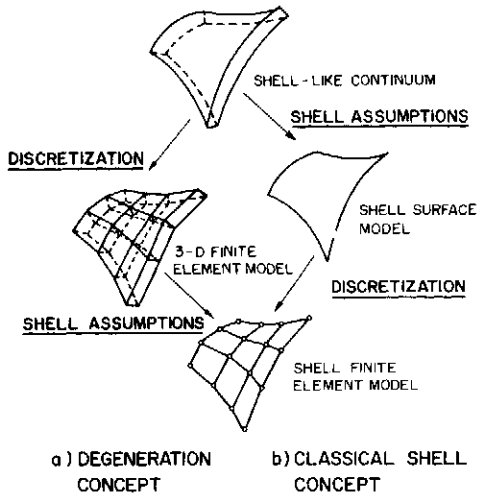

Fig. 1. Strategies for shell element derivation.

Since shell approximations are enforced in individual shell elements in total disregard of the global form of shell geometry, the shell element is unrestricted to any specific shell surface.

In the shell element to be presented, the following thick shell approximations are made: (1) a plane-stress state is assumed for each shell lamina and (2) straight normals to the undeformed shell midsurface remain straight throughout the deformation. The first assumption avoids the ill-conditioning that could result from displacement dependency across a shell normal. The second assumption allows the displacement profile along a shell normal to be completely described by two parameters: the midsurface displacement and one outer-face displacement relative to the midsurface are employed here.

The usual rotational degree-of-freedom is abandoned because of its inconvenience when its magnitude is finite. Since finite rotation can not be represented by a vector, its coordinate transformation often requires a complex and unorthodox treatment. The element formulation ends up with highly complicated expressions involving products of trigonometric functions [8]. In the proposed shell element, the field variables (displacement and relative displacement) are vectorial regardless of their magnitude. Consequently, the formulation of element characteristics is relatively simple and straightforward.

Another problem often encountered in thin shell applications of a degenerate shell element is the so-called shear-locking phenomenon [2, 3]. In a thin shell limit, each of the transverse shear strains is minute and its associated strain energy becomes a penalty function [9]. The first variation of this function leads to a constraint which enforces zero transverse shear strain everywhere on the shell surface and adversely affects the bending behavior.

Reduced integration techniques were introduced and employed effectively in many degenerate elements [1, 3] as a means to remedy the shear-locking problem. In this technique, the transverse shear strain energy is evaluated with a reduced quadrature: the associated shear constraint is only enforced pointwise at the integration sampling points without degrading the thin shell solution. Rational explanations for this remedy can be found in many references [10–12] and therefore are omitted here.

FORMULATION OF LARGE DEFORMATION SHELL ELEMENT

Element concepts

The present shell element shown (Fig. 2) evolves from a 3-D continuum (brick) element. Two opposite bilinear faces portray the top and the bottom surfaces of a shell whereas the mean surface between them defines shell mid-surface. The element consists of eight nodes, four reference nodes on the midsurface and four relative nodes on the top surface. Nodal variables assigned to each of the reference nodes are three components of displacement, while those assigned to each relative node are three components of the relative displacement with respect to the reference node located at the same corner.

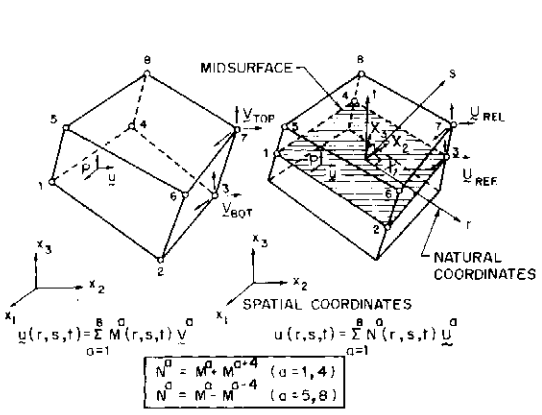

Fig. 2. Shape functions employed in the shell element evolving from a three-dimensional continuum element.

Geometry of the shell element can be described by a set of natural curvilinear coordinates $\{r, s, t\}$ such that a cube of bi-unit sides is uniquely mapped into the shell element. Displacement vector of a particle P located at (r, s, t) in a shell element can be expressed in terms of nodal variables as

$$\mathbf{u}(r, s, t) = \sum_{a=1}^{8} N^a(r, s, t)\mathbf{U}^a \tag{1}$$

where $\mathbf{U}^a$ denotes the absolute displacement vector at node "a" for $a = 1, 4$ and the relative displacement vector at node "a" for $a = 5, 8$. The shape function N^a consistent with this definition of $\mathbf{U}^a$ can be given by

$$N^a(r, s, t)\begin{cases} = \frac{1}{4}(1 + r^a r)(1 + s^a s) & \text{for } a = 1, 4 \\ = \frac{1}{4}(1 + r^a r)(1 + s^a s) & \text{for } a = 5, 8 \end{cases} \tag{2}$$

This element is isoparametric provided that relative position vector is input for each relative node; hence,

$$\mathbf{x}(r, s, t) = \sum_{a=1}^{8} N^a(r, s, t)\mathbf{x}^a \tag{3}$$

where $\mathbf{x}^a (a = 1, 4)$ is the position vector of a reference node and $\mathbf{x}^a (a = 5, 8)$ is the relative position vector of a relative node with respect to the reference node "$a-4$" (Fig. 2).

Formulation of discretized equations of motion

The motion of a body B is a one-parameter family of its configuration B_t in the Euclidean space. The spatial Cartesian coordinate system $\mathbf{x}$ serves to describe motions of particles in the space. Another set of Cartesian coordinates $\mathbf{X}$, known as the reference coordinates, describes the material framework of a configuration B_0 which is employed as a deformation reference. Motion of a particle P can be given in terms of the displacement vector $\mathbf{u}$ from its reference position in B_0, $\mathbf{X}(P)$, as

$$x_j(\mathbf{X}, t)=\delta_{jJ}X_J+d_j+u_j(\mathbf{X}, t) \tag{4}$$

where δ_{jJ} denotes the Cartesian shifter between $\mathbf{x}$ and $\mathbf{X}$ systems and $\mathbf{d}$ is the position vector of the origin of $\mathbf{X}$ (Fig. 3). Throughout this presentation, upper-case and lower-case subscripts are used to differentiate between the components associated with $\mathbf{X}$ and $\mathbf{x}$ respectively. Also, a repeated index in a term implies summation over its range.

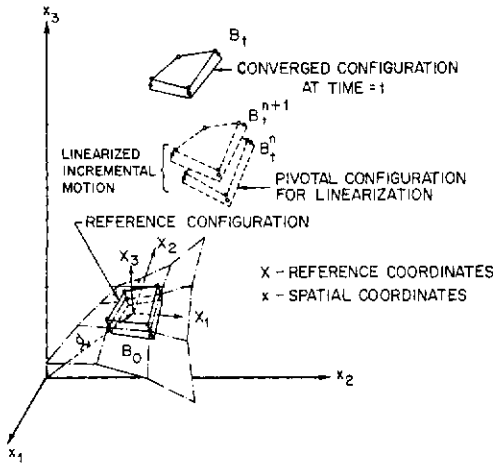

Fig. 3. Motion of a shell finite element.

Physical principles governing the motion and thermal responses of deformable bodies include conservation of mass, balance of linear and angular momenta, balance of energy and the entropy production inequality [13]. Restricting our attention to elastic bodies under isothermal deformation, the balance equation of energy becomes trivial. The balance of angular momentum is satisfied through the use of a symmetric stress tensor. On the other hand, the conservation of mass is satisfied through $\rho_t=\rho_0/J_t$ where ρ_0 and ρ_t are mass densities of the body at B_0 and B_t respectively and J_t is the determinant of the deformation gradient matrix. With a constitutive model constructed to comply with the entropy production inequality, an elastodynamic problem reduces to the determination of deformation and stress response that satisfy the balance equation of linear momentum.

The balance of linear momentum, together with constitutive equations, strain–displacement relations, and appropriate initial and boundary conditions, constitutes an initial boundary value problem. By the finite element method, a weak form of this initial boundary value problem can be used to establish a system of discretized equations of motion.

First, the local balance equation of linear momentum is expressed in the Lagrangian mode as [13]

$$(S_{IJ}F_{jJ})_{,I}+\rho_0 b_j-\rho_0\ddot{u}_j=0 \qquad \text{for } P\in B \tag{5}$$

in which $\mathbf{b}$ is the body force vector, $\mathbf{S}$ the second Piola–Kirchhoff stress tensor and $\mathbf{F}$ the deformation gradient associated with a motion from B_0 to B_t. Assuming that the motion is sufficiently smooth for differentiation, $\mathbf{F}$ is given by

$$F_{jJ}=\frac{\partial x_j}{\partial X_J}. \tag{6}$$

The traction boundary condition associated with boundary surface ∂B_0 is as follows.

$$n_I S_{IJ}F_{jJ}-\hat{T}_j^{(n)}=0 \quad \text{on } \partial B_0 \tag{7}$$

where $\mathbf{n}$ is the unit normal vector of ∂B_0 and $\hat{\mathbf{T}}^{(n)}$ is the prescribed traction acting on ∂B_0.

The Galerkin weighted residual method is applied to eqns (5) and (7) to construct a Galerkin's weak form of the problem, i.e.

$$G(\mathbf{u}, \eta)=-\int_{B_0}(S_{IJ}F_{jJ})_{,I}\eta_j\,dV-\int_{B_0}(\rho_0 b_j-\rho_0\ddot{u}_j)\eta_j\,dV+\int_{\partial B_0}(n_I S_{IJ}F_{jJ}-\hat{T}_j^{(n)}\eta_j)\,dA=0 \tag{8}$$

in which η denotes a weight field over B_0. Applying the Gauss–Green Theorem to the first integral leads to a corresponding canonical form of eqn (8). If both $\mathbf{u}$ and η are continuous over the shell domain, the Galerkin function can be written as an accumulation of individual element contributions, i.e. $G(\mathbf{u}, \eta)=\Sigma_e G^e(\mathbf{u}, \eta)$ where the canonical form of a typical G^e associated with eqn (8) is

$$G^e(\mathbf{u}, \eta)=\int_{B_0^e}S_{IJ}F_{jJ}\eta_{j,I}\,dV-\int_{B_0^e}(\rho_0 b_j-\rho_0\ddot{u}_j)\eta_j\,dV-\int_{\partial B_0^e}\hat{T}_j^{(n)}\eta_j\,dA. \tag{9}$$

In the present shell element, the displacement field is expressed in terms of nodal displacements and nodal relative displacements according to eqns (1) and (2) in compliance with the thick shell assumption. The Galerkin method also employs η which belongs to the same function space as the displacement field. In addition, η is chosen to satisfy homogeneous essential boundary conditions.

Let $\mathbf{X}$ be constructed at the element center so that X_3 is normal to the element midsurface. The unit vectors associated with $\mathbf{X}$ are given as follows.

$$\hat{\mathbf{e}}_{X_3}=\mathbf{x}_{,r}(0,0,0)\times\mathbf{x}_{,s}(0,0,0)/|\mathbf{x}_{,r}(0,0,0)\times\mathbf{x}_{,s}(0,0,0)| \tag{10a}$$

$$\hat{\mathbf{e}}_{X_2}=\hat{\mathbf{e}}_{X_3}\times\mathbf{x}_{,r}(0,0,0)/|\hat{\mathbf{e}}_{X_3}\times\mathbf{x}_{,r}(0,0,0)| \tag{10b}$$

$$\hat{\mathbf{e}}_{X_1}=\hat{\mathbf{e}}_{X_2}\times\hat{\mathbf{e}}_{X_3}. \tag{10c}$$

The displacement field and the weight field of a particle $P(\mathbf{X})$ in the shell element can be represented as

$$\mathbf{u}(\mathbf{X})=N^a(\mathbf{X})\mathbf{U}^a \qquad \mathbf{X}\in B_0^e \tag{11}$$

$$\eta(\mathbf{X})=N^a(\mathbf{X})\mathbf{H}^a \qquad \mathbf{X}\in B_0^e \tag{12}$$

where N^a is given in eqn (2) and $\mathbf{H}^a$ denotes element nodal values of η. Note that the repeated superscript index such as "a" in eqns (11) and (12) implies summation over the element nodes ($a=1, 8$). Substituting eqns (11) and (12) into eqn (9) yields

$$G^e(\mathbf{U}, \mathbf{H})=H_j^b(M_{ji}^{ba}\dot{U}_i^a+K_j^b-R_j^b) \tag{13}$$

in which the internal force vector, the mass matrix and

the generalized force vector are respectively

$$K_j^b = \int_{B_0^e} S_{IJ} F_{jJ} N_{,I}^b \, dV \tag{14}$$

$$M_{ji}^{ba} = \int_{B_0^e} N^a N^b \, dV \delta_{ij} \tag{15}$$

and

$$R_j^b = \int_{\partial B_0} {}_e\hat{T}_j^{(n)} N^n \, dA + \int_{B_0^e} \rho_0 b_j N^b \, dV. \tag{16}$$

Observe that superscript refers to a node number while subscript refers to a spatial basis. For example, K_j^a denotes the j-component of the internal force vector at node "a". Assembling all individual element contributions leads to

$$G(\mathbf{U}, \mathbf{H}) = \mathbf{H}^T[\mathbf{M}\ddot{\mathbf{U}} + \mathbf{K}(\mathbf{U}) - \mathbf{R}] = \mathbf{0} \tag{17}$$

in which $\mathbf{H}$ is a vector of nonprescribed weight parameters associated with global nodes. Since $\mathbf{H}$ can be arbitrary, eqn (17) reduces to

$$\mathbf{M}\ddot{\mathbf{U}} + \mathbf{K}(\mathbf{U}) - \mathbf{R} = \mathbf{0} \tag{18}$$

which is the system of discretized equations of motion in terms of shell generalized variables $\mathbf{U}$.

Linearization of the internal force vector

In quasi-static analysis, dropping the inertia term in eqn (18) directly gives a nonlinear algebraic system, from which $\mathbf{U}$ corresponding to a load step is computed. For dynamic problems, a time integration scheme such as the Newmark method or the Wilson θ-method can be used to establish an algebraic system of pseudostatic equilibrium equations from eqn (18). Solving these nonlinear equations by the Newton–Raphson technique requires the linearization of nonlinear term $\mathbf{K}(\mathbf{U})$ with respect to $\mathbf{U}$.

For quasi-static analysis, it is not difficult to show that a typical linearized equilibrium system associated with eqn (18) is

$$\mathbf{DK}(\mathbf{U}_n^m)\Delta\mathbf{U}_n^m = \mathbf{R}_n - \mathbf{K}(\mathbf{U}_n^m) \tag{19}$$

where $\mathbf{DK}(\mathbf{U}_n^m)$ denotes tangent stiffness matrix about a trial displacement $\mathbf{U}_n^m$ (assumed at the mth iteration for $\mathbf{U}_n$, the solution corresponding to the nth load step). The iterative increment, $\Delta\mathbf{U}_n^m$, is computed from eqn (19) and added to $\mathbf{U}_n^m$ for a more accurate solution.

It is very convenient to evaluate $\mathbf{DK}$ from the componential form as

$$DK_{ji}^{ba}(\mathbf{U}_n^m) = \frac{\partial K_j^b}{\partial U_i^a}\bigg|_{\mathbf{U}=\mathbf{U}_n^m} \tag{20}$$

An expression for the shell element tangent stiffness is obtained by substituting eqn (14) into eqn (20) as

$$DK_{ji}^{ba}(\mathbf{U}_n^m) = \int_{B_0^e} \left[\frac{\partial S_{IJ}}{\partial U_i^a} F_{jJ} N_{,I}^b + S_{IJ} \frac{\partial F_{jJ}}{\partial U_i^a} N_{,I}^b \right] dV \bigg|_{\mathbf{U}=\mathbf{U}_n^m}. \tag{21}$$

In view of eqns (3), (4) and (6), the deformation gradient $\mathbf{F}$ can be evaluated from

$$F_{jJ} = \delta_{jJ} + N_{,J}^a U_j^a. \tag{22}$$

Using the chain rule $\partial S_{IJ}/\partial U_i^a = (\partial S_{IJ}/\partial E_{KL})(\partial E_{KL}/\partial U_i^a)$ in eqn (21), the Green strain definition $E_{IJ} = \frac{1}{2}(F_{kI}F_{kJ} - \delta_{IJ})$ and eqn (22), we can obtain $\mathbf{DK}$ for the shell element as

$$DK_{ji}^{ba}(\mathbf{U}_n^m) = \left\{ \int_{B_0^e} \left[F_{jJ}(\mathbf{U}) N_{,I}^b \right] \left[\frac{\partial S_{IJ}}{\partial E_{KL}}(\mathbf{U}) \right] \left[F_{iL}(\mathbf{U}) N_{,K}^a \right] \times dV + \int_{B_0^e} \delta_{ij} N_{,I}^a S_{IJ}(\mathbf{U}) N_{,J}^b \, dV \right\}_{\mathbf{U}=\mathbf{U}_n^m}. \tag{23}$$

The first term on the r.h.s. of eqn (23) constitutes an elastic tangent stiffness with the effect of finite motion included, and the other term represents the effect of initial stresses.

Constitutive model

So far, the formulation is valid for any material constitution in which $\mathbf{S}$ is a function of $\mathbf{F}$. To avoid distractions from using too complicated constitutive models, our scope will be further limited to the class of hyperelastic solids. In this case, main attention can be focused on the performance of the shell element. The constitutive model for hyperelastic solids takes the form [13]

$$S_{IJ} = \rho_0 \frac{\partial \hat{\Psi}(\mathbf{E})}{\partial E_{IJ}} \tag{24}$$

in which $\hat{\Psi}$ is the Helmholz free energy function. To provide a simple presentation of constitutive equations, a fourth-order elasticity tensor is introduced such that

$$C_{IJKL} = \frac{1}{2}\frac{\partial S_{IJ}}{\partial E_{KL}} = \frac{1}{2}\rho_0 \frac{\partial^2 \hat{\Psi}}{\partial E_{IJ}\partial E_{KL}} \tag{25}$$

from which one can show that $C_{IJKL} = C_{KLIJ} = C_{JIKL} = C_{IJLK}$.

In practice, constitutive relation can be obtained by assuming $\hat{\Psi}$ as a convenient function of $\mathbf{E}$. From eqn (25), if $\hat{\Psi}$ is taken as a quadratic function of $\mathbf{E}$, all C_{IJKL}'s are constant parameters. This class of material constitution corresponds to the first-order theory of elasticity [13]. For isotropic, linear elastic materials, the elasticity tensor can be described by two Lame's constants, λ and μ, as

$$2C_{KLMN} = \lambda\delta_{KL}\delta_{MN} + \mu(\delta_{KM}\delta_{LN} + \delta_{KN}\delta_{LM}). \tag{26}$$

In the present shell element formulation, the elasticity tensor must be modified to include the effect of the plane-stress assumption. With an orientation of $\mathbf{X}$ following eqns (10a), (10b) and (10c), the generalized plane-stress tensor $\bar{\mathbf{C}}$ with respect to $\mathbf{X}$ at the element center can be obtained as

$$\bar{C}_{KLMN} = C_{KLMN} - C_{KL33}C_{33MN}/C_{3333}. \tag{27}$$

In addition, $\bar{\mathbf{C}}$ at any point on the element midsurface is approximated by $\bar{\mathbf{C}}$ at the element center. This does not affect convergence because each individual element approaches a point as the shell element model is refined; thus, $\bar{\mathbf{C}}(\mathbf{X}) \to \bar{\mathbf{C}}(\mathbf{0})$ at the center of each element.

Computational implementation

A reduced numerical integration will be used to evaluate the transverse shear effect in both $\mathbf{K}$ and $\mathbf{DK}$. To allow the selective integration scheme, $\mathbf{K}$ and $\mathbf{DK}$ must be partitioned into two parts: the transverse shear effect and the rest. Rewrite $\mathbf{K}$ given by eqn (14) in a matrix form as

$$\mathbf{K}^b = \int_{B_0^e} \mathbf{F}\mathbf{S}\nabla\mathbf{N}^b \, dV \tag{28}$$

where $\nabla \mathbf{N}^b = \langle N^b_{,1} N^b_{,2} N^b_{,3} \rangle^T$. If the matrix of the second Piola–Kirchhoff stress tensor $\mathbf{S}$ is decomposed into two submatrices as

$$\mathbf{S} = \mathbf{S}_m + \mathbf{S}_s = \begin{bmatrix} S_{11} & S_{12} & 0 \\ S_{21} & S_{22} & 0 \\ 0 & 0 & S_{33} \end{bmatrix} + \begin{bmatrix} 0 & 0 & S_{13} \\ 0 & 0 & S_{23} \\ S_{31} & S_{32} & 0 \end{bmatrix} \quad (29)$$

The internal force vector can be split into two parts, $\mathbf{K}^b = \mathbf{K}^b_m + \mathbf{K}^b_s$, in which the membrane-bending effect is given by

$$\mathbf{K}^b_m = \int_{B^e_0} \mathbf{F}\mathbf{S}_m \nabla \mathbf{N}^b \, dV \quad (30)$$

and the transverse shear effect by

$$\mathbf{K}^b_s = \int_{B^e_0} \mathbf{F}\mathbf{S}_s \nabla \mathbf{N}^b \, dV. \quad (31)$$

Similar partitioning will be applied to the tangent stiffness matrix. By restricting the present scope to the class of isotropic hyperelastic material, the term $\partial S_{IJ}/\partial E_{KL}$ in eqn (23) is replaced by $\bar{C}_{IJKL}$ in view of eqns (25)–(27). Since no coupling terms in $\bar{\mathbf{C}}$ between the shear and the in-plane strains exist, the partition of $\mathbf{DK}$ into the two effects is straightforward. Rewrite $\mathbf{DK}$ of eqn (23) in a matrix form as

$$\mathbf{DK}^{ba} = \int (\mathbf{B}^b)^T \mathbf{D} \mathbf{B}^a \, dV + \int_{B^e_0} (\nabla \mathbf{N}^b)^T \mathbf{S} \nabla \mathbf{N}^a \, dV \cdot \mathbf{I} \quad (32)$$

in which $\mathbf{I}$ is the identity matrix, $\mathbf{B}^a$ relates the vector of Green strains $E = \{E_{11} E_{22} E_{33} 2E_{12} 2E_{23} 2E_{31}\}^T$ to the nodal parameters $\mathbf{U}^a$ and $\mathbf{D}$ is a matrix deduced from the generalized plane-stress tensor to give $\partial \mathbf{S}/\partial \mathbf{E} = \mathbf{D}$ when $\mathbf{S} = \{S_{11} S_{22} S_{33} S_{12} S_{23} S_{31}\}^T$. The matrices $\mathbf{B}$ and $\mathbf{D}$ can be partitioned as

$$\mathbf{B}^a = \begin{bmatrix} \mathbf{B}^a_m \\ \mathbf{B}^a_s \end{bmatrix} = \begin{bmatrix} F_{11}N^a_{,1} & F_{21}N^a_{,1} & F_{31}N^a_{,1} \\ F_{12}N^a_{,2} & F_{22}N^a_{,2} & F_{32}N^a_{,2} \\ F_{13}N^a_{,3} & F_{23}N^a_{,3} & F_{33}N^a_{,3} \\ F_{11}N^a_{,2}+F_{12}N^a_{,1} & F_{21}N^a_{,2}+F_{22}N^a_{,1} & F_{31}N^a_{,2}+F_{32}N^a_{,1} \\ F_{13}N^a_{,2}+F_{12}N^a_{,3} & F_{23}N^a_{,2}+F_{22}N^a_{,3} & F_{33}N^a_{,2}+F_{32}N^a_{,3} \\ F_{13}N^a_{,1}+F_{11}N^a_{,3} & F_{23}N^a_{,1}+F_{21}N^a_{,3} & F_{33}N^a_{,1}+F_{31}N^a_{,3} \end{bmatrix} \quad (33)$$

and

$$\mathbf{D} = \begin{bmatrix} \mathbf{D}_m & \mathbf{0} \\ \mathbf{0} & \mathbf{D}_s \end{bmatrix} = \begin{bmatrix} \bar{\lambda}+2\mu & \bar{\lambda} & 0 & 0 & 0 & 0 \\ \bar{\lambda} & \bar{\lambda}+2\mu & 0 & 0 & 0 & 0 \\ 0 & 0 & \varepsilon & 0 & 0 & 0 \\ 0 & 0 & 0 & \mu & 0 & 0 \\ 0 & 0 & 0 & 0 & \mu & 0 \\ 0 & 0 & 0 & 0 & 0 & \mu \end{bmatrix} \quad (34)$$

with respect to the system $\mathbf{X}$. The reduced Lame's constant $\bar{\lambda} = 2\lambda\mu/(\lambda+2\mu)$ and ε is a fictitious coefficient employed for numerical stability to be discussed in the Appendix.

In view of eqns (33) and (34), we can show that

$$\mathbf{DK}^{ab} = \mathbf{DK}^{ab}_m + \mathbf{DK}^{ab}_s \quad (35)$$

where the membrane-bending effect is given by

$$\mathbf{DK}^{ab}_m = \int_{B^e_0} (\mathbf{B}^a_m)^T \mathbf{D}_m \mathbf{B}^b_m \, dV + \int_{B^e_0} (\nabla \mathbf{N}^a)^T \mathbf{S}_m \nabla \mathbf{N}^b \, dV \cdot \mathbf{I} \quad (36)$$

and the transverse shear effect by

$$\mathbf{DK}^{ab}_s = \int_{B^e_0} (\mathbf{B}^a_s)^T \mathbf{D}_s \mathbf{B}^b_s \, dV + \int_{B^e_0} (\nabla \mathbf{N}^a)^T \mathbf{S}_s \nabla \mathbf{N}^b \, dV \cdot \mathbf{I}. \quad (37)$$

The $2 \times 2 \times 2$ Gaussian quadrature is used to evaluate $\mathbf{K}_m$ and $\mathbf{DK}_m$, while the one-point Gaussian quadrature is used to evaluate $\mathbf{K}_s$ and $\mathbf{DK}_s$.

Choice of B_0

Figure 3 shows a configuration B_t at time t and also a reference configuration denoted by B_0. During the $(n+1)$st Newton–Raphson iteration, the configuration B^{n+1}_t is obtained by solving the linearized equilibrium system based upon the last known configuration B^n_t.

Distinction should be made between a configuration about which linearization is performed (B^n_t) and a configuration that is employed for deformation reference (B_0). The total Lagrangian formulation takes the undeformed configuration as B_0, while the updated Lagrangian formulation employs B^n_t as reference. In the general case, there is no obvious, clear-cut advantage for choosing one formulation over the other. Many factors need to be considered including the nature of the problem, computational efficiency, and program implementation effort.

For shell structures, for which the constitutive model is transversely isotropic, the total Lagrangian formulation is found to be superior. The elementary elasticity tensor $\mathbf{D}$ with respect to $\mathbf{X}$ (eqn (34)) can be used in the

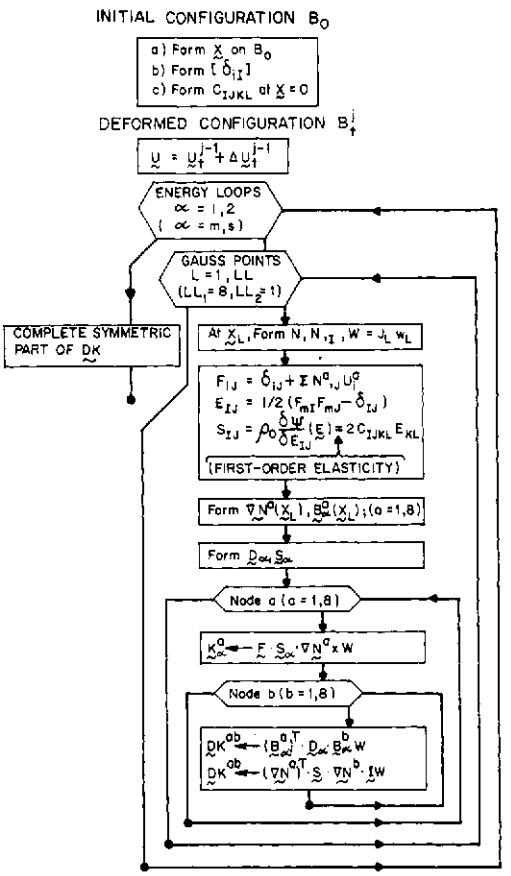

Fig. 4. Flow diagram showing the computation of $\mathbf{K}$ and $\mathbf{DK}$.

computation of **DK** at any state of the motion without a need to be updated or transformed; hence, computational effort is kept at a minimum. In addition, the reference frame **X** can be constructed locally to accommodate a convenient energy splitting in the evaluation of **K** and **DK**. For the above reasons, the total Lagrangian formulation is chosen in this study. The flow chart showing steps to evaluate **DK** and **K** of the proposed nonlinear shell element is given in Fig. 4.

NUMERICAL EXAMPLES

Numerical examples are solved to test the performance of the shell element in nonlinear applications. The first-order, linear elasticity tensor of eqn (26) is used in these examples to allow relevant solution comparisons. All nonlinear solutions employ the Newton–Raphson iteration technique within each load increment. The Euclidean norm of incremental displacements less than 10^{-4} times the current displacement norm is used as the condition for convergence. The respective number of iterations required to meet this criterion is stated in each problem.

All problems were solved with the FEAP macro programming language [14]. The calculations were performed on the University of California CDC 6400 computer.

A stiff bar undergoing finite rotations

The shell element is used to model a very stiff bar (Fig. 5) which is hinged at one end and attached to soft springs at the other end to allow large rotations. Load-deflection curves are plotted in Fig. 5 to compare with the one-dimensional nonlinear truss solution. The comparison shows good agreement between the two solutions.

Cylindrical bending of a cantilever shell strip

Five shell elements are used to model the cantilever shell strip shown in Fig. 6. The strip is subjected to a bending moment at the tip. Since relative displacements, not rotations, are employed in this shell element model, an appropriate transformation is needed to obtain equivalent relative nodal forces from the tip bending moment with respect to the displaced position. This is done conveniently through a fictitious surface element detailed in Fig. 6.

The analytical solution for this problem is available: the deformed midsurface forms a constant curvature $= ML/EI$, where M is the applied bending moment at the tip, L is the strip length, and I is the moment of inertia about the axis of bending. The present solution is plotted in Fig. 7. A deviation of 7% is observed at the last load step when the crude mesh of 5 elements attempts to form a half circular ring. A plot of the deformed configurations is also given in Fig. 8.

The elastica

A clamped beam-column in Fig. 9 is subjected to vertical load at the top. The beam-column is tilted initially with a slope of 1:1000 to initiate non-neutral stability solution after the bifurcation point (buckling).

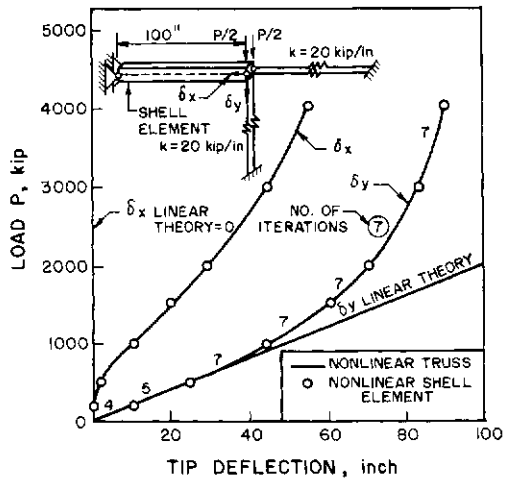

Fig. 5. Finite rotation of a stiff bar modelled by shell element; load-deflection curves. The bar has $A = 100$ in^2, $E = 10^7$ psi and $\nu = 0$.

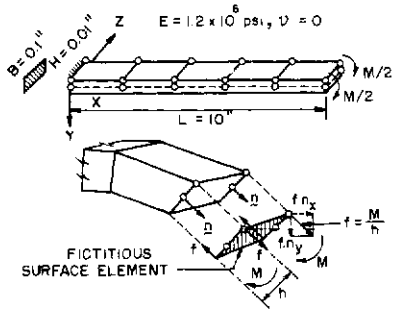

Fig. 6. Finite-element mesh of a cantilever shell strip and a fictitious surface element to transform bending moment to relative nodal forces on the deformed configuration.

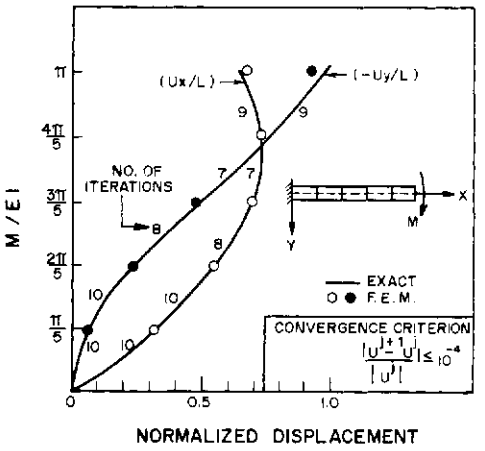

Fig. 7. Load-displacement curves of a 5-element model cantilever strip.

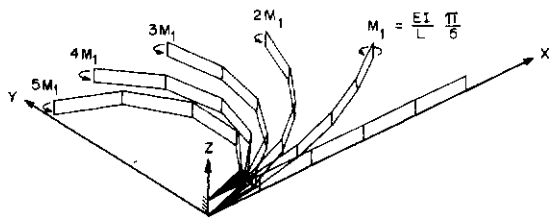

Fig. 8. Deformed configurations of the cantilever strip subjected to pure bending.

Ten shell elements are employed for the beam-column of a unit width. The tip displacements plotted in Fig. 9 show excellent agreement with the analytical solution [15].

Square clamped plate subjected to a uniform pressure

Figure 10 shows a sixteen shell element model of square clamped plate quadrant. Finite deflection of the plate center is plotted vs the magnitude of uniform pressure for comparison with other solutions. The present solution shows better agreement with the analytical solution [16] than the solution of 16 cubic plate elements, reported by Kawai *et al.* [17]. The values of the extreme fiber stresses are also plotted in Fig. 11.

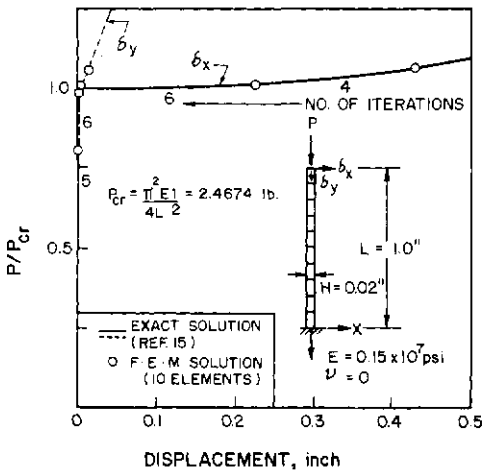

Fig. 9. Elastica problem: load-deflection curves.

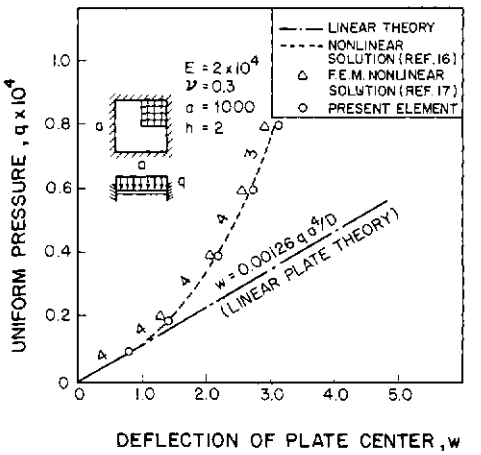

Fig. 10. Square clamped plate subjected to a uniform pressure. Comparison of solutions for plate deflection at the center.

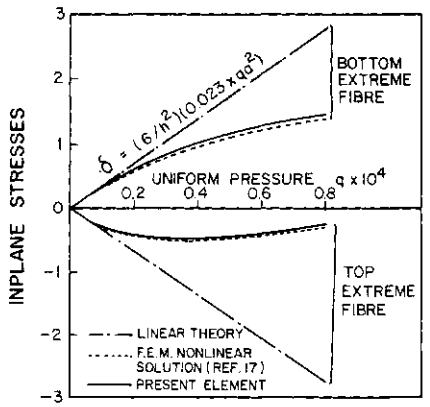

Fig. 11. Top and bottom fiber stresses at the plate center; values extrapolated from stresses at Gauss points.

A shallow, clamped cylindrical panel subjected to normal pressures

In this problem, 16 shell elements are employed for a quadrant of a shallow cylindrical shell shown in Fig. 12. Four iterations are needed in each load step to pass the convergence criterion. In the same figure, the present solution is compared with those due to Gallagher [18], Brebbia *et al.* [19], and Dhatt [20]. The compar-

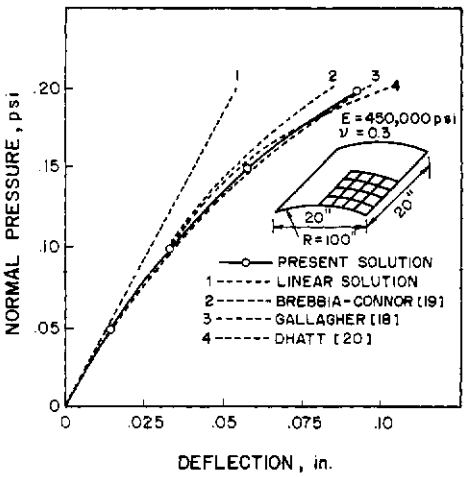

Fig. 12. Clamped cylindrical shell problem. Comparison of solutions for vertical deflection at the shell center.

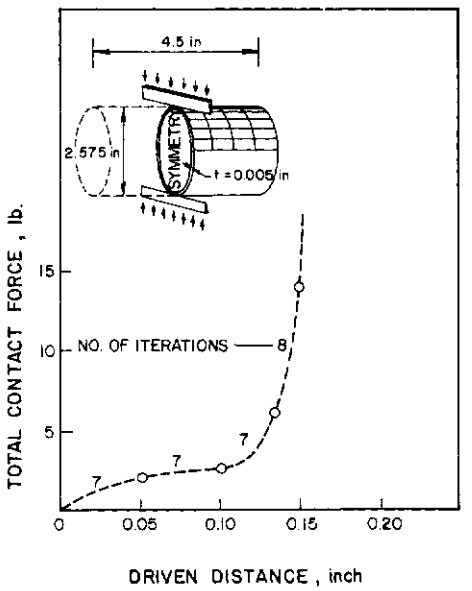

Fig. 13. An aluminum can squeezed at the midsection between two rigid edges. Total contact force versus driven distance.

ison shows good agreement between the present solution and Gallagher's solution.

An aluminum can squeezed at the midsection between two rigid edges

The last example is an aluminum can being squeezed between two rigid, straight edges as shown in Fig. 13. Young's modulus of aluminum is taken as 10^6 and Poisson's ratio as 1/3.

For simplicity, clamped ends are assumed at both ends of the cylindrical shell. A quadrant of the can is modelled with 24 shell finite elements. Four Hertzian contact elements developed by Hughes *et al.* [21] are employed around the contact periphery of the can midsection. The driven distance of a rigid edge is prescribed at a uniform increment of 0.05 in. The value of total contact force is plotted vs the driven distance in Fig. 13. A plot of the deformed configurations is also presented in Fig. 14 along with contact pressure profiles.

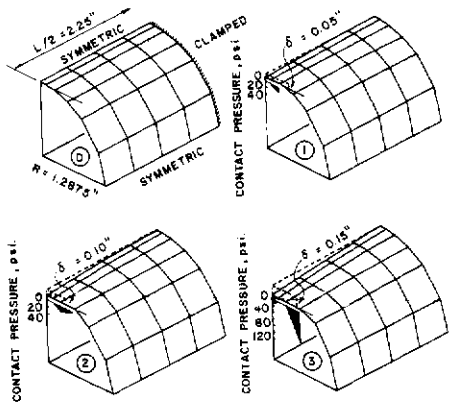

Fig. 14. Plot of deformed configurations of the finite-element aluminum can quadrant.

CONCLUSIONS

A highlight of the present finite element for general nonlinear shells is its rigorous, but surprisingly simple formulation. The key to this success is the introduction of relative displacements in place of the customary shell rotation variables. As a result, the finite element formulation can be presented within the context of nonlinear continuum mechanics. The simplicity of the formulation stems from the fact that no unorthodox treatment of finite shell rotation is encountered.

The total Lagrangian formulation is chosen in this study because of its simplicity and efficiency in establishing a degenerate shell element. All the numerical examples show excellent performance of the present shell element, despite the crude finite element meshes. Undoubtedly, this shell element, which is simple, cheap, versatile, and yet accurate, will serve as an attractive basis for large-deformation problems of general shells.

Acknowledgements—The research reported in this paper was conducted, in part, under the support of the National Highway Traffic Safety Administration of the U.S. Department of Transportation. The support of the University of California Computer Center is also acknowledged.

REFERENCES

1. O. C. Zienkiewicz, R. L. Taylor and J. M. Too, Reduced integration technique in general analysis of plates and shells. *Int. J. Numer. Meth. Engng* **3**, 275–290 (1971).
2. T. J. R. Hughes, R. L. Taylor and W. Kanoknukulchai, A simple and efficient finite element for plate bending. *Int. J. Numer. Meth. Engng* **11**, 1529–1543 (1977).
3. W. Kanok-Nukulchai, A simple and efficient finite element for general shell analysis. *Int. J. Numer. Meth. Engng* **14**, 179–200 (1979).
4. S. Ahmad, B. M. Irons and O. C. Zienkiewicz, Analysis of thick and thin shell structures by curved finite elements. *Int. J. Numer. Meth. Engng* **3**, 275–290 (1971).
5. E. L. Wilson, R. L. Taylor, W. P. Doherty and J. Ghaboussi, Incompatible displacement models. In *Numerical and Computer Methods in Structural Mechanics* (Edited by S. J. Fenves *et al.*). Academic Press, New York (1973).
6. S. W. Key and Z. E. Beisinger, The analysis of thin shells with transverse shear strains by the finite element method. *Proc. Conf. Matrix Meth. Struct. Mech.*, pp. 667–710, Wright-Patterson A.F.B., Ohio, AFFDL-TR-68-150, (1968).
7. O. C. Zienkiewicz, J. Bauer, K. Morgan and E. Onate, A simple and efficient element for axisymmetric shells. *Int. J. Numer. Meth. Engng* **11**, 1545–1558 (1977).
8. J. H. Argyris, P. C. Dunne, G. A. Malejannakis and E. Schelkle, A simple triangular facet shell element with applications to linear and non-linear equilibrium and elastic stability problems. *Comput. Meth. Appl. Mech. Engng* **10**(3), 371–403 and **11**(1), 97–131 (1977).
9. C. A. Fellipa, Error analysis of penalty function techniques for constraint definition in linear algebraic systems. *Int. J. Numer. Meth. Engng* **11**, 709–728 (1977).
10. O. C. Zienkiewicz and E. Hinton, Reduced integration, function smoothing and non-conformity in finite element analysis. *J. Franklin Inst.* **302**, 443–461 (1976).
11. T. J. R. Hughes and D. S. Malkus, On the equivalence of mixed finite element methods with reduced/selective integration displacement method. *Proc. Symp. Applic. Comput. Meth. Engng* **1**, 23–32, University of Southern California, Los Angeles (1977).
12. T. J. R. Hughes, M. Cohen and M. Haroun, Reduced and selective integration techniques in the finite element analysis of plates. *Nucl. Engng Design* **46**, 203–222 (1978).
13. A. C. Eringen, *Continuum Physics*. Vols. I and II. Academic Press, New York (1974).
14. O. C. Zienkiewicz, *The Finite Element Method*, 3rd Edn. McGraw-Hill, London (1977).
15. S. Timoshenko and J. M. Gere, *Theory of Elastic Stability*. McGraw-Hill, New York (1961).
16. S. Way, A laterally loaded clamped square plate with large deformation. *Proc. 5th Int. Cong. Appl. Mech.*, Cambridge, Mass. (1938).
17. T. Kawai and N. Yoshimura, Analysis of large deflection of plates by the finite element method. *Int. J. Number. Meth. Engng* **1**, 123–133 (1969).
18. R. H. Gallagher, The finite element method in shell stability analysis. *Comput. Structures* **3**, 543–557 (1973).
19. C. Brebbia and J. Connor, Geometrically nonlinear finite-element analysis. *Proc. ASCE, J. Engng Mech. Div.* **95**(EM2), 463–483 (1969).
20. G. S. Dhatt, Instability of thin shells by the finite element method. *Proc. Symp. Int. Assoc. Shell Struct.*, Vienna (1970).
21. T. J. R. Hughes, R. L. Taylor, J. L. Sackman, A. Curnier and W. Kanoknukulchai, A finite element method for a class of contact-impact problems. *Comput. Meth. Appl. Mech. Engng* **8**, 249–276 (1979).

APPENDIX

The fictitious coefficient ε in eqn (34) is employed to prevent the system from being ill-conditioned in certain situations. The reason can be explained as follows. Along the interelement boundaries of a bilinear element assemblage, kinks normally occur. Despite the plane-stress assumption,

the complete (three) components of relative displacement must be assigned to each relative node to accommodate coupling among non-planar elements surrounding the node. Although no stiffness for the transverse component has been accounted within the individual elements, the coupling among them serves to prevent free thickness deformation of each element. Nevertheless, whenever neighboring elements to a node are close to being co-planar, the weak coupling only generates minute stiffness to restrain the zero-energy thickness deformation mode and the system tends to be ill-conditioned. Under this situation, a fictitious thickness modulus ε is introduced to maintain the numerical condition of the system.

The value of ε must be large enough so that the relative degrees-of-freedom represent rotations; on the other hand, it must not be so large as to effectively cancel out the in-plane stiffness due to limited computer word length. There exists a range of ε however for which correct shell solutions can be obtained with little sensitivity of ε. The magnitude comparison shows that the stiffness associated with a transverse relative degree-of-freedom is $0(l^e/h^e)^2$ times the in-plane stiffness, where l^e/h^e is a characteristic length-to-thickness aspect ratio of shell element. To prevent exorbitant magnitude of this stiffness in the thin shell limit ($h^e \to 0$), a smaller ε must be used for the thinner shell. Numerical experiments are conducted on the range of the fictitious thickness modulus ε.

The result indicates that ε should be proportional to $(h^e/l^e)^2$ times the in-plane modulus. Figure A1 shows a two-

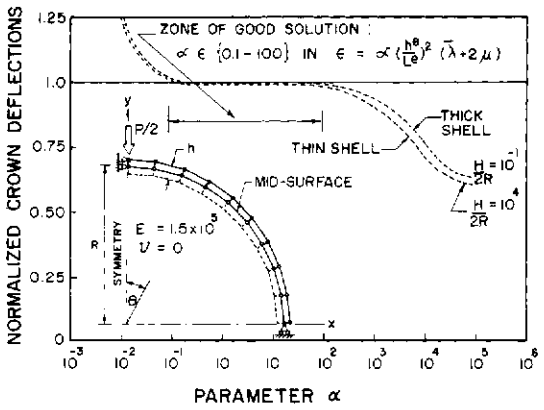

Fig. A1. A two-hinged arch finite element model (unit width) subjected to concentrated load at the crown. Vertical deflection at the crown versus fictitious thickness modulus ε.

hinged arch finite element model subjected to a point load at the crown. A small magnitude load is employed so that the solution can be relevantly compared with analytical small-displacement solution. Crown deflections are obtained with different values of ε as shown in Fig. A1. Good solutions are attainable with values of ε within 10^{-1} and 10^2 times $(h^e/l^e)^2(\bar{\lambda}+2\mu)$. In Fig. A2. solutions of the same problem using 3, 9 and 27 shell elements are plotted; all are obtained with $\varepsilon = (h^e/l^e)^2(\bar{\lambda}+2\mu)$. Solution of the 9-element model with $\varepsilon = (\bar{\lambda}+2\mu)$ is also presented for comparison; its failure in the thin shell limit is attributed to exorbitant magnitude of the corresponding transverse stiffness when $h^e \to 0$. Midsurface displacements, relative displacements and stress resultants of the 3 and 9 element meshes are very accurate as shown in Figs. A3 and A4. The solution of the 27-element mesh is accurate to the third decimal place and is in fact indistinguishable from the exact solution.

It is therefore recommended that magnitude of ε be given by

$$\varepsilon = \alpha(h^e/l^e)^2(\bar{\lambda}+2\mu) \qquad \text{(A1)}$$

in which the parameter α may vary within 10^{-1}–10^2 to ensure reliable thin shell solutions.

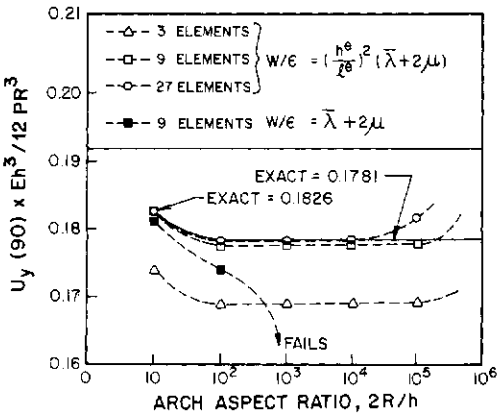

Fig. A2. Vertical deflection at the crown versus arch aspect ratio for models of 3, 9 and 27 elements.

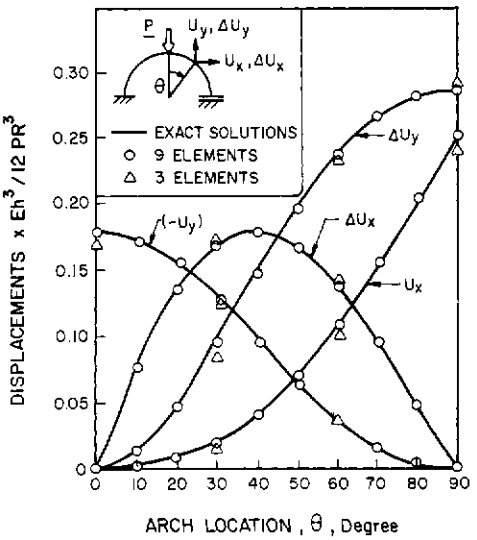

Fig. A3. Displacements and relative displacements along the arch for 3 and 9 element models. Solution obtained by 27 elements, not plotted here, are accurate to the third decimal place.

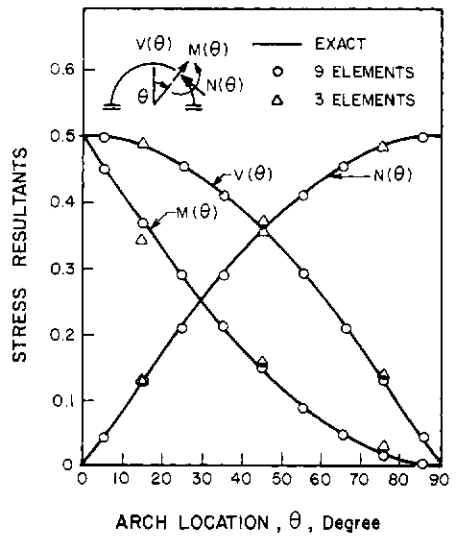

Fig. A4. Stress resultants of the arch by 3 and 9 element models.

Computers & Structures, Vol. 13, pp. 31–44, 1981
Printed in Great Britain.

0045-7949/81/010031-14/$02.00/0

RECENT ADVANCES IN REDUCTION METHODS FOR NONLINEAR PROBLEMS

AHMED K. NOOR†
George Washington University Center at NASA Langley Research Center, Hampton, VA 23665, U.S.A.

Abstract—Status and some recent developments in the application of reduction methods to nonlinear structural mechanics problems are summarized. The aspects of reduction methods discussed herein include: (a) selection of basis vectors in nonlinear static and dynamic problems (b) application of reduction methods in nonlinear static analysis of structures subjected to prescribed edge displacements, and (c) use of reduction methods in conjunction with mixed finite element models.

Numerical examples are presented to demonstrate the effectiveness of reduction methods in nonlinear problems. Also, a number of research areas which have high potential for application of reduction methods are identified.

NOMENCLATURE

E elastic modulus of the material
e error norm defined in eqns (16) and (28)
$[F]$ linear global flexibility matrix
$\{\mathscr{F}\}$ vector of internal nodal forces defined in eqn (38)
$\{f_H(H,X,\lambda)\}$, $\{f_X(H,X,\lambda)\}$ and $\{\tilde{f}(\phi,\lambda)\}$ vectors defined in eqns (30) and (33)
$\{f(X,\lambda)\}$ and $\{\tilde{f}(\psi,\lambda)\}$ vectors defined in eqns (1) and (4), respectively
$\{G_1(X)\}, \{G_2(X)\}$ partitions of $\{G(X)\}$ defined in eqns (19) and (45)
$\{G(X)\}$ and $\{\mathscr{G}(X)\}$ vectors of nonlinear terms defined in eqns (1) and (30), respectively
$\{\tilde{G}(\psi)\}, \{\tilde{\mathscr{G}}(\phi)\}$ vectors of nonlinear terms of the reduced system of equations defined in eqns (6) and (35), respectively
$\{H\}$ vector of nodal forces (or force parameters)
h thickness of the shell
K total kinetic energy of the structure
$[K]$ global linear stiffness matrix
$[K_{ff}], [K_{fc}], [K_{cf}], [K_{cc}], [K_{aa}], [K_{ab}], [K_{ba}], [K_{bb}]$ partitions of the matrix $[K]$ defined in eqns (19) and (45)
$[\tilde{K}], [\tilde{\mathscr{K}}]$ linear stiffness matrices of the reduced system defined in eqns (5) and (34), respectively
$[M], [\tilde{M}]$ mass matrices of the full and reduced systems
$\{\mathscr{M}(H,X)\}$ vector of nonlinear terms defined in eqn (30)
n number of displacement degrees of freedom in the model
P applied concentrated load
p intensity of uniform pressure loading
$\{\bar{Q}\}$ normalized load vector of the full system
$\{\tilde{Q}\}, \{\tilde{\mathscr{Q}}\}$ normalized load vectors of the reduced systems defined in eqns (7) and (36), respectively
$\{Q_a\}, \{Q_b\}$ partitions of the vector $\{\bar{Q}\}$ defined in eqn (45)
$\{Q_f\}, \{Q_c\}$ vectors of external and constraint forces defined in eqn (19)
q load parameter
R radius of curvature of the shell
$\{R\}$ and $\{R_f\}$ residual vectors defined in eqns (15) and (29), respectively
r number of reduced basis vectors
$S_{(i)}$ current stiffness parameter corresponding to point i of the solution path
$[S]$ linear generalized stiffness matrix defined in eqn (30)
U total strain energy of the structure
u_1, u_2, w displacement components in the coordinate directions
$\{X\}$ vector of nodal displacements
$\{X_a\}, \{X_b\}$ partitions of the vector $\{X\}$ defined in eqn (45)
$\{X_f\}, \{X_c\}$ vectors of free and prescribed (nonzero) nodal displacements defined in eqn (17)
x_1, x_2, x_3 orthogonal curvilinear coordinates
$\{Z\}$ vector of displacement parameters defined in eqn (18)
β condition number of the Gram matrix of basis vectors
$[\Gamma], [\Gamma_H], [\Gamma_X]$ matrices of basis vectors defined in eqns (3) and (32)
λ path parameter
ν Poisson's ratio of the material
ρ mass density of the material
ϕ_1, ϕ_2 rotation components of the middle surface of the shell
$\{\psi\}$ vector of unknowns of the reduced equations

1. INTRODUCTION

In recent years nonlinear analysis of static and dynamic problems has become the focus of intense research efforts. The increasing importance of nonlinear analysis is largely due to the emphasis placed by manufacturers, contractors and certifying agencies on realistic modeling and accurate analysis of critical structural components. This endeavor has prompted the development of versatile and powerful finite element discretization methods as well as of improved numerical methods and programming techniques for nonlinear static and dynamic analysis of structures (e.g. Refs. [1–16]). In spite of these advances the solutions of most large-scale nonlinear structural and solid mechanics problems require excessive amounts of computer time even on present-day large computers and thus are very expensive.

An examination of the static load–deflection characteristics and dynamic response-time histories of a num-

†Professor of Engineering and Applied Science.

ber of complex structural systems revealed that they are generally not more complicated than those for simple structures. The large numbers of degrees of freedom in complex structures are often dictated by their topology rather than by the expected complexity of the behavior. This fact has been recognized and techniques for reducing the degrees of freedom have long been proposed in vibration analysis and automated optimum design (Refs. [17–22]), and more recently in nonlinear analysis (Refs. [23–30]). The techniques for reducing the degrees of freedom are referred to herein as *reduction methods*.

In the case of nonlinear analysis most of the reduction methods that have been proposed are hybrid procedures which combine contemporary finite elements (or finite differences) and classical Rayleigh–Ritz (or Bubnov–Galerkin) technique. Such approaches preserve the modeling versatility of the finite element (or finite difference) method, and at the same time reduce the number of degrees of freedom through Rayleigh–Ritz (or Bubnov–Galerkin) approximation.

The essence of reduction methods for nonlinear analysis is to limit the deformation modes of the discretized structure to some known modes (basis vectors or global Rayleigh–Ritz approximation functions) which are considerably smaller in number than the number of degrees of freedom of the initial discretization. Due to the high potential of reduction methods for nonlinear analysis, increasing interest has recently been shown in the application of these methods to nonlinear static and dynamic problems. This paper summarizes the status and some recent developments of reduction methods and their application to nonlinear structural mechanics problems. Discussion focuses herein on a number of aspects of reduction methods which are of interest to the author including: (a) selection of basis vectors in nonlinear statics and dynamics problems, (b) application of reduction methods to static nonlinear analysis of structures subjected to prescribed edge displacements, and (c) use of reduction methods in conjunction with mixed finite element models.

Numerical examples are presented to demonstrate the effectiveness of reduction methods. Also, a number of research areas which have high potential for application of reduction methods are identified.

2. REDUCTION METHODS FOR NONLINEAR STATIC PROBLEMS

For static problems the response of the discretized structure is described by a system of nonlinear algebraic equations. Rayleigh–Ritz (or Bubnov–Galerkin) technique is then used to replace the governing equations of the structure by a reduced system of equations with considerably fewer unknowns. This section gives a summary of the basic equations used in reduction methods along with some recent developments relative to the selection of basis vectors. The loading is assumed to be conservative and proportional. A total Lagrangian formulation is used and the spatial discretization is done by using displacement finite element models. The advantages of using reduction methods in conjunction with mixed finite element models, in which the fundamental unknowns consist of both stress and displacement parameters, are discussed in the succeeding sections.

2.1 *Governing finite element equations*

The governing finite element (or finite difference) equations of the discretized structure can be cast in the following form:

$$\{f(X,\lambda)\} = [K]\{X\} + \{G(X)\} - q\{\bar{Q}\} = 0 \tag{1}$$

where $[K]$ is the $n \times n$ linear global stiffness matrix; n is the total number of displacement degrees of freedom; $\{X\}$ is the vector of unknown nodal displacements; $\{G(X)\}$ is the vector of nonlinear terms; $\{\bar{Q}\}$ is a normalized load vector; q is a load parameter, and λ is a path parameter which may be identified with a loading or displacement parameter.

2.2 *Reduced system of equations*

A Rayleigh–Ritz technique is used to replace eqn (1) by a reduced system of equations. This is accomplished by approximating $\{X\}$ by a linear combination of r linearly independent vectors $\{\tilde{X}\}_1, \{\tilde{X}\}_2, \ldots, \{\tilde{X}\}_r$ where r is much less than n, i.e.

$$\{X\} = [\Gamma]\{\psi\} \tag{2}$$

where

$$[\Gamma]_{n,r} = [\{\tilde{X}\}_1, \{\tilde{X}\}_2, \ldots, \{\tilde{X}\}_r] \tag{3}$$

and $\{\psi\}_{r,1}$ is a vector of undetermined coefficients which are obtained by solving the reduced system of nonlinear equations.

$$\{\tilde{f}(\psi,\lambda)\} = [\tilde{K}]\{\psi\} + \{\tilde{G}(\psi)\} - q\{\tilde{Q}\} = 0 \tag{4}$$

and

$$[\tilde{K}] = [\Gamma]^T[K][\Gamma] \tag{5}$$

$$\{\tilde{G}(\psi)\} = [\Gamma]^T\{G(\psi)\} \tag{6}$$

$$\{\tilde{Q}\} = [\Gamma]^T\{\bar{Q}\} \tag{7}$$

where superscript T denotes transposition and $\{G(\psi)\}$ is obtained from $\{G(X)\}$ by replacing $\{X\}$ by its expression in terms of $\{\psi\}$, eqn (2).

2.3 *Selection of reduced basis vectors*

As would be expected, the effectiveness of reduction methods depends, to a great extent, on the proper choice of the reduced basis vectors. Various choices for basis vectors were proposed in the literature. These include linear bifurcation buckling modes (Refs. [26–27]); linear solution and corrections to it (Ref. [25]), and nonlinear solution and its various order path derivatives (Refs. [28, 29]). In order to assess the relative merits of these various choices of basis vectors it is useful to identify the qualities important in an ideal set of basis vectors. An ideal set of basis vectors is defined herein as one which maximizes the quality of the results and minimizes the total effort in obtaining them. The criteria which these basis vectors must satisfy are:

(a) The vectors must be linearly independent and span the space of solutions in the neighborhood of the point considered on the solution path, in the sense that they fully characterize the nonlinear response in that neighborhood.

(b) Their generation should be both simple and computationally inexpensive, and their number can be automatically selected for any given problem.

(c) The vectors must have good approximation properties in the sense that they provide highly accurate solutions on a large interval of the solution path.

(d) Their use should simplify the tracing of post-buckling and post-limit-point paths.

The first criterion is necessary for the convergence of the Rayleigh–Ritz approximation. The last three criteria significantly enhance the efficiency of the reduction method and increase its effectiveness in solving nonlinear structural problems. If the various choices for basis vectors reported in the literature are examined in the light of these criteria, one finds that the generation of bifurcation buckling modes for large structural problems is computationally expensive. The use of the linear solution as a basis vector necessitates frequent additions of corrective basis vectors; each additional vector is obtained by solving the full system of nonlinear finite element equations. On the other hand, *the use of a nonlinear solution and its various order path derivatives (which are commonly used in the static perturbation technique) satisfies all the aforementioned criteria.* These basis vectors are:

$$\{\bar{X}\}_1 = \{X\} \tag{8}$$

$$\{\bar{X}\}_2 = \left\{\frac{\partial X}{\partial \lambda}\right\} \tag{9}$$

$$\vdots$$

$$\{\bar{X}\}_r = \left\{\frac{\partial^{r-1} X}{\partial \lambda^{r-1}}\right\}. \tag{10}$$

The vectors are linearly independent and span the space of solutions in the neighborhood of the point considered on the solution path. As is known from the static perturbation technique, the use of the path derivatives, eqns (9) and (10), simplifies the tracing of post-buckling and post-limit-point paths. The path derivatives are obtained by successive differentiation of the governing finite element equations of the discretized structure. An efficient algorithm for evaluating the basis vectors and generating the reduced system of equations is given in Ref. [29]. The generation of all the vectors is done with only one matrix factorization, and therefore, the effort in generating the second and succeeding basis vectors reduces to that of evaluating the right hand sides of the recursion formulas used in their evaluation (see Refs. [28, 29]).

A criterion for the automatic selection of the number of basis vectors was proposed in Ref. [28]. This criterion is based on monitoring the condition number β of the Gram matrix of the basis vectors, and terminating the generation of these vectors when β exceeds a prescribed value. Along with the prescribed value of β, upper and lower limits for the number of basis vectors must be prescribed (e.g. 10 and 2). The high accuracy and effectiveness of using the proposed set of basis vectors in nonlinear shell problems was demonstrated in Ref. [29].

3. COMPUTATIONAL PROCEDURE USED WITH REDUCTION METHODS

A problem-adaptive computational procedure for use with reduction methods has been presented in Refs. [28, 29]. The five key elements of this procedure are: (a) efficient evaluation of basis vectors and generation of the reduced system of equations; (b) characterization of the nonlinear response by means of a single scalar; (c) automatic selection of load (or displacement) step size and evaluation of the corresponding displacements and forces; (d) sensing and controlling the error in the reduced system of equations; (e) tracing post-buckling and post-limit-point paths. Only some of the key features of these elements are outlined herein.

3.1 *Characterization of nonlinear response and selection of load (or displacement) step size*

For the efficient application of reduction methods to complex structural systems, it is desirable to characterize the changes in the nonlinear response of the structural system by means of a single parameter. The selection of load (or displacement) increments and the frequency of error sensing are then related to changes in this parameter.

A convenient scalar for characterizing the nonlinear response is the current stiffness parameter S introduced in Refs. [31, 32]. This parameter has the major advantage of being easily computed from the reduced system of equations. The parameter $S_{(i)}$ corresponding to point i in the load–displacement path is defined as follows:

$$S_{(i)} = \frac{\left.\dfrac{\partial q}{\partial \lambda}\right|_{(i)}}{\left\{\dfrac{\partial X}{\partial \lambda}\right\}^T_{(i)} \{\bar{Q}\}} / S_0 \quad \text{for the full system} \tag{11}$$

$$= \frac{\left.\dfrac{\partial q}{\partial \lambda}\right|_{(i)}}{\left\{\dfrac{\partial \psi}{\partial \lambda}\right\}^T_{(i)} \{\hat{Q}\}} / S_0 \quad \text{for the reduced system} \tag{12}$$

where

$$S_0 = \frac{\left.\dfrac{\partial q}{\partial \lambda}\right|_0}{\left\{\dfrac{\partial X}{\partial \lambda}\right\}^T_0 \{\bar{Q}\}} \tag{13}$$

and the subscript 0 refers to the value at $\lambda = 0$.

The parameter $S_{(i)}$ provides a global measure for the stiffness of the structure at point i. It has an initial value of 1.0, increases when the structure stiffens and decreases when the structure softens. For stable equilibrium paths, S is positive; for unstable paths, it is negative; and at limit points, S is zero.

An automatic load (and displacement) incrementation procedure is described in Refs. [28, 31]. The load (or displacement) steps are selected in such a way as to maintain almost equal changes of S for the different load (or displacement) steps. The load increment of the ith step $\Delta q_{(i)}$ is related to the load increment of the $(i-1)$ step $\Delta q_{(i-1)}$ as follows:

$$\Delta q_{(i)} = \frac{\Delta q_{(i-1)}}{|\Delta S_{(i-1)}|} |\Delta \bar{S}| \tag{14}$$

where $\Delta \bar{S}$ is the chosen increment of S and $\Delta S_{(i-1)}$ is the actual change in the current stiffness parameter during the $(i-1)$ step. Along with eqn (14) maximum and minimum values must be specified for Δq.

3.2 *Sensing and controlling the error in the reduced system of equations*

In order to check the accuracy of the solution obtained by the reduced system of equations at any value of the load parameter q, the current solution $\{X\}$ is generated using eqn (2) and then the residual vector $\{R\}$ of the finite

element equations, eqn (1), is computed, where

$$\{R\} = [K]\{X\} + \{G(X)\} - q\{\bar{Q}\}. \tag{15}$$

A weighted Euclidean norm of $\{R\}$ is used as an error measure, namely:

$$e = \frac{1}{nq}\sqrt{\left(\frac{\{R\}^T\{R\}}{\{\bar{Q}\}^T\{\bar{Q}\}}\right)}. \tag{16}$$

If the error norm e is less than a prescribed tolerance, the solution is continued; otherwise, a corrected (or improved) estimate of $\{X\}$ is obtained using Newton–Raphson technique in conjunction with eqn (1). Then a new set of basis vectors is generated (with no matrix factorization needed).

To improve the efficiency of the computational procedure, it is desirable to reduce the frequency of computing the error norm without sacrificing the solution accuracy. This is accomplished by relating the frequency of error sensing to changes in the current stiffness parameter S (see Refs. [28, 29]).

3.3 *Tracing post-buckling and post-limit-point paths*

At limit points of the load deflection path, $S = 0$ and the stiffness matrix $[\overset{*}{K}](= [K] + [(\partial G_i/\partial X_j)])$ is singular. To avoid such singularities, S is continuously monitored and load incrementation is discontinued when S falls below a prescribed tolerance (e.g. 0.05). A new set of basis vectors are then computed, with λ chosen to be a displacement parameter instead of the load parameter. The solution is then advanced using a displacement incrementation procedure.

To trace the unstable load deflection path in snap-through and snap-back problems, the change $\Delta X_{\max}$ in the maximum displacement component is monitored. If a large value $\Delta X_{\max}$ is observed in one load step (e.g. ten times the preceding value of $X_{\max}$) the solution step is rejected before switching to displacement incrementation. The maximum displacement $X_{\max}$ at each step is chosen as the path parameter to be incremented. Note that the location of the maximum displacement can shift from step to step. The displacement increments are chosen to correspond to almost equal changes of S for the different steps.

4. CASE OF PRESCRIBED EDGE DISPLACEMENTS

In the case of a loading applied by means of prescribed displacements, as would occur in a laboratory compression test, it is convenient to partition the vector of nodal displacements as follows:

$$\{X\} = \begin{Bmatrix} X_f \\ X_c \end{Bmatrix} \tag{17}$$

where $\{X_f\}$ and $\{X_c\}$ are the free and prescribed (nonzero) displacements, respectively. The constrained zero displacements, and their associated equations are eliminated from eqn (1). For simplicity, the prescribed (nonzero) displacements are assumed to be proportional to the path parameter λ, i.e.

$$\{X_c\} = \lambda\{Z\}. \tag{18}$$

4.1 *Governing finite element equations*

Equation (1) can be conveniently partitioned into two sets of matrix equations as follows:

$$\begin{bmatrix} K_{ff} & K_{fc} \\ K_{cf} & K_{cc} \end{bmatrix}\begin{Bmatrix} X_f \\ X_c \end{Bmatrix} + \begin{Bmatrix} G_1(X_f, X_c) \\ G_2(X_f, X_c) \end{Bmatrix} - \begin{Bmatrix} Q_f \\ Q_c \end{Bmatrix} = 0. \tag{19}$$

In the absence of externally applied loading (case of prescribed displacements only), $\{Q_f\} = 0$ and $\{Q_c\}$ equals the vector of constraint forces associated with the prescribed displacements $\{X_c\}$. The first set of eqns (19) can be used to determine $\{X_f\}$ and the second set is then used to evaluate the constraint forces $\{Q_c\}$.

4.2 *Basis vectors and reduced system of equations*

It is convenient to write the matrix $[\Gamma]$, eqn (3), in the following form:

$$[\Gamma]_{n,r} = \left[\begin{Bmatrix} 0 \\ Z \end{Bmatrix} \begin{Bmatrix} X_f \\ 0 \end{Bmatrix} \frac{\partial}{\partial\lambda}\begin{Bmatrix} X_f \\ 0 \end{Bmatrix} \cdots \frac{\partial^{r-2}}{\partial\lambda^{r-2}}\begin{Bmatrix} X_f \\ 0 \end{Bmatrix}\right]. \tag{20}$$

The corresponding reduced system of equations has a slightly different structure from that of eqn (4), namely:

$$[\tilde{K}]\{\psi\} + \{\tilde{G}(\psi)\} - \{\tilde{Q}\} = 0 \tag{21}$$

where

$$\{\tilde{Q}\} = [\Gamma]^T\begin{Bmatrix} 0 \\ Q_c \end{Bmatrix}. \tag{22}$$

Note that $\{\tilde{Q}\}$ has only one nonzero component, namely $\tilde{Q}_1$. Equations (21) are solved for the reduced unknowns $\{\psi\}$ subject to the condition $\psi_1 = \lambda$.

4.3 *Current stiffness parameter*

In the absence of external loading the current stiffness parameter, defined in eqns (11)–(13) needs to be modified as follows:

$$S_{(i)} = \frac{1}{\left\{\frac{\partial Q_c}{\partial\lambda}\right\}^T_{(i)}\{Z\}}/S_0 \quad \text{for the full system} \tag{23}$$

$$= \frac{1}{\left.\frac{\partial\tilde{Q}_1}{\partial\lambda}\right|_{(i)}}/S_0 \quad \text{for the reduced system} \tag{24}$$

where

$$\left\{\frac{\partial Q_c}{\partial\lambda}\right\} = \left[[K_{cf}] + \left[\frac{\partial G_{2_i}}{\partial X_{f_j}}\right]\right]\left\{\frac{\partial X_f}{\partial\lambda}\right\} + \left[[K_{cc}] + \left[\frac{\partial G_{2_i}}{\partial X_{c_j}}\right]\right]\{Z\} \tag{25}$$

$$\frac{\partial\tilde{Q}_1}{\partial\lambda} = \sum_{j=1}^{r}\left[[\tilde{K}_{1j}] + \left[\frac{\partial\tilde{G}_1}{\partial\psi_j}\right]\right]\frac{\partial\psi_j}{\partial\lambda} \tag{26}$$

and

$$S_0 = \frac{1}{\left\{\frac{\partial Q_c}{\partial\lambda}\right\}^T_0\{Z\}}. \tag{27}$$

4.4 *Error norm*

A convenient error norm that can be used for checking the accuracy of the reduced solution is given by:

$$e = \sqrt{(\{R_f\}^T\{R_f\}/\{Q_c\}^T\{Q_c\})} \tag{28}$$

where

$$\{R_f\} = [K_{ff}]\{X_f\} + [K_{fc}]\{X_c\} + \{G_1(X_f, X_c)\}. \quad (29)$$

Except for the aforementioned modifications, the computational algorithm to be used for the case of prescribed edge displacements is the same as that outlined in Refs. [28, 29].

5. USE OF REDUCED-BASIS TECHNIQUE IN CONJUNCTION WITH MIXED FINITE ELEMENT MODELS

In a number of applications of the reduced basis technique with displacement finite element models it was found that the accuracy of stress resultants produced by the approximate reduced equations was, in general, lower than that of displacements. To remedy this drawback the use of the reduced basis technique in conjunction with mixed finite element models was proposed in Ref. [30]. The basic idea of this approach as applied to geometrically nonlinear static problems with conservative proportional loading is discussed in the succeeding subsections.

5.1 *Governing finite element equations*

The governing finite element equations of the discretized structure consist of both the constitutive equations and the equilibrium equations and can be cast in the following form:

$$\begin{Bmatrix} f_H(H, X, \lambda) \\ f_X(H, X, \lambda) \end{Bmatrix} = \begin{bmatrix} -[F] & [S] \\ [S]^T & 0 \end{bmatrix} \begin{Bmatrix} H \\ X \end{Bmatrix} + \begin{Bmatrix} \mathscr{G}(X) \\ \mathscr{M}(H, X) \end{Bmatrix} - q \begin{Bmatrix} 0 \\ \bar{Q} \end{Bmatrix} = 0 \quad (30)$$

where $[F]$ and $[S]$ are the linear global flexibility and generalized stiffness matrices; $\{H\}$ and $\{X\}$ are the vectors of stress parameters and nodal displacements; $\{\mathscr{G}(X)\}$ and $\{\mathscr{M}(H, X)\}$ are vectors of nonlinear contributions; and $\{\bar{Q}\}$ is a normalized external load vector.

5.2 *Basis vectors and reduced system of equations*

As in the case of displacement models discussed in the preceding sections, the basis vectors are chosen to consist of a nonlinear solution and its various order path derivatives as follows:

$$\begin{Bmatrix} H \\ X \end{Bmatrix} = \begin{bmatrix} \Gamma_H \\ \Gamma_X \end{bmatrix} \{\phi\} \quad (31)$$

$$\begin{bmatrix} \Gamma_H \\ \Gamma_X \end{bmatrix} = \left[\begin{Bmatrix} H \\ X \end{Bmatrix} \frac{\partial}{\partial \lambda} \begin{Bmatrix} H \\ X \end{Bmatrix} \cdots \frac{\partial^{r-1}}{\partial \lambda^{r-1}} \begin{Bmatrix} H \\ X \end{Bmatrix} \right]. \quad (32)$$

A Rayleigh–Ritz (or Bubnov–Galerkin) procedure is then used to replace the governing finite element equations by the following reduced system of equations

$$\{\tilde{f}(\phi, \lambda)\} = [\tilde{\mathscr{K}}]\{\phi\} + \{\tilde{\mathscr{G}}(\phi)\} - q\{\tilde{\mathscr{Q}}\} = 0 \quad (33)$$

where

$$[\tilde{\mathscr{K}}] = -[\Gamma_H]^T[F][\Gamma_H] + [\Gamma_H]^T[S][\Gamma_X] + [\Gamma_X]^T[S]^T[\Gamma_H] \quad (34)$$

$$\{\tilde{\mathscr{G}}(\phi)\} = [\Gamma_H]^T\{\mathscr{G}(\phi)\} + [\Gamma_X]^T\{\mathscr{M}(\phi)\} \quad (35)$$

and

$$\{\tilde{\mathscr{Q}}\} = [\Gamma_X]^T\{\bar{Q}\}. \quad (36)$$

In eqns (35), $\{\mathscr{G}(\phi)\}$ and $\{\mathscr{M}(\phi)\}$ are obtained from $\{\mathscr{G}(X)\}$ and $\{\mathscr{M}(H, X)\}$ by replacing $\{H\}$ and $\{X\}$ by their expressions in terms of $\{\phi\}$, eqn (31).

The computational algorithm for applying reduction methods with mixed models is similar to that described in the preceding sections in connection with displacement models and is outlined in Ref. [30].

5.3 *Assets and labilities of using reduced basis technique with mixed models*

If the proposed approach for applying reduced basis technique in conjunction with mixed models is contrasted with the corresponding displacement approach the following two major advantages can be identified:

1. *Simplicity of generation of reduced basis vectors.* The nonlinear terms in the finite element equations of the mixed method have simple mathematical structure and are bilinear (or quadratic) in the nodal parameters (see Refs. [30, 33]). In contrast, the nonlinear terms in the displacement finite element equations are cubic in the nodal displacement parameters. As a consequence of this, the evaluation of the path derivatives for mixed finite elements involves less arithmetic operations than that of the corresponding displacement models.

2. *Better approximation properties.* Numerical results reported in Ref. [30] have shown that for a given number of basis vectors, the accuracy of the solutions obtained by reduced basis-mixed models is higher than that of the corresponding displacement approach. This is particularly true for the stress predictions. As a consequence of this, the basis vectors in the mixed method are less frequently updated than in the displacement method. This will also be demonstrated in the section of numerical studies.

While there are a number of advantages of the proposed reduced basis-mixed model approach two major difficulties also arise: (a) the first results from the large number of degrees of freedom used in the mixed model. This leads to a substantial increase in the number of simultaneous equations used in generating and updating the basis vectors; and (b) the second difficulty is due to the nondefiniteness of the matrix of the algebraic equations used in generating the basis vectors. The two difficulties can be alleviated by using *mixed models with discontinuous stress fields at interelement boundaries.* Such mixed models have been shown to have better performance that mixed models with continuous stress fields (see Ref. [34]). Moreover, the stress parameters as well as their path derivatives can be eliminated on the element level, thereby considerably reducing the size of the system of equations used for evaluating the path derivatives. Also, the use of mixed models with discontinuous stress fields simplifies the implementation of the reduced basis-mixed model approach in existing nonlinear programs based on the displacement formulation.

6. REDUCTION METHODS FOR NONLINEAR DYNAMIC PROBLEMS

The semi-discrete form of the governing equations for nonlinear structural systems at time t can be written in the following form:

$$[\ddot{M}]\{X\}_t = \{Q\}_t - \{\mathscr{F}\}_t \quad (37)$$

where $[M]$ is the mass matrix; $\{Q\}$ is the vector of externally applied discretized loads; $\{\ddot{X}\}$ is the vector of

nodal accelerations; $\{\mathscr{F}\}$ is the vector of internal nodal forces which can be expressed in terms of the vector of nodal displacements as follows:

$$\{\mathscr{F}\}_t = [K]\{X\}_t + \{G(X)\}_t \tag{38}$$

and $[K]$ is the linear global stiffness matrix. For simplicity, the effect of damping has been neglected in eqn (37).

With a specification of the initial conditions, the governing system of nonlinear ordinary differential equations, eqn (37), can be integrated to produce the time history response of the structure. A wide variety of explicit and implicit techniques have been proposed in the literature for integrating eqn (37) and obtaining the response-time history of the structure. However, the computational effort involved in applying these techniques to large systems can be quite substantial. Therefore, the reduction of degrees of freedom in nonlinear dynamic problems is even more important than in nonlinear static analysis.

6.1 *Modal methods*

Modal superposition technique is a very effective reduction method for linear dynamic problems when only few vibration modes are excited by the external loading (case of structural dynamics problems as opposed to wave propagation problems, see Ref.[13]). The basis vectors in this technique consist of few vibration mode shapes. Several studies have been made on improving the accuracy and efficiency of modal superposition techniques in linear problems (see, for example, Refs. [35, 36]).

The use of modal methods in nonlinear problems appears, at a first glance, to violate the well-known fact that superposition principles are not applicable to nonlinear systems. However, Ref.[37] suggests the use of the *principle of local modal superposition* which states that small harmonic motions may be superimposed upon large static motion and that small forced motion may be represented in terms of the nonlinear (tangent stiffness) frequency spectrum.

If a total Lagrangian displacement formulation is used, the vector of nodal displacements is expressed as a linear combination of the lowest vibration modes as follows:

$$\{X\} = [\Gamma]\{\psi\} \tag{39}$$

where the columns of the matrix $[\Gamma]$ are the basis vectors which consist of the lowest vibration modes.

The semi-discrete governing equations of the structure, eqn (37), are then approximated by the following reduced system of ordinary differential equations

$$[\tilde{M}]\{\ddot{\psi}\}_t = \{\tilde{Q}\}_t - \{\tilde{\mathscr{F}}\}_t \tag{40}$$

where

$$[\tilde{M}] = [\Gamma]^T[M][\Gamma] \tag{41}$$

$$\{\tilde{Q}\} = [\Gamma]^T\{Q\} \tag{42}$$

$$\{\tilde{\mathscr{F}}\} = [\tilde{K}]\{\psi\} + [\Gamma]^T\{G(\psi)\} \tag{43}$$

and

$$[\tilde{K}] = [\Gamma]^T[K][\Gamma] \tag{44}$$

Both the $[\tilde{M}]$ and $[\tilde{K}]$ in this case are diagonal matrices. The effectiveness of modal superposition technique in nonlinear dynamic problems depends on:

(a) The number of basis vectors (vibration modes) required to accurately simulate the response;

(b) The frequency of updating the basis vectors (or recalculating the vibration modes); and,

(c) The efficiency of the algorithms used in extracting the initial eigenmodes and updating them.

The number of basis vectors required depends on the structural properties of the system as well as on the spatial distribution and frequency content of the loading (see Refs. [37, 38]). The frequency of updating the basis vectors depends on the rate of change of these vectors with time.

The computational cost of extracting the vibration modes can be reduced by applying one of the condensation schemes (e.g. Guyan reduction or static "zero mass" condensation method) to the discrete system prior to extracting the eigenvectors. An efficient algorithm should be used for extracting *only* the lowest modes for the generalized eigenvalue problem that represents the initial state of the structure. Then an iterative scheme such as subspace iteration technique is applied for determining the subsequent modal spectrum (or mode shapes) using the most recently determined spectrum as an initial estimate (see Ref.[37]).

For mildly nonlinear problems, the use of modal technique in conjunction with the residual force method holds much promise. This is because a single set of modes (based on linear analysis) could be used throughout the analysis. Only the residual force due to nonlinearities needs to be transformed (modified) in each time step (see eqn (40)). This approach was suggested in Ref.[38] but no numerical results were presented. In a number of simple nonlinear structural dynamics problems, modal methods were found to be competitive with direct integration operators (see Refs. [37–40]).

6.2 *Modified modal method*

For the case of step loading on arches and spherical shells, it was found that reasonably accurate solutions can be obtained by the simultaneous use of the following two sets of vibration modes as basis vectors:

(a) Lowest vibration modes of the initial state of the structure;

(b) Lowest vibration modes of the nonlinear, steady-state of the structure.

The latter set of modes is obtained by first finding the steady-state (or static) nonlinear solution and using it to evaluate the stiffness of the structure, then extracting the lowest vibration modes from the corresponding generalized eigenvalue problem. Note that the resulting mass and linear stiffness matrices $[\tilde{M}]$ and $[\tilde{K}]$ of the reduced system, eqns (41) and (44), are sparse but not diagonal. The effectiveness of the aforementioned choice of basis vectors for the solution of nonlinear dynamic problems is discussed in the succeeding sections.

7. TWO-STAGE RAYLEIGH–RITZ AND BUBNOV–GALERKIN TECHNIQUES

The discussion to this point has been focused on the methodology of establishing reduction methods in conjunction with finite element (or finite difference) techniques. Reduction methods can also be used to improve the efficiency of the classical Rayleigh–Ritz and Bubnov–Galerkin techniques by considerably reducing the number of degrees of freedom of the discretized structure. This is accomplished by applying these techniques in two stages. The first stage is that of spatial discretization

wherein the structure is discretized by using coordinate functions which cover the entire region of the structure. In the second stage the vector of unknown parameters is expressed as a linear combination of a small number of basis vectors. The Rayleigh–Ritz (or Bubnov–Galerkin) procedure is then applied a second time to approximate the nonlinear equations of the discretized structure by a reduced system of nonlinear algebraic equations. For static problems, the basis vectors used in the second stage are the same as those used in the reduced basis-finite element method; namely, a nonlinear solution and a number of its path derivatives. Also, the computational procedure for the two-stage Rayleigh–Ritz and Bubnov–Galerkin techniques is similar to that outlined in the preceding sections in conjunction with reduced basis-finite element method. A detailed discussion of the two-stage technique is given in Ref.[41] and its effectiveness is demonstrated by means of numerical examples of axisymmetric deformation of shallow spherical caps.

8. NUMERICAL STUDIES

Numerical studies which demonstrate the effectiveness of the reduction methods presented in the preceding sections for the solution of nonlinear static problems have been presented in Refs. [28–30]. Herein the results of three typical problems are discussed. The three problems are: (a) elastic collapse analysis of cylindrical shell with a rectangular cutout (b) large deflections of clamped cylindrical panel, and (c) nonlinear dynamic response of a shallow spherical cap subjected to a point load applied as a step function at the apex.

The first problem was selected to test the effectiveness of the proposed approach when applied to structures problems with loading applied as a prescribed edge displacement. The second problem is used to assess the relative merits of reduced basis-mixed model approach over the corresponding displacement method and the third problem gives an indication of the potential of the modified modal method in solving nonlinear dynamic problems.

8.1 *Elastic collapse analysis of cylindrical shell with a cutout*

The first problem considered is that of the cylindrical shell with rectangular cutout shown in Fig. 1. The problem is one of three problems used in Ref.[42] to assess the capability of various programs to analyze shell structures. The load is applied to the cylinder by means of a uniform axial shortening which is increased incrementally until the cylinder collapses.

Due to symmetry, only one octant of the cylinder was modeled using the grid of shear-flexible elements shown in Fig. 1. Bicubic Lagrangian interpolation functions were used to approximate each of the displacement and rotation components (a total of 2996 nonzero displacement degrees of freedom). Finite difference solutions to this problem using the STAGS (*ST*ructural Analysis of *G*eneral *S*hells) computer code are presented in Refs. [42, 43].

Figure 2 shows the variation of the current stiffness parameter S with loading. Figure 3 gives an indication of the accuracy of the normal displacement w, at the centers of two sides of the rectangular cutout, obtained by the reduced-basis technique. Figure 4 gives an indication of the accuracy of the total strain energy and Fig. 5 shows the error norms of the reduced basis technique with seven basis vectors at various load levels. Figure 6 shows contour plots of the normal displacement w at

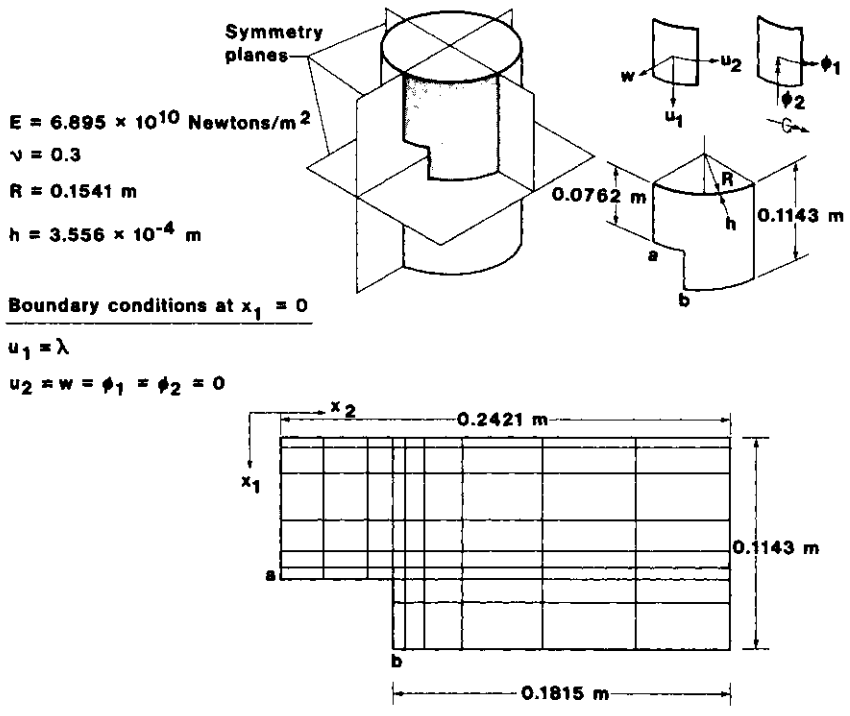

Fig. 1. Cylindrical shell with cutout and finite element model used in the present study.

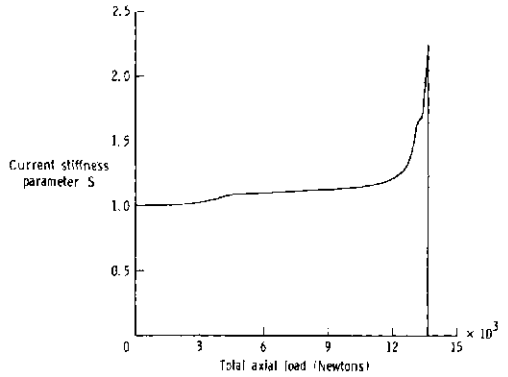

Fig. 2. Variation of current stiffness parameter with loading for the cylindrical shell with cutout shown in Fig. 1.

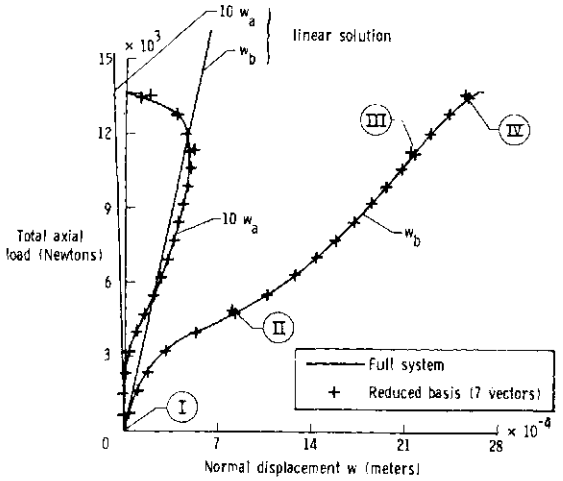

Fig. 3. Accuracy of normal displacements obtained by reduced basis technique at various load levels. Cylindrical shell with cutout shown in Fig. 1. Roman numerals indicated points of generating basis vectors.

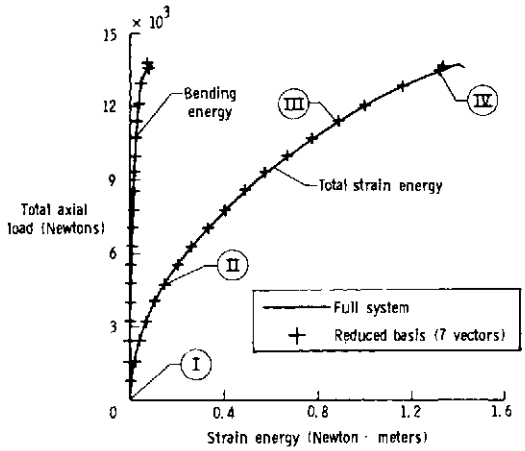

Fig. 4. Accuracy of strain energies obtained by reduced basis technique at various load levels. Cylindrical shell with cutout shown in Fig. 1. Roman numerals indicate points of generating basis vectors.

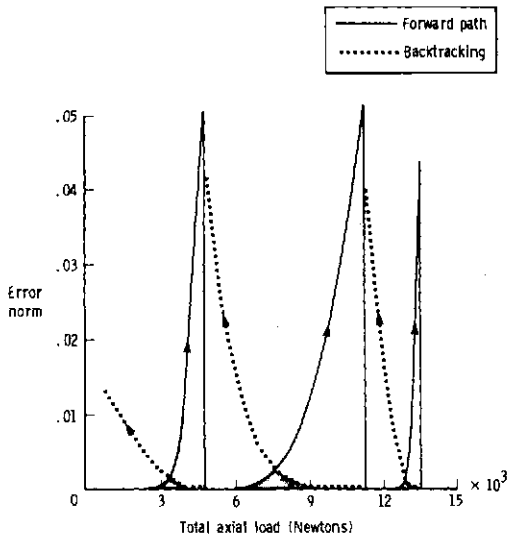

Fig. 5. Error norms of reduced basis technique (using 7 vectors) at various load levels. Cylindrical shell with cutout shown in Fig. 1.

four different load levels, each normalized by dividing by w_{max} for that load level.

In the present study the path parameter λ was chosen to be equal to the axial edge displacements, and therefore, the components of the vector $\{Z\}$ are equal to unity. The basis vectors were first computed for the unloaded shell ($\lambda = 0, \{X_I\} = 0$). An error tolerance $e \leq 0.05$ was prescribed. The seven basis vectors were used to advance the solution to $\lambda = 3.048 \times 10^{-5}$ m. at which value the error norms were checked and were found to exceed the prescribed tolerance (see Fig. 5). New (updated) set of seven basis vectors were generated and the solution was continued until $\lambda = 7.620 \times 10^{-5}$ m. The same process was repeated and new set of seven vectors were generated and used to advance the solution until $\lambda = 9.398 \times 10^{-5}$. The predicted collapse load of the cylinder was 13.656×10^3 Newtons corresponding to $\lambda = 9.70 \times 10^{-5}$ m.

The high accuracy of the normal displacements and strain energies obtained by the reduced system of equations is demonstrated in Figs. 3 and 4. At $\lambda = 9.398 \times 10^{-5}$ m. the errors in the maximum normal displacement w_b and the total strain energy U obtained by using seven basis vectors were 0.53% and 0.023%, respectively.

Higher accuracy of the reduced solutions can be achieved by backtracking the equilibrium paths every time a new (updated) set of basis vectors is generated. This amounts to effectively reducing the error norm well below the prescribed tolerance. When this technique was used in the present problem, the maximum value of the error norms using seven vectors reduced to less than 0.003. The computational expense involved in the backtracking process was insignificant.

Figure 6 shows that a large change in loading (or prescribed axial end shortening) is associated with a small change in the spatial distribution of the response quantities (manifested by small changes in the normalized contour plots). *It is this fact that suggested the separation of the spatial distribution of the response quantities at any load level from the variation of these*

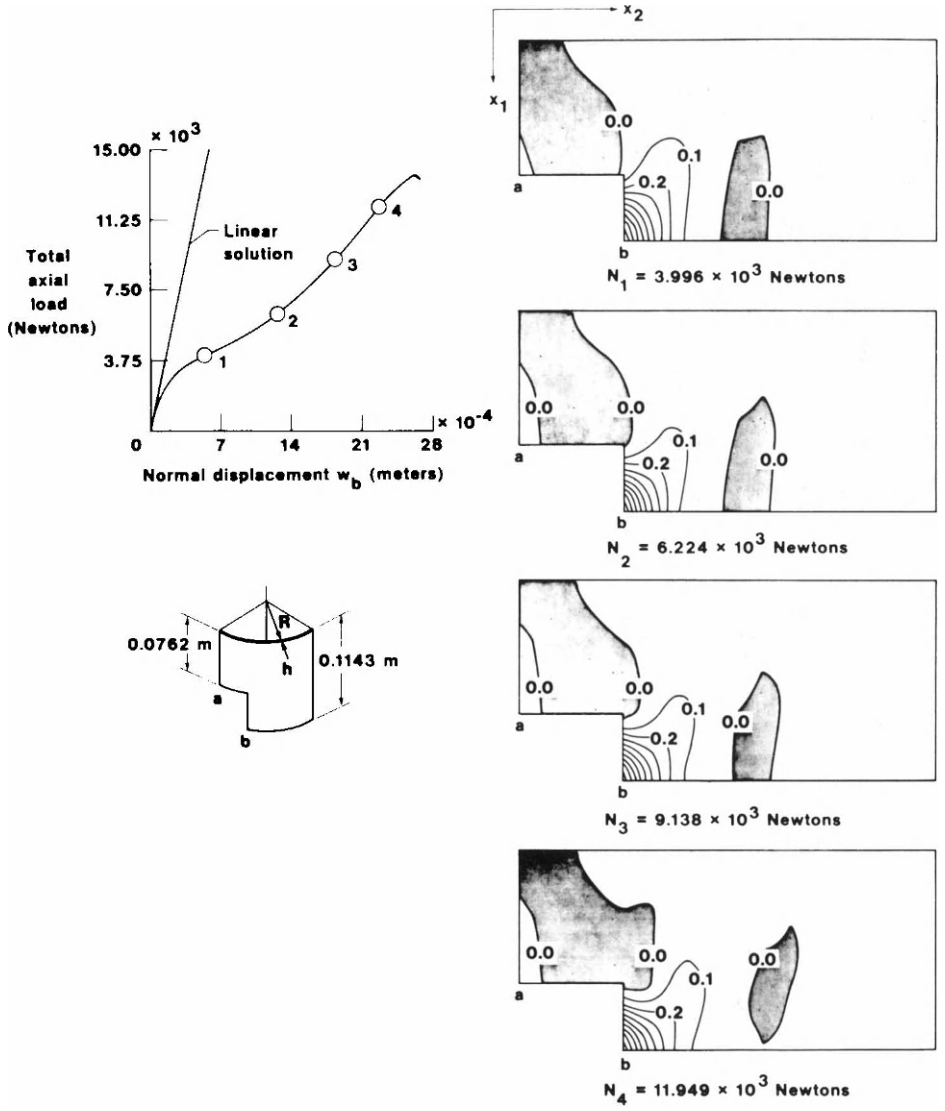

Fig. 6. Contour plots for the normal displacements w at various load levels (each normalized by dividing by w_{max} for that load level). Cylindrical shell with cutout (see Fig. 1).

quantities with loading, and is the primary reason for the success of the proposed approach.

In summary, the generation of the whole solution path up to collapse of the cylinder involved: (a) generation of an initial set of basis vectors at $\lambda = 0$, and (b) updating the basis vectors three times.

The use of reduced basis technique in this problem resulted in *reducing the number of degrees of freedom by a factor of over* 400 (from 2996 degrees of freedom for the original finite element model to seven degrees of freedom for the reduced system).

8.2 *Large deflections of clamped cylindrical panel*

The second problem considered is that of a clamped cylindrical panel subjected to uniform pressure loading. The material and geometric characteristics of the panel are given in Fig. 7. Finite element solutions to this problem were given in Refs. [44, 45]. Also, the same problem was analyzed in Ref. [29] using the reduced basis displacement approach. Due to symmetry, only one quarter of the panel was considered and was modeled by a grid of 4×4 shear-flexible, shallow shell mixed elements. Biquadratic

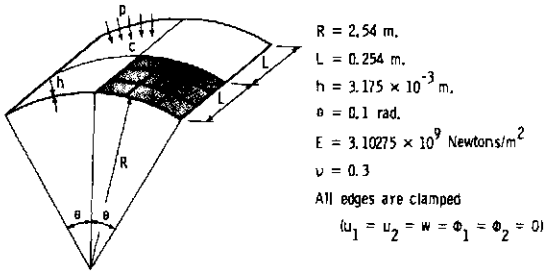

Fig. 7. Cylindrical panel used in present study.

Lagrangian interpolation functions were used for approximating each of the displacement and rotation components and bilinear interpolation functions were used for approximating each of the eight stress resultants. The analysis model had a total of 287 nonzero displacement degrees of freedom and 512 stress-resultant parameters. No continuity requirements were imposed on the stress resultants at the interelement boundaries, and therefore, they were eliminated on the element level.

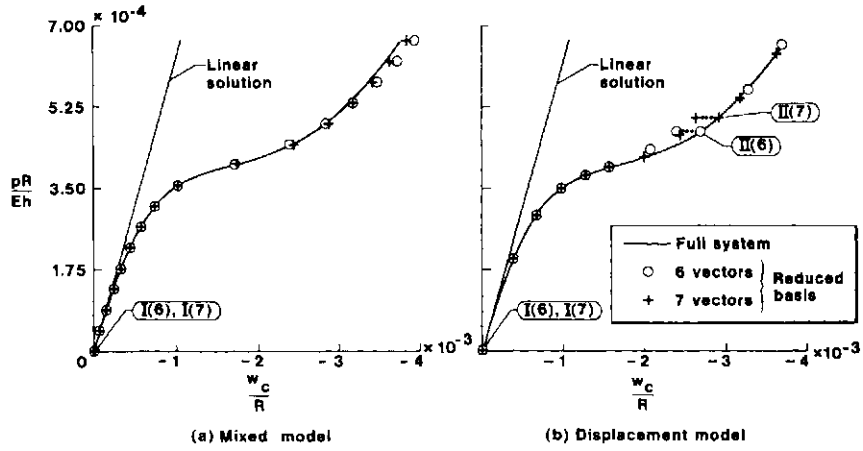

Fig. 8. Accuracy of normal displacement w_c obtained by reduced basis mixed and displacement models at various load levels. Clamped cylindrical panel subjected to uniform pressure loading (see Fig. 7). Roman numerals indicate points of generating basis vectors and numbers between parentheses refer to numbers of basis vectors.

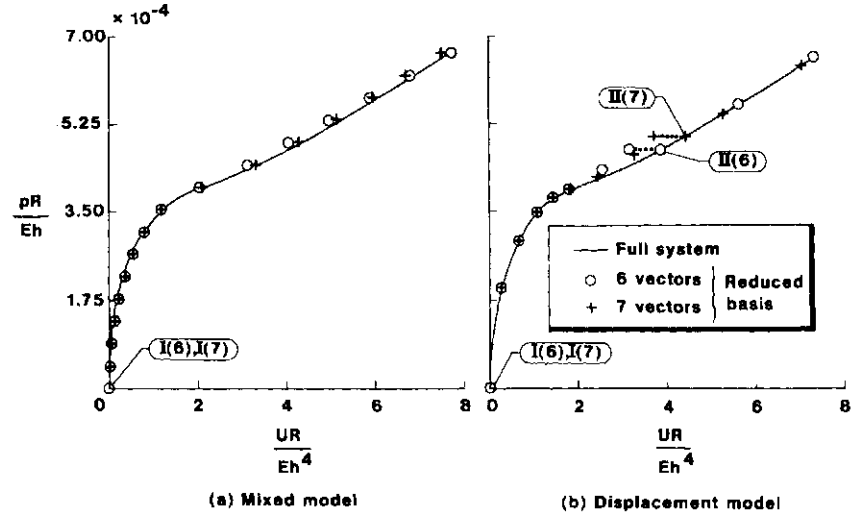

Fig. 9. Accuracy of strain energy obtained by reduced basis mixed and displacement approaches at various load levels. Clamped cylindrical shell subjected to uniform pressure loading (see Fig. 7). Roman numerals indicate points of generating basis vectors and numbers between parentheses refer to number of vectors.

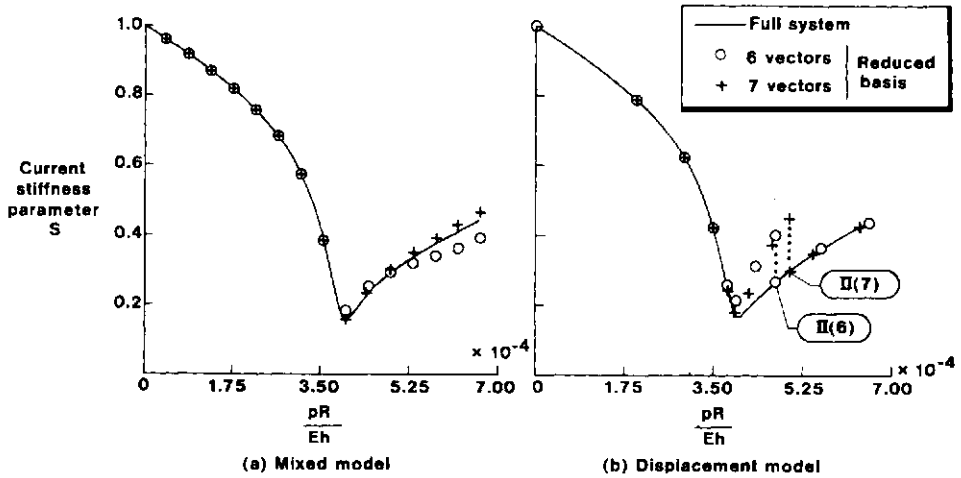

Fig. 10. Accuracy of current stiffness parameter obtained by reduced basis mixed and displacement approaches at various load levels. Clamped cylindrical panel subjected to uniform pressure loading (see Fig. 7).

Figures 8–10 give an indication of the accuracy of the solutions obtained using the reduced basis-mixed and displacement approaches.

The basis vectors were first computed for the unloaded shell ($\lambda = 0, \{H\} = \{X\} = 0, \{\mathscr{G}(X)\} = \{\mathscr{M}(H, X)\} = 0$), and were thus obtained by solving a linear set of finite element equations. An error tolerance $e \leq 0.02$ was prescribed. *With the reduced basis-mixed model approach that error tolerance was not exceeded when the solution was advanced to* $\lambda = (pR/Eh) = 0.667 \times 10^{-3}$, *and therefore, no updating of the basis vectors was needed.* On the other hand, ther error norms of the reduced basis-displacement approach with six and seven basis vectors exceeded the prescribed tolerance at $\lambda = 0.472 \times 10^{-3}$ and $\lambda = 0.499 \times 10^{-3}$, respectively. A new (updated) set of six and seven basis vectors were generated at these values of λ. Also, the strain energy obtained by the reduced basis-mixed approach was found to be more accurate than that obtained by the corresponding displacement approach (see Fig. 9).

Figure 10 shows the high accuracy of the current stiffness parameter predicted by the reduced basis mixed approach, with six and seven basis vectors through the softening region and up to where a stiffening behavior is again experienced. Then the reduced basis mixed solutions with six basis vectors tend to underestimate the value of S. The corresponding solutions with seven vectors slightly overestimate the value of S.

8.3 *Nonlinear dynamic response of a shallow spherical cap*

The last problem considered is that of the dynamic response of the clamped shallow spherical cap shown in Fig. 11. The cap is subjected to a point load at the apex applied as a step function in time. Solutions to this problem using Houbolt temporal integration scheme were presented in Refs. [46, 47]. Also, several modal solutions, with successively higher number of modes, were presented in Ref. [37]. The modes were updated very frequently (every one microsecond).

Due to axial symmetry, only the meridian was considered and was modeled by using ten shear-flexible curved elements with quintic interpolation functions for each of the displacements and rotation components (a total of 148 nonzero displacement degrees of freedom).

An indication of the accuracy of the response time histories obtained by the modified modal approach, for a duration of 0.5 milliseconds is given in Figs. 11 and 12. A set of ten basis vectors consisting of (a) the five lowest vibration modes of the initial (linear) state of the structure and (b) the five lowest vibration modes of the nonlinear steady-state (static equilibrium state) of the structure. *The same set of vectors was used throughout the response analysis.* The reduced system of ten equations was integrated using the central difference temporal integration scheme with $\Delta t = 0.4$ μsec. Figures 11 and 12 show that in spite of the slight phase shift, the chosen set of

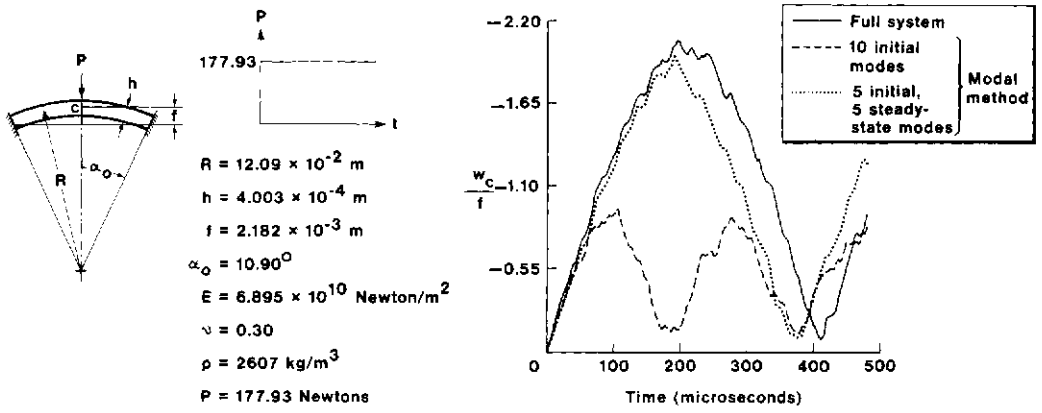

Fig. 11. Accuracy of normal displacement w_c obtained by modal methods. Clamped shallow spherical cap subjected to a point load at the apex.

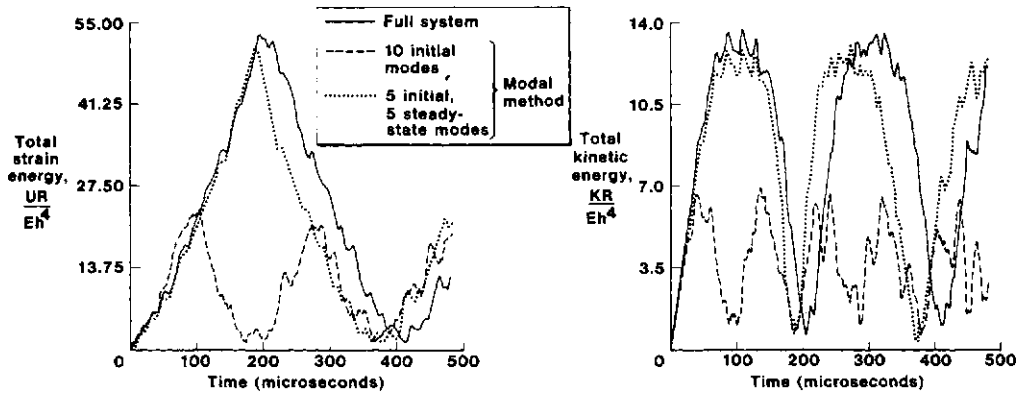

Fig. 12. Accuracy of total strain and kinetic energies obtained by modal methods. Clamped shallow spherical cap subjected to a point load at the apex (see Fig. 11).

basis vectors predicts accurately the shape of the response-time histories. In contrast the use of ten linear vibration modes leads to grossly inaccurate solutions. It may be noted that Ref. [37] reported significant inaccuracies in the predictions of the modal method at about 50 μsec when twelve modes or less were used (even when these modes were updated every microsecond).

9. FUTURE DIRECTIONS FOR RESEARCH ON REDUCTION METHODS

Among the different aspects of reduction methods which have high potential for research are the following:

9.1 *Use of reduction methods in conjunction with substructuring (partitioning) techniques*

In many structural problems the nonlinearities are either more pronounced in, or limited to, a few local regions. The rest of the structure either exhibits mild nonlinearity or remains completely linear. The use of reduction methods in conjunction with substructuring techniques can lead to substantial savings in computer time in these problems. A possible approach for applying this procedure to static problems with localized strong nonlinearities is to partition the governing finite element equations of the discretized structure as follows:

$$\begin{bmatrix} K_{aa} & K_{ab} \\ K_{ba} & K_{bb} \end{bmatrix} \begin{Bmatrix} X_a \\ X_b \end{Bmatrix} + \begin{Bmatrix} G_1(X_a, X_b) \\ G_2(X_a, X_b) \end{Bmatrix} - q \begin{Bmatrix} Q_a \\ Q_b \end{Bmatrix} = 0 \qquad (45)$$

where the vector $\{X_a\}$ represents the nodal displacements in the region with strong nonlinearity and the vector $\{X_b\}$ represents the nodal displacements in the rest of the structure.

The initial set of basis vectors (corresponding to $\lambda = 0$) are generated in the manner described in the previous sections. The parameter λ is incremented and for each nonzero value of λ the vector $\{X_b\}$ is first obtained by using the static perturbation technique (i.e. Taylor series expansion) as follows:

$$\{X_b\} = \{X_b\}_0 + \Delta\lambda \left\{\frac{\partial X_b}{\partial \lambda}\right\}_0 + \frac{(\Delta\lambda)^2}{2!}\left\{\frac{\partial^2 X_b}{\partial \lambda^2}\right\}_0 + \cdots. \qquad (46)$$

Then the vector $\{X_a\}_\lambda$, at the same value of λ, is obtained by using the reduced basis technique with $\{X_b\}_\lambda$ given by eqn (46).

Also, in updating the basis vectors, the path derivatives associated with $\{X_b\}$ are approximated by their Taylor series expansions, thereby considerably reducing the size of the system of equations used in generating the path derivatives associated with $\{X_a\}$.

Moreover, if the region of strong nonlinearity is not known in advance it can be identified by comparing the norms of the higher-order derivatives $\{(\partial^2 X/\partial\lambda^2)\}$, $\{(\partial^3 X/\partial\lambda^3)\}$ and $\{(\partial^4 X/\partial\lambda^4)\}$ of the displacement vector at each node with the norm of the first derivative $\{(\partial X/\partial\lambda)\}$ for the same node. The region of strong nonlinearity usually consists of the nodes with large norms for the higher-order derivatives.

9.2 *Improving the effectiveness of reduction methods in nonlinear dynamic problems*

In order to realize the full potential of reduction methods in nonlinear dynamic problems, a problem-adaptive computational strategy needs to be developed which includes the following key elements:

(a) Characterization of nonlinear dynamic response by means of a single (or few) scalar(s);

(b) Proper selection of basis vectors. This also includes a procedure for efficient generation of basis vectors and automatic selection of their number.

(c) Sensing and controlling the error in the reduced system of equations. This includes relating the frequency of sensing the error to the changes in the values of the scalar(s) characterizing the nonlinear dynamic response.

9.3 *Application of reduction methods to inelastic analysis and optimization problems*

The key element in the application of reduction methods to inelastic analysis is the proper selection of basis vectors. In static problems the validity of using the path derivatives as basis vectors should be examined. In optimization problems reduction methods can be used for: (a) reducing the number of degrees of freedom in the analysis model; (b) reducing the number of design variables; and (c) reducing the number of constraints. Some ideas along these lines were presented in Ref.[48], but algorithms need to be developed for the automatic implementation of these ideas.

10. CONCLUDING REMARKS

Status and recent developments in the application of reduction methods to nonlinear structural mechanics problems are summarized. A number of aspects of reduction methods are discussed herein including: (a) selection of basis vectors in nonlinear static and dynamic problems, (b) application of reduction methods to nonlinear analysis of structures subjected to prescribed edge displacements, and (c) use of reduction methods in conjunction with mixed finite element models.

Numerical examples are presented to demonstrate the effectiveness of reduction methods in nonlinear problems. Also, a number of research areas which appear to have high potential for application of reduction methods are identified.

The results of the present study suggest several conclusions relative to the effectiveness of reduction methods in nonlinear static problems and the particular choice of basis vectors in these problems:

1. The proposed reduced basis technique for nonlinear static problems outlined in the paper is a hybrid method which combines the major advantages of contemporary finite element method, classical Rayleigh–Ritz technique and static perturbation method, namely:

(a) modeling versatility

(b) reduction in total number of degrees of freedom; and,

(c) simplicity of tracing post-buckling and post-limit-point equilibrium paths.

Moreover, it greatly alleviates the following major drawbacks of the aforementioned three techniques:

(a) excessive amounts of computer time required for the nonlinear finite element analysis of complex structures;

(b) difficulty of selecting global approximation functions for classical Rayleigh-Ritz (and Bubnov–Galerkin) technique; and,

(c) small radius of convergence of the Taylor series expansions used in the static perturbation technique.

2. The use of path derivatives as basis vectors in nonlinear static problems allows highly accurate solutions to be obtained with a small number of basis vectors. Therefore, the time required to solve the reduced system of equations is fairly small and the analysis time,

to a first approximation, equals the time required to generate and update the basis vectors.

3. The success of the foregoing reduced basis technique in static problems can be mainly attributed to the separation of spatial distribution of the response quantities at any load level from the variation of these quantities with loading. The numerical studies have shown that a large change in loading (or prescribed end displacements) is associated with a small change in the spatial distribution of the response quantities. On the other hand, large changes in the spatial distribution of the response quantities require updating the basis vectors.

4. For static problems with conservative external and internal forces, the efficiency of the reduced-basis technique can be increased if the error tolerance is increased and the accuracy of the reduced system of equations is maintained by backtracking the solution path every time a new (updated) set of basis vectors is generated.

5. The use of reduction methods in conjunction with mixed models offers the following two major advantages over displacement models:

(a) lower computational expense in generating the basis vectors; and,

(b) better approximation for stresses and less frequent updating of basis vectors.

If the mixed models have discontinuous stress fields at interelement boundaries, the stress parameters as well as their path derivatives can be eliminated on the element level and the efficiency of the reduction method is thereby greatly enhanced.

Acknowledgements—The present work is partially supported by a National Science Foundation Grant No. PFR-7916263, and by a NASA Langley Research Center Grant No. 09-010-078.

REFERENCES

1. R. F. Hartung (Editor), *Numerical Solution of Nonlinear Structural Problems*, AMD-Vol. 6. American Society of Mechanical Engineers (1973).
2. T. Belytschko, J. R. Osias and P. V. Marcal (Editors), *Finite Element Analysis of Transient Nonlinear Structural Behavior*, AMD-Vol. 14. American Society of Mechanical Engineers (1975).
3. K. J. Bathe, J. T. Oden and W. Wunderlich (Editors), *Formulations and Computational Algorithms in Finite Element Analysis: U.S.-German Symp.* Massachusetts Institute of Technology (1977).
4. P. G. Bergan, P. K. Larsen, H. Pettersson, A. Samuelsson, T. H. Søreide, and N. E. Wiberg (Editors), *Finite Elements in Nonlinear Mechanics*. TAPIR, Trondheim (1978).
5. K. J. Bathe, An assessment of current finite element analysis of nonlinear problems. In *Numerical Solution of Partial Differential Equations* III (Edited by B. Hubbard). Academic Press, New York (1976).
6. C. A. Felippa, Procedures for computer analysis of large nonlinear structural systems. In *Large Engineering Systems* (Edited by A. Wexler), pp. 60–100. Pergamon Press, London, (1976).
7. W. F. Schmidt, Adaptive step-size selection for use with the continuation method. *Int. J. Num. Meth. Engng* **12**, 677–694 (1978).
8. W. C. Rheinboldt, Numerical methods for a class of finite dimensional bifurcation problems. *SIAM J. NUM. Analysis* **15**(1), 1–11 (Feb. 1978).
9. E. Riks, An incremental approach to the solution of snapping and buckling problems. *Int. J. Solids Structures*, **15**, 529–551 (1979).
10. M. A. Crisfield, A faster modified Newton–Raphson iteration. *Comput. Meth. Appl. Mech. Engng* **20**, 267–278 (1979).
11. P. G. Bergan, Solution algorithms for nonlinear structural problems. *Proc. Int. Conf. Engng Application Finite Element Meth.* pp. 13.1–13.38. Computas, Oslo (1979).
12. J. H. Argyris, J. St. Doltsinis and K. J. Willam, New developments in the inelastic analysis of quasistatic and dynamic problems. *Int. J. Num. Meth. Engng* **14**, 1813–1850 (1979).
13. C. A. Felippa and K. C. Park, Direct time integration methods in nonlinear structural dynamics. *Comput. Meth. Appl. Mech. Engng* **17/18**, 277–313 (1979).
14. E. Schrem, Structural aspects of software systems for nonlinear finite element analysis. In *Finite Elements in Nonlinear Mechanics*, pp. 621–645 TAPIR, Trondheim (1978).
15. P. Hermann, W. Knudson and S. Schneider, Considerations for the design of programs for nonlinear finite element analysis. In *Computational Aspects of the Finite Element Method*, pp. 177–178. Budesanstalt fur Materialprufung, Berlin (1979).
16. R. H. Dodds and L. A. Lopez, A generalized software system for nonlinear analysis. In *Engng Software*, pp. 55–77. Pentech Press, Plymouth, (1979).
17. A. Jennings and D. R. L. Orr, Application of simultaneous iteration method to undamped vibration problems. *Int. J. Num. Meth. Engng.* **3**, 13–24 (1971).
18. S. B. Dong, J. A. Wolf, Jr. and F. E. Peterson, On a direct-iterative eigensolution technique. *Int. J. Num. Meth. Engng* **4**, 151–161 (1972).
19. K. J. Bathe and E. L. Wilson, Large eigenvalue problems in dynamic analysis. *J. Engng Mech. Div., ASCE*, **98**, 1471–1485 (1972).
20. R. H. MacNeal, The solution of large structural dynamic problems. *Proc. Symp. Applications Comput. Meth. Engng*, pp. 77–86. University of Southern California, Los Angeles, (23–26 Aug. 1977).
21. R. L. Fox and H. Miura, An approximate analysis technique for design calculations. *AIAA J.* **9**, 177–178 (Jan. 1971).
22. A. K. Noor and H. E. Lowder, Approximate techniques of structural reanalysis. *Comput. Structures* **4**(4), 801–812 (Aug. 1974).
23. J. F. Besseling, Nonlinear analysis of structures by the finite element method as a supplement to a linear analysis. *Comput. Meth. Appl. Mech. Engng* **3**, 173–194 (1974).
24. J. F. Besseling, Post-buckling and nonlinear analysis by the finite element method as a supplement to a linear analysis. *ZAMM* **55**, T3-T16 (1975).
25. B. O. Almroth, F. A. Brogan and P. Stern, Automatic choice of global shape functions in structural analysis. *AIAA J.* **16**, 525–528 (1978).
26. D. A. Nagy, Modal representation of geometrically nonlinear behavior by the finite element method. *Comput. Structures* **10**, 683–688 (1979).
27. D. A. Nagy and M. König, Geometrically nonlinear finite element behavior using buckling mode superposition. *Comput. Meth. Appl. Mech. Engng* **19**, 447–484 (1979).
28. A. K. Noor and J. M. Peters, Reduced basis technique for nonlinear analysis of structures. *AIAA J.* **18**(4), 455–462 (Apr. 1980).
29. A. K. Noor, C. M. Andersen and J. M. Peters, Global-local approach for nonlinear shell analysis. *Proc. Seventh ASCE Conf. Electronic Computation*, pp. 634–657 Washington University, St. Louis, Missouri (6–8 Aug. 1979).
30. A. K. Noor and J. M. Peters, Nonlinear analysis via global-local mixed finite element approach. *Int. J. Num. Meth. Engng* (to appear).
31. P. G. Bergan, I. Holand and T. H. Søreide, Use of current stiffness parameter in solution of nonlinear problems, In *Energy Methods in Finite Element Analysis*, pp. 265–282. Wiley, New York (1979).
32. P. G. Bergan, G. Horrigmoe, B. Kråkeland and T. H. Søreide. Solution techniques for nonlinear finite element problems. *Int. J. Num. Meth. Engng* **12**, 1677–1696 (1978).
33. A. K. Noor and S. J. Hartley, Nonlinear shell analysis via mixed isoparametric elements. *Comput. Structures* **7**, 615–626 (1977).

34. A. K. Noor and J. M. Peters, Mixed models and reduced/selective integration displacement models for nonlinear analysis of curved beams. *Int. J. Num. Meth. Engng* (to appear).
35. B. M. Fraeijs de Veubeke, M. Geradin, A. Huck and M. A. Hogge, Structural dynamics and heat conduction. *Lecture Notes for Course No.* 126, International Center for Mechanical Sciences, Udine, Italy. Pergamon Press, Oxford (1972).
36. K. Bell, DYNOGS—A computer program for dynamic analysis of off-shore gravity platforms. *Theoretical Manual-SINTEF.* Norwegian Institute of Technology, Trondheim (1978).
37. R. E. Nickell, Nonlinear dynamics by mode superposition. *J. Comput. Meth. Appl. Mech. Engng* **7**, 107–129 (1976).
38. K. J. Bathe, Finite element formulation, modeling and solution of nonlinear dynamic problems. In *Numerical Methods for Partial Differential Equations.* Academic Press, New York (1979).
39. S. N. Remseth, Nonlinear static and dynamic analysis of framed structures. *Comput. Structures* **10**, 879–897 (1979).
40. N. F. Morris, The use of modal superposition in nonlinear dynamics. *Comput. Structures* **7**, 65–72 (1977).
41. A. K. Noor, J. M. Peters and C. M. Andersen, Two-stage Rayleigh–Ritz technique for nonlinear analysis of structures. In *Innovative Numerical Analysis for the Applied Engineering Sciences, Proc. Second Int. Symp. Innovative Num. Analysis in Appl. Engng Sci.* June 16–20 1980, *Montreal, Canada*, pp. 743–753. University Press of Virginia, Charlottesville, Virginia (1980).
42. R. F. Hartung and R. E. Ball, A comparison of several computer solutions to three structural shell analysis problems. *AFFDL-TR-73-15* (Apr. 1973).
43. B. O. Almroth and A. M. C. Holmes, Buckling of shells with cutouts, experiments and analysis. *Int. J. Solids Structures* **8**, 1057–1071 (1972).
44. G. R. Thomas and R. H. Gallagher, A Triangular Thin Shell Finite Element: Nonlinear Analysis, *NASA CR-2483* (July 1975).
45. T. Matsui and O. Matsuoka, A new finite element scheme for instability analysis of thin shells. *Int. J. Num. Meth. Engng* **10**, 145–170 (1976).
46. J. A. Stricklin, Geometrically nonlinear static and dynamic analysis of shells of revolution. In *High Speed Computing of Elastic Structures* **1**, pp. 383–412. University of Liege (1971).
47. J. F. McNamara and P. V. Marcal, Incremental stiffness method for finite element analysis of the nonlinear dynamic problem. In *Numerical and Computer Methods in Structural Mechanics*, 353–376. Academic Press, New York (1973).
48. L. A. Schmit and H. Miura, Approximation concepts for efficient structural synthesis. *NASA CR-2552*, (Mar. 1976).

Computers & Structures, Vol. 13, pp. 45–53, 1981
Printed in Great Britain.

0045-7949/81/010045-09$02.00/0

ADAPTIVE LOAD INCREMENTATION IN ELASTIC–PLASTIC FINITE ELEMENT ANALYSIS†

DENNIS M. TRACEY and COLIN E. FREESE

Mechanics and Engineering Laboratory, Army Materials and Mechanics Research Center, Watertown, MA 02172, U.S.A.

(*Received* 9 *May* 1980)

Abstract—The paper presents a strategy to control load path discretization error in elastic–perfectly plastic finite element analysis. The load path discretization is included as part of the nonlinear problem, using the strategy. At each stage in the incrementation, the load step size is treated as a variable which is forced to adapt to the current structural stiffness gradient. The step size is determined during the numerical solution, using a selection criterion which restricts changes in yield surface stress state at points within the plastic zone.

The strategy has been developed for a particular, assumed displacement, "incremental secant stiffness" formulation. The formulation *per se* is not new; it has been presented by Rice and Tracey [1]. Average stiffnesses are used to account for elastic plastic boundary and flow rule changes during the step. The formulation is examined in detail, to allow discussion of the approximations which are made and also to guide implementation. The 2D problems of plane stress, plane strain and axisymmetric deformation are considered. Simple test solutions are used to demonstrate that solution error can be effectively monitored by the yield surface deviatoric stress change, and this suggests the step size selection criterion that is employed.

A new solution algorithm for adaptive incrementation is the major contribution of the paper. With the algorithm, the nonlinear incremental secant equilibrium equation is solved subject to the selection criterion which is viewed as a constraint condition on the nodal variables. It appears that the algorithm could be used to advantage in other structural mechanics problem areas.

INTRODUCTION

Finite element solutions of flow theory plasticity problems in general are dependent upon load path discretization. This poses a problem of error control in practice, and here we consider the issue for small deformation elastic–plastic problems which use the Prandtl–Reuss constitutive relationships. When employing this constitutive theory, it is necessary to trace the stress and strain history of material points during the application of load, to account for the continually changing character of the plastic flow throughout the structure. The load path discretization dependency results from approximations used in representing the constitutive equations over the finite load steps of an analysis. The nature of the approximations vary with formulation, thus specialized error control strategies must be established. Here we consider the problem for the elastic perfectly plastic, assumed displacement formulation that was developed by Rice and Tracey [1].

In the formulation, the spatial distribution of displacement is assumed, and at each load step the basic unknown is the array of nodal displacement increments, $\Delta \mathbf{U}_i$. The load step number is denoted by the subscript i. If the vector $\mathbf{P}$ represents a segment of the load path, with property that over the segment individual nodal load components increase from zero in fixed proportion to each other, then the incremental equilibrium equation to be solved corresponding to a load step $\lambda_i \mathbf{P}$ is given by

$$\mathbf{K}\Delta \mathbf{U}_i = \lambda_i \mathbf{P}. \tag{1}$$

The stiffness matrix $\mathbf{K}$ is defined to account for the plastic yielding, and hence we use what is commonly called a "tangent modulus" formulation.

The most primitive tangent modulus formulation determines $\mathbf{K}$ on the basis of the stress and deformation state, and plastic zone at the beginning of a step. Such a "tangent stiffness" approach leads to problems of load imbalance, in the sense that calculated stress distributions do not equilibrate applied loads. The source of this imbalance is largely due to corrective procedures that are necessary to satisfy the yield condition after a step solution. It occurs whenever different constitutive relationships are used for stiffness definition and stress computation,

In the Rice and Tracey [1] formulation step average stiffnesses are used, with the averages defined as functions of the undetermined displacement increment. It is perhaps best called an "incremental secant stiffness" formulation. The load imbalance problem is essentially alleviated with this formulation because it is self-consistent as regards the constitutive law. Step average element stiffnesses are used which approximately account for elastic–plastic boundary changes and also for changes which occur in the flow rule at locations within the plastic zone. Importantly, the averages are defined so as to guarantee satisfaction of the yield condition at the end of a step, and thus corrective procedures

†To be presented at the Symposium on Computational Methods in Nonlinear Structural and Solid Mechanics (Oct. 1980), Arlington, Virginia.

are not required. Whereas a tangent stiffness formulation poses a linear problem at each step, the incremental secant stiffness problem is nonlinear. At each load step, the problem is to determine $\Delta \mathbf{U}_i$ which satisfies the nonlinear equation

$$\mathbf{K}(\Delta \mathbf{U}_i)\Delta \mathbf{U}_i = \lambda_i \mathbf{P}. \tag{2}$$

It is clear that in general a different endpoint stress, strain and displacement solution, i.e. $\mathbf{U} = \Sigma \Delta \mathbf{U}_i$, results for each discretization of the vector $\mathbf{P}$. Differences from that solution which would result with infinitesimal step sizes constitutes the discretization error that concerns us in this report. From test solutions, we show in the following that an effective way to control discretization error when using the incremental secant stiffness formulation is by limiting the yield surface deviatoric stress change that occurs during the plastic deformation of a step. This serves to define the step size selection criterion for our adaptive load incrementation solution algorithm.

With the adaptive algorithm, discretization is accomplished automatically, as part of the solution process. The scheme is designed to adjust step size according to a specified maximum allowable stress change. In essence at each step the equilibrium equation is solved subject to a constraint

$$g(\Delta \mathbf{U}_i) = 0 \tag{3}$$

which follows from the selection criterion. Using the algorithm allows a set of incremental solutions to be obtained which are consistently spaced along the load path, in contrast to the arbitrary spacing that can result with *a priori* discretization choices. Efficient convergence studies can be readily performed by systematically decreasing the specified maximum allowable stress change value.

The adaptive algorithm was developed during the course of a study aimed at improving our quantitative understanding of errors which might follow from the incremental secant stiffness formulation [1]. The error control strategy which we present here is designed specifically for this formulation. Being that the strategy is so specialized, we have elected to start the report with a basic review of the formulation. This serves three useful purposes. It allows a thorough discussion of a previously unrecognized complication in the plane stress problem, which has to do with the proper definition of the yield surface secant approximation. Next, it clearly identifies the nature of the approximations being made, thus providing the background for the subsequent discussion. Lastly, the review should allow rapid implementation by specialists who may be interested in testing the solution algorithm.

Following the formulation section, we motivate the choice of our step size selection criterion by considering solution errors for two trivial homogeneous deformation problems. A detailed description of the adaptive algorithm is then given. We conclude with a discussion of solutions for a thick-walled cylinder under monotonic and cyclic pressurization to demonstrate the performance of the algorithm.

INCREMENTAL SECANT STIFFNESS FORMULATION

Here we describe the formulations for the "two-dimensional" problems of plane stress, plane strain, and axisymmetric deformation. We start with the incremental equilibrium equations and then concentrate on the operations involved in the computation of the step-wise average element stiffness matrix. To meet the above mentioned purposes of this section, the discussion by necessity is very detailed and methodical.

It suffices to consider equilibrium of a single element. If the nodal degrees of freedom $\Delta \mathbf{U}_i$ involve motion in the x, y plane, then the group of strain increment components involved in the internal work of deformation are $(\Delta\varepsilon_{xx}, \Delta\varepsilon_{yy}, \Delta\gamma_{xy})$ for the planar problems and $(\Delta\varepsilon_{xx}, \Delta\varepsilon_{yy}, \Delta\varepsilon_{zz}, \Delta\gamma_{xy})$ for problems of axisymmetry. Using the vector $\Delta\boldsymbol{\varepsilon}_i$ to represent these respective groups at load step i, the element interpolation function provides the relationship

$$\Delta\boldsymbol{\varepsilon}_i = \mathbf{B}\Delta \mathbf{U}_i. \tag{4}$$

If $\Delta\boldsymbol{\sigma}_i$ is the stress increment vector that is the work conjugate to $\Delta\boldsymbol{\varepsilon}_i$ then the principle of virtual work gives the equilibrium condition of the element as

$$\int \mathbf{B}^T \Delta\boldsymbol{\sigma}_i \, \mathrm{d}V = \lambda_i \mathbf{P}. \tag{5}$$

The constitutive relationship

$$\Delta\boldsymbol{\sigma}_i = \mathbf{D}\Delta\boldsymbol{\varepsilon}_i \tag{6}$$

allows us to write the matrix stiffness equation as

$$\left[\int \mathbf{B}^T\mathbf{D}\mathbf{B} \, \mathrm{d}V\right] \Delta \mathbf{U}_i = \lambda_i P. \tag{7}$$

Of the system of equations represented by (7), those corresponding to specified components of $\Delta \mathbf{U}_i$ must be deleted, and the load vector must include terms corresponding to specified non-zero values. Furthermore, in general there is the need to assembly equations for a group of elements. For our present purposes these considerations need not be addressed in depth. Here we are concerned mainly with the details of computation of the stiffness matrix in eqn (7) for a generic element.

The tangent stiffness approach evaluates $\mathbf{K}$ using constitutive matrices $\mathbf{D}$ that represent the current state of yielding, both as regards the elastic–plastic boundary and flow capability within the plastic zone. The incremental secant formulation on the other hand uses a step average $\mathbf{D}$ which accounts for elastic–plastic boundary changes and flow direction changes during the step. The designation "secant stiffness" is used to underscore the fact that the averaging is done over the (undetermined) deformation interval. The $\mathbf{D}$ matrix is dependent upon $\Delta \mathbf{U}_i$; thus the nonlinear functional form of eqn (2) involving $\mathbf{K}(\Delta \mathbf{U}_i)$.

By the nature of flow theory plasticity there is no explicit functional relationship $\mathbf{D}(\Delta \mathbf{U}_i)$ that can be used in the formulation. The matrix must be numerically generated as part of the iterative solution process. The process used in previous fixed load step analyses (where $\lambda_i \mathbf{P}$ was specified) involves the formation of a trial stiffness matrix and solution for an estimate to $\Delta \mathbf{U}_i$ at each iteration cycle. If $\Delta \mathbf{U}_i^{j-1}$ is the solution for cycle $j-1$, then for cycle j, $\mathbf{D}$ (and thus $\mathbf{K}$) is computed on the basis of $\Delta \mathbf{U}_i^{j-1}$ and the improved solution follows from

$$\mathbf{K}(\Delta \mathbf{U}_i^{j-1})\Delta \mathbf{U}_i^{j} = \lambda_i \mathbf{P}. \tag{8}$$

The solution to the true nonlinear problem results by iterating to convergence. The adaptive solution algorithm modifies this process by treating λ_i as an unknown. Nonetheless, for either fixed or variable load step size

the nature of the incremental secant stiffness formulation [1] is defined by the operations involved in computing $\mathbf{K}(\Delta\mathbf{U}_i^{j-1})$. We concentrate on these operations in the remainder of the section.

The components of the stiffness matrix are defined as volume integrals, eqn (7), and these are evaluated using Gaussian quadrature. The main problem then lies in evaluating the matrix product $\mathbf{B}^T\mathbf{D}\mathbf{B}$ at a few distinct "integration stations" within the element volume. If there are N degrees of freedom, $\mathbf{B}$ is of order $3\times N$ and $\mathbf{D}$ is of order 3×3 for the planar problems, while for axisymmetric problems these respective orders are $4\times N$ and 4×4. To be able to compute $\mathbf{D}$ at a station requires that the starting stress state be known at that location, and also that the strain increments suggested by the active solution vector $\Delta\mathbf{U}_i^j$ be calculated using eqn (4). We will not consider strain hardening here so that further state data is not needed. In the planar formulations it proves convenient to use four component arrays $\mathbf{S}^0$ and $\Delta\mathbf{E}$ to represent the starting stress state and strain increment. The arrays use an xx, yy, zz, xy component ordering. For plane strain the zz component of $\Delta\mathbf{E}$ is identically zero. For plane stress the zz component of $\mathbf{S}^0$ is identically zero, while the zz component of $\Delta\mathbf{E}$ is initially unknown and must be determined along with $\mathbf{D}$. Of course for axisymmetric problems there is no predetermined knowledge concerning any of the eight components of $\mathbf{S}^0$ and $\Delta\mathbf{E}$.

Along with the vectors $\mathbf{S}^0$ and $\Delta\mathbf{E}$, it proves convenient in the planar formulations to work with temporary 4×4 constitutive matrices. This also allows a parallel discussion ot the three problem classes. The necessary 3×3 $\mathbf{D}$ matrices are obtained through a concluding reduction operation. If $\mathbf{C}$ is such a 4×4 constitutive matrix, its function is simply defined according to

$$\begin{Bmatrix}\Delta\sigma_{xx}\\ \Delta\sigma_{yy}\\ \Delta\sigma_{zz}\\ \Delta\tau_{xy}\end{Bmatrix}=\begin{bmatrix}C_{11}&C_{12}&C_{13}&C_{14}\\ C_{21}&C_{22}&C_{23}&C_{24}\\ C_{31}&C_{32}&C_{33}&C_{34}\\ C_{41}&C_{42}&C_{43}&C_{44}\end{bmatrix}\begin{Bmatrix}\Delta\varepsilon_{xx}\\ \Delta\varepsilon_{yy}\\ \Delta\varepsilon_{zz}\\ \Delta\gamma_{xy}\end{Bmatrix}. \tag{9}$$

We concern ourselves with computing the components C_{ij}, and then for plane strain, since $\Delta\varepsilon_{zz}=0$, the 3×3 matrix follows as

$$\mathbf{D}_{plane\ strain}=\begin{bmatrix}C_{11}&C_{12}&C_{14}\\ C_{21}&C_{22}&C_{24}\\ C_{41}&C_{42}&C_{44}\end{bmatrix}. \tag{10}$$

For plane stress, the $\Delta\sigma_{zz}=0$ condition implies that $\Delta\varepsilon_{zz}$ depends upon the inplane strain increment components according to

$$\Delta\varepsilon_{zz}=\begin{bmatrix}-C_{31}/C_{33} & -C_{32}/C_{33} & -C_{34}/C_{33}\end{bmatrix}\begin{Bmatrix}\Delta\varepsilon_{xx}\\ \Delta\varepsilon_{yy}\\ \Delta\gamma_{xy}\end{Bmatrix} \tag{11}$$

Using eqn (11) to eliminate $\Delta\varepsilon_{zz}$ from the 1st, 2nd and 4th equations of (9) gives the 3×3 plane stress matrix as

$$\mathbf{D}_{plane\ stress}=\begin{bmatrix}C_{11}&C_{12}&C_{14}\\ C_{21}&C_{22}&C_{24}\\ C_{41}&C_{42}&C_{44}\end{bmatrix}-1/C_{33}\begin{Bmatrix}C_{13}\\ C_{23}\\ C_{43}\end{Bmatrix}\begin{bmatrix}C_{31}&C_{32}&C_{34}\end{bmatrix} \tag{12}$$

Of course for the axisymmetric case,

$$\mathbf{D}_{axisymmetric}=\mathbf{C}. \tag{13}$$

The 4×4 elastic matrix is given by

$$\mathbf{C}^e=2G\begin{bmatrix}1+\omega&\omega&\omega&0\\ \omega&1+\omega&\omega&0\\ \omega&\omega&1+\omega&0\\ 0&0&0&1/2\end{bmatrix} \tag{14}$$

where G is the shear modulus, and in terms of Poisson's ratio ν, $\omega=\nu/(1-2\nu)$.

The above serves as the background against which the constitutive matrix computations for an integration station we determine whether the station's strain increment $\Delta\mathbf{E}$ is purely elastic: purely elastic over a portion of the interval, elastic–plastic over the remainder; or elastic–plastic over the entire interval. We start with the hypothesis that it is purely elastic and compute the corresponding final stress state $\mathbf{S}^2$ according to

$$\mathbf{S}^2=\mathbf{C}^e\Delta\mathbf{E}+\mathbf{S}^0. \tag{15}$$

For plane stress, $\Delta\varepsilon_{zz}$ in $\Delta\mathbf{E}$ is tentatively considered to be given by eqn (11) using C^e_{3j}. If $\mathbf{S}^2$ falls within the Mises yield surface, the elastic hypothesis is taken to be correct and $\mathbf{C}^e$ is then used to define $\mathbf{D}$ for the point, using either (10), (12) or (13). It perhaps should be emphasized here that points which have $\mathbf{S}^0$ satisfying the yield criterion could fall into this elastic category for the step, indicating that the point unloads. In terms of the modulus of the deviatoric stress vector $\mathbf{s}$ and tensile flow stress Y, the Mises yield surface is defined by

$$\sqrt{3/2}|\mathbf{s}|=Y. \tag{16}$$

To account for the complementary shear stress τ_{yx}, $\mathbf{s}$ is a five component vector. The stress states used in the formulation are illustrated in Fig. 1 relative to the yield surface in deviatoric stress space.

If $\mathbf{S}^2$ falls outside the yield surface, the next operation determines whether or not there is a subinterval of purely elastic response before yield occurs. The total strain increment $\Delta\mathbf{E}$ is taken to be the result of a proportional straining process, i.e. components of $\Delta\mathbf{E}$ are treated as though they increase in fixed proportion to each other throughout the interval. Then the elastic subinterval is established by the scalar f_e ("fraction elastic") which is the non-negative root to the quadratic equation

$$\sqrt{3/2}|\mathbf{s}^0+f_e(\mathbf{s}^2-\mathbf{s}^0)|=Y. \tag{17}$$

In this expression $\mathbf{s}^0$ and $\mathbf{s}^2$ are the deviatoric parts of the stress states $\mathbf{S}^0$ and $\mathbf{S}^2$. The strain $f_e\Delta\mathbf{E}$ is considered purely elastic, and it brings the point to yield at the yield surface stress state

$$\mathbf{S}^1=\mathbf{S}^0+f_e(\mathbf{S}^2-\mathbf{S}^0). \tag{18}$$

The strain $(1-f_e)\Delta\varepsilon$ is taken to be elastic–plastic, and it is considered to occur after $\mathbf{S}^1$ is reached. This case of elastic/elastic-plastic partitioning of the deformation applies not only for cases of first yield, but in general. For instance, it applies when there is unloading from a yield surface stress state $\mathbf{S}^0$ and reyielding at $\mathbf{S}^1$ during the interval. For cases of elastic–plastic straining over the entire interval, $f_e=0$.

The weighting factor f_e is used to define the average constitutive matrix at the integration station in question, for the current solution iteration cycle. If $\mathbf{C}^{ep}$ is the constitutive matrix that applies over the elastic–plastic subinterval--a matrix which follows from the Prandtl–Reuss equations and the averaging techniques discussed below--and if $\mathbf{D}^{ep}$ is the reduced matrix

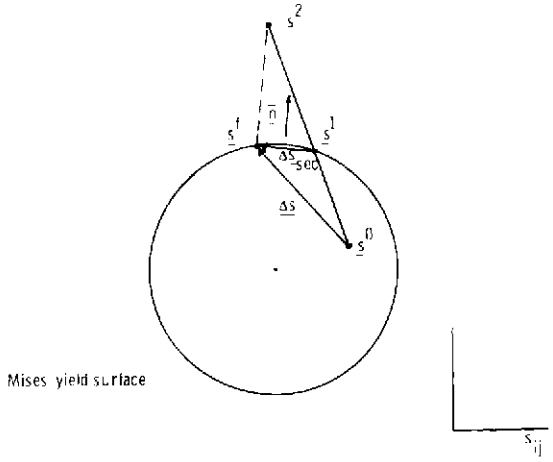

Fig. 1. Illustration of stress states of the formulation in deviatoric space.

following from $\mathbf{C}^{ep}$, then the average $\mathbf{D}$ matrix is given by

$$\mathbf{D}=f_e\mathbf{D}^e+(1-f_e)\mathbf{D}^{ep}. \tag{19}$$

$\mathbf{D}^e$ is the elastic matrix that follows from $\mathbf{C}^e$. This partitioning of the interval into elastic and elastic–plastic subintervals, and the use of a corresponding step average stiffness was suggested by the work of Marcal and King [2]. They referred to the approach as the "partial-stiffness" method.

Our next concern is to define $\mathbf{C}^{ep}$ in a way that is appropriate to the elastic–plastic strain increment $(1-f_e)\Delta\varepsilon$. We will in our discussion employ the dimensionless deviatoric stress vector $\mathbf{n}=\sqrt{3/2}\mathbf{s}/Y$. This vector considered in stress space is directed normal to the yield surface, and it has unit length when s satisfies the yield criterion. The Prandtl–Reuss equations for infinitesimal deformation starting at $\mathbf{S}^1$ would suggest that $\mathbf{C}^{ep}$ be given by

$$\mathbf{C}^e-2G\begin{Bmatrix} n^1_{xx}\\ n^1_{yy}\\ n^1_{zz}\\ n^1_{xy}\end{Bmatrix}\begin{bmatrix} n^1_{xx} & n^1_{yy} & n^1_{zz} & n^1_{xy}\end{bmatrix}. \tag{20}$$

However, this choice of $\mathbf{C}^{ep}$ would allow a stress change which is tangent to the yield surface, and thus result in a final stress state $\mathbf{S}^0+\Delta\mathbf{S}$ which violates the yield criterion. We define $\mathbf{C}^{ep}$ using an average normal vector so that the yield criterion is satisfied exactly at the end of the step. This approach can be contrasted with formulations which use the instantaneous matrix (20) and satisfy the yield criterion by *a posteriori* scaling of the stress solution. This latter procedure carries the penalty of creating a load imbalance, i.e. a violation of the incremental equilibrium equation (5).

Rice and Tracey [1] have demonstrated that if the average unit normal is defined, in terms of $\mathbf{s}^1$ and the elastically calculated final deviatoric stress state $\mathbf{s}^2$, as

$$\bar{\mathbf{n}}=(\mathbf{s}^1+\mathbf{s}^2)/|\mathbf{s}^1+\mathbf{s}^2| \tag{21}$$

and used in (20) instead of $\mathbf{n}^1$, then the yield condition is satisfied at the end of the step. Using this average normal corresponds to a chord approximation to the yield circle. It essentially states that the material offers no resistance to straining proportional to $\bar{\mathbf{n}}$. Hence in terms of $\bar{\mathbf{n}}$, $\mathbf{C}^{ep}$ is given by

$$\mathbf{C}^{ep}=\mathbf{C}^e-2G\begin{Bmatrix} \bar{n}_{xx}\\ \bar{n}_{yy}\\ \bar{n}_{zz}\\ \bar{n}_{xy}\end{Bmatrix}\begin{bmatrix} \bar{n}_{xx} & \bar{n}_{yy} & \bar{n}_{zz} & \bar{n}_{xy}\end{bmatrix}. \tag{22}$$

For plane stress problems, there is a complication in the above definition of $\mathbf{C}^{ep}$ which follows from the indeterminacy of $\Delta\varepsilon_{zz}$. The elastically calculated final stress state $\mathbf{S}^2$ used in the definition of $\bar{\mathbf{n}}$ depends upon $\Delta\mathbf{E}$, according to eqn (15). The original hypothesis that the strain increment is purely elastic for the step allows an elastic computation for $\Delta\varepsilon_{zz}$. From this a provisional $\mathbf{S}^2$ is employed to determine f_e and $\mathbf{S}^1$. However, computation of the proper $\mathbf{S}^2$ is predicated upon knowing the elastic–plastic portion of $\Delta\varepsilon_{zz}$, $\Delta\varepsilon^{ep}_{zz}$, which corresponds to the inplane strain $(1-f_e)\Delta\varepsilon$. To satisfy the $\Delta\sigma_{zz}=0$ condition over the elastic–plastic subinterval, $\Delta\varepsilon^{ep}_{zz}$ is determined from the following (nonlinear) equation

$$0=(1-f_e)(C^{ep}_{31}\Delta\varepsilon_{xx}+C^{ep}_{32}\Delta\varepsilon_{yy}+C^{ep}_{34}\Delta\gamma_{xy})+C^{ep}_{33}\Delta\varepsilon^{ep}_{zz}. \tag{23}$$

This equation is solved using an iterative algorithm. The incipient yield matrix (20) provides starting values for C^{ep}_{3j}. Solving for a trial $\Delta\varepsilon^{ep}_{zz}$ allows computation of a trial $\mathbf{S}^2$ and improved C^{ep}_{3j}, etc. The process has shown rapid convergence properties. The solution provides a constitutive matrix which insures that both the yield criterion and the planar stress condition are satisfied at the conclusion of the step.

With $\mathbf{C}^{ep}$ established, the step average $\mathbf{D}$ follows from either eqns (10), (12) or (13), and (19) for the integration point in question. Next, the product $\mathbf{B}^T\mathbf{DB}$ is computed and scaled by the necessary volume weighting factor, and this represents the contribution of one station to $\mathbf{K}(\Delta\mathbf{U}^{j-1}_i)$ in eqn (8). The total stiffness results from contributions from all integration points of all elements of the structure. The linear system of equations is solved for $\Delta\mathbf{U}^j_i$ and the process is continued until successive solutions show insignificant differences.

This completes our description of the incremental secant stiffness formulation for 2D elastic–perfectly plastic problems. The character of the formulation *per se* is as outlined regardless of whether the load step size is prescribed, as in the standard analysis procedure or treated as a variable, as in our adaptive scheme. By virtue of the subinterval partitioning and average flow rule techniques, the formulation is able to accommodate an arbitrary size load step. An equilibrium state which satisfies the yield condition throughout the plastic zone is always obtained, regardless of step size. However, the need for averaging over a step implies that solutions will always possess some degree of discretization error. We consider the means to controlling this error in the next section.

CONTROLLING LOAD PATH DISCRETIZATION ERROR

When considering the issue of error control, it is first necessary to identify the approximations of the formulation, and then find a convenient way to quantitatively monitor the solution errors which follow from these approximations. In our formulation, error stems from the averaging techniques used to approximate elastic–plastic boundary and plastic flow direction

changes during a load step. We have found that the level of solution error which results from either of these approximations can be conveniently monitored in terms of the yield surface deviatoric stress change $\Delta \mathbf{s} = (\mathbf{s}^f - \mathbf{s}^1)$, Fig. 1. To demonstrate this, we consider the errors in solutions for two simple homogeneous deformation problems. These solutions were gained by prescribing the discretization and using the standard solution algorithm. The results suggest that an effective general error control strategy would be one which selects step size according to a $\Delta \mathbf{s}_{sec}$ limitation.

We begin by considering the tensile loading of a thin-walled cylinder which is first twisted from a stress free state to incipient yield. During the tensile loading a constraint is imposed so that shear strain remains fixed at the magnitude $1/\sqrt{3}Y/G$, hence additional deformation is strictly extensional. As the tensile stress σ increases from zero, the shear stress τ decreases to follow the Mises yield surface, which for this problem is given by

$$\sigma^2 + 3\tau^2 = Y^2. \tag{24}$$

As τ decreases, so does the cylinder's resistance to further extension, and hence uncontrolled plastic extensional straining results as $\sigma \to Y$.

At a given value of σ, the extensional strain ε is given by the relationship

$$\varepsilon = \frac{Y}{3E}\left[(1+\nu)\ln\left(\frac{1+\sigma/Y}{1-\sigma/Y}\right) + (1-2\nu)\sigma/Y\right]. \tag{25}$$

This exact solution is derived in Hill [3]. We can use it here to quantify finite element solution discretization errors. The problem has no spatial variations, so it can be readily treated using a single constant state triangular element, with the plane stress formulation. In eqn (25) and below, E represents Young's modulus.

Consider the case of loading from the incipient yield state to a σ value of $0.8Y$. According to eqn (25) ε then equals $1.059Y/E$, for $\nu = 0.3$. However, numerically the solution for ε depends upon how the tensile loading is discretized. For instance, using one step, so that the applied load increment corresponds to $\Delta\sigma = 0.8Y$, gives an ε value of $0.973Y/E$. With four steps of $\Delta\sigma = 0.2Y$, the ε value results as $1.051Y/E$. If we consider loading to $\sigma = Y$, the exact solution suggests that $\varepsilon \to \infty$, corresponding to the attainment of limit load. However, numerically we obtained ε values of 1.770, 2.208 and $2.985Y/E$ for 1,2 and 10 uniform step discretizations, respectively.

These deviations from the exact solution are due entirely to the average flow rule that is used to define the stiffness at each step. The approximation can be geometrically constructed as a piecewise linear model of the yield ellipse (24). The solution improvements following from the step size refinements correspond to the decrease of the chordal segments of the model. In general terms, the improvements correspond to decreasing $|\Delta \mathbf{s}_{sec}|$ magnitudes. We expect that a strategy of controlling this stress variable will be effective in limiting the average flow rule approximation in the general problem, where $\Delta \mathbf{s}_{sec}$ varies from point to point. Of course in general, contrary to the case for this problem, it is not possible to predict the relationship between load step size and the $\Delta \mathbf{s}_{sec}$ distribution. This is why an adaptive load incrementation procedure is desirable.

Another distinctly different source of error is the method used for partitioning strain increments into elastic and elastic-plastic parts to account for yielding during a step. The solution gained using this scheme can be exact only if there is proportional straining in the load interval. The nature of the approximation can be readily appreciated by considering the problem of homogeneous uniaxial extension to a strain level beyond yield—starting from a stress free state. Strain components do not increase in fixed proportion for this problem: if U is the imposed extension over a length L and if the contraction over a length L is V, then before yield occurs $\Delta V/\Delta U = \nu$, while afterwards $\Delta V/\Delta U = 1/2$. Numerical solutions show discretization dependency. Using a plane stress constant state triangle we solved for the case having the imposed extensional strain U/L equal to 10 Y/E, and $\nu = 1/4$. V should result as 4.75 YL/E according to the formula

$$V/L = \nu Y/E + 1/2(U/L - Y/E) \tag{26}$$

which applies when $U/L > Y/E$. In the table we give solutions for eight uniform step size discretizations. A one step analysis resulted in a 23% error in V. The exact solution was obtained using 10 steps and 20 steps, but not when 16 steps were used. The exact solution results only when partitioning is not done!

The error occurs because the incipient yield state $\mathbf{S}^1$ is determined on the basis of the ratio of the components of the total strain change, as defined at the current iteration cycle. For instance, in the case of one step loading, the exact ratio $\Delta V/\Delta U$ is 4.75. Considered to be the result of proportional straining, this ratio suggests that first yield occurs at a biaxial stress state. In all cases, $\mathbf{S}^f$ resulted as a uniaxial stress state of magnitude Y, as is necessary to satisfy the yield condition and equilibrium. But since an inexact partitioning is done, the approximate contraction results. From the table, we see that the degree of error is reflected by the value of $|\Delta \mathbf{s}_{sec}|$. It is expected that partitioning error in the general problem can be monitored in terms of this variable.

The issue of accurately tracing elastic plastic boundary movement is of course much more complicated than the above example would suggest. In general, within an arbitrary load interval, the deformation at a point can be non-monotonic, possibly involving multiple unloadings and reyieldings. The simple elastic/elastic plastic partitioning could then be a gross approximation. However, we expect that such approximations can be monitored in terms of $|\Delta \mathbf{s}_{sec}|$. As this "secant stress" decreases, the possibilities of non-monotonic deformation occurring should likewise decrease.

Having a way to quantitatively monitor solution error gives rise to the next concern, which is choosing a viable criterion to be used for step size selection. We have chosen a criterion which places a limit on the maximum value of $|\Delta \mathbf{s}_{sec}|$ that can occur in the structure during a load step. The standard analysis approach of prescribing step size is clearly unsuited for such an error control strategy. Hence, we have developed the following adaptive solution algorithm which allows a numerical determination of the required discretization.

ADAPTIVE SOLUTION ALGORITHM

With this adaptive incrementation approach, the size of each load step is determined so that the max-

imum $|\Delta \mathbf{s}_{sec}|$ results equal to a prescribed fraction of the yield stress, αY. This selection criterion is viewed as a constraint condition on the nodal variables, and we express this condition as

$$g(\Delta \mathbf{U}_i) = |\Delta \mathbf{s}_{sec}|^{max} - \alpha Y = 0. \tag{27}$$

The solution for a step consists of the vector $\Delta \mathbf{U}_i$ and step size scalar λ_i which satisfy the stiffness equation (2) and the constraint condition (27).

The algorithm is designed to automatically discretize a load history which may involve a combination of prescribed tractions, body forces and displacements. The history is considered in segments, selected so that during each one the prescribed loading parameters increase from base values of zero in fixed proportion to each other. $\mathbf{P}$ represents the nodal load vector that would correspond to the final values of the parameters in a particular segment. If there are non-zero specified components of displacement, then at each step within the segment, $\lambda_i \mathbf{P}$ involves elements of $\mathbf{K}$ multiplying the specified values.

Often at the beginning of a load segment, there is an interval during which the behavior is purely elastic. For instance in reverse loadings, such as for the pressure cycling of the example problem below, there is purely elastic behavior until incipient reverse yield conditions are reached. Hence, as a standard practice, at the first step of each load segment, it is assumed that the problem is linear. The elastic stiffness is employed and the solution is scaled to have λ_1 correspond to the incipient yield state.

Beyond incipient yield the explicit form of the equilibrium equation is undetermined at a step, as has been discussed above. An iterative process is necessary and it begins with an estimate for the load step size, λ_i^0, and a choice of a starting displacement increment vector $\Delta \mathbf{U}_i^0$ to define the first trial stiffness. For these starting values we have used λ_{i-1}, and the null vector $\mathbf{0}$; the latter choice implying that the current stress state defines the flow conditions for the first iteration cycle. The matrix equation for $\Delta \mathbf{U}_i^1$ then takes the form

$$\mathbf{K}(\Delta \mathbf{U}_i^0) \Delta \mathbf{U}_i^1 = \lambda_i^0 \mathbf{P}. \tag{28}$$

Components of $\mathbf{K}(\Delta \mathbf{U}_i^0)$ enter the definition of $\mathbf{P}$ for cases having non-zero specified displacement components.

In general $\Delta \mathbf{U}_i^1$ will not satisfy the constraint condition, so that a search is performed for a scalar multiple of $\Delta \mathbf{U}_i^1$ which does satisfy it. This scaled solution is used as the trial vector for the next cycle of iteration. The improved step size trial follows from interpreting the scale factor as being equal to λ_i^1/λ_i^0. In general terms, the problem after (28) is solved for $\Delta \mathbf{U}_i^1$ is to determine λ_i^1 which satisfies

$$g(\Delta \mathbf{U}_i^1 \cdot \lambda_i^1/\lambda_i^0) = 0. \tag{29}$$

The search procedure which gives λ_i^1 is as follows. Once $\Delta \mathbf{U}_i^1$ is obtained, the "secant stress" $\Delta \mathbf{s}_{sec}$ is computed at all plastically deforming points in the structure. The maximum $|\Delta \mathbf{s}_{sec}^1|/\alpha Y$ is used to scale $\Delta \mathbf{U}_i^1$. The scaled solution suggests a revised stress distribution, so that the search and scaling is repeated until convergence. The only difficulty encountered in this procedure is when limit load is being approached, since then straining is purely plastic and only slight stress changes are possible. Actually, we have found this to be a convenient way to detect the attainment of limit conditions. Prior to the computation of the stress change, a test is employed which compares the plastic and elastic strain changes. If the ratio of the moduli of these strain vectors exceeds 1000, then execution terminates with the message UNCONTROLLED PLASTIC FLOW.

The above operations for the first cycle of iteration sets the pattern for subsequent cycles. At cycle j, a stiffness matrix is formed according to the estimated displacement $\Delta \mathbf{U}_i^{j-1} \cdot \lambda_i^{j-1}/\lambda_i^{j-2}$, and a new displacement $\Delta \mathbf{U}_i^j$ is determined from

$$\mathbf{K}(\Delta \mathbf{U}_i^{j-1} \cdot \lambda_i^{j-1}/\lambda_i^{j-2}) \Delta \mathbf{U}_i^j = \lambda_i^{j-1} \mathbf{P}. \tag{30}$$

Once $\Delta \mathbf{U}_i^j$ is obtained, λ_i^j follows from

$$g(\Delta \mathbf{U}_i^j \cdot \lambda_i^j/\lambda_i^{j-1}) = 0. \tag{31}$$

This iterative process is continued until convergence; that is, until *both* $\Delta \mathbf{U}_i^j$ and λ_i^j show insignificant changes with further iteration. Since λ_i is determined on the basis of the secant stress distribution, a function of $\Delta \mathbf{U}_i$, λ_i^j and $\Delta \mathbf{U}_i^j$ converge concurrently. Hence, convergence can be conveniently monitored by observing the cycle to cycle change in the scalar λ_i^j. We have used a test which terminates iteration when the relative change in λ_i^j in two successive cycles falls below a specified tolerance δ. For the fixed load step algorithm, we use a test which terminates iteration when the relative change in the maximum secant stress modulus falls below δ.

Numerical results have shown the importance of using a strict convergence test in analysis. The value of δ in effect determines the relative degree of applied load-internal stress imbalance. The equilibrium condition (5) can be satisfied only if there are insignificant differences in the vectors $\Delta \mathbf{U}_i^{j-1}$ and $\Delta \mathbf{U}_i^j$. Data from the cylinder problem illustrates the point. Consider the case of loading from $\sigma = 0$ to $\sigma = Y/2$ in one step: The element stress results after the first four iteration cycles were found to be 0.4757, 0.4972, 0.4997 and 0.5000 Y. The rate of convergence varies with problem and step size of course. For the above problem with a final $\sigma = Y$, the stress results were 0.825, 0.915, 0.950 and 0.960 after the first four cycles. Hence, the value assigned to δ weighs heavily on the ultimate accuracy of a solution, and this must be considered in the accuracy/cost deliberations when undertaking an analysis.

To complete our discussion of the adaptive solution algorithm, we mention some additional restrictions that must be placed on the allowable magnitude of λ_i. Corresponding to the specification of definite load vectors $\mathbf{P}$, there is the need to restrict $\lambda_i < 1$, and furthermore $\Sigma \lambda_i = 1$. The final step to reach the total load will usually be smaller than that allowed by the constraint condition. For this case, the algorithm reverts to the fixed load step procedure. When $\mathbf{P}$ is indefinite in the sense that the final magnitude of the loading parameters are not specified, then λ_i is not restricted. This latter case applies to studies which seek to determine limit load values.

EXAMPLE ANALYSES USING ADAPTIVE INCREMENTATION

In practice, the most obvious value of the adaptive algorithm is that it produces a solution which has a consistent level of error from step to step, and this is accomplished by simply prescribing a value for the constraint parameter α. Clearly, the approach becomes more and more attractive as problem complexity

increases. However, when discussing the algorithm's performance characteristics, it is best to consider a problem that is well understood; so we consider here the analysis of a thick-walled cylinder under monotonic and cyclic pressure loadings.

A cylinder with an inner/outer radius ratio of 1/4 is considered. In the problem, axial strain is prevented, so that spatial variations are limited to the radial direction. Using an (r, θ, z) cylindrical coordinate system, only the displacement component U_r is non-zero. The analysis was undertaken using the 2D axisymmetric formulation, with a mesh of 60 four-node bilinear interpolation ring elements, and with nodal values of ΔU_z set equal to zero. In the (r, z) plane, the mesh would appear as a row of uniformly spaced square elements of edge length $a/20$. At each pressure step Δp, the loading consists of radial forces $\Delta p\, \pi a^2/20$ applied to the 2 nodes at $r = a$.

First we consider the results for a monotonic increase in pressure from a stress free state to limit conditions. The value for α was specified as 0.05. The incipient yield conditions were found at the expected pressure level $p_1 = 0.560\,Y$. During the computations of the 14th pressure step, execution terminated with the UNCONTROLLED PLASTIC FLOW message. This was at a pressure level of $1.609\,Y$, which agrees, to within a factor of 1.005, with the theoretical limit pressure $(2/\sqrt{3}) \ln (b/a)\,Y$. There is a precipitous drop in step size during the loading, and this is shown in Fig. 2. The

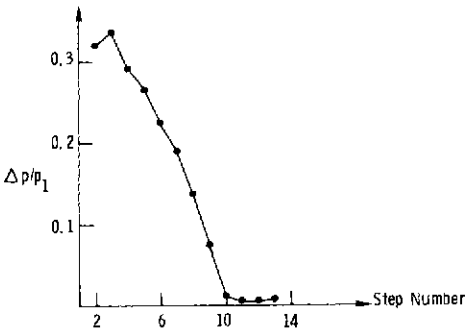

Fig. 2. Pressure steps as determined by adaptive algorithm for monotonic loading to limit conditions.

highly accurate determination of the limit pressure suggests that both the spatial and the load path discretizations incurred minor levels of approximation. The significant result here, of course, is that this very accurate load path discretization was obtained automatically, with the adaptive algorithm. In this analysis, the tolerance parameter δ was equal to 0.001. Four iterations were required, on the average, to meet the convergence test.

We can gain an appreciation for the nonlinear character of this problem and for some general features of solutions which are obtained with the formulation and solution algorithm by considering the yield surface stress changes which occur across the cylinder wall, corresponding to different pressure steps. Figure 3 shows $|\Delta \mathbf{s}\ |/Y$ plotted versus r/a, for 6 pressure steps. The distributions take on oscillatory forms, with the peak values of 0.05 following from the constraint condition. The peak always occurs at the elastic-plastic boundary, as defined by the previous step solution. By

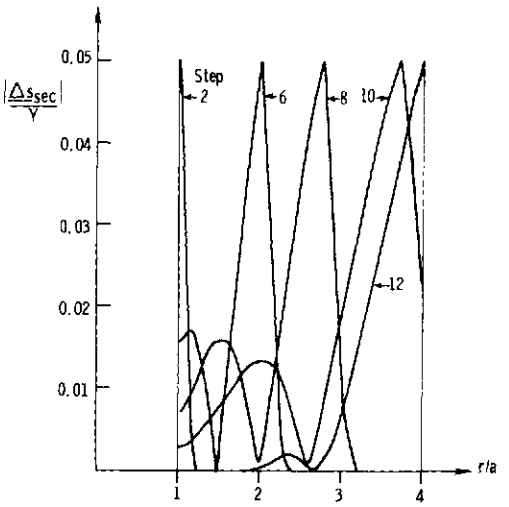

Fig. 3. Radial variation of yield surface deviatoric stress change for pressure steps in monotonic loading case.

definition, $\Delta \mathbf{s}_{sec}$ falls to zero at the newly determined elastic–plastic boundary and equals zero in the elastic region. Generally, the peaks and valleys of the distributions occur at the elastic plastic boundaries of previous steps. The outer surface of the cylinder yielded during the 10th pressure step. During steps 11–13, the maximum stress change was at this location, as the stress state there followed a history similar to that of plane strain uniaxial extension. It is perhaps worth restating here, relating to Figs. 2 and 3, that the basis of our error control strategy is that step size *per se* is immaterial. What is important is consistency of approximation, and this can be effectively achieved by limiting the yield surface deviatoric stress change at each step, as in Fig. 3.

In the cyclic analysis, pressure varied between the values of zero and $2.8p_1$. We followed the loading for $1\frac{1}{2}$ cycles using an α of 0.05, and the resulting discretization is illustrated in Fig. 4. As can be seen, 18 steps were found necessary to trace this load path. At peak load, the elastic–plastic boundary had advanced to $r = 3.38\,a$. The plastic zone elastically unloads during step 10 to a state of reverse incipient yield at the inner surface. The zone of reverse plastic flow spreads during steps 11–13 to $r = 1.23\,a$, at $p = 0$. For incompressible materials this boundary is known to be at $r = 1.26\,a$, [4]. We have taken ν as 0.3 in this problem. During step 14, the reverse plastic zone elastically unloads to a renewed state of forward incipient yield at the inner surface. The forward yielding spreads across the wall as the pressure increases during steps 15–18. At peak load, it was found that the elastic–plastic boundary had re-

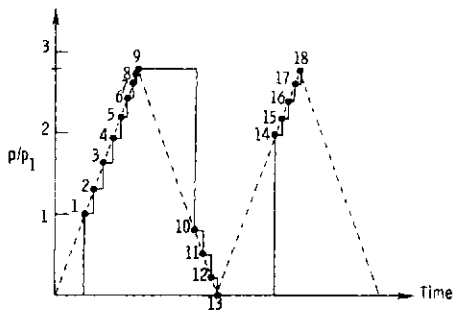

Fig. 4. Pressure discretization results in cyclic analysis.

gained its previous position at $r = 3.38$ a.

The radial distribution of the hoop stress $\sigma_{\theta\theta}$ takes on interesting variations during the pressure cycling, as displayed in Fig. 5. The monotonic and tensile character of the elastic solution is seen to give way to jagged distributions with peaks and valleys at the elastic–plastic boundaries and compression in the interior of the wall. Take the curve labeled 17, for instance. The first peak marks the current plastic boundary, the valley is at the boundary of the reverse plastic zone and the tensile peak is at the maximum pressure, forward plastic zone boundary. We determined that plastic flow during step 18 was essentially limited to $a < r < 1.23$ a, even though the entire region $a < r < 3.38$ a satisfied the yield condition at the conclusion of the step. Hence this smaller zone would be aptly called a cyclic plastic zone. The hoop stress distribution at step 18 shows no perceptible differences from that at step 9. This is a surprising result, as the stress state would be expected to display this cyclic character only for radial loading, such as for the incompressible case. The axial stress showed differences up to 6% at peak load levels 9 and 18, and these differences were confined to the cyclic plastic zone.

Further details of this problem could be discussed, including the dependence of the solution on the prescribed value of α, but this would not have general import. Our intention here has been to provide some simple data to illustrate the performance of the adaptive algorithm. In complex problems, entailing totally unpredictable conditions of yielding and plastic flow, we have found, as in this example, that the adaptive approach is a very efficient way to achieve accurate solutions.

CONCLUSIONS AND FUTURE RESEARCH DIRECTIONS

The adaptive load incrementation approach is a major development when considered in the context of standard practice, which requires the analyst to prescribe the load path discretization. With this standard approach, load steps which provide a consistent level of error can only be determined by performing a series of analyses, and this can entail excessive labor and expense. While the error control strategy represents an improvement, we are not claiming that is is the optimum approach. Various questions remain, as discussed below. Although we have focused on 2D analysis, the general considerations apply to 3D problems. Of course, the strategy presented—adaptively selecting step size according to a constraint on the maximum value of $|\Delta \mathbf{s}_{sc}|$-has been developed for a single finite element formulation, for the elastic–perfectly plastic model. For strain hardening materials, it appears that an effective constraint would be one which simultaneously limits the hardening law and yield surface approximations in a load step.

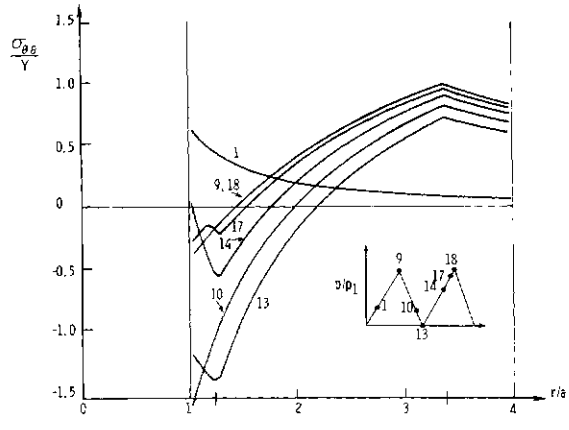

Fig. 5. Radial variation of hoop stress at different positions along the cyclic loading path.

Table 1. Homogeneous uniaxial extension solution data

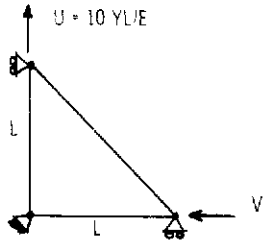

1	5.530	1.227	0.309
2	5.165	1.087	0.134
3	4.960	1.023	0.058
5	4.800	1.013	0.021
8	4.755	1.001	0.006
10	4.75	1	0
16	4.751	1.000	0.000
20	4.75	1	0

There is a need for further research to examine the possibilities of achieving a uniformity of error from step to step. Krieg and Krieg [5] have considered this issue for homogeneous, proportional strain situations. Work is also needed to establish convergence study guidelines. Whereas we have concentrated on load path discretization, there is the obvious need for a strategy to control error which stems from spatial as well as load path discretization. Related to this are restrictions, which must be placed on element interpolation functions and mesh patterns, to allow spatially nonuniform, near-incompressible straining when fully plastic conditions develop. These restrictions have been discussed by Nagtegaal *et al.* [6].

It would appear that the adaptive solution algorithm could be used to advantage in many other incremental structural mechanics problems. It applies only to tangent modulus formulations, of course; but in the algorithm's generalized form, the nature of the problem nonlinearity, whether it be constitutive, geometric or both, is immaterial. The effectiveness of the algorithm is always dependent upon the propriety of the constraint condition which is chosen for the particular problem class.

REFERENCES

1. J. R. Rice and D. M. Tracey, Computational fracture mechanics. In *Numerical and Computer Methods in Structural Mechanics* (Edited by S. J. Fenves *et al.*) pp. 585–623. Academic Press, New York (1973).
2. P. V. Marcal and I. P. King, Elastic–plastic analysis of two-dimensional stress systems by the finite element method. *Int. J. Mech. Sci.* **9**, 143–155 (1967).

3. R. Hill, *The Mathematical Theory of Plasticity*. Oxford University Press, London (1950).
4. W. Prager and P. G. Hodge, Jr., *Theory of Perfectly Plastic Solids*. Wiley, New York (1951).
5. R. D. Krieg and D. B. Krieg, Accuracies of numerical solution methods for the elastic–perfectly plastic model. *Trans. ASME, J. Pressure Vessel Tech.* 510–515 (1977).
6. J. C. Nagtegaal, D. M. Parks and J. R. Rice, On numerically accurate finite element solutions in the fully plastic range. *Comp. Meths. Appl. Mech. Engng* **4** 153–177 (1974).

Computers & Structures Vol. 13, pp. 55–62
Printed in Great Britain.

0045-7949/81/01055-08$02.00/0

A FAST INCREMENTAL/ITERATIVE SOLUTION PROCEDURE THAT HANDLES "SNAP-THROUGH"

M. A. CRISFIELD

Transport and Road Research Laboratory, Department of the Environment, Crowthorne, Berkshire RG11 6AV, England

(*Received* 25 *April* 1980)

Abstract—Riks [1] has recently proposed a new solution procedure for overcoming limit points. To this end, he adds, to the standard equilibrium equations, a constraint equation fixing the length of the incremental load step in load/deflection space. The applied load level becomes an additional variable.

The present paper describes a means of modifying Rik's approach so that it is suitable for use with the finite element method. The procedure is applied in conjunction with the modified Newton–Raphson method in both its original and accelerated forms. The resulting techniques not only allow limit points to be passed, but also, improve the convergence characteristics of the unconstrained iterative procedures. Illustrative examples include the large deflection analysis of shallow elastic shells and the collapse analysis of a stiffened steel diaphragm from a box-girder bridge.

INTRODUCTION

Snap-through and snap-back buckling phenomena (Fig. 1) pose some of the most difficult problems in non-linear structural analysis. For most practical problems, it is quite unnecessary to trace such a convulated load/deflection path as that shown in Fig. 1. Indeed, were such a path to be traced, most analyses would trace the static path ABCDEFGHIJ and thus infer the dynamic "snaps". Although the analyses are therefore somewhat artificial, they may be very important.

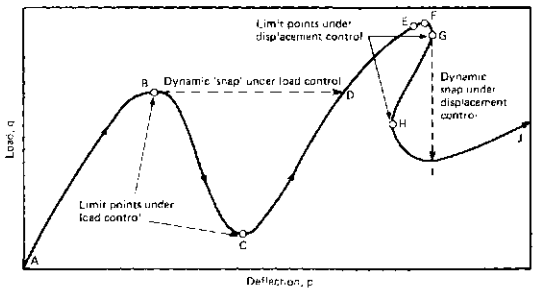

Fig. 1. "Snap buckling".

For some problems, all that may appear to be required is the load level at the first limit point. However, without analysis techniques that allow the limit points to be passed, even this information may be unavailable or unreliable. "Collapse loads" are often associated with a failure to achieve convergence with the iterative solution procedure. However, it may only be the iterative solution procedure that has collapsed (possibly as a consequence of round-off error). For other problems, the analysis may be performed on an individual component of a complete structure. In such a situation, it may be important to obtain information on the nature of the load shedding, following the limit points, in order to assess the performance of the complete structure.

When analysing relatively simple structures, it is tempting to try and avoid the full complexities of a "snap analysis" by applying a simple form of displacement control. Such "displacement control" may simulate a physical testing procedure. For instance, referring to Fig. 1, if the displacement p were to be prescribed, the limit point B could be passed and the load-shedding curve BC could be traced. However, a similar procedure would fail at, or just before, the limit point G. This failure might not matter if the analyst could conclude "Following the (local) maximum at F, there is a very sharp drop-off in load". However, the dramatic non-linear behaviour associated with the limit point G may induce a failure in the incremental/iterative solution procedure at point E (Fig. 1). In such a situation, the analyst is left with no information on the nature of the failure and may not even be sure that he has a structural (rather than numerical) collapse. Consequently, non-linear finite element computer programs should be provided with solution procedures that will handle such "snapping phenomena" particularly if this can be achieved without resorting to many "special techniques" [2]. Present procedures generally involve the use of fictitious springs [3] or adopt some form of "displacement control" [4, 5]. The main disadvantage of the former method is the trial and error often involved in the selection of the appropriate springs [6]. The disadvantages of the latter method relate to the selection of the appropriate displacement variable. For instance, Maewal and Nachbar [7] note the necessity to change the prescribed displacement variable following slow convergence or divergence of the iterative solution procedure.

Began *et al.* [6, 8] use the "current stiffness parameter" [8], to predict the position of the local maximum or minimum. They then suppress the equilibrium iterations in the neighbourhood of the extremum (limit) point and reverse the sign of the load following a change in the sign of the determinant of the tangent stiffness matrix. The supression of the equilibrium iterations dictates the provision of very small load increments

close to the limit point and also leads to a local drift from equilibrium.

RIKS METHOD

Figure 2(a) illustrates the application of Rik's procedure [1] to the solution of a one-dimensional problem. Riks used the normal to the tangent rather than the circular path. The latter method is slightly less likely to fail (Fig. 2a) and has been applied in the

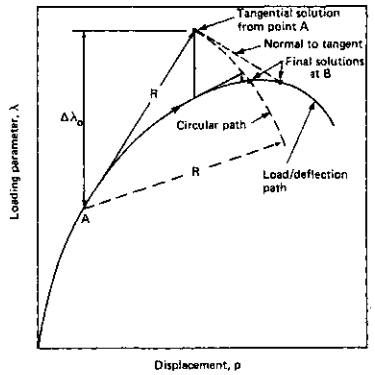

(a) WITH NEWTON-RAPHSON TECHNIQUE

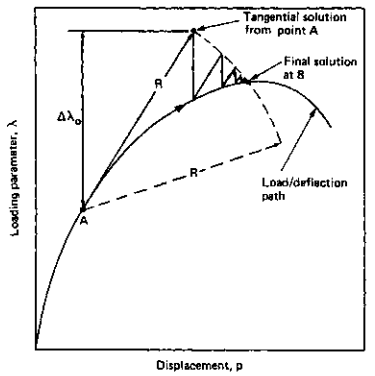

(b) WITH MODIFIED NEWTON-RAPHSON TECHNIQUE

Fig. 2. Riks's method (1). (a) With Newton–Raphson technique; (b) with modified Newton–Raphson technique.

present work. For a problem with N displacement variables, the following constraint equation is added to the usual N equilibrium equations.

$$\Delta\mathbf{p}^T\Delta\mathbf{p}+\Delta\lambda^2\mathbf{q}^T\mathbf{q}=\Delta l^2 \tag{1}$$

$\Delta\mathbf{p}$ is the incremental displacement vector and $\mathbf{q}$ is the total applied loading vector. The "loading parameter" is the scalar λ while Δl fixes the "length" of the increment in N+1 dimensional space. The N equilibrium equations involve the N+1 unknowns $\mathbf{p}$ and λ and can be written in the form

$$\mathbf{q}_{\text{int}}(\mathbf{p},\lambda)-\lambda\mathbf{q}_{\text{ext}}=0. \tag{2}$$

(The external load vector $\mathbf{q}_{\text{ext}}$ will normally be referred to as $\mathbf{q}$.) Riks applied his technique to the analysis of a shallow circular arch and solved the N+1 equations using the Newton–Raphson (N–R) method.

The Newton–Raphson method is not often used with the finite element method, the modified Newton–Raphson method (m.N–R) being generally preferred [9]. When using the m.N–R procedure, the tangent stiffness matrix is neither re-formed nor re-factorised at each iteration but is, instead held fixed. In the current version, the tangent stiffness matrix is only formed and factorised at the beginning of each load increment. Figure 2(b) illustrates the combination of Rik's procedure with the m.N–R method for the one-dimensional problem of Fig. 2(a).

A MODIFIED RIKS METHOD

Even having substituted the m.N–R method for the N–R procedure, Rik's technique is still not suitable for use with the standard finite element method. Unfortunately, the direct simultaneous solution of eqns (1) and (2) destroys the symmetric banded nature of the equilibrium equations (eqns 2) on their own (with λ taken as a constant). Fortunately, the problem can be overcome by adopting a technique similar to that advocated by Batoz and Dhatt [5] for standard "displacement control". Using such a procedure, eqn (2) is re-written to express the out-of-balance force vector (or gradient of the total potential energy), $\mathbf{g}$, as:

$$\mathbf{g}(\lambda+\delta\lambda)=\mathbf{g}(\lambda)-\delta\lambda\mathbf{q}=0. \tag{3}$$

Consequently, the iterative change (δ_i) given by the m.N–R method, can be expressed as:

$$\delta_i=-\mathbf{K}^{-1}\mathbf{g}(\lambda_i+\delta\lambda_i)=\delta_i(\lambda_i)+\delta\lambda_i\delta_T \tag{4}$$

where $\delta_i(\lambda_i)$ is the standard iterative change for some known fixed out-of-balance force vector, $\mathbf{g}_i(\lambda_i)$ with known λ_i and $\mathbf{K}$ is the tangent stiffness matrix at the beginning of the "load increment", i.e.

$$\delta_i(\lambda_i)=-\mathbf{K}^{-1}\mathbf{g}_i(\lambda_i) \tag{5}$$

while δ_T is the tangential displacement,

$$\delta_T=\mathbf{K}^{-1}\mathbf{q} \tag{6}$$

which was required for the original tangential solution

$$\Delta\mathbf{p}_0=\Delta\lambda_0\delta_T \tag{7}$$

with $\Delta\lambda_0$ being some assumed initial incremental loading parameter (see Fig. 2) and $\Delta\mathbf{p}_i$ being the incremental displacement vector such that

$$\Delta\mathbf{p}_{i+1}=\Delta\mathbf{p}_i+\delta_i. \tag{8}$$

Instead of applying the constraint of eqn (1), numerical experience has shown that it is preferable to fix the "incremental length", Δl, in N dimensional space, i.e. eqn (1) is replaced by

$$\Delta\mathbf{p}_i^T\Delta\mathbf{p}_i=\Delta l^2 \tag{9}$$

for all iterations, i. Substituting from eqns (4) and (8) into eqn (9) gives the following quadratic equation for the change, $\delta\lambda_i$, in the loading parameter:

$$a_1\delta\lambda_i^2+a_2\delta\lambda_i+a_3=0 \tag{10}$$

where

$$\begin{aligned} a_1&=\delta_T^T\delta_T\\ a_2&=2(\Delta\mathbf{p}_i+\delta_i(\lambda_i))^T\delta_T\\ a_3&=(\Delta\mathbf{p}_i+\delta_i(\lambda_i))^T(\Delta\mathbf{p}_i+\delta_i(\lambda_i))-\Delta l^2. \end{aligned} \tag{11}$$

The two roots of this scalar quadratic equation will be designated $\delta\lambda_{i1}$ and $\delta\lambda_{i2}$. To avoid "doubling back" on the original load/deflection path, the "angle" between the incremental displacement vector, $\Delta\mathbf{p}_i$ before the present iteration, and the incremental vector, $\Delta\mathbf{p}_{i+1}$ after the current iteration, should be positive. From

eqns (4) and (8) there are two alternative values for $\Delta\mathbf{p}_{i+1}$ (called say $\Delta\mathbf{p}_{i+1,1}$ and $\Delta\mathbf{p}_{i+1,2}$) which correspond to the two solutions $\delta\lambda_{i1}$ and $\delta\lambda_{i2}$. Hence, the two "angles" θ_1 and θ_2 are given by:

$$\theta_1=\Delta\mathbf{p}_{i+1,1}^T\Delta\mathbf{p}_i,\quad \theta_2=\Delta\mathbf{p}_{i+1,2}^T\Delta\mathbf{p}_i. \tag{12}$$

The appropriate root, $\delta\lambda_{i1}$ or $\delta\lambda_{i2}$, is that which gives a positive "angle" unless both "angles" are positive, in which case, the appropriate root is that closest to the linear solution:

$$\delta\lambda_i=-a_3/a_2. \tag{13}$$

The first load increment will generally be started using a given approximate increment, $\Delta\lambda_0$ (Fig. 2). The "length" of the increment, Δl, is then fixed using eqns (7) and (9), i.e.

$$\Delta l=\Delta\lambda_0\sqrt{\boldsymbol{\delta}_T^T\boldsymbol{\delta}_T}. \tag{14}$$

For subsequent increments, the lengths may be adjusted with a view to achieving "a nearly constant number of iterative cycles being needed at each level of loading in order to restore equilibrium" [6]. To this end, the following very simple approach may be adopted [10].

$$\Delta l_j=\Delta l_{j-1}\frac{I_d}{I_{j-1}}. \tag{15}$$

The "length" Δl_{j-1} was used for the $j-1$th increment, I_{j-1} was the number of iterations required to achieve equilibrium at the $j-1$th increment and I_d is the desired number of iterations (between 3 and 5 in the present work). This procedure will automatically lead to small lengths in the areas of the most severe non-linearity and longer lengths when the response is nearly linear. To avoid the danger of converging on a higher equilibrium path, and in the presence of plasticity (which is path dependent) to limit the departure from the true equilibrium path during the iterations, maximum lengths should be specified [8, 10]. A maximum number of iterations (in the present work 12) should also be given. Failure to converge within this limit would result in an automatic reduction in the increment size [10].

For all increments other than the first, the initial incremental loading parameter $\Delta\lambda_0$ (Fig. 2) would be obtained from

$$\Delta\lambda_0=\pm\Delta l/\sqrt{\boldsymbol{\delta}_T^T\boldsymbol{\delta}_T}. \tag{16}$$

The sign is chosen following an approach due to Bergan and Soreide [8] in which the sign follows that of the previous increment unless the determinant of the tangent stiffness matrix has changed sign, in which case, a sign reversal is applied. Provided the adopted factorisation procedure takes the form

$$\mathbf{K}=\mathbf{L}\mathbf{D}\mathbf{L}^T \tag{17}$$

the determinant is easily calculated and there are no problems in obtaining solutions if $\mathbf{K}$ is negative definite. However, the procedure does fail if $\mathbf{K}$ is exactly singular. Fortunately, as noted by Batoz and Dhatt [5], this is extremely unlikely to occur in practise. Indeed, neither they, nor the author, have ever encountered such a situation.

For some problems, it may be required that the scalar λ_i should relate to a set of prescribed displacements rather than to a fixed load vector, $\mathbf{q}$. For example, when "loading" elasto-plastic structures, the distribution of stress across some "loaded boundary" may be unknown and may vary with the load so that it is essential to prescribe displacements unless constraint equations are to be introduced. In such circumstances, the vector $\mathbf{q}$ in eqn (6) would be replaced by the tangent load vector $\mathbf{q}_{T,i}$ which may be formed at the end of each iteration at the same time as the gradient (or out-of-balance force vector), $\mathbf{g}_i(\lambda_i)$, is calculated. The vector $\boldsymbol{\delta}_T$ in eqns (6) and (11) would then be replaced by $\boldsymbol{\delta}_{T,i}$ which would need to be re-formed at each iteration. This can be achieved by operating simultaneously on two "load vectors" ($\mathbf{g}_i(\lambda_i)$ and $\mathbf{q}_{T,i}$) when applying the forward and backward substitution to find $\boldsymbol{\delta}_i(\lambda_i)$ and $\boldsymbol{\delta}_{T,i}$.

AN ACCELERATED MODIFIED NEWTON–RAPHSON METHOD WITH FIXED LENGTH INCREMENTS

At the expense of extra storage and complexity, the previous "modified Riks approach" can be adapted to apply to an "accelerated m.N–R" method [11]. Various such acceleration procedures have been proposed [11–13]. The particular technique used in the present work [11] is both efficient and fully automatic and is closely related [14] to conjugate gradient [14–16], conjugate-Newton [17] and quasi-Newton [18–20] solution procedures. The method has been shown [20] to be among the most efficient of a set of so-called "secant-Newton" solution techniques. Assuming for the present fixed load levels, the accelerated iterative procedure replaces eqn (5) by

$$\boldsymbol{\delta}_i=e_i\boldsymbol{\delta}_{i-1}+h_i\overset{*}{\boldsymbol{\delta}}_i \tag{17}$$

where

$$\overset{*}{\boldsymbol{\delta}}_i=-\mathbf{K}^{-1}\mathbf{g}_i \tag{18}$$

is the standard m.N–R iteration vector and the scalars e_i and h_i are given by

$$h_i=-\frac{a_i}{b_i}$$
$$e_i=h_i\left(1-\frac{c_i}{b_i}\right)-1. \tag{19}$$

The scalars a_i, b_i and c_i are given by the inner products

$$\begin{aligned} a_i&=\boldsymbol{\delta}_{i-1}^T\mathbf{g}_{i-1}\\ b_i&=\boldsymbol{\delta}_{i-1}^T(\mathbf{g}_i-\mathbf{g}_{i-1})=\boldsymbol{\delta}_{i-1}^T\gamma_i\\ c_i&=\overset{*}{\boldsymbol{\delta}}_i^T\gamma_i. \end{aligned} \tag{20}$$

In comparison with the standard m.N–R method (of eqn 18), eqn (17) requires the storage of two extra vectors, $\boldsymbol{\delta}_{i-1}$ and $\mathbf{g}_{i-1}$.

By applying eqns (3) and (4), eqn (17) can be modified to relate to a variable load level. (The procedure is analogous to the modification of the fixed load level m.N–R method of eqn (5) to the variable load level approach of eqn 4.) As a consequence of the modification, eqn (17) can be replaced by

$$\boldsymbol{\delta}_i(\lambda_i+\delta\lambda_i)=\boldsymbol{\delta}_i(\text{eqn }17)+\delta\lambda_i\boldsymbol{\delta}_{Te} \tag{21}$$

where all the terms in eqns (17)–(20) relate to the fixed load level λ_i and $\boldsymbol{\delta}_{Te}$ is given by:

$$\boldsymbol{\delta}_{Te}=h_i\boldsymbol{\delta}_T+d_i\overset{*}{\boldsymbol{\delta}}_i+t_i\boldsymbol{\delta}_{i-1} \tag{22}$$

where the scalar h_i has already been defined (eqn 19) and the scalars d_i and t_i are given by:

$$d_i=\frac{\boldsymbol{\delta}_{i-1}^T\mathbf{q}}{b_i} \tag{23}$$

$$t_i = d_i\left(1-\frac{c_i}{b_i}\right) - \frac{h_i}{b_i}\delta_T^T\gamma_i.$$

Equation (17) satisfies the "generalised secant" relationship [14, 20]

$$\delta_i^T\gamma_i = -\delta_{i-1}^T\mathbf{g}_i \tag{24}$$

while eqn (21) satisfies the equivalent relationship for a variable load level

$$\delta_i^T\gamma_i = -\delta_{i-1}^T(\mathbf{g}_i - \delta\lambda_i\mathbf{q}). \tag{25}$$

It should be emphasised that the vectors $\mathbf{g}_i$, $\mathbf{g}_{i-1}$ and $\gamma_i = \mathbf{g}_i - \mathbf{g}_{i-1}$ all relate to the load level λ_i. Consequently, following the calculation of $\delta\lambda_i$, the vector $\mathbf{g}_i$ is adjusted using eqn (3) to relate to the new load level $\lambda_{i+1} = \lambda_i + \delta\lambda_i$ before being stored for the next iteration as $\mathbf{g}_{i-1}$.

The calculation of the load adjustment scalar $\delta\lambda_i$ follows the procedure previously described for the "constrained m.N–R method". To that end, eqns (8) and (9) are used to set up a scalar quadratic equation which is identical to eqns (10) and (11) with the exception that $\delta_i(\lambda_i)$ and δ_T in eqns (11) are replaced by δ_i (eqn 17) and δ_{Te} (eqn 22) respectively.

Numerical experience has shown that in some situations, the accelerated m.N–R iteration gives a worse solution than the standard m.N–R procedure. This appears to occur whenever the scalar multiplying $\overset{*}{\delta}_i$ is much different from unity or whenever the scalar multiplying δ_{i-1} becomes large in comparison with the scalar multiplying $\overset{*}{\delta}_i$. Consequently, the acceleration is only applied if

$$R_1 > h_i + \delta\lambda_i d_i > \frac{1}{R_1} \tag{26}$$

and

$$R_2 > \frac{e_i + \delta\lambda_i t_i}{h_i + \delta\lambda_i d_i} > -\tfrac{1}{2}R_2$$

where the "cut out parameter", R_1 lies between 2.0 and 3.0 and the "cut out parameter", R_2 lies between 0.3 and 1.0. (Further work is required to obtain the optimum values or to derive new "cut out criteria".)

APPLICATIONS

The solution procedures have been incorporated in a finite element computer program for the large-deflection elasto–plastic analysis of imperfect stiffened plates and shallow shells. The program is based on a Lagrangean formulation for moderately large deflections. The elements are rectangular with quadratic shape functions [4] being used for the in-plane displacement fields, while the restricted quartic non-conforming shape functions [21] (which pass the patch test) are used for the out-of-plane deflections. Reduced two-point Gaussian integration is adopted in order to reduce the "self straining". Details are given in [20, 22].

The following convergence criterion has been adopted

$$\frac{\|\bar{\mathbf{g}}\|}{\max.(\lambda\|\bar{\mathbf{q}}\|, \|\bar{\mathbf{r}}\|)} < \varepsilon \tag{27}$$

where $\bar{\mathbf{g}}$, $\bar{\mathbf{q}}$ and $\bar{\mathbf{r}}$ are the scaled gradient (out-of-balance force), total applied force and reaction vectors. The applied scaling is that proposed by Peano and Riccioni [23], i.e.

$$\|\bar{\mathbf{g}}\| = \sqrt{\mathbf{g}^T\mathbf{D}^{-1}\mathbf{g}}\,, \text{ etc.}; \tag{28}$$

where $\mathbf{D}$ is a diagonal matrix containing the leading diagonal elements of the tangent stiffness matrix (at the beginning of the load increment). Unless it is stated otherwise, the convergence constant ε of eqn (27) is set to 10^{-4} while the cut-out parameters of eqn (26) are set as $R_1 = 3.0$ and $R_2 = 0.8$.

Hinged elastic cylindrical shells subject to point loads

A five by five mesh was used to idealise a quarter of the elastic cylindrical shell shown in Fig. 3. The

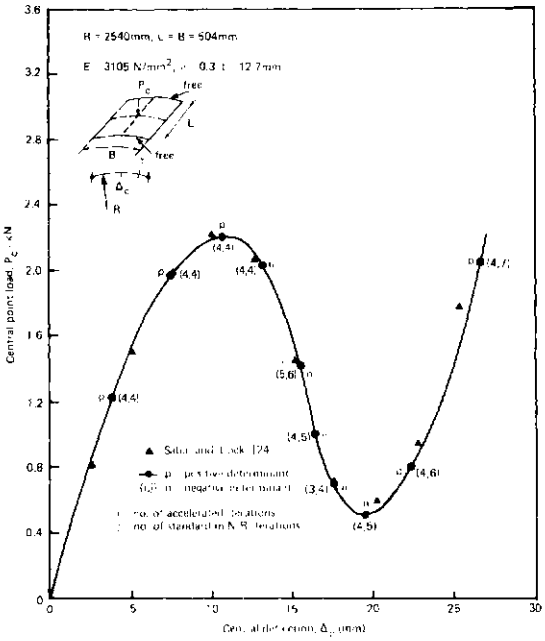

Fig. 3. Hinged cylindrical shell with a central point load.

results are in close agreement with an alternative solution due to Sabir and Lock [24] who used a N–R solution procedure combined with displacement control at the centre of the shell. The present analysis combines applied loading with the "length constraint" so that the tangent stiffness matrix changes from positive to negative to positive definite as the load/deflection path is traced (Fig. 3). The analysis was first performed using the accelerated m.N–R method combined with the automatic procedure for selecting the incremental lengths. The desired number of iterations, I_s (eqn 15), was set to 4 which equals the average number of iterations taken over the complete load/deflection path.

This analysis was followed by a second analysis in which the incremental lengths derived from the first analysis were used to define the increment sizes for a "constrained m.N–R" solution. The average number of iterations came to 4.9 (Fig. 3) which is significantly more than were required when the acceleration was added. The benefits of the acceleration were most noticeable in the region where the structure is hardening. In this zone, the coefficient of the m.N–R iteration vector, $\overset{*}{\delta}_i$ (which is $h_i + \delta\lambda_i d_i$) is generally less than unity.

Both solution procedures allowed the limit points to be passed without resorting to very small increments or surpressing the equilibrium iterations. In order to derive a load/deflection path involving both horizontal

and vertical tangent (limit) points, Sabir and Lock [24] halved the thickness of the shell. They traced the load/deflection behaviour (Fig. 4) by switching from displacement to load and back to displacement control. The present solution, which is in reasonable agreement with Sabir and Lock's solution (Fig. 4), was obtained by combining load control (via the parameter λ_i) with the length constraint. The solution process was the same as that described for the previous shell.

The desired number of iterations, I_d, was again set to 4 which is very close to the average number of iterations (4.1) required when using the accelerated m.N–R solution procedure. When the acceleration was removed, the average number of iterations increased to 6.9. Once more, the limit points were passed without any particular problems. The adopted convergence criterion ($\varepsilon = 10^{-4}$) is excessively harsh. This probably contributes towards the larger number of increments required in comparison with Sabir and Lock's solution (No details are given [24] on the convergence criterion or characteristics.)

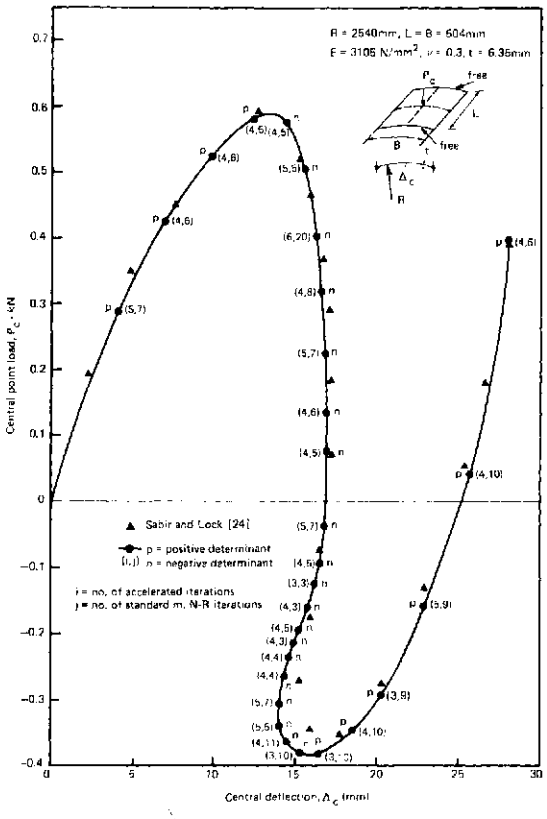

Fig. 4. Thin hinged cylindrical shell with a central point load.

Stiffened steel diaphragm from box-girder bridge

As part of a study [25] into the collapse behaviour of steel box-girder diaphragms, TRRL commissioned a set of tests [26] on lightly stiffened large-scale models. Figure 5 shows such a model and gives load/deflection curves obtained from a finite element analysis which allows for plasticity, geometric nonlinearities and imperfections. An elastic sub-structuring technique was combined with some structural idealisations [22, 25] so that only the diaphragm itself was analysed in a non-linear manner. A 5 × 7 mesh was used to represent one half of the diaphragm. Details are given in [10] which includes comparisons with the experimental results [26].

In order to bracket the experimental behaviour, two extreme boundary conditions were applied to the out-of-plane deflections at the edges of the diaphragm. For analysis A (curve A, Fig. 5), the boundaries were assumed to be simply supported while for analysis B (curve B, Fig. 5) they were assumed to be encastré. In both cases the structure was "loaded" by incrementing prescribed displacements across the bearings and combining this "displacement control" with the addition of "length constraints". The accelerated m.N–R method was used for the first analyses and was combined with the automatic procedure for calculating the incremental lengths (I_d being set to 3). Maximum increment sizes were also specified [10]. The later analyses, using the standard (constrained) m.N–R method, maintained the same lengths as had been derived using the accelerated procedure. The convergence constant, ε (eqn 27) was set to 10^{-3} while the "cut-out" factors R_1 and R_2 (eqns 26) were set to 3.0 and 0.5 respectively.

Despite the applied "displacement control", analysis

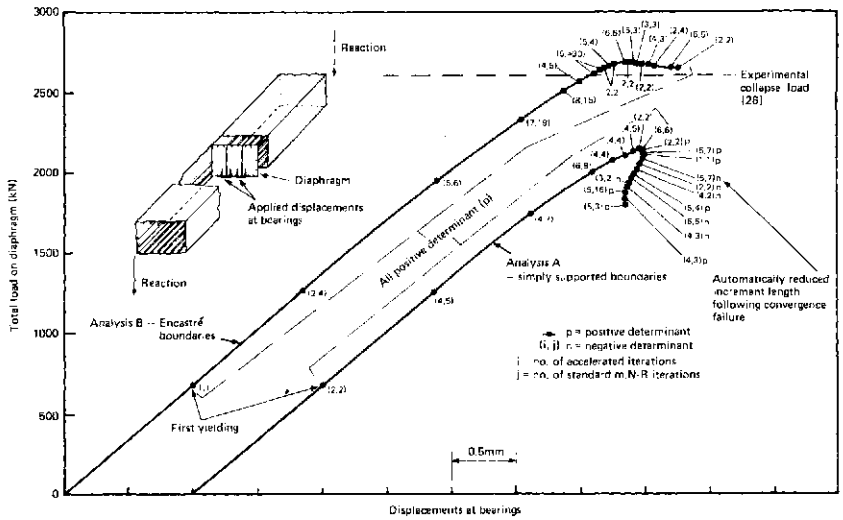

Fig. 5. Stiffened diaphragm from steel box-girder.

A (curve A, Fig. 5 with 348 degrees-of-freedom) was expected to encompass limit points since an earlier analysis [10], without the addition of the "length constraint", had to be abandoned following a failure to achieve convergence. Clearly, the addition of the length constraint has overcome these problems and allowed four limit points (or changes in the sign of the determinant of the tangent stiffness matrix) to be passed. Up to the 12th increment, while the determinant was positive (under displacement control), the accelerated solution procedure gave slightly better convergence (average number of iterations = 3.7) than the standard technique (average number of iterations = 4.4). However, following the first limit point, the response involves a dramatic reduction in load while the determinant of the tangent stiffness matrix oscillates between positive and negative. In these circumstances, the accelerated solution procedure gave a slightly worse performance than the standard technique (Fig. 5, curve A) before the final stiffening response again favoured the acceleration. It is not surprising that the acceleration is relatively unsuccessful when the structure oscillates between stable and unstable equilibrium. The technique was designed to satisfy the "secant relationship" of eqns (24) or (25) which were in turn derived [14, 20] by approximating the total potential energy to a quadratic function. Clearly such an approximation is unreasonable when the determinant of the tangent stiffness matrix is close to zero.

Analysis B (with the encastré boundaries) involved 324 degrees-of-freedom. Under the applied "displacement control", the response was everywhere stable (Fig. 5, curve B) so that no limit points were encountered. The accelerated solution technique (average number of iterations = 3.9 in comparison with the desired number of iterations = 4.0) gave substantially better convergence characteristics than the standard procedure (average number of iterations greater than 7.4).

Clamped elastic cylindrical shell

The previous examples have shown that both of the "constrained iterative procedures" can be successfully used to pass limit points. In general, the use of the accelerated m.N–R procedure has led to an appreciable reduction in the required number of iterations. However the advantages have been less dramatic than those previously experienced [10, 11, 14] when the length constraint was omitted. Following this observation, it was decided to directly compare the performance of the constrained and unconstrained iterative procedures. This was achieved by analysing the clamped shell of Fig. 6 which responds to load without exhibiting any limit points. To this end, a 5×5 mesh was used to idealise a quarter of the shell (196 degrees-of-freedom).

The first analysis combined the constrained accelerated m.N–R procedure with the technique for automatically selecting the increment lengths. The average number of iterations required to restore equilibrium was 3.6 while the desired number of iterations, I_d had been set to 4. The incremental lengths derived from this analysis were next used to generate a solution without acceleration. The average of the required number of iterations increased to 6.4.

Unconstrained solutions were now obtained using the load increments that had been derived from the previous analyses (Fig. 6). The accelerated m.N–R

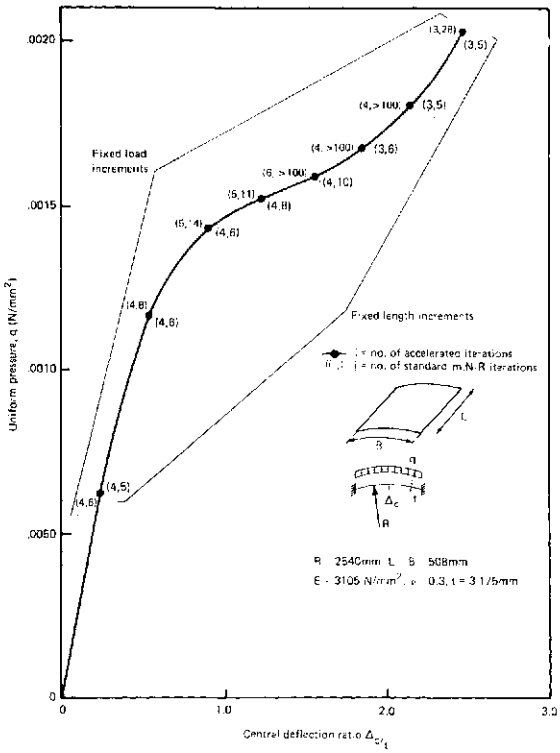

Fig. 6. Fully clamped cylindrical shell with uniform pressure loading.

method was still fairly successful, the average number of iterations having increased from 3.6 to 4.4 as a result of the removal of the length constraint. However, the performance of the standard m.N R method showed a dramatic deterioration following the removal of the length constraint. The average number of iterations increase from 6.4 to over 46. This supports the hypothesis that the addition of the length constraint is far more beneficial to the standard m.N–R method than it is to the accelerated technique.

Solution of linear simultaneous equations

The previous solution techniques can be used [14, 20] with the matrix **K** (eqns 5 and 6) approximating the tangent stiffness matrix at the beginning of the increment. In the extreme, if the matrix K is replaced by the identity matrix, the solution procedures can be used to solve sets of linear simultaneous equations. Without the length constraint, the m.N–R method becomes the simple Jacobi iteration [16] while the accelerated m.N–R method becomes a form of accelerated Jacobi iteration which coincides with the conjugate gradient method *if* line searches [14, 18] are introduced [14, 20]. However, following the previous nonlinear solutions, line searches will not be introduced in the present work. The following set of linear simultaneous equations [16] was used to investigate the effect of adding the length constraint to the standard and accelerated Jacobi methods:

$$\begin{bmatrix} 1.0 & & \text{symmetric} & \\ -0.30009 & 1.0 & & \\ 0.0 & -0.46691 & 1.0 & \\ -0.30898 & 0.0 & -0.27471 & 1.0 \end{bmatrix} \{p\} = \{q\}$$

$$= \begin{Bmatrix} 5.32088 \\ 6.07624 \\ -8.80455 \\ 2.67600 \end{Bmatrix} \quad (24)$$

The convergence constant ε of eqn (27) was set to 10^{-3}. When using the standard Jacobi iteration (m.N–R with $\mathbf{K} = \mathbf{I}$), the required number of iterations was reduced by 30% (from 24 to 17) when the "length constraint" was added. In contrast, when using the accelerated Jacobi method (accelerated m.N–R with $\mathbf{K} = \mathbf{I}$), the required number of iterations was only marginally reduced (from 11 to 10) when the length constraint was added. A similar trend followed from other examples although, in line with the standard Jacobi method [16], convergence could not always be achieved. Better methods are clearly available for solving linear equations. However the object of the example is to show in a different context, the advantages that can be gained by adding Riks's "length constraint". Hopefully, the work may stimulate a rigorous mathematical-study of the convergence properties.

CONCLUSIONS

Riks's solution procedure [1] for passing limit points has been adapted so that it is suitable for implementation with the finite element method. As a result of the modification, the "length constraint equation" is no longer solved directly in combination with the equilibrium equations. Instead, the iterative change, resulting from the usual treatment of the equilibrium equations, is augmented by the addition of a multiple of the tangential displacement vector. This fixed vector is derived from the external load vector and the tangent stiffness matrix at the beginning of the load increment. The scalar multiplying the tangential displacement vector is obtained from the solution of a scalar quadratic equation derived from the "length constraint equation". The technique is implemented in conjunction with the modified Newton–Raphson (m.N–R) method in both standard and accelerated forms.

The solution procedure has been successfully applied to problems involving both horizontal tangent (limit) points, which could otherwise be passed using displacement control, and vertical tangent points, which could otherwise be passed using load control. Such switching is no longer required and there is no need to suppress the equilibrium iterations in the vicinity of the limit points. When applied with the standard m.N–R procedure, only one extra vector need be stored. The added computation is negligible. Not only can the limit points be passed, but also, the convergence characteristics are significantly improved so that the technique can be beneficially applied to problems for which limit points are not anticipated.

Numerical experience with the accelerated m.N–R method is not quite so encouraging. Better convergence characteristics were generally obtained when the acceleration was included. However, the benefits gained by adding the length constraint to the accelerated m.N–R method were less dramatic than those obtained as a result of the similar addition to the standard m.N–R procedure. As anticipated, the performance of the "constrained accelerated m.N–R" solution procedure was least satisfactory when the structure was oscillating over a short length of the load/deflection path between stable and unstable equilibrium. Further work in this area should concentrate on the development of better "cut out" criteria designed to temporarily suppress the accelerations.

Acknowledgements—The work described in this Paper forms part of the programme of the Transport and Road Research Laboratory and the Paper is published by permission of the Director.

REFERENCES

1. E. Ricks, An incremental approach to the solution of snapping and buckling problems. *Int. J. Solids Structures* **15**, 524–551 (1979).
2. C. A. Felippa, Procedures for computer analysis of large nonlinear structural systems. *Proc. Int. Symp. on Large Engng Systems* (Edited by A. Wexler), Univ. Manitoba, Canada. Pergamon Press, New York (1977).
3. P. Sharifi and E. P. Popov, Non linear buckling analysis of sandwich arches. *J. Engng Mech. Div., ASCE* **97**, 1397–1312 (1971).
4. J. H. Argyris, Continua and discontinua. *Proc. 1st Conf. Matrix Meth. Struct. Mech.*, Wright-Patterson A.F.B., Ohio, pp. 11–189 (1965).
5. J. L. Batoz and G. Dhatt, Incremental displacement algorithms for non linear problems. *Int. J. Num. Meth. Engng* **14**, 1262–1266 (1979).
6. P. G. Bergan, G. Horrigmoe, B. Krakeland and T. H. Soreide, Solution techniques for non-linear finite element problems. *Int. J. Num. Meth. Engng* **12**, 1677–1696 (1978).
7. A. Maewal and W. Nachbar, Stable postbuckling equilibria of axially compressed elastic circular cylindrical shells: a finite element analysis and comparison with experiments. *J. Appl. Mech.* **44**, 475–481 (1977).
8. P. G. Bergan and T. Soreide, Solution of large displacement and instability problems using the current stiffness parameter. In *Finite Elements in Non-linear Mechanics*, pp. 647–669 Tapir Press 3 (1978).
9. O. C. Zienkiewicz, *The Finite Element Method*, 3rd Ed. McGraw-Hill, New York (1977).
10. M. A. Crisfield, The automatic nonlinear analysis of stiffened plates and shallow shells using finite elements. *Proc. Inst. Civ. Engrs*, Part 2, Paper 8335. To be published.
11. M. A. Crisfield, A faster modified Newton–Raphson iteration. *Comp. Meth. Appl. Mech. Engng* **20**, 267–278 (1979).
12. G. C. Nayak and O. C. Zienkiewicz, Note on the 'alpha'-constant stiffness method for the analysis of non-linear problems. *Int. J. Num. Meth. Engng* **4**, 579–582 (1972).
13. A. Jennings, Accelerating the convergence of matrix iterative processes. *J. Inst. Math. Appl.* **8**, 99–110 (1971).
14. M. A. Crisfield, Iterative solution procedures for linear and non linear structural analysis. TRRL Report LR900, Crowthorne, England (1979).
15. M. Hestenes and E. Steifel, Method of conjugate gradients for solving linear systems. *J. Res. Natl Bur. of Standards* **49**, 409–436 (1952).
16. A. Jennings, *Matrix Computation for Engineers and Scientists*. Wiley, New York (1977).
17. B. Irons and A. Elsawaf, The conjugate-Newton algorithm for solving finite element equations. *Proc. U.S.–German Symp. on Formulations and Algorithms in Finite Element Analysis* (Edited by Bathe, Oden and Wunderlich), pp. 599–631. MIT, Mass. (1977).
18. J. Dennis, Jr. and J. More, Quasi-Newton methods, motivation and theory. *SIAM Rev.* **19**, 46–84 (1977).
19. H. Matthies and G. Strang, The solution of nonlinear finite element equations. *Int. J. Num. Meth. Engng* **14**, 1613–1626 (1979).
20. M. A. Crisfield, Incremental/iterative solution procedures for non-linear structural analysis. *Int. Conf. on*

Numerical Methods for Non-linear Problems, Swansea (Sept. 1980).
21. O. C. Zienkiewicz and Y. K. Cheung, The finite element method for the analysis of elastic isotropic and orthotropic slabs. *Proc. Inst. Civ. Engrs* **28**, 471–488 (1964).
22. M. A. Crisfield and R. S. Puthli, Approximations in the non-linear analysis of thin plated structures. *Finite Elements in Non-linear Mechanics*, pp. 373–392. Tapir Press (1978).
23. A. Peano and R. Riccioni, Automated discretisation error control in finite element analysis. In *Finite Elements in the Commercial Environment* (Edited by J. Robinson), pp. 368–387. Robinson & Assoc., Verwood, England (1978).
24. A. B. Sabir and A. C. Lock, The application of finite elements to the large-deflection geometrically non-linear behaviour of cylindrical shells. In *Variational Methods in Engineering* (Edited by C. A. Brebbia and H. Tottenham), pp. 7/54-7/65. Southampton University Press (1972).
25. M. A. Crisfield and R. S. Puthli, A finite element method applied to the collapse analysis of stiffened box girder diaphragms. In *Steel Plated Structures* (Edited by P. J. Dowling, J. E. Harding and P. A. Frieze), pp. 311–337. Crosby Lockwood Staples, London (1977).
26. B. Einarsson and P. J. Dowling, Tests on simply stiffened rectangular diaphragms. CESLIC Repts BG54 and BG57, Imperial College, London (1979).

Computers & Structures, Vol. 13, pp. 63–71, 1981
Printed in Great Britain.

0045-7949/81/010063-09$02.00/0

AN EFFICIENT AND ACCURATE ITERATIVE METHOD, ALLOWING LARGE INCREMENTAL STEPS, TO SOLVE ELASTO-PLASTIC PROBLEMS

C. NYSSEN
Novatome, 20 Avenue Edouard-Herriot, 92350 Le Plessis Robinson, France

(*Received* 11 *May* 1980)

Abstract—In non linear structural analysis, an economical computation algorithm should be able to compute for large load increments and the number of iterations per step must remain little sensitive to the increment size. In case of elasto-plasticity, several difficulties are encountered in deriving an efficient solution scheme. A state determination algorithm is proposed which, combined with slight adaptations of the classical Newton–Raphson method, allows to obtain the required property and to compute for accurate solutions.

Evenmore, the solutions obtained are reasonably independent on the chosen calculation strategy. Several examples, including combined geometric and elasto-plastic non linearities, illustrate the performance of the derived algorithm.

1. INTRODUCTION

A large number of theoretical and computation advances in the analysis of nonlinear structures have been made in recent years. Many computer analyses have been carried out and a number of general purpose computer programs for nonlinear elastic and inelastic analyses have been developed.

Nevertheless, the choice for an efficient, accurate and economical calculation algorithm to solve elasto-plastic problems with a great number of degrees of freedom is still a tricky task [1–3]. It seems to be a general agreement that a good algorithm should be able to deal with large load increments, this requirement being obtained without alteration of the solution accuracy. The main difficulties in case of elasto-plasticity arise from the irreversibility of the plastic strains and from the discontinuous change of the material properties.

From this, two distinct phases must be considered when deriving a computation algorithm in elasto-plasticity: the numerical iterative method to solve the system of nonlinear equations and the numerical algorithm for accurate state determination of the material. As will be shown, these two fundamental aspects are closely bounded.

We propose here a particular state determination algorithm which allows to maintain good convergence properties to the Newton–Raphson method, provided it is slightly modified. It will be shown that the numerical solution computed is quite independent of the particular calculation strategy adopted, which is also an essential requirement.

2. SYSTEM OF EQUATIONS TO SOLVE

In this analysis, it will be assumed that the elasto-plastic materials obey the Prandtl–Reuss–von Mises plastic flow rules [4]. Only isotropic materials with isotropic hardening and at uniform temperature will be considered in the formulation for brevity. All considerations can be straightforwards generalized to include temperature dependence of mechanical properties and kinematic hardening if necessary.

If small strains are assumed, the increments of total Green strains may be split into an elastic part and a plastic part:

$$\dot{\varepsilon}_{ij} = \dot{\varepsilon}^e_{ij} + \dot{\varepsilon}^p_{ij}. \tag{1}$$

The elastic strains are related to the stresses by the classical linear elastic constitutive relations:

$$\sigma_{ij} = C_{ijkl}\varepsilon_{kl}, \tag{2}$$

where the C_{ijkl} are the elastic moduli. The stresses should always satisfy the plasticity criterium:

$$F(\sigma, \bar{\varepsilon}_p) = \bar{\sigma}^2 - X^2 = 0 \tag{3}$$

with

$$\bar{\sigma}^2 = f(\sigma_{ij}); \; X = X_0 + \int H' \, \mathrm{d}\bar{\varepsilon}_p, \tag{4}$$

where f is a convex function which defines the plasticity criterium used. X_0 is the initial elasticity limit, while $\mathrm{d}\bar{\varepsilon}^p$ is an equivalent plastic strain. H' is the coefficient of strain hardening. During the plastic flow, the stresses must be plastically admissible and satisfy eqn (3).

Following the Drucker stability postulate [5], the plastic strains are given by

$$\dot{\varepsilon}^p_{ij} = \dot{\lambda} \frac{\partial f}{\partial \sigma_{ij}} = \dot{\lambda} a_{ij}. \tag{5}$$

The exact solution of the plasticity problem should satisfy relations (1)–(3) and (5), the equilibrium equations and the appropriate boundary conditions.

During plastic flow, the increments should satisfy the consistency condition:

$$a_{ij}\dot{\sigma}_{ij} = 2XH'\dot{\bar{\varepsilon}}^p = 4\bar{\sigma}^2 H'\dot{\lambda} = A\dot{\lambda}. \tag{6}$$

From (1), (2), (5) and (6), $\dot{\lambda}$ may always be expressed in terms of strain increments to obtain the classical elasto-plastic incremental stress-strain relations:

$$\dot{\sigma}_{ij}=D_{ijkl}\dot{\varepsilon}_{kl}, \tag{7}$$

with

$$D_{ijkl}=[C_{ijkl}-\alpha C_{ijst}a_{st}C_{klmn}a_{mn}/(A+a_{pq}C_{pqrs}a_{rs})]. \tag{8}$$

In (8), the α parameter takes a value of unity during plastic flow, i.e. if $f(\sigma_{ij})=X^2$ and $f\geqslant 0$; it takes a zero value otherwise.

In a finite element static analysis based on the displacement formulation, the equation of equilibrium may be stated as

$$\int_V B'(q)\sigma\,\mathrm{d}V=g, \tag{9}$$

where σ are the Kirchhoff–Trefftz stresses, B is the incremental strain matrix which generally depends on the generalized displacements q, and g is a vector of generalized loads. Since the strains are assumed to be small, the stresses are related to the total strains through the constitutive equations (7), i.e.

$$\sigma=\int_\varepsilon D(\sigma)\,\mathrm{d}\varepsilon, \tag{10}$$

where the integration is taken along the deformation path since plasticity is essentially path dependent. The nonlinear equations to solve in an elasto-plastic problem may be written

$$\int_V B'(q)\left(\int_\varepsilon D(\sigma)\,\mathrm{d}\varepsilon\right)\mathrm{d}V=g. \tag{11}$$

3. REQUIRED PROPERTIES OF AN EFFICIENT SOLUTION METHOD

3.1. *Solution procedures*

It is now generally admitted that an iterative procedure must be used to achieve sufficient accuracy in solving the nonlinear system (11) [1–3, 6–8]. The main iterative methods can be considered as particular cases of the Newton–Raphson method.

Suppose that we know an approximation of the solution at iteration k, noted

$$(\sigma,\ \varepsilon,\ q), \tag{12}$$

which satisfy the compatibility requirements and the constitutive relations (7). The exact solution may always be written as

$$q=q+\Delta q \quad \varepsilon=\varepsilon+\Delta\varepsilon \quad \sigma=\sigma+\Delta\sigma, \tag{13}$$

where Δq, $\Delta\varepsilon$ and $\Delta\sigma$ denote the corrections to be done on the solution (12), which are not necessary infinitesimal. Expressing that the solution (13) must satisfy eqns (11), it is then possible to compute for the corrections Δ, after linearization in these corrections. Noting that

$$\int_0^{\varepsilon+\Delta\varepsilon} D(\sigma)\,\mathrm{d}\varepsilon\simeq\int_0^{\varepsilon} D(\sigma)\,\mathrm{d}\varepsilon+D(\sigma)\Delta\varepsilon=\sigma+D(\sigma)\Delta\varepsilon, \tag{14}$$

one obtains

$$K^T(q)\Delta q=g-\int_V B'(q)\sigma\,\mathrm{d}V=r, \tag{15}$$

where

$$K^T(q)=\int_V [B'(q)D(\sigma)B(q)+\frac{\partial B}{\partial q}(q)\sigma]\,\mathrm{d}V \tag{16}$$

is the tangential stiffness matrix computed using the tangent material properties evaluated at the approximate state (12). In (15), r states for the out-of-balance forces. Solving (15) for Δq, a new estimation of the displacements is obtained. The corresponding state of the material is then obtained by computing the corresponding strain increments to which the stress increments are related through the elasto-plastic constitutive relations:

$$\Delta\sigma=\int_\varepsilon^{\varepsilon+\Delta\varepsilon} D(\sigma)\,\mathrm{d}\varepsilon. \tag{17}$$

From the new stress state, the new out-of-balance forces may be computed and the procedure repeated until an appropriate norm of $\mathbf{r}$ becomes less than a user fixed tolerance ε. It is worth noting that a solution is then reached whatever the stiffness matrix used for the iterations.

Constant stiffness method. If the stiffness matrix is formed and decomposed only once, the constant stiffness method [9, 10] is recovered. In case of strong nonlinearities, the method often fails to converge even if an acceleration scheme is used and this method cannot be retained solely for a general purpose computing code.

Strict and modified Newton–Raphson method. In the strict Newton–Raphson method, the tangential stiffness is changed at every iteration. A disadvantage of this procedure is that a large amount of computational effort may be required to form and decompose the stiffness matrix. But, if the convergence of the method is sufficiently fast, it can be compensated for by saving time in the state determination phase. In fact, when evaluating the computational efficiency of a solution scheme, it should be noted that the computational cost of this phase can be significant as compared with the solution phase cost [1–3].

Depending on the degree of nonlinearity, computing time can sometimes be saved by reforming the stiffness matrix on each few iterations (modified Newton–Raphson method). It is also interesting to note that the factorized tangent stiffness matrix may also be gradually constructed at low cost while iterating using quasi Newton methods [11, 12]. These methods seem very promising but were not investigated in this work.

When only geometric nonlinearities are present and in absence of instability, the convergence of the Newton–Raphson method is quadratic and in structural analysis, convergence is almost always obtained in a few iterations. Due to the ability of the method to converge even in case of strong nonlinearities, the method is widely used in nonlinear structural analysis. When applied to elasto-plastic problems, some difficulties are still encountered due to the irreversibility of the plastic stress and the discontinuous variation of material properties due to elasto-plastic state transition. Its use and efficiency is sometime controverted in

this case [13]. The main problems of the method may be summarized as follows.

The first difficulty is inherent to each type of iterative method. To each computing strategy corresponds a particular path in the load space given by

$$g = \int_V B^t \sigma \, dV \tag{18}$$

where the σ are the stresses computed during the iterations. This path can be quite sophisticated. Since an elasto-plastic solution is essentially path dependent, the value of the final solution must be discussed.

Convergence difficulties may be encountered if the method is applied without special care.

In case of combined material and geometric non-linearities, the convergence of the Newton–Raphson method can excessively slow down and even be lost in particular cases [13, 14].

Due to these difficulties, some modifications of the classical Newton Raphson method should be introduced to retain the decisive advantages of reliability of the method.

3.2 *Definition of an efficient iterative scheme*

A solution method to be included in a general purpose nonlinear computer program should have a great reliability and offer a great flexibility in the choice of computing strategy since the best one vary with each particular problem. The computed solution should be reasonably independent of the particular strategy adopted. Finally, the method should be economic to use which implies two aspects. Firstly, in order to save engineer time, convergence should be reached whatever the reasonable choice of the load incrementation may be. Secondly, in order to save computing time, the rate of convergence should be sufficiently fast to insure that the total computing cost, including the stiffness matrix reformations and the state determinations, should be acceptable.

It is now well recognized [3, 14, 15] that these requirements can only be achieved if the computation algorithm is able to deal with large load increments, provided the number of iterations per step remains quite independent of the increment size. The state determination algorithm should consequently be very accurate, which can significantly increase the computation cost of the corresponding phase and leads to limit the number of iterations per step.

It will be shown that the required properties can be reached using a Newton–Raphson type method with an appropriate state determination algorithm.

4. STATE DETERMINATION ALGORITHM

Computing of strain increments from displacement increments involves only kinematics. The problem of computing a stress increment from a given strain increment involves the material constitutive relations at two levels: i.e. how to determine the increment of stress $\Delta\sigma$ for a given strain increment $\Delta\varepsilon$ and how to determine the total increment of stress over a whole increment.

4.1 *Stress increment associated to a given strain increment*

The stress increment during plastic flow must be such that the plastic flow rule and the plasticity criterium should be satisfied with about the same degree of accuracy. Due to the nonlinearity of (3) and (5), the true stress increment must be computed using,

$$\Delta\sigma^v = \int_{\varepsilon}^{\varepsilon+\Delta\varepsilon} D(\sigma)\, d\varepsilon. \tag{19}$$

Various algorithms have been designed for this purpose.

4.1.1 *Single step methods.* A first approximation of (19) is obtained using a Euler one step forward integration scheme:

$$\Delta\sigma^a \simeq D(\sigma)\Delta\varepsilon. \tag{20}$$

The fact that the direction of the plastic flow is only correct in the beginning of the increment can lead to important error in the final orientation of the stress vector in the stress space [15, 16]. Moreover the final stress σ^a will not lie on the yield surface. An additional correction is then needed and generally, the stresses are brought radially back to the yield surface. The plastic flow which takes place during this correction is usually completely neglected. So, the radial return seems not very consistent.

To eliminate this difficulty, a single step Euler backward method can be used. In this case the flow rule is satisfied only at the end of the interval considered while the elastic stresses are again projected radially to the yield locus. But in this implicit method, the additional plastic flow occuring during this return can easily be taken into account if the von Mises criterium is used [15–17]. Schreyer *et al.* [15] have demonstrated in a parametric study that for a single step method, the error associated with the implicit scheme is usually much less than the error obtained with the Euler forward method, but if the increments are large, the error can still be unacceptable. Moreover, the convergence properties of the iterative method singularly degrades when using the implicit scheme if the stress state is far from uniaxial.

4.1.2 *Subincrementation schemes.* Improvements of the accuracy of integration (19) can be achieved by multi-stepping [3, 6, 14, 16, 18]. In this case, both implicit and Euler schemes lead to results that may be considered quite satisfactory for most engineering problems, for approximately the same number of subincrements [15], the errors being even less for the explicit Euler scheme in the case considered in [15].

The algorithm implemented is based on an Euler forward multistep integration scheme since it is the most easy to use in plane stress problem and for multilinear hardening law. It is coupled with a consistent correction to bring the stresses back to the yield surface at each subincrement and is formulated as follows.

Since higher derivatives are not available, a constant strain rate is assumed like in most structural programs. This assumption may be violated in the true physical loading path. Strictly speaking, small enough load steps should be used. However the proposed algorithm performs very well even for quite large increments of load.

When plastic loading occurs, the increment of strain $\Delta\varepsilon$ is then divided into m equal subincrements. To estimate the parameter m, the troncature error of a one step integration is first estimated. If σ_Δ designate

the difference between the stress state reached in a single step and in a double step Euler forward integration, a measure of the troncature error for one step is taken as

$$2f^{1/2}(\sigma_\Delta)/X. \tag{21}$$

It is then assumed that the total error is roughly $1/m$ of the single step error if a m substep procedure is used. The number of subincrements is then taken equal to

$$m=2f^{1/2}(\sigma_\Delta)/x\varepsilon, \tag{22}$$

where ε is roughly equal to the required relative error level. Sufficient accuracy was always obtained using $\varepsilon=0.05$ and the number m was almost always less than 30. More sophisticated algorithms could be used to determine m, based on the variation of the plastic flow direction during the integration process [14, 18], but the simple formula (22) has always proven to be sufficient in the applications. If the strain hardening law is multilinear, a strain subincrement

$$\Delta\varepsilon_{(m)}=\Delta\varepsilon/_m \tag{23}$$

is divided into the required number of substeps so that no discontinuity occurs within as subinterval. For each subinterval, the associated stress increment is computed by

$$\Delta\sigma_{(m)}=D(\sigma)\Delta\varepsilon_{(m)}, \tag{24}$$

where σ states for the stresses at the beginning of the subinterval.

At the end of each subincrement an additional correction is made to bring the stresses back to the yield surface. To do this, the following scheme, which is consistent with all plasticity laws to the first order, is proposed. In a displacement iterative scheme, this correction denoted δ must be done at fixed total strains, which implies

$$\delta\varepsilon^e+\delta\varepsilon^p=0. \tag{25}$$

On the other hand, we would like to have

$$f(\sigma+\delta\sigma)=(X+\delta X)^2, \tag{26}$$

or linearizing

$$\frac{\partial f}{\partial\sigma}\delta\sigma=X^2-f(\sigma)+4\bar{\sigma}XH'\delta\lambda. \tag{27}$$

If due account is taken from plastic flow rule (5), it comes that

$$\delta\lambda=\frac{f(\sigma)-X^2}{4\bar{\sigma}XH'+a'Ha}>0 \tag{28}$$

where H is the Hooke matrix. The corresponding correction for the stresses is given by

$$\delta\sigma=-\delta\lambda Ha. \tag{29}$$

As demonstrated by (28), plastic flow always occurs during this correction.

4.2 *Total stress increment evaluation over an increment*

From strict application of the Newton–Raphson method the total strain increment at iteration i of increment n should be evaluated by

$$(\Delta\sigma^v)_n^i=\sum_{k=0}^{i-1}\int_{\varepsilon_m^k}^{\varepsilon_m^{k+2}}D\,\mathrm{d}\varepsilon, \tag{30}$$

with $\varepsilon_n^0=\varepsilon_n^*$, where a starred value is a value at the beginning of the considered increment. Nevertheless, if (30) is applied without care, the solution obtained may be very path dependent, and depends strongly of the particular calculation strategy adopted [3]. Moreover, fictitious numerical unloadings may occur during the iterative process. If they are considered as irreversible, these can lead to erroneous results especially in cases of combined geometric and material nonlinearities. Evenmore, convergence may be lost due to loading–unloading cycles.

To avoid this difficulty and obtain a reasonable path independent algorithm for a given load increment, many authors [1, 7, 14, 18] have proposed to compute the stress increment by integration on the total strain increment at each iteration, i.e. for iteration i of increment n, on

$$\Delta\varepsilon_n^i=\sum_{k=1}^{i}\mathrm{d}\Delta\varepsilon_k, \tag{31}$$

where $\mathrm{d}\Delta\varepsilon_k$ is the new strain increment at iteration k. Nevertheless, this technique has a serious drawback: the cost of the state determination does not decrease during the iterative procedure since the whole strain increment is always integrated. Moreover, the strain path used to compute for $(\Delta\sigma^v)_n^i$ differs from the strain path used in the Newton–Raphson iteration for the approximated stress:

$$(\Delta\sigma^a)_n^i=(\Delta\sigma^v)_n^{i-1}+D[(\sigma^a)_n^i]\,\mathrm{d}\Delta\varepsilon_n^i. \tag{32}$$

Consequently, the new state of stress may differ from the approximated value by a quantity which is not quadratic in $\mathrm{d}\Delta\varepsilon_n^i$. This technique can lead to serious convergence difficulties especially in case of combined geometric and material nonlinearities. This fact has led Bushnell [14] to separate in this case the geometric and material iterations to maintain the convergence of the iterative scheme. But this procedure may be costly since each material iteration requires several geometric iterations.

All these drawbacks may be eliminated in another way. The path dependence of the state determination may be eliminated using an assumption of incremental reversibility. "A point which deforms plastically during one increment is assumed to unload plastically until the plastic work done become again equal to its value at the beginning of the considered increment. Then only will elastic unloading take place". The corresponding stress–strain relation is given on Fig. 1 for a one dimensional case. Due to this assumption, the stress increment may be computed using (30). The number of integration subincrements decrease rapidly as the iterations converge, which save computing time for the state determination. Moreover, the procedure is more consistent with the Newton–Raphson method and good convergence properties are maintained by this procedure. The solution becomes also reasonably

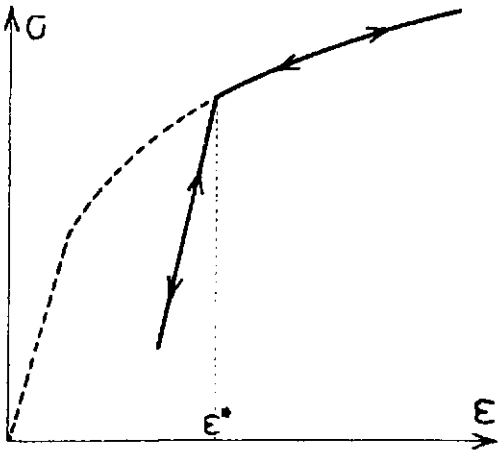

Fig. 1. Incremental reversibility assumption.

independent of the particular computing strategy adopted for the increment.

5. IMPROVEMENTS OF THE NEWTON RAPHSON METHOD FOR ELASTO-PLASTIC CASES

Two additional adaptations have been introduced in the classical Newton–Raphson method.

When the loads are decreased, the plastic points undergo too large unloading when the first iteration of the corresponding increment is made using the tangent stiffness matrix. The convergence of the Newton–Raphson method may then excessively be slowed down. To avoid this difficulty, the possibility to restore the elastic stiffness matrix at the first iteration of each increment of loads was introduced. In the case of continuous loading, this additional iteration is not very time consuming since the elastic stiffness matrix triangulation, made at the first iteration of the problem, may be saved and does not need to be re-run. Moreover, when the incremental reversibility assumption is introduced, this iteration does not generally change the solution.

Secondly, non convergent loading–unloading cycles may be observed when a plastic point unloads as far as to reload plastically during the same iteration. This phenomenon was often observed numerically in case of combined material and geometric nonlinearities. To avoid these spurious cycles, the elastic stiffness is automatically restored at this point during the increment until a new elastic state is reached during the iterative process (Fig. 2). In this way, the convergence of the Newton–Raphson method has always been restored in all the cases where the loss of convergence was due to the considered phenomenon.

The final algorithm obtained has been tested on numerous examples including thermoplasticity with isotropic or kinematic hardening and combined geometric and material nonlinearities. The convergence rate reached has been always satisfactory even for very large load increments. Moreover, the number of iterations needed per step was nearly independent of the increment amplitude and the solution computed reasonably insensitive to the particular strategy adopted on the linear parts of the loading path. A few examples will now be presented to illustrate the accuracy and the efficiency of the proposed algorithm.

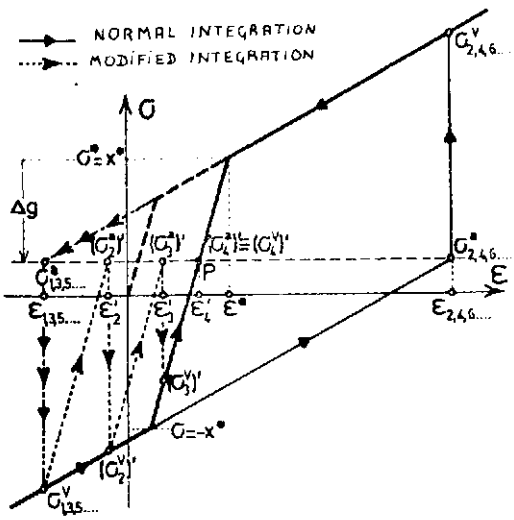

Fig. 2. Unloading-loading cycles in a uniaxial case.

6. EXAMPLES

The proposed algorithm was implemented in general purpose computer programs [19, 20]. The results presented here were obtained using either of these programs.

6.1 *Tension–torsion tube*

Problem description. The physical problem being solved is that of a thin walled cylindrical tube which is subjected to axial tension and torsion. Since the stress distribution in the tube, remote from ends, is constant everywhere, the only requirements for the finite element model is that it represents material subjected to uniform tension and shear. This could be accomplished by a single plane constant stress isoparametric quadrilateral element. The material constants are given in Fig. 3. The non proportional loading path is specified in the same figure. The elasto-plastic nonlinearities are very severe for this case, which was retained by Clinard *et al.* [21] as a benchmarking problem for testing nonlinear computing codes.

Results and discussion. To compute the solution, a systematic incremental history was chosen, as if the final solution was unknown. Each linear segment of the loading path was equally divided in n increments. To obtain a reference solution, n was firstly chosen equal to 80. The solution obtained agree with the averaged computed solution using ADINA, ANSYS, CREEPLAST, CREEPABSA and PLACRE as given in [21], within 5%. Then n was chosen equal to 5 which corresponds to quite large increments. In this case, two different computing strategies were adopted: pure Newton–Raphson iteration and modified Newton–Raphson method with a first elastic iteration at each step.

Axial and shear stress strain results are plotted in Fig. 4. The results agree closely with the reference solution. When the elastic stiffness matrix is used at the first iteration, the shear stress–strain curves differ slightly, but the maximum difference is less than 9%. Figure 5 gives the convergence curves of the algorithm for a few increments and demonstrates its quality.

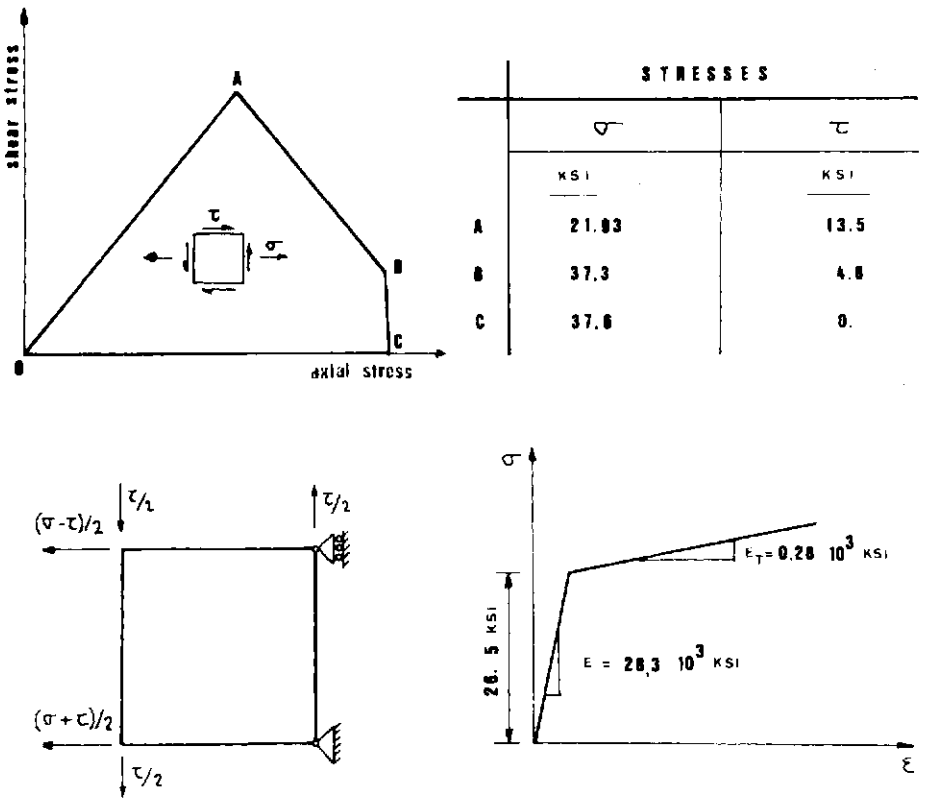

Fig. 3. Tension–torsion test on a tube.

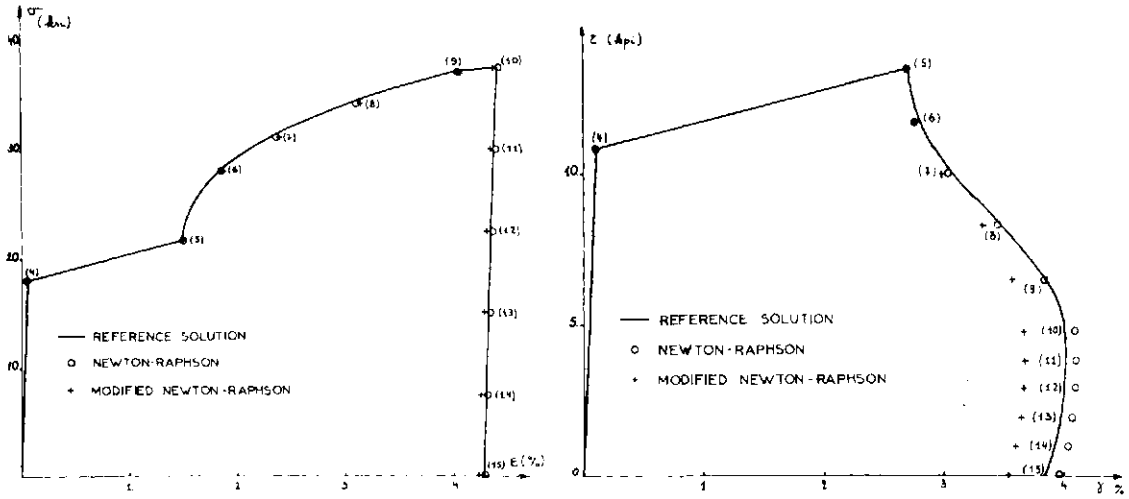

Fig. 4. Stress–strain response in the tension–torsion test.

6.2 *Flat circular plate under concentrated load*

Problem description. A simply supported aluminium circular plate is submitted to a concentrated load at its center. Geometric and material data are given in Fig. 6. Isotropic hardening was adopted using a piecewise linear law with eight segments. The plate was tested by Levine *et al.* [22], which present also computed results in good agreement with the test results, but they use about 100 load steps to reach the final load of 1000 lbs. Computed results using BOSOR 5 are also available in [14] with separate material and geometric iterations.

As reported by Bushnell [14], the stress path differs significantly from radial path near the center of the plate and since both geometrical and material non-linearities are significant, this is a good configuration on which to verify the analysis and the strategy.

Results obtained. The total loads of 1000 lbs was applied in ten, two and one increments respectively. The deflections of the center of the plate is given in Fig. 6, where they are compared to the other available results. Good agreement with the experimental results should be noted.

Computed results and CPU times are compared in Table 1. It is a striking fact that the differences between the central deflections, computed in the different load incrementation cases, are less than 1%. The differences on the final stresses computed in one or ten steps may

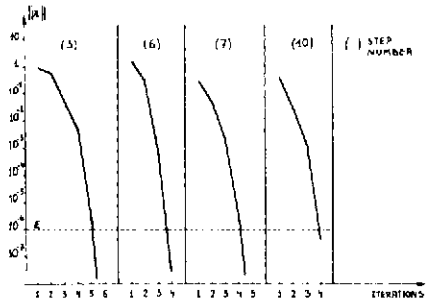

Fig. 5. Convergence curves obtained in the tension–torsion test applying large increments of load.

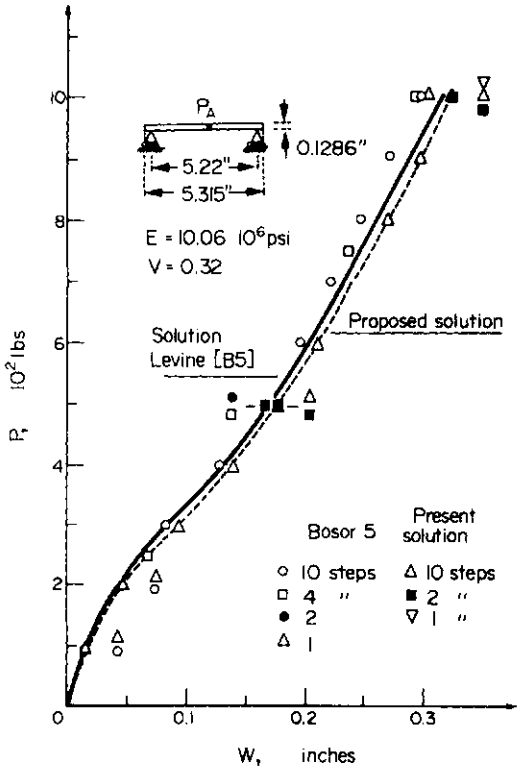

Fig. 6. Central deflection of an aluminium plate.

be locally more important and reach 5–10%. The comparison of the CPU times shows clearly that computing cost can be saved using large incremental steps.

It is also interesting to compare the proposed algorithm to the method developed by Bushnell in Bosor 5. For the first load step of 500 lbs, this last required 12 cycles of material iterations, for each of which two to three Newton–Raphson geometric iterations were needed, leading to a total of 30 geometric iterations. Up to 45 subincrements were needed in the material iterations to ensure that the stresses remain on the yield locus. With the proposed algorithm, this number was always less than 30 and decreases rapidly for successive iterations. The total number of iterations was only 7, which emphasize the economy that can result by simultaneously iterating on material and geometric nonlinearities.

6.3 *Evaluation of the burst pressure of a rocket motor*

Problem description. The last example comes from an industrial study. It consists of a rocket motor case for which experimental results are available. The complete structure shown in Fig. 4 has three different material properties. In the first part, denoted composite material, we have anisotropic material which behaves elastically. The second part, denoted rubber joint, ensures the bounding between the vessel and the polar boss. The third part is made of aluminium alloy and undergoes important plastic deformations during loading. Internal pressure is raised up to the burst failure of the rocket motor. Geometric nonlinearities in the vessel and in the rubber joint, which undergoes very large strains (shear up to 200%), are very important in the behaviour of the structure [3, 22]. Experimental results are available for strains on the surface of the polar boss.

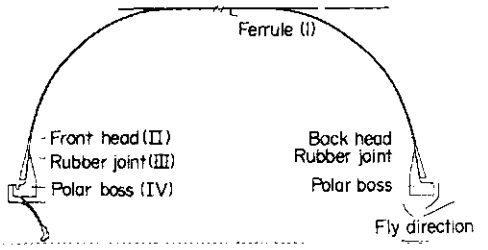

Fig. 7. Typical rocket motor.

Results. The internal pressure up to 63.35 bars was applied in only four increments, as given in Table 2. The finite element mesh used leads to 1965 DOF for a total of 271 quadrangular isoparametric axisymetric elements. Since the geometric nonlinearities were significant, the pure Newton–Raphson method was used throughout the analysis. More details about the calculation may be found in [22]. The characteristics of the solution are summarized in Table 2. As can be seen the convergence properties obtained were very

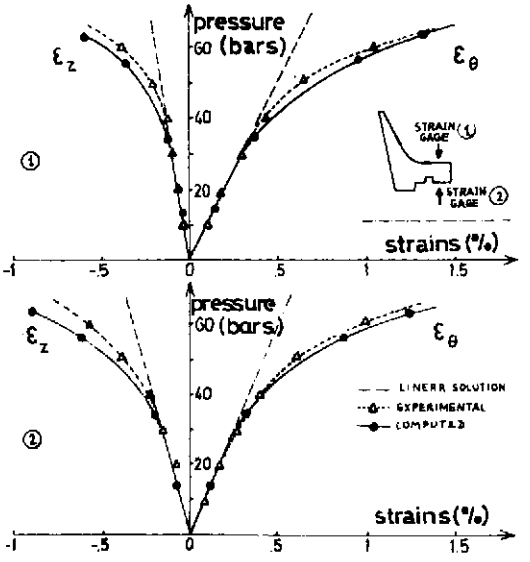

Fig. 8. Evolution of the skin strains of the polar boss.

Table 1. Aluminium plate under concentrated load. Comparison of computed solutions

Increments number	Load (lbs)	Central deflection (10^{-2} in.)	Number of iterations	CPU times (sec) IBM 370/158
10	100.	1.849	4	69.
	200.	4.979	5	74.
	300.	9.624	5	76.
	400.	14.16	5	77.
	500.	18.01	7	98.
	600.	21.52	4	61.
	700.	24.74	4	62.
	800.	27.81	4	60.
	900.	30.76	4	60.
	1000.	33.66	4	68.
2	500.	17.95	7	114.
	1000.	33.79	6	99.
1	1000.	33.70	12.	204.

Table 2. Nonlinear analysis of a rocket motor

Increment	1	2	3	4
Pressure (bars)	14	34	56	63.35
Number of iterations	4	4	6	5
Number of plastic elements	0	58	154	167
CPU times (sec) IBM370/158	1 213	1 130	1 684	1 422
CPU time for linear analysis	390			

good and the total CPU time is about ten times the time of the linear analysis of the same structure. Figure 8 shows the comparison of the measured and computed strains for the polar boss. The agreement is quite satisfactory.

7. CONCLUSIONS

The Newton–Raphson method has been adapted to solve for elasto-plastic calculations. Combined with the proposed stress state determination algorithm it leads to a very efficient iterative method. Fast convergence and accurate solutions have always been achieved for stable structures even if large incremental loads were applied. The computed solution is quite independent of the solution strategy. This allows to save both computing time and analysts time, since the loading history may be defined more easily even for an unknown structural response.

Additional computational efficiency could certainly be gained by using an automatic decision for reformation or not of the stiffness matrix at each iteration, depending on the value of the residual loads norm and its rate of decay.

REFERENCES

1. D. P. Mondkar and G. H. Powell, Evaluation of solution schemes for nonlinear structures. *Comput. Structures* **9**, 223–236 (1978).
2. J. A. Stricklin and W. E. Haisler, Formulations and solution procedures for nonlinear structural analysis. *Comput. Structures* **7**, 125–136 (1977).
3. C. Nyssen, Modelisation par éléments finis du comportement non linéaire de structures aérospatiales. Ph.D. dissertation, Liège (1979).
4. R. Hill, The mathematical theory of plasticity. Oxford (1950).
5. D. C. Drucker, A more fundamental approach to plastic stress–strain relations. *Proc. 1st U.S. Nat. Cong. of Appl. Mech.*, 487–491, Chicago (1951).
6. G. C. Nayak and O. C. Zienkiewicz, Elasto-plastic stress analysis. A generalization for various constitutive relations including strain softening. *Int. J. Num. Meth. Engng* **5**, 113–135 (1972).
7. K. J. Bathe, E. Ramm and E. L. Wilson, Finite element formulations for large deformation dynamic analysis. *Int. J. Num. Meth. Engng* **9**, 353–386 (1975).
8. H. Jr. Armen, A. B. Pifko, H. S. Levine and G. Isakson, Plasticity. In *Finite Element Techniques in Structural Mechanics* (Edited by H. Tottenham and C. rebbia), Southampton (1972).
9. O. C. Zienkiewicz, S. Valliapan and I. P. King, Elasto-plastic solutions of engineering problems. "Initial stress" finite element approach. *Int. J. Num. Meth. Engng* **1**, 75–100 (1969).
10. J. H. Argyris and D. W. Scharpf, Methods of elasto-plastic analysis. *Proc. of Symp. on Finite Element Technology at ISD*, Stuttgart, Germany (1969).
11. J. Dennis and J. More, Quasi-Newton methods, motivation and theory. *SIAM Rev.* 19 (1977).
12. H. Matthies and G. Strang, The solution of nonlinear

finite element equations. *Int. J. Num. Meth. Engng*. To appear.
13. J. A. Stricklin and W. E. Haisler. Evaluation of solution procedures for material and for geometrically nonlinear structural analysis by the direct stiffness method. *AIAA/ASME* 13th *Struct., Structure Dyn. Material Conf*. San Antonio (1972).
14. D. Bushnell, A strategy for the solution of problems involving large deflections, plasticity and creep. *Int. J. Num. Meth. Engng* **10**, 1343–1356 (1976).
15. H. L. Schreyer, R. F. Kulak and J. M. Kramer. Accurate numerical solution for elasto-plastic models. *J. Pressure Vessel Technol.* **101**, 226–234 (1979).
16. R. D. Krieg and D. B. Krieg, Accuracies of numerical solution methods for the elastic-perfectly plastic model. *J. Pressure Vessel Technol.* 512–515 (1977).
17. Q. S. Nguyen and J. Zarka. Quelques méthodes de résolution numérique en élasto-plasticité classique et en élastoviscoplasticité. *Séminaire Plasticité et Viscoplasticité*, Ecole Polytechnique, Paris (1972).
18. D. P. Mondkar and G. H. Powell, Evaluation of state determination calculation in nonlinear analysis. *4th Int. Conf. on Structure Mech. in React. Technol.*, L2/5. San Francisco (1977).
19. NOVNL, Fiche signalétique. NOVATOME technical note MSD 78.057.
20. S.A.M.C.E.F., Système d'Analyse des Milieux Continus par Eléments Finis. *Theoretical Manuel*. University of Liège, Belgium.
21. J. A. Clinard, D. A. McKinley, W. C. Kroencke and W. K. Sartory, Verification by comparison of independent computer program solutions. Pressure vessels and piping computer program evaluation and qualification, ASME PVB-PB-024, 27–50 (1977).
22. H. S. Levine, H. Armen Jr., R. Winter and A. Pifko, Nonlinear behavior of shells of revolution under cyclic loading. Grumman Research Department Report RE-426J (1972).
23. C. Nyssen, Nonlinear incremental analysis up to failure of aeronautical structures. *Proc. of Int. Conf. on Engng Appl. of the Finite Element Methods*, p. 22. Hovik, Norway (1979).

Computers & Structures Vol. 13, pp. 73–81
Printed in Great Britain.

0045-7949/81/010073-09$02.00/0

COMPUTATIONAL STRATEGIES FOR THE SOLUTION OF LARGE NONLINEAR PROBLEMS VIA QUASI-NEWTON METHODS

M. GERADIN†, S. IDELSOHN‡ and M. HOGGE §
Aerospace Laboratory of the University of Liège, Rue E. Solvay, 21, B-4000 Liege, Belgium

(*Received* 9 *May* 1980)

Abstract - The usefulness of quasi-Newton methods for the solution of nonlinear systems of equations is demonstrated. After a review of the Newton iterative method, several quasi-Newton updates are presented and tested. Special attention is devoted to the solution of large sparse systems of equations such as those issued from spatial discretization of continua by finite elements.

The numerical examples presented comprise static and dynamic analyses of geometrical, material and combined nonlinear structural problems and a model fluid flow problem with different levels of nonlinearity. All the results are assorted with a complete discussion of the different methods used, of the convergence rates and of the associated computer costs.

From the present studies, it can be concluded that computational costs for the solution of large nonlinear systems of equations can be reduced drastically by using convenient quasi-Newton updates or by adequate combined Newton/quasi-Newton strategies.

The best known method for solving large systems of nonlinear equations iteratively is Newton's method, sometimes modified so as to improve its computational efficiency. Davidon, for the minimization problem, and Broyden, for systems of equations, introduced in the early sixties new methods which, although iterative in nature, were quite unlike any other one in use at the time [1]. This new class of algorithms has been called by the names quasi-Newton, variable metric, secant, update or modification methods, the basic idea being to replace the costly evaluation of the effective Jacobian or Hessian matrix involved by some economically obtained approximation.

In recent years there has been a proliferation of quasi-Newton methods applicable to the unconstrained minimization problem. The same is not true for solving nonlinear equations: according to [1], the only quasi-Newton method that has been seriously used to solve nonlinear equations is the one proposed by Broyden. In the context of nonlinear structural and continuum analysis using the finite element method, the application of quasi-Newton methods for the solution of the associated systems of equations has been suggested for the first time by Strang and Mathies [2]. Since then a growing amount of literature has developed on the subject through various nonlinear finite element applications [3–8, 10]. At first sight, quasi-Newton methods seem to be particularly attractive to dynamic analysis where the unknown increments are necessarily kept small in order to achieve a sufficient accuracy in the time-marching procedure [3, 4, 7]. In this paper it will be shown that various quasi-Newton updates are also of interest for static nonlinear problems, either of structural or continuum nature and that important savings can be obtained on the total cost of such problems too. It will also be demonstrated how, in the context of nonlinear analysis using the finite element method, advantage can be taken of the sparse pattern of the structural matrices to achieve an optimum implementation of the method.

The remaining of the paper is divided into five sections: in the second one, we recall the basic Newton method for the solution of systems of nonlinear equations and the composition of such systems issued from finite element structural and fluid problems. In Section 3, the most common quasi-Newton updating formulas are described, including rank-one and rank-two updates. Approximations to the inverse Jacobian are presented together with the concept of line search that can be associated with the iterative procedure. A brief outline of stability and convergence properties of Newton and quasi-Newton procedures is given. Section 4 deals with the practical implementation of the updating method in relation with sparse finite element systems of equations. Coupling between Newton and quasi-Newton methods is proposed for highly nonlinear problems and a shifting strategy is presented and tested. Several numerical applications are described in Section 5 where nonlinear structural and fluid flow problems with different level of nonlinearity are analyzed by Newton method and various quasi-Newton updates. The final section draws the conclusions of the analysis and present research directions that should be explored in the future.

2. NEWTON METHODS

Consider the problem of finding a solution to the system of equations

$$\mathbf{r}(\mathbf{q}) = \mathbf{0} \tag{1}$$

where $\mathbf{r}$ and $\mathbf{q}$ are n-dimensional vectors.

Newton's method of solution can be derived by assuming that we have an approximation $\bar{\mathbf{q}}$ to $\mathbf{q}$, and

‡Visiting scientist from CONICET; Professor, Univ. Nacional, Rosario, Rep. Argentina.
§Senior Assistant.

that in the neighbourhood of $\bar{\mathbf{q}}$ the linear mapping

$$\mathbf{r}_L(\mathbf{q}) = \mathbf{r}(\bar{\mathbf{q}}) + \frac{\partial \mathbf{r}(\bar{\mathbf{q}})}{\partial \mathbf{q}} (\mathbf{q} - \bar{\mathbf{q}}) \tag{2}$$

is a good approximation to $\mathbf{r}(\mathbf{q})$. A presumably better approximation to $\mathbf{q}$ can then be obtained by equating (2) to zero.

Thus, Newton's method takes an initial approximation $\mathbf{q}_0$ to $\mathbf{q}$, and attempts to improve it iteratively by

$$\mathbf{q}_{k-1} = \mathbf{q}_k - \mathbf{S}_k^{-1} \mathbf{r}_k, \quad k = 0, 1, \ldots \tag{3}$$

taking $\mathbf{r}_k = \mathbf{r}(\mathbf{q}_k)$ and with the definition of the Jacobian matrix

$$\mathbf{S}_k = \mathbf{S}(\mathbf{q}_k) = \left(\frac{\partial \mathbf{r}}{\partial \mathbf{q}} \right)_{\mathbf{q}_k}. \tag{4}$$

The finite element discretization of static nonlinear structural problems leads to systems of type (1) with

$$\mathbf{r}(\mathbf{q}) = \mathbf{K}(\mathbf{q})\mathbf{q} - \mathbf{g} = \mathbf{0} \tag{5}$$

where $\mathbf{q}$ is the vector of the unknown displacements and $\mathbf{g}$ the vector of the applied nodal loads.

Nonlinearities arise in general from material behavior or adaptation of the geometry; they are implicitly contained in the internal forces $\mathbf{K}(\mathbf{q})\mathbf{q}$ which result from the spatial integration of the internal stresses σ

$$\mathbf{K}(\mathbf{q})\mathbf{q} = \int_V \mathbf{B}^T \sigma \, dV \tag{6}$$

where $\mathbf{K}(\mathbf{q})$ is the structural stiffness matrix. The Jacobian matrix (4) is in this case the tangent stiffness matrix

$$\mathbf{S}(\mathbf{q}) = \mathbf{K}^t(\mathbf{q}) = \frac{\partial}{\partial \mathbf{q}} [\mathbf{K}(\mathbf{q})\mathbf{q}] \tag{7}$$

plus a contribution of the external forces $\partial \mathbf{g}/\partial \mathbf{q}$ if these forces are dependent upon geometry changes; this term is generally omitted to preserve the symmetry of the Jacobian matrix.

In nonlinear structural dynamics, the effective loads in (5) are the difference between externally applied loads and inertia forces, so that the spatially discretized systems read

$$\mathbf{r}(\mathbf{q}) = \mathbf{K}(\mathbf{q})\mathbf{q}(t) + \mathbf{M}\ddot{\mathbf{q}}(t) - \mathbf{g}(t) = \mathbf{0}. \tag{8}$$

The Jacobian matrix of Newton's method is thus not only a function of the tangent stiffness matrix $\mathbf{K}^t$ but also of the temporal integration scheme used in the response. If such schemes are limited to those contained in Newmark's formula:

$$\begin{aligned} \dot{\mathbf{q}}_{i+1} &= \dot{\mathbf{q}}_i + (1-\gamma)h\ddot{\mathbf{q}}_i + \gamma h \ddot{\mathbf{q}}_{i+1} \\ \mathbf{q}_{i+1} &= \mathbf{q}_i + h\dot{\mathbf{q}}_i + (\tfrac{1}{2} - \beta)h^2 \ddot{\mathbf{q}}_i + \beta h^2 \ddot{\mathbf{q}}_{i+1} \end{aligned} \tag{9}$$

where the subscript i denotes the ith time-step, h the time-step size and β, γ the Newmark's parameters, the Jacobian matrix becomes

$$\mathbf{S}(\mathbf{q}) = \mathbf{K}^t(\mathbf{q}) + \frac{1}{\beta h^2} \mathbf{M} + \frac{\partial \mathbf{g}}{\partial \mathbf{q}}. \tag{10}$$

The last term appears only for geometry-dependent external forces and again is usually omitted for symmetry purposes.

In viscous incompressible fluid flow problems [8], the system of discretized nonlinear equations of motion reads

$$\mathbf{r}(\mathbf{q}) = [\mathbf{K} + \mathbf{C}(\mathbf{q})]\mathbf{q} - \mathbf{g} = \mathbf{0} \tag{11}$$

where $\mathbf{K}$ and $\mathbf{C}(\mathbf{q})$ are the diffusive and convective matrices, $\mathbf{q}$ is the vector of unknown nodal velocities and pressures and $\mathbf{g}$ is the vector representing "virtual work" equivalent body forces and surface tractions. Note that only $\mathbf{K}$ is symmetrical and unknown-independent, so that the Jacobian matrix

$$\mathbf{S}(\mathbf{q}) = \mathbf{K} + \frac{\partial}{\partial \mathbf{q}} [\mathbf{C}(\mathbf{q})\mathbf{q}] \tag{12}$$

is always unsymmetrical.

3. QUASI-NEWTON METHODS

3.1 *Direct updates*

The major expense in Newton's method is the calculation of the Jacobian $\mathbf{S}(\mathbf{q}_k)$ and its inversion.

In contrast, quasi-Newton methods consist in deriving an approximation $\mathbf{G}$ to the Jacobian by evaluating $\mathbf{r}(\mathbf{q})$ at two successive points $\bar{\mathbf{q}}$ and $\mathbf{q}$. Indeed if we expand $\mathbf{r}$ around $\mathbf{q}$ by Taylor's theorem

$$\mathbf{S}(\mathbf{q})\mathbf{d} = \mathbf{r}(\mathbf{q}) - \mathbf{r}(\bar{\mathbf{q}}) + \Delta \mathbf{r} \tag{13}$$

where $\mathbf{d} = \mathbf{q} - \bar{\mathbf{q}}$ and $\Delta \mathbf{r} \to \mathbf{0}$ as $\mathbf{q} \to \bar{\mathbf{q}}$. When neglecting the term $\Delta \mathbf{r}$ in eqn (13), we obtain

$$\mathbf{G}(\mathbf{q})\mathbf{d} = \mathbf{r}(\mathbf{q}) - \mathbf{r}(\bar{\mathbf{q}}) = \mathbf{y} \tag{14}$$

which is called the quasi-Newton equation. It is exact if $\mathbf{r}$ derives from a quadratic functional and nearly exact in a sufficiently small neighbourhood of the solution if that functional is not quadratic but strictly convex. Therefore it is desirable that any matrix candidate to $\mathbf{G}$ satisfies eqn (14). It is also desirable that the approximation $\mathbf{G}$ to $\mathbf{S}$ be easily computable from $\mathbf{G}(\bar{\mathbf{q}})$, $\mathbf{y}$ and $\mathbf{d}$ by adding to $\mathbf{G}(\bar{\mathbf{q}})$ a correction matrix which depends upon the above quantities while satisfying eqn (14). The simplest among such relations is the single-rank update

$$\mathbf{G} = \tilde{\mathbf{G}} + \frac{[\mathbf{y} - \tilde{\mathbf{G}}\mathbf{d}]\mathbf{u}^T}{\mathbf{u}^T\mathbf{d}} \tag{15}$$

where $\mathbf{u}$ is an arbitrary vector such that $\mathbf{u}^T\mathbf{d} \neq 0$.

Quasi-Newton iteration consists thus, given initial arbitrary $\mathbf{q}_0$ and $\mathbf{G}_0$, to calculate a new direction by eqn (3) and next, to generate a new matrix $\mathbf{G}_{k+1}$ by eqn (15), i.e.

(1) $\mathbf{d}_k = -\mathbf{G}_k^{-1} \mathbf{r}_k$ (16)

(2) Compute $\mathbf{y}_k$, $\mathbf{u}_k$ $k = 0, 1, \ldots$.

(3) $\mathbf{G}_{k+1} = \mathbf{G}_k + \dfrac{(\mathbf{y}_k - \mathbf{G}_k\mathbf{d}_k)\mathbf{u}_k^T}{\mathbf{u}_k^T\mathbf{d}_k}$ (17)

Several rank-one updates are possible, Obviously it is highly desirable that $\mathbf{u}$ depends only on $\mathbf{d}$, $\mathbf{y}$ and $\tilde{\mathbf{G}}$. Broyden proposes $\mathbf{u} = \mathbf{d}$, so that

$$\mathbf{G}_B = \tilde{\mathbf{G}} + \frac{[\mathbf{y} - \tilde{\mathbf{G}}\mathbf{d}]\mathbf{d}^T}{\mathbf{d}^T\mathbf{d}}. \tag{18}$$

It has been shown that in this way $\mathbf{G}$ is the "closest" to $\mathbf{S}$ when measuring the distance by the Frobenius norm [1]. Note that Broyden's update is unsymmetric and hence does not preserve the eventual symmetry of $\tilde{\mathbf{G}}$.

For symmetric systems of equations, Davidon suggests to use the direction $\mathbf{u} = \mathbf{y} - \tilde{\mathbf{G}}\mathbf{d}$. The new corrective matrix becomes

$$\mathbf{G}_D = \tilde{\mathbf{G}} + \frac{(\mathbf{y} - \tilde{\mathbf{G}}\mathbf{d})(\mathbf{y} - \tilde{\mathbf{G}}\mathbf{d})^T}{(\mathbf{y} - \tilde{\mathbf{G}}\mathbf{d})^T\mathbf{d}} \tag{19}$$

which insures the symmetry of the successive approximation matrices. It is known to dispense with accurate line searches [12] but there is no guarantee that $\mathbf{G}_D$ is positive definite even if $\tilde{\mathbf{G}}$ exhibits this property.

Rank-two formulas are often proposed, for instance the Powell symmetric Broyden update (PSB), the Brodie update, etc... Several of them, in addition to preserving symmetry, have the property of safeguarding positive definite matrices. Among them, the most widely used are the Davidon–Fletcher–Powell update (DFP):

$$\mathbf{G}_{\mathrm{DPF}}=\left(\mathbf{I}-\frac{\mathbf{y}\mathbf{d}^T}{\mathbf{y}^T\mathbf{d}}\right)\tilde{\mathbf{G}}\left(\mathbf{I}-\frac{\mathbf{d}\mathbf{y}^T}{\mathbf{y}^T\mathbf{d}}\right)+\frac{\mathbf{y}\mathbf{y}^T}{\mathbf{y}^T\mathbf{d}} \tag{20}$$

and the Broyden–Fletcher–Goldfard–Shanno formula (BFGS):

$$\mathbf{G}_{\mathrm{BFGS}}=\tilde{\mathbf{G}}+\frac{\mathbf{y}\mathbf{y}^T}{\mathbf{y}^T\mathbf{d}}-\frac{\tilde{\mathbf{G}}\mathbf{y}\mathbf{y}^T\tilde{\mathbf{G}}}{\mathbf{d}^T\tilde{\mathbf{G}}\mathbf{d}}. \tag{21}$$

Both formulas satisfy the quasi-Newton equation (14). In the same manner as for eqn (17), the iterative procedure is obtained by setting in eqns (20) and (21) $\mathbf{G}=\mathbf{G}_{k+1}$, $\tilde{\mathbf{G}}=\mathbf{G}_k$, $\mathbf{y}=\mathbf{y}_k$, $\mathbf{d}=\mathbf{d}_k$.

3.2 *Inverse updates*

To solve the linear problem (16) at least expense, it is convenient to obtain directly from (15) the new approximation to the inverse Jacobian. This is possible using the property that [12]:

$$(\mathbf{A}\quad \alpha\mathbf{u}\mathbf{v}^T)^{-1}=\mathbf{A}^{-1}-\beta\mathbf{x}\mathbf{z}^T \tag{22}$$

with $\mathbf{x}=\mathbf{A}^{-1}\mathbf{u}$, $\mathbf{z}=\mathbf{A}^{-T}\mathbf{v}$ and $\beta=\alpha(1+\alpha\mathbf{v}^T\mathbf{A}^{-1}\mathbf{u})^{-1}$. Thus, the general rank-one update (15) becomes

$$\mathbf{G}^{-1}=\tilde{\mathbf{G}}^{-1}+\frac{(\mathbf{d}-\tilde{\mathbf{G}}^{-1}\mathbf{y})\mathbf{v}^T}{\mathbf{v}^T\mathbf{y}} \tag{23}$$

for an arbitrary vector $\mathbf{v}$, with $\mathbf{v}^T\mathbf{y}\neq 0$. Broyden's update is obtained when $\mathbf{v}=\tilde{\mathbf{G}}^{-T}\mathbf{d}$, and Davidon's symmetric update when $\mathbf{v}=\mathbf{d}-\tilde{\mathbf{G}}^{-1}\mathbf{y}$, i.e.

$$\mathbf{G}_B^{-1}=\tilde{\mathbf{G}}^{-1}+\frac{(\mathbf{d}-\tilde{\mathbf{G}}^{-1}\mathbf{y})\mathbf{d}^T\tilde{\mathbf{G}}^{-1}}{\mathbf{d}^T\tilde{\mathbf{G}}^{-1}\mathbf{y}} \tag{23'}$$

$$\mathbf{G}_D^{-1}=\tilde{\mathbf{G}}^{-1}+\frac{(\mathbf{d}-\tilde{\mathbf{G}}^{-1}\mathbf{y})(\mathbf{d}-\tilde{\mathbf{G}}^{-1}\mathbf{y})^T}{(\mathbf{d}-\tilde{\mathbf{G}}^{-1}\mathbf{y})^T\mathbf{y}} \tag{23''}$$

All the rank-two updates may also be transformed in the same manner to obtain directly the inverse matrix $\mathbf{G}^{-1}$, yielding

$$\mathbf{G}_{\mathrm{DPF}}^{-1}=\tilde{\mathbf{G}}^{-1}+\frac{\mathbf{d}\mathbf{d}^T}{\mathbf{d}^T\mathbf{y}}-\frac{\tilde{\mathbf{G}}^{-1}\mathbf{y}\mathbf{y}^T\tilde{\mathbf{G}}^{-1}}{\mathbf{y}^T\tilde{\mathbf{G}}^{-1}\mathbf{y}} \tag{24}$$

and

$$\mathbf{G}_{\mathrm{BFGS}}^{-1}=\left(\mathbf{I}-\frac{\mathbf{d}\mathbf{y}^T}{\mathbf{y}^T\mathbf{d}}\right)\tilde{\mathbf{G}}^{-1}\left(\mathbf{I}-\frac{\mathbf{y}\mathbf{d}^T}{\mathbf{y}^T\mathbf{d}}\right)+\frac{\mathbf{d}\mathbf{d}^T}{\mathbf{y}^T\mathbf{d}}. \tag{25}$$

It is useful to note that DFP and BFGS updates are related by the transformation

$$\mathbf{d}\rightarrow\mathbf{y};\quad \mathbf{G}\rightarrow\mathbf{G}^{-1}$$

(see eqns 20–25 and 21–24); these updates are called "dual" or "complementary" updates [1].

3.3 *Line search*

In order to improve the convergence rate, an optimal step length σ_k in the direction determined by eqn (16) can be evaluated such as to cancel the projection of the residual vector in that direction, i.e.

$$\delta=\mathbf{d}_k^T\mathbf{r}(\mathbf{q}_k+\sigma_k\mathbf{d}_k)=0 \tag{26}$$

and then

$$\mathbf{q}_{k+1}=\mathbf{q}_k+\sigma_k\mathbf{d}_k. \tag{27}$$

This is an expensive operation since it may involve numerous evaluations of the residual vector to achieve great accuracy. One may expect, however, that the more accurate the line search is, the better is the chance of achieving convergence in a minimum number of iterations.

In Ref. [3], the authors report that satisfactory rate of convergence is obtained without line search when

$$|\mathbf{d}_k^T\mathbf{r}(\mathbf{q}_k+\mathbf{d}_k)|\leqslant\eta|\mathbf{d}_k^T\mathbf{r}(\mathbf{q}_k)|\quad\text{with}\quad\eta=0.5 \tag{28}$$

This has been confirmed by the numerical experiments described in the present paper. When eqn (28) is not satisfied, successive linear interpolations may be performed in order to determine the optimal length σ_k such that

$$|\mathbf{d}_k^T\mathbf{r}(\mathbf{q}_k+\sigma_k\mathbf{d}_k)|\leqslant\eta|\mathbf{d}_k^T\mathbf{r}(\mathbf{q}_k)|. \tag{29}$$

Strang [13] reports that the choice $\eta=0.9$ should be a good compromise for accuracy vs cost of the line search, especially for fluid problems.

3.4 *Stability and convergence of quasi-Newton methods* [1, 12]

Under the assumption that $\mathbf{r}$ is continuously differentiable in an open convex set C pertaining to R^n and that there is a solution $\mathbf{q}^*$ to eqn (1) for which $\mathbf{S}(\mathbf{q}^*)$ is nonsingular, then Newton algorithm is known to possess a domain of attraction A, which is an open set containing $\mathbf{q}^*$ such that for any $\mathbf{q}_0\in A$ the Newton iterates are well-defined, remain in A and converge to $\mathbf{q}^*$. This implies that if Newton iterates pertain to A, they will remain in A and insures in some sense the stability of the iterative procedure.

Moreover, there exists a sequence $\{\alpha_k\}$ which converges to zero and such that

$$\|\mathbf{q}_{k+1}-\mathbf{q}^*\|\leqslant\alpha_k\|\mathbf{q}_k-\mathbf{q}^*\|,\quad k=0,\ldots \tag{30}$$

where $\|\cdot\|$ stands for the L_2 vector norm $\|x\|=(\Sigma_i x_i^2)^{1/2}$ or the consistent matrix norm. This result is known as superlinear convergence. This is more than linear convergence for which with $\alpha\in(0,1)$

$$\|\mathbf{q}_{k+1}-\mathbf{q}^*\|\leqslant\alpha\|\mathbf{q}_k-\mathbf{q}^*\|\quad k\geqslant k_0 \tag{31}$$

and guarantees only that the error will eventually be decreased by the factor $\alpha<1$. If in addition $\mathbf{r}$ satisfies a Lipshitz condition at $\mathbf{q}^*$, i.e. if there is a constant β such that

$$\|\mathbf{S}(\mathbf{q})-\mathbf{S}(\mathbf{q}^*)\|\leqslant\beta\|\mathbf{q}-\mathbf{q}^*\|,\quad \mathbf{q}\in C \tag{32}$$

then second order or quadratic convergence is obtained, i.e. there is a constant γ such that

$$\|\mathbf{q}_{k+1}-\mathbf{q}^*\|\leqslant\gamma\|\mathbf{q}_k-\mathbf{q}^*\|^2,\quad k=0,\ldots \tag{33}$$

which is a well-known property of Newton method seldom obtained in practice due to requirement (32).

Any quasi-Newton iteration generated by eqn (16):

$$\mathbf{q}_{k+1}=\mathbf{q}_k-\mathbf{G}_k^{-1}\mathbf{r}_k\quad k=0,1,\ldots$$

will be locally convergent at $\mathbf{q}^*$, i.e. $\{\mathbf{q}_k\}$ is well-defined and converges to $\mathbf{q}^*$, if there is an $\varepsilon>0$ and a $\delta>0$ such

that whenever $\mathbf{q}_0 \in A$ and $\mathbf{G}_0 \in A_M$ (A_M is the set of the various Jacobian approximations which might be used in the iterative process) they satisfy

$$\begin{aligned} &\|\mathbf{q}_0 - \mathbf{q}^*\| < \varepsilon \\ &\|\mathbf{G}_0 - \mathbf{S}(\mathbf{q}^*)\| < \delta. \end{aligned} \tag{34}$$

Now such a sequence converges superlinearly to $\mathbf{q}^*$ if and only if

$$\lim_{k \to \infty} \frac{\|[\mathbf{G}_k - \mathbf{S}(\mathbf{q}^*)](\mathbf{q}_{k+1} - \mathbf{q}_k)\|}{\|\mathbf{q}_{k+1} - \mathbf{q}_k\|} = 0. \tag{35}$$

An equivalent but more geometric formulation of this condition is that it requires $\mathbf{d}_k$ in the iterative method to asymptotically approach the Newton correction

$$\mathbf{d}_k^N = -\mathbf{S}_k^{-1}\mathbf{r}_k$$

in both magnitude and direction. This follows from the fact that

$$\mathbf{d}_k - \mathbf{d}_k^N = \mathbf{d}_k + \mathbf{S}_k^{-1}\mathbf{r}_k = \mathbf{S}_k^{-1}[\mathbf{S}_k - \mathbf{G}_k]\mathbf{d}_k$$

and thus eqn (35) is equivalent with

$$\lim_{k \to \infty} \frac{\|\mathbf{d}_k - \mathbf{d}_k^N\|}{\|\mathbf{d}_k\|} = 0. \tag{36}$$

This characteristic of local and superlinear convergence is shared by Broyden's method eqn (15) and its modification by Schubert for sparse Jacobians (see next section). Convergence of the other direct updates or of the inverse updates has only been proved in the frame of unconstrained minimization, in which case $\mathbf{r}$ is the gradient vector (and $\mathbf{S}$ the Hessian matrix) of an objective function [1, 12].

4. COMPUTATIONAL IMPLEMENTATION OF QUASI-NEWTON UPDATES

The natural way of performing quasi-Newton corrections to the Jacobian matrix is in the form implied by the updates of Section 3, i.e. by adding a correction matrix to the previous approximation or by implementing a correction in product form [2].

Inspection of the procedure in a finite element context, where most of the elements of the Jacobian matrix $\mathbf{S}$ are known to be zero owing to the topology of the discretization mesh and where a frontal solution technique is used with substructuring to perform block elimination, reveals that careful attention has to be devoted to the correction procedure in order to preserve the sparse pattern of the true Jacobian. Schubert [9] has proposed a variant of Broyden's unsymmetric update in which $\mathbf{G}_{k+1}$ is forced to have the same sparsity as $\mathbf{S}$. Such a technique has been developed for symmetric correction in [7] since we expect an optimal correction procedure for symmetric systems using symmetric updates.

The procedure is however rather heavy to handle and another way of performing the quasi-Newton update [2, 7] consists of applying the correction on the direction of search $\mathbf{d}$ instead of modifying the matrix $\mathbf{G}$ itself. In fact, using the inverse update as described by eqn (23), at the kth iteration, $\mathbf{G}^{-1}$ can be written as

$$\mathbf{G}_k^{-1} = \mathbf{G}_0^{-1} + \sum_{i=0}^{k} \beta_i \mathbf{v}_i \mathbf{v}_i^T. \tag{37}$$

For instance, for Davidon's update, eqn (23′), we have $\mathbf{v}_i = \sigma_i \mathbf{d}_i - \mathbf{G}_i^{-1}\mathbf{y}_i$ and $\beta_i = [\sigma_i \mathbf{d}_i - \mathbf{G}_i^{-1}\mathbf{y}_i)^T \mathbf{y}_i]^{-1}$. If at each iteration the correction vector $\mathbf{v}_i$ and coefficient β_i are stored on auxiliary memory, the kth direction can be obtained from (16) as

$$\mathbf{d}_k = -(\mathbf{G}_0^{-1} + \sum_{i=0}^{k} \beta_i \mathbf{v}_i \mathbf{v}_i^T)\mathbf{r}(\mathbf{q}_k). \tag{38}$$

The new correction vector for Davidon's update is then

$$\mathbf{v}_k = \sigma_k \mathbf{d}_k - \mathbf{G}_0^{-1}\mathbf{y}_k - \sum_{i=0}^{k} \beta_i \mathbf{v}_i \mathbf{v}_i^T \mathbf{y}_k. \tag{39}$$

This procedure is also applied by Crisfield using only one correction vector at each iteration [5].

Computational efficiency of this updating technique stems from the fact that, if an initial sparse Jacobian $\mathbf{G}_0$ is given, it may be triangularized and stored only once. The successive products $\mathbf{G}_0^{-1}\mathbf{r}(\mathbf{q}_k) = \mathbf{d}_k^0$ needed in eqns (38) and (39) may easily be performed solving the triangularized system of equation

$$\mathbf{G}_0 \mathbf{d}_k^0 = \mathbf{r}(\mathbf{q}_k).$$

In this manner only the nonzero elements of $\mathbf{G}_0$ after Gauss elimination, the vectors $\mathbf{v}_i$ and the coefficients β_i have to be stored. When the number of correction vectors becomes too large [from our experience, say around 10 without exceeding this limit since convergence will not be reached later on], the algorithm may be restarted with the initial matrix $\mathbf{G}_0^{-1}$.

In practice a new problem should be attacked first with the quasi-Newton iteration procedure. If strong nonlinearities are present and require Newton method, this latter technique should be used for k iterations until the convergence test ε be reasonably approached (say $\|\mathbf{r}_k\| < 10^2\,\varepsilon$); then the iterative scheme should be shifted to the quasi-Newton update for the end of the solution procedure. This changing strategy is illustrated in the next section for fluid problems and requires obviously the simultaneous implementation of the two algorithms into the associated computer program. Such an implementation is symbolized on the flow chart of Fig. 1.

A last observation is about the theoretical profit that one can expect between Newton and quasi-Newton iteration. In Newton method, the computation and triangularization of S_k requires $0(n^3)$ arithmetic operations. In quasi-Newton method, for every iteration from the second, this expense is reduced to $0(n^2)$.

5. NUMERICAL APPLICATIONS

5.1 *Clamped spherical cap*

The first example considered is the nonlinear structural analysis of a clamped spherical cap submitted to a sudden pressure loading, and where geometric and material nonlinearities are simultaneously present. Its geometric and material properties are summarized on Fig. 2. This is a classical example taken from [10].

The structure is modelled with 8 axisymmetric cubic shell elements [14]. The resulting finite element model numbers 72 degrees of freedom. Only 3 Gauss points are used to integrate the constitutive law over the thickness: this relatively crude integration rule may be foreseen to generate oscillations in the numerical solution when plasticity develops.

Static analysis. The structure was first tested statically with the pressure load described on Fig. 2.

The iterative procedure is stopped when

$$\|\mathbf{r}_k\| / (\|\mathbf{g}\| + \|\mathbf{g}_{\text{int}}\|) \leq 10^{-4}$$

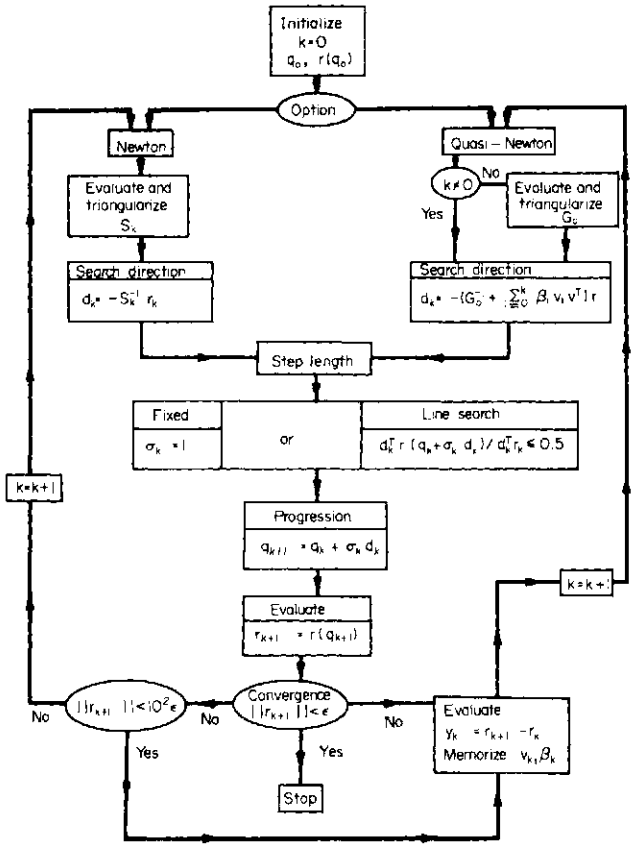

Fig. 1. Flow chart for Newton and quasi-Newton iterative procedures.

where $\mathbf{g}_{int}$ stands for $\mathbf{K}(\mathbf{q})\mathbf{q}$ in eqn (5).

The purpose of this analysis is the comparison in computer times necessary to obtain the solutions with Newton and quasi-Newton methods.

In this problem, the only external existing loads are the pressure loads. These loads introduce an unsymmetrical contribution to the Jacobian matrix which is neglected in the present analysis (see Section 2). Therefore, it seems natural that an unsymmetrical quasi-Newton update would give the best results.

Table 1 summarizes the performances obtained when using a Newton technique and quasi-Newton iterations, with the symmetrical Davidon's update and the unsymmetrical Broyden's update respectively.

In opposition to what was expected Davidon's updates give the best efficiency with a gain of 35% with respect to the standard Newton method. In fact, in this problem the geometrical nonlinearities are mild and thus the successive Jacobian matrices are nearly symmetrical. It is the reason why a symmetrical update is the most efficient.

Dynamic analysis. For the nonlinear response to step loading, time integration is performed with Newmark's scheme ($\beta = 1/4$, $\gamma = 1/2$) and a relatively large time step Δt of 1.5 10^{-5} sec has been adopted. Equilibrium iteration is now stopped within each time step n when

$$\|\mathbf{r}_k^n\| / (\|\mathbf{g}(t_n)\| + \|\mathbf{g}_{int}^n\|) \leq 10^{-3}.$$

Figure 3 displays the time history of the axial displacement at the apex of the cap for the following material and geometrical behaviors:

—linear elastic,

—elastic–plastic material, geometrically linear,

—material and geometrical nonlinearities simultaneously present.

Very little difference is observed in the numerical results with different methods of solution. For this example also, the only interest of the comparison lies in computer times and numbers of iterations to obtain the solution.

To solve this problem, the comparison has been made between Newton iterations and the quasi-Newton method using successively the Davidon and BFGS updates. The performances obtained to integrate the first 17 steps have been summarized in Table 2 for the combined nonlinear response.

The Newton solution corresponds to a strategy in which the stiffness is reevaluated at iterations 1, 2, 5 and 8 of each time step.

Quasi-Newton iterations have been performed with and without line search. Davidon's update has been tested using the vectorial correction (starting from $\mathbf{K}_0$ at each time step). The best results were obtained without line search.

The last two columns correspond to the BFGS updates with substructure correction (starting from the tangent stiffness matrix at each time step) [7]. One observes a significant increase in the number of iterations when the process is not restarted at each time step, due to the fact that the number of updates on $\mathbf{G}_0$ becomes excessive.

In spite of the small size of this problem (involving only 72 d.o.f.), the difference of computer costs between the reevaluation of stiffness (with Gauss elimination)

Table 1. Spherical cap static analysis. Efficiency of Newton and quasi-Newton iterations

		NEWTON	QUASI-NEWTON	
			G_D update	G_B update
1	Total number of Jacobian evaluations	4	1	1
2	Total number of residual evaluations	5	7	9
3	C.P.U.* Time per iteration	5.34	5.34/2.	5.34/2.2
4	Total number of iterations	5	6	8
5	Total C.P.U. Time*	32.	20.6	25.9

* IBM 370/158

Table 2. Spherical cap dynamic analysis. Efficiency of Newton and quasi-Newton iterations

	NEWTON	QUASI-NEWTON			
		G_D update	G_D update	G_{BFGS} update	G_{BFGS} update
Number of iteration per step	3.35	5.0	4.88	3.29	6.0
Total number of Jacobian evaluations	40	1	1	17	1
Total number of residual evaluations	57	102	111	73	135
Total number of Line Search	-	-	11	-	16
C.P.U. time per iteration	5.40	2.75	2.97	4.83	3.6
Total number of iterations	57	85	83	56	102
Total C.P.U. time	308.	233.6	247.	271.	368.

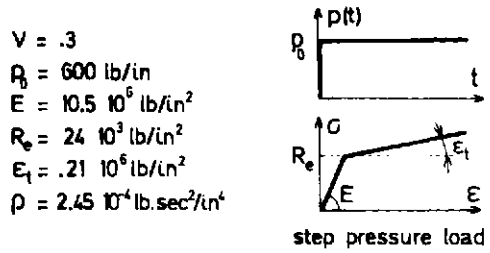

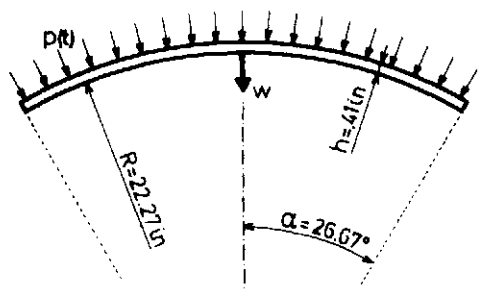

Fig. 2. Spherical cap submitted to step pressure loading.

and the calculation of the residual vector is yet significant. Quasi-Newton iteration is the most efficient procedure.

5.2 *Two-dimensional fluid flow*

In fluid flow problems the relation between the viscosity and the density of the fluid plays an important role in the nonlinear character of the solution. Thus similar problems with differents Reynolds number become nearly linear or largely nonlinear for lower or higher Reynolds number. This interacts with the convergence properties of the solution and is an easy way of testing the differents methods proposed here. The second example deals thus with the computation of the velocity profiles of two-dimensional fluid flow between two parallel walls.

A 4×4 isoparametric finite element mesh is used yielding a total of 129 d.o.f. Each element possesses a quadratic velocity field and a linear pressure field [8]. The boundary condition are represented on Fig. 4.

Table 3 shows the efficiency of the different methods used for $Re = 10$. In all cases the starting solution $\mathbf{q}_0$ corresponds to the Stokes solution, i.e. the solution of eqn

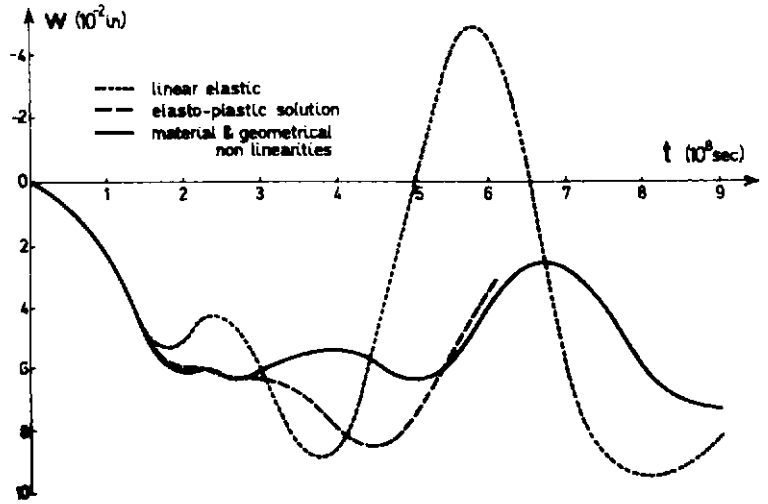

Fig. 3. Spherical cap, displacement W at apex node.

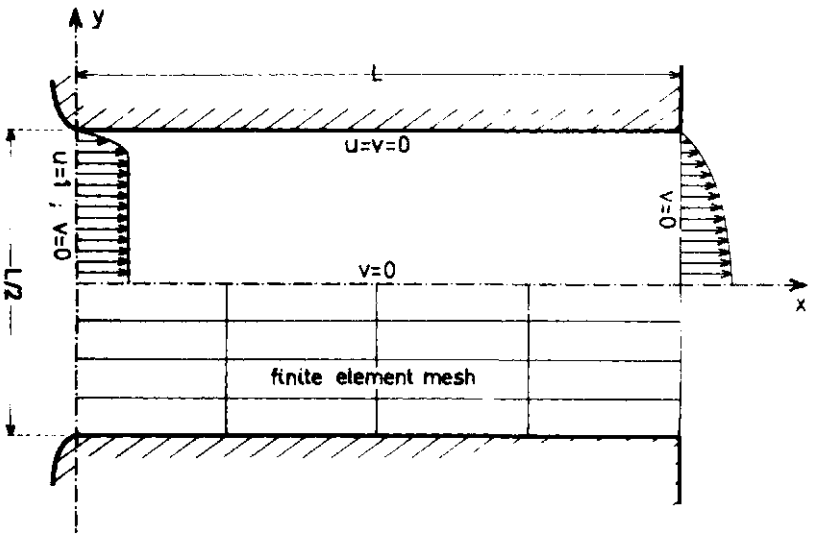

Fig. 4. 2 D-Flow between parallel walls.

Table 3. Fluid flow problem (Re = 10). Efficiency of Newton and quasi-Newton iterations

	NEWTON	QUASI-NEWTON	
		G_D update	G_B update
Total number of Jacobian evaluations	4	1	1
Total number of residual evaluations	4	4	3
C.P.U. Time per iteration	15.1	15.1/3.3	15.1/3.4
Number of iterations	4	3	2
Total C.P.U. time	68.8	35.2	31.4

(11) with $\mathbf{C}=\mathbf{0}$, and the iteration is stopped when

$$\|\mathbf{r}_k\|/(\|\mathbf{g}\|+\|\mathbf{g}_{int}\|) \quad 10^{-3}$$

where $\mathbf{g}$ includes the reactions to the imposed velocity field and $\mathbf{g} = [\mathbf{K}+\mathbf{C}(\mathbf{q})]\mathbf{q}$ (see Section 2).

Up to Reynolds number 10, quasi-Newton updates can be performed from a single Jacobian evaluation. They reveal to be quite competitive in comparison to standard Newton iterations. It is remarkable to note that for the present problem the need for an approxim-

Table 4. Fluid flow problem (Re = 100.). Efficiency of Newton and quasi-Newton iterations

	NEWTON	QUASI-NEWTON	
		G_D update	G_B update
Total number of Jacobian evaluations	10	6	6
Total number of residual evaluations	10	12	11
C.P.U. Time per iteration	14.	14./2.8	14./3.8
Number of iterations	10	11	10
Total C.P.U. Time	154.	111.	139.

ate unsymmetrical Jacobian matrix makes Broyden's update the most adequate.

For Reynolds number higher than 10, the problem becomes strongly nonlinear and a quasi-Newton method using directly the linear matrix **K** as initial matrix does not converge. Nevertheless, another strategy was successfully tested: during the first iterations the Jacobian matrix was evaluated and then, the processus is continued with quasi-Newton updates according to the procedure outlined in the flow chart of Fig. 1.

Table 4 shows the comparison of procedures for Re = 100. The above procedure is applied as follows: the first 6 iterations are done evaluating the Jacobian matrix, then the remaining 5 for the Davidon's update, or the remaining 4 for the Broyden's update, are done by quasi-Newton corrections of the last Jacobian matrix. This is the only way to keep quasi-Newton methods very competitive.

Unsymmetrical Broyden's updates exhibit a better convergence rate than Davidon's ones but are more expensive since the former require the solution of two linear systems of equations against only one for the latter [see eqns (23′)–(23″)]. In the present case the quasi-Newton procedure was started, in accordance with the flow diagram (Fig. 1), when

$$\|\mathbf{r}_k\|/(\|\mathbf{g}\| + \|\mathbf{g}_{int}\|) \leqslant 10^{-1}.$$

Similar conclusions can be drawn from other fluid flow applications [8].

CONCLUSIONS

The adequacy of various updating methods to solve nonlinear systems of equations of finite element structural and continuum mechanics applications has been demonstrated, and their implementation for sparse systems has been discussed.

Quasi-Newton methods converge almost always in a larger number of steps than an "optimal" Newton strategy. The former become thus competitive only when the cost of Jacobian evaluation is significantly larger than that of the residual vector calculation. This superiority of quasi-Newton methods is thus increased with the number of unknowns in a problem.

Conversely, it is observed that strong nonlinearities lead to large number of quasi-Newton updates which in turn can lead to an ill-conditioned iteration matrix. It is thus advised to restart periodically the iteration procedure either using the initial Jacobian or by calculating the effective one in the actual stage of the response.

As a corollary, the so-called vectorial correction is well adapted since it allows for an easy restart of the updating procedure from the initial Jacobian.

The line search does not introduce a significant improvement in the convergence of quasi-Newton methods for the problems at hand, and should be performed only in exceptional cases.

Rank-two corrections do not yield an important improvement of the convergence rates. Hence, Davidon and Broyden rank-one corrections should be preferred due to their lower cost. In problems where Jacobians are definitely unsymmetrical, Broyden's formula should be preferred despite the need for a double linear system solution.

Future research and numerical tests should be devoted to optimal coupling between Newton and quasi-Newton strategies to reach always the minimal cost. Safeguarding methods described for these methods in the context of unconstrained minimization [12] should be explored to ascertain stability and convergence properties even in cases when the solution does no longer correspond to a minimum of a functional.

REFERENCES

1. J. E. Dennis and Jorge J. More, Quasi-Newton methods, motivation and theory. *SIAM Rev.* **19**(1), 46–89 (1977).
2. H. Mathies and G. Strang, The solution of nonlinear finite element applications. *Int. J. Num. Meth. Engng* **14**, 1613–1626 (1979).
3. K. J. Bathe and A. Cimento, Some practical procedure for the solution of nonlinear finite element applications. *Comp. Meth. Appl. Mech. Engng* **22**, 59–85 (1980).
4. K. J. Bathe and V. Sonnad, On effective implicit time integration in analysis of fluid-structure problems. *Int. J. Num. Meth. Engng* **15**, 943–948 (1980).
5. M. A. Crisfield, Iterative solution procedures for linear and nonlinear structural analysis Transport and Road Research Laboratory—TRRL Lab. Rep. 900, ISSN 0305-1293. Crowthorne, Berkshire (1979).
6. M. A. Crisfield, A faster modified Newton Raphson

iteration. *Comp. Meth. Appl. Mech. Engng* **20**, 267–278 (1978).
7. M. Geradin, S. Idelsohn and M. Hogge, Nonlinear structural dynamics via Newton and quasi-Newton methods. *Nucl. Engng Des.* **54**, 339–348 (1980).
8. P. Beckers and S. Idelsohn, A comforming finite element for the analysis of viscous incompressible fluid flow. 3rd Int. Conf. Finite Elements in Water Resources, Univ. Mississippi, 19–23 May 1980.
9. L. K. Schubert, Modification of a quasi-Newton method for nonlinear equations with a sparse Jacobian. *Math. Comp.* **24**, 27–30 (1970).
10. M. P. Kamat and N. F. Knight, Nonlinear transient analysis via energy minimization. *AIAA J.*, **17**(9), 968–969 (1979).
11. S. Nagarajan and P. Popov, *Comput. Structures* **4**, 1117–1134 (1974).
12. M. A. Wolfe, *Numerical Methods for Uncontrained Optimization*. Van Nostrand Reinhold, Wokingham (1978).
13. G. Strang, Private communication (January 1980).
14. M. Geradin *et al.*, Module d'analyse dynamique non-linéaire NLDYN. L.T.A.S. Report VF-40, Aerospace Lab., Universite de Liège (1979).

Computers & Structures Vol. 13, pp. 83–87, 1981
Printed in Great Britain.

0045-7949/81/010083-05$02.00/0

OPTIMAL FINITE ELEMENT DISCRETIZATION FOR NONLINEAR CONSTITUTIVE RELATIONS

D. Siu and D. Turcke†
Department of Civil Engineering, Queen's University, Kingston, Ontario, Canada K7L 3N6

(*Received* 11 *May* 1980)

Abstract An investigation of optimum grid layouts and its consequences on the approximate solution in the finite element method for nonlinear constitutive relations is carried out. The criterion for an optimum grid is based on direct minimization of the total potential energy of the discrete model with respect to the nodal locations contained within the entire continuum. Both the exact solution and the finite element formulations are examined. A computer-directed search procedure which can "move" nodes of an initial grid to generate a sequence of "improved" grids, which have progressively smaller discretization errors, is presented in this paper. A significant reduction in computational cost is observed by uncoupling the optimization variables (nodal locations) in the minimization algorithm. In order to study the differences between optimum mesh configurations in linear and nonlinear analyses one-dimensional tapered bars will be examined with a nonlinear constitutive relation. From these studies optimum grid characteristics were identified and consequently led to strategies for obtaining near optimal discretizations in two and three-dimensional nonlinear analyses. A set of guidelines is developed such that near optimum grids can be obtained by the analyst without using the solution algorithm explicitly.

E Young's modulus of elasticity, α_1
σ_x nominal axial stress
ε_x nominal axial strain, $\partial u/\partial x$
α coefficient of constitutive non-linearity, α_2/α_1
u axial deformation
P axial force applied at the end of tapered bar
$A, \bar{A}$ Section area
x generalized co-ordinate
π_p total potential energy for a conservative system
U_0 strain energy density. $\int_0^{\varepsilon_x} \sigma_x \, d\varepsilon_x$
R residual slope

INTRODUCTION

Over the past several years there has been a growing interest in Finite Element Grid Optimization [1, 2]. That is, the generation of a finite element discretization which provides the required solution accuracy with minimum cost. There are essentially two fundamental approaches to achieve this required accuracy.

Initially an optimal grid can be attained through mesh modification wherein the number of elements and order of trial functions are kept constant [2, 3]. It has been demonstrated that the use of isoenergetics to obtain near optimal grid patterns are most effective where there are high variations in strain energy density.

An alternate approach is also available in which improved accuracy can be achieved through mesh refinement. In this research the main effort is focused on permitting the discretization process to be adaptive. Specifically, the discretization algorithm endeavours to improve the solution or minimize the discretization error through refining the mesh by increasing the number of degrees of freedom in regions where the initial model is inadequate. This refinement procedure or change in the number of degrees of freedom can be accomplished by adding more elements (h-convergence) and/or by increasing the order of the element trial functions (p-convergence) [4, 5].

Essentially all of the above research has been directed at linear elastostatic analyses. However, since the computational costs and solution accuracy in nonlinear analyses depends extensively on the level of discretization, the implications of optimal grids for statically nonlinear problems require special attention.

Thus the objective of this paper is to thoroughly investigate the characteristics of optimal grids for nonlinear analyses. Specifically, attention is focused on nonlinear constitutive relations.

STUDY OF OPTIMAL GRIDS IN NONLINEAR ANALYSIS

Early investigations on mesh optimization dealt with a class of one-dimensional tapered bars [3, 6]. From these studies optimal grid characteristics were identified and consequently led to computational strategies and adaptive methods for obtaining near optimal discretizations in two-dimensional linear analyses. Thus in order to study the differences between optimum mesh configurations in linear and nonlinear analyses the same class of tapered bars shown in Fig. 1 will be

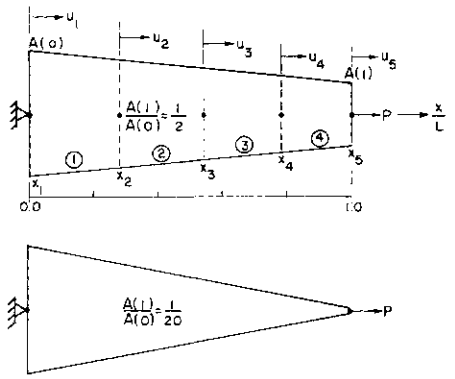

Fig. 1. Finite element model of tapered bar.

examined with a nonlinear constitutive relation. Not only do these examples afford a means of comparison but their exact solutions can be obtained.

The criterion for an optimum grid is based on direct minimization of the total potential energy of the discrete model with respect to the nodal locations contained within the continuum [7]. The theorem of minimum potential energy is valid for nonlinear, as well as linear stress–strain laws as long as the system remains conservative [8].

MATHEMATICAL FORMULATION

For the tapered bar shown in Fig. 1, the following non-linear stress–strain relation was incorporated

$$\sigma_x = \alpha_1 \varepsilon_x \pm \alpha_2 \varepsilon_x^2 \tag{1}$$

where + is for compression and − is for tension. This can be rewritten as

$$\sigma_x = E(\varepsilon_x \pm \alpha \varepsilon_x^2) \tag{2}$$

where $E = \alpha_1$ and $\alpha = \alpha_2/\alpha_1$. α is a measure of the constitutive nonlinearity which is zero for linear stress–strain relations. Given the above material definition (2) and assuming small deformations, the governing differential equation at a point in static equilibrium is

$$\left(\frac{\partial u}{\partial x}\right)^2 \pm \frac{1}{\alpha}\left(\frac{\partial u}{\partial x}\right) \mp \frac{P}{\alpha E A_{(x)}} = 0, \quad \alpha > 0. \tag{3}$$

The solution to which is

$$u(x) = -\frac{x}{2\alpha} + \int_0^x \sqrt{\left(\frac{1}{2\alpha}\right)^2 + \frac{P}{\alpha E A_{(x)}}}\, dx \quad \text{for compression} \tag{4}$$

and

$$u(x) = +\frac{x}{2\alpha} - \int_0^x \sqrt{\left(\frac{1}{2\alpha}\right)^2 - \frac{P}{\alpha E A_{(x)}}}\, dx \quad \text{for tension} \tag{5}$$

$$\left|\frac{P}{\alpha E A_{(x)}}\right| \leqslant \left(\frac{1}{2\alpha}\right)^2 \quad \text{and} \quad \alpha > 0.$$

Deformation is assumed to be positive for tension. With the appropriate definition for $A_{(x)}$, (4) and (5) can be evaluated exactly.

Having obtained the exact solution, the finite element method applied to the principle of minimum potential energy will be developed for the class of one-dimensional problems being studied. The total potential energy π_p for the ith element is

$$\pi_{pi} = \int_{v_i} U_0\, dV_i + Pu_i - Pu_{i+1} \tag{6}$$

assuming no body forces.

Following the usual procedures of minimization, and incorporating the nodal displacements and co-ordinates as variables the following two general equations must be satisfied

$$\frac{\partial \pi_p}{\partial u_i} = \frac{\partial \pi_{pi-1}}{\partial u_i} + \frac{\partial \pi_{pi}}{\partial u_i} = 0 \tag{7}$$

and

$$\frac{\partial \pi_p}{\partial x_i} = \frac{\partial \pi_{pi-1}}{\partial x_i} + \frac{\partial \pi_{pi}}{\partial x_i} = 0 \tag{8}$$

Using a linear Lagrange interpolating polynomial for the problem being considered, we have

$$u(x) = \left(\frac{x - x_{i+1}}{x_i - x_{i-1}}\right) u_i + \left(\frac{x - x_i}{x_{i+1} - x_i}\right) u_{i+1}. \tag{9}$$

Thus (6) can be rewritten as

$$\pi_{pi} = E\left[\frac{1}{2}\left(\frac{u_{i+1} - u_i}{x_{i+1} - x_i}\right)^2 \pm \tfrac{1}{3}\alpha\left(\frac{u_{i-1} - u_i}{x_{i+1} - x_i}\right)^3\right] \times \int_{x_i}^{x_{i+1}} A(x)\, dx - P(u_{i+1} - u_i) \tag{10}$$

Substituting (10) into (7) and (8) one obtains for the ith element

$$(DEL)_i^2 \pm \frac{1}{\alpha}(DEL)_i \mp \frac{P}{\alpha E \bar{A}(x)_i} = 0 \tag{11}$$

for the ith node

$$\frac{P}{E}\left[(DEL)_i\left(2 - \frac{A(x_i)}{\bar{A}(x)_i}\right) - (DEL)_{i-1}\left(2 - \frac{A(x_i)}{\bar{A}(x)_{i-1}}\right)\right] \pm \tfrac{1}{3}\alpha A(x_i)\left[(DEL)_i^3 - (DEL)_{i-1}^3\right] = 0 \tag{12}$$

where

$$(DEL)_i = \frac{u_{i+1} - u_i}{x_{i-1} - x_i} \quad \text{and} \quad \bar{A}(x)_i = \frac{\int_{x_i}^{x_{i+1}} A(x)\, dx}{x_{i+1} - x_i}$$

Complete formulation of (11) and (12) is contained in Appendix A. Employing the above non-linear algebraic equations (11) and (12) optimal grids were obtained for various tapers, material definitions and load levels.

SOLUTION SEARCHING TECHNIQUE

Equation (11) is the finite difference expression for (3) by which all nodal displacements can be determined. There are two boundary conditions prescribed for this system. At the left extreme end, the displacement is prescribed as zero and at the right extreme end, the surface traction is prescribed as the force P. Thus for the 1st element, (11) gives

$$\left(\frac{u_2 - u_1}{x_2 - x_1}\right)^2 \pm \frac{1}{\alpha}\left(\frac{u_2 - u_1}{x_2 - x_1}\right) \mp \frac{P}{\alpha E \bar{A}(x)_1} = 0 \tag{13}$$

where $u_1 = 0$ and $x_1 = 0$.
This can be rewritten as

$$u_2^2 \pm \left(\frac{x_2}{\alpha}\right) u_2 \mp \frac{P x_2^2}{\alpha E \bar{A}(x)_1} \tag{14}$$

For a given grid configuration, the only unknown quantity in (14) is u_2 which can be determined directly as

$$u_2 = x_2\left[-\frac{1}{2\alpha} + \sqrt{\left(\frac{1}{2\alpha}\right)^2 + \frac{P}{\alpha E \bar{A}(x)_1}}\right] \text{for compression} \tag{15}$$

and

$$u_2 = x_2\left[+\frac{1}{2\alpha} - \sqrt{\left(\frac{1}{2\alpha}\right)^2 - \frac{P}{\alpha E \bar{A}(x)_1}}\right] \text{for tension} \tag{16}$$

Knowing u_2, we can proceed to the 2nd element and determine u_3 from (11). This procedure can be repeated successively until all nodal displacements are obtained for the given grid configuration.

In order to obtain an optimum grid, (12) must be satisfied simultaneously by all variable nodes within the model. The determination of such a configuration is tedious and requires a substantial computational effort. A non-linear programming would far exceed the cost of re-analysing the problem with manually improved models. To overcome these obstacles, a simplified algorithm is developed using computer-directed search techniques resulting in fast convergence with high accuracy.

The first variable node in the model is node 2 and the last is node m; nodes 1 and $(m+1)$ define the boundaries of the model, they cannot be varied. Thus for node 2, (12) gives

$$\frac{P}{E}\left[\left(\frac{u_3-u_2}{x_3-x_2}\right)\left(2-\frac{A(x_2)}{A(x)_2}\right)-\frac{u_2}{x_2}\left(2-\frac{A(x_2)}{A(x)_1}\right)\right] \pm\tfrac{1}{3}\alpha A(x_2)\left[\left(\frac{u_3-u_2}{x_3-x_2}\right)^3-\left(\frac{u_2}{x_2}\right)^3\right]=R. \qquad (17)$$

If the model has an optimum grid configuration, R is zero. However by assuming an initial grid, we can determine u_2 and u_3 from (11) with which R can be calculated. The term R has a physical meaning. It is the gradient of the total potential energy with respect to the generalized co-ordinate x. Thus if R turned out to be negative, the minimization criterion guarantees that node 2 is left of its optimum location. Likewise if R turned out to be positive, node 2 must be right of its optimum location as illustrated in Fig. 2. Thus with R, we can "move" node 2 towards its optimum location in a directed manner.

The computer-directed search algorithm is shown in Fig. 3. Select node 2 as the target node to be moved first. The range of movement for node 2 is between the limits of nodes 1 and 3. If $R<0$, node 2 must be moved towards node 3. When $R=0$, node 2 remains unchanged and if $R>0$, node 2 must be moved towards node 1. Each increment of movement is one-tenth the distance between node 2 at the starting position and its limiting node. Movement will continue in the same direction until the condition with $R=0$ or a change in sign for R is obtained. Depending on the relative magnitudes of R in the last step, a new generalized co-ordinate for node 2 is determined as illustrated in Fig. 4. Then node 3 becomes the target node with nodes 2 and 4 as its limiting nodes. A similar procedure is applied until all variable nodes are "optimized" for this iteration. This new configuration is then compared with that from the previous iteration. If the difference is below a specified tolerance, near optimal grid configuration is established. Otherwise, the entire model is optimized again in the next iteration.

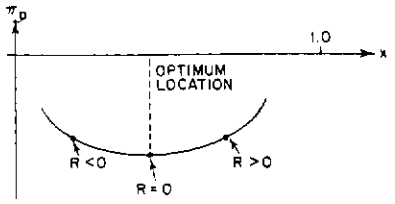

Fig. 2. Variation of total potential energy with respect to generalized co-ordinate.

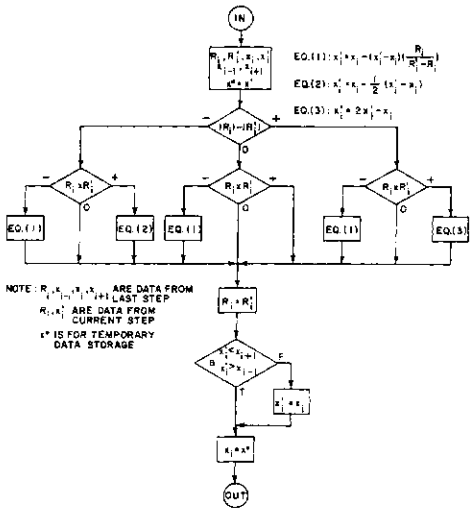

Fig. 3. Flow chart of the computer-directed search algorithm.

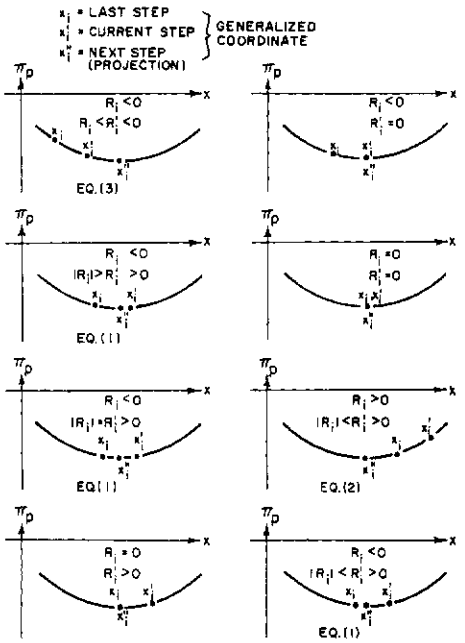

Fig. 4. Graphical representation of the search algorithm.

SAMPLE PROBLEMS

A series of taper bars with a linear taper geometry of the form $A(x)=ax+b$ were examined. The taper ratio, defined to be the ratio of the section area at $x=l$ and that at $x=0$, was between 0.5 and 0.005. A generalized co-ordinate system was used. The coefficient of constitutive nonlinearity, α, was assumed to be 1.0. The load applied at $x=1.0$ was chosen to be such that $P/EA(0)=1\times10^{-3}$. This was to ensure that a small deformation condition was maintained. A series of models having two to five finite elements (one to four variable nodes) were examined. An unoptimized grid is defined to be one with the nodes equally spaced along the entire length of the bar, while an optimized grid is assumed to be the one obtained from the computer-directed search algorithm. Exact solutions were evaluated and used as the basis for comparison.

From the various tapered bar examples studied,

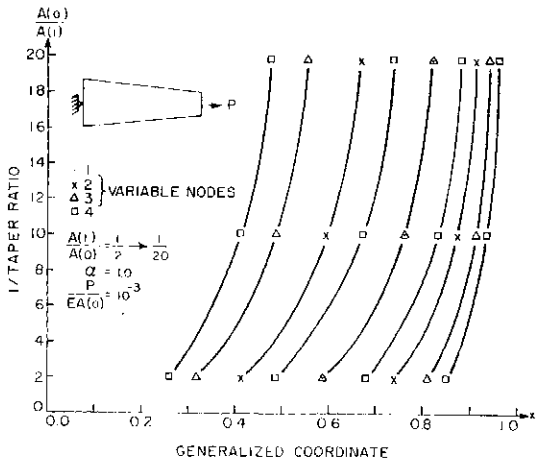

Fig. 5. Optimal grid configuration for tapered bars of the form $A(x)=ax+b$.

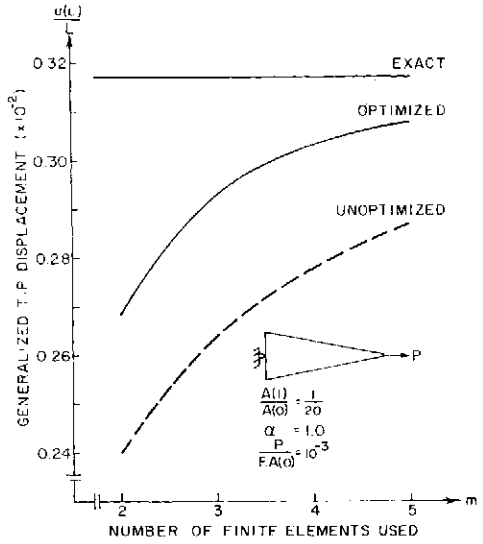

Fig. 6. Grid sensitivity of generalized tip displacement.

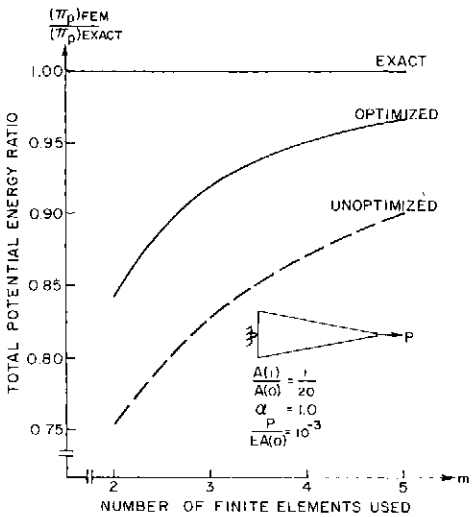

Fig. 7. Grid sensitivity of total potential energy ratio.

the following factors will be considered in the comparison of optimized and unoptimized grids:

(a) approximations of the displacements and strains
(b) global minimum total potential energy
(c) potential energy content per element.

DISCUSSION

Typical results are shown in Figs. 5–9 from which the following conclusions have been made:

(1) In order to achieve the same level of accuracy for this class of problems the optimal grid required 50% fewer degrees of freedom than an unoptimized grid.

(2) Each element in an optimal grid had the same energy content.

(3) The nodal strains from the optimized mesh were exact even though only an approximate solution was obtained for the displacements.

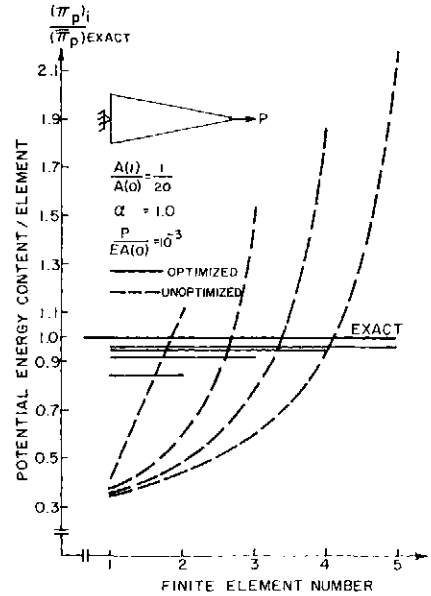

Fig. 8. Grid sensitivity of potential energy content/element.

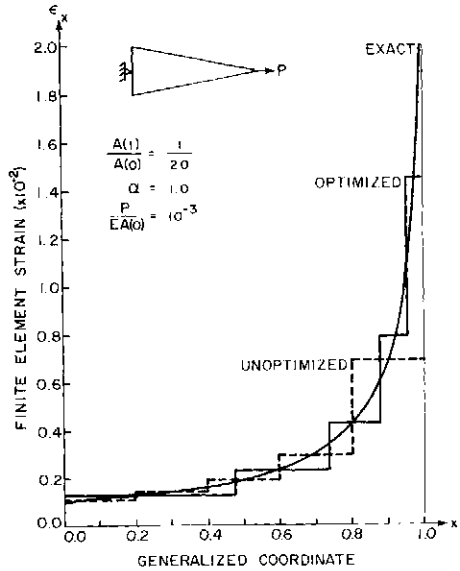

Fig. 9. Grid sensitivity of finite element strain.

(4) The same algorithm in general can be applied to other taper configurations.

(5) Standardized charts can be developed to aid finite element engineers in planning grid layouts.

Thus from this initial investigation optimal grid characteristics for nonlinear constitutive relations indicate that substantial savings can be achieved and suggests possible computational strategies for mesh modification and/or mesh refinement.

FUTURE WORK

Other nonlinear constitutive relations can be incorporated in the algorithm together with new taper configurations. As for two-dimensional analyses, the use of isoenergetics can assist design engineers in grid layouts. Each line orthogonal to the isoenergetic contours can be treated as a one-dimensional tapered bar. The variation of section area along its length will be half the distance between the above lines. However, the Poisson ratio effect has not been taken into account and further research is required. This concept can also be projected to three-dimensional models.

Finite element analyses with geometric nonlinearity have been investigated in a similar manner and promising results were obtained [9]. However the combined effect of both types of nonlinearities are still open for further research and development. Other types of loading conditions can be examined, such as variable traction along the length of the bar.

REFERENCES

1. M. S. Shephard, Finite element grid optimization—a review. *The Third Nat. Cong. Pressure Vessels and Piping*, San Francisco, California, June, 1979.
2. D. J. Turcke, Characteristics of piecewise approximations in numerical analysis. *The Third Nat. Cong. on Pressure Vessels and Piping*, San Francisco, California, June, 1979.
3. D. J. Turcke, Optimum mesh configurations in the finite element method. Ph.D. Thesis, University of Waterloo, 1974.
4. B. A. Szabo, Adaptive finite element approximations: state of the art. *Symposium on Mathematical Modeling in Structural Engineering*, NASA—Langely Research Center, Oct. 1979.
5. I. Babuska *et al.*, Mathematical problems of discrete modeling and *a posteriori* reliability estimates. *Symp. on Mathematical Modeling in Structural Engineering*, NASA—Langely Research Center, Oct., 1979.
6. W. Prager, A note on the optimal choice of finite element grids. *Comput. Meth. Appl. Mech. Engng* **6** 363–366 (1975).
7. C. A. Felippa, Numerical experiments in finite element grid optimization by direct energy search. *Appl. Math. Modelling* **1**, 239–244 (1977).
8. Y. C. Fung, *Foundations of Solid Mechanics*, Chap. 10.7. Prentice-Hall, Englewood Cliffs, New Jersey (1965).
9. D. Siu and D. J. Turcke, Optimum grids in nonlinear finite element analysis. *Symp. on Mathematical Modeling in Structural Engineering*, NASA—Langely Research Center, Oct., 1979.

APPENDIX A

Development of general nonlinear algebraic equations

The detailed formulation of eqns (11) and (12) in the main text is presented here. Considering eqn (10) and differentiating with respect to u_i gives

$$\frac{\partial \pi_{pi}}{\partial u_i} = -E\left[\left(\frac{u_{i+1}-u_i}{x_{i+1}-x_i}\right)+\alpha\left(\frac{u_{i+1}-u_i}{x_{i+1}-x_i}\right)^2\right]\frac{\int_{x_i}^{x_{i+1}} A(x)\,dx}{x_{i+1}-x_i}+P \tag{A1}$$

and

$$\frac{\partial \pi_{pi-1}}{\partial u_i} = E\left[\left(\frac{u_i-u_{i-1}}{x_i-x_{i-1}}\right)+\alpha\left(\frac{u_i-u_{i-1}}{x_i-x_{i-1}}\right)^2\right]\frac{\int_{x_{i-1}}^{x_i} A(x)\,dx}{x_i-x_{i-1}}-P. \tag{A2}$$

Substituting (A1) and (A2) into (7) gives

$$E[(DEL)_{i-1}+\alpha(DEL)_{i-1}^2]\bar{A}(x)_{i-1} - E[(DEL)_i+\alpha(DEL)_i^2]\bar{A}(x)_i=0. \tag{A3}$$

However, for the $(m+1)$th node at the boundary where a traction is prescribed, (7) reduces to

$$\frac{\partial \pi_{pm}}{\partial u_{m+1}}=0 \tag{A4}$$

and (A3) for the mth element is

$$E[(DEL)_m+\alpha(DEL)_m^2]\bar{A}(x)_m-P=0. \tag{A5}$$

Thus (7) reduces to the general recurring form

$$E[(DEL)_i+\alpha(DEL)_i^2]\bar{A}(x)_i-P=0 \tag{A6}$$

or

$$(DEL)_i^2+\frac{1}{\alpha}(DEL)_i-\frac{P}{\alpha E\bar{A}(x)_i}=0 \tag{A7}$$

by direct substitution of (A5) into (A3).

Again, employing eqn (10) and differentiating with respect to x_i gives

$$\frac{\partial \pi_{pi}}{\partial x_i} = E\left[\left(\frac{u_{i+1}-u_i}{x_{i+1}-x_i}\right)^2+\alpha\left(\frac{u_{i+1}-u_i}{x_{i+1}-x_i}\right)^3\right]\frac{\int_{x_i}^{x_{i+1}} A(x)dx}{x_{i+1}-x_i} - E\left[\frac{1}{2}\left(\frac{u_{i+1}-u_i}{x_{i-1}-x_i}\right)^2+\frac{1}{3}\alpha\left(\frac{u_{i+1}-u_i}{x_{i+1}-x_i}\right)^3\right]A(x_i) \tag{A8}$$

and

$$\frac{\partial \pi_{pi-1}}{\partial x_i} = -E\left[\left(\frac{u_i-u_{i-1}}{x_i-x_{i-1}}\right)^2+\alpha\left(\frac{u_i-u_{i-1}}{x_i-x_{i-1}}\right)^3\right]\frac{\int_{x_{i-1}}^{x_i} A(x)\,dx}{x_i-x_{i-1}} + E\left[\frac{1}{2}\left(\frac{u_i-u_{i-1}}{x_i-x_{i-1}}\right)^2+\frac{1}{3}\alpha\left(\frac{u_i-u_{i-1}}{x_i-x_{i-1}}\right)^3\right]A(x_i). \tag{A9}$$

Substituting (A8) and (A9) into (8) gives

$$\begin{aligned}&-E[(DEL)_{i-1}^2+\alpha(DEL)_{i-1}^3]\bar{A}(x)_{i-1}\\&+E[\tfrac{1}{2}(DEL)_{i-1}^2+\tfrac{1}{3}\alpha(DEL)_{i-1}^3]A(x_i)\\&+E[(DEL)_i^2+\alpha(DEL)_i^3]\bar{A}(x)_i\\&-E[\tfrac{1}{2}(DEL)_i^2+\tfrac{1}{3}\alpha(DEL)_i^3]A(x_i)=0.\end{aligned} \tag{A10}$$

This can further be reduced with direct substitution of (A6) into (A10) which gives

$$\begin{aligned}&-P(DEL)_{i-1}+\tfrac{1}{2}P(DEL)_{i-1}\frac{A(x_i)}{\bar{A}(x)_{i-1}}\\&+\tfrac{1}{6}\alpha E(DEL)_{i-1}^3A(x_i)\\&+P(DEL)_i-\tfrac{1}{2}P(DEL)_i\frac{A(x_i)}{\bar{A}(x)_i}+\tfrac{1}{6}\alpha E(DEL)_i^3A(x_i)=0\end{aligned} \tag{A11}$$

and then

$$\frac{P}{E}\left[(DEL)_i\left(2-\frac{A(x_i)}{\bar{A}(x)_i}\right)-(DEL)_{i-1}\left(2-\frac{A(x_i)}{\bar{A}(x)_{i-1}}\right)\right] \pm\tfrac{1}{3}\alpha A(x_i)[(DEL)_i^3-(DEL)_{i-1}^3]=0. \tag{A12}$$

Computers & Structures, Vol. 13, pp. 91–96, 1981
Printed in Great Britain.

0045-7949/81/010091-06$02.00/0

EXPERIMENTS WITH DIRECT INTEGRATION ALGORITHMS FOR ORDINARY DIFFERENTIAL EQUATIONS IN STRUCTURAL DYNAMICS

JON BRAEKHUS
Det norske Veritas, 1322 Høvik, Norway

and

JAN OLE AASEN
Norges Tekniske Høgskole, 7034 Trondheim-NTH, Norway

(*Received* 6 *May* 1980)

Abstract—Various explicit integration methods are compared with an implicit method on two dynamic problems in solid mechanics. Methods of steplength-control are discussed. Some effects of steplength-control on the behaviour of explicit and implicit methods are pointed out and illustrated by the problems studied.

1. INTRODUCTION

In numerical solution of the partial differential equations of structural dynamics one usually proceeds by discretizing the space-variables by the FEM and choosing some discretization scheme for the time-variable. As is well known this procedure can be regarded as consisting of two steps in which the partial differential equations are first converted into a system of ordinary differential equations (ODEs) which one then solves by some discrete variable method

We report here some numerical experiments based on various implications of the above point of view, that we believe should be taken into consideration in the solution of dynamical problems in structural analysis.

Our experiments involved the design of a program for computing plane, finite deformations of an elastic beam. The equations of motion, in a total Lagrangian formulation, were discretized by ordinary finite element techniques resulting in a nonlinear ODE of the form

$$M\ddot{\mathbf{u}} + \mathbf{k}(\mathbf{u}) = \mathbf{f}(t) \tag{1.1}$$

where $\mathbf{u}(t)$ is a displacement-vector, M is a mass matrix, $\mathbf{k}$ specifies the elastic response, and $\mathbf{f}$ is a load-vector.

A set of initial value problems for (1) were then solved by several methods, viz.

(i) Runge–Kutta–Fehlberg methods of orders 1–3 [1].

(ii) An adaptive Runge–Kutta method with optimized stability-properties [2].

(iii) The central difference method.

(iv) The trapezoidal rule or average acceleration method.

The problems and the methods chosen were intended to throw some light on various problems that arise in the solution of non-linear differential equations.

In principle, (1.1) can be solved by any of the existing methods for ODEs. It is known [8] that an ODE-solver can be more or less well-matched with the particular FEM applied to the PDEs, so several ODE-solvers should be considered for any given problem. To make this freedom of choice feasible, a computer program should be designed in a modular form so that the time integrator "sees" only the ODE to be solved. In our program this is done by writing the ODE integrators for equations of the form

$$M\ddot{\mathbf{u}} = \mathbf{F}(t, \mathbf{u}, \dot{\mathbf{u}}), \tag{1.2}$$

basing all computations including approximations to Jacobians (i.e. tangential stiffness and damping matrices) on values of the vector $\mathbf{F}$. The task of the element-part of the program is then to deliver values of $\mathbf{F}$.

With any ODE-solver, the steplengths used are subject to requirements of local accuracy and stability, the last term meaning that local errors committed in any step should not be unduly amplified in subsequent steps. An ODE is classified as non-stiff or stiff depending on which of the two requirements is the over-riding one. Usually a non-stiff ODE can be solved effectively by an explicit method, whereas a stiff equation requires some form of impliciteness in the integration method. Explicit methods involve so much less work per step than implicit ones that we think they should be utilized more than they are at present in structural problems. Besides, coded with a steplength-control, an explicit method can detect stiffness [3] and will therefore not become unstable, only possibly inefficient. Three of the integration methods tested were explicit, having slightly differing stability properties. We believe that two of them (i) and (ii) have not been tested on structural problems before.

Whether the method chosen is explicit or implicit, there remains the problem of deciding which steplengths should be used. Automatic step-control based or estimates of local errors is contained in all standard ODE-solvers, while apparently very few of the programs presently used for structural problems have this feature. Without a step-control one has no indication of the accuracy of the results obtained, and in case an implicit method is used, its stability-properties can mislead one into choosing too large steps. Of the algorithms tested, (i) and (iv) have step-control. Runge–Kutta–Fehlberg methods are designed with this problems in mind and compute a local error-estimate

as a difference between values delivered by two R-K-formulas of different order. In method (iv) we estimate local error by the difference between values computed in one full step and in two half-steps. How to utilise local error-estimates effectively in a step-control mechanism is no straight forward matter [4]. Our results on method (i) show that a specified accuracy can be obtained, but a diagram of steplengths produced by the program appear ragged, suggesting that the mechanism could be improved. With an implicit method like (iv) the problem is complicated by the fact that the steplength affects the convergence-rate of the iterations performed in each step and that the tolerance used in the acceptance-test of an iterated value must be related to the tolerance used in an acceptance-test of a step-length.

We have not found any general solution to these problems. Improvements in the basic algorithms can probably be obtained for some class of problems by a "tuning" of the parameters involved on representative problems from the given class.

2. ONE-STEP METHODS AND STEPLENGTH CONTROL

An initial value problem

$$\begin{aligned} &M\ddot{\mathbf{u}} = \mathbf{F}(t, \mathbf{u}, \dot{\mathbf{u}}), \quad t \geqslant 0, \\ &\mathbf{u}(0) = \mathbf{u}_0, \quad \dot{\mathbf{u}}(0) = \mathbf{v}_0, \end{aligned} \tag{2.1}$$

may be converted into an equivalent first-order problem

$$\begin{cases} \dot{\mathbf{y}} = \mathbf{f}(t, \mathbf{y}), \quad t \geqslant 0, \\ \mathbf{y}(0) = \mathbf{y}_0, \end{cases} \tag{2.2}$$

by defining

$$\begin{aligned} &\mathbf{v} = \dot{\mathbf{u}}, \quad \mathbf{y} = \begin{bmatrix} \mathbf{u} \\ \mathbf{v} \end{bmatrix}, \quad \mathbf{y}_0 = \begin{bmatrix} \mathbf{u}_0 \\ \mathbf{v}_0 \end{bmatrix}, \\ &\mathbf{f}(t, \mathbf{y}) = \begin{bmatrix} \mathbf{v} \\ M^{-1}\mathbf{F}(t, \mathbf{u}, \mathbf{v}) \end{bmatrix}. \end{aligned} \tag{2.3}$$

The algorithms (i), (ii) and (iv) are best described in terms of (2.2), and algorithm (iii) may also be described this way if the special structure of $\mathbf{f}$ is taken into account.

A one-step method for (2.2) may be characterized by a function $\mathbf{E}(t, \mathbf{x}, h)$, depending on $\mathbf{f}$, such that approximations $\mathbf{y}(t_n)$ are defined by the rule

$$\mathbf{y}_{n+1} = \mathbf{E}(t_n, \mathbf{y}_n, h_n). \tag{2.4}$$

Here h_n denotes the steplength employed at step n. A local error for $\mathbf{E}$ is defined as follows: let $\mathbf{L}(\tau, \mathbf{x}, t)$ denote the solution of the problem

$$\begin{aligned} &\dot{\mathbf{y}} = \mathbf{f}(t, \mathbf{y}), \quad t \geqslant \tau, \\ &\mathbf{y}(\tau) = \mathbf{x}. \end{aligned}$$

Then the local error $\mathbf{d}(t, \mathbf{x}, h)$ is given by

$$\mathbf{d}(t, \mathbf{x}, h) = \mathbf{E}(t, \mathbf{x}, h) - \mathbf{L}(t, \mathbf{x}, t+h). \tag{2.5}$$

The global error in $\mathbf{y}_n$ will be denoted by

$$\mathbf{e} = \mathbf{y}_n - \mathbf{y}(t_n).$$

Let $\|\cdot\|$ denote a vector-norm, and suppose that $\mathbf{E}$ and $\mathbf{L}$ are Lipschitz-continuous, i.e. that $\alpha(t, h)$ and $\beta(t, h)$ exist such that

$$\begin{aligned} &\|\mathbf{E}(t, \mathbf{x}, h) - \mathbf{E}(t, \mathbf{x}', h)\| \leqslant \alpha(t, h)\|\mathbf{x} - \mathbf{x}'\|, \\ &\|\mathbf{L}(t, \mathbf{x}, t+h) - \mathbf{L}(t, \mathbf{x}', t+h)\| \leqslant \beta(t, h)\|\mathbf{x} - \mathbf{x}'\|. \end{aligned}$$

The following relations are easily established.

$$\|\mathbf{e}_{n+1}\| \leqslant \alpha(t_n, h_n)\|\mathbf{e}_n\| + \|\mathbf{d}(t_n, \mathbf{y}(t_n), h_n)\|, \tag{2.6}$$

$$\|\mathbf{e}_{n+1}\| \leqslant \beta(t_n, h_n)\|\mathbf{e}_n\| + \|\mathbf{d}(t_n, \mathbf{y}_n, h_n)\|. \tag{2.7}$$

If the solution $\mathbf{y}(t)$ is bounded, (2.6) shows that to get small global errors, we must impose an accuracy-condition,

$$\|\mathbf{d}(t_n, \mathbf{y}(t_n), h_n)\| \quad \text{small}, \tag{2.8}$$

and a stability-condition

$$\alpha(t_n, h_n) \leqslant 1 \tag{2.9}$$

(to avoid exponential growth in $\mathbf{e}_n$).

If solutions of the differential equations are stable, i.e. if

$$\beta(t, h) \leqslant 1$$

for relevant values of t and h, then (2.7) shows that global errors will be small if $\|\mathbf{d}(t_n \mathbf{y}_n, h_n)\|$ is kept small.

This last quantity contains the actually computed vector $\mathbf{y}_n$, and can be estimated. Such estimates are usually made in one of two ways: The first employs an additional formula $\mathbf{E}'$ of an order 1 higher than $\mathbf{E}$, and the local error is estimated by

$$\mathbf{d}(t, \mathbf{x}, h) \approx \mathbf{E}(t, \mathbf{x}, h) - \mathbf{E}'(t, \mathbf{x}, h). \tag{2.10}$$

The Runge–Kutta–Fehlberg methods have been constructed for effective application of (2.10). Since values given by $\mathbf{E}'$ are available at each step, it seems natural to compute the vectors $\mathbf{y}_n$ by $\mathbf{E}'$ instead of $\mathbf{E}$. This is called local extrapolation [3]. In the second method one calculates the difference between results of a full step and two half-steps and sets

$$\begin{aligned} \mathbf{d}(t, \mathbf{x}, h) &\approx (\mathbf{x}' - \mathbf{x}'')/(1 - 2^{-p}), \\ \mathbf{x}' &= \mathbf{E}(t, \mathbf{x}, h), \\ \mathbf{x}'' &= \mathbf{E}(t + h/2, \mathbf{E}(t, \mathbf{x}, h/2), h/2). \end{aligned}$$

In this case it is natural to define the solution vectors by the values of $\mathbf{x}''$ calculated at each step. We have based steplength-control for the trapezoidal rule on (2.11).

In our programs the mechanisms for selecting steplength are as follows. Let δ_n be an estimate of $\mathbf{d}(t_n, \mathbf{y}_n, h_n)$ and let $|||\cdot|||$ denote the maximum norm. The integration is to proceed such that

$$|||\delta_n||| \leqslant \varepsilon \tag{2.12}$$

where ε is a specified tolerance. If a value of h_n, calculated at step $n-1$ results in a $|||\delta_n|||$ larger than ε, h_n is reduced by repeated use of the formula

$$h_n := \varphi \cdot (\varepsilon / |||\delta_n|||)^{1/(p+1)} h_n \tag{2.13}$$

until (2.12) is satisfied. Here φ is a fixed factor and p is the order of the method. If (2.12) is satisfied, h_{n+1} is set equal to the r.h.s. of (2.13), with some restrictions on the size of h_{n+1}/h_n. A detailed discussion of the above technique may be found in [5].

With an implicit method there are two additional problems that must be considered when steplength-control is to be implemented. We discuss them for the trapezoidal rule. This method defines $\mathbf{E}(t, \mathbf{x}, h)$ as the solution $\mathbf{z}$ of the equation

$$\mathbf{z} = \mathbf{x} + (h/2)(\mathbf{f}(t, \mathbf{x}) + \mathbf{f}(t+h, \mathbf{z})). \tag{2.14}$$

The equation cannot in general be solved exactly so instead of $\mathbf{z}$, we have to use an approximation $\bar{\mathbf{z}}$. Put

$$\mathbf{s} = \bar{\mathbf{z}} - \mathbf{z}.$$

The local error is then not $\mathbf{d}$, but $\mathbf{d}+\mathbf{s}$, and $\mathbf{s}$ should be small compared to $\mathbf{d}$. Let $D\mathbf{f}$ denote the Jacobian w. r. to the second variable of $\mathbf{f}$, and let $\mathbf{r}(\bar{\mathbf{z}})$ denote the difference between l.h.s. and r.h.s. of (2.14) with $\mathbf{z}$ replaced by $\bar{\mathbf{z}}$.

Then it can be shown that

$$\mathbf{s} = -(I-(h/2)J)^{-1}\mathbf{r}(\bar{\mathbf{z}}),$$

$$J = \int_0^1 D\mathbf{f}(t+h,\ \mathbf{z}+\xi\mathbf{s})\,d\xi.$$

Suppose that (2.14) is solved by a quasi-Newton method

$$\begin{cases} \mathbf{z}^{(m+1)} = \mathbf{z}^{(m)} - \mathbf{w}^{(m)}, \\ \mathbf{w}^{(m)} = N^{-1}\mathbf{r}(\mathbf{z}^{(m)}), \end{cases} \tag{2.15}$$

and the convergence is rapid. We may then infer that $N \approx I-(h/2)J$, and that an $\mathbf{s}^{(m)}$ corresponding to $\mathbf{z}^{(m)}$ satisfies

$$\mathbf{s}^{(m)} \approx \mathbf{w}^{(m)}.$$

Hence the tolerance for the iterations at each step should be related to the specified tolerance ε for local errors. In our program we terminate iterations when

$$\|\mathbf{w}^{(m)}\| \leqslant \varepsilon/10.$$

The next problem concerns the calculation of the Newton-matrix N and the influence of the steplength on the convergence rate of (2.15). We want to calculate and factorize N as infrequently as possible. In our method N is an approximation of $I-(h/2)D\mathbf{f}$ evaluated at some previously calculated solution-point $(t_k, \mathbf{y}_k)$. At step n, the iteration (2.15) is first performed with the most recently calculated N. If convergence fails after a specified number of iterations, we calculate $D\mathbf{f}(t_n, \mathbf{y}_n)$ and a corresponding N, and start iterations anew with the same steplength. If convergence still fails, the steplength is reduced by a fixed, specified factor, and a new N is calculated from $D\mathbf{f}(t_n, \mathbf{y}_n)$. This process is continued until convergence is obtained. With this method we do not have to specify in advance how often N should be evaluated.

We should remark here that while the discussion has been in terms of a general first-order equation (2.2), the methods tested have been implemented for equations specified by (2.1)–(2.3). This means that the Newton-matrix needed in iterations will in fact be an approximation of

$$M-(h/2)^2\partial\mathbf{F}/\partial\mathbf{u}-(h/2)\partial\mathbf{F}/\partial\mathbf{v}. \tag{2.16}$$

Also, when we call an integration method explicit, we disregard inversion (factorization) of the mass matrix M.

3. THE METHODS TESTED.

A Runge–Kutta–Fehlberg method consists of two Runge–Kutta formulas $\mathbf{E}$ and $\mathbf{E}'$ of orders p and $p+1$. We have implemented methods of orders $p=1, 2, 3$ given by Tables 3, 5 and 7 in [1]. The methods will be denoted by $RKFp(p+1)$ with an X appended if local extrapolation has been used. Steplength-control is incorporated, but may be switched off.

An adaptive Runge Kutta method [2] defines an $\mathbf{E}(t, x, h)$ as follows. Put

$$\mathbf{x}_0 = \mathbf{x}, \quad \mathbf{x}_j = \mathbf{x} + c_j\mathbf{f}(t + c_{j-1}h,\ \mathbf{x}_{j-1}), \quad j = 1(1)q.$$

Then

$$\mathbf{E}(t, \mathbf{x}, h) = \mathbf{x}_q.$$

The method is of second order if $q \geqslant 1$, $c_q = 1$, and $c_{q-1} = 1/2$. c_0 is always 0, while c_j, $1 \leqslant j \leqslant q-2$ may be chosen to optimize the stability-properties of the method in some sense (see below). Our implementations will be denoted by ARK(q). Steplength-control has not been included.

The central difference method becomes explicit for equations of the form (2.1) only when $\mathbf{F}$ is independent of $\dot{\mathbf{u}}$. We have implemented the method, without steplength-control, for equations of the form (1.1). The method is denoted by *CD*.

Finally, our implementation of the trapezoidal rule for equations (2.1)–(2.3) will be denoted TRAP.

Some data for our implementations of the methods are listed below.

Table 1.

Method	# evaluations of $\mathbf{F}$ per step	Required storage
RKFp(p+1)	p+1	M (factorized)
RKFp(p+1)X	p+2	2(p+5) vectors *)
ARK(q)	q	M (fact.), 6 vectors
CD	1	M (fact.), 6 vectors
TRAP	variable	M, ∂F/∂u, ∂F/∂v, Newton-mat., 13 vectors

*) A vector is a value of $\mathbf{u}$, $\mathbf{v}$ or $\mathbf{F}$.

4. STABILITY PROPERTIES.

We assume now that the equation to be integrated has the form

$$M\ddot{\mathbf{u}} + \mathbf{k}(\mathbf{u}) = \mathbf{q}(t) \tag{4.1}$$

with a symmetric, positive definite Jacobian (tangential stiffness-matrix)

$$K(u) = \partial\mathbf{k}/\partial\mathbf{u}.$$

An integration method will be called unconditionally stable if, when applied to (4.1), the resulting $\mathbf{E}$ satisfies (2.9) without restrictions on h_n. The explicit methods do not have this property. Arguments based on local linearizations of (4.1) indicate that to satisfy (2.9), h_n must be chosen such that

$$\rho_n^{1/2}h_n \leqslant \beta, \tag{4.2}$$

where ρ_n is the spectral radius of $M^{-1}K(\mathbf{u}_n)$ and β is a constant depending on the method. If K is constant, (2.9) and (4.2) are equivalent.

The trapezoidal rule is unconditionally stable if K is constant. The unconditional stability probably does

Table 2.

Method	β
RKF1(2)	0
RKF1(2)X	0
RKF2(3)	1.7
RKF2(3)X	1.7
RKF3(4)	2.8
RKF3(4)X	3.0
ARK(p)	p-1
CD	2

not hold in general, but it seems unlikely that step-lengths will have to be delimited for stability-reasons with this method.

5. EVALUATIONS OF THE JACOBIANS FOR THE TRAPEZOIDAL RULE

As was mentioned in the introduction, our test-program consists of two independent parts, of which one is the ODE-solver. The task of the other part is to deliver a mass matrix and a response-vector. It then seemed logical to calculate Jacobians, if needed, by use of the response-vector alone. To do this efficiently, we have employed a method described in [6]. The idea is as follows. Suppose that we want an approximation of

$$K(u)=\partial\mathbf{k}(\mathbf{u})/\partial\mathbf{u}.$$

A simple way is to use differences

$$\frac{\partial k_i}{\partial u_j}\approx\frac{k_i(\mathbf{u}+\delta e_j)-k_i(\mathbf{u})}{\delta}$$

where δ is an increment and $\mathbf{e}_j$ the jth coordinate vector. If K is a bandmatrix of bandwidth $b=2m-1$ so that k_i is independent of u_j if $|i-j|\geq m$, we may find simultaneously approximations of columns $j+kb, k=0,1,2,\ldots$ of K from the difference

$$k(\mathbf{u}+\delta\Sigma\mathbf{e}_{j+kb})-k(\mathbf{u}).$$

In this way we need $b+1$ evaluations of $\mathbf{k}$ to calculate an approximation of K. We do not know any general rule for selecting a value of δ. In our test-cases $K(0)$ is known and δ chosen so that the error in the approximation is small for $\mathbf{u}=0$.

6. TEST-EQUATIONS

Two test-cases are presented. Both concern motions of a beam of length l, with a rectangular cross-section of breadth b and height h. The material constants are: density $\rho=7850$ kg/m^3, mod. of elasticity $\xi=3.2\times10^{11}$ N/m^2. In both cases the resulting equation takes the form

$$M\ddot{\mathbf{u}}+\mathbf{k}(\mathbf{u})=\mathbf{q}(t)$$
$$\mathbf{k}(\mathbf{u})=K\mathbf{u}+C\mathbf{uuu}.$$

K is a matrix and C a trilinear operator.

Case 1. *Axially loaded rod*

A rod is kept fixed at one end, and a load

$$P(t)=\begin{cases}P_0\sin(\pi t/0.004), & t\leq0.004\text{ sec},\ P_0=8\times10^8\ N\\ 0, & t>0.004\text{ sec.}\end{cases}$$

is applied at the other. Denote displacements by $U(x,t)$. The equations for U are

$$bh\int_0^l(\rho U_{tt}\delta U+S\delta E)\,dx=P\delta U(0),$$
$$S=\xi E,\ E_x=U_x+U_x^2/2,$$
$$U(x,0)=U_t(x,0)=0,\ U(l,t)=0.$$

Indices denote partial differentiations. The dimensions used are $l=100, b=h=1.935\times10^{-2}$. U is approximated by a piecewise linear function with 50 elements of equal length.

Case 2. *Free oscillations of a hinged beam*

Let x and y denote coordinates parallel and perpendicular to the beam-axis, and let $U(x,t)$, $v(x,t)$ denote displacements in the x- and y-direction of points along the axis. The equations of motion are

$$\int_0^l\int_{-h/2}^{h/2}(\rho U_{tt}\delta U+\rho V_{tt}\delta V+S\delta E)\,dy\,dx=0,$$
$$S=\xi E,\quad E=U_x-yV_{xx}+V_x^2/2.$$

Initial and boundary-values for U and V are

$$U(x,0)=U_0(x)=-l(\delta\alpha)^2(\pi/8)\sin(2\pi x/l),$$
$$V(x,0)=V_0(x)=l\delta\alpha\sin(\pi x/l),$$
$$U_t(x,0)=V_t(x,0)=0,$$
$$U(x,t)=V(x,t)=V_{xx}(x,t)=0,\quad x=0,l,$$
$$\delta=h/(l\sqrt{12}).$$

α is a constant. If $\delta\ll1$, then with errors of $O(\delta^2)$,

$$U(x,t)=U_0(x)(cn(\omega t,k^2))^2,$$
$$V(x,t)=V_0(x)cn(\omega t,k^2),$$
$$\omega^2=(1+\alpha^2/4)\pi^4\xi I/(\rho hl^4),\ k^2=\alpha^2/(8+2\alpha^2),$$
$$cn=\text{elliptic cosine.}$$

See e.g. [9]. The dimensions of the beam are $l=50$, $h=0.5$. U is approximated by a piecewise linear function and V by a cubic Hermite-spline. The beam is divided into 10 elements of equal length. Two values of α have been used. With $\alpha=10^{-6}$ the equations are in effect linear, while for $\alpha=4$, the nonlinear terms become significant.

7. RESULTS

Tables 3 and 4 contain results of various runs with the methods tested. Where steplength control has been employed, the tolerances listed are given relative to the maximum value of $\left\|\begin{bmatrix}\mathbf{u}(t)\\ \dot{\mathbf{u}}(t)\end{bmatrix}\right\|$ over the integration interval. The relative errors at a given t_n are defined as

$$\left\|\begin{bmatrix}\mathbf{u}_n\\ \mathbf{v}_n\end{bmatrix}-\begin{bmatrix}\mathbf{u}(t_n)\\ \dot{\mathbf{u}}(t_n)\end{bmatrix}\right\|\Big/\left\|\begin{bmatrix}\mathbf{u}(t_n)\\ \dot{\mathbf{u}}(t_n)\end{bmatrix}\right\|.$$

Here $\mathbf{v}_n$ is the calculated approximation of $\dot{\mathbf{u}}(t_n)$, and $\|\cdot\|$ is the maximum norm. In both cases a reference solution was calculated by a RKF3(4)X using a fixed, very small steplength.

8. COMMENTS

The two test-cases show different behaviour with respect to stiffness. We regard case 1 as a non-stiff problem. The quantity $\rho_n^{1/2}$ in eqn (4.2) is $O(10^4)$, but

Table 3. Case 1: Equations integrated over [0, 0.008].

Method	rel. tolerance	# steps	# attempt. steps	# deriv. calc. *)	time used	rel. error at 0.008
RKF1(2)	5.6E-5	146	166		177	1.3E-1
RKF2(3)	- " -	88	124		197	2.2E-2
RKF3(4)	- " -	110	148		315	3.7E-3
RKF1(2)	2.8E-4	142	173		184	6.3E-1
RKF2(3)	- " -	59	79		125	5.2E-2
RKF3(4)	- " -	74	99		210	1.3E-2
ARK(4)		80			116	8.4E-2
- " -		32			46	UNSTABLE
ARK(6)		32			77	1.1E-1
- " -		20			48	UNSTABLE
CD		80			39	6.4E-2
-"-		50			25	1.3E-1
-"-		40			20	UNSTABLE
TRAP	2.8E-4	113	151	1	1084	1.3E-2
-"-	1.1E-3	66	91	2	634	3.5E-2
-"-	5.6E-3	28	46	8	308	1.2E-1

*) No. of calculations of $\partial k/\partial u$.

Table 4. Case 2: $\alpha = 4$. Equations integrated over one full period [0, 0.874] of $cn(\omega t, k^2)$, where $\omega = 8.135$ and $k^2 = 0.4$.

Method	rel. tolerance	# steps	# attempt. steps	# deriv. calc. *)	time used	rel. error at 0.874
RKF2(3)	2.8E-4	2268	3297		3385	1.8E-5
RKF3(4)	- " -	1417	1935		2658	1.8E-5
RKF2(3)	1.4E-2	2227	3220		3368	2.8E-5
RKF3(4)X	- " -	1526	1740			1.8E-5
ARK(6)		3496			5498	2.1E-5
CD		8740			2747	9.0E-6
TRAP	1.4E-3	934	1673	160	7882	6.9E-5
-"-	2.8E-3	22	48	19	239	2.6E-3
-"-	2.8E-2	16	44	15	190	5.1E-2

*) No. of calculations of $\partial k/\partial u$.

the solution is changing so rapidly (the solution of the *PDE* develops into a shock after about 0.01 sec) that to get a reasonable accuracy in the results, the steplengths must be chosen such that $\rho_n^{1/2} h_n = O(1)$, irrespective of method. Hence, on this problem, explicit methods should be more efficient than implicit ones as regards computing time. Table 3 shows this to be the case. Computing times per step for the methods are as follows:

Method	CD	RKF1(2)	ARK(4)	RKF2(3)	ARK(6)	RKF3(4)	TRAP
Time per step	0.5	1.3	1.4	2.2	2.4	2.9	9.6–11

The superiority of *CD* w.r.t. speed is of course evident from Table 1. When compared to RKF2(3) (to take a method of the same order) the speed of CD should however be related to the lack of any means for detecting instability.

Case 2 is a (moderately) stiff problem. The quantity $\rho_n^{1/2}$ is $O(10^4)$ in this case also, but the solution $u(t)$ has the form

$$\mathbf{u}(t) = \mathbf{a}(t) + \mathbf{b}(t) \tag{8.1}$$

where $\mathbf{a}$ contains the functions $cn(\omega t)$ and $(cn(\omega t))^2$ with $\omega = 8.135$, $\mathbf{b}$ is rapidly oscillating, and $\|\mathbf{b}\| \ll \|\mathbf{a}\|$. On this problem the explicit methods must use steplengths $h_n = O(10^{-4})$ to remain stable.

Steplength-control appears to be able to detect instability: When an equation is integrated by an explicit method with a local error criterion (2.12), the steplengths selected will satisfy (4.2). The reason for this is that the local error estimate δ_n grows rapidly with n if h_n violates (4.2). If the problem is stiff, the computed steplengths, accepted as well as rejected, will oscillate around $\beta/\rho_n^{1/2}$, and the method does not become unstable, only possibly inefficient [3]. A consequence is that the number of steps used and the accuracy obtained may be more or less independent of the specific error tolerance. Table 4 shows an example of this. An increase of the tolerance by a factor of 50 has almost no effect on the behaviour of RKF2(3).

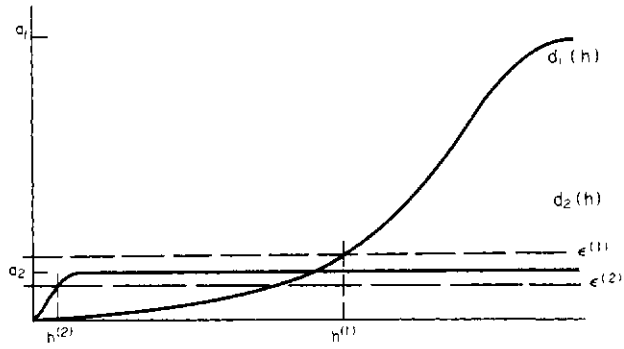

Fig. 1.

With the trapezoidal rule steplengths are delimited by the local error criterion (2.12) and convergence requirements for the iterative method used to solve the implicit equations at each step.

Table 4 shows that the choice of local error tolerance may have a large effect on the behaviour of the method. When the tolerance is decreased from 2.8×10^{-4} to 1.4×10^{-4}, the number of steps goes up by a factor of 42.5. This can be explained by the form (8.1) of the solution. It can be shown that if $\mathbf{u}$ consisted of $\mathbf{a}(t)$ alone, a relative error tolerance of 1.4×10^{-3} can be satisfied by a steplength 0.02, so the interval considered could be covered is less than 50 steps. The number of steps actually used, depend strongly on whether the relative tolerance is larger or smaller than $\|\mathbf{b}\|/\|\mathbf{a}\|$. A model for this behaviour can be found in an equation

$$\ddot{\mathbf{u}} + \Lambda \mathbf{u} = 0$$

with Λ diagonal and constant, and a solution

$$\mathbf{u}(t) = \begin{bmatrix} a_1 \exp(i\omega_1 t) \\ a_2 \exp(i\omega_2 t) \end{bmatrix}$$

with $a_1 \gg a_2 > 0$, and $\omega_1 \ll \omega_2$. With the trapezoidal rule, the local errors satisfy

$$|d_i| = 2a_i g(\omega_i h), \quad i = 1, 2$$

where h is a steplength, and

$$g(x) = |\sin(x - \arctan x)|.$$

Figure 1 below shows the effect of a criterion

$$\max_i \ |d_i| \leqslant \varepsilon$$

on the steplength. For simplicity we have replaced g by a function equal to g when x-arctan $x \leqslant \pi/2$, and equal to 1 for larger values of x.

Table 3 and 4 indicate how the number of calculations of Jacobians is affected by the local error tolerance. With a small tolerance, the steplengths have to be small. Convergence-rates are then less dependent on the Jacobian which consequently does not have to be recomputed very often. When tolerance and steplengths increase the Jacobian becomes more important for convergence, and the number of steps per evaluation decreases. In conclusion we note that explicit methods are probably more efficient than implicit ones on problems involving wave-propagation and may even be more effective on some stiff problems, for low error tolerance. In our opinion steplength controls should be incorporated in programs for dynamic problems. The resulting increase in work per step should be set against an increased ability of judging the computed results as well as the ability to detect instability and inefficiency of a method.

9. REFERENCES

1. E. Fehlberg, Klassische Runge-Kutta-Formeln vierter und niedriger Ordnung. *Computing* **6**, 61–67 (1970).
2. K. Dekker *et al.* Comparing stabilized Runge–Kutta methods for semidiscretized parabolic and hyperbolic equations. Report NW 45/77, Stichting Mathematisch Centrum, Amsterdam.
3. L. F. Shampine, Stiffness and non-stiff differential equation solvers. In *Numerische Behandlung von Differentialgleichungen* (Edited by R. Ansorge *et al.*). Birkhäuser (1975).
4. L. F. Shampine, Local error controls in codes for ordinary differential equations. *Appl. Math. Computations* **3**, 189–210 (1977).
5. L. F. Shampine and H. A. Watts, Practical solution of ordinary differential equations by Runge–Kutta methods. Report SAND 76-0585, Sandia Laboratories, Albuquerque (1976).
6. A. R. Curtis *et al.*, On the estimation of sparse Jacobian matrices. *J. Inst. Maths. Appl.* **13**, 117–119 (1974).
7. A. R. Curtis and J. K. Reid, The choice of steplength when using differences to approximate Jacobian matrices. *J. Inst. Maths. Appl.* **13**, 121–126 (1974).
8. R. D. Krieg and S. W. Key, Transient shell response by numerical time integration. *Int. J. Num. Math. Engng* **7**, 273–286 (1973).
9. D. Burgreen, Free vibrations of a pin-ended column with constant distance between pin ends. *J. Appl. Mech.* **18**, 135–139 (1951).
10. J. F. McNamara, Solution schemes for problems of nonlinear structural dynamics. *J. Pressure Vessels Tech.* 96–102 (May 1974).
11. J. O. Aasen and J. Braekhus, Evaluation of direct integration algorithms for ordinary differential equations used in structural dynamics. Tech. Rep. 79-0463, Det norske Veritas, 1322 Høvik, Norway.

Computers & Structures, Vol. 13, pp. 97–101, 1981
Printed in Great Britain.

0045-7949/81/010097-05$02.00/0

STABILITY OF SOME EXPLICIT DIFFERENCE SCHEMES FOR FLUID-STRUCTURE INTERACTION PROBLEMS

H. NEISHLOS†, M. ISRAELI and Y. KIVITY
Department of Computer Science, Technion—Israel Institute of Technology, Haifa, Israel

(*Received* 6 *May* 1980)

Abstract—The spectral stability theory of initial boundary value explicite finite-difference schemes is used to develop a stability analysis method for problems of fluid-structure interaction. By this analysis it is shown that due to the interaction between the structure and fluid stability restrictions on the time step may be more severe than commonly assumed. Four schemes of practical interest are analyzed in detail. The validity of the stability analysis is tested by simulating the effects of underwater explosion on a submarine. The computational results corroborate the prediction of the analysis concerning the stability boundary.

1. INTRODUCTION

In the explicit numerical integration of fluid-structure interaction problems there may be stability restrictions on the time step which are more severe than commonly assumed. Denote by Δt_f the maximum time step for stable integration in a fluid, by Δt_s the corresponding time step in a structure, and by Δt the time step for stable integration in the coupled problem. Then it was found [1, 2] computationally that Δt is smaller than either Δt_f or Δt_s in certain difference schemes. The stability analysis currently available [3, 4] do not exhibit this restriction because of incomplete treatment of the interaction at the interface.

In this work we consider a fluid continuum interacting with a thin shell at the boundary. The interaction effects at the interface, namely (a) the coupling via the pressure, (b) the normal velocity continuity are included in the analysis while sliding between the fluid and shell is allowed.

Three classes of schemes are possible. They are defined by the magnitude of the time step Δt required for stable integration of the coupled problem:

$$\Delta t \begin{cases} = \min(\Delta t_f, \Delta t_s), & \text{for schemes of class I} \\ < \min(\Delta t_f, \Delta t_s), & \text{for schemes of class II} \\ \leqslant \min(\Delta t_f, \Delta t_s), & \text{for schemes of class III.} \end{cases}$$

We present and discuss four explicit difference schemes which demonstrate these three classes. Only schemes of class I are free from reduction of stability due to the interaction between the fluid and the shell. It should be noted here that the stability restrictions may be overcome by integrating the structure implicitly, but only with considerable additional computational expense [5]. Thus the explicit approach remains attractive, especially for three dimensional problems.

2. EQUATIONS OF MOTION

The structural-hydrodynamic problem consists of solving the equations of structure and fluid together with contact, initial and boundary conditions.

We make these assumptions: the fluid is acoustic and the structure is a thin shell. Furthermore, we use linearized shallow shell equations adequate for stability analysis.

We consider an orthogonal curvilinear coordinate system (x_1', x_2', x_3'), where coordinates x_1' and x_2' coincide with the principal curvature directions of the shell midsurface and x_3' is normal to the shell surface. The fluid extends from $x_3' = 0$. We suppose that for a given shell region the principal curvatures κ_1 and κ_2 are constant and the diagonal components A_1 and A_2 of the metric tensor are equal to one. Then in various cases of practical interest, the use of simplifying assumptions followed by an appropriate orthogonal expansion leads to the following one dimensional model [2, 4, 6]:

$$\frac{\mathrm{d}^2 w}{\mathrm{d}t^2} + \omega^2 w = -p\Big|_{x_3 = 0}. \tag{2.1}$$

Here w is the normal displacement into the fluid, p is the hydrodynamic pressure, t is the time, w, p, t and $x_j (j = 1, 2, 3)$ are non-dimensionalized by $L, \rho_f a_f^2, L/a_f, L$ respectively, where $L = \rho_s h/\rho_f$, and ρ_s, a_s, h are the density, sound velocity and thickness of the shell, ρ_f and a_f are the density and sound velocity of the fluid. The frequency ω of the shell depends on the mode of deformation (for stability analysis, normally the extensional mode), type of the shell theory and on the boundary conditions. Thus ω is a function of wave numbers in the reduced directions, and the parameters ρ_s/ρ_f, a_s/a_f, $\kappa_1 L$, $\kappa_2 L$.

The fluid motion in the acoustic approximation is governed by the dimensionless wave equation in the (x_1, x_2, x_3) coordinate system

$$\frac{1}{H_1 H_2 H_3}\left[\frac{\partial}{\partial x_1}\left(\frac{H_2 H_3}{H_1}\frac{\partial}{\partial x_2}\right) + \frac{\partial}{\partial x_2}\left(\frac{H_3 H_1}{H_2}\frac{\partial}{\partial x_2}\right) + \frac{\partial}{\partial x_3}\left(\frac{H_1 H_2}{H_3}\frac{\partial}{\partial x_3}\right)\right] p = \frac{\partial^2 p}{\partial t^2} \tag{2.2}$$

where

$$H_1 = A_1(1 + L\kappa_1 x_3), \quad H_2 = A_2(1 + L\kappa_2 x_3), \quad H_3 = 1.$$

Considering the fluid motion in a thin layer near the shell surface we can assume $L\kappa_i x_3 \ll 1$ $(i = 1, 2)$.

Using the previous assumptions on the shell metric and the above mentioned orthogonal expansion, we

†For correspondence: Computer Science Dept., Technion—Israel Institute of Technology, Haifa, Israel.

obtain from (2.2) the following:

$$\frac{\partial^2 p}{\partial t^2}=\frac{\partial^2 p}{\partial x^2}-k^2 p, \tag{2.3}$$

where k is a function of the wave numbers in the reduced direction and of the parameters $\kappa_1 L$ and $\kappa_2 L$.

The contact condition at the interface is:

$$\frac{\mathrm{d}^2 w}{\mathrm{d}t^2}=-\frac{\partial p}{\partial x_3}\bigg|_{x_3=0}. \tag{2.4}$$

Equations (2.1), (2.3) and (2.4) together with initial and boundary conditions will be the basic model for our fluid-structure interaction problem.

More details on the model and justification of the assumptions may be found in [2].

3. NUMERICAL FORMULATION

We approximate the eqns (2.1), (2.3) and (2.4) by the following explicit finite difference scheme:

$$D_f^2 p_j^n=(G_f^2-k^2)p_j^n \tag{3a}$$

$$(D_s^2+\omega^2)w^n=-p_0^n \tag{3b}$$

$$D_c^2 w^n=-G_c p_0^n \tag{3c}$$

where D_f^2, D_s^2, D_c^2 are the difference operators for second time derivatives with time step Δt, G_f^2 and G_c are difference operators for second and first spatial derivatives with step Δx; j and n are space and time reference indices; j equal to zero denotes the shell surface.

In the present work we consider a nondissipative case in which $D_f^2=D_s^2=D_c^2=D^2$, where D^2 is the central difference operator. This choice gives rise to a time scheme, where the amplitude remains constant. Furthermore, the operator G_f^2 is centered and G_c is any operator involving two or three spatial points.

The solution procedure for the scheme (3) is:

(1) Solve the shell and contact equations (3b) and (3c) for w^{n+1} and p_0^n using the known displacements w^{n-1}, w^n and pressures p_1^n or p_1^n and p_2^n for the two or three point operators respectively.

(2) Solve the fluid equation (3a) for p_j^{n+1} using the previous pressures p_j^n and p_j^{n+1} $(j=1, 2, \ldots)$.

The schemes (3) with different types of G_c will be the basic model for the present stability analysis.

4. MATHEMATICAL APPROACH

The system of eqns (3) may be considered as an approximation to an initial boundary value problem, where the eqn (3a) describes the fluid (interior) and the eqns (3b, c) describe the shell (boundary). By this approach the spectral stability theory of initial boundary value finite difference schemes may be applied. The state of the art of this theory may be found in [7].

For stability analysis the substitution

$$p_j^n=\binom{s+1}{s-1}^n\binom{r+1}{r-1}^j p$$

$$w^n=\binom{s+1}{s-1}^n$$

is made for the scalers p and w.

The system (3) takes the form

$$d^2=g^2-k^2$$

$$d^2=\omega^2\frac{g_c}{1-g_c}. \tag{4.1}$$

The functions $d(s, \Delta t)$, $g(r, \Delta x)$, $g_c(r, \Delta x)$ correspond to the operators D, G, G_c, following the substitution above, and are given by

$$d^2(s, \Delta t)=\frac{4}{(s-1)^2\Delta t^2}, \quad g^2(r, \Delta x)=\frac{4}{(r-1)^2\Delta x^2}. \tag{4.2}$$

The following theorem is proved in [2]:

Theorem The system of eqns (3) is stable if and only if the following hold:

(i) the equation

$$h(r, \Delta x)=f(r, \Delta x) \tag{4.3}$$

where

$$h=g^2-k^2 \quad \text{and} \quad f=\omega^2\frac{g_c}{1-g_c} \tag{4.4}$$

has no roots r with $Re\{r\}<0$ and $Im\{r\}\neq 0$,

(ii) the eqn (4.3) has no real roots in the interval $(-(1+4/k^2\Delta x^2)^{1/2}, -1)$,

(iii) the time step Δt must satisfy the following condition

$$\Delta t\leqslant \min(\Delta t_f, \Delta t_s, \Delta t_i), \tag{4.5}$$

where Δt, Δt_s and Δt_i are equal to

$$\Delta t_f=2\Delta x(4+k^2\Delta x^2)^{-1/2} \tag{4.6}$$

$$\Delta t_s=2\omega^{-1}, \tag{4.7}$$

$$\Delta t_i=\begin{cases}\min 2|f|^{-1/2}, & \text{over all roots of equation (4.4) in the interval } (-1, 0]\\ \Delta t_s & \text{if there are no roots of equation (4.4) in the interval } (-1, 0].\end{cases} \tag{4.8}$$

In the following section we shall use this theorem to analyze the stability of the system (3) for different contact operators G_c.

5. STABILITY ANALYSIS

Let us consider four difference schemes, where the operators G_c and the corresponding functions g_c and f are given in Table 1.

In the following we prove that conditions (i) and (ii) of the theorem are satisfied for all operators defined in Table 1. The proofs are based upon a separation principle in the complex plane.

Lemma 1. The functions f which are defined in Table 1 and the function h satisfy the following condition:

$$\text{sign } Im\{h\}=\text{sign } Im\{-f\} \tag{5.1}$$

for all $\Delta x>0$ and r such that $Re\{r\}<0$.

Proof. Let $r=a+ib$, and taken for example, case (c), where $f(r, \Delta x)=[2r/(r^2-1)\Delta x-2r]$. We find:

$$\text{sign } Im\{h\}=\text{sign}\left\{\frac{-8ab}{|r^2-1|^2\Delta x^2}\right\}=\text{sign}\{-ab\}$$

and

$$\text{sign } Im\{f\}=\text{sign}\left\{\frac{-2\Delta x(|r|^2+1)}{|(r^2-1)\Delta x-2r|}b\right\}=\text{sign}\{-b\}.$$

Since, $a<0$ by assumption, (5.1) is proved. Similarly for the other three cases.

Lemma 2. For real r, the functions f and h satisfy:

$$f<0 \quad \text{and} \quad h>0, \tag{5.2}$$

for all $\Delta x>0$ and r in the interval $(-(1+4/k^2\Delta x^2)^{1/2}, -1)$.

Table 1.

Description	Class I		Class II	Class III
Type	(a) Forward two point first order in Δx	(b) Forward three-point second order in Δx	(c) Central two-point second order in Δx	(d) Backward two-point first order in Δx
$G_c\, p_c^n$	$\frac{p_1^n - p_c^n}{\Delta x}$	$\frac{-3p_0^n + 4p_1^n - p_2^n}{2\Delta x}$		
$G_c p^-$			$\frac{p_2^n - p_0^n}{2\Delta x}$	$\frac{p_1^n - p_0^n}{\Delta x}$
g_c	$\frac{2}{(r-1)\Delta x}$	$\frac{2(r-2)}{(r-1)^2\Delta x}$	$\frac{2r}{(r-1)\Delta x}$	$\frac{2}{(r+1)\Delta x}$
f	$\frac{2}{(r-1)\Delta x - 2}$	$\frac{2(r-2)}{(r-1)^2\Delta x - 2(r-2)}$	$\frac{2}{(r+1)\Delta x - 2}$	$\frac{2r}{(r^2-1)\Delta x - 2r}$

Proof. For r restricted as above we find:

$$h(r, \Delta x) = \frac{4}{(r^2-1)\Delta x^2} - k^2 > \frac{4}{\left(1 + \frac{4}{k^2\Delta x^2} - 1\right)\Delta x^2} - k^2 = 0.$$

On the other hand it follows from (4.4) that f is negative when g_c is negative, but all g_c in Table 1 are negative if $r < -1$, and (5.2) is proved.

Now we consider three classes I, II and III of schemes:

Class I: Schemes where the interaction between the fluid and the shell does not reduce the stability for all Δx

Lemma 3. For functions f defined by schemes (a) and (b) from the Table 1 and for function h the following holds for all Δx and $0 \geqslant r > -1$:

$$\Delta t_i \geqslant \Delta t_s. \tag{5.3}$$

Proof. For r and Δx restricted as above functions f are continuous and decrease monotonically for all x from $-\omega^2$ at $r = -1$ to $f(0, \Delta x) > -\omega^2$ at $r = 0$. Therefore, if the eqn (4.3) has a root r_0, then

$$\Delta t_i \geqslant \frac{2}{\sqrt{\max |f(r_0, \Delta x)|}} > \frac{2}{\omega} = \Delta t_s,$$

but if the eqn (4.3) has no roots then

$$\Delta t_i = \Delta t_s$$

by definition, and (5.3) is proved.

To summarize, by Lemmas 1, 2 and 3 we have two forward, first and second order schemes for the contact condition (3c), where the interaction does not reduce the stability, the stability is defined completely by the stability of the fluid and of the shell separately. The value of $\tilde{\Delta x}$ separating the regions of fluid dominated stability as opposed to shell dominated stability is given by

$$\tilde{\Delta x} = 2(\omega^2 - k^2)^{-1/2}, \quad \text{if} \quad \omega > k. \tag{5.4}$$

The typical stability boundaries for schemes of class I are given in Figs. 1 and 2 by full curve.

Class II: Schemes where the stability is reduced for all Δx as a result of the interaction between fluid and shell

To this class belong the scheme with G_c defined by (c) from Table 1. This case may be important for practical purposes being a second order scheme with a small truncation error.

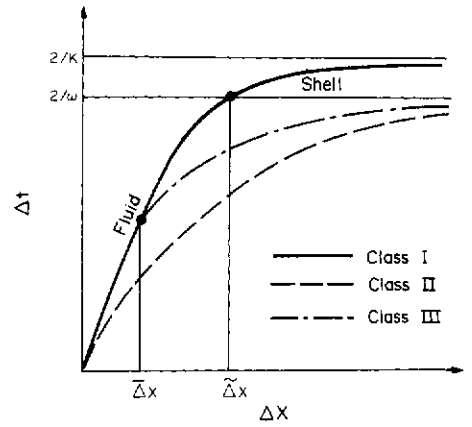

Fig. 1. Stability boundaries for the three classes of schemes, I, II and III ($\omega > k$).

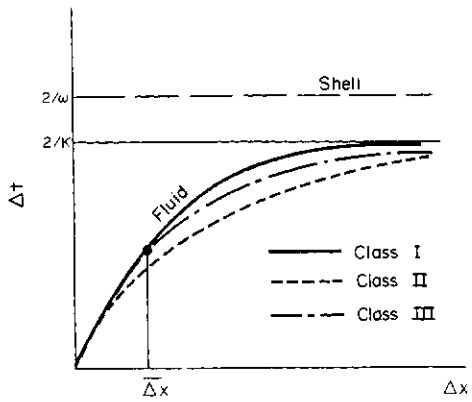

Fig. 2. Stability boundaries for the three classes of schemes, I, II, and III ($\omega < k$).

Lemma 4. For function f, defined by the scheme (c) from the Table 1, and for function h the following holds for all x and $0 \geqslant r > -1$

$$\Delta t_i < \min(\Delta t_f, \Delta t_s). \tag{5.5}$$

Proof: The function $f(r, \Delta x) = 2r\omega^2[(r^2-1)\Delta x - 2r]^{-1}$ decreases monotonically from $-\omega^2$ at $r = -1$ to $-\infty$ at $r = r_A = (1 - \sqrt{1 + \Delta x^2})/\Delta x$. On the other hand the

function $h(r, \Delta x)$ increases monotonically from $-\infty$ at $r=-1$ to $4/(\Delta t_f)^2$ at $r=0$. It follows that there is a single root, r_0, of eqn (4.3) in the interval $(-1, 0]$ where $|f(r_0, \Delta x)| = |h(r_0, \Delta x)|$ is larger than both $|f(-1, \Delta x)|$ and $|h(0, \Delta x)|$. Consequently the lemma is proved.

To estimate the effect of the interaction on stability we investigate some limiting cases. We find [2] assymptotic expressions for Δt_i as follows:

$$\text{for } \Delta x \to 0,\ \Delta t_i = \Delta t_f \left[1 - \frac{\Delta x^2}{2(4+k^2\Delta x^2)} + \cdots \right]. \quad (5.6)$$

$$\text{for } \Delta x \to \infty,\ \Delta t_i = \begin{cases} \Delta t_f \left[1 - \dfrac{1}{(k^2-\omega^2)\Delta x} + \cdots \right], & \text{if } \omega < k \\ \Delta t_s \left[1 - \dfrac{1}{(\omega^2-k^2)\Delta x} + \cdots \right], & \text{if } \omega > k \\ \Delta t_s \left[1 - \dfrac{1}{\sqrt{2\omega\Delta x^{1/2}}} + \cdots \right], & \text{if } \omega = k. \end{cases} \quad (5.7)$$

We see that Δt_i approach Δt_f and Δt_s when Δx approaches 0 and ∞ respectively. The typical stability boundary is given on Figs. 1 and 2 by the dashed curve.

The influence of the interaction may be measured by the quantity:

$$Q(\Delta x, k, \omega) = \frac{\min(\Delta t_f, \Delta t_s) - \Delta t_i}{\min(\Delta t_f, \Delta t_s)}. \quad (5.8)$$

An important practical case is $\omega > k$, which corresponds to a shell having higher sound velocity than the fluid. Then the region of the greatest reduction of stability is the vicinity of $\widetilde{\Delta x}$, defined in (5.4). In this case the influence of the interaction on a specific scheme may be estimated by:

$$\tilde{Q}(k, \omega) = \left. \frac{\Delta t_s - \Delta t_i}{\Delta t_s} \right|_{\Delta x = \widetilde{\Delta x}}. \quad (5.9)$$

Using (5.4) and the assymptotic expressions (5.6) and (5.7b) $\tilde{Q}$ may be approximated by:

$$\tilde{Q}(k, \omega) \sim \tilde{Q}_A(k, \omega) = (\omega^2 - k^2)^{-1/2}. \quad (5.10)$$

In [2] we considered the response of a steel cylindrical shell, submerged in water, to a transverse shock wave. For this case the extensional frequency is given by

$$\omega = \alpha k$$

where $\alpha = a_s/a_f$ (≈ 3.3 for steel shell and water), $k = n\rho_s h/\rho_f R$; n is the circumferential wave number and R is the radius of the cylinder.

The estimate (5.10) for $\tilde{Q}$ reduces to

$$\tilde{Q}_A = k^{-1}(\alpha^2 - 1)^{-1/2}. \quad (5.11)$$

In Fig. 3 we present the curve $\tilde{Q}_A$ according to (5.11) and the curve $\tilde{Q}$ which is obtained numerically from the complete analysis. It is observed that for $k > 0.35$ $\tilde{Q}_A$ gives a very good estimate for $\tilde{Q}$, whereas for $k < 0.35$ $\tilde{Q}_A$ gives an overconservative estimate.

In [1] it was found computationally for a problem using the scheme (c) that the time step Δt for stable interpretation of the coupled problem must satisfy $\Delta t < \sqrt{2/3}\ \min(\Delta t_f, \Delta t_s)$. This is in agreement with the above analysis.

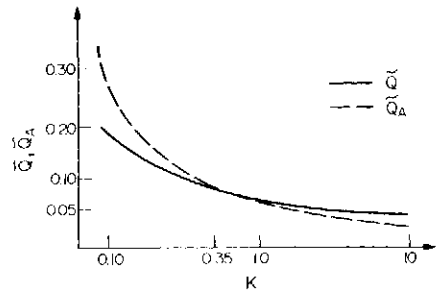

Fig. 3. Comparison between influence of the interaction, $\tilde{Q}$, and its estimate $\tilde{Q}_A$.

Class III: Schemes where the stability is reduced for some Δx *as a result of the interaction between fluid and shell*

Lemma 5. For function f defined by scheme (d) from Table 1, and for function h, the following hold for $0 \geqslant r > -1$

$$\begin{aligned} &\Delta t_i \geqslant \min(\Delta t_f, \Delta t_s), \quad \text{for } \Delta x < \Delta x < 2 \\ &\Delta t_i < \min(\Delta t_f, \Delta t_s), \quad \text{for } \overline{\Delta x} \leqslant \Delta x. \end{aligned} \quad (5.12)$$

where $\overline{\Delta x}$ is the single real root in the interval $(0, 2]$ of the equation

$$f(0, \Delta x) = h(0, \Delta x). \quad (5.13)$$

Proof. For $\Delta x < 2$ the function $f(r, \Delta x) = 2\omega/[(r+1)\Delta x - 2]$ decreases monotonically from $-\omega^2$ at $r=-1$ ro $f(0, \Delta x) < -\omega^2$ at $r=0$, while the function $h(r, \Delta x)$ increases monotonically from $-\infty$ at $r=-1$ to $h(0, \Delta x)$ at $r=0$. Therefore, there exists a root r_0 of eqn (4.3) in the interval $(-1, 0]$, if

$$f(0, \Delta x) \leqslant h(0, \Delta x). \quad (5.14)$$

It may be easily shown (graphically, for instance), that eqn (5.13) always has a single real solution $\overline{\Delta x} < 2$, thus the inequality (5.14) holds for $\Delta x \geqslant \overline{\Delta x}$.

For $\Delta x \geqslant 2$ the function f has a vertical asymptotic at $0 \geqslant r_A = (2 - \Delta x/\Delta x) > -1$, and there exists a root r_0 such that $|f(r_0)| > \omega^2$. Consequently, the lemma is proved.

The typical stability boundaries for schemes of class III are presented at Figs. 1 and 2 by dotted curve.

For an important case $k\Delta x = 2$ (i.e. a square mesh in the fluid) the solution of the eqn (5.13) is

$$\Delta x = 4(1 + \sqrt{1 + \omega^2})^{-1/2}. \quad (5.15)$$

For $\omega \to \infty$, $\overline{\Delta x} \to 0$, and the stability behaviour of the scheme of class III approaches the stability behaviour of the schemes of class II.

Asymptotic analysis may be produced for the schemes of class III, as we have done for the schemes of class II [2].

6. APPLICATIONS

The validity of the stability analysis was tested with a nonlinear Lagrangian two-dimensional program DISCO [8]. The problem considered is that of a submerged cylindrical shell subjected to a step shock wave, simulating the effects of underwater explosions on a submarine. The code employs the scheme (a) of Table 1. The computational results corroborate the predictions of the analysis concerning the stability boundary. As an example, for a 50mm-thick steel shell cylinder with a diameter of 10m for a 2MPa pressure wave (acoustic

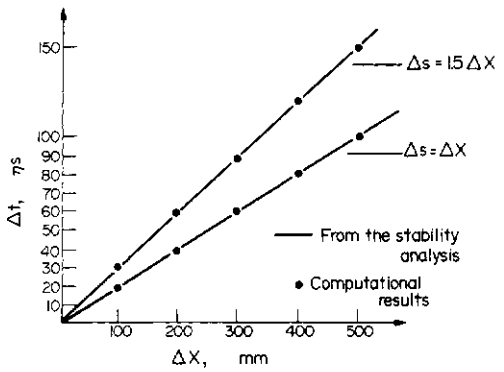

Fig. 4. Comparison between the computed and estimated stability boundaries, for a submerged cylindrical shell subjected to a step shock wave.

region) the results are illustrated in Fig. 4, where $k\Delta x \approx 2$, Δs is a typical mesh size in the shell and Δt is the maximum allowed time step.

7. FURTHER STUDIES

Using the same approach, we are able to produce a stability analysis, involving two dynamical equations for the shell without reduction to the one shell equation model (2.1). We find that the results of such two-dimensional analysis are similar to results which are presented in present work. That means we can estimate the stability behaviour of the numerical schemes by analyzing a one-dimensional model. The effectiveness of this approach depends only on the estimate of the highest shell frequence, that which is determining the numerical stability. This is confirmed by the agreement between the computed stability boundary of a two-dimensional problem and the estimated stability boundary of a one-dimensional analysis, as illustrated in Section 6.

These studies will be presented in a forthcoming publication.

REFERENCES

1. J. D. Bitzberger, *Two Dimensional Analysis of Fluid-Structure Interaction by Method of Finite-Difference-Hydraulic Ram*, The Fuel Tank Problem, NTIS, AD-783839 (1979).
2. H. Neishlos, Dynamic Fluid-Structure Interaction, Ph.D. Thesis, Computer Science Dept., Technion-IIT, Haifa, Israel (1980).
3. T. Belytschko, H. J. Yen and R. Mullen, Mixed methods for time integration. *Comput. Meth. Appl. Mech. Engng* **17/18**, 259–275 (1979).
4. K. C. Park, C. A. Felippa and J. A. DeRuntz, Stabilization of staggered solution procedures for fluid-structure interaction analysis. In *Computational Methods for Fluid-Structure Interaction Problems* (Edited by T. Belytschko *et al.*), Vol. 26, pp. 95–124 A.S.M.E. Applied Mechanics Symposia Series, AMD (1977).
5. T. Belytschko and R. Mullen, Stability of explicit-implicit mesh partitions in time integration. *Int. J. Numer. Meth. Engng* **12**, 1575–1586 (1978).
6. K. Forsberg, Influence of boundary conditions on the model characteristics of thin cylindrical shells. *AIAA J.* **2**, 2150–2157 (1964).
7. K. W. Morton, Initial-value problems by finite-difference and other methods. In *The State of the Art in Numerical Analysis* (Edited by D. A. H. Jacob), pp. 699–745. Academic Press, New York (1977).
8. Y. Kivity and D. Tzur, Study of projectile formation in lined shallow cavity charges. *Proc. 4th Int. Symp. on Ballistics*, Monterey, California (1972).

Computers & Structures, Vol. 13, pp. 103–113, 1981
Printed in Great Britain.

0045-7949/81/010103-11$02.00/0

NUMERICAL ANALYSIS OF CONTINUATION METHODS FOR NONLINEAR STRUCTURAL PROBLEMS†

WERNER C. RHEINBOLDT
Department of Mathematics and Statistics, University of Pittsburgh, Pittsburgh, PA 15261, U.S.A.

(*Received* 17 *May* 1980)

Abstract – Continuation methods are considered here in a broad sense as the collection of methods needed for the computational analysis of specified parts of the solution field of "under-determined" equations $Fx = c$ where $F: R^m \to R^n$, $m > n$, is given and any suitable m-n of the variables x_i are designated as parameters. Such equations arise frequently in structural mechanics. In general, the solutions are $(m-n)$-dimensional manifolds in R^m. Some basic existence results for the case $m = n+1$ are presented, and a procedure for the computational trace of the corresponding one-dimensional solution manifolds in R^{n+1} is discussed in detail. Then a general approach is formulated which allows, under certain assumptions, the computation of the derivative of F, and which includes, the usual incremental formulations in structural mechanics. In finite element applications it is possible to combine the continuation procedure with adaptive mesh-refinements; for a model problem it is shown that such a combined process can be surprisingly effective. The article ends with some comments about the general case $m > n+1$ and the possibility of assessing numerically the structural stability of a structure.

1. INTRODUCTION

There appears to be little question that the socalled incremental methods represent by far the most popular procedures for the solution of problems in nonlinear structural mechanics. While these procedures were developed more or less independently in the engineering literature, it is now also recognized that they belong to the general class of continuation methods used for some time in mathematics in general and in numerical analysis in particular. The literature in this area is extensive; we refer only to [13] for a description of the incremental approach to structural problems as a continuation procedure, to [8] for a historical overview of uses of continuation techniques in mathematics, and to [24] for a more recent literature survey of some numerical aspects of continuation methods.

Basically, in structural mechanics, the discretized equations of equilibrium have the generic form

$$P(x) = p \tag{1.1}$$

with a given nonlinear mapping P: $D_P \subset R^n \to R^n$ and vector $p \in R^n$. In many cases, x represents here the displacement vector and p the load vector.

In order to focus the subsequent discussion we use as an illustration the very simple model of a plane structure shown in Fig. 1. Two equal, straight rods with longitudinal elastic modulus γ are pin-jointed at the two supports and at the tip where a dead-load p acts along the vertical symmetry axis. As indicated in Fig. 1, this symmetry axis is used as the x-axis with the origin at the unloaded position of the tip. Then the total potential energy of the structure under load p is given by

$$2[\tfrac{1}{2}\gamma(\sqrt{1+h^2} - \sqrt{1+(h-x)^2}))^2] - px$$

and hence the equilibrium equation (1.1) here has the form

$$P(x) \equiv \gamma\left[\sqrt{\frac{1+h^2}{1+(h-x)^2}} - 1\right](h-x) = p, \tag{1.2}$$

where the nonlinear function P on the left is now a mapping of R^1 into itself.

In general, (1.1) has to be solved for a number of load vectors p in order to assess the behavior of the structure under different conditions. Often the linear set $\{tp;\ t \in R^1\}$ of loads is used and hence the family of equations

$$P(x) = tp \tag{1.3}$$

involving the real parameter $t \in R^1$ is considered in place of (1.1). The interest then centers on determining continuous paths in R^n

$$x: J \subset R^1 \to R^n, \tag{1.4}$$

such that $x(t)$ is a solution of (1.3) for each t in the interval of definition J. More specifically, a path (1.4) is to be found which passes for $t = t_0 \in J$ through a point $x^0 = x(t_0)$ that is a known solution of (1.3) for t_0. Broadly speaking, a continuation method is now any procedure which, starting from x^0 at t_0, produces acceptable approximations x^i of $x(t_i)$ for a sequence of parameter values $t_1, \ldots, t_N$ in J.

In our simple example (1.2) the load p is already one-dimensional and thus p may be used in place of the parameter t. Clearly for $p = 0$ we have the solution $x^0 = 0$ and hence we want here a real function $x = x(p)$ which solves (1.2) for all p in some interval J and satisfies $x(0) = 0$, $0 \in J$. For $\gamma = 1$, $h = 0.5$ and $J = [0, 0.021457\ldots)$

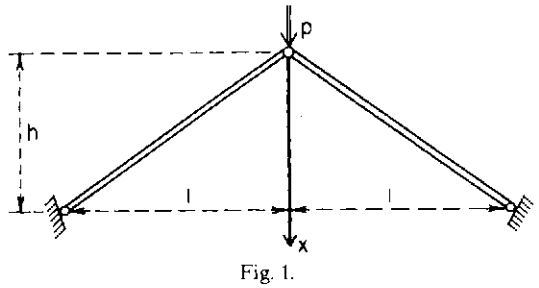

Fig. 1.

†This work was in part supported by the National Science Foundation under grant MCS-78-05299.

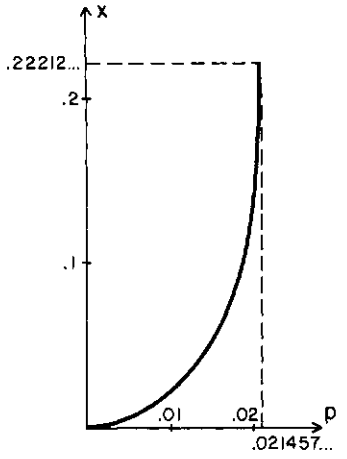

Fig. 2.

the solution is shown in Fig. 2. The right end point of J is a limit point where the derivative $x'(p)$ of the solution becomes infinite. This represents a buckling point of the structure.

The above description of continuation methods corresponds with the standard concept of these methods. However, it does not allow us to focus on two important aspects of our problem. Since a vector $x \in R^n$ can be said to solve (1.3) only if a corresponding value of $t \in R^1$ has been given, the solutions of (1.3) are in actuality points $(x_1, \ldots, x_n, t)$ of R^{n+1}. From differential geometry it is known, that, in general, the set of these solutions in R^{n+1} defines a one-dimensional manifold in the space. This means that we should look for parametric solutions $x_i = x_i(s)$, $i = 1, \ldots, n$, $t = t(s)$ involving a suitable parameter s. The choice of $s = t$ is only locally permissible. This is evident from Fig. 3 which shows for our model problem with $\gamma = 1$, $h = 0.5$, a portion of the solution manifold in R^2 through the origin. Clearly, the parametrization $s = t$ breaks down at the limit points. It would also fail at bifurcation points which our model does not possess. Both types of points signify a loss of stability and hence are of considerable importance in our assessment of the structure. This suggests that from the outset it may be well to consider instead of the solution paths (1.4) in R^n the manifold of solutions of (1.3) in R^{n+1}. This will be discussed further in the next Section.

The second of the indicated two aspects lacking in our earlier formulation concerns the degree of controllability of the structure. The variable t in (1.3) represents an albeit somewhat artificial control parameter in the description of the system. In general, there are other parameters entering into the specification of P which are in some sense under our control and may have a strong influence on the behavior of the structure. Even if no such parameters are readily available, more general load condition than those of the set $\{tp;\ t \in R^1\}$ may need to be considered. In other words, the description of the system usually involves not only the "behavior" variables $x_1, \ldots, x_n$ but also a certain number $q > 0$ of assignable "control" parameters $u_1, u_2, \ldots, u_q$. Hence instead of (1.3) our problem has the generic form

$$F(x, u) = c \tag{1.5}$$

where $F: D_F \subset R^n \times R^q \to R^n$ is again a given mapping and $c \in R^n$ a fixed vector. In our example, we have the control parameters $u_1 = p$, $u_2 = h$ and hence the mapping

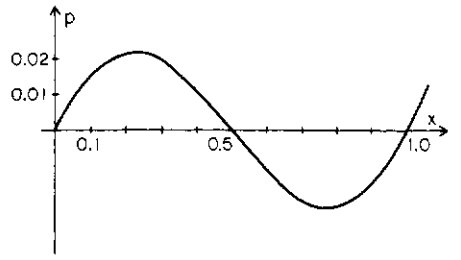

Fig. 3.

$$F(x, u_1, u_2) = \gamma\left[\sqrt{\frac{1+u_2^2}{1+(u_2-x)^2}} - 1\right](u_2 - x) - u_1, \tag{1.6}$$

from R^3 into R^1. The right side c of (1.5) is here zero.

In analogy to the case of the equation (1.3) the set of all solutions (x, y) of (1.5) is a q-dimensional manifold in R^{n+q}. For our model problem (with $\gamma = 1$), Fig. 4 shows the contour lines $p = \text{constant}$ of this 2-dimensional "surface" in (x, p, h)-space.

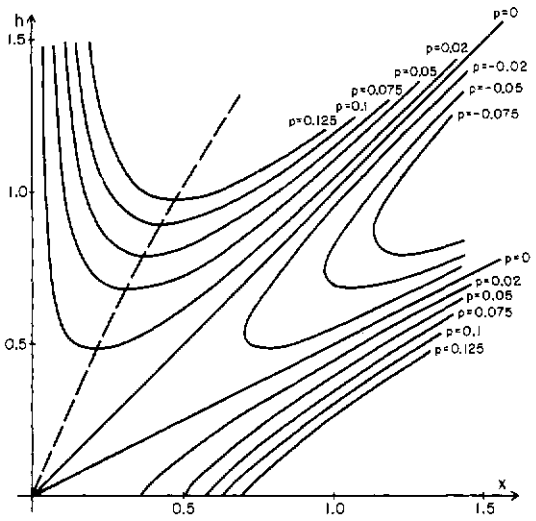

Fig. 4.

M. J. Sewell [19] called the solution manifold of (1.5) in R^{n+q} the equilibrium surface of the structure. In [21] several simple, but instructive examples are given for model structures with $n = 1$, $q = 2$, including, in essence, our model problem (1.2). The equilibrium surface provides global information about the behavior of the system under changes of the parameters. For instance, the limit points (and bifurcation points) are those points on the structure for which the matrix $F_x(x, u)$ of partial derivatives of F with respect to x is singular. Figure 4 shows one line of limit points for our model problems; it gives immediate information about the buckling loads and deformations for different initial heights h.

Since the advent of catastrophe theory the interest in a deeper study of such equilibrium surfaces has certainly intensified (see, e.g. [20]). But, the computational analysis of these surfaces is still very much in its infancy. More general continuation methods are required which permit a trace of any specific path on the surface. For example, we may wish to compute directly the line of limit points in Fig. 4. Some comments about this will be given later.

The aim of this paper is to present an overview of certain recent results as well as of various open questions about continuation methods in the setting described above. More specifically, Section 2 gives a summary of some of the basic properties of the set of solutions in R^{n+1} of the equation (1.5) in the case $q=1$, that is, when there is only one parameter. Then in Section 3 we discuss in reasonable detail a complete algorithm for the numerical trace of these solutions in R^{n+1}. Finally, Section 4 covers a number of aspects arising in connection with structural problems and leading to modifications or extensions of the method most of which involve as yet unresolved questions.

2. THE SOLUTION MANIFOLD FOR ONE-PARAMETER PROBLEMS

This section presents a brief summary of some of the basic properties of the set of solutions (x, u_1) in R^{n+1} of the equations (1.5) when $q=1$. This includes the case of the original equations (1.3). But in order to simplify the notation, it will be useful to set $x_{n+1}=u_1$ in (1.5) (or $x_{n+1}=t$ in (1.3)) and hence to write the equation in the "under-determined" form

$$Fx=c \tag{2.1}$$

involving a function F: $R^{n+1}\to R^n$ from R^{n+1} into R^n and a given vector $c\in R^n$. For ease of discussion we assume that F is defined and twice continuously differentiable on all of R^{n+1}. As before some specific solution $x^0\in R^{n+1}$ of (2.1) is supposed to be known.

A (non-trivial, parametric) solution of (2.1) is defined as any continuously differentiable function

$$x: J\subset R^1\to R^{n+1}, \quad x'(s)\neq 0, \qquad s\in J, \tag{2.2}$$

on some open interval J of R^1 such that $Fx(s)=c$ for all s in J. Evidently, such a solution remains one under any continuously differentiable parameter transformation with non-zero derivative. Hence there is no restriction to assume that in (2.2) the parameter s is the arc-length. This choice has certain advantages and has been used by various authors. Without attempting any historical survey, we mention only the articles [10, 11, 16, 18].

The set

$$\mathbb{R}(F)=\{x\in R^{n+1}; \operatorname{rank} F'(x)=n\} \tag{2.3}$$

will be termed the regularity set of the function F. Here $F'(x)$ is the derivative of F represented by the $n\times(n+1)$ Jacobian matrix of all partial deterivatives. This set excludes essentially only the bifurcation points. For instance consider the case of our simple model problem (1.6) when x_1 is the displacement, $x_2=u_1=p$ and the height $u_2=h$ is a fixed constant. Then (with $\gamma=1$) we have

$$F'(x)=\left(1-\frac{(1+h^2)^{1/2}}{[1+(h-x_1)^2]^{3/2}}, -1\right), \qquad x=\begin{pmatrix}x_1\\ x_2\end{pmatrix},$$

and hence $\mathbb{R}(F)=R^2$. On the other hand, if we use the displacement x_1, $x_2=u_2=h$, and keep the load $u_1=p$ constant, then

$$F'(x)=\left(1-\frac{(1+x_2^2)^{1/2}}{[(1+(x_2-x_1)^2]^{3/2}}, \frac{(1+x_2^2)^{1/2}}{[1+(x_2-x_1)^2]^{3/2}} + \frac{x_2(x_2-x_1)}{[(1+x_2^2)(1+(x_2-x_1)^2]}, -1\right) \tag{2.5}$$

and for $x_1=x_2=0$ the rank of $F'(x)$ reduces to zero. In other words, here we have $\mathbb{R}(F)=\{x\in R^2; x\neq 0\}$ and, in fact, Fig. 4 shows that in this case the origin is a bifurcation point.

A proof of the following result is given in [16]:

Theorem 2.1. For any $x^0\in\mathbb{R}(F)$ with $Fx^0=b$ there exists a unique solution (2.2) of (2.1) in $\mathbb{R}(F)$ for which the interval of definition J is maximal under set inclusion, the parameter s is the arclength, and $0\in J$, $x(0)=x^0$. If $\alpha\in\partial J$ is finite then $x(s)\to\partial\mathbb{R}(F)$ or $\|x(s)\|\to\infty$ as $s\to\alpha$, $s\in J$.

The task of the desired continuation process is now to compute an approximation of this solution for a given $x^0\in\mathbb{R}(F)$. A possible process of this type is discussed in the next Section. Here we mention only a few properties of the solutions characterized by the Theorem.

Since $F'(x)$ is an $n\times(n+1)$ matrix which for $x\in\mathbb{R}(F)$ has n linearly independent columns, there exists a non-zero vector $v\in R^{n+1}$ for which $F'(x)v=0$. Obviously, v has the direction of the tangent of the solution curve of (2.1) through x. In order to obtain a unique vector v we need to fix the sign of its direction and its length. For theoretical purposes this may be accomplished by requiring that

$$F'(x)v=0, \quad v^Tv=1, \quad \det\begin{pmatrix}F'(x)\\ v^T\end{pmatrix}>0. \tag{2.6}$$

Then

$$T: \mathbb{R}(F)\to R^{n+1}, \quad v=Tx \tag{2.7}$$

is a well defined mapping from $\mathbb{R}(F)$ into R^{n+1}. For instance in the particular case of our model problem when $F'(x)$ is given by (2.5), we have

$$Tx=\frac{1}{[1+(1-A)^2]^{1/2}}\begin{pmatrix}1\\ 1-A\end{pmatrix}, \quad A=\frac{(1+h^2)^{1/2}}{(1+(h-x_1)^2)^{3/2}}$$
$$x=\begin{pmatrix}x_1\\ x_2\end{pmatrix}\in\mathbb{R}(F). \tag{2.8}$$

It is easily seen that in $\mathbb{R}(F)$ any solution of the (autonomous) system of differential equations $x'=Tx$ is a parametric solution of (2.1) with the arc-length as parameter,

A point $x\in\mathbb{R}(F)$ is a limit-point (or turning point) of (2.1) with respect to the ith variable x_i, $1\leqslant i\leqslant n+1$, if the ith-component of Tx is zero. In the case of (2.8) this may happen only for $i=2$ when $A=1$, that is, when

$$x_1=h\pm\sqrt{(1+h^2)^{1/3}-5} \tag{2.9}$$

This is the heavy-dashed curve in Fig. 4. It represents the location of the buckling points of the structure of Fig. 1 as a function of the height. The corresponding buckling loads are found by a simple evaluation of the function P of (1.3) and hence are given by $p=\{(1+h^2)^{1/3}-1\}^{3/2}$.

In the case when $F'(x)$ is given by (2.5) there are limit points with respect to both variables x_1, x_2. In Fig. 4 these are the points where the tangent of the curve is parallel to the x_2-axis or x_1-axis, respectively. Then, for example, the x_2-coordinate of an x_1-limit point respresents the critical height for the given load p such that for all lower heights the structure is instable at that load.

3. NUMERICAL DETAILS OF A CONTINUATION PROCESS

Let $x^0\in\mathbb{R}(F)$ with $Fx^0=c$ be a given point and

$$x;\ J\subset R^1\to\mathbb{R}(F),\quad \|x'(s)\|_2=1,\qquad s\in J,\quad x(0)=x^0, \tag{3.1}$$

the solution of (2.1) through x^0 which is guaranteed to exist in $\mathbb{R}(F)$ by Theorem 2.1. By requiring that the Euclidean norm of the tangent equals one we automatically ensure that the parameter s is the arc-length.

Our task is now to compute a suitable sequence of points

$$x^j\doteq x(s_j),\quad j=0,1,\ldots,N,\qquad s_0<s_1<\ldots<s_N, \tag{3.2}$$

approximating (3.1). Essentially all numerical continuation processes for doing this now are of the predictor-corrector type. Suppose that the points $x^0, x^1,\ldots,x^k$ have already been computed for some $k\geq 0$. Then a suitable predictor

$$y=\pi(t),\quad \pi: J_\pi\subset R^1\to R^{n+1},\quad \pi(0)=x^k, \tag{3.3}$$

is calculated which approximates (3.1) on some small interval $[s_k, s_k+\delta]$, $\delta>0$ beyond s_k. For example, π may be the polynomial of degree at most m defined by the interpolatory requirements $\pi(s_i)=x^j$, $j=k, k-1,\ldots,k-m$. Alternatively, if the tangents Tx^j at these points are also available, Hermite-interpolation may be applied as well. Other than in the case of the multistep ODE-solvers for the computer solution of initial value problems for ordinary differential equations, we appear to gain very little from the use of high order interpolation polynomials for the predictor π of our continuation process. Some reasons for this will be given later. Generally, the simple Euler predictor

$$\pi(t)=x^k+tTx^k,\quad t\geq 0 \tag{3.4}$$

has been found to be computationally optimal.

Before we can use (3.4), the tangent vector Tx^k needs to be computed, that is, we have to determine the vector v specified by (2.6) at the point $x=x^k$. For this the $n\times(n+1)$ system of equations $F'(x^k)v=0$ has to be augmented by some $(n+1)$st scalar equation. There are various possible choices for this (see, e.g. [1]), but from a practical viewpoint an affine equation $w^Tv=\xi$ has obvious advantages. The vector $w\in R^{n+1}$ has to be such that the resulting $(n+1)\times(n+1)$ system of equations is nonsingular. In order to reduce the computational work it is natural to consider the choice $w=e^i$ where e^i is the ith natural basis vector of R^{n+1} with a suitable index i, $1\leq i\leq n+1$. It is easily seen that

$$\det\begin{pmatrix}F'(x^k)\\(e^i)^T\end{pmatrix}=((Tx^k)^Te^i)\det\begin{pmatrix}F'(x^k)\\(Tx^k)^T\end{pmatrix} \tag{3.5}$$

and that the determinant on the right will be non-singular for any $x^k\in\mathbb{R}(F)$. Hence, the index i should be chosen such that $|(Tx^k)^Te^i|$ is as large as possible. Generally, let

$$|(Tx^j)^Te^{i_j}|=\max\{|(Tx^j)^Te^l|,\ l=1,\ldots,n+1\},\qquad j=0,1,\ldots. \tag{3.6}$$

Then it is reasonable to use $w=e^i$ with $i=i_{k-1}$. Of course, this applies only for $k\geq 1$; for $k=0$ a suitable index i is assumed to have been given with x^0. Recall that x^{k-1} is a limit point with respect to the ith variable if $(Tx)^{k-1}e^i=0$. Hence for $k\geq 1$ we choose the index $i=i_{k-1}$ for which Tx^{k-1} is in some sense furthest from a limit point with respect to x_i.

Our basic task is now to solve the system of equations

$$\begin{pmatrix}F'(x^k)\\(e^i)^T\end{pmatrix}v=e^{n+1}, \tag{3.7}$$

which will be non-singular if $(Tx^k)^Te^i\neq 0$ and hence if x^k is not too far from x^{k-1}. Basically, any standard method for the solution of a non-singular system of linear equations is applicable here. However, $F'(x)$ often has a special structure and the addition of the last row may lead to complications. For example, when F is derived from (1.3), that is, when

$$Fx=P\bar{x}-x_{n+1}p,\quad x=\begin{pmatrix}\bar{x}\\x_{n+1}\end{pmatrix}\in R^{n+1},\quad \bar{x}\in R^n \tag{3.8}$$

we frequently find in applications that $P'(\bar{x})$ is a banded, symmetric matrix. Obviously, the matrix of (3.7) has lost these advantageous properties and hence some special consideration is required to prevent an increase in the complexity of the solution process.

In the particular case of the mapping (3.8) our system (3.7) has the particular form

$$Av=c,\ A=\begin{pmatrix}B & p\\(e^i)^T & \end{pmatrix},\quad B=P'(\bar{x}^k). \tag{3.9}$$

For $i=n+1$ we need to solve only the subsystem with the matrix B and hence no complications arise. Suppose therefore that $1\leq i\leq n$. Then A is a bordered matrix and our basic approach will be to introduce a decomposition

$$A=A_0+ab^T \tag{3.10}$$

of A into the sum of a suitable non-singular matrix A_0 and a rank-one matrix ab^T. Once the two systems

$$A_0y=r,\quad A_0z=a \tag{3.11}$$

with the same matrix A_0 have been solved, the solution of (3.9) itself is given by

$$v=y-\frac{b^Ty}{1+b^Tz}z. \tag{3.12}$$

Here, it follows from the well-known Sherman–Morrison formula that $b^Tz\neq -1$ as long as A and A_0 are non-singular.

Among the various possible decompositions (3.9) the following one has been found very effective in applications:

$$A=A_0+a(e^{n+1})^T,\quad A_0=\left(\begin{array}{c|c}B & e_n^i\\\hline (e_n^i)^T & 0\end{array}\right),\quad a=\begin{pmatrix}p\\0\end{pmatrix}-e^i \tag{3.13}$$

Here e_n^i denote the natural basis vectors of R^n while as before, e^i are those of R^{n+1}. It turns out that A_0 is generally non-singular although there are situations when this is not true. Without entering into a theoretical discussion about conditions ensuring the non-singularity of A_0, we consider here only the solution of the systems (3.11) for this particular A_0. These systems have the common form

$$\left(\begin{array}{c|c|c|c}B_1 & b_1 & C & 0\\\hline b^T & \beta & b_2^T & 1\\\hline C^T & b_2 & B_2 & 0\\\hline 0 & 1 & 0 & 0\end{array}\right)\begin{pmatrix}w_1\\\eta_1\\w_2\\\eta_2\end{pmatrix}=\begin{pmatrix}d_1\\\delta_1\\d_2\\\delta_2\end{pmatrix} \tag{3.14}$$

where B_1, B_2 are square symmetric matrices. Hence we

need to solve merely the banded, symmetric $(n-1)\times(n-1)$ system

$$\left(\begin{array}{c|c} B_1 & C \\ \hline C^T & B_2 \end{array}\right)\begin{pmatrix} w_1 \\ w_2 \end{pmatrix}=\begin{pmatrix} d \\ d_2 \end{pmatrix}$$

which has a non-singular matrix exactly if A_0 has the property and for which the band-width does not exceed that of B itself. Since always $\eta_1=\delta_2$ the remaining unknown of the system (3.14) is given by $\eta_2=\delta_1-\beta\delta_2-b_1^Tw_1-b_2^Tw_2$.

Evidently, if $B=P'(\bar{x}^k)$ has been stored in some banded format, then it is unnecessary to store the matrix of (3.15) separately. In fact, after saving the vectors b_1, b_2 and the scalar β of (3.14) we need only zero-out the locations occupied by b_1, b_2 and store 1 in the location of β. Then we may work with this $n\times n$ banded, symmetric matrix in place of the matrix of (3.15).

Once the—necessarily non-zero—solution v of the system (3.7) has been obtained, the tangent vector

$$Tx^k=\sigma\frac{v}{\|v\|_2} \tag{3.16}$$

can be computed. Here $\sigma=\pm1$ is the direction specified in (2.6). By (3.5) we have

$$\sigma_{k,i}=\sigma_k\ \text{sign}\,(Tx^k)^Te^i,\quad \sigma_{k,i}=\text{sign det}\begin{pmatrix} F'(x^k) \\ (e^i)^T \end{pmatrix},$$

$$\sigma_k=\text{sign det}\begin{pmatrix} F'(x^k) \\ (Tx^k)^T \end{pmatrix} \tag{3.17}$$

Here $\sigma_{k,i}$ is the sign of the determinant of our system (3.7) which is easily computed during the solution of that system. By (2.6) we want $\sigma_k=+1$ and hence we should set $\sigma=\sigma_{k,i}$ sign (v^Te^i). As long as the solution curve remains in $\mathbb{R}(F)$ this approach is satisfactory. However, it does not permit us to detect when we may have passed a bifurcation point. More specifically, suppose that $x^*\in\mathbb{R}(F)$ is a bifurcation point where several solutions x^j: $J_j\subset R^1\to\mathbb{R}(F)$, $j=1,2,\ldots,$ of (2.1) (for different c) terminate, that is, for which $x^j(s)$ tends to x^* when s tends to one of the endpoints of J_k. In structural applications it frequently happens that there are pairs of these solutions, say, $x=x^1(s)$, $x=x^2(s)$ for which $\lim Tx^1(s)=-\lim Tx^2(s)$, (see Fig. 5). In other words, if we disregard the direction of the solutions, they appear to form one smooth curve through x^*. In such a case, when the process moves along $x^1(s)$ toward x^* it usually "jumps" over x^* onto $x^2(s)$. Then, unless we reverse the sign of σ_k we will not move along $x^2(s)$ away from x^* but again toward x^* instead. In order to avoid this problem the factor σ in (3.16) is defined by

$$\sigma=\begin{cases} +1 & \text{if sign } v^Te^i_{n+1}=\text{sign }(Tx^{k-1})^Te^i_{n+1} \\ -1 & \text{otherwise} \end{cases} \tag{3.18}$$

and then σ_k is computed from (3.17). Now for $\sigma_k\neq\sigma_{k-1}$ we have a situation as in Fig. 5 and hence we change the sign of Tx^k. Otherwise Tx^k is used as computed. Note, however, that in this case we may well have jumped over a bifurcation point of even multiplicity.

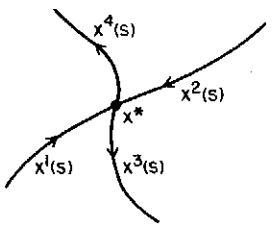

Fig. 5.

With Tx^k we now know the predictor (3.4). In order to define the corrector, some $(n+1)$st equation has to be added again to the system (2.1). As in the case of the tangent calculation it is natural to use for this purpose the following augmented system

$$\hat{F}x=\begin{pmatrix} Fx-c \\ (e^{i_k})^T(x-\pi(t_{k+1}))-\gamma \end{pmatrix}=0. \tag{3.19}$$

Here i_k is defined by (3.6), t_{k+1} represents the step to be taken along the predictor line (3.4) and the scalar γ will be fixed shortly. Any locally convergent iterative process for solving (3.19) may now be used as the corrector. For instance, if Newton's method is chosen then the corrector has the form

$$\begin{pmatrix} F'(y^j) \\ (e^{i_k}_{n+1})^T \end{pmatrix}(y^j-y^{j+1})=\hat{F}y^j,\ y^0=\pi(t_{k+1}),\quad j=0,1\ldots \tag{3.20}$$

and the systems of equations to be solved have exactly the same form as those in the tangent computations.

The choice of the step t_{k+1} to be taken along the predictor depends on the selection of γ. This is equivalent with the selection of the point $x(s_k+\Delta s)$ on the solution (3.1) which is to be approximated by the corrector. In fact, as long as t_{k+1} is not too large the equation

$$(e^{i_k})^Tx(s_k+\Delta s)=\gamma+(e^{i_k})^T\pi(t_{k+1}) \tag{3.21}$$

defines a one-to-one correspondence between Δs and γ for all sufficiently small Δs. Evidently, $\Delta s=t_{k+1}$ is a natural but by no means required choice for Δs.

In order to compute γ for $\Delta s=t_{k+1}$ and to estimate the distance between the predicted point $\pi(t_{k+1})$ and the desired solution $x(s_k+t_{k+1})$ of (3.18) we proceed as in the case of the ODE solvers. The quadratic polynomial

$$q(s)=x^k+(s-s_k)Tx^k+(s-s_k)^2w^k \tag{3.22}$$

$$w^k=\frac{1}{h_k}\left[Tx^k-\frac{1}{h_k}(x^k-x^{k-1})\right],$$

$$h_k=\|x^k-x^{k-1}\|_2\doteq s_k-s_{k-1}$$

represents a "better" approximation of $x(s)$ than the predictor (3.4). In fact, for three-times continuously differentiable F the error $\|q(s)-x(s)\|$ is asymptotically of order h^3 where $h=\max(h_k,|s-s_k|)$ while for the predictor it is only of order h^2. This suggests that for sufficiently small h we may replace $x(s)$ by $q(s)$. If this is done in (3.21) then we obtain for $\Delta s=t_{k+1}$ the value of γ as

$$\gamma=\frac{t_{k+1}^2}{h_k}\left[(e^{i_k})^TTx^k-\frac{1}{h_k}(e^{i_k})^T(x^k-x^{k-1})\right]. \tag{3.23}$$

At the same time, the requirement, that the distance between $\pi(t_{k+1})$ and $x(s_k+t_{k+1})$ is below some tolerance $\rho_{k+1}>0$, may be approximated by

$$\|\pi(t_{k+1})-q(s_k+t_{k+1})\|\leq\rho_{k+1}. \tag{3.24}$$

This leads immediately to the estimate

$$t_{k+1}\leq\sqrt{\frac{\rho_{k+1}}{\|w^k\|_2}}. \tag{3.25}$$

Before we discuss the choice of ρ_{k+1} it may be useful to comment on the computation of the quantities in

(3.23) and (3.24). The norm of w^k represents an estimate of the curvature of $x(s)$ at x^k and hence it is small when the curve is fairly straight. Since w^k is proportional to the difference of two vectors of length one, the explicit computation of this vector may lead to severe loss of accuracy due to subtractive cancellation. In (3.23) only one component of w^k is needed, and it should be computed with care and preferably in double precision. For the computation of $\|w^k\|_2$ in (3.25) we use

$$\|w^k\|_2 = \frac{1}{h_k}\sqrt{2(1-\cos\alpha_k)} = \frac{2}{h_k}\left|\sin\frac{\alpha_k}{2}\right|,$$
$$\alpha_k = \arccos\left((Tx^k)^T\frac{x^k - x^{k-1}}{h_k}\right). \qquad (3.26)$$

which is a numerically reliable formula as long as the last step h_k was not overly small.

We turn now to the choice of the tolerance $\rho_{k+1} > 0$. Ideally, ρ_{k-1} should be chosen such that the corrector iteration, when started from $\pi(t_{k-1})$, is known to converge to a point on the solution curve. In [16] it was shown that for any closed segment $\{x(s),\ s \leqslant s \leqslant \bar{s}\}$ of the solution curve which is completely contained in $\mathbb{R}(F)$ there exists a fixed positive tolerance $\rho > 0$ such that the Newton method (3.20) converges to a point on the curve as long as the predicted point has at most a distance ρ from it. This will be the case for all sufficiently small steps t_{k+1} along the predictor. But then the achievable error $\|x^{k+1} - x(s_{k+1})\|$ is solely determined by the termination criterion for the corrector iteration. In contrast to this the standard multistep ODE-solvers involve a corrector equation which is obtained by interpolation and hence for which the solutions are not, in general, on the exact curve. As a consequence the achievable error for the ODE-solvers depends on the history of the process up to that point, and this in turn has a strong influence on the selection of the steps. On the other hand, in the case of the continuation process any step t_{k+1} is acceptable in principle if only the corrector converges from $\pi(t_{k+1})$. This is the basic reason why it has little sense to use higher order predictors; in fact, they rarely provide consistently better starting points to save sufficient work in the corrector iteration to balance the added effort and storage requirements needed for their computation.

This still leaves us with the question how to choose the tolerance $\rho_{k+1} > 0$ in (3.25). By definition, for any locally convergent corrector iteration at $x(s_{k+1})$ there exists a convergence radius $r_{k+1} > 0$ such that for all starting points within the distance r_{k+1} from $x(s_{k+1})$ the process is guaranteed to converge. A natural idea is then to estimate $r_1, \ldots, r_k$ from the performance of the corrector iterates at the computed points. In [6] it is also $x^1, \ldots, x^k$ and to select ρ_{k+1} by extrapolation from these r^j. Various schemes of this type have been discussed in the literature (see e.g. [1, 16, 18]), but the results appear to be very sensitive to the properties of the problem at hand. Now a recent result in [6] has provided new insight into the reason for this.

It is natural to attempt to estimate any convergence radius r_j on the basis of the corrector iterates at x^j and our knowledge of F and F' at these points. In [6] it is proved that this information is insufficient to obtain any lower or upper bound of r_j. In other words, we would need more global information about the problem to obtain such bounds for r_j and this would require more computational efforts than is reasonably justifiable. The quantities used in the cited articles do not represent bounds of the convergence radii but of the quality of the convergence of the particular sequence of corrector iterates at the compute points. In [6] it is also shown that for Newton's method such assessments of the convergence quality can be used effectively for the determination of suitable tolerances ρ_j even though such ρ_j are not estimates of the radii r_j.

We proceed here in a more straightforward way which is not restricted to a particular corrector process. As in the ODE-solvers we need to control both the relative growth and the absolute size of the predictor step t_{k+1}. Thus we require that

$$\text{(i)}\ \frac{1}{p}h_k \leqslant t_{k+1} \leqslant p h_k, \quad \text{(ii)}\ t_{\min} \leqslant t_{k+1} \leqslant t_{\max}, \qquad (3.27)$$

where p is some factor, say $p = 3$, and $t_{\min}$, $t_{\max}$ depend on the machine as well as on the requirements of the problem. A natural tolerance at the last computed point x^k is the distance $\delta_k = \|(x^{k-1} + t_k T x^{k-1}) - x^k\|$ between the points where the corrector started and ended. However, it turns out that the corresponding tentative step

$$t_{k+1} = \sqrt{\frac{\delta_k}{\|w^k\|}} = h_k\sqrt{\frac{\delta_k/h_k}{2|\sin\alpha_k/2|}},$$

tends to lead to numerical instabilities even if it is adjusted to satisfy (3.27). For instance, for small δ_k the step will be small and the next distance δ_{k-1} is likely to be even smaller. Thus, especially when the curvature does not decrease, the algorithm ends up taking minimal steps only. Clearly we need to introduce thresholds for the quantities in (3.28).

Let $\alpha_0 > 0$ be a small lower threshold for $|\alpha_k|$ and set

$$\omega_k = 2\min\left(\tfrac{1}{2}\sqrt{2}, \max\left(\left|\sin\frac{\alpha_0}{2}\right|, \left|\sin\frac{\alpha_k}{2}\right|\right)\right). \qquad (3.29)\text{(a)}$$

Moreover, let

$$\eta_{\max} = 2p^2\left|\sin\frac{\alpha_0}{2}\right|, \quad \eta_{\min} = \frac{2}{p^2}\sin\frac{\pi}{4} = \frac{\sqrt{2}}{p^2} \qquad (3.29)\text{(b)}$$

and introduce the relative tolerance

$$\eta_{k+1} = \begin{cases} \eta_{\max}, & \text{if } \left|\sin\frac{\alpha_k}{2}\right| \leqslant \sin\frac{\alpha_0}{2} \text{ or } \delta_k \leqslant h_k\eta_{\min}, \\ \eta_{\min} & \text{if } \left|\sin\frac{\alpha_k}{2}\right| \geqslant \sqrt{2} \text{ or } \delta_k \leqslant h_k\eta_{\min} \\ \delta_k/h_k, & \text{otherwise.} \end{cases} \qquad (3.29)\text{(c)}$$

Clearly we need $\alpha_0 > \alpha_0 = 2\arcsin[(\sqrt{2}p^2)^{-1}]$ to ensure that $\eta_{\min} < \eta_{\max}$. Then for $\alpha_0 < \alpha_0 < \pi/2$ the tentative step

$$\tilde{t}_{k+1} = h_k\sqrt{\frac{\eta_{k+1}}{\omega_k}}$$

satisfies (3.27)(i), and hence for the step

$$t_{k+1} = \min\{\max(\tilde{t}_{k+1}, t_{\min}), t_{\max}\}. \qquad (3.30)$$

both conditions (3.27) hold. With $p = 3$ and $\alpha_0^* = 0.05$ and various values of $t_{\min}$ and $t_{\max}$ this step-length has been used extensively with excellent results.

Once the predictor step t_{k+1} has been chosen, the corrector iteration is started from $\pi(t_{k+1})$. This process has to incorporate provisions for monitoring the convergence and for aborting the iteration as soon as divergence is detected. These provisions depend of course on the type of corrector used. In the case of Newton's

method (3.20) it has been found satisfactory to declare non-convergence if either one of the following the three conditions is true

$$\begin{aligned}&\text{(i)}\ \ \|\hat{F}y^j\| \geqslant \theta \|\hat{F}y^{j-1}\| \text{ for some } j \geqslant 1\\ &\text{(ii)}\ \ \|y^j - y^{j-1}\| \geqslant \theta \|y^{j-1} - y^{j-2}\| \text{ for some } j \geqslant 2 \qquad (3.31)\\ &\text{(iii)}\ \ j \leqslant j_{\max}\end{aligned}$$

with a suitable constant θ, say $\theta = 1.05$, and an integer $j_{\max}$, say $j_{\max} = 6$. On the other hand, the iterate y^j is accepted as the next point x^{k+1} if either one of the two conditions holds

$$\begin{aligned}&\text{(i)}\ \ \|\hat{F}y^0\| \leqslant \varepsilon_1\\ &\text{(ii)}\ \ (\|\hat{F}y^j\| \leqslant \varepsilon_2) \text{ and } (\|y^j - y^{j-1}\| \leqslant \varepsilon_3 + \varepsilon_4 \|y^j\|) \qquad (3.32)\\ &\qquad\qquad \text{for some } j \geqslant 1\end{aligned}$$

with given tolerances $\varepsilon_1, \ldots, \varepsilon_4$ which depend on the machine and on the problem.

In the case of non-convergence the predictor step is halved and the corrector is restarted from $\pi(\frac{1}{2}t_{k+1})$ with the corresponding value (3.23) of γ. However, it is required here that $\frac{1}{2}t_{k+1} \geqslant t_{\min}$ otherwise some user dependent action needs to be taken to modify $t_{\min}$ or to stop the overall process. On the other hand, if the convergence is declared with $x^{k+1} = y^j$ as the last iterate then we approximate the exact arc-length by

$$s_{k+1} = s_k + \|x^{k+1} - x^k\|_2 \qquad (3.33)$$

and, if required, proceed to take a new predictor-corrector step.

The continuation procedure described in this section has been used extensively with excellent success on many problems from structural mechanics and other fields. For space reasons we forego including here some graphs of the solution of a particular, large problem obtained by the procedure. Only a few of the many data characterizing any practically meaningful problem can ever be sketched and this does provide little or no insight into the way the continuation procedure actually works. Therefore, in the interest of giving a more detailed picture of the operation of the process, we present here computational results for a small, simple problem for which all relevant data can be exhibited.

More specifically, for a two-bar structure of the form of Figure 1 with $h = 2$ we use the following model derived in [13], p. 232:

$$Fx = \begin{pmatrix} (x_1 - 2)^3 + (x_1 - 2)(x_2^2 - 4) - 2x_3 \cos\alpha \\ x_2(x_1 - 2)^2 + x_2(x_2^2 - 2) - 2x_3 \sin\alpha \end{pmatrix} = 0. \qquad (3.34)$$

The load of size $2x_3$ is here tilted by an angle α from the vertical direction. Table 1 gives results computed on a PDP-10 for the case $\alpha = 0$, that is, for a vertically downward load. All data are rounded to three digits. In this case the horizontal component x_2 of the displacement vector x and of the tangent vector Tx is always zero and hence is not given. The change of the sign of the determinant σ_k (see (3.17)) between steps 1 and 2 signifies that a bifurcation point has been passed and that the direction of the trace had to be reversed. Between steps 2 and 3 a limit point with respect to the load variable x_3 is encountered. Note that the number of corrector steps is essentially constant except—as expected—near the bifurcation point where of course the Newton method used here becomes singular. The value $t_{\max} = 1$ was used; the decrease of the predicted steps near the limit points is caused solely by the increased curvature: otherwise limit points have no effect whatsoever on the process.

Table 2 gives results for the case $\alpha = \arcsin 0.75 \doteq 0.8481$. Here the limit point for the load variable occurs between steps 3 and 4 and a limit point for the horizontal deformation component x_2 is encountered between steps 4 and 5. If the run is continued a limit point with respect to the first variable x_1 will be found between steps 6 and 7. The solution is here more strongly curved and hence the steps are smaller and the number of corrector steps is larger.

Table 1.

k	s_k	x_1^k / $(Tx^k)_1$	x_3^k / $(Tx^k)_3$	i_k	h_k / t_{k+1}	Corr. Steps	α
0	0	0 .243	0 .970	3	- .500	3	16.5
1	.503	.135 .297	.485 .955	3	.503 1.00	4	9.98
2	1.55	.595 .721	1.42 .693	1	1.04 .703	3	-.0697
3	2.20	1.23 .666	1.31 -.746	3	.650 .540	3	-4.24
4	2.99	1.66 .479	.649 -.878	3	.787 1.00	2	-7.89
5	4.03	2.14 .453	-.282 -.892	3	1.05		-8.75

Table 2.

	s_k	x_1^k $(Tx^k)_1$	x_2^k $(Tx^k)_2$	x_3^k $(Tx^k)_3$	i_k	h_k t_{k+1}	# of Corr. Steps	α_e
0	0	0 .131	0 .595	0 .793	3	- .500	5	20.2
1	.595	.181 .309	.404 .745	.397 .591	2	.595 .829	4	14.9
2	1.55	.568 .709	1.10 .682	.921 .180	1	.951 .544	7	13.5
3	2.21	1.05 .894	1.50 .398	1.15 -.206	1	.665 .375	7	13.1
4	2.66	1.42 .856	1.59 .140	.910 -.498	1	.452 .496	6	12.4
5	3.45	1.86 .631	1.50 -.183	.260 -.754	3	.790 1.00	-	10.9

4. EXTENSIONS AND MODIFICATIONS

In this section we consider various special aspects of our problem, in particular, as they arise in structural applications. Up to now, the function F of (1.5) was simply assumed to be given. In practice, however, this mapping is derived in a more or less complicated manner from the original problem formulation and it depends strongly on the form of this derivation how much information is actually available about F during the solution process.

In structural applications the mapping F is typically obtained by finite element techniques. As a consequence, each evaluation of the vector Fx for a given point $x \in R^{n-1}$ involves computations of elemental stiffness data, their assembly into global form, etc. Hence there is no readily apparent way of computing the derivative matrix $F'(x)$, and without it the process of the previous section requires substantial modifications.

The derivative F' is an integral part of the computation of the predictor and it may or may not be needed in the corrector iteration. While the various forms of Newton's method certainly are well suited as corrector processes, there are many other choices available which do not depend on an explicit knowledge of F'. For instance, quasi-Newton-(update)-methods have been proposed for this purpose (see e.g. [23]). Another possibility arises when F has the quasi-linear form

$$Fx = A(x)\bar{x} - x_{n+1}p, \quad x = \begin{pmatrix} \bar{x} \\ x_{n+1} \end{pmatrix} \varepsilon R^{n-1}, \quad \bar{x} \in R^n. \tag{4.1}$$

This is frequently the case for geometrically nonlinear problems. Then the "corrector equation" (3.19) has the same generic form.

$$\hat{A}(x)x = d, \quad \hat{A}(x) = \begin{pmatrix} A(\bar{x}) & -p \\ \hline (e^i)^T & \end{pmatrix}, \tag{4.2}$$

and this suggests the well-known iterative process

$$\hat{A}(y^{j+1})y^j = d, \quad y^0 = x^k, \quad j = 0, 1, \ldots \tag{4.3}$$

as a corrector method.

Evidently, the derivative F' may also be avoided in the definition of the predictor. For instance, as indicated in the previous section we may use the standard Lagrangian interpolation polynomial π based on the data $\pi(s_j) = x^j$, $j = k, k-1, \ldots, k-m$. Unfortunately, this requires that the last $m+1$ points are kept in storage. Moreover, it is well-known that the quality of the approximation of the solution by π deteriorates rapidly outside the interpolation interval $[s_{k-m}, s_k]$.

Generally, continuation processes not involving the derivative perform noticeably more poorly than those based on it. As indicated, the predictions tend to be less reliable, and, in most cases, derivative-free corrector processes, such as (4.3), converge more slowly or may fail to converge altogether in parts of $\mathbb{R}(F)$. Fortunately, there is a technique which often allows us to obtain F' without unreasonable effort. It involves what in structural mechanics is usually called the incremental formulation of the basic equations.

For simplicity we consider the case of the equations (1.3). Moreover, before the discretization the original equilibrium problem is assumed to have the form

$$Hu = tw, \quad t \in R^1, \tag{4.4}$$

involving a mapping $H: X \to X$ on some infinite dimensional space X. Usually, X is a Banach- or Hilbert-space of suitable functions on a given finite-dimensional domain. The finite-element approximation then introduces a discretization mapping

$$\phi: X \to R^n \tag{4.5}$$

from X onto R^n and with it the discretized version $P: R^n \to R^n$ of H defined by $P(x) = \phi(Hu)$ for all $x = \phi(u)$, $u \in X$. Note, however, that P is only well-defined if ϕ is compatible with ϕ in the sense that $\phi(u) = \phi(v)$ for any $u, v \in X$ implies that $\phi(Hu) = \phi(Hv)$. Now, if, say, $\phi(w) = p$, then our discretized problem assumes the form (1.3).

In most applications, H possesses a (Frechet) derivative H' which maps X into the space $L(X)$ of

bounded linear operators on X. Moreover, it is usually rather straightforward to obtain H' from H. The incremental forms, discussed, for instance, in [13], are simply H' in the differential form $H'(u)v$. Now our discretization (4.5) induces also the matrix valued mapping $M: R^n \to L(R^n)$ with $M(x)y = \phi(H'(u)v)$, $x = \phi(u)$, $y = \phi(v)$, provided only that H' satisfies the appropriate compatibility condition. Evidently, the same mechanism used in the computation of Px also allows us to compute $M(x)y$. The question then arises under what conditions this discretization M of the derivative H' turns out to be the derivative P' of the discretization P. In other words we have the (Fig. 6) diagram

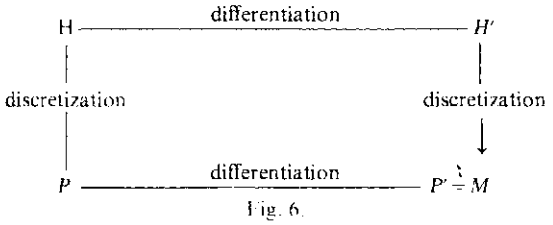

Fig. 6.

and the question is whether the operations of differentiation and discretization are commutative. Since M can be computed this would provide us with the desired method for computing the derivative P' of P.

In [14] it was shown that, under suitable assumptions, the answer is indeed affirmative. Unfortunately, in practical situations these assumptions -and, in particular, the mentioned compatibility conditions— are difficult to verify. There are also simple examples where the commutativity does not hold. However, it is conjectured that in most of the finite element applications to structural problems the result does hold and hence that in these cases P' can be computed as the discretization of H'. A formal proof is expected to be given elsewhere. In addition, the general "incremental approach" sketched here is beginning to find applications in fluid-flow problems, etc., where formerly derivative-based continuation methods were thought to be out of the question. There is certainly a need for a broader study of this incremental approach to the computation of the derivative of discretizations of practically important operators H.

Generally, in the application of the finite element method a very critical decision involves the choice of the mesh and the elements. Various approaches have been proposed for the design of meshes which are optimal in some sense. In particular, in [2–5] a theory of *a posteriori* error estimates for finite elements solutions has been developed which permits the construction of an adaptive mesh refinement algorithm that has been found to be highly effective for a range of problems.

Suppose again that in its basic form our problem is given by the equation (4.4). Then the desired solution may be expected to have the form

$$u: J \to X, \quad t: J \to R^1 \tag{4.6}$$

involving suitable functions u and t on some open interval J. Evidently, now, our principal aim should be to approximate this solution (4.6) of the infinite-dimensional problem. In order to accomplish this we construct first the discretization (1.3) of (4.4) and in turn compute its solution curve in R^{n+1}. This curve depends on the discretization (4.5) we have used; moreover the approximation-error between it and (4.6) is likely to vary considerably when we move along the solution (4.6). Since our main aim is to approximate (4.6), it is natural to consider different discretizations (4.5) (and hence dimensions n) in different parts of the parameter interval J.

In the finite-element setting the discretization (4.5) represents a particular selection of the mesh and the elements. Thus we are interested in methods for adapting the mesh and/or the elements to ensure an approximation of (4.6) within a given tolerance throughout the entire parameter interval. This is at present still a largely unresolved problem. In order to measure the approximation error, a theory of *a posteriori* error estimates for nonlinear finite element problems is needed, and such a theory is as yet little developed. Moreover, each change of the discretization (4.5) represents a change of the finite-dimensional problem and its dimension. Hence each such change implies a restart of the continuation process for a modified problem in a different space, and at present the interaction between these problem changes and the stability of the continuation procedure is only barely understood.

Nevertheless, so far all experience with processes that combine continuation and mesh-adaptation have been almost startingly effective. As an example consider the elliptic two-point boundary-value problem

$$-\frac{\mathrm{d}}{\mathrm{d}x}\left(a\left(\frac{\mathrm{d}u}{\mathrm{d}x}\right)\right)+b(u)=tf(x),\ x\in I=[0,1],\ t\in R^1, \tag{4.7}$$

$$u(0)=u(1)=0,$$

with suitable coefficient functions a, b, f. Let

$$\Delta:\ x_0=0<x_1<\ldots<x_n<x_{n+1}=1, \quad n=n(\Delta), \tag{4.8}$$

be a given mesh on I and $S(\Delta)$ the set of continuous functions on I which are linear on each subinterval $I_j(\Delta)=[x_{j-1}, x_j]$, $j=1,\ldots,n+1$, and zero at the endpoints of I. For any $t\in R^1$ the finite element solution $u(\Delta)\in \mathring{S}(\Delta)$ of (4.7) is defined by

$$\int_0^1 [a(u')v'+b(u)v]\,\mathrm{d}x = t\int_0^1 fv\,\mathrm{d}x, \quad v\in\mathring{S}(\Delta). \tag{4.9}$$

For fixed $j=1,\ldots,n+1$ let

$$\omega_j(x)=u(\Delta)(x)+z_jq_j(x),\ q_j(x)=(x-x_{j-1})(x_j-x),$$

$$x\in I_j(\Delta), \tag{4.10}$$

where $z_j\in R^1$ is the solution of the scalar nonlinear equation

$$\int_{I_j(\Delta)} [a(\omega_j)q_j'+(b(\omega_j)-tf)q_j]\,\mathrm{d}x=0. \tag{4.11}$$

Then

$$\varepsilon(\Delta)=\left[\sum_{j=1}^{n}|z_j|^2\right]^{1/2} \tag{4.12}$$

represents an *a posteriori* estimate for the error between $u(\Delta)$ and the exact solution u^* of (4.7) under the seminorm $\|(u-u(\Delta))'\|_{L_2^2(I)}$ which -under proper conditions about a, b is equivalent to the norm of the Sobolev space $\mathring{H}_2^1(I)$.

Evidently (4.9) defines the finite dimensional problem (1.3) for the particular mesh (4.8) to which we apply our continuation process. At each continuation step the error estimate (4.12) can be computed. Then, in line with the mesh-refinement algorithm discussed in [5] (see also [17]) those subintervals $I_j(\Delta)$ are halved for which $|z_j|$ exceeds a certain tolerance. On the new mesh

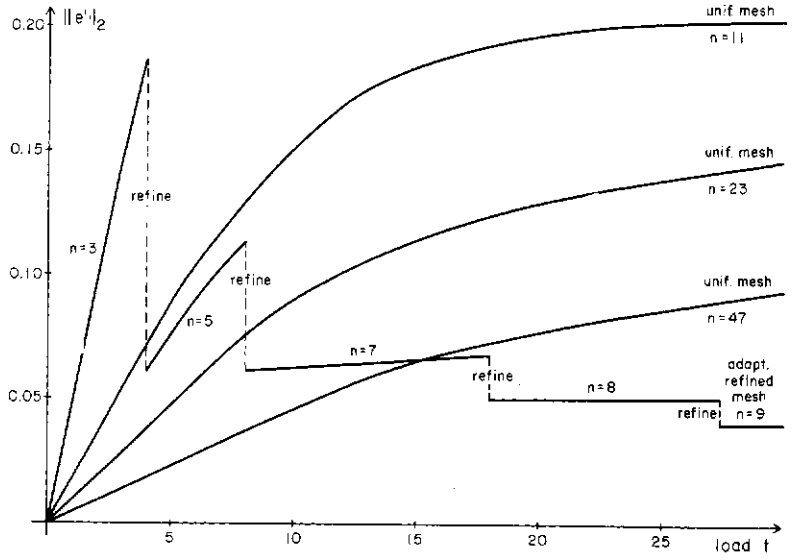

Fig. 6.

an approximate solution is obtained by interpolation and then corrected by means of a few Newton steps. Now the continuation process is applied again until a further refinement becomes necessary.

Some numerical results with this combined process have been given in [5] and are summarized in Fig. 6 for the problem (4.7) with

$$a(s)=\frac{s}{1+s}, \quad -1<s<\infty\,; \; b(s)\equiv 0, \quad s\in R^1$$

$$f(s)=\begin{cases}1, & \text{for } \frac{1}{4}<s<\frac{3}{4}\\ 0, & \text{otherwise}\end{cases}$$

This may be viewed as a model of a one-dimensional rod of length one which is clamped at the endpoints and subjected to a load in the direction of its axis specified by tf. The effectiveness of the procedure is certainly evident.

We end our discussion with some words about the general continuation problem (1.5) involving more than one parameter. As mentioned before, the solution then is a q-dimensional manifold in R^{n+q}, the equilibrium surface of the structure. Various authors have used perturbation techniques to analyse local features of this surface (see [19] and the many references given there, as well as [9, 12] for the same approach in a different context). In essence, these techniques allow for an analysis of the behavior of a given path on the equilibrium surface under certain perturbations of a parameter. In [19] these techniques are placed in the general context of the study of the equilibrium surface itself. This permitted a broader exploration of the close relationship between the shape of the surface and the structural stability of the mechanical system. In a more general setting these ideas are pursued further in [20, 21].

These studies certainly suggest the possibility of analyzing the structural stability of a system by exploring numerically the shape of the equilibrium surface, that is, by computing appropriate paths on the surface. A natural aim, for example, is to find and trace any paths on the surface consisting entirely of limit-points with respect to a given parameter. Since the continuation process discussed in Section 3 is not affected by such limit points, this task has certainly become feasible.

For small-dimensional problems with two parameters u_1, u_2 such a trace of the limit-point curves has been successfully accomplished. Basically, from a given starting point a primary curve is followed along which, say, u_2 is constant. As soon as a limit point with respect to u_1 is encountered the trace is turned to follow the curve of these limit points. The technical difficulty is here to specify an appropriate auxiliary equation which defines this curve on the equilibrium surface. It is easy to identify such equations, but in most cases their forms are numerically cumbersome. This was the reason for the restriction to small dimensional problems. Yet the results were in all cases highly interesting and encouraging. It is hoped that the indicated technical difficulties can be removed to provide a more general numerical approach to the study of the structural stability of complex mechanical systems.

REFERENCES

1. J. P. Abbott, An efficient algorithm for the determination of certain bifurcation points. *J. Comp. Appl. Math.* **4**, 19–27, (1978).
2. I. Babuska and W. Rheinboldt, Error estimates for adaptive finite element computations. *SIAM J. Numer. Anal.* **15**, 736–754 (1978).
3. I. Babuska and W. Rheinboldt, *A-posteriori* error estimates for the finite element methods. *Int. J. Numer. Meth. Engng* **12**, 1597–1615 (1978).
4. I. Babuska and W. Rheinboldt, Analysis of optimal finite element meshes in R^1. *Math Comput.* **33**, 435–463 (1978).
5. I. Babuska and W. Rheinboldt, Reliable error estimation and mesh adaptation for the finite element methods. In *Computational Methods in Nonlinear Mechanics* (Edited by J. T. Oden), pp. 67–108. North Holland, Amsterdam (1980).
6. C. den Heijer and W. C. Rheinboldt, On steplength algorithms for a class of continuation methods. University of Pittsburgh, Inst. for Computational Math. and Applications. *Tech. Rep., ICMA*-80-16, 1980.
7. P. Deuflhard, A stepsize control for continuation methods with special applications to multiple shooting techniques. *Numer. Math.* **33**, 115–146 (1979).

8. F. Ficken, The continuation method for functional equations. *Comm. Pure Appl. Math.* **4**, 435–456 (1951).
9. J. P. Keener and H. B. Keller, Perturbed bifurcation theory. *Arch. Rat. Mech. Anal.* **50**, 159–175 (1973).
10. H. B. Keller, Numerical solution of bifurcation and nonlinear eigenvalue problems. In *Applications of Bifurcation Theory* (Edited by P. Rabinowitz), pp. 359–384. Academic Press, New York (1977).
11. H. B. Keller, Global homotopies and Newton methods. In *Recent Advances in Numerical Analysis* (Edited by C. deBoor and G. H. Golub), pp. 73–94. Academic Press, New York (1978).
12. B. J. Matkowsky and E. L. Reiss, Singular perturbations of bifurcations. *SIAM J. Appl. Math.* **33**, 230–255 (1977).
13. J. T. Oden, *Finite Elements of Nonlinear Continua*. McGraw-Hill, New York (1972).
14. M. Ortega and W. C. Rheinboldt, On discretization and differentiation of operators with application to Newton's method. *SIAM J. Numer. Anal.* **3**, 143–156 (1966).
15. W. C. Rheinboldt, An adaptive continuation process for solving systems of nonlinear equations. Polish Academy of Science, *Banach Ctr. Publ.* **3**, 129–142 (1977).
16. W. C. Rheinboldt, Solution fields of nonlinear equations and continuation methods. *SIAM J. Numer. Anal.* **17**, 221–237 (1980).
17. W. C. Rheinboldt, On a theory of mesh-refinement processes. Univ. of Pittsburgh. *Int. F. Comput. Math. Appl., Tech. Rep. ICMA*-80-12, 1980; to appear in *SIAM J. Numer. Anal.*.
18. E. Riks, A unified method for the computation of critical equilibrium states of nonlinear elastic systems. National Aerospace Laboratory NLR, The Netherlands, *Tech. Rep., NLR-MP*-77041*U*, 1977.
19. M. J. Sewell, On the connection between stability and the shape of the equilibrium surface. *J. Mech. Phys. Solids* **14**, 203–230 (1966).
20. M. J. Sewell, Some mechanical examples of catastrophe theory. *Bull. Inst. Math. Appl.* **12**, 163–172 (1976).
21. M. J. Sewell, Some global equilibrium surfaces. University of Wisconsin-Madison, Mathematics Research Center, *MRC-Rep.* 1714, Feb. 1977.
22. M. J. Sewell, Some catastrophe problems in mechanics. University of Reading, Department of Mathematics, *Tech. Rep.*, Jan. 1978.
23. W. G. Strang, The quasi-Newton method in finite-element computations. In *Computational Methods in Nonlinear Mechanics* (Edited by J. T. Oden). North Holland, Amsterdam (1980).
24. H. J. Wacker (Ed.), *Continuation Methods*. Academic Press, New York (1978).

Computers & Structures, Vol. 13, pp. 115–119, 1981
Printed in Great Britain.

0045-7949/81/010115-05$02.00/0

METHODS FOR OPTIMAL ENGINEERING DESIGN PROBLEMS BASED ON GLOBALLY CONVERGENT METHODS

LAYNE WATSON†
Department of Computer Science, Virginia Polytechnic Institute and State University, Blacksburg, VA 24061, U.S.A.

and

W. H. YANG
Department of Applied Mechanics and Engineering Science, The University of Michigan, Ann Arbor, MI 48109, U.S.A.

(*Received* 25 *April* 1980)

Abstract—An optimal design problem is formulated as a system of nonlinear equations rather than the extremum of a functional. Based on the Chow–Yorke algorithm, another globally convergent homotopy method, and quasi-Newton methods, two algorithms are developed for solving the nonlinear system. Although the base algorithms are globally convergent (under certain fairly general assumptions), there is no theoretical proof of global convergence for the new methods. Some low dimensional numerical results are given.

1. INTRODUCTION

Most engineering designs are based on linear theories of physical phenomena. But since the parameters in the design problems are treated as variables, the mathematical formulations of the design problems are nonlinear. The usual formulation of an optimal design problem is to seek the extremum of a functional. If the optimality conditions are stated as differential or algebraic equations, the optimal design problem can be formulated directly as a system of nonlinear equations.

The finite element method is used to approximate the differential equations. The resulting nonlinear algebraic system is the projection of the original optimal design problem into a finite dimensional space. The solution of the algebraic system approximates that of the original problem. The algorithms developed here are based on globally convergent algorithms that have been used successfully in situations where Newton's method for nonlinear systems fails to converge. Examples of this approach are some nonlinear two-point boundary value problems [1], some fluid mechanics problems [2], the nonlinear complementarity problem [3], and the generalized plane stress problem of elasticity [4].

Two algorithms are developed here. One is a homotopy method and the other is a least change secant update (quasi-Newton) method. To illustrate the techniques, in this paper they are applied to a nonlinear algebraic system originating from a generalized plane stress problem of elasticity. This same model problem was solved in [4] by a globally convergent homotopy method. The homotopy map used in [4] was rather complicated, more so in order to be able to prove global convergence than from practical necessity. The homotopy map used here retains some of the essential features of the map in [4], but is much simpler, hence easier to implement. Unfortunately preliminary numerical results indicate that the homotopy method is not globally convergent. Creation of a new homotopy method is justified because both Newton's method and standard continuation diverge (unless the starting point is close to the solution) for this model problem [4]. Quasi-Newton methods are not theoretically globally convergent and in fact are known to fail for the model problem here [4], but a quasi-Newton method with a twist was very successful on the model problem.

The generalized plane stress problem of elasticity is chosen as a model problem of optimal design. The thickness of the sheet is assumed variable. The goal is to find the optimal thickness distribution of a given loading such that the strain energy density is uniform in the sheet.

The problem reduces to a nonlinear algebraic system by the use of the finite element approximation given in the next section.

2. FORMULATION

A generalized plane stress problem of elasticity describes the behavior of an elastic sheet under edge loading conditions. The sheet can be manufactured with an arbitrary thickness distribution. The optimal design problem is to seek a thickness distribution for a given loading such that the strain energy density is constant. This design uses material optimally in the elastic range. If the given load increases proportionally, the elastic limit of the material will be reached simultaneously throughout the sheet.

The problem must satisfy the equations of equilibrium,

$$\frac{\partial}{\partial x}(h\sigma_{xx})+\frac{\partial}{\partial y}(h\sigma_{xy})=0 \tag{2.1}$$

$$\frac{\partial}{\partial x}(h\sigma_{xy})+\frac{\partial}{\partial y}(h\sigma_{yy})=0$$

†The work of this author was partially supported by NSF Grant MCS 7821337.

where h is the thickness and σ_{xx}, σ_{xy} and σ_{yy} are the components of the stress tensor.

The elastic material properties are described by the generalized Hooke's law

$$\begin{aligned} &\frac{\partial u}{\partial x}-\frac{1}{E}(\sigma_{xx}-\nu\sigma_{yy})=0 \\ &\frac{\partial v}{\partial y}-\frac{1}{E}(\sigma_{yy}-\nu\sigma_{xx})=0 \\ &\frac{\partial u}{\partial y}+\frac{\partial v}{dx}-\frac{2(1+\nu)}{E}\sigma_{xy}=0 \end{aligned} \tag{2.2}$$

where u, v are the displacement components in the x, y directions respectively; E is the Young's modulus; and ν is the Poisson's ratio.

There are six unknowns in the system of eqns (2.1)–(2.2) in terms of the thickness, stress and displacement components.

If the thickness is regarded as a known parameter, the problem can be interpreted as an operator equation,

$$\begin{matrix} 0 & 0 & \frac{\partial}{\partial x} & \frac{\partial}{\partial y} & 0 & u \\ 0 & 0 & 0 & \frac{\partial}{\partial x} & \frac{\partial}{\partial y} & v \\ \frac{\partial}{\partial x} & 0 & \frac{-1}{Eh} & 0 & \frac{\nu}{Eh} & q_1 \\ \frac{\partial}{\partial y} & \frac{\partial}{\partial x} & 0 & \frac{-2(1+\nu)}{Eh} & 0 & q_2 \\ 0 & \frac{\partial}{\partial y} & \frac{\nu}{Eh} & 0 & \frac{-1}{Eh} & q_3 \end{matrix} = 0 \tag{2.3}$$

where

$$q_1=h\sigma_{xx},\ q_2=h\sigma_{xy},\ q_3=h\sigma_{yy} \tag{2.4}$$

are the edge stress resultants. The differential matrix operator is a function of the thickness. A finite element method given by Jespersen [8] may reduce (2.3) to an algebraic system,

$$K(\mathbf{h})\mathbf{u}=\mathbf{f} \tag{2.5}$$

where K is an n by n positive definite matrix called the stiffness matrix, $\mathbf{h}$ is the vector of thicknesses of the elements, $\mathbf{u}$ is the nodel displacement vector and $\mathbf{f}$ is the load vector. If $\mathbf{h}$ is known, (2.5) may be solved uniquely.

We shall assume the strain energy density

$$(\sigma_{xx}-\sigma_{yy})^2+\sigma_{xy}^2=U_0 \tag{2.6}$$

to be constant, U_0, everywhere. In terms of displacements, (2.6) is a differential equation. By the same finite element scheme, the condition (2.6) for each element has the form

$$\mathbf{u}^t B_i \mathbf{u}=1 \quad i=1,2,\ldots,m \tag{2.7}$$

where the B_i are n by n positive semidefinite matrices, and the constant U_0 is used for normalization. The total number of elements m is usually smaller than the number of nodes n.

Since the thickness $\mathbf{h}$ is non-negative, let $h_i=t_i^2$. The nonlinear algebraic system is

$$\begin{aligned} &K(\mathbf{t})\mathbf{u}=\mathbf{f} \\ &\mathbf{u}^t B_i \mathbf{u}=1 \quad i=1,\ldots,m \end{aligned} \tag{2.8}$$

where $\mathbf{t}$ is an m-vector; $\mathbf{u}$ is an n-vector and $\mathbf{f}$ is a given vector ($m<n$). The stiffness matrix has the structure

$$K(\mathbf{t})=\sum_{i=1}^{m} t_i^2 K_i \tag{2.9}$$

where the K_i are the element stiffness matrices which are positive semidefinite.

3. HOMOTOPY ALGORITHM

The algorithm developed here has the same theoretical basis as the fixed point algorithm in [5] and [6]. The theory is summarized in the following lemmas. See [5] for the proofs and [6] for an elementary exposition. Let E^n denote n-dimensional real Euclidean space.

Lemma 1. Let $\rho: E^n \times [0, 1) \times E^n \to E^n$ be a C^2 map such that the Jacobian matrix $D\rho(a, \lambda, x)$ has full rank on $\rho^{-1}(0)=\{(a, \lambda, x) | \rho(a, \lambda, x)=0\}$. Then for almost all $a \in E^n$, the Jacobian matrix of $\rho_a(\lambda, x)=\rho(a, \lambda, x)$ also has full rank on $\rho_a^{-1}(0)=\{(\lambda, x) | \rho_a(\lambda, x)=0\}$.

This is expressed in differential geometry jargon by saying if $\rho(a, \lambda, x)$ is transversal to zero, then for almost all a $\rho_a(\lambda, x)$ is also transversal to zero. "Almost all" means every point except those in a set of Lebesgue measure zero. Alternatively one could say $\rho_a(\lambda, x)$ is transversal to zero with probability one. Lemma 1 is known as a "parameterized Sard's Theorem". Now suppose ρ_a is chosen such that $\rho_a(0, x)=s(x)$ is a simple function with unique zero $x=\alpha$, and $\rho_a(1, x)=f(x)$ is the function for which a zero is desired. The next lemma merely spells out the implications of Lemma 1.

Lemma 2. Under the hypothesis of Lemma 1, for almost all a there exists a zero curve γ of ρ_a emanating from $(0, \alpha)$ along which the Jacobian matrix $D\rho_a(\lambda, x)$ has full rank. γ is a simple C^1 curve, is disjoint from any other zeros ρ_a might have, and either wanders off to infinity or reaches a zero of $f(x)$ (at $\lambda=1$).

Note that if the zero curve γ is bounded, it *must* reach a zero of $f(x)$. In general terms, the homotopy method is: construct the homotopy map $\rho_a(\lambda, x)$, then track the zero curve γ emanating from $(0, \alpha)$. If γ is bounded, then the algorithm is *globally divergent* with probability one. It turns out that γ is bounded for many important problems [1–6], hence there are globally convergent algorithms for these problems. The homotopy map ρ_a may be simple, as for the Brouwer fixed point problem [6], or quite complicated, as for the optimal design problem [4].

Another observation is that this homotopy algorithm is *not* just continuation or embedding. λ is not an embedding parameter that increases monotonically from 0 to 1, but is a *dependent* variable that can both increase and decrease along γ. Furthermore, the full rank of $D\rho_a$ along γ and the way in which the algorithm is implemented guarantee that there are never any "singular points" along γ. Singular points occur frequently in standard embedding techniques, resulting in their failure.

The nonlinear system under consideration here is (2.8). For comparison, the homotopy map used in [4] will be given. Define

$$\psi: E^n \times (0, 1)^m \times [0, 1) \times E^m \times E^n \to E^{m+n}$$

by

$$\psi(a, b, \lambda, t, u) \begin{pmatrix} [\lambda K(t) + (1-\lambda)\,\mathrm{diag}(t_1^2, \ldots, t_m^2, 1, \ldots, 1)]u \\ \qquad\qquad -f - (1-\lambda)a \\ u^t[\lambda B_1 + (1-\lambda)e_1 e_1^t]u - 1 - (1-\lambda)b_1 \\ \vdots \\ u^t[\lambda B_m + (1-\lambda)e_m e_m^t]u - 1 - (1-\lambda)b_m \end{pmatrix}$$

where e_j is an n-vector with 1 in the jth component and zeros elsewhere, diag $(t_1^2, \ldots)$ is an $n \times n$ diagonal matrix with diagonal elements $t_1^2, \ldots$. Now regard a, b, t, u as being complex vectors, so that ψ defines a complex map

$$\tilde{\psi}: \mathbf{C}^{n+m} \times [0, 1) \times \mathbf{C}^{m+n} \to \mathbf{C}^{m+n}.$$

Next convert every complex vector $v = (v_1, v_2, \ldots)$ to a real vector $(Re\ v_1, Im\ v_1, Re\ v_2, \ldots)$. This converts $\tilde{\psi}$ back to a real map

$$\rho: E^{2n+2m} \times [0, 1) \times E^{2m+2n} \to E^{2m+2n},$$

and

$$\rho_d(\lambda, x) = \rho(d, \lambda, x)$$

is the homotopy map actually used. The obtuse definition of ψ and the complexification of ψ make it possible to prove that the zero curve γ of ρ_d emanating from $(0, \alpha)$ reaches a zero of (2.8) at $\lambda = 1$.

The proposal here is to use a simpler ψ, but the same complexification process. Let $v = (t, u)$,

$$F(v) = \begin{pmatrix} K(t)u - f \\ u^t B_1 u - 1 \\ \vdots \\ u^t B_m u - 1 \end{pmatrix}$$

and take

$$\psi(a, \lambda, v) = \lambda F(v) + (1-\lambda)(v - a).$$

Converting ψ to complex and back to real again as above leads to the homotopy map

$$\rho_d(\lambda, x) = \lambda G(x) + (1-\lambda)(x - d), \qquad /(3.1)$$

where $x \in E^{2m+2n}$. Lemmas 1 and 2 apply to this ρ_d, hence the proposed homotopy method is to track the zero curve γ of ρ_d emanating from $(0, d)$. There is no proof that γ reaches $\lambda = 1$ but it is possible to prove that γ cannot turn back toward $\lambda = 0$.

The details of tracking γ are in [6], so that aspect will only be sketched here. Parameterize γ by arc length so $\lambda = \lambda(s)$, $x = x(s)$ along γ, and

$$\rho_d(\lambda(s), x(s)) = \lambda(s)G(x(s)) + (1 - \lambda(s))(x(s) - d) = 0.$$

Then

$$\frac{\mathrm{d}}{\mathrm{d}s}\rho_d(\lambda(s), x(s)) = D\rho_d(\lambda, x)\begin{pmatrix} \mathrm{d}\lambda/\mathrm{d}s \\ \mathrm{d}x/\mathrm{d}s \end{pmatrix} = 0, \qquad (3.2)$$

and since the parameter is arc length,

$$\left\| \left(\frac{\mathrm{d}\lambda}{\mathrm{d}s}, \frac{\mathrm{d}x}{\mathrm{d}s} \right) \right\|_2 = 1. \qquad (3.3)$$

Thus γ is the trajectory of the initial value problem (3.2)–(3.3) with initial conditions

$$\lambda(0) = 0, \quad x(0) = d. \qquad (3.4)$$

Note that (3.2) does not explicitly specify the derivative $(\mathrm{d}\lambda/\mathrm{d}s, \mathrm{d}x/\mathrm{d}s)$, which is required by any ODE subroutine. However, the full rank of $D\rho_d(\lambda(s), x(s))$, the condition (3.3), and the continuity of $(\mathrm{d}\lambda/\mathrm{d}s, \mathrm{d}x/\mathrm{d}s)$ along γ permit the unique determination of the derivative. The details of the numerical calculation of $(\mathrm{d}\lambda/\mathrm{d}s, \mathrm{d}x/\mathrm{d}s)$ are in [6] for dense $D\rho_d$ and in [4] for sparse $D\rho_d$.

The initial value problem (3.2)–(3.4) is most efficiently solved by a variable step, variable order Adams algorithm as in [7], for example. Since the ultimate goal is to solve $G(x) = 0$ and not to track γ, some special strategies are called for. These strategies, based on computational experience, are discussed in [6] and [1]. Since λ is a dependent variable and the ODE solver is taking discrete steps, it is unlikely that λ will hit 1 exactly. As soon as $\lambda(s) > 1$, inverse interpolation with previous points saved by the ODE solver yields an $\bar{s}$ such that $\lambda(\bar{s}) = 1$. The corresponding $x(\bar{s})$ is a zero of $G(x)$. Note that no extra derivative evaluations or steps by the ODE solver are required for the inverse interpolation.

4. QUASI-NEWTON ALGORITHM

Define $v = (t, u)$ and

$$F(v) = \begin{pmatrix} K(t)u - f \\ u^t B_1 u - 1 \\ \vdots \\ u^t B_m u - 1 \end{pmatrix}$$

as in Section 3. The most modern quasi-Newton methods, known as least change secant update methods, are based on solving

$$F(v) = 0$$

by minimizing

$$\|F(v)\|_2.$$

When intelligently programmed, they are in practice usually globally convergent because they guarantee a decrease in $\|F(v)\|$ at each move [10]. This feature is necessary for robustness, but it results in their failure on (2.8), because $\|F(v)\|$ has local minima at which $F(v) \neq 0$.

A least change secant update method applied directly to $F(v)$ will generally fail (unless the starting point is sufficiently close to the solution). The proposal here is to apply the least change secant update method in [12] to the *complexification*

$$G(x)$$

of $F(v)$, where G is the same as in Section 3. At least for the model problems tried here, this trick worked very well. $G(x)$ does not have the local minima difficulties afflicting $F(v)$. The drawback is that the dimension of the problem doubles, but clever programming can partially overcome this.

Least change secant update methods have the form

$$x^{(k+1)} = x^{(k)} - \gamma H_k G(x^{(k)}),$$

where H_k is an approximation to the inverse of the Jacobian matrix $DG(x^{(k)})$, and γ is chosen to guarantee certain desirable properties of the sequence $\{x^{(k)}\}$. H_k is updated at each iteration in $0((n+m)^2)$ operations, compared to $0((n+m)^3)$ for Newton's method. The precise details are complicated, and can be found in [10]. The efficiency per iteration, ultimate superlinear convergence, and robustness make least change secant update methods very attractive.

5. NUMERICAL RESULTS

To illustrate the dependence on m and n, the problem (2.8) was solved for various m and n using the data described below. Let $n=km$, and K_i be an $n\times n$ block diagonal matrix with $k\times k$ diagonal blocks. All the diagonal blocks are zero except the ith, which is

$$B=\begin{pmatrix} 2 & -1 & 0 & & & \\ -1 & 2 & -1 & & & \\ 0 & -1 & 2 & & & \\ & & & \ddots & & \\ & & & & 2 & -1 \\ & & & & -1 & 2 \end{pmatrix}$$

Thus

$$K_i=\begin{pmatrix} 0 & & & & \\ & \ddots & & & \\ & & 0 & & \\ & & & B & \\ & & & & 0 \\ & & & & & \ddots \\ & & & & & & 0 \end{pmatrix} \tag{5.1}$$

B_i is an $n\times n$ block diagonal matrix with the same block structure as K_i, and has the form (4.1) with $B=I$. f is an n-vector with the jth component being $0.01j$.

Table 1 shows the results. The execution times are in seconds on an IBM 370/158. The stopping criterion was $\|G(x)\|_\infty \le 10^{-4}$, and the starting points were chosen arbitrarily, but always at least a distance 1 from the solution. Failure of the homotopy method to converge is indicated in Table 1 by a dash. The number of Jacobian evaluations is reported in parentheses after the CPU times. The computer code used for the homotopy method was the fixed point code in [11], which also produced the numerical results in [1] and [6]. The quasi-Newton code used was the FORTRAN subroutine HYBRJ, part of the MINPACK package being developed at Argonne National Laboratory [12].

The CPU times in Table 1 are from codes which assume that the Jacobian matrix is dense, and use direct (elimination) methods to compute the kernel of the Jacobian matrix $D\rho_d(\lambda, x)$ (for the homotopy algorithm) or factor the Jacobian matrix $DG(x)$ (for the quasi-Newton method). Typically the Jacobian matrix in optimal design problems is very sparse, and a production code would use iterative sparse matrix techniques to find the kernel of $D\rho_d$ or factor DG. An important aspect of Table 1 is the number of Jacobian evaluations, which would be the same independent of how the matrix calculations are done. Note that the number of Jacobian evaluations is relatively insensitive to the dimensions m and n for the homotopy method, which is typical behavior [6]. Since the whole point of quasi-Newton methods is to avoid explicitly calculating the Jacobian, the quasi-Newton CPU times are the important figures.

Large scale computational results for a realistic generalized plane stress problem in elasticity will be

Table 1.

			CPU time	
m	n	total dimension	homotopy	quasi-Newton
2	4	12	8.8 (95)	.4 (1)
2	6	16	----	.6 (1)
3	6	18	----	.9 (1)
4	8	24	98.0 (109)	1.8 (1)
3	9	24	80.1 (86)	2.0 (1)
2	10	24	60.0 (70)	3.0 (2)
5	10	30	----	3.6 (1)
4	12	32	----	8.3 (2)
3	15	36	----	20.8 (4)
5	15	40	----	18.9 (2)
4	20	48	----	61.1 (4)
10	20	60	----	41.0 (1)
5	25	60	----	131.1 (4)
6	30	72	----	262.6 (4)
10	30	80	----	310.4 (3)
15	30	90	----	183.5 (1)

reported in a future paper.

In conclusion, recall that Newton's method, quasi-Newton methods and standard continuation fail when applied directly to (2.8). A complicated nonlinear homotopy based on the Chow-Yorke algorithm was developed in [4], and proven globally convergent for (2.8). The existence of a globally convergent homotopy algorithm for (2.8) motivated the algorithm of Section 3. Unfortunately the simple homotopy algorithm of Section 3 is not always globally convergent, which suggests that the intricacies of the homotopy map in [4] may be necessary. Hence there is no completely satisfactory homotopy algorithm for optimal design problems of the form (2.8) yet. The Section 4 algorithm is perhaps obvious, but it is interesting that it works. At present the best least change secant update methods destroy sparsity (H_k is dense even though $DG(x)$ may be very sparse), and thus the quasi-Newton approach is (at present) infeasible for large $m+n$. There are sparse matrix techniques for the quasi-Newton updating and factoring of a new quasi-Newton method (which retains sparsity and superlinear convergence) [13-16], but the global behavior and ultimate convergence rate of this new method are untested on real problems. Sparsity is maintained by sacrificing other desirable features of the quasi-Newton update (such as symmetry or positive definiteness), and a satisfactory compromise remains to be found. Note that the kernel of a homotopy Jacobian can be computed by sparse matrix algorithms.

There is no simple, globally convergent, feasible algorithm for large dimensional problems like (2.8). The advantages of both homotopy and least change secant update methods are too great to rule either approach out, and both should be pursued with regard to optimal design problems.

REFERENCES

1. L. T. Watson, An algorithm that is globally convergent with probability one for a class of nonlinear two-point boundary value problems. *SIAM J. Numer. Anal.* **16**, 394–401 (1979).
2. L. T. Watson, T.-Y. Li and C.-Y. Wang, Fluid dynamics of the elliptic porous slider. *J. Appl. Mech.* **45**, 435–436 (1978).
3. L. T. Watson, Solving the nonlinear complementarity problem by a homotopy method. *SIAM J. Control Optimization* **17**, 36–46 (1979).
4. L. T. Watson and W. H. Yang, Optimal design by a homotopy method. *Applicable Anal.*, **10**, 275-284 (1980).
5. S. N. Chow, J. Mallet-Paret and J. A. Yorke, Finding zeros of maps: homotopy methods that are constructive with probability one. *Math. Comput.* **32**, 887–899 (1978).
6. L. T. Watson, A globally convergent algorithm for computing fixed points of C^2 maps. *Appl. Math. Comput.* **5**, 297-311 (1979).
7. L. F. Shampine and M. K. Gordon, *Computer Solution of Ordinary differential Equations: The Initial Value Problem*. W. H. Freeman, San Francisco (1975).
8. D. Jespersen, A least squares decomposition method for elliptic equations. Ph.D. thesis, Department of Mathematics, Univ. of Michigan, Ann Arbor, Michigan (1976).
9. J. E. Dennis, Jr. and J. J. More, Quasi-Newton methods, motivation and theory. *SIAM Rev.* **19**, 46-89 (1977).
10. J. E. Dennis, Jr. and A. Schnabel, Quasi-Newton methods for unconstrained nonlinear problems. *Book Manuscript* (1979).
11. L. T. Watson and D. Fenner, Chow-Yorke algorithm for fixed points or zeros of C^2 maps. *ACM Trans. Math. Software* **6**, 252–260 (1980).
12. J. J. More, MINPACK documentation, Applied Math. Div., Argonne National Lab Argonne, Illinois, 1979.
13. Ph. L. Toint, On sparse and symmetric matrix updating subject to a linear equation. *Math. Comput.* **31**, 954–961. (1977).
14. Ph. L. Toint, Some numerical results using a sparse matrix updating formula in unconstrained optimization. *Math. Comput.* **32** 839–851 (1978).
15. Ph. L. Toint, On the superlinear convergence of an algorithm for solving a sparse minimization problem. *SIAM J. Numer. Anal.* **16**, 1036–1045 (1979).
16. M. J. D. Powell and Ph. L. Toint, On the estimation of sparse Hessian matrices. *SIAM J. Numer. Anal.* **16**, 1060–1074 (1979).

Computers & Structures, Vol. 13, pp. 123–128, 1981
Printed in Great Britain.

0045-7949/81/010123-06$02.00/0

NON-LINEAR VISCOELASTICITY BASED ON FREE VOLUME CONSIDERATION

W. G. KNAUSS and I. J. EMRI
Graduate Aeronautical Laboratories, California Institute of Technology, Pasadena, CA 91125, U.S.A.

(*Received* 17 *May* 1980)

Abstract—Many advanced engineering problems suffer from inadequate solution because the appropriate constitutive behavior for the materials involved is not available. This is certainly true where polymers are concerned because in many situations involving failure analysis the non-linear viscoelastic material properties become important.

In this paper a non-linear viscoelastic constitutive law is considered. It starts from the assumption that linear viscoelasticity is appropriate under infinitesimal strains and that the material description must revert to this case. The non-linearity of this development is derived from the stress dependent time response in the deformation process. The physical basis for the description derives from the observation that stress induced dilatation effects the mobility of molecular chains through changing the free volume in the polymer. Test data for polyvinyl acetate are compared with computations under conditions of relaxation and constant strain rate deformation. Excellent agreement is obtained between the proposed model and experiments. This agreement would indicate that the free volume model is definitely a possible way of describing non-linear viscoelastic behavior under small to moderate strains.

1. INTRODUCTION

The use of high speed computers in mechanics has removed a great many obstacles to scientific and design problem solving. In solid mechanics and structural engineering finite element techniques have made great strides in solving problems that were considered extremely complex by the earlier standards. These advances were made possible by the discretization of the well known field equations for virtually arbitrary geometries. The exploitation of these methods has become often more a matter of finances than of basic ability.

Besides possibly finances, a severe limitation on physically realistic problem solving arises from our lack of knowledge of material constitutive behavior. By far most structural or "continuum" codes incorporate linearly elastic material behavior with only some possessing capability of modelling non-linearly elastic and plastically deforming solids. With regard to time or rate sensitive materials only the (physically unrealistic) rudiments of linear viscoelasticity seem to be considered. In connection with today's increased use of structural polymers in advanced engineering designs, these material descriptions pose severe limitations. All the power of computational mechanics developed so far is compromised critically if the constitutive behavior of the structure is modelled insufficiently well.

In this presentation we are concerned with non-linearly viscoelastic material behavior. There are several physical reasons why materials behave in a non-linear manner. We distinguish polymeric solids as being single-phase or filled with soft or stiff inclusions in the form of particulates or continuous and chopped fibers. Examples are solid propellent rocket fuels, impact toughened polystyrene, tire tread shock, glass and graphite fiber reinforced plastic and structural adhesives.

Macroscopical non-linear material response in such materials may be associated with the development of discontinuities such as (micro) cracks and separation of the phases. On the other hand, grossly non-linear behavior in single phase materials may be the result of the appearance of crazes which qualitatively have the same effect as the generation of multiple cracks.

Here we wish to address non-linearly viscoelastic behavior from more molecular forces which do not occur as the result of such internal damage. Thus, this type of non-linearity is (possibly) present before damage mechanisms become operative.

Specifically, we are concerned here with the effect of stress or strain induced changes in the rate of relaxation or creep. In related work [1] we have noted that the intrinsic time scale of a material can be modified by moisture in the same manner as by temperature. In fact, we observed that the time scale was affected by the volume dilatation whether the latter was occasioned thermally or by swelling. The deduction is then close at hand that also stress induced volume dilatation will affect the intrinsic time scale of the material.

The effect of pressure on rheological behavior has been studied by several authors, first with a change in the glass transition behavior in mind [2–4] and later with rheological implications [5]. There seems to be no systematic study involving the effect of stress state on rheological behavior as a result of associated volume changes. Gent has attributed the crazing phenomenon in glassy plastic to stress-induced softening and void formation in the craze [14]. Very recently Bernstein and Shokooh [7] have considered the phenomenological concept of a "stress clock" which concept is akin to the physical basis underlying Gent's considerations and those of volume increase developed here in the sequel. It should be mentioned that in connection with fibrous and particulate composite thermodynamic reasoning led Schapery and Lou [8, 9] to examine modification of the relaxation or creep rate through a "strain dependent" shift factor.

For our present purposes we confine ourselves to relatively small strains which seems appropriate for the deformation of rigid polymers. We thus exclude spec-

ifically considerations of the large deformations [10] associated with rubber elasticity and viscoelasticity. Therefore, we may feel justified to begin our considerations with the linearly viscoelastic behavior of an isotropic solid which must describe its constitution under truly small strains or stresses; in other words, the nonlinear description of material behavior reduces then automatically to linear viscoelasticity in the limit of vanishing stresses and strains.

2. THEORETICAL BACKGROUND

As mentioned in the introduction, several investigators have studied the effect of temperature and pressure on the thermorheology of high polymers [2–5, 11–15]. These effects are commonly associated with changes in the free volume of the material. According to our experimental studies mentioned in the introduction and involving parametric variations in temperature and in water concentration, the (free) volume offers a unifying parameter to describe changes in the time scale of the material response. We proceed now to enlarge this concept by including the effect of mechanically (stress) induced volume dilatation.

The time dependence or viscosity of the rheological response is modified by a time-multiplying factor a which depends on the temperature, solvent concentration and mechanical dilatation,

$$a = a(T, c, \theta). \tag{1}$$

Doolittle expressed this factor in terms of the free volume by

$$\log a = \frac{B}{2.303}\left(\frac{1}{f} - \frac{1}{f_0}\right). \tag{2}$$

where f is the fractional free volume defined in terms of the total volume v_0 of the solid and the free volume v_f as

$$f = \frac{v_f}{v_f + v_0} \cong \frac{v_f}{v_0}. \tag{3}$$

and denotes by f_0 the fractional free volume at some reference conditions. We consider the fractional free volume to depend on three variables: temperature T, solvent concentration c, and mechanically induced dilatation θ, or

$$f = f(T, c, \theta). \tag{4}$$

Let us assume that the change in fractional free volume due to any one of the three variables is additive. This assumption appears entirely adequate for our present purposes since an examination of the partial derivitives of f with respect to T, c and θ reveals that only a small error results for ranges of the variables encountered normally. We then have differentially

$$\mathrm{d}f = \alpha\,\mathrm{d}T + \gamma\mathrm{d}c + \delta\cdot\mathrm{d}\theta, \tag{5}$$

where α, γ and δ are, in general, functions of T, c and θ. Let us assume further that α, γ and δ are constants, a condition that does not seem poor if we remain below the glass transition temperature and below the boiling point of the solvent. Then

$$f = f_0 + \alpha\cdot\Delta T + \gamma\cdot c + \delta\cdot\theta, \tag{6}$$

†Repeated indices indicate summation.

where we allow for zero solvent concentration and zero mechanical dilatation in stress free reference conditions. In terms of (6) eqn (1) becomes then

$$\log a(T, c, \theta) = -\frac{B}{2.303 f_0}\,\frac{\alpha\cdot\Delta T + \gamma\cdot c + \delta\cdot\theta}{\dfrac{f_0}{f_0} + \dfrac{\alpha\cdot\Delta T + \gamma\cdot c + \delta\cdot\theta}{f_0}}. \tag{7}$$

Through its dependence on the stress induced volume changes this shift factor $a(T, c, \theta)$ becomes instrumental in the non-linear material response described below.

Let us consider first the linearly viscoelastic constitutive description of an isotropic solid under infinitesimal deformations, in terms of the deviatoric stress and strain components (S_{ij}, e_{ij}) which are derived from the components of stress, τ_{ij} and (infinitesimal) strains ε_{ij} through the relations

$$S_{ij} = \tau_{ij} - \tfrac{1}{3}\tau_{kk}\delta_{ij}, \tag{8a}$$

$$e_{ij} = \varepsilon_{ij} - \tfrac{1}{3}\theta\delta_{ij} \qquad \theta = \varepsilon_{kk}. \tag{8b}$$†

Let $\mu(t)$ and $K(t)$ be, respectively, the relaxation moduli in shear and volume deformation. We have then at reference conditions

$$S_{ij} = 2\int_{-\infty}^{t} \mu(t-\xi)\frac{\partial e_{ij}}{\partial\xi}\,\mathrm{d}\xi, \tag{9}$$

$$\tau_{kk} = 3\int_{-\infty}^{t} K(t-\xi)\frac{\partial}{\partial\xi}(\theta + \alpha^*\Delta T + \gamma^* c)\,\mathrm{d}\xi. \tag{10}$$

If all macroscopic change in volume equal the change in free volume then $\alpha = \alpha^*$, $\gamma = \gamma^*$ and $\delta = 1$; we are not prepared to make that assertion now, nor is such an assertion absolutely necessary at this time for our later development. However, we point out that the comparison of our analysis with that data produces that $\delta = 1 (= 0.98)$. Also we note that for comparison of our computation with that data the terms $\alpha^*\Delta T$ and $\gamma^* c$ shall not enter our considerations.

Generalizing Lee's suggestions [16–18] that the time-temperature shifting under non-isothermal conditions be valid instantaneously, i.e. the temperature reduced time t' relates to the actual time t by the differential relation

$$\mathrm{d}t' = \frac{\mathrm{d}t}{a[T(t)]}. \tag{11}$$

We have, more generally, in view of (7)

$$t' = \int_0^t \frac{\mathrm{d}\xi}{a[T(\zeta), c(\zeta), \theta(\zeta)]}\,; \quad \xi' = \int_0^\xi \frac{\mathrm{d}\xi}{a[T(\zeta), c(\zeta), \theta(\zeta)]}. \tag{12}$$

Under conditions of time varying temperature, solvent concentration and stress dilatation

$$S_{ij}(t) = 2\int_{-\infty}^{t} \mu(t'-\xi')\frac{\partial e_{ij}}{\partial\xi}\,\mathrm{d}\xi, \tag{13}$$

$$\tau_{kk}(t) = 3\int_{-\infty}^{t} K(t'-\xi')\frac{\partial}{\partial\xi}(\theta + \alpha^*\Delta T + \gamma^* c)\,\mathrm{d}\xi. \tag{14}$$

Inasmuch as the reduced time in the argument of the relaxation function depends on the total stress or strain history, these relations no longer represent linear operations that connect stresses with deformations. Thus while the appearance of a linearly viscoelastic material behavior appears preserved considerable deviation from small strain linearity will become apparent.

3. EXAMPLES FOR TWO SPECIAL LOAD HISTORIES

From eqn (12) it is apparent that holding the temperature, concentration and dilatation constant during a test would produce a time independent shift of the test result since thus $t' = \text{constant} \cdot t$. Experimentally such a condition is extremely difficult, if not impossible, to impose. The next constraint is posed by available test equipment. With a view toward later comparison of test data with the evaluations of eqns (13) and (14) we therefore consider, for the present, the problems of stress relaxation and monotonic loading by a history of constant strain rate.

(1) *Relaxation at constant temperature and concentration*

We consider a uniaxial tensile specimen and impose the Heaviside strain history

$$\varepsilon_{11} = \varepsilon_0 h(t), \tag{15}$$

while all stresses except τ_{11} vanish. The pertinent equations become then

$$\tfrac{3}{2}S_{11} = \tau_{11} = 2\int_{-\infty}^{t} \mu(t'-\xi')\frac{\partial}{\partial \xi}(\varepsilon_{11}-\varepsilon_{22}), \tag{16}$$

$$\tfrac{1}{3}\tau_{kk} = \tfrac{1}{3}\tau_{11} = \int_{-\infty}^{t} K(t'-\xi')\frac{\partial}{\partial \xi}(\varepsilon_{11}+2\varepsilon_{22}), (\varepsilon_{33}=\varepsilon_{22}). \tag{17}$$

Since these relations constitute non-linear operations between τ_{11} and the strains ε_{11} and ε_{22} there is no direct analytical way of eliminating ε_{22} in order to obtain a relation between τ_{11} and ε_{11} only, except for infinitesimal strains ($a(T, c, \theta) = \text{constant}$). In this case

$$\tau_{11} = \int_{-\infty}^{t} E(t-\xi)\frac{\partial e_{11}}{\partial \xi}\,\mathrm{d}\xi, \tag{18}$$

$$\theta = \int_{-\infty}^{t} \tfrac{1}{3}K^{-1}(t-\xi)\frac{\partial \tau_{11}}{\partial \xi}\,\mathrm{d}\xi, \tag{19}$$

where the tensile relaxation modulus $E(t)$ is achieved by

$$\bar{E} = \frac{9\bar{K}\bar{\mu}}{3\bar{K}+\bar{\mu}}, \tag{20}$$

bars denoting Laplace transformed quantities.

The increase $K^{-1}(t)$ of the bulk modulus $K(t)$ is determined by

$$\int_0^t \tfrac{1}{3}K^{-1}(t-\xi)K(\xi)\,\mathrm{d}\xi = t. \tag{21}$$

Because the non-linear effects considered here are due to the stress induced changes in the scale of relaxation times, it is reasonable to assume that the same effect is prevalent in the simple tensile test. We therefore generalize the eqns (18) and (19) by applying the time reduction (12) to render

$$\tau_{11} = \int_{-\infty}^{t} E(t'-\xi')\frac{\partial e_{11}}{\partial \xi}\,\mathrm{d}\xi, \tag{22}$$

$$\theta = \int_{-\infty}^{t} \tfrac{1}{3}K^{-1}(t'-\xi')\frac{\partial \tau_{11}}{\partial \xi}\,\mathrm{d}\xi. \tag{23}$$

We note once more that (22, 23) do not follow directly from (16, 17); however, since the representation of linearly viscoelastic behavior can be given in several ways, each of which involves two independent material functions, it seems justifiable to start with the representations (18) and (19) in order to lead to stress induced non-linear behavior.

We now specialize (22) and (23) for step strain loading according to (15) to obtain

$$\tau_{11} = \varepsilon_0 \int_{-\infty}^{t} E(t'-\xi')\delta(\xi)\,\mathrm{d}\xi, \tag{24}$$

with $\delta(\xi)$ denoting the delta function; this reduces further to

$$\tau_{11} = \varepsilon_0 E(t'), \quad t' = \int_0^t \frac{\mathrm{d}\zeta}{a[T(\zeta), c(\zeta), \theta(\zeta)]}, \tag{25}$$

which, for infinitesimal strains ($\theta \to 0$) render

$$\tau_{11} = \varepsilon_0 E(t), \tag{26}$$

where $E(t)$ is the relaxation modulus for infinitesimal strains. Note that (25) represents a decaying stress history; however, because t' depends on the stress history, which in turn depends on the applied strain ε_0, the decay history will vary with the applied strain. Nevertheless, for short times the same glassy limit modulus will be achieved.

We particularize (17) now to the case of constant temperature and zero solvent concentration. There results then

$$\log a(\theta) = -\frac{B}{2.303 f_0}\frac{\delta\cdot\theta}{f_0 - \delta\cdot\theta}, \tag{27}$$

with θ being given by (23). In order to evaluate (27) we need to specify the bulk modulus $K(t)$ or its inverse $K^{-1}(t)$. We started this investigation by assuming a constant bulk modulus, but when we effected a comparison with the experimental data found that a time dependent description in the form of a standard linear solid yielded much better results. Accordingly, we chose

$$K^{-1}(t) = M_0 + M_1(1 - \mathrm{e}^{-t/\tau}). \tag{28}$$

The complete set of equations governing $\tau_{11}(t)$ is then, with $E(t)$ as the relaxation modulus at infinitesimal strain

$$\tau_{11} = \varepsilon_0 E(t'), \tag{25a}$$

$$t' = \int_0^t \frac{\mathrm{d}\zeta}{a[T_0, o, \theta(\zeta)]} \tag{25b}$$

$$\log a = -\frac{B}{2.303 f_k}\frac{\delta\cdot\theta}{f_0 + \delta\cdot\theta}, \tag{27a}$$

$$3\cdot\theta = (M_0 + M_1)\tau_{11} - \int_0^t \mathrm{e}^{-t'-\xi'/\tau}\frac{\partial \tau_{11}}{\partial \xi}\,\mathrm{d}\xi. \tag{29}$$

These equations are solved numerically. In order to avoid extensive iteration in their solution, we approximated (29) by replacing $t'-\xi'$ with $t-\xi$, since we believe that difference to be relatively unimportant. In fact, for our experimental study we have no information on $K(t)$, so that M_0, M and τ must be extracted by data fit; the physical reasonableness of the values so determined would then constitute a further test of the present considerations.

(2) *Constant rate of strain extension*

Prescription of constant rate of straining in the form of

$$\varepsilon_{11} = \dot{\varepsilon} t \tag{30}$$

results in the full set of response equations, analogous to (25a, b), (27a) and (29) as

$$\tau_{11}(t) = \dot{\varepsilon}\int_0^t E(t'-\xi')\,\mathrm{d}\xi, \tag{31a}$$

$$t'-\xi'=\int_{\xi}^{t}\frac{ds}{a[T,o,\theta(s)]}, \tag{31b}$$

$$\log a=\frac{-B}{2.303f_0}\,\frac{\alpha_T\Delta T+\delta\cdot\theta(t)}{f_0+\alpha_T\Delta T+\delta\cdot\theta(t)} \tag{31c}$$

$$3\cdot\theta(t)=(M_0+M_1)\tau_{11}(t)-\int_0^t e^{-t-\xi/\tau}\frac{\partial\tau_{11}}{\partial\xi}\,d\xi. \tag{31d}$$

Again, according to the remarks following eqn (29) we have replaced $t'-\xi'$ by $t-\xi$ in (31d). For later reference when we compare the evaluation of (31a–d) with test data we point out that the experiments with constant strain rates involve relatively short times; the transition behavior of the bulk modulus is not involved and it is entirely adequate to consider the bulk modulus to be constant at its glassy or short time value. Also, because test data were obtained at different temperatures, we include here the effect of different but constant temperatures. Since all test temperatures are below the glass transition temperature we allow only for the simple proportionality of the free volume to the temperature change.

4. COMPARISON WITH EXPERIMENTAL DATA

In order to test the proposed theory we compare the computations with data from measurements on polyvinyl acetate. In the interest of brevity we do not account here the method of specimen preparation but content ourselves with stating that the specimens were machined in a cylindrical shape with a test section 0.8 cm (0.312 in.) in diameter and a test section of 5 cm (2 in.). The measurements were made with the aid of an Instron tensile tester†. Measurements of strain in the relaxation tests were accomplished via bench marks on the specimen test section, the relative distance of which was monitored with an Optron. Such direct strain measurement also allowed continued monitoring of whether specimen slippage occurred in the grips.

(1) *Relaxation tests*

Relaxation tests were conducted at uniaxial tensile strains of 1, 3 and 5%. While the method of strain measurement allows an accuracy of a fraction of a percent the prescription of the applied strain through the mechanism of the straining machine was difficult. We were therefore not able to prescribe small strains well though it could be measured well; as a consequence, we lack precise data at "infinitesimal" strains.

Relaxation tests were conducted at different temperatures at each of the indicated strains. For each of the latter a master curve was prepared by shifting the segments for a best fit as a master curve. Strictly speaking this temperature shifting should not be independent of the strain at which measurements are made; however, as a first approximation we assume that procedure to be adequate.

The experimental master curves are compared with those calculated in Fig. 1. Note that a 1% strain produces a high stress and thus a significant dilatation. As a result the 1%-relaxation data should not agree well with the relaxation behavior for infinitesimal strain. Accordingly, we have also calculated the relaxation behavior of

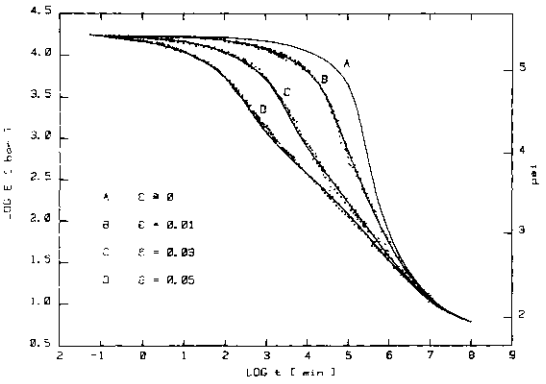

Fig. 1. Relaxation behavior of polyvinyl acetate in uniaxial tension at different strain levels. Dots represent experimental results; solid lines indicate non-linear analysis.

infinitesimal strain, shown as curve *A* in Fig. 1.

The calculated curves exhibit some apparent "unevenness" which is the result of our uncertainty of the true bulk behavior. Apart from this blemish it is clear, however, that the general response of the specimens is well followed by the calculations, provided we let

$$K(t)=[1.34+2.01\exp(-t/\tau)]\cdot 10^3 \text{ bar}$$
$$\tau=4\cdot 10^5 \text{ min}.$$

Note that at least a partial check on the validity of the representation of $K(t)$ is given by comparing the computation of Section 3 with appropriate and independent experiments, as described next, as long as the same bulk representation is used.

(2) *Constant rate of strain test*

Tensile specimens were strained in a closely controlled (dry) thermal environment to produce typical "stress-strain" response curves. Since we found that the discrepancy between theory and experiment was on the order of 5% we saw no urgency to compensate for changes in specimen cross section. Accordingly, the stress is referred to the original, undeformed cross section.

In Figs. 2(a–c) we show experimental results (dotted curves) together with the responses computed from eqns (31a–d) (solid lines). Also shown are the responses which a linearly viscoelastic solid would produce if linear viscoelasticity were valid at non-infinitesimal strains. It is apparent from eqn (7) and how the instantaneous shift factor affects the stress–strain response (27a) and (31c) that the apparently non-linear behavior is noticeably affected by the environmental temperature. The polyvinyl acetate used possesses a glass transition temperature of 28–29°C. To illustrate the effect of change in temperature on the stress-strain behavior we show in Fig. 2(a) and 2(b) the response at two temperatures (24.3 and 26.5°C). The difference is so noticeable because the higher temperature is fairly close to the glass transition temperature. To illustrate the effect of strain rate we include Fig. 2(c) which results from an increase in strain rate by a factor of 10 over that in Fig. 2(b). Here it is interesting to note that the range of apparent agreement with the linearly viscoelastic behavior extends to higher stresses or strains than for the slower strain rate, thus emphasizing the fact that the non-linear behavior is a rate or time related non-linearity.

†We gratefully acknowledge Prof. Tschoegl's assistance, in whose laboratory we could perform the relaxation measurements.

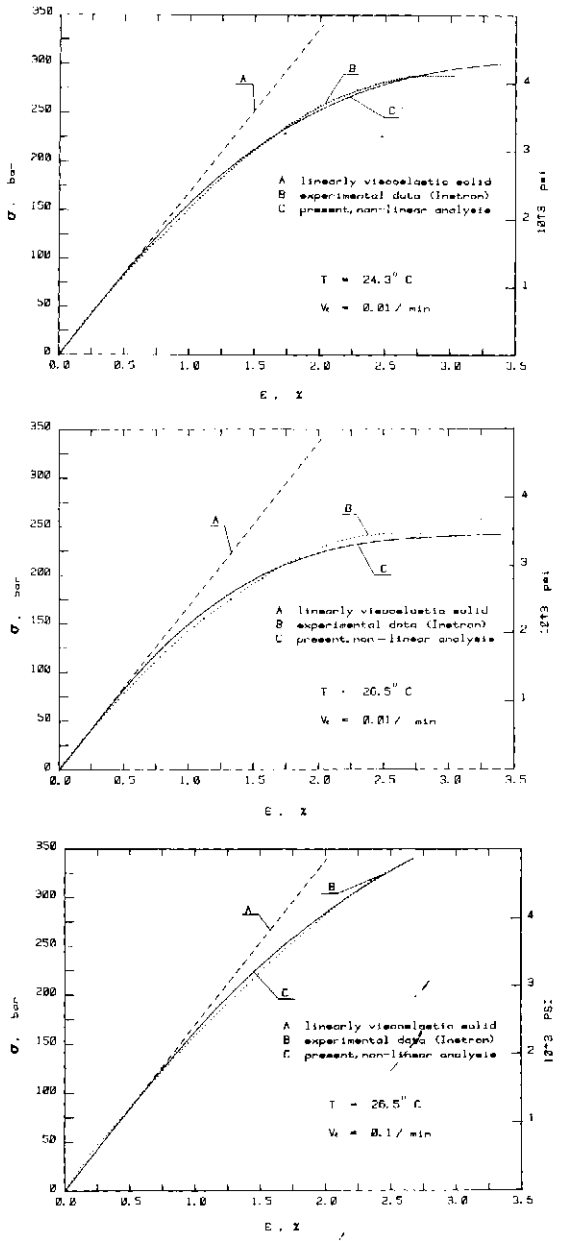

Fig. 2. Uniaxial tensile stress as a function of strain in constant rate of strain test. (a) and (b) illustrate different temperatures at the same strain rate. (b) and (c) illustrate the effect of different strain rate at constant temperature.

CONCLUSIONS

We have presented a theory of non-linearly viscoelastic behavior which is based on the concept of how the free volume affects the internal time scale of the material. We have demonstrated that a formulation consistent with linearly viscoelastic behavior for infinitesimal strains leads to good agreement with the test data in uniaxial tension. The computation requires numerical evaluation and can be incorporated into numerical stress analysis codes.

While it is not our primary purpose to have to justify the polymer physical aspects of the problem, it is of interest to note that the constants required for the evaluation of the model are either determined by measurements independent from those reported here

$B = 0.16$†

$f_0 = 0.01$†

$\alpha_T = 5.98 * 10^{-4}/°C$ (coefficient of thermal volume expansion)†

and by fitting the theory to the test data with the bulk representation of eqn (28). Note also that, as mentioned before the constant $\delta = 1$; this means that the mechanically (stress) induced dilatation is equal to the increase of the free volume.

†Determined at our laboratory by Mr. Luc Heymans, graduate student.

Acknowledgements—The authors wish to acknowledge the support of the Office of Naval Research under Contract N00014-78-C-0634 and are grateful for the support of Dr. R. S. Miller. We also acknowledge the support of Air Force Office of Scientific Research Contract F49620-77-C-0051 and are grateful for the personal support of Lt. Col. J. D. Morgan, who was associated with this program until very recently.

REFERENCES

1. W. G. Knauss and V. H. Kenner, On the hygrothermomechanical characterization of polyvinyl acetate. California Institute of Technology, Graduate Aeronautical Laboratories, *GALCITSM* 80-8.
2. J. D. Ferry and R. A. Stratton, The free volume interpretation of the dependence of viscosities and viscoelastic relaxation times on concentration, pressure and tensile strain, *Kolloid-Z* **171**(2), 107–111 (1960).
3. D. Turnbull and M. H. Cohen, Free-volume model of the amorphous phase-glass transition. *J. Chem. Phys.* **34**(1), 120 (1961).
4. A. Quach and R. Simha, Pressure-volume-temperature properties and transitions of amorphous polymers; polystyrene and poly (orthomethylstyrene). *J. Appl. Phys.* **82**(12), 4592–4606 (1971).
5. R. W. Fillers and N. W. Tschoegl, The effect of pressure on the mechanical properties of polymers. *Trans. Soc. Rheology* **21**(1), 51–100 (1977).
6. A. N. Gent, Hypothetical mechanism of crazing in glassy plastic. *J. Mater. Sci.* 325–932 (1970).
7. B. Bernstein and A. Shokooh, The stress clock function in viscoelasticity. *J. Rheology* **24**(2), 189–211 (1980).
8. R. A. Schapery, An engineering theory of nonlinear viscoelasticity with applications. *Int. J. Solids Structures* **2**, 407–425 (1966). See also R. A. Schapery, On the characterization of nonlinear viscoelastic materials. *Polymer Engng Sci.* **9**(4) (1969).
9. Y. C. Lou and R. A. Schapery, Viscoelastic characterization of a nonlinear fiber-reinforced plastic. *J. Composite Mater.* **5** (1971).
10. W. V. Chang, R. Bloch and T. W. Tschoegl, Study of the viscoelastic behavior of uncrosslinked (gum) rubbers in moderately large deformations. *J. Polymer Sci.* **15**, 923–944 (1977).
11. H. Leaderman, Elastic and creep properties of filamentous materials and other high polymers. The Textile Foundation, Washington (1943).
12. J. D. Ferry, M. L. Williams and R. F. Landel, The temperature dependence of relaxation mechanisms in amorphous polymers and other glass-forming liquids. *J. Am. Chem. Soc.* **77**, 3701 (1955).
13. J. D. Ferry and R. F. Landel, Molecular friction coefficients in polymers and their temperature dependence. *Kolloid-Z* **148** 1/2), 1 (1956).
14. M. L. Williams, Free volume approach to polystyrene melt viscosity. *J. Appl. Phys.* **23**(10), 1395 (1958).

15. K. H. Hellwege, W. Knappe and P. Lehmann, Die Isotherme Kompressibilitaet Einiger Amorpher und Teilkristalliner Hochpolymerer im Temperaturbereich von 20–25° C und bei Drucken bis zu 2000 kp/cm². *Kolloid-Z* **143**(2), 110 (1961).
16. M. L. Morland and E. H. Lee, Stress analysis for linear viscoelastic materials with temperature variation. *Trans. Soc. Rheology* **4**, 233–263 (1960).
17. E. H. Lee, Some recent developments in linear viscoelastic stress analysis. *Proc. 11th Int. Cong. of Applied Mechanics*, Munich (Germany), Springer-Verlag, Berlin (1964).
18. E. H. Lee and T. G. Roberts, On the generation of residual stresses in thermoviscoelastic bodies, *J. Appl. Mech.* No. 65, APMW-g (1965).

Computers & Structures Vol. 13, pp. 129–135
Pergamon Press Ltd., 1981. Printed in Great Britain

0045-7949/81/010129-07$02.00/0

A THEORY FOR ANALYSIS OF THERMOPLASTIC MATERIALS

DAVID H. ALLEN†
Engineering Science and Mechanics Department, Virginia Polytechnic Institute and State University, Blacksburg, VA 24061, U.S.A.

and

WALTER E. HAISLER
Associate Professor, Aerospace Engineering Department, Texas A&M University, College Station, TX 77843, U.S.A.

(*Received* 8 *May* 1980)

Abstract—The purpose of this paper is to present a theoretical model for predicting the behavior of elastic-plastic materials subjected to cyclic mechanical and thermal loading. The considerable literature in this area gives ample evidence of its significance. Solutions are sought in the areas of laser technology, nuclear reactor design, and turbine analysis, to name but a few.

There are four sections contained in this paper: (1) the formulation of a special purpose constitutive law; (2) review of a variational principle for use with the constitutive law; (3) a discussion of the application of the model to a computer code; and (4) a comparison of several experiments to results obtained in the theoretical model.

INTRODUCTION

In this paper the classical isothermal rate independent theory of plasticity is extended to obtain a nonisothermal theory for thermoplastic materials. This extension is performed in two parts: first, it is assumed that material properties are temperature dependent; and second, an uncoupled rate dependent strain term is included to account for creep. In order to account for the Bauschinger effect during cyclic loading the theory includes a combined isotropic–kinematic workhardening rule. The resulting incremental constitutive law includes a term attributable to nonisothermal loading and not contained in the isothermal theory. The addition of this temperature dependent stress increment into the constitutive law necessitates the derivation of a variational principle which differs from the well-known isothermal principle. Thus, a virtual work equation is presented for use with the finite element method. This section is followed by a short discussion of the computational procedure used to implement the constitutive law to a computer.

In the final section results of several example problems are presented. The impetus of these sample problems is twofold in nature. First, examples will be utilized to clarify certain computational aspects of the constitutive theory, and second, experimental data will be compared to theoretical results as a means of verification of the theory.

PRESENTATION OF THE CONSTITUTIVE THEORY

Recall that in the incremental theory of plasticity the workhardening rule is defined by a yield function in stress space, which for temperature dependent combined isotropic-kinematic hardening is:

$$F(S_{ij}-\alpha_{ij})=k^2(\int \mathrm{d}\bar{\varepsilon}^P, T), \tag{1}$$

where S_{ij} = second Piola Kirchhoff stress tensor α_{ij} = coordinates of the yield surface center in stress space, $\mathrm{d}\bar{\varepsilon}^P$ = uniaxial plastic strain increment, T = temperature, and $\int \mathrm{d}\varepsilon^P$ is a state variable representing the plastic strain history dependence in the yield function. Note that the explicit temperature dependence on the r.h.s. of eqn (1) precludes kinematic hardening due to temperature changes [1]. A schematic representation of eqn (1) is shown in Fig. 1.

Differentiating eqn (1) gives the following consistency condition during plastic loading:

$$\frac{\partial F}{\partial S_{ij}}\mathrm{d}S_{ij}-\frac{\partial F}{\partial S_{ij}}\mathrm{d}\alpha_{ij}-2k\frac{\partial k}{\partial \bar{\varepsilon}^P}\mathrm{d}\varepsilon^P-2k-2k\frac{\partial k}{\partial T}\mathrm{d}T=0, \tag{2}$$

where the term $(\partial F/\partial S_{ij})$ represents $\partial F(S_{ij}-\alpha_{ij})/\partial S_{ij}$ evaluated at $S_{ij}-\alpha_{ij}$ which can be seen to be equivalent to $\partial F/\partial(S_{ij}-\alpha_{ij})$. Since during neutral loading the plastic strain increment and $\mathrm{d}\alpha_{ij}$ are zero, it is apparent that a statement governing loading is:

$$\frac{\partial F}{\partial S_{ij}}\mathrm{d}S_{ij}-2k\frac{\partial k}{\partial T}\mathrm{d}T>0. \tag{3}$$

In addition to the statement of consistency during loading given by (2), the following associated flow rule is employed:

$$\mathrm{d}E^P_{ij}=\mathrm{d}\lambda\frac{\partial F}{\partial S_{ij}}, \tag{4}$$

where $\mathrm{d}E^P_{ij}$ represents the plastic strain increment tensor.

†Formerly at Texas A&M University.

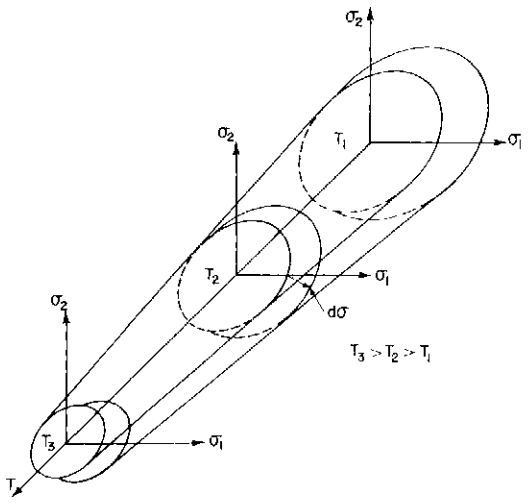

Fig. 1. Yield surface as a function of stress and temperature.

The stress at any time is assumed to be given by:

$$S_{ij}=D^{t}_{ijmn}(E_{mn}-E^{P}_{mn}-E^{C}_{mn}-E^{T}_{mn}), \tag{5}$$

where D^{t}_{ijmn} is the elastic constitutive tensor at time t. Incrementation of eqn (5) was shown in our previous paper [2] to give:

$$\begin{aligned}\mathrm{d}S_{ij}=&D^{t+\Delta t}_{ijmn}(\mathrm{d}E_{mn}-\mathrm{d}E^{P}_{mn}-\mathrm{d}E^{C}_{mn}-\mathrm{d}E^{T}_{mn})\\&+\mathrm{d}D_{ijmn}(E^{t}_{mn}-E^{Pt}_{mn}-E^{Ct}_{mn}-E^{Tt}_{mn}),\end{aligned} \tag{6}$$

where $D^{t+\Delta t}_{ijmn}$ = elastic modulus tensor at time $t+\Delta t$, $\mathrm{d}D_{ijmn}$ = change in the elastic constitutive tensor (due to a temperature change) during time step Δt, E_{mn} = total strain tensor, E^{P}_{mn} = plastic strain tensor, E^{C}_{mn} = creep strain tensor, E^{T}_{mn} = thermal strain tensor, and all superscripts t indicate measurement at time t. The superscript $t+\Delta t$ on the elastic constitutive tensor is necessary due to the fact that the time step is finite rather than infinitesimal. Note that incrementation of the constitutive law results in a stress rate which is not rotationally invariant unless an infinitesimal strain measure is used. Therefore, the resulting theory is applicable only to small deformations.

The final expression required to complete the constitutive law is the hardening rule. According to Ziegler's modification [3] a tensorially correct statement is:

$$\mathrm{d}\alpha_{ij}=\mathrm{d}\mu(S_{ij}-\alpha_{ij}), \tag{7}$$

where μ is a scalar to be determined by the consistency condition (eqn 2).

The constitutive law is thus obtained by substituting eqn (4) into eqns (2) and (6) and solving for the stress increment tensor. The resulting equation is:

The above constitutive law differs from that obtained by Yamada [4, 5] in that the term containing $\mathrm{d}T$ is written as a separate portion of the stress increment in the latter's derivation. It will be shown, however, that the two are mathematically equivalent. Unfortunately, in the form presented in eqn (8) it is not possible to determine the stress increment due to the occurrence of several undetermined parameters on the r.h.s. Yamada has accounted for these terms by introducing the plastic work rate. We have chosen a slightly different method for determining the effect of these unknowns.

As presented in a previous paper by us [6], we assume that there exists a scalar parameter c, called the hardening modulus, which when multiplied by the plastic strain increment and subtracted from the stress increment will be parallel to a tangent to the yield surface. Mathematically, this may be stated as:

$$(\mathrm{d}S_{ij}-c\mathrm{d}E^{P}_{ij})\frac{\partial F}{\partial S_{ij}}=0. \tag{9}$$

It can be seen from an examination of the consistency condition (eqn 2), that in order for the above statement to be valid, the following must hold:

$$c\mathrm{d}E^{P}_{ij}\frac{\partial F}{\partial S_{ij}}=\frac{\partial F}{\partial S_{ij}}\mathrm{d}\alpha_{ij}+2k\frac{\partial k}{\partial \bar{\varepsilon}^{P}}\mathrm{d}\bar{\varepsilon}^{P}+2k\frac{\partial k}{\partial T}\mathrm{d}T. \tag{10}$$

If one employs the normality condition in eqn (10) and substitutes the result into the constitutive relation (eqn 8), the result is:

$$\begin{aligned}\mathrm{d}S_{ij}=&\left(D^{t+\Delta t}_{ijmn}-\frac{D^{t+\Delta t}_{ijmn}\dfrac{\partial F}{\partial S_{vw}}\dfrac{\partial F}{\partial S_{tu}}D^{t+\Delta t}_{tumn}}{c\dfrac{\partial F}{\partial S_{pq}}\dfrac{\partial F}{\partial S_{pq}}+D^{t+\Delta t}_{pqrs}\dfrac{\partial F}{\partial S_{pq}}\dfrac{\partial F}{\partial S_{rs}}}\right)\\&\times(\mathrm{d}E_{mn}-\mathrm{d}E^{C}_{mn}-\mathrm{d}E^{T}_{mn})\\&-\left(\frac{D^{t+\Delta t}_{ijvw}\dfrac{\partial F}{\partial S_{vw}}\dfrac{\partial F}{\partial S_{tu}}\mathrm{d}D_{tumn}}{c\dfrac{\partial F}{\partial S_{pq}}\dfrac{\partial F}{\partial S_{pq}}+D^{t+\Delta t}_{pqrs}\dfrac{\partial F}{\partial S_{pq}}\dfrac{\partial F}{\partial S_{rs}}}\right)\\&\times(E^{t}_{mn}-E^{Pt}_{mn}-E^{Ct}_{mn}-E^{Tt}_{mn})\\&+\mathrm{d}D_{ijmn}(E^{t}_{mn}-E^{Pt}_{mn}-E^{Ct}_{mn}-E^{Tt}_{mn}).\end{aligned} \tag{11}$$

The simplicity of the above formulation can be seen when one uses the normality condition in conjunction with eqn (9) to obtain

$$c=\frac{\dfrac{\partial F}{\partial S_{ij}}\mathrm{d}S_{ij}}{\dfrac{\partial F}{\partial S_{ij}}\mathrm{d}E^{P}_{ij}}=\frac{2}{3}\frac{\mathrm{d}\sigma_{x}}{\mathrm{d}\bar{\varepsilon}^{P}}. \tag{12}$$

Thus, for isothermal loading it can be seen that the hardening modulus is simply two-thirds the instantan-

$$\begin{aligned}\mathrm{d}S_{ij}=&\left(D^{t+\Delta t}_{ijmn}-\frac{D^{t+\Delta t}_{ijvw}\dfrac{\partial F}{\partial S_{vw}}\dfrac{\partial F}{\partial S_{tu}}D^{t+\Delta t}_{tumn}}{\dfrac{\partial F}{\partial S_{tu}}\dfrac{\mathrm{d}\alpha_{tu}}{\mathrm{d}\lambda}+2k\dfrac{\partial k}{\partial \bar{\varepsilon}^{P}}\dfrac{\mathrm{d}\bar{\varepsilon}^{P}}{\mathrm{d}\lambda}+2k\dfrac{\partial k}{\partial T}\dfrac{\mathrm{d}T}{\mathrm{d}\lambda}+D^{t+\Delta t}_{pqrs}\dfrac{\partial F}{\partial S_{pq}}\dfrac{\partial F}{\partial S_{rs}}}\right)(\mathrm{d}E_{mn}-\mathrm{d}E^{C}_{mn}-\mathrm{d}E^{T}_{mn})\\&-\left(\frac{D^{t+\Delta t}_{ijvw}\dfrac{\partial F}{\partial S_{vw}}\dfrac{\partial F}{\partial S_{tu}}\mathrm{d}D_{tumn}}{\dfrac{\partial F}{\partial S_{tu}}\dfrac{\mathrm{d}\alpha_{tu}}{\mathrm{d}\lambda}+2k\dfrac{\partial k}{\partial \bar{\varepsilon}^{P}}\dfrac{\mathrm{d}\bar{\varepsilon}^{P}}{\mathrm{d}\lambda}+2k\dfrac{\partial k}{\partial T}\dfrac{\mathrm{d}T}{\mathrm{d}\lambda}+D^{t+\Delta t}_{pqrs}\dfrac{\partial F}{\partial S_{pq}}\dfrac{\partial F}{\partial S_{rs}}}\right)\times(E^{t}_{mn}-E^{Pt}_{mn}-E^{Ct}_{mn}-E^{Tt}_{mn})+\mathrm{d}D_{ijmn}(E^{t}_{mn}-E^{Pt}_{mn}-E^{Ct}_{mn}-E^{Tt}_{mn})\end{aligned} \tag{8}$$

eous slope of the uniaxial stress plastic strain diagram. However, for nonisothermal loadings this is not the case. To see this, note that since the uniaxial stress is a function of both the plastic strain history and temperature, an increment of uniaxial stress is given by:

$$d\sigma = \frac{\partial \sigma}{\partial \bar{\varepsilon}^P} d\bar{\varepsilon}^P + \frac{\partial \sigma}{\partial T} dT. \tag{13}$$

Combining eqns (12) and (13) gives:

$$c = \frac{2}{3}\left(H' + \frac{\partial \sigma}{\partial T}\frac{dT}{d\bar{\varepsilon}^P}\right), \tag{14}$$

where H' is the instantaneous slope of the stress–plastic strain diagram. Substituting the above equation into the constitutive relation (eqn 11), then rearranging and employing the normality condition, gives

$$dS_{ij} = C^t_{ijmn}(dE_{mn} - dE^C_{mn} - dE^T_{mn}) + dP_{ij}, \tag{15}$$

where

$$C^t_{ijmn} = D^{t+\Delta t}_{ijmn} - \frac{D^{t+\Delta t}_{ijvw}\frac{\partial F}{\partial S_{vw}}\frac{\partial F}{\partial S_{tu}} D^{t-\Delta t}_{tumn}}{\frac{2}{3}H'\frac{\partial F}{\partial S_{pq}}\frac{\partial F}{\partial S_{pq}} + D^{t+\Delta t}_{pqrs}\frac{\partial F}{\partial S_{pq}}\frac{\partial F}{\partial S_{rs}}}, \tag{16}$$

and

$$dP_{ij} = -\left(\frac{D^{t+\Delta t}_{ijvw}\frac{\partial F}{\partial S_{vw}}\frac{\partial F}{\partial S_{tu}} dD_{tumn}}{\frac{2}{3}H'\frac{\partial F}{\partial S_{pq}}\frac{\partial F}{\partial S_{pq}} + D^{t+\Delta t}_{pqrs}\frac{\partial F}{\partial S_{pq}}\frac{\partial F}{\partial S_{rs}}}\right) \times (E^t_{mn} - E^{Pt}_{mn} - E^{Ct}_{mn} - E^{Tt}_{mn}) + dD_{ijmn}(E^t_{mn} - E^{Pt}_{mn} - E^{Ct}_{mn} - E^{Tt}_{mn}) + \left(\frac{\sqrt{\frac{2}{3}}\frac{\partial F}{\partial S_{tu}}\frac{\partial F}{\partial S_{tu}} D^{t+\Delta t}_{ijmn}\frac{\partial F}{\partial S_{mn}}\frac{\partial \sigma}{\partial T}}{\frac{2}{3}H'\frac{\partial F}{\partial S_{pq}}\frac{\partial F}{\partial S_{pq}} + D^{t+\Delta t}_{pqrs}\frac{\partial F}{\partial S_{pq}}\frac{\partial F}{\partial S_{rs}}}\right) dT, \tag{17}$$

and the terms H' and $\partial\sigma/\partial T$ may be determined from uniaxial stress–strain data at time t. It can be seen that C_{ijmn} is superscripted at time t since the hardening parameters are determined there. Note that the first two terms in dP_{ij} represent the change in the effective modulus tensor during the load increment multiplied by the elastic strain tensor at time t, and the last term represents a correction term which results from using the hardening modulus, H', at time t.

The translation of the yield surface in stress space may now be obtained by substituting eqn (7) into eqn (2) and solving for $d\mu$. The resulting relation is:

$$d\mu = \frac{\frac{\partial F}{\partial S_{ij}} dS_{ij} - 2k\frac{\partial k}{\partial T} dT - 2k\frac{\partial k}{\partial \bar{\varepsilon}^P} d\bar{\varepsilon}^P}{(S_{mn} - \alpha_{mn})\frac{\partial F}{\partial S_{mn}}}. \tag{18}$$

Equation (18) thus guarantees that the state of stress will remain consistent with the yield surface during loading even under nonisothermal conditions.

To summarize, then, the constitutive law is obtained by solving, in the following order, eqns (17), (16), (15), (18) and (7).

It should also be noted here that the above constitutive theory satisfies thermodynamic restrictions [7], where the entropy generation term is introduced as an uncoupled rate independent (plastic) and rate dependent (creep) dashpot in a Maxwell model with nonlinear temperature dependent modulus and viscosity. The resulting constitutive law is reduced from a set of nonlinear coupled first order differential equations by using a first order Runge Kutta process.

THE VARIATIONAL PRINCIPLE

The constitutive law may be applied to the conservation of momentum via an appropriate variational principle. We present here briefly an incremental principle utilized in several nonlinear programs such as AGGIE I [8], NONSAP [9] and ADINA [10]. First consider the virtual work expression within a total Lagrangian description [11]:

$$\int_{V_0} S^{t+\Delta t}_{ij}\delta E^{t+\Delta t}_{ij} dV = \int_A T_k \delta u_k dA + \int_{V_0} \rho_0 F_k \delta u_k dV \tag{19}$$

where $S^{t+\Delta t}_{ij}$ = the 2nd Piola–Kirchhoff stress tensor at time $t+\Delta t$ referred to the initial configuration at time $t=0$, $\delta E^{t+\Delta t}_{ij}$ = the variation in the Green–Lagrange strains at $t+\Delta t$ referred to the initial configuration V_0, T_k = the surface tractions at time $t+\Delta t$ referred to the surface of the configuration A, δu_k = the variation in the displacements, ρ_0 = the local density in the initial configuration and F_k = the body force per unit mass at time $t+\Delta t$ referred to the initial configuration V_0.

We consider finite strain measure here for two reasons: this is the formulation already contained within the above mentioned nonlinear computer codes; and the constitutive law presented herein may be extended to encompass finite strain using an appropriate hypoelasticity theory [12, 13].

The virtual work equation is incrementalized using:

$$S^{t+\Delta t}_{ij} = S^t_{ij} + \Delta S_{ij}, \tag{20}$$

and

$$E^{t+\Delta t}_{ij} = E^t_{ij} + \Delta E_{ij}. \tag{21}$$

The stress increment ΔS_{ij} is then substituted using eqn (15) and the strain increment is implaced by incremantalizing the Green–Lagrange kinematic relation [2]. The resulting variational principle is then linearized by neglecting terms nonlinear in the displacement increment, and this approximation is accounted for later by using an appropriate iterative technique [14, 15]. The linearized variational principle is then cast in a finite element matrix formulation by using an assumed displacement function. The resulting equations of motion are:

$$[M]\{\ddot{u}^{t+\Delta t}\} + ([K^t_L] + [K^t_{NL}])\{\Delta u\} = \{R^{t+\Delta t}\} - \{F^t\}, \tag{22}$$

where

$$[M] = \int_{V_0} \rho_0 [H]^T [H] dV, \tag{23}$$

$$[K_L] = \int_{V_0} [B_L]^T [C][B_L] dV, \tag{24}$$

$$[K_{NL}] = \int_{V_0} [B_{NL}]^T([S] - [C][\Delta E^C] - [C][\Delta E^T] + [\Delta P])[B_{NL}] dV, \tag{25}$$

$$R^{t+\Delta t}_i = \int_A T_k \frac{\partial \Delta u_k}{\partial \Delta u_i} dA + \int_{V_0} \rho_0 F_k \frac{\partial \Delta u_k}{\partial \Delta u_i} dV, \tag{26}$$

and

$$-\{F^t\} = \int_{V_0} [B_L]^T(\{S\} - [C]\{\Delta E^C\} - [C]\{\Delta E^T\} + \{\Delta P\}) dV, \tag{27}$$

and $[B_L]$ and $[B_{NL}]$ are the linear strain displacement transformation matrix and the nonlinear strain displacement transformation matrix [2, 11], respectively. Also, H is the matrix relating nodal displacements to the displacement field [11].

COMPUTER CODE IMPLEMENTATION

The constitutive law and variational principle presented herein have been implaced in the finite element code AGGIE I [8]. This code has the capability to model both geometric and material nonlinear structural response, and contains two and three dimensional isoparametric elements [16]. Under certain loading conditions the constitutive law (eqn 15) may be specialized for computational efficiency [2, 17]. Thus, the theory presented herein has been implanted in the code as four different material models: quasiisothermal elastic, nonisothermal elastic, quasi-isothermal elastic - plastic, and nonisothermal elastic plastic, where quasi-isothermal is defined to mean that although the component undergoes thermal loading the material properties may be assumed to be unaffected in the temperature range considered. Utilizing the appropriate model has been shown to give significant computational savings [17].

The amount of input data required will depend on the model being used. For the nonisothermal elastic–plastic model (eqn 15) with negligible creep the required input data are shown in Fig. 2. If significant creep is expected it will be necessary to input additional data which will depend on the creep model being used. Currently, there are three creep models within the code [8]: a microphenomenological equation of state approach, an intepolation scheme using creep vs time curves, and a nonlinear viscoelasticity model. Normally, it will be necessary to input either creep curves at specified loads and temperatures, or a creep compliance tensor [18].

One will recall that in order to solve the thermal stress problem one must characterize the temperature distribution within the medium. It is assumed in this theory that the mechanical deformation and heat transfer problem may be solved *a priori*. AGGIE I does not have the capability to solve this problem. Therefore, an additional input requirement is that the spacial and time dependent temperature distribution be input to the code on a nodal basis.

The procedure for utilizing the constitutive law is to assume a strain increment for each integration point based on information from the previous load step. One may then check for yielding by assuming eqn (6) holds and applying the resulting stress tensor to eqn (1). If yielding is not predicted then eqn (6) is correct. If yielding occurs, then the stress state is updated using eqn (15) and the yield surface location is updated using eqn (7). A complete outline of this procedure is contained in Ref. [19].

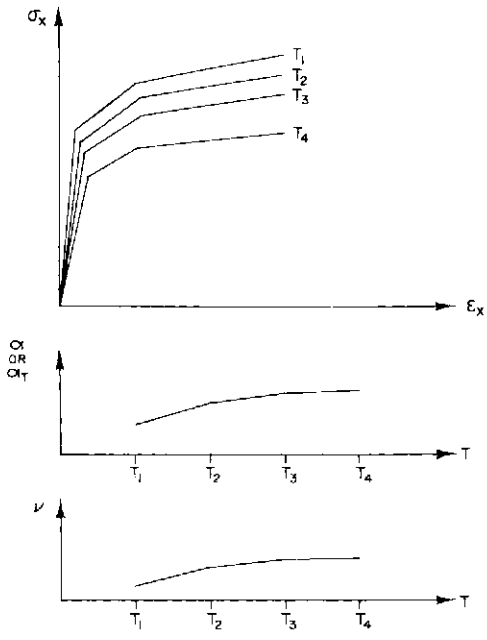

Fig. 2. Materials input data.

EXAMPLE PROBLEMS

1. *Nonisothermal elastic axial bar subjected to simultaneous mechanical load and heat input*

The first example demonstrates the capability of the code to predict the static response of elastic materials with strongly temperature dependent material properties to simultaneous mechanical and thermal loading. A significant factor in the accuracy of the theory is the correct determination of the thermal strain increment during a nonisothermal load step. Suppose one assumes that the thermal strain increment is given by:

$$d\varepsilon^T = \alpha^{t+\Delta t}(T_{t_2} - T_{t_1}). \tag{28}$$

This assumption can introduce significant error into the analysis. The proper definition is given by:

$$\begin{aligned} d\varepsilon^T &= {}_{\alpha}{}^{t+\Delta t}(T_{t_2} - T_R) - \alpha^t(T_{t_1} - T_R) \\ &= \alpha^{t+\Delta t}(T_{t_2} - T_{t_1}) + (\alpha^{t+\Delta t} - \alpha^t)(T_{t_1} - T_R), \end{aligned} \tag{29}$$

where T_R is the reference temperature at which the thermal strain is zero. It can be seen that the second term in eqn (29) represents the error incurred by using eqn (28). Mathematically, eqn (29) may be interpreted as representing a chain rule differentiation.

To illustrate the error which may be incurred by utilizing eqn (28), the code is now compared to an experiment. An aluminum (6061–T6) axial bar with material properties as shown in Fig. 3 is subjected to the thermomechanical load history shown in Fig. 4. Due to the relatively short time period and low stress level, creep strain is assumed to be negligible. Analytical results are compared in Fig. 4. Experimental results as well as the theoretical result denoted CREEPARHS [20] are due to Stone. Three solutions were performed in AGGIE I using a single plane stress isoparametric element and 26 load steps. In the first analysis it is assumed that material properties are not temperature dependent and room temperature data are used. In the second solution, properties are assumed to vary with temperature, and the definition of the thermal strain increment given by eqn (28) is used. Finally, the third analysis employs temperature dependent material properties as well as the definition of the thermal strain increment given in (29). It is found that all theoretical results except the last are in error by approx. 10% or more. Thus, the importance of temperature dependent material properties as well as a correct definition of the

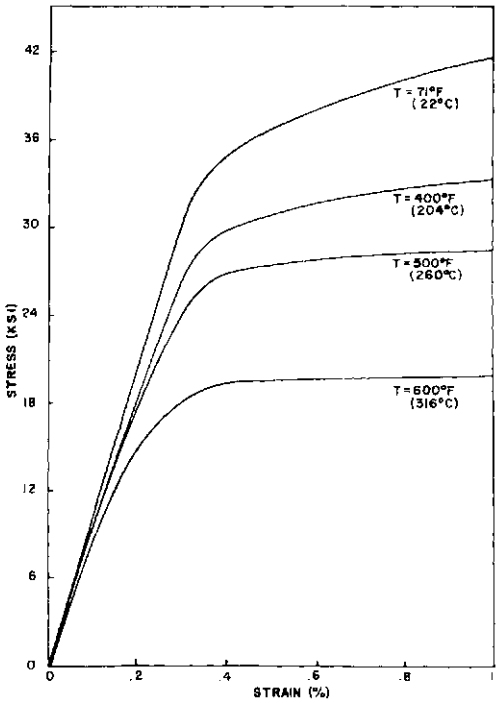

Fig. 3. Material data for Al 6061-T6 experimental test samples.

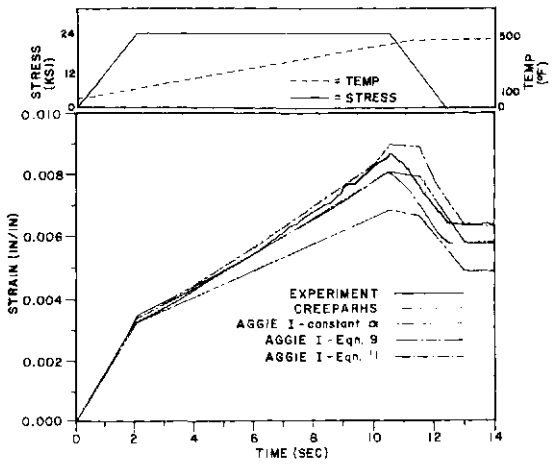

Fig. 4. Comparison of analysis to experiment for uniaxial elastic thermomechanical loading.

thermal strain increment are illustrated by this example problem.

II. *Nonisothermal elastic–plastic axial bar*

In this example an axial bar with material properties shown in Fig. 5 is subjected to the load history shown in the same figure. Attempts at experimental verification of this problem have failed due to the fact that the relatively long heat up time required with the equipment available at this institution induces significant creep. Additional equipment is on order and it is hoped that experimental verification will be forthcoming in the near future. This example is included not as a verification of the theory, but rather as a corroboration of the computational efficiency of the model.

One will recall that in our previous papers [2, 19], we

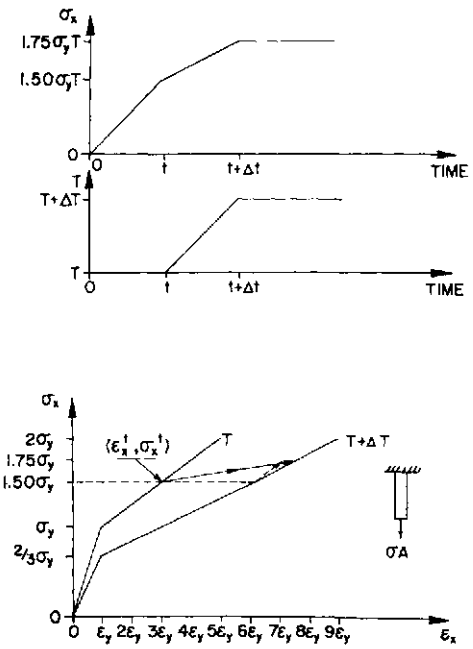

Fig. 5. Nonisothermal elastic–plastic axial bar with thermomechanical load history.

proposed that to obtain the effective modulus tensor C_{ijmn} for a load step one should use the elastic constitutive tensor D_{ijmn} at the end of the load step. This was shown to be mathematically correct and is computationally supported by this example. In the example, an axial bar is loaded isothermally to some plastic state and is then simultaneously subjected to a mechanical load and spacially constant slow heat input. According to the classical incremental theory of plasticity it is required that the state of stress and strain move to a point on the uniaxial stress–strain diagram for the temperature at the end of the step. This requirement must be satisfied in order to remain consistent with the yield surface during plastic loading. Using the elastic modulus proposed by us the theory will predict this result exactly. If one utilizes the elastic modulus at the start of the load step the state of stress and strain will converge incorrectly to a point denoted by the head of the dashed line in Fig. 5. This point corresponds to a horizontal translation from $(\varepsilon_x^t, \sigma^t)$ to the stress–strain curve at the temperature at the end of the step, followed by a translation parallel to the stress strain curve at time Thus, utilizing the elastic modulus at the start of a load step does not satisfy the consistency condition. Further, if one employs equilibrium iteration and correctly updates the elastic modulus during the iteration procedure, the solution will converge to the correct solution, but in exactly twice the computation time encountered in our theory. Therefore it is suggested that using the elastic constitutive tensor at the end of the step is not only consistent but also computationally efficient.

III. *Nonisothermal elastic–plastic axial bar with significant creep*

This problem illustrates the ability of the theory to predict the response of materials near their ultimate strength. An aluminum (6061–T6) axial bar is subjected to the load history shown in Fig. 6, such that ultimate failure of the specimen occurs. Experimental and

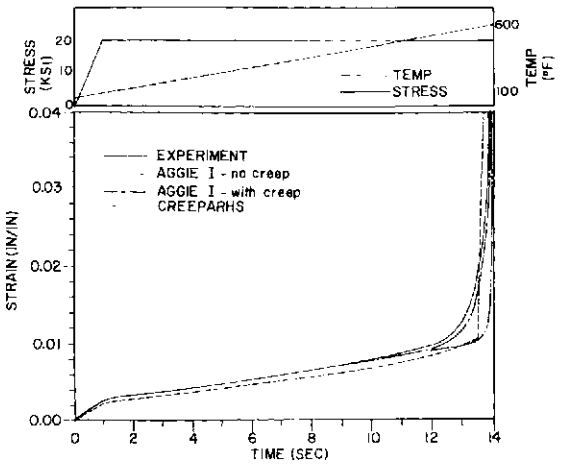

Fig. 6. Comparison of analysis to experiment for uniaxial elastic–plastic thermomechanical loading.

CREEPARHS [20] results are due to Stone. Two analyses were performed using AGGIE I. In the first, creep is assumed to be negligible. In the second, linear interpolation of isothermal creep data at a load of 20 ksi is used. It is seen from results plotted in Fig. 6 that the theory produces accurate results even near the ultimate strength of the material.

IV. *Nonisothermal elastic–plastic axial bar subjected to cyclic load history*

One of the primary purposes of this research has been to obtain a theory which can effectively model the response of elastic–plastic media to cyclic mechanical and thermal loading. Although the literature contains abundant verification tools for isothermal cyclic loading histories, we have been unable to obtain experimental data to verify the nonisothermal problem. Therefore, we have undertaken to perform certain nonisothermal tests using axial bars on the MTS system. Although results of our experiments are incomplete at this time, analytical results of a cyclic test are presented herein. Although the theory is capable of modelling creep response, this study is meant to verify the time independent behavior of the material. Therefore, we have chosen the test case shown in Fig. 7. Note that the specimen is heated at zero load after prestrain so that no creep occurs. This problem thus tests the expansion and translation of the yield surface in stress space caused by a temperature change. In order to verify the applicability of the theory it is necessary to perform three materials data tests. Isothermal stress–strain curves are generated at room temperature and 200°F. In addition, an isothermal cyclic load test is performed to determine the ratio of isotropic to kinematic hardening (β) used in the model. Theoretical results are presented in Fig. 7. It is seen that the combined hardening model produces results which differ significantly from both kinematic and isotropic nonisothermal hardening theory as well as isothermal isotropic hardening theory, indicated by the dashed line in Fig. 7. A schematic representation of the transformation of the yield surface is shown in Fig. 8. A future paper will compare experimental results to the analytical solution presented here.

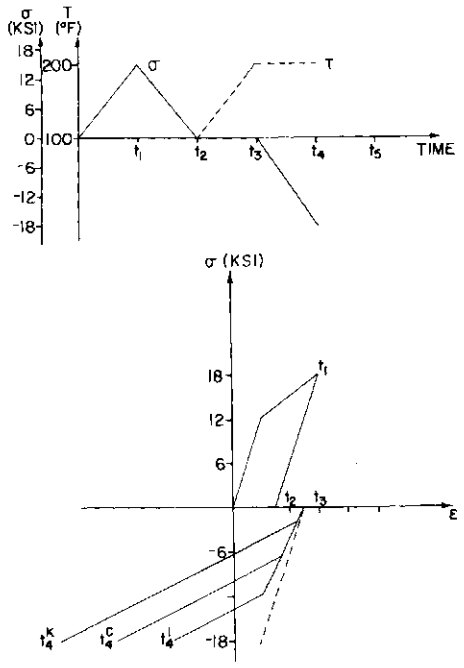

Fig. 7. Elastic–plastic axial bar subjected to cyclic thermomechanical load history.

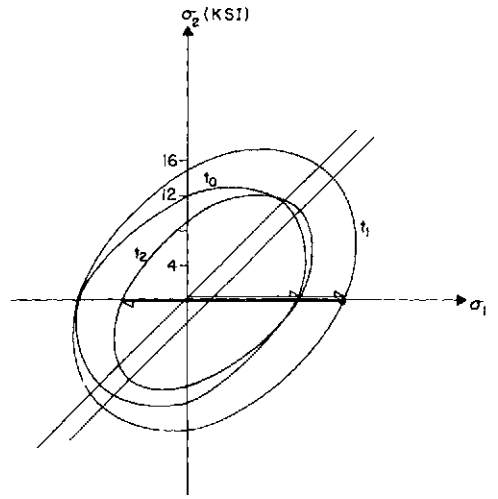

Fig. 8. Nonisothermal combined hardening ($\beta = 0.5$) of yield surface for elastic plastic axial bar.

CONCLUSION

We have proposed herein a theory for modelling the response of thermoplastic materials. The theory has been shown in this report to be adequate in predicting response of many solid media. In addition, it has been shown that certain computationally simplified forms of the theory are correctly in place in the computer code AGGIE I. However, the theory may be inadequate in modelling certain physical phenomena. Among these are rate dependence, instability near ultimate strength, finite stress and strain, phase changes, and violation of other assumptions in the theory such as the normality condition. Research is currently underway to incorporate the above additions to the theory.

REFERENCES

1. A. Phillips and R. Kasper, On the foundations of thermoplasticity—an experimental investigation. *J. Appl. Mech.* 891 896 (Dec. 1973).
2. D. H. Allen and W. E. Haisler. The application of thermal and creep effects to the combined isotropic kinematic hardening model for inelastic structural analysis by the finite element method. Office of Naval Research, No. 3275-79-3 (May 1979).
3. H. Ziegler, A modification of Prager's hardening rule. *Q. Appl. Math.* **17**, 55–56 (1959).
4. Y. Yamada and T. Sakurai, Basic formulation and a computer program for large deformation analysis. *Pressure Vessel Technology*, Part I, pp. 341–352. ASME, New York (1977).
5. Y. Yamada, Constitutive modelling of inelastic behavior and numerical solution of nonlinear problems by the finite element method. *Comput. Structures* **8**, 533–543 (1978).
6. D. H. Allen, An investigation into the combined isotropic-kinematic workhardening rule. Office of Naval Research, No. 3275-79-2 (May 1979).
7. D. H. Allen, A survey of current temperature dependent elastic-plastic-creep constitutive laws for applicability to finite element computer codes. 21st AIAA/ASCE/ASME SDM Conference, Seattle (May 1980).
8. W. E. Haisler, AGGIE I. A finite element program for nonlinear structural analysis. Office of Naval Research, No. 3275-77-1 (June 1977).
9. K. J. Bathe and E. L. Wilson, NONSAP—A nonlinear structural analysis program. *Nucl. Engng and Design* (June 1974).
10. M. D. Snyder and K. J. Bathe, *Formulation and Numerical Solution of Thermo-elastic–Plastic and Creep Problems*. NTIS (1977).
11. B. Hunsaker, Jr., The application of combined kinematic-isotropic hardening and the mechanical sublayer model to small strain inelastic structural analysis by the finite element method. Dissertation, Texas A&M University (Aug. 1976).
12. C. A. Truesdell and W. Noll, The non-linear field theories of mechanics. In *Encyclopedia of Physics*, Vol. 3, Part 3. Springer-Verlag, Berlin (1964).
13. S. W. Key, J. H. Biffle and R. D. Krieg, A study of the computational and theoretical differences of two finite strain elastic–plastic constitutive models. *Formulations and Computational Algorithms in Finite Element Analysis*: U.S.–Germany Symposium. MIT, New York (1976).
14. J. A. Stricklin, W. E. Haisler and W. A. Von Riesemann, Formulation, computation, and solution procedures for material and/or geometric nonlinear structural analysis by the finite element method. Sandia Laboratories, No. SC-CR-73-3102 (July 1972).
15. G. Strang and H. Matthies, Numerical computations in nonlinear mechanics. *Pressure Vessels and Piping Conference*. ASME, New York (1979).
16. O. C. Zienkiewicz, *The Finite Element Method*. McGraw-Hill, New York (1977).
17. D. H. Allen and W. E. Haisler, The prediction of response of solids to thermal loading using the finite element code AGGIE I. Office of Naval Research, No. 3275-80-1 (June 1980).
18. D. R. Sanders and W. E. Haisler, An incremental form of the single-integral nonlinear viscoelastic theory for elastic plastic-creep finite element analysis. *Pressure Vessels and Piping Conference*. ASME, New York (1979).
19. D. H. Allen and W. E. Haisler, Thermoplastic analysis using the finite element code AGGIE I. Office of Naval Research, No. 3275-79-4 (Dec. 1979).
20. S. J. Stone, Effects of material behavior on the response of rapidly heated structures. McDonnell Douglas Astronautics Company, MDC G8432 (Jan. 1980).
21. C. E. Pugh, J. M. Corum, K. C. Lin and W. L. Greenstreet, Currently recommended constitutive equations for inelastic design analysis of FFTF components. ORNL TM-3602, Oak Ridge National Laboratories (Sept. 1972).
22. W. E. Haisler, Numerical and experimental comparison of plastic work hardening rules. *Trans. 4th Int. Conf. on Structural Mechanics in Reactor Technology*, San Francisco (15–19 Aug. 1977).
23. W. E. Haisler, B. J. Hunsaker and J. A. Stricklin, On the use of two hardening rules of plasticity in incremental and pseudo force analysis. Presented at the Winter Annual Meeting of the ASME, New York; also in *Constitutive Equations in Viscoplasticity Computational and Engineering Aspects*, AMD Vol. 20, pp. 139–170 (5–10 Dec. 1976).
24. M. Tanaka, Large deflection analysis of elastic–plastic circular plates with combined isotropic and kinematic hardening. *Ingenieur-Archiv* **41**, 342–356 (1972).
25. B. Hunsaker, Jr., An evaluation of four hardening rules of the incremental theory of plasticity. Thesis, Texas A&M University (Dec. 1973).
26. W. E. Haisler and D. R. Sanders, Elastic–plastic-creep large strain analysis at elevated temperature by the finite element method. Office of Naval Research, No. 2375-78-1 (Apr. 1978).
27. D. R. Sanders and W. E. Haisler, An incremental form of the single-integral nonlinear viscoelastic theory for elastic–plastic-creep finite element analysis. Office of Naval Research, No. 3275-79-1 (Apr. 1979).
28. K. H. Bathe, H. Ozdemir and E. L. Wilson, Static and dynamic geometric and material nonlinear analysis. Structural Engineering Laboratory, University of California, Berkeley, California, Rep. UCSESM 74-4 (Feb. 1974).
29. P. Sharifi and D. N. Yates, Nonlinear thermo-elastic-plastic and creep analysis by the finite-element method. *AIAA J.* **12**, 1210–1215 (1974).

Computers & Structures, Vol. 13, pp. 137–144, 1981
Printed in Great Britain.

0045-7949/81/010137-08$02.00/0

PREDICTION OF STABLE CRACK GROWTH IN TYPE 304 STAINLESS STEEL

A. ZAHOOR and I. S. ABOU-SAYED

Battelle's Columbus Laboratories, Columbus, OH 43201, U.S.A.

(*Received* 17 *May* 1980)

Abstract—Crack growth resistance curves using the J integral for Type 304 stainless steel at room temperature and at 400° F were generated using experimental data from center-cracked tension panels. Two methods were used. The first utilized a finite strain based finite element analysis. The second used an estimation procedure. Good agreement was obtained up to maximum load. However, past maximum load, the estimation procedure overestimated the J values. Stable crack growth predictions were made on a center-cracked tension panel with a different initial crack length. Good predictions were obtained up to about maximum load. Limitations on the applicability of the J integral approach to extended amounts of stable crack growth is presented and a possible alternative approach is discussed.

INTRODUCTION

Type 304 stainless steel is the principal structural material for Boiling Water Reactor (BWR) piping systems. Because stress corrosion cracks may occur in these pipes, it is of interest to determine the margin of safety against fracture. Typically, Type 304 stainless steel is a highly ductile and very tough material, and as a consequence, extensive plastic deformation occurs before the initiation of crack growth along with considerable resistance to crack growth [1]. Despite this, pipe cracking problems in the nuclear industry have been analyzed using techniques of linear elastic fracture mechanics (LEFM). Applications of LEFM using crack initiation as a fracture criterion are likely to be overly conservative because of the ability of materials like Type 304 stainless steel to exhibit considerable resistance to crack growth. This clearly suggests the need of a fracture criterion which can properly account for the effects of plasticity and can accommodate crack growth prior to general instability.

Several plastic fracture criteria have been proposed [2–5]. Of them, the J integral-Tearing Modulus approach, the crack opening angle (COA), and the crack tip opening angle (CTOA) seem most promising [6]. This paper focuses on the applicability of the J integral. In an effort to assess the applicability of a J-resistance curve approach for Type 304 steel, a program which involved experimental, analytical and numerical work was conducted. The experiments were performed on several center-cracked tension panels [1, 7]. J-resistance curves (J vs crack growth) were generated from these experimental data at room temperature and at 400° F.

The J-resistance curve at room temperature was generated by two independent methods. The first method involved a full scale finite element analysis of the center-cracked panel, whereas the second utilized a J integral estimation procedure [8, 9]. The finite element analysis was conducted using the computer program BCLFEM [10] which is based on finite strain, large deformation, and the incremental theory of plasticity. A comparison of the results permits an assessment of the accuracy of the estimation procedure.

The J-resistance curve at 400° F was generated from the test results of an initial 3 in. long crack in a center-cracked tension (CCT) panel by using an estimation procedure. This resistance curve was then used to predict crack growth in a 5.18 in. long crack in a CCT panel tested at 400° F via a J integral-Tearing Modulus approach [3, 11, 12]. These predictions were found to agree well with the experimental results up to maximum load. Because this involves only a small amount of stable crack growth even in the favorable conditions considered here, alternative methods for considering extended amounts of stable crack growth are needed. For this purpose, a method to improve the predictive capability through a combined J/CTOA fracture criterion is also presented.

PLASTIC FRACTURE CRITERIA

The incentive for the development of elastic–plastic fracture mechanics can be attributed to the inability of linear elastic fracture mechanics (LEFM) to treat conditions where the plastic behavior of real materials is important. The very first effort was a plasticity correction to the LEFM crack tip characterizing parameter. This was followed by the use of strip yield plastic zone models such as that of Durgdale. This, however, had limited capability for handling many cases of practical interest, such as large scale contained plasticity and full plasticity throughout the uncracked ligament.

Tough and ductile nuclear reactor materials undergo large plastic deformation before the initiation of crack growth. Moreover, crack growth instability in materials like 304 stainless steel is always preceeded by some amount of stable crack growth. Consequently, application of LEFM to such materials, using crack initiation as the fracture criterion, gives a considerable underestimate of their strength.

Attempts to account for the extensive plastic deformations preceeding initiation of crack growth and the additional resistance to growth before crack instability led to the development of various plastic fracture criteria [1, 2, 5, 6, 13]. A detailed discussion

of the applicability and limitations of a resistance curve approach based on various fracture criteria is given in [6]. The most promising are the J integral-Tearing Modulus approach, CTOA, COA, and a combination of J integral and crack tip opening angle, hereafter denoted by J/CTOA. These will be described briefly in the following.

The J integral-Tearing Modulus approach is based on the use of the J integral as a crack tip characterizing parameter, the change in J due to crack growth da, that is dJ/da, and a J-resistance curve, supposedly a material property. The applied value of the J integral is equated with the value characterizing the resistance to crack growth. Hence, during crack growth,

$$J(\sigma, a, W, t) = J_{\text{matl}}(\Delta a) \tag{1}$$

where J is the applied value of the J integral. It will depend upon the applied stress σ, crack length a, and other dimensions such as width W, thickness t, etc. of the cracked body. The parameter J_{matl}, however, is solely the materials response to crack growth and is generally considered to be a function of crack growth, Δa, only, at least for a given temperature and degree of constraint at the crack tip.

The J integral is based on the deformation theory of plasticity; i.e. the value J depends only on the current loads and crack length. This is valid provided no unloading is permitted. Stable crack growth, however, invariably involves unloading behind the crack tip which somewhat limits the use of J. Recently, Hutchinson and Paris [14] have shown that J can be used for situations involving crack growth provided the amount of crack growth, Δa, is small and the parameter

$$\omega \equiv \frac{dJ}{da} \cdot \frac{b}{J} \gg 1, \tag{2}$$

where b is the length of the body ahead of the crack tip, i.e. remaining ligament. They suggested ω values above about 50. But experimental results [2] and work by others [5] indicate that values of ω as low as 15 may be sufficient to permit the use of the J-resistance curve approach.

Other fracture criteria like COA, CTOA and J/CTOA were studied in [6]. The average crack opening angle (COA) is defined as the ratio of the crack opening displacement at the original crack tip to the total amount of crack growth that has occurred. Because of this definition, COA is undefined for a fully blunted crack tip and has a large value at small amounts of crack growth. But, it decreases with crack growth and is found to attain almost a constant value during subsequent growth. The crack tip opening angle (CTOA), defined as the ratio between crack opening displacement at a short and fixed distance s behind the current crack tip and s, shows similar behavior. That is, there is an initial transition to a constant value after some stable growth.

The attainment of a constant value of COA or CTOA is a very attractive feature in that they can be easily used for numerical computations involving substantial amounts of crack growth. The COA is much easier to define and measure experimentally than is CTOA, but its relation to the processes occuring at the crack tip is somewhat unclear. The CTOA criterion must be directly connected to the events at the crack tip, but it is difficult to measure experimentally. From a computational point of view, CTOA looks more promising.

The J/CTOA criterion [6] utilizes the attractive features of both the J and CTOA criteria. Where J-controlled growth conditions exist at initiation and early stages of crack growth, J is used as a fracture criterion. The CTOA is computed simultaneously with J in a finite element computation, and when a constant value of CTOA is obtained, further crack growth is dictated by CTOA. A drawback of this approach is that a finite element method must be used, however.

J-RESISTANCE CURVES

Several center-cracked tension (CCT) panels of Type 304 stainless steel were tested at room temperature and at 400° F [1, 7]. Figure 1 shows the CCT panel, the fixtures and the specimen dimensions. The panels were loaded in stroke control and crack growth was recorded by means of a movie camera. Relevant information, such as panel displacement, LVDT, load, cross head displacement, crack opening displacement, and remote strains across the width of the panel were also recorded. This information was then utilized to generate a variety of crack growth resistance curves.

The center-cracked panels that were chosen for generating resistance curves (room temperature and 400° F) had an initial crack length of 3.0 in. Two independent methods were utilized in this study: the finite element analysis and the estimation procedure [8, 9]. The finite element analysis was conducted only for the panel which was tested at room temperature.

Finite element analysis

The 12 × 24 in. panel was modeled through a set of two dimensional finite elements under plane stress

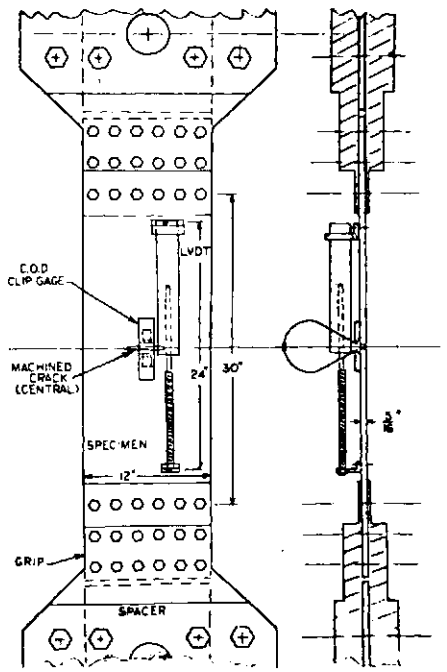

Fig. 1. Specimen assembly for the center-cracked tension (CCT) panel experiment.

conditions. Because of symmetry, only one quadrant of the panel was modeled as shown in Fig. 2. The model consisted of 476 nodes and 498 elements. The computer program BCLFEM [10], which is based on finite strain, large deformation and incremental theory of plasticity, was used for the analysis. Thickness changes due to large deformation are accounted for in this computer program. Constant strain triangular elements were used in the neighborhood of the crack tip to properly simulate the nearly incompressible plastic deformation. The remaining elements were of the 4-noded isoparametric quadrilateral type. A (2×2) G integration scheme was used for generating the stiffness of the elements. The mesh contained 40 nodes across the crack plane.

The nodal spacing in the immediate vicinity of the crack tip was chosen to be 0.0625 in. Along a 2 in. length of the uncracked ligament, 19 spring-like general elastic elements were located at the nodes to provide restraint in the direction of the load. A high stiffness (1.0×10^{14} lb/in.) was ascribed to each of these general elastic elements to model the homogeneous symmetry condition. The simulation of crack growth was achieved by gradually releasing the force developed in these spring-like elements to zero. The multi-linear stress–strain curve (room temperature) shown in Fig. 3 was used in the analysis.

The model was loaded to match the remote displacements that were measured during the experiment. The consecutive releases of the spring-like general elastic elements to simulate crack growth were forced to follow the experimental curve shown in Fig. 4. The numerically calculated load versus remote displacement curve is shown in Fig. 5 along with the experimental record. It is seen that the model underpredicted the maximum load by about 5%. This difference is thought to be due to the stress–strain

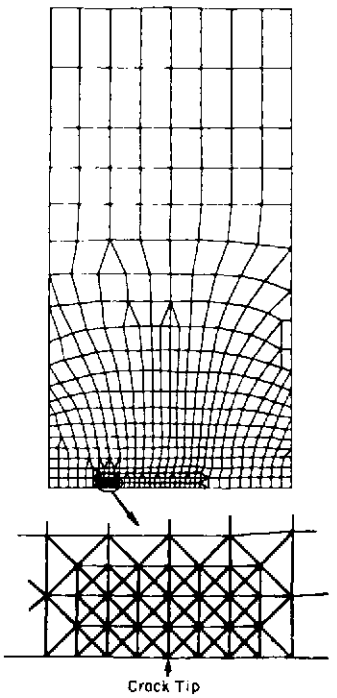

Fig. 2. Finite element model for the center-cracked tension (CCT) panel with a 3 in. crack.

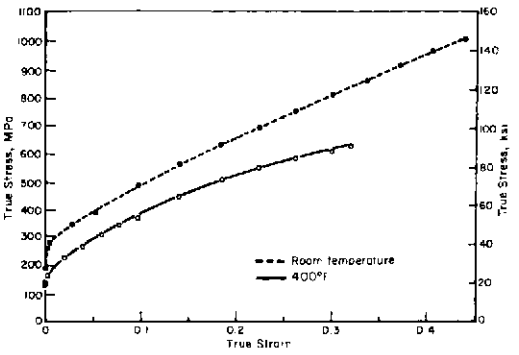

Fig. 3. Stress strain properties for type 304 stainless steel.

curve used in the simulation which differs from the actual experimental curve for that plate due to scatter in the mechanical properties from one plate to another. Some error is also introduced from the difference between the simulated and experimental $\delta-\Delta a$ curves (see Fig. 4). This may cause the crossover of the predicted and experimental $P-\delta$ records in Fig. 5. Nevertheless, the agreement between the predicted and experimental curve is believed to be satisfactory.

Figure 6 shows the deformed mesh just prior to the initiation of crack growth (remote displacement, $\delta=0.26$ in.). It is easily seen that the elements near the

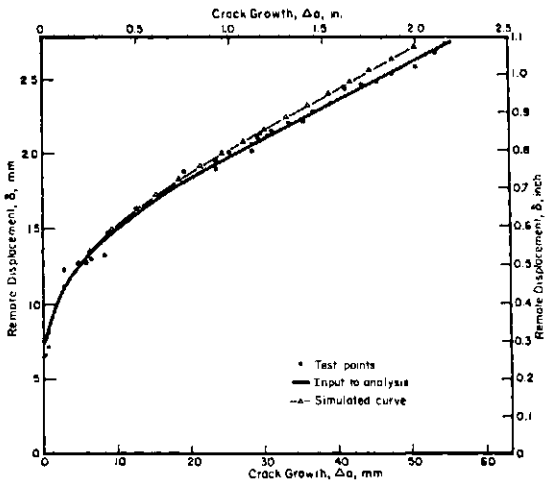

Fig. 4. Experimental displacement vs crack growth data for the 3 in. CCT panel tested at room temperature.

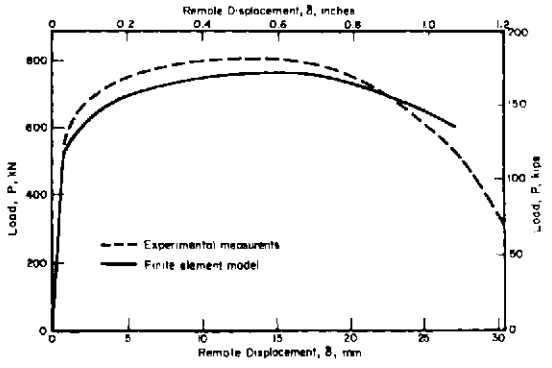

Fig. 5. Comparison of finite element calculations with the experimental load-displacement data on CCT panel.

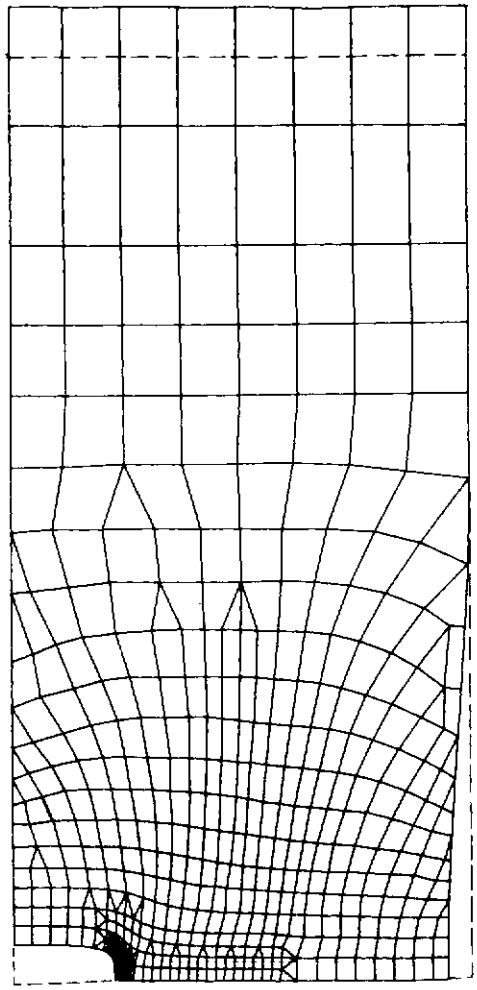

Fig. 6. The crack profile at initiation of crack growth ($\delta = 0.26$ in., displacements are magnified five times).

crack tip undergo severe distortion, and that the crack tip elements rotate nearly 90 degrees. The finite element analysis also indicated that due to severe blunting the crack tip moved inward by about 30–35 mils, giving a crack tip blunting of about 100–120 mils. It should be pointed out that even the remote ends of the CCT panel had yielded prior to the initiation of crack growth.

Figure 7 shows the variations of thickness and the true stress normal to the crack plane as a function of the distance along the uncracked ligament. At the blunted crack tip a reduction in thickness of as much as 25% is obtained at the initiation load†.

Figure 8 shows the crack profile at various stages of stable crack growth. Notice that in Figs. 8(b) and (c) the leading portion of the crack is almost straight. This indicates that crack growth occurs with a constant crack tip opening angle. This has been confirmed by the movie records from the experiments [7] as shown in Fig. 8(d).

†Moreover, the average stress in the uncracked ligament (σ_{net} is significantly higher than the yield stress (38.0 ksi). The initial yielding of the entire ligament (based on average stress) occurs at a load of about 110 kips ($\delta = 0.026$ in.).

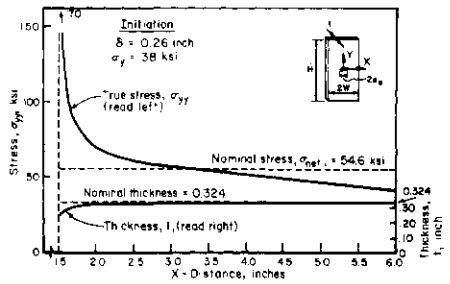

Fig. 7. The variation of thickness and true stress σ_{yy} with the distance along uncracked ligament at initiation of crack growth.

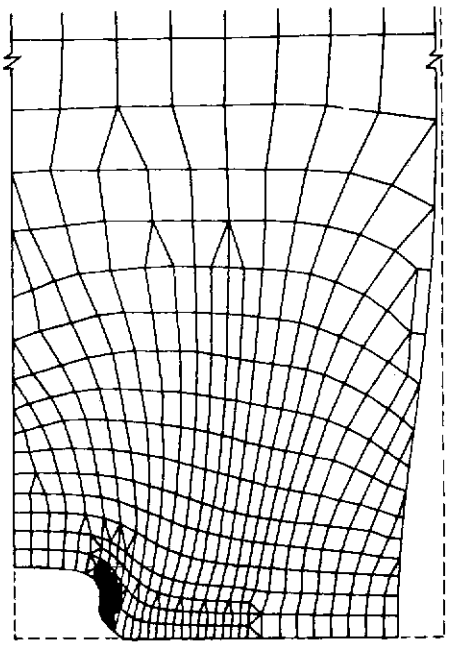

Fig. 8(a). The crack profile after 0.361 in. of crack growth (displacements are magnified five times).

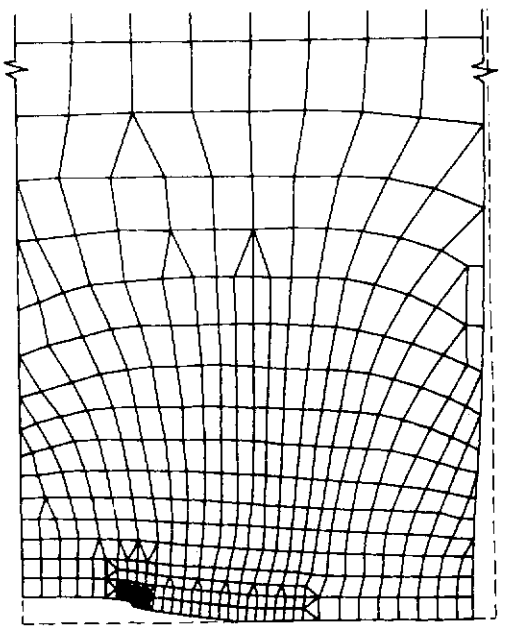

Fig. 8(b). The crack profile after 1.296 in. of crack growth.

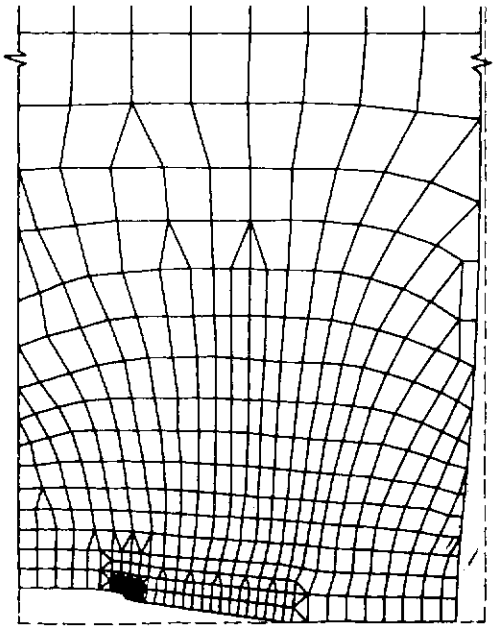

Fig. 8(c). The crack profile after 1.983 in. of crack growth.

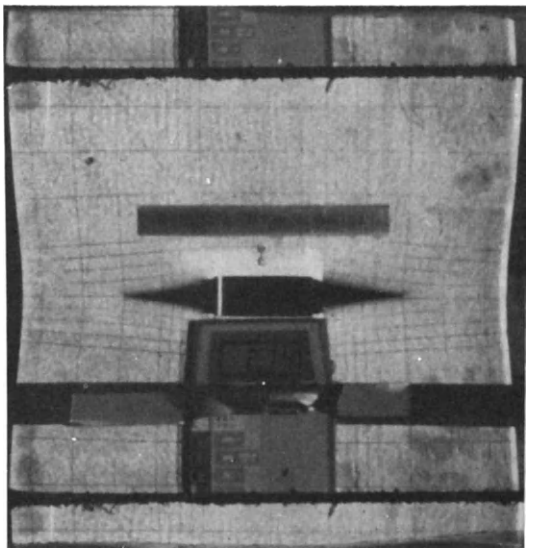

Fig. 8(d). Photograph of the CCT panel after some stable crack growth.

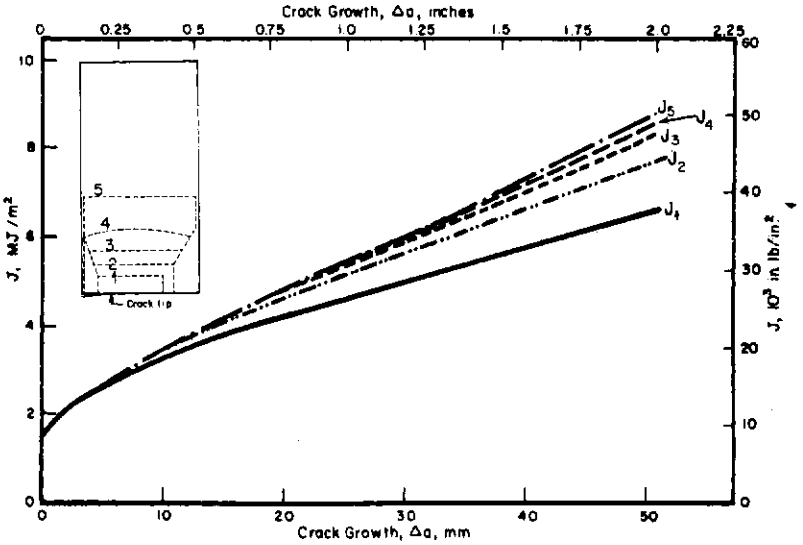

Fig. 9. Computed J values vs Δa.

Having established that the finite element analysis is consistent with the experimental record (see Fig. 5), attention can be turned to crack growth resistance curves. While the model was forced to follow the experimental curve shown in Fig. 4, J integral computations were made at each step before node release. Computations were done for five different contours, shown in Fig. 9. The nearest contour was at a distance of 2.6 in. from the original crack tip. The definition of J integral used was consistent with the finite strain formulation, the details of which can be found in [7]. Figure 9 shows the computed J-Δa curves. (Crack growth refer to growth at one crack tip only.) It is important to note that during crack growth J increased to as much as four times its value at initiation. J integral values computed through small strain formulation for the same problem were 6–7% smaller than those of the finite strain presented here [7].

Figure 10 shows the crack growth resistance curves based on COA and CTOA. As discussed earlier CTOA shows a transition to a plateau value after about 0.6–0.8 in. of crack growth.

Estimation procedure

For the case of an elastic–plastic loading, the J-integral can be split up into its elastic and plastic parts as

$$J = J_{el} + J_{pl} \tag{3}$$

where

$$J_{el} = G = \frac{K_I^2}{E}$$

J_{pl} = plasticity contribution to J.

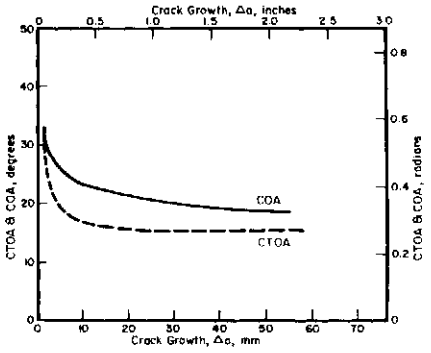

Fig. 10. Crack growth resistance curves based on COA and CTOA.

The Pseudo-potential energy rate interpretation leads to an alternate but equivalent definition of the line integral J as [8]

$$J=J_{el}+\frac{1}{t(b-a)}\left[\int_0^{\delta_{pl}} P d\delta_{pl}-\frac{1}{2}P\delta_{pl}\right] \quad (4)$$

where P is the load and δ_{pl} is the plasticity contribution to the remote displacements of the panel ends (24 in. long), i.e.,

$$\delta_{pl}=\delta-\delta_{\text{elastic}}$$

where $2b$, $2a$ and t are the CCT panel width, crack length and thickness, respectively.

The load–displacement record shown in Fig. 5 can be replotted in terms of load versus δ_{pl} by subtracting the elastic contribution to δ. For a given load, the quantity in the square bracket in (4) is equal to the area contained between the $P-\delta_{pl}$ curve and a straight line joining that load point and the origin (Fig. 11). Equation (4) is valid only for a non-growing crack and it assumes that a deep crack exists such that the plasticity is confined to the remaining ligaments only.

The experimental strain gage data at the remote ends of the 3 in. crack CCT panel showed plastic strains existed there near the initiation load. These remote plastic strains increase up to maximum load. The plastic displacement due to the remote plastic strain was subtracted from the measured δ (LVDT) in order to make use of (4) properly. Equation (4) gives accurate values of J at the initiation load and provides a good approximation up to maximum load. Past maximum load large errors are introduced in J because the load–displacement record (non-growing crack case) of a longer crack would be lower. Thus, the actual J values are smaller than these obtained by using eqn (4). Recently, a method called a Key Curve method which utilizes a modification of eqn (4) for a growing crack has been proposed [9]. This method requires more than one specimen to generate a J-resistance curve. Since pertinent data from other CCT panel experiments [1, 7] could not be extracted to use the Key Curve method, eqn (4) was used instead.

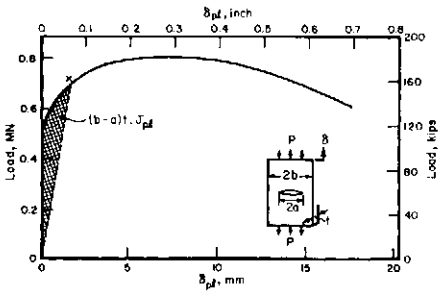

Fig. 11. Load vs δ_{pl} curve obtained from the experimental data of Fig. 5.

Figure 11 shows a load versus δ_{pl} curve which was obtained from the experimental load-displacement record of Fig. 5. As shown for the point X on the curve, the shaded area gives the quantity in the square bracket of eqn (4). For this point, J_{el} can be computed easily from handbook solutions [15]. Thus, the value of J is estimated easily. Its corresponding crack growth is obtained from Figs. 4 and 5.

A plot of the J values with crack growth is shown in Fig. 12. For comparison purposes, the results of the finite element analysis are also shown on that figure. It is seen that good agreement is obtained up to a crack growth of approx. 0.5 in. which, incidentally, corresponds to the maximum load (Figs. 4 and 5). Past maximum load, the disagreement between the two solutions becomes larger due to the fact mentioned earlier that J values obtained through the estimation procedure are overestimated past maximum load.

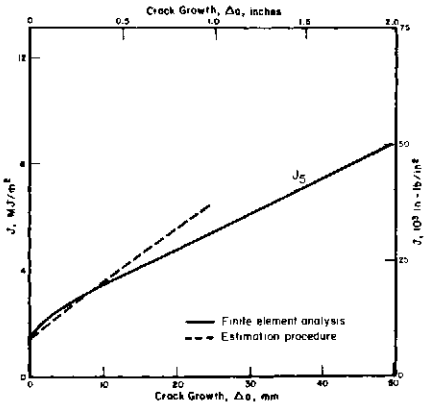

Fig. 12. J-Resistance curves for type 304 stainless steel at room temperature obtained from 3 in. crack CCT panel.

The same procedure was repeated to generate J-resistance curve for a 3 in. crack in a CCT panel tested at 400° F [1], the details of which can be found in [6]. The J-resistance curve at 400° F is shown in Fig. 13, where it is compared with the room temperature J-resistance curve of Fig. 12 (estimation procedure).

PREDICTION OF CRACK GROWTH

For a material like Type 304 stainless steel, the stress–strain curve in the plastic range may be represented as

$$(\varepsilon/\varepsilon_0)=\alpha(\sigma/\sigma_0)^n \quad (6)$$

where n is the hardening index, α is a material constant, σ_0 and ε_0 are the reference stress and strain, respectively. The latter two quantities may be related to each other by $\sigma_0/\varepsilon_0=E$, the elastic modulus.

The applied value of J can be written as [3, 16]

$$J_{\text{appl}}=\alpha b\sigma_0\varepsilon_0 G_{1n}(a/b, n)(P/P_0)^{n+1} \quad (7)$$

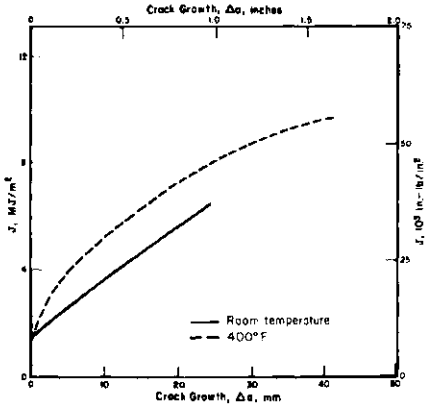

Fig. 13. J-Resistance curves for type 304 stainless steel.

where $P=2b\sigma_\infty$ (σ_∞ = remote uniformly applied stress), $P_0=2(b-a)\sigma_0$ and $2a$ and $2b$ are the crack length and the panel width, respectively. G_{1n} is a nondimensional function which depends on the crack length to width ratio and the hardening index, n. Numerical values of $G_{1n}(a/b,\ n)$ were obtained through an incremental plasticity J-integral calculation and are reported elsewhere [3, 16].

The 5.18 in. crack CCT panel had a test fixture similar to that of Fig. 1 with the exception that it had a free panel length of 18 in. (instead of 24 in., Fig. 1) and LVDT was not monitored to measure panel displacement. The test was performed in stroke control and only cross-head displacement, δ_{CH}, was measured. Hence, the panal was essentially subjected to uniform remote displacement. For a uniform remote displacement, eqn (7) takes the form

$$J_{appl}=(\alpha)^{-1/n}\frac{b\sigma_0^2}{E}(1-a/b)^{-n-1}G_{1n}(a/b,\ n)\cdot(\varepsilon_\infty/\varepsilon_0)\frac{n+1}{n}. \tag{8}$$

A curve fit to the true stress-true strain curve for Type 304 stainless steel at 400° F (Fig. 3) was used to obtain a relation of the form given in eqn (6). The best fit within the range of stresses and strains encountered by the 5.18 in. CCT panel gave $\alpha=6.0, n=3.1, \sigma_0=20.0$ ksi, and $\varepsilon_0=7.634\times10^{-4}$ in./in. The nondimensional function G_{1n} for $n=3$ is shown in Fig. 14.

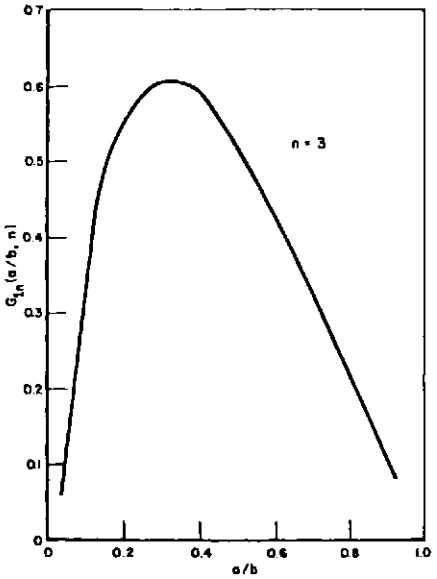

Fig. 14. Non-dimensionalized function $G_{1n}(a/b,\ n)$ vs a/b.

The experimental data for the 5.18 in. crack CCT panel are shown in the first four columns of Table 1. It should be pointed out that the displacement, δ, of the panel is not the same as that imposed by the cross-head, δ_{CH}, due to the compliance of the fixture. The fixture compliance, C_f, was estimated to be 1.317×10^{-6} in./lb [6]. The panel displacement, δ, was obtained by subtracting the fixture displacement from the crosshead displacement. Remote applied strains, ε_∞, were then computed through δ, assuming a uniform displacement across the remote ends of the panel.

Other entries in Table 1 came from the analysis. J_{appl} values were calculated by using eqn (8) and Fig. 14. With these J_{appl} values, the J-resistance curve at 400° F (Fig. 13) was used to predict crack growth. The predicted crack growth, Δa, is in fairly good agreement with those of the measured values up to a $\delta_{CH}=0.81$ in. as shown in Table 1. For $\delta_{CH}>0.81$ in. predictions are poor.

The parameter ω (see eqn (2)) which is a measure of J-controlled crack growth is also shown in Table 1. It is interesting to note that crack growth predictions were good for ω values as low as 4. As mentioned earlier, ω values around 15 were suggested as necessary for a J-controlled condition in some cases [2, 5]. This

Table 1. Crack growth prediction in a 5.18 in. CCT panel

$\alpha = 6.0,\ n = 3.1,\ a = 2.59,\ b = 6.0,\ c_F = 1.317\times10^{-6}$ in./lb

Experimental Data				Analytical Prediction			
P, 10^3 lb	δ_{CH}, inch	δ inch	Δa, inch	$J_{applied}$ in.-lb/in.^{2}	Δa, inch	Δa/(b-a)', %	ω
100.0	0.374	0.2423	0.0	5,136.1			
102.0	0.554	0.41971	0.09	10,445.7	0.10	2.9	27.0
103.0	0.624	0.4884	0.155	14,961.9	0.17	5.2	13.0
104.0	0.70	0.56307	0.165	18,191.8	0.22	7.3	10.0
103.0	0.766	0.6304	0.36	27,274.3	0.38	12.5	6.0
102.0	0.810	0.6757	0.51	33,409.3	0.52	18.0	3.3
100.0	0.834	0.70234	0.53	36,520.8	0.62	22.2	2.5
97.0	0.874	0.7463	0.59	41,974.2	0.80	30.7	1.7
93.5	0.914	0.7909	0.76	54,767.8	1.50	78.5	0.4
88.0	0.950	0.83414	1.00	79,023.1	--		

may imply that for Type 304 steel which has a high hardening material lower ω values may be justifiable. However, it should be clear that this work does not severely test the applicability of the approach. That is, the J-resistance curve was obtained from a geometry that is quite similar to the one where it was applied. All that can really be definitely said is that $\omega = 4$ is a lower bound for Type 304 steel.

CONCLUSIONS

The simplicity and ease with which resistance curves can be generated by a simple estimation procedure offers tremendous advantages over expensive finite element analyses. The analysis presented in this paper further indicates that the estimation procedure may be adequate for generation of J-resistance curve up to maximum load. However, estimation of J past maximum load begins to be in error. This error is primarily due to the use of eqn (4) which is valid for a non-growing crack. The key curve method [9] offers some advantages in that J-values can be estimated more accurately in the stable crack growth portion of the load displacement record even past maximum load. To date, the key curve method has not been checked against a more rigorous analysis such as the full finite element analysis. Further work in this direction is presently being conducted.

The predictive analysis seems to indicate that the applicability of J may be extended to ω values as low as 4 for material with high strain hardening rates such as 304 stainless steel. Crack growth up to 15% of the remaining ligament was predicted well by the J integral-tearing modulus approach. This amount of growth corresponded roughly to crack growth slightly past maximum load. Since the accuracy of the J-resistance curve is in doubt past maximum load, the results of the predictive analysis cannot be relied on in this region. Moreover, due to loss of J-controlled growth, any analysis based on J-integral will be invalid. Recent studies [5, 6, 7] indicate that the loss of J-controlled growth occurs around crack growth of 6–10% of the remaining ligament. This suggests that reliable predictions of extended amounts of crack growth would require a more general approach.

Acknowledgements– The results reported in this paper were obtained in two separate research programs supported by the Electric Power Research Institute. The authors thank Drs. T. U. Marston, D. M. Norris, Jr. and R. Jones of EPRI for their encouragement. The experiments described in this paper were performed at Battelle's Columbus Laboratories by Drs. D. Broek, C. W. Marschall and Mr. A. Nagar. Drs. M. F. Kanninen and S. G. Sampath contributed to the analysis phase of the work.

REFERENCES

1. M. F. Kanninen *et al.*, Mechanical fracture predictions for sensitized stainless steel piping with circumferential cracks. Electric Power Research Institute. *Rep. EPRI NP-192* (Sept. 1976).
2. P. C. Paris, H. Tada, A. Zahoor and H. Ernst, The Theory of instability of the tearing mode of elastic-plastic crack growth. In *Elastic–plastic fracture. ASTM STP* **668**, 5–36 (1979).
3. A. Zahoor, Tearing instability of elastic-plastic crack growth. D.Sc. Dissertation, Washington University, Saint Louis (1978).
4. M. F. Kanninen *et al.*, Elastic-plastic fracture mechanics for two dimensional stable crack growth and instability problems. In Elastic plastic fracture. *ASTM STP* **668**, 121–150 (1979).
5. C. F. Shih, H. G. DeLorenzi and W. R. Andrews, Studies on crack initiation and stable crack growth. In Elastic-plastic fracture, *ASTP STP* **668**, 65–120 (1979).
6. M. F. Kanninen *et al.*, The development of a plastic fracture methodology. Battelle's Columbus Laboratories, *Final Rep. to EPRI on RP* 601–1 (Apr. 1980).
7. M. F. Kanninen *et al.*, Instability predictions for circumferentially cracked pipes. Battelle's Columbus Laboratories. *Rep. to EPRI on Project* T118-2 (Apr. 1980).
8. J. R. Rice, P. C. Paris and J. G. Merkle, Some further results of J-integral analysis and estimates. In Progress in flaw growth and fracture toughness testing. *ASTM STP* **536**, 231–245 (1973).
9. H. Ernst, P. C. Paris, M. P. Rossow and J. W. Hutchinson, Analysis of load-displacement relationship to determine J-R curve and tearing instability material properties. In Fracture mechanics. *ASTM STP* **677**, 581–599 (1979).
10. "BCLFEM", Battelle's Columbus Laboratories, *Internal Rep.* (1979).
11. A. Zahoor and P. C. Paris, Instability analysis of a fully plastic center-cracked strip of an elastic plastic strain hardening material. *Proc. CSNI Specialist Meeting on Elastic–Plastic Fracture Mechanics*, Dearsbury, England, May 1978, Committee on the Safety of Nuclear Installations, CSNI-32, Vol. 2 (1979).
12. A. Zahoor and P. C. Paris, A preliminary fracture analysis on the integrity of HSST intermediate test vessels. *Proc. CSNI Specialist Meeting on Plastic Tearing Instability*, Committee on the Safety of Nuclear Installations (CSNI) of the OECD Nuclear Energy Agency, NUREG/CP-0010, CSNI-39, 477–518 (1979).
13. J. R. Rice, A path independent integral of the approximate analysis of strain concentration by notches and cracks. *J. Appl. Mech.* 379–386 (1968).
14. J. W. Hutchinson and P. C. Paris, Stability Analysis of J-controlled crack growth. In Elastic-plastic fracture. *ASTM STP* **668**, 37–64 (1979).
15. H. Tada, P. C. Paris and G. R. Irwin, The stress analysis of cracks handbook. Del Research Corporation, 226 Woodbourne Drive, St. Louis, MO 63105 (1973).
16. C. F. Shih and J. W. Hutchinson, Fully plastic solutions and large scale yielding estimates for plane stress crack problems. *J. Engng Mater. Tech.* **94**, 289–295 (1976).

Computers & Structures, Vol. 13, pp. 145–154, 1981
Printed in Great Britain.

0045-7949/81/010145-10$02.00/0

FRACTURE ANALYSIS OF NOTCHED COMPOSITES

JAN BACKLUND
Department of Mechanical Engineering, Linkoping Institute of Technology,
581 83 Linkoping, Sweden

(*Received* 21 *May* 1980)

Abstract Static fracture of notched composites has drawn the attention of numerous researchers in recent years and it has been studied both experimentally and theoretically. One of the proposed theories for predicting fracture of composites is the "average stress criterion" due to Whitney and Nuismer. A similar theory based on fracture mechanics has been used by Waddoups *et al.* Pipes et al have recently generalized these concepts by introducing a three-parameter fracture model and a radius superposed method.

In the present paper the mechanisms behind the cut-off of the stress peak at the notch are investigated using the fictitious crack model (FCM). In the intense energy region close to the notch, a fictitious crack is assumed to form when the uniaxial tensile strength is exceeded. On the surfaces of this fictitious crack, cohesive forces act. These forces reduce with increased width of the fictitious crack and vanish at a certain crack width. Hereafter the crack is considered as a real crack. The reduction of the cohesive forces can be assumed to follow various curves, three of which are shown in Fig. 1(b). A common feature for all curves is, however, that the area under the curve is equal to the fracture energy $\mathcal{G}_f$. It should also be emphasized that the fictitious crack merely represents a damaged zone in the composite than a sharp crack.

Some preliminary finite element calculations performed with the fictitious crack model show good correlation with experimental results and the redistribution of stresses at increased external load is illustratively demonstrated.

1. INTRODUCTION

1.1 *Background*

With the increased use of advanced fibre-reinforced composite materials, the characterization of these materials for various loadings and geometries has become a primary concern for the designer. Incorporation of composites into vehicles and structures requires that holes be drilled into laminates to facilitate joining of structural parts or to provide access to the interior of the structure. These holes introduce stress concentrations which significantly reduce the failure load, but the extent of this reduction is not completely understood. Considerable literature is available, both analytical and experimental, which addresses the problem of fracture of anisotropic plates with circular holes. However, a generally accepted method for failure analysis is still lacking.

1.2 *Aim and scope of this work*

According to the opinion of the author, new analytical or computational methods have to be established, which in a better way than the now existing ones describe the increased "damage" in the composite at increased external load and hence the accompanied redistribution of stresses and strains. The word damage is here used as a general expression for crack formation, fibre pull-out, crack bridging, matrix microcracking, matrix yielding, fibre debonding, delamination, etc., see Fig. 2. The aim of the present work is, after having given a survey of existing methods of failure analysis, to make a preliminary investigation of a new method termed the fictitious crack model (FCM), which earlier has been applied by Hillerborg *et al.* [1, 2] to failure analysis of concrete. Two other approaches, which should be investigated with respect to their ability of modelling fracture of composites, are also mentioned. These are the work by Janson and Hult on continuous damage mechanics (CDM) [3, 4] and the blunt crack band propagation approach (BCB) proposed by Bazant and Cedolin [5].

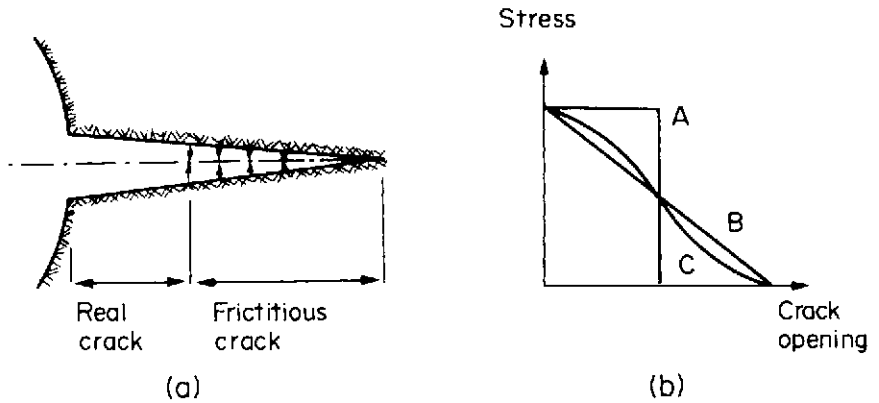

Fig. 1. The fictitious crack model: (a) real and fictitious crack, (b) reduction of stress with crack opening.

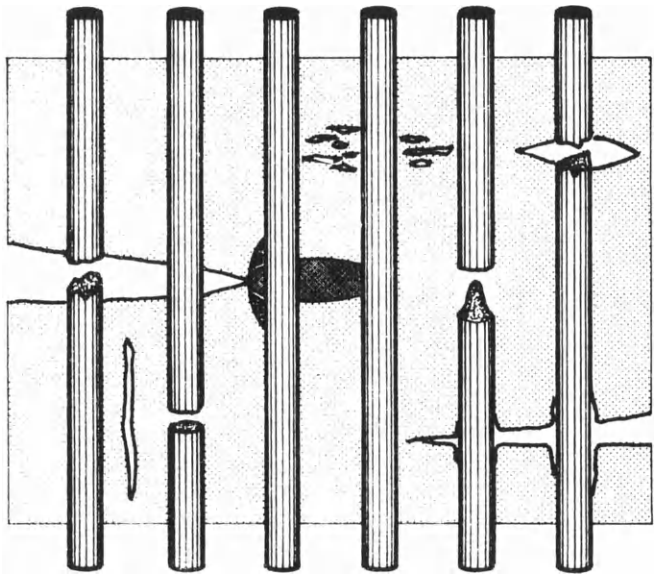

Fig. 2. Possible failure modes in a fibre reinforced material.

2. REVIEW OR PREVIOUS APPROACHES

2.1 *General remarks*

This chapter contains a survey of various proposed methods for static failure analysis of fibre reinforced composites. Many of these approaches are general with respect to the type of material studied. Despite this fact, this survey will be restricted to deal with fibre reinforced plastics (FRP) and with high strength fibre materials such as carbon, glass and aramid. In this initial state of the research project, the interest will be focused on FRP:s with continuous fibres. A strongly increased use of chopped-fibre reinforced plastics, especially within the automotive industry, will however probably result in a special study of non-continuous-fibre reinforced plastics later on in this project.

The three up to now most widely used fracture criteria for notched composites are briefly described in Sections 2.2 and 2.3. In Section 2.4 some other works are surveyed.

2.2 *Inherent flaw criterion*

Waddoups *et al.* [6] were among the first to apply linear elastic fracture mechanics (LEFM) to notched composites. On the basis of experimental results such as those summarized in Tables 1 and 2 and Fig. 3, they used the Bowie solution [7] for the stress intensity factor for cracks emanating from a circular hole in an isotropic plate to explain the hole size effect.

The starting point of Waddoups *et al.* is illustrated in Fig. 4. They assumed an intense energy region to exist at the hole, "a" being a characteristic length of this region. The isotropic stress intensity factor K_I for two symmetric cracks of length a is

$$K_I = \sigma\sqrt{\pi a} f(a/R) \tag{2.1}$$

where the function $f(a/R)$, which is given by Bowie [7], takes the value 1 if the hole vanishes.

The fracture stress σ_c for the plate with a hole is according to eqn (2.1)

$$\sigma_c = \frac{K_{IC}}{\sqrt{\pi a} f(a/R)} \tag{2.2}$$

where K_{IC} is the fracture toughness. For the case with no hole but an inherent crack of length $2a$, the fracture

Table 1. Test results for 25.4 mm wide $[0/\pm 45]_{2s}$ graphite-epoxy tensile coupons

Specimen	Static strength (MPa)
Without hole	464
ϕ 1.57 mm hole	310
ϕ 0.79 mm hole	355
ϕ 0.38 mm hole	420

Table 2. Test results for 127 mm wide $[0/\pm 45]_{2s}$ graphite-epoxy tensile coupons

Specimen	Static strenght (MPa)
Without hole	524
ϕ 25.4 mm hole	192
ϕ 63.5 mm hole	157
ϕ 76.2 mm hole	159

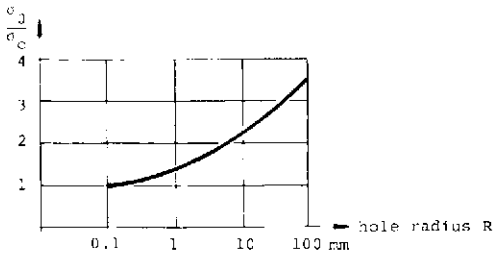

Fig. 3. Unnotched strength σ_0/notched strength σ_c vs hole radius of $[0/\pm 45]_{2s}$ graphite-epoxy.

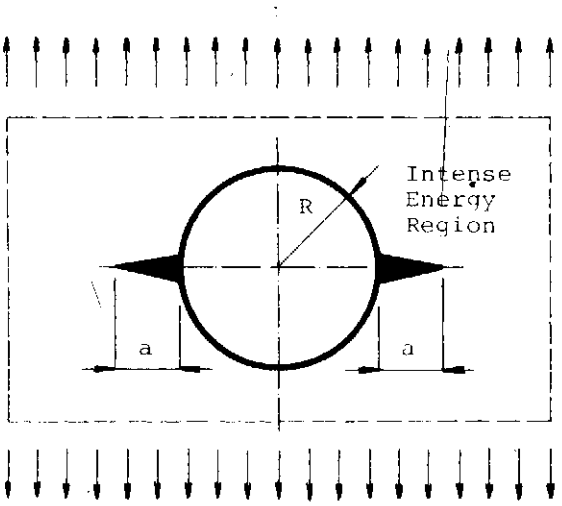

Fig. 4. Intense energy region at the hole.

stress σ_0 is

$$\sigma_0=\frac{K_{IC}}{\sqrt{\pi a}}. \tag{2.3}$$

Hence the ratio σ_0/σ_c of unnotched to notched strength can be obtained by dividing eqns (2.2) and (2.3)

$$\frac{\sigma_0}{\sigma_c}=f(a/R). \tag{2.4}$$

A parametric representation of the function $f(a/R)$ is given in Fig. 5, where also the experimental results in Fig. 3 are shown. The experimental behavior is approximated fairly well by an inherent crack a of length 1 mm.

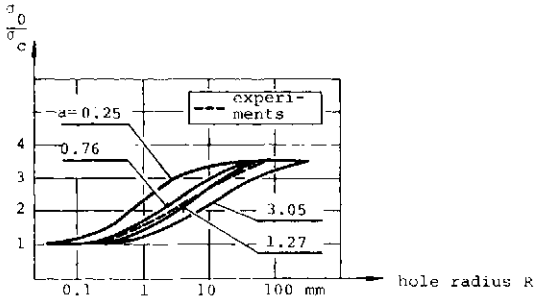

Fig. 5. Theoretical and experimental curves relating unnotched strength σ_0/notched strength σ_c to hole radius.

The existence of an intense energy region was also illustrated by Waddoups *et al.* by strain gauge measurements at the net section of a notched specimen, Fig. 6. The maximum strain measured exceeded the ultimate strain of an unnotched specimen of the same material considerably.

2.3 *Point and average stress criteria*

In a number of papers, Nuismer *et al.* [8 11] have presented a theoretical basis, experimental verification and practical application of stress criteria which are similar to the inherent flaw criterion. However, LEFM is not applied and the stress distribution ahead of the notch is obtained using linear elasticity.

As a starting point we take the stress field in an infinite

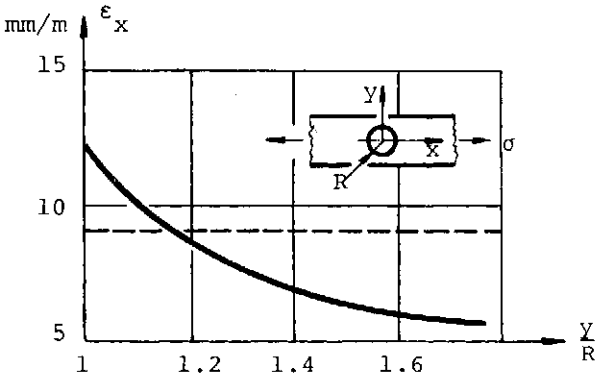

Fig. 6. Net section strains compared to ultimate strain of unnotched specimen. $\sigma=260$ MPa, $R=9.5$ mm.

isotropic plate subjected to uniaxial tension and with a circular hole, Fig. 7. The variation of the stress component σ_y can be expressed as in eqn (2.5), where R is the radius of the hole and σ is the stress applied at infinity [12]

$$\sigma_y=\left[1+\frac{1}{2}\left(\frac{R}{x}\right)^2+\frac{3}{2}\left(\frac{R}{x}\right)^4\right]\sigma. \tag{2.5}$$

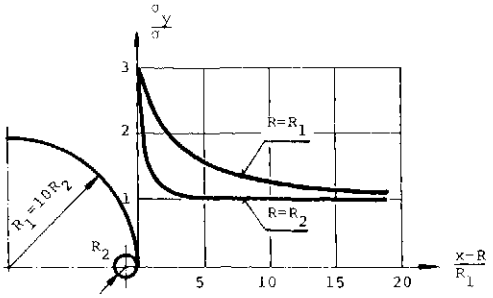

Fig. 7. Stress distribution ahead of circular holes of different radii in an infinite isotropic plate.

For $x=R$, the well-known value 3 of the stress concentration factor (SCF) is obtained from eqn (2.5). The stress concentration is however much more localized for the smaller hole than for the larger hole. For the larger hole, a larger volume of material is subjected to high stresses and, hence, the probability of having a large flaw in highly stressed regions is greater than for the plate having a smaller hole. The conclusion that large hole plates should have a lower fracture stress σ_c than small hole plates was also verified experimentally by Nuismer and Whitney [8, 9].

In the point stress criterion (PSC), it is assumed that the notched strength σ_c is obtained when the stress σ_y at a certain distance d_0 from the notch equals the unnotched strength σ_0, eqn (2.6)

$$\sigma_0=\sigma_y(x=d_0)=\left[1+\tfrac{1}{2}\xi_1^2+\tfrac{3}{2}\xi_1^4\right]\sigma_c \tag{2.6}$$

which can be expressed as

$$\frac{\sigma_c}{\sigma_0}=\frac{2}{2+\xi_1^2+3\xi_1^4} \tag{2.7}$$

where

$$\xi_1=\frac{R}{R+d_0}. \tag{2.8}$$

For pedagogical reasons, the notched to unnotched strength ratio in eqn (2.7) was derived for an isotropic material. If the material is anisotropic, eqn (2.5) has to be modified in accordance with eqn (2.9) [13]

$$\sigma_y=\left\{2+\left(\frac{R}{x}\right)^2+3\left(\frac{R}{x}\right)^4-(K_{T\infty}-3)\left[5\left(\frac{R}{x}\right)^6-7\left(\frac{R}{x}\right)^8\right]\right\}\frac{\sigma}{2} \tag{2.9}$$

where the stress concentration factor $K_{T\infty}$ for the infinite plate is expressed by in-plane laminate stiffnesses A_{ij} [14] in eqn (2.10) and, alternatively, by effective elastic moduli in eqn (2.11).

$$K_{T\infty}=1+\sqrt{\frac{2}{A_{11}}\left(\sqrt{A_{11}A_{22}}-A_{12}+\frac{A_{11}A_{22}-A_{12}^2}{2A_{66}}\right)} \tag{2.10}$$

$$K_{T\infty}=1+\sqrt{2\left(\sqrt{\frac{E_x}{E_y}}-\nu_{yx}\right)+\frac{E_x}{G_{xy}}}\,. \tag{2.11}$$

In its generalized form, the point stress criterion now is expressed as in eqn (2.12)

$$\frac{\sigma_c}{\sigma_0}=2/[2+\xi_1^2+3\xi_1^4-(K_{T\infty}-3)(5\xi_1^6-7\xi_1^8)]. \tag{2.12}$$

In the average stress criterion (ASC), it is assumed that the notched strength σ_c is obtained when the average of the stress σ_y over a certain distance a_0 ahead of the notch equals the unnotched strength σ_0, eqn (2.13)

$$\sigma_0=\frac{1}{a_0}\int_R^{R+a_0}\sigma_y(x,0)\,\mathrm{d}x. \tag{2.13}$$

Substituting eqn (2.9) into (2.13) yields after integration

$$\frac{\sigma_c}{\sigma_0}=2(1-\xi_2)/[2-\xi_2^2-\xi_2^4+(K_{T\infty}-3)(\xi_2^6-\xi_2^8)] \tag{2.14}$$

where

$$\xi_2=\frac{R}{R+a_0}. \tag{2.15}$$

Figures 8–11 show how the point and average stress criteria correlate with experiments performed by Nuismer and Whitney [9] on glass/epoxy and graphite/epoxy.

At the representation in Figs. 8–11 of the notched strength obtained at the experiments is was transformed to "infinite plate notched strength" by multiplying by the isotropic finite width correction factor $K_T/K_{T\infty}$ according to eqn (2.16) [15]

$$\frac{K_T}{K_{T\infty}}=\frac{2+(1-2R/W)^3}{3(1-2R/W)}\,. \tag{2.16}$$

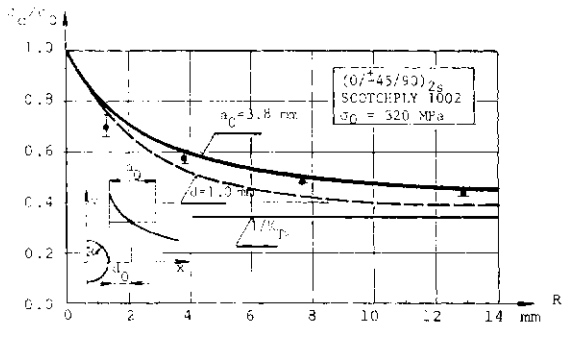

Fig. 8. Notched to unnotched strength of $(0,\pm45,90)_{2s}$ Scotchply 1002 laminates with circular holes.

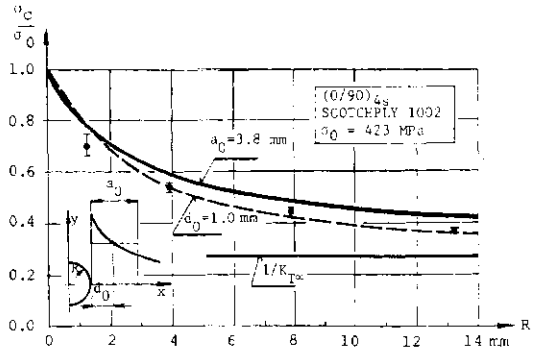

Fig. 9. Notched to unnotched strength of $(0/90)_{4s}$ Scotchply 1002 laminates with circular holes.

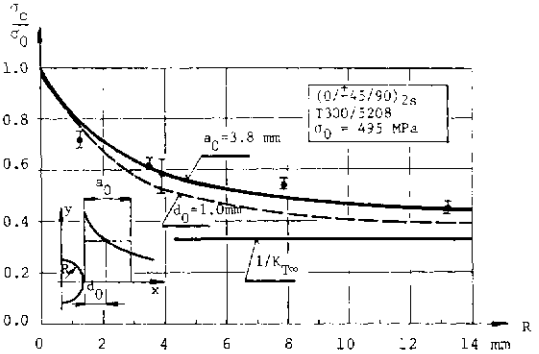

Fig. 10. Notched to unnotched strength of $(0/\pm45/90)_{2s}$ T300/5208 laminates with circular holes.

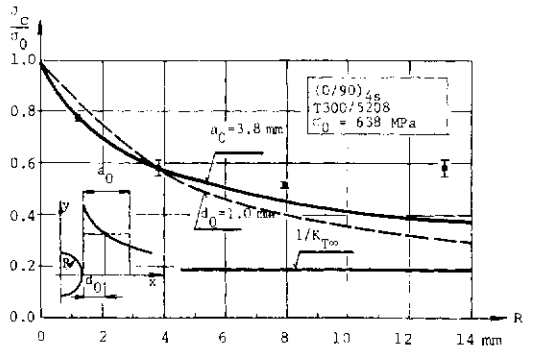

Fig. 11. Notched to unnotched strength of $(0/90)_{4s}$ T300/5208 laminates with circular holes.

2.4 *Other approaches*

The application of fracture mechanics to composites has been investigated in a number of papers such as Phillips [16], Hahn [17], Morris and Hahn [18], Brinson and Yeow [19], Yeow *et al.* [20, 21] and Awerbuch and Hahn [22]. In these papers the main interest was to evaluate experimentally such fracture parameters as the crack opening displacement (COD) or the fracture toughness expressed as critical stress intensity factor (SIF) K_{IC} or fracture energy $\mathcal{G}_c$. They are mainly concerned with laminates with sharp notches or cracks. Lau and Chow [23] present finite element calculations of SIF:s in orthotropic plates. An excellent review article by Dharan [24] on the subject should also be mentioned.

Kanninnen *et al.* [25, 26] have also reviewed the current knowledge on fracture in composites. Furthermore, they have proposed a new model in which a local heterogeneous region (LHR) is studied which surrounds the crack tip. In this model various micromechanical failure processes are taken into consideration.

Two other approaches which deserve to be noticed are those due to Snyder and Cruse [27] and Pipes *et al.* [28]. In the previous work a boundary-integral equation (BIE) method was developed by which finite width effects and stress intensity factors for Modes I and II could be calculated for various geometries and in-plane loadings avoiding the assumption of an isotropic correction factor. Pipes et al presented a three-parameter relationship for the notched strength of composites which was based on the works by Waddoups *et al.* [6] and Nuismer and Whitney [9]. They put the notched to unnotched strength in the following form,

$$\frac{\sigma_c}{\sigma_0}=2/[2+f^{-2}+3f^{-4}-(K_{T\infty}-3)(5f^{-6}-7f^{-8})] \tag{2.17}$$

where

$$f=1+\frac{R^{m-1}}{R_0^m C}. \tag{2.18}$$

Equation (2.17) can be regarded as a generalization of eqn (2.12), which was derived from the point stress fracture criterion [9]. The undetermined parameters in the model are the notch sensitivity factor C and the exponential parameter m.

Finally, two works dealing with the compressive failure of notched composites will be mentioned. The overwhelming majority of papers addressing fracture of notched composites deal with tensile fracture. However, Nuismer and Labor [11] have demonstrated some successful applications of the average stress criterion to the compressive strength of graphite/epoxy laminates with countersunk holes. Knauss *et al.* [29] performed an experimental study of graphite/epoxy plates with different layups.

3. THE FICTITIOUS CRACK MODEL

3.1 *General remarks*

The inherent flaw criterion of Waddoups *et al.* [6], the point and average stress criteria of Nuismer *et al.* [8–11] and the three-parameter criterion of Pipes *et al.* [28] are all of the empirical type, i.e. they all rely upon some parameter, eg a, d_0, a_0, c, m, etc., which has to be chosen in such a way that the experimental results are approximated by the theory. These parameters can not be calculated or postulated on the basis of fundamental data of the constituent materials of the composite but they are selected on a best-fit basis.

A theory by which the notched fracture strength could be computed from known fundamental material data would be much more appealing. It would, however, not be realistic to expect such a theory to be able of modelling all micromechanical fracture mechanisms in detail (see Fig. 2). The fracture energy $\mathscr{G}_c$ represents the sum of all energies dissipated in these various mechanisms, see Beaumont and Harris [30], and it is selected as a suitable parameter for characterizing the material. The fictitious crack model (FCM) is a model which originally was used by Hillerborg *et al.* [1] and Modéer [2] for fracture analysis of concrete and cement. It fulfills the requirements discussed above, i.e. only basic material parameters such as stiffnesses, unnotched fracture stress σ_0 and fracture energy $\mathscr{G}_c$ are required as input parameters. The entire process of crack formation and crack growth, both stable and unstable, can be modelled. The fracture load can be calculated for various shapes of notches and not only circular holes.

3.2 *Description of the model*

The basic principle of FCM is to gather all microcracks and other local fractures to a fictitious crack, see Fig. 12. From a computational point of view, the fictitious crack is identical to a real crack with uniting stresses acting on the crack surfaces. The fictitious crack is formed when the unnotched tensile strength σ_0 of the material is exceeded. Fig. 13(a).

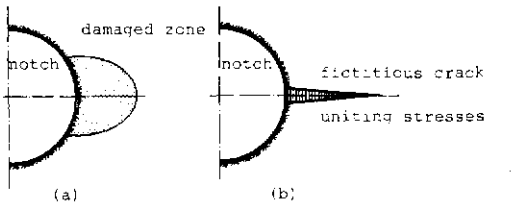

Fig. 12. Modelling of damaged zone as a fictitious crack: (a) Damaged zone. (b) Fictitious crack.

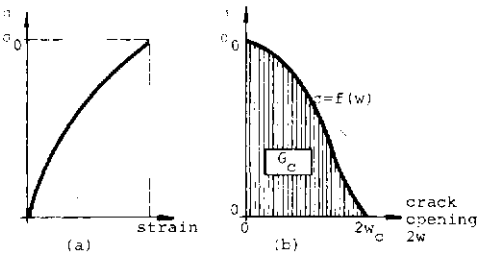

Fig. 13. Stress vs strain and crack opening: (a) stress–strain curve of unnotched composite, (b) reduction of the stress acting on the crack surfaces with crack opening $2w$. The area under the curve is equal to the fracture energy $\mathscr{G}_c$.

When the crack opening $2w$ increases, due to an increase of the external load, the uniting stresses are reduced, Fig. 13(b). This reduction can be expressed with a general function $f(w)$, eqn (3.1)

$$\sigma=f(w). \tag{3.1}$$

The area under the $\sigma-w$ curve corresponds to the fracture energy $\mathscr{G}_c$, Fig. 13(b).

At a limiting value of w, which is denoted w_c, the stress is reduced to zero and a real crack is formed, Fig. 14(a). Upon a further increase of the external load the real crack grows. This growth is generally stable in a first phase and then it changes to be unstable. The load at which the crack growth changes from stable to unstable is in the following taken as the fracture load according to the computations, Fig. 14(b).

A very nice property of the fictitious crack model is that both formation, stable growth and unstable growth of cracks can be followed for quasi-static loadings. The

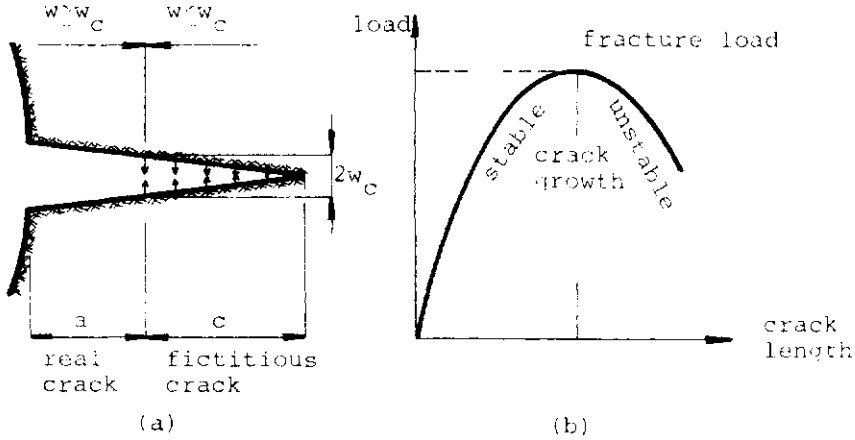

Fig. 14. Crack growth according to the FCM: (a) real and fictitious cracks, (b) computational fracture load.

latter is true if the analysis is displacement controlled. This general property of modelling the behaviour of an unloaded and undamaged structure up to fracture is unique for FCM and has no counterpart in either conventional fracture mechanics or the criteria developed for composites such as the inherent flaw, point or average stress criteria.

Various approximations can be used both for the stress–strain curve and for the stress-crack opening curve. In this work a linear stress-strain curve is assumed, ie the material is assumed to be linearly elastic. For the stress–crack opening curve two different approximations are used, Fig. 15. In the first one, a constant stress σ_0 is assumed to act on the surfaces of the crack as long as the crack opening is less than $2w_{c1}$, eqn (3.2)

$$w_{c1}=\frac{\mathcal{G}_c}{2\sigma_0}. \tag{3.2}$$

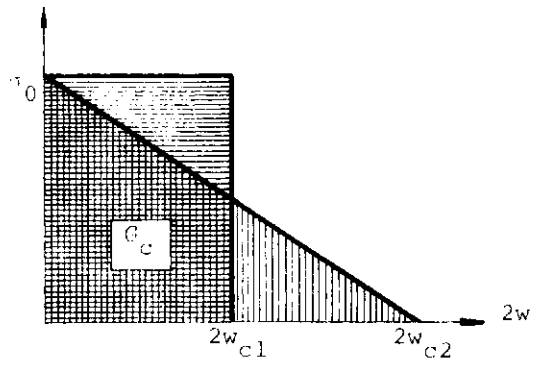

Fig. 15. Constant and linearly decreasing stress–crack opening curves.

In the second case a linearly decreasing stress-crack opening curve is employed with the limiting value $2w_{c2}$ of the crack opening, eqn (3.3)

$$w_{c2}=\frac{\mathcal{G}_c}{\sigma_0}. \tag{3.3}$$

4. NUMERICAL RESULTS

4.1 *General remarks*

In the present applications of the fictitious crack model, $(0/90)_{4s}$ Thornel 300/Narmco 5208 graphite/epoxy laminates were studied. Experimental results and theoretical results obtained from the average and point stress criteria have been published by Nuismer and Whitney [9], see also Fig. 11 in Section 2.3.

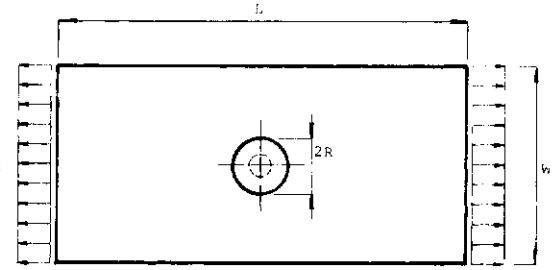

Fig. 16. Geometry of and loading of analysed plate $L=52.0$ mm, $E=25.1$ mm, $2R=7.6$ mm and 2.8 mm, thickness $=2.16$ mm.

The geometries of the analysed plates are given in Fig. 10 and the data for the material are given in Tables 3 and 4. These Tables give the elastic data of the graphite/epoxy lamina and the elastic and fracture data of the laminate, respectively. In Table 4 the values of the fracture energy $\mathcal{G}_c$ and the limiting crack openings w_{c1} and w_{c2} are questionable. Nuismer and Whitney did unfortunately not give the value of $\mathcal{G}_c$ in their paper [9] so it had to be taken from the work by Phillips [16], who reported experimental results for a similar laminate. Hence, the value of $\mathcal{G}_c$ which has been given in Table 4 can be considerably erroneous. To check the influence of the value of $\mathcal{G}_c$ on the computed results, complementary calculations were performed with half and twice the value of $\mathcal{G}_c$, see Section 4.5 and Section 5.

Table 3. Stiffness properties of graphite/epoxy lamina

Stiffness property	Value	Units
Young's modulus in the fibre direction E_{11}	147.7	GPa
Young's modulus in the transverse direction E_{22}	11.05	GPa
Shear modulus G_{12}	5.32	GPa
Major Poisson's ratio ν_{12}	0.29	–

The stiffness coefficients A_{ij} are defined in equation (4.1), where N_x, N_y and N_{xy} are membrane forces and

Table 4. Stiffness and fracture properties of graphite/epoxy laminate with thickness 2.16 mm. The stiffnesses are defined in eqn (4.1) and the crack openings in Fig. 15.

Property	Value	Units
Stiffness A_{11}	172.6	MN/m
Stiffness A_{22}	172.6	MN/m
Stiffness A_{12}	7.0	MN/m
Stiffness A_{66}	11.6	MN/m
Unnotched strength σ_0	638	MPa
Fracture energy G_c	20	kJ/m^2
Crack opening w_{c1}	15.7	μm
Crack opening w_{c2}	31.3	μm

ε_x, ε_y and γ_{xy} are strains of the laminate [14]

$$\begin{bmatrix} N_x \\ N_y \\ N_{xy} \end{bmatrix} = \begin{bmatrix} A_{11} & A_{12} & 0 \\ A_{12} & A_{22} & 0 \\ 0 & 0 & A_{66} \end{bmatrix} \begin{bmatrix} \varepsilon_x \\ \varepsilon_y \\ \gamma_{xy} \end{bmatrix}. \qquad (4.1)$$

In Figs. 12 and 17 the two finite element meshes used at the computations are shown. The mesh signified as "fine", Fig. 12, differs from the "coarse" mesh in Fig. 18 only in the element layout along the x-axis. This refinement was made to get a check of the discretization errors in the analysis.

At the places in these meshes where two element sides coinside with a single side, displacement continuity was assured by using the "master-slave" technique and subsidiary conditions [42]. In all computations the general purpose finite element code GENFEM-3 developed by Glemberg, Petersson and Wennerström [43-45] was used.

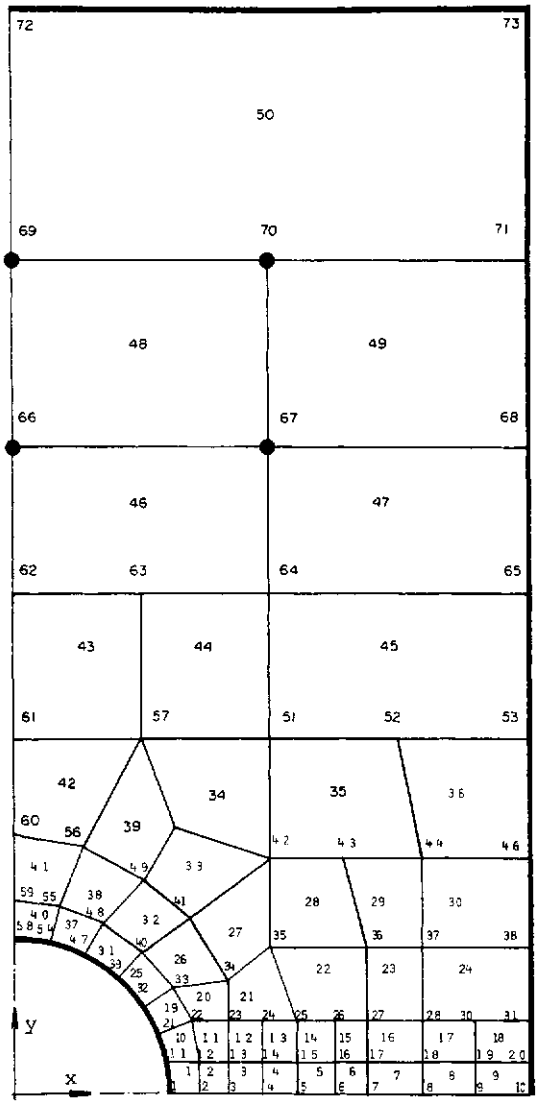

Fig. 17. Coarse finite element mesh.

4.2 *Large hole*

When the large hole analysis is discussed, we first look at the results obtained using the coarse mesh in Fig. 17. According to the calculation of the undamaged plate, the external stress $\sigma = 100$ MPa gives a nodal force $F_1 = 172$ N in node No. 1, which gives an average stress of $172/0.4 = 430$ MPa along half the distance between nodes 1 and 2. Hence, the external stress $\sigma = 100 \cdot 638/430 = 148$ MPa is causing a fictitious crack of length $c = 0.4$ mm, where 638 MPa is the unnotched tensile strength, Table 4. The next step in the calculation is split into two load cases, see Fig. 19.

By adjusting the external stress σ such that the nodal force F_2 equals the unnotched strength σ_0 multiplied by the sum of the two adjacent half element lengths, and at the same time checking w_1 with respect to w_c, the growth of the fictitious crack can be simulated. The procedure is repeated, and in each step the number of load cases that have to be considered is increased by one. It is, of course, also necessary to check if any w behind the front of the fictitious crack exceeds w_c. In this way the growth of the real crack is also followed.

The resulting curves relating external stress σ to total crack length $a+c$ for the coarse and fine meshes are shown in Fig. 20.

4.3 *Small hole*

In the same way as described in the preceding section, a plate with a ϕ 2.8 mm hole was analysed using a modified version of the coarse mesh. The maximum stress obtained was $\sigma = 443$ MPa. If we now apply a factor $349/328 = 1.064$, see Fig. 20 to this result, a predicted maximum stress $\sigma = 471$ MPa is obtained for a fine mesh calculation of this plate.

4.4 *Variation of fracture energy and stress with crack opening curve*

As discussed in Section 4.1, two separate analyses were carried out to clarify the influence of the value of the fracture energy. For the large hole and the fine mesh, the values $\mathcal{G}_c = 10$ kJ/m^2 and 40 kJ/m^2 were used in addition to the previously applied value 20 kJ/m^2. The maximum stress obtained for these two cases was 330 MPa and 412 MPa, respectively, as compared with 349 MPa, Fig. 20.

The sensitivity of the results to the shape of the stress vs crack opening curve was also analysed. In all calculations discussed so far, the constant stress vs crack open-

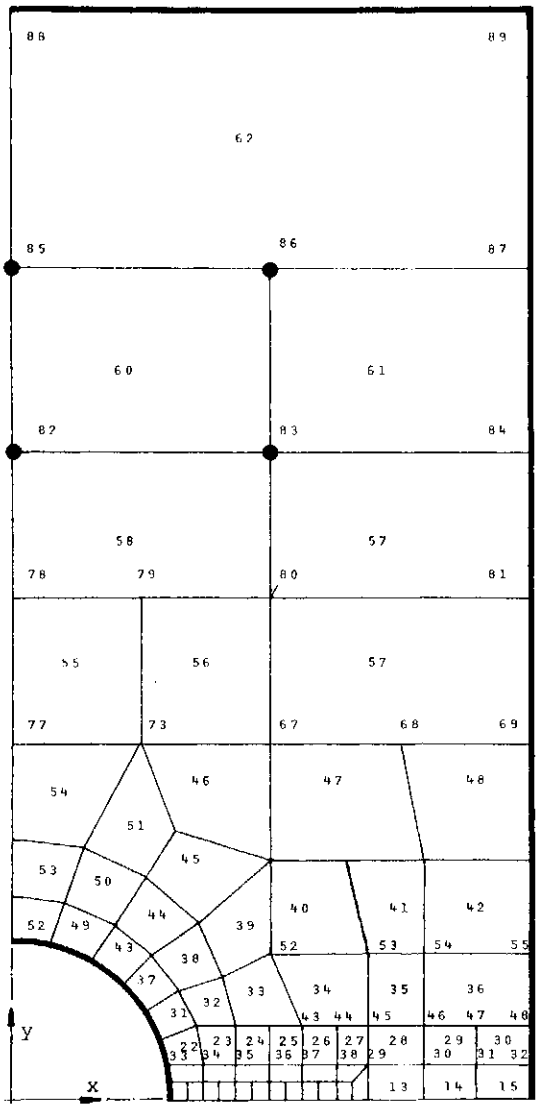

Fig. 18. Fine finite element mesh.

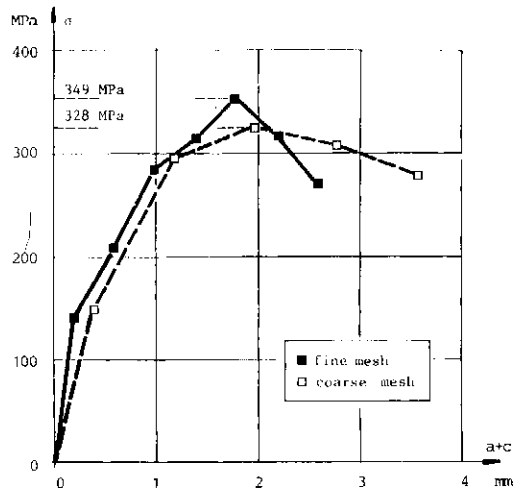

Fig. 20. External stress σ vs total crack length $a + c$ for plate with ϕ 7.6 mm hole.

ing relationship has been used, see Fig. 15. Now, for the large hole fine mesh case, the linearly-decreasing curve was used in combination with a simplified procedure. The resulting maximum stress for this case was 326 MPa.

4.5 *Comparison with previous results*

In Fig. 21 the results of the pilot study computations described in the preceding sections are compared with experimental and theoretical results by Nuismer and Whitney [9], see Fig. 11. Before the present results were plotted, they were modified by the isotropic finite width correction factor according to eqn (2.16), which for the large and small hole was 1.12 and 1.01, respectively.

5. DISCUSSION, FUTURE RESEARCH

The results obtained in this pilot study are encouraging. The fictitious crack model seems to be able to cope

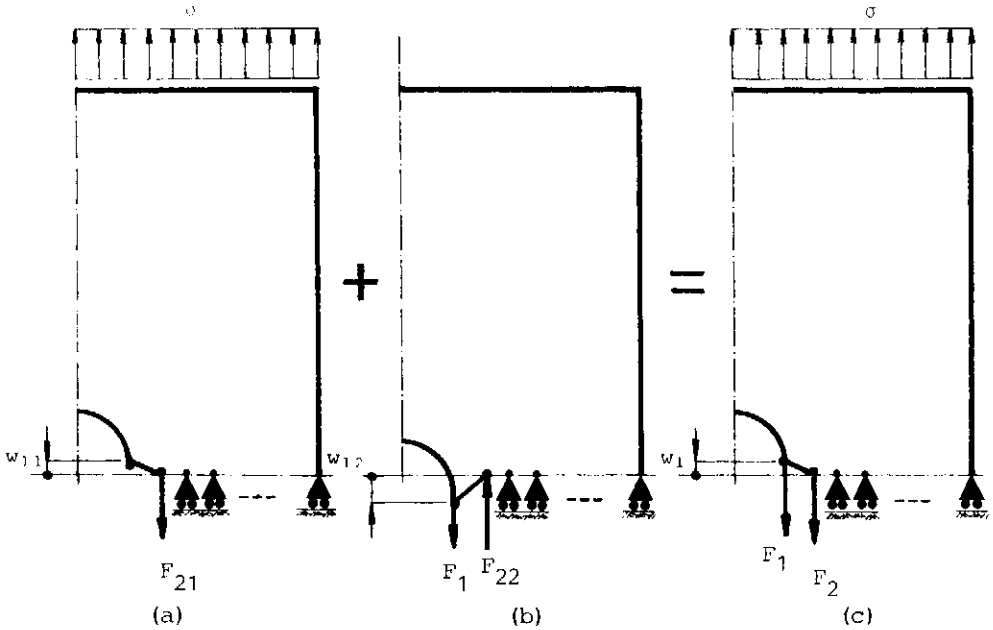

Fig. 19. Superposition of load cases: (a) external stress σ acting, (b) uniting nodal force F_1 acting, (c) total load case.

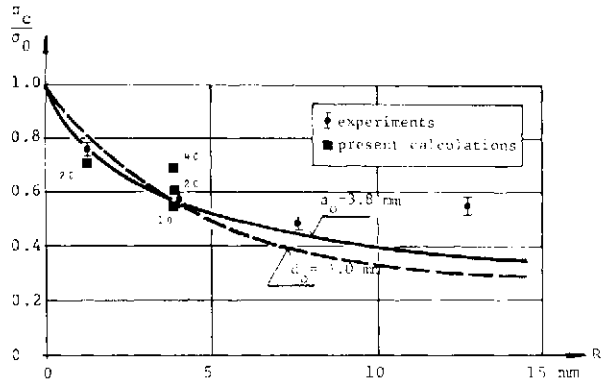

Fig. 21. Comparison of present results with experimental and theoretical results by Nuismer and Whitney [9]. The numbers denote the values of fracture energies $\mathcal{G}_c$

with the problem of static fracture in notched composites. Even if the results are somewhat uncertain with reference to the value of $\mathcal{G}_c$ the hole size effect is described in a qualitatively correct way. The major advantage of the new technique over existing theories is that only basic stiffness and fracture data of the material are required.

Hence, a further study of FCM applied to notched composites seems well motivated. Some of the issues which then should be investigated more closely are listed below:

(a) Experiments should be searched for, or performed, where both the stiffnesses, unnotched fracture stress, fracture energy and notched fracture stress are known

(b) A general computer code based on the procedure described in Section 3.3 should be developed. This program could preferably be written for a mini or micro computer communicating with a large computer. Then the condensed stiffness matrix could be evaluated in the large computer and sent over to the small one, where all FCM computations could be performed

(c) A careful study of discretization errors and of various stress vs crack opening relationships should be undertaken

(d) The FCM technique should then be applied to other notches than circular holes and to various types of composites

Parallel to this work, the author feels that it would be fruitful to apply the principles of two other recent techniques for fracture analysis to composites also. These are the continuous damage mechanics approach described by Janson and Hult [3, 4] and the blunt crack band propagation technique proposed by Bazant and Cedolin [5].

REFERENCES

1. A. Hillerborg, M. Modéer and P. E. Pettersson, Analysis of crack formation and crack growth in concrete by means of fracture mechanics and finite elements. *Cement Concrete Res.* **6**, 773–782 (1976).
2. M. Modéer, A fracture mechanics approach to failure analyses of concrete materials. diss, University of Lund, Division of Building Materials, *Rep. TVBM-1001*, Lund (1979).
3. J. Janson and J. Hult, Fracture mechanics and damage mechanics, a combined approach. *J. de Mécanique Appliquée* **1**, 69–84 (1977).
4. J. Jansson, Dugdale crack in a material with continuous damage formation. *Engng Fracture Mech.* **9**, 891–899 (1977).
5. Z. P. Bazant and L. Cedolin, Blunt crack band propagation in finite element analysis. *Proc. ASCE, J. Engng Mech. Div.* **105**, (EM2), 297–315 (1979).
6. M. E. Waddoups, J. R. Eisenmann and B. E. Kaminski, Macroscopic fracture mechanics of advanced composite materials. *J. Composite Mater.* **5**, 446–454 (1971).
7. O. L. Bowie, Analysis of an infinite plate containing radial cracks originating from the boundary of an internal circular hole. *J. Math. Phys.* **35** 60 (1956).
8. J. M. Whitney and R. J. Nuismer, Stress fracture criteria for laminated composites containing stress concentrations. *J. Composite Mater.* **8**, 253–265 (1974).
9. R. J. Nuismer and J. M. Whitney, Uniaxial failure of composite laminates containing stress concentrations In Fracture mechanics of composites. *ASTM STP* **593**, 17–142 (1975).
10. R. J. Nuismer and J. D. Labor, Applications of the average stress failure criterion: Part I—Tension. *J. Composite Mater.* **12** 238–249 (1978).
11. R. J. Nuismer and J. D. Labor, Applications of the average stress failure criterion: Part II - Compression. *J. Composite Mater.* **13**, 49–60 (1979).
12. S. Timoshenko and J. N. Goodier, *Theory of Elasticity*, 3rd Edn. McGraw-Hill, New York (1970).
13. S. G. Lekhnitskii, *Anisotropic Plates*. Gordon & Breach, New York (1968).
14. R. M. Jones, *Mechanics of Composite Materials*. McGraw-Hill, New York (1975).
15. R. E. Peterson, *Stress Concentration Factors*. Wiley, New York (1974).
16. D. C. Phillips, The fracture mechanics of carbon fibre laminates. *J. Composite Mater.* **8**, 130–141 (1974).
17. H. T. Hahn, Fracture behaviour of composite laminates. *Proc., Int. Conf. on Fracture Mechanics and Technology* (Edited by G. C. Sih and C. L. Chow). Sijthoff Noordhoff, Hong Kong (1977).
18. D. H. Morris and H. T. Hahn, Fracture resistance characterization of graphite/epoxy composites. In Composite materials: testing and design (*4th Conf.*). *ASTM STP* **617**, 5–17 (1977).
19. H. F. Brinson and Y. T. Yeow, An experimental study of the fracture behaviour of laminated graphite/epoxy composites. In Composite Materials: testing and design (*4th Conf.*). *ASTM STP* 617, 18–38 (1977).
20. Y. T. Yeow, D. H. Morris and H. E. Brinson, The fracture behaviour of graphite/epoxy laminates. *Exper. Mech.* **19**, 1–8 (1979).
21. Y. T. Yeow, D. H. Morris and H. F. Brinson, A correlative study between analysis and experiment on the fracture behaviour of graphite/epoxy composites. *J. Testing Evaluation* **7**, 117–125 (1979).
22. J. Awerbuch and H. T. Hahn, Crack-tip damage and fracture toughness of boron/aluminum composites. *J. Composite Mater.* **13**, 82–107 (1979).
23. K. J. Lau and C. L. Chow, A finite element method of stress intensity factor determination in cracked orthotropic plates. *Proc., Int. Conf. on Fracture Mechanics and Technology* (Edited by G. C. Sih and C. L. Chow). Sijthoff Noordhoff, Hong Kong (1977).
24. C. K. H. Dharan, Fracture mechanics of composite materials. *J. Engng Mater. and Tech.* **100** 233–24 (1978).
25. M. F. Kanninnen, E. F. Rybicki and H. F. Brinson, A critical look at current applications of fracture mechanics to the failure of fibre-reinforced composites. *Composites* **8**, 17–22 (1977).
26. M. F. Kanninen, E. F. Rybicki and W. J. Griffith, Preliminary development of a fundamental analysis model for crack growth in a fiber reinforced composite material. In Composite materials: testing and design (*4th Conf.*), *ASTM STP* **617**, 53–69 (1977).
27. M. D. Snyder and T. A. Cruse, Boundary-integral equation analysis of cracked anisotropic plates. *Int. J. Fracture* **11**, 315–328 (1975).
28. R. B. Pipes, R. C. Wetherhold and J. W. Gillespie Jr, Notched strength of composite materials. *J. Composite Mater.* **13**, 148–160 (1979).

29. J. F. Knauss, J. H. Starnes Jr and F. G. Henneke II, The compressive failure of graphite/epoxy plates with circular holes. Department of Engineering Science and Mechanics, College of Engineering, Virginia Polytechnic Institute and State University, *Rep. VPI-E*-78-5, Blacksburg, Virginia (1978).
30. P. W. R. Beaumont and B. Harris, The energy of crack propagation in carbon fibre-reinforced resin systems. *J. Mater. Sci.* **7**, 1265–1279 (1972).
31. J. Bäcklund, H. Wennerström and K. Axelsson, PIFEM, a computer program for analysis of elasto-plastic structures. The Swedish Ship Research Foundation, *Rep. No.* 125, Göteborg (1976).
32. J. Bäcklund, F. Nilsson and K. Markström, A singular element with variable crack length. *Int. J. Fracture* **13**, 250–252 (1977).
33. J. Bäcklund, On isoparametric elements. *Int. J. Numer. Meth. Engng* **12**, 731 (1978).
34. J. Bäcklund and K. Lindberg, Optimum design of structural details of ships using elasto-plastic finite element analysis. *Proc. Int. Symp. Practical Design in Shipbuilding*, pp. 109–112, Tokyo (1977).
35. J. Bäcklund and H. Ansell, Cracks at loaded holes. *Proc. Euromech Colloquium No.* 110 *on Contact Problems and Load Transfer in Mechanical Assemblages*, pp. 97–102, Rimforsa, Sweden (1978).
36. A. Karlsson and J. Bäcklund, Summary of SIF design graphs for cracks emanating from circular holes. *Int. J. Fracture* **14**, 585–596 (1978).
37. A. Karlsson and J. Bäcklund, J-integral at loaded crack surfaces. *Int. J. Fracture* **14**, R311–R314 (1978).
38. J. Bäcklund and J. Mackerle, Stress intensity and crack opening of compact tension specimens. *Engng Fracture Mech.* **12** 99–101 (1979).
39. J. Bäcklund and J. Mackerle, Stress analysis of composite material plates by isoparametric finite elements. Linköping Institute of Technology, Department of Mechanical Engineering, Division of Solid Mechanics, *Rep. R*-130, Linköping (1979).
40. J. Bäcklund and C.-G. Aronsson, Effects of geometrical incompatibilities on stress intensity factors calculated by the finite element method. *Proc. 1st Int. Conf. on Numerical Methods in Fracture Mechanics*, pp. 281–291, SHansea (1978).
41. O. C. Zienkiewicz, *The Finite Element Method* 3rd Edn. McGraw-Hill, New York (1977).
42. H. Petersson and E. P. Popov, Substructuring and equation system solution in finite element analysis. *Comput. Structures* **17**, 197–206 (1977).
43. H. Wennerström, R. Glemberg and H. Petersson, GENFEM-3, a computer program for general finite element analysis. *User's Manual*. Chalmers University of Technology, Department of Structural Mechanics, Publication 79:4, Göteborg (1979).
44. H. Wennerström and H. Petersson, GENFEM-3, a computer program for general finite element analysis. *Verification Manual*, Chalmers University of Technology, Department of Structural Mechanics, Publication 79:5, Göteborg (1979).
45. R. Glemberg, H. Petersson and H. Wennerström, GENFEM-3, a computer program for general finite element analysis. *Theoretical Manual*, Chalmers University of Technology, Department of Structural Mechanics, Göteborg (in preparation).

Computers & Structures, Vol. 13, pp. 157–162, 1981
Printed in Great Britain.

0045-7949/81/010157-06$02.00/0

COMPUTATIONAL METHOD FOR SOIL/STRUCTURE INTERACTION PROBLEMS†

Y. MARVIN ITO‡ and RUSSELL H. ENGLAND §
California Research & Technology, Inc., Woodland Hill, California, U.S.A.

and

RICHARD B. NELSON¶
University of California, Los Angeles, California, U.S.A.

(*Received* 9 *May* 1980)

Abstract This paper describes a computational method for soil/structure interaction problems, with particular emphasis on reinforced concrete structural response. The computational method involves the modeling capabilities of the CRT/NONSAP finite-element computer code which has been extended to address soil/structure interaction problems. Some of the relevant improvements include:
•Refined elastic–plastic material models for concrete and geologic materials.
•Interface element to model shear transfer and sliding at soil/structure interfaces.
•Element deletion (removal) procedure for representation of cracking in brittle materials, or failure in ductile material caused by large strains.
The details of these improvements regarding their applicability to dynamic analysis of reinforced concrete structures and the effects of soil/structure interaction are described. Also, the nonlinear response analysis of a buried reinforced concrete cylinder to an air blast environment is presented.

INTRODUCTION

Problems involving nonlinear response of soil/structure systems are complicated by three features: (1) nonlinearity in the structural components, e.g. inelasticity in concrete and steel reinforcements of reinforced concrete structures; (2) nonlinearity in soils, e.g. compaction and (3) slip and/or gap at the interface between the soil and structure. In this paper a nonlinear finite-element computer program developed at California Research & Technology, Inc. (CRT) is used to analyze problems of this type. This code, termed CRT/NONSAP, is an extensively modified version of the code originally developed at the University of California, Berkeley [1, 2], and has the capability of dealing with elastic–plastic large deformation dynamical response of complex structure/media systems.

The nonlinear material models for soil and structure now available in this code include elastic–plastic models for complex pressure sensitive materials. These models are generalized versions of Drucker–Prager and Mohr–Coulomb associated flow models [3, 4], and can represent soil, rock or concrete types of materials, including, if necessary, tension failures, cracking, effects of compaction and shear failure dependency on pressure. These models have successfully predicted the nonlinear response of geologic media and reinforced concrete structures to dynamical blast and shock loading.

†This work was partially supported by the Defense Nuclear Agency.
‡Principal Engineer.
§Research Engineer.
¶Professor of Engineering and Applied Science.

The combined soil/structure problem is complicated by the interface between the soil and structure. In fact, experiments [5] have shown that sliding between concrete/soil and steel/soil interfaces occurs at interface shear levels which are significantly less than the shear limit of the soil. Thus, analyses which assume a perfectly bonded interface condition overpredict the shear transfer and depending on the specific application, either over- or underestimate structural response.

Typical interface data indicates that shear associated with interface slipping resembles a Coulomb law. That is, the shear limit for bonding is dependent in some fashion on the interface normal pressure. Various plasticity constitutive models exist which fit the general form of the interface shear/normal sliding stress data. For example, the Drucker–Prager and Mohr–Coulomb yield criterion give a good approximate representation of interface sliding data. Interface behavior can be simulated numerically by explicitly representing the interface boundary with a finite element having a small thickness and using a constitutive model that reflects the interface shear/normal stress limits. Since the interface element is to simulate the shear/pressure limits on the surface between two dissimilar materials, its material constituents should reflect interface sliding data and not necessarily the constituent laws for either of the two adjoining materials.

Theoretical calculations performed wherein interface behavior is simulated using either a Drucker–Prager or Mohr–Coulomb yield law and an *associated* flow rule generally do not compare well with experimental data. This is due to the fact that the sliding which occurs in an interface typically results in large interface shear strain. According to the associated flow rule this shear strain

causes volumetric expansion in the interface element of the order of the shear strains to occur during the process of interface slipping. This volumetric expansion can cause significant, unrealistic buildup of pressure in the structure and surrounding media, especially if the problem is confined.

To avoid this difficulty, a special interface element was developed. The yield law employed is a simple Coulomb friction law, and the plastic flow rule used assumes the direction of plastic strain increment lies colinear with the interface sliding, i.e. sliding causes plastic shear strains only. This flow rule is nonassociated and prevents plastic dilatation. The selection of a nonassociated flow rule to alleviate plastic volumetric dilatation results in a loss of symmetry in the incremental constitutive law (incremental stress strain matrix) and hence leads to nonsymmetric interface tangent stiffness matrices. Furthermore, nonassociated flow rules can lead to indefinite or negative definite systems. An incremental solution procedure is employed in which only the symmetric portion of the interface constitutive law is used to represent the system incremental tangent stiffnesses. The errors induced by neglecting the nonsymmetric terms are eliminated through iteration and the accumulation of errors is prevented by reapplication of the errors obtained from the previous cycle to the next load step. This approach is computationally efficient and permits the retention of the usual symmetric linear equation solution procedure.

In the following sections the detailed mathematical features of the numerical modeling and solution techniques are described. Also, the nonlinear response analysis of a buried reinforced concrete cylinder to an air blast environment is presented.

GENERALIZED DRUCKER–PRAGER MATERIAL MODEL

Inelastic deformation in geologic media and concrete materials results from two separate mechanisms: (1) plastic strains which accumulate when slippage occurs due to excess shear stress and (2) compaction (the closing of gaps and voids) which occurs under hydrostatic states of compression. Both these mechanisms can absorb significant energy, thus modeling their effects is essential if theoretical nonlinear models are to accurately predict behavior in soil/structure interaction problems.

In the analyses performed herein, the geologic material is characterized using a hysteretic pressure dependent elastic–plastic model. With this model, shear failure is governed by a pressure/plastic work dependent yield law and its associated flow law. The general form of the law in terms of the stress invariants J_1 and J_2' is as follows:

$$F = \alpha J_1 + \sqrt{J_2'} - K \tag{1}$$

where

$$\alpha = \alpha(J_1, W_p) \tag{2a}$$

$$K = K(J_1, W_p) \tag{2b}$$

$$J_1 = \sigma_{ii}$$

$$J_2' = \frac{1}{2}\left(\sigma_{ij} - \frac{\sigma_{kk}}{3}\delta_{ij}\right)\left(\sigma_{ij} - \frac{\sigma_{mm}}{3}\delta_{ij}\right) \tag{3b}$$

W_p denotes plastic work, and α and J are scalar parameters. Expressing the material parameters α and K as a function of the hydrostatic pressure ($-J_1$) permits an accurate representation of triaxial compression test data. Typical shear failure data for geologic materials are shown in Fig. 1.

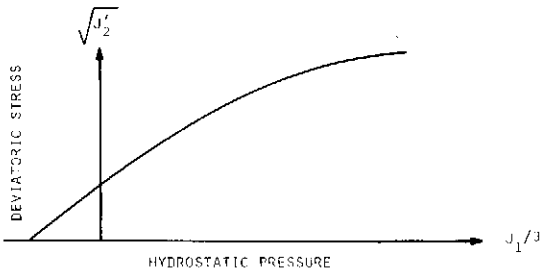

Fig. 1. Typical shear failure data for geologic materials.

The constitutive model represents the hysteretic effects of compaction using a variable loading and unloading bulk moduli formulation where the incremental bulk modulus depends both on the current volumetric strain state and the peak volumetric strain occurring during the loading history. Figure 2 shows typical compaction behavior generally obtained from either uniaxial strain or hydrostatic compressions tests which are used to fit the variable bulk modulus model.

The effect of compaction is most significant in soils and may be ignored for certain types of rock and concrete. Similarly, plastic work has little significance on the yield/flow surfaces in soils. Thus this general material model can be specialized to represent various soils, rock and other geologic material such as concrete.

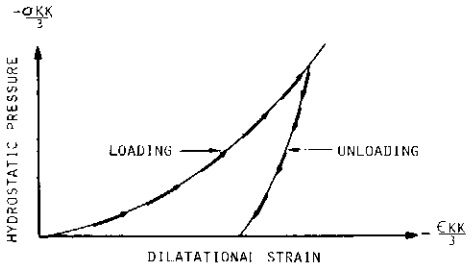

Fig. 2. Typical compaction data for geologic materials.

REINFORCED CONCRETE MATERIAL MODEL

The reinforced concrete model developed for the numerical calculations presented herein includes an explicit representation of the steel reinforcement bars (one-dimensional elastic–plastic elements) and the plain concrete (elastic plastic continuum elements). Plain concrete is idealized using an isotropic pressure dependent yield law with strain hardening and softening capabilities and an associated flow law. The yield criterion has the form given in eqn (1). Expressing the yield parameters α and K in terms of J_1 (hydrostatic pressure) and plastic work (W_p) allows for an analytical representation of both the pressure dependency on yielding and post-yield strain hardening and softening formulations.

The material parameters for the concrete model were evaluated to fit concrete biaxial stress data. This stress data was preferred to triaxial because of the basic

geometry of the structures analyzed (thin wall cylinder) where states of stress remain essentially biaxial ($\sigma_{rr} \ll \sigma_{\theta\theta}$). Figure 3 shows a typical failure surface for plain concrete in states of plane stress. This biaxial failure data can be used to evaluate corresponding values of the invariants J_1 and $\sqrt{J_2'}$; thus when the failure data is mapped to J_1, $\sqrt{J_2'}$ space (see Fig. 4), the material parameters α and K can be evaluated to fit experimental data.

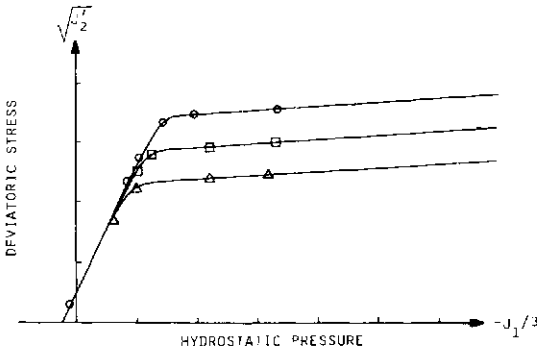

Fig. 3. Biaxial failure data for plain concrete.

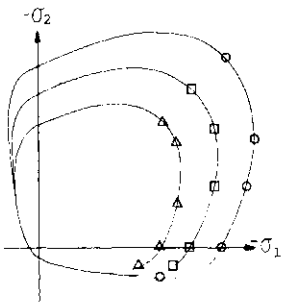

Fig. 4. Plain concrete biaxial failure data mapped to J_1, $\sqrt{J_2'}$ space.

This concrete constitutive model gives an accurate representation of concrete behavior until either compressive crushing and spalling or tensile cracking occurs. In this event an element deletion (removal) procedure has been developed where at any cycle of the solution procedure, failed elements are physically removed from the grid. Two distinct approaches can be exercised: (1) removal of both the mass and stiffness of the element (simulating the complete removal of the material), or (2) removal of the stiffness but retaining the mass (idealization of a crack section). This element removal technique is by no means an attempt to simulate crack propagation. It is, however, an effective means for evaluating the effects on structural response caused by changes in load path resulting from localized failures occurring in concrete (and steel reinforcing bars).

STRUCTURE/MEDIA INTERFACE MATERIAL MODEL

This section describes the basic fundamental relations used to evaluate the incremental constitutive equations for the structure/media interface element. This includes the stress criterion for slippage and the plastic flow rule from which the incremental constitutive laws are derived.

Experimental data suggests that sliding in structure/soil interfaces in governed by a Coulomb-type criterion, i.e. the critical shear stress which causes debonding is dependent on the normal interface pressure. Furthermore, experimental data shows that the critical shear stress limit is essentially a linear function of the normal pressure for a rather large range of interface pressures. A general form of the criterion for interface slip which defines all combinations of stress states corresponding to sliding is as follows:

$$F(\sigma_n, \tau) = 0 \tag{4}$$

where σ_n = interface normal stress; τ = interface shear stress; and $F(\sigma_n, \tau) \equiv 0$ denotes interface sliding, and $F(\sigma_n, \tau) < 0$ corresponds to interface bonding. Assuming the critical shear limit is linearly dependent on the interface normal stress leads to the following criterion for slip:

$$F = \sqrt{\tau^2} + \mu\sigma_n - C \tag{5}$$

where μ = interface coefficient of friction and C = interface cohesion.

During interface sliding a flow rule is required which specifies the direction of the plastic flow given the interface stresses. In order to prevent plastic dilatation the following nonassociated flow law was selected:

$$\mathrm{d}\varepsilon_n^p = 0 \tag{6a}$$

$$\mathrm{d}\gamma^p = \mathrm{d}\gamma^p \tag{6b}$$

where $\mathrm{d}\varepsilon_n^p$ = incremental interface plastic normal strain and $\mathrm{d}\gamma^p$ = incremental interface plastic shear strain. Again, an associated flow rule will produce considerable volumetric expansion if sliding occurs on the interface. Figure 5 illustrates the difference between interface element response for associated and nonassociated flow rules.

From the definition of the criterion for slip (i.e. that during sliding $F \equiv 0$) and the plastic flow rule, the incremental constitutive relations are obtained. During sliding, the sliding criterion requires

$$F(\sigma_n + \mathrm{d}\sigma_n, \tau + \mathrm{d}\tau) \equiv 0 \tag{7a}$$

or

$$\frac{\partial F}{\partial \sigma_n}\mathrm{d}\sigma_n + \frac{\partial F}{\partial \tau}\mathrm{d}\tau = 0 \tag{7b}$$

or

$$\frac{\tau \mathrm{d}\tau}{\sqrt{\tau^2}} + \mu \mathrm{d}\sigma_n = 0. \tag{7c}$$

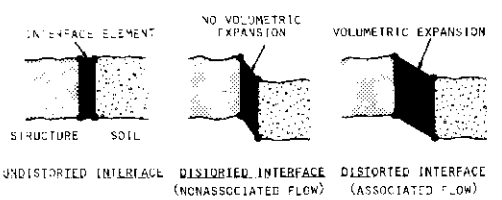

Fig. 5. Effect of flow rule on distortion of interface element during sliding.

The stress increments are evaluated from the elastic strain increments and the elastic constitutive relations

$$d\tau = G(d\gamma - d\gamma^p) \tag{8a}$$

$$d\sigma_n = E(d\varepsilon_n - d\varepsilon_n^p). \tag{8b}$$

Use of the nonassociated flow rule which stipulates that sliding causes plastic shear strain only (i.e. $d\varepsilon_n^p = 0$) and eqns (8) and (7) leads to the following expression for $d\gamma^p$:

$$d\gamma^p = d\gamma + \frac{\sqrt{\tau^2}}{\tau}\,\mu\,\frac{E}{G}\,d\varepsilon_n. \tag{9}$$

Finally, the incremental constitutive matrix is determined by substituting eqn (9) into (8),

$$\begin{Bmatrix} d\tau \\ d\sigma_n \end{Bmatrix} = [C]\begin{Bmatrix} d\gamma \\ d\varepsilon_n \end{Bmatrix} \tag{10}$$

where

$$[C] = \begin{matrix} 0, & -\frac{\sqrt{\tau^2}}{\tau}\mu E \\ 0, & E \end{matrix}. \tag{11}$$

Note that the elastic-plastic constitutive law is nonsymmetric and indefinite.

Finally, it is recognized that positive normal strain (tension on the interface is an indication of a gap forming between the two material boundaries. When this occurs, a free surface exists on both material surfaces and the materials are no longer coupled through the interface. This is simulated by zeroing the interface stress and the constitutive laws.

NUMERICAL SOLUTION PROCEDURE

Perhaps the most versatile and preferred implicit solution procedure for nonlinear problems is an incremental technique wherein effects of nonlinearity are taken into account by means of a series of piece-wise linear analyses. Each analysis is based through linearization of the nonlinear constitutive law and strain-displacement relations (for large displacement theory) which gives a linear system incremental tangent stiffness for use in the analysis. Errors induced from linearization can be eliminated by an iteration scheme in which the errors in system equilibrium are reapplied using the previous tangent stiffness to reduce errors in the equilibrium equations (modified Newton–Raphson method). If iteration is not performed, then the errors in system equilibrium can be reapplied to the next load increments to prevent the accumulation of error build-up.

When nonlinear material behavior is idealized using plasticity models with associated flow rules, the system tangent stiffness is symmetric even for large displacement theory, provided the external loading is conservative. The symmetry of the system tangent stiffness is advantageous since it greatly reduces storage requirements and linear equation solution. If nonassociated flow rules are required, linearization leads to nonsymmetric constitutive laws and nonsymmetric tangent stiffness matrices. Storage requirements for nonsymmetric matrices are nearly double the requirements for the symmetric stiffness and solution times may increase by an order of magnitude due to additional data management problems in large systems.

In many applications it is computationally more efficient to neglect the nonsymmetric portion of the incremental tangent stiffness and account for the errors induced by this approximation either through an iterative modified Newton–Raphson approach and/or by reapplication of the unbalanced loads which result from neglecting the nonsymmetric terms and from linearization of a nonlinear system to the next load step. This solution approach was used for the calculation presented herein and was found to give excellent results, i.e. this approach gave very stable behavior and generally, satisfactory solutions could be obtained without iteration.

The steps outlined below illustrate the basic procedures employed to evaluate the interface stress state and the approximate constitutive laws used in evaluating the interface tangent stiffness matrix:

(1) From the previous interface normal strain and the current incremental normal strain, determine closure of the interface.

(a) If $(\varepsilon_n + \Delta\varepsilon_n) < 0$ (closed interface), go to 2.

(b) If $(\varepsilon_n + \Delta\varepsilon_n) > 0$ (open interface), zero out interface normal and shear stresses. If interface tangent stiffness is to be calculated, set all terms in constitutive matrix to zero and return.

(2) From previous interface strains, stresses, and the current incremental strain, calculate the updated interface stress state from elastic analysis:

$$\Delta\sigma_n = E\Delta\varepsilon_n$$
$$\Delta\tau = G\Delta\gamma.$$

(3) If $F(\sigma_n + \Delta\sigma_n,\ \tau + \Delta\tau) \leqslant 0$, interface behavior is elastic (bonding), update stress and strains accordingly:

$$\sigma_n = \sigma_n + \Delta\sigma_n$$
$$\tau = \tau - \Delta\tau$$
$$\varepsilon_n = \varepsilon_n + \Delta\varepsilon_n$$
$$\gamma = \gamma + \Delta\gamma.$$

If interface tangent stiffness is to be calculated, select the elastic constitutive matrix and return.

(a) If $F(\sigma_n + \Delta\sigma_n,\ \tau + \Delta\tau) > 0$, and if previous cycle was plastic, then set RATIO to zero. Otherwise, a transition occurs between elastic and plastic response. In this case determine RATIO from the equation

$$F(\sigma_n + \text{RATIO}\ \Delta\sigma_n,\ \tau + \text{RATIO}\ \Delta\tau) = 0$$

Update the stresses to obtain the stress state prior to yielding

$$\sigma_n = \sigma_n + \text{RATIO}\ \Delta\sigma_n$$
$$\tau = \tau + \text{RATIO}\ \Delta\tau.$$

(b) Use the remaining portion of the strain increment associated with an elastic–plastic response to evaluate the corresponding stress increment. Since the constitutive law is dependent on the stress state, divide the strain increment subintervals and determine the updated stress increments through integration of the constitutive equation, i.e.

$$(1 - \text{RATIO})\begin{Bmatrix} \Delta\gamma \\ \Delta\varepsilon_n \end{Bmatrix}$$

$$\begin{Bmatrix} \Delta\tau \\ \Delta\sigma_n \end{Bmatrix} = \int_0^{\cdot} \begin{bmatrix} 0, & (-\sqrt{\tau^2}/\tau)\mu E \\ 0, & E \end{bmatrix} \begin{Bmatrix} d\gamma \\ d\varepsilon_n \end{Bmatrix}.$$

Update the total stress and strain states:

$$\sigma_n = \sigma_n + \Delta\sigma_n$$
$$\tau = \tau + \Delta\tau$$

$$\sigma_n = \sigma_n + \Delta\sigma_n$$
$$\gamma = \gamma + \Delta\gamma$$

If the interface tangent stiffness is to be updated, use the approximate symmetric elastic plastic constitutive law:

$$[C] = \begin{bmatrix} 0, & 0 \\ 0, & E \end{bmatrix}.$$

NUMERICAL APPLICATION

This section presents the results of a numerical simulation to demonstrate the ability of the analytical models to predict buried structure response. Figure 6 shows the numerical configuration of a buried reinforced concrete model experiment under explosive air blast loading (conducted by SRI International). Figure 7 gives the details of the element representation of the test model. The results of pre-test calibration experiments were used to select appropriate concrete, reinforcement, soil and interface material parameters. Figure 8 shows the corresponding numerical results for concrete strain histories at various axial stations. The numerical results compare very well with those observed in the test. The failure in the text model corresponds to the calculated region of peak concrete strain.

Additional sensitivity analyses show the effect of the soil/structure interface condition. As shown in Fig. 9, moderate changes in the coefficient of friction has a small effect on concrete response. However, a high value of cohesion gives significantly different results.

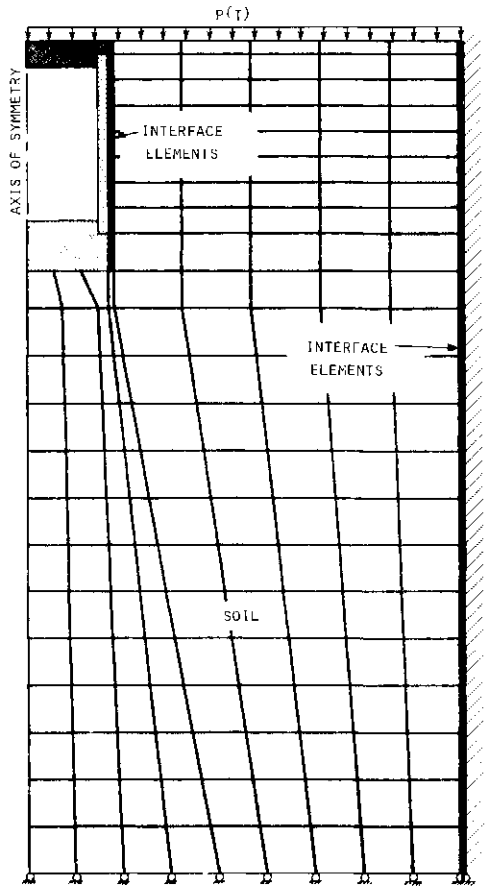

Fig. 6. Finite element description of surrounding media and interface of a buried reinforced concrete cylinder.

DISCUSSION

The results presented in the last section give a clear indication of the ability of the CRT/NONSAP code to simulate a complex nonlinear dynamical soil/structure response, involving elastic plastic behavior of soil and structure constituents and the soil/structure interface behavior. This last effect was modeled using a structure/media interface element which incorporates incremental plasticity theory to predict interface sliding stress states. A nonassociated flow rule was selected to prevent volumetric expansion of the interface when sliding occurs. The nonsymmetric incremental system

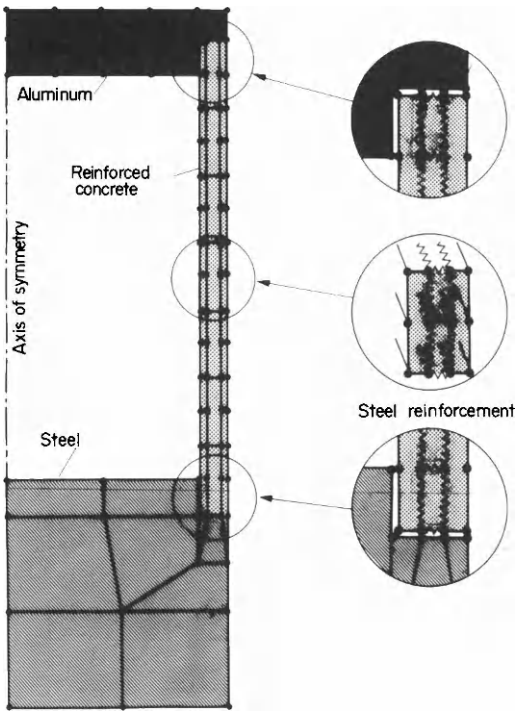

Fig. 7. Finite element description of the reinforced concrete structure.

tangent stiffness which results from the selection of a nonassociated flow rule was neglected, and the errors associated with this approximation were eliminated through iteration and by reapplication of the errors to the next load step to prevent error accumulation. This approach was very successful. In fact, in most applications, satisfactory results were obtained without any iteration.

The basic idea of limiting the surface stress conditions along boundaries of dissimilar materials using a thin interface element whose material constituents reflect typical interface behavior can be extended to other applications. For example, the basic approach can be modified to account for initial gaps existing between material boundaries. That is, closing of a gap can be detected by monitoring the normal strain in a gap element. Subsequently, stress along the interface after closure can be limited using the identical procedure as employed by the interface element. This gap element will be implemented into the CRT/NONSAP finite element code for both two- and three-dimensional applications.

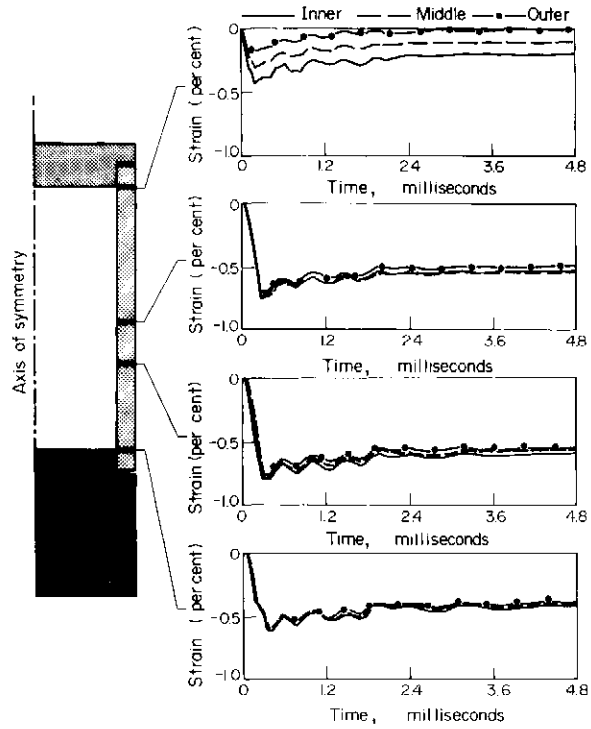

Fig. 8. Calculated axial concrete strain histories.

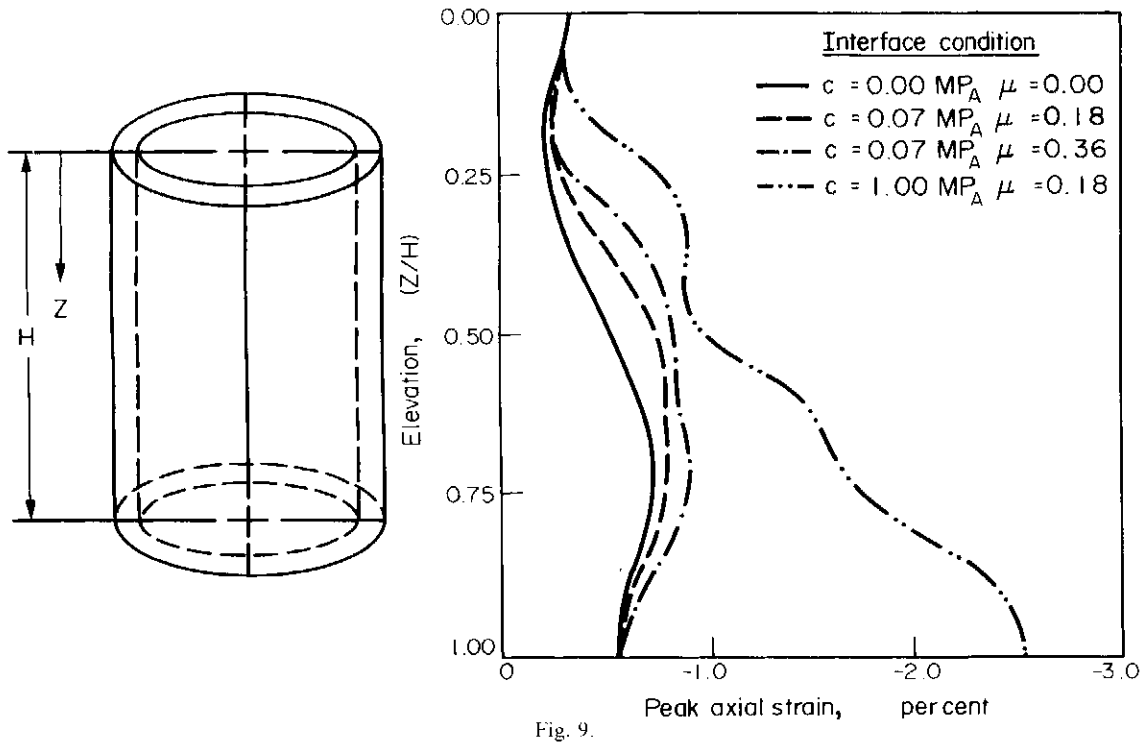

Fig. 9.

REFERENCES

1. K. J. Bathe, E. L. Wilson and R. H. Iding, NONSAP, A structural analysis program for static and dynamic response of nonlinear systems. SESM Rep. 74-3, Dept. of Civil Engineering, University of California, Berkeley, California (Feb. 1974).
2. K. J. Bathe, H. Ozpemir and E. L. Wilson, Static and dynamic geometric and material nonlinear analysis. *SESM Rep.* 74-4, Dept. of Civil Engineering, University of California, Berkeley, Calif. (Feb. 1974).
3. D. C. Drucker and W. Prager, Soil mechanics and plastic analysis of limit design. *Q. Appl. Mech.* **10**, 157 163 (1952).
4. G. C. Nayak and O. C. Zienkiewicz, Convenient form of stress invariants for plasticity. *Proc. ASCE* **98**(ST4), 949 954 (1972).
5. P. Huck, T. Liber, R. L. Chiapetta, N. T. Thomopoulos, Jr. and M. M. Singh, Dynamic response of soil/concrete interfaces at high pressures. *AFWL-TR*-73-264, Air Force Weapons Laboratory, Kirtland A.F.B., New Mexico (Apr. 1974).

Computers & Structures, Vol. 13, pp. 163–166, 1981
Printed in Great Britain.

0045-7949/81/010163-04$02.00/0

FLUID STRUCTURE COUPLING ALGORITHM

W. H. McMaster, E. Y. Gong, C. S. Landram and D. F. Quinones

University of California, Lawrence Livermore Laboratory, P.O. Box 808, Livermore, CA 94550, U.S.A.

(*Received* 25 *April* 1980)

Abstract—A fluid-structure-interaction algorithm has been developed and incorporated into the two dimensional code PELE-IC. This code combines an Eulerian incompressible fluid algorithm with a Lagrangian finite element shell algorithm and incorporates the treatment of complex free surfaces. The fluid structure, and coupling algorithms have been verified by the calculation of solved problems from the literature and from air and steam blowdown experiments. The code has been used to calculate loads and structural response from air blowdown and the oscillatory condensation of steam bubbles in water suppression pools typical of boiling water reactors. The techniques developed here have been extended to three dimensions and implemented in the computer code PELE-3D.

INTRODUCTION

We have developed a fluid-structure-interaction algorithm for the analysis of the dynamic response of coupled fluid structure systems. The method is incorporated into a two-dimensional semi-implicit Eulerian hydrodynamics code, PELE-IC. The code is quasi-two phase since we can couple to either a one-dimensional or a lumped parameter description of compressible gases. The code is written in both plane and cylindrical coordinates in order to handle a variety of geometrical configurations. The coupling algorithm is general in nature and can accommodate a wide variety of structural shapes. It is capable of following large interface motions through the calculational grid. By the use of a variable time step we are able to accommodate varying flow conditions and maintain computational stability. The fluid, structure and coupling algorithms have been verified by calculations of solved problems from the literature and by comparison with air and steam blowdown experiments (1) and (2).

The basic semi-implicit solution algorithm contained in the SOLA code (3) was used as a foundation for the development of the PELE-IC code. We track the movement of free surfaces using a donor cell treatment based on a combination of void fractions and interface orientation. This gives us great versatility in following fluid-gas interfaces for bubble definition and water surface motion without the use of marker particles.

The structural motion is computed by a finite element code [4] from the applied fluid pressure at the fluid structure interface. The finite element shell structure algorithm uses conventional thin-shell theory with transverse shear. The spacial discretization employs piecewise-linear interpolation functions and one-point quadrature applied to conical frustra. We use the Newmark implicit time integration method implemented as a one step module. The fluid code then uses the structure's resultant position and velocity as boundary conditions. The fluid pressure field and the structure's response are corrected iteratively until the normal velocities of the fluid and structure are equal. This results in a strong coupling between the two algorithms.

GENERAL DESCRIPTION OF THE SOLUTION ALGORITHMS

The underlying approach used by PELE-IC for the solution of general flow fields is the use of the semi-implicit SOLA algorithm. The basic assumption of this approach is that all flow variables within the computational grid satisfy the continuity equation for each cell, regardless of whether or not the computational cell contains a free surface or a moving structure. For incompressible fluids this means that all cells are divergence free. This assumption permits freedom of motion for all surfaces throughout the grid. Superimposed on this basic algorithm we have applied the boundary conditions for free surfaces, compressible gases, and moving structures.

In this section we will give a brief description of the solution algorithms.

SOLA solution algorithm

The SOLA algorithm uses a Newton–Raphson iteration on the pressure field to solve the mass conservation equation. At each iterative step the pressure in each fluid cell is adjusted to satisfy the divergence criteria. In this algorithm the pressure is a cell centered variable and the velocity components are specified on cell sides.

The algorithm is solved by first writing the Navier–Stokes equation for the fluid velocity, u, in terms of the time level:

$$\partial u/\partial t = (-\nabla \cdot uu + g + \nu\nabla^2 u)^n - \nabla p^{n+1} \qquad (1)$$

where the superscript n indicates the time level and $p = P/\rho$ is the ratio of the pressure to the density of the fluid. The body acceleration is given by g and the kinematic viscosity is specified by the constant ν. Setting $p^{n+1} = p^n + \delta p$ gives

$$u^{n+1} = [u + \delta t(-\nabla \cdot uu - \nabla p + g + \nu\nabla^2 u)]^n - \delta t \delta \nabla p. \qquad (2)$$

Defining the term inside the brackets as $\tilde{u}$, then the equation to be solved is

$$u^{n+1} = \tilde{u} - \delta t \delta \nabla p \qquad (3)$$

where $\tilde{u}$ is found using a slightly modified form of the

finite difference formulation of Hirt *et al.* [3]. This equation is solved iteratively where we define the divergence error, D, for each cell at the ith iteration as

$$\nabla \cdot u_i = D_i \tag{4}$$

and $\tilde{u}$ is used as the first trial velocity to start the iteration process. The pressure increment in each cell necessary to update the velocity field is given by

$$\delta p_i = -\frac{(1+\phi)D_{i-1}}{\partial D/\partial p} \tag{5}$$

where ϕ is a correction term ($0 < \phi < 1$) dependent upon adjacent cells in the direction of the sweep through the grid, and $\partial D/\partial p$ is a constant dependent only upon the cell size, the time step, and the presence of a structural boundary. We update the velocity field in each cell with the pressure increment, using

$$\delta u_i = \pm \delta p_i \delta t/\delta z \tag{6}$$

where δz is the cell side in the direction of u, and the sign is chosen dependent upon which side centered velocity component is being adjusted. Satisfaction of the continuity equation in any particular cell perturbs the velocity field of its neighbors. Hence, the method is applied in sweeps throughout the grid until the divergence error everywhere satisfies

$$\nabla \cdot u_i = D_i \leqslant \varepsilon \tag{7}$$

where ε is a preset convergence tolerance which should be set according to the minimum flow field of interest in the solution. The final velocity and pressure fields are then

$$u^{n+1} = \tilde{u} + \Sigma_i \delta u_i \quad \text{and} \quad p^{n+1} = p^n + \Sigma_i \delta p_i. \tag{8}$$

Since the solution procedure is a Newton–Raphson iteration, the rate of convergence is dependent upon the magnitude of $\partial D/\partial p$ which has the form

$$\frac{\partial D}{\partial p} = 2\delta t \left(\frac{F_x}{\delta x^2} + \frac{F_y}{\delta y^2} \right) \tag{9}$$

where F_x and F_y are dependent upon structural interfaces coupled to the fluid cell. If there is no structure, then $F_x = F_y = 1$. From the formula for $\partial D/\partial p$ we see that convergence is accelerated by the use of large time steps and small cell sizes. However, the user is limited in his choice by the physics of the problem. In general, we require that

$$\frac{u\delta t}{\delta z} < 0.4 \tag{10}$$

where δz is the component δx or δy in the direction of the maximum velocity u.

Thin shell algorithm

The finite element module uses simple shell theory with transverse shear (see Kraus [5]). The element formulation was described by Hughes and Taylor [6] for beams and plates, and was extended to axisymmetric and plane shells by Goudreau [7]. (Similar results were obtained by Zienkiewicz *et al.* [8] at about the same time.) The element is a two-node, conical frustrum with three degrees of freedom per node. Shape functions are piecewise-linear for displacements and rotations. The shear "locking" associated with low-order interpolation is removed by one-point quadrature. Large deformation (here two to three shell thicknesses) is accounted for in an approximate way by reformulating the stiffness matrix at every time step.

The Newmark implicit time integration scheme (see Goudreau and Taylor [7]) is used at each time step to move the shell. The algorithm has the form

$$(K + 4M/(\delta t))^2 Q^{n+1} = p^{n+1} - 4MA^n/(\delta t)^2 \tag{11}$$

where

$$A^n = Q^n + \dot{Q}^n \delta t + \ddot{Q}^n (\delta t)^2/4. \tag{12}$$

Goudreau [2] gives the derivation of K and a FORTRAN listing of the one-step module.

The thin shell algorithm has been made more general by the addition of the following four features:

(1) Each element may have its own thickness.

(2) Each node can be specified to have its own separate restraints and prescribed initial displacement.

(3) The code computes the static deflection of the structure as a result of the initial loading before beginning the dynamic solution.

(4) The gas pressure in the ullage region is applied to the shell as well as fluid pressures.

Fluid structure interface algorithm

This algorithm couples the fluid motion to the structure's motion within the SOLA iteration loop. Normal velocity compatibility between the structure and fluid is required where the Lagrangian shell crosses either the I-line or J-line intercept which defines the centroid of the Eulerian cell. The choice depends on the angular orientation of the structure, e.g. for angles equal or less than 45° we use the I-line coupling. The cell side coupled velocity is the one closest to the structure along the intercept line. In this manner, we maintain a smooth coupling whenever the structure crosses an Eulerian grid line. The finite element module uses the pressure field supplied by the fluid and provides the fluid code with the resultant position and velocity of the interface. Each change in the pressure field causes a different structural reponse, and each different response changes the flow field of the fluid. Therefore, the iteration proceeds until both conditions are satisfied. Within a single iteration, all Eulerian fluid zones are adjusted one by one, using the latest values available, and then all the Lagrangian shell nodes are simultaneously adjusted by the implicit time step solution.

The pressure applied to an element is determined by an interpolation along each intersection I or J line to the neighboring full fluid cell. These interpolated values are weighted by the liquid content of the cell so that the proper pressure is applied when a free surface is in the same cell. The interpolation procedure provides a smooth pressure history whenever the structure crosses a grid line.

The solution strategy is to first set the normal fluid velocity equal to the normal structure velocity at the coupling point. The structure's normal velocity is found by an interpolation between nodal values and the intercept angle. The normal fluid velocity is found by an interpolation between all four of the cell side velocities. This determines the cell side velocity which is coupled to the structure. This first step of setting the coupled Eulerian cell velocity to satisfy the boundary conditions imposed by the structure causes the cell not to satisfy the divergence criteria; therefore, the second step is to adjust the cell pressure using the SOLA algorithm

so that the cell is divergence free. This two step process is repeated each iteration until both conditions are satisfied.

The free surface algorithm

Accurate free surface tracking is necessary to allow the application of velocity and pressure boundary conditions at fluid-gas interfaces. We track the free surface by a combination of void fraction and surface orientation in each cell. The void fraction provides for the conservation of mass and the surface orientation allows us to apply the proper boundary conditions and follow the flow from cell to cell.

The free surface algorithm performs four functions:

(1) Determines the surface orientation within the calculational cell based upon its fluid content and that of neighboring cells. This orientation is specified by its intercepts on two sides of the cell. Within the cell, the interface is considered to be a straight line segment. Thus, the surface is tracked by its intersection of grid lines.

(2) Applies the prescribed boundary pressure to the fluid surface. This is done by finding the appropriate cell centered pressure by an interpolation from the nearest full fluid cell to the boundary. Recent additions to the code also allow the application of a prescribed boundary velocity to the fluid surface. This option allows one to drive the surface with a moving piston. Both these options allow the boundary conditions to be a function of time.

(3) Calculates the fluid advection based on surface orientation using the donor cell method where the amount of liquid advected is determined from the contents of the upstream cell, the orientation of the surface, and the velocity of the common liquid side. This method guarantees the conservation of mass during advection.

(4) Uses velocity boundary conditions for the void sides of the cell to maintain continuity of the flow field. This assures a smooth flow when a surface crosses grid lines.

Special features

The main application of the code to date has been to studies of the pressure suppression systems of boiling-water reactors during postulated loss-of-coolant accidents. Consequently, various special features have been added directed toward the solution of these problems. Some of these special features are described in this section.

Downcomer pipes. Downcomer pipes are modeled by specifying the bounding grid lines as rigid. A special algorithm has been added to the code to allow this option. In this manner, pipe wall thicknesses small in comparison with a calculational cell can be correctly modeled. For vent clearing problems, the specified driving pressure is applied as a boundary condition between the grid lines defining the pipe. The code has the capability of handling up to two rigid downcomer pipes with driving pressures in this manner.

Obstacles and baffles. Obstacles and baffles which restrict the flow can be modeled by specifying portions of grid lines as rigid boundaries. The code will then apply the boundary condition of zero normal velocity at this boundary. There is no restriction on the number of such obstacles that can be specified.

Coupling to compressible gas flow. In many applications the downcomer is driven from a drywell with either variable or constant pressure. Sometimes this flow is further controlled by the use of an orifice. To provide for these situations, a flow model coupled to the fluid dynamics was developed. This model couples the bubble pressure to the drywell and current bubble volume by the equation

$$P(t)=P_u\left(\frac{V_0}{V}\right)^{\gamma}\left[1+\frac{\gamma}{P_u V_0}\int_0^t \dot{m}V^{\gamma-1}\,\mathrm{d}\tau\right] \tag{13}$$

where $\dot{m}$ = mass flow rate through the orifice as specified in Vennard [9]. The formula used depends upon whether the flow is choked or unchoked, V_0 = original downcomer volume from the orifice to the water level, V = current steam volume including the bubble and P_u = initial ullage pressure. The time of integration, t, covers vent clearing and subsequent bubble formulation and growth.

In application we find that the mass flow is initially choked and dependent only upon the drywell pressure and density. Subsequently, during vent clearing, the flow becomes unchoked and is dependent upon both the drywell pressure and the bubble pressure. Since the bubble pressure is dependent upon the bubble growth in the pool, there is a coupling between the suppression pool and the drywell.

Variable ullage pressure. During a vent clearing event, the bubble growth causes a pool swelling in the confined ullage region. This compressed air region then provides an upload on the confining structure. We derive this pressure pulse from the perfect gas law using the ullage volume change as calculated from the rise of the water surface. In experiments performed at the Massachusetts Institute of Technology [10], the test configuration applied this ullage pressure to the bottom flexible plate. The code has been modified to simulate these experiments.

Collapsing bubbles. In chugging studies of collapsing bubbles, we have applied a condensation model to provide the applied bubble pressure. This pressure is dependent upon the inflow rate of steam and the condensation rate; both of which are dependent upon the bubble volume time history. The use of the void fraction and surface orientation algorithms allow us to monitor the bubble volume accurately.

Compressibility effects. In the mass continuity equation, the incompressible assumption sets $\partial\rho/\partial t=0$. We may take into account small changes in compressibility by substituting the wave equation

$$\frac{\partial\rho}{\partial t}=\frac{1}{c^2}\frac{\partial P}{\partial t} \tag{14}$$

into the mass equation, where c is the speed of sound in the fluid. This, then, changes the specification of the divergence leading to

$$D=\nabla\cdot u+\frac{1}{c^2}\frac{\partial P}{\partial t} \tag{15}$$

and

$$\frac{\partial D}{\partial p}=2\delta t\left[\frac{F_x}{\delta x^2}+\frac{F_y}{\partial y^2}+\frac{1}{2c^2\delta t^2}\right] \tag{16}$$

which are used in the iteration and for setting the velocity boundary conditions.

SUMMARY

We have developed three new algorithms to treat free surfaces, fluid-structure boundaries, and steam condensation. The first is an air-water surface algorithm that has been used to model bubble growth and pool swell in reactor pressure suppressure systems. The second is a fluid-structure coupling algorithm that correctly couples the Lagrangian structure overlaying the Eulerian grid. The third provides the driving pressure for bubble growth and collapse dominated by steam condensation.

These algorithms have been incorporated into a three-dimensional version of the code, called PELE-3D. With this version, we are able to study nonsymmetric effects.

Acknowledgements—This work was performed under the auspices of the U.S. Department of Energy by Lawrence Livermore Laboratory under contract No. W-7405-Eng-48. The work was sponsored by the Nuclear Regulatory Commission, Office of Nuclear Regulatory Research, and is designated Task 189:A0116 under interagency agreement DOE 40-550-75.

REFERENCES

1. W. McMaster, D. Norris, G. Goudreau, D. Quinones, E. Gong, B. Moran and N. Macken, Coupled fluid-structure method for pressure suppression analysis. *NUREG/CR*-0607, *UCRL*-52620, 1979, University of California, Lawrence Livermore Laboratory, Livermore, California.
2. W. McMaster and E. Gong, User's manual for PELE-IC: a computer code for Eulerian hydrodynamics. *UCRL*-52609, 1979, University of California, Lawrence Livermore Laboratory, Livermore, California.
3. C. Hirt, B. Nickols and N. Romero, SOLA—a numerical solution algorithm for transient fluid. *LA*-5852, 1975, Los Alamos Scientific Laboratory, Los Alamos, New Mexico.
4. G. Goudreau, A computer module for one step dynamic response of an axisymmetric or plane linear elastic thin shell. *UCID*-17730, 1978, University of California, Lawrence Livermore Laboratory, Livermore, California.
5. H. Kraus, *Thin Elastic Shells*. Wiley, New York (1967).
6. T. Hughes and R. Taylor, Computational methods in applied mechanics and engineering. *SMIRT*5 *Proc.* M2/1, 1977.
7. G. Goudreau and R. Taylor, *Computational Meth. Appl. Mech. Engng* **2**(1), 69–97 (1978).
8. O. Zienkiewicz, J. Bayer, K. Morgan and E. Omate, A simple and efficient element for axisymmetric shells. *Int. J. Numer. Meth. Engng* **11**(10), 1545 (1977).
9. J. Vennard, *Elementary Fluid Mechanics*, 3rd Edn, pp. 110–111, 301–305. Wiley, New York (1954).
10. W. Anderson, P. Huber and A. Sonin, Small scale modeling of hydrodynamic forces in pressure suppression systems. *NUREG/CR*-0003, prepared for the U.S. Nuclear Regulatory Commission, Massachusetts Institute of Technology (Dec. 1977).

Computers & Structures, Vol. 13, pp. 167–170, 1981
Printed in Great Britain.

0045-7949/81/010167-04$02.00/0

FINITE ELEMENT SOLUTION OF NONLINEAR FLUID-STRUCTURE INTERACTION PROBLEMS UNDER HYDRODYNAMIC SHOCK CONDITIONS

J. E. JACKSON, JR.
Department of Mechanical Engineering, Clemson University, Clemson, SC 29631, U.S.A.

and

T. L. COST
Department of Aerospace Engineering, Mechanical Engineering, and Engineering Mechanics, The University of Alabama, Tuscaloosa, AL 35486, U.S.A.

Abstract—A method of solution for the transient response of nonlinear fluid-structure systems is presented. Finite element discretization is applied to the nonlinear hydrodynamic equations in Eulerian form. The resulting system of equations is solved by Galerkin's method via a Newton–Raphson technique. Interaction between fluid and structure is accounted for by iteratively enforcing the interface conditions. The fluid finite element mesh is redefined by linear interpolation as the system deforms. The procedures are demonstrated by solution of a one-dimensional system consisting of a single-degree-of-freedom spring-mass in contact with a perfect gas through which a shock is propagated.

1. INTRODUCTION

Fluid-structure interaction occurs whenever a fluid and a structure are in contact and their motions are interdependent. The phenomenon is present in many physical systems, yet has received incomplete attention in the literature.

The present investigation is concerned with fluid-structure systems in which fluid compressibility must be considered. Such would be the case for systems in which the fluid medium is gaseous or for liquid-structure systems in which shocks occur. For example, a problem currently receiving much attention is a reactor core accident in which shock waves radiate from the core through a fluid medium to strike a surrounding structure [1].

The use of finite-difference fluid discretization schemes in the solution of fluid-structure interaction problems in liquid metal fast breeder reactors (LMFBR) has been demonstrated in Refs. [2] and [3]. Belytschko and Kennedy [4] have addressed a similar problem by use of two-dimensional finite element models for fluid discretization. This approach makes use of a quasi-Eulerian fluid element in which the motion of the nodes may differ from the motion of the fluid. In this case additional transport terms appear in the momentum equation.

The use of the finite element method for fluid discretization is advantageous because of the ease with which complex boundary geometries may be handled. The Eulerian formulation of the hydrodynamic equations provides large deformation analysis capability [1]. Of significance in this study is the method by which fluid and structural systems are solved separately with iterative enforcement of interface conditions. This procedure allows combination of the fluid calculations with those of standard structural computer programs.

The governing compressible fluid equations are stated in Section 2. Finite element discretization and solution of the resulting set of nonlinear, nonsymmetric equations are outlined in Section 3. Solution of coupled fluid-structure systems is discussed in Section 4, including applicable interface conditions and redefinition of the fluid mesh to model deformed geometries. A one-dimensional example problem is defined in Section 5 and results are discussed in Section 6. Suggestions for future investigation and conclusions are noted in Sections 7 and 8.

2. GOVERNING EQUATIONS

The governing equations for a fluid medium are obtained from the principles of conservation of mass, conservation of momentum, and balance of energy. Application of these conservation laws gives the continuity equation, the equations of motion, and the energy equation, respectively. Thus,

$$\rho_{,t}+(\rho u)_{,i}=0, \tag{1}$$

$$(\rho u_j)_{,t}+(\rho u_i u_j)_{,j}+p_{,i}=0, \tag{2}$$

and

$$E_{,t}+(Eu_j)_{,j}+(p_j u_j)_{,j}=0, \tag{3}$$

where ρ, p, E and u_i denote the mass density, pressure, total energy, and the velocity components. Equations (1) (3) assume no body forces, heat input, or fluid viscosity. In addition an equation of state,

$$f(\rho, E, u_i)=f(\rho, I)=0, \tag{4}$$

is required, where I is internal energy.
Assuming a perfect gas equation of state and rewriting, eqns (1) (4) become

$$\rho_{,t}+m_{j,j}=0, \tag{5}$$

$$m_{i,t}+(m_i u_j)_{,j}+(\gamma-1)(E-\tfrac{1}{2}m_j u_j)_{,i}=0, \tag{6}$$

$$E_{,t}+\gamma(Eu_j)_{,j}+\frac{1-\gamma}{2}(m_k u_k u_j)_{,j}=0, \tag{7}$$

and

$$m_i-\rho u_i=0, \quad i, j, k=1 \ldots n, \tag{8}$$

where the m_i are components of linear momentum and γ

is the ratio of specific heats. The value of the index n depends upon the dimensionality of the problem and can range from one to three. In the above notation repeated indices indicate summation, and a comma denotes differentiation.

3. FINITE ELEMENT DISCRETIZATION

Consider a fluid system governed by eqns (5)–(8). Discretization and solution of these nonlinear equations are accomplished as follows:

(a) Replace all time derivatives with temporal operators of the form

$$\phi^r_{,t} = C_1\phi^r + C_2, \tag{9}$$

where $\phi^r(x_i, t) = \phi(x_i, t = r\Delta t)$.

The symbol ϕ represents the vector of unknowns as defined in eqns (5)–(8). For a one-dimensional system ϕ would represent

$$\phi^{rT} = [\rho^r r^r E^r m^r]. \tag{10}$$

Applicable temporal operators include the method of Park [5], Gear 2-step and 3-step procedures [5], a first-order backward difference operator, and others which can be written in the form of eqn (9).

(b) Approximate the fluid continuum by finite elements. Thus,

$$\phi^r(x_i) = \sum_{l=1}^{N} h_l\phi^r_l, \tag{11}$$

where N is the number of nodal points per element and the h_l defines the shape function.

(c) Linearize by assuming

$$\phi^{k+1,r}_l = \phi^{k,r}_l + \Delta\phi_l, \tag{12}$$

and dropping higher order $\Delta\phi_l$ terms, which results in a set of equations,

$$L(\Delta\phi_l, \phi^{k,r}_l) = 0. \tag{13}$$

(d) Apply Galerkin's method to the set of discrete linearized equations. That is,

$$\int_V L(\Delta\phi_l, \phi^{k,r}_l)h_M \, dV = 0, \tag{14}$$

where V represents the finite element volume. Equation (14) results in a set of algebraic equations of the form

$$J^{k,r}_{ij}\Delta\phi_j = R_i(\phi^{k,r}_j). \tag{15}$$

Note that eqn (15) is in the form of a Newton–Raphson method, where k is an iteration cycle and $J^{k,r}_{ij}$ is the Jacobian evaluated at the kth iteration. Solution of the fluid system is achieved by application of eqns (13) and (15) at each successive time step r. Convergence has been achieved when the delta quantities vanish. Variations of the numerical method, such as a modified Newton–Raphson method or an incremental procedure, are easily programmable and may save computation time in certain cases [6].

(e) Structural equations are cast in the usual finite element form,

$$M_{ij}\ddot{q}^r_j + C_{ij}\dot{q}^r_j + K_{ij}q^r_j = F^r_i. \tag{16}$$

Substituting a temporal operator for the time derivatives results in a set of equations

$$S_{ij}q^r_j = T^r_i, \tag{17}$$

at each time step r. If the structural equations are nonlinear they may be written in the form of eqn (15) and solved in a manner similar to the fluid system.

4. SOLUTION OF COUPLED NONLINEAR FLUID-STRUCTURE SYSTEMS

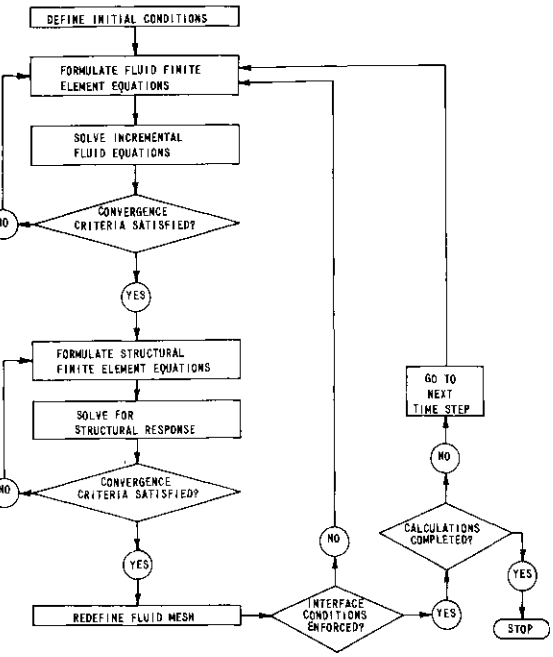

Fig. 1. Flow chart for solution of nonlinear fluid-structure interaction problems.

Solution of coupled fluid-structure systems is accomplished using a "substructure" approach. Figure 1 is a flow chart illustrating a substructure solution technique for cases in which either the fluid system, the structural system, or both are nonlinear. A converged solution of the fluid system is obtained separately from that of the structure. Note that the substructure approach necessitates an iterative enforcement of the fluid-structure interface conditions. The limiting case is the marching scheme in which the solution of the structural system at time step $r-1$ is used as data for solution of the fluid system at time step r. Thus, only one solution of each system is calculated for each time step.

If it is assumed that the surrounding fluid must always remain in contact with the structure, the fluid-structure interface condition is

$$u_i n_i = \dot{q}_i n_i. \tag{18}$$

Equation (18) expresses the fact that at the fluid-structure interface the velocity components of the fluid and of the structure normal to the surface of the structure are equal. The n_i are components of a unit vector normal to the interface surface.

Since the hydrodynamic equations (5)–(8) were derived in an Eulerian coordinate system, the finite element nodal points do not follow the fluid motion but represent a fixed location at which the fluid properties are evaluated. However, as a structure in contact with a fluid deforms, the fluid must deform in order to remain in contact with the structure. Depending upon the structural deformations, the fluid finite element mesh is compressed or extended so that the location of the interface nodal points will coincide with the deformed

surface of the structure. In these studies, the fluid pressure and other system parameters are redefined by a linear interpolation of these parameters at the "old" nodal point locations. The portion of the fluid mesh to be redefined depends upon the extent of the change in the fluid domain. Logically, it would seem that numerical inaccuracies would be minimized for a given finite element mesh when the change in shape of a given element is small in relation to the dimensions of the element.

5. EXAMPLE PROBLEM

The one-dimensional system illustrated by Fig. 2 was investigated. Twenty-nine one-dimensional fluid elements were bounded on the right by a linear single-degree-of-freedom spring-mass. By specifying discontinuous initial condition a shock was propagated through the fluid, striking the mass. Applying the

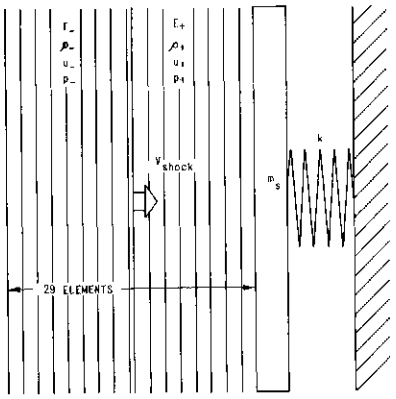

Fig. 2. Diagram of fluid-structure system utilized in calculations for one-dimensional fluid-structure interaction problem.

methods discussed above and illustrated in Fig. 1, the dynamic response of the fluid-solid system was calculated. The Gear 3-step temporal operator was utilized for the fluid while the Newark [7] operator was applied in solution of the structural (spring-mass) system. Solution of the nonlinear simultaneous equations was accomplished by a standard Newton-Raphson procedure. For each time step, iteration between fluid and structural system was continued until the solid and fluid interface normal velocities agreed within 0.1%. As the mass displacement varied, redefinition of the fluid finite element mesh by linear interpolation was performed on the ten elements bordering the solid. Calculations were performed in single precision on a CDC Cyber 175 computer. Results are presented in Fig. 3.

6. DISCUSSION OF RESULTS

For the one-dimensional example problems solved, convergence to a solution at a given time step was generally achieved within three to eight iterations.

Note from Fig. 3 that the fluid-structure interaction solution was compared to a no-interaction solution. The no-interaction solution was obtained by applying to the spring-mass a Heaviside forcing function of magnitude equal to the theoretical rigid wall reflected

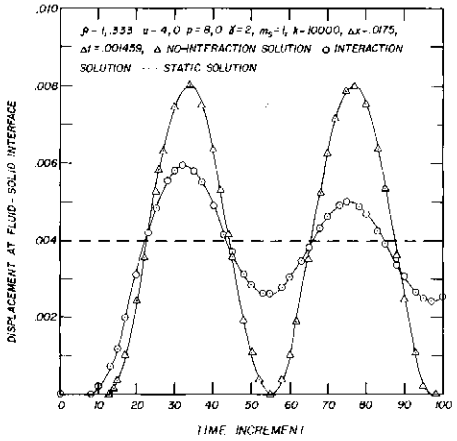

Fig. 3. One-dimensional structural response due to shock wave loading.

pressure. Comparison of the two solutions demonstrates that considering interaction effects significantly alters the structural response.

Although only one-dimensional systems were investigated, extension of the method to multidimensional systems is straightforward. A chief feature of the proposed solution procedure is the fact that fluid and structural systems are solved separately. Such a technique possesses the advantage that the fluid formulation can be easily combined with many standard structural dynamics programs. Moreover, such separate solutions may result in fewer numerical difficulties than would be the case for a truly simultaneous solution of systems possessing widely different characteristics.

Although the example problem considered only a linear structure, it is clear that the methodology may be easily extended to include structural nonlinearities.

7. FUTURE INVESTIGATIONS

This work was unfunded research and was consequently limited to one-dimensional systems. More work is needed on more complex two-dimensional problems to better ascertain computational costs and the accuracy and generality of the methodology. Comparisons of the above factors for this finite element formulation with those of other approaches, such as the finite difference methods of Refs. [1–3] and the quasi-Eulerian finite element approach of Ref. [4] would be useful.

8. CONCLUSIONS

A method of solution for fluid-structure interaction problems was proposed. The procedures were demonstrated for a one-dimensional example and appear to be feasible for complex multidimensional systems. Separate solution of fluid and structural systems with iterative enforcement of interface conditions allows a fluid system to be readily incorporated into standard structural analysis programs. The methodology is also compatible with structurally nonlinear systems. An Eulerian fluid formulation permits large deformation analysis of the fluid-region.

REFERENCES

1. Y. W. Chang and C. Y. Wang, An Eulerian method for

large displacement fluid-structure interaction in reactor containments. *Computational Methods for Fluid-Structure Interaction Problems*, pp. 1 14, AMD26, *ASME*, New York, (1977).
2. C. Y. Wang, Y. W. Chang, and S. H. Fistedis, Analysis of nonlinear fluid-structure interaction in LMFBR containment. *Nucl. Engng Design* **49**, 93–105 (1978).
3. H. Y. Chu and Y. W. Chang, Analysis of LMFBR containment response using a multifield implicit continuous fluid Eulerian code (MICE). *Nucl. Engng Design* **49**, 107 117 (1978).
4. T. B. Belytschko and J. M. Kennedy, Computer models for subassembly simulation. *Nucl. Engng Design* **49**, 17–38 (1978).
5. K. C. Park, Practical aspects of numerical time integration. *Comput. Structures* **7**, 343 353 (1977).
6. J. E. Jackson and T. L. Cost, Nonlinear hydrodynamic shock propagation analysis by the finite element method. *2nd Int. Conf. on Computational Methods in Nonlinear Mechanics*, Houston, Texas, March, 1979, *Int. J. Engng Sci.* **18**, 351–356 (1980).
7. N. M. Newmark, A method of computation for structural dynamics. *J. Engng Mech. Div., ASCE* **85**, 67–94 (1959).
8. T. J. Chung, Finite element analysis in fluid dynamics. Department of Mechanical Engineering, University of Alabama in Huntsville, Alabama (1974).
9. J. E. Jackson, Analysis of fluid-structure interaction under hydrodynamic shock conditions by the finite element method. Doctoral Dissertation, University of Alabama, Tuscaloosa, Alabama (1977).

Computers & Structures, Vol. 13, pp. 171–178, 1981
Printed in Great Britain.

0045-7949/81/010171-08$02.00/0

FINITE ELEMENT MODELING OF FLUID/THERMAL/STRUCTURAL INTERACTION FOR A GAS-COOLED FAST REACTOR CORE

JOEL G. BENNETT† and FREDERICK D. JU‡

Los Alamos Scientific Laboratory, Los Alamos, NM 87545, U.S.A.

(*Received* 27 *May* 1980)

Abstract Two nonlinear finite element formulations for application to a series of experiments in the Gas-Cooled Fast Reactor (GCFR) development program are described. An efficient beam column element for moderately large deformations is combined with a finite element developed for an engineering description of a convecting fluid. Typical results from both elements are illustrated. A combined application for a problem typical of the GCFR loss-of-coolant experiments is illustrated. These problems are not the usual fluid structural interaction problems in that the inertia coupling is negligible while the thermal coupling is very important.

1. INTRODUCTION

At the Los Alamos Scientific Laboratory (LASL), out-of-pile facilities are currently in use for simulating a Protected Loss of Flow Accident (PLOF) for the Gas-Cooled Fast Reactor (GCFR) development program. The description and results of one of two such destructive tests carried out thus far are given in Refs. [1, 2]. Design activities are currently underway for an even larger test that will employ 438 simulated fuel rods to simulate an hexagonally shaped GCFR core module and its six boundaries. One of the objectives of this series of tests is to demonstrate the behavior of one of the GCFR modules in the event of a loss of coolant flow and subsequent shutdown of the reactor to the power level provided by the decay heat. Another objective is to provide some insight into the structural design for the module by identifying areas for which current designs can be improved. This safety program is being carried out at LASL in cooperation with the General Atomic Company and the U.S. Department of Energy.

One area that has been identified as being of significant importance in the post-test reviews is the effect of the convective heat transfer by the free convection of helium. In addition, evidences of duct bowing and undue frictional interaction between fuel rod cladding and their spacer grids have been observed. Free convection appears to drive the duct bowing process. In cases for which thermal bowing of the rods is sufficient to cause two-sided contact between the rods and their supporting grids (and thus a tendency to "lock up"), the subsequent rod deformation caused by the axial expansion also appears to be affected by the free convection. This paper is aimed at describing the analytical developments and applications for examining the complex processes of the fluid/thermal/structural interaction of these experiments.

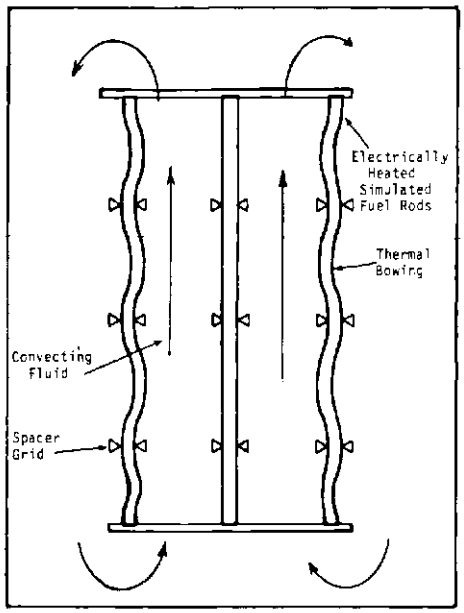

Fig. 1. Description of the physical problem of interest.

2. DESCRIPTION OF THE PHYSICAL MODEL

The physical problem that is representative of these experiments is illustrated in Fig. 1. The electrically heated simulated fuel rods are very closely spaced and are loosely supported at various points along their length by spacer grids. Large thermal gradients cause thermal bowing of the rods and a tendency to become bound up axially in their spacer grids. The initial thermal bowing is then increased by the resulting axial loads as the temperature increases. In addition, thermal bowing will affect the geometry of the flow channel. The temperature field is determined by both free convection and conduction through the fluid.

†Staff Member, LASL.
‡University of New Mexico and Visiting Staff Member, LASL.

These problems are not the usual fluid structural interaction problems in that the inertial coupling is negligible. However, the thermal coupling appears to be very important. A survey of the literature reveals that no satisfactory finite element formulations are readily available for application to these experiments. Section 3 describes an efficient beam column finite element formulation while Section 4 describes the fluid element formulation. A coupled example is given in Section 5.

3. A BEAM COLUMN ELEMENT FOR MODERATELY LARGE ELASTIC DEFORMATION

The development of the beam-column element is considered in detail in a 1966 Jet Propulsion Lab report by Martin [3]. Subsequently, several texts on the finite element method have presented beam-column elements, such as: Martin and Carey, Prezemieniecki and Zienkiewicz [4-6]. A more elaborate and general treatment is available in the Massachusetts Institute of Technology report by Bolourchi and Bathe as an addendum to the ADINA finite element code [7, 8]. In both the first two references, the stiffness matrix is derived from second derivatives of the strain energy with respect to the spatial coordinates. Such approximation is permissible only when the quadratic terms in the strain energy function dominate, while the nonlinear effect is essentially perturbative. Prezemieniecki, though following a different approach, basically employed the assumption of Martin. Zienkiewicz separated the membrane and the bending strains at an early stage. As a result, the bending effect of the membrane force in an element is only secondary. Zienkiewicz developed the element only for a plate, and the example shows the result of covering the plate with 32 elements. The ADINA finite element is formulated in three-dimensional space and takes into account nonlinear symmetrical problems. The method of approach is based on the virtual work principle, which is considered most appropriate for nonlinear problems.

3.1 *Formulation of the beam column element*

Because the mathematical model of the element is based on the structural theory of the beam column, we stipulate that for every element the following conditions are satisfied: that the cross section is uniform; that its characteristic dimension (d) is of small order to the element length (l); that the slope is small everywhere in the element; and that the material properties are uniform with respect to the axial coordinate for one element.

In this formulation, there is no material nonlinearity, but the geometrical nonlinearity will be emphasized. The strain energy in general will not be a quadratic function of the spatial coordinates. This condition will govern the method in deriving the element stiffness matrix.

The kinematic and the loading states of a finite element are uniquely defined by the displacement vector and the force vector **a** and **f** at its nodes. Their components are shown in their respective positive directions in Fig. 2. Figure 2 shows the coordinates (x, y), the nodal point designation (I, J), the material and geometrical properties (E, A, $\bar{I}$), the components of the displacements (u, w, θ), and the force vectors (S, R, M) for the element.

Since both the lateral displacement and its derivative, $w(x)$ and θ, are defined at a node, a cubic function in x will be used, while a linear function will be sufficient for the axial displacement of a particle along the centroidal axis. Hence, the shape function $\mathbf{N}(x, y)$ is defined as

$$\mathbf{N}^T(x, y)=[\mathbf{N}_u(x, y)\mathbf{N}_w(x, y)]^T=\begin{bmatrix}\mathbf{N}_u(x, y)^T\\ \mathbf{N}_w(x, y)^T\end{bmatrix} \tag{1}$$

$$=\begin{bmatrix}(1-\xi) & \xi & (6/l)y\xi(1-\xi) & -y(1-\xi)(1-3\xi) & -(6/l)y\xi(1-\xi) & y\xi(2-3\xi)\\ 0 & 0 & (1-\xi)^2(1+2\xi) & l(1-\xi)^2\xi & \xi^2(3-2\xi) & -l(1-\xi)\xi^2\end{bmatrix},$$

material properties. It also takes into account the short beam effect by allowing the constant plane cross section to change its angle with respect to the neutral plane of the beam. However, as a result of simplifications for a symmetric stiffness matrix, it takes a number of elements for a single span of a beam column. Other noteworthy literature includes the formulation by Belytschko *et al.* [9] and the subsequent application to a problem of a reactor structure by Kennedy and Belytschko [10].

In the current development, the following conditions will be observed as applicable to the GCFR experiments. The material shall be linearly elastic. The deformation is moderately large according to von Karman's postulation. Two or three elements should be adequate to cover a single span of the beam column. The Euler–Bernoulli condition will be used; i.e. the cross sectional plane remains undeformed and orthogonal to the neutral plane. Planar deformation is assumed and considered adequate for plane and axi-

where $\xi = x/l$.

The displacement field in the element is defined uniquely by the nodal displacement vector through the shape function, as

$$\begin{Bmatrix}u(x, y)\\ w(x)\end{Bmatrix}=\begin{Bmatrix}\mathbf{N}_u^T\mathbf{a}\\ \mathbf{N}_w^T\mathbf{a}\end{Bmatrix}=\mathbf{N}^T\mathbf{a}, \tag{2}$$

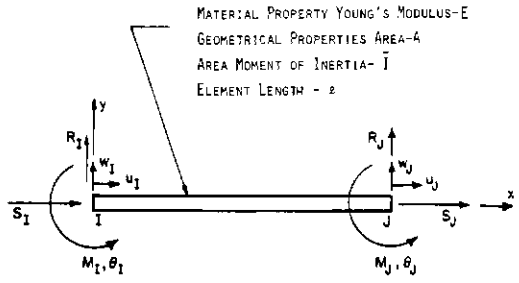

Fig. 2. Beam column element quantities and coordinates.

where

$$\mathbf{a}^T=[u_I\ u_J\ w_I\ \theta_I\ w_J\ \theta_J].$$

For a system in equilibrium, the principle of virtual work must hold regardless of the linearity of the system, that is

$$\delta U=\delta U^{(i)}+\delta U^{(e)}=0, \tag{3}$$

where the internal virtual work is the negative virtual change of strain energy, that is, $\delta U^{(i)}=-\delta U_e$.

With the postulation of the small strain (not small displacement) theory and by considering residual stress separately, we can use the Hookian Law†

$$\sigma_{ij}=C_{ijkl}\varepsilon_{lk}.$$

Because of the geometrical nonlinearity,

$$\varepsilon_{kl}=e_{kl}+\eta_{kl},$$

where $e_{kl}=\frac{1}{2}(u_{k,l}+u_{l,k})$ and $\eta_{kl}=\frac{1}{2}u_{j,k}u_{k,l}$.

The global strain energy is

$$U_e=\int_V\int_\varepsilon \sigma_{ij}\,\mathrm{d}\varepsilon_{ij}\,\mathrm{d}V.$$

Hence,

$$-\delta U^{(i)}=\delta U_e=\int_V \sigma_{ij}\delta\varepsilon_{ij}\,\mathrm{d}V$$
$$=\left\{\int_V C_{ijkl}e_{kl}\delta e_{ij}\,\mathrm{d}V+\int_V C_{ijkl}\eta_{kl}\delta e_{ij}\,\mathrm{d}V+\int_V \sigma_{ij}\delta\eta_{ij}\,\mathrm{d}V\right\}. \tag{4}$$

We shall find the internal virtual work in the form of

$$\delta U^{(i)}=-\delta\mathbf{a}^T\mathbf{K}\mathbf{a}. \tag{5}$$

Equation (5) combined with the known external virtual work expression

$$\delta U^{(e)}=\delta\mathbf{a}^T\mathbf{f}$$

is substituted into eqn (3) to yield

$$\delta\mathbf{a}^T(-\mathbf{K}\mathbf{a}+\mathbf{f})=0.$$

Since the virtual displacement is arbitrary, the equilibrium equation results as

$$\mathbf{f}=\mathbf{K}\mathbf{a}. \tag{6}$$

$\mathbf{K}$ is the stiffness matrix. In the derivation there is no differentiation of the strain energy density function.

In eqn (4) the first term on the right hand side contains only the linear portion of the strain tensor, while both of the last two terms contain the nonlinear portion of the strain tensor. We may express eqn (4) as

$$\delta U=\delta U_L+\delta U_N^{(1)}+\delta U_N^{(2)}, \tag{7}$$

where the subscripts L and N denote the linear and the nonlinear portions of the virtual change in strain energy respectively.

For the structural theory of beam column, the only nontrivial strain component is the longitudinal fiber strain $\varepsilon_{xx}=e_{xx}+\eta_{xx}$. Using the shape functions, eqn (2), the linear portion is

$$e_{xx}=\partial_x u(x,y)=\partial_x\mathbf{N}_u(x,y)^T\mathbf{a}=\mathbf{a}^T\partial_x\mathbf{N}_u$$

and the nonlinear portion is

$$\eta_{xx}=\tfrac{1}{2}\mathbf{a}^T[\partial_x\mathbf{N}_u\partial_x\mathbf{N}_u^T+\mathbf{N}_w'\mathbf{N}_w'^T]\mathbf{a}, \tag{8}$$

where ∂_i indicates the partial derivative with respect to coordinate i, and the prime indicates the derivative with respect to x. Their virtual variations are

$$\delta e_{xx}=\delta\mathbf{a}^T\partial_x\mathbf{N}_u$$
$$\delta\eta_{xx}=\delta\mathbf{a}^T[\partial_x\mathbf{N}_u\partial_x\mathbf{N}_u^T+\mathbf{N}_w'\mathbf{N}_w'^T]\mathbf{a}. \tag{9}$$

The elastic coefficient C_{ijkl} becomes Young's Modulus E. When eqn (8) and (9) are substituted in eqn (4) or a term thereof, there will be volume integrals of the products of shape functions of varying complexity.

For the linear term in eqn (4)

$$\delta U_L=\int_V Ee_{xx}\delta e_{xx}\,\mathrm{d}V$$
$$=\delta\mathbf{a}^T\left[E\int_0^l\int_A\partial_x\mathbf{N}_u\partial_x\mathbf{N}_u^T\,\mathrm{d}A\,\mathrm{d}x\right]\mathbf{a}.$$

We shall define K_L as the integrals in the brackets that can be carried out in closed form.

For the first nonlinear term in eqn (5) we have

$$\delta U_N^{(1)}=E\int_V\eta_{xx}\delta e_{xx}\,\mathrm{d}V$$
$$=\delta\mathbf{a}^T\left[\tfrac{1}{2}El\int_0^1\int_A\partial_x\mathbf{N}_u\mathbf{a}^T(\partial_x\mathbf{N}_u\partial_x\mathbf{N}_u^T+\mathbf{N}_w'\mathbf{N}_w'^T)\,\mathrm{d}A\,\mathrm{d}\xi\right]\mathbf{a}.$$

We again define the term inside the brackets as $\mathbf{K}_N^{(1)}$.

In the second nonlinear term of eqn (4), the fibre stress is

$$\sigma_{xx}(x,y)=\sigma(x,y)=\frac{S}{A}+\frac{M_R(x)y}{I},$$

where S is the axial force in the beam element, tensile being positive, and $M_R(x)$ is the resistant moment in the element such that

$$M_R=\left[m_I\left(1-\frac{x}{l}\right)-m_J\left(\frac{x}{l}\right)\right]-S[w(x)-w_I]$$
$$=[(1-\xi)\ \ -\xi]\begin{Bmatrix}m_I\\ m_J\end{Bmatrix}-S(\mathbf{N}_w^T\mathbf{a}-w_I).$$

The first term represents the bending moment due to the beam effect alone, excluding the bending from the column effect in that element. It is the result of the lateral load, the external moment and the thermal moment. Its distribution in the element is approximated by a linear function. The last term gives the column effect. $\{m_I\,m_J\}^T$ are the resistant moments at the leading and terminal ends of the element because of the beam effect only. The last term in eqn (4) becomes

$$\delta U_N^{(2)}=\int_V\sigma_{xx}\delta\eta_{xx}\,\mathrm{d}V$$
$$=\delta\mathbf{a}^T\left[\int_V\sigma(\partial_x\mathbf{N}_u\partial_x\mathbf{N}_u^T+\mathbf{N}_w'\mathbf{N}_w'^T)\,\mathrm{d}V\right]\mathbf{a}.$$

The expression inside the brackets is designated $\mathbf{K}_N^{(2)}$. Based on eqn (4), we obtain

$$\mathbf{K}=\mathbf{K}_L+\mathbf{K}_N^{(1)}+\mathbf{K}_N^{(2)}. \tag{11}$$

The integration that is defined in writing in eqn (11) is carried out and the element stiffness matrix for an

†Summation convention is used and applied to subscripts of Roman minuscules.

element with superscript I is written as

$$\mathbf{K}^I = \frac{(E\bar{I})^I}{l_I^3}\left(1+\frac{u_J-u_I}{2l_I}+\frac{S^I}{(EA)^I}\right)$$
$$\times\begin{bmatrix} \rho_I^{-2} & & & & & \text{sym} \\ 0 & 12 & & & & \\ 0 & 6l_I & 4l_I^2 & & & \\ -\rho_I^{-2} & 0 & 0 & \rho_I^{-2} & & \\ 0 & -12 & -6l_I & 0 & 12 & \\ 0 & 6l_I & 2l_I^2 & 0 & -6l_I & 4l_I^2 \end{bmatrix}$$

$$+\frac{S^I}{30l_I}\begin{bmatrix} 0 & & & & & \text{sym} \\ 0 & 36 & & & & \\ 0 & 3l_I & 4l_I^2 & & & \\ 0 & 0 & 0 & 0 & & \\ 0 & -36 & -3l_I & 0 & 36 & \\ 0 & 3l_I & -l_I^2 & 0 & -3l_I & 4l_I^2 \end{bmatrix}$$

$$+\frac{1}{2l_I^2}\left[6\left(\frac{(E\bar{I})^I}{l_I^2}-\frac{S^I}{5}\right)(w_I-w_J)+3\left(\frac{(E\bar{I})^I}{l_I}-\frac{S^I l_I}{30}\right)\right.$$
$$\left.\times(\theta_I+\theta_J)+(m_I^I+m_J^I)\right]\begin{bmatrix} 0 & & & & & \text{sym} \\ -2 & 0 & & & & \\ -l_I & 0 & 0 & & & \\ 0 & 2 & l_I & 1 & & \\ 2 & 0 & 0 & -2 & 0 & \\ -l_I & 0 & 0 & l_I & 0 & 0 \end{bmatrix}$$

$$+\frac{1}{2l_I}\left[S^I(w_I-w_J)+\left(\frac{(E\bar{I})^I}{l_I}-\frac{S^I l_I}{6}\right)(\theta_I-\theta_J)+(m_I^I-m_J^I)\right]$$
$$\times\begin{bmatrix} 0 & & & & & \text{sym} \\ 0 & 0 & & & & \\ -1 & 0 & 0 & & & \\ 0 & 0 & 1 & 0 & & \\ 0 & 0 & 0 & 0 & 0 & \\ 1 & 0 & 0 & -1 & 0 & 0 \end{bmatrix}$$

$$+(EA)^I\left\{\frac{w_I-w_J}{20l_I^2}\begin{bmatrix} 0 & -12 & -l & 0 & 12 & l \\ 0 & 0 & 0 & 0 & 0 & 0 \\ 0 & 0 & 0 & 0 & 0 & 0 \\ 0 & 12 & l & 0 & -12 & l \\ 0 & 0 & 0 & 0 & 0 & 0 \\ 0 & 0 & 0 & 0 & 0 & 0 \end{bmatrix}\right.$$
$$+\frac{\theta_I+\theta_J}{40l_I}\begin{bmatrix} 0 & -2 & -l & 0 & 2 & -l \\ 0 & 0 & 0 & 0 & 0 & 0 \\ 0 & 0 & 0 & 0 & 0 & 0 \\ 0 & 2 & l & 0 & -2 & l \\ 0 & 0 & 0 & 0 & 0 & 0 \\ 0 & 0 & 0 & 0 & 0 & 0 \end{bmatrix}$$
$$\left.+\frac{\theta_I-\theta_J}{24}\begin{bmatrix} 0 & 0 & -1 & 0 & 0 & 1 \\ 0 & 0 & 0 & 0 & 0 & 0 \\ 0 & 0 & 0 & 0 & 0 & 0 \\ 0 & 0 & 1 & 0 & 0 & -1 \\ 0 & 0 & 0 & 0 & 0 & 0 \\ 0 & 0 & 0 & 0 & 0 & 0 \end{bmatrix}\right\}. \tag{12}$$

The corresponding displacement and force vectors are

$$\mathbf{a}^T=[u_I\ w_I\ \theta_I\ u_J\ w_J\ \theta_J]$$
$$\mathbf{f}^T=[S_I\ R_I\ M_I\ S_J\ R_J\ M_J].$$

In the stiffness matrix, there are the nodal displacement terms (u_I, u_J, w_I, w_J, θ_I, θ_J) and the element resistant forces (S^I, m_I^I, m_J^I). These terms may or may not be known. Consequently, a numerical iteration scheme is necessary to derive the solution. The displacement terms are solved for at each iteration, while the element resistant forces must be computed or updated from the nodal forces, which are divided into internal and external components.

The nonsymmetry of this stiffness matrix can be handled by separating the bending and axial effects as shown in Ref. [11]. Because we will combine this element with a fluid element, and we will work with an available direct nonsymmetric banded solver, we choose to maintain this nonsymmetric form.

A beam column under a thermal load is equivalent to one subject to the mechanical load resulting from constraints to free thermal expansions. In the linear structural member such as the beam column, the thermal strain generates two effects. The mean value of the thermal strain over the cross sectional area results in the axial expansion. Its gradient across the cross section effectively bends the member as if there were an exterior moment.

The axial expansion comes from the areal mean of the temperature field over the cross sectional area, with the coefficients of thermal expansion and the Young's moduli as weighting functions. Free axial thermal expansion is ignored in the present formulation. A column effect results only when free axial thermal expansion is restricted. This restriction is treated as prescribed axial displacements at a pair of nodes.

The thermal strain gradient is input as a thermal moment. It can result from either a temperature gradient or a difference in coefficients of thermal expansion across the beam. The external moment is further separated into mechanical and thermal components with the thermal moment being linearly interpolated along the element length. Details are available in Ref. [11].

3.2 *Example problem*

The element formulation has been tested on a number of problems for which the solutions are known. The type of problem of interest in the GCFR experiments has dimensions and properties similar to that illustrated in Fig. 3. This figure shows the exact solution, a one element solution, and a two-element solution for a beam-column that is bent by a thermal gradient M_T until the end rotations reach 0.015 radians. At this rotation, which is typical of the end restrictions in a GCFR experimental test fixture, the ends become "locked" preventing further axial thermal expansion. This figure illustrates that the single element representation of a beam column span is inadequate while a two element representation of a single span can hardly be distinguished from the exact solution. These results are typical of the accuracy that can be achieved using

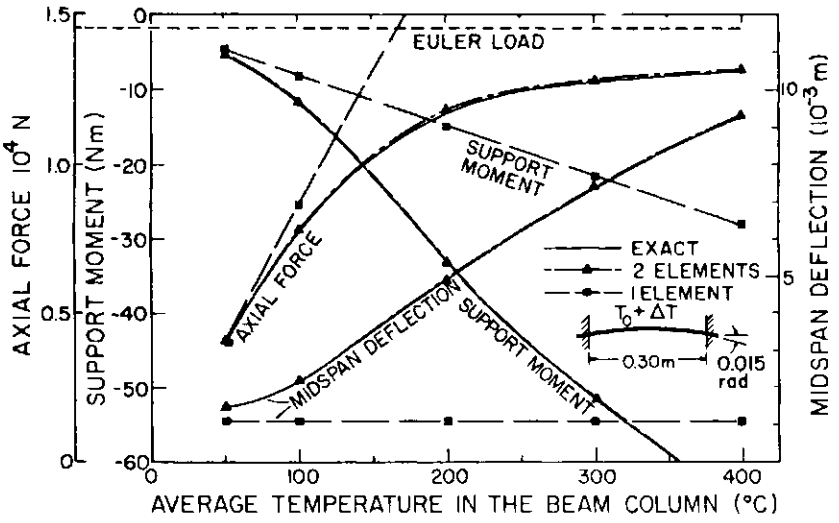

Fig. 3. Results from a 1- and 2-element thermally loaded beam column.

only two elements per span. The more accurate results are achieved by maintaining the full nonlinear unsymmetric element stiffness matrix.

4. FLUID ELEMENT FORMULATION

Another tool that has been developed for analysis of these experiments is a finite element description of a convecting fluid. A number of finite element formulations for convective heat transfer analysis are in the current literature [12-19]. Several international symposia have been held on the use of finite element analysis in fluid mechanics [20, 21], and summer courses have been given in the subject by the Texas Institute of Computational Mechanics at the University of Texas, Austin [22]. In addition, the 1979 ASME Winter Annual featured a special symposia on "Finite Element Methods for Convective Dominated Flows" [23].

Nearly all approaches currently in use are illustrated in Ref. [15], which features a discretization of the Navier–Stokes equations. Early in this program, these approaches were examined and were rejected as being computationally impractical if not impossible for application to the experiments of the GCFR program. This statement does not detract from their merit, but rather emphasizes the difficulties inherent in attempting to numerically model a GCFR module consisting of 237 fuel pins, the supporting spacer grids, and hexagonal duct walls with all the associated fluid flow channels. Even using gross axisymmetry the problem is a formidable one. For these reasons, a fluid description is needed that captures the relevant physics of a convecting fluid flow through the fuel rod bundle without a costly description of the fluid. This formulation, then, is based on the fact that there are numerous empirical, usually nonlinear, experimental relationships in the engineering literature relating the hydraulic gradient and velocity field for steady flows. Reference [24] rigorously shows that these relationships should exist for porous media based on the Navier–Stokes equations.

The linear form of this relationship is commonly known as Darcy's law and we begin the formulation with these expressions:

$$u=-\frac{k_x}{\mu}\left(\frac{\partial p}{\partial x}\right),\quad v=-\frac{k_y}{\mu}\left(\frac{\partial p}{\partial y}+\rho g\right),\quad w=-\frac{k_z}{\mu}\left(\frac{\partial p}{\partial z}\right) \tag{13}$$

where u, v, w = the bulk velocity of the fluid in the x, y and z directions; k_x, k_y, k_z = anisotropic flow resistance coefficients, which can be functions of the velocities; p = the pressure; μ = the fluid viscosity; ρ = the fluid density and g = the acceleration of gravity.

For steady incompressible laminar flow, the continuity equation can be written as

$$\frac{\partial u}{\partial x}+\frac{\partial v}{\partial y}+\frac{\partial w}{\partial z}=0.$$

Substituting the Darcy relationship into the incompressibility condition gives an equation of the form

$$\frac{\partial}{\partial x}\left(-\frac{k_x}{\mu}\frac{\partial p}{\partial x}\right)+\frac{\partial}{\partial y}\left(-\frac{k_y}{\mu}\frac{\partial p}{\partial y}\right)+\frac{\partial}{\partial z}\left(-\frac{k_z}{\mu}\frac{\partial p}{\partial z}\right)+\frac{\partial}{\partial y}\left(\frac{k_y}{\mu}\alpha g\rho_0 T\right)=0, \tag{14}$$

where we have incorporated the Boussinesq condition, $\rho=\rho_0[1-\alpha(T-T_0)]$, with T and T_0 being the fluid temperature and reference temperature for ρ_0, respectively, and α is the bulk coefficient of thermal expansion.

The energy equation for steady flow becomes

$$\rho C_p\left(u\frac{\partial T}{\partial x}+v\frac{\partial T}{\partial y}+w\frac{\partial T}{\partial z}\right)-\left[\frac{\partial}{\partial x}\left(\lambda_x\frac{\partial T}{\partial x}\right)+\frac{\partial}{\partial y}\left(\lambda_y\frac{\partial T}{\partial y}\right)+\frac{\partial}{\partial z}\left(\lambda_z\frac{\partial T}{\partial z}\right)\right]+Q_g=0, \tag{15}$$

where C_p = the fluid heat capacity; $\lambda_x, \lambda_y, \lambda_z$ = the anisotropic conduction coefficients and Q_g = the heat generation per unit volume.

(A) *Finite element equations*

The method of Weighted Residuals via the Galerkin approximation is applied to eqns (14) and (15) to give the following finite element equations

$$\int_v\left\{[B]\left[\frac{k}{\mu}\right][B]^T\{P\}+\frac{k_y}{\mu}\alpha g\rho_0\{N\}\frac{\partial\{N\}^T}{\partial y}\{T\}\right\}dV$$

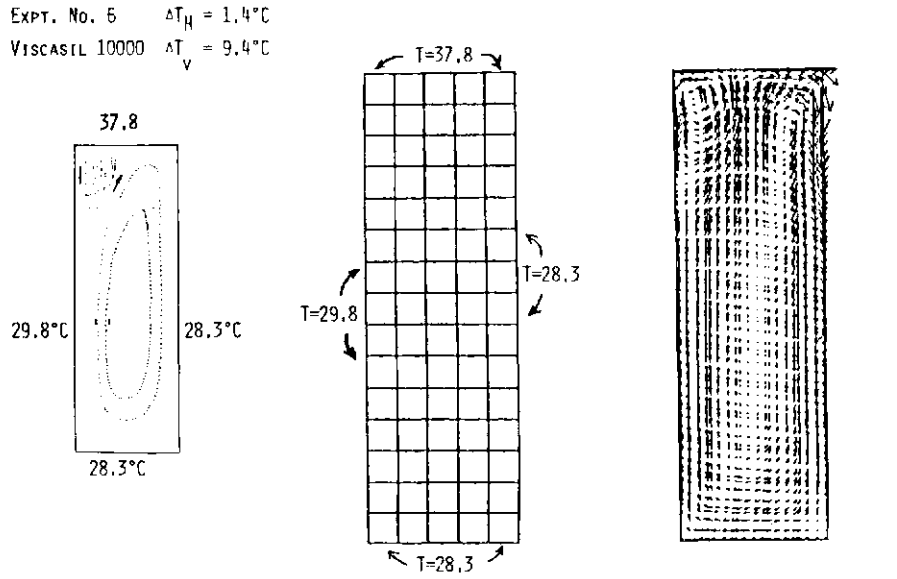

Fig. 4. Computer simulation of a convective flow experiment.

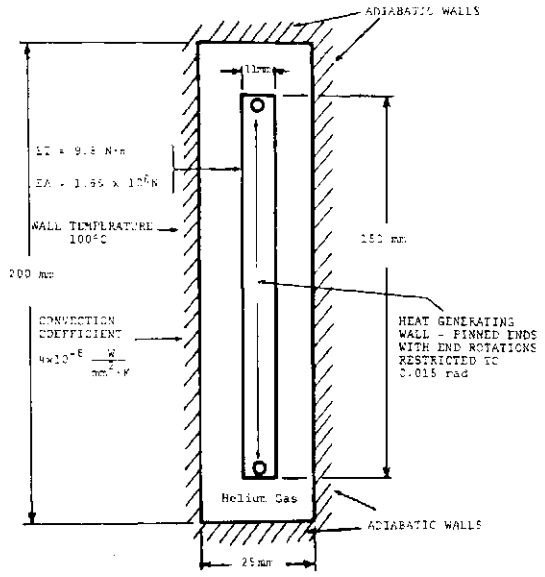

Fig. 5. Sample problem representing GCFR core module dimensions used for studying fluid/thermal/structure interaction effects.

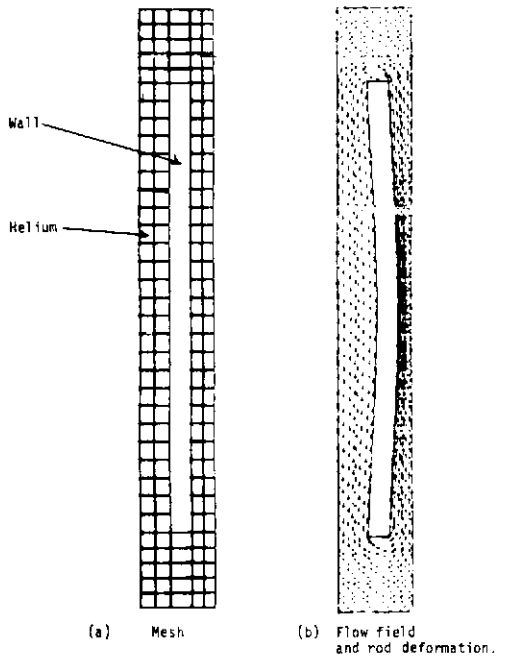

Fig. 6. Finite element mesh, wall deformation, and velocity field.

$$-\int_S \{N^*\} v_n \, dS = 0 \qquad (16)$$

and

$$\int_v \{\rho C_p \{N\}\{u\}^T [B]^T \{T\} + [B][\lambda][B]^T \{T\}\} \, dV + \int_v Q_g \{N\} \, dV - \int_S \{N^*\} q_n \, dS = 0 \qquad (17)$$

where $\{N\}$ is the vector of element interpolation functions, $[B]$ is the matrix of its derivatives with respect to the spatial variables, $\{T\}$ and $\{P\}$ are the vectors of the nodal point temperatures and pressures, $\{u\}$ is the velocity vector evaluated at Gauss points, $\{N^*\}$ are the element boundary shape functions, v_n and q_n are the boundary velocities and heat fluxes normal to the surface, respectively. Equations (15) and (16) were programmed into a finite element code using 8-node isoparametric elements, Gaussian quadrature, and "serendipity" shape functions. The details of this procedure are readily available in the literature [6, 25]. Since eqns (15) and (16) constitute a nonsymmetric but banded set of nonlinear algebraic equations, a Newton–Raphson scheme using a banded nonsymmetric solver was implemented for their solution. Temperature, pressure, heat fluxes, velocity, and convective boundary conditions are available options for the fluid boundaries.

This formulation differs from the usual formulation in that the pressure rather than velocity is the nodal point variable. In effect, the pressure takes the role of a velocity potential with velocities being evaluated from the discretized versions of eqn (13) at the element Gauss points.

4.2 *Sample analyses*

In an effort to illustrate the ability of the program to simulate the relevant physics of a convecting fluid flow, experimental work was sought such as in Ref. [25]. Several problems in this experimental study have been simulated. Figure 4 shows one such simulation in which an experimental apparatus was used to measure the effect of a vertical "stabilizing" temperature gradient on a convective flow established by a horizontal temperature gradient. Figure 4(a), from Ref. [24], shows the experimental boundary conditions and the streamline pattern that developed. Figure 4(b) shows the mesh and boundary conditions used to simulate the experiment and Fig. 4(c) shows the resulting velocity field.

The experiment clearly shows the two convection cells that develop, as does the computer simulation. Because of a lack of meaningful data, no direct velocity values were compared, but the streamline prediction appears to be in agreement for all problems simulated in this study.

5. FLUID/THERMAL/STRUCTURAL INTERACTION EXAMPLE

The sample problem shown in Fig. 5 has been studied to identify areas in the formulations that are important in simulating the GCFR experiments. The geometric dimensions boundary conditions, and thermal loadings were chosen to be representative of those encountered in the experiments. For this problem, notice that as the thermal gradient deforms the wall, the convective flow path for the right hand channel will become constricted, causing higher temperatures and further flow constriction. Clearly the mechanism is self reinforcing to some extent. Figure 6 shows the final rod deformation and velocity field obtained for this problem. The reinforcing mechanism was evidenced, but not strongly, in the iteration process by a further average temperature rise of about 5°C over the temperature initially calculated for the rod as the channel became restricted.

In this example, the average rod temperature is calculated as 500°C while the average thermal gradient across the rod is 80°C/mm. The maximum moment in the rod is computed to be 13.8 N-m occurring at the rod supports, while the axial force is computed to be 1.0×10^4 N. The original gap of 7 mm between the rod and the adiabatic wall is closed to 3.8 mm.

Although this sample problem is only a gross representation of the GCFR experiments, these tools show promise of being able to accurately characterize the relevant physics associated with them.

6. FUTURE PROJECTIONS AND RESEARCH

Results of our studies to date indicate that the convective flow field does not significantly influence the structural response but does significantly influence the temperature fields and thus the fuel rod cladding melting position. We have also determined that the end conditions on the fuel rods are important. Modifications to the beam column element are underway to allow frictional constraints for end conditions that will be closer to the actual conditions in the experiments.

Clearly the experiments are complex and three-dimensional in nature. Methods for the best usage of these analytical tools are being studied. Hopefully, conclusions drawn from the numerical simulations can be used as a guide in future experimental planning and research.

REFERENCES

1. D. L. Hanson and A. J. Giger, Experimental assessment of the effect of helium pressure on heat transfer in the GCFR core during a protected loss of flow accident. ASME Paper 79-HT-4 presented at the *Joint ASME/AiChe 18th Nat. Heat Transfer Conf.*, 6–8 Aug. 1979, San Diego, California.
2. D. L. Hanson and A. J. Giger, PLOF accident preview results of a test employing 34 simulated GCFR fuel rods. Los Alamos Scientific Laboratory report LA-UR-79-119 presented at the ANS meeting, 19 Aug. 1979, Seattle, Washington.
3. C. Martin, Large deflection and stability analysis by the direct stiffness method. Jet Propulsion Laboratory, *Tech. Rep. No.* 32-931, pp. 19–25 (1966).
4. H. C. Martin and G. F. Carey, *Introduction to Finite Element Analysis*, pp. 151–177. McGraw-Hill, New York (1973).
5. J. S. Prezemieniecki, *Theory of Matrix Structure Analysis*, pp. 384–397. McGraw-Hill, New York (1968).
6. O. C. Zienkiewicz, *The Finite Element Method*, 3rd Edn, pp. 500–512. McGraw-Hill, New York (1977).
7. Said Bolourchi and K. J. Bathe, A geometric and material nonlinear three-dimensional beam element. Dept. of Mech. Eng. Massachusetts Institute of *Tech. Rep. No.* 82448-4 (1977).
8. K. J. Bathe, ADINA: a finite element program for automatic dynamic incremental nonlinear analysis. *MITRep.* 82448-1, Sept. 1975 (Revised Dec. 1978).
9. T. B. Belytschko, L. Schwas and M. J. Klein, Large displacement, transient analysis of space frames. *Int. J. Numer. Meth. Engng* **11**, 65–84 (1977).
10. J. M. Kennedy and T. B. Belytschko, Formulation and application of a three-dimensional structural model for upper internal structures. Argonne National Laboratory report to the published (1980).
11. F. D. Ju, An efficient beam-column finite element including application to thermoelastic deformation. *Los Alamos Scientific Laboratory Report* LA-8229-MS, (Feb. 1980).
12. C. Taylor and P. Hood, A numerical solution of the Navier–Stokes equations using the finite element technique. *Int. J. Comput. Fluids* **1**(1), 73–100 (1973).
13. D. K. Gartling and E. B. Becker, Finite element analysis of viscous imcompressible flow, Part I: basic methodology. *Comput. Meth. Appl. Mech. Engng* **8**, 51–60 (1976).
14. D. K. Gartling and E. B. Becker, Finite element analysis of viscous incompressible flow, Part II: applications. *Comput. Meth. Appl. Mech. Engng* **8**, 127–138 (1976).
15. D. K. Gartling, Convective heat transfer analysis by the finite element method. *Comput. Meth. Appl. Mech. Engng* **12**, 365–382 (1977).
16. D. K. Gartling, NACHOS—a finite element computer program for incompressible flow problems, Part I and II, Sandia Laboratories SAND77-1333 and SAND77-1334 (1978).
17. D. K. Gartling, R. E. Nickell and R. I. Tanner, A finite element convergence study for accelerating flow problems. *Int. J. Numer. Meth. Engng* **11**, 1155 (1977).

18. R. H. Gallagher, *Finite Elements in Fluids*. Vols. 1–3. Wiley, New York (1978).
19. T. J. Chung, *Finite Element Analysis in Fluid Dynamics*. McGraw-Hill, New York (1978).
20. J. T. Oden, O. C. Zienkiewicz, R. H. Gallagher and C. Taylor, Finite element methods in flow problems. Univ. Alabama, Huntsville Press, Huntsville (1974).
21. International Centre for Computer Aided Design, preprints of the *2nd Int. Symp. on Finite Element Methods in Flow Problems*, Rapallo, Italy (1976).
22. Finite Element Analysis in Fluids Dynamics, 16–20 July 1979, The Texas Institute for Computational Mechanics, The University of Texas at Austin.
23. T. J. R. Hughes (Ed.), *Finite Element Methods for Convection Dominated Flows*, AMD-Vol 34. ASME (1979).
24. N. Ahmed and D. K. Sunada, Nonlinear flow in porous media. *Proc. ASCE J. Hydraulic Div.*, pp. 1843–8557 (1979).
25. S. Ostrach and C. Raghaven, Effect of stabilizing thermal gradients on natural convection in rectangular enclosures. *J. Heat Transfer* **101**, 239–243 (1979).

Computers & Structures, Vol. 13, pp. 181–188, 1981
Printed in Great Britain.

0045-7949/81/010181-08$02.00/0

TRANSIENT RESPONSE ANALYSIS OF STRUCTURAL SYSTEMS WITH NONLINEAR BEHAVIOR†

M. A. BHATTI and K. S. PISTER
University of California, Berkeley, CA 94720, U.S.A.

(*Received* 11 *May* 1980)

Abstract—This paper presents a mixed algorithm for integration of equations of motion for structural systems having evolutionary type models for cyclic behavior of their constituent elements. The global equations of motion are integrated using Newmark's method while the internal resisting forces are calculated using an explicit, fourth order Runge–Kutta scheme with the option of using a time-step smaller than that used for Newmark's method. The algorithm also takes advantage of the spatially localized nonlinear nature of the problem, in the case where nonlinearity is concentrated in discrete parts of the structure. As a numerical example, earthquake-induced response of a three-story steel frame tested on an Earthquake Simulator, is presented.

1. INTRODUCTION

A number of models has been employed to specify the force-deformation relationship for inelastic structural elements under cyclic loading. Two of the most common are the bilinear and the Ramberg–Osgood models. The bilinear model exhibits sharp transition from elastic to inelastic states. Kinematic or isotropic hardening rules are used for unloading and reloading. The model fails to represent actual material behavior and is computationally quite inefficient because it requires one to keep track of all stiffness transition points.

The Ramberg–Osgood model coupled with Masing's rule for unloading and reloading gives a continuous transition from elastic to inelastic states. This model is quite adequate for steel members but suffers from other limitations. For example, it is not possible to include isotropic hardening, stiffness degradation, etc. From a computational viewpoint, it is a very difficult model to use, because it specifies deformation as a function of force and therefore determination of forces given deformations requires iterative techniques. Moreover, Matzen and McNiven [1] have pointed out that the model as presented originally is not suitable for random earthquake-type excitations. At least thirteen new rules have been added to make it applicable to this case, making the model even harder to use. Figure 1 shows sample hysteresis loops generated by a Ramberg–Osgood model in which different parts requiring special attention have been identified.

Recently a series of models utilizing internal variables has been proposed for cyclic behavior of structural elements [2]. These models take the form of rate-type evolutionary equations and are sufficiently general to include strain-hardening, stiffness degradation, etc. Computations are facilitated since the same set of equations govern initial loading, unloading and reloading and the models behave well in case of arbitrary excitations. Since these models are in the form of differential equations, conventional methods for integration of global structural dynamics equations cannot be used directly. This paper presents a mixed algorithm for integration of equations of motion for the structural systems having evolutionary type models for cyclic behavior of their constituent elements. The global equations of motion are integrated using Newmark's method while the internal resisting forces are calculated using an explicit, fourth order Runge-Kutta scheme with the option of using a time-step smaller than that used for Newmark's method. The algorithm also takes advantage of the spatially localized nonlinear nature of the problem, in the case where non-linearity is concentrated in discrete parts of the structure, such as in rigid frames.

As a numerical example, earthquake-induced response of a three-story steel frame containing nonlinear energy-absorbing devices is presented. The frame chosen was tested on the Earthquake Simulator at the University of California, Berkeley. In addition, the significance of controlled, localized energy dissipation in earthquake-resistant design of structures is illustrated.

†This research was supported by the National Science Foundation Grant ENV76-04264.

2. A MODEL FOR HYSTERETIC BEHAVIOR OF NONLINEAR ELEMENTS

In Ref. [2], a number of models for describing hysteretic behavior of nonlinear elements are presented. The particular rate-independent model to be used for nonlinear elements in this study is given by the following equations:

$$\dot{F}(t)=K_0\left[\dot{\delta}(t)-|\dot{\delta}(t)|\left(\frac{F(t)}{F_0}-S\right)^n\right] \tag{1}$$

$$S(t)=\alpha\begin{bmatrix}\delta(t) & F(t)\\ \delta_0 & F_0\end{bmatrix} \tag{2}$$

where, $F(t)$ is the generalized force, $\delta(t)$ is generalized deformation and $\dot{\delta}(t)$ is the deformation rate of the nonlinear element. F_0, δ_0, α and n are material parameters. Physically, F_0 is generalized yield force, δ_0 is a generalized yield displacement, $K_0=F_0/\delta_0$ the initial stiffness, α is a constant which controls slope after yielding ($K_y\approx K_0[\alpha/1+\alpha]$), and n is taken as an odd integer which controls the sharpness of transition from the elastic to the inelastic region. As $n\to\infty$ the model approaches a bilinear model. Typical loops generated

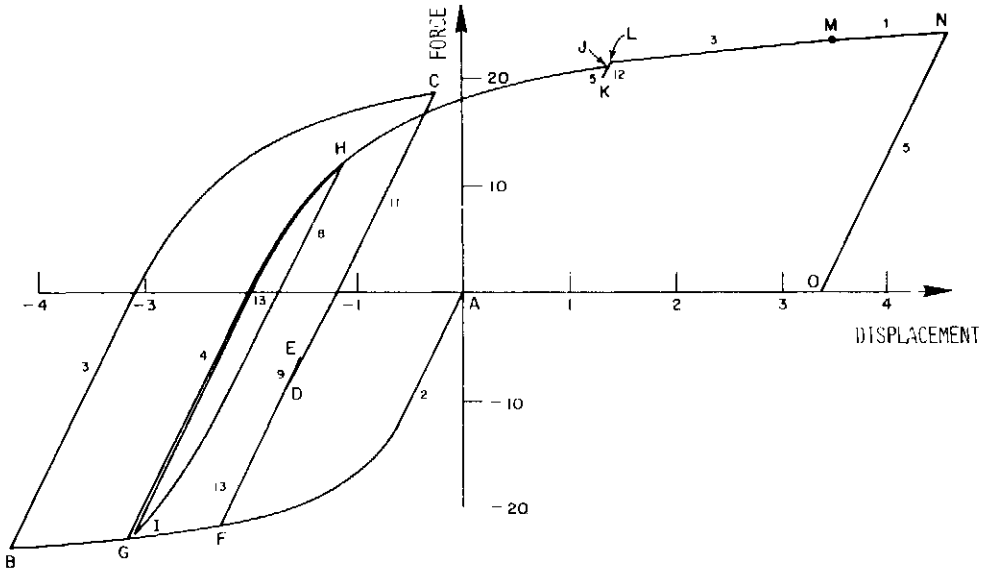

Fig. 1. Sample hysteresis loops from Ramberg-Osgood model.

by this model under deformation varying sinusoidally with time are shown in Fig. 2.

It should be pointed out that the above model is just one of a class of models for inelastic behavior. This particular choice was made for the immediate application of the present work to optimal design of frames with energy-absorbing devices. More complicated models, such as models exhibiting stiffness degradation, etc., can be obtained by introducing more parameters into the basic model, as explained in Ref. [2]. These models can be introduced into the present formulation without any difficulty.

3. EQUATIONS OF MOTION FOR THE SYSTEM

Equations of motion for a discrete, N degree-of-freedom structural system subjected to earthquake ground motion can be written as follows [3]:

$$\mathbf{M}\ddot{\mathbf{u}}(t)+\mathbf{C}\dot{\mathbf{u}}(t)+\mathbf{F}(t)=-\mathbf{M}\mathbf{r}\ddot{u}_g(t) \tag{3}$$

where $\mathbf{u}(t)=[u_1(t), u_2(t), \ldots, u_N(t)]^T$ is the nodal point displacement vector; $\dot{\mathbf{u}}(t)$ = nodal point velocity vector; $\ddot{\mathbf{u}}(t)$ = nodal point acceleration vector; $\mathbf{M}$ = mass matrix of the system, $\mathbf{M}\in\mathbb{R}^N\times\mathbb{R}^N$; $\mathbf{C}$ = structural damping matrix, $\mathbf{C}\in\mathbb{R}^N\times\mathbb{R}^N$; $\mathbf{F}$ = nodal force vector, $\mathbf{F}\in\mathbb{R}^N$; $\mathbf{r}$ = earthquake influence coefficient vector, $\mathbf{r}\in\mathbb{R}^N$. This vector represents displacements at nodal degrees of freedom resulting from a unit support displacement. For example, $\mathbf{r}=(1, 1, \ldots, 1)^T$ for an N story shear frame (with one degree of freedom at each story) subjected to horizontal ground motion and $\ddot{u}_g(t)$ = ground acceleration time history.

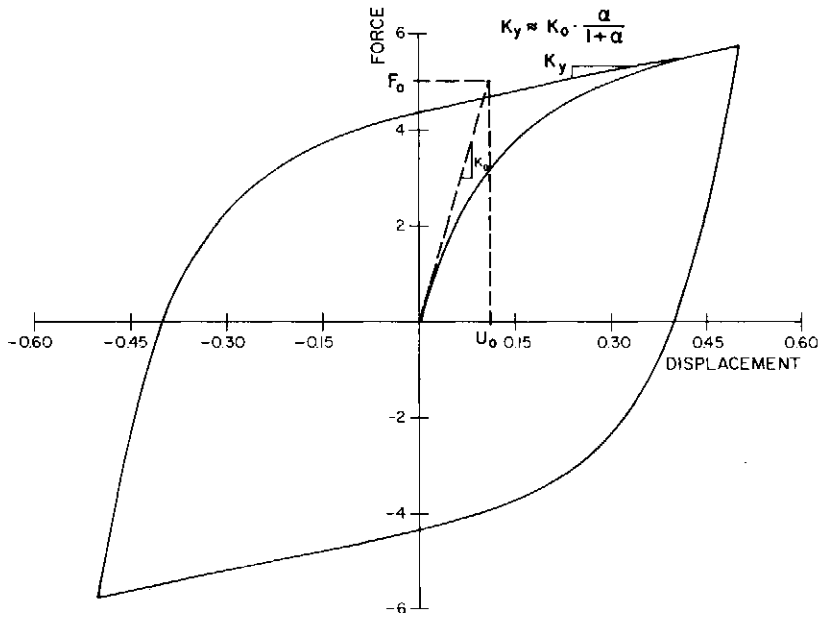

Fig. 2. Hysteresis loops generated by rate-independent model under sinusoidal excitation.

4. NUMERICAL SOLUTION OF THE DIFFERENTIAL EQUATIONS OF MOTION

The equations of motion (3) are solved numerically with the exact solution $\mathbf{u}(t)$, $\dot{\mathbf{u}}(t)$ and $\ddot{\mathbf{u}}(t)$ approximated by $\mathbf{u}_t$, $\dot{\mathbf{u}}_t$ and $\ddot{\mathbf{u}}_t$, respectively, at discrete time intervals. The step-by-step integration procedures start with the known initial conditions and march forward in time giving the solution at discrete points in time. The process for a nonlinear system has two distinct phases. The first phase is the linearization phase, in which the equations are linearized about the current state by retaining only first-order terms of a Taylor series expansion. Estimates of the solution at the next step are then obtained by using these linearized equations. The second phase is the state determination phase, in which the internal forces in equilibrium with the new state of motion are calculated. If the discrepancy between these internal forces and the external applied loads is within some tolerance level, the solution is accepted and the process repeated for the next step. Otherwise, a Newton–Raphson type iteration is used until the unbalanced forces are within acceptable limits.

In this study, estimates of the solution are obtained using Newmark's method, and internal forces in the nonlinear elements are computed using a fourth-order Runge–Kutta scheme. Details of the process are given below.

The equations of motion (3) at time $\tau = t + \Delta t$ can be written as

$$\mathbf{M}\ddot{\mathbf{u}}_\tau + \mathbf{C}\dot{\mathbf{u}}_\tau + \mathbf{F}_\tau = \mathbf{P}_\tau \tag{4}$$

$$\text{where } \mathbf{P}_\tau = -\mathbf{M}\mathbf{r}\ddot{u}_g(\tau).$$

Define the increments in acceleration, velocity, displacement and force occurring in the time increment Δt by

$$\begin{aligned}
\Delta\ddot{\mathbf{u}}_t &= \ddot{\mathbf{u}}_\tau - \ddot{\mathbf{u}}_t \\
\Delta\dot{\mathbf{u}}_t &= \dot{\mathbf{u}}_\tau - \dot{\mathbf{u}}_t \\
\Delta\mathbf{u}_t &= \mathbf{u}_\tau - \mathbf{u}_t \\
\Delta\mathbf{F}_t &= \mathbf{F}_\tau - \mathbf{F}_t \\
&\approx \frac{\partial \mathbf{F}_t}{\partial \mathbf{u}_t}\Delta\mathbf{u}_t = \mathbf{K}_t\Delta\mathbf{u}_t
\end{aligned} \tag{5}$$

Substituting these expressions in eqn (4), the incremental form of the equations of motion is obtained as follows:

$$\mathbf{M}\Delta\ddot{\mathbf{u}}_t + \mathbf{C}\Delta\dot{\mathbf{u}}_t + \mathbf{K}_t\Delta\mathbf{u}_t = \mathbf{P}_t^* \tag{6}$$

where $\mathbf{P}_t^* = \mathbf{P}_\tau - [\mathbf{M}\ddot{\mathbf{u}}_t + \mathbf{C}\dot{\mathbf{u}}_t + \mathbf{F}_t]$.

4.1 *Newmark's method*

An implicit, single-step, two parameter family of integration operators described by Newmark [4] is used for the numerical integration of the equations of motion. The method assumes that the increments in velocity and acceleration are related to the increment in displacement and the state of motion at time t, as follows:

$$\Delta\dot{\mathbf{u}}_t = \frac{\gamma}{\beta\Delta t}\Delta\mathbf{u}_t - \frac{\gamma}{\beta}\dot{\mathbf{u}}_t - \Delta t\left(\frac{\gamma}{2\beta} - 1\right)\ddot{\mathbf{u}}_t \tag{7}$$

$$\Delta\ddot{\mathbf{u}}_t = \frac{1}{\beta(\Delta t)^2}\Delta\mathbf{u}_t - \frac{1}{\beta\Delta t}\dot{\mathbf{u}}_t - \frac{1}{2\beta}\ddot{\mathbf{u}}_t \tag{8}$$

where Δt is time step of integration and γ, β are integration parameters. A "constant average acceleration" operator, which is unconditionally stable for linear problems, is obtained with $\beta = 1/4$ and $\gamma = 1/2$. A "linear acceleration" operator is obtained with $\beta = 1/6$ and $\gamma = 1/2$.

Substituting (7) and (8) into the incremental equations of motion (6) and simplifying gives

$$\mathbf{K}_t^*\Delta\mathbf{u}_t = \mathbf{R}_t^* \tag{9}$$

where

$$\mathbf{K}_t^* = \frac{1}{\beta\Delta t}\mathbf{M} + \frac{\gamma}{\beta\Delta t}\mathbf{C} + \mathbf{K}_t$$

$$\mathbf{R}_t^* = \mathbf{P}_t^* + \mathbf{M}\left[\frac{1}{\beta\Delta t}\dot{\mathbf{u}}_t + \frac{1}{2\beta}\ddot{\mathbf{u}}_t\right] + \mathbf{C}\left[\frac{\gamma}{\beta}\dot{\mathbf{u}}_t + \Delta t\left(\frac{\gamma}{2\beta} - 1\right)\ddot{\mathbf{u}}_t\right].$$

4.2 *Solution of* $\mathbf{K}_t^*\Delta\mathbf{u}_t = \mathbf{R}_t^*$

The most expensive part of the integration process is the solution of the above set of linear equations. Fortunately, for spatially localized nonlinear problems, it is not necessary to form and decompose the whole matrix $\mathbf{K}_t^*$ at each step. The substructuring technique is used to separate effectively the nonlinear part from the linear part of the problem as follows:

Partition the displacement vector such that displacements corresponding to the nonlinear degrees of freedom are separated from the remaining displacements:

$$\Delta\mathbf{u}_t = \begin{bmatrix}\Delta\mathbf{u}^E \\ \Delta\mathbf{u}^N\end{bmatrix}$$

where $\Delta\mathbf{u}^N$ = incremental displacements corresponding to the nonlinear degrees of freedom and $\Delta\mathbf{u}^E$ = incremental displacements corresponding to the rest of the system.

Partition $\mathbf{K}_t^*$ and $\mathbf{R}_t^*$ accordingly, as follows:

$$\begin{bmatrix}\mathbf{K}_{EE} & \mathbf{K}_{EN} \\ \mathbf{K}_{NE} & \mathbf{K}_{NN}\end{bmatrix}\begin{Bmatrix}\Delta\mathbf{u}^E \\ \Delta\mathbf{u}^N\end{Bmatrix} = \begin{Bmatrix}\mathbf{R}^E \\ \mathbf{R}^N\end{Bmatrix}. \tag{10}$$

The first submatrix equation gives:

$$\mathbf{K}_{EE}\Delta\mathbf{u}^E + \mathbf{K}_{EN}\Delta\mathbf{u}^N = \mathbf{R}^E$$

or

$$\Delta\mathbf{u}^E = \mathbf{K}_{EE}^{-1}[\mathbf{R}^E - \mathbf{K}_{EN}\Delta\mathbf{u}^N] \tag{11}$$

The second submatrix equation in eqn (10) gives:

$$\mathbf{K}_{NE}\Delta\mathbf{u}^E + \mathbf{K}_{NN}\Delta\mathbf{u}^N = \mathbf{R}^N. \tag{12}$$

Substitute eqn (11) into eqn (12):

$$\mathbf{K}_{NE}\mathbf{K}_{EE}^{-1}[\mathbf{R}^E - \mathbf{K}_{EN}\Delta\mathbf{u}^N] + \mathbf{K}_{NN}\Delta\mathbf{u}^N = \mathbf{R}^N.$$

Define

$$\mathbf{Q} = -\mathbf{K}_{EE}^{-1}\mathbf{K}_{EN},$$

then

$$\mathbf{Q}^T = -\mathbf{K}_{NE}\mathbf{K}_{EE}^{-1}.$$

Thus,

$$[\mathbf{K}_{NE}\mathbf{Q} + \mathbf{K}_{NN}]\Delta\mathbf{u}^N = \mathbf{R}^N + \mathbf{Q}^T\mathbf{R}^E,$$

or

$$\Delta\mathbf{u}^N = [\mathbf{K}_{NE}\mathbf{Q} + \mathbf{K}_{NN}]^{-1}[\mathbf{R}^N + \mathbf{Q}^T\mathbf{R}^E]. \tag{13}$$

Once the $\Delta\mathbf{u}^N$ are known, $\Delta\mathbf{u}^E$ are calculated from eqn (11).

The computational steps can be summarized in the following algorithm.

Algorithm

In the beginning of the integration loop
(i) form $\mathbf{K}_{EE}$, $\mathbf{K}_{EN}$, $\mathbf{K}_{NE}=\mathbf{K}_{EN}^T$,
(ii) triangularize $\mathbf{K}_{EE}$,
(iii) obtain $\mathbf{Q}$ by forward reduction and back substitution from $\mathbf{K}_{EE}\mathbf{Q}=-\mathbf{K}_{EN}$,
(iv) form $\mathbf{Q}^T$ and the product $\mathbf{K}_{NE}\mathbf{Q}$.
At each time step of integration,
(i) form $\mathbf{K}_{NN}$ at the current step,
(ii) form load vectors $\mathbf{R}^E$ and $\mathbf{R}^N$,
(iii) solve $[\mathbf{K}_{NE}\mathbf{Q}+\mathbf{K}_{NN}]\Delta\mathbf{u}^N=\mathbf{R}^N+\mathbf{Q}^T\mathbf{R}^E$ for $\Delta\mathbf{u}^N$,
(iv) obtain $\Delta\mathbf{u}^E$ by forward reduction and back substitution from

$$\mathbf{K}_{EE}\Delta\mathbf{u}^E=\mathbf{R}^E-\mathbf{K}_{EN}\Delta\mathbf{u}^N.$$

4.3 *Computation of internal resisting forces*

After the increments in the displacements and velocities are obtained, the next step is to compute the internal resisting forces in equilibrium with this new state of motion. The internal forces in the linear elements are obtained simply by multiplying the current displacement by the appropriate stiffnesses of these elements. Computation of forces in the nonlinear elements, however, is not so simple, because of lack of an algebraic expression for their force-deformation behavior, which is described by a set of first-order differential equations. These differential equations must be integrated numerically to obtain the internal forces in the nonlinear elements. An explicit fourth-order Runge–Kutta scheme, with the option of using a smaller time step than the one used in Newmark's method, is used in this study. An explicit scheme is favored over an implicit scheme because of the added complexity of an implicit scheme, which would involve an additional iteration cycle. The details of the process are given below.

To integrate force-deformation equations of nonlinear elements from time t to time $\tau=t+\Delta t$, some assumptions regarding the variation of acceleration, velocity and displacement during the time interval (t,τ) are needed. Since the Newmark's linear acceleration method has been demonstrated to be quite effective for solving nonlinear structural dynamic problems [5], it seems reasonable to assume linear variation in the acceleration during the time interval. This implies quatratic variation of velocity and cubic variation of displacement. These variations are shown in Fig. 3.

The force corresponding to the ith nonlinear degree of freedom is given by eqns (1) and (2).

$$\dot{F}_i(x)=K_0\left\{\dot{\delta}_i(x)-|\dot{\delta}_i(x)|\left[\frac{F_i(x)}{F_0}-S_i(x)\right]^n\right\} \tag{14}$$

$$S_i(x)=\alpha\left[\frac{\delta_i(x)}{\delta_0}-\frac{F_i(x)}{F_0}\right] \tag{15}$$

$$x\in[0,\Delta t],$$

where $\delta_i(x)$ is the deformation corresponding to the ith degree of freedom. The deformations are related to nodal displacements by a transformation matrix which depends upon the type of structural system. For example, for a shear frame $\delta_i=u_i-u_{i-1}$, while more

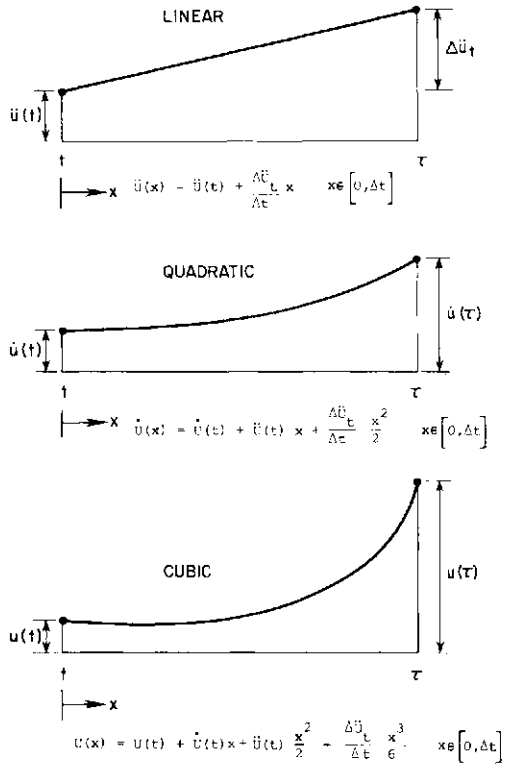

Fig. 3. Variations in acceleration, velocity and displacement during time interval $[t,\tau=t+\Delta t]$.

complicated expressions are required for other types of frames. Combining eqns (14) and (15) then

$$\dot{F}_i(x)=K_0\left[\dot{\delta}_i(x)-|\dot{\delta}_i(x)|\left\{(\alpha+1)\frac{F_i(x)}{F_0}-\alpha\frac{\delta_i(x)}{\delta_0}\right\}^n\right]$$
$$x\in[0,\Delta t]. \tag{16}$$

Equation (16) is integrated by employing a fourth-order Runge–Kutta method with time step Δx, where $\Delta x\leqq\Delta t$, and initial condition $F_i(0)=F_i(t)$.

The following calculations advance the solution from $x_K\to x_{K+1}=x_K+\Delta x$.

$$K_1=\Delta x\,K_0\left[\dot{\delta}_i(x_K)-|\dot{\delta}_i(x_K)|\left\{(\alpha+1)\frac{F_i(x_K)}{F_0}-\alpha\frac{\delta_i(x_K)}{\delta_0}\right\}^n\right]$$

$$K_2=\Delta x\,K_0\left[\dot{\delta}_i(x_K+\tfrac{1}{2}\Delta x)-|\dot{\delta}_i(x_K+\tfrac{1}{2}\Delta x)|\left\{(\alpha+1)\frac{F_i(x_K)+\frac{1}{2}K_1}{F_0}-\alpha\frac{\delta_i(x_K+\frac{1}{2}\Delta x)}{\delta_0}\right\}^n\right]$$

$$K_3=\Delta x\,K_0\left[\dot{\delta}_i(x_K+\tfrac{1}{2}\Delta x)-|\dot{\delta}_i(x_K+\tfrac{1}{2}\Delta x)|\times\left\{(\alpha+1)\frac{F_i(x_K)+\frac{1}{2}K_2}{F_0}-\alpha\frac{\delta_i(x_K+\frac{1}{2}\Delta x)}{\delta_0}\right\}^n\right]$$

$$K_4=\Delta x\,K_0\left[\dot{\delta}_i(x_K+\Delta x)-|\dot{\delta}_i(x_K+\Delta x)|\times\left\{(\alpha+1)\frac{F_i(x_K)+K_3}{F_0}-\alpha\frac{\delta_i(x_K+\Delta x)}{\delta_0}\right\}^n\right]$$

where

$$\dot{\delta}_i(y)=\dot{\delta}_i(t)+\ddot{\delta}_i(t)y+\frac{\Delta\ddot{\delta}_i}{\Delta x}\frac{y^2}{2}$$

$$\delta_i(y)=\delta_i(t)+\dot{\delta}_i(t)y+\ddot{\delta}_i(t)\frac{y^2}{2}+\frac{\Delta\ddot{\delta}_i}{\Delta x}\frac{y^3}{6}.$$

then

$$F_i(x_{K+1}) = F_i(x_K) + \frac{1}{6}(K_1 + 2K_2 + 2K_3 + K_4). \tag{17}$$

4.4 *Algorithm for integration of the equations of motion*

The process of numerical integration of the equations of motion (3) can now be summarized in the following algorithm.

A. *Initial calculations*

Data: Integration parameters, β, γ; Time steps, Δt and Δx; Convergence tolerance parameter, TOL; Structural property matrices, $\mathbf{K}^E$, $\mathbf{M}$ and $\mathbf{C}$; Parameters of hysteretic model for nonlinear elements, F_0, δ_0, α and n.

Step 1: Compute the constants

$$a_1 = \frac{1}{\beta(\Delta t)^2} \quad a_2 = \frac{1}{\beta \Delta t} \quad a_3 = \frac{1}{2\beta}$$

$$a_4 = \frac{\gamma}{\beta \Delta t} \quad a_5 = \frac{\gamma}{\beta} \quad a_6 = \Delta t\left[\frac{\gamma}{2\beta} - 1\right]$$

Step 2: Initialize the state of motion, i.e. specify $\mathbf{u}_0$, $\dot{\mathbf{u}}_0$ and $\ddot{\mathbf{u}}_0$.

Step 3: Form structural property matrices, $\mathbf{M}$ and $\mathbf{C}$. Partition the stiffness matrix as explained in eqn (10), triangularize $\mathbf{K}_{EE}$ and form $\mathbf{Q}$.

B. *For each time step*

Step 4: Form $\mathbf{K}_t^*$ and $\mathbf{R}_t^*$

$$\mathbf{K}_t^* = a_1\mathbf{M} + a_4\mathbf{C} + K^t$$
$$\mathbf{R}_t^* = \mathbf{P}_t^* + \mathbf{M}[a_2\dot{\mathbf{u}}_t + a_3\ddot{\mathbf{u}}_t] + \mathbf{C}[a_5\dot{\mathbf{u}}_t + a_6\ddot{\mathbf{u}}_t]$$

where $\mathbf{P}_t^* = \mathbf{P}_\tau - [\mathbf{M}\ddot{\mathbf{u}}_t + \mathbf{C}\dot{\mathbf{u}}_t + \mathbf{F}_t]$ and $\mathbf{P}_\tau = -\mathbf{M}\mathbf{r}\ddot{u}_g(\tau)$.

Step 5: Solve

$$\mathbf{K}_t^* \Delta\mathbf{u}_t = \mathbf{R}_t^*$$

for $\Delta\mathbf{u}_t$, using the algorithm given previously.

Step 6: Update the state of motion at $\tau = t + \Delta t$

$$\ddot{\mathbf{u}}_\tau = \ddot{\mathbf{u}}_t + a_1\Delta\mathbf{u}_t - a_2\dot{\mathbf{u}}_t - a_3\ddot{\mathbf{u}}_t$$
$$\dot{\mathbf{u}}_\tau = \dot{\mathbf{u}}_t + a_4\Delta\mathbf{u}_t - a_5\dot{\mathbf{u}}_t - a_6\ddot{\mathbf{u}}_t$$
$$\mathbf{u}_\tau = \mathbf{u}_t + \Delta\mathbf{u}_t.$$

Step 7: Compute the internal resisting forces, $\mathbf{F}_\tau$, in equilibrium with the current state, as explained previously.

Step 8: Compute the unbalanced force at time τ

$$\mathbf{f} = \mathbf{P}_\tau - [\mathbf{M}\ddot{\mathbf{u}}_\tau + \mathbf{C}\dot{\mathbf{u}}_\tau + \mathbf{F}_\tau].$$

Step 9: Compute $\|\mathbf{f}\|_2$, the Euclidean norm of $\mathbf{f}$. If $\|\mathbf{f}\|_2 \leq$ TOL, no iteration is needed in this step. Go to Step 4 for the next step calculations, else proceed to Step 10.

C. *Iteration within a time step*

Step 10: Compute $\mathbf{K}_\tau^* = a_1\mathbf{M} + a_4\mathbf{C} + \mathbf{K}_\tau$.

Step 11: Solve $\mathbf{K}_\tau^*\delta\mathbf{u}_\tau = \mathbf{f}$ for $\delta\mathbf{u}_\tau$.

Step 12: Update the state of motion

$$\text{new } \ddot{\mathbf{u}}_\tau = \ddot{\mathbf{u}}_\tau + a_1\delta\mathbf{u}_\tau$$
$$\text{new } \dot{\mathbf{u}}_\tau = \dot{\mathbf{u}}_\tau + a_4\delta\mathbf{u}_\tau$$
$$\text{new } \mathbf{u}_\tau = \mathbf{u}_\tau + \delta\mathbf{u}_\tau.$$

Step 13: Compute the unbalance as in Step 8. See if convergence criterion of Step 9 is satisfied. If yes, go to Step 4 for next time step. Else go to Step 10.

5. NUMERICAL EXAMPLE

As an example, the technique is applied to compute earthquake-induced response of a steel frame with an earthquake isolation system, tested on the Earthquake simulator at the Earthquake Engineering Research Center, University of California, Berkeley. The test structure is a three-story steel frame with added masses at each floor as shown in Fig. 4. The structure is supported vertically by specially designed rubber bearings whose properties are specified. The bearings also provide nominal shear resistance. An energy-absorbing device is linked to the base of the structure as shown. This device acts as a hysteretic passive controller, supplying a time-dependent horizontal force to the base. Details of the test configuration and the results can be found in reference [6]. The tests show that for strong earthquakes the energy-absorbing device yields and absorbs amounts of energy equivalent to as much as 35% of critical viscous damping. Thus the frame itself is left without damage.

In the following sections, equations of motion for the test frame are given and the response is computed using the algorithm given in section 4. It is assumed that the frame itself remains elastic, so that the only nonlinearity is in the energy-absorbing device.

5.1 *Equations of motion for the test frame*

As shown in Fig. 4, the structural system consists of an assemblage of beam and column sections. Masses are assumed to be lumped at the floor levels and rotary inertia is neglected. Axial deformations in both beams and columns are neglected. Thus, the frame has 12 degrees of freedom; one lateral and two rotational degrees of freedom per floor. Rotational degrees of freedom may be eliminated by appropriate partitioning of the mass, damping and stiffness matrices associated with the discretized structural model of the frame. The resulting equations of motion can be written [3]:

$$\mathbf{M}\ddot{\mathbf{u}}(t) + \mathbf{C}\dot{\mathbf{u}}(t) + \mathbf{K}^E\mathbf{u}(t) - \mathbf{F}(t) = -\mathbf{M}\mathbf{r}\ddot{u}_g(t) \tag{18}$$

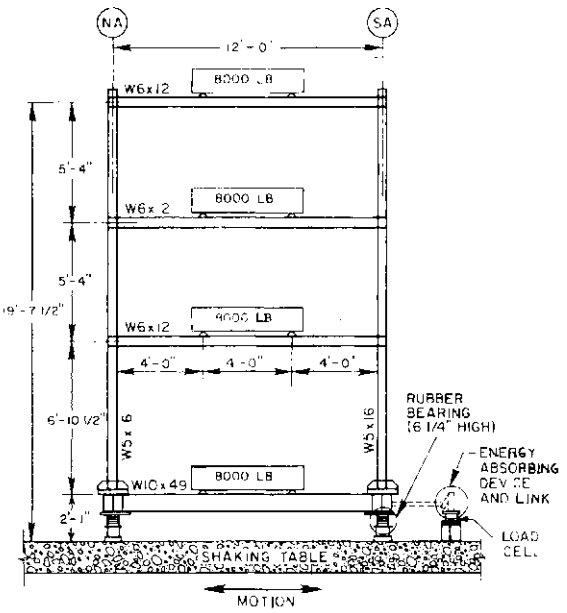

Fig. 4. Steel test frame.

where $\mathbf{K}^E$ = stiffness matrix of the frame including the rubber bearings but not the energy-absorbing device; $\mathbf{F}$ = force in the energy-absorbing device. The only nonzero entry in this vector corresponds to the degree of freedom at which the energy-absorbing device is connected. In this case, only F_4 will be nonzero and $\mathbf{r}^T = [1111]$.

The structural property matrices, $\mathbf{K}^E$, $\mathbf{M}$ and $\mathbf{C}$ can be calculated from the material and section properties shown in Fig. 4. Thus, the lateral, elastic stiffness matrix of the complete structure, including the stiffness of the rubber bearings is (units are kip-inches):

$$\mathbf{K}^E = \begin{bmatrix} 46.38 & -66.64 & 23.04 & -2.78 \\ & 144.40 & -96.50 & 18.74 \\ & & 122.43 & -48.97 \\ \text{SYMMETRIC} & & & 34.21 \end{bmatrix}.$$

The mass matrix of the structure corresponding to the lateral degrees of freedom is (in kip-inch units):

$$\mathbf{M} = \begin{bmatrix} 0.02438 & & & \\ & 0.02438 & & \\ & & 0.02514 & \\ & & & 0.02832 \end{bmatrix}.$$

Rayleigh damping is assumed in constructing the damping matrix:

$$\mathbf{C} = \alpha\mathbf{M} + \beta\mathbf{K}^E. \tag{19}$$

The coefficients α and β are computed from:

$$\begin{bmatrix} \frac{1}{\omega_1} & \omega_1 \\ \frac{1}{\omega_2} & \omega_2 \end{bmatrix} \begin{Bmatrix} \alpha \\ \beta \end{Bmatrix} = \begin{Bmatrix} \xi_1 \\ \xi_2 \end{Bmatrix}, \tag{20}$$

where ω_1 and ω_2 are first and second mode frequencies, and ξ_1 and ξ_2 are the respective critical damping ratios in these modes. The damping matrix for the present structures, assuming $\xi_1 = 3\%$ and $\xi_2 = 1\%$, is given below.

$$\mathbf{C} = \begin{bmatrix} 0.0279 & -0.0332 & 0.0115 & 0.0014 \\ & 0.0768 & -0.0481 & 0.0093 \\ & & 0.0660 & -0.0244 \\ \text{SYMMETRIC} & & & 0.0226 \end{bmatrix} \tag{14}$$

The force in the device is computed from eqns (1) and (2), which for this application take the form:

$$\dot{F}_4(t) = K_0 \left[\dot{u}_4(t) - |\dot{u}_4(t)| \left(\frac{F_4(t)}{F_0} - S \right)^n \right] \tag{21}$$

$$S(t) = \alpha \left[\frac{u_4(t)}{\delta_0} - \frac{F_4(t)}{F_0} \right].$$

The tangent stiffness matrix $\mathbf{K}_t$ at any time is obtained by adding $\partial F_4(t)/\partial \dot{u}_4$ to K^E_{44} as follows:
Equation (21) gives

$$\dot{F}_4(t) = K_0 \dot{u}_4(t) \left[1 - \text{sign} \left(\frac{F_4(t)}{F_0} - S(t) \right)^n \right]$$

where

$$\text{sign} = 1 \text{ if } \dot{u}_4(t) > 0$$
$$= -1 \text{ if } \dot{u}_4(t) < 0.$$

Thus,

$$\frac{\partial F_4(t)}{\partial u_4} = K_0 \left[1 - \text{sign} \left(\frac{F_4(t)}{F_0} - S(t) \right)^n \right].$$

5.2 *Numerical results*

The hysteresis model presented in eqns (1) and (2) contains four parameters, namely, F_0, δ_0, α and n. The values for these parameters must be chosen so that the experimental response closely matches with the predicted response. From the test results on the mild steel energy-absorbing devices [7], the following set of

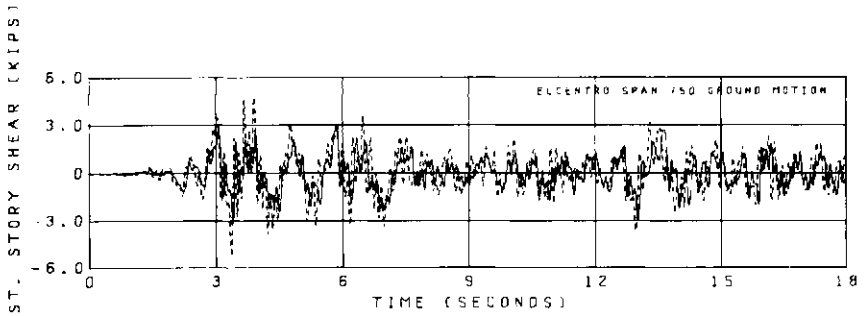

Fig. 5. First story shear time history.

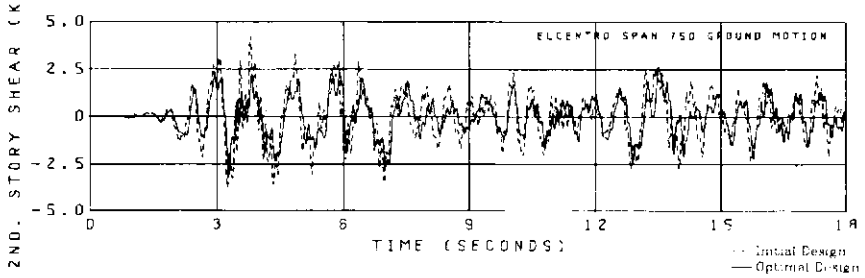

Fig. 6. Second story shear time history.

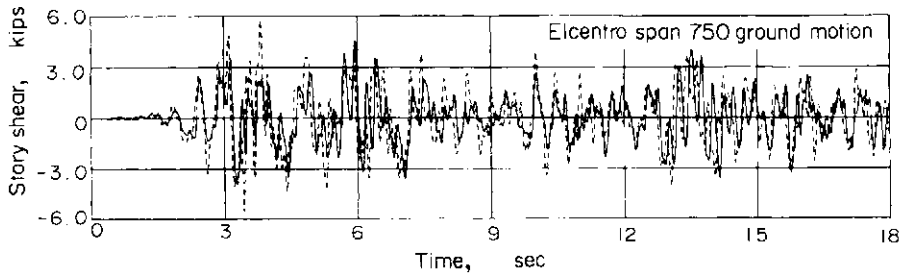

Figure 7 Third Story Shear Time History

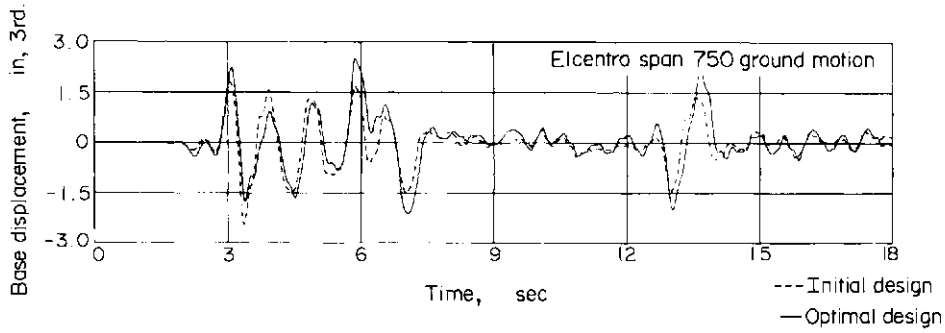

Fig. 8. Base displacement time history.

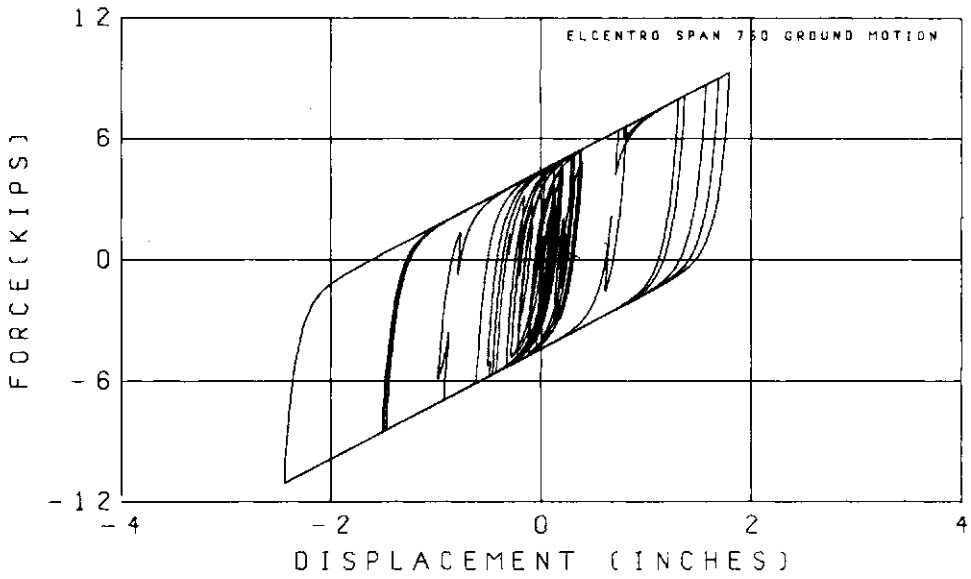

Fig. 9. Energy-absorber hysteresis loops (initial design).

parameters is obtained:

$$F_0 = 5.0 \quad \delta_0 = 0.11 \quad \alpha = 0.064 \quad n = 1 \qquad (22)$$

Since the purpose of an earthquake isolation system is to minimize forces in the structure, other sets of parameters could be obtained which minimize some function of these forces. In Ref. [8], an optimal design problem was formulated in which the device parameters were adjusted so that the sum of story shears in the frame were minimized. The optimal values of the parameters were found to be:

$$F_0 = 4.337 \quad \delta_0 = 0.2503 \quad \alpha = 0.05831 \quad n = 1. \qquad (23)$$

The response of the structure, subjected to modified El Centro 1940NS (see Ref. [8]), is computed by using the above two sets of parameters. The parameters given in eqn (22) are labeled "initial design" and those in eqn (23) are labeled as 'optimal design'. The story shears and base displacement time histories are shown in Figs. 5–8. The energy absorber hysteresis loops are

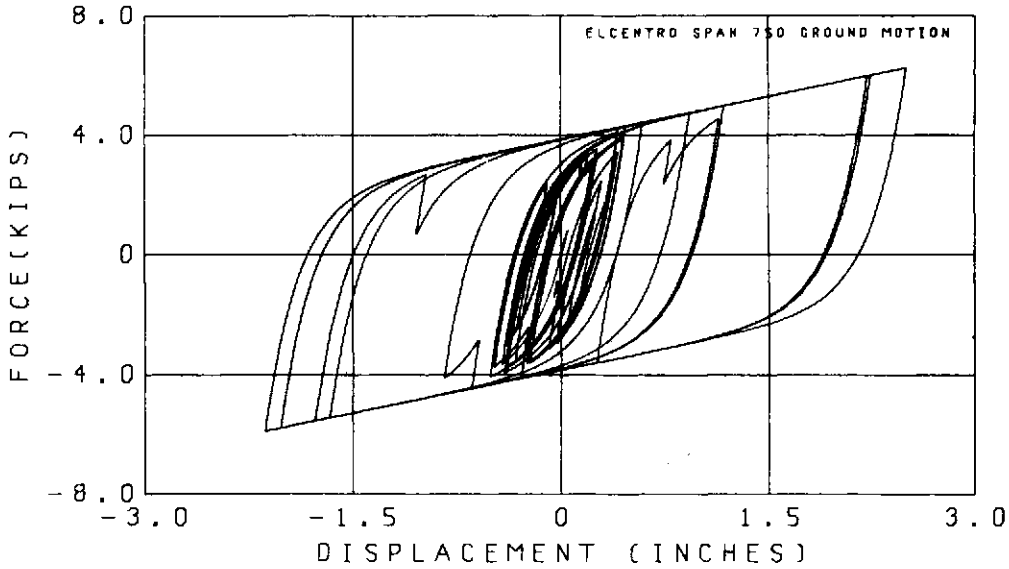

Fig. 10. Energy-absorber hysteresis loops (optimal design).

shown in Figs. 9 and 10. The response was computed with a time-step of 0.01 for the Newmark's method and 0.005 for the Runge–Kutta method. Only one iteration within each time-step was required in the large motion area and none in the rest. The algorithm was very stable and was not very sensitive to the global time-step as long as internal resisting forces were computed with reasonable accuracy.

It is interesting to note that the story shears obtained by using parameters of eqn (23) are much lower than those obtained by using values of eqn (22). This shows that by proper design of the isolation system, considerable reductions in the forces could be achieved in the structure.

6. CONCLUSIONS

An algorithm for integration of the equations of motion for structural systems having evolutionary type models for cyclic behavior of their constituent elements is presented. One of the principal advantages of the rate type of the models, obtained from using internal variables, is the generality they offer. For example, while it is not possible to account for stiffness or yield force degradation in a Ramberg–Osgood model, it is very easy to incorporate a new internal variable, described by a suitable equation, to account for these effects. Work is underway to include stiffness degrading models for analyzing concrete structures.

REFERENCES

1. V. C. Matzen and H. D. McNiven, Investigation of the inelastic characteristics of a single-story steel structure using system identification and shaking table experiments. *Rep. No. EERC* 76-20, Earthquake Engineering Research Center, University of California, Berkeley, Aug. 1976.
2. H. Ozdemir, Nonlinear transient dynamic analysis of yielding structures. Ph.D. Dissertation, Division of Structural Engineering and Structural Mechanics, Department of Civil Engineering, University of California, Berkeley, 1976.
3. R. W. Clough and J. Penzien, *Dynamics of Structures*. McGraw-Hill, New York (1975).
4. N. M. Newmark, A method of computation for structural dynamics. *J. Engng Mech. Div., ASCE* **85**, (EM3) 67–94 (1959).
5. D. P. Mondkar and G. H. Powell, Static and dynamic analysis of nonlinear structures. *Rep. No. EERC* 75-10, Earthquake Engineering Research Center, University of California, Berkeley, March 1975.
6. J. M. Kelly, J. M. Eidinger and C. J. Derham, A practical soft-story earthquake isolation system. *Rep. No. UCB/EERC*-77/27, Earthquake Engineering Research Center, University of California, Berkeley, Nov. 1977.
7. J. M. Kelly and D. F. Tsztoo, The development of energy-absorbing devices for aseismic base isolation system. *Rep. No. UCB/EERC*-78/01, Earthquake Engineering Research Center, University of California, Berkeley, Jan. 1978.
8. M. A. Bhatti, Optimal design of localized nonlinear systems with dual performance criteria under earthquake excitations. *Rep. No. UCB/EERC*-79/15, Earthquake Engineering Research Center, University of California, Berkeley, July 1979.

Computers & Structures, Vol. 13, pp. 189–196, 1981
Printed in Great Britain.

0045-7949/81/010189-08$02.00/0

INELASTIC ANALYSIS OF 3-D MIXED STEEL AND REINFORCED CONCRETE SEISMIC BUILDING SYSTEMS

FRANKLIN Y. CHENG

Civil Engineering Department, University of Missouri-Rolla, Rolla, MO 65401, U.S.A.

(*Received* 17 *May* 1980)

Abstract—This paper presents partial results of a NSF research project for studying the response behavior of inelastic building systems subjected to the simultaneous input of static loads and multicomponent earthquake motions that can be applied in any direction of the structural plan. The analysis includes the second-order moment resulting from the gravity load and the vertical ground motion.

The building systems may have elevator cores, floor diaphragms, and shear walls of reinforced concrete as well as steel beams, columns, and bracings. The material behavior of the steel members is based on the Ramberg–Osgood hysteresis loop with the consideration of the Bauschinger effect. Takeda's model is employed for the reinforced concrete elements. The system stiffness and geometric matrices, and the numerical integration procedures are developed consistantly with the building characteristics that each floor has dynamic degrees of freedom associated with the axial displacements of the columns and one torsional and two transverse displacements at the mass center. Thus, computation efficiency can be achieved by eliminating structural joint rotations from floor to floor with only the displacements associated with the lumped masses left for the motion equation. The yielding surface of a steel member is based on the nonlinear interactions and the von Mises yield criterion.

A computer program, INRESB-3D, has been developed for the inelastic response behavior of (1) the transverse, vertical, and torsional movements of a structure; (2) the internal moments and their associated rotations of the members; (3) the energy absorption characteristics of a structure; and (4) the requirement of the ductility factors and the excursion ratios of various building systems. Included in the paper is an example of unsymmetric eight-story building with steel columns and a concrete wall.

INTRODUCTION

The effect of a static gravity load on the dynamic response of plane structures has been studied by a number of investigators [1, 2]. They generally recognized that a gravity load can significantly increase plastic drift. Cheng and his associates, among other investigators, studied the effect of interacting earthquake motions (one horizontal and one vertical) on the response behavior of plane structural systems of elastic, elastoplastic and bilinear hysteresis models [3, 4]. The dynamic analysis of three-dimensional structures can be divided into space frameworks [5–8] and building systems [9–11]. References [5–8] mainly emphasize the various aspects of deriving force-displacement relationships, numerical procedures, and yielding criteria. Methods of analyzing tied buildings for static loads, buckling loads, and time-dependent forces are proposed in Refs. [9–11]. Inelastic seismic building systems can be analyzed by using the computer program DRAIN-TAB that is, however, actually devised to analyze plane inelastic frames, which are tied by floor diaphragms. Thus, the yielding criteria for individual columns are based on one-dimensional bending and axial forces [12].

This paper is to present partial results of a NSF project for investigating the effect of two horizontal and one vertical interacting ground motions on the response behavior of elastic and inelastic three-dimensional structural systems. The earthquake motions could be applied in any direction to a structural plan whose shape was not necessarily rectangular. The building systems were subjected to the simultaneous input of static loads and earthquake excitations for which the $P-\Delta$ effect of the second-order moment resulting from a gravity load and vertical initial forces acting on columns was considered. The material behavior of the steel members was based on the Ramberg Osgood hysteresis loop for which the loading, reversal of loading, and Bauschinger effect were included in the stiffness derivation. The hysteresis system for the reinforced concrete elements was based on stiffness degrading model. The von Mises' yield condition was used to determine the interaction between the yielding axial force and the plastic torsional capacity. The influence of the interacting axial force with bending moments on the flexural capacity of a cross section was based on the approximate yielding surface resulting from both the theoretical and experimental work that has been done on steel wide flange sections. Because the shear walls and flexural shear panels mainly have moments about their major axes, these members were treated as plane elements for which the moments about the minor axes were not considered.

A computer program, which was identified as INRESB-3D [13] (INelastic analysis of REinforced concrete and Steel Building systems for 3-Dimensional ground motions) was developed for the research, and the results presented herein were obtained by using an IBM 370/168 computer through the computer network of the University of Missouri.

METHOD OF ANALYSIS

Structural model and its characteristics. The struc-

tural model is three-dimensional and has the following characteristics:

(1) The structure consists of steel columns, beams, and bracings as well as floor diaphragms, shear walls and flexural shear panels. The floor plan does not need to be rectangular. The floor levels, however, must be horizontal, and the columns, shear walls, and panels must be vertical.

(2) The floor and roof diaphragms are idealized as laminae having infinite rigidity in their own planes but flexibility out of them. The diaphragms can be thin, cast-in-place, concrete slabs on open web steel joists or cold formed steel-deck panels with concrete placed on them. Because of the rigidity, each floor can have three common degrees of freedom: two translations and one rotation. However, the individual columns can have axial deformations and be able to bend about strong and weak axes.

(3) The structure can be subjected to static vertical loads on beams and joints and lateral loads at the floor levels as well as to three-dimensional interacting ground motions. The dead load of all the floor masses and their inertial forces resulting from vertical ground motion can induce an overturning moment which is also included in the analysis as the second-order moment of the P-Δ effect.

(4) The bracing members are axially-loaded members either in tension or compression. The beams may have torsion and bending about the horizontal axes but cannot have axial deformation nor bending about the vertical axis. However, the columns can have torsional, axial and bending deformations (about both major and minor axes). The torsional and translational displacements of the columns and shear walls as well as translational displacements of the shear panels at each floor can be transformed to three common degrees of freedom. The finite length of the rigid structural joints is considered in the system stiffness formulation.

Stiffness condensation. Because the lumped masses at each floor are associated with the floor displacements of two translations and one rotation as well as with the axial deformations of the columns, the rotational degrees of freedom at the structural joints can be condensed in the motion equation for the purpose of increasing the computation efficiency. The reduction of degrees of freedom is similar to stiffness condensation and is performed through a process of forward eliminations of the structural stiffness matrix, story-by-story, from the top of the building. Thus, during the dynamic response analysis, the displacements associated with the rigid-body motion of the floor displacements as well as the vertical column displacements are calculated first, then the joint rotations and member-end forces are obtained by using backward substitution.

Step-by-step integrations. Let the incremental dynamic motion equation including the P-Δ effect be expressed in global coordinates as

$$\mathbf{M}\Delta\ddot{\mathbf{r}}+\mathbf{c}\Delta\dot{\mathbf{r}}+(\mathbf{K}_e-\mathbf{K}_g)\Delta\mathbf{r}=-\mathbf{M}\Delta\ddot{\mathbf{r}}_g \tag{1}$$

in which $\mathbf{M}$ = diagonal mass matrix; $\mathbf{c}$ = damping matrix; expressed as $\alpha\mathbf{M}+\beta(\mathbf{K}_e-\mathbf{K}_g)$; $\mathbf{K}_e$ = structural stiffness matrix; $\mathbf{K}_g$ = geometric stiffness matrix including $\mathbf{M}g$ and $\mathbf{M}\ddot{\mathbf{r}}_g$; $\Delta\mathbf{r}$, $\Delta\dot{\mathbf{r}}$, $\Delta\ddot{\mathbf{r}}$ = incremental displacement, velocity, and acceleration vectors; and $\Delta\ddot{\mathbf{r}}_g$ = incremental ground acceleration vector including the vertical ($\Delta\ddot{\mathbf{v}}_g$) and horizontal ($\Delta\ddot{\mathbf{v}}_x$, $\Delta\ddot{\mathbf{v}}_y$) components. Based on the step-by-step integration method, eqn (1) can be expressed as

$$\left(1+\frac{3}{\Delta t}\beta\right)\mathbf{K}\Delta\mathbf{r}+\left(\frac{6}{\Delta t^2}+\frac{3\alpha}{\Delta t}\right)\mathbf{M}\Delta\mathbf{r}-\beta\mathbf{K}\mathbf{B}_n-\left(\frac{6}{\Delta t^2}+\frac{3\alpha}{\Delta t}\right)\times\left(\frac{1}{1+(3/\Delta t)\beta}\right)\beta\mathbf{M}\mathbf{B}_n$$
$$=\Delta\mathbf{P}+\mathbf{M}(\mathbf{A}_n+\alpha\mathbf{B}_n)-\left(\frac{6}{\Delta t^2}+\frac{3\alpha}{\Delta t}\right)\left(\frac{1}{1+(3/\Delta t)\beta}\right)\beta\mathbf{M}\mathbf{B}_n \tag{2}$$

in which Δt is the time interval; n represents the response time; $\mathbf{A}_n=(6/\Delta t)\dot{\mathbf{r}}_{n-1}+3\ddot{\mathbf{r}}_{n-1}$; $\mathbf{B}_n=3\dot{\mathbf{r}}_{n-1}+(\Delta t/2)\ddot{\mathbf{r}}_{n-1}$; $\mathbf{K}=\mathbf{K}_e-\mathbf{K}_g$, and $\Delta\mathbf{P}=-\mathbf{M}\Delta\ddot{\mathbf{r}}_g$. Let $c_0=3/\Delta t+6/\Delta t^2$, $c_1=1/c_4$, $c_2=c_0c_1$, $c_3=\alpha-c_2\beta$, $c_4=1+3\beta/\Delta t$, then eqn (3) becomes

$$\bar{\mathbf{K}}\bar{\mathbf{r}}=\Delta\bar{\mathbf{P}} \tag{3}$$

in which $\bar{\mathbf{K}}=\mathbf{K}+c_2\mathbf{M}$, $\Delta\bar{\mathbf{r}}=(1/c_1)\Delta\mathbf{r}-\beta\mathbf{B}_n$, and $\Delta\mathbf{P}=\mathbf{M}(-\Delta\ddot{\mathbf{r}}_g+\mathbf{A}_n+c_3\mathbf{B}_n)$. The expression of the pseudal dynamic equation in eqn (3) is identical to the force-displacement relationship for static loads. Thus the well-known Gaussian elimination technique can be used both for static and dynamic cases. In the solution procedures, the displacements at the foundation are set to zero; the complete computation of local displacements and member forces are then carried out floor by floor.

Structural material characteristics. The stress and stress reversal of steel members are typically shown in Figs. 1–3 and those of concrete elements are sketched in Fig. 4. In the figures, the skeleton and branch curves are respectively associated with stress and stress reversal. Figure 1 signifies the moment curvature relationship

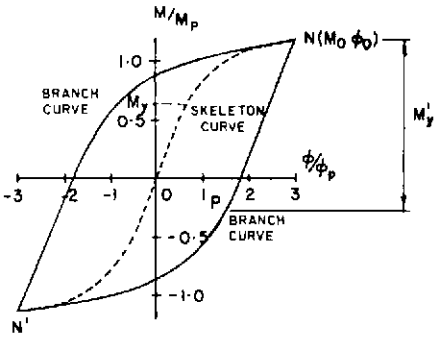

Fig. 1. Ramberg–Osgood moment reversal.

$(M-\phi)$ for the skeleton curve which may be expressed as

$$\phi=\frac{M}{EI}\left(1+a\left|\frac{M}{M_p}\right|^{r-1}\right) \tag{4}$$

in which ϕ is the curvature, M the bending moment, I the moment of inertia of a cross section, and M_p the plastic moment capacity whose associated yielding moment is $M_y=CM_p$. C is the ratio of the elastic section modulus to the plastic section modulus. a and r are positive constants chosen to fit the material characteristics. For the limiting cases of the elastic and the elasto-plastic, one may use $a=1$, $r=1$, and $a>0$, $r=\infty$, respectively.

A general description of the moment-curvature

relationship of the Ramberg–Osgood model may be found in Fig. 1. As shown in the figure, immediately after the load is applied, the moment-curvature follows the skeleton curve from 0 to N (or from 0 to N'). The load is then released, and finally in the opposite direction, the moment-curvature follows the branch curve from N to N'. The point N is treated as the origin of the branch curve. In the process of load reversal, the moment-curvature relationship is linear for a range of moments designated as M_y'. Because of the Bauschinger effect, the magnitude of M_y' is less than or at most equal to $2M_y$. The curvature associated with the branch curve may be expressed as

$$\phi=\phi_0+\frac{M-M_0}{EI}\left(1+a\left|\frac{M-M_0}{2M_p}\right|^{r-1}\right) \tag{5}$$

in which ϕ_0 and M_0 are the curvature and moment at the returning point. Figure 2 similar to Fig. 1 is for the moment rotation ($M-\phi$) relationship.

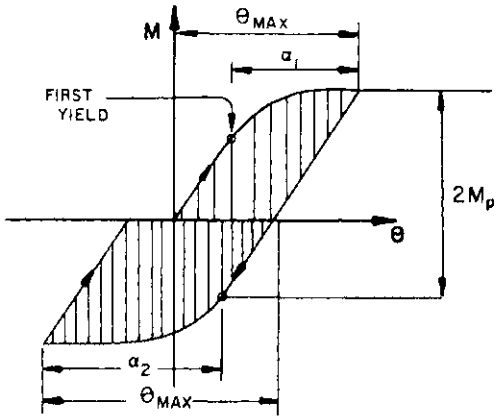

Fig. 2. Ductility based on rotation.

When a member is subjected to an axial force, P, which can be either tension or compression, the linear tensile load is limited by the yielding capacity, P_y, and the linear compression should be limited by the critical load of buckling capacity, P_{cr}. The loading and its reversal are sketched in Fig. 3. Because the Ramberg–Osgood model is an increasing function, the analysis yields a greater flexibility of the member and does not provide collapse conditions. From Fig. 3, one may express the skeleton curves for tension and compression in eqns (6) and (7) respectively as follows:

$$\varepsilon=\frac{PL}{AE}\left(1+a\left|\frac{P}{P_y}\right|^{r-1}\right),\quad \varepsilon=\frac{PL}{AE}\left(1+a\left|\frac{P}{P_{cr}}\right|^{r-1}\right). \tag{6,7}$$

For the branch curve,

$$\varepsilon=\varepsilon_0+\frac{L}{AE}(P-P_0)\left(1+a\left|\frac{P-P_0}{P_y+P_{cr}}\right|^{r-1}\right) \tag{8}$$

in which P_0 is the point at which the load release begins, and P_{cr} is a result of the critical stress, σ_{cr}, of long or short column [14] multiplied by the cross sectional area, A.

The Ramberg–Osgood torsional hysteresis loop is not shown and is similar to Fig. 1. The skeleton curve and branch curve can be respectively expressed as:

$$\gamma=\frac{TL}{GI_z}\left(1+a\left|\frac{T}{T_p}\right|^{r-1}\right) \tag{9}$$

$$\gamma=\gamma_0+\frac{L}{GI_z}(T-T_0)\left(1+a\left|\frac{T-T_0}{2T_p}\right|^{r-1}\right) \tag{10}$$

in which γ is the total angle of twist, T the torque, G the shear modulus, I_z the polar moment of inertia, and T_p the plastic torsional capacity of a given section.

The moment-rotation relationship ($M-\theta$) of concrete elements is based on the experimental work and is sketched in Fig. 4 in which the numerals signify the rules for generating stiffness coefficients in the computer program during various loading, unloading, and load reversal [15].

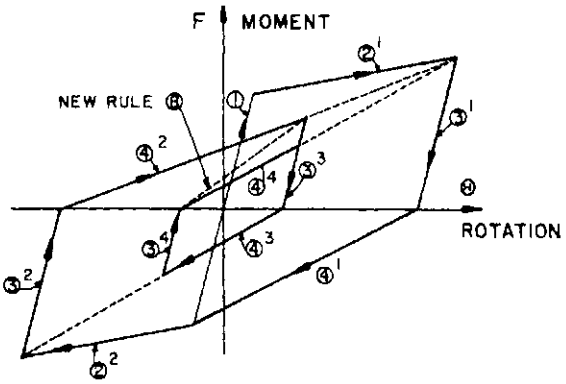

Fig. 4. Stiffness degrading model.

Stiffness coefficients for Ramberg–Osgood hysteresis loops—skeleton curve. The stiffness derivation is based on the principle of incremental analysis and the transfer matrix technique. A typical member is shown in Fig. 5 where the forces (M_i, V_i, M_j and V_j) and their associated deformations (τ_i, v_i, τ_j, and v_j) are positive as

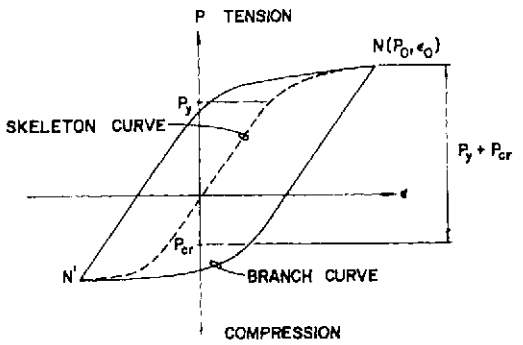

Fig. 3. Ramberg–Osgood axial load reversal.

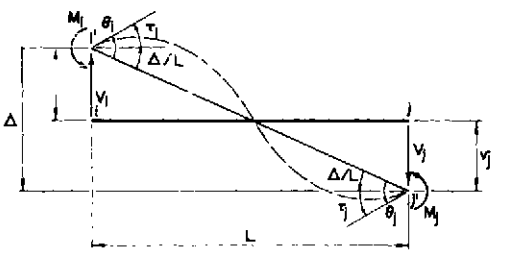

Fig. 5. Positive forces and deformations of a member.

indicated. Because of the cycling loading process, the force-deformation relationships must be expressed in two groups of loading and unloading corresponding to skeleton curve and branch curve respectively.

Let us consider a stable determinate beam shown in Fig. 6 for which the elastic curvature associated with the given moments may be sketched in the accompanying figure. The slope at end-i may be expressed on the basis of structural mechanics and eqn (4) as

$$\tau_i = -\int_0^L \phi \, dx \tag{11}$$

where the moment, M, in the equation of ϕ should be substituted by $M_x = V_i x - M_i$. The deflection at end-i may be similarly obtained

$$v_i = \int_0^L \phi x \, dx. \tag{12}$$

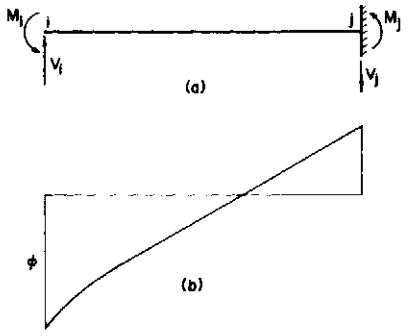

Fig. 6. Forces applied at end-I, (a) given beam, (b) curvature.

Since an incremental procedure must be used for analyzing the inelastic structure, the force-deformation relationships at end-i can be expressed in the following derivative forms:

$$\frac{d\tau_i}{dM_i}, \quad \frac{d\tau_i}{dV_i}, \quad \frac{dv_i}{dM_i}, \quad \frac{dv_i}{dV_i}. \tag{13}$$

Equations (13) are obtained by just using the derivative of the integral solutions of eqns (11) and (12) with respect to the independent variables M_i and V_i and then substituting the equilibrium condition, $V_i = (M_i + M_j)/L$, to eliminate V_i. These equations are actually an incremental form of flexibility matrix and can be symbolically expressed as

$$\begin{Bmatrix} dv_i \\ d\tau_i \end{Bmatrix} = \begin{bmatrix} f_{11} & f_{12} \\ f_{21} & f_{22} \end{bmatrix} \begin{Bmatrix} dV_i \\ dM_i \end{Bmatrix} \quad \text{or} \quad d\Delta_i = \mathbf{f}\, dF_i. \tag{14}$$

Using the equilibrium condition, one may find the incremental forces at end-j. The stiffness coefficients are then obtained by using the transfer matrix technique in the following form:

$$\begin{Bmatrix} dV_i \\ dM_i \\ dV_j \\ dM_j \end{Bmatrix} = \left[\begin{array}{c|c} \mathbf{S}_{ii} & \mathbf{S}_{ij} \\ \hline \mathbf{S}_{ij}^T & \mathbf{S}_{jj} \end{array}\right] \begin{Bmatrix} dv_i \\ d\tau_i \\ dv_j \\ d\tau_j \end{Bmatrix} \tag{15}$$

in which

$$\begin{bmatrix} \mathbf{S}_{ii} & \mathbf{S}_{ij} \\ \mathbf{S}_{ij}^T & \mathbf{S}_{jj} \end{bmatrix} = \begin{bmatrix} \mathbf{f}^{-1} & \mathbf{f}^{-1}\mathbf{E}^T \\ \mathbf{E}\mathbf{f}^{-1} & \mathbf{E}\mathbf{f}^{-1}\mathbf{E}^T \end{bmatrix}, \quad \mathbf{E} = \begin{bmatrix} -1 & 0 \\ L & -1 \end{bmatrix}. \tag{16, 17}$$

The stiffness coefficients in eqn (15) can be expressed in terms of the angles, θ_i, θ_j, measuring from the chord to the tangents. The chord is defined as the line connecting two ends, i' and j', of a member, whether the member is displaced or not. Using the analogy of θ_i and θ_j to τ_i and τ_j, one may find another set of stiffness coefficients for which the shears are not treated as independent forces and are dependent on the moments.

The stiffness coefficients for axial force and torsion can be directly derived from eqns (6, 7 and 9).

Stiffness coefficients for Ramberg Osgood hysteresis loops branch curve. The unloading case can be classified into four groups: (a) moment reversal at end-i, (b) moment reversal at end-j, (c) axial load reversal, and (d) torsional moment reversal. The moment reversals and their associated curvatures for groups (a) and (b) are sketched in Figs. 7 and 8, respectively.

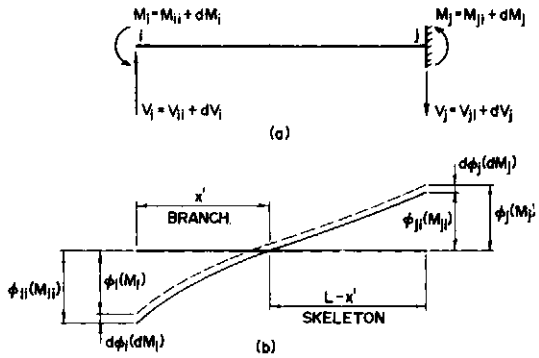

Fig. 7. Moment reversal at end-I, (a) given beam, (b) curvature.

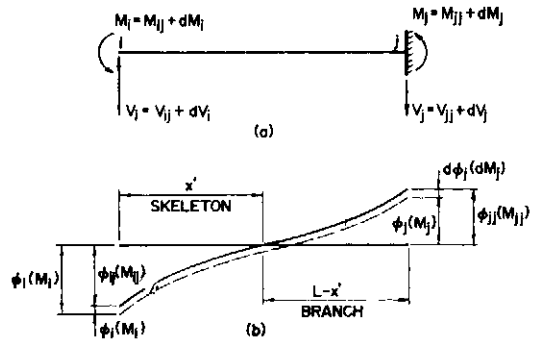

Fig. 8. Moment reversal at end-J, (a) given beam, (b) curvature.

Let the member end-i be subjected to a moment reversal, dM_i, for which the curvature changes from the solid line to dashed line as shown in Fig. 7(b). Because of the moment reversal, the curvature between o and $x'(\phi_{ox'})$ is reduced while the curvature between x' and $L(\phi_{x'L})$ is increased, where $x' = M_{ii}/V_{ii}$, $\phi_{ox'}$ and $\phi_{x'L}$ are respectively corresponding to the branch curve and skeleton curve for which the slope may be calculated as

$$\tau_i = -\int_0^L \phi_{ox'} \, dx - \int_{x'}^L \phi_{x'L} \, dx \tag{18}$$

from eqns (4) and (5)

$$\tau_i = -\int_0^{x'} \left[\phi_0 \frac{M_x - M_0}{EI}\left(1 + a\left(\frac{M_x - M_0}{2M_p}\right)^{r-1}\right)\right] dx - \int_{x'}^L \frac{M_x}{EI}\left(1 + a\left(\frac{M_x}{M_p}\right)^{r-1}\right) dx \tag{19}$$

in which

$$M_0 = V_{ii}x - M_{ii} \tag{20}$$

$$\phi_0 = \frac{M_0}{EI}\left(1 + a\left|\frac{M_0}{M_p}\right|^{r-1}\right). \tag{21}$$

Similarly

$$v_i = \int_0^{x'} x\left[\phi_0 + \frac{M_x - M_0}{EI}\left(1 + a\left|\frac{M_x - M_0}{2M_p}\right|^{r-1}\right)\right]dx + \int_{x'}^{L} x\,\frac{M_x}{EI}\left(1 + a\left|\frac{M_x}{M_p}\right|^{r-1}\right)dx. \tag{22}$$

Similar to the derivation of eqn (14), one must first find the derivatives of the integrals of eqns (19) and (22) with respect to M_i and V_i and then substituting the following equilibrium equation into the derivative equations: $M_j = V_iL - M_i$, $M_{ji} = V_{ii}L - M_{ii}$, $M_{iid} = M_i - M_{ii}$, $M_{jid} = M_j - M_{ji}$, and $M'_p = 2M_p$. Thus the final incremental force-deformation relations are obtained from the derivative forms of eqn (13) and the stiffness coefficients are then obtained in the similar manner shown in eqns (14)–(17).

For the moment reversal at end-j, one may follow Fig. 8 and eqns (18)–(22) to find four derivative equations of $d\tau_i/dM_i$, $d\tau_i/dV_i$, dv_i/dM_i, dv_i/dV_i for which the following equilibrium equation are substituted: $M_j = V_iL - M_i$, $M_{jj} = V_{ij}L - M_{ij}$, $M_{ijd} = M_i - M_{ij}$, $M_{jjd} = M_j - M_{jj}$, and $M'_p = 2M_p$. The stiffness coefficients are obtained from the final expressions of the incremental force-deformation relations.

The stiffness coefficient for the branch curve of axial force or torsion can be directly obtained by inverting the incremental form of the flexibility coefficient associated with eqns (8) or (10).

Interaction relations. The values of the bending, axial, and torsional capacities of a member are dependent upon the interaction among the internal forces at the cross section. Let the shearing stress and the shearing yield stress induced by torsion be τ and τ_y, and

$$m = \frac{\tau}{\tau_y}, \tag{23}$$

then on the basis of the von Mises' yield criterion, one may find the maximum normal stress, σ, which can occur at a cross section having a torsion, T, as

$$\sigma = \sigma_y[1 - m^2]^{1/2} \tag{24}$$

in which σ_y is the normal yield stress. The result implies that the effect of torsional moment can be taken into account in axial force and bending moments by reducing their magnitudes by a factor of $\sqrt{1-m^2}$.

The interaction relations between the biaxial bending and the axial force were employed in this study have two sets of interaction equations for checking strength and stability. Since the strength criteria was used for the numerical example included in this paper, the interaction equation introduced herein (eqn 25) is for strength only [14].

$$\left(\frac{M_x}{M_{pcx}}\right)^{\alpha} + \left(\frac{M_y}{M_{pcy}}\right)^{\alpha} = 1 \tag{25}$$

in which M_x and M_y are the applied moments about the major and minor axes respectively, and M_{pcx} and M_{pcy} are the modified plastic moments that include the effect of the axial compressive force, P. Let $p = P/P_y$, then

$$M_{pcx} = 1.18(1-p)M_{px} \leqslant M_{px} \tag{26}$$

and

$$M_{pcy} = 1.19(1-p^2)M_{py} \leqslant M_{py} \tag{27}$$

M_{px} and M_{py} are plastic moments about the major and minor axes respectively. The exponent, α, is a numerical factor whose value depends on the shape of a particular cross section and on the magnitude of the axial load. The variation of α can be approximately expressed by

$$\alpha = 1.6 - \frac{p}{\ln p} \tag{28}$$

in which ln is the natural logarithm.

The procedures for reducing the plastic capacities are as follows: At any time step in the structural analysis, a reduction of plastic moments, M_{px}, M_{py}, must be made to include the influence of the compressive axial force based on eqns (26) and (27). These modified plastic moments, M_{pcx}, M_{pcy}, must then be reduced because of the torsional effect in the amount of $\sqrt{1-m^2}$ shown in eqn (24). The torsional influence should also be applied to the axial force to change its capacity. The final reduced moments, M_{rpx}, M_{rpy}, and the axial force, P_r, are employed in the stiffness coefficients for the next time step in the analysis. Because the stiffness coefficients are derived on the basis of the Ramberg-Osgood hysteresis with strain-hardening that is not considered in the interaction equations, the internal actions at some loading stage can be greater than the plastic capacities at that stage, which must be approximately reduced in order to fit the interaction equations.

Response parameters. The response parameters observed in this study are displacements, internal forces, seismic input and output energies, ductilities, and excursion ratios. This paper only presents some numerical results of ductility studies which are therefore briefly discussed herein. The ductility factor, which is commonly used as the maximum required deformation of a structure, is generally defined as the deformation in a region of a system (or an overall response of system) that is divided by the corresponding deformation present when yield occurs (see Fig. 2). The excursion ratio is used as an index of the total severity of the inelastic deformation during a response history. The excursion is normally expressed in terms of a summation of ductility factors. If the ductility factors are used to describe the deformations of individual regions, they are normally measured on the basis of rotations, curvatures or strains. In this work, the ductility factors based on rotation, variable strain energy, and hybrid strain energy were used. The numerical example given in the paper, however, is based on the definition of rotation as sketched in Fig. 2. Observation of the figure reveals that the ductility factor is measured as the maximum absolute nodal rotation, $|\theta|_{\max}$, divided by the yield rotation, θ_y, as

$$\mu = \frac{|\theta|_{\max}}{\theta_y} = \frac{\theta_y + \alpha}{\theta_y} = 1 + \frac{\alpha}{\theta_y} \tag{29}$$

in which the yield rotation is based on the antisymmetrical bending of a member when its two ends are subjected to the plastic moment, M_p; thus, $\theta_y = M_pL/6EI$ in which L is the length of the member, and EI is the member's flexural rigidity. The angle, α, is measured from the first yield at which the member stiffness coefficients pass beyond the elastic limit.

The excursion ratio, ε, corresponding to the duc-

tility ratio can be defined as the total plastic rotation of a node of a member divided by the yield rotation of the joint. In terms of ductility

$$\varepsilon = \sum_{i=1}^{N_\mu} (\mu_i - 1) \tag{30}$$

in which μ_i is the ductility factor for the half plastic rotation, i, and N_μ is the total number of times the node becomes inelastic.

NUMERICAL EXAMPLE, OBSERVATIONS AND FUTURE

Numerical example. More than one hundred cases of several structural systems were investigated in this study. The example given is an eight-story building of L-shape plan with steel columns and a shear wall as shown in Fig. 9. The mass center is at point "A". The

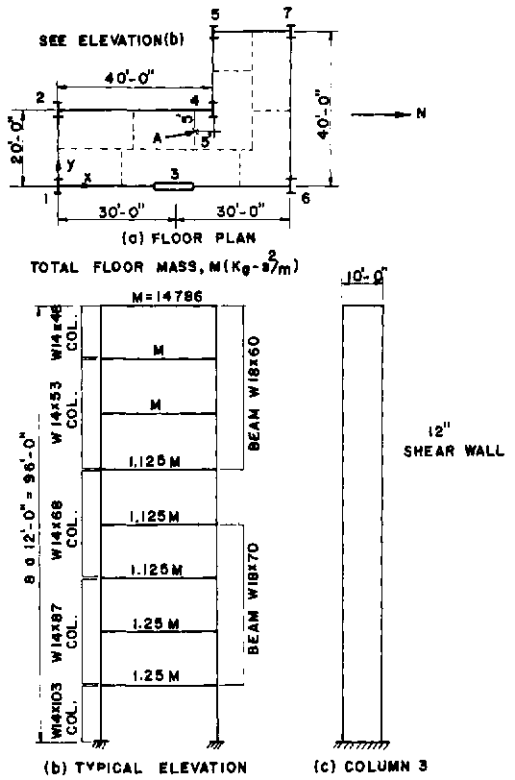

Fig. 9. Eight-story building of L-shape with steel columns and shear-wall, (1 ft = 0.305 m).

transverse masses are shown in the accompanying figure. The torsional masses are 62,111.8 k-in-sec^2 (715,604 kg-m-s^2) for the first and second floor, 55,900.62 k-in-sec^2 (644,044 kg-m-s^2) for the third through fifth floor, and 49,689.44 k-in-sec^2 (572,483 kg-m-s^2) for the sixth through eighth floor. The masses associated with the axial displacements of columns are distributed according to the dashed lines shown for the floor masses in the figure. The cross-sectional properties of the shear wall are that the yield moment is 40,000 in-k (4520 kN-m), the moment of inertia about the major axis is 864,000 in^4 (0.3596 m^4), and the effective cross sectional area is 720 in^2 (0.4645 m^2). The torsional moment of inertia and the moment of inertia about the minor axis are assumed to be negligible. For the steel members, $a=1$ and $r=20$ were employed. The first five seconds of the El Centro 1940 earthquake are used with the scale of one, and the N-S component is applied in the N-S structural plan. In the analysis, five percent damping ($\alpha=0.4305$ and $\beta=0.00581$) and $\Delta t=0.005$ sec were employed.

Response observations. The effect of the interaction of the three earthquake components on the response was investigated by considering (c) the N-S component with the $P-\Delta$ effect of dead load, (d) the N-S and E-W components with the $P-\Delta$ effect of dead load, and (e) the N-S, E-W, and vertical components with the $P-\Delta$ effect of both dead load and the vertical earthquakes. Thus the ratio, d/c, indicates how the E-W component affects the response behavior. e/d shows the increase caused by the vertical ground motion, and e/c signifies the influence of both the E-W and vertical components. The ductility demands in the x-direction shown in Fig. 10 of the vertical members are mainly

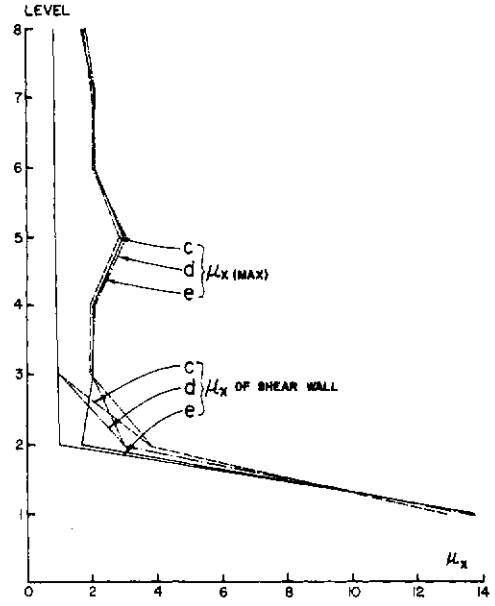

Fig. 10. Comparison of max. ductilities in X-direction of columns with shear-wall ductilities.

developed at the shear wall for which the maximum required ductility is at the first floor. From the second floor to the top, the ductilities are demanded slightly by the other columns, and the shear wall remains elastic. The ductilities in the y-direction sketched in Fig. 11 are mainly developed at column 7, for which the critical location is at the fifth floor. Because the shear wall and column 7 suffer severe damage, the ductilities of these two members are plotted along with the maximum required numbers for each floor of the system. The ductilities and excursion ratios of the beams in the y-direction of the floor plan are shown in Figs. 12 and 13. Inclusion of the E-W component and the vertical component apparently demands more ductilities than those occasioned by the N-S components only.

Future research. The future research work may be emphasized on the comparative studies of the optimum design of building systems for various interacting ground motions and code provisions; recommendation on how to strengthen the structural parameters at the critical regions of a system and how to improve the code provisions. The study is currently undertaken at UMR.

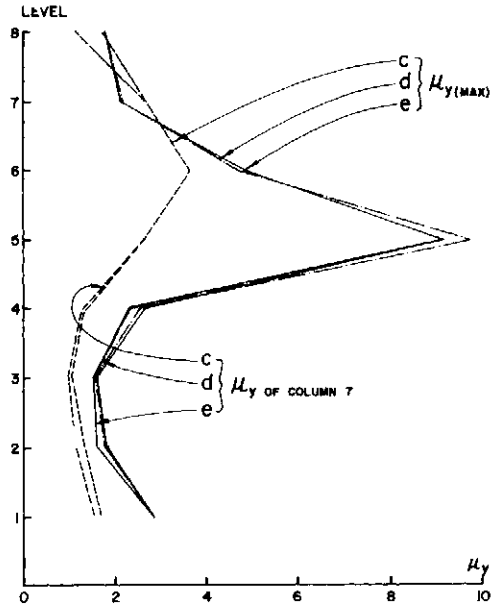

Fig. 11. Comparison of max. ductilities in Y-direction with Col. 7 ductilities.

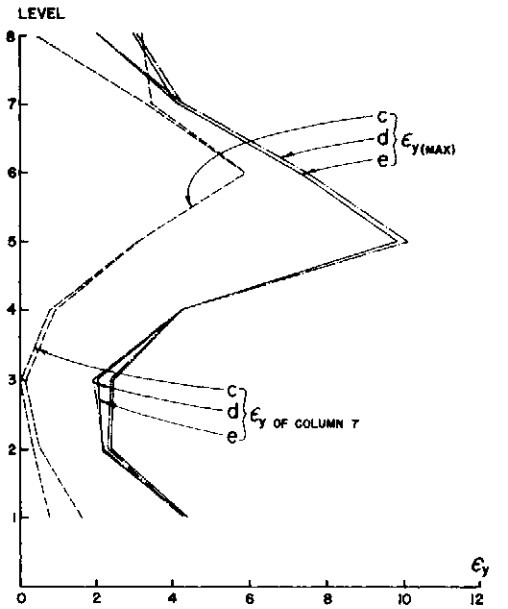

Fig. 13. Comparison of max. excursion ratios in Y-direction of columns with Col. 7 excursion ratios.

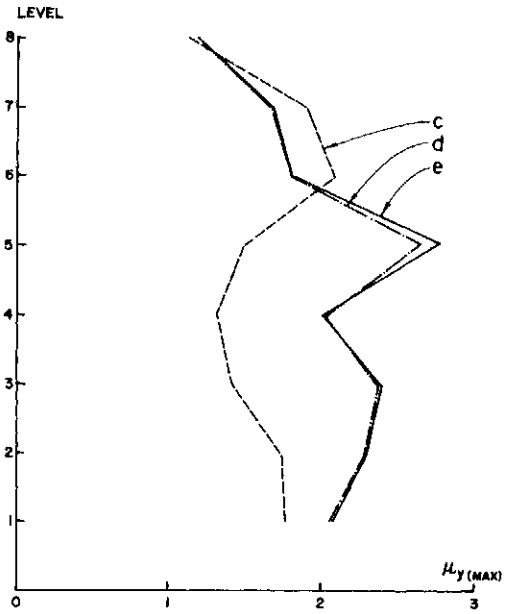

Fig. 12. Max. ductility factors in Y-direction of beams.

Acknowledgements—This research project was sponsored by the National Science Foundation under Grant No. ENV-7518372-A01. The author deeply appreciates the financial support and the continuous encouragement and advice that Dr. S. C. Liu, Program Manager, provided during the course of the investigation. Dr. P. Kitipitayangkul, former graduate student, is also acknowledged for his capable assistance.

REFERENCES

1. S. C. Goel, *P-Δ* and axial column deformation in aseismic frames. *J. Struct. Div., ASCE*, **95**(ST8), 1693–1711 (1969).
2. F. Y. Cheng and M. E. Botkin, Second-order elasto-plastic analysis of tall buildings with damped dynamic excitations. *Proc. Finite Element Method in Civil Engineering*, pp. 549–564. McGill University, Montreal (1972).
3. F. Y. Cheng and K. B. Oster, *Dynamic Instability and Ultimate Capacity of Inelastic Systems Parametrically Excited by Earthquakes—Part II*. Technical Report for the National Science Foundation, available at Technical Information Service, U.S. Department of Commerce (1976).
4. F. Y. Cheng and K. Oster, Ultimate instability of earthquake structures. *J. Struct. Div., ASCE* **102**(ST5), 961–972 (1976).
5. F. Y. Cheng, E. Uzgider and P. Kitipitayangkul, Analysis of space frames subject to multicomponent earthquakes. *Proc. Conf. Centro American De Ingenieria Sismica*, Vol. I, pp. 105 116, San Salvador, El Salvador (1978).
6. R. K. Wen and F. Farhoomand, Dynamic analysis of inelastic space frames. *J. Engng Mech. Div. ASCE* **96**(EM5), (1970).
7. N. F. Morris, Dynamic analysis of elastic plastic space frames. *Proc. Int. Symp. Earthquake Structural Engineering* (Edited by F. Y. Cheng), Vol. I, pp. 285 298 (1976).
8. F. Y. Cheng, Inelastic analysis of dynamic space frameworks. *Proc. 7th Conf. Electronic Computation*, ASCE, pp. 537 552 (1979).
9. W. Weaver and M. F. Nelson, Three-dimensional analysis of tier buildings. *J. Struct. Div., ASCE* **93**(ST2), (1967).
10. R. S. Nair, Overall elastic stability of multistory buildings. *J. Struct. Div., ASCE* **101**(ST12) (1975).
11. F. Y. Cheng, Comparative studies of buckling capacity of three-dimensional building systems. *Proc. Int. Colloquium on Stability of Structures Under Static and Dynamic Loads*, ASCE, pp. 158–178 (1977).
12. R. Guendelman-Israel and G. H. Powell, *DRAIN-TABS, Rept. No. UCB/EERC-77/08*, University of California-Berkeley (1977).
13. F. Y. Cheng and P. Kitipitayangkul, *INRESB-3D A Computer Program for INelastic Analysis of REinforced-Concrete Steel Buildings Subjected to 3-Dimensional Ground Motions, Tech. Rep. No. 2* prepared for the National Science Foundation, available at NTIS, U.S. Dept. of Commerce (1979).
14. W. F. Chen and T. Atsuta, *Theory of Beam-Columns*, Vol. II. McGraw-Hill, New York (1977).

15. T. Takeda, M. A. Sozen and N. N. Nielson, Reinforced concrete response to simulated earthquakes. *J. Struct. Engng Div., ASCE*, No. St12 (1970).
16. F. Y. Cheng and P. Kitipitayangkul, *Investigation of the Effect of 3-D Parametric Earthquake Motions on Stability of Elastic and Inelastic Building Systems*, Rep. No. 1, prepared for the National Science Foundation, available at the U.S. NTIS and the University of Missouri-Rolla (1979).

Computers & Structures, Vol. 13, pp. 197–204, 1981
Printed in Great Britain.

0045-7949/81/010197-08$02.00/0

COUPLING IN THE DYNAMIC RESPONSE OF NONLINEAR UNSYMMETRIC STRUCTURES

O. A. PEKAU† and PRADIP K. SYAMAL‡
Department of Civil Engineering, Concordia University, Montreal, Canada H3G 1M8

(*Received* 17 *May* 1980)

Abstract—A procedure is presented for investigating the stability of the torsional component of response in a nonlinear unsymmetric structure subjected to translational excitation. The torsional motion is found to be unstable due to the nonlinearity of the resisting elements if the parameters of the system are such that they fall within the region bounded by the upper and the lower instability curves. Furthermore, relationships for torsional damping and other system parameters determine the minimum torsional damping necessary to stabilize the torsional component of the motion. Thus, the procedure presented herein may be applied to structures that are susceptible to lateral-torsional coupling arising from nonlinearity of the resisting elements, eccentricity between the centres of resistance and mass, or a combination of both of these factors.

NOMENCLATURE

a, b	plan dimensions of building
c_x, c_y, c_θ	viscous damping coefficients
D	square of non-dimensional amplitude of a single-degree-of freedom system
E_x, E_y	non-dimensional eccentricities
e_x, e_y	static eccentricities
P, Q R	average non-dimensional response amplitudes in x-, y- and θ-directions, respectively aspect ratio (a/b)
r	aspect ratio (a/b)
$R_x(\delta_j), R_y(\delta_j)$	resisting forces in element j
t	time
U	amplitude of sinusoidal ground acceleration
$u(t), v(t)$	lateral displacements of mass centre
x, y	principal coordinate directions
β, γ	geometric parameters of L-shaped building
Γ	mass radius of gyration
δ_0	reference displacement
δ_j	in-plane displacement of resisting elements
$\zeta_x, \zeta_y, \zeta_\theta$	critical damping ratios
$\theta(t)$	rotational displacement
$\Lambda_x(\tau), \Lambda_y(\tau), \Lambda_\theta(\tau)$	non-dimensional response
λ	coefficient of nonlinearity
ξ_x, ξ_y, ξ_θ	non-dimensional displacement perturbations
τ	non-dimensional time
Ω_y	translational fundamental frequency ratio (ω_y/ω_x)
Ω_θ	torsional fundamental frequency ratio (ω_θ/ω_x)
Ω	sinusoidal ground excitation frequency ratio (ω/ω_x)
$\omega_x, \omega_y, \omega_\theta$	uncoupled building frequencies
ω	frequency of sinusoidal ground excitation

1. INTRODUCTION

Generally, all buildings are torsionally unbalanced to some extent and any form of translational excitation will therefore cause torsional response associated with the lateral vibration. Field observations of earthquake damage show numerous examples of structural failure due to such simultaneous torsional motion.

Earthquake response of linear elastic structures where the centre of mass is eccentric to the centre of resistance has been the subject of a number of studies [1–3]. Hoerner [1] indicated that strong modal coupling can occur in a rectangular building with a uniform distribution of columns in plan if eccentricities and translational-torsional frequency differences are small. Kan and Chopra [2], after studying the elastic response of a torsionally coupled building for idealized flat or hyperbolic response spectra, concluded that coupling between lateral and torsional motions induces torsion and generally reduces the base shear. They also demonstrated a relation for the base shear and torque between the torsionally coupled and the corresponding uncoupled system when excitation is applied in one direction. Employing a partially symmetric single-storey model and the design spectrum concept together with suitably conservative procedures for combining the modal maxima, Dempsey and Irvine [3] evaluated the dimensionless torque and shear as functions of two independent parameters, viz. frequency ratio and dimensionless eccentricity.

However, recent studies [4–6] indicate that coupling also exists between the lateral and torsional responses of symmetric structures. Newmark [4] examined symmetric structures exited into torsional motion by the rotational component of ground motion about a vertical axis. Tso and Asmis [5, 6] studied the coupled lateral-torsional motion of elastic, nonlinear, symmetric structures subjected to lateral ground motion and showed that nonlinear coupling exists between the translational and torsional response.

As a general conclusion of these studies, strong modal coupling will occur if the torsional and translational

†Associate Professor Department of Civil Engineering, Concordia University, Montreal.
‡Graduate student: also. Senior Engineer, Canatom Inc., Montreal Canada H4Z 1K3.

frequencies coincide, for symmetric as well as for unsymmetric buildings.

The preceding studies of linear unsymmetric and nonlinear symmetric structures are not directly applicable in predicting the behaviour of structures that are both nonlinear and unsymmetric. Thus, the objective of the present study is directed towards (1) providing an understanding of the coupled behaviour of buildings that are nonlinear as well as unsymmetric, (2) identifying the basic parameters controlling the response of the system, and (3) investigating the influence of these parameters.

In this paper, it is shown that the nonlinear equations of motion are governed by a set of three damped, coupled Mathieu–Hill type equations which exhibit regions of instability. For illustration, torsional response stability curves for an example building system are presented and the effect of torsional damping on the instability is investigated. Convergence problems, encountered in the form of "gaps" in the solution, are examined.

DERIVATION OF EQUATIONS OF MOTION

An idealized one-storey structure consisting of a rigid deck supported on massless, axially inextensible columns having eccentric centre of mass with respect to the centre of resistance is considered (Fig. 1). This system has three degrees-of-freedom, namely the two horizontal displacements u and v of the mass centre relative to the ground along the x- and y-axes and the rotation θ about the vertical axis. The earthquake ground motion

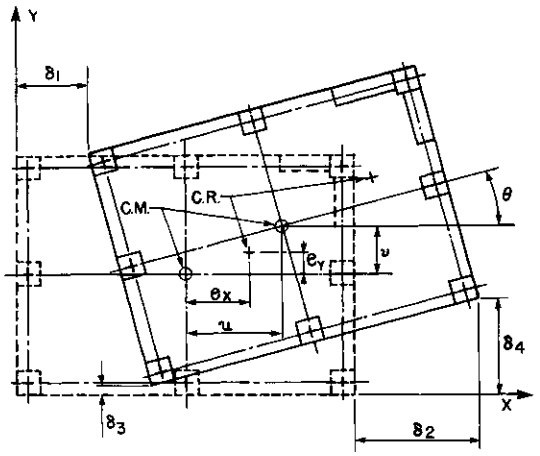

Fig. 1. Geometric relationships for building displacements.

is defined by accelerations $\ddot{u}_g(t)$ and $\ddot{v}_g(t)$ in the x- and y-directions.

Letting k_{ix} and k_{iy} represent the translational stiffnesses of the ith resisting element, the translational stiffnesses K_x and K_y and the torsional stiffness of the structure with respect to the centre of mass, $K_{\theta m}$, are given by

$$K_x=\Sigma k_{ix}, \quad K_y=\Sigma k_{iy} \tag{1}$$

$$K_{\theta m}=\Sigma(k_{ix}y_i^2+k_{iy}x_i^2). \tag{2}$$

The centre of resistance is located at distances e_x and e_y, the eccentricities measured from the centre of mass along the x- and y-axes and defined by

$$e_x=\frac{1}{K_y}\Sigma x_i k_{iy}, \quad e_y=\frac{1}{K_x}\Sigma y_i k_{ix} \tag{3}$$

The equation of motion of the system can then be written as

$$\begin{bmatrix} M & 0 & 0 \\ 0 & M\Gamma^2 & 0 \\ 0 & 0 & M \end{bmatrix}\begin{Bmatrix} \ddot{u} \\ \ddot{\theta} \\ \ddot{v} \end{Bmatrix}+\begin{bmatrix} c_x & 0 & 0 \\ 0 & c_\theta & 0 \\ 0 & 0 & c_y \end{bmatrix}\begin{Bmatrix} \dot{u} \\ \dot{\theta} \\ \dot{v} \end{Bmatrix}$$

$$+\begin{bmatrix} K_x & -K_x e_y & 0 \\ -K_x e_y & K_{\theta m} & K_y e_x \\ 0 & K_y e_x & K_y \end{bmatrix}\begin{Bmatrix} u \\ \theta \\ v \end{Bmatrix}=-\begin{Bmatrix} M\ddot{u}_g \\ 0 \\ M\ddot{v}_g \end{Bmatrix} \tag{4}$$

in which M is the mass of the deck, Γ is the mass radius of gyration of the deck about the vertical axis through the centre of mass, and c_x, c_y and c_θ are the translational and torsional viscous damping coefficients, respectively; the dots represent differentiation with respect to time t.

Describing the displaced position of the centre of mass of the deck by u, v and θ as shown in Fig. 1, the three equations of motion (eqn 4) can be written as

$$M\ddot{u}+c_x\dot{u}+s_1R_x(\delta_1)+s_2R_x(\delta_2)=-M\ddot{u}_g \tag{5}$$

$$M\Gamma^2\ddot{\theta}+C_\theta\dot{\theta}+s_3R_x(\delta_1)+s_4R_x(\delta_2)+s_5R_y(\delta_3)+s_6R_y(\delta_4)=0 \tag{6}$$

$$M\ddot{v}+c_y\dot{v}+s_7R_y(\delta_3)+s_8R_y(\delta_4)=-M\ddot{v}_g \tag{7}$$

where s_j ($j=1, 2, \ldots, 8$) are the parametric constants describing the plan profile and dimensions (i.e. length, width) of the building; and δ_j ($j=1, \ldots, 4$) are the displacements of the lateral resisting elements (Fig. 1); and $R_x(\delta_j)$ and $R_y(\delta_j)$ respresent the restoring forces in the x- and y-directions of element j. The displacement δ_j can be expressed as linear functions of displacements u, v, θ and the building dimensions as follows:

$$\delta_1=u+\theta F_1(l_y, \bar{y}_m) \tag{8}$$

$$\delta_2=u+\theta F_2(l_y, \bar{y}_m) \tag{9}$$

$$\delta_3=v+\theta F_3(l_x, \bar{x}_m) \tag{10}$$

$$\delta_4=v+\theta F_4(l_x, \bar{x}_m) \tag{11}$$

where l_x, l_y and $\bar{x}_m$, $\bar{y}_m$ are the plan dimensions and distances of the centre of mass from the resisting elements, respectively; F_j ($j=1, \ldots, 4$) are functions of these parameters.

The force-displacement relationship of the lateral resisting elements is assumed to be elastic and weakly nonlinear with cubic softening-type nonlinearity expressed as

$$R_x(\delta_j)=k_x\delta_j\left[1-\lambda\left(\frac{\delta_j}{\delta_0}\right)^2\right], \quad j=1, 2 \tag{12}$$

$$R_y(\delta_j)=k_y\delta_j\left[1-\lambda\left(\frac{\delta_j}{\delta_0}\right)^2\right], \quad j=3, 4 \tag{13}$$

in which k_x, k_y are the linear stiffnesses of the resisting elements along x- and y-directions, respectively; δ_0 is some convenient reference displacement; and λ is a measure of the nonlinearity of the force-displacement relation, with $\lambda \ll 1.0$.

Substituting eqns (8)–(13) into equations (5)–(7) results in

$$\ddot{u}+2\zeta_x\omega_x\dot{u}+\{s_{11}u-(s_{12}u^3+s_{13}u^2\theta+s_{14}u\theta^2+s_{15}\theta+s_{16}\theta^3)\}=-\ddot{u}_g \tag{14}$$

$$\ddot{\theta}+2\zeta_\theta\omega_\theta\dot{\theta}+\{s_{31}\theta-(s_{32}\theta^3+s_{33}\theta^2u+s_{34}\theta u^2+s_{35}u^3)-(s_{36}\theta^3+s_{37}\theta^2v+s_{38}\theta v^2+s_{39}v^3)$$

$$-(s_{41}u+s_{42}v)\}=0 \tag{15}$$

$$\ddot{v}+2\zeta_y\omega_y\dot{v}+\{s_{21}v-(s_{22}v^3+s_{23}v^2\theta+s_{24}v\theta^2+s_{25}\theta+s_{26}\theta^3)\}=-\ddot{v}_g \tag{16}$$

where $\zeta_x, \zeta_y, \zeta_\theta$ represent the ratios of critical damping in x-, y- and θ-directions, respectively; ω_x, ω_y, ω_θ are frequency parameters that may be interpreted as uncoupled frequencies of the system, i.e. the natural frequencies of the system if it were torsionally uncoupled ($e_x=e_y=0$). They are given by

$$\omega_x=\sqrt{\frac{K_x}{M}};\quad \omega_y=\sqrt{\frac{K_y}{M}} \text{ and } \omega_\theta=\sqrt{\frac{K_{\theta m}}{M\Gamma^2}}. \tag{17}$$

The coefficients s_{ij} are constants consisting of various functions of parameters s_1–s_8, λ, δ_0, ω_x, ω_y, ω_θ and F_1–F_4.

For simplicity, ground motion is assumed to be sinusoidal and directed along the x-axis only. Therefore,

$$\ddot{u}_g=U\cos\omega t;\quad \ddot{v}_g=0. \tag{18}$$

It is convenient to express eqns (14)–(16) in non-dimensional form with the following changes of variables:

$$\tau=\omega_x t \tag{19}$$

$$\delta_0=\frac{U}{\omega_x^2};\quad \delta_1=\frac{U}{\omega_y^2};\quad \theta_A=\frac{U}{\Gamma\omega_\theta^2} \tag{20}$$

$$\Lambda_x(\tau)=\frac{u(t)}{_0};\quad \Lambda_y(\tau)=\frac{v(t)}{\delta_1};\quad \Lambda_\theta(\tau)=\frac{\theta(t)}{\theta_A} \tag{21}$$

$$\Omega_y=\frac{\omega_y}{\omega_x};\quad \Omega_\theta=\frac{\omega_\theta}{\omega_x};\quad \Omega=\frac{\omega}{\omega_x} \tag{22}$$

where τ represents non-dimensional time and $\Lambda_x, \Lambda_y, \Lambda_\theta$ represent non-dimensional response of the system as functions of τ.

Denoting $d\Lambda/d\tau$ by $\dot{\Lambda}$ and substituting eqns (19)–(22) into eqns (14)–(16) yields the following three coupled, non-dimensional equations of motion for sinusoidal ground acceleration directed along the x-axis:

$$\ddot{\Lambda}_x+f_1\dot{\Lambda}_x+\{f_2\Lambda_x-(f_3\Lambda_x^3+f_4\Lambda_x^2\Lambda_\theta+f_5\Lambda_x\Lambda_\theta^2+f_6\Lambda_\theta+f_7\Lambda_\theta^3)\}=-\cos\Omega\tau \tag{23}$$

$$\ddot{\Lambda}_\theta+h_1\dot{\Lambda}_\theta+\{h_2\Lambda_\theta-(h_4\Lambda_\theta^3+h_9\Lambda_\theta^2\Lambda_x+h_3\Lambda_\theta\Lambda_x^2+h_8\Lambda_x^3)-(h_6\Lambda_\theta^3+h_{12}\Lambda_\theta^2\Lambda_y+h_5\Lambda_\theta\Lambda_y^2+h_{11}\Lambda_y^3)-(h_7\Lambda_x+h_{10}\Lambda_y)\}=0 \tag{24}$$

$$\ddot{\Lambda}_y+g_1\dot{\Lambda}_y+\{g_2\Lambda_y-(g_3\Lambda_y^3+g_4\Lambda_y^2\Lambda_\theta+g_5\Lambda_y\Lambda_\theta^2+g_6\Lambda_\theta+g_7\Lambda_\theta^2)\}=0 \tag{25}$$

where f_i, g_i and h_i are non-dimensional constants that may be expressed as functions of $\zeta_x, \zeta_y, \zeta_\theta, s_{ij}, \Omega_y$ and Ω_θ.

STABILITY OF COUPLED RESPONSE

Equations (23)–(25) can be solved by applying the method of averaging, i.e. method of slowly varying amplitude popularly known as the Kryloff–Bogoliuboff method [7]. This method has been successfully applied by Evensen [8] in the vibration of circular rings and by Zaouk and Dym [9] for shallow shell vibrations. It is assumed that the solution exists in the form

$$\left.\begin{aligned}\Lambda_x(\tau)&=P(\tau)\cos[\Omega\tau+\Phi(\tau)]\\ \Lambda_y(\tau)&=Q(\tau)\cos[\Omega\tau+\Psi(\tau)]\\ \Lambda_\theta(\tau)&=R(\tau)\cos[\Omega\tau+\chi(\tau)]\end{aligned}\right\} \tag{26}$$

where variables P, Q, R, Φ, ψ, and χ are approximated by their average values $\mathbf{P}$, $\mathbf{Q}$, $\mathbf{R}$, $\mathbf{\Phi}$, $\mathbf{\Psi}$ and χ respectively. The averaging procedure thus leads to a set of six nonlinear simultaneous algebraic equations, which yield the approximate solution

$$\left.\begin{aligned}\Lambda_x(\tau)&=\mathbf{P}\cos(\Omega\tau+\mathbf{\Phi})\\ \Lambda_y(\tau)&=\mathbf{Q}\cos(\Omega\tau+\mathbf{\Psi})\\ \Lambda_\theta(\tau)&=\mathbf{R}\cos(\Omega\tau+\chi)\end{aligned}\right\} \tag{27}$$

The stability of the solution can be examined by the perturbation technique [8, 9]. The form of the solution expressed by eqn (27) is perturbed by letting

$$\left.\begin{aligned}\Lambda_x(\tau)&=\mathbf{P}\cos(\Omega\tau+\mathbf{\Phi})+\xi_x(\tau)\\ \Lambda_y(\tau)&=\mathbf{Q}\cos(\Omega\tau+\mathbf{\Psi})+\xi_y(\tau)\\ \Lambda_\theta(\tau)&=\mathbf{R}\cos(\Omega\tau+\chi)+\xi_\theta(\tau)\end{aligned}\right\} \tag{28}$$

where $\xi_x(\tau), \xi_y(\tau)$ and $\xi_\theta(\tau)$ represent small perturbations.

Substituting the expressions of eqn (28) into differential equations (23)–(25) and retaining only the first order terms in perturbations ξ_x, ξ_y and ξ_θ lead to the following set of variational equations (damped coupled Mathieu-Hill equations):

$$\begin{bmatrix}\frac{1}{f_2}&0&0\\0&\frac{1}{h_2}&0\\0&0&\frac{1}{g_2}\end{bmatrix}\begin{Bmatrix}\ddot{\xi}_x\\\ddot{\xi}_\theta\\\ddot{\xi}_y\end{Bmatrix}+\begin{bmatrix}\frac{f_1}{f_2}&0&0\\0&\frac{h_1}{h_2}&0\\0&0&\frac{g_1}{g_2}\end{bmatrix}\begin{Bmatrix}\dot{\xi}_x\\\dot{\xi}_\theta\\\dot{\xi}_y\end{Bmatrix}+\left(\begin{bmatrix}1&0&0\\0&1&0\\0&0&1\end{bmatrix}-\frac{1}{2}\begin{bmatrix}\frac{A_{11}}{f_2}&\left(\frac{A_{12}}{f_2}+\frac{2f_6}{f_2}\right)&0\\\left(\frac{A_{21}}{h_2}+\frac{2h_7}{h_2}\right)&\frac{A_{22}}{h_2}&\left(\frac{A_{23}}{h_2}+\frac{2h_{10}}{h_2}\right)\\0&\left(\frac{A_{32}}{g_2}+\frac{2g_6}{g_2}\right)&\frac{A_{33}}{g_2}\end{bmatrix}-\frac{1}{2}\cos 2\Omega\tau\begin{bmatrix}\frac{A_{11}}{f_2}&\frac{A_{12}}{f_2}&0\\\frac{A_{21}}{h_2}&\frac{A_{22}}{h_2}&\frac{A_{23}}{h_2}\\0&\frac{A_{32}}{g_2}&\frac{A_{33}}{g_2}\end{bmatrix}\right)\begin{Bmatrix}\xi_x\\\xi_\theta\\\xi_y\end{Bmatrix}=0 \tag{29}$$

in which

$$\left.\begin{aligned}A_{11}&=3f_3\mathbf{P}^2+2f_4\mathbf{PR}+f_5\mathbf{R}^2\\ A_{12}&=f_4\mathbf{P}^2+2f_5\mathbf{PR}+3f_7\mathbf{R}^2\\ A_{21}&=h_9\mathbf{R}^2+2h_3\mathbf{PR}+3h_8\mathbf{P}^2\\ A_{22}&=3h_4\mathbf{R}^2+2h_9\mathbf{PR}+h_3\mathbf{P}^2+3h_6\mathbf{R}^2+2h_{12}\mathbf{QR}+h_5\mathbf{Q}^2\\ A_{23}&=h_{12}\mathbf{R}^2+2h_5\mathbf{QR}+3h_{11}\mathbf{Q}^2\\ A_{32}&=g_4\mathbf{Q}^2+2g_5\mathbf{QR}+3g_7\mathbf{R}^2\\ A_{33}&=3g_3\mathbf{Q}^2+2g_4\mathbf{QR}+g_5\mathbf{R}^2\end{aligned}\right\}. \tag{30}$$

Equation (29) may be written in condensed form as

$$\mathbf{C}\ddot{\xi}+2\mathbf{C}\varepsilon\dot{\xi}+[\mathbf{E}-\tfrac{1}{2}\mathbf{A}-\tfrac{1}{2}\cos 2\Omega\tau\mathbf{B}]\xi=0 \tag{31}$$

where

$$\underline{\varepsilon}=\frac{1}{2}\begin{bmatrix} f_1 & 0 & 0 \\ 0 & h_1 & 0 \\ 0 & 0 & g_1 \end{bmatrix} \tag{32}$$

and $\underline{\mathbf{C}}$, $\underline{\mathbf{E}}$, $\underline{\mathbf{A}}$ and $\underline{\mathbf{B}}$ are defined by eqn (29).

The principal region of instability of the above equation can be approximated by [10]

$$\begin{vmatrix} \underline{\mathbf{E}}-\frac{1}{2}\underline{\mathbf{A}}+\frac{1}{4}\underline{\mathbf{B}}-\Omega^2\underline{\mathbf{C}} & -2\Omega\underline{\mathbf{C}}\underline{\varepsilon} \\ 2\Omega\underline{\mathbf{C}}\underline{\varepsilon} & \underline{\mathbf{E}}-\frac{1}{2}\underline{\mathbf{A}}-\frac{1}{4}\underline{\mathbf{B}}-\Omega^2\underline{\mathbf{C}} \end{vmatrix}=0 \tag{33}$$

which, upon expansion, becomes a sixth-order algebraic equation in Ω^2. For the first approximation, let

$$\Omega=\Omega_\theta. \tag{34}$$

Upon substituting this value into all the elements of determinantal eqn (33), except the second and fifth elements of the principal diagonal, the following equation is obtained:

$$\begin{vmatrix}
\left(1-\frac{A_{11}}{4f_2}-\frac{\Omega_\theta^2}{f_2}\right) & -\left(\frac{A_{12}}{4f_2}+\frac{f_6}{f_2}\right) & 0 & -\frac{\Omega_\theta f_1}{f_2} & 0 & 0 \\
-\left(\frac{A_{21}}{4h_2}+\frac{h_7}{h_2}\right) & \left(1-\frac{A_{22}}{4h_2}-\frac{\Omega^2}{h_2}\right) & -\left(\frac{A_{23}}{4h_2}+\frac{h_{10}}{h_2}\right) & 0 & -\frac{\Omega_\theta h_1}{h_2} & 0 \\
0 & -\left(\frac{A_{32}}{4g_2}+\frac{g_6}{g_2}\right) & \left(1-\frac{A_{33}}{4g_2}-\frac{\Omega_\theta^2}{g_2}\right) & 0 & 0 & -\frac{\Omega_\theta g_1}{g_2} \\
\frac{\Omega_\theta f_1}{f_2} & 0 & 0 & \left(1-\frac{3A_{11}}{4f_2}-\frac{\Omega_\theta^2}{f_2}\right) & -\left(\frac{3A_{12}}{4f_2}+\frac{f_6}{f_2}\right) & 0 \\
0 & -\frac{\Omega_\theta h_1}{h_2} & 0 & -\left(\frac{3A_{21}}{4h_2}+\frac{h_7}{h_2}\right) & \left(1-\frac{3A_{22}}{4h_2}-\frac{\Omega^2}{h_2}\right) & -\left(\frac{3A_{23}}{4h_2}+\frac{h_{10}}{h_2}\right) \\
0 & 0 & \frac{\Omega_\theta g_1}{g_2} & 0 & -\left(\frac{3A_{32}}{4g_2}+\frac{g_6}{g_2}\right) & \left(1-\frac{3A_{33}}{4g_2}-\frac{\Omega_\theta^2}{g_2}\right)
\end{vmatrix}=0. \tag{35}$$

The foregoing equation is expanded, neglecting terms of higher than the second order in f_1, g_1 and h_1. To express the solution for Ω in concise form the following substitutions are made:

$$\left.\begin{aligned}
E_1&=\left(1-\frac{A_{11}}{4f_2}-\frac{\Omega_\theta^2}{f_2}\right)\left(1-\frac{A_{33}}{4g_2}-\frac{\Omega_\theta^2}{g_2}\right)\\
E_2&=\left(1-\frac{3A_{11}}{4f_2}-\frac{\Omega_\theta^2}{f_2}\right)\left(1-\frac{3A_{33}}{4g_2}-\frac{\Omega_\theta^2}{g_2}\right)\\
E_3&=\left(\frac{A_{22}}{2h_2}\right)E_2\\
&\quad+\left(1-\frac{3A_{11}}{4f_2}-\frac{\Omega_\theta^2}{f_2}\right)\left(\frac{3A_{23}}{4h_2}+\frac{h_{10}}{h_2}\right)\left(\frac{3A_{32}}{4g_2}+\frac{g_6}{g_2}\right)\\
&\quad+\left(1-\frac{3A_{33}}{4g_2}-\frac{\Omega_\theta^2}{g_2}\right)\left(\frac{3A_{12}}{4f_2}+\frac{f_6}{f_2}\right)\left(\frac{3A_{21}}{4h_2}+\frac{h_7}{h_2}\right)\\
E_4&=\left(1-\frac{A_{11}}{4f_2}-\frac{\Omega_\theta^2}{f_2}\right)\left(\frac{A_{23}}{4h_2}+\frac{h_{10}}{h_2}\right)\left(\frac{A_{32}}{4g_2}+\frac{g_6}{g_2}\right)\\
&\quad+\left(1-\frac{A_{33}}{4g_2}-\frac{\Omega_\theta^2}{g_2}\right)\left(\frac{A_{12}}{4f_2}+\frac{f_6}{f_2}\right)\left(\frac{A_{21}}{4h_2}+\frac{h_7}{h_2}\right)
\end{aligned}\right\} \tag{36}$$

This allows the solution of equation (35) to be expressed as

It should be noted that the above equation contains the torsional damping term, h_1, within the inner radical term.

If $(E_1E_3-E_2E_4)^2-4\left(\frac{\Omega_\theta h_1}{h_2}\right)^2E_1^2E_2^2<0$,

Ω yields complex

values for the boundary frequencies. Thus, the largest value of torsional damping for which dynamic instability is still possible is defined by

$$(E_1E_3-E_2E_4)^2\%4\left(\frac{\Omega_\theta h_1}{h_2}\right)^2E_1^2E_2^2. \tag{38}$$

This results in the following expression defining the minimum value of torsional damping necessary to ensure stability:

$$\begin{aligned}
2\Omega_\theta h_1=&\frac{A_{22}}{2}+\frac{\left(\frac{3A_{23}}{4}+h_{10}\right)\left(\frac{3A_{32}}{4}+g_6\right)}{\left(g_2-\frac{3A_{33}}{4}\Omega_\theta^2\right)}\\
&+\frac{\left(\frac{3A_{12}}{4}+f_6\right)\left(\frac{3A_{21}}{4}+h_7\right)}{\left(f_2-\frac{3A_{11}}{4}-\Omega_\theta^2\right)}\\
&-\frac{\left(\frac{A_{23}}{4}+h_{10}\right)\left(\frac{A_{32}}{4}+g_6\right)}{\left(g_2-\frac{A_{33}}{4}-\Omega_\theta^2\right)}\\
&-\frac{\left(\frac{A_{12}}{4}+f_6\right)\left(\frac{A_{21}}{4}+h_7\right)}{\left(f_2-\frac{A_{11}}{4}-\Omega_\theta^2\right)}
\end{aligned} \tag{39}$$

$$\Omega=\left(h_2-\frac{A_{22}}{4}-h_2\frac{(E_1E_3+E_2E_4)\pm\left[(E_1E_3-E_2E_4)^2-4\left(\frac{\Omega_\theta h_1}{h_2}\right)^2E_1^2E_2^2\right]^{1/2}}{2E_1E_2}\right)^{1/2} \tag{37}$$

However, if torsional damping is neglected eqn (37) gives rise to two equations, one representing an upper bound and the other expressing a lower bound for the zone of instability. The upper bound curve is given by

$$\Omega^2 = h_2 - \frac{3A_{22}}{4} - \frac{\left(\frac{3A_{23}}{4}+h_{10}\right)\left(\frac{3A_{32}}{4}+g_6\right)}{\left(g_2-\frac{3A_{33}}{4}-\Omega_\theta^2\right)} - \frac{\left(\frac{3A_{12}}{4}+f_6\right)\left(\frac{3A_{21}}{4}+h_7\right)}{\left(f_2-\frac{3A_{11}}{4}-\Omega_\theta^2\right)} \quad (40)$$

whereas the lower bound curve is

$$\Omega^2 = h_2 - \frac{A_{22}}{4} - \frac{\left(\frac{A_{23}}{4}+h_{10}\right)\left(\frac{A_{32}}{4}+g_6\right)}{\left(g_2-\frac{A_{33}}{4}-\Omega_\theta^2\right)} - \frac{\left(\frac{A_{12}}{4}+f_6\right)\left(\frac{A_{21}}{4}+h_7\right)}{\left(f_2-\frac{A_{11}}{4}-\Omega_\theta^2\right)}. \quad (41)$$

Typical results obtained from the foregoing analysis are presented in the following discussion of an illustrative unsymmetric building structure.

TYPICAL RESULTS AND DISCUSSION

It is clear that eqns (39)–(41) involve the geometric parameters, damping coefficients, fundamental frequencies, input frequency and the nonlinearity parameter λ. Although these equations have been formulated for an unsymmetric system, they are equally applicable for symmetric structures as well. These equations are useful in studying the torsional instability of the system as well as in identifying values of the system parameters for which such instability may take place.

Torsional stability in a symmetric structure means having no torsional response for purely translational excitation. For an unsymmetric system, on the other hand, torsional stability is defined as a bound on the magnitude of the rotational displacement of the system over time.

To demonstrate the application of the method described above, a typical unsymmetrical building, L-shaped in plan as shown in Fig. 2, is selected for study.

Application of analysis to example structure

The elements of lateral resistance are assumed to be distributed along the perimeter of the structure as shown in Fig. 2. The building is assumed to be nominally symmetric, i.e. eccentricities e_x and e_y are small. (For the L-shaped building, values of the geometric parameters β and $\gamma \geqslant 0.3$ correspond to eccentricities $\leqslant 10\%$). For this condition, one may neglect the response amplitudes **Q** and **R** in eqns (30) and (39)–(41). The upper and lower bounds of eqns (40) and (41) are then transformed, respectively, as follows:

$$\Omega_\theta^2 = \Omega^2 + \frac{3h_3\mathbf{P}^2}{4} + \frac{h_{10}g_6}{(\Omega_y^2-\Omega_\theta^2)} + \frac{\left(\frac{3f_4\mathbf{P}^2}{4}+f_6\right)\left(\frac{9h_8\mathbf{P}^2}{4}+h_7\right)}{\left(1-\frac{9f_3\mathbf{P}^2}{4}-\Omega_\theta^2\right)} \quad (42)$$

and

$$\Omega_\theta^2 = \Omega^2 + \frac{h_3\mathbf{P}^2}{4} + \frac{h_{10}g_6}{(\Omega_y^2-\Omega_\theta^2)} + \frac{\left(\frac{f_4\mathbf{P}^2}{4}+f_6\right)\left(\frac{3h_8\mathbf{P}^2}{4}+h_7\right)}{\left(1-\frac{3f_3\mathbf{P}^2}{4}-\Omega_\theta^2\right)} \quad (43)$$

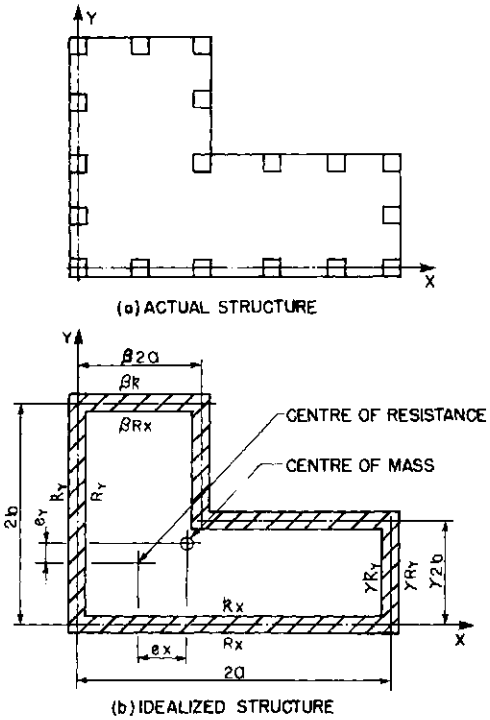

Fig. 2. Plan of example L-shaped building.

It is instructive to transform eqns (42) and (43) in terms of the non-dimensional eccentricities of the system. The non-dimensional eccentricities, E_x and E_y, are given by

$$E_x = \frac{e_x}{\Gamma}, \quad E_y = \frac{e_y}{\Gamma} \quad (44)$$

All coefficients, except h_3, of eqns (42) and (43) can now be expressed in terms of E_x, E_y, λ, Ω_y and Ω_θ; namely,

$$\left.\begin{aligned} f_3 &= \lambda, & h_7 &= E_y\Omega_\theta^2 \\ f_4 &= -\frac{3\lambda E_y}{\Omega_\theta^2}, & h_8 &= -\lambda E_y\Omega_\theta^2 \\ f_6 &= \frac{E_y}{\Omega_\theta^2}, & h_{10} &= -E_x\Omega_\theta^2 \\ g_6 &= -\frac{E_x\Omega_y^4}{\Omega_\theta^2} \end{aligned}\right\} \quad (45)$$

It is somewhat complicated to express h_3 in terms of E_x and E_y; therefore, the expression for h_3 is written in

terms of the geometric parameters as

$$h_3 = 3\lambda\gamma_1^2\left(\frac{c_3}{c_1}\right)^2 \tag{46}$$

in which

$$\left.\begin{aligned}
\gamma_1 &= -\frac{\sqrt{3}c_1}{\sqrt{c_6 r^2 + c_7}}\\
c_1 &= 1-(1-\beta)(1-\gamma)\\
c_2 &= 1-(1-\beta^2)(1-\gamma)\\
c_3 &= 1-(1-\beta)(1-\gamma^2)\\
c_4 &= \gamma(1-\gamma)(1-\beta)^2\\
c_5 &= \beta(1-\beta)(1-\gamma)^2\\
c_6 &= c_2^2 + 4\beta c_4\\
c_7 &= c_3^2 + 4\gamma c_5
\end{aligned}\right\} \tag{47}$$

and where r is the aspect ratio, a/b, of the building and parameters β and γ, defined in Fig. 2, represent the two geometric parameters of a particular L-shaped building plan.

An approximation for the translational amplitude, **P**, in the direction of ground motion for the nominally symmetric building is necessary. Kan and Chopra [2] provided the following relationship for the two translational and the torsional responses in a three-degree-of-freedom linear unsymmetric system:

$$\mathbf{V}_x^2 + \mathbf{V}_y^2 + \mathbf{T}^2 = 1 \tag{48}$$

in which

$$\mathbf{V}_x = \frac{V_x}{V_{x0}}, \quad \mathbf{V}_y = \frac{V_y}{V_{x0}}, \quad \text{and} \quad \mathbf{T} = \frac{T}{rV_{x0}} \tag{49}$$

Here V_{x0} is the response in the x-direction of the single-degree-of-freedom uncoupled system whose mass and stiffness are the same as those of the coupled system; V_x, V_y and T are the translational and torsional responses of the coupled system in the x-, y- and θ-directions, respectively.

Equation (48) can readily be transformed into

$$\frac{\mathbf{P}}{\sqrt{D}}(1+E_y) + \frac{\mathbf{Q}}{\sqrt{D}}\Omega_y^2(1+E_x) = 1 \tag{50}$$

where

$$D = [(1-\Omega^2)^2 + (2\zeta_x\Omega)^2]^{-1}. \tag{51}$$

For input ground excitation in the x-direction, the response $\mathbf{P} \gg \mathbf{Q}$, since eccentricities are assumed small and the building is nominally symmetric. Hence, **Q** can be set to zero and eqn (50) transforms into

$$\mathbf{P}^2 = \frac{D}{(1+E_y^2)} \tag{52}$$

Substituting eqns (45), (46) and (52) into eqns (42) and (43) yields the following upper and lower bound instability equations:

$$\Omega_\theta^2 = \Omega^2 + \left(\frac{9\lambda D}{4(1+E_y^2)}\right)\left(\frac{c_3}{c_1}\gamma_1\right)^2 + \left(\frac{E_x^2\Omega_y^4}{\Omega_y^2-\Omega_\theta^2}\right) + \left(\frac{\left[1-\dfrac{9\lambda D}{4(1+E_y^2)}\right]^2 E_y}{\left[1-\dfrac{9\lambda D}{4(1+E_y^2)}\right]-\Omega_\theta^2}\right) \tag{53}$$

$$\Omega_\theta^2 = \Omega^2 + \left(\frac{3\lambda D}{4(1+E_y^2)}\right)\left(\frac{c_3}{c_1}\gamma_1\right)^2 + \left(\frac{E_x^2\Omega_y^4}{\Omega_y^2-\Omega_\theta^2}\right) + \left(\frac{\left[1-\dfrac{3\lambda D}{4(1+E_y^2)}\right]^2 E_y}{\left[1-\dfrac{3\lambda D}{4(1+E_y^2)}\right]-\Omega_\theta^2}\right). \tag{54}$$

The foregoing allows eqn (39) to be expressed in terms of the non-dimensional eccentricites. The largest value of torsional damping in a nominally symmetric building for which dynamic instability is still possible is thus given by

$$\zeta_\theta = \left(\frac{3\lambda D}{8\Omega_\theta^2(1+E_y^2)}\right)\left(\frac{c_3}{c_1}\gamma_1\right)^2 + \frac{E_y^2}{4\Omega_\theta^2} \times \left[\frac{\left\{1-\dfrac{9\lambda D}{4(1+E_y^2)}\right\}^2}{\left\{1-\dfrac{9\lambda D}{4(1+E_y^2)}\right\}-\Omega_\theta^2} - \frac{\left\{1-\dfrac{3\lambda D}{4(1+E_y^2)}\right\}^2}{\left\{1-\dfrac{3\lambda D}{4(1+E_y^2)}\right\}-\Omega_\theta^2}\right]. \tag{55}$$

Stability curves for example structure

Figures 3 and 4 present the stability curves in $\Omega_\theta - \Omega$ parameter space computed from eqns (53) and (54). An interesting feature in the computation of Ω_θ is the appearance of a discontinuity or "gap" in the solution to the left of $\Omega = 1$, where the approximate solution for Ω_θ from both the upper and the lower bound equations breaks down. To investigate the possible reason for this behaviour, examination of eqns (53) and (54) shows that when the denominator of the fourth term in these equations approaches zero, the term becomes large.

Curves plotted in Fig. 3 trace the behaviour of the

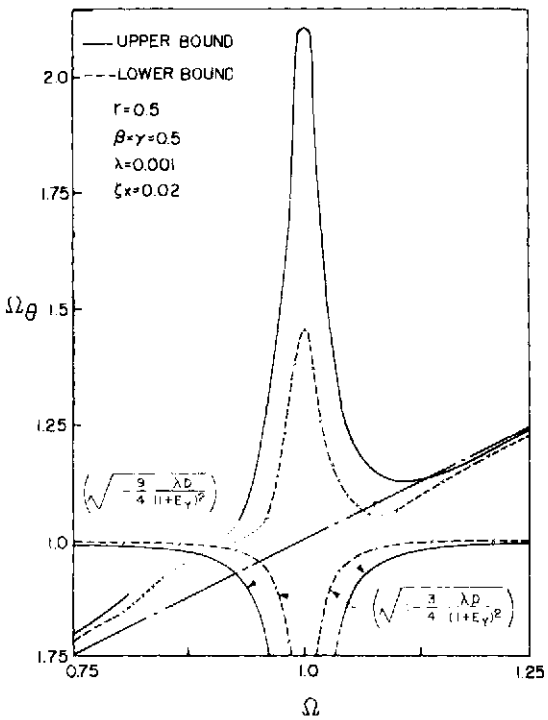

Fig. 3. Instability curves for example L-shaped building.

fourth term; the curves for the partial denominators, $\sqrt{1-\frac{9\lambda D}{4(1+E_y^2)}}$ and $\sqrt{1-\frac{3\lambda D}{4(1+E_y^2)}}$ from eqns (53) and (54), are seen to cross the upper and lower bound instability curves at the location of the gap. A similar breakdown in the solution is also noticed for some of the lower bound curves, this time to the right of $\Omega=1$. However, here the partial denominator curves do not cross the expected solutions of the lower bound equation. It is found that the gaps diminish with a decrease in eccentricity. This is evident also from the fact that the numerator of the fourth term contains the eccentricity as a compensating factor. A time history investigation needs to be performed to understand more fully the significance of the gap. It is interesting to note that a similar "gap" phenomenon was observed by Evensen [8] in the study of nonlinear vibrations of thin circular rings.

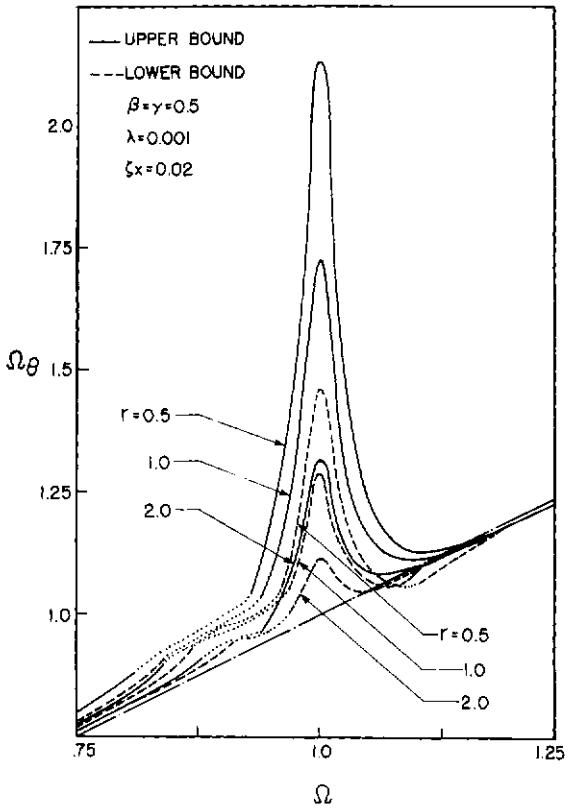

Fig. 4. Effect of aspect ratio r on instability.

Figure 4 is the plotting of some instability curves similar to those described in Fig. 3 for various values of aspect ratio r, to demonstrate the influence of this parameter on the zone of instability of the system. It is seen that the instability zone decreases and shifts towards the $\Omega_\theta=\Omega$ line as r increases in magnitude. Also the length of gap decreases with the increased r values for both upper and lower bound curves.

The effect of torsional damping ζ_θ (eqn 55) is demonstrated in Figs. 5 and 6. A value of ζ_θ less than the magnitude plotted for a particular system implies that the structure is unstable. This equation also exhibits computational difficulties, producing a "gap" at or somewhat to the left of $\Omega_\theta=1$ (Fig. 5), similar to that The denominator of the second term of eqn (55), when approaching small values, is responsible for this gap. In Fig. 6 the same equation is replotted in ζ_θ–Ω plane for several ζ_x and Ω_θ values to demonstrate the influence of the aspect ratio, r. The results show that the smaller the value of the aspect ratio, the larger the value of ζ_θ required to stabilize the system.

In the present study, the resisting elements have been assumed to be distributed along the perimeter of the structure. However, in actual buildings the resisting elements are frequently distributed over the plan area. To handle such systems, appropriate expressions for E_x, E_y, K_x, and K_y should be employed in the general formulation expressed by eqns (39)–(41).

The system considered here is subjected sinusoidal ground motion in only one direction, although earthquake ground motion is multi-directional and more complex in nature. However, this would not significantly alter the parametric conditions for torsional instability.

SUMMARY AND CONCLUSIONS

The purpose of this paper is to present the mathematical relationships for the parameters of an unsymmetric structure subjected to ground motion, in order to identify situations where the system will be torsionally unstable.

Two mathematical relationships have been formulated, one for the upper bound and the other for the lower bound instability curve. The torsional motion is found to be unstable due to nonlinearity of the resisting elements as well as the eccentricities between centres of resistance and mass, provided that parameters of the system are such that they fall within the zone between the upper and lower bound instability curves. Also, an

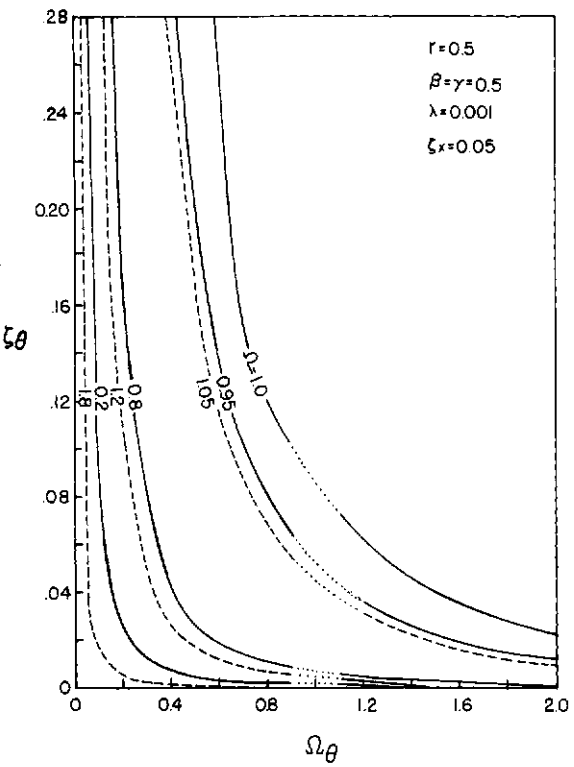

Fig. 5. Minimum torsional damping for stability.

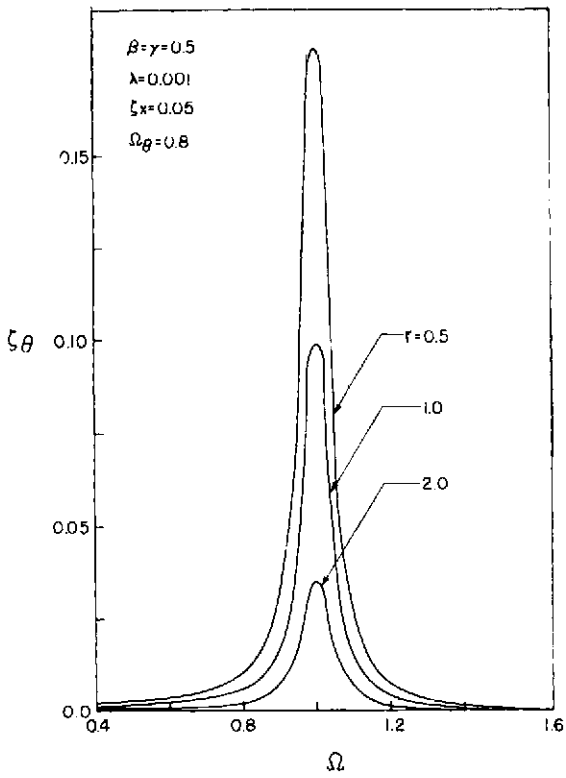

Fig. 6. Effect of aspect ratio r on minimum torsional damping.

expression has been presented for torsional damping, in terms of the system parameters. This expression may be used to determine the minimum torsional damping necessary to stabilize torsional response accompanying purely translational excitation.

Some numerical problems in the computation of instability and torsional damping curves have been encountered in the form of "gaps". Otherwise, the numerical computation is simple enough to be used for both truly symmetric and the nominally symmetric structures of the present study.

FUTURE RESEARCH

In terms of future research, additional study is needed to apply the procedure presented herein to buildings of other geometries, particularly those exhibiting large eccentricities. Further study is also needed to understand more fully the occurrence of "gaps" in the solution. Time-history analysis appears necessary for the latter.

REFERENCES

1. J. B. Hoerner, Modal coupling and earthquake response of tall buildings. Ph.D. Thesis, California Institute of Technology (1971).
2. C. L. Kan and A. K. Chopra. Coupled lateral torsional response to buildings to ground shaking. Report No. EERC 76-13, University of California, Berkeley (1976).
3. K. M. Dempsey and H. M. Irvine, Envelopes of maximum seismic response for a partially symmetric single-storey building model. *J. Earthquake Engng Struct. Dynamics* **7**, 161–180 (1979).
4. N. M. Newmark, Torsion in symmetrical buildings. Proc. *4th World Conf. Earthquake Engng*, Vol. 2, A-3, pp. 19–32. Santiago, Chile (1969).
5. W. K. Tso. Induced torsional oscillations in symmetrical structures. *J. Earthquake Engng Struct. Dynamics* **3**, 337–346 (1975).
6. W. K. Tso and K. G. Asmis, Torsional vibration of symmetrical structures. *Proc. 1st Can. Conf. Earthquake Engr*, pp. 178–186 Vancouver (1971).
7. N. Kryloff and N. Bogoliuboff. *Introduction to Nonlinear Mechanics*. Princeton University Press, New Jersey (1947).
8. D. A. Evensen, Nonlinear flexural vibrations of thin circular rings. *J. Appl. Mech.* **33**, 553–560 (1966).
9. B. R. El-Zaouk and C. L. Dym, Non-linear vibrations of orthotropic doubly-curved shallow shells. *J. Sound Vib.*, **31**(1), 89–103 (1973).
10. V. V. Bolotin. *The Dynamic Stability of Elastic Systems*. Holden-Day, San Francisco (1964).
11. K. Klotter and E. Pinney, A comprehensive stability criterion for forced vibrations in nonlinear systems. *J. Appl. Mech., ASME Trans.* **20**, 9–12 (1953).

Computers & Structures, Vol. 13, pp. 205–211, 1981
Printed in Great Britain.

0045-7949/81/010205-07$02.00/0

ELASTIC-PLASTIC SEISMIC RESPONSE ANALYSES OF STRUCTURES SUPPORTING STEAM GENERATORS

Y. NAKAO† and Y. MURASE‡
Senior Research Engineer, Structure and Vibration Research Laboratory, Hiroshima Technical Institute, Technical Headquarters

and

H. KOHATA
Manager, Civil Engineering Section, Power System Headquarters, Mitsubishi Heavy Industries, Ltd., Tokyo, Japan

(*Received* 6 *May* 1980).

Abstract Three dimensional elastic–plastic seismic response analysis of structures supporting steam generators is carried out. The structural system is idealized as a finite element model composed of elastic beam elements and partially of non-linear spring elements. In the equation of motion the nonlinear restoring force term is divided into a linear term and a nonlinear term, the latter being moved to the right hand side of the equation and regarded as an external force term. The equation is solved by using the mode superposition method accompanied by the mass condensation method. The analysis method is shown to be of practical use by applying it to a scaled model and to an actual structure.

1. INTRODUCTION

In the past, during strong earthquakes in Japan, the structures supporting steam generators as shown in Fig. 1 have been damaged in such localized parts as stoppers. Although these damages are not detrimental to the function of the generators, analytical approaches to these occurrence are desired to evaluate the damages and to keep the safety factors of the structures adequate.

Generally the elastic–plastic seismic response analysis of framed structures such as tall buildings has been performed by using the simplified method of idealizing the structures by mass-spring systems with dashpots [1]. However, with such a simplified idealization, it seems difficult to analyze the response of the structure supporting the generator and to evaluate directly the stresses of each of the structural members, because of the complexity involved in the structural system (Fig. 1).

In this paper, an elastic–plastic response analysis in which the structure is idealized as a three dimensional finite element model is carried out by applying the mode superposition method [2] in conjunction with the mass condensation method [3–5].

First, considering the aforementioned experiences of the damages of actual structures, it can be assumed that the structural members of the supporting structure and the generator remain elastic, while the stoppers, which are provided for the lateral support of the generator, are elastic-plastic during an earthquake. The system is, thus, idealized to be an assemblage of elastic beam elements and elastic plastic spring elements having bi-linear restoring force characteristics.

Next, the nonlinear restoring force term in the equation of motion of the above system is divided into a linear term and a nonlinear term, the latter being moved to the right hand side of the equation and regarded as an external force vector. The equation is

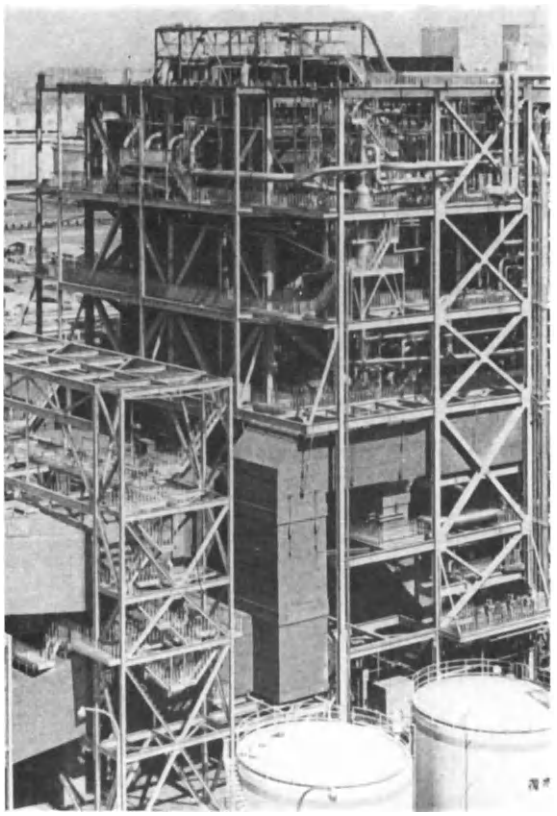

Fig. 1. Bird's-eye view of steam generator and its supporting structure.

†Assistant Chief Research Engineer.
‡Senior Research Engineer, Structure and Vibration Research Laboratory.

reduced by the mass condensation method [3] and subsequently solved by the mode superposition method. The response of each mode is calculated by Newmark's β method [6], and the effect of the nonlinear term is corrected by the iteration method at each step of the integration.

Finally, a seismic shaking table test was carried out on a scaled model, and experimental and calculated responses are compared to show that the accuracy is practically good. Moreover, calculated and measured natural frequencies and modes of an actual structure are shown to be in good agreement. Then, the analysis method is applied to an actual structure subjected to a strong earthquake, and it is shown that the previously mentioned actual damages can be explained well by the results of the analysis.

6. IDEALIZATION OF THE STRUCTURE

The structure supporting the steam generator is of complicated construction, consisting of columns, beams, vertical braces, and horizontal braces provided on each floor, etc. (Fig. 1). The elevation and plan views of the structure are shown in Figs. 2 and 3, respectively. The steam generator is suspended from the top of the supporting structure through rods and is horizontally supported by stoppers which are located along the height of the generator. The stoppers prevent only the horizontal movement of the generator, as shown in Fig. 3.

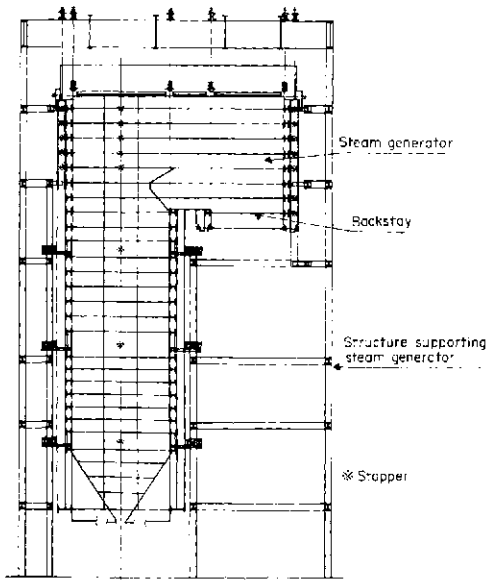

Fig. 2. Elevation view of steam generator and supporting structure and location of stoppers.

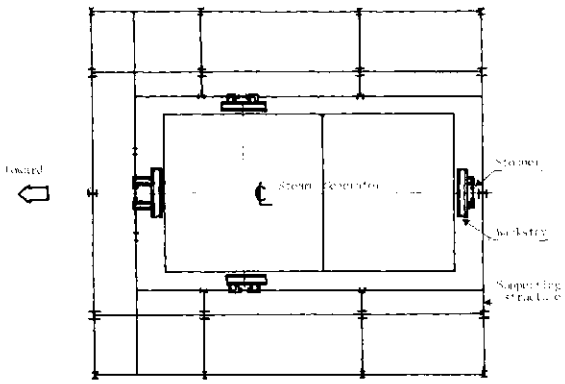

Fig. 3. Plan view of steam generator and supporting structure.

Each member of the supporting structure is idealized as the elastic beam element and treated as the three-dimensional finite element model shown in Fig. 4. The steam generator is also idealized as the equivalent beam elements in Fig. 4 and the lumped masses as shown in Fig. 5(a). The stoppers are idealized as the non-linear spring elements having a bilinear restoring force characteristics, as shown in Fig. 5(b).

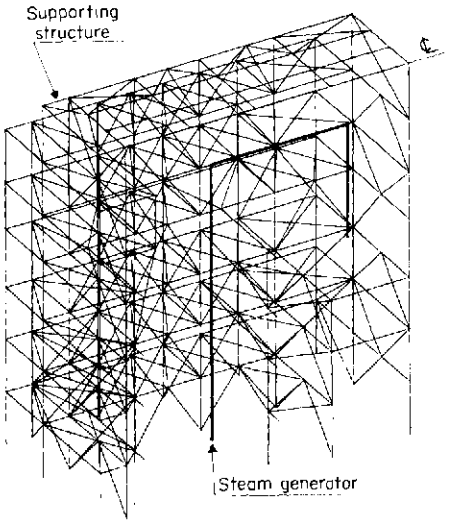

Fig. 4. Finite element model of a prototype.

3. METHOD OF ANALYSIS

According to the finite element analysis procedure, the basic equation of seismic response for the above mentioned structural system can be expressed as:

$$[M]\{\ddot{u}\}+[C]\{\dot{u}\}+[K_N(\{u\})]\{u\}=-[M]\{E\}\ddot{u}_0 \qquad (1)$$

where $\{u\}$: unknown nodal parameter vector consisting of displacements and rotations relative to movement of the base of the structure,

$[M]$: mass matrix,

$[C]$: damping matrix,

$[K_N(\{u\})]$: stiffness matrix (including non-linear spring stiffness; the function of $\{u\}$),

$\{E\}$: vector showing external force distribution corresponding to the ground movement,

$\ddot{u}_0$: seismic acceleration at the base of the structure (the function of time),

$\dot{} \equiv \frac{d}{dt}$

The non-linear restoring force term $[K_N(\{u\})]\{u\}$ can be divided into the linear restoring force term $[K_L]\{u\}$ and the non-linear term $\{P_N(\{u\})\}$ by dividing the restoring force of the non-linear spring element into a linear term and a non-linear term. By moving the non-linear external force term to the r.h.s. of eqn (1),

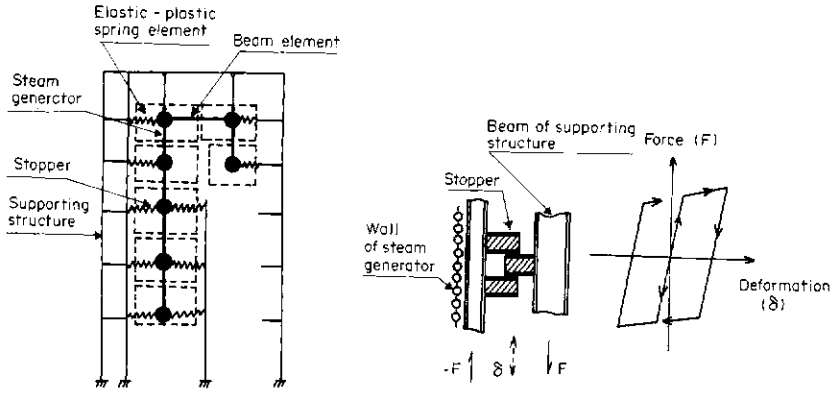

Fig. 5. Idealization of steam generator and stopper.

the following equation is obtained:

$$[M]\{\ddot{u}\}+[C]\{\dot{u}\}+[K_L]\{u\}=-[M]\{E\}\ddot{u}_0-\{P_N(\{u\})\}. \tag{2}$$

To reduce degrees of freedom, the mass condensation method is applied, by dividing $\{u\}$ into the master parameter vector $\{u_m\}$ and the slave parameter vector $\{u_s\}$, where all the parameters corresponding to the elastic-plastic stoppers are selected to be contained in the master parameter vector $\{u_m\}$. Then, eqn (2) can be divided into the equations with respect to the master and slave parameters, respectively, as follows:

$$[M_m]\{\ddot{u}_m\}+[C_{mm}]\{\dot{u}_m\}+[C_{ms}]\{\dot{u}_s\}+[K_{Lmm}]\{u_m\}+[K_{Lms}]\{u_s\}=-[M_m]\{E_m\}\ddot{u}_0-\{P_{Nm}(\{u_m\})\} \tag{3a}$$

$$[M_s]\{\ddot{u}_s\}+[C_{sm}]\{\dot{u}_m\}+[C_{ss}]\{\dot{u}_s\}+[K_{Lsm}]\{u_m\}+[K_{Lss}]\{u_s\}=-[M_s]\{E_s\}\ddot{u}_0 \tag{3b}$$

where

$$\begin{bmatrix}\{u_m\}\\ \{u_s\}\end{bmatrix}\equiv\{u\},\quad \begin{bmatrix}[M_m] & 0\\ 0 & [M_s]\end{bmatrix}\equiv[M],$$

$$\begin{bmatrix}[C_{mm}][C_{ms}]\\ [C_{sm}][C_{ss}]\end{bmatrix}\equiv[C]$$

$$\begin{bmatrix}[K_{Lmm}][K_{Lms}]\\ [K_{Lsm}][K_{Lss}]\end{bmatrix}\equiv[K_L],\quad \begin{bmatrix}\{E_m\}\\ \{E_s\}\end{bmatrix}\equiv\{E\},\quad \begin{Bmatrix}\{P_{Nm}(\{u_m\})\}\\ 0\end{Bmatrix}$$

In eqn (3b), assuming that the inertia and damping terms are small and negligible, the vector $\{u_s\}$ can be solved in approximation as the function of the solution $\{u_m\}$ and $\ddot{u}_0$[5]; as follows:

$$\{u_s\}=-[K_{Lss}]^{-1}[K_{Lsm}]\{u_m\}+[K_{Lss}]^{-1}[M_s]\times[K_{Lss}]^{-1}[K_{Lsm}]\{\ddot{u}_m\}-[K_{Lss}]^{-1}[M_s]\{E_s\}\ddot{u}_0. \tag{4}$$

By substituting eqn (4) in eqn (3a), the basic equation relating to the master parameter vector can be obtained as follows:

$$[M_m^*]\{\ddot{u}_m\}+[C_m^*]\{\dot{u}_m\}+[K_m^*]\{u_m\}=-[M_m^*]\{E_m^*\}\ddot{u}_0-\{P_{Nm}(\{u_m\})\} \tag{5}$$

where

$$[M_m^*]=[M_m]+[K_{Lms}][K_{Lss}]^{-1}[M_s][K_{Lss}]^{-1}[K_{Lsm}]$$
$$[C_m^*]=[C_{mm}]$$
$$[K_m^*]=[K_{Lmm}]-[K_{Lms}][K_{Lss}]^{-1}[K_{Lsm}]$$
$$[M_m^*]\{E_m^*\}=[M_m]\{E_m\}-[K_{Lms}][K_{Lss}]^{-1}[M_s]\{E_s\}.$$

Equation (5) is solved by the method of mode superposition which, comparing calculation time, is considered to be more economical than the ordinary direct integration method in the current problem, because considerable degrees of freedom are still there.

The elastic natural vibration mode vectors of eqn (5) are obtained from the following eigen-value equation:

$$-\omega_n^2[M^*]\{\phi_{mn}\}+[K_m^*]\{\phi_{mn}\}=0,\quad (n=1, 2\ldots) \tag{6}$$

where ω_n: nth natural circular frequency.
$\{\phi_{mn}\}$: nth natural vibration mode vector of master parameter vector.

Using $\{\phi_{mn}\}$ and ω_n $(n=1, 2\ldots)$, eqn (5) can be expressed, as:

$$\{u_m\}=\sum_n \alpha_n\{\phi_{mn}\} \tag{7a}$$

$$\ddot{\alpha}_n+2h_n\omega_n\dot{\alpha}_n+\omega_n^2\alpha_n=-\beta_n^*\ddot{u}_0-N_n^*(\{u_m\}),\quad (n=1, 2\ldots) \tag{7b}$$

where

$$\beta_n^*=\frac{\{\phi_{mn}\}^T[M_m^*]\{E_m^*\}}{\{\phi_{mn}\}^T[M_m^*]\{\phi_{mn}\}},$$

$$N_n^*(\{u_m\})=\frac{\{\phi_{mn}\}^T\{P_{Nm}(\{u_m\})\}}{\{\phi_{mn}\}^T[M_m^*]\{\phi_{mn}\}}.$$

The modal damping ratio h_n can be determined by referring to the measured values, etc. as is usually performed.

A step-by-step integration of eqn (7) is performed using the Newmark's β method with $\beta=1/6$ or $1/4$, the non-linear terms in the right-hand side of eqn (7b) being corrected in each step of the integration by means of the iteration method starting from the elastic solution. Judgement of convergence is performed by the following equation:

$$\frac{\ddot{\alpha}_n(i+1)}{\ddot{\alpha}_n(i)}-1\leqslant\varepsilon$$

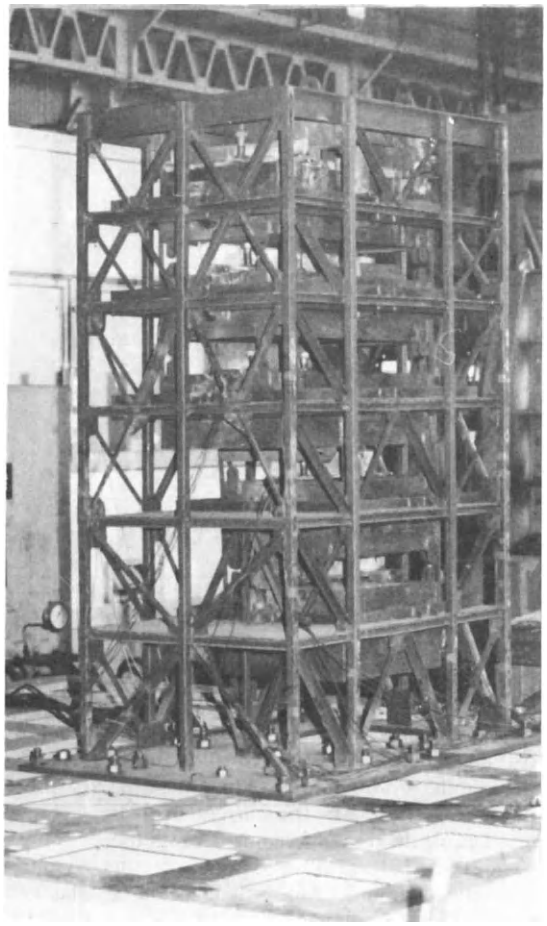

Fig. 6. View of experimental model on shaking table.

where i: number of iteration ($=1, 2 \ldots$)
ε: convergence tolerance.

If the dynamic force terms can be neglected in higher order vibration modes compared with their static force terms, the higher order equation in eqn (7b) may be approximated as follows:

$$\omega_n^2 \alpha_n = -\beta_n^* \ddot{u}_0 - N_n^*(\{u_m\}). \tag{9}$$

By the use of eqn (9), the time interval of the integration can reasonably be enlarged without any fear of divergence of the solution.

The slave parameter vector $\{u_s\}$ is calculated from eqn (4), using $\{u_m\}$ obtained in the above manner, and stresses of all elements for any arbitrary time can also be obtained.

4. MODEL TEST AND COMPARISON WITH THE THEORY

A vibration test was performed and analyzed, on a scaled model of an appropriate prototype. As shown in Fig. 6, due to the size of the shaking table, the model was made of steel and about one to thirty scale. The steam generator was divided vertically into five blocks, which were suspended one by one from the top of the supporting structure through flexible rods.

The stoppers were designed so that plastic hinges may be produced only in the local regions near fixed ends (Fig. 7). The restoring force characteristics were obtained from a static loading test, as shown in Fig. 7.

First, an elastic natural vibration characteristic test was performed on the shaking table by applying small vibration to measure the natural frequencies, natural vibration modes and damping ratios. Second, the responses of accelerations and strains at the typical points were measured by applying simulated seismic vibrations, and gradually increasing the levels of their input accelerations.

In the analysis of model, 30 parameters were selected; 20 lateral displacements at both ends of 10 stoppers, and 10 respresentative displacements of the supporting structure.

The CPU time for calculation of the natural vibration was about 350 sec on CDC Cyber 173.

4.1 *Natural vibration*

Figures 8 and 9 shows a comparison between the computed and tested values of the first and second vibration modes and their frequencies. The calculated values of the first vibration mode show good agreements both for frequency and displacement mode. Some greater error is shown for the second vibration mode, but it may be said to be permissible for earthquake resistant design of these structures.

4.2 *Elastic response*

The elastic response at the base acceleration of 150 gal was calculated using the first and second vibration modes, and the measured values as the damping ratios ($h_1 = 0.02$, $h_2 = 0.043$) for the modal response analysis.

Figure 10 shows the comparison of the experimental and calculated responses at the typical points. Both are in good correspondence.

4.3 *Elastic–plastic seismic response*

The elastic–plastic response at the base acceleration of 950 gal was calculated using all of the vibration modes up to 30th order, where eqn (7b) for frequencies higher than 8th order (85 Herz) was approximated by eqn (9). In this analysis, it was assumed that the 1st and 2nd modal damping ratios were the same as those in the case of the foregoing elastic response, and the ratios of the modes higher than 2nd order also were replaced by the 2nd order damping ratio (0.043). The time increment and the convergence tolerance were taken as 1/4000 sec and 0.0005, respectively. The CPU time for calculation of the response was about 700 sec on CDC Cyber 173.

Figure 11 shows the comparison of the experimental and the calculated results, in which the elastic–plastic calculation results coincide comparatively well with the experimental ones, while elastic calculation results show a quite different tendency. And it can be seen that the stress response of the stopper tends to remain on the same level due to yielding of the stopper. From the effects of such elastic–plastic deformations of the stoppers, the accelerations and the stress responses of the structure also show the phenomena of reduction of their responses in comparison with those obtained by elastic analysis.

5. APPLICATION TO ACTUAL STRUCTURE

This section discusses the practicability of this analysis method by applying it to actual structures. First, the results of the measurement and the analysis of the natural frequencies and modes of an actual

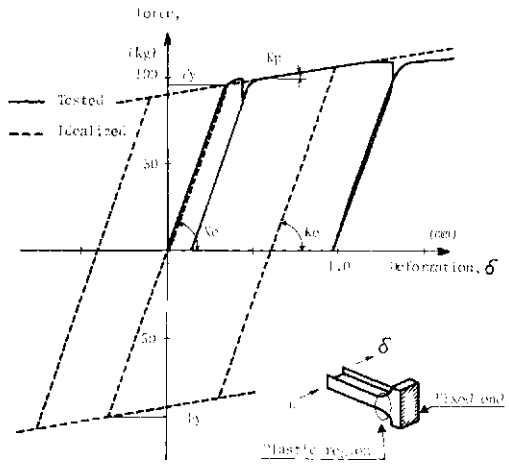

Fig. 7. Idealization of restoring force characteristics of stopper of experimental model.

structure are in comparatively good agreement as shown in Table 1 and Fig. 12 [7]. Thus, the aforesaid idealizing technique can be considered nearly applicable to actual structures.

Next, the response analysis was performed on an actual supporting structure that had in fact encountered a strong earthquake in which only its stoppers were damaged while its main members remained sound. Using the acceleration wave recorded in the vicinity of the site as the seismic input, two types of calculations were performed: one for the elastic response and the other for the elastic–plastic response considering the previously mentioned elastic-plastic deformations of the stoppers.

Figures 13 and 14 show the response waves at the typical points and the maximum axial stress ratios of the main members of the supporting structure, respectively. (The stress ratio is defined as a ratio of the axial stress to the allowable stress.) As clear from Fig. 13, the elastic responses are still increasing in the vicinity

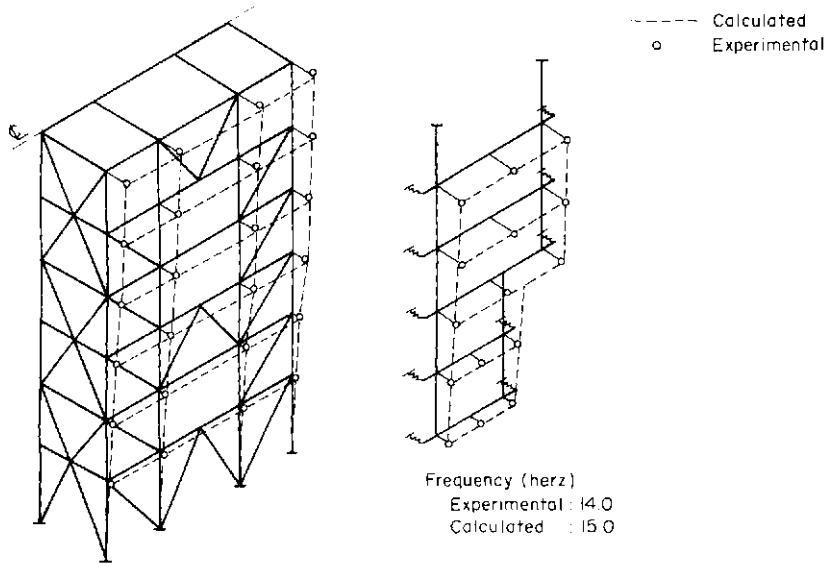

Fig. 8. Comparison of calculated experimental values of first vibration mode and its frequency.

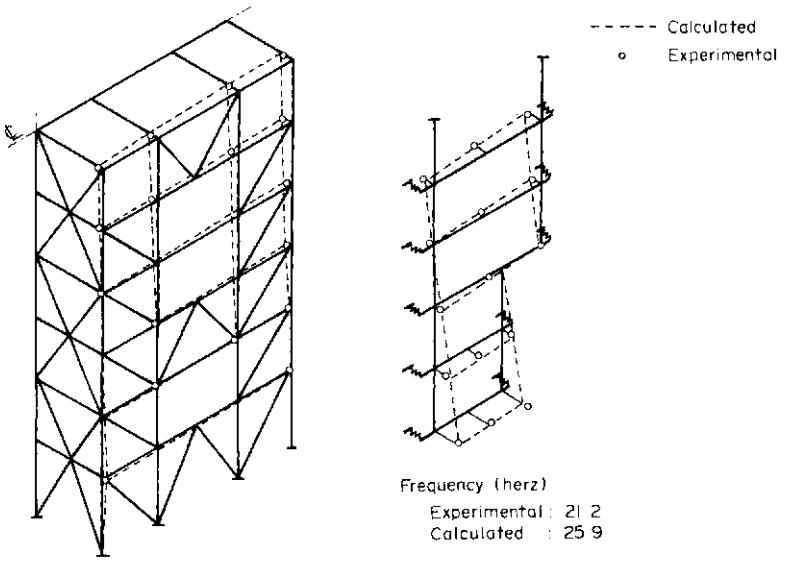

Fig. 9. Comparison of calculated and experimental values of second vibration mode and its frequency.

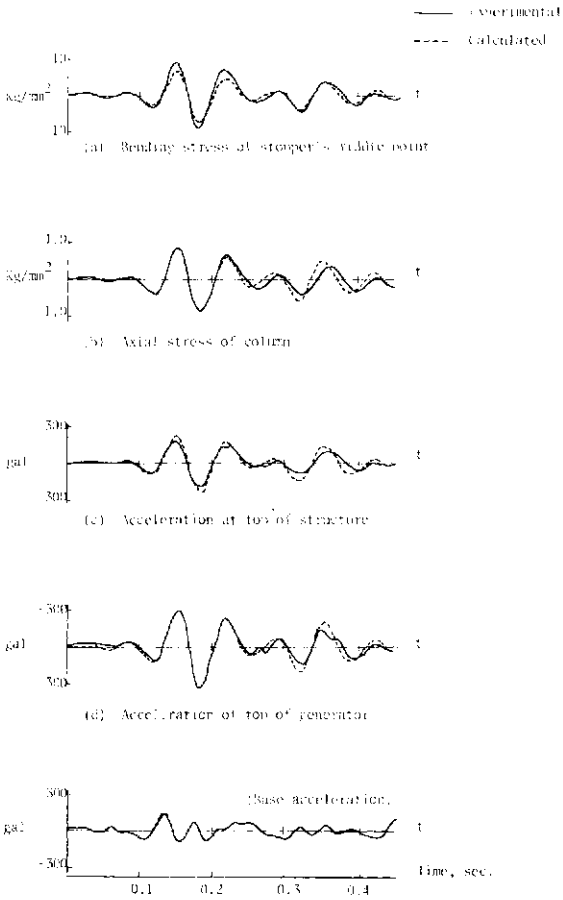

Fig. 10. Comparison of calculated and experimental values in elastic response.

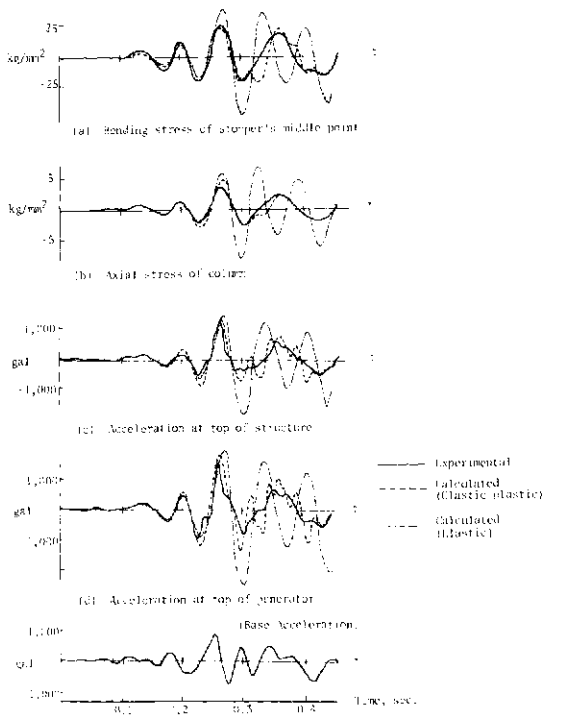

Fig. 11. Comparison of calculated and experimental values in elastic-plastic response.

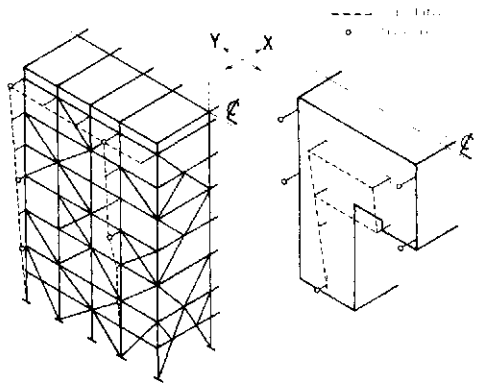

Fig. 12. Comparison of calculated and measured first vibration mode on prototype.

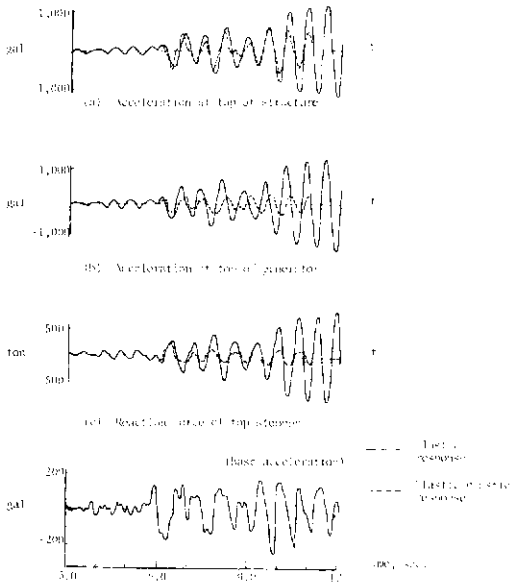

Fig. 13. Elastic and elastic-plastic seismic responses calculated on an actual structure.

Table 1. Comparison of calculated and measured natural frequencies on prototype.

Vibration mode	Frequency (herz)	
	Calculated	Measured
First mode in X-di	1.04	1.1
First mode in Y-di.	1.15	1.25
Torsional mode	1.74	–
Second mode in X-di	2.61	–
Second mode in Y-di	4.69	–

of 11 sec, while the elastic-plastic responses are flat after 6 seconds, nearly at which time the stoppers begin to yield. From Fig. 14, it can also be seen that the axial stresses of the main members of the supporting structure are all within the allowable stresses in regard to the elastic plastic response; whereas, in the case of the elastic response, there are members exceeding the allowable stresses. Thus, the results of the elastic-plastic response calculation can explain the aforementioned damaged condition of the actual structure, demonstrating the practicability of this elastic-plastic response analysis method.

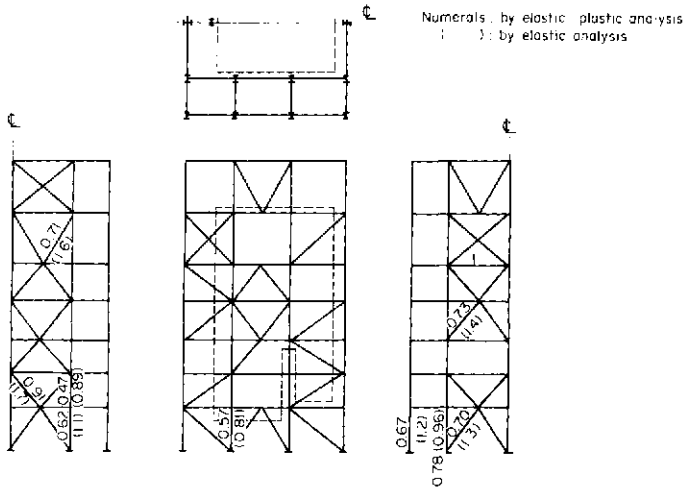

Fig. 14. Stress ratios in main structural members on acctual structure.

6. CONCLUSION

The three dimensional analysis of the elastic–plastic seismic response of structures supporting steam generators has been carried out by applying the mode superposition method in conjunction with the mass condensation method. The following results have been obtained from some examinations.

(1) The comparison between the results of the scaled model test and the calculation has shown that the accuracy of the analysis is comparatively good.

(2) The results of the measurement and the analysis of the natural frequencies and modes of an actual structure are in comparatively good agreement.

(3) The phenomena of actual structures during strong earthquakes in the past, in which only localized stoppers were damaged, can be well explained qualitatively using the elastic–plastic analysis.

(4) Thus, the present method of analysis is considered to be of practical use for seismic response analyses of structures supporting steam generators and similar heavy-framed structures.

REFERENCES

1. K. Muto, Seismic response analysis of building by the matrix method, Preprint., *Japan U.S. Seminar on Matrix Methods of Structural Analysis and Design*, Tokyo, 1969.
2. R. W. Clough, Analysis of structural vibrations and dynamic response. *Recent advances in Matrix Method of Structural Analysis and Design*. University of Alabama Press (1971).
3. B. Irons, Structural eigenvalue problem: elimination of unwanted variables. *J. AIAA* **3**, 961–962 (1965).
4. Y. Nakao and M. Kawashima, Practical analysis of steel structures using higher-order elements. *Advances in Computational Methods in Structural Mechanics and Design*, pp. 537–589. University of Alabama Press (1972).
5. Y. Nakao and S. Takano, Elastic–plastic seismic response analysis of framed structures by mode superposition. *Theory and Practice in Finite Element Structural Analysis*, pp. 423–436. University of Tokyo Press (1973).
6. N. M. Newmark, A method of computation for structural dynamics. *J. Engng Mech. Div., ASCE* **85**, 67–94 (1959).
7. K. Narita, Y. Nakao *et al.*, Study on seismic response of structure supporting steam generator (in Japanese). *Trans. Ann. Meeting of the Architectural Institute of Japan*, pp. 861–862 (Sept., 1978).

Computers & Structures, Vol. 13, pp. 213–221, 1981
Printed in Great Britain.

0045-7949/81/010213-09$02.00/0

MODELS FOR THE POST-CRACKING BEHAVIOR OF PLAIN CONCRETE UNDER SHORT TERM MONOTONIC LOADING

EUGENE YU-TZE CHEN† and WILLIAM C. SCHNOBRICH‡

Department of Civil Engineering, University of Illinois, Urbana-Champaign, Urbana, IL 61801, U.S.A.

(*Received* 28 *May* 1980)

Abstract—Experimental studies indicate that post-cracking behavior of concrete has a significant influence on the intermediate response characteristics of a number of structural members. In order to numerically reproduce this post-cracking response of concrete, a significant amount of effort has been invested. Thus far this effort has had limited success. In this paper a new concept of the relative strain is introduced. Based on this concept together with available test results, constitutive relations for plain concrete in a cracked state are proposed. The implementation of these relations into a integrated post-cracking model for the plain concrete is also included.

INTRODUCTION

Concrete is a composite mixture of a hydrated cement paste matrix interspersed with fine and coarse aggregate particles. This composite material exhibits an intrinsic brittleness (low tensile strength) through the formation of cracks [1–3]. Cracking results in the permanent loss of both tensile stiffness and tensile strength. Once cracking occurs the internal stress pattern of concrete changes to accommodate the associated geometric discontinuities. However, through the cross-crack transmission of both shear and normal stress a somewhat continuous internal stress flow is still possible even in cracked concrete. Depending on the degree of internal redundancy, cracked concrete still may possess a significant amount of load carrying capacity before its final collapse. Furthermore, any crack closure will restore part or all of the compressive strength and compressive stiffness. The fact that these additional strengths exist makes the post-cracking behavior most important in the study of the ultimate load carrying capacity and the deformation characteristics of concrete.

In this paper one methodology is proposed for handling concrete in the post cracked state. Based on this concept, phenomenological models pertaining to the normal and shear stress transfer across the crack are suggested. These models are contrived with realistic parameters to reproduce the most important facets of the mechanical behavior of cracked concrete without violating fundamental principles of mechanics. The proposed methodology and its concept together with the suggested models are intended to provide a more realistic qualitative interpretation as well as a better quantitative evaluation of the post-cracking behavior of concrete.

CRACK REPRESENTATION

Currently, there are two basic approaches for the spatial idealization of concrete cracking within a finite element modelling, namely, the smeared crack representation and the discrete crack representation. If overall load deflection is sought, the smeared crack representation, which distributes damage over a certain area of the material, is probably the better choice. On the other hand, if detailed local behavior is of interest, the discrete crack representation becomes a must. However, detailed local behavior generally is of very limited practical significance in an engineering application. From the computational standpoint, the constant changing of topology inherent in the use of the discrete crack representation makes the approach very cumbersome and undesirable. In order to reduce this computational inefficiency, a new network-topological approach has been proposed [4], but to implement such an approach requires a major overhaul of most existing computer programs. The smeared crack representation, which corresponds to an averaging (smoothing) procedure of local discontinuities, allows an equivalent continuum treatment with localized anisotropy. It simplifies the solution algorithms substantially, and fits well into the approximate nature of the finite element method with C_0—continuity of displacement and bounded nonsingular strain and stress fields. Because of its generality and simplicity the smeared crack representation attracts much of the attention of the researchers.

By passing the question of the validity of fracture mechanics as applied to concrete, recently Bazant and Cedolin have incorporated the concept of fracture mechanics with the smeared crack representation to study crack propagation [5]. Ingraffea also has proposed a fracture mechanics discrete crack idealization for crack propagation, in which crack initiation is by a strength concept [6]. Additional research is being investigated at other institutions, however, the processes are still in the formative stages and will require additional investigation before any conclusive evaluations can be made.

CONCEPT OF RELATIVE STRAIN ACROSS THE CRACK

From the standpoint of continuum mechanics, a crack may be identified as a separation of two neighboring material particles [6]. Upon cracking certain

†Teaching and Research Assistant.
‡Professor.

components of displacement will become discontinuous, which implies "relative movements" between the two sides of the crack surface. Since in continuum mechanics displacement and strain are related through kinematic equations, it is only natural to assume that a set of relative strains exist which represent the relative displacements across the cracks.

In the equivalent continuum treatment of cracked concrete (smeared crack approach) the "relative strain" is defined as the elastic portion of the corresponding strain. The rational behind this assumption roots from basic considerations of continuum mechanics. Before cracking occurs a complete bonding exists between two neighboring particles. It is this bonding that allows them to deform or to be strained together. Once cracking starts, a separation which implies relative movements between these two neighboring particles will occur. These relative movements can be interpreted as a relaxation of deformation (straining) of one particle with respect to the other. Since the plastic portion of deformation (straining) is nonrecoverable, it is logical to assume that the elastic portion must account for the relaxation and the corresponding relative movements. In summary, this proposed strategy can be outlined as follows:

(a) The "initial" relative strain across a crack is defined as the elastic portion of the corresponding total strain which exists just before crack occurs;

$$(\tilde{\sigma}_n)_{\text{initial}} = \frac{(\sigma_n)_{\text{crack}}}{E}$$
$$(\tilde{\varepsilon}_s)_{\text{initial}} = \frac{(\tau)_{\text{crack}}}{G} \tag{1.1}$$

(b) The "incremental" relative strain across the crack is defined as the elastic portion of the corresponding strain increment or decrement due to crack propagation or crack closure;

$$\Delta\tilde{\varepsilon}_n = \frac{\Delta\sigma_n}{E}$$
$$\Delta\tilde{\varepsilon}_s = \frac{\Delta\tau_s}{G}. \tag{1.2}$$

(c) The "accumulated" relative strain across the crack is defined as the summation of initial and incremental ones;

$$\begin{cases} \tilde{\varepsilon}_n = (\tilde{\varepsilon}_n)_{\text{initial}} + \Sigma(\Delta\tilde{\varepsilon}_n) \\ \tilde{\varepsilon}_s = (\tilde{\varepsilon}_s)_{\text{initial}} + \Sigma(\Delta\tilde{\varepsilon}_s) \end{cases} \tag{1.3}$$

where subscripts n and s represent the normal and tangential directions to the crack surfaces respectively; E is the Youngs modulus; and $G = E/1+\nu$ is the elastic shear modulus with ν the elastic poisson's ratio. Schematically the initial and incremental relative strain can be illustrated as shown in Fig. 1.

INTERFACE-STRESS-TRANSFER MODEL FOR CRACKS IN PLAIN CONCRETE

Let **n**, **s** and **t** be a set of right-handed orthogonal coordinate directions with **n** normal and **s**, **t** tangential to the cracked surface as shown in Fig. 2.

The 3-D constitutive relations of a crack in terms of stress and relative strain components across the crack can be described in a matrix form as follows:

$$\begin{Bmatrix} \sigma_n \\ \tau_s \\ \tau_t \end{Bmatrix} = \begin{bmatrix} K_{nn} & K_{ns} & K_{nt} \\ K_{sn} & K_{ss} & K_{st} \\ K_{tn} & K_{ts} & K_{tt} \end{bmatrix} \begin{Bmatrix} \tilde{\varepsilon}_n \\ \tilde{\varepsilon}_s \\ \tilde{\varepsilon}_t \end{Bmatrix} \tag{2.1}$$

where K_{nn} is the normal stiffness coefficient; K_{ss}, K_{tt} are the shear stiffness coefficients; K_{sn}, K_{tn} are the coupled shear stiffness coefficients; K_{ns}, K_{nt} are the dilatant-contractant stiffness coefficients and K_{st}, K_{ts} are the cross shear stiffness coefficients.

The stiffness matrix in eqn (2.1) is generally unsymmetric. Because a symmetric matrix is always desirable from a numerical point of view, eqn (2.1) is modified so that a symmetric constitutive matrix is achieved as shown in eqn (2.2).

$$\begin{Bmatrix} \sigma_n \\ \tau_s \\ \tau_t \end{Bmatrix} = \begin{bmatrix} K_{nn} & K_{ns} & K_{nt} \\ K_{ns} & \left\{K_{ss}+(K_{sn}-K_{ns})\dfrac{\tilde{\varepsilon}_n}{\tilde{\varepsilon}_s}\right\} & K_{st} \\ K_{nt} & K_{st} & \left\{K_{tt}+(K_{tn}-K_{nt})\dfrac{\tilde{\varepsilon}_n}{\tilde{\varepsilon}_t}+(K_{ts}-K_{st})\dfrac{\tilde{\varepsilon}_s}{\tilde{\varepsilon}_t}\right\} \end{bmatrix} \begin{Bmatrix} \tilde{\varepsilon}_n \\ \tilde{\varepsilon}_s \\ \tilde{\varepsilon}_t \end{Bmatrix} \tag{2.2}$$

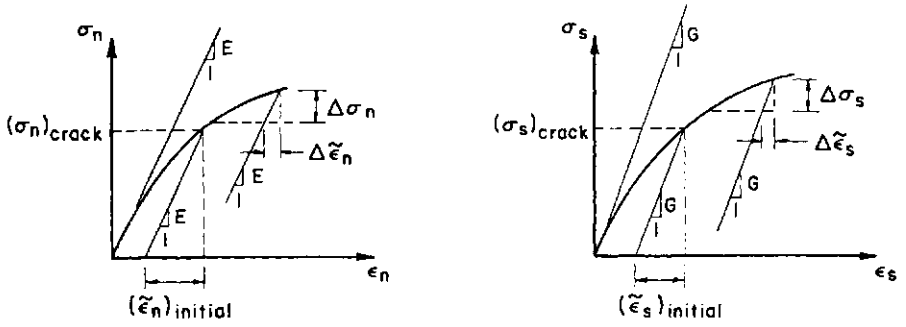

Fig. 1. Relative normal and shear strains and strain increments.

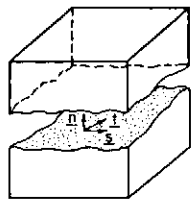

Fig. 2. Material coordinate system for cracked concrete.

Unfortunately, this modification introduces relative strain components into the stiffness matrix, and consequently, nonlinearizes the constitutive relations in eqn (2.2). This shortcoming is minimal because all the stiffness coefficients in eqn (2.1) are intrinsically nonlinear. As a result of this nonlinearity an incremental and/or iterative solution procedure is virtually unavoidable. Based on this argument, the symmetric constitutive matrix in eqn (2.2) is adopted in the solution algorithm. Upon replacing the stress and relative strain components in eqn (2.2) by the corresponding stress and relative strain increments a set of incremental constitutive relations of a crack medium are thus obtained in eqn (2.3).

$$\begin{Bmatrix} \Delta\sigma_n \\ \Delta\tau_s \\ \Delta\tau_t \end{Bmatrix} = \begin{bmatrix} K_{nn} & K_{ns} & K_{nt} \\ K_{ns} & \left\{K_{ss}+(K_{sn}-K_{ns})\dfrac{\bar{\varepsilon}_n}{\bar{\varepsilon}_s}\right\} & K_{st} \\ K_{nt} & K_{st} & \left\{K_{tt}+(K_{tn}-K_{nt})\dfrac{\bar{\varepsilon}_n}{\bar{\varepsilon}_t}+(K_{ts}-K_{st})\dfrac{\bar{\varepsilon}_s}{\bar{\varepsilon}_t}\right\} \end{bmatrix} \begin{Bmatrix} \Delta\bar{\varepsilon}_n \\ \Delta\bar{\varepsilon}_s \\ \Delta\bar{\varepsilon}_t \end{Bmatrix} \tag{2.3}$$

POST-CRACKING MODEL FOR PLAIN CONCRETE

The 3-D incremental constitutive relations of intact concrete with respect to an arbitrary coordinate system can be expressed in a symmetric matrix form as follows:

$$\begin{Bmatrix} \Delta\sigma_{11} \\ \Delta\sigma_{21} \\ \Delta\sigma_{31} \\ \Delta\sigma_{22} \\ \Delta\sigma_{32} \\ \Delta\sigma_{33} \end{Bmatrix} = \begin{bmatrix} K_{11\,11} & K_{11\,21} & K_{11\,31} & K_{11\,22} & K_{11\,32} & K_{11\,33} \\ & K_{21\,21} & K_{21\,31} & K_{21\,22} & K_{21\,32} & K_{21\,33} \\ \text{symmetric} & & K_{31\,31} & K_{31\,22} & K_{31\,32} & K_{31\,33} \\ & & & K_{22\,22} & K_{22\,32} & K_{22\,33} \\ & & & & K_{32\,32} & K_{32\,33} \\ & & & & & K_{33\,33} \end{bmatrix} \begin{Bmatrix} \Delta\varepsilon_{11} \\ \Delta\varepsilon_{21} \\ \Delta\varepsilon_{31} \\ \Delta\varepsilon_{22} \\ \Delta\varepsilon_{32} \\ \Delta\varepsilon_{33} \end{Bmatrix} \tag{3.1}$$

Cracking occurs when a certain limiting stress or strain condition is reached. Once cracking occurs, locally concrete loses its isotropy and homogeneity. As a result, the material coordinate system is locally fixed to either the principle stress or the principle strain directions. In the current study, a strain-based cracking condition and the principle strain directions are adopted to delineate the crack initiation in plain concrete. Since cracking is assumed to be perpendicular to the maximum principle strain direction, if two or three maximum principle strain components are of equal values, multiple cracks will occur simultaneously. Additional cracks are allowed to occur by the same process in the intact subspace of concrete if the same strain-based condition is satisfied at a later time. Based on this procedure, multi-directional cracks are thus possible.

Upon cracking, eqn (3.1) written in the current principle strain directions need to be modified to account for the existence of cracks. For this purpose, the interface-stress-transfer (IST) model is used, while the constitutive relations for the intact concrete are still enforced in the uncracked subspace of concrete. The modified 3-D incremental constitutive relations for three different cases are outlined as follows.

(a) *One crack in the first direction*

$$\begin{Bmatrix} \Delta\sigma_{11} \\ \Delta\sigma_{21} \\ \Delta\sigma_{31} \\ \Delta\sigma_{22} \\ \Delta\sigma_{32} \\ \Delta\sigma_{33} \end{Bmatrix} = \begin{bmatrix} \text{IST model} & & 0 \\ & & \\ & & \\ & \text{2-D intact model} & \\ 0 & & \end{bmatrix} \begin{Bmatrix} \Delta\bar{\varepsilon}_{11} \\ \Delta\bar{\varepsilon}_{21} \\ \Delta\bar{\varepsilon}_{31} \\ \Delta\varepsilon_{22} \\ \Delta\varepsilon_{32} \\ \Delta\varepsilon_{33} \end{Bmatrix} \tag{3.2}$$

(b) *Two orthogonal cracks in the first and second directions*

$$\begin{Bmatrix} \Delta\sigma_{11} \\ \Delta\sigma_{21} \\ \Delta\sigma_{31} \\ \Delta\sigma_{22} \\ \Delta\sigma_{32} \\ \Delta\sigma_{33} \end{Bmatrix} = \begin{bmatrix} \text{IST model} & & 0 \\ & & \\ & & \\ & \text{IST model} & 0 \\ 0 & & \\ & 0 & \text{1-D intact model} \end{bmatrix} \begin{Bmatrix} \Delta\bar{\varepsilon}_{11} \\ \Delta\bar{\varepsilon}_{21} \\ \Delta\bar{\varepsilon}_{31} \\ \Delta\bar{\varepsilon}_{22} \\ \Delta\bar{\varepsilon}_{32} \\ \Delta\bar{\varepsilon}_{33} \end{Bmatrix} \tag{3.3}$$

(c) *Three orthogonal cracks in the directions*

$$\begin{Bmatrix} \Delta\sigma_{11} \\ \Delta\sigma_{21} \\ \Delta\sigma_{31} \\ \Delta\sigma_{22} \\ \Delta\sigma_{32} \\ \Delta\sigma_{33} \end{Bmatrix} = \begin{bmatrix} \text{IST model} & & 0 \\ & & \\ & & \\ & \text{IST model} & 0 \\ 0 & & \\ & 0 & \text{IST model} \end{bmatrix} \begin{Bmatrix} \Delta\bar{\varepsilon}_{11} \\ \Delta\bar{\varepsilon}_{21} \\ \Delta\bar{\varepsilon}_{31} \\ \Delta\bar{\varepsilon}_{22} \\ \Delta\bar{\varepsilon}_{32} \\ \Delta\bar{\varepsilon}_{33} \end{Bmatrix} \tag{3.4}$$

Upon cracking, some amount of tensile normal stress as well as shear stress across the crack will be released and must be redistributed to the remaining material. This stress releasing is necessary to accommodate the initial opening and slipping between the two sides of the crack surfaces. As to how gradual this releasing of stresses should be carried out, depends on (a) the reinforcement in the vicinity of the crack, (b) the crack representation used, and (c) the density of cracks that already exist in the material. For reinforced concrete

with a smeared crack representation during the early stage of its loading when cracks are not densely populated, a gradual stress releasing is believed to be realistic. Whereas, for plain concrete and a discrete crack representation a sudden release is often used. However, from the computational point of view, a gradual stress releasing tends to improve the numerical stability of the solution algorithm and is thus generally more preferable.

A new crack(s) in a new direction(s) is conceivable after the old one(s) is closed. In order to always maintain an orthogonal set of opening cracks, a new crack(s) in a new direction(s) can occur only when the number of currently opened cracks is no more than one.

In the following sections, a series of comprehensive mathematical models are proposed for the complete definition of eqn (2.1). Considering the randomness of irregularities of crack surfaces, it is logical to assume that identical relations can be used for shear in both the s and t directions.

INTERFACE SHEAR TRANSFER CAPACITY OF CRACKED CONCRETE

Mattock and his co-workers have conducted a series of studies on the peak interface shear transfer capacity of reinforced concrete subjected to short term monotonic loading [8–11]. Based on their test findings and the work of others [12–15], a mathematical model is herein proposed to reproduce the observed relations between the peak interface shear transfer capacity, τ_p, and the normal stress, σ_n, across the crack. In order to be more general in its formulation, both τ_p and σ are normalized by the magnitude of the unconned uniaxial compressive strength of concrete, $|\sigma_K|$, such that,

$$\tilde{\tau}_p = \tau_p/|\sigma_K|, \quad \textit{and } \tilde{\sigma}_n = \sigma_n/|\sigma_K|.$$

The proposed model comprises two parts; the first part represents the concrete strength "independent" portion, and the second part represents the concrete strength "dependent" portion of the peak interface shear transfer capacity of concrete [8]. The schematic illustration of the normalized proposed model is shown in Fig. 3. In this model there are four independent parameters.

(a) $\tilde{\sigma}_t = \sigma_t/|\sigma_c|$, where σ_t is the direct uniaxial tensile strength of concrete. $\sigma_t = 0.08$–0.12 is commonly used.

(b) θ, the internal friction angle of concrete, $\theta = 37°$–$39°$ is commonly used for normal weight concrete.

(c) a, the parameter which controls the interface shear transfer capacity of concrete under small tensile stress normal to the crack. $a = \tilde{\sigma}_t$ is commonly used,

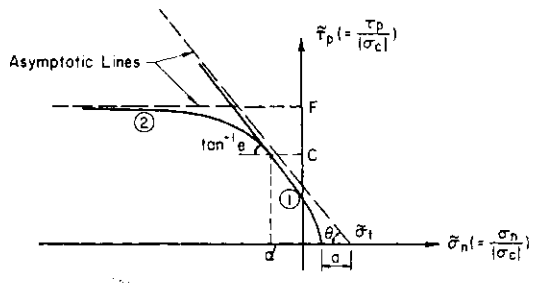

Fig. 3. Normalized model for peak interface shear transfer capacity of cracked concrete.

which means there is no interface shear transfer under tensile normal stress.

(d) c, the upper limit of the normalized peak interface shear transfer capacity, below which it is concrete strength independent. It corresponds to the "dividing point" of the two parts in the proposed model. $c = 0.3$ is commonly used [11].

Besides the afore-mentioned independent parameters, there are additional dependent ones shown in the figure,

(e) d, the normalized normal stress corresponding to the dividing point;

(f) e, the slope of the proposed model at the dividing point.

(g) F, the upper bound of the normalized peak interface shear transfer capacity predicted by the proposed model. ASCE-ACI 426 suggested $F = 0.3$–0.45 [16].

Part 1—Concrete Strength "Independent" Portion

$$(d \leqslant \tilde{\sigma}_n \leqslant (\tilde{\sigma}_t - a), \quad 0 \leqslant \tilde{\tau}_p \leqslant c).$$

The proposed equation is a hyperbola:

$$\frac{(\tilde{\sigma}_n - \tilde{\sigma}_t)^2}{a^2} - \frac{\tilde{\tau}_p^2}{a^2 \tan^2 \theta} = 1 \tag{4.1}$$

with

$$d = \tilde{\sigma}_n|_{\tilde{\tau}_p = c} = \tilde{\sigma}_t - \sqrt{a^2 + c^2/\tan^2 \theta} \tag{4.2}$$

and

$$e = \frac{\partial \tilde{\tau}_p}{\partial \tilde{\sigma}_n}\bigg|_{\substack{\tilde{\sigma}_n = d \\ \tilde{\tau}_p = c}} = -\frac{\tan^2 \theta}{c}\sqrt{a^2 + c^2/\tan^2 \theta}. \tag{4.3}$$

Part 2—Concrete Strength "Dependent" Portion

$$(\tilde{\sigma}_n \leqslant d, \; c \leqslant \tilde{\tau}_p \leqslant F).$$

The proposed equation is also a hyperbola:

$$\tilde{\tau}_p = F\left(1 + \frac{1}{H\tilde{\sigma}_n}\right). \tag{4.4}$$

In order to make the transition between part 1 and part 2 C_3—continuous, which is numerically desirable, the following two conditions are enforced;

(a) $c = \tilde{\tau}_p|_{\tilde{\sigma}_n = d} = F\left(1 + \frac{1}{Hd}\right)$

(b) $e = \frac{\partial \tilde{\tau}_p}{\partial \tilde{\sigma}_n}\Big|_{\substack{\tilde{\sigma}_n = d \\ \tilde{\tau}_p = c}} = -\frac{F}{Hd^2}$

which lead to

$$F = c + ed \tag{4.5}$$

and

$$H = -\frac{c + ed}{ed^2}. \tag{4.6}$$

In Fig. 4 the proposed model for $\tilde{\tau}_p$ with $\tilde{\sigma}_t = 0.1$, $\theta = 38°$, $a = 0.05$ and $c = 0.3$ is plotted, along with an averaged $\tilde{\tau}_{ave}$ calculated from the following equations.

$$\tilde{\tau}_1 = \frac{33.5\sqrt{|\sigma_n|}}{|\sigma_c|}, \leqslant 0.3 \tag{4.7}$$

$$\tilde{\tau}_2 = \frac{400 + 0.8|\sigma_n|}{|\sigma_c|}, \leqslant 0.3 \tag{4.8}$$

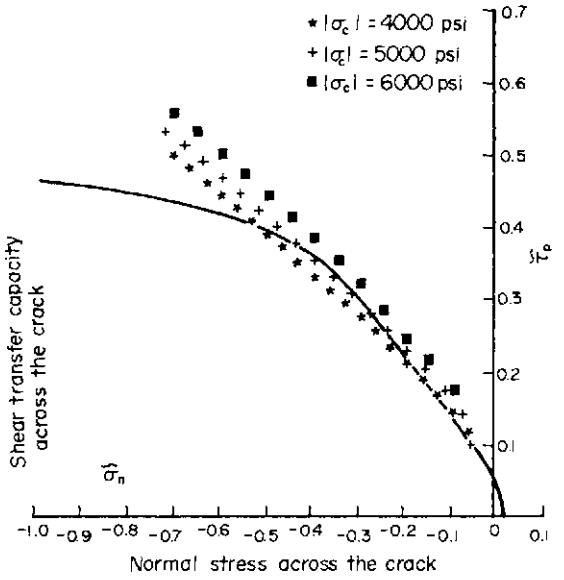

Fig. 4.

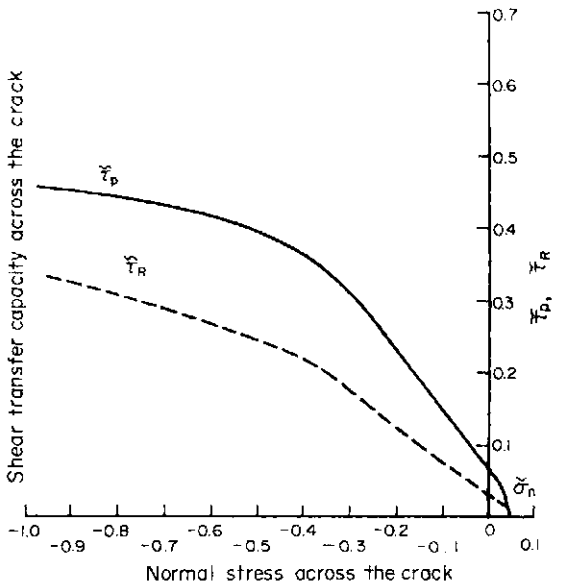

Fig. 5.

$$\tilde{\tau}_{ave}=\frac{\tilde{\tau}_1+\tilde{\tau}_2}{2}, \quad \tilde{\tau}_{ave}\leqslant 0.3.$$

Equations (4.7) and (4.8) were originally proposed by Birkeland and Mattock, respectively [11]. Because both of the equations represent test results reasonably well within $0\leqslant\tilde{\tau}\leqslant 0.3$, the averaged value between them is used for comparison with the proposed model. In order to study the effect of concrete strength, $\tilde{\tau}_{ave}$, calculated for three different values of $|\sigma_c|=4000$, 5000 and 6000 psi, are plotted in Fig. 4. From this plot we observe that,

(a) concrete of lower strength tends to have a "better" interface shear transfer behavior;

(b) $\tilde{\tau}_p=0.3$ is a good dividing point between the concrete strength "independent" and "dependent" portions, with a much reduced increase rate for the latter;

(c) $\tilde{\tau}_p=0.45$ proposed by the ASCE-ACI 426 is a conservative upper bound limit for the peak interface shear transfer capacity of concrete.

RESIDUAL INTERFACE SHEAR TRANSFER CAPACITY OF CRACKED CONCRETE

As observed in frictional materials, the peak interface shear transfer capacity will drop to a smaller value when the abrupt slip occurs [17-19]. This smaller value is commonly referred to as the "residual interface shear transfer capacity", τ_R. Under constant normal load with negligible amount of surface deterioration, the residual interface shear transfer remains virtually constant. As the number of stick-slip cycles increases the local roughness deteriorates. Consequently, the crack surfaces must travel a longer distance before their next match. This smoothing of local roughness causes degradation of the peak and the residual interface shear transfer capacities as well as their stiffness [17, 20].

It has been verified through test results that:

(a) the residual interface shear transfer capacity under short term monotonic loading is a function of the normal stress across the crack;

(b) when the compressive normal stress exceeds a threshold value, $|Q\sigma_c|$, the ratio between the residual and the peak interface shear transfer capacities becomes one.

Based on these observations together with some reasoning, a mathematically simple but conceptually logical model is herein proposed as follows.

$$\tilde{\tau}_R=\frac{\tau_R}{|\sigma_c|}=R\tilde{\tau}_p, \qquad 0\leqslant R\leqslant 1 \tag{5.1}$$

$$R=B+(1-B)\left[\frac{(\tilde{\sigma}_t-a)-\tilde{\sigma}_n}{(\tilde{\sigma}_t-a)-Q}\right]$$

$$\text{when } Q\leqslant\tilde{\sigma}_n\leqslant(\tilde{\sigma}_t-a) \tag{5.2}$$

$$=1, \quad \text{when} \quad \tilde{\sigma}_n \quad Q$$

where $\tilde{\tau}_R$ is the normalized residual interface shear transfer capacity; R is the residual index and B and Q are parameters which depend on the type and loading history of the material.

In Fig. 5 the proposed model for $\tilde{\tau}_R$ with $B=0.5$ and $Q=-2.0$ is plotted, along with the corresponding $\tilde{\tau}_p$ for direct comparison.

CRACK OPENING AND CLOSING, NORMAL STRESS AND NORMAL STIFFNESS OF A CRACK

The fundamental crack property which governs the normal deformation of cracked concrete is the maximum amount of crack closure. Mathematically it can be described by the maximum amount of the relative compressive normal strain across a crack, ε_p, before the crack is considered closed. Under compression the crack-closed concrete behaves very similarly to the intact concrete. On the other hand, due to the permanent nature of damage caused by tensile cracking, the already closed crack will reopen whenever there is any tensile stress normal to it [19]. As to the initial amount of this reopening expressed in terms of the relative strain, it is proposed that the same quantities defined in eqn (1.1) are used. In this paper a mathematical model is postulated to relate the normal stress, σ_n, and the relative normal strain, $\tilde{\varepsilon}_n$, across a crack. The der-

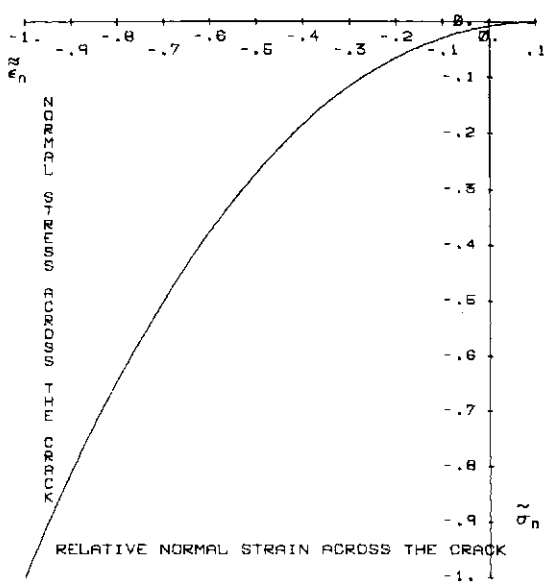

Fig. 6.

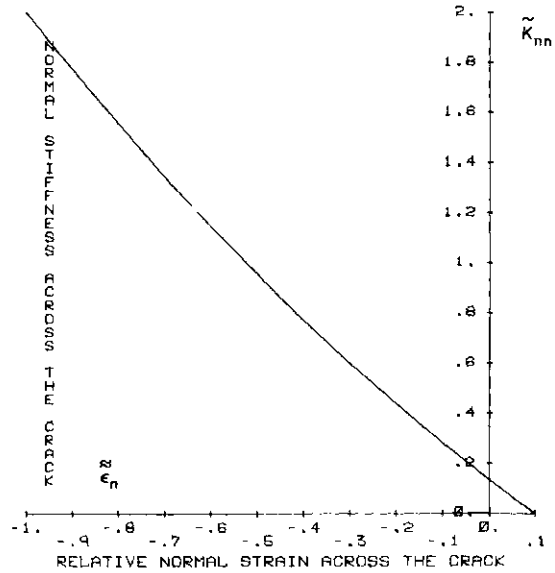

Fig. 7.

ivative of it with respect to $\bar{\varepsilon}_n$ yields the normal stiffness, K_{nn}. In order to be more general in the formulation, σ_n, $\bar{\varepsilon}_n$ and K_{nn} are normalized by the magnitude of the unconfined uniaxial compressive strength of concrete, $|\sigma_c|$, its corresponding normal strain, $|\varepsilon_c|$, and the secant modulus, $E_c = \sigma_c/\varepsilon_c$, respectively, such that,

$$\tilde{\sigma}_n = \frac{\sigma_n}{|\sigma_c|}, \quad \tilde{\bar{\varepsilon}}_n = \frac{\bar{\varepsilon}_n}{|\varepsilon_c|}, \quad \text{and} \quad \tilde{K}_{nn} = \frac{K_{nn}}{E_c}.$$

The proposed relation in terms of the normalized quantities can be written as,

$$\tilde{\sigma}_n = -\left[1 - 3\left(\frac{y}{x}\right)^2 + 2\left(\frac{y}{x}\right)^3\right] + K \cdot x \cdot \left[\frac{y}{x} - 2\left(\frac{y}{x}\right)^2 + \left(\frac{y}{x}\right)^3\right] \tag{6.1}$$

$$\tilde{K}_{nn} = \frac{\mathrm{d}\tilde{\sigma}_n}{\mathrm{d}\tilde{\bar{\varepsilon}}_n} = -\left[-6\frac{y}{x^2} + 6\frac{y^2}{x^3}\right] + K \cdot \left[1 - 4\frac{y}{x} + 3\left(\frac{y}{x}\right)^2\right] \tag{6.2}$$

where $K = E/E_c$, $x = \varepsilon_q - \varepsilon_p$, $y = \tilde{\bar{\varepsilon}}_n - \varepsilon_p$, and $\varepsilon_p \leqslant \tilde{\bar{\varepsilon}}_n \leqslant \varepsilon_q$ in which ε_p is the normalized relative strain quantity chosen as the threshold value which defines a fully closed crack, $\varepsilon_p \leqslant 0$ and ε_q is the normalized relative strain quantity chosen to define an open crack with no normal strength and stiffness across the crack, $\varepsilon_q \geqslant 0$.

In Fig. 6 and Fig. 7 relations for $\tilde{\sigma}_n$ and $\tilde{K}_{nn}$ with respect to $\tilde{\bar{\varepsilon}}_n$ are plotted. Parameters used are $\varepsilon_p = -1$, $\varepsilon_q = 0.1$, and $K = 2$.

INITIAL SHEAR MODULUS, SHEAR STRESS AND SHEAR STIFFNESS OF A CRACK

The shear response of concrete across a crack has been experimentally investigated by White, Holley, Laible, Gergely, Houde and Mirza [13–15]. Based on these tests and supplemented by the test results of jointed rock the following observations can be drawn.

(a) the relation of shear stress vs relative shear displacement (slip) is strongly dependent on the initial crack width. Slip increases rather sharply with respect to the increase of the initial crack width;

(b) the above relation is virtually linear between the zero stress point and the point where slip is equal to 40–65% of the current crack width. It deviates from linear rather rapidly under further slip;

(c) considerable variation in shear stiffness has been experienced when the normal stress across the crack is changed.

Based on these observations, two mathematical models are proposed for the initial shear modulus, A, and the shear stress τ_s, across a crack. Using the concept of relative strain introduced in this paper, crack width (relative normal displacement) and slip (relative shear displacement) are denoted by the relative normal strain, $\bar{\varepsilon}_n$, and the relative shear strain, $\bar{\varepsilon}_s$, respectively. In order to be more general normalized quantities are used in the proposed models, they are

$$\tilde{\tau}_s = \tau_s/|\sigma_c|, \quad \tilde{\bar{\varepsilon}}_n = \bar{\varepsilon}_n/|\varepsilon_c|, \quad \tilde{\bar{\varepsilon}}_s = \bar{\varepsilon}_s/|\varepsilon_c|,$$
$$\tilde{A} = A/G, \quad \text{and} \quad \tilde{\bar{A}} = A/E_c,$$

or $\tilde{\bar{A}} = (K/(1+\nu))\tilde{A}$ where $K = E/E_c$, and $\tilde{K}_{ss} = K_{ss}/E_c$.

(1) *Initial shear modulus*

The initial linear relationship between the shear stress and the relative shear strain is described by the initial shear modulus of a crack. The value of the initial shear modulus depends on the crack width and is bounded by zero and the shear modulus of the uncracked concrete, G. It can be written as,

$$\tilde{A} = 1 - \frac{1}{A_s(1/(\tilde{\bar{\varepsilon}}_n - \varepsilon_p))^{N_s} + 1}, \quad \text{when } \tilde{\bar{\varepsilon}}_n \geqslant \varepsilon_p \tag{7.1}$$

where ε_p is defined in eqn (6.2);

A_s and N_s are parameters which control the shape of the proposed model to fit the test results, $A_s \geqslant 0$ and $N_s \geqslant 0$.

In Fig. 8 the relation for $\tilde{A}$ vs $\tilde{\bar{\varepsilon}}_n$ with $\varepsilon_p = -1$, $A_s = 1$, and $N_s = 4$ is plotted.

(2) *Shear stress*

The normalized relation between the shear stress, τ_s, and the relative shear strain, $\bar{\varepsilon}_s$, which is a function of the current normal stress, σ_n, and the relative normal strain, $\bar{\varepsilon}_n$, across a crack, is proposed in eqn (7.2). Its schematic illustration is given in Fig. 9

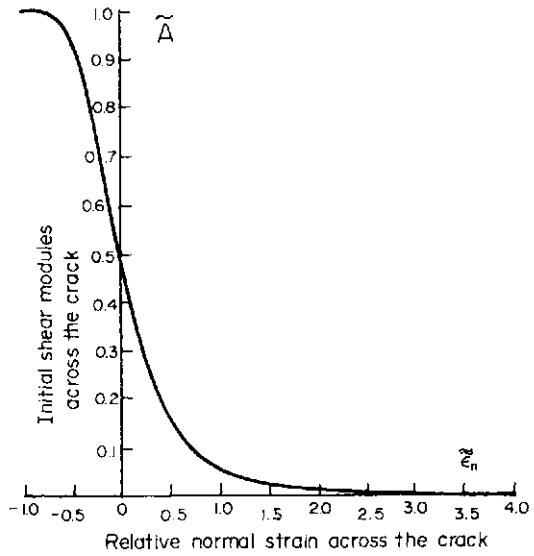

Fig. 8.

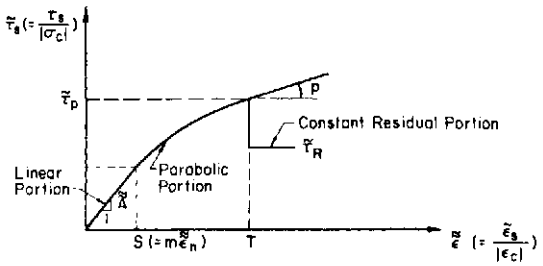

Fig. 9. Normalized model for interface shear transfer across a crack.

$$\begin{cases} \tilde{\tau}_s = \tilde{\tilde{A}}\tilde{\tilde{\varepsilon}}_s, & \text{when } 0 \leqslant \tilde{\tilde{\varepsilon}}_s \leqslant S(=m\tilde{\tilde{\varepsilon}}_n) \\ \tilde{\tau}_s = A_0 + A_1\tilde{\tilde{\varepsilon}}_s + A_2\tilde{\tilde{\varepsilon}}_s^2, & \text{when } S \leqslant \tilde{\tilde{\varepsilon}}_s \leqslant T \\ \tilde{\tau}_s = \tilde{\tau}_R, & \text{when } T \leqslant \tilde{\tilde{\varepsilon}}_s \end{cases} \tag{7.2}$$

where p is the slope at the normalized peak shear stress, $\tilde{\tau}_p$, designed to allow a more flexible fitting with experimental data and m is the percentage of the normalized current relative normal strain, $\tilde{\tilde{\varepsilon}}_n$. $m\tilde{\tilde{\varepsilon}}_n$ sets the upper limit of $\tilde{\tilde{\varepsilon}}_s$ for the linear shear response across a crack.

Depending on the current values of $\tilde{\sigma}_n$ and $\tilde{\tilde{\varepsilon}}_n$, two special cases which complement eqn (7.2) exist.

(a) If $\tilde{\sigma}_n$ is such that $T(=\tilde{\tau}_p/\tilde{A}) \leqslant S(=m\tilde{\tilde{\varepsilon}}_n)$, then

$$\begin{cases} \tau_s = \tilde{\tilde{A}}\tilde{\tilde{\varepsilon}}_s, & \text{when } 0 \leqslant \tilde{\tilde{\varepsilon}}_s \leqslant T \\ \tilde{\tau}_s = \tilde{\tau}_R, & \text{when } T \leqslant \tilde{\tilde{\varepsilon}}_s \end{cases} \tag{7.3}$$

(b) If $\tilde{\tilde{\varepsilon}}_n \leqslant 0$, then $S = 0$, and

$$\begin{cases} \tilde{\tau}_S = A_0 + A_1\tilde{\tilde{\varepsilon}}_S + A_2\tilde{\tilde{\varepsilon}}_S^2, & \text{when } 0 \leqslant \tilde{\tilde{\varepsilon}}_S \leqslant T \\ \tilde{\tau}_S = \tilde{\tau}_R, & \text{when } T \leqslant \tilde{\tilde{\varepsilon}}_S \end{cases} \tag{7.4}$$

In order to determine the coefficients, while maintaining C_1-continuity between the linear part and the parabolic part of eqn (7.2), the following conditions are imposed,

(a) $\tilde{\tau}_S\big|_{\tilde{\tilde{\varepsilon}}_S = S} = \tilde{\tilde{A}}S = A_0 + A_1 S + A_2 S^2$

(b) $\dfrac{\partial \tilde{\tau}_S}{\partial \tilde{\tilde{\varepsilon}}_S}\Big|_{\tilde{\tilde{\varepsilon}}_S = S} = \tilde{\tilde{A}} = A_1 + 2A_2 S$

(c) $\dfrac{\partial \tilde{\tau}_S}{\partial \tilde{\tilde{\varepsilon}}_S}\Big|_{\tilde{\tilde{\varepsilon}}_S = T} = p = \sqrt{A_1^2 - 4A_2A_0 + 4A_2\tilde{\tau}_p}$.

These conditions provide the means to determine the coefficients as,

$$\begin{aligned} A_0 &= A_2 S^2 \\ A_1 &= \tilde{\tilde{A}} - 2A_2 \cdot S \\ A_2 &= \frac{p^2 - \tilde{\tilde{A}}^2}{4(\tilde{\tau}_p - \tilde{A} \cdot S)} \end{aligned} \tag{7.5}$$

where $\tilde{\tilde{A}} = \tilde{\tilde{A}}(\tilde{\tilde{\varepsilon}}_n)$, and $\tilde{\tau}_p = \tilde{\tau}\ (\tilde{\sigma}_n)$.

(3) *Shear stiffness*

The normalized shear stiffness, $\tilde{K}_{ss}$, is obtained by differentiating eqn (7.2) with respect to $\tilde{\tilde{\varepsilon}}_s$. Such that,

$$\begin{cases} \tilde{K}_{ss} = \tilde{\tilde{A}}, \text{ when } 0 \leqslant \tilde{\tilde{\varepsilon}}_s \leqslant S \\ \tilde{K}_{ss} = A_1 + 2A_2\tilde{\tilde{\varepsilon}}_s, \text{ when } S \leqslant \tilde{\tilde{\varepsilon}}_s \leqslant T \\ \tilde{K}_{ss} = 0, \text{ when } T \leqslant \tilde{\tilde{\varepsilon}}_s. \end{cases} \tag{7.6}$$

COUPLED SHEAR STIFFNESS OF A CRACK

Due to the roughness of the crack surface, the relative normal displacement across a crack will introduce additional slip [18]. If somehow this additional slip is restrained, extra interface shear transfer capacity as well as the coupled shear stiffness will be mobilized. The normalized coupled shear stiffness of a crack, $\tilde{K}_{sn} = K_{sn}/E_c$, is defined as,

$$\tilde{K}_{sn} = \frac{\partial \tilde{\tau}_S}{\partial \tilde{\tilde{\varepsilon}}_n}\Big|_{\tilde{\tilde{\varepsilon}}_S \text{ constant}} \tag{8.1}$$

From eqn (7.1) we get

$$Z_1 = \frac{\partial \tilde{\tilde{A}}}{\partial \tilde{\tilde{\varepsilon}}_n} = \frac{K}{1+\nu}\frac{\partial \tilde{A}}{\partial \tilde{\tilde{\varepsilon}}_n} = \frac{-K}{1+\nu} \times \{A_s[A_s(\tilde{\tilde{\varepsilon}}_n - \varepsilon_p)^{-N_s} + 1]^{-2} \cdot N_s \cdot (\tilde{\tilde{\varepsilon}}_n - \varepsilon_p)^{-(N_s+1)}\} \tag{8.2}$$

when

$$\tilde{\tilde{\varepsilon}}_n \geqslant \varepsilon_p.$$

From eqns (4.1)–(4.6) and (6.2) we get

$$Z_2 = \frac{\partial \tilde{\tau}_p}{\partial \tilde{\tilde{\varepsilon}}_n} = \frac{\partial \tilde{\tau}_p}{\partial \tilde{\sigma}_n}\frac{\partial \tilde{\sigma}_n}{\partial \tilde{\tilde{\varepsilon}}_n} = \begin{cases} \left(\dfrac{-\tan\theta \cdot \sqrt{(a \cdot \tan\theta)^2 + \tilde{\tau}_p^2}}{\tilde{\tau}_p}\right) \cdot \tilde{K}_{nn}, & \text{when } \tilde{\sigma}_n \geqslant d \\ \dfrac{-F}{H} \cdot \dfrac{1}{(\tilde{\sigma}_n)^2} \cdot \tilde{K}_{nn}, & \text{when } \tilde{\sigma}_n < d. \end{cases} \tag{8.3}$$

From eqns (7.2) and (7.4) we get

$$Z_3 = \frac{\partial S}{\partial \tilde{\tilde{\varepsilon}}_n} = \frac{\partial(m\tilde{\tilde{\varepsilon}}_n)}{\partial \tilde{\tilde{\varepsilon}}_n} \begin{cases} = m, & \text{when } \tilde{\tilde{\varepsilon}}_n > 0 \\ = 0, \end{cases} \tag{8.4}$$

Equations (7.5) and (8.2)–(8.4) give us

$$Z_4=\frac{\partial A_2}{\partial \tilde{\bar{\varepsilon}}_n}=\frac{-\tilde{\bar{A}}\cdot Z_1}{2\cdot(\tilde{\bar{\tau}}_p-\tilde{\bar{A}}\cdot S)} - \frac{(p^2-\tilde{\bar{A}}^2)(Z_2-Z_1\cdot S-\tilde{\bar{A}}\cdot Z_3)}{4\cdot(\tilde{\bar{\tau}}_p-\tilde{\bar{A}}\cdot S)^2} \quad (8.5)$$

$$Z_5=\frac{\partial A_1}{\partial \tilde{\bar{\varepsilon}}_n}=Z_1-2\ Z_4\cdot S-2A_2\cdot Z_3 \quad (8.6)$$

$$Z_6=\frac{\partial A_0}{\partial \tilde{\bar{\varepsilon}}_n}=Z_4\cdot S^2+2A_2\cdot S\cdot Z_3. \quad (8.7)$$

Equations (5.2), (6.1), and (6.2) lead to

$$Z_7=\frac{dR}{d\tilde{\bar{\varepsilon}}_n}=-\left(\frac{1-B}{(\tilde{\sigma}_t-a)-Q}\right)\cdot\tilde{K}_{nn}, \quad \text{when } Q\leqslant\tilde{\sigma}_n\leqslant(\tilde{\sigma}_t-a)$$
$$=0, \text{ when } \tilde{\sigma}_n\leqslant Q \quad (8.8)$$

Based on the proposed model for $\tilde{\tau}_s$ in eqns (7.2)–(7.4) together with the definitions for Z_1 through Z_7, $\tilde{K}_{sn}$ can be formulated in two cases as follows:

(a) If $S\leqslant T$, then

$$\tilde{K}_{sn}=Z_1\cdot\tilde{\bar{\varepsilon}}_s, \quad \text{when } 0\tilde{\bar{\varepsilon}}_s S$$
$$\tilde{K}_{sn}=Z_6+Z_5\cdot\tilde{\bar{\varepsilon}}_s+Z_4\cdot\tilde{\bar{\varepsilon}}_s^2, \quad \text{when } S\leqslant\tilde{\bar{\varepsilon}}_s\leqslant T \quad (8.9)$$
$$\tilde{K}_{sn}=Z_7\cdot\tilde{\bar{\tau}}_p+Z_2\cdot R \quad \text{when } T\leqslant\tilde{\bar{\varepsilon}}_s$$

(b) If $T\leqslant S$, then

$$\begin{cases}\tilde{K}_{sn}=Z_1\cdot\tilde{\bar{\varepsilon}}_s, & \text{when } 0\leqslant\tilde{\bar{\varepsilon}}_s\leqslant T\\ \tilde{K}_{sn}=Z_7\cdot\tilde{\bar{\tau}}_p+Z_2\cdot R & \text{when } T\leqslant\tilde{\bar{\varepsilon}}_s\end{cases} \quad (8.10)$$

DILATANT–CONTRACTANT STIFFNESS OF A CRACK

Due to the rough and irregular nature of crack surfaces, any slip between the opposite sides of crack surfaces has the tendency to cause additional relative dilating or contracting normal displacement. If the crack width is restrained from changing, then additional counteracting normal stress will be introduced. Depending on whether the crack is contracting or dilating, the additional normal stress may be of either tension or compression. This cross effect either weakens or strengthens the interface shear transfer capacity of concrete [18, 21–24]. The significance of dilatancy and contractancy in interface stress transfer mechanisms has been reported in Ref. [17–20, 25–27]. The normalized dilatant-contractant stiffness of a crack, $\tilde{K}_{ns}=K_{ns}/E_c$, is defined as,

$$\tilde{K}_{ns}=\left.\frac{\partial\tilde{\bar{\sigma}}_n}{\partial\tilde{\bar{\varepsilon}}_s}\right|_{\tilde{\bar{\varepsilon}}_n=constant}=\frac{\partial\tilde{\bar{\sigma}}_n}{\partial\tilde{\bar{\varepsilon}}_n}\frac{\partial\tilde{\bar{\varepsilon}}_n}{\partial\tilde{\bar{\tau}}_s}\left.\frac{\partial\tilde{\bar{\tau}}_s}{\partial\tilde{\bar{\varepsilon}}_s}\right|_{\tilde{\bar{\varepsilon}}_n=constant}$$
$$=\tilde{K}_{nn}\left(\frac{1}{\tilde{K}_{sn}}\right)\tilde{K}_{ss} \quad (9.1)$$

where, $\tilde{K}_{nn}$, $\tilde{K}_{sn}$ and $\tilde{K}_{ss}$ are defined in eqn (6.2), eqns (8.9), (8.10) and eqn (7.6), respectively.

CROSS SHEAR

The term "cross shear" is used to refer to the interaction between shears in two orthogonal directions across a crack. Although the existence of the cross shear phenomenon is quite conceivable, its effect is neglected

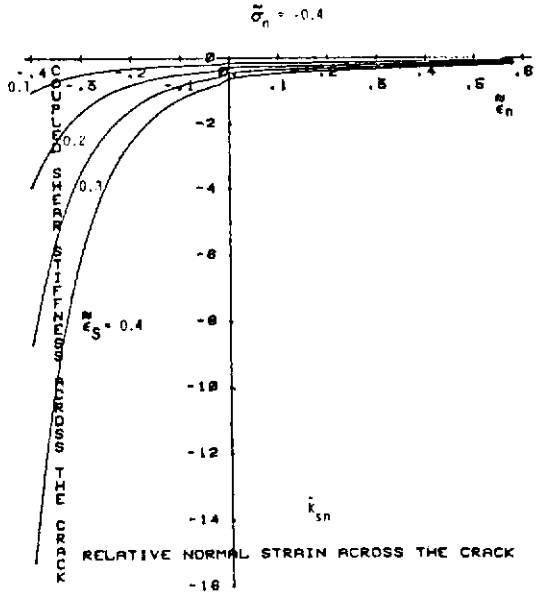

Fig. 11.

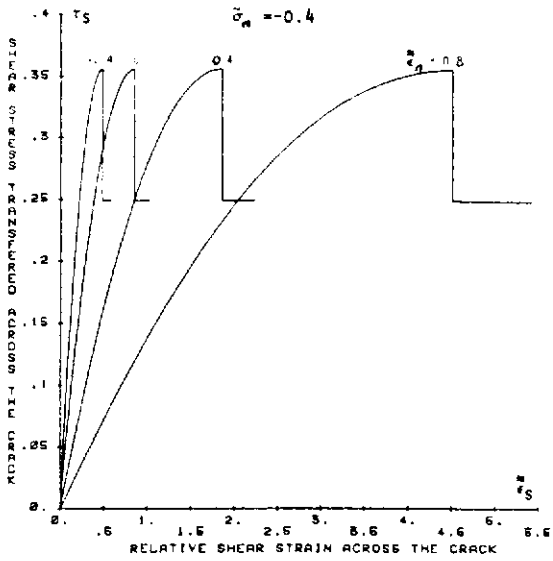

Fig. 10.

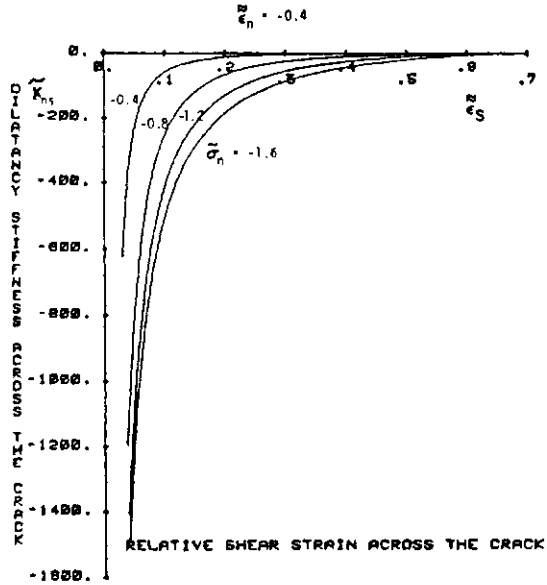

Fig. 12.

in this study due to the lack of experimental information and practical significance.
Using $\tilde{\sigma}_t=0.1$ $\theta=37$, $a=0.05$, $c=0.3$ for $\tilde{\tau}_p$;

$B=0.5$, $Q=1$ for $\tilde{\tau}_R$;
$\varepsilon_p=-1$, $\varepsilon_q=0.1$, $K=2$ for $\tilde{\sigma}_n$ and $\tilde{K}_{nn}$;
$\varepsilon_p=-1$, $A_s=1$, $N_s=4$, $\nu=0.2$, $K=2$ for $\tilde{\tilde{A}}$; and
$m=0.5$, $p=0$.

Equations (7.2) and (7.4) are plotted in Fig. 10 with $\tilde{\sigma}_n=-0.4$ and $\tilde{\tilde{\varepsilon}}_n=-0.4, 0, 0.4, 0.8$;
Equations (8.9) and (8.10) are plotted in Fig. 11 with $\tilde{\sigma}_n=-0.4$ and $\tilde{\tilde{\varepsilon}}_s=0.1, 0.2, 0.3, 0.4$;
Equation (9.1) is plotted in Fig. 12 with $\tilde{\tilde{\varepsilon}}_n=-0.4$ and $\tilde{\sigma}_n=-0.4, -0.8, -1.2, -1.6$.

CONCLUSION

In this paper the concept of the relative strain is introduced. Based on this concept, together with the available experimental data and reasoning, a series of mathematical models are proposed. These models are designed to simulate the interface stress transfer mechanisms of a crack in plain concrete subjected to short term monotonic loading. In order to verify the validity of these models and to broaden their application to reinforced concrete, bond slip and dowel action require immediate attention. Investigation on these subjects and the development of them into an integrated analytical system for the behavior of reinforced concrete under static as well as dynamic loading is felt to be the direction of future research.

REFERENCES

1. T. T. C. Hsu, F. O. Slate, G. M. Sturman and G. Winter, Microcracking of plain concrete and the shape of the stress–strain curve. *ACI J., Proc.* **60** (1963).
2. M. D. Kotsovos and J. B. Newman, Behavior of concrete under multiaxial stress. *ACI J., Pro.* **74** (1977).
3. M. D. Kotsovos, Fracture processes of concrete under generalized stress state. *Mater. Structures* **12** (1979).
4. D. Ngo, A network-topological approach to the finite element analysis of progressive crack growth in concrete members. Ph.D. Thesis, University of California, Berkeley (1975).
5. Zdenek P., Bazant and Luigi Cedolin, Blunt crack band propagation in finite element analysis. *J. Engng Mech., Div., ASCE, Proc.* **105**(EM2) (1979).
6. A. R. Ingraffea, On discrete fracture popagation in rock loaded in compression. *Proc. 1st Int. Conf., on Numerical Methods in Fracture Mechanics*, Swansea, 9–13 Jan., 1978.
7. L. E. Malvern, *Introduction to the Mechanics of a Continuous Medium*, 1st Edn. Prentice-Hall, Englewood Cliffs, New Jersey (1969).
8. J. A. Hofbeck, I. O. Ibrahim and A. H. Mattock, Shear transfer in reinforced concrete. *ACI J., Proc.* **66** (1969).
9. A. H. Mattock and N. M. Hawkins, Shear transfer in reinforced concrete—Recent research. *PCA J.* **17**(2) (1974).
10. A. H. Mattock, Shear transfer in concrete having reinforcement at an angle to the shear plane. *ACI Publication SP-42, Shear in Reinforced Concrete*, Vol. 1 (1974).
11. A. H. Mattock, Shear transfer in reinforced concrete with moment or tension across the shear plane. *PCA J.* **20**(4) (1975).
12. R. F. Mast, Auxiliary reinforcement in concrete connections. *J. Struct. Div., ASCE, Proc.* **94**(ST6), (1968).
13. J. Hovde and M. S. Mirza, A finite element analysis of shear strength of reinforced concrete beams, *ACI Publication SP-42, Shear in Reinforced Concrete*, Vol. 1 (1974).
14. R. N. White and M. J. Holley, Jr., Experimental studies of membrane shear transfer. *J. Struct. Div., ASCE, Proc.* **98**(ST8) (1972).
15. J. P. Laible, R. N. White and P. Gergely, Experimental investigation of seismic transfer across cracks in concrete nuclear containment vessels. *ACI Publication SP-53, Reinforced Concrete Structures in Seismic Zones*, 1977.
16. ASCE-ACI Task Committee 426, The shear strength of reinforced concrete members. *J. Struct. Div., ASCE, Proc.* **99**(ST6) (1973).
17. N. R. Barton, A model study of rock-joint deformation. *Int. J. Rock Mech. Mining Sci.* **9** (1972).
18. R. E. Goodman and J. Dubois, Duplication of dilatancy in analysis of jointed rocks. *J. Soil Mech. Foundations Div., ASCE, Proc.* **98**(SM4) (1972).
19. R. E. Goodman and C. St. John, Finite element analysis for discontinuous rocks. In *Numerical Methods in Geotechnical Engineering*. McGraw-Hill, New York (1976).
20. R. E. Goodman, Analysis in jointed rocks. In *Finite Element in Geomechanics*. Wiley, New York (1977).
21. Z. P. Bazant and T. Tsubaki, Concrete reinforcing net: optimum slip-free limit design. *J. Struct. Div., ASCE, Proc.* **105**(ST1) (1979).
22. Z. P. Bazant and T. Tsubaki, Friction-dilatancy model for cracked reinforced concrete. Structural Engineering, *Rep. No.* 79-8/640*f*, Department of Civil Engineering, Northwestern University (Aug. 1979).
23. M. N. Fardis and O. Buyukozturk, Shear transfer model for reinforced concrete. *J. Engng Mech. Div., ASCE, Proc.* **105**(EM2) (1979).
24. Joost C. Walraven, Fundamental analysis of aggregate interlock. *ASCE Spring Convention*, Portland, 14–18 (Apr. 1980).
25. H. H. Einstein and R. C. Hirschfeld, Model studies on mechanics of jointed rock. *J. Soil Mech. Foundations Div., ASCE, Proc.* **99**(SM3) (1973).
26. R. E. Goodman, R. L. Taylor and T. L. Brekke, A model for the mechanics of jointed rock. *J. Soil Mech. Foundations Div., ASCE, Proc.* **94**(SM3) (1968).
27. M. Hittinger and R. E. Goodman, JTROCK—a computer program for stress analysis of two-dimensional, discontinuous rock masses. *Geotechnical Engineering Rep. No. UCB/GT/78-04*, Department of Civil Engineering, University of California, Berkeley.

Computers & Structures, Vol. 13, pp. 223–227, 1981
Printed in Great Britain.

0045-7949/81/010223-05$02.00/0

NONLINEAR ANALYSIS OF REINFORCED CONCRETE FRAMES

CHENG-TZU THOMAS HSU†
Department of Civil and Environmental Engineering, New Jersey Institute of Technology, Newark, NJ 07102, U.S.A.

M. SAEED MIRZA‡
Department of Civil Engineering and Applied Mechanics, McGill University, Montreal, Quebec, Canada Canada H3A 2K6

and

C. S. SUNNY SEA§
Carolina Dewatering Corporation, Irvington, New York, U.S.A.

(*Received* 25 *April* 1980)

Abstract—A computer analysis is described for the elastic–perfectly plastic analysis of reinforced concrete planar frames. This computer program requires less computer time and memory space and is intended as practical analysis and design uses. The computer program is capable of complete analysis of reinforced concrete frames from zero load until failure under any system of static gravity and lateral loads. The program can cater for any given geometry and end conditions. The analysis of reinforced concrete frames uses a computer program as a subroutine to calculate the moment-curvature characteristics under a constant load applied at the section centroid. A reinforced concrete frame tested by Cranston and Cracknell [1] are analyzed using the computer program developed and the results are compared with the experimental results. It is noted that the proposed nonlinear analysis satisfactorily reproduced the behavior of reinforced concrete plane frames from zero loads until failure.

INTRODUCTION

Many rigorous and computationally complex methods [2–9] for predicting the non-linear behavior of reinforced concrete frames have been developed over the last two decades. Various ones of these methods have been devised to include some of the following aspects: (i) the nonlinear concrete stress strain relationship; (ii) the varying cross section due to nonuniform cracking and inelastic behavior; (iii) the effect of axial load; (iv) the effects of creep and shrinkage; (v) the post yielding behavior of sections; (vi) the residual effects of overloading. Most of the effort in this area has been concentrated on developing suitable computer programs to provide information on strength, ductility and elastic and plastic behavior including deflections at specific load levels. These analyses were based on the matrix flexibility, matrix displacement and finite element methods and assumed that a structure behaves linearly under small increments of load or deformation. Many of these computer programs require a great deal of computer time and memory space and are therefore intended as a research tool.

This paper presents a more practical and time-saving computer analysis for reinforced concrete plane frames. A computer program developed by Wang [13–14] for an elastic-perfectly plastic analysis of steel plane frames was modified to account for the behavior of reinforced concrete materials and structures.

PRESENT METHOD

General

In any inelastic analysis, it is necessary to consider the rotation capacity of the hinging regions before establishing the redistribution of bending moments in the frame. The post-elastic behavior of the concrete frames for both of these aspects is dependent on the shape of the moment-curvature and the moment-rotation curves for the frame members.

Load-moment-curvature and inelastic rotation

It is well known that the plastic hinges formed in a steel frame have a very large rotation capacity. However, the rotation capacity of hinging regions in a structural concrete member is dependent on several parameters, e.g. material properties, member geometry, applied loads, etc. Recent limit design research in structural concrete has led to the definition of the hinge length; the rotation capacity of the hinge can then be calculated from the constitutive relationships for the materials and the section geometry. Hsu and Mirza [7] have developed a computer program to determine the moment curvature characteristics of a reinforced concrete section subjected to a constant axial load applied at the section centroid. The inelastic rotation capacity of the hinge can be calculated using the following equations (Mattock [11] and Corley [12]):

$$\theta_{pl}=\left(\phi_u-\phi_y\frac{M_u}{M_y}\right)\frac{d}{2} \tag{1a}$$

where θ_{pl} = the inelastic rotation of the hinge; d = the effective depth; ϕ_y = the curvature at yield; M_y = the bending moment at yield; ϕ_u = the curvature at ultimate load and M_u = the ultimate bending moment.

For an under-reinforced section, the moment-curvature curve can be approximated by an elastic-

perfectly plastic relationship without any serious error. The plastic rotation capacity is then given by

$$\theta_{pl}=\left(\phi_u-\phi_y\right)\frac{d}{2}. \tag{1b}$$

The following points must be considered in developing a computer program for an elastic–perfectly plastic analysis of reinforced concrete frames:

(a) The inelastic rotation capacity of the hinging region in a reinforced concrete section is dependent on the section geometry, material properties and applied axial load and can be limited in some cases. The axial loads applied at the members are based on the values obtained from the linear structural analysis for plane frames.

(b) The appearance of cracks in a structural concrete member gives rise to a varying flexural rigidity (EI) along its length. Flexural rigidity (EI) used in the present method is on the basis of the flexural rigidity after concrete cracking. The zero flexural rigidity is assumed after yielding of the tension steels.

(c) The descending branch of the moment-curvature curve at a section (or the moment-rotation curve at a hinge) provides the section with added ductility although its bending strength decreases.

(d) The strength of a reinforced concrete section in positive and negative bending is dependent on the quantity and the arrangement of tension and compression steels. The bending strength of a reinforced concrete section can therefore, be significantly different under reversal of applied loads. Similarly, the ductility of a reinforced concrete section is dependent on the reinforcement details.

(e) The provision of stirrups in a reinforced concrete beam does not only prevent shear failures, but also increases the ductility of the concrete. This increased compressive strain capacity significantly improves the rotation capacity of the hinging region although it does not add to the strength of the section.

Elastic–plastic computer analysis and design method

A computer program was developed by the writers [10] for elastic–perfectly plastic analysis of reinforced concrete plane frames, based on a modification of Wang's program [13, 14] which was developed as a general purpose program (matrix displacement formulation) for limit analysis of steel plane frames (see Appendix). Wange [13, 14] used the conventional mechanism approach to handle the collapse stage in steel plane frames. The present program was based on an assumed rotational capacity of the "plastic hinges" and the formation of a "mechanism" at the ultimate load stage

The reinforced concrete frame was divided into several small elements. For each element, the section geometry, material properties and inelastic hinge rotation are known through the input data and subprograms. The computer program developed is capable of complete analysis of reinforced concrete plane frames from zero load until failure under any system of loads. The computer output gives the complete load-deformation behavior, the location and the sequence of the formation of "plastic hinges" until a "collapse mechanism" is formed. The program can cater for any given geometry (structural layout, member length, section geometry) material properties and end conditions (fixed and/or pinned end conditions).

The details of computer program can be found in the Ref. [10]. The flow diagram is shown in Fig. 1. The program is coded in FORTRAN IV and can be run either on the RAX or O/S systems of IBM 370/155 or IBM 360/75.

Example and discussion of results

The specimen analysed using the present computer program is Frame FP4 tested by Cranston and Cracknell [1] (Figs. 2 and 3). It must be noted that the value of flexural rigidity (EI) used in the main computer program is the slope of the moment-curvature curve (under a constant axial force at the section centroid). Moment-curvature curves for typical sections are shown in Figs. 4 and 5. The location of formation of hinges and the final collapse mechanism are shown in Fig. 6; these have been obtained from the computer analysis results. The failure mechanism obtained experimentally shows excellent agreement with the present analysis results (Fig. 7).

The experimental and the computed load-deformation curves are shown in Fig. 8. The computed ultimate strengths of the frame is lower than the experimental

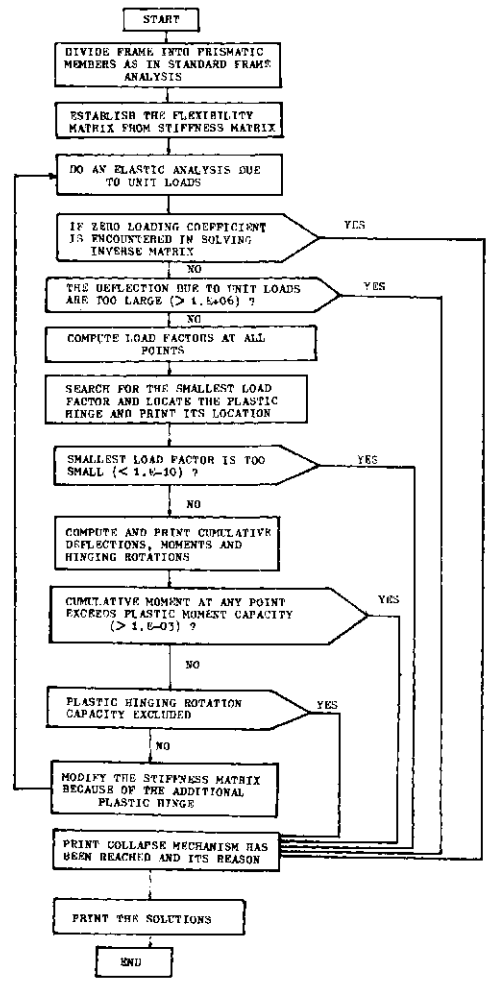

Fig. 1. Flow diagram: elastic perfectly plastic analysis of reinforced concrete plane frames.

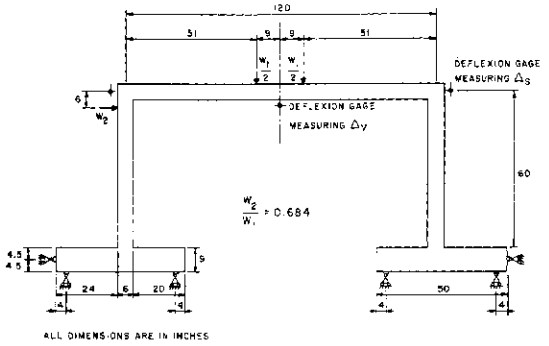

Fig. 2. Dimensions and loading of frame FP4 (after Cranston and Cracknell [1]).

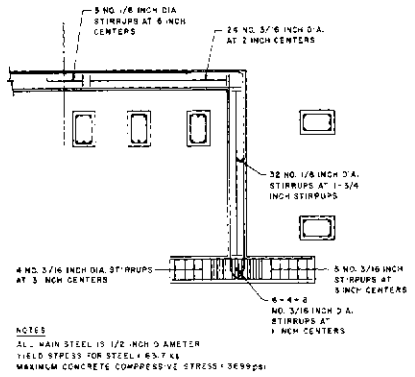

Fig. 3. Reinforcement details for Frame FP4 (after Cranston and Cracknell [1]).

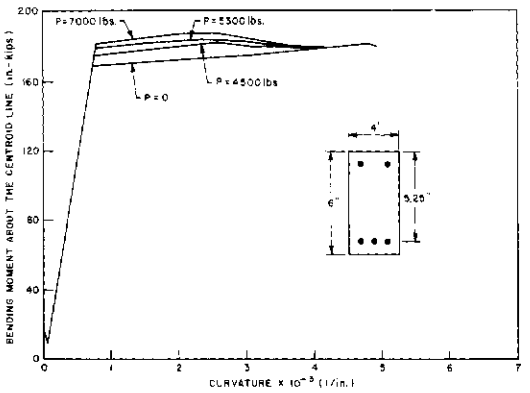

Fig. 5. Moment—curvature curves.

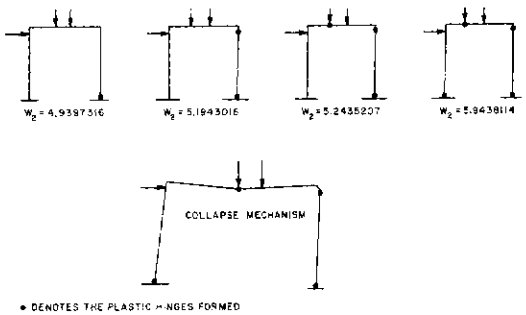

Fig. 6. Process of mechanism formed by the present analysis.

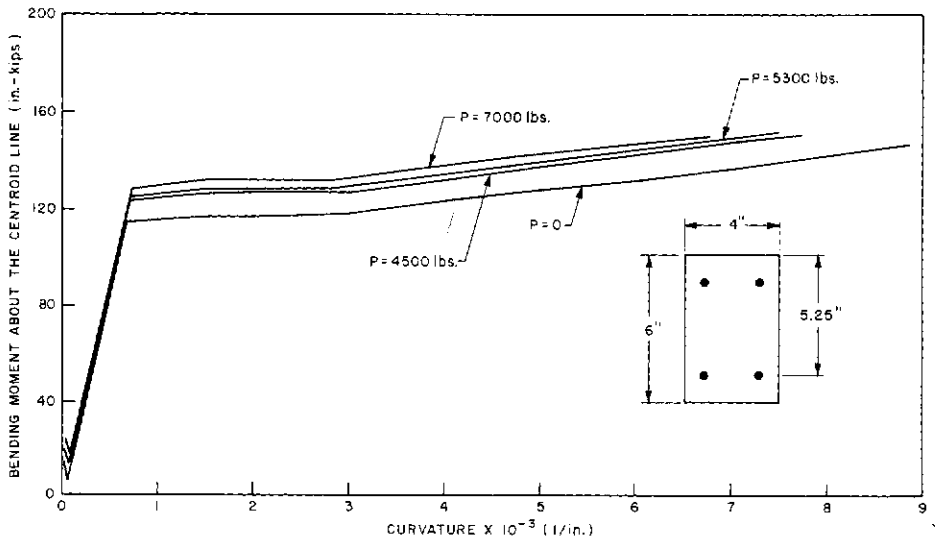

Fig. 4. Moment—curvature curves.

value because the moment-curvature relationship used in analysis is a conservative elastic–plastic idealization of the moment-curvature results obtained from the present computer program. However, both horizontal and the vertical deflections at the maximum load agree well with the test results showing that the curvature formulation used is satisfactory. Moreover, there is excellent agreement between the experimental and the computed $\Delta_v - \Delta_s$ curves.

CONCLUSIONS

A computer-aided limit analysis and design of reinforced concrete frames was developed to predict the failure mechanism and the load-deflection curves. The computer program basically follows the limit analysis of steel plane frames, and has been outlined for incorporating the effects of rotational capacity of the plastic hinges by modifying a general purpose computer program developed by Wang [13, 14].

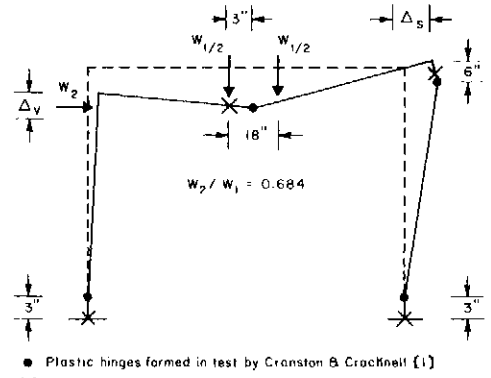

Fig. 7. Modes of failure for Frame FP4.

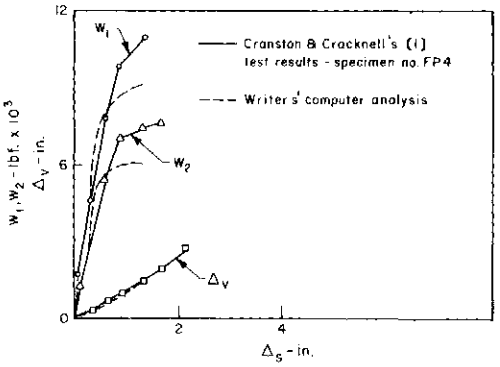

Fig. 8. Load–deflection curves for Frame FP4.

The program can be used to examine the strength and ductility of reinforced concrete plane frames and the resulting factor of safety against failure.

Acknowledgements—The writers are grateful to the Canada Emergency Measures Organization for the financial assistance to the continuing program of study of the strength and behavior of three-dimensional reinforced and prestressed concrete structures. The financial assistance of the National Research Council of Canada and New Jersey Institute of Technology towards the computer costs of this program is gratefully acknowledged.

REFERENCES

1. W. B. Cranston and J. A. Cracknell, Tests on reinforced concrete frames 2: Portal frames with fixed feet. Cement and Concrete Association TRA/420, London, England (1969).
2. J. Ferry-Borges and E. R. Oliveira, Non-linear analysis of reinforced concrete structures. *Pub. LABSE* **23**, 51–69 (1963).
3. W. B. Cranston, A computer method for inelastic analysis of plane frames. Cement and Concrete Association, TRA/386, London, England (1965).
4. J. M. Becker, Inelastic analysis of reinforced concrete frames. M.Sc. Diss., Cornell University, Ithaca, New York (1967).
5. R. G. Drysdale, Prediction of the behavior of concrete frames. IABSE Symp., Design of Concrete Structures for Creep, Shrinkage and Temperature Changes, Madrid (1970)
6. H. A. Franklin, Non-linear analysis of reinforced concrete frames and panels. Ph.D. Diss., Univ. of California, Berkeley, Calif. (1970).
7. C. T. Hsu, Behavior of structural concrete subjected to biaxial flexure and axial compression. Ph.D. Dissertation, McGill Univ., Montreal, Quebec (1974).
8. B. L. Gunnin, F. N. Rad and R. W. Furlong, A general non-linear analysis of concrete structures and comparison with frame tests. *Comput. Structures* **7**, 257–265 (1977).
9. J. S. Ford, D. C. Chang and J. E. Breen, Experimental and analytical modeling of unbraced multi-panel concrete frames. Part 2, Final Report, RCRC Project # 31, Civil Engineering Structures Research Laboratory, The Univ. of Texas at Austin, Texas, 39 pp. (1978).
10. C. T. Hsu, M. S. Mirza and A. A. Mufti, An elastic–plastic computer analysis of steel and reinforced concrete plane frames. Structural Concrete Series 72–5, Dept. of Civil Engineering and Applied Mechanics, McGill Univ., Montreal, Quebec (1972).
11. A. H. Mattock, Rotational capacity of hinging regions in reinforced concrete beams. *Proc. Int. Symp. Flexural Mechanics and Reinforced Concrete*, Miami, Florida, ASCE-ACI SP-12, pp. 143–182 (1964).
12. W. G. Corley, Rotation capacity of reinforced concrete beams. *Proc. ASCE Structl. Div.* **92**(ST4), 121–146 (1966).
13. C. K. Wang, General computer program for limit analysis. *J. Struct. Div. ASCE* **89**(ST6), 101–118 (1963).
14. C. K. Wang, *Matrix Methods of Structural Analysis*, 2nd Edn. International Textbook, Pennsylvania (1970).
15. R. K. Livesley, Automatic design of structural frames. *Q. J. Mech. Appl. Math.* **9**(3), 257–278 (1956).
16. A. Jennings and K. Majid, An elastic–plastic analysis by computer for framed structures loaded up to collapse. *The Structural Engr* **43**(12), 407–412 (1965).

APPENDIX

Formulations for elastic–perfectly plastic analysis of plane frames

The stiffness matrix of a member **S** relates the joint moments $\boldsymbol{F}$ and the corresponding rotations $\boldsymbol{e}$ as follows:

$$\boldsymbol{F}=\mathbf{S}\boldsymbol{e}. \tag{2a}$$

Equation (2a) can be written explicitly for a member ij as

$$\boldsymbol{F}_i=\mathbf{S}_{ii}\boldsymbol{e}_i+\mathbf{S}_{ij}\boldsymbol{e}_j \tag{2b}$$

$$\boldsymbol{F}_j=\mathbf{S}_{ji}\boldsymbol{e}_i+\mathbf{S}_{jj}\boldsymbol{e}_j. \tag{2c}$$

It must be noted that eqns (2) account only for flexural deformations in the member ij while the axial and sheer deformations are neglected. This follows an earlier formulation by Wang [13, 14]. A more complete formulation for an elastic–plastic material has been developed by Livesley [15] and Jennings and Majid [16].

Using the results from basic slope deflection equation, the member stiffness matrix is given by,

$$\mathbf{S}=\begin{bmatrix} S_{ii} & S_{ij} \\ S_{ji} & S_{jj} \end{bmatrix}=\begin{bmatrix} 4EI/L & 2EI/L \\ 2EI/L & 4EI/L \end{bmatrix} \tag{3}$$

where E = the modulus of elasticity; I = the moment of inertia and L = the length of the member ij.

If a simple or a plastic hinge is introduced at the jth end of the member ij, the stiffness matrix **S** gets modified as

$$\mathbf{S}=\begin{bmatrix} S_{ii} & 0 \\ 0 & 0 \end{bmatrix}=\begin{bmatrix} 3EI/L & 0 \\ 0 & 0 \end{bmatrix}. \tag{4}$$

Similarly if a simple or plastic hinge is introduced at the ith end of the member ij, then **S** gets modified as

$$\mathbf{S}=\begin{bmatrix} 0 & 0 \\ 0 & S_{jj} \end{bmatrix}\quad\begin{bmatrix} 0 & 0 \\ 0 & 3EI/L \end{bmatrix}. \tag{5}$$

For a typical member ij in bending

$$\boldsymbol{F}=\mathbf{S}\boldsymbol{e}$$

or

$$\boldsymbol{e}=\mathbf{S}^{-1}\boldsymbol{F}=\mathbf{D}\boldsymbol{F} \tag{6}$$

where **D** is the flexibility matrix for the member ij and is given by

$$\mathbf{D}=\begin{bmatrix} L/3EI & -L/6EI \\ -L/6EI & L/3EI \end{bmatrix} \tag{7}$$

The external rotations X_i, X_j, and the deflection X_{ij} of end j relative to end i are related to the internal rotations e_i and e_j by the equation

$$\boldsymbol{e}=\mathbf{B}\boldsymbol{X} \tag{8}$$

where **B** = the deformation matrix

$$=\begin{bmatrix} 1 & 0 & -1/L \\ 0 & 1 & -1/L \end{bmatrix} \tag{9a}$$

and

$$\boldsymbol{X}=\begin{bmatrix} X_i \\ X_j \\ X_{ij} \end{bmatrix} \tag{9b}$$

Equation (8) can be rewritten as

$$\boldsymbol{e}=\mathbf{A}^t\boldsymbol{X} \tag{10}$$

where $\mathbf{A}^t=\mathbf{B}$ and t denotes transport of a matrix and **A** is the statics matrix relates the externally applied forces $\boldsymbol{P}$ to internal end moments $\boldsymbol{F}$ as follows:

$$\boldsymbol{P}=\mathbf{A}\boldsymbol{F}. \tag{11}$$

If there are no hinges either at i or at j, then continuity requires that the internal end rotations $\boldsymbol{e}$ as caused by the end moments $\boldsymbol{F}$, be equal to those caused by the external joint rotations or displacements. Therefore it follows from eqns (6) and (10), that

$$\mathbf{D}\boldsymbol{F}=\mathbf{A}^t\boldsymbol{X} \tag{12}$$

whence

$$\boldsymbol{F}=\mathbf{D}^{-1}\mathbf{A}^t\boldsymbol{X}=\mathbf{S}\mathbf{A}^t\boldsymbol{X} \tag{13}$$

which is familiar equation from the displacement method of rigid frame analysis.

If there is a hinge at any member end, then the hinge rotation $\boldsymbol{H}$ is given by the angle from the direction of the member as required by the external joint rotations or displacements to that caused by the end moments. Therefore

$$\boldsymbol{H}=\mathbf{D}\boldsymbol{F}-\mathbf{A}^t\boldsymbol{X}. \tag{14}$$

Computers & Structures, Vol. 13, pp. 231–240, 1981
Printed in Great Britain.

0045-7949/81/010231-10$02.00/0

FUTURE NEEDS FOR INELASTIC ANALYSIS IN DESIGN OF HIGH-TEMPERATURE NUCLEAR PLANT COMPONENTS†

J. M. CORUM
Oak Ridge National Laboratory, Oak Ridge, TN 37830, U.S.A.

(*Received* 17 *May* 1980)

Abstract - The purpose of this paper is to describe the role that inelastic analyses play in the design of high-temperature nuclear plant components and to identify the problem areas and needs. The design methodology, which explicitly accounts for nonlinear material deformation and time-dependent failure modes, requires a significant level of realism in the prediction of structural response. Thus, material deformation and failure modeling are, along with computational procedures, key parts of the methodology. Each of these is briefly discussed along with validation by comparisons with benchmark structural tests, and problem areas and needs are discussed for each.

1. INTRODUCTION

High-temperature nuclear plant components, by definition, operate at temperatures where creep effects and time-dependent failure mechanisms are significant. For the austenitic stainless and ferritic steels used in liquid-metal fast-breeder reactors (LMFBRs), these effects are implicity assumed by the ASME Boiler and Pressure Vessel Code, Section III, to occur upon significant exposure to temperatures above 800 and 700°F, respectively [1, 2]. Since normal operating temperatures of LMFBRs are in the range from 900 to 1100°F, it has been necessary to develop and utilize a design methodology that explicitly accounts for the effects of nonlinear material deformation and time-dependent damage mechanisms and failure modes.

This methodology has sought a new level of realism in the prediction of inelastic structural behavior. Efforts to develop increasingly realistic mathematical descriptions of elastic–plastic-creep material behavior (constitutive equations) have been underway, and a number of inelastic structural analysis computer programs, which are capable of treating the thermal and mechanical loadings and the typical structural geometries that are encountered, have been developed and made available to the design community.

This paper describes the role of inelastic analysis in the design of high-temperature nuclear plant components, with the objective of delineating current uncertainties and problem areas as well as future needs and directions. Because inelastic analyses are just one ingredient of the total integrated design methodology—consisting of design specifications, analysis methods for predicting structural response, and rules and criteria to guard against structural failure the requirements placed on such analyses, as well as the problem areas that exist, cannot be easily divorced from the remainder of the methodology. Thus, the problem areas and needs are identified herein in the context of this total design methodology, and they must be addressed in terms of the ultimate goal of the design process—to assure a level of structural integrity consistent with the high levels of safety and integrity required for nuclear equipment.

The following section provides an overview of the high-temperature structural design problem in fast-breeder reactors, and it summarizes the structural design ingredients and the role of inelastic analysis. Section 3 then reviews material deformation modeling. Currently used models and their shortcomings, as well as promising new developments, are briefly discussed. Section 4 addresses time-dependent failure modeling and current design criteria. Again, shortcomings and needed developments are discussed with respect to their effect on analysis. The fifth section then addresses current inelastic analyses and the problems encountered in their validation. Results from representative high-temperature structural tests are compared with analysis predictions for illustration. The final section is a summary of the problem areas and needs.

2. THE HIGH-TEMPERATURE STRUCTURAL DESIGN METHODOLOGY

The methodology for the structural design of high-temperature nuclear plant components has developed rapidly during the past decade concurrently with the effort to design and build LMFBRs. These plants are sodium cooled and consist of primary and secondary coolant loops. The primary loop includes the reactor, housed in a reactor vessel, a pump, and the primary side of an intermediate heat exchanger (IHX). The secondary loop includes the secondary side of the IHX, a pump, and a steam generator.

Two features lead to the unique high-temperature design problems in LMFBRs. The first is that the sodium outlet temperature is well within the creep range for the alloys currently used in plant construction - types 304 and 316 stainless steel and 2 1/4 Cr–1 Mo steel. The second feature is the relatively large temperature rise of the coolant as it passes through the reactor core—about 300°F vs typically 60°F for a

†Research sponsored by the Division of Reactor Research and Technology, U.S.Department of Energy, under contract W-7405-ENG-26 with the Union Carbide Corporation.

light-water reactor plant. Reactor scrams and power changes result in rapid changes in this temperature rise, and because of the good heat transfer properties of the sodium coolant, thermal transient loadings can be imposed throughout the system.

The potential structural effects of such transients can be described by means of a simple example—a straight section of pipe in a coolant loop, as depicted in Fig. 1. Assume that the sodium temperature drops 300°F in several seconds (*a–b*), rises slowly (*b–c*), and then is constant for several hundred hours (*c–d*), after which there is another thermal cycle. The predicted response of the pipe is depicted in (c). Starting with point *a*, the inner surface of the pipe first yields in tension as it

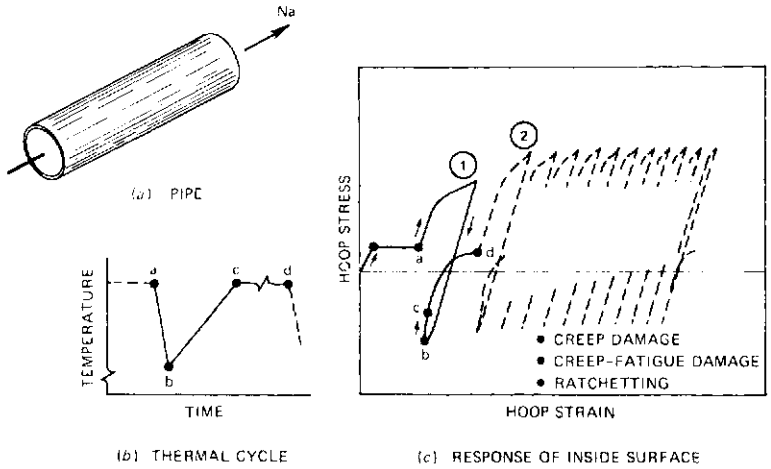

Fig. 1. Schematic representation of effects of repeated thermal transient loadings.

contracts, but as the outer surface subsequently begins to cool the inner surface stress reverses sign and goes into compression. At *b*, the wall is uniformly at the lower temperature; slow heating from *b* to *c* causes the residual stress to decrease because of the decreasing yield condition with increasing temperature. At *c*, a compressive residual stress remains, which relaxes during the subsequent hold period. The response to subsequent cycles is depicted in the figure.

The behavior shown in Fig. 1 illustrates three key potential failure modes. First, creep-rupture damage is accumulated during the hold periods; second, the plastic cycles introduce fatigue damage which interacts with the creep to produce a creep-fatigue interaction damage mode; and third, ratchetting occurs, introducing the potential for failure due to excessive deformation. These are the primary concerns of the LMFBR structural designer. He must have inelastic analysis procedures to predict the response, and he must have criteria that guard against failure by time-dependent cracking or rupture and by excessive deformation.

In reality, of course, the components to be assessed are generally more complex than a straight pipe. Figure 2 depicts an intermediate heat exchanger as an example. Critical structural areas include the primary inlet nozzle-to-cylinder attachment, with its relatively thick reinforcing, and several areas such as the tube-sheet-to-shell attachments, where thick and thin sections must be joined.

The design methodology for a component such as the IHX has three constituents: (1) design specifications, which give the normal operating and overload thermal and mechanical loading histories for which the component must be designed, (2) structural analysis procedures, guidelines for which are provided by Oak Ridge National Laboratory and described in the following section, and (3) the criteria for guarding against structural failure, which are provided in Code Case N-47 of the ASME Boiler and Pressure Vessel Code [2]. The specified loading conditions are developed to provide an upper bound to what might be expected, both in number and severity of events, and the design analyst is expected to combine these into loading histograms that will provide worst case predictions. Likewise, the ASME Code criteria, which

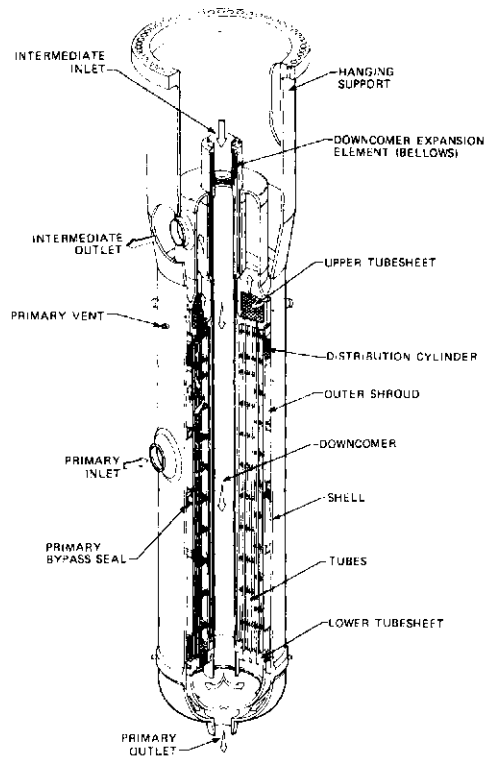

Fig. 2. Intermediate heat exchanger for LMFBR. (Courtesy of Clinch River Breeder Reactor Plant Project Office).

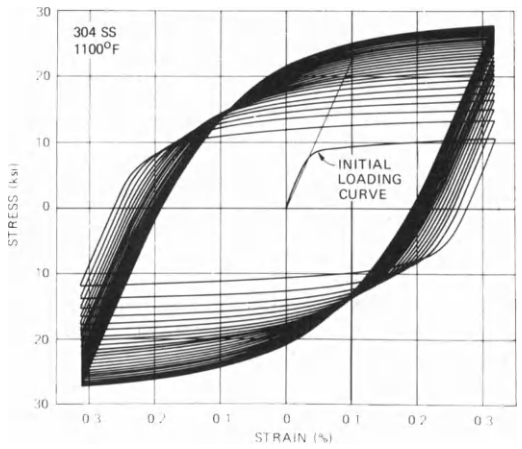

Fig. 3. Typical cyclic stress–strain curve for uniaxial specimen cycled between fixed strain limits.

will be briefly reviewed in Section 4, contains margins of safety to cover unknowns in the material models, material variability, etc.

Together, these three constituents design specification, structural analysis procedures, and design criteria must provide an integrated approach to assuring the high level of structural integrity required for nuclear components, where a failure might result in severe economic, political, and safety consequences. But whereas the design specifications and the design criteria contain built-in margins of safety, the inelastic analysis cannot very easily do so, because a prediction that is conservative for one failure mode, e.g. ratchetting, can be nonconservative for another, e.g. creep-fatigue damage. This introduces a complicating factor into evaluating and validating inelastic analysis. Analysis procedures are *valid* if they guide the designer to correct decisions in the structural design process and if, when utilized correctly and appropriately, they assure compliance with the design requirements.

3. MATERIAL DEFORMATION MODELING

Mathematical models (constitutive equations) that describe the time-dependent inelastic response of a material to time-varying thermal and mechanical multiaxial loadings are the key ingredient of inelastic analysis procedures. These models must be capable of predicting the significant behavioral features of a material, while at the same time being tractable in terms of incorporation into computing tools. The purpose of this section is to outline the currently recommended models [3] and potential new models, and to discuss problems and shortcomings as they relate to, and influence, structural analysis.

Briefly, the currently recommended models assume that total strain is the sum of elastic, plastic, creep, and thermal components. Use is made of the classical theories of plasticity and creep, but these are augmented by modifications and ad hoc rules to account for observed nonclassical behavioral features and interactions between plastic deformation, creep deformation, and time.

The plasticity theory makes use of a yield criterion, a multiaxial flow rule, a combination isotropic-kinematic hardening law to define yielding subsequent to initial yield, and cyclic uniaxial stress–strain curves to characterize the material. Both the initial yield surface and the subsequent plastic loading surfaces are described by an equation of the von Mises form:

$$f=\frac{1}{2}S_{ij}S_{ij}=\kappa(\varepsilon^p_{kl},\varepsilon^c_{kl},T), \tag{1}$$

where

$$S_{ij}=\sigma'_{ij}-\alpha_{ij}. \tag{2}$$

The prime of σ'_{ij} indicates deviatoric stress, the superscripts p and c denote plastic and creep quantities, T denotes temperature, and α_{ij} denotes the center of the yield surface, which is shifted according to

$$\mathrm{d}\alpha_{ij}=\frac{1}{2\kappa}S_{ij}\,(S_{kl}\,\mathrm{d}\sigma_{kl}-\mathrm{d}\kappa). \tag{3}$$

The plastic strain increment is given by the flow law:

$$\mathrm{d}\varepsilon^p_{ij}=\frac{1}{2C\kappa}S_{ij}\left(S_{kl}\,\mathrm{d}\sigma_{kl}-\frac{\partial\kappa}{\partial T}\,\mathrm{d}T-\frac{\delta\kappa}{\delta\bar{\varepsilon}^c}\,\mathrm{d}\bar{\varepsilon}^c\right). \tag{4}$$

In this formulation, bilinear representations of the cyclic stress–strain curves are used. The size of the yield surface is characterized by κ, which is related to the cyclic bilinear yield points. The hardening coefficient C is related to the slope of the elastic–plastic portion of the bilinearized stress–strain curve.

Numerous experiments have been performed to provide the bases for the plasticity recommendations outlined above. Representative data are illustrated in Figs. 3–5. Figure 3 is a typical cyclic stress–strain curve, and it illustrates the cyclic hardening that must be characterized. Figure 4 is the result of a test on a tube in which the yield surface was probed at various points along a nonradial loading path. These surfaces represent points at which nonlinear response just begins (the proportional limits), and they clearly indicate the appropriateness of a kinematic hardening model (kinematic movement of the surface without change in size or shape) and of the von Mises surface representation.

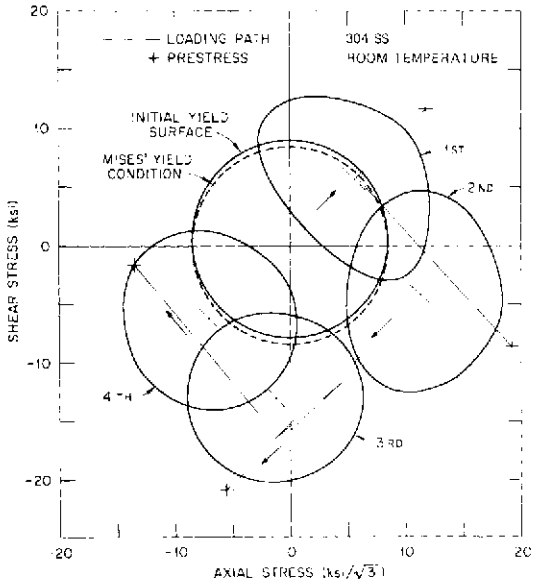

Fig. 4. Yield surfaces measured during nonproportional loading of tubular specimen subjected to torsional and axial loadings.

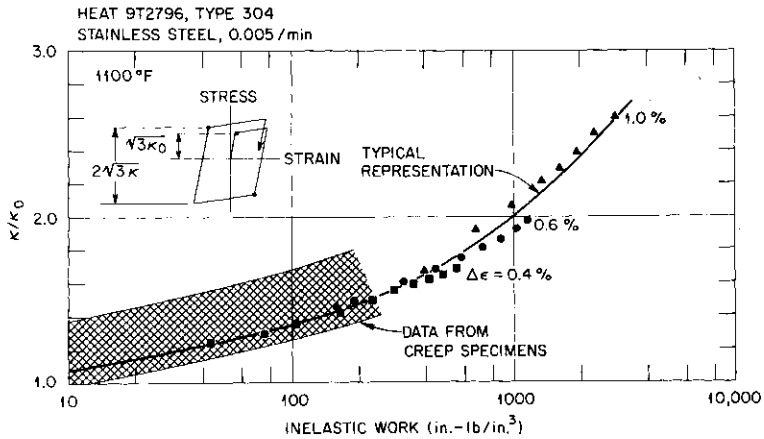

Fig. 5. Dependence of cyclic yield stress on inelastic (plasticity or creep) work.

Although kinematic hardening alone is appropriate for the "proportional limit surfaces," some isotropic hardening becomes necessary to describe the bilinear surfaces that derive from Fig. 3. Figure 5 depicts experimental results for 304 stainless steel showing the dependence of κ on the accumulation of both plastic and creep strains. The data points show results from cyclic stress–strain tests plotted against inelastic work; the shaded band represents data from stress-strain tests on precrept specimens. The resulting representative curve is typical of the relation used for κ in eqn (1).

The model for creep makes use of a multiaxial flow rule, a strain-hardening law with auxiliary rules for determining creep response under changing stresses and temperatures, and a uniaxial creep equation for characterizing the material. The flow rule is given by

$$d\varepsilon_{ij}^{c} = \frac{3}{2}\frac{\dot{\bar{\varepsilon}}^{c}(\bar{\sigma}, \bar{\varepsilon}^{H})}{\bar{\sigma}}\sigma_{ij}\,dt, \tag{5}$$

where $\dot{\bar{\varepsilon}}^{c}$ is the effective creep strain rate obtained from the creep equation for an effective stress $\bar{\sigma}$ and a modified effective total creep strain, $\bar{\varepsilon}^{H}$, which is the measure of strain hardening. Multiaxial data for monotonic creep loadings exist to show the reasonableness of the flow rule. Likewise, step-load uniaxial data (Fig. 6) exist to generally support the strain-hardening rule. The auxiliary rules handle the cases of reversal creep, and again uniaxial data show the general reasonableness of these rules.

Additional complications arise due to the interactions of creep and plasticity. Rules have been added to approximately account for the effect that creep has on α_{ij}, the measure of yield surface movement. Likewise, plastic strains can affect creep hardening, so additional rules are furnished to account for this, as illustrated in Fig. 7. Here, a hold period was introduced at one end of the measured cyclic loop shown in Fig. 7(a). Normally, strain hardening would lead to progressively less relaxation from one cycle to the next, but for 2 1/4 Cr–1 Mo steel the reversed plastic strain loop cancels the creep-strain hardening [Fig. 7(b)]. Note that in the case where the specimen was loaded from c to d and allowed to relax without the plastic reversal, hardening does occur.

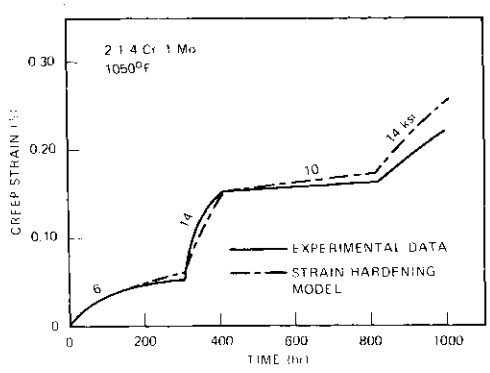

Fig. 6. Result of typical uniaxial step-load creep test compared with strain-hardening prediction.

As a final example of the need to augment the classical rules, it has been observed in certain types of problems that the kinematic hardening plasticity model can lead to unrealistic situations because of a lack of restraint on the movement of the *bilinear* yield surface. The analytical prediction in Fig. 8(a), which is again for the surface of a pipe subjected to repeated thermal cycle, illustrates this difficulty—peak stresses are becoming very high, and gross yielding occurs even before reversed loading in the later cycles. For these cases a special "α-reset" procedure has been recommended. Results for the same problem with the α-reset procedure, which resets α_{ij} to zero when significant stress reversals occur, are depicted in Fig. 8(b).

The point of reviewing the currently used constitutive models has been to illustrate that the rules are complex. Subtle changes can have large effects on inelastic analysis deformation and failure predictions. Also, although most features have been demonstrated experimentally, at least through relatively short-term uniaxial tests, many of the features remain to be validated, particularly for long-term nonproportional multiaxial loadings.

Much of the increasing complexity introduced into the current constitutive equations was necessary because of the inherent limitations of the bilinear theory and, more generally, of the classical framework. Nonlinear theories are being developed and validated to overcome the former, and a more general unified theory, which simultaneously represents both rate-dependent plasticity and time-dependent creep without distinguishing between the two, is being pursued which shows promise of overcoming both limitations. The unified theory makes use of two state variables—a

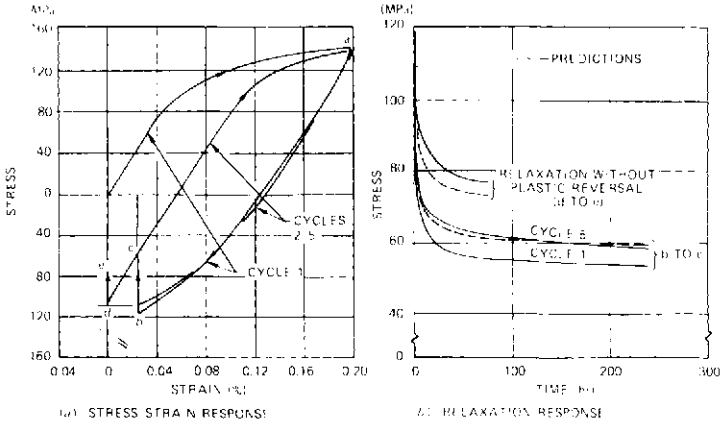

Fig. 7. Measured and predicted relaxation responses for hold periods interspersed with plastic cycles (2 1/4 Cr–1 Mo steel at 1000°F).

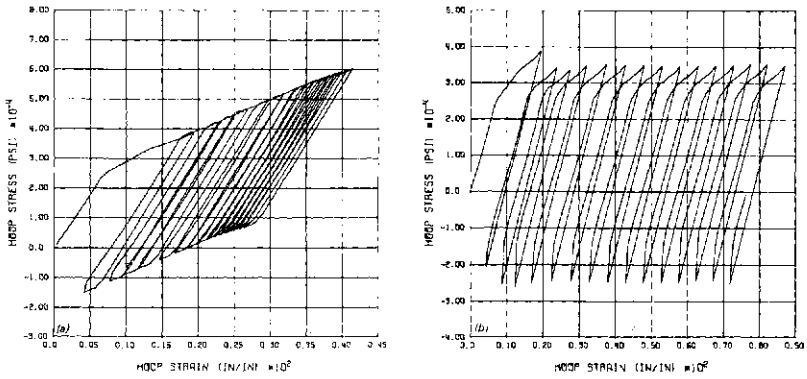

Fig. 8. Predicted stress-strain response of pipe wall subjected to repeated thermal downshocks. (a) Without restriction on kinematic movement of yield surface; (b) with α-reset procedure.

tensorial quantity representing internal stresses or back stresses, and a scalar quantity representing isotropic hardening—to allow for both hardening and recovery to occur simultaneously. The theory is akin to classical plasticity in that surfaces are utilized, but they are surfaces of constant strain rate. Of importance to inelastic analysis is the fact that some solution complications result from the time integration, which requires that a system of differential equations be simultaneously solved for each loading step. Nonetheless, it is believed that the unified theory will become a practicable tool in inelastic design analysis. It has been used to solve a number of practical structural problems, and it captures most of the behavioral features that have required modifications and ad hoc rules for the current classically-based constitutive theory. One example will be given here to illustrate this capability. Figure 9(a) shows a calculated stress-strain loop in which constant strain hold times are introduced at 1, 2, ..., 7. The predicted response is shown in Fig. 9(b) and qualitatively matches the observed behavior of 2 1/4 Cr–1 Mo steel. Note in particular that the effect of the plastic reversal on subsequent relaxation is correctly predicted.

A final point should be made regarding deformation modeling. The foregoing discussion has centered on the constitutive equation framework and formulation, while actual material response is characterized by the results of uniaxial stress-strain tests and creep tests. Studies at Oak Ridge National Laboratory on some 20 heats of type 304 stainless steel indicate that the yield stress can vary by more than $\pm 20\%$ from one heat to the next. For a given stress level and time, measured creep strain can vary by $\pm$ a factor of 2 from one heat to the next. Yet, the designer generally uses one set of properties to represent all 304 stainless steel; he doesn't know *a priori* the behavior of the particular heats from which his component will be built. Heat-to-heat variations can significantly affect deformation predictions; and failure predictions, even more so. Studies have shown that much of the intended Code design margins can be exhausted by such variations. This then is an additional complicating factor which must be considered when addressing the requirements for, and validity of, inelastic analysis methods.

4. TIME-DEPENDENT FAILURE CRITERIA

Although failure modeling and criteria are not a part of inelastic analysis, they are a part of the integrated design approach, and the validity of inelastic analysis for high-temperature reactor components can be addressed only in the framework of that total approach. The purpose of this section is to briefly review the current Code criteria along with problems and shortcomings.

ASME Code Case N-47 has two general categories of limits. The first consists of primary stress limits placed

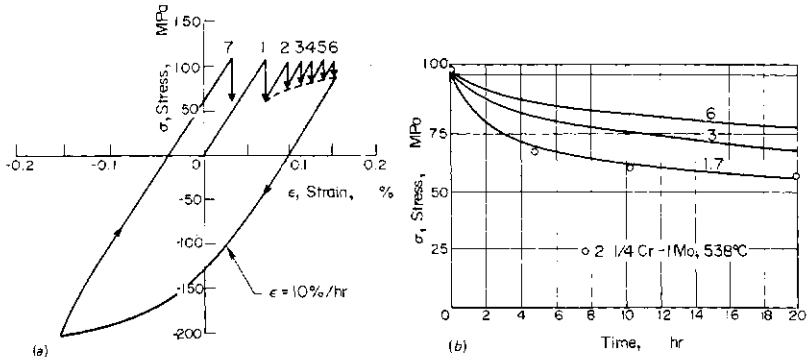

Fig. 9. Typical example of unjaxial loading illustrating capability of unified constitutive theory to capture key behavioral features. The experimental points correspond to the initial relaxation period.

on elastically-calculated load-controlled quantities, such as the internal pressure stresses. The second consists of strain, creep-fatigue, and buckling limits. It is in meeting these latter limits that inelastic analysis is frequently required.

The creep-fatigue rules are, by far, the most frequently limiting criteria, so only they will be reviewed here. A linear time- and cycle-fraction damage accumulation rule, expressed as

$$\sum_j \left(\frac{n}{N_d}\right)_j + \sum_k \left(\frac{t}{T_D}\right)_k \leqslant D, \tag{6}$$

is used by the Code along with von Mises effective quantities to represent multiaxial effects. The time fraction represents the time, t, at a given condition (stress and temperature) divided by the allowable time at that condition. The cycle fraction represents the number of cycles at a given condition (strain range and temperature) divided by the allowable number of cycles at that condition. The quantity, D, which is less than or equal to one, comes from an interaction diagram that is experimentally determined from creep-fatigue tests. Both the quantities N_d, which comes from a design fatigue curve, and T_D, which comes from a minimum creep-rupture curve, have design margins built into them.

The Code creep-fatigue rules were chosen on the basis of available data. Since then, extensive efforts have been underway to validate or improve the criteria. Multiaxial creep and fatigue data, although generally restricted to relatively short-time, proportional, monotonic loadings, tend to confirm the adequacy of the multiaxial strength theories for those limited conditions.

The damage accumulation rules are more questionable. An extensive test series is currently underway to provide data for more fully validating the time-fraction rule. Existing creep-fatigue data, which are restricted to short times and large strain ranges, indicate several shortcomings of the linear damage summation rule, including excessive data scatter relative to the correlation and questionable predictions obtained from extrapolations. Nonetheless, alternative methods have not been shown to be clearly superior to the satisfaction of the Code groups.

In summary, efforts are still underway to validate the failure models, although there are known shortcomings in the damage accumulation rules. The design margins included in the Code procedures are intended to cover the uncertainties. However, these uncertainties introduce another complication to the task of validating inelastic analysis for design.

5. INELASTIC ANALYSES AND THEIR VALIDATION

The incremental and iterative finite-element method is the procedure generally employed for inelastic design analyses. This approach and its application to high-temperature design analyses have been reviewed in an interpretive report by Gallagher [4]. Because the resulting computer programs involve complex constitutive models and computational procedures, their use must be accompanied by a large measure of experience and judgment on the part of the analyst. At best they are costly and time-consuming to use, and as a result their use is limited in practice to only the most critical few locations.†

As with any complex computing procedure, questions of validity and acceptance of the results naturally arise, and they involve more than just verification of the computer program. The real question is one of qualification of the entire analysis procedure—does the combination of mathematical models, geometric discretization, description of material behavior, representation of the thermal and mechanical loading histories, and boundary conditions, all consistent with the program limitations, give an acceptable solution to the physical problem?

What constitutes an acceptable solution? It is one that leads to a correct design. Thus, it must ultimately be shown that analysis predictions, together with design criteria, preclude structural failures, and in the absence of long-term service experience, this demonstration must come from comparisons with the results of benchmark structural tests. A major portion of the high-temperature structural design technology development activities funded by the U.S. Department of Energy has thus been devoted to the generation of high-temperature, inelastic structural test data on a variety of geometries ranging from the simple to the complex. A number of representative test results from this series of tests was published in 1975 by the ASME [6] along with typical comparisons with inelastic analysis predictions. Since then, tests to failure have been emphasized.

To illustrate the process and the problems encoun-

†Reference [5] describes a large inelastic analysis performed on an IHX inlet nozzle-to-cylinder attachment similar to that shown in Fig. 2.

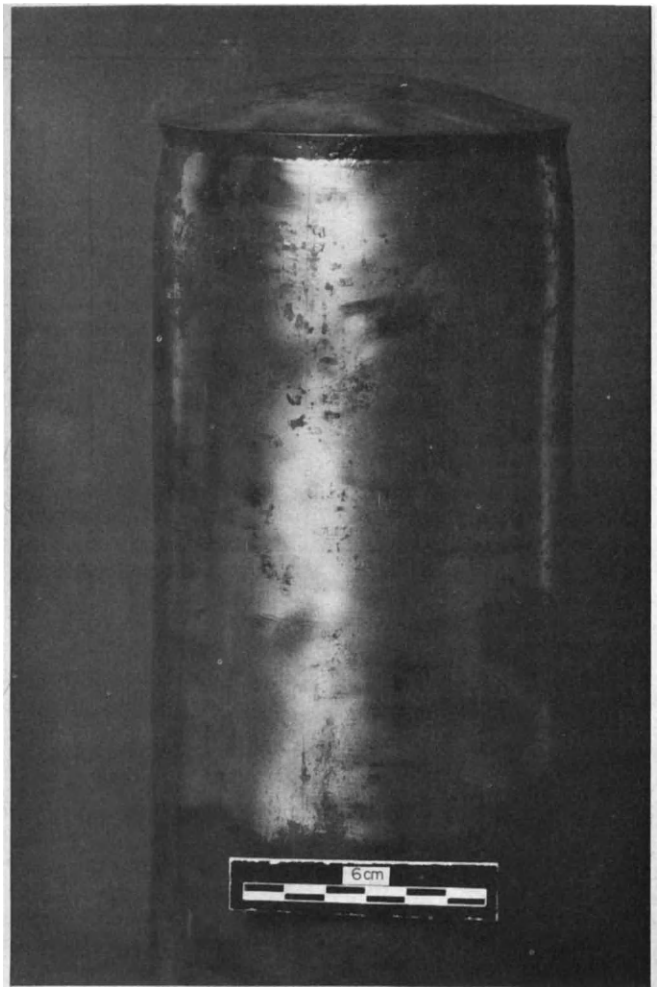

Fig. 10. Thin capped cylindrical shell after long-term pressurization test to failure.

tered in evaluating high-temperature inelastic analysis methods, three benchmark problem examples are briefly presented here. All three structures were fabricated from a single well-characterized heat of type 304 stainless steel, and all were tested in the annealed condition.

The first example is a thin-walled cylindrical shell with a flat head. The structure, which was machined from a solid bar, was subjected to a step history of internal pressure and temperature during an initial deformation test period. The pressure was then increased and held constant until failure at 1100°F after 3300 hr of testing. Figure 10 depicts the specimen after testing; failure occurred by opening of a creep crack which propagated circumferentially in the junction region between the flat head and cylinder.

Figure 11 shows typical results from a circumferentially oriented capacitive strain gage, located in the most highly strained region of the head, compared with analysis predictions. Although the agreement between theory and experiment was somewhat better at this point than at others where strain gages were located, the overall agreement was judged to be reasonable for the deformation phase. Large deformations prevented completion of the failure phase of the analysis; extrapolation of results, however, gave a very conservative creep-rupture prediction.

The second example consists of an 8-in. $\times$0.375-in. dia. wall pipe subjected to 13 thermal transient cycles in a sodium test loop. Results from two diametrically opposed capacitive strain gages are compared with the predicted ratchetting strains in Fig. 12. The predictions shown are from an analysis based on properties of the actual pipe product form. Qualitatively, the agreement is good; however, the quantitative error is significant. Furthermore, comparisons for a second test show the analysis overpredicting the measured response by more or less the same amount as the underprediction in Fig. 12.

The final example is the nozzle-to-sphere model shown in Fig. 13. Again, the model was subjected to a deformation phase, in which step-pressure and step-moment loadings on the nozzle were imposed, followed by a pressure increase which was held until failure. Figure 14 shows measured and predicted elastic plastic and creep strains in the critical region of the junction for the pressure loading. Except for the recovery strains during the zero pressure hold periods, the agreement is reasonably good. However, this is the best comparison of eight capacitive gage locations. A symmetrically located gage, whether due to gage problems or real variations, gave a significantly smaller strain response than that shown in Fig. 14.

Based on the scatter band of creep rupture for the

heat of material, failure, interpreted as crack initiation, was predicted to occur in the junction region somewhere between about 200 and 20,000 hr, with a target of 2400 hr. Photomicrographs of replicas of the junction region were made at 1000 and 2000 hr, and a typical result for 1000 hr is shown in Fig. 15. Intergranular cracking was visible in the meridional direction and extended in some instances for several grain boundary facets. Does this cracking constitute failure?

The previous examples illustrate that essential

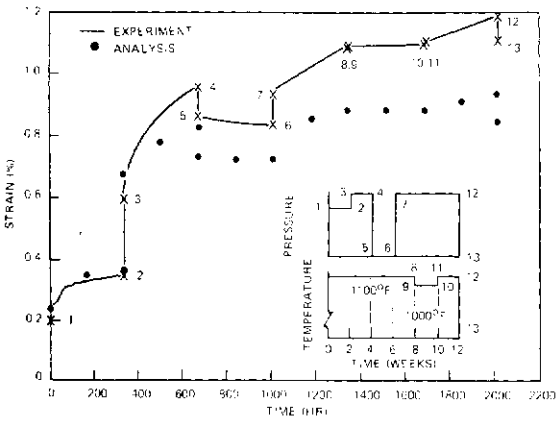

Fig. 11. Typical comparison of measured vs predicted strain-time response in capped cylindrical shell.

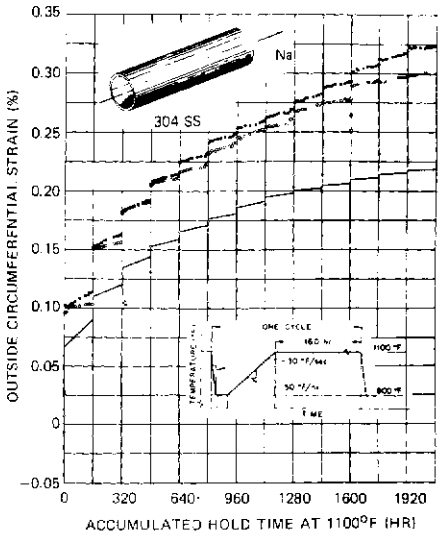

Fig. 12. Measured vs predicted ratchetting strains for pipe subjected to repeated thermal transients.

Fig. 13. Instrumented nozzle-to-sphere specimen of type 304 stainless steel.

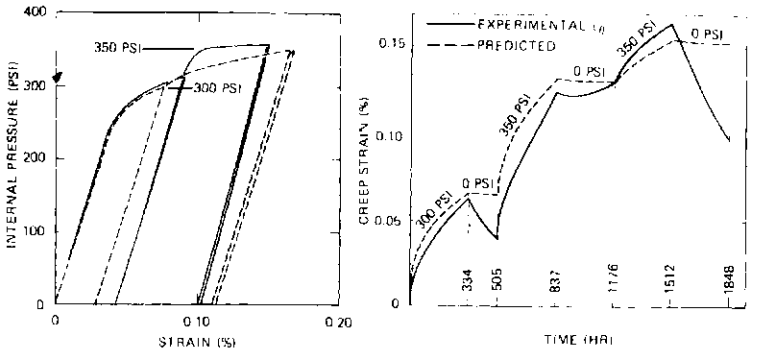

Fig. 14. Measured vs predicted circumferential ratchetting strains in junction region for initial pressure phase of nozzle-to-sphere test.

Fig. 15. Micrograph obtained from surface replica in nozzle-to-sphere intersection after 43 days of internal pressure testing. Wedge cracks are indicative of creep damage.

deformation features can be predicted, but they also point up the difficulties in judging the validity of the analysis procedure, especially for predicting failure. We have discussed uncertainties in the constitutive and failure models and the variations in material behavior, even within a single heat. In addition, uncertainties and variations must be associated with the test results; high-temperature experiments are difficult to perform, and great care is required to obtain meaningful strain measurements. Also, failures are difficult to define. Thus, exact comparisons cannot be expected, and a large group of test results will ultimately be required to make a conclusive assessment.

6. SUMMARY

The goal of this paper has been to give the reader a brief overview of inelastic analysis in the design of high-temperature nuclear plant components and of the uncertainties and problem areas that require attention. Material deformation and failure modeling along with computational procedures were addressed. Significant strides have been made in the last decade in the development and application of detailed inelastic analyses. Experimentally based constitutive models have been developed for the three alloys—types 304 and 316 stainless steel and 2 1/4 Cr–1 Mo steel—of most concern in LMFBRs, and these have been incorporated into computer programs available to the designer. Successful inelastic design-type analyses can be, and are, performed.

Practically, however, detailed analyses are often still cumbersome, time-consuming, and costly; permissible loading and geometric complexities are limited by computing equipment and by pre- and postprocessor software. Thus, if detailed inelastic analyses are to play an increasing role in the design process, we must have more efficient solution algorithms, and more attention must be given to pre- and postprocessors that are patterned to the high-temperature structural design methodology.

Program developers and users must be aware of the shortcomings and problems associated with material deformation modeling and with failure modeling and design criteria. Likewise, they should be aware of forthcoming developments in material modeling, such as the unified constitutive equations, which will place new computational requirements on analysis procedures.

Current constitutive models, although believed to capture most significant behavioral features, are complex and have identified shortcomings. They have not been completely verified, particularly with respect to complex and long-term multiaxial loadings. Furthermore, material modeling is made less exact by the significant heat-to-heat variations that exist.

Time-dependent failure models and criteria, while believed to be conservative, also have shortcomings and are in need of long-term multiaxial verification. Of particular significance is the need for improved creep-fatigue criteria, which are generally the limiting requirement in current design assessments.

It has been suggested in this paper that a valid inelastic analysis is one that will guide the designer to a economic, reliable, and safe design. Thus, the analysis cannot be divorced from the material models and the design criteria, nor can questions of validation be ignored. The general range of accuracy that can be obtained from the analysis process must be established. Likewise, the accuracy requirements that are inherently assumed in the design criteria must be ascertained. Ultimately, collective assessment of comparisons with a significant number of representative benchmark structural test results will play a key role in resolving these problems.

Perhaps the biggest need, however, is for developers and users of computer programs to work hand-in-hand with those who are developing the overall high-temperature structural design technology. Only through such a cooperative effort can the future role of inelastic analysis in high-temperature structural design be assured and placed on a firm basis.

Acknowledgements The author acknowledges with appreciation the contributions of several colleagues at the Oak Ridge National Laboratory to the material presented in this paper. A special note of thanks is due J. A. Clinard with whom many discussions over the past several years have helped to mold the thoughts expressed herein.

REFERENCES

1. American Society of Mechanical Engineers, *ASME Boiler and Pressure Vessel Code, Section III, Nuclear Power Plant Components, Division 1* (Sept. 1977).
2. ASME Code Case N-47-17, *Class 1 Components in Elevated Temperature Service, Section III, Division 1*. American Society of Mechanical Engineers, New York (Sept. 1977).
3. D. N. Robinson, C. E. Pugh and J. M. Corum, Constitutive Equations for Describing High-Temperature Inelastic Behavior of Structural Alloys. *Specialists Meeting on High-Temperature Structural Design Technology of LMFBRs, 27–30 April, 1976*. International Atomic Energy Agency, IWGFR/11, 44–57 (October 1976).
4. R. H. Gallagher, *Computational Methods in Nuclear Reactor Structural Design for High-Temperature Applications: An Interpretive Report*. ORNL-4756, Oak Ridge National Laboratory (Feb. 1973).
5. R. S. Barsoum and R. W. Loomis, Inelastic Finite Element Cyclic Analysis of a Nozzle-to-Cylinder Intersection. ASME 76-PVP-29, presented at the Joint Petroleum Mechanical Engineering and Pressure Vessels and Piping Conference, Mexico City (19–24 Sept. 1976).
6. J. M. Corum and W. B. Wright, (Eds.), *Pressure Vessels and Piping: Verification and Qualification of Inelastic Analysis Computer Programs*. G00088, American Society of Mechanical Engineers, New York (1975).

Computers & Structures, Vol. 13, pp. 241–248, 1981
Printed in Great Britain.

0045-7949/81/010241-08$02.00/0

ELASTIC–PLASTIC BENDING AND BUCKLING OF PIPES AND ELBOWS

DAVID BUSHNELL
Lockheed Palo Alto Research Laboratory, Palo Alto, CA 94304, U.S.A.

(*Received* 6 *May* 1980)

Abstract—A summary of previous work is first presented. Then an axisymmetric model is presented in which the bending of an infinite straight or curved pipe with external or internal pressure is simulated by thermal loading. The model includes geometric and material nonlinearity in the prebuckling analysis and bifurcation buckling from the nonlinear prebuckled state. Comparisons with tests on straight pipes and elbows are given. The calculations are performed with use of a slightly modified version of the BOSOR5 computer program. Qualitative agreement with test results is demonstrated.

INTRODUCTION

The elastic–plastic collapse and bifurcation buckling analysis of straight and curved tubes subjected to bending is needed for design and evaluation of nuclear power plant piping components, offshore pipelines, and other structures involving tubular members. Most of the recent work on piping has been motivated by a desire to be able to predict stress, stiffness, and limit moments of piping systems in nuclear reactors. Since the most flexible and highly stressed piping components are elbows, a significant portion of the total effort has been focused on test and analysis of various elbows under in-plane and out-of-plane moments. In the offshore oil industry, the laying of under-water oil pipelines involves bending of rather large diameter straight pipes in the presence of external hydrostatic pressure. The degree of ovalization of the pipe cross section under bending is very much affected by the external pressure, as will be seen later.

Elastic models

The bending of elastic piping components is explored in Refs. [1–11]. Brazier [1] was the first to calculate collapse moments, including in his theory the important effect of increasing ovalization (flattening) of the pipe cross section as the bending moment increased. Clark and Reissner [2] used an asymptotic formulation in which ovalization of initially curved tubes under bending is assumed to be symmetric about a tube diameter normal to the plane of curvature of the tube axis. Wood [3] expanded Brazier's treatment to include pressure, and Reissner [4] further improved the theory by including higher order nonlinear terms and introducing the effect of pressure on the bending of slightly curved tubes. Aksel'rad [5] was the first to predict bifurcation buckling of straight pipes under bending, including the effect of flattening of the cross section in the prebuckling analysis. In all of the analyses just cited, end effects are ignored; the pipes are assumed to be infinitely long. Stephens *et al.* [6] used the STAGS computer program [12] to calculate collapse and bifurcation buckling of initially straight tubes of finite length. For tubes with radius-to-thickness $R/t = 100$ they carried out a parameter study, predicting limit and bifurcation bending moments for length-to-radius ratios $3.4 \leqslant L/R \leqslant 20$. They included internal and external pressure in their analysis.

Elastic analyses of piping elbows have been performed by Dodge and Moore [7], who wrote a computer program, ELBOW, based on a model similar to Clark and Reissner's [2]. Hibbitt *et al.* [8] introduced a curved piping finite element into the MARC computer program [13]. This element, called No. 17 in the MARC element library, is based on neglect of elbow end effects. Discretization is in the circumferential coordinate only. Sobel [9] used the MARC No. 17 element in a convergence study with mesh size. He referred to Clark and Reissner's asymptotic formulas to establish optimal finite element nodal point density in the hoop direction as a function of elbow geometry. Rodabaugh *et al.* [10] performed a study of 45°, 90° and 180° elbows, determining the stiffening effects of straight pipes attached to the ends of the elbows. They used the EPACA computer program [14] for their analysis in which end effects are included. Although EPACA includes the capability to treat structures made of elastic–plastic material, the work described in Ref. [10] is restricted to elastic behavior. Fabian [11] accounts for geometric nonlinearities in determining limit moments of long elastic cylinders and bifurcation from the nonlinear prebuckled state. Bifurcation is found to occur at moments just below the limit moments, a result in agreement with Aksel'rad's [5].

Bending tests on elastic–plastic straight pipes and elbows

Several test programs on bending of elastic–plastic straight pipes and elbows have been carried out in the past decade. Bolt and Greenstreet [15] give load–deflection curves for 14 commercial 6-in. diameter carbon steel elbows and one 6 in. diameter stainless steel elbow with and without internal pressure. Vrillon *et al.* [16] compare test and theory for the in-plane bending of a 180° elbow subjected to both opening and closing moments. They used the TRICO program [17] for their analysis. Sherman [18] tested several straight pipes, noting formation of relatively short axial wavelength buckles just before collapse. A comparison between one of Sherman's experiments and theoretical results obtained with a modified version of the BOSOR5 computer program [19] is given later. Peters [20] de-

scribes a test on a 90° elbow carried out on the multiload test facility (MLTF) at the Westinghouse Advanced Reactors Division. Bung *et al.* [21] ran tests at elevated and room temperature on 304 stainless steel elbows. Comparisons between the test results of Peters [20] and Bung *et al.* [21] and theoretical predictions obtained with the modified version of BOSOR5 referred to above are presented in a following section. Reddy [22] presents experimentally measured maximum strains in long tubes under pure bending for the range of radius-to-thickness, $10 < a/h < 100$.

Elastic–plastic piping analysis

With one exception known to the writer [23], there are basically three types of elastic–plastic piping analysis for the prediction of stress, stiffness, and buckling failure of straight and curved tubes and combinations thereof:

(1) a "brute force" method in which the tubes are divided into a two-dimensional field of finite elements;

(2) simplified models in which tube end effects are ignored and discretization or trigonometric expansion is in the circumferential coordinate only;

(3) a further simplified model in which resultant forces and moments integrated over the tube cross section are related to strains and changes in curvature of the tube axis.

The STAGSC computer program [12], the EPACA code [14], and the TRICO code [17] have been used for the "brute force" analysis of elastic–plastic elbows attached to straight pipes. Vrillon *et al.* [16], Roche and calculate moment–deflection curves for combinations of straight pipes and elbows, including elastic–plastic material behavior and moderately large deflections. These nonlinear analyses require large amounts of computer time. The more economical but less rigorous one-dimensionally discretized or trigonometric-series models have been employed by Mello and Griffin [26] and Sobel and Newman [27, 28], who used the MARC computer program [13] element No. 17 [8], and by Gellin [29], who used trigonometric series expansion. The most economical and more approximate beam-type models have been used by Roche *et al.* [30], Spence and Findlay [31, 32] and Calladine [33]. An efficient analysis method suitable for piping systems is derived by Hibbitt and Taylor [23]. This method does not fall into any of the three categories identified above. It involves linear superposition of beam strains and cross section deformation.

In the following sections an approximate analysis of the second type (one-dimensional discretization) is described and results given for various configurations. The theoretical results were obtained with a modified version of BOSOR5 [19].

AXISYMMETRIC MODEL OF PIPE OR ELBOW BENDING PROBLEM

In the following analysis an initially uniformly curved pipe is treated as if it were part of a toroidal shell. The model is similar to that described in Ref. [34]. Bending in the plane of the curvature of the pipe centerline is applied by means of an appropriate temperature distribution over the pipe cross section, as will be described next.

Development of the expression for axial strain. Every cross section of the uniformly curved pipe is assumed to deform identically. Therefore, the structure can be treated as a shell of revolution, a torus. Figure 1 shows

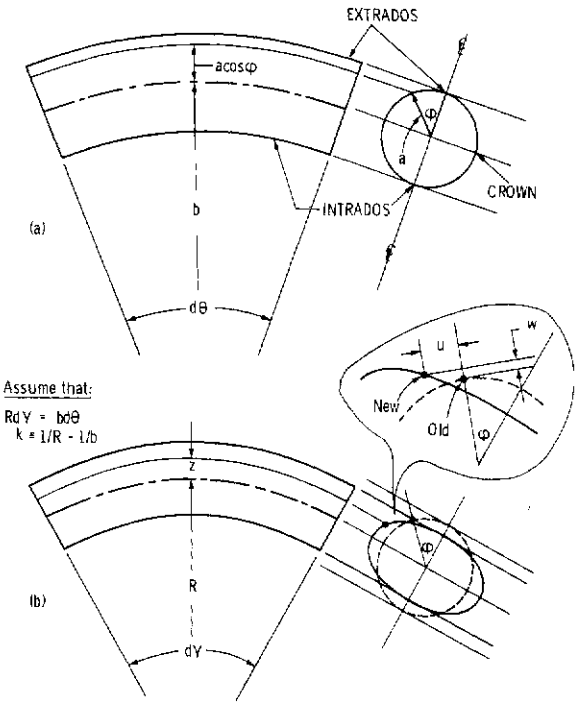

Fig. 1. In-plane bending of curved pipe: (a) initial configuration, (b) uniformly bent configuration.

the undeformed pipe reference surface with centerline radius of curvature b and meridional radius of curvature a. The centerline radius of curvature of the deformed pipe reference surface is R and the cross section has ovalized such that a generator that was originally at a radius $r = b + a\cos\phi$ is now at a radius $R + z$, where z is given by

$$z = (a + w)\cos\phi - u\sin\phi. \tag{1}$$

If we assume that the centerline remains inextensional, the reference surface axial strain is

$$\varepsilon = \frac{(R + z)b/R - (b + a\cos\phi)}{b + a\cos\phi}. \tag{2}$$

Rearrangement of eqn (2) and use of the relationships

$$\cos\phi = r/R_2; \quad \sin\phi = -r' \equiv -\mathrm{d}r/\mathrm{d}s \tag{3}$$

leads to the expression

$$\varepsilon = \frac{b}{R}(w/R_2 + ur'/r) + \frac{a(1/R - 1/b)\cos\phi}{1 + a/b\cos\phi} \tag{4}$$

in which R_2 is the normal circumferential radius of curvature of the reference surface of the undeformed torus, r is the radius to a point on the torus reference surface, and r' is the derivative of r with respect to meridional arc length s. Figure 2 shows these quantities.

Simulation of the pipe bending problem by thermal loading of a torus. In order to use BOSOR5 to treat the problem of elastic–plastic bending and bifurcation buckling of a curved pipe, it is necessary to write the axial strain given by eqn (4) as a stress-producing pre-buckling hoop strain for the shell-of-revolution (torus)

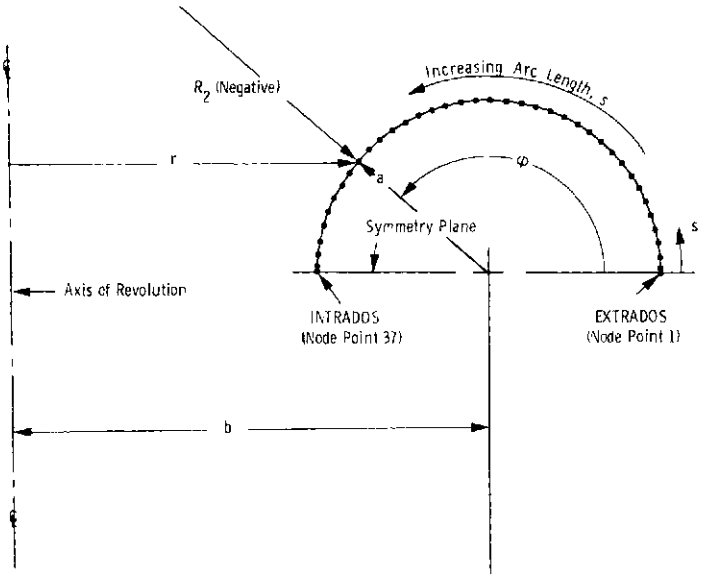

Fig. 2. Discretization of pipe modeled as toroidal segment.

analysis. This is easily done by definition of the prebuckling stress-producing hoop strain as

$$\varepsilon = \varepsilon_2 - \alpha_2 \Delta T \tag{5}$$

in which, from eqn (4), it is seen that

$$\varepsilon_2 = \frac{b}{R}(w/R_2 + ur'/r) \tag{6}$$

$$\alpha_2 \Delta T = -a\left(\frac{1}{R} - \frac{1}{b}\right)\left[\frac{\cos\phi}{1 + a/b\cos\phi}\right]. \tag{7}$$

In this way, the problem of bending of a curved pipe is simulated by a problem of a nonuniformly heated torus.

In BOSOR5 the temperature rise ΔT is assumed to be of the form

$$\Delta T = f(t)g(s) \tag{8}$$

in which $f(t)$ is a function of "pseudo" time t and $g(s)$ is a function of meridional arc s. In this application of BOSOR5 we can set

$$f(t) = T_0 t = T_0\left(\frac{1}{R} - \frac{1}{b}\right) = T_0 k \tag{9}$$

$$g(s) = -\cos\phi \Big/ \left(1 + \frac{a}{b}\cos\phi\right) \tag{10}$$

$$\alpha_2 = a/T_0 \tag{11}$$

in which T_0 is arbitrary. (In the cases studied here T_0 is set equal to 10^{-5} in order to generate values of ΔT in the program list output which have enough significant figures to provide a check of the input data.)

To perform the large-deflection, elastic–plastic pipe bending and bifurcation buckling analyses, the prebuckling analysis part of the BOSOR5 program must be modified in a simple way: the expression for reference surface prebuckling hoop strain, which for the usual shell-of-revolution analysis is

$$\varepsilon_2 = w/R_2 + ur'/r \tag{12}$$

must be changed, *in the prebuckling analysis branch of BOSOR5 only*, to

$$\varepsilon_2 = b\left(t + \frac{1}{b}\right)(w/R_2 + ur'/r) \tag{13}$$

in which the time t is given from eqn (9) by

$$t = k = \frac{1}{R} - \frac{1}{b}. \tag{14}$$

Thus the prebuckling "axisymmetric" problem is solved by imposition of a change in torus centerline curvature k and calculation of equilibrium with use of the same techniques and strategies described in detail in [19] and [35]. (The plasticity theory used in BOSOR5 is based on isotropic strain hardening and the von Mises yield criterion.) No further program changes are required for inclusion of internal or external pressure in the analysis. No changes at all are needed for calculation of axisymmetric or nonaxisymmetric bifurcation buckling, since the above prebuckling analysis generates a prebuckling state consisting of appropriate membrane stress resultants and cross section deformations that are axisymmetric about the torus axis of revolution.

Elastic–plastic bending and bifurcation buckling of straight pipes can be predicted by use of a very large b/a (see Fig. 1a). The behavior of a pipe bend under an opening moment can be predicted with use of a negative time t, or $k = (1/R - 1/b) < 0$.

Discretization. Figure 2 shows an example of how the pipe meridian can be discretized in the BOSOR5 analysis. Sobel [9] has shown that this nodal point density is more than sufficient for reasonably accurate solutions in the elastic regime. A preliminary study of an elastic–plastic pipe-bending problem with BOSOR5 indicates that use of three times as many nodal points does not change the predicted behavior by more than one percent.

Bifurcation buckling. The nonaxisymmetric bifurcation buckling modal displacement field is assumed to vary harmonically in the circumferential direction (normal to the plane of the paper in Fig. 2), as described in [36]. The strategy for calculation of bifurcation buckling loads (or times) is described in [37].

Boundary conditions. In the prebuckling analysis the displacement field is constrained to be symmetric about the equator of the torus. Thus the axial displacement u, meridional rotation χ, and normal displacement w are given by $u=0$, $\chi=0$ and $w=$ free at the extrados and intrados (shown in Fig. 2). In the bifurcation buckling analysis the buckling modal displacements may be either symmetric on antisymmetric at the equatorial symmetry plane. In all cases studied here it turns out that the critical bifurcation buckling condition corresponds to a buckling modal displacement field which is symmetric about the equatorial symmetry plane.

NUMERICAL RESULTS

Bending, limit moment and bifurcation buckling moment of straight pipes. The straight pipe is simulated by a torus with b/a greater than about 10^3. The theory presented in eqns (1)–(14) was checked by comparison with results from Reissner's analysis of elastic tubes [4]. An example is shown in Fig. 3. The equation numbers in Fig. 3 refer to equations in Ref. [4]. Agreement of the modified BOSOR5 analysis with Reissner's results is excellent. Figures 4–9 pertain to the elastic–plastic bending, collapse and bifurcation buckling of a straight pipe tested by Sherman [18]. (In Sherman's tests there was no pressure, however.)

Figure 4 shows test results and the results of two BOSOR5 runs, one in which the external pressure is zero and the other in which the external pressure is one-half the external pressure p_{cr} that would cause buckling in the absence of an applied bending moment, M. The pipe material is elastic perfectly plastic with a yield strength of 421 N/mm^2. For the case with $p=0$ the BOSOR5 program predicts bifurcation buckling (non-axisymmetric wrinkling) with $n=52500$ full waves

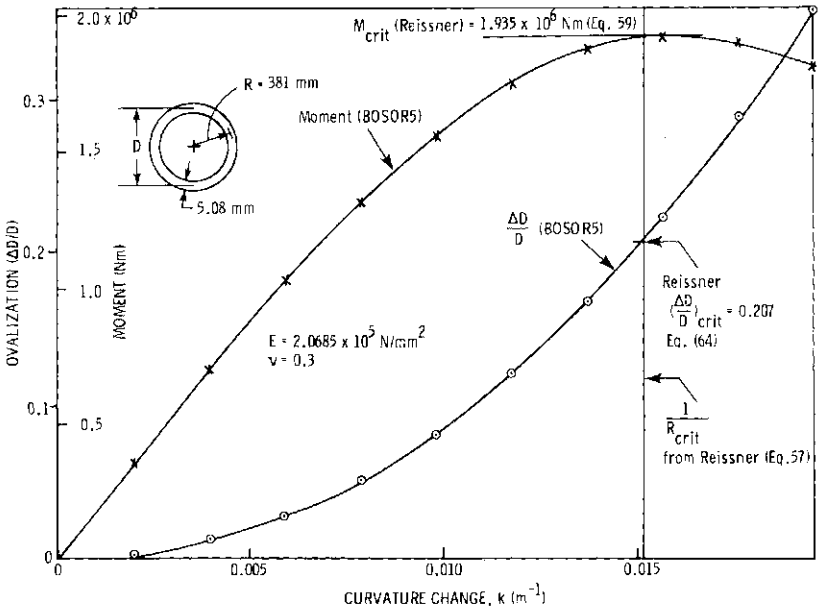

Fig. 3. Moment-curvature-change and ovalization of infinitely long elastic cylindrical shell under pure bending; comparison of BOSOR5 model with Reissner's results.

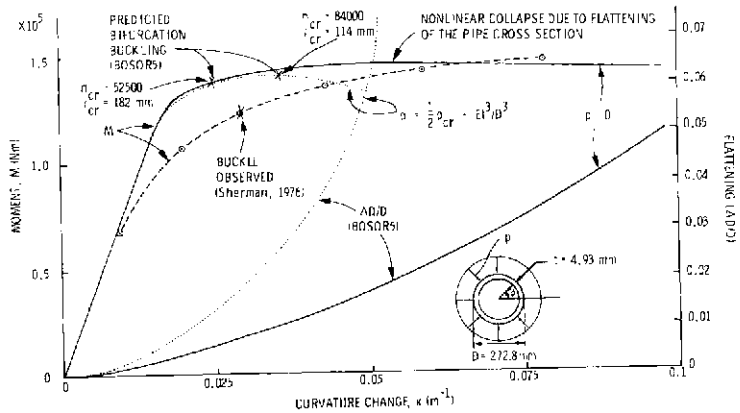

Fig. 4. Bending of straight elastic-plastic pipe with and without external pressure and comparison with test by Sherman.

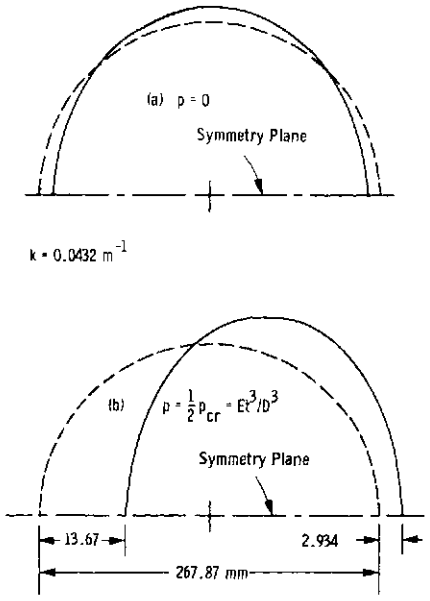

Fig. 5. Ovalization of straight pipe of dimensions shown in Fig. 4 with and without external pressure under imposed curvature $k=0.0432\ m^{-1}$.

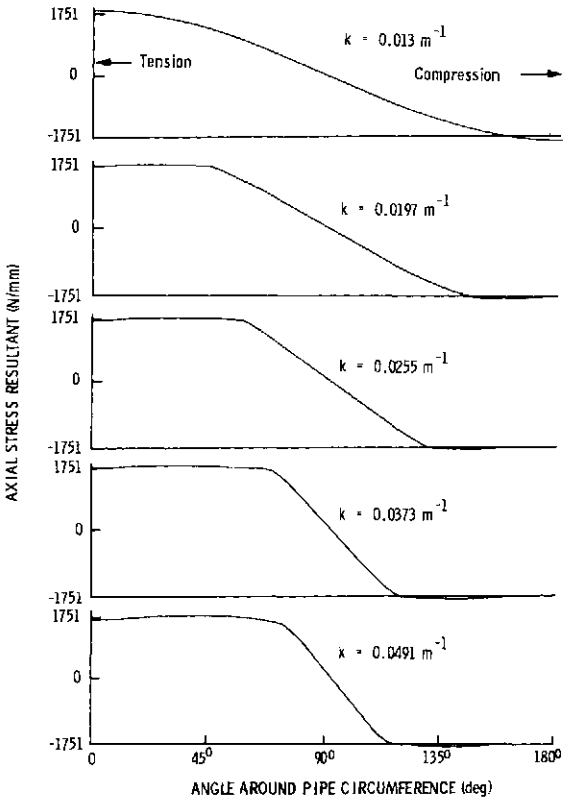

Fig. 6. Growth of plastic region in straight pipe as imposed curvature, k, is increased ($p=Et^3/D^3$).

around the circumference of the torus, the centerline radius of which is taken to be $b=1524$ m. Thus, the predicted bifurcation buckling wavelength is

$$l_{cr}=2\pi b/n=182\ \text{mm}. \tag{15}$$

With $p=0$, bifurcation buckling is predicted to occur at an applied moment slightly below that corresponding to nonlinear collapse due to flattening of the cross section. Thus, in a test of such a pipe (if it were perfect!) one would expect to see relatively short axial-wavelength wrinkles or a single wrinkle appear just before failure. Indeed Sherman observed the formation of such buckles in his tests.

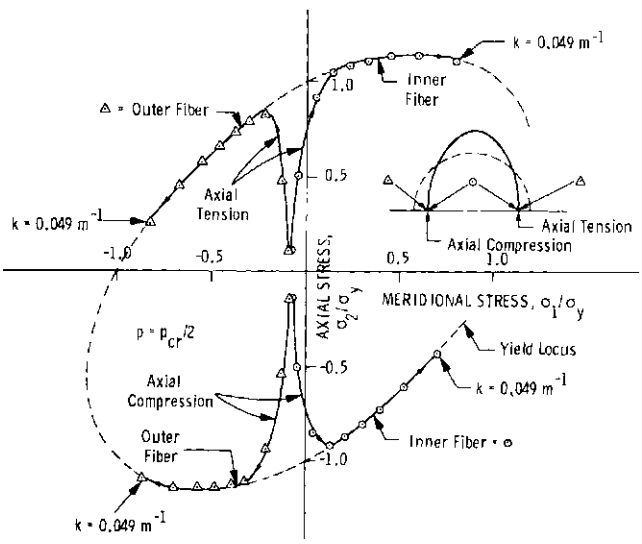

Fig. 7. Paths in stress space followed by inner and outer fiber points on the plane of symmetry as externally pressurized straight pipe is bent ($p=p_{cr}/2=Et^3/D^3$).

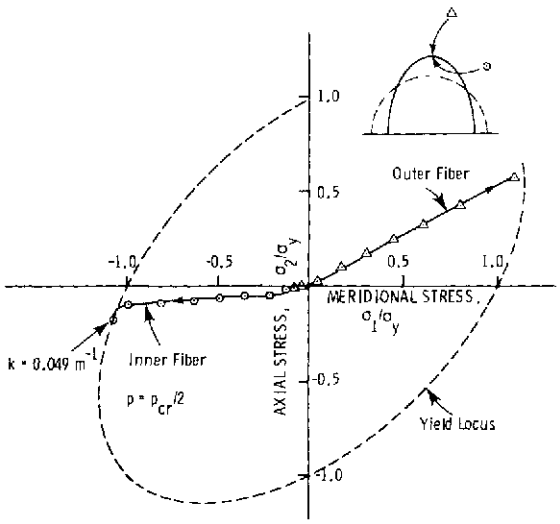

Fig. 8. Paths in stress space followed by inner and outer fiber points at $\phi=90^\circ$ as externally pressurized straight pipe is bent ($p=Et^3/D^3$).

With external pressure, ovalization or flattening of the pipe cross section is predicted to occur more precipitously with increasing applied curvature change $k=(1/R-1/b)$. Note, however, that the maximum moment-carrying capability of the pipe is not much less than that of the pipe without external pressure. In the case treated here bifurcation buckling occurs with a somewhat shorter axial wavelength

$$l_{cr}=2\pi b/84000=114\ \text{mm} \tag{16}$$

at a value of k slightly greater than that corresponding to collapse due to flattening of the cross section. Hence,

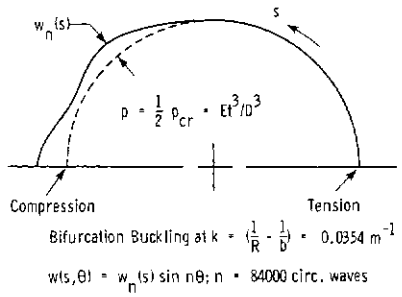

Fig. 9. Bifurcation buckling mode for externally pressurized straight pipe.

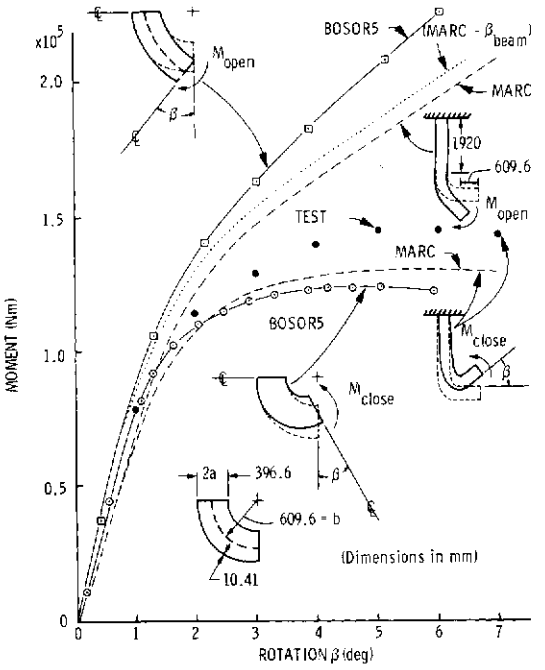

Fig. 10. Comparison of test and theory for bending of 90° elbow. Test by Westinghouse Advanced Reactor Division, 1978.

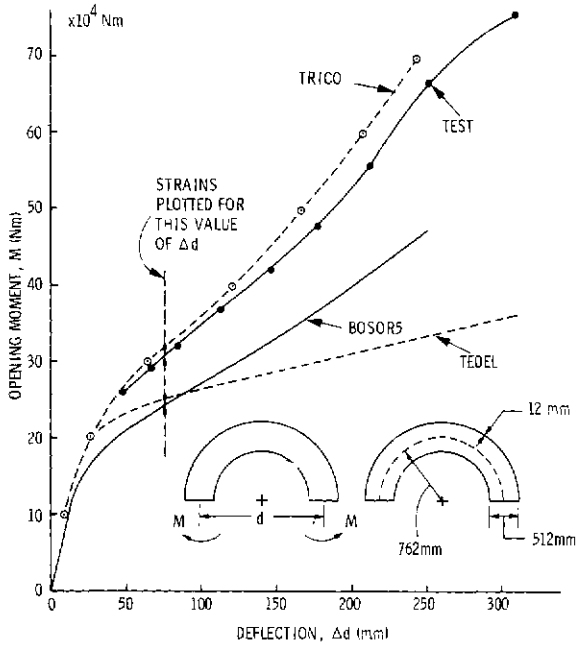

Fig. 11. Moment-deflection curves from test and theory for 180° elbow with opening moment.

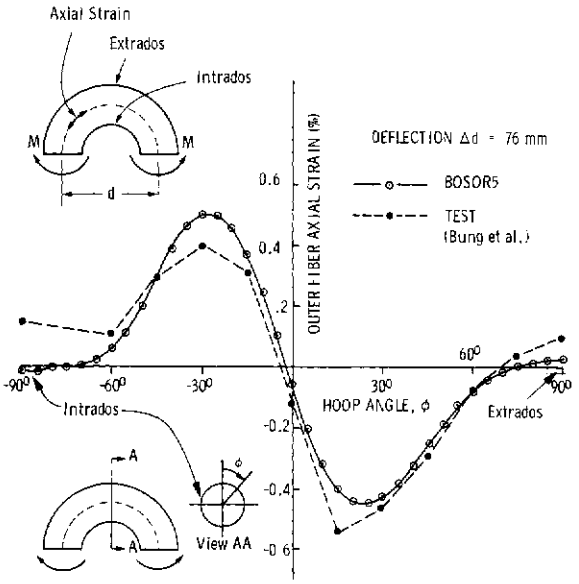

Fig. 12. Outer fiber axial strain at symmetry plane in 180° elbow with opening moment.

if the moment M is applied rather than the curvature change k, axial wrinkles might not appear before failure. Figure 5 shows the predicted deformations of the pipe cross sections with and without external pressure at $k = 0.0432\ m^{-1}$. The deformations are exaggerated but plotted to the same scale in Figs. 5(a) and (b).

Figure 6 shows the circumferential stress resultant N_{20} in the torus at several values of applied curvature change k for the case with external pressure $p = 1/2\ p_{cr} = Et^3/D^3$. Remember that the *circumferential* stress resultant N_{20} in the BOSOR5 *torus* model is actually the *axial* stress resultant in the *pipe*. The plots clearly show the growth of the plastic regions as the applied curvature is increased. Yielding begins when the applied moment is about 10^5 Nm, well below the maximum moment. The development of extreme fiber stresses at the equator and crown are shown respectively in Figs. 7 and 8 for the case $p = p_{cr}/2$. The plastic biaxial loading of the elastic–perfectly plastic material at the equator is far from being proportional as the centerline curvature k is monotonically increased. Figure 9 shows the plastic bifurcation mode.

Bending and limit moment of elastic–plastic elbows. Figures 10–13 show results from application of the modified BOSOR5 analysis to in-plane bending of 90° and 180° piping elbows. The BOSOR5 predictions are compared to tests and to other analyses.

Figure 10 gives a comparison of BOSOR5 results with a test of a 90° elbow by Peters [20] and an analysis in which the MARC element No. 17 is used for the elbow [28]. The test was for a closing moment. Analytical predictions are shown for both opening and closing moments. The quantity β_{beam} is the part of the end cross-section rotation attributable to beam-type bending, which is not included in the BOSOR5 model.

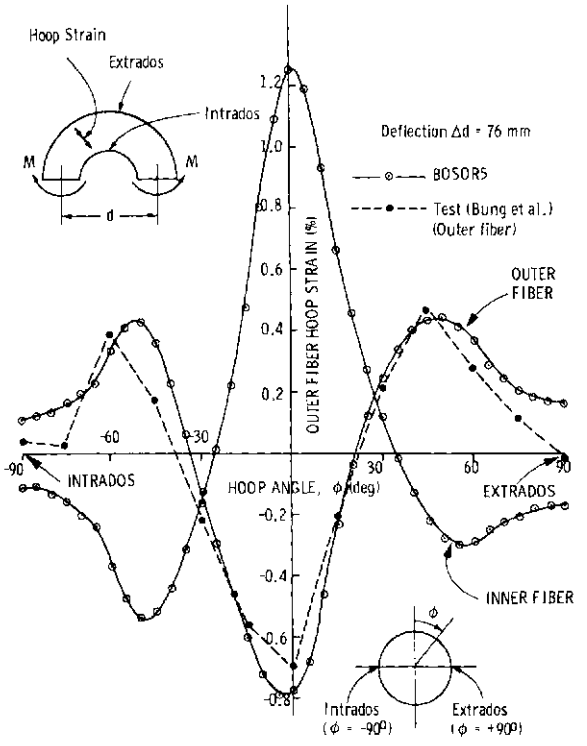

Fig. 13. Hoop strain at symmetry plane in 180° elbow with an opening moment.

Figure 11 shows a comparison of test and theory for a 180° elbow tested by Bung *et al.* [21]. The theoretical results labeled "TRICO" and "TEDEL" were obtained, respectively, by Roche and Hoffman [24] and Roche, *et al.* [30]. TRICO is a general nonlinear computerized shell analyzer [17] and TEDEL is a program based on a simplified nonlinear beam model. The axial and hoop strains plotted in Figs. 12 and 13 correspond to an increase in d of 76 mm. There is reasonably good agreement between the BOSOR5 predictions and measured strains. (Note that the definition of hoop angle ϕ differs from that in Fig. 2.)

CONCLUSIONS

The excellent agreement with Reissner's results for an infinite elastic tube reveals that the model introduced here, although approximate, is correct. That the results might be said to be only in qualitative rather than quantitative agreement with tests on elbows and finite length pipes is doubtless due primarily to initial imperfections, residual stresses, and end effects. In the case of bending of elbows, the straight legs act to prevent ovalization near the ends of the elbow, as is clearly shown by Sobel and Newman in Ref. [28]. In the case of straight pipes, such as those tested by Sherman, it appears that the deleterious effects of residual stresses and initial imperfections outweigh the strengthening effect of end restraint.

Acknowledgements—This work was supported by the 1979 Independent Development Program at Lockheed. The author is indeed grateful to Bill Sable for his support, to Jörgen Skogh for his helpful suggestions, to Colleen Miller for drafting the figures, and to Christy Morgan for typing the manuscript.

REFERENCES

1. L. G. Brazier, On the flexure of thin cylindrical shells and other 'thin' sections. *Proc. R. Soc.*, Series A **116**, 104–114 (1927).
2. R. A. Clark and E. Reissner, Bending of curved tubes. *Adv. Appl. Mech.* **2**, 93–122 (1951).
3. J. D. Wood, The flexure of a uniformly pressurized circular cylindrical shell. *J. Appl. Mech.* **25**, 453–458 (1958).
4. E. Reissner, On finite bending of pressurized tubes. *J. Appl. Mech.* **26**, 386–392 (1959).
5. E. L. Aksel'rad, Refinement of the upper critical loading of pipe bending taking account of the geometric nonlinearity. *Izv. An. SSSR, OTN, Mekhanika* No. 4, 133–139 (1965).
6. W. B. Stephens, J. H. Starnes, Jr. and B. O. Almroth, Collapse of long cylindrical shells under combined bending and pressure loads. *AIAA J.* **13**, 20–24 (1975).
7. W. G. Dodge and S. E. Moore, ELBOW: a FORTRAN program for the calculation of stresses, stress indices, and flexibility factors for elbows and curved pipes. *ORNL-TM-4098* (April 1973).
8. H. D. Hibbitt, E. P. Sorensen and P. V. Marcal, The elastic-plastic and creep analysis of pipelines by finite elements. *2nd Int. Conf. Pressure Vessel Technology*, ASME, San Antonio, TX, Part 1, pp. 239–251 (Oct. 1973).
9. L. H. Sobel, In-plane bending of elbows. *Comput. Structures* **7**, 701–715 (1977).
10. E. C. Rodabaugh, S. K. Iskander, S. E. Moore, End effects on elbows subjected to moment loadings. Battelle Columbus Laboratories, Ohio, *Rep. ORNL/Sub-2913/7* (March 1978).
11. O. Fabian, Collapse of cylindrical elastic tubes under combined bending, pressure, and axial loads. *Int. J. Solids Structures* **13**, 1257–1270 (1977).
12. B. O. Almroth, F. A. Brogan and G. M. Stanley, Structural analysis of general shells, Vol. II: User instructions for STAGSC. Lockheed Missiles & Space Co., *Rep. LMSC-D633873* (Jan. 1979).
13. MARC-CDC nonlinear finite element analysis program. *User Information Manual*, Vol. 1. Control Data Corp. (1971).
14. Z. Zudans *et al.*, Theory and user's manual for EPACA. *Franklin Institute Rep. F-C-3038* (June 1972).
15. S. E. Bolt and W. L. Greenstreet, Experimental determination of plastic collapse loads for pipe elbows. *ASME Paper 71-PVP-37*.
16. B. Vrillon, C. Montfort and J. Befre, Experimental analysis of piping components of fast breeder reactors. *3rd Int. Conf. on Structural Mechanics in Reactor Technology*, Vol. 2, Part F, Paper F3/4. American Elsevier, New York (1975).
17. A. Hoffman, M. Livolant and R. Roche, Plastic analysis of shell by finite element method: global plasticity model for any shapes of shells. *2nd SMiRT Conf.*, Berlin, Paper L6/2 (1973).
18. D. R. Sherman, Tests of circular steel tubes in bending. *ASCE J. Structural Div.* **102**(ST11), 2181–2195 (1976).
19. D. Bushnell, BOSOR5—program for buckling of elastic plastic complex shells of revolution including large deflections and creep. *Comput. Structures* **6**, 221–239 (1976).
20. F. E. Peters, Results from a buckling test of a 16-in (406-mm) diameter piping elbow. Westinghouse Advanced Reactors Division, *Rep. WARD-HT-3045-35* (*July* 1978).
21. H. Bung, G. Clement, A. Hoffman and H. Jakubowicz,

Piping benchmark problems-computer analysis with the CEASEMT finite element system. *CEASEMT Rep. EMT/78/61* (Oct. 1978).
22. B. D. Reddy, An experimental study of the plastic buckling of circular cylindrical shells in pure bending. *Int. J. Solids Structures*, **15**, 669–683 (1979).
23. H. D. Hibbitt and L. M. Taylor, A family of simple pipe bend elements: Formulation and preliminary testing. Hibbitt & Karlsson, Inc., Providence, Rhode Island. *Final Rep.* on Contract N926007-MP (Sept. 1979).
24. R. Roche and A. Hoffman, Global plastic models for computerized structural analysis. *4th SMiRT*, San Francisco, Paper L5/5 (1977).
25. J. Skogh and F. Brogan, Collapse analysis of finite-length pipe bends. Lockheed Missiles & Space Co., *Rep.* (Dec. 1978).
26. R. M. Mello and D. S. Griffin, Plastic collapse loads for pipe elbows using inelastic analysis. *J. Pressure Vessel Tech.* **96**, 177–183 (Aug. 1974).
27. L. H. Sobel and S. Z. Newman, Instability analysis of elbows in the plastic range. *4th Int. Conf. on Structural Mechanics in Reactor Technology, Vol. L, Inelastic Analysis of Metal Structures*, San Francisco, Paper L3/2 (1977).
28. L. H. Sobel and S. Z. Newman, Comparison of experimental and simplified analytical results for the in-plane plastic bending the buckling of an elbow. Westinghouse Advanced Reactors Div., Madison, Pennsylvania, paper presented at the 1980 *Pressure Vessels and Piping Conf.* held 13–15 Aug., San Francisco.
29. S. Gellin, The plastic buckling of long cylindrical shells under pure bending. (submitted for publication).
30. R. Roche, A. Hoffman and B. Vrillon, Piping systems, inelastic analysis—a simplified numerical method. *3rd Int. Conf. on Pressure Vessel Technology*, ASME Tokyo, Japan, pp. 133–142 (1977).
31. J. Spence and G. Findlay, Limit load for pipe bend under plane bending. *Proc. 2nd Int. Conf. on Pressure Vessel Technology*, Vol. I ASME, pp. 393–399 (1973).
32. J. Spence and G. E. Findlay, Limit moments for non-circular cross section (elliptical) pipe bends. *4th SMiRT Conf.*, San Francisco, California, Vol. F, Paper F 4/6 (1977).
33. C. R. Calladine, Limit analysis of curved tubes. *J. Mech. Engng Sci.* **16**(2), 85–87 (1974).
34. D. Bushnell, Stress, buckling and vibration of prismatic shells. *AIAA J.* **9**(10), 2004–2013 (1971).
35. D. Bushnell, A strategy for the solution of problems involving large deflections, plasticity and creep. *Int. J. Numer. Meth. Engng* **11**, 683–708 (1977).
36. D. Bushnell, Bifurcation buckling of shells of revolution including large deflections, plasticity and creep. *Int. J. Solids Structures* **10**, 1287–1305 (1974).
37. G. Lagae and D. Bushnell, Elastic–plastic buckling of internally pressurized torispherical vessel heads. *Nucl. Engng Design* **48**, 405–414 (1978).

Computers & Structures, Vol. 13, pp. 249–256, 1981
Printed in Great Britain.

0045-7949/81/010249-08$02.00/0

HIGH-TEMPERATURE INELASTIC ANALYSIS†

A. LEVY

Grumman Aerospace Corporation, Bethpage, NY 11714, U.S.A.

(*Received* 11 *May* 1980)

Abstract—Computationally efficient, finite-element methods for accurately predicting small strain, isothermal, three-dimensional, elastic–plastic creep responses of thick and thin shell structures are being developed. This work has been performed, in part, to support Oak Ridge National Laboratory's (ORNL) High-Temperature Structural Design (HTSD) Program. In order to verify the analytic capabilities developed and the constitutive relations used for high-temperature inelastic behavior, a high-temperature creep test of a nuclear reactor inlet nozzle test model was simulated analytically. (The test is being conducted at ORNL as part of the HTSD Program.) The discrepancies between analytic and experimental results are discussed and an explanation is given consistent with previous experimental findings.

INTRODUCTION

Three-dimensional elastic–plastic creep finite element analytic capabilities are being developed at Grumman Aerospace Corporation. This work has been performed, in part, to support Oak Ridge National Laboratory's (ORNL) High-Temperature Structural Design Program. The HEX Program [1, 2] of Grumman's PLANS system of finite element programs [3] is being used for this purpose. Currently this program is capable of analyzing small-displacement, isothermal, three-dimensional, elastic–plastic creep responses of thick and thin-shell structures subjected to mechanical and thermal loads.

The program is discussed in general, including constitutive equations, solution algorithm, the use of variable inelastic integration points and general strategy for solving large problems. The constitutive relations and general procedures are in accordance with ORNL guidelines for design of nuclear system components at elevated temperatures [4].

In order to verify the analytic capabilities developed, as well as the constitutive relations used for high-temperature inelastic behavior, a high-temperature creep test being conducted at ORNL [5] is simulated analytically. The test model is representative of nozzle attachments in pressure vessels used in the nuclear industry. The analysis indicates the need for more sophisticated elastic–plastic creep interactive constitutive relations. The discrepancies between analytic and experimental results are discussed and an explanation is given consistent with the experimental findings presented in Ref. [4].

PROGRAM DESCRIPTION

Constitutive equations

Consistent with small strain theory, we write the differential equation

$$de_{ij} = d\varepsilon^e_{ij} + d\varepsilon^p_{ij} + d\varepsilon^c_{ij} + d\varepsilon^t_{ij} \tag{1}$$

where de_{ij}, $d\varepsilon^e_{ij}$, $d\varepsilon^p_{ij}$, $d\varepsilon^c_{ij}$ and $d\varepsilon^t_{ij}$ are the changes in total, elastic, plastic, creep and thermal strain tensors, respectively. Here we choose the more classical approach of separating the inelastic strains into two parts, one time dependent (creep) and the other time independent (plasticity). This is in contrast to the unified theories, in which plasticity and creep are basically indestinguishable, such as the treatments presented in Refs. [6–8].

Continuing on the basis that inelastic strains can be separated into plastic and creep components we discuss each separately. The isothermal plasticity theory incorporated into the HEX Program includes: Hill's yield criterion for orthotropic materials, which reduces to the von Mises yield criterion for isotropic materials, is used to predict initial yield and the subsequent loading surface

$$f(\sigma_{ij} - \alpha_{ij}) - \kappa(\bar{\varepsilon}^p, T) = 0 \tag{2}$$

where α_{ij} represents the translation of the loading surface in stress space σ_{ij}, $\bar{\varepsilon}^p$ corresponds to effective plastic strain

$$\bar{\varepsilon}^p = \sqrt{\tfrac{2}{3}\varepsilon^p_{ij}\varepsilon^p_{ij}} \tag{3}$$

and T corresponds to temperature; the Prandtl–Reuss associative flow rule

$$d\varepsilon^p_{ij} = \lambda \frac{\partial f}{\partial \sigma_{ij}} \tag{4}$$

in which the change in the plastic strain tensor is normal to the loading surface; and a hardening law based on the Prager–Ziegler kinematic hardening theory,

$$d\alpha_{ij} = \mu(\sigma_{ij} - \alpha_{ij}) \tag{5a}$$

$$d\alpha_{ij}\frac{\partial f}{\partial \sigma_{ij}} = c(\bar{\varepsilon}^p, T)\, d\varepsilon^p_{ij}\frac{\partial f}{\partial \sigma_{ij}} \tag{5b}$$

where $c(\bar{\varepsilon}^p, T)$ is the hardening parameter.

Differentiating eqn (2) and assuming

$$\frac{d\kappa}{d\bar{\varepsilon}^p} = g(\beta) \tag{6}$$

where β is the accumulated plastic strain, we arrive at

$$\frac{\partial f}{\partial \sigma_{ij}} d\sigma_{ij} + \frac{\partial f}{\partial \alpha_{ij}} d\alpha_{ij} - g\, d\bar{\varepsilon}^p = 0. \tag{7}$$

†This work was funded, in part, by DoE/ORNL High-Temperature Structural Design (HTSD) program, and in part by Grumman's Independent Research and Development Program.

Substituting eqn (5a) into eqn (7) we arrive at

$$\mu=\frac{\dfrac{\partial f}{\partial \sigma_{ij}}\,d\sigma_{ij}-g\,d\bar{\varepsilon}^{p}}{\dfrac{\partial f}{\partial \sigma_{ij}}(\sigma_{ij}-\alpha_{ij})} \tag{8}$$

and combining eqns (3), (4), (5b) and (7) we arrive at

$$\lambda=\frac{\dfrac{\partial f}{\partial \sigma_{ij}}\,d\sigma_{ij}}{c\dfrac{\partial f}{\partial \sigma_{ij}}\dfrac{\partial f}{\partial \sigma_{ij}}+g\left(\dfrac{2}{3}\dfrac{\partial f}{\partial \sigma_{ij}}\dfrac{\partial f}{\partial \sigma_{ij}}\right)^{1/2}}. \tag{9}$$

Substituting eqn (9) into eqn (4) we arrive at a stress–plastic strain relation

$$d\varepsilon^{p}_{ij}=C_{ijkl}\,d\sigma_{kl} \tag{10}$$

where

$$C_{ijkl}=\frac{\dfrac{\partial f}{\partial \sigma_{ij}}\dfrac{\partial f}{\partial \sigma_{kl}}}{c\dfrac{\partial f}{\partial \sigma_{mn}}\dfrac{\partial f}{\partial \sigma_{mn}}+g\left(\dfrac{2}{3}\dfrac{\partial f}{\partial \sigma_{mn}}\dfrac{\partial f}{\partial \sigma_{mn}}\right)^{1/2}}$$

The stress–elastic strain relation can be written

$$d\varepsilon^{e}_{ij}=E^{-1}_{ijkl}\,d\sigma_{kl} \tag{11}$$

where E_{ijkl} contains the usual elastic constants.

Substituting eqns (10) and (11) into eqn (1) and solving for $d\sigma_{ij}$ we arrive at

$$d\sigma_{ij}=D_{ijkl}\,(de_{kl}-d\varepsilon^{c}_{kl}-d\varepsilon^{t}_{kl}) \tag{12}$$

where $D_{ijkl}=[C_{ijkl}+E_{ijkl}{}^{-1}]^{-1}$. Substituting eqn (12) into eqn (10) gives

$$d\varepsilon^{p}_{ij}=C_{ykl}D_{klmn}(de_{mn}-d\varepsilon^{c}_{mn}-d\varepsilon^{t}_{mn}). \tag{13}$$

Equations (12) and (13) indicate that the states of stress and plastic strain can be determined once the states of total, creep and thermal strains are known. Alternatively, using the elastic stress–strain relation, eqn (11), along with eqns (4) and (9) we can arrive at λ as

$$\lambda=\frac{\dfrac{\partial f}{\partial \sigma_{ij}}E_{ijkl}(d\varepsilon_{kl}-d\varepsilon^{c}_{kl}-d\varepsilon^{t}_{kl})}{c\dfrac{\partial f}{\partial \sigma_{ij}}\dfrac{\partial f}{\partial \sigma_{ij}}+g\left(\dfrac{2}{3}\dfrac{\partial f}{\partial \sigma_{ij}}\dfrac{\partial f}{\partial \sigma_{ij}}\right)^{1/2}+\dfrac{\partial f}{\partial \sigma_{ij}}E_{ijkl}\dfrac{\partial f}{\partial \sigma_{kl}}}$$

A detailed description of the complete elastic-plastic cyclic theory used in the present program, which includes elastic-ideally plastic, linear and nonlinear strain hardening behavior, and proportional and nonproportional cyclic loading conditions are presented in Ref. [3].

The constitutive equations for time dependent creep are somewhat similar to those for plasticity in that they require a flow rule, a prescribed uniaxial "creep law" relating creep strain rate to time at constant stress and temperature levels, and a hardening rule.

The flow rule for a multiaxial stress is similar to the Prandt–Reuss flow rule for plasticity, i.e.

$$\dot{\varepsilon}^{c}_{ij}=\lambda\sigma'_{ij} \tag{14}$$

where $\dot{\varepsilon}^{c}_{ij}$ and σ'_{ij} are components of the creep strain rate and deviatoric stress tensors, respectively. The scalar factor λ can be found to be

$$\lambda=\frac{3}{2}\frac{\dot{\bar{\varepsilon}}^{c}(\bar{\sigma}, t, T, \bar{\varepsilon}^{c})}{\bar{\sigma}} \tag{15}$$

where $\dot{\bar{\varepsilon}}^{c}$ is the effective creep strain rate, $\bar{\sigma}$ is the effective stress,

$$\dot{\bar{\varepsilon}}^{c}=\sqrt{\tfrac{2}{3}\dot{\varepsilon}^{c}_{ij}\dot{\varepsilon}^{c}_{ij}}$$
$$\bar{\sigma}=\sqrt{\tfrac{3}{2}\sigma_{ij}\sigma_{ij}} \tag{16}$$

t denotes time and T denotes temperature.

Uniaxial creep tests are performed at constant stress and temperature levels to determine the "creep law"

$$\bar{\varepsilon}^{c}=\bar{\varepsilon}^{c}(\bar{\sigma}, t, T).$$

Usually this is prescribed in equation form, e.g.

$$\bar{\varepsilon}^{c}=f(\bar{\sigma}, T)[1-e^{-r(\sigma,T)t}]+h(\bar{\sigma}, T)t \tag{17}$$

where f, r and h are chosen to best fit the data. It is easier to handle $\bar{\varepsilon}^{c}(\bar{\sigma}, t, T)$ if it is prescribed in equation form. Usually an equation can be found to fit the data. If needed different equations can be used at different stress levels.

Among the many hardening rules that can be considered the two most generally compared are strain-hardening and time-hardening. These hardening rules dictate the path from one stress state to another. The strain-hardening rule

$$\dot{\bar{\varepsilon}}^{c}=\dot{\bar{\varepsilon}}^{c}(\bar{\sigma}, T, \bar{\varepsilon}^{c}) \tag{18}$$

assumes that at constant stress and temperature the creep strain rate depends on the existing total creep strain while the time-hardening rule

$$\dot{\bar{\varepsilon}}^{c}=\dot{\bar{\varepsilon}}^{c}(\bar{\sigma}, T, t) \tag{19}$$

assumes that at constant stress and temperature, the creep strain rate depends on the existing time (from the beginning of the creep process). While other more complicated models may be more accurate it has been determined that, in most cases, strain-hardening adequately describes the hardening behavior. The strain-hardening rule is acceptable as long as load reversals do not occur. In order to eliminate observed inconsistencies an auxiliary procedure must be used, when stress reversal occurs, as described by Greenstreet *et al.* [9]. Stress reversal occurs whenever

$$\varepsilon^{c}_{ij}\sigma_{ij}<0 \tag{20}$$

where ε_{ij} is measured from its current creep strain origin. At these points the creep strain origin is switched to a new value and the analysis continued.

In addition, because of the assumption of creep strain incompressibility, delayed strain recovery upon unloading cannot be exhibited. For small strain behavior, however, this phenomenon may be more of theoretical interest than practical importance.

Although we have presented the plasticity and creep constitutive equations independent of each other, at high-temperature both are present and influence each other, i.e. plastic behavior is influenced by prior creep behavior and creep behavior is influenced by prior plastic behavior. ORNL has been experimenting with, among other materials common in nuclear reactors, annealed type 304 stainless steel. Their conclusions [4] are that prior small plastic strains have little effect on subsequent creep strain rates, but that prior creep strains have a significant effect on subsequent plastic

strains, especially at elevated temperatures. In particular, accumulated creep strains reduce the development of subsequent plastic strains through, predominantly, an increase in the yield stress. In an attempt to account for this behavior, Pugh, Clinard and Swinderman [10] have recommended modifications to the constitutive equations. These modifications allow the plastic loading surface to translate with changes in creep strains, and expand with accumulated creep strains in a similar manner as with plastic strains. As an alternative, Robinson [8] suggests a unified creep-plasticity model which is shown to represent qualitatively most of the important phenomenological features observed in materials used in high temperature reactors. At the present time neither of these approaches has been incorporated into ORNL's guidelines for inelastic analysis of high-temperature reactor system components.

Solution algorithm

From energy considerations the governing equation associated with the incremental initial strain method is written as

$$[K]\{\Delta U\} = \{\Delta P\} + \{\Delta Q^c\} + \{\Delta Q^p\} \tag{21}$$

$\{\Delta U\}$ is the incremental nodal displacement vector, from which total strains are obtained

$$\{\Delta e\} = [B]\{\Delta U\} \tag{22}$$

$\{\Delta P\}$ is the incremental applied load vector, including thermal loads, $[K]$ is the elastic stiffness matrix defined as

$$[K] = \int [B]^T [E][B]\, dV \tag{23}$$

and $\{\Delta Q^p\}$ and $\{\Delta Q^c\}$ are the pseudo-load vectors associated with plastic and creep strains, respectively, and defined by

$$\{\Delta Q^p\} = \int [B]^T [E]\{\Delta \varepsilon^p\}\, dV$$

and

$$\{\Delta Q^c\} = \int [B]^T [E]\{\Delta \varepsilon^c\}\, dV. \tag{24}$$

Here we use finite incremental quantities, denoted by Δ. We assume that the differential equations, including the constitutive equations, can be integrated over a small but finite interval, Δ, by using linear functional forms during the interval.

The material constitutive model, as described earlier, enters the governing matrix equation, eqn (21), through the pseudo-load vectors as described in eqn (24). Note that the pseudo-load vectors, and hence the right hand side of eqn (21), are unknown at the start of an incremental step. Note also that the formulation is isothermal in the sense that the elastic stiffness matrix does not change in time, as a function of temperature.

In the following, we outline an iterative method as described in Ref. [11]. Equation (21) is written, for the ith the incremental step and nth iteration, as

$$[K]\{\Delta U\}_i^n = \{\Delta P\}_i + \{\Delta Q^c\}_i^n + \{\Delta Q^p\}_i^n + \{R\}_i \tag{25}$$

For the starting value we write,

$$\{\Delta Q^p\}_i^0 = \int [B]^T [E]\{\Delta \varepsilon^p\}_i^0\, dV$$

$$\{\Delta Q^c\}_i^0 = \int [B]^T [E]\{\Delta \varepsilon^c\}_i^0\, dV \tag{26}$$

with the inelastic strain increment,

$$\{\Delta \varepsilon^p\}_i^0 = \{\Delta \varepsilon^p\} \text{ and } \{\Delta \varepsilon^c\}_i^0 = \{\Delta \varepsilon^c\}_i^{PR} \tag{27}$$

taken as a predicted value.

The predictor value for the creep strain is written as

$$\{\Delta \varepsilon^c\}_i^{PR} = \Delta t_i \{\dot{\varepsilon}^c\}_{i-1} + \frac{(\Delta t)^2}{2\Delta t_{i-1}} [\{\dot{\varepsilon}^c\}_{i-1} - \{\dot{\varepsilon}^c\}_{i-2}] \tag{28}$$

where $\{\dot{\varepsilon}^c\}_j$ corresponds to the converged value for the jth step. Equation (28) is a two-term expansion of the creep strain rate in time, with a backwards difference for the second term and a time increment, Δt_i. The corrector term is the average of the previous two iterations,

$$\{\Delta \varepsilon^c\}_i^{COR,n} = [\{\Delta \varepsilon^c\}_i^n + \{\Delta \varepsilon^c\}_i^{n-1}]/2 \tag{29}$$

noting once again that $\{\Delta \varepsilon^c\}_j$ corresponds to $\{\Delta \varepsilon^c\}_j^{COR,n}$ upon convergence. The predicted value of plastic strain is,

$$\{\Delta \varepsilon^p\} = \{\Delta \varepsilon^p\}_{i-1} \tag{30}$$

and the corrector,

$$\{\Delta \varepsilon^p\}_i = \{\Delta \varepsilon^p\}_i^n. \tag{31}$$

In this manner

$$\{\Delta Q^p\}_i^n = \int [B]^T [E]\{\Delta \varepsilon^p\}_{i-1}\, dV$$

$$\{\Delta Q^c\}_i^n = \int [B]^T [E]\{\Delta \varepsilon^c\}_i^{COR,n-1}\, dV$$

The equilibrium corrector term in eqn (25), $\{R\}_i$, remains constant within an iterative cycle and represents any equilibrium imbalance brought forward from the previous incremental step, i.e.

$$\{R\}_i = \int [B]^T [E][\{\Delta \varepsilon^p\}_{i-1} + \{\Delta \varepsilon^c\}_{i-1} - \{\Delta \varepsilon^p\}_{i-1}^{PR} - \{\Delta \varepsilon^c\}_{i-1}^{PR}]\, dV \tag{32}$$

This procedure is an extension of the one outlined for creep by Mendelson, Hirschberg and Manson [12] and modified by Dahl [13]. Within this procedure there are a number of options available, including: the basic predictor–corrector iterative method, a predictor corrector method, i.e. no iterations take place as the solution marches forward. In either case, the predictor or the corrector can be modified so that the initial value is the converged one from the previous step and the corrector is the calculated value from the current iteration. Different procedures are most practical for different problems as discussed in Ref. [11].

Much attention has been given to the time step increment strategy at this governs efficiency and accuracy. The time step is always kept within certain bounds. If the time step is too large, accuracy suffers and instability may occur, and if the time step is too small the expense of solving a problem may be very high. The criterion for the time step solution follows those outlined by Zienkiewicz and Cormeau [7], and is described in Ref. [11].

Description of isoparametric solid element

The basic finite element used is an isoparametric solid element as described by Zienkiewicz *et al.* [14]. A variable number of nodes of between eight and twenty

is allowed for each element as described by Levy [15]. In practice this variable node feature is especially useful when a mesh changes character, e.g. going from a coarser to a finer mesh. It is also applicable to problems in which the mechanical behavior is directional, e.g. when bending is significant in one direction and shear deformation is significant in another. The use of this "variable node" isoparametric element allows the user to specify the number of nodes contained in an element without resorting to external methods such as node elimination or constraint equations, which may be costly.

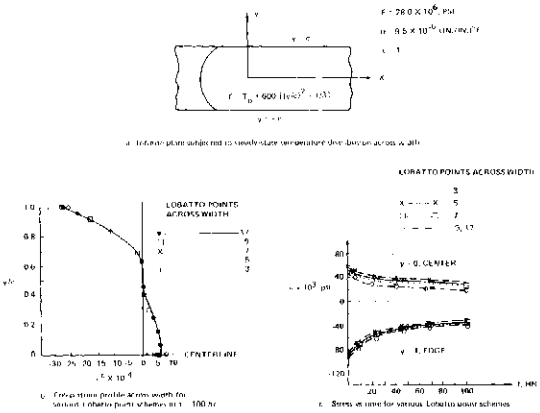

Fig. 1. Thermal stress relaxation.

Variable inelastic integration points

The calculation of the incremental displacements, eqn (21) requires the evaluation of integrals involving inelastic behavior. Consequently, the accuracy of the solution depends on the accuracy of the inelastic strain representation. An accurate representation of the elastic-plastic creep behavior within an element is achieved by introducing a variable set of inelastic integration points, within an element, at which stress and strain histories are monitored. Within an element the order of the allowable kinematic strain distribution depends on the assumed displacement field while the order of the allowable elastic plastic strain distribution (or inelastic material properties) and/or allowable creep strain distribution depends on the choice of inelastic integration points as well as the allowable stress distribution. Either Gauss or Lobatto integration points can be specified within each element. Lobatto points, in which boundary points are included, are of particular importance where it is necessary to detect initial and subsequent yielding on the surface of the element. We can then choose a finite element grid based on the kinematic strain variation expected while choosing inelastic integration points based on the inelastic behavior expected. This results in the use of a minimum number of degrees of freedom for a given analysis, which is particularly important for elastic plastic creep analyses where computational costs can be prohibitive.

Examples are presented in Ref. [11] to demonstrate the use of a variable set of inelastic integration points for plasticity and creep. Here we repeat one of the problems, that of "thermal stress relaxation" involving creep alone.

An infinite plate of width $2c$ is subjected to a steady state temperature distribution across the width, as shown in Fig. 1(a). Secondary creep is assumed with the creep rate given as

$$\dot{\varepsilon}^c = 3\cdot 10^{-24}\sigma^4 \operatorname{sgn}(\sigma) \tag{33}$$

The solution to this problem can be found by substituting

$$\sigma = E(\varepsilon - \varepsilon^c) \tag{34}$$

into eqn (33), yielding

$$\frac{\mathrm{d}\varepsilon^c}{(\varepsilon - \varepsilon^c)^4} = 3\times 10^{-24} E^4\,\mathrm{d}t \tag{35}$$

along with

$$\varepsilon = -0.0057(y^2 - 1/3) + \int_0^1 \varepsilon^c\,\mathrm{d}y \tag{36}$$

where $\varepsilon = e - \alpha T$.

If ε was constant, then eqn (35) would be the stress relaxation equation and integrable directly. As it is, a numerical procedure must be used to integrate eqns (35) and (36).

One element is sufficient since the element allows for a quadratic thermal strain distribution across the width. The creep strain will vary through the element dependent on the choice of inelastic integration points as well as the allowable stress distribution from eqn (34).

The finite element solution is found for various Lobatto point schemes across the width. The creep strain distribution at $t = 100$ hr is shown in Fig. 1(b), and the stress relaxation is shown in Fig. 1(c). As the number of Lobatto points is increased across the width, the creep strain profile is represented more accurately, resulting in a better approximation of the integration performed in eqn (36). A single eight node element is sufficient to represent the exact kinematic strain distribution. The inelastic part of the total strain is found to be more accurate as the number of inelastic strain integration points is increased. This is equivalent to stating that the integral of creep strain in eqn (36) is more accurate as the number of integration points is increased. Nine Lobatto points appear to be sufficient for this problem as the solution is within 1% of the solution using 17 Lobatto points. Thus, an accurate representation of the creep strain distribution within an element can be obtained with the use of a variable set of inelastic integration points, eliminating the need for a finer idealization. For this problem eight Gauss points gives the same accuracy as nine Lobatto points which is consistent with the accuracy of these integration schemes.

General solution procedures

In general, the procedures outlined in Fig. 2 should be followed for a large scale inelastic analysis. Model generation includes determination of the finite element grid and choice of inelastic strain integration points. Preprocessors include initial data checks, bandwidth optimization and model plots. Since inelastic deformation is a path-dependent process, a restart capability is an important feature for large analyses, allowing the user to examine the deformation history at intermediate load levels before proceeding further. The restart pro-

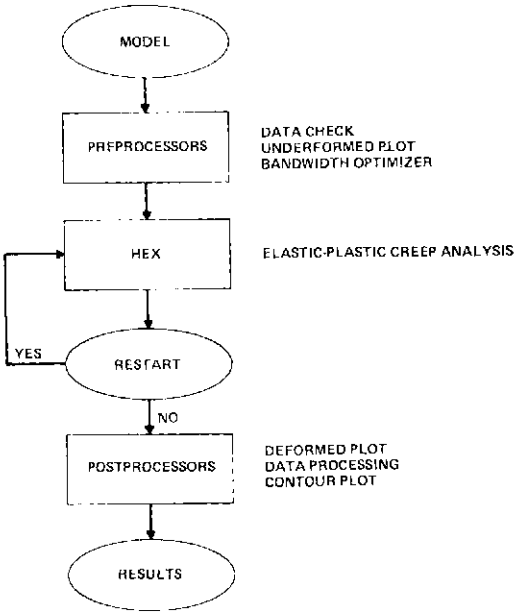

Fig. 2. Problem flow chart.

cedure incorporates some special features that are useful for load cycling. During the initial load-time history, restart information can be saved at a number of load-time points along the way. The user can then restart the computations by loading or unloading from any given point in the load history. The restart intervals can be decided on as the analysis proceeds. Postprocessors include deformed model and contour plots. Data processing is also included whereby data for specific times and stress points can be gathered, sorted and processed to obtain contour plots of such quantities as effective and principal stresses and strains.

ANALYSIS OF HIGH-TEMPERATURE REACTOR PIPING COMPONENT

In order to verify the analytic capabilities developed, as well as the constitutive relations used for high-temperature inelastic behavior, we performed an elastic–plastic analysis of a test model, designated NS-2 by ORNL. The model is represented in Fig. 3 and is representative of nozzle attachments in pressure vessels used in the nuclear industry. This model is composed of type 304 stainless steel and consisting of a cylindrical nozzle-toroidal fillet-spherical shell con-

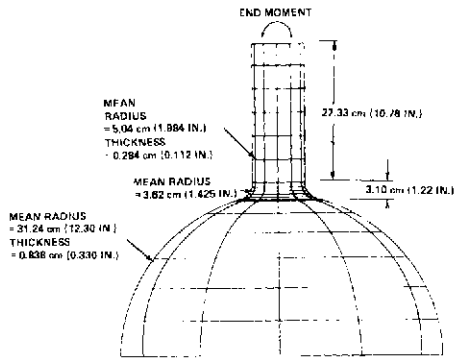

Fig. 3. Overall dimensions of piping component.

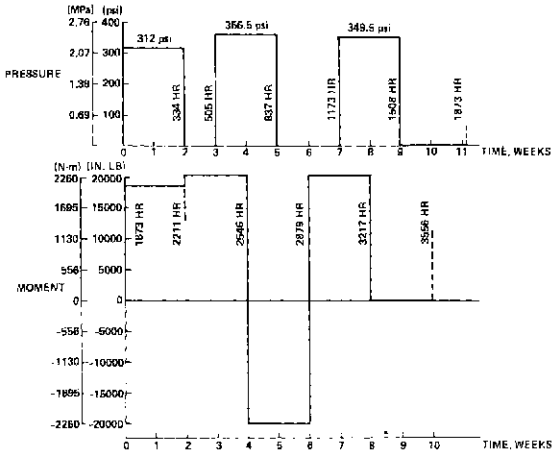

Fig. 4. Pressure and moment histogram.

figuration, and is being tested at ORNL [5]. The test is being conducted at 1100°F for a period of 21 weeks under combined internal pressure and end moment loadings as shown in Fig. 4.

The creep-strain rate time relation was modeled after experimental findings which did not fit the usual "creep laws" based on powers of stress and time. The data, presented in Ref. [16], was approximated by the expression

$$\varepsilon^c = \varepsilon_m t + \sum_{i=1}^{3} A_i[1-\exp(-R_i t)] \tag{37}$$

by Clinard [16]. Linear strain hardening was found to be representative of the material (304 Stainless Steel) behavior at operating temperature (1100°F) [4].

The finite element model, shown in Figs. 3 and 5, are based on expected total strains. A model composed of a grid with four times the number of degrees of freedom was tested elastically and found to give the same total strain results as the coarser model so that the accuracy of the present model was assured. Based on the findings mentioned in the section on modeling, one element was sufficient in the thickness direction while the set of inelastic integration points in each element was chosen based on the expected inelastic strains. As an example, combined bending and membrane stresses in the fillet region dictated the use of a five point Lobatto scheme

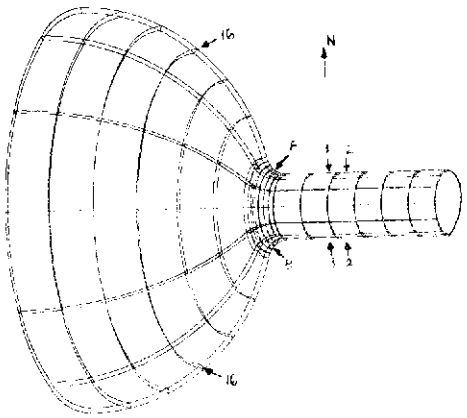

Fig. 5. Finite element representation including gauge locations.

through the thickness. In order to further verify the model, including inelastic integration point selection, and elastic–plastic analysis was compared to an ORNL experiment reported by Gwaltney, Richardson and Battiste [17] for the same model at room temperature. The analytic and experimental results are shown in Fig. 6 and are in good agreement.

The findings mentioned earlier, pertaining to plasticity–creep interaction, indicate in which directions we anticipate the finite element analysis to differ from the true response. In particular, the effect of prior creep strain accumulation should increase the subsequent yield stress and therefore reduce the development of plastic strains. Thus, not accounting for this interactive behavior should lead to an overprediction of plastic strains in the presence of creep strain accumulation.

The actual analysis was run in 15 segments using restart procedures. Typical results are shown at gauge location S8, in Figs. 7 and 8 for the pressure loading phase and Figs. 9 and 10 for the moment loading phase. The experimental results shown were obtained from Clinard, Richardson and Battiste [5]. The results show an overprediction of plastic strain during the pressure loading, which occurs predominantly during the first creep period where stress redistribution is pronounced, and during the second time-independent reloading period. After the first period the increase in plastic strain during the time-dependent pressure loading phases is negligible, due to the lack of stress redistribution. In addition, as mentioned earlier, the delayed strain recovery exhibited experimentally was not predictable analytically. The present results agree almost identically with those found by ORNL using axisymmetric analytic methods [18], the only difference being

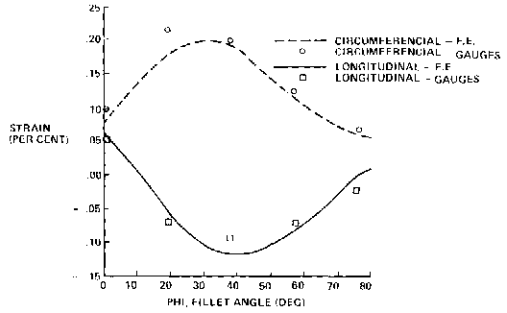

Fig. 6. Comparison between experimental and finite element analysis results for strain at inside south surface for piping component under combined pressure (500 psi) and end moment (20 k-in) at room temperature (zero degrees corresponds to cylindrical–toroidal intersection).

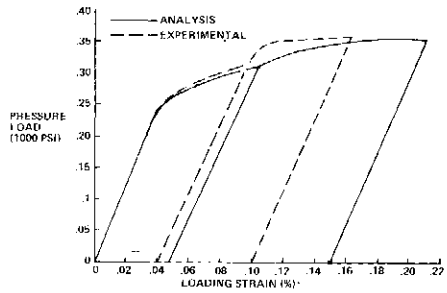

Fig. 7. Pressure load vs circumferential strain at gauge 8, at 1100°F.

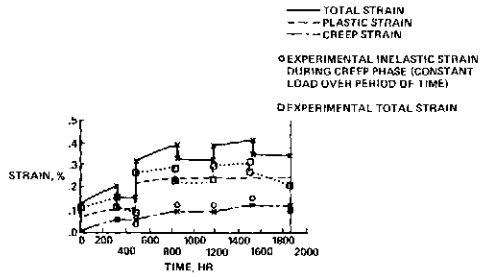

Fig. 8. Circumferential strain at gauge 8 during pressure loading, at 1100°F.

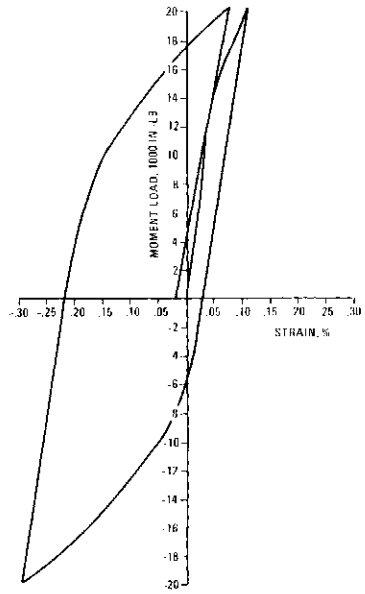

Fig. 9. Moment load vs circumferential strain (during loading) at gauge location S8.

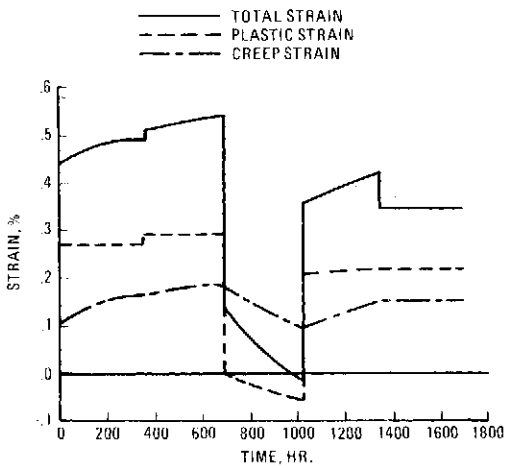

Fig. 10. Circumferential strain at gauge location S8 vs time during moment loading.

that the present solution predicts plastic behavior during the first creep phase. The results shown in Figs. 9 and 10 are not compared to experiment since the experimental results during this phase are still in progress as of this writing. However, the limited data available indicates that for the time-independent load-

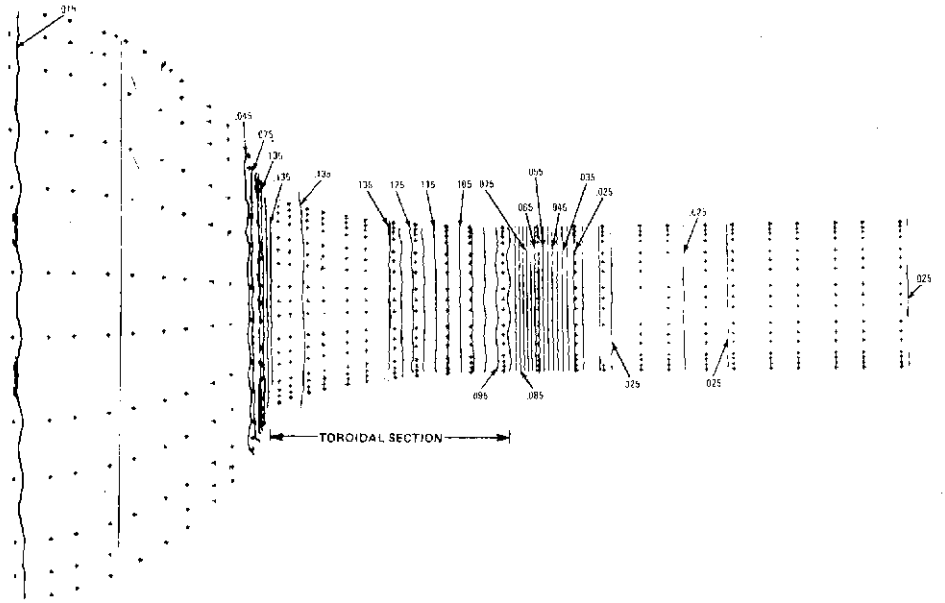

Fig. 11. Contour plot of effective creep strain % at end of pressure phase.

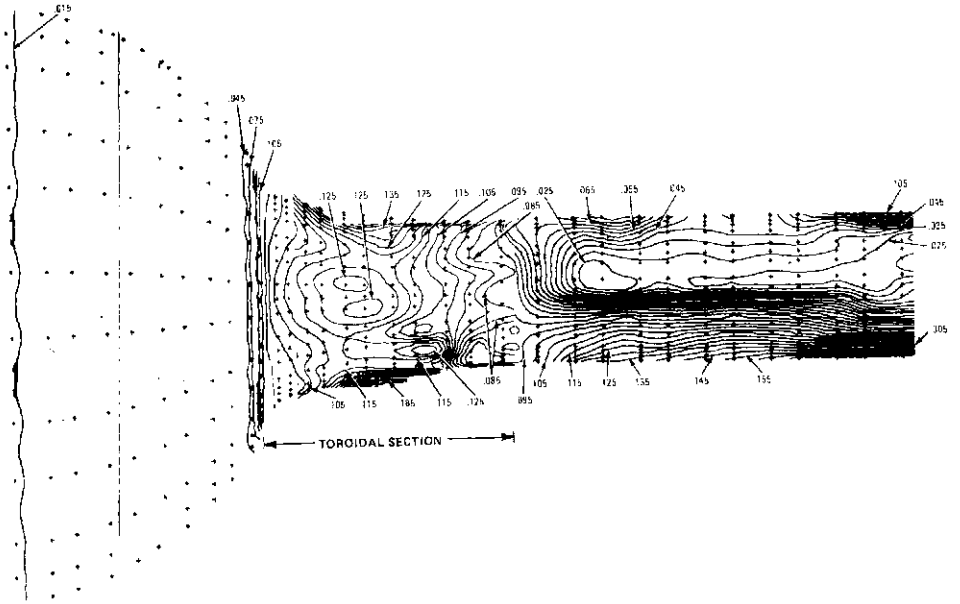

Fig. 12. Contour plot of effective strain % at end of moment phase.

ing phases the plastic strains are overpredicted and for the time-dependent loading phases the creep strains are reasonable.

The discrepancies between experiment and analysis can be accounted for qualitatively if we consider the lack of interactive behavior between creep and plasticity as discussed earlier, i.e. creep strains at high temperatures tend to reduce the development of subsequent plastic strains, and accumulated creep strains tend to raise the yield stress of the material.

Typical contour plots are shown in Figs. 11 and 12. Note that the geometry is distorted. Here we show contour plots of effective creep strain at the end of the pressure and moment loading phases. Creep strains are directly related to stresses and therefore Figs. 11 and 12 represent the accumulated effect of the stress history. The stresses and creep strains developed in the spherical shell are almost completely due to the pressure loading, while those in the toroidal and cylindrical sections are redistributed due to the moment load as shown. The peak stress occurs at gauge location S8 in the toroidal region, except for the edge effect near the application of the moment.

FUTURE RESEARCH DIRECTIONS

In the near future, large scale computer programs will be capable of analyzing nonisothermal, large strain, inelastic three-dimensional behavior. Solution algorithms, finite elements and modeling techniques are in a relatively advanced state and have been demonstrated by many researchers. The area of most

uncertainty appears in the constitutive relations. It is apparent that even for general cyclic inelastic behavior alone (i.e. isothermal, small displacement, inelastic behavior) the present state-of-the-art constitutive relations are inadequate. An accurate representation of the general inelastic material behavior must be established. Research in the areas of unified theories and interactive relations for a wide range of materials and environments may solve this problem.

Acknowledgements—I would like to thank my colleague, Dr. A. B. Pifko, for his expert help in building the HEX Program and for his attention and advise whenever needed. My thanks to J. A. Clinard (ORNL) for his very helpful discussions and to Dr. S. Iskander (ORNL) for his suggestion to investigate the use of the Lobatto integration scheme.

REFERENCES

1. A. Levy, A. Pifko and H. Armen, Jr., Finite element elastic–plastic analysis of LMFBR components. *Nucl. Engng Des.* **45**, 411–418 (1977).
2. A. Levy, Development of the PLANS computer program for elastic-plastic creep analysis of nuclear reactor structural components. Grumman Research Department Report RE-567, ORNL-Sub-4485-2. Grumman Aerospace Corporation (1979).
3. A. B. Pifko, H. S. Levine and H. Armen, Jr., PLANS—A finite element program for nonlinear analysis of structures, Volume I—Theoretical Manual. Grumman Research Department Report RE-501, Grumman Aerospace Corporation (1974)
4. Energy Research and Development Administration, *Guidelines and Procedures for Design of Nuclear System Components at Elevated Temperatures.* FDT Standard F9-5T (1974).
5. J. A. Clinard, M. Richardson and R. L. Battiste, Nozzle-to-sphere tests. In *High-Temperature Structural Design Program Semiannual Progress Report for Period Ending December* 31, 1979, ORNL-5622. Oak Ridge National Laboratory (in preparation).
6. S. R. Bodner and Y. Partom, Constitutive equations for elastic viscoplastic strain-hardening materials. *J. Appl. Mech.* **39**, 751–757 (1972).
7. O. C. Zienkiewicz and J. C. Cormeau, viscoplasticity plasticity and creep in elastic solids—a unified numerical approach. *Int. J. Num. Meth. Engng* **8**, 821–845 (1974).
8. D. N. Robinson, A unified creep-plasticity model for structural metals at high temperatures. ORNL/TM-5969. Oak Ridge National Laboratory (1978).
9. W. L. Greenstreet, J. M. Corum, C. E. Pugh and K. C. Liu, Currently recommended constitutive equations for inelastic design analysis for FFTF components, ORNL-TM-36-02. Oak Ridge National Laboratory (1971).
10. C. E. Pugh, J. A. Clinard and R. W. Swindeman, Recommended modifications to constitutive equations in RDT standard F9-5T. In *High-Temperature Structural Design Program Semiannual Progress Report for Period Ending* 31 *December* 1978, ORNL-5540, pp. 2–16. Oak Ridge National Laboratory (1979).
11. A. Levy, A. B. Pifko, On computational strategies for problems involving plasticity and creep, *Proc. of the Fifth Invitational Symposium on the Unification of Finite Elements, Finite Differences and Calculus of Variations.* The University of Connecticut (1980).
12. A. Mendelson, M. H. Herschberg and S. S. Mason, A general approach to the practical solution of creep problems. *J. Bas. Engng* **81**, 585–593 (1959).
13. N. C. Dahl, Discussion of (A general approach to the practical solution of creep problems, A Mendelson *et al.*, *J. Bas. Engng* **81**, 585–593, 1959); *J. Bas. Engng* **81**, 595 (1959).
14. O. C. Zienkiewicz, J. E. Irons, S. Admad and F. C. Scott, Isoparametric and associated element families for two and three-dimensional analysis. In *Finite Element Methods in Stress Analysis* (Edited by I. Holand and K. Bell), pp. 383–432. Tapir Press, Trondheim, Norway (1972).
15. A. Levy, A Three-dimensional "variable node" isoparametric solid element. Gruman Research Department Report RM-587, Grumman Aerospace Corporation (1974).
16. J. A. Clinard, Creep equation. In *High-Temperature Structural Design Program Semiannual Progress Report for Period Ending June* 30, 1978, ORNL-5433, pp. 137–140, Oak Ridge National Laboratory (1978).
17. R. C. Gwaltney, M. Richardson and R. L. Battiste, Room temperature enelastic test of a nozzle-to-spherical-shell model subjected to pressure and moment loading, ORNL/TM-6170. Oak Ridge National Laboratory (1978).
18. R. C. Gwaltney, M. Richardson and R. L. Battiste, Nozzle-to-sphere tests and analyses. In *High-Temperature Structural Design Program Semiannual Progress Report for Period Ending* 31 *December* 1978. ORNL-5540, p. 120. Oak Ridge National Laboratory (1979).

Computers & Structures, Vol. 13, pp. 257–262, 1981
Printed in Great Britain.

0045-7949/81/010257-06$02.00/0

DYNAMIC ANALYSES OF ELASTO–PLASTIC PIPING SYSTEMS UNDERGOING LARGE DEFORMATIONS

J. HEIFETZ†, M. BENJAMIN‡, and L. LISTVINSKY‡
EBASCO Services Inc., 2 World Trade Center, 79th Floor, New York, NY 10048, U.S.A.

(*Received* 9 *May* 1980)

Abstract—A finite element program development is presented for elasto plastic piping systems subjected to severe pipe rupture blowdown forces and finite deformations. The piping consists of straight and curved elements with relatively thin walls. The effects of varying internal pressure on yielding are included but remain uncoupled from the dynamic solution process.

The elasto-plastic materials are modeled as bilinear with isotropic strain hardening. An incremental flow rule associated with the Von Mises yield surface completes the constitutive laws governing these materials except for the requirement that stress rates be frame indifferent (as part of a more general requirement on constitutive equations). Frame indifference is satisfied by writing the Prandtl-Reuss equations in terms of "stretching" (or strain rate) and Jaumann flux.

In the context of this paper, "large deformations" result from second order effects due to gross changes in frame geometry and due to local bending and membrane strains.

The solution to the typical initial value problem representing the postulated blowdown event within a nuclear piping system consists of a step-by-step integration of a set of ordinary differential equations in the time domain. The authors have chosen the Newmark Beta method, with variable integration steps for this purpose. At each integration step "correction" forces $\mathbf{P}_n$ and $\mathbf{H}_n$ are found by determining plastic strains and rigid body rotations at Gaussian grid points within a pipe element and then performing numerical integration over appropriate pipe volumes.

At regular intervals, direction cosines of applied blowdown forces are transformed to follow the rotations of traction surfaces, and the stiffness matrix is updated. The optimal interval spacing for solution accuracy appropriate and economy is under investigation.

Comparisons with solutions and experiments in the open literature will be made, wherever possible.

Despite its low probability, the postulated pipe rupture event represents one of the major concerns of nuclear plant design. Efforts at restraining high energy pipes following such an event include the use of energy absorbing restraints, i.e. yielding U-bars, crushable materials. Hard restraints, i.e. concrete walls and rigid steel frames, occur where clearences are minimal or functional operability of components must be maintained. Characteristically all such restraints must be gapped to allow for free pipe movement during normal operating conditions.

Frequently it is impossible or uneconomical to place restraints in certain crowded or otherwise inaccessable regions, with the result that long stretches of pipe remain unrestrained. The validity of a pipe whip analyses for such cases (using small deformation theory) may then be questioned (and often is) with regard to the accuracy of restraint reactions and pipe deflections that result. This paper represents an outgrowth of earlier works on large deformations in solids [1] and PLAST [2], a computer program for the dynamic analysis of elasto-plastic piping systems. In these developments the Von Mises yield surface and its incremental, associated flow rule [3] are coupled with an isotropic strain hardening material.

BACKGROUND

The large deformation of flexible systems (i.e. plates, shells, frames) is characterized by significant rigid body rotations of local segments of the system. Local deformation gradients may be small but the effect of rigid body rotations on these gradients remain significant [4].

In formulating the solution to dynamic problems in large deformations, consideration must be given to the "frame indifference" of the constitutive equations [5]. Therefore, such terms as strain rate, stress rate, etc. must themselves be frame indifferent. The associated flow rule for incremental plasticity is sometimes parameterized with respect to time, causing plastic materials to appear to be rate dependent. Thus, when materials undergoing large deformation have elastic components of strain that are infinitesmal, the flow rule for an elasto plastic material may be written:

$$D'_{ij}=\frac{T^{(J)}_{ij}}{2G}+\lambda\frac{\partial f(\tau_{ij})}{\partial\tau_{ij}} \tag{1}$$

where

$$D'_{ij}=D_{ij}-\tfrac{1}{3}\delta_{ij}D_{kk} \tag{2a}$$

is the deviator of "stretching";

$$D_{ij}=\frac{1}{2}\left(\frac{\partial U_i}{\partial x_j}+\frac{\partial U_j}{\partial x_i}\right) \tag{2b}$$

defines "stretching";

$$\tau'_{ij}=\tau_{ij}-\tfrac{1}{3}\delta_{ij}\tau_{kk} \tag{3}$$

is the stress deviator;

$$T^{(J)}_{ij}=\dot{\tau}_{ij}-\tau_{kj}\omega_{ik}-\tau_{ik}\omega_{jk} \tag{4}$$

†Applied Physics Department.
‡Analytic and Computer Department

defines the Jaumann "flux" or stress rate [6] (see Appendix A).

$$\omega_{ik}=\frac{1}{2}\left(\frac{\partial \dot{U}_k}{\partial x_i}-\frac{\partial \dot{U}_i}{\partial x_k}\right) \tag{5}$$

defines a term of the "spin" tensor. G is the shear modulus, λ is a proportionality factor dependent on the current state of stress and condition of yielding, U is the material point displacements, δ_{ij} is the kroneker delta and $f(\tau_{ij})=0$ defines a yield surface in stress space.

The flow rule, as indicated in (1), refers to a current coordinate system attached to each particle of a continuum. As the continuum deforms, individual particles experience rigid body rotation as well as straining. The Jaumann flux is therefore a rate of stress increment due to both the deformation of the particle and the rotation of its stress field. This definition of stress rate implies [6] stationarity of the stress invariants (and hence the yield function) when $T_{ij}^{(J)}=0$. The virtual work equations may be written in incremental form as follows:

$$\int_V (\tau_{ij}^{(n-1)}+\Delta\tau_{ij}^{(n)})\delta c_{ij}\,dV=\int_V \rho F_i^{(n)}\delta U_i^{(n)}\,dV+\int_S [\overset{v}{T}_i^{(n)}\delta U_i^{(n)}\,dS \tag{6}$$

where n refers to time $t^{(n)}$, $\Delta()^{(n)}=()^{(n)}-()^{(n-1)}$, $[\overset{v}{T}_i(n)$ is the traction on a surface with outdrawn normal v, F_i is the body force/unit mass, $S=S_\sigma+S_U$, S_σ is the surface with tractions specified, S_U is the surface with displacements specified and V is the volume in current configuration.

Prior to transforming (6) into usable matrix form, several finite element definitions and equations will be listed:

$$\{\dot{U}\}=[\Phi]\{\dot{X}\} \tag{7}$$

defines the velocity of any point within an element in terms of the element nodal velocities.

$$\{D\}=[B]\{\dot{X}\} \tag{8}$$

defines stretching in terms of nodal velocities.

$$\{T^{(J)}\}=[E]\{\mathbf{D}^{(T)}-\mathbf{D}^{(P)}\} \tag{9}$$

defines the constitutive equations in rate form and is really a restatement of (1), where $[\Phi]$ is a shape function matrix, $\{\dot{X}\}$ is the vector of nodal velocities, $[B]$ is the matrix obtained by applying the differential operators of (2b) on (7), i.e.

$$[B(\xi)]=[\Gamma][\Phi(\xi)] \tag{10}$$

U is the vector of element internal displacements, $[E]$ is an elasticity matrix relating stress rate to stretching and $D^{(T)}$, $D^{(P)}$ in (9) refer to "total" and "plastic" components of stretching respectively.

Equation (4) may be rewritten in matrix form as:

$$\{T\}=\{\dot{\tau}\}+[W]\{\tau\}. \tag{11}$$

Multiplying both sides of (11) by Δt_n using (1), (8), (9), and rearranging, results in:

$$\{\Delta\tau_n\}=[E]\{[B_n]\{\Delta X_n\}-\dot{\lambda}_n\{\tau'_{n-1}\}\}-[\Delta W_n]\{\tau_{n-1}\}. \tag{12}$$

The virtual work equations in matrix form are then:

$$\delta\mathbf{X}_n^T\int_V \mathbf{B}_n^T\{(\mathbf{I}-\Delta\mathbf{W}_n)\tau_{n-1}+\mathbf{E}(\mathbf{B}_n\Delta\mathbf{X}_n-\dot{\lambda}_n\tau'_{n-1})\}\,dV=\delta\mathbf{X}_n^T\int_V(\rho_n\Phi_n^T\mathbf{F}_n)\,dV+\delta\mathbf{X}_n^T\int_S(\Phi_n^T T_n)dS \tag{13}$$

where $\mathbf{I}$ is the identity matrix. The body force is here identified as an inertial quantity:

$$\mathbf{F}_n=-\dot{U}_n=-\Phi\ddot{\mathbf{X}}_n. \tag{14}$$

The vector δX_n^T is eliminated from both sides of (13) and eqn (13) is rewritten as:

$$[M_n]\{\ddot{X}_n\}+[K_n]\{\Delta X_n\}=\{\overline{T}_n\}-\{P_n\}+\{H_n\} \tag{15}$$

where

$$[M_n]=\int_V \rho_n(\Phi_n^T\Phi_n)\,dV \tag{16a}$$

$$[K_n]=\int_V [\mathbf{B}_n^T\mathbf{E}\mathbf{B}_n]\,dV \tag{16b}$$

$$\{\overline{T}_n\}=\int_S \Phi_n^T\mathbf{T}_n\,dS \tag{16c}$$

$$\{H_n\}=\int_V \dot{\lambda}_n\mathbf{B}_n^T\mathbf{E}\tau'_{n-1}\,dV \tag{16d}$$

$$\{P_n\}=\int_V B_n^T(\mathbf{I}-\Lambda\mathbf{W}_n)\tau_{n-1}\,dV \tag{16e}$$

dV and dS are the differential volume and differential surface with specified tractions, respectively, of a single pipe element referred to a current configuration.

The computation of integrals (16a)–(16e) can be aided by noting that:

$$dV=J\,dV_0 \tag{17a}$$

and

$$dS=|J|\left(\frac{\partial\bar{x}}{\partial\bar{x}}\right)dS_0 \tag{17b}$$

where $\mathbf{J}=(\partial x/\partial\bar{x})$ is the Jacobian of a transformation (see Appendix B) from the initial to a current configuration, $|J|$ = determinant of J and $(\partial\bar{x}/\partial x)=\mathbf{J}^{-1}$, and dV_0 and dS_0 are the differential volume and traction surface, respectively of a single pipe element referred to the initial configuration.

Equation (15) was written to represent the equation of motion for a single element subject to externally applied and inertial forces. As connecting elements share common nodes, the matrices $[M_n]$ and $[K_n]$ may be "assembled" at common nodes to provide the total mass and stiffness for each node in each of its degrees of freedom. A similar assembly procedure applies to vectors $\{P_n\}$ and $\{H_n\}$. This leads to a set of matrix equations of motion for the entire assembly of nodal points that is identical to (15) in form.

SOLUTION METHOD

Equation (15) may be solved by stepwise integration methods subject to appropriate boundary and initial conditions. In the pipe rupture analysis, the boundary conditions include:

(a) Phased blowdown (inertial plus pressure) forces at each elbow of the system, available as time histories. Such forces may be obtained from one-dimensional, two-phase fluid dynamic codes and are included in (16c).

(b) Gapped, radial, external elastic-plastic, springs acting intermittantly and unidirectionally with the additional constraint to displace co-directionally with pipe. These springs are treated as non-linear "correction forces" similar to those of (16d) and (16e).

(c) Conventional fixed/free displacement boundaries.

The step-wise integration procedure in this further development of the PLAST Program, is by Newmark [7] with parameter $\beta=\frac{1}{6}$. The method is explicit and uses criteria suggested by Newmark as the basis for adjusting each time-integration step. Thus, numerical instability is anticipated and the integration interval optimized based on these criteria. When frequent opening and closing of gapped restraints occurs, integration intervals must be adjusted to assure adequate sampling of the restraint responses in addition to satisfying the above criteria. An alternative, implicit integration procedure [8], using constant integration intervals, is unconditionally stable for $\beta\geqslant\frac{1}{4}$ and leads to more rapid (and somewhat less accurate) solutions. However, restraint peak responses will be markedly truncated unless the integration interval is very small. An additional factor that limits the integration interval is the magnitude of incremental plastic deformation components. These depend on the stress state close to, but just prior to the current stress state. If the variation of stress states are large during any integration interval, one may expect computational inaccuracy.

Integrals (16d) and (16e) are evaluated by the application of four point Gaussian quadrature along the pipe element axis and eight point Filon Quadrature around the pipe element circumference. As the pipe walls are considered to be thin, these quadrature points lie in the mid-plane of the pipe wall. See Appendix C for detailed description of pipe element.

The algorithm used in this analysis is similar to that given in [2], with the exception that updating of reference frames must now be included.

As magnitudes in levels of frame distortion increase, nodal coordinates are updated. This is followed by updating of $[B]$ and $[K]$ matrices and the integrals of eqns (16a)–(16e) for each pipe element involved in the frame distortion.

EXAMPLES

The rigid frame indicated in Figs. 1 and 2 is subjected to simultaneous vertical and horizontal loads (indicated in Fig. 1). The frame itself consists of 4 in. pipe with the following physical properties:

Area $=3.174$ in^2
$I=7.2333$ in^4
$E=29\times10^6$ psi
$\sigma_y=4.6$ ksi (at initial yield)
$v=0.3$
$w=10.79\#/$ft. *Note*: This was multiplied by 675 to obtain a period 25 times its normal minimum.

The applied forces are:

$$\max F_H=5K$$
$$\max F_v=20K.$$

The material is treated as bilinear and strain hardens isotropically. In the examples chosen, the alternative options of allowing the applied forces to remain constantly in the same direction, or of allowing the

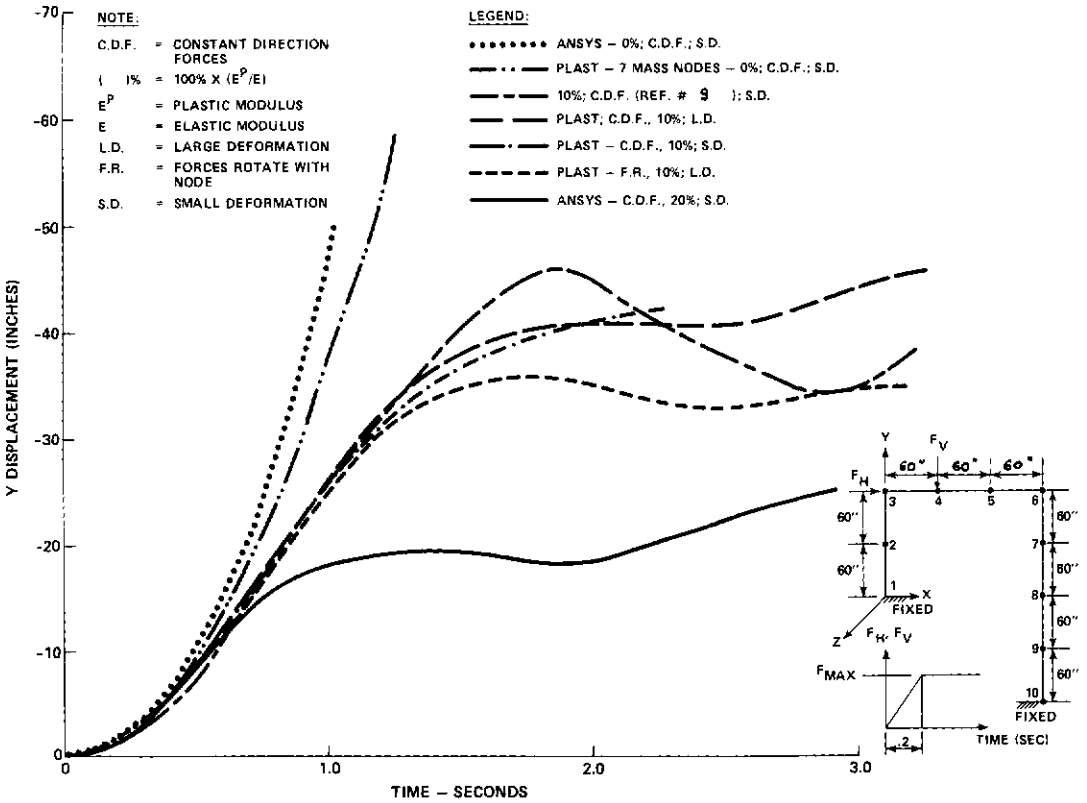

Fig. 1. Vertical displacement of node 4 vs time.

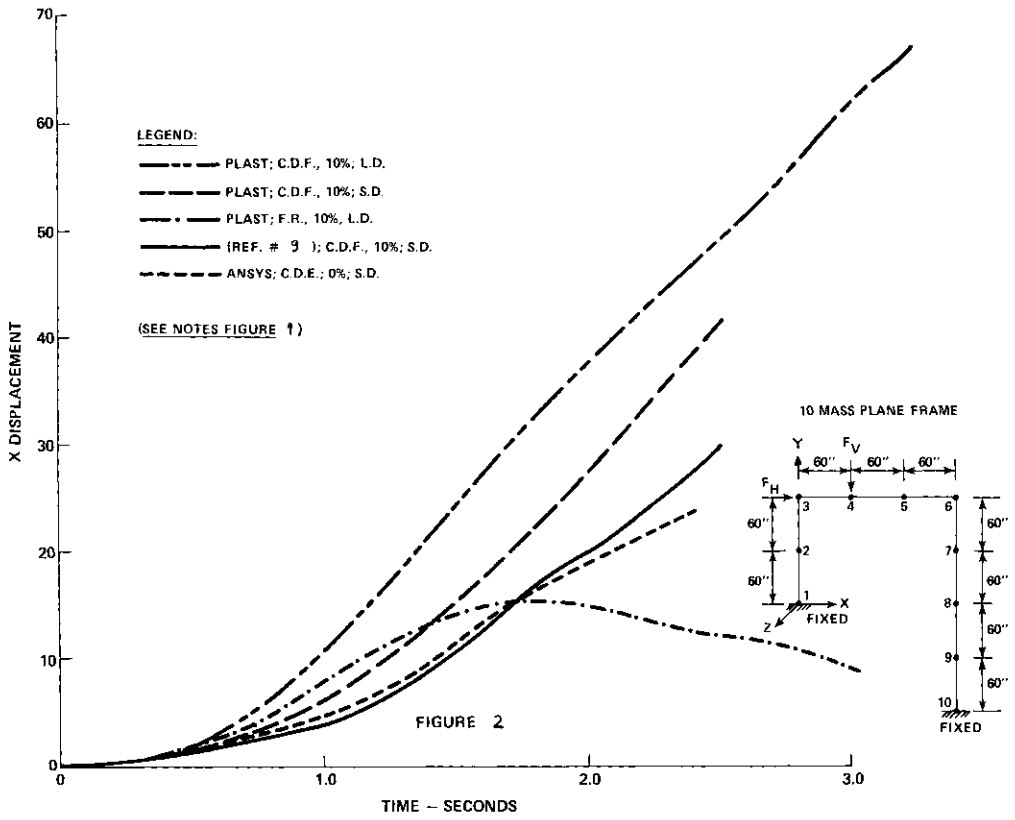

Fig. 2. Node 3—horizontal deflection vs time.

same forces to rotate with the nodal load application points are considered.

An examination of the results in Figs. 1 and 2 indicate the following:

(1) The effects of strain hardening are not significant until large distortions of the frame occur.

(2) In the large deformation regime significant differences occur in solutions due to different strain hardening rates (all other parameters remaining equal).

(3) The effect on the solution of allowing applied forces to rotate with their point of application is much larger than that of switching from small to large deformation theory.

DISCUSSION

The assumptions of large deformations, in this paper, encompass large rigid body rotations accompanied by relatively small deformation gradients locally. This may be interpreted to mean either than the relative rotation of one end of a pipe element with respect to its other end is "large" or that the relative rotation of two nodes separated by two or more elements is large. In the latter instance, it is assumed that the element retains its original shape (either straight or curved) following a large deformation. In the former case, a straight element may become curved or a curved element may change curvature (i.e. radius) subsequent to a large deformation. Each of these two instances would be realized in coarse and fine meshed systems respectively.

As the time-history solution procedes, each increment in nodal displacements is referred to its current configuration, i.e. to a set of coordinate axes located at each nodal point of the distorted continuum. However, if each element retains its original shape after a configuration change, the form of the shape function remains unchanged. This condition, which is consistant with the characterization of flexible systems made earlier in this paper, has the effect of minimizing the "rate-of-rotation" term in the Jauman Flux, i.e. as local element axes undergo rapid rigid body rotations, the particular rotations, within each element, referred to these moving axes diminish.

If elemental shapes change, subsequent to large deformations, then the shape functions must change to account for curvature changes in each element.

CONCLUSIONS

The characterization of large deformations of piping systems, indicate that gross geometric changes and traction transformations (rotation of applied loads) are primary factors in selecting a solution method. Since local deformation gradients are small, local volumetric and surface area changes are negligible, i.e. jacobians are always close to 1. Since reference axes in the step by step solution method move with each node and elemental distortions are assumed to be small, and the "spin" components of the Jaumman Flux terms are negligible.

FUTURE TRENDS IN NON-LINEAR STRUCTURAL ANALYSIS

There are three main areas requiring significant work to improve the efficiency and applicability of large scale non-linear dynamic structural analysis programs.

First, is the development of more accurate models for non-linear elements [10, 11, 13, 14]. Second is improvements in techniques for integrating the resulting dynamic equations [12–14] and finally substructuring of structural systems into linear and non-linear regions and/or stiff and flexible regions [15, 16].

REFERENCES

1. J. H. Heifetz and C. J. Costantino, Dynamic response of non-linear media at large strains. *J. Engng Mech. Division, ASCE* **98** (EM6) 1511–1528 Procedures Paper No. 9451, (1972).
2. J. Heifetz and P. Flanagan, Non-localized yielding and strain hardening in the finite element analysis of elasto plastic space frames. *3rd Int. Conf. Pressure Vessel Technology*, April 1977, Tokyo, Japan.
3. A. Mendelson, *Plasticity: Theory and Application*. Macmillan, New York (1968).
4. V. V. Novozhilov, *Foundations of the Non-Linear Theory of Elasticity*. Graylock Press, Rochester, New York (1953).
5. Truesdell, *The Elements of Continuum Mechanics*. Springer Verlag, Berlin (1966).
6. W. Prager, An elementary discussion of definitions of stress rate. *Q. Appl. Math.* **18**, 403–407 (1961).
7. N. M. Newmark, A method of computation for structural dynamics. *J. Engng. Mech. Div. Procedure ASCE* 67–94 (July 1969).
8. R. H. MacNeal and C. W. McCormick, The NASTRAN computer program for structural analyses. *Comput. Structures* **1**, 389–412 (1971).
9. E. A. Akboush, *et al.*, Inelastic deformations of geometrically nonlinear frames. ASCE Meeting, Baltimore, Maryland, Preprint No. 1405, April 1971.
10. L. Lazzeri, Application of plastic analysis to the pipe whip problem. *Int. J. Pressure Vessels Piping* **7**, 183–187 (1979).
11. K. J. Bathe and C. A. Almeida, A simple and effective pipe elbow element-linear analysis. *J. Appl. Mech.* **47**, 93–100 (1980).
12. S. N. Remseth, Nonlinear static and dynamic analysis of framed structures. *Comput. Structures* **10**, 879–897 (1979).
13. J. H. Argyris, *et al.*, Finite element method the natural approach. *Comput. Meth. Appl. Mech. Engng* **17/18**, 1–106 (1979).
14. B. O. Almroth, P. Sterm and F. A. Brogan, Future trends in nonlinear structural analysis. *Comput. Structures* **10**, 369–374 (1979).
15. A. Alizadeh and G. T. Will, A substructured frontal solver and its application to localized material nonlinearity. *Comput. Structures* **10**, 275–231 (1979).
16. C. P. Stavrinides, A procedure for coupling dynamic equations. *Comput. Meth. Appl. Mech. Engng* **20**, 1–7 (1979).

APPENDIX A

Jauman flux

The estimates for Jaumann flux at a material point are predicated on the assumptions that: (a) transverse shear terms in the pipe cross sections are negligible, and (b) pipe wall thicknesses correspond to those of thin shells. Therefore:

$$\tau_{xr} = \tau_{rx} \approx 0$$
$$\tau_{\theta r} = \tau_{r\theta} \approx 0 \qquad \text{(A1)}$$
$$\tau_{rr} \approx 0.$$

Consideration of the anti-symmetry of the rate of rotation tensor and eqns (A1) in the expansion of eqn (4) lead the expression;

$$\begin{Bmatrix} T_{xx} \\ T_{x\theta} \\ T_{\theta\theta} \end{Bmatrix}^{(J)} = \begin{Bmatrix} \tau_{xx} \\ \tau_{x\theta} \\ \tau_{\theta\theta} \end{Bmatrix} + \omega_{0x} \begin{bmatrix} -2 & 0 & 0 \\ 1 & 0 & -1 \\ 0 & 0 & 0 \end{bmatrix} \begin{Bmatrix} \tau_{xx} \\ \tau_{x\theta} \\ \tau_{\theta\theta} \end{Bmatrix} \qquad \text{(A2)}$$

which represents the expansion of eqn (11).

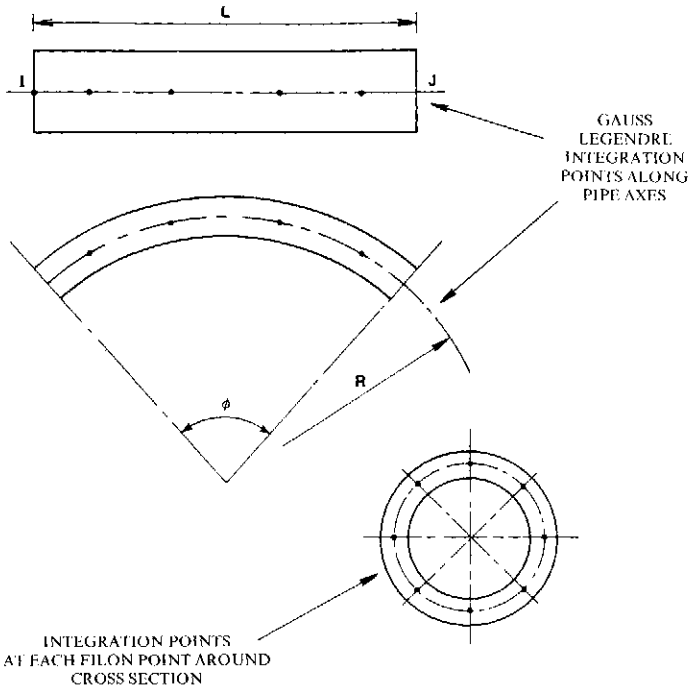

Fig. 3.

APPENDIX B

Deformation gradient

$$[J]=\left[\frac{\partial x_i}{\partial X_j}\right]=\begin{bmatrix}\left(1+\frac{\partial U_r}{\partial r}\right) & \frac{1}{r}\left(\frac{\partial U_r}{\partial \theta}-U_\theta\right) & \left(\frac{\partial U_r}{\partial x}\right)\\ \left(\frac{\partial U_\theta}{\partial r}\right) & \left\{\frac{1}{r}\left(U_r+\frac{\partial U_\theta}{\partial \theta}\right)+1\right\} & \left(\frac{\partial U_\theta}{\partial x}\right)\\ \left(\frac{\partial U_x}{\partial r}\right) & \left(\frac{1}{r}\frac{\partial U_x}{\partial \theta}\right) & \left(1+\frac{\partial U_x}{\partial x}\right)\end{bmatrix} \tag{B1}$$

represents the deformation gradient of a material particle in cylindrical, physical coordinates.

Consideration of thin wall assumptions reduces all variations with respect to r to zero, i.e.

$$\frac{\partial U_r}{\partial r}=\frac{\partial U_\theta}{\partial r}=\frac{\partial U_x}{\partial r}=0. \tag{B2}$$

Further assumptions include:

(a) Uniform hoop strain

$$\frac{\partial U_\theta}{\partial \theta}=0. \tag{B3}$$

(b) Unwarped cross-sections due to torsion, i.e. planes remain plane

$$\frac{\partial U_x}{\partial \theta}=0. \tag{B4}$$

This results in the following determinant:

$$|J|=\left(1+\frac{\partial U_x}{\partial x}\right)\left[1+\frac{U_r}{r}\right]. \tag{B5}$$

APPENDIX C

Pipe elements

The piping systems is modeled as a series of Euler–Bernouli prismatic and curved beams connected to one another at lumped mass points (nodes). The element is defined by two nodes I, J with six degrees of freedom at each node. Vector $\{X\}$ represents the displacements of nodes I and J.

$$\{X\}=\{U^I, V^I, W^I, \theta^I, \theta^I, \theta^I, U^J, V^J, W^J, \theta^J, \theta^J, \theta^J\}$$

where U, V, W=displacements along x, y, z, axes and θ_x, θ_y, θ_z=rotations about x, y, z, axes respectively, The typical straight and curved pipe elements are shown in Fig. 3. In Fig. 3 are shown interpolation points of Gaussian quadrature and Filon Quadrature which are used to evaluate the plastic correction force (Integral 16D) and the updating correction force (Integral 16E) for each element.

Computers & Structures, Vol. 13, pp. 263–274, 1981
Printed in Great Britain.

0045-7949/81/010263-12$02.00/0

AIRCRAFT IMPACT ON REINFORCED CONCRETE SHELLS

INFLUENCE OF MATERIAL NONLINEARITIES ON EQUIPMENT RESPONSE SPECTRA

TH. ZIMMERMANN

Motor-Columbus Consulting Engineers Inc., CH-5401 Baden, Switzerland

and

B. REBORA and C. RODRIGUEZ

IENER, Institut d'économie et d'aménagements énergétiques, Swiss Federal Institute of Technology Ecublens, CH-1015 Lausanne, Switzerland

(*Received* 6 *May* 1980)

Abstract—The effects of material nonlinearities on response spectra resulting from the impact of a commercial aircraft on the secondary containment of a BWR reactor are investigated. A finite element model taking into account concrete cracking and crushing and steel yielding is used for the analysis. The results show that, for the design considered here, no reduction of the response spectra due to material nonlinearity in the impact zone can be expected. As a matter of fact, an amplification results close to the impact area.

1. INTRODUCTION

Nuclear regulations in several countries require that the reactor building and the equipment be designed to resist the impact of a commercial aircraft.

The present study investigates the effects of material nonlinearities on equipment response spectra for the impact of a Boeing 707-320 on the secondary containment of a BWR reactor.

Much work has been devoted recently to this subject [1–5], motivated by the extremely high accelerations observed from linear analysis, the hope being that nonlinear analysis should prove them to be too conservative. These studies, however, do not show a general consensus about possible influences of material nonlinearity.

The emphasis is placed here on the influence of concrete cracking and crushing and steel plasticity in the immediate vicinity of the impact zone. Nonlinearities of the component support or other design related influences on response spectra are not addressed herein.

A finite element analysis of both linear and nonlinear response is performed. A loading function corresponding to an impact on a rigid target is used throughout the study

The problem statement is given in Section 2, followed by a description of the finite element model in Section 3. Numerical results are described in Section 4 and conclusions are drawn in Section 5.

2. PROBLEM STATEMENT

The impact of a Boeing 707-320 onto the dome of the secondary containment of a BWR reactor is being investigated (Fig. 1).

Since mainly qualitative results are being looked for, we restrict the model to a dome sector of radius 22 m (without boundary elements), thickness 1.2 m (reduced to 1.12 in order to account for the reinforcement's position), subject to a vertical impact.

Geometry

Figure 2 shows the geometry and describes the load. The shell is discretized into three layers of finite elements. A special boundary element combining a dashpot (following [6]) with a weakened stiffness reduces wave reflections and allows for some tuning of the first mode, in order to obtain a satisfactory similitude between the model and the containment structure.

Load

The load is uniformly distributed over an impact area of 24.63 m^2 (radius 2.8 m). The load time-history is shown in Fig. 2a). This impact area corresponds to the probable average according to [7]. It is smaller than the area usually adopted (37 m^2), in order to favor nonlinear influences, which we expect to be moderate.

As already mentioned we use a preassumed loading function (following [7]). If strong energy dissipation occurs we could expect the load time-history to be significantly reduced, but earlier computations show that this is unlikely to reach 10% and since it would require a much more costly modelling (including the aircraft), we limit the analysis to the induced vibration.

The total load duration is 400 ms and the adopted time step 2 ms, giving satisfactory mode representation upto about 80 Hz.

3. FINITE ELEMENT MODEL

3.1 *Elements*

We use 60-D serendipity isoparametric finite elements to simulate the massive concrete structure. Reinforcement is simulated by degenerated 24-D membrane elements without shear stiffness. Typical elements are shown in the upper part of Fig. 3.

The structure is divided into 30 brick-type elements, distributed over three layers and 99 membrane elements. It has 267 nodes (Fig. 3, lower part).

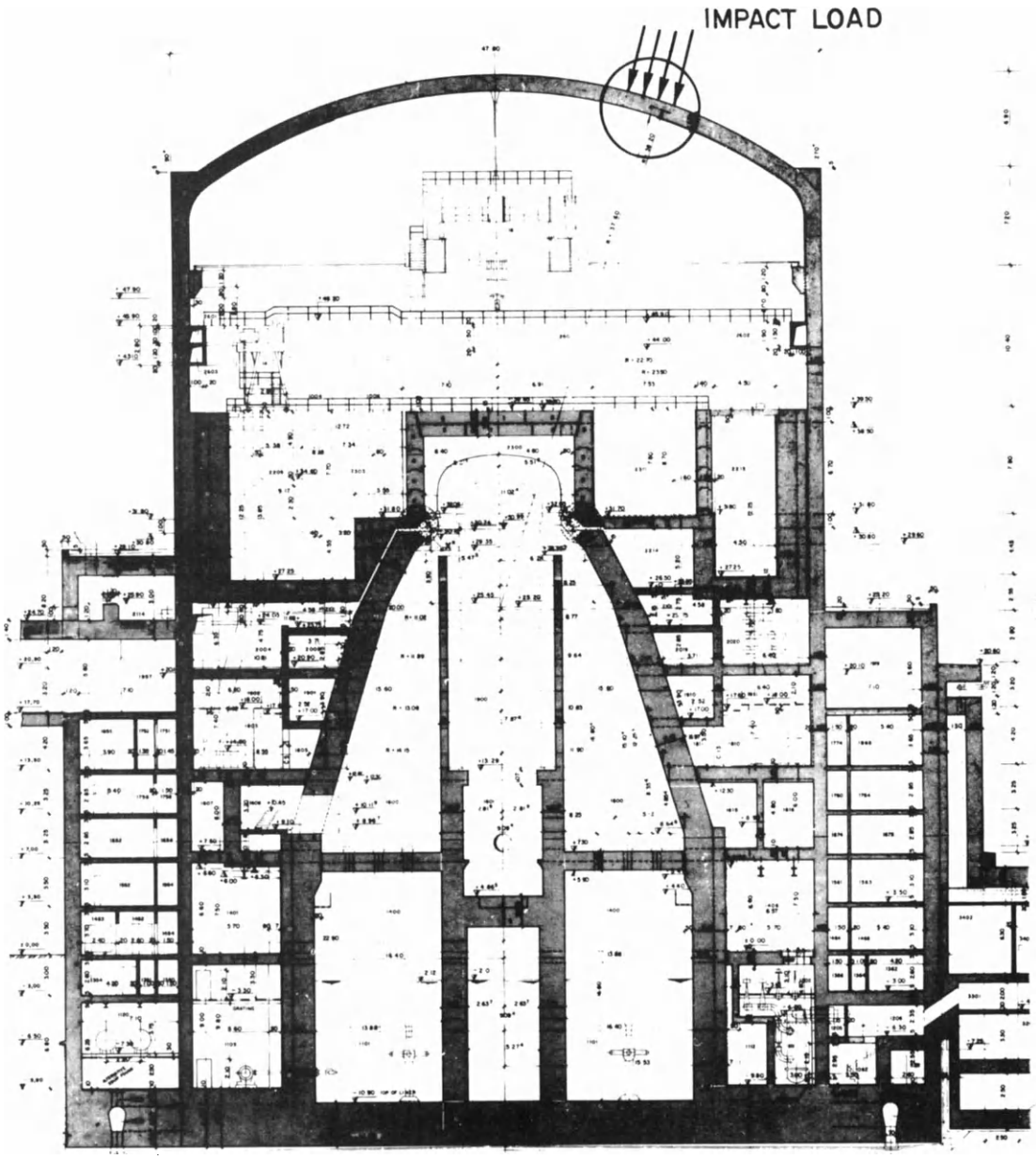

Fig. 1. Impact on reactor building.

3.2 *Constitutive equations*

A detailed account of the material model is given in [8]. We limit here the discussion to an overview completed by the more recent modifications.

Concrete. Concrete in a three-dimensional state of strain can be considered as a statistically isotropic material. In tension and for moderate compression, a linear constitutive law is selected. In the domain of higher compressive stress, a nonlinear stress-strain relationship is introduced. The failure criterion is expressed as a function of the stress invariants, specified in the spatial coordinates of the three principal stresses. The same failure criterion governs the failure in tension (cracking), as well as that in compression (crushing) and of course all combinations thereof. All states of the material behavior are described in the following paragraphs.

The nonlinear behavior of concrete is described by a variable shear modulus $\mu(=G)$, function of the second stress invariant I_2. The bulk modulus K remains constant. No volumetric dilatancy is considered, as this effect appears only close to failure. The following set of equations defines the stress–strain behavior:

Hooke's law,

$$\sigma_m = 3K\varepsilon_m \tag{3.1}$$

$$s_{ij} = 2\mu e_{ij} \tag{3.2}$$

where

$$\sigma_{ij} = \sigma_m + s_{ij} \tag{3.3}$$

$$\sigma_m = \sigma_{ii/3} \text{ (sum)} \tag{3.4}$$

and similarly for ε_{ij}. Further

$$K = \text{constant} \tag{3.5}$$

$$\mu = \mu_c \quad I_2 \leqslant I_{2e} \tag{3.6a}$$

$$I_2 > I_{2e}. \tag{3.6b}$$

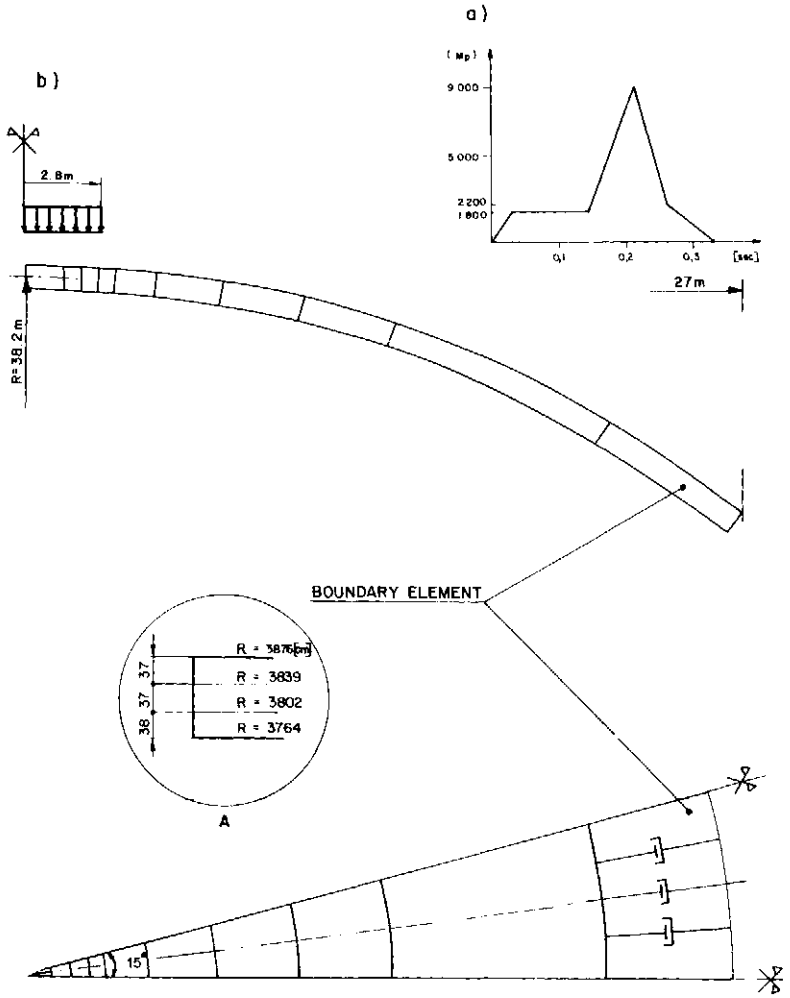

Fig. 2. Geometry, load and boundary conditions.

A typical "μ-law" is shown on Fig. 4(a). The parameters which define the law are: the limit of linearity (e.g. $1/3\beta p = 1/3$ uniaxial strength on prism) and the failure strain ($\varepsilon_r = 2$–3%).

Under cyclic loading, we check for unloading on the second stress invariant I_2. When the increment ΔI_2 is negative we set:

(1) $I'_{2e} = I_{2u}$† as the new limit of linearity (3.7a)

(2) $\mu = \mu_e$ (3.7b)

(3) $\Delta\varepsilon_0 = \mathbf{D}^{-1}\sigma_0$: the out-of-balance stress‡ becomes a permanent strain (this is merely a formal transformation). (3.7c)

Upon reloading, the same μ-law holds again, with the new I'_{2e} defined above. A secant shear modulus μ' is defined through a new origin on $II_2^{1/2}$ as indicated in Fig. 4(c).

The failure surface is shown in Fig. 4(b). The surface is a general cone centered along the average axis of the principal stresses. Any state of stress which is on or outside the surface represents a failure. For rupture under short-time loading, this failure surface was adopted, although much more complicated than the more commonly used ones, in order to give the best correlation with published experimental results. The analytical form of the failure surface can be found in [9]. The parameters to be established by experiments are the uniaxial compressive strength of a prism β_p, the uniaxial tensile strength $\beta_t (= \gamma \cdot \beta_p)$, and the biaxial compressive strength $n \cdot \beta_p$. Figure 4b shows the surface for $\beta_p = -1$, $\gamma = -0.1$ and $n = 1.3$.

Post-failure behavior can take different aspects depending on the stress state. Following a tensile failure, the concrete is orthotropic; for increasing load the principal axes will change leading to tangential stresses in the crack plane, while tensile stresses normal to crack are forced to zero by means of an "initial stress technique" (see Section 3.3). Following a compressive failure (crushing), the behavior becomes similar to that of a granular material so that a new failure surface can be defined by a conic criterion, i.e.

$$\sqrt{1.5} I_2^{1/2} + \kappa I_1 = 0 \tag{3.8}$$

(suggested $\kappa = 0.38$).

Steel. Yielding of the steel is determined by the von Misès criterion

$$I_2 - \frac{2}{3}\bar{\sigma}^2(k) = 0 \tag{3.9}$$

where $\bar{\sigma}(k)$ is the uniaxial tensile yield stress function

†Subscript u holds for unloading point, e for limit of linearity.

‡See the initial stress algorithm in Section 3.3.

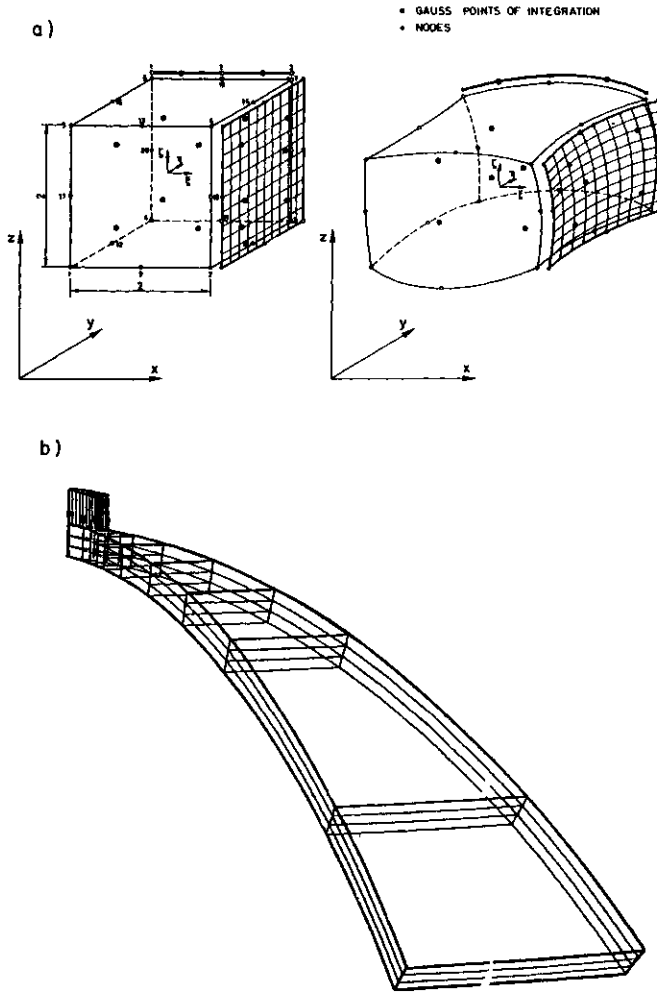

Fig. 3. Finite elements and mesh.

of a hardening parameter k. Kinematic hardening (Fig. 4d) coupled with total strain theory is used here. As the deformation of the steel is strongly influenced by that of the concrete, the global response should, in general, be insensitive to the material model used for steel.

3.3 *Solution of the nonlinear equation of motion*

We want to solve the equation of motion

$$\mathbf{Ma}+\mathbf{N}(\mathbf{d})=\mathbf{R}\dagger \tag{3.10}$$

where $\mathbf{N}$ is a nonlinear algebraic function of $\mathbf{d}$, corresponding to the type of constitutive laws previously defined, i.e.

$$\sigma=\mathbf{f}(\varepsilon) \tag{3.11}$$

with $\mathbf{f}$ a specific function. This covers, in particular, the nonlinear inelastic behavior described in the previous paragraph.

In order to solve eqn (3.10) we employ an implicit Newmark algorithm [10], which consists of the following equations‡

$$\mathbf{Ma}_{n+1}+\mathbf{N}(\mathbf{d}_{n+1})=\mathbf{R}_{n+1} \tag{3.12}$$

$$\mathbf{d}_{n+1}=\mathbf{d}_n+\Delta t\mathbf{v}_n+\frac{\Delta t^2}{2}(2\beta\mathbf{a}_{n+1}+(1-2\beta)\mathbf{a}_n) \tag{3.13}$$

$$\mathbf{v}_{n+1}=\mathbf{v}_n+\Delta t(\delta\mathbf{a}_{n+1}+(1-\delta)\mathbf{a}_n). \tag{3.14}$$

Assuming a nonlinear material behavior as described in the previous section, a solution can be achieved by adjustment of the elasticity matrix $\mathbf{D}$, the initial strain vector ε_0 or the initial stress vector σ_0 in the following stress–strain equation:

$$\sigma=\mathbf{D}(\varepsilon-\varepsilon_0)+\sigma_0. \tag{3.15}$$

The initial stress approach with constant stiffness is used here throughout the nonlinear and dynamic iterations. First, we eliminate $\mathbf{a}_{n+1}$ in (3.12) using (3.13) and define an "effective static problem"

$$\mathbf{K}_0^*\mathbf{d}_{n+1}=\mathbf{R}_{n+1}^*. \tag{3.16}$$

At each time step, we perform then the following computations:

(1) Initialization

$$i=0,\ \mathbf{F}_{n+1}^i=0$$

(2) Iteration

$$\text{(a) } \mathbf{R}^{*i+1}_{n+1}=\mathbf{R}^*_{n+1}+\mathbf{F}^i_{n+1}, \tag{3.17}$$

i.e. effective force = constant part + "initial stress

†Since we introduce material nonlinearity explicitely, no viscous damping is considered.

‡See [11] for implementation details.

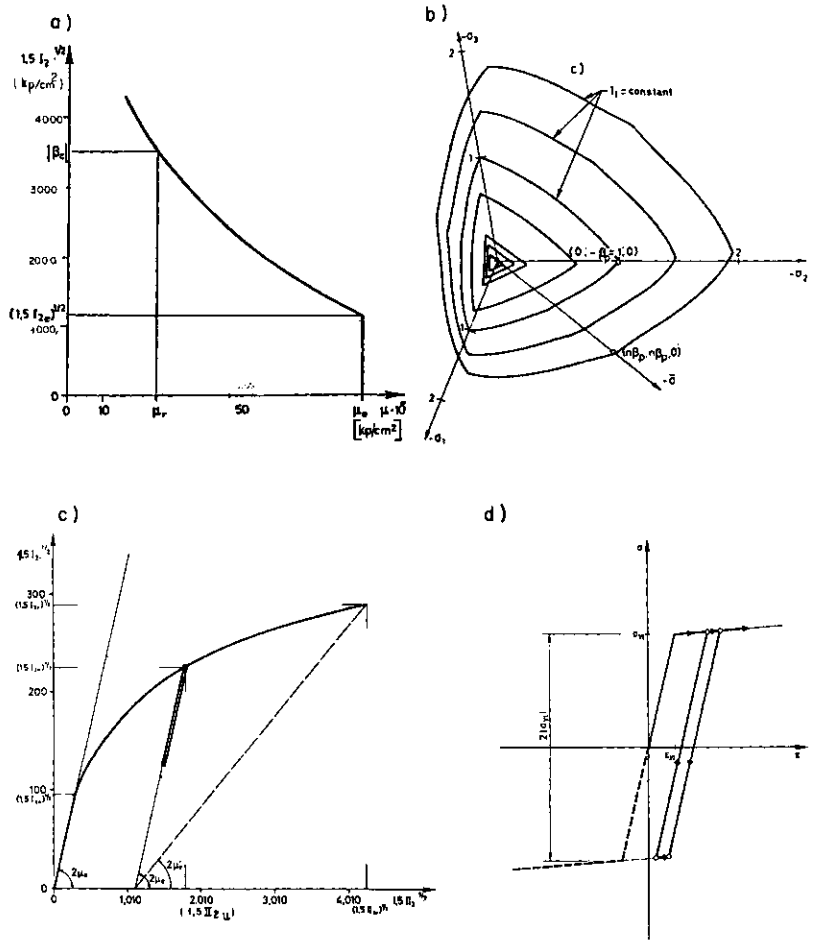

Fig. 4. Constitutive laws (a) concrete shear modulus, (b) concrete failure surface, (c) concrete hysteresis, (d) steel hysteresis.

equivalent force"

$$\text{(b)}\ \mathbf{d}_{n+1}:\mathbf{K}_0^*\mathbf{d}_{n+1}^{i+1}=\mathbf{R}^{*i+1}_{n+1} \tag{3.18}$$

$$\text{(c)}\ \mathbf{F}_{n+1}^{i+1}=-\int_e B^T\sigma_0^{i+1}\,dV \tag{3.19}$$

where

$$\sigma_0^{i+1}=\mathbf{f}(\varepsilon)-\mathbf{D}(\varepsilon_{n+1}^{i+1}-\varepsilon_0), \tag{3.20}$$

i.e. fictive force increment = integral over the element of the out-of-balance stresses (computed at Gauss integration points).

(d) Convergence check

$$\|\mathbf{F}^{i+1}-\mathbf{F}^i\|/\|\mathbf{F}^{i+1}\|<\text{tolerance}.$$

(e) As needed, increment i and go to (a).

3.4 *Data*

The geometry, the load and the discretization have been described previously. The material data corresponding to both concrete and steel are given in Table 1.

Boundary conditions. Rotational symmetry is imposed in both lateral planes of the shell sector. The outer edge of the shell is fixed and smeared radial dashpots are introduced in the boundary elements in order to damp out wave reflexions.

The dashpots are dimensioned following [6], i.e.

$C=\rho\cdot u\cdot A\,\{\text{kg/s}\}$: damping constant
$A=\{\text{m}^2\}$: area
$u=(E/\rho)^{1/2}\{\text{m/s}\}$: axial wave speed
$\rho=2.5\cdot 10^3\{\text{kg/m}^3\}$: density
$E=4.2\cdot 9.81\cdot 10^9\ \{\text{N/m}^2\}$: modulus of elasticity
hence, $C=10.15\cdot 10^6\ \{\text{kg/s}\cdot\text{m}^2\}\cdot A$.

Reinforcement. Radial and tangential reinforcement is introduced via membrane elements with no in-plane shear resistance. Steel sections as a function of horizontal radius are shown in Fig. 5b. For ease of implementation average values, constant over elements, are introduced. For simplicity, the same sections are taken in both directions, radial and tangential, and for both, upper and lower, reinforcement.

Shear reinforcement consists of 4 Ø 18/m (10.2 cm^2) in each direction, i.e. 16 Ø 18/m^2 (40.8 cm^2). The shear reinforcement is smeared over the element's faces and discretized as described on Fig. 5a. As for bending reinforcement we use elements with preferential directions, normal here to the shell's midplane.

4. NUMERICAL RESULTS

In a first step, a linear elastic analysis was performed and the corresponding response spectra generated at several points. A second computation was then done, restarting at $t=140$ ms. This corresponds approxi-

Table 1. Material data

Concrete

β_p = -240 (kp/cm2) (= 0.8 β_w = 0.8·(-300)))*
β_{pd} = 1.2 ·β_p = -288 (kp/cm2))
β_b = 1.2 β_p = -288 -"-) strengths
β_{bd} = 1.2 β_{pd} = -345.6 -"-)
β_t = 2.5 $\sqrt{|\beta_w|}$ = 43.3 -"-)
β_{td} = 1.2 β_t = 52 -"-

E_o = 19,000 $\sqrt{1.2|\beta_w|}$ = $3.6\ 10^5$) elastic moduli
E_{od} = 1.1 E_o = $3.96\ 10^5$)

υ_d = 0.2 Poisson's coefficient

γ_c = 2.5 (10^3kp/m3) specific mass

ϵ_r = 0,003 uniaxial failure strain

Bulk modulus $K = \frac{Ed}{3(1-2\upsilon_d)} = 2.2\ 10^5$ (kp/cm2)

Initial shear modulus $\mu_o = \frac{Ed}{2(1+\upsilon_d)} = 1.65\ 10^5$ (kp/cm2)

Shear modulus $\mu = \mu_o - \alpha \ln \frac{I_2}{I_{2e}}$, $\alpha = 0.596\ 10^5$(kp/cm2)

Steel

E_s = $2.1\ 10^6$ (kp/cm2)
E'_s = 2.10^4 (kp/cm2)
σ_y = 4,600 (kp/cm2)
β_t = 5,600 (kp/cm2)
γ_s = 7.85 (t/m3) (set to γ_s = 0)

Subscripts:
* p = prism, d = dynamic, w = cube, b = biaxial, o = initial, t = traction, r = rupture, c = concrete, e = limit of linearity, s = steel

mately to the initiation of material nonlinear behavior.

Comparison of the nonlinear versus linear displacement time-histories show a significant increase in the vertical displacement (28%) in the impact zone (Fig. 6, Point A), which fades out rapidly when we move away from the impact point (Fig. 6, Points B, C).

Only moderate and local disturbances appear: multiaxial cracking, no steel yielding. In Fig. 7, we show typical stress fields at $t = 214$ and 330 ms†.

Examining the stress time-histories at three locations (Fig. 8), we observe exclusively tensile failures. During loading, the first cracks appear at the intrados, simultaneously in radial and tangential direction (Fig. 8, Point D, time 150 ms), opposite to the impact point. Later on, radial cracks propagate (Fig. 8, Point F, time 170 ms). During unloading tensile cracks also appear at the extrados and within the shell (Fig. 8, Point E, time 300 ms), again in both directions. This cracking is related to the hysteresis hypothesis as follows: during loading permanent compression strains form at the extrados, which lead to tensile stresses and cracking upon unloading, when the shell recovers its initial configuration (Fig. 8, Point E, time 300 ms).

Accelerations time-histories are shown in Fig. 9§. Again we observe, due to nonlinearity, an amplification in the impact area (Point A), which fades out when moving away (Points B, C). Besides, the nonlinear response shows an abnormally high frequency content about 250 Hz ($T = 2\Delta t$) (Fig. 9, Point A). This is also indicated by the Fourier transform of the acceleration curve (Fig. 10, top). The observed vibration is related to progressive cracking: each new crack generates a jump in acceleration amplitude, within one Δt, which equals

$$\Delta \mathbf{a} = \mathbf{M}^{-1} \Delta \mathbf{K} \cdot \mathbf{d}$$

and excites eigenfrequencies about 250 Hz.

Our interest being in response spectra in the frequency range of 10^{-2}–10^2 Hz we truncate the Fourier

†The arrows give the orientation and magnitude of principal stresses and the shaded zones indicate cracks traces in the section's plane, represented at Gauss points.

‡Stress time-histories are defined in the principal coordinates of the final state of stress (at $t = 400$ ms). Line i of the orientation matrix gives the cosinus of σ_i.

§In vertical direction.

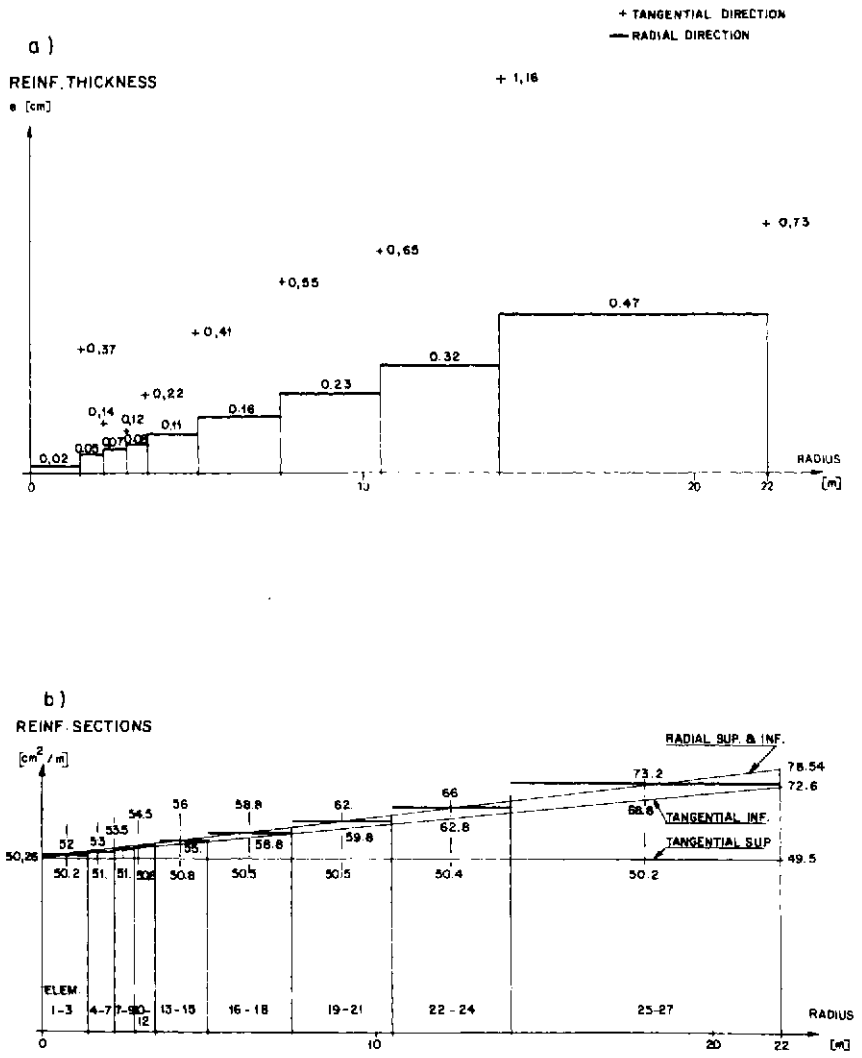

Fig. 5. Reinforcement.

transform of both linear and nonlinear signals at some reasonable frequency (150 Hz†). The corresponding nonlinear acceleration time-history is shown in Fig. 10 (bottom) and should be compared to Fig. 9 (Point A, dotted line).

Response spectra resulting from "smoothed" accelerograms are shown in Fig. 11. In our problem, material nonlinearity provokes increased accelerations close to the impact point over the whole frequency range, but especially above 10 Hz. Away from the impact the "nonlinear response spectra" tend towards the linear ones.

5. CONCLUSIONS

For the specific type of structure considered in the present analysis, and with the given loading function, material nonlinearity leads to an increase of equipment response spectra in the immediate vicinity of the impact area (Fig. 11, Point A). Away from the impact zone, about 11–14 m, effects of nonlinearity vanish (Fig. 11, Point C).

The structure being designed in a way that material nonlinear behavior appears only close to the maximum load ($t > 150$ ms), these results are by no means surprising.

In order to induce a reduction in the response spectra amplitudes, at least in a certain frequency range, design should be modified in order to increase the nonlinear part of structural response. This point is presently being further investigated.

Also, possible modifications of the numerical algorithm in order to avoid interferences between the time-stepping procedure and the initial-stress technique, which were discussed in Section 4, are subject to further study.

Acknowledgements—This work is an outgrowth of the impact analysis done for the Kaiseraugst nuclear power plant. The authors wish to thank Messrs' Jemielewski and Gaehler of Motor-Columbus for allowing publication.

†Results are not very sensitive to this particular choice.

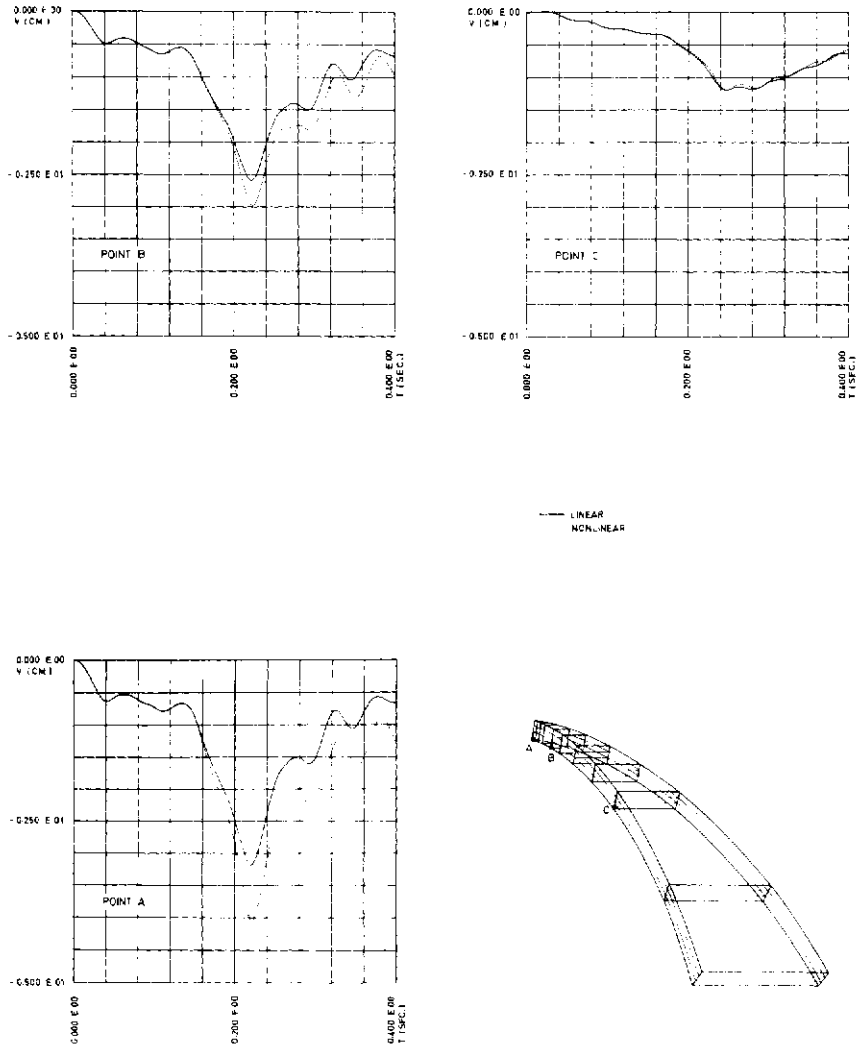

Fig. 6. Displacements time-histories.

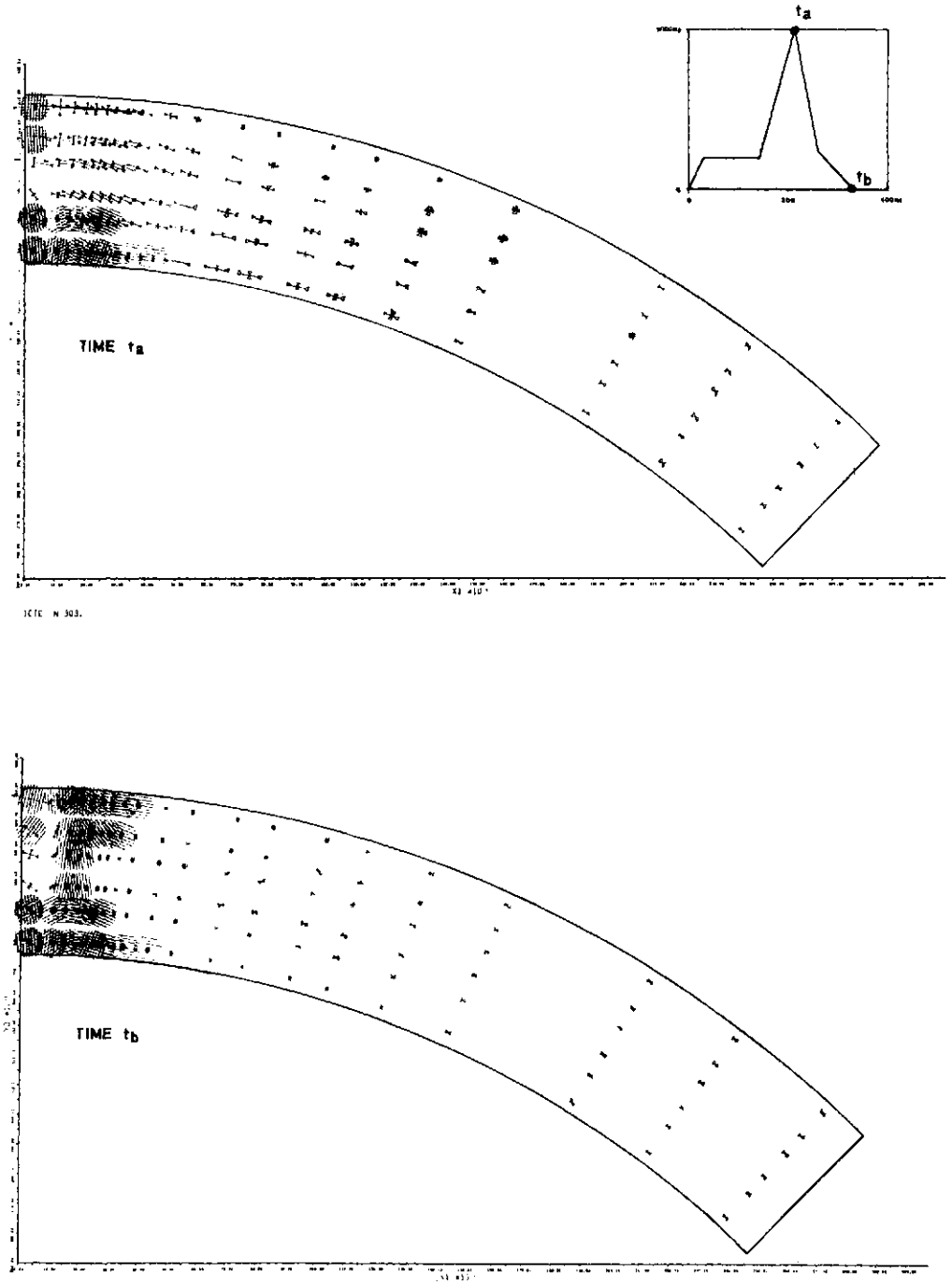

Fig. 7. Principal stresses.

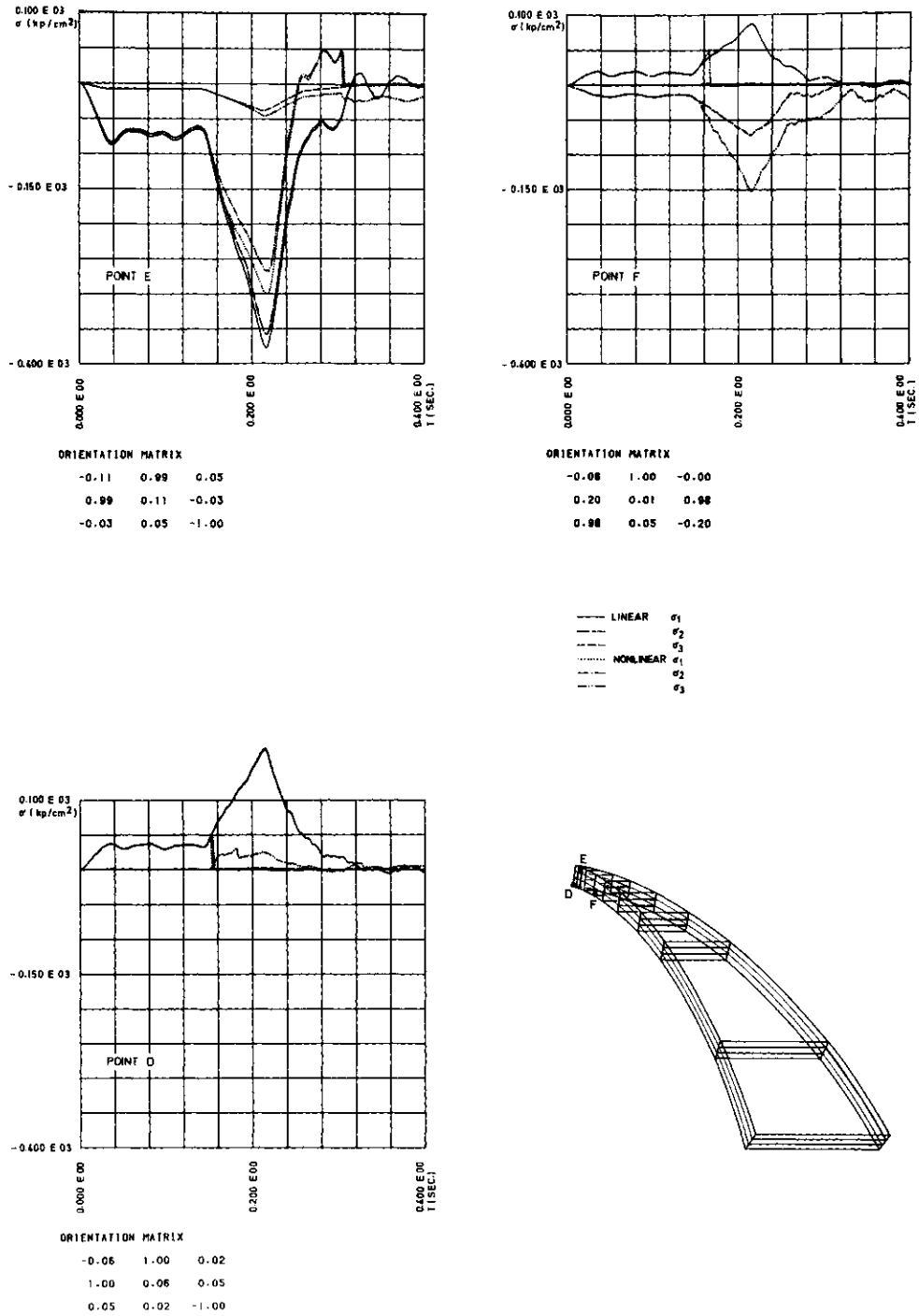

Fig. 8. Stresses time-histories.

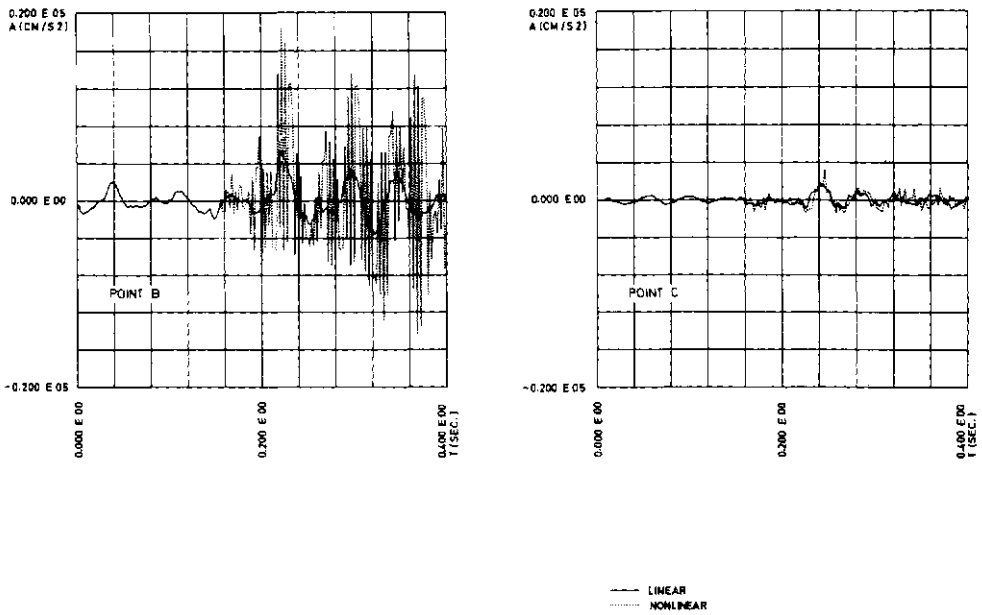

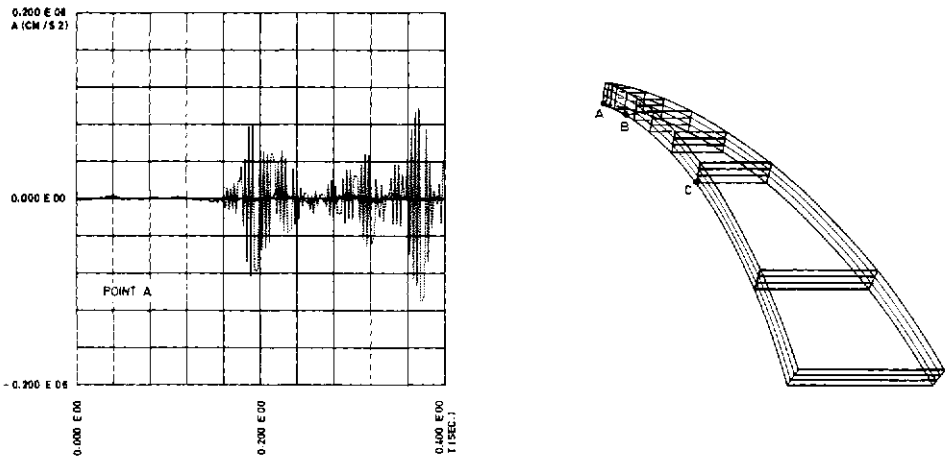

Fig. 9. Accelerations time-histories.

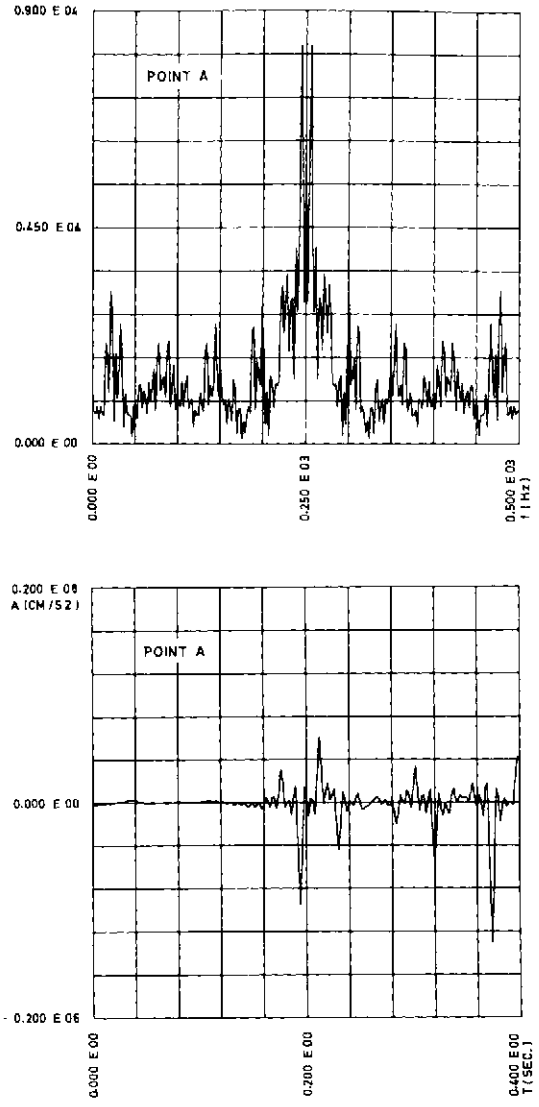

Fig. 10. Fourier transform and "smoothed" acceleration time-history.

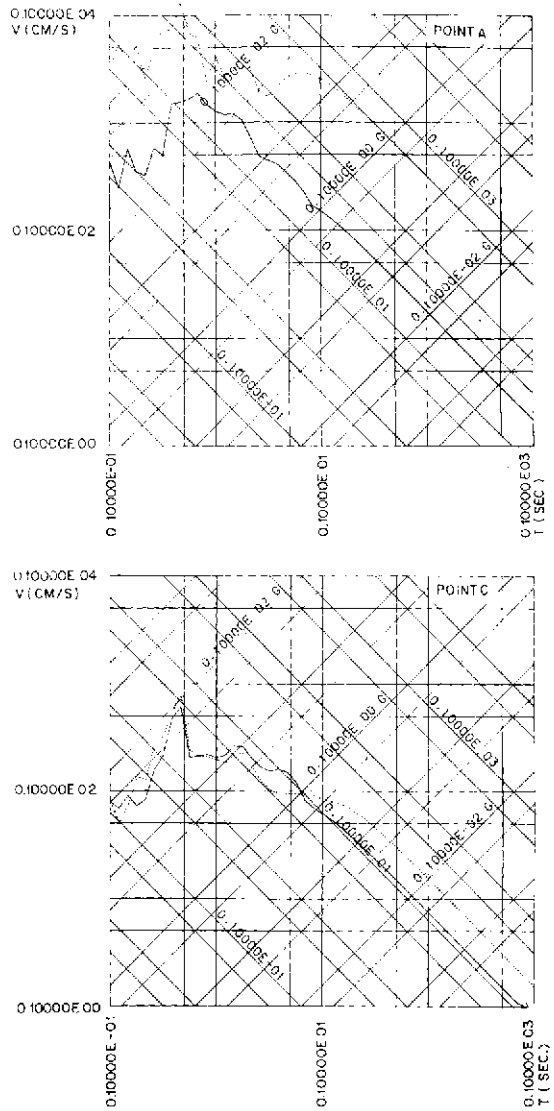

Fig. 11. Response spectra (1% damping).

REFERENCES

1. M. Schalk and H. Wölfel, Response of equipment in nuclear power plants to airplane crash. *Nucl. Engng Design* **38**, 567–582 (1976).
2. J. P. Wolf, K. M. Bucher and P. E. Skikerud, Response of equipment to aircraft impact. *Nucl. Engng Design* **47**, 169–193 (1978).
3. H. Kamil, N. Krutzik, G. Kost and R. Sharpe, An overview of major aspects of the aircraft impact problem. *Nucl. Engng Design* **46**, 109–121 (1978).
4. H. J. Krutzik, *Analysis of aircraft impact problems.* Lecture notes, Advanced course on structural dynamics, Ispra, Italy (Oct. 1978).
5. F. Stangenberg, K. Düspohl and R. Zinn, Deformations of reinforced concrete structures subjected to extreme dynamic loads. Presentation at *5th SMiRT Conf.*, Paper J5/5, Berlin (1979).
6. J. Lysmer and R. L. Kuhlmeyer. Finite dynamic model for infinite media. *ASCE J. Mech. Div.* 859–877 (1969).
7. J. D. Riera, On the stress analysis of structures subjected to aircraft impact forces. *Nucl. Engng Design* **8**, 415–426 (1968).
8. B. Rebora, Th. Zimmermann and J. P. Wolf, Dynamic rupture analysis of reinforced concrete shells. *Nucl. Engng Design* **37**, 269–297 (1976).
9. B. Saugy, Structures massives hétérogènes. Thèse No. 323, EPFL, Lausanne (1979).
10. N. Newmark. A method of computation for structural dynamics. *ASCE J. Mech. Div.* **45**, 67–94 (1959).
11. K. J. Bathe and E. L. Wilson, *Numerical Methods in Finite Element Analysis.* Prentice Hall, Englewood Cliffs, New Jersey (1976).

Computers & Structures, Vol. 13, pp. 277–285, 1981
Printed in Great Britain.

0045-7949/81/010277-09$02.00/0

THEORY AND APPLICATION OF FINITE ELEMENT ANALYSIS TO STRUCTURAL CRASH SIMULATION

A. B. PIFKO and R. WINTER†

Research Department, Grumman Aerospace Corporation, Bethpage, NY 11714, U.S.A.

(*Received* 27 *May* 1980)

Abstract—An increasing emphasis is currently being placed on the crashworthy design of occupant-carrying vehicles. The goal of this effort is to design vehicles that can minimize the dynamic forces experienced by occupants during a crash event while at the same time maintaining them in a survivable structural envelope. To accomplish this goal it is necessary to evaluate the dynamic crush behavior of the vehicle structure in specific crash situations.

It is the purpose of this paper to discuss the computational aspects of this problem. This is accomplished by outlining the computational methods used for crash simulation, discussing the requirements of a finite element solution to the problem and then summarizing results of two large structural crash simulation problems.

INTRODUCTION

An increased emphasis is currently being placed on crashworthiness as a structural design requirement for occupant-carrying vehicles. This requirement has been expressed recently in the form of military standards for U.S. Army troop carrying aircraft and federal motor vehicle safety standards for passenger automobiles. Consequently, by contract or by law, the crash impact condition has been added to the traditional set of structural design criteria. The goal of crashworthy design is to produce vehicles that during a specified crash event, will reduce the dynamic forces experienced by the occupants to specified acceptable levels, while maintaining a survivable envelope around them. Generally, the structure outside of this envelope must absorb and dissipate most of the impact energy in a well-controlled manner in order to fulfill this goal. In order to meet crashworthiness criteria with a minimum of effort and time, it is essential that adequate crashworthiness evaluation methods be used as early as possible in the design process.

It is the purpose of this paper to discuss the computational aspects of this problem. This is accomplished by outlining the development of computational methods used for crash simulation, discussing the requirements of a finite element solution to the problem, and then summarizing results of two large structural crash simulation problems performed at Grumman Aerospace Corporation.

Current techniques for structural crashworthiness evaluation can be characterized as experimental, hybrid, or fully theoretical. These methods have been discussed in Refs. [1-4] and can be summarized as follows:

Experimental—crash tests of actual full scale vehicles or scale models.

Hybrid—a combined experimental and numerical method in which the structure is divided into a number of relatively large sections or subassemblies that are treated as beam/nonlinear spring elements. The crush behavior of these components as represented by the varying stiffness characteristics of the elements are determined externally by test or separate analysis.

Theoretical—the finite element method in which the structure is divided into natural components, i.e. beam, stringer, skin panels, etc. The varying stiffness characteristics are calculated internally and depend interactively on the loading path, the material properties, and the changing shape and position of the structure.

There are a number of computer programs in existence that implement the hybrid method. The most generally useful one is the computer program KRASH, (Ref. [6]). Numerous nonlinear finite element programs are in use, and several surveys are available in Refs. [1, 6–8]. Some of these specifically designed for vehicle crash simulation, with the capability to model beams and thin panels are: ACTION (Ref. [9]), DYCAST (Refs. [10, 11]), and WRECKER (Ref. [12]).

Each of the methods outlined has its virtues and faults. Tests can provide the best accuracy and realism but can be costly and time consuming. Some tests are nevertheless absolutely essential. For example, the full scale tests at NASA Langley Research Center are providing essential insight into many general aspects of the light aircraft situation (Refs. [3, 4]). These will direct the efforts of researchers and designers into the most meaningful areas, and are providing data for verifying mathematical methods (Ref. [13]). Small scale model tests may also be useful, depending on the compromises between small size and realistic construction detail. Scale model tests on automobiles have been shown to yield useful results (Ref. [14]). At early stages of design however, test articles may not be available for destructive evaluation.

While some impact tests will always be required to verify actual performance, the number of tests can be reduced by the use of theoretical crash simulation. In this sense theoretical crash simulation can be viewed as a numerical experiment in which a discretized model of a structure is subjected to crash conditions.

The basic difference between hybrid and theoretical simulation models is in the manner in which they

†Staff Scientists.

represent the details of the actual structural stiffness and mass characteristics. In the hybrid method, the vehicle is modelled by a relatively small number of lumped masses connected by nonlinear springs or beam elements. Representative structural sections are built or cut from existing vehicles and tested statically for their crush characteristics which provide the nonlinear stiffnesses for the model. In this manner, the behavior of any material or special type of construction can be evaluated by means of these component crush tests. Alternatively, the deformation may be approximated by analytical estimates, a detailed static finite element analysis, or educated guesses.

The external generation of crush data input can in itself be costly and time consuming. In addition the data are usually derived by varying only one force or moment at a time, whereas the actual nonlinear deformation takes place under combinations of several load components that are not known in advance. Thus it cannot be assumed that the accuracy in one particular case will be as good for a variety of impact orientations and velocity vectors because the loading combinations on the structure will vary. The number of structural elements in the model must be limited because of the engineering effort required to generate their nonlinear stiffnesses. Consequently, hybrid methods usually require less computer time than finite element methods so that, if stiffness approximations can be made, the method is suitable for providing preliminary information or gross estimates of vehicle response.

Since the full finite element method does not rely on the existence of an actual structure, in principle it can provide a detailed analysis without the need for component tests. Once the vehicle finite element model is assembled and checked out, it can be easily modified by changing material or geometry of individual components. Thus detailed design evaluations and optimizations can be carried out. One modelling disadvantage is that some new material or construction type may not have an adequate finite element representation available when needed. This possibility can be covered by incorporating hybrid elements whose nonlinear stiffnesses are externally supplied. Such hybrid elements can also be useful to model a special energy-absorbing device or structural component whose deformation characteristics are already known.

The computational problem associated with finite element crash simulation is formidable, requiring consideration of several interdisciplinary areas that include nonlinear structural mechanics, numerical analysis, and computer sciences. These areas include: the appropriate theory to treat large elastic-plastic deformation, techniques to handle nonlinear boundary conditions required by variable contact/rebound, a library of finite elements appropriate for crash simulation, and accurate and efficient numerical time integration methods. Although investigations are still underway in each of these areas, theories have reached a sufficient level of maturity to be implemented into a program for crash simulation. Central to any implementation is the capability to treat nonlinear dynamic effects. Here nonlinearities that arise in a crash event are due to both material and geometric effects. Material nonlinearities are a consequence of plastic deformation while geometric nonlinearities are due to large displacements, the nonlinearity of the strain displacement relations, and any change in the boundary conditions due to intermittent contact/rebound.

Methods to treat various aspects of this problem have been developed by a number of researchers. Initially methodology was developed separately for each of the phenomena cited above. Reference [15] surveys computational methods for nonlinear structural analysis in its entirety and presents an extensive reference list to the pertinent literature.

Given that there is a sufficient understanding of these individual problems to permit crash analyses, the most vexing question associated with finite element methods is: how detailed a model is required to simulate the salient features of a crash, while still permitting the resulting analysis to be made economically viable?

Experience has shown that, while an accurate, versatile computer code is essential for an adequate crash analysis, it is not enough. Some expertise in the "art" of modelling a vehicle for a nonlinear dynamic analysis is also required, in order to produce sufficiently accurate results with a minimum of time and cost. A thorough understanding of the capabilities of the theory, and sufficient experience to know what will and will not work, is required by the analyst who prepares the model and its input data for the computer code.

This problem of modelling efficiency is much more acute in large-deflection nonlinear analysis than in the linear cases, because the solution involves a sequence of incremental steps each one similar to a complete linear analysis in itself. Thus, a dynamic event requiring hundreds or thousands of time increments can be prohibitively costly, unless the model is reduced to the minimum complexity required to produce sufficiently accurate results.

Generally, finite element crash analysis cannot be done efficiently in a data vacuum but should use all available information, such as past impact tests on similar vehicles and existing component crush data. In particular, important local deformation modes such as the collapse of hollow thin walled tubes in compression and bending require special modelling procedures.

Static crush tests on selected individual components or subassemblies can be useful to guide the modelling choices, but caution must be exercised since there are cases in which static collapse modes do not agree with the dynamic modes. Some steel structures that collapse statically after much plastic yielding can be greatly stiffened in a dynamic crush by the increase in the material's yield stress due to strain rate sensitivity. In addition, the effects of inertial forces due to added mass can significantly change the local behavior in some sensitive cases.

In this paper we will address some of these problems through the description of the main features of the DYCAST program (DYnamic Crash Analysis of STructures) and some experience gained in the crash evaluation of an automobile and an aircraft structure. DYCAST is an outgrowth of the PLANS system (Ref. [16]) of finite element programs for static nonlinear structural analysis. It is the result of an on-going effort at Grumman Aerospace, partially funded by the Langley Research Center of NASA, under a joint FAA-NASA project in aviation crashworthiness. Reference [4] summarizes the scope and goals of this project. Usage of DYCAST for the crash simulations

of aircraft type structures was reported in Refs. [11, 17], and more recently, automobile barrier impact analyses have been performed.

DYCAST FORMULATION

Constitutive relations

The methods used to implement plasticity theories into a finite element code by now are well developed and have been reported in many references (see for example, Ref. [18]). Here we outline the form of constitutive equations in a general way. DYCAST makes use of a flow theory of plasticity. Basic to this approach is the definition of an initial yield criterion, flow, and hardening rule. The initial yield criterion used is based on Hill's equations for orthotropic material behavior which reduces to the von Mises yield criterion for an isotropic material. From the flow and hardening rules the following incremental relation between the increment of plastic strain and stress is obtained

$$\{\Delta\varepsilon^p\} = [C]\{\Delta\sigma\} \tag{1}$$

where the terms of $[C]$ are path dependent quantities that reflect the instantaneous states of stress and hardening of the material and the choice of plasticity theory. In DYCAST use is made of the Prager–Ziegler kinematic hardening theory. Also contained in $[C]$ is a material parameter characterizing the hardening of the material. In the one dimensional case this is represented by the slope of the stress versus plastic strain curve. This is generalized to multiaxial stress conditions by assuming an effective plastic strain—effective stress relation. In either case these data must be input either in tabular form or as an appropriate nonlinear representation.

Another assumption that is used to develop the appropriate equations is that the increment of total strain may be decomposed into an elastic and plastic component. This assumption leads to the incremental constitutive relations for the stresses and plastic strains in an elastic–plastic material

$$\{\Delta\sigma\} = [D]\{\Delta\varepsilon\} \tag{2}$$

and

$$\{\Delta\varepsilon^p\} = [C][D]\{\Delta\varepsilon\} \tag{3}$$

where $\{\Delta\varepsilon\}$ is the increment in total strain, $[D] = [E^{-1} + C]^{-1}$ and $[E]$ contains the usual elastic material parameters.

Explicit forms for the relations in eqns (2) and (3) that are used in DYCAST are in Ref. [16]. Equations similar in form to eqn (2) for perfect plasticity are also shown in Ref. [16].

Development of equations of motion

The approach implemented in DYCAST is the updated Lagrangian formulation (Refs. [19–21]) for geometric nonlinearity. The derivation of the governing equations based on this approach follows that originally presented in Refs. [20, 21] for static analysis. The essentials of this method are that the solution is obtained incrementally, starting from a reference state, Γ_R, defined at time t for which the states of stress, strain, and deformation are known. The next state, Γ_c, termed the current state at time $t+\Delta t$ is assumed to be incrementally adjacent to Γ_R. The problem then reduces to solving for the incremental quantities, Δu_i, $\Delta\sigma_{ij}$, $\Delta\varepsilon_{ij}$ which are the increments in displacement, stress and strain in going from Γ_R to Γ_c. Once these quantities are obtained the coordinates of all points are updated by

$$x_i = X_i + \Delta u \tag{4}$$

where X_i is the coordinate locaton in Γ_R and the stress measure is transformed to Γ_c so that Γ_c is now the reference state for the next increment.

Based on these concepts, the equations of motion can be developed by one of several alternative procedures. Using the principle of virtual work and neglecting body forces and damping we can write

$$\int_{V_R} [N]^t \rho [N]\, \mathrm{d}V \{\ddot{u}\}_{n+1} + \int_{V_R} [B]^t [D][B]\, \mathrm{d}V + \int_{V_R} [\Omega]^t [\hat{\Sigma}][\Omega]\, \mathrm{d}V \{\Delta u\}_{n+1} = \int_{S_R} [N]^t \{T + \Delta T\}\, \mathrm{d}S - \int_{V_R} [B]^t \{\hat{\Sigma}\}\, \mathrm{d}V \tag{5}$$

where $[N]$ and $[B]$ are function matrices arising from the finite element field assumptions that map nodal displacements to the element displacement field and linear component of strain, $[\Omega]$ is a matrix containing first derivatives of the components of $[N]$, $[\hat{\Sigma}]$ and $\{\hat{\Sigma}\}$ are a matrix and vector of stress referred to Γ_R. The matrix $[D]$ comes from eqn (2) and in the absence of plasticity is equal to the matrix of elastic constants, $[E]$.

The integral quantities of eqn (5) are respectively, the consistent mass matrix, $[m]$ the material stiffness matrix, $[k_t]$, the initial stress stiffness matrix, $[k_g]$, the consistent load vector, $\{P\}$ and the vector of internal forces in Γ_R at time t, $\{F\}$. Summing these integrals over every finite element with respect to a common coordinate system then leads to the global equations of motion,

$$[M]\{\ddot{u}\}_{n+1} + [K_t + K_g]\{\Delta u\}_{n+1} + \{F\}_n = \{P\}_{n+1}. \tag{6}$$

Here n denotes the state at the end of the nth increment at time t, and $n+1$ at time $t+\Delta t$.

The updated Lagrangian approach outlined above is particularly effective for the nonlinear problem associated with crash simulation using beam, membrane, and plate elements. This is because large shape changes due to the progressive crushing and folding of the structure are accounted for by successive updating of the nodal coordinates. The nonlinearities due to the internal loads (for example, the change in stiffness due to the "beam column effect") are included through the initial stress stiffness matrix. Thus compressive forces dominant in a crash event will act through the geometric nonlinearities to reduce the stiffness of the structure.

Discrete time integration

Much attention has been given to methods for obtaining solutions to eqn (6). References [22–25] discuss methods for nonlinear dynamic analysis. The

starting point for these is the choice of an appropriate scheme to integrate eqn (6) in time. Various methods for both linear and nonlinear structural analysis have been surveyed in Refs. [26, 27]. We shall not attempt to repeat the survey of these procedures here, but rather make some general comments on the integrators used in DYCAST.

One measure used to evaluate a time integrator is the size of the allowable time step that can be used to yield accurate solutions. At the outset we state that a significant factor affecting time step size for a nonlinear dynamic analysis is the degree of nonlinearity active in the analysis. That is, the time step must be small enough so that the assumptions intrinsic to the governing equations, i.e. plasticity theory and geometric nonlinearity, must not be violated. Because the nonlinearities may vary during an analysis it is our view that an integator implemented in a general purpose code for nonlinear dynamic analysis should be a variable time step procedure. A variable time step procedure is one that enables the time step to be changed at different instants of the response, generally subject to stability and accuracy requirements. Such a procedure has obvious advantages over one with a constant time step, particularly in complex problems arising in practical applications because the system nonlinearities and dynamic response are varying continuously throughout the response history. This is particularly true for problems typical in crash simulation. Based on these comments, variable time step integrators have been implemented in DYCAST. These fall into two categories, i.e. explicit and implicit. These are the explicit Modified Adams (Ref. [28]), and the implicit Newmark-β (Ref. [29]), and Wilson-θ (Ref. [30]) methods. An explicit constant time step central difference (Ref. [26]) integrator is also available. The formulation of the explicit integrators in DYCAST are presented in Ref. [10]. The implicit technique is more useful for the structural dynamic response seen in a crash analysis. Implementation of the implicit technique in DYCAST is essentially as presented in Refs. [22–25]. The technique used solves eqn (6) iteratively at each time step subject to the recurrence relations for either the Newmark-β or Wilson-θ method.

A variable time step procedure is defined by requiring that the number of iterations in each time step be less than a prescribed value. If this criterion is violated the time step is halved. Conversely, if the solution converges in one iteration for a prescribed number of consecutive steps the time step is increased. An upper bound for the time step is also specified.

Finite element library

The basis for the derivation of the elements in DYCAST are in Ref. [16]. There are currently four element types available for structural modelling, as follows;

Membrane Triangles – Three classes are available: a uniform strain triangle, a linear strain triangle, and a set of hybrid triangles with one or two sides having linear strain variation.

Stringer Element – Two types are available: one having a uniform axial strain, and the other having a linear variation of axial strain.

Beam Element—There are with six degrees of freedom at each node, three displacements and three rotations. The element is based on a linear axial displacement field and cubic transverse displacement. In the completely elastic case, the beam stiffness matrix involves elastic material properties and integrated quantities that depend on the cross section, the area, and moments of inertia. Once points on the beam are plastic, these integrals must be numerically integrated.

To accomplish this, the shape of the cross section must be known *a priori* and the state of stress and strain must be evaluated at each integration point in the cross section. Towards this end twelve distinct cross sections can be specified, including eleven preformed shapes plus a thin-walled section of arbitrary closed or open configuration.

Nonlinear Spring Element—A nonlinear spring elements becomes an important element in modelling a complex structure. It can be used as follows;

- to stimulate structural sections for which the axial load versus elongation behavior (or moment versus rotation) has been obtained either by a crush test or by some other means.
- to simulate an energy absorbing device
- as a gap element to approximate variable contact/rebound.

The force versus elongation for this element is specified in tabular form. In general, nonlinear spring elements dissipate energy by unloading rapidly from their last deformation state along some specified unloading slope, thereby accumulating nonrecoverable permanent deformation. Upon reloading, the path is along the unloading line to the previous maximum deformation state, at which point deformation continues along the originally specified load vs deflection curve.

The nonlinear spring element in principle can be used as a gap element in order to simulate variable kinematic constraints that describe contact/rebound. However in practice, use of a gap element in a dynamic analysis leads to high frequency oscillations because of the large stiffness associated with a small nodal mass. To surmount this difficulty, viscous damping is introduced to the nonlinear spring when used as a gap element. The damping coefficient is defined as proportional to the current stiffness so that before contact, i.e. zero stiffness, the damping coefficient is zero. Spurious rebound is prevented by a "capture" technique in which both the stiffness and damping parameter are maintained as long as the contact point oscillates within a certain tolerance of the actual contact position. This technique has been effective for a number of sample problems.

Failure criterion

Assuming continuing and unlimited elastic or plastic deformation in a crash simulation is equivalent to assuming that a structural element will dissipate unlimited energy as it deforms along a particular load-deformation path. Obviously this can overpredict the energy that can be dissipated since actual materials will fail at some maximum deformation. To accommodate this behavior, maximum strain failure criteria have been implemented for every element in DYCAST. Once these criteria are satisfied the stiffness and force in the elements are deleted. Computationally this is straightforward requiring that these quantities not be

assembled in eqn (6). Provision has also been made to delete elements "manually" based on some other failure criterion or on engineering judgment. A complete discussion of structural failure modes for use in crash simulation is in Ref. [31].

Additional considerations

An important and necessary component of the solution strategy outlined here is the implementation of a restart capability. This capability enables an analyst to perform a crash simulation in manageable time segments. In keeping with the path dependent nature of nonlinear analysis it also allows the results of a segment in time to be carefully examined to see if they appear to be meaningful, and to see if any critical failures have occurred, before deciding if the analysis should be continued. Typically, the crash simulations that we have already performed have involved restarts for many time segments.

Another practical consideration involves graphically displaying the results of an analysis. This has been accomplished within the framework of the restart procedure by using the saved data set on the restart tape with two peripheral post-processing programs that can produce views of the deformed structure as well as time histories of displacement, velocity, and acceleration. Examples of these are shown in the next section.

AUTOMOBILE CRASH SIMULATION

A crash simulation was performed on a preliminary design concept of an automobile in a frontal impact into a rigid barrier at 30 mph. This was essentially a simulation of a test required by the U.S. Federal Motor Vehicle Safety Standards for occupant protection in frontal barrier crashes.

The structure of the vehicle body was made of primarily glass fiber/vinyl ester resin with steel members in the front end assembly and engine support structure.

A three-dimensional finite-element model was prepared, including all the mass distributions corresponding to a fully-loaded condition, as shown in Fig. 1. The body from the rear door post forward was modelled as deformable structure. Aft of the rear door post all components were lumped into a single rigid mass. The deformable body components were idealized using flat membrane triangles, straight rod segments, straight beam segments, and nonlinear springs. As to be expected, the model contained the most detail at its front end, with progressively less detail towards the rear. Only the left half of the vehicle was modelled and analyzed because of the symmetric loading and the nearly perfect symmetry of the vehicle about the longitudinal mid-plane.

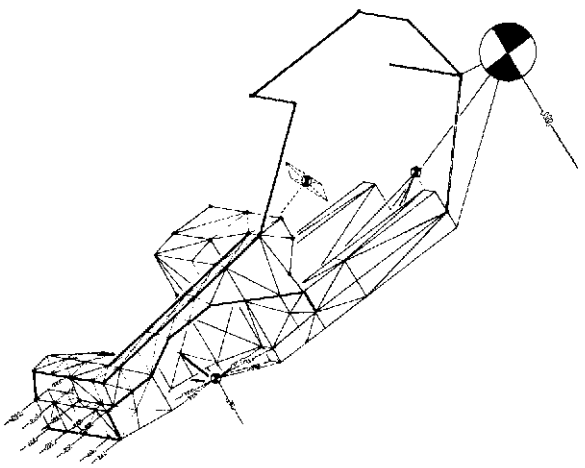

Fig. 1. Finite element model of left half of rear engined automobile.

The resulting model contained 259 nodes, 504 elements, and 663 degrees-of-freedom. Triangular membrane elements were used to form the body panels and beam elements for body stiffeners, door posts, body cross members, and roof. The beams are indicated by double lines in Fig. 1. Use of energy-dissipating nonlinear spring elements was an important consideration in the overall modelling philosophy. These elements were used to approximate the behavior of certain structural parts whose force versus deflection behavior had been obtained by test or analysis. Modelling these components in detail in order to calculate their deformation behavior would be expensive at best, even if it could be assured that the resulting model could indeed produce the essentials of the behavior. The dissipative nonlinear spring elements were used to represent the longitudinal crush behavior of the front bumper, front end energy absorbing struts, the radiator and fan assembly, the tire and wheel assembly, and the steel front cross-member. The front cross-member was formed from steel sheet. While the cross-car bending stiffness of this member was modelled by beam elements, its fore-and-aft crush was approximated with a number of nonlinear springs whose properties approximated the expected behavior.

Two energy absorbing struts were imbedded in the front end as part of an exploratory study and represented the primary load path and energy dissipating capability for front end impacts. Each of these struts was simulated by two nonlinear springs deforming at a constant force over a maximum distance of 18.5 in. These struts, if fully effective, were designed to completely absorb the kinetic energy of a 30 mph impact in 12 in.

The non-structural items were included in the model as point masses and placed in the finite element model at the node points closest to their actual locations in the vehicle. The occupants were not modelled dynamically, but the loads they imposed on the structure were accounted for in a simplified manner by adding mass to the steering wheel hub and lower instrument panel, assuming an air-bag restraint system. The suspension behavior was modelled by linear elastic springs of appropriate stiffness, one at the outer ends of the front cross-member at the wheel attachments, and one at the rear body mass, connected vertically to freely sliding ground points.

The material properties of the body structure were determined by tests on small coupons and larger panels. The panel test data were significantly different from those of the smaller coupons, and were considered more representative of the actual body panel crushing behavior. Accordingly, the stress-strain curves for the body panels were prepared primarily from the panel test data.

The computer simulations produced output data in the form of printed values of displacement, velocity,

acceleration, strain, stress, forces, and moments as well as the locations of material failures, at each time increment. Computer-generated graphical output was also produced, in the form of plots of displacement, velocity, and acceleration vs time for pre-selected points in the vehicle, and in the form of drawings of the deformed structure at selected instants during the crash event. All these output data, involving thousands of pages, were examined to evaluate the dynamic structural response of the vehicle model, and to check on the validity of the numerical calculations.

The structural deformations and damage due to the impact event are illustrated in Fig. 2 in side views at the instants of wall contact and at maximum forward motion (zero forward velocity). Only the exterior panels visible from the side are shown. At 15.4 msec, the 8-in. bumper stroke was completed, and the front edge of the body structure contacted the wall. At this instant the bumper had absorbed 7.8% of the kinetic energy, reducing the speed to 28.8 mph.

Just after body contact, the brittle body structure nearest the wall began to fail. Each succeeding body panel, as it approached the wall, experienced increasing stress, strain, and deformation, until it failed at some point before reaching the wall. The failed structural elements were automatically deleted from the model during the analysis, and they were also deleted from the computer-generated drawings of Fig. 2. The greatest portion of the wall thrust was generated by the energy-absorbing struts. Note that the front body is distorted downward near the wall, and that an overall nosedown rotation of the vehicle is visible. This was caused by the fact that the wall thrust was located at the level of the energy absorbing structure, low on the body, below the center of gravity. In fact, as time progressed, the nose dropped and the rear engine mass rose, so as to increase the offset.

The structural performance is further illustrated by the motion histories of the rear mass shown in Fig. 3. The acceleration versus time reveals the effect of key events in the front end of the structure. First a small acceleration pulse occurs during the 8 in. bumper stroke. After the body hit the wall, the acceleration rose quickly to the 40–50 g range as the energy absorbing members began to stroke. These components behind the struts had to carry the strut loads. Thus, the strut loads (and the acceleration) dropped momentarily when the steel cross-member yielded suddenly, they rose again as the strain hardening behavior of the steel halted the cross-member collapse. Similarly, when the outer supports to the cross-member failed, the strut load dropped momentarily until the central tunnel took over the full load. In spite of the local failures, the vehicle came satisfactorily to rest after 19 in. of total motion (at the rear engine), in about 65 msec, with an average deceleration of 32 g during the body crush phase. The exploratory energy absorbing struts accounted for 95% of the kinetic energy dissipated, and performed well. An alternative concept

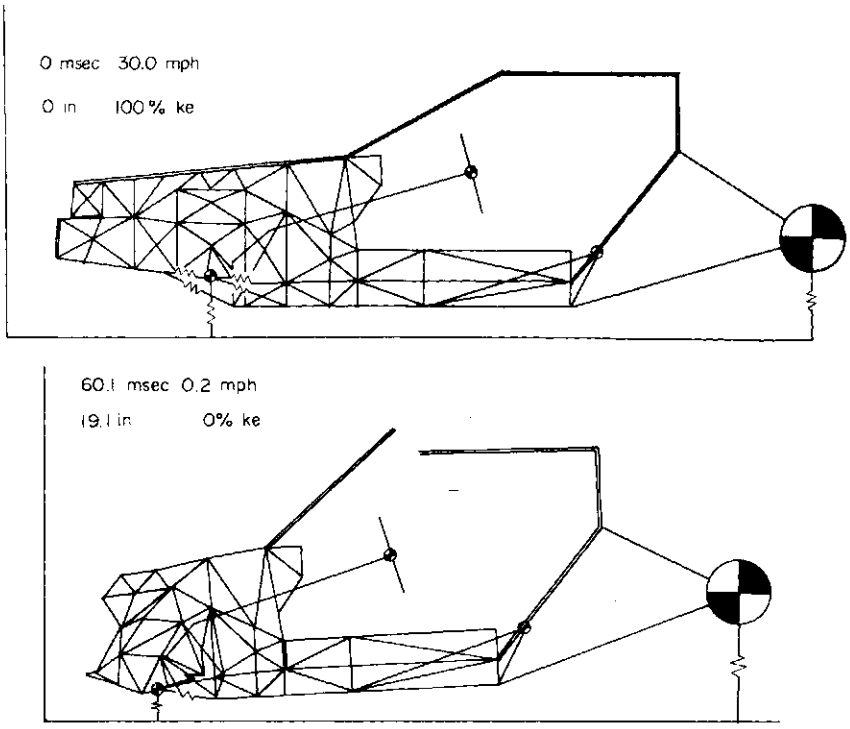

Fig. 2. Side view of model before and after impact.

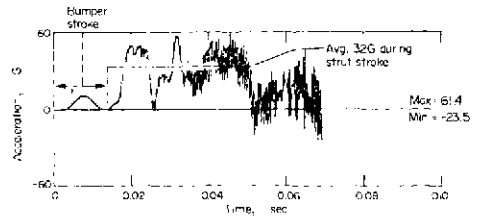

Fig. 3. Predicted acceleration history for rear body/engine mass of automobile.

would be to redesign the front end to allow a greater stroking distance in the energy absorbing structure, thereby reducing the internal loads and the average acceleration levels, while dissipating the same energy.

As a result of this analysis of the preliminary design concept, we were able to recommend certain specific changes to increase the structural integrity of the vehicle for the 30 mph frontal crash.

The simulation covered 70 msec, in 352 time steps, using 91 min computer (CPU) time on an IBM 370/168.

AIRCRAFT CRASH SIMULATION

As part of an on-going investigation of crashworthy design concepts for U.S. Army Research and Technology Laboratories and Bell Helicopter Textron, a series of crash-impact investigations are underway. At the time of this writing, the most recent one of these to be completed was a comparison of the crash responses of two helicopter cockpit sections—one of all composite material with an energy-absorbing concept, the other of conventional aluminum construction. This work was part of a project in which Bell and Grumman jointly surveyed and assessed available data and analytical methods for evaluating crash-impact characteristics of composite helicopter airframe structures. The final results of the entire project appear in Ref. [32], and a separate description of the finite-element crash simulations was presented in Ref. [17].

This preliminary study was done primarily for the purpose of exploring the applicability of the DYCAST finite-element code for crash simulation of future helicopter airframes constructed of advanced composite materials.

A cockpit section of fuselage structure (Fig. 4) of a typical troop transport helicopter was selected for analysis. Details of the two cockpit designs are shown in Fig. 5. The all-composite section incorporated an energy absorbing concept below the floor. Identical vertical impact conditions of 30 fps onto a rigid horizontal surface were used for both sections, representing the condition in which the landing gear had already reduced the initial velocity.

The metal section was taken from a representative helicopter, and the composite section was designed by Bell to replace it. The two cockpits therefore had the same overall dimensions and were designed for the same flight loads. Their floor structures were composed mainly of longitudinal beams, transverse bulkheads, an outer skin, and a floor panel covering. The roof and door posts were deep channel beams built-up from

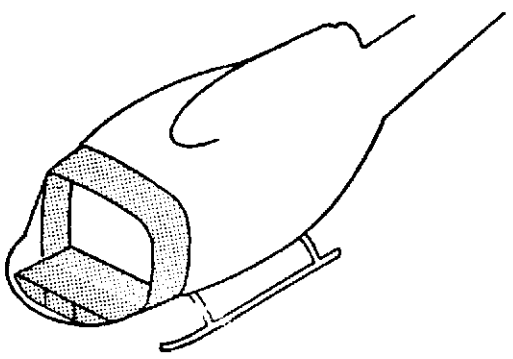

Fig. 4. Location of analyzed helicopter fuselage section.

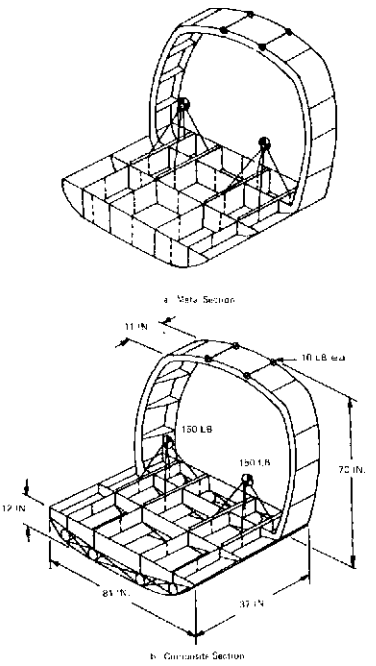

Fig. 5. Original cockpit sections, floor panels not shown.

thin webs and flanges with angle stiffeners at the corners and edges.

Both sections carried two 150 lb point masses, representing crew members, each on four rigid seat legs.

The conventional aluminum section had full depth webs on the floor beams and bulkheads. The composite section had the lower portion of the longitudinal beams replaced by hollow foam-filled tubes, while the lower parts of the bulkheads were replaced by diagonal tension straps and transverse formers attached to the skin. The tubes were PVC foam-filled, and were design to dissipate energy while being diametrally crushed.

The metal cockpit had all aluminum structure except for the titanium seat rails. The composite section had Kevlar/epoxy laminates for the beam and bulkhead webs, skins, floor covers, tube walls, and diagonal straps, while all the web caps and stiffeners were of graphite/epoxy laminates.

The finite-element idealizations of the two fuselage sections are shown in Fig. 6. Only the left half of each cockpit was modelled because of symmetry.

In the metal cockpit floor section all webs, skins, and floor covers were idealized by membrane triangles, while beam elements were used to model the web caps, stiffeners, and seat rails. Forward of the second bulkhead, the web caps and stiffeners were modelled by stringer elements because of the absence of local bending. The floor cover, crew masses, and seat legs were removed from the drawings in order to show the sub-floor details. Since the belly skin panels were expected to buckle under in-plane compression, a beam grid was added to those skin panels to account for their transverse bending stiffness. The roof frame and upper door post were modelled by a single arch of beam elements. The roof-mounted equipment masses were replaced by a single mass with rotary inertia.

The material behavior of the aluminum and titanium was represented by elastic-perfectly plastic stress-strain curves to the failure point.

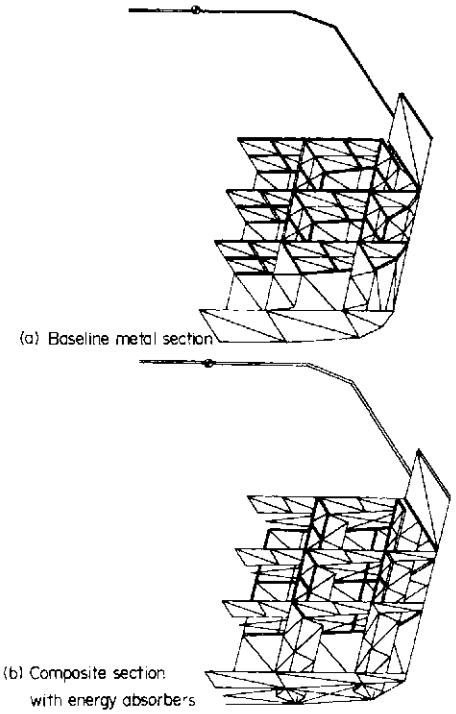

Fig. 6. Finite-element idealization of left half of cockpit sections—floor panels and crew seat are not shown.

The metal half-section model contained 111 nodes, 348 elements, and 419 degrees-of-freedom.

The composite section had the same idealization scheme, except that orthotropic membrane triangles were used. The tubes were modelled by membrane triangles to form hollow, square-diamond tube walls that could flatten as the tubes crushed. In this way, the changing values of longitudinal bending, shear, and axial stiffnesses of the tube cross section could be approximated. The vertical crush behavior of the tubes was represented by a series of vertical nonlinear spring elements inside each tube, whose force–displacement curves were derived from tests. The diagonal tension straps were modelled by nonlinear springs having no compressive stiffness; that is, as cables.

The composite laminate's material properties were represented by linear elastic stress-strain curves to failure, with no plasticity.

The composite cockpit half-section model contained 144 nodes, 422 elements, and 471 degrees-of-freedom.

The Newmark Beta numerical time integrator with variable time step was used in both cases. The aluminum section required 10 msec of event time, with 71 time steps, using 19 min (CPU) of computer time on an IBM 370/168 computer. The composite section analysis covered 30 msec, with 197 time steps, using 56 CPU min.

The vertical acceleration histories of the 150 lb rigid crew/seat masses are compared for both cases in Fig. 7. The baseline aluminum floor structure was very stiff vertically and developed little plastic deformation in this impact condition. Consequently, its potential for energy dissipation and force attenuation was not used. The composite section transmitted much less acceleration because of the crushing action of its energy-absorbing tubes. The analysis indicated a partial local failure under the inboard seat legs of the

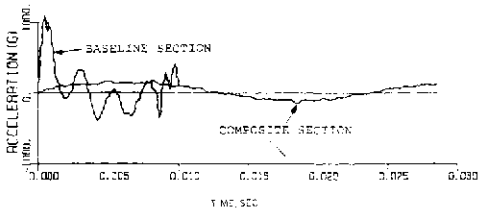

Fig. 7. Comparison of vertical accelerations of the rigid crew and seat.

composite section, which could easily be prevented by addition of vertical stiffeners to the beam webs under the legs. It is clear that for both sections, the crew compartment was sufficiently intact, but the composite section benefitted greatly from the great compliance and energy dissipation provided by the crushable tubes. Certainly, the aluminum section would also benefit from such devices. However, the composite cockpit weighed about 30% less than the metal section. Therefore, this study indicates that the use of advanced composite materials in helicopter fuselages, while greatly reducing structural weight, need not prevent the achievement of crashworthiness goals.

These results showed that DYCAST could be a useful tool for evaluating the crash performance of advanced composite helicopter fuselages.

This preliminary investigation is being followed by an investigation of the impact behavior of a more complete all-composite helicopter fuselage incorporating engine and transmission masses in the roof.

CONCLUDING REMARKS

The application of nonlinear finite element techniques to the crashworthiness evaluation of structures is a very exciting and challenging endeavor. It is an example of the maturing of theoretical techniques that have been the subject of vigorous investigation in recent years to the point of application to pertinent engineering design evaluations. However, because of the complexities of the theoretical basis of nonlinear dynamic analysis, it is important for users of these computer programs to clearly understand their underlying theories and to exercise engineering judgment in order to interpret results meaningfully. In addition, experience has shown that, while an accurate and versatile program is essential for adequate crash analysis, expertise in the "art" of modelling a vehicle for a crash analysis is also required in order to produce sufficiently accurate results with a minimum of time and cost. The results shown for the two sample analyses indicate that theoretical crash simulations can be economically used as part of the overall design process. Finally, the effort to develop a tool for crash simulation is an on-going effort so that the description of DYCAST in the paper represents an already obsolete progress report. Developments in a number of areas are continuing, driven by the requirements revealed by the increasingly more complex crash simulations underway for both aircraft and automobiles.

REFERENCES

1. K. J. Saczalski and W. D. Pilkey, Techniques for predicting vehicles crash impact response. In *Aircraft Crashworthiness* (Edited by K. Saczalski, G. T. Singley

III, W. D. Pilkey and R. L. Huston), pp. 467–484. University Press of Virginia, Charlottesville, Virginia (1975).
2. K. J. Saczalski, Modelling and computational solution procedure of prediction of structural crash-impact response. In *Finite Element Analysis of Transient Nonlinear Structural Behavior* (Edited by T. Belytschko, J. R. Osias and P. V. Marcal), AMD-Vol. 14, pp. 99–118. ASME (1975).
3. E. Alfaro-Bou, R. J. Hayduk, R. G. Thomson and V. L. Vaughan, Simulation of aircraft crash and its validation. In *Aircraft Crashworthiness* (Edited by K. Saczalski, G. T. Singley III, W. D. Pilkey and R. L. Huston), pp. 485–498. University Press of Virginia, Charlottesville, Virginia (1975).
4. R. G. Thomson and R. C. Goetz, NASA/FAA General Aviation Crash Dynamics Program *A Status Rep., AIAA/ASME/ASCE/AHS 20th Structures, Structural Dynamics and Materials Conf.*, A Collection of Technical Papers on Design and Loads, pp. 224–232 (1979).
5. G. Wittlin and M. A. Gamon, A method of analysis for general aviation airplane structural crashworthiness. In *Measurement and Prediction of Structural and Biodynamic Crash-Impact Response* (Edited by K. J. Saczalski and W. D. Pilkey), pp. 63–82. ASME (1976).
6. M. P. Kamat, Survey of computer programs for prediction of crash response and its experimental validation. In *Measurement and Prediction of Structural and Biodynamic Crash Impact* (Edited by K. J. Saczalski and W. D. Pilkey), pp. 33–48. ASME (1976).
7. D. S. Fine, Elastic-plastic finite element analysis of vehicle structural components. SAE Paper 770614, Presented at *2nd Int. Conf. on Vehicle Structural Mechanics*, Southfield, Michigan (April 1977).
8. A. K. Noor, Computer programs for solution of nonlinear structural and solid mechanics problems. In *Symposium on Computational Methods in Nonlinear Structural and Solid Mechanics* (Edited by A. K. Noor and H. G. McComb, Jr.). Pergamon Press, Oxford (1980).
9. M. P. Kamat, Nonlinear transient analysis of aircraftlike structures - theory and validation. Virginia Polytechnic Institute and State University, Blacksburg, Virginia, *Rep. VPI-E*-79-10 (1979).
10. H. Armen, A. B. Pifko and H. S. Levine, Nonlinear finite element techniques for aircraft crash analysis. *Aircraft Crashworthiness*, pp. 517–548. University Press of Virginia, Charlottesville, Virginia (1975).
11. R. Winter, A. B. Pifko and H. Armen, Crash simulation of skin-frame structure using a finite element code. *SAE paper* 770484 (1977).
12. K. S. Yeung and R. C. Welsh, Refinement of finite element analysis of automobile structures under crash loading. *Tech. Final Rep.*, Vol. II. Department of Transportation, National Highway Traffic Administration, Contract DOT-HS-6-01364 (1977).
13. R. Hayduk, R. G. Thomson, G. Wittlin and M. P. Kamat, Nonlinear structural crash dynamic analysis. *SAE Paper* 790588 (1979), SAE Business Aircraft Meeting, Wichita, April 1979.
14. B. S. Holmes, J. K. Gran, J. D. Colton, Developing a new vehicle structure with scale modeling techniques. In *Measurement and Prediction of Structural and Biodynamic Crash-Impact Response* (Edited by K. J. Saczalski and W. D. Pilkey), pp. 17–32. ASME (1976).
15. A. K. Dhalla and R. H. Gallagher, Computational methods for nonlinear structural analysis. In *ASME—Decade of Progress Design Analysis, Elevated Temperature Design Techniques* (in preparation).
16. A. Pifko, H. S. Levine and H. Armen, Jr., PLANS—A finite element program for nonlinear analysis of structures, Vol. I- Theoretical manual. *NASA CR*-2568 (1975).
17. R. Winter, J. D. Cronkhite and A. B. Pifko, Crash Simulation of composite and aluminum helicopter fuselages using a finite element program. *AIAA/ASME/ASCE/AHS 20th Structures, Structural Dynamics and Materials Conf.*, A Collection of Technical Papers on Design and Loads, pp. 233–240 (1979).
18. H. Armen, Plastic analysis. In *Structural Mechanics Computer Programs* (Edited by W. Pilkey, K. Saczalski and H. Schaeffer), pp. 103–122. University Press of Virginia, Charlottesville, Virginia (1974).
19. L. A. Hofmeister, G. A. Greenbaum and D. A. Evensen, Large strain elasto-plastic finite element analysis. *AIAA J.* **9**, 1248–1254 (1971).
20. H. S. Levine, H. Armen, R. Winter and A. Pifko, Nonlinear behavior of shells of revolution under cyclic loading. *J. Comput. Structures* **3**, 589–617 (1973).
21. K. J. Bathe, E. Ramm and E. L. Wilson, Finite element formulations for large deformation dynamic analysis. *Int. J. Numer. Meth. Engng* **9**, 353–386 (1975).
22. J. F. McNamara, Solution schemes for problems of nonlinear structural dynamics. *J. Pressure Vessel Tech., ASME* **96**, 96–102 (1974).
23. D. P. Mondkar and G. H. Powell, Finite element analysis of non-linear static and dynamic response. *Int. J. Numer. Meth. Engng*, **11**, 499–522 (1977).
24. J. A. Stricklin and W. E. Haisler, Comments on nonlinear transient structural analysis. In *Finite Element Analysis of Transient Nonlinear Structural Behavior* (Edited by T. Belytschko, J. R. Osias and P. V. Marcal), AMD-Vol. 14, pp. 157–178. ASME (1975).
25. T. Belytschko and D. F. Schoebeule, On the unconditional stability of a implicit algorithm for nonlinear structural dynamics. *J. Appl. Mech.* **97**, 865–869 (1975).
26. T. Belytschko, Transient analysis. In *Structural Mechanics Computer Programs* (Edited by W. Pilkey, K. Saczalski and H. Schaeffer), pp. 255–276. University Press of Virginia, Charlottesville, Virginia (1974).
27. J. R. Tillerson, Selecting solution procedures for nonlinear structural dynamics. *The Shock and Vibration Digest* **7** (1975).
28. H. Garnet and H. Armen, A variable time step method for determining plastic stress reflections from boundaries. *AIAA J.* **13**, 532–534 (1975).
29. N. Newmark, A method of computation for structural dynamics. *J. Engng Mech. Div., ASCE* **85**, 67–94 (1959).
30. E. L. Wilson, L. Forhoomand and K. J. Bathe, Nonlinear dynamic analysis of complex structures. *Earthquake Engng Struct. Dyn.* **1**, 241–252 (1973).
31. R. Winter, A study of structural failure modes for a computer crash simulation. Grumman Aerospace Corporation Research Department, *Memo. RM*-630 (March 1977).
32. J. D. Cronkhite, T. J. Haas, V. L. Berry and R. Winter, Investigation of the crash-impact characteristics of advanced airframe structures. U.S. Army Research and Technology Laboratories, *TR*-79-11 (Sept. 1979).

Computers & Structures, Vol. 13, pp. 287–294, 1981
Printed in Great Britain.

0045-7949/81/010287-08$02.00/0

PROJECTILE IMPACT DAMAGE ANALYSIS

W. J. STRONGE and J. C. SCHULZ
Naval Weapons Center, China Lake, CA 93555, U.S.A.

(*Received* 25 *April* 1980)

Abstract – Small, flat-fronted cylindrical steel projectiles have been fired at normal obliquity against simulated concrete and steel plate targets. Deformation measurements from these firings are compared with nonlinear finite element analysis results. For firings against simulated concrete, good agreement between analysis and experiment is obtained when an initial transient is added to a quasi-steady-state penetration theory. For firings against steel plates, large element distortions result in computational difficulties.

INTRODUCTION

An analysis technique for determining the deformation and fracture of projectiles impacting hard targets has been developed [1]. This technique involves finding an approximate pressure loading to be applied to the front of a projectile to represent forces at the target-projectile interface and then using this approximate loading in a nonlinear finite element analysis to calculate stresses and displacements in the projectile. For impact against thick targets, such as concrete half-spaces, impact forces cause breakup and flow of the target material ahead of the advancing projectile. Penetration theory equations [2] can be used to calculate these forces. For impact against thin metal plates at velocities where perforation occurs, impact forces both shear a plug from the plate and accelerate that plug to the residual velocity [3]. In some cases, these shear forces are relatively small and can be neglected.

In the present paper a series of experiments involving small, flat-fronted, cylindrical steel projectiles fired at normal obliquity against simulated concrete and steel plate targets are described. The purpose of the tests was to gather data for comparison with the above-described analysis technique. Two types of information were recovered: the impact velocities at which failure occurred (as well as an idea of the nature of the failures) and the final deformed shapes of the projectiles after the tests. This second information, in particular, has been compared directly with projectile deformations predicted from finite element analysis. Modifications to the penetration theory equations to include an initial impact pressure pulse result in good agreement between theory and experiment for the projectiles penetrating simulated concrete targets. Difficulties have been encountered with the finite element analysis of the projectiles perforating steel plates due to severe element distortion.

DESCRIPTION OF EXPERIMENTS

Projectiles

Three types of blunt, steel projectiles were fired. Their cross sectional views are shown in Fig. 1. These projectiles were all flat-fronted, hollow cylinders, 2 in. long and 0.5 in. in diameter. However, their internal geometries varied. Test projectile No. 1 (TP1) has an internal cavity with a wall thickness of 0.05 in. The front end of the cavity is flat with a radius at its outer edge less than 0.0312 in. The solid disk to the front of the cavity is 0.25 in. thick. Test projectile No. 2 (TP2) is similar to TP1 except that its cavity wall thickness is 0.075 in. Test projectile No. 3 (TP3) has the same wall thickness as TP1, but the front end of its cavity is hemispherical rather than flat. All the projectiles were machined from 4340 steel rods and were heat-treated to a Rockwell "C" hardness of 38–40.

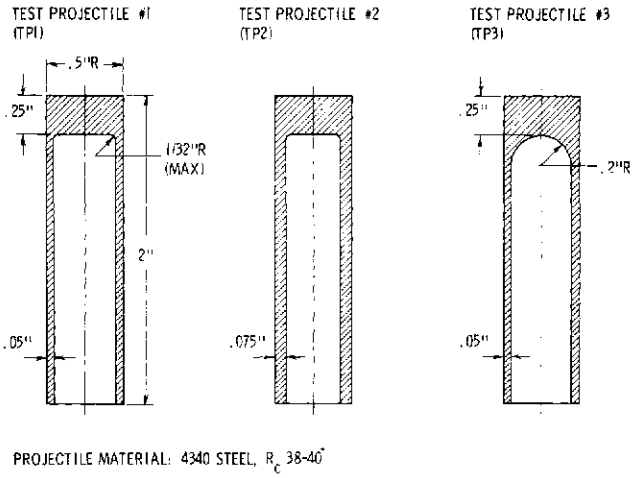

Fig. 1. Cross sectional views of test projectiles.

Targets

These projectiles were fired against two different targets: simulated concrete and steel plate.

Simulated concrete targets were made of "Thorite" (trademark of Standard Dry Wall Products), a fast-setting, high-strength concrete patching compound consisting of sand, cement, and additives to promote rapid curing. The largest sand grains are about 0.04 in. in diameter. The targets were cured for seven days before being fired into. Half were cured wet for the entire period (with their surfaces covered with water),

and half were wet-cured for 24 hr and allowed to dry-cure (with their surfaces exposed to air) for the remaining six days.

Steel plate targets were cut from 0.0625-in.-thick sheets of a hot-rolled, low-carbon steel with a Rockwell "B" hardness of 55.

Experimental procedure

The projectiles were fired from a smooth-bore, 50-caliber powder gun. Impact velocities were measured in the gun barrel with a photo diode system coupled to an interval counter. The targets were placed about 18 in. from the end of the barrel. The projectiles impacted the targets at normal obliquity. Projectiles that perforated steel plate targets were captured in a recovery trough filled with Celotex slabs placed immediately behind the targets. The apparatus is described more fully by Goldsmith and Finnegan [4].

EXPERIMENTAL RESULTS

Results against thorite targets

Thirty shots were fired against Thorite targets. The results are summarized in Table 1. Figure 2 is a photograph of selected projectiles after test.

Impact damage to the TP1 projectiles occurred predominantly near the front of the cavity where stress waves propagating from the front end encounter a greatly reduced cross sectional area. A bulge formed in this region (Fig. 2b). The average distance from the front end to the point of maximum bulging was about 0.34 in. For impact velocities above about 2150 fps the TP1 projectiles fractured. (One TP1 projectile fractured at a lower velocity of 2044 fps.) In some cases the front disk sheared completely off across the cavity side wall, and the wall then fractured longitudinally into long, thin petals (Fig. 2e). In other cases the front disk remained attached to one of the petals, resulting in a non-axisymmetric final configuration (Fig. 2d).

The TP2 projectiles also bulged just to the rear of the front disk. The average distance from the front end to the point of maximum bulging was 0.33 in. The degree of bulging for a given impact velocity was less for the TP2 projectiles due to their greater wall thickness. None of the TP2 projectiles fractured for the range of impact velocities in the tests.

The TP3 projectiles bulged further back near the transition point between the hemisphere and side wall (Fig. 2c). The average distance from the front end to the point of maximum bulging was 0.45 in. The degree of bulging that these projectiles withstood without fracture was over twice as great as for the TP1 projectiles (0.579 in. maximum bulge diameter vs 0.532 in). For the TP3 projectiles, fracture occurred at velocities above about 2600 fps (again with one exception). Impact at higher velocities resulted in shearing off of the front portion (back to the hemisphere-to-side-wall transition) and peeling back of the rear portion into several short, stubby petals (Fig. 2f). There was a tendency for some of the petals to break off. It is apparent that the hemispherical cavity front is effective in increasing the impact velocity at which projectile fracture occurs.

Table 1. Summary of results for projectile firing against thorite targets

Proj. type	Target cure	Impact velocity, fps	Penetration depth, in.	Bulge diameter, in.	Fracture description
TP1	Wet	1745	2.66	.512	...
TP1	Dry	1750	3.2	.519	...
TP1	Dry	1900	3.4	.521	...
TP1	Wet	1910	3.19	.517	...
TP1	Dry	2044	2.9	..	Non-axisymmetric
TP1	Dry	2044	3.9	.529	...
TP1	Wet	2090	3.66	.525	...
TP1	Wet	2105	3.65	.518	...
TP1	Dry	2140	3.4	.532	...
TP1	Dry	2145	3.75	.531	...
TP1	Wet	2150	2.38	..	Long petals
TP1	Dry	2170	3.4	..	Non-axisymmetric
TP1	Wet	2370	2.19	..	Long petals
TP1	Dry	2370	2.6	..	Long petals
TP2	Wet	1830	3.94	.503	...
TP2	Wet	1990	4.72	.505	...
TP2	Wet	2130	4.69	.510	...
TP2	Dry	2190	5.1	.511	...
TP2	Wet	2390	6.84	.513	...
TP2	Dry	2630	6.75	.517	...
TP3	Wet	1930	3.75	.515	...
TP3	Wet	2140	4.44	.515	...
TP3	Wet	2270	4.78	.527	...
TP3	Wet	2435	4.19	.552	...
TP3	Dry	2510	2.94	..	Stubby petals
TP3	Dry	2570	4.28	.579	...
TP3	Wet	2580	4.84	.568	...
TP3	Dry	2600	3.41	..	Stubby petals
TP3	Dry	2720	3.53	..	Stubby petals
TP3	Dry	2955	3.09	..	Stubby petals

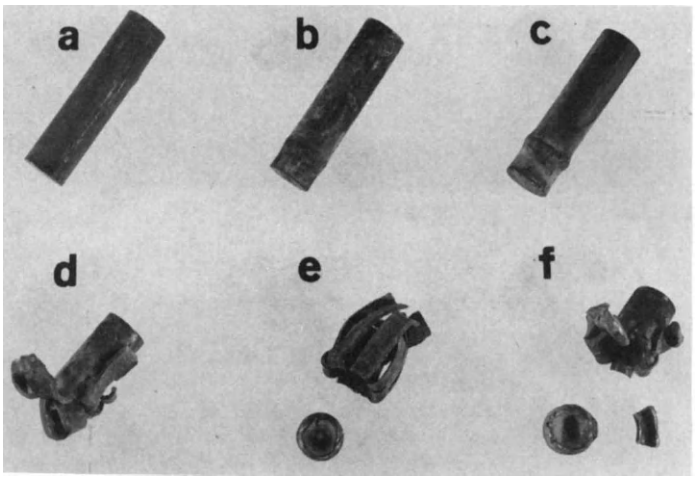

Fig. 2. Photograph of selected projectiles fired against thorite targets. (a) Unfired TP1; (b) TP1 at 2140 fps; (c) TP3 at 2580 fp; (d) TP1 at 2170 fp; (e) TP1 at 2370 fp; (f) TP3 at 2720 fp.

Results against steel plate targets

Twenty-one shots were fired against steel plate targets. The results are summarized in Table 2. Figure 3 is a photograph of selected projectiles after test. As indicated in the table some of the shots yawed coming out of the gun or hit the recovery trough and are of questionable value.

Table 2. Summary of results for projectiles fired against steel plate targets

Proj. type	Impact velocity, fps	Description of projectile after test
TP1	1685	Front bulged.
TP1	1800	Front bulged.
TP1	2025	Front bulged, projectile yawed, deformation not axisymmetric.
TP1	2060	Front bulged, spall at rear of front disk.
TP1	2180	Incipient circumferential fracture near rear of disk, spalled piece wedged in cavity.
TP1	2430	Crack around half of outside circumferene at rear of disk, spalled, central portion of front fractured.
TP1	2640	Front disk almost sheared out, two .25-inch longitudinal cracks in side wall, may have hit recovery trough.
TP1	2670	Crack around half of outside circumference, front fractured, spalled, part of spalled piece recovered.
TP2	1990	Front bulged, spalled piece wedged in cavity.
TP2	2200	Front end fractured, spalled.
TP2	2440	Front end fractured, spalled.
TP2	2500	Front end mashed on one side, can see light through small cracks, spalled, projectile yawed up, deformation not axisymmetric.
TP2	2640	Front end fractured, hole through disk, spalled.
TP2	2870	Front end mashed on one side, spalled, hit recovery trough.
TP2	2900	Front end mashed on one side, spalled, hit recovery trough.
TP2	3080	Front end mashed on one side, spalled, hit recovery trough.
TP3	1670	Front bulged, second bulge at rear of hemisphere.
TP3	1910	Front bulged, second bulge at rear of hemisphere.
TP3	2330	Front bulged, second bulge at rear of hemisphere.
TP3	2640	Front bulged, central portion fractured, second bulge at rear of hemisphere.
TP3	2930	Front bulged, central portion fractured, second bulge at rear of hemisphere.

The TP1 projectiles bulged at the front end (Fig. 3b). There was no distinct bulge to the rear of the front disk as was the case for penetration into Thorite. At higher velocities the amount of bulging increased and was accompanied by fracturing of the central portion of the front end. Characteristically, a number of tensile cracks could be seen criss-crossing the fractured region, presumably due to mushrooming or spreading out of the front end. In addition, the higher impact loads caused a disk-shaped piece to spall off the rear of the front disk. (One such spalled disk, actually from a TP2 projectile, is shown in Fig. 3d.) At still higher impact velocities a circumferential crack appeared at the rear of

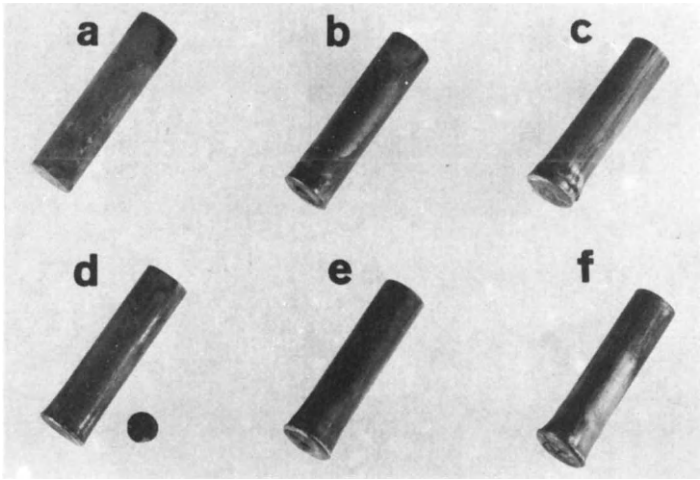

Fig. 3. Photograph of Selected Projectiles Fired Against Steel Plate Targets. (a) Unfired TP1; (b) Tp1 at 1655 fps; (c) TP1 at 2430 fps; (d) TP2 at 2200 fps; (e) TP2 at 2640 fps; (f) TP3 at 2930 fps.

the front disk (Fig. 3c). In some instances the front disk was almost sheared off.

The TP2 projectiles behaved in a similar fashion except that due to the increased side wall thickness no circumferential crack formed at the rear of the front disk and visible damage was confined to the central portion of the front disk. In one case (Fig. 3e), fracturing was so severe that a hole about 0.0625 in. in diameter was formed through the front disk.

In addition to bulging at the front end, the TP3 projectiles also bulged at the hemisphere-to-side-wall transition, about 0.45 in. from the front end (Fig. 3f). At higher velocities fracturing of the central portion of the front end occurred, similar to the TP1 and TP2 projectiles, but no fracturing was observed at this second bulge. Furthermore, there was no apparent spalling at the front of the hemispherical cavity. Again, the hemispherical front end would appear to be desirable for enhancing warhead survivability.

COMPARISON OF EXPERIMENTAL RESULTS WITH ANALYSIS

Penetration into thorite targets

The penetration theory of Bernard and Creighton [2] was used to determine forces acting on a projectile. Application of this theory to a projectile penetrating concrete has been described in [1]. A similar approach been adopted here.

Use of the theory requires a knowledge of several target material properties. In particular, the cohesion (taken as one-half the ultimate compressive stress), the index of rigidity (defined as the reciprocal of the maximum deviatoric strain at failure), and the density are required. In an attempt to determine these quantities for Thorite, compression tests in an Instron machine were made of cylindrical test specimens, 4 in. long and 2 in. in diameter, prepared at the same time as the targets. These tests yielded an unreasonably low value for ultimate stress (around 2500 psi). This may have been because the specimens had too many voids in them. In any case rather than use this questionable experimental value, a compressive strength supplied by the manufacturer (3910 psi) was used in the analysis. Our experimental compression test data were used, however, to estimate the index of rigidity, since no other data were available. Within the range of these tests, penetration theory results are relatively insensitive to the index of rigidity.

The theory of Bernard and Creighton applies to conical-nosed projectiles, while the projectiles tested here are flat-fronted. Experiments with small cylindrical, flat-fronted projectiles fired into plaster of paris or simulated concrete targets [5] have shown, however, that conical caps of target material form on the front of blunt projectiles shortly after initial impact. These caps are carried along by the projectiles as they penetrate. The presence of these caps means that flat-fronted projectiles become effectively conical-nosed during penetration and can be analyzed using this theory. For the projectiles analyzed here, the cone half-angle was assumed to be 45 degrees.

The property values used in determining force-time histories and penetration depths for the three test projectiles against Thorite targets are given in Table 3.

A plot of penetration depth versus impact velocity is given in Fig. 4. Experimental points are shown only for those projectiles that did not fracture. The filled points are for impacts against wet-cured targets, while the non-filled points are for impacts against dry-cured targets. There is no apparent effect of type of cure on the penetration results. Also shown are lines corresponding to penetration theory calculations for the three types of projectiles. Agreement between theory and experiment is reasonably good. For the three highest velocity TP3 projectiles the experimental penetration depths are considerably less than theoretical predictions. This difference may be associated with the extreme bulging of these projectiles. Bulging may have increased their resistance to penetration.

Bulging against thorite targets

Finite element analyses of the projectiles were carried out in a manner similar to [1]. The penetration resistance force as a function of time for a given impact velocity was applied to the finite element model of a projectile in the form of a normal pressure uniformly

Table 3. Property values for penetration calculations.

Target density, lb sec^2/in^4	.000198
Cohesion, psi	1955
Index of rigidity	80
Cone half-angle, deg	45
Projectile radius, in	.25
TP1 projectile mass, lb sec^2/in	.000122
TP2 projectile mass, lb sec^2/in	.000161
TP3 projectile mass, lb sec^2/in	.000125

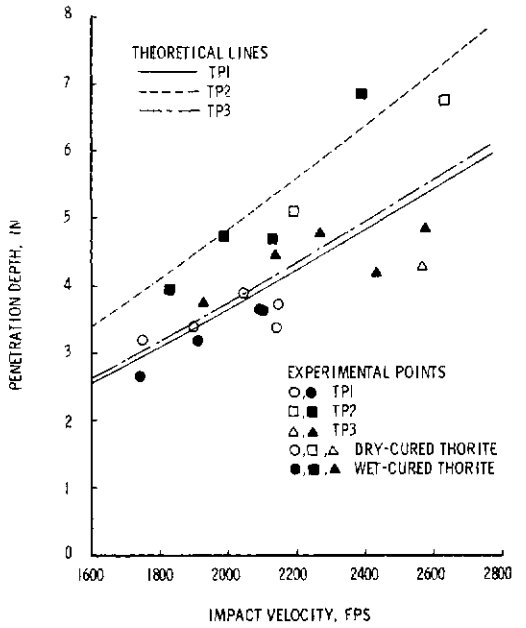

Fig. 4. Penetration depth for test projectiles fired against thorite.

distributed over the front end. Program HONDO II [6] was used for the analyses. Runs were made for a time of 500 m sec (longer in a couple of instances to ensure that all plastic deformation had occurred). The material properties used for the 4340 steel projectiles are given in Table 4.

Table 4. Material properties for 4340 steel projectiles

Elastic modulus, psi	30,000,000
Poisson's ratio	.3
Yield stress, psi	150,000
Density, lb sec^2/in^4	.000733

A plot of cavity bulge height versus impact velocity is given in Fig. 5. Again, there is no apparent difference in the results for the two types of cure. Theoretical points for the three projectiles at an impact velocity of 2400 fps (the circled points) are also shown. It is apparent that the amount of bulging predicted for these three projectiles is much less than actually measured. An explanation for this discrepancy and a modification to the analytical procedure that improves the comparison have been developed.

Improved penetration theory including initial pressure

The Bernard and Creighton penetration theory is for conical-fronted projectiles. At the moment of initial impact, however, the test projectiles are flat-fronted. A certain period of time is required before a cone is formed and the conical penetrator model is valid. During this initial period forces on the front of the projectile are very large. An estimate for the peak impact pressure can be obtained from plane wave theory ([7], p. 66).

$$p_I = \rho c u \tag{1}$$

where ρ is the target density, c is the wave speed for compressive forces in the target, and u is the impact velocity of the projectile. The duration of this load pulse, t_I, can be taken as the time for a disturbance to travel from the front end of the projectile to the surface of the cone formed on its front, or

$$t_I = \frac{r}{2c} \tag{2}$$

The loading applied to the front of the projectile during this initial pulse can then be represented as a rectangular pulse of magnitude p_I and duration t_I. This pulse will reduce the velocity of the projectile by an amount

$$\Delta V = \pi r^2 p_I t_I / m \tag{3}$$

where r is the projectile radius and m its mass. If this amount is subtracted from the original impact velocity, the new impact velocity can be used in the penetration theory equations to calculate the force-time curve. The total loading will then consist of the initial pulse plus this force-time curve.

Curves corresponding to the new initial pulse loading are also shown in Fig. 5. Agreement with experimental results is now quite good despite the gross assumptions made in determining the initial pulse. It is significant that agreement is so consistent for all three projectiles over the entire range of test velocities.

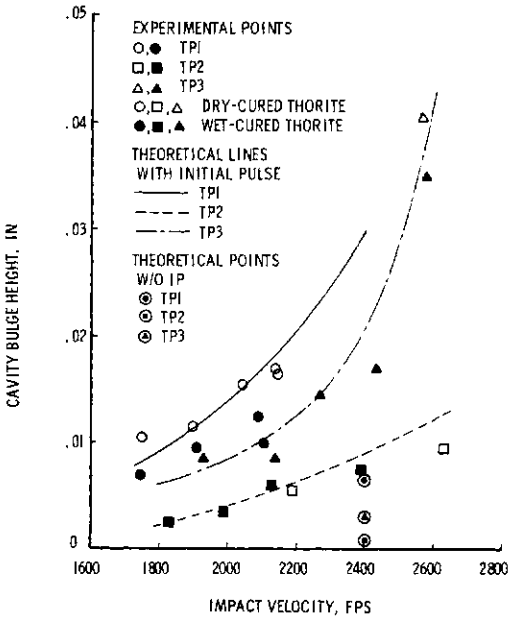

Fig. 5. Cavity bulge height for test projectiles fired against thorite

In addition to bulging near the front of the cavity, the test projectiles also bulged at their front ends. Measurements of the front bulged diameters were made. A plot of front bulge height versus impact velocity is shown in Fig. 6. The experimental points show considerable scatter. It is possible that the front bulge may be sensitive to a very slight degree of impact obliquity. also shown are theoretical lines corresponding to the initial pulse loading. The lines are almost coincident, indicating that the front bulge is not dependent on the cavity geometry. The agreement between theory and experiment in this case is still fairly good considering the amount of scatter. The experimental points on the figure reveal a dependence of front bulge height on type of cure, the degree of bulging being greater for wet-cured targets. Apparently, the type of cure affects material properties primarily near the surface (where the front bulge is formed), and to a lesser extent inside the material so that the penetration depth and height of the cavity bulge (which depend on the entire penetration path) are not different.

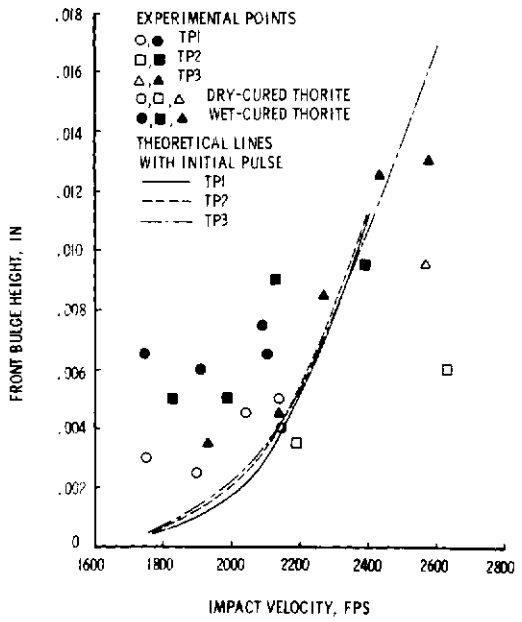

Fig. 6. Front bulge height for test projectile fired against thorite.

The final deformed shapes of the finite element models of the three projectiles using the initial pulse loadings corresponding to an impact velocity of 2100 fps are shown in Fig. 7. The final deformed shape for the TP3 projectile at 2600 fps is also shown. In addition to quantitative agreement with experimental bulge heights, these shapes also agree quite well qualitatively with the overall shapes of the projectiles as shown in Fig. 2.

Use of the initial pulse loading curve will change the theoretical penetration depth versus impact velocity lines shown in Fig. 4. The amount of this change, however, is small, amounting in effect to a shift of the lines by about 100 fps in the direction of increasing velocity. This would, if anything, result in slightly better agreement between analysis and experiment.

Bulging against steel plate targets

An approximate loading to be applied to the front end of a projectile to represent impact with a steel plate target can be derived based primarily on the assumption that the forces applied are associated with the acceleration of the punched-out disk of plate material up to the speed of the projectile and that the strength of the steel can be neglected [8]. For an impact velocity of 1700 fps (approximately the lowest test velocity) the impulse required for this acceleration can be calculated as 0.182 lb sec. The time of application of this impulse can be taken as roughly twice the transit time for a stress disturbance to propagate across the thickness of the plate, about 0.625 msec. A force-time curve yielding the calculated impulse can be obtained by assuming a constant force for this time interval with 5 msec half-sine transient added at each end to smooth out the loading slightly. If this force is applied as a uniform pressure over the front end the maximum applied pressure is 980,600 psi.

Difficulties were encountered in the finite element analysis of test projectiles using this loading. Due to the very high pressure applied, extreme plastic deformation of the front ends occurred. After about 2 msec, the elements at the front outer edge became so distorted that the solution stopped. In order to force a longer time solution, a nonuniform pressure distribution over the front end was tried. Specifically, a sinusoidal distribution was assumed with the pressure at center twice the pressure at the outer edge. This reduced the amount of deformation at the outer edge and allowed the solution to proceed. Final deformed shapes for the TP1, TP2 and TP3 projectiles perforating 0.0625-in. steel plate at 1700 fps using this sinusoidal load distribution are shown in Fig. 8. Analytical bulge heights and measured heights for TP1 and TP3 projectiles fired at 1685 and 1670 fps respectively are compared in Table 5. No measurements were made for a TP2 projectile because none was fired at that low a velocity. The front bulge heights were measured immediately to the rear of the lip, and for the TP2 projectile the analytical cavity bulge height was taken as the radial displacement 0.25 in. from the front end.

The experimental bulges are considerably less than the analytically determined ones, indicating that the analytically determined loading is too severe. Nevertheless, there is fairly good qualitative agreement between theory and experiment for the TP1 and TP3 projectiles. The lip that forms at the front outer edge and the severe distortion of the elements in this region are apparent. Most of this lip would be sheared off of an actual test projectile.

Finite element analysis of projectiles at higher impact velocities does not appear feasible using program HONDO II. Even with a sinusoidal pressure distribution, solutions would probably stop prematurely at higher velocities as element distortion increases. Also, the use of an engineering property description of the steel rather than an equation of state representation is questionable at the extremely high pressure levels encountered.

CONCLUSIONS

The purpose of the experimental work described here was to provide data for comparison with analytical results. The results indicate that the Bernard and

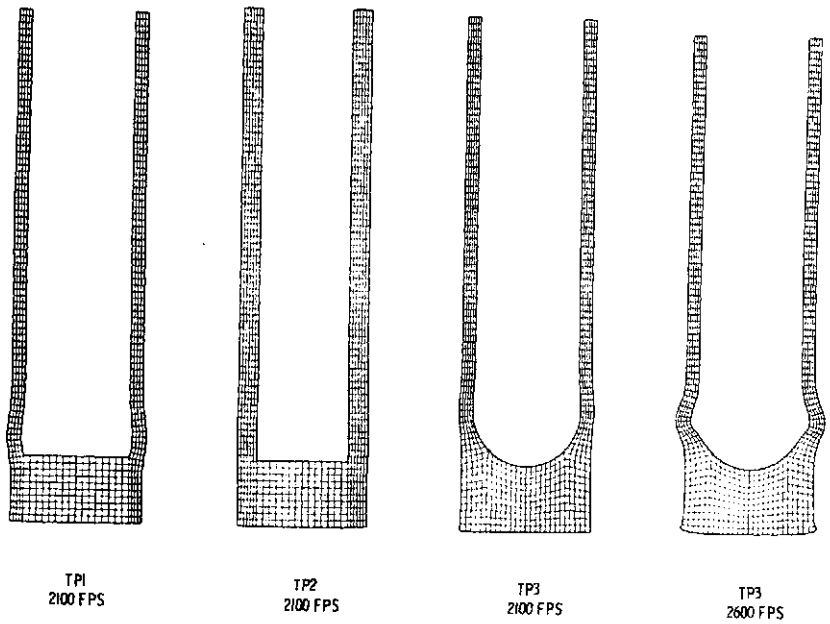

Fig. 7. Final deformed shapes of finite element models of test projectiles penetrating into thorite.

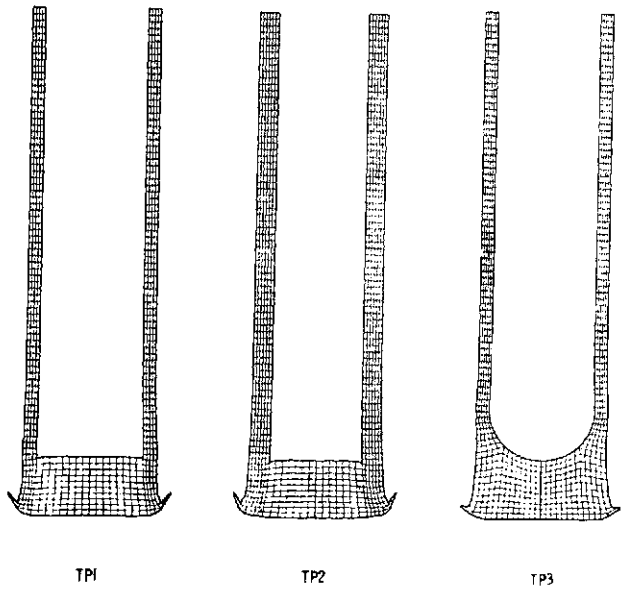

Fig. 8. Final deformed shapes of finite element models of test projectiles perforating steel plates at 1700 fp.

Table 5. Bulge height comparison for projectiles perforating steel plates.

Project type	Front bulge height, in.		Cavity bulge height, in.	
	Experiment	Analysis	Experiment	Analysis
TP1	.0195	.0282	.0065	.0101
TP2	...	.0407	...	.0113
TP3	.0165	.0271	.004	.0074

Creighton penetration theory for conical projectiles can be used for blunt projectiles impacting half-space targets at normal obliquity if an initial impact pulse is added to the theory. This initial pulse is related to the formation of a conical cap of target material on the front of the blunt projectile. With this integrated penetration force theory, the HONDO II program predictions of residual shapes of plastically deforming projectiles were in good agreement with experimentally observed values. For perforation of steel plate targets, larger local deformation at the impact surface of the projectile caused analytical difficulties for HONDO II.

Acknowledgements—The authors would like to thank S. A. Finnegan and K. G. Whitham for conducting the firings and assisting in preparation of the targets.

REFERENCES

1. J. C. Schulz, Finite element analysis of a kinetic energy warhead penetrating concrete. In *Proc. 4th Intl. Symp. on Ballistics*, Monterey California, Oct., 1978. (Sponsored by American Defense Preparedness Association.) Publication UNCLASSIFIED.
2. R. S. Bernard and D. C. Creighton, *Projectile Penetration in Earth Materials: Theory and Computer Analysis*. Defense Nuclear Agency, Washington, D.C., Nov. 1977. (*Contract Rep.* S-76-13, publication UNCLASSIFIED.)
3. W. Goldsmith and M. E. Backman. The mechanics of penetration of projectiles into targets. *Int. J. Engng Sci.* **16**, 1–99 (1978).
4. W. Goldsmith and S. A. Finnegan, Penetration and perforation processes in metal targets at and above ballistic velocities. *Int. J. Mech. Sci.* **13**, 843–866 (1971).
5. M. W. Backman, S. A. Finnegan and K. G. Whitham, Displacement patterns and cap formation in the penetration of concrete simulants by long rods of blunt nose shapes. In *Proc. DEA-G-1060 Ballistic R&D Meeting*, NWSC, Dahlgren Virginia, 25–28 April 1978. Vol. 1, p. TB-v-1, publication UNCLASSIFIED.
6. S. W. Key, Z. E. Beisinger and R. D. Krieg, *HONDO II, a Finite Element Computer Program for the Large Deformation Dynamic Response of Axisummetric Solids*. Sandia Laboratories, Albuquerque, New Mexico, (1978). (*Sandia Laboratories Rep. SAND*78-0422, publication UNCLASSIFIED.)
7. M. E. Backman, *Terminal Ballistics*. Naval Weapons Center, China Lake, California, Feb. 1976. (*NWC Tech. Publication* 5780, publication UNCLASSIFIED.)
8. J. C. Schulz, *Finite Element Analysis of a Steel Canister Perforating a Steel Plate*. Naval Weapons Center, China Lake, California, Jan. 1978. (*NWC Tech. Memo.* 3345, publication UNCLASSIFIED.)

Computers & Structures, Vol. 13, pp. 295–301, 1981
Printed in Great Britain.

0045-7949/81/010295-07$02.00/0

NONLINEAR ANALYSIS OF A MITIGATING STEEL NOSE CONE†

M. L. CHIESA and M. L. CALLABRESI
Analytical Mechanics Division 8121, Sandia National Laboratories, Livermore, CA 94550, U.S.A.

(*Received* 11 *May* 1980)

Abstract—The ability of a structure to mitigate energy associated with impacting hard surfaces plays a significant role in the design and survivability of internal components. This paper summarizes the design and analysis of an efficient nose cone for impacting rigid surfaces. A two-dimensional finite element quasi-static model, utilizing large displacement, large strain formulations, contact-impact surfaces and elastic-plastic material models, was used in the design-iteration phase of the study. Results from the analyses agreed with experimentally tested scaled nose cones, thus permitting the design changes which resulted in an efficient structure for axisymmetric loading to be completed in minimal time. A three-dimensional explicit, dynamic, finite element program was used in the evaluation of an asymmetrical static crush. The solution, obtained on a CRAY-1 computer also agreed extremely well with experimental tests. Efforts to model the material property variation with strain rate led to encouraging results and more work will be required in this area.

INTRODUCTION

Various parts of a modern strategic bomb are designed to mitigate considerable energy when impacting a hard surface in order to ensure the survivability of the internal components. Unfortunately, many factors affect the design of each part and their interactions can only be clearly understood through a detailed analysis. The present study concerns the design and analysis of a mitigating nose cone or frontal section of a 1000 k bomb, delivered as shown in Fig. 1.

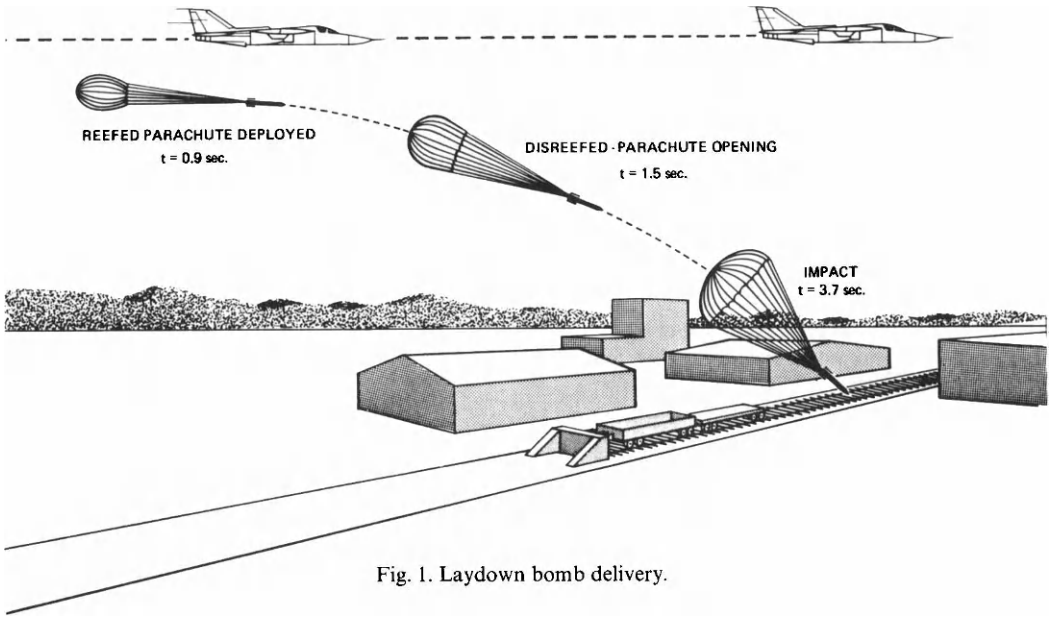

Fig. 1. Laydown bomb delivery.

This study was initiated when the impact requirements placed on the bomb were changed requiring the nose cone to absorb significantly more kinetic energy. Based on previous experience, the time required to fabricate and test a particular redesign would be approximately four months. Therefore, it was felt that if an analytical approach could be used to optimize the design, a reliable nose design could be obtained in much less time. The analysis would also provide a means to better understand how certain design changes affect energy absorption.

The design conditions limits the crush displacement of the nose cone and the peak deceleration of the bomb when it impacts a rigid surface. The impact conditions selected for this study were the head on, symmetric condition, and an oblique impact of ten degrees from the centerline axis. In order to minimize the changes associated with a redesign, the nose section was still required to be machined from a 21-6-9 stainless steel forging using the same exterior contour. Therefore, only the interior contour and the shape of the external sliding inhibitors (commonly referred to as teeth) could be significantly modified.

†Work supported by the U.S. Dep. of Energy under Contract DE-ACO4-76DP00789.

The analytical design approach selected for optimizing the nose configuration consisted of first using a two-dimensional model for the axisymmetric load case and verifying the analytical results through scale model testing. These scale model tests would be tested at a slow load rate thereby eliminating any strain rate effects exhibited by the material. Once the two-dimensional model was verified, the nose cone would be optimizied for the symmetric load case. A three-dimensional analytical model of the optimized nose would then be analyzed for the oblique load case in order to evaluate the optimized design when subjected to nonsymmetric loadings. A scale model static test simulating the oblique load would be used to verify the three-dimensional analysis. After the optimized nose design, subject to low strain rates, was verified, the efficiency of the design for impact loading conditions would be evaluated using both dynamic numerical analysis and scaled dynamic tests.

TWO-DIMENSIONAL ANALYSIS

The analytical design-iteration program was implemented using a two dimensional finite element computer program to model the nose section of the bomb. This symmetric impact case was studied first since a two-dimensional model allowed quick evaluation of proposed designs. To eliminate the strain rate effects, verification tests, in which the nose tip was crushed 1.35 in. at a rate of 0.1 in./min, were used to provide the data to be simulated by the two-dimensional static analysis.

The two-dimensional model was analyzed using GNATS [1], a general nonlinear finite element program for quasi-static two-dimensional structures. The program used a total Lagrangian [2–4] formulation for describing the equilibrium of a body in the displaced position. At each iteration, Green's strains are computed from the total displacements using the Green–Lagrange strain-displacement equations. An Almansi strain increment, calculated by transformation of the Green strain increment, is then input into the material subroutines to obtain a Cauchy stress increment. The program then iterates using a full Newton scheme until the equilibrium equation has converged to a prescribed tolerance.

An efficient numerical material model, developed by Krieg [5], for time independent plasticity has been incorporated into the GNATS code. This material model allows the inelastic material behavior to be modeled by several different functions. A very close numerical fit to the experimental true stress–strain curve for 21-6-9 stainless steel, shown in Fig. 2, was obtained using the following function:

$$\bar{\sigma} = \sigma_y + R_1(\varepsilon_p)^{R_2} + R_3 \tan^{-1}(R_4\varepsilon_p)$$

where $\bar{\sigma}$ is the effective stress, σ_y is the yield stress, ε_p is the effective plastic strain, and R_1, R_2, R_3, R_4 are constants which were determined from a nonlinear least squares fit of experimental data.

Implementation of a contact-impact algorithm using a modification of work by Hallquist [6, 7] was required so that the contacting tooth problem during loading could be solved. The algorithm, based on a penalty function formulation, allows sliding of arbitrary mesh lines regardless of differences in materials or mesh density of the two contacting surfaces. At each

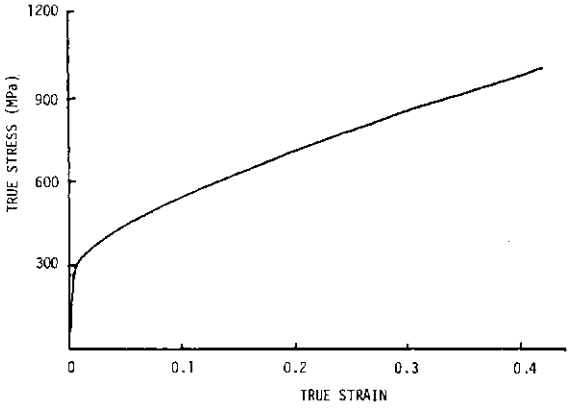

Fig. 2. Stress–strain curve for 21-6-9 stainless steel.

iteration, nodes lying on user defined sliding interfaces are tested for penetration by a series of vector cross and dot products. For each node that has penetrated, a linear spring is inserted that couples the penetrating node with the two nearest nodes on the opposite interface and a resisting force, proportional to the depth of penetration, is applied to each of the three spring nodes.

The solution is moderately sensitive to the spring stiffness, which can be input by the user or internally calculated using the bulk modulus of the material. The amount of penetration can become excessive if a low stiffness is used and numerical problems can arise when using a very high stiffness. Although the formulation results in slower convergence, larger bandwidths and does not entirely preclude penetration, it is logistically simple to implement into implicit codes and yields excellent results.

The finite element mesh, shown in Fig. 3, was used in modeling the axisymmetric static crushing. Complicated geometry definition and significant bending required 591 nodes and 165 eight-node isoparametric quadrilaterals to accurately describe and analyze the problem. In addition, sizable geometry changes and bending necessitated the use of five elements through the thickness. The initial half-bandwidth of the problem was increased from 40 to 58 by the inclusion of three

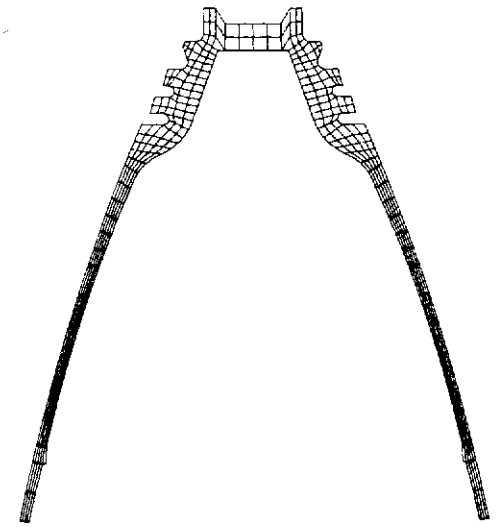

Fig. 3. Axisymmetric finite element mesh used in two-dimensional analysis.

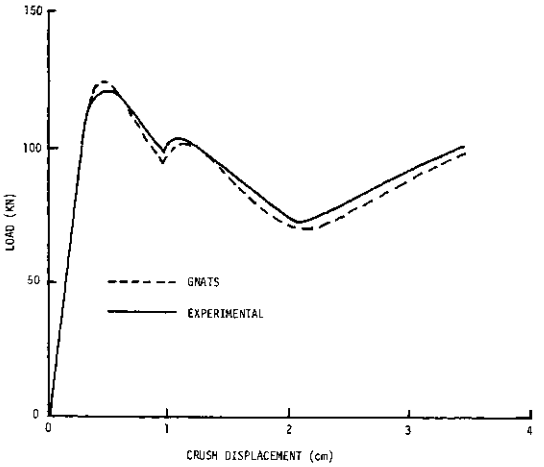

Fig. 4. Two-dimensional analytical experimental static load-crush curves.

sets of sliding interfaces (which were required at each contacting tooth).

Two-ninths scale test units of several intermediate design iterations were manufactured and statically tested. The excellent agreement between experimental and analytical results, depicted in the load-displacement curve (force required to crush the nose versus crush displacement) shown in Fig. 4, resulted in the curtailment of experimental tests and complete reliance on the computer analyses. Results from an intermediate iteration are shown in Fig. 4 as this was the last design in which accurate stress–strain material data from a nose forging was available. Comparisons of the final design were also excellent although a slight deviance was attributable to material property changes (primarily a change in the yield strength due to modifications in the heat treatment). The initial teeth shape and inner contour were significantly changed, based on the computer analyses of more than 40 design iterations, until an optimum nose design was obtained. The analytical deformation history of the static axisymmetric loading is pictured in Fig. 5 and the final

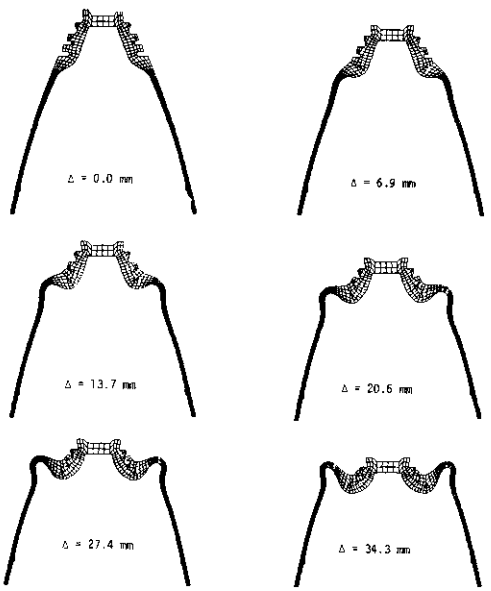

Fig. 5. Deformation history of axisymmetric analysis.

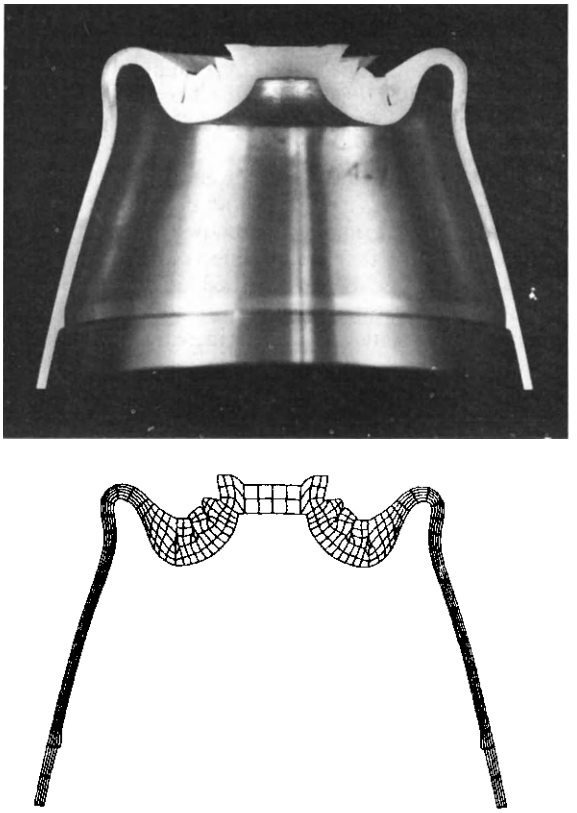

Fig. 6. Comparison of experimental and GNATS final deformed shapes.

displaced shape of the computer analyzed optimized nose is compared in Fig. 6 with a photograph of the scaled test unit.

In an attempt to more accurately describe the actual impact conditions, two-ninths scale test units were tested dynamically using a drop table with a scaled mass, simulating the weapon, from a height calculated to provide the kinetic energy required to be absorbed by

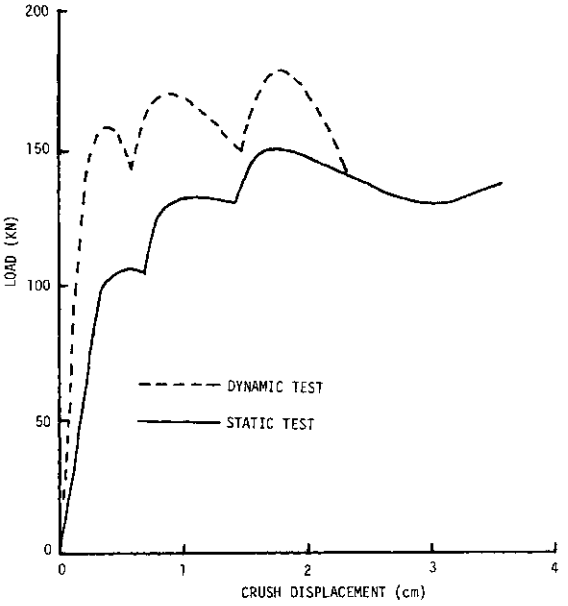

Fig. 7. Load-crush curves of dynamic and static axisymmetric tests.

the nose. Dimensions and masses were scaled so that stresses, time and thus strain-rates were identical in the full and two-ninth scale models. A computer analysis of a full scale nose verified that the load-displacement curve of the smaller nose would scale as the theory predicts.

The load-displacement curve from the axisymmetric dynamic test is shown in Fig. 7 with the curve from the static test. The maximum rigid body deceleration was increased 22% by the dynamic effects and the deceleration at the first peak increased 56%. Frequency calculations indicated that the loading could be assumed quasi-static and that the increase in load must be attributable to the strain-rate sensitivity of the material. An attempt was not made at this point to analytically solve the strain-rate problem on the two-dimensional model.

Average solution time for the two-dimensional model was 1800 central processor seconds per analysis with approx. 300 equilibrium iterations. New designs based on changes from results of the previous design could thus not only be evaluated within two days via the computer, but also resulted in significant cost savings. The time to reach an optimum design was reduced from possibly years to only several months.

THREE-DIMENSIONAL ANALYSIS

Since the probability of vertical impact is small, a combined experimental and analytical test program was initiated to study the relationship between angle of attack and amount of kinetic energy absorbed. Scaled nose cones were tested statically by crushing at an inclined angle of 10° from vertical while the three-dimensional impact problem was numerically modeled using three-dimensional brick finite elements. Due to problem size and complexity, the choices of computer codes available for the analysis were limited. The requirements, similar to those of the two-dimensional model, were large strain, large displacement, three-dimensional contacting interfaces and elastic-plastic material model capabilities. The three-dimensional dynamic explicit code DYNA3D [8] was selected to analyze the problem as it was the only finite element computer program that met the requirements and could solve the problem in a reasonable length of time. An explicit dynamic code was used because of the unavailibility of an acceptable three-dimensional static implicit code and because of the large bandwidth that would have been generated. DYNA3D, programmed to take full advantage of vector optimization on the CRAY-1 (a Class VI machine) executes at less than 0.67 CPU (central processor units) minutes per million mesh cycles. Usage of only eight node bricks and one point integration in element stiffness calculations significantly reduce core memory requirements and permit the solution of very large three-dimensional structures.

The nose cone mesh consisted of 4356 eight node bricks and 6074 nodes as shown in Fig. 8. The final two rows of elements, containing a very dense material (131 kg/cm^3), was used to model the mass of the aft section. Five sets of sliding interfaces were required in the model, three for the contacting teeth and two sets of tied interfaces that allow a reduction in mesh density. One tied interface is used near the base to allow a reduction from four to three elements through the thickness and another tied interface near the tip to prevent irregular or wedge shaped elements. The material was modeled by a bilinear isotroptic hardening law, further reducing computational time by increased optimization of the vector calculations, although this method results in reduced accuracy for small plastic strains. The two-ninths scale nose was impacted into perfectly rigid and frictionless wall, modeled by the large one element block shown in Fig. 8, with an initial

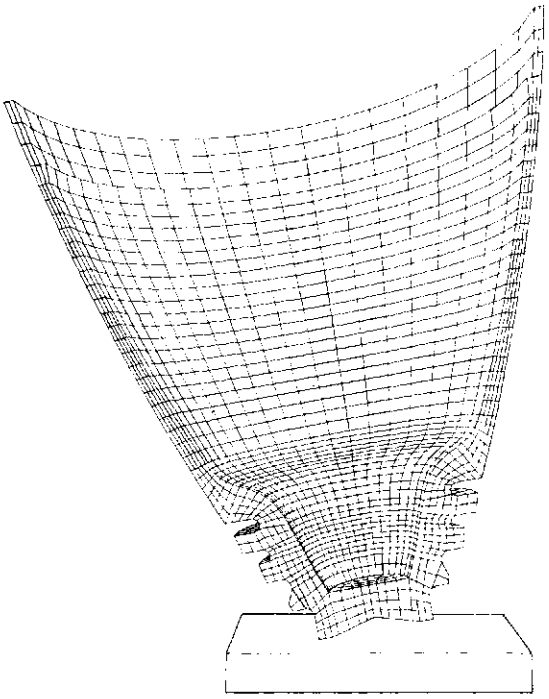

Fig. 8. Finite element mesh used in three-dimensional analysis.

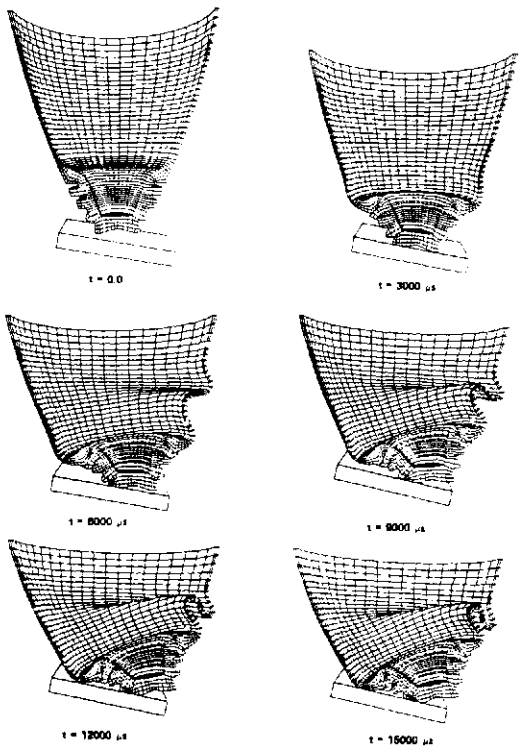

Fig. 9. Deformation history of asymmetric analysis.

axial velocity of 574 c/sec.

Due to the size of the model, the problem was analyzed at the Lawrence Livermore National Laboratory on their CRAY-1 computer. After an initial three-dimensional analysis of the symmetric impact verified the model was working correctly, the oblique analysis was run requiring 15 CPU hours. Deformed shapes, plotted by the post-processor GRAPE [9] program at three millisecond intervals are shown in Fig. 9 and a buckle can be seen to be developing in the leeward wall within the first 3 msec. A zero energy mode, the result of a one point integration in an eight node brick, caused the hourglassing which is noticeable in the tooth area at the larger deformations. The hourglassing is controlled to a large extent by use of an artificial viscosity and although aesthetically displeasing, will not affect the final

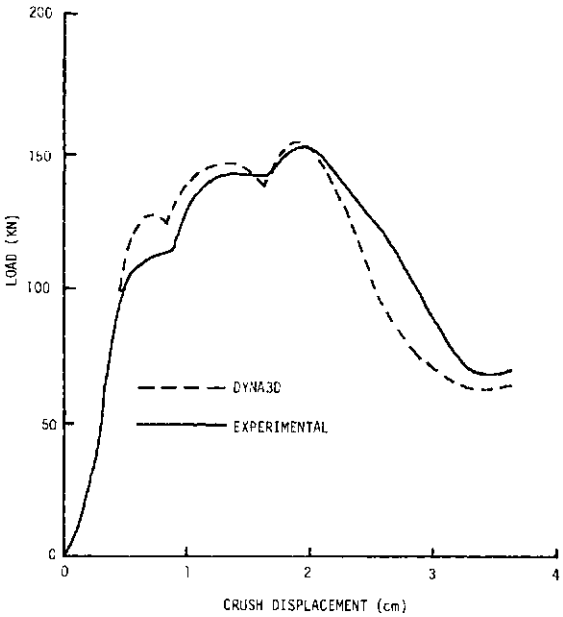

Fig. 10. Three-dimensional analytical and experimental static load-crush curves.

results. The crush force, calculated from the global rigid body accelerations, is plotted versus the crush displacement in Fig. 10 with the results from the experimental static test.

The discrepancy in load values at the first two peaks is primarily due to the bilinear stress–strain model in which the yield stress (480 MPa) used in this model is larger than the actual yield (380 MPa). The three-dimensional model accurately predicted the buckling load since the material model is more representative at higher plastic strain values. The final deformed shapes of the analytical and experimental noses, shown in Fig. 11, agree extremely well with the exception of a slight difference in location of the buckle, attributable to the imperfect modeling of the impact surface (rigid and frictionless).

As initially suspected, the difference between the dynamic analysis and static test results is small indicating that inertia effects in the problem are minimal and that the increase in load, shown in a dynamic test, must be entirely due to material strain rate sensitivity. A dynamic test, in which the scaled nose was dropped and impacted a nearly rigid steel block at 574 c/sec, showed that the lower wall did not buckle indicating that the strain rate in the wall must increase the yield stress enough to prevent the wall buckling that occurred in the slow rate test. An attempt was made to model the strain-rate behavior in the DYNA3D code using the Symonds-Ting model [10] as implemented in the HONDO [11] computer program. The yield stress for this model is defined as a function of an effective strain rate and the plastic modulus is held constant for simplicity, although strain rate tests conducted at Sandia on the 21-6-9 stainless steel indicated a significant decrease in modulus with increasing strain rate. For the Symonds–Ting model, if σ_0 is the uniaxial yield stress at zero strain rate, then the yield stress, σ_y, at any other strain rate, $\dot{\varepsilon}$, is given by

$$\left[\sigma_y = \sigma_0 \left[1 + \left(\frac{\dot{\varepsilon}}{D}\right)^{1/p}\right]\right.$$

where p and D are constants which have been evaluated from a nonlinear least squares fit. Results of the strain rate tests on 21-6-9, shown in Fig. 12, reveal a significant increase in yield stress at high strain rates. Since strain rates at locations in the nose exceed 1000 $\sec^{-1}$, while the maximum rate achieved in the laboratory tests were 300 $\sec^{-1}$ due to test equipment limitations, the constants for the rate model were extrapolated to the higher strain rates.

Data from the three-dimensional analysis, with the rate model included, show an increase in crushing force and that the lower wall does not buckle. Although the load curve does not increase enough to match the experimental dynamic tests, the results have been

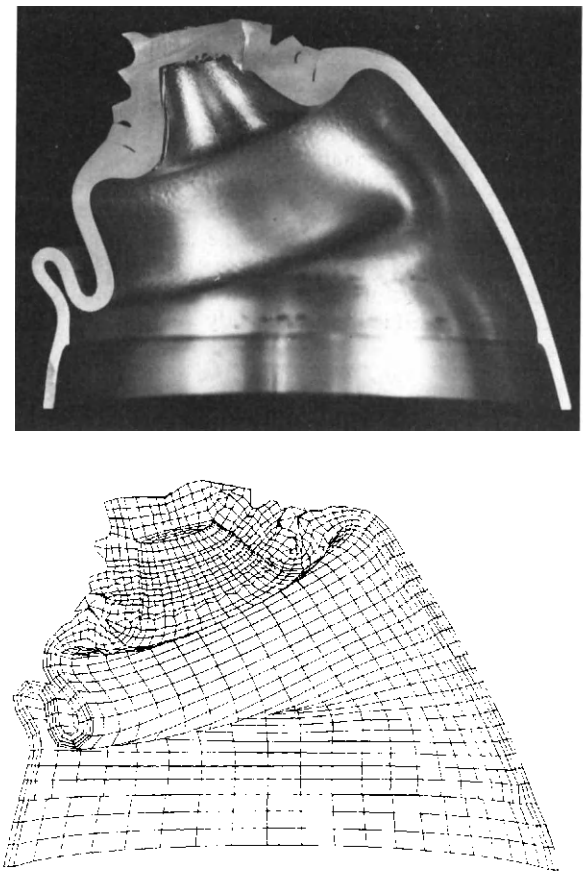

Fig. 11. Comparison of experimental and DYNA3D final deformed shapes.

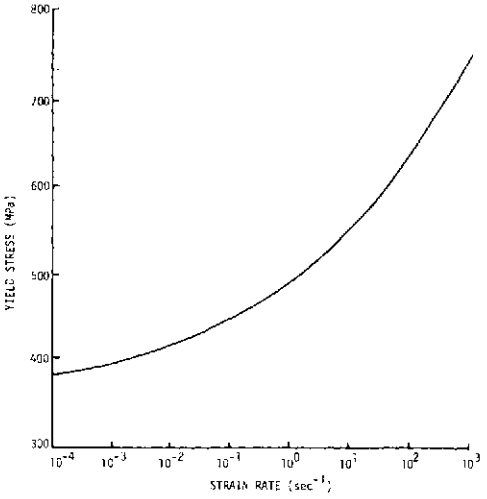

Fig. 12. Yield stress variation with strain rate.

encouraging and work is presently proceeding to determine the discrepancy.

CONCLUDING REMARKS

The two- and three-dimensional nonlinear finite element models have been shown to be very accurate in predicting the response of the crushing nose. The two-dimensional analysis was invaluable in the design iteration of the nose, drastically reducing costs and time. Designs were analyzed and results were evaluated within two days while manufacture and testing often required three to four months per iteration. It was shown that accurate and valuable results can be achieved from three-dimensional analyses in a reasonable amount of time providing, as illustrated in the Appendix, an efficient numerical program and a Class VI computer are available.

Future work in the area will be to develop a more accurate strain rate model based on experimental tests of tensile bars and the nose cone data. Noses were tested dynamically at three different velocities to provide ample data for correlation with the analytical results. Included in the future study will be a determination of why the present material strain rate model yielded inaccurate results.

REFERENCES

1. R. C. Young and M. L. Callabresi, GNATS—A finite element computer program for the general nonlinear analysis of two-dimensional structures. Sandia National Laboratories Livermore, SLL-74-0023 (Oct. 1974).
2. H. D. Hibbitt, P. B. Marcal and J. R. Rice, Finite element formulation for problems of large strain and large displacements, *Int. J. Solids Structures* **6**, 1069–1086 (1970).
3. K. J. Bathe, E. Ramm and E. L. Wilson, Finite element formulations for large dynamic analysis, *Int. J. Num. Meth. Engrs* **9**, 353–386 (1975).
4. M. L. Callabresi and R. C. Young, Large strain elastic–plastic analysis of two-dimensional quasi-static structures, Sandia National Laboratories Livermore SAND 77-8632, (April 1977).
5. R. D. Krieg, Private communication. Sandia National Laboratories, Albuquerque, New Mexico (1977).
6. J. O. Hallquist, NIKE2D - An implicit, finite-deformation, finite element code for analyzing the static and dynamic response of two-dimensional solids, Lawrence Livermore National Laboratory, UCRL-52678 (March 1979).
7. J. O. Hallquist, A numerical treatment of sliding interfaces and impact, In *Computational Techniques for Interface Problems*, (Edited K. C. Punk and D. K. Gartling), AMD Vol. 30, ASME, New York (1978).
8. J. O. Hallquist, Preliminary user's manual for DYNA3D and DYNAP, Lawrence Livermore National Laboratory, UCID-17268, Revision 1 (Oct. 1979).
9. B. E. Brown, Displaying the results of three-dimensional analysis using GRAPE, Lawrence Livermore National Laboratory, UCID-18507, (Oct. 1979).
10. P. S. Symonds and T. C. T. Ting, Longitudinal impact on visco plastic rods - Approximate methods and comparisons, *JAM* **31**, 611–620 (1964).
11. S. W. Key, Z. E. Beisinger and R. D. Krieg, HONDO II—A finite element computer program for the large deformation dynamic response of axisymmetric solids, Sandia National Laboratories, Albuquerque, New Mexico, SAND78-0422 (Oct. 1978).
12. J. O. Hallquist, DYNA2D - An explicit finite element and finite difference code for axisymmetric and plane strain calculations (User's Guide), Lawrence Livermore National Laboratory, UCRL-52429 (March 1978).
13. J. H. Biffle and M. H. Gubbels, WULFF--A set of

Table A1. Comparative solution times in CPU hours for finite element codes and scientific computers

FINITE ELEMENT CODE	CDC 6600	CDC 7600	CRAY-1
TWO-DIMENSIONAL			
GNATS	.50	(.10)	(.02)
DYNA2D	15	2.1	0.4
HONDO	20	3.0	(0.6)
THREE-DIMENSIONAL			
DYNA3D	450	75	15
WULFF	4500	750	(150)

computer programs for the large displacement dynamic response of three-dimensional solids, Sandia National Laboratories, Albuquerque, New Mexico, SAND76-0096 (Aug. 1976).

APPENDIX

Solution times, calculated for possible two- and three-dimensional analyses using five codes,GNATS [1], a static implicit code, and HONDO [11], DYNA2D [12], WULFF [13] and DYNA3D [8], dynamic explicit codes are listed in Table A1. Value in parentheses indicate that the code is currently not available on the respective computer and that timings have been approximated from past experience. The factor of ten difference in efficiency between WULFF and DYNA3D is primarily due to the number of numerical integration points used. WULFF, however, does not have the hourglass problem since the eight point gaussian quadrature eliminates that zero energy mode.

Computers & Structures, Vol. 13, pp. 303–309, 1981
Printed in Great Britain.

0045-7949/81/010303-07$02.00/0

COMPUTER DESIGN OF A HIGH EXPLOSIVE VELOCITY AUGMENTED KINETIC ENERGY PENETRATOR

D. B. TUFT and M. J. MURPHY
University of California, Lawrence Livermore Laboratory, Livermore, CA 94550, U.S.A.

(*Received* 17 *May* 1980)

Abstract—The results of a combined analytical/experimental design of a high-explosive velocity augmented kinetic energy penetrator are presented. The objective of the analysis is the design of a velocity augmentor and main charge case. The augmentor design must conform to restrictive volume constraints and provide maximum impulse to the main charge which, in turn, must survive the augmentor loading and penetrate the target.

An explicit finite element hydrodynamic computer code, DYNA2D, employing arbitrary zoning, two-way sliding with gaps, and high explosive equation-of-state is employed as the analytical tool. High strain rate material models are used and predictions are compared to experimental deformations. Shock wave interactions in the main charge case are analyzed and a combination of shock attenuation and wave trapping is employed to reduce loads below failure limits.

The final design provides maximum velocity augmentation while staying within volume constraints and maintaining main charge case integrity. Computed deformations and velocities are experimentally verified. This design analysis method using state-of-the-art code and computer capabilities is shown to be an effective method of simplifying the design process as well as providing necessary design optimization data not previously available.

INTRODUCTION

This paper presents the combined analytical/experimental design of a high explosive velocity augmented kinetic energy penerator being developed at the Lawrence Livermore Laboratory. A Lagrangian hydrodynamic finite-element computer analysis was combined with high explosive testing to develop the penetrator assembly, which consists of a main charge (MC) and a velocity augmentor (VA) as shown in Fig. 1. At target impact the velocity augmentor detonates increasing the main charge velocity allowing it to penetrate the target and come to rest at the desired depth.

OBJECTIVE

The overall objective of this analysis is the design of the velocity augmentor and main charge case within restrictive volume constraints. This objective has two parts:

(1) Design a velocity augmentor to provide maximum impulse to the main charge within the volume available.

(2) Design a main charge case that will survive the augmentor impulse while delivering the maximum payload to the target.

In order to meet these objectives, a combined analytical/experimental program was developed. The approach used to solve this problem applied the unique resources of the Lawrence Livermore Laboratory which combines an extensive scientific computing capability with a conveniently located explosives test facility.

APPROACH

The approach used to solve this problem was a combined analytical/experimental program that was subdivided into four distinct tasks. An objective was met in each task before going on to the next. The following describes these objectives:

(1) *Computer Model Development.* Select an appropriate analytical code and computer. Generate a finite element mesh and mathematically characterize material properties.

(2) *Computer Model Calibration.* Validate the computer model by correlating analytical predictions to experimental results.

(3) *MC and VA Design Optimization.* Optimize the VA and design the MC case to withstand the VA impulse.

(4) *Final Experimental Verification.* Experimentally confirm the computer predictions.

COMPUTER MODEL DEVELOPMENT

The computer code selected for the analysis, DYNA2D, was developed at LLL by Hallquist [1]. DYNA2D is an explicit, two-dimensional, plane strain and axisymmetric, Lagrangian hydrodynamic finite-element code. Particular features distinguish DYNA2D from codes previously available for hydrodynamic modeling. First, DYNA2D allows gaps and arbitrary two-way sliding between adjacent materials. This improves the modeling of complex geometries with intersecting material interfaces. Specialization of a contact-impact algorithm allows such interfaces to be rigidly tied allowing variable zoning without the need for transition regions. Because less simplification or compromise is required in the model, more accurate predictions are possible. Another feature of DYNA2D is its use of quadrilateral finite element zones. These allow arbitrary zoning in which a logically regular mesh is not required. Finite elements offer an alternative meshing scheme that for certain geometric configurations can result in reduced mesh entanglement. Moreover, the quadrilateral zones afford an added degree of freedom and are less stiff than triangular zones used in some finite element codes. The third feature is the large number of material models incorporated into the code.

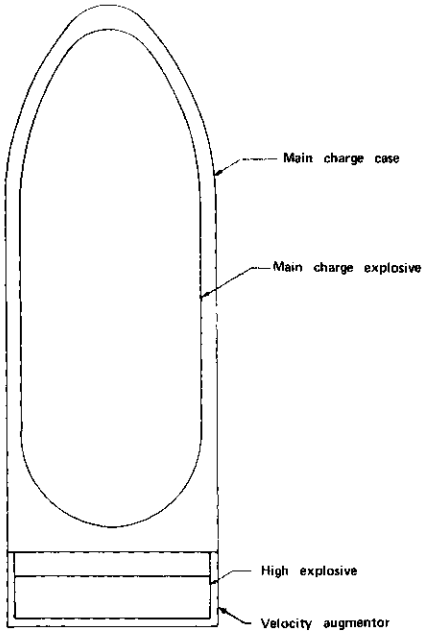

Fig. 1. Kinetic energy penetrator assembly.

Four of the thirteen available material models in DYNA2D were used in this analysis. The four material models are described briefly below:

(1) *Elastic/plastic/hydrodynamic*

The shear modulus (G), yield strength (S_y), and hardening modulus (E_t) are required to define the standard engineering properties. An equation of state defines the pressure, P, as

$$P = C_\phi + C_1\mu + C_2\mu^2 + C_3\mu^3 + (C_4 + C_5\mu + C_6\mu^2)E_i$$

where $\mu = \rho/\rho_0 - 1$, ρ/ρ_0 = ratio of current density over initial density and E_i = internal energy

(2) *Steinberg/Guinan high strain rate model*

The Steinberg/Guinan model is an advanced plasticity model that accounts for thermal softening and strain hardening. It assumes that the elastic shear modulus and the yield strength of an isotropic material depend upon pressure and internal energy [2]. The yield strength is also governed by effective plastic strain that controls strain hardening. The model is rate-independent and was formulated for use at strain rates greater than $10^5\ \text{sec}^{-1}$. In this domain it is assumed that strain rate enhancement has saturated and is no longer a variable affecting yield strength.

The expected flow curve for a typical material subjected to high strain rate explosive loading is shown in Fig. 2. When strain hardening alone is the dominant effect, the curve begins at Y_0 and strain hardens to Y_{max}. The value of Y_{max} is the maximum yield strength to be attained from cold work of the material. The dotted curve in Fig. 2 shows the effect of pressure and temperature on the flow curve. During the early stages of deformation when *HE* pressure is high, the pressure dominates and raises the yield strength. Later in the process when the *HE* pressure is no longer dominant, the effects of heating due to a rise in internal energy begin to degrade the strength of the material.

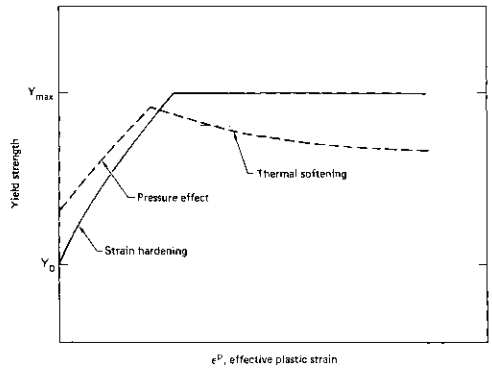

Fig. 2. Steinberg–Guinan high strain rate model.

(3) *Jones/Wilkins/Lee high explosive equation of state* [3]

The *JWL* equation of state defines the pressure, P, as

$$P = A\left(1 - \frac{\omega}{R_1 V}\right)e^{-R_1 V} + B\left(1 - \frac{\omega}{R_2 V}\right)e^{-R_2 V} + \frac{\omega E_i}{V}$$

where A, B, R_1, R_2 and ω are empirical constants, V is the relative volume, and E_i is the internal energy. A programmed burn model based on detonation velocity is used to define detonation times for each explosive zone.

(4) *Reactive material equation of state*

The fourth material model used in the analysis was the reactive material model. This model characterizes a high explosive material acting as a structural member. However, if the energy input into any zone exceeds a minimum energy in the form of the integral of p^2t, the material in that zone detonates using a modified form of the JWL equation of state.

The post processor used for the analysis, THOR, was also developed at LLL by Hallquist [4]. THOR reads the binary plot files generated by DYNA2D and plots contours, time histories, and deformed shapes. It can compute a variety of strain measures at either Gauss integration or nodal points, interface pressure along slidelines, forces along constrained boundaries, response spectra, and momentum.

This analysis was run on the Cray-I computer, the most advanced scientific computer currently available in the world. DYNA2D coding was vectorized to take advantage of the computor's speed capabilities. This reduced the computing time (and cost) by a factor of seven over the equivalent time of a CDC 7600.

The computational mesh used in the preliminary analysis is presented in Fig. 3(a). The finite-element mesh generator, ZONE, developed at LLL by Burger [5], was used to develop this mesh. The mesh utilizes 1033 nodes, 838 quadlateral elements, 5 materials and 7 slide lines located at material interfaces.

The models used for the materials shown in Fig. 3(a) were as follows:

4330 V Mod Steel—elastic/plastic/hydrodynamic
Titanium —elastic/plastic/hydrodynamic
Copper —Steinberg/Guinan high strain rate
VA Explosive —JWL high explosive equation of state
MC Explosive —Reactive material model.

The constants used for the titanium, copper, and VA explosive were found in the literature [2, 3, 6]. However, the properties of the steel case and main charge

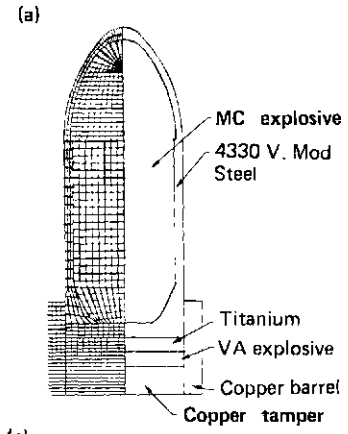

(b)

	YIELD STRENGTH (Mbar)	DEFORMATION (cm)		
		ΔA	B	ΔC
RUN 1	0.0113	1.88	1.40	1.28
RUN 2	0.0136	1.66	1.20	1.10
RUN 3	0.0170	1.30	1.02	0.840
GUN 1	TEST	1.32	1.03	0.838
GUN 2	TEST	1.31	1.03	0.836

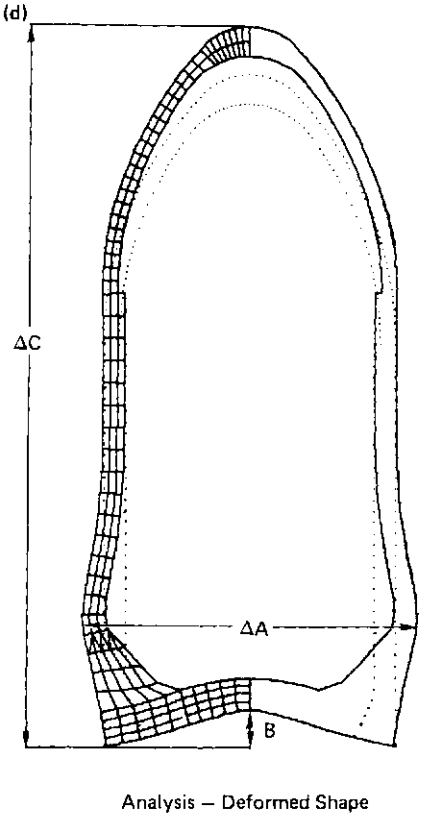

Fig. 3. Preliminary experimental/analytical correlation.

explosive needed additional consideration in order to accurately correlate computer predictions to experimental data.

Static stress–strain data and split Hopkinson bar test data were obtained for the MC explosive [7]. This data showed that the static yield strength of (0.000217) Mbar increased to (0.000374) Mbar at a strain rate of 2500 sec^{-1}. The bulk modulus of 0.10355 Mbar was obtained from ultrasonic tests [8].

High strain rate split Hopkinson bar tests were also run on the 4330 vanadium modified steel case [7]. Strain rates up to 10^3 sec^{-1} are obtainable with the test apparatus at LLL. However, rates as high as 10^5 sec^{-1} can be expected for HE interaction problems. To account for the effect of higher strain rates, the tangent modulus in the elastic/plastic/hydrodynamic material model was held constant while the yield strength was increased until correlation to experimental data was achieved.

CODE CALIBRATION AND EXPERIMENTAL RESULTS

The objective of this portion of the design/analysis was to calibrate and/or validate computer predictions of a non-optimized experimental configuration and to determine acceptable limits of case strain. The initial computer runs were made using three yield strength models. Figure 3(b) presents various computed deformations for $S_y = 0.0113$, 0.0136, and 0.0170 Mbar. Also shown are the corresponding experimental deformations from two tests. The predictions of radial deformation (ΔA), base deformation (B) an overall length change (ΔC) were compared to the results of two explosive experiments. Excellent correlation was found using the yield strength at 0.0170 Mbar which corresponds to a 51% increase over the quasi-static value. Figures 3(c) and (d) show a comparison of the experimental and computed deformed ($s_y = 0.0170$ Mbar) geometries.

Further code verification was accomplished by comparing the computed to experimental MC rigid-body

velocity from detonation of the velocity augmentor. The experimental velocity was determined using a flash X-ray system. The computed value of 95 msec compared well with the experimental value of 92.6 msec. The case deformation of 16% was also used as a limit for further designs since the MC survived the augmentor detonation. Although laboratory tests have shown up to 20% strain for this material at static rates, it was decided that 16% deformation should be used for analytical design purposes. A secondary factor in this consideration was the increased cross sectional area of the MC at the higher deformation levels which reduces penetration.

Although this preliminary velocity augmentor design did not meet volumetric constraints, the analysis and experiment met the objectives of the first two tasks outlined in the program. The following summarizes the results of the first half of the development of the kinetic energy penetrator assembly.

(1) Analytical code calibrated and verified.

(2) Material models defined and confirmed with experimental results.

(3) Deformation limits defined.

VELOCITY AUGMENTOR OPTIMIZATION

The next step was optimization of the velocity augmentor within the imposed volume constraints. Variables chosen for this optimization study were tamping thickness, tamping materials, and shock wave attenuator thickness. These parameters were identified as having a major impact on performance and each was isolated and studied. Maximum MC case velocity and the experimentally determined limit of 16% radial case strain were used as performance criteria. Designs not meeting augmentor volume and case deformation constraints were not considered.

Because case survivability is a necessity, the velocity augmentor should be designed to do as little damage as possible while producing the highest possible velocity. One of the parameters affecting case damage is shock waves propagating from the augmentor. To reduce the effect of these shock waves on the MC case, a shock attenuator is required. The attenuator material should have high strength, be as light as possible, and have a shock impedence mismatch with the steel case. Titanium was initially chosen as the attenuator material due to its weight, strength, and shock impedence properties. At this point in the design analysis, the thickness of titanium attenuator was set at 0.953 cm because this proved acceptable in the preliminary design.

H.E. TAMPING OPTIMIZATION

The next parameter to be studied in the velocity augmentor design was the explosive tamper. With the above defined attenuator, tamping was added first in unequal increments. Throughout the tamping optimization, the attenuator thickness and overall outside VA envelope was held constant. This results in a trade off between HE mass and tamper mass. Figure 4(a) shows MC calculated rigid-body velocity and Fig. 4(b) shows calculated maximum radial case strain plotted vs augmentor charge-to-mass ratio. From this figure it can be seen that both MC velocity and strain reach a maximum at a charge to mass ratio of 0.17. This configuration was considered to be optimum. Additional points at higher and lower tamper densities were also calculated.

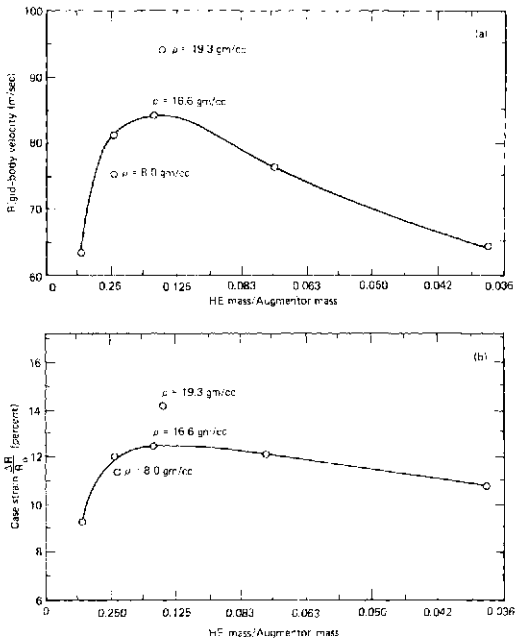

Fig. 4. Calculated velocity and strain vs charge to mass ratio.

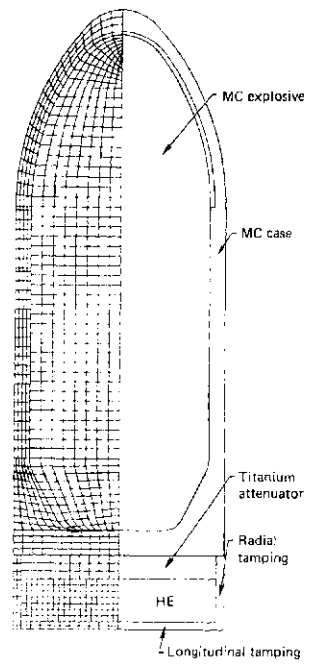

Fig. 5. Penetrator assembly with optimized velocity augmentor.

The resulting optimized velocity augmentor design, shown in Fig. 5, consists of radially and axially tamped high explosive and a titanium shock attenuator. During the velocity augmentor optimization process, shock wave attenuation was not optimized and case stress levels were not considered. An experimental test of the optimized VA design produced catastrophic MC case failure. Although the calculated maximum radial case deformation for this design was below the acceptable level, the tensile stress in the case far exceeded the ten-

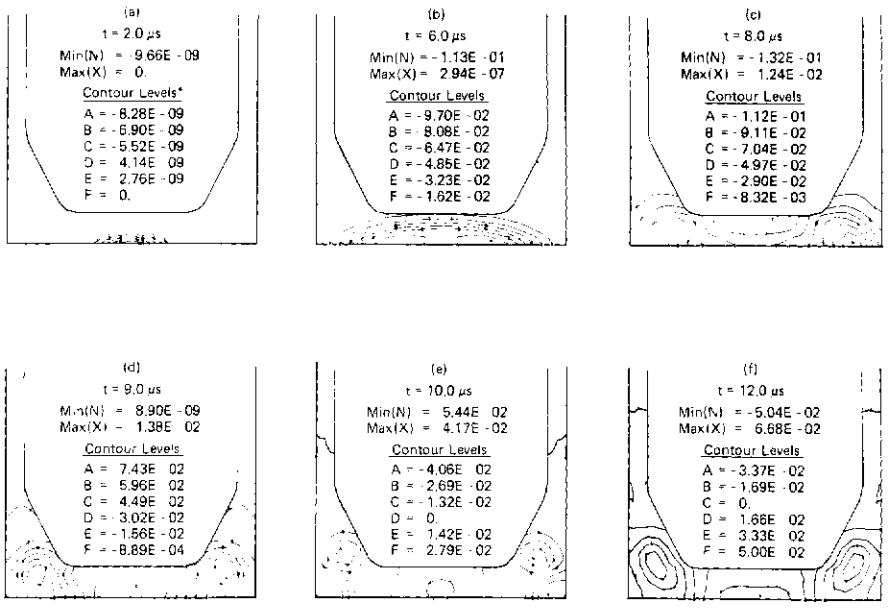

*Contour Levels in Mbar

Fig. 6. Shock wave propagation in main charge case.

sile strength of the case material. A study of the HE shock wave interaction at the MC base showed a compression wave reflecting off the outer case diameter was responsible for the tensile stress failure in the case. Figure 6 illustrates the sequence of shock interactions leading to high tensile stresses. The spherical wave created by the HE detonation enters the base center beginning at about 2μs. The wave then propagates striking the upper side of the case base at about 6μs and reflecting as a tensile wave as shown in Fig. 6(c). The initial wave continues to propogate radially outward impacting the outer case wall and reflecting as a strong tensile wave beginning at about 10μs. The stress level of the reflected wave grows in magnitude until reaching a maximum of about 66 kbar at 12μs, as shown in Fig. 6(f). The location of failure in the tested MC case corresponds to the location of this calculated maximum stress.

Two approaches toward reducing tensile stress in the case were taken. First, the magnitude of the compression wave impacting the outer wall was reduced by optimizing the shock wave attenuator. Second, a radial momentum trap was incorporated to absorb the compressive wave at the outer diameter and not allow the reflected tensile wave to propagate back into the case.

SHOCK ATTENUATOR OPTIMIZATION

The shock attenuator, located between the augmentor explosive and the MC case, is intended to reduce shock loading produced by the explosive while at the same time allowing maximum impulse to be imparted to the MC. From one-dimensional shock theory we know that alternating materials of high and low shock impedence will result in minimum stress transmitted.

To evaluate the relative effectiveness of different material combinations and layer thicknesses, several hydrodynamic calculations were performed with KOVEC, a one-dimensional code [9]. KOVEC solves the Lagrangian finite-difference equations for one-dimensional elastic-plastic flow and allows explosive burn using the JWL equation-of-state [3].

The overall geometry for this study is shown at the top of Fig. 7(a). The total augmentor length was kept constant to reflect VA volume constraints while the attenuator materials and thicknesses were varied. Hence, explosive thickness varied with changes in attenuator thickness. The MC case was represented by a steel plate with the same thickness as the bottom center thickness of the MC case.

The parameters of interest in this attenuator study were total impulse delivered to the case and maximum pressure in the case. As a baseline, a calculation of impulse for zero attenuation was made and all subsequent impulse numbers were expressed as a fraction of the baseline impulse I_0.

Figure 7(a) shows a plot of impulse ratio I/I_0, pressure transmission ratio P_t/P_i, and maximum case pressure as a function of plate thickness for the tantalum–lucite combination. This material combination represents one of the highest possible difference in shock impedence available in common materials. The rise in case pressure between 0.0 and 0.159 cm plate thickness is due to pressure magnification differences between a shock impinging on steel or tantalum. Thus, in this instance, two thin attenuator plates are worse than no attenuation at all. The pressure ratio decreases more rapidly than the impulse ratio for plate thicknesses beyond 0.318 cm. This thickness was selected as an optimum configuration.

Several other material and thickness combinations were also considered. The results indicated the optimum attenuator among those investigated is a 0.318 cm tantalum −0.318 cm lucite combination. This attenuator produced the maximum relative impulse while reducing case pressure below the calculated acceptable level.

Figure 7(b) shows a comparison of a two-dimensional calculation of pressure versus time in the bottom center of the MC case for the titanium attenuator and

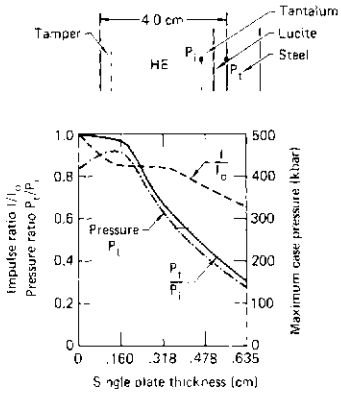

Fig. 7(a). One-dimensional shock attenuation study.

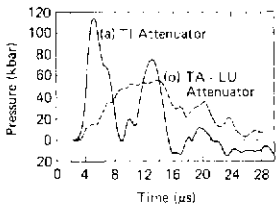

Fig. 7(b). Calculated two-dimensional base pressure for two attenuators.

tantalum–lucite attenuator. The maximum pressure has been reduced by 44% and the pulse spread out producing a longer duration, less severe push on the MC case.

MOMENTUM TRAP DESIGN

With the magnitude of the incident stress reduced, it was then desirable to prevent the compression wave from reflecting as a tensile wave at the outer diameter of the case. The momentum trap design shown in Fig. 8 was incorporated to achieve this effect. The momentum trap, which is actually a combination of a third attenuator plate and a radial momentum ring, is made of the MC case steel so that the initial compression wave will pass from the case into the ring with zero reflection. This initial compression wave then reflects from the outer surface of the ring as a tensile wave which cannot propogate through the material interface back into the case. Thus, the tensile wave is trapped and damage is limited to the ring. Calculations showed the momentum trap design completely eliminated any tensile stress in the case resulting from radial wave reflection. By improving the shock attenuation and preventing radial wave reflection, the maximum tensile stress in the case was reduced from about 66 kbar to below 20 kbar. Computed stress from our preliminary experiments suggested that 20 kbar was an acceptable level for dynamic stress and that the MC case should survive with the new velocity augmentor design.

The new design was tested twice and case integrity was achieved in both experiments. A comparison of calculated to actual deformed geometry of the MC case is shown in Fig. 9. The predicted length, base and

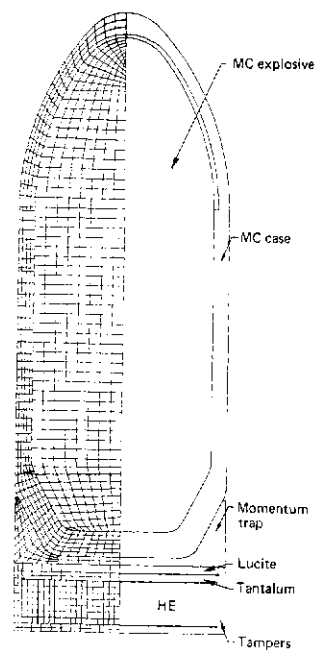

Fig. 8. Optimized penetrator assembly with momentum trap.

radial deformation[2] are within 13% of the experimental deformations. At this point all of the objectives were met. The augmentor provided sufficient impulse to the main charge while staying within the volumetric constraints. In addition, the main charge survived the impulse and penetrated the target.

CONCLUSIONS

The results of this study indicate that the finite-element calculational method employing arbitrary geometry, two-way slide lines, and HE equation-of-state is a valid method for predicting the mechanics of the HE detonation phenomena and resulting shock wave interactions. A high-explosive augmented kinetic energy penetrator was designed using this tool and the results were experimentally verified. Maximum velocity augmentation was obtained while staying within VA volume constraints and maintaining MC case integrity. This method can be used to accelerate and simplify the design process as well as provide necessary data for design optimization not previously available.

FUTURE EFFORT

At the present time a baseline for a velocity augmented kinetic energy penetrator assembly has been designed. Feasibility of using a high explosive augmentor within the volumetric and weight constraints has been shown. Our future effort is concerned with optimizing key parameters affecting the overall performance. The following areas of study are planned:

(1) Optimize Momentum Trap—The current momentum trap design eliminated undesirable tensile stresses in the case. However, a large portion of the augmentor energy was absorbed in this process. Future effort is directed toward minimizing the absorbed

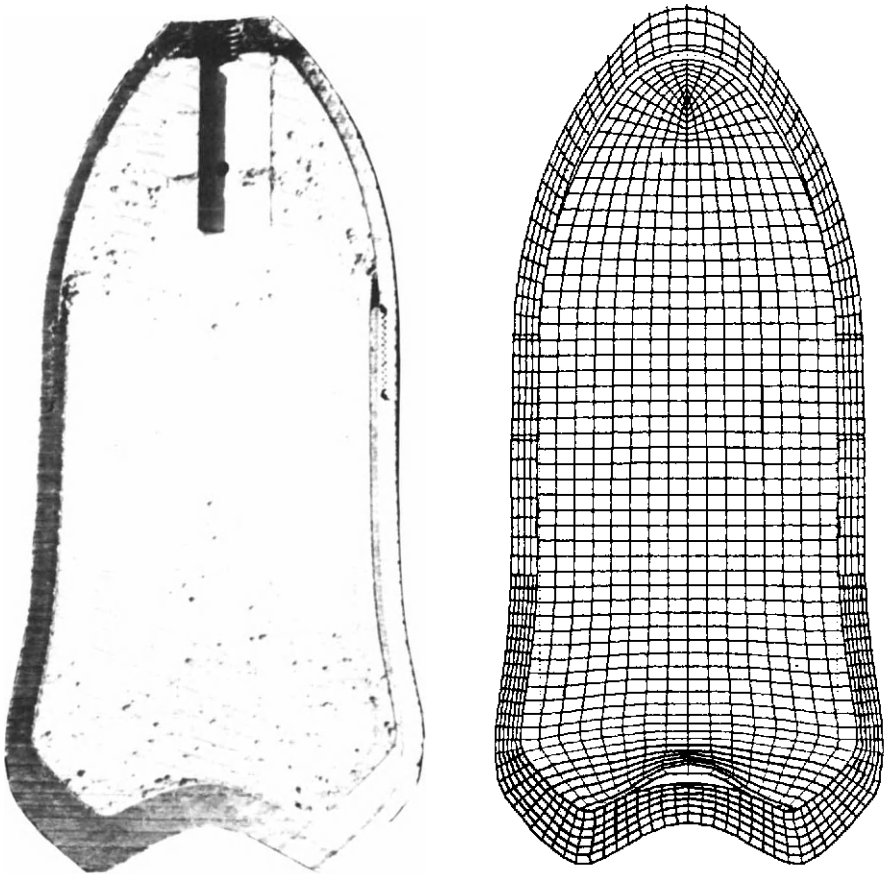

Fig. 9. Comparison of final experimental and computed deformed geometries.

energy while maintaining the current stress levels in the case.

(2) Improve overall charge/mass ratio –Effort will continue to reduce case weight and increase the amount of MC explosive.

Acknowledgements—The authors wish to acknowledge Dr. J. O. Hallquist, Mr. R. E. Varosh and Dr. R. W. Werne for their technical contributions to this work. Our appreciation also goes to Ms. Toni Dry who typed the manuscript.

Work performed under the auspices of the U.S. Department of Energy by the Lawrence Livermore Laboratory under contract number W-7405-ENG-48.

REFERENCES

1. J. O. Hallquist, DYNA2D—An explicit finite element and finite difference code for axisymmetric and plane strain calculations. Lawrence Livermore Laboratory, *Rep. UCRL*-52529.
2. D. J. Steinberg and M. W. Guinan. A high-strain-rate constitutive model for metals. Lawrence Livermore Laboratory, *Rep. UCRL*-80465 (1978).
3. B. M. Dobratz [Ed.], Properties of chemical explosives and explosive simulants. Lawrence Livermore Laboratory, *Rep. UCRL*-51319, Rev. 1 (1974).
4. J. O. Hallquist, THOR a post-processor for two-dimensional analysis codes Lawrence Livermore Laboratory, *Rep. UCRL*-52852.
5. M. J. Burger, ZONE a finite element mesh generator. Lawrence Livermore Laboratory, *Rep. UCID*-17139, Rev. 1.
6. *Aerospace Structural Metals Handbook*.
7. D. Breithaupt, Lawrence Livermore Laboratory, Private communication (1979).
8. A. Weston, Lawrence Livermore Laboratory, Private communication (1979).
9. J. P. Woodruff, KOVEC user's manual. Lawrence Livermore Laboratory, *Rep. UCID*-17306 (1976).

Computers & Structures, Vol. 13, pp. 311–318, 1981
Printed in Great Britain.

0045-7949/81/010311-08$02.00/0

STRAIN-RATE EFFECTS ON TURBINE MISSILE CASING IMPACT

JAMES T. GORDON, JR. and JOHN E. REAUGH
Science Applications, Inc., 2450 Washington Avenue, Suite 120, San Leandro, CA 94577, U.S.A.

(*Received* 11 *May* 1980)

Abstract—Results from two-dimensional plane stress and plane strain computations simulating the impact of a 120° turbine disk fragment on a turbine internal stator blade ring are presented and compared with data obtained in recent full-scale experiments. These computations were performed using the nonlinear explicit finite-difference computer code STEALTH developed for the Electric Power Research Institute. The numerical model employed represents the turbine missile as a rigid body which acts as a kinematic boundary condition on the stator ring. A work hardening, strain-rate dependent material model was used to characterize the strength behavior of the stator ring. Friction effects were not modeled.

Predictions of the deformed shape of the stator ring, line-of-flight displacement of the missile c.g., missile rotation angle and rotational velocity agreed well with experimental values. Predicted values of missile kinetic energy and line-of-flight velocity were lower than observed experimentally, but showed reasonable agreement up to about 3.3 msec after impact, at which time the hold-down bolts were observed to move in the experiment. These bolts were not modeled in the analysis. For times less than 3.0 msec, the predicted strains compared reasonably well with measured values.

INTRODUCTION

The capability to predict the effect of turbine missile impact due to the rare failure of a shrunk-on disk is a necessity in the design and safe operation of both nuclear and fossil-fueled power plants. Recent full-scale experiments [1] have demonstrated the large plastic deformations resulting from turbine missile impact and the extent to which a simulated internal stator blade ring and a simulated steam turbine outer wall can slow the velocity of 120° turbine disk fragments in two orientations—blunt and piercing. The objective was to provide benchmark data on both the energy-absorbing mechanisms of the impact process and, if break-through occurred, the exit conditions of the fragment.

This paper documents numerical studies conducted using the explicit finite-difference computer code STEALTH† to simulate and predict the transient, large strain, nonlinear behavior resulting from the blunt orientation impact of a turbine disk fragment on the internal stator blade ring in the full-scale experiment. The goals of this numerical simulation were to aid in understanding the process by which missile fragments are slowed by the stator blade ring, and to demonstrate the applicability of the STEALTH code in determining the energy absorption of the stator blade ring (due principally to plastic flow), by comparison with the experiments.

TARGET STRUCTURE

The target structure being modeled is shown in Fig. 1. The inner structure, representing the last-stage stationary-blade support ring, was 12.7 cm (5 in.) thick, 50.8 cm (20 in.) wide and 431.8 cm (170 in.) in dia. The outer shell, representing a casing cover, was 3.2 cm (1.26 in.) thick, 182.9 cm (72 in.) wide and 635 cm (250 in.) in dia. The ring and the shell were fabricated from ASTM A515, Grade 65 cold-rolled steel with a tensile yield of 300 MPa (43.6 ksi), a tensile ultimate of 491 MPa (71.4 ksi), and an elongation of 26% at room temperature.

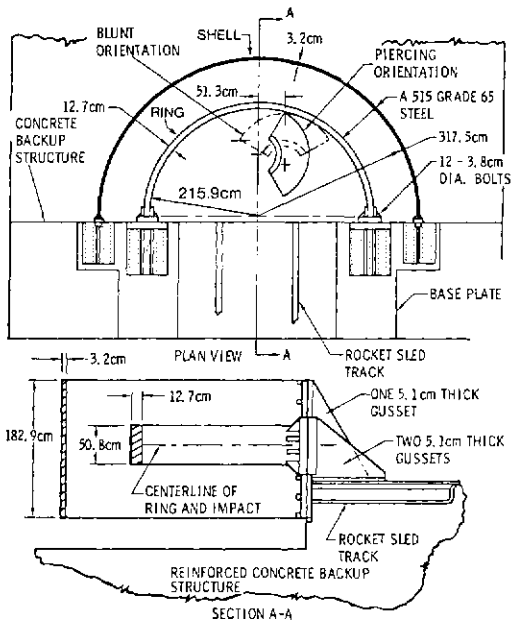

Fig. 1. Target structure, missile and impact orientations.

The ring and the shell were bolted to a massive concrete structure and soil overburden weighting 1633 metric tons (1800 tons). The bolted connections simulated as closely as practicable the horizontal joints in an actual turbine. Twelve bolts that were 3.8 cm (1.5 in.) in diameter held down each end of the ring; these had

†Solids and Thermal hydraulics codes for EPRI Adapted from Lagrange TOODY and HEMP", developed for Electric Power Research Institute by Science Applications, Inc. under EPRI Contract RP307.

an ultimate strength of 11.5 MN (2.6×10^6 lbf) and an active length of 25.4 cm (10 in.). Fourteen bolts 2.54 cm (1 in.) in diameter held down each end of the shell; these had an ultimate strength of 6.7 MN (1.5×10^6 lbf) and an active length of 15.2 cm (6 in.). The bolts were fabricated from A490 steel.

MISSILE IMPACT CONDITIONS

The missile was a 120° sector of a last-stage shrunk-on disk. Dimensions and mass properties of the 1527-kg (3366-lb) missile are given in Fig. 2. The missile was made from high-strength alloy steel (ultimate strength of 896 MPa or 130 ksi). Note that the turbine sector has no blades; it is assumed that the blades break off or are crushed during exit.

MATERIAL MODEL

The material model used in these calculations was a work hardening, strain-rate dependent representation for A515 steel. Static tensile stress–strain data from the A515 steel used to fabricate the experimental test ring are given in Table 1 in terms of true stress $\sigma = \sigma_E(1+\varepsilon_E)$ and true strain $\varepsilon = \ln(1+\varepsilon_E)$.

Since no data were found in the literature on the dynamic behavior of A515 steel, published dynamic data for similar types of mild cold-rolled steels were taken as the basis for the strain-rate law used. The strain-rate dependence of the dynamic flow stress σ_D used for these calculations is given by

$$\sigma_D = \sigma_0 \left[1 + \left(\frac{\dot{\varepsilon}}{40.4} \right)^{1/5} \right], \quad \dot{\varepsilon} \sim \text{sec}^{-1} \tag{1}$$

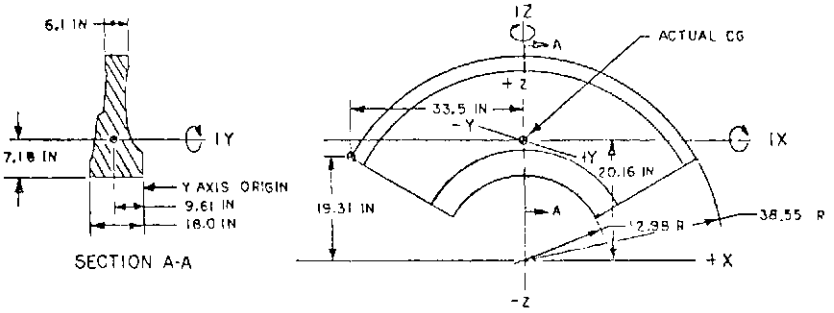

Fig. 2. Dimensions and mass properties of steel missile segment (120° hub section).

The missile was mounted on a lightweight support sled, which was pushed by a rocket sled. After the acceleration stage the rocket sled was braked, allowing the missile and support sled to coast toward the target. Activation of explosive bolts just before impact separated the missile from the support sled, which was diverted by a striker plate beneath the target structure. The missile then traveled in free flight before its 15.5 cm wide (6.1 in.) edge struck the center of the 50.8 cm wide (20 in.) ring.

As indicated in Fig. 1, the flight path of the missile's center of gravity was offset 51.3 cm (20.2 in.) from the centerline of the track and the structure. This simulated the trajectory of a turbine segment that leaves the shaft translating tangentially from a circle through the segment's center of gravity. The rotation of the segment, which would be at the rotational velocity of the turbine at failure, was not simulated in the tests. Instead, the total translational and rotational energy of the hypothetical turbine segment was included in the translational energy of the test missile.

The nominal impact velocity was 151 m/sec (495 ft/sec). This translational velocity gave the same total kinetic energy (17.4×10^6 J, or 12.8×10^8 ft-lbf) as a segment leaving a shaft spinning at 2160 rpm, or 120% of operating speed (the so-called design overspeed condition).

Table 1. True stress vs true strain for A515 steel

σ(MPa)	σ(psi)	ε
0	0	0
258.893	37,548	0.001293
413.893	60,000	0.050
491.614	71,300	0.095
954.958	138,500	0.75

where σ_0 is the static yield stress. This simple strain-rate law has been used to characterize the behavior of mild steel by Bodner and Symonds [2] using experimental data from Manjoine [3].

The stress invariant $\sigma^2 = 3J_2$ is calculated assuming the stress changes are elastic. Then, if

$$\sigma < \sigma(\varepsilon^P, 0) \tag{2}$$

the elastic state is appropriate, and no plasticity results.

The fundamental equation for plasticity, using the Prandtl–Reuss flow rule to second order accuracy is

$$\dot{\varepsilon}^P = \frac{\sigma - \sigma(\varepsilon^P, \dot{\varepsilon}^P)}{3\mu\Delta t} \tag{3}$$

where μ is the shear modulus. This equation is solved by Newton's method to obtain the consistent yield stress

and plastic strain rate.

$$\dot{\varepsilon}^p_{(n+1)} = \dot{\varepsilon}^p_{(n)} - \frac{3\mu\Delta t\dot{\varepsilon}^p_{(n)} - (\sigma - \sigma_{(n)})}{3\mu\Delta t + \left(\frac{d\sigma}{d\dot{\varepsilon}^p}\right)_{(n)}}. \quad (4)$$

The first guess $\dot{\varepsilon}^p_{(1)}$ is taken to be

$$\dot{\varepsilon}^p_{(1)} = \min\left(\frac{\sigma - \sigma(\varepsilon^p, 0)}{3\mu\Delta t}, \dot{\varepsilon}\right) \quad (5)$$

where $\dot{\varepsilon}$ is the total equivalent strain rate. In all cases, the plastic strain dependence is evaluated at the value of plastic strain from the previous time-step.

The calculations were performed using the inelastic portion of the true stress vs true strain curve defined in Table 1. Table 2 shows the values of Young's modulus E, bulk modulus K, Poisson's ratio Y, and shear modulus G, used in these calculations where $K = E/3(1-2\nu)$ and $G = E/2(1+\nu)$.

Table 2. Elastic constants used for A515 steel

E M bar (psi)	ν Poisson's ratio	K Mbar(psi)	G Mbar(psi)
2.0 (2.9006×10^7)	0.287	1.5649452 (2.2694×10^7)	0.777700077 (1.1268842×10^7)

The mean stress (equation-of-state) model was considered to be a linear function of the compression μ where

$$p = K\mu = K(\rho_0/\rho - 1) \quad (6)$$

where p is the pressure, ρ the density and ρ_0 a reference density (7.85 gm/cm^3).

PROBLEM SIMULATION

The geometry of blunt impact in plan view is shown in Fig. 3. The turbine missile is considered to be a rigid body which acts as a kinematic boundary condition on the finite-difference grid representing the stator ring. Although the STEALTH code does allow for multi-material impact (using slidelines), the approximation of a rigid missile would seem to be a good one since missile deformation was not observed in the full-scale blunt orientation tests. Furthermore, to simulate the missile with a finite-difference grid would double the computer cost.

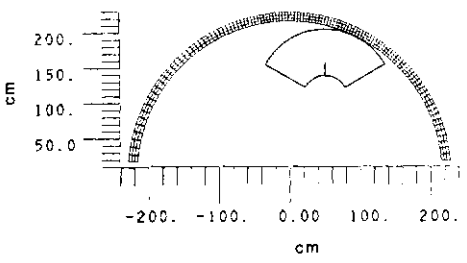

Fig. 3. Undeformed stator ring and turbine missile.

The turbine missile, is represented as a rigid body by straight line segments describing the impact face and perimeter of the disk. The disk center of mass is shown in Fig. 3 as the end point of the line segment perpendicular to the inner arc of the disk to aid in visualization of missile rotation.

The stator ring is represented by a (4×111) finite-difference grid consisting of 3 zones through the thickness of the ring and 110 zones circumferentially. As indicated in Fig. 1, each end of the test ring was attached to a thick base plate by eight thick flanges. Each base plate was attached to the back-up structure by 12 pre-torqued bolts. Early examination of test results indicated that these bolts failed at about 9 msec after impact. Inspection of the failed bolts showed little or no inelastic elongation before failure. This suggested that the supports displaced little during the impact response of the ring prior to bolt failure (the base plate would have no motion at all until the reaction load exceeded the pre-load). In consideration of these factors, the numerical calculations were performed with the assumption of rigid fixed supports. Subsequent test data evaluation has indicated that the base plates had begun to lift as early as 3.3 msec after impact. Thus, this fixed support boundary condition is strictly applicable only to about 3.3 msec after impact.

COMPUTATIONAL ALGORITHM

The STEALTH computer code solves the partial differential equations of continuum mechanics using an explicit finite-difference method formulated in a Lagrange (moving) coordinate frame. The STEALTH code is based entirely on the computer code technology published by Lawrence Livermore Laboratory, Livermore, Calif. and Sandia Laboratories, Albuquerque, New Mexico. The description that follows has been summarized from a descriptive report [4]. The computer code documentation is a separate report [5–8].

In the Lagrange system, fixed mass units translate, rotate compress, expand, and distort. Momentum is associated with the motion of the mass and internal energy is fixed to the mass unit. The STEALTH solutions are second-order accurate in space and time. A complete description of the Lagrangian equations solved by the STEALTH code is given in the user's manual [5].

Several rezoning options are available in STEALTH for updating grid point locations and variables in problems with large mesh distortion or grid tangling. Pressure discontinuities are handled by smearing out the discontinuity with a von Neumann quadratic artificial viscosity [9]; zone-to-zone oscillations may be damped out by using a linear artificial viscosity [10]; grid instability (hourglassing) is controlled by a "tensor-triangle" artificial viscosity [10]. Stability of the differential equations is automatically regulated by the Courant stability criterion [5].

The computational procedure used in modeling the blunt orientation impact process can be summarized as follows:

On a given cycle, n:

- The disk perimeter acts as a fixed boundary for the finite-difference grid.
- STEALTH computes the stresses in the ring and new grid point positions due to the blunt orientation impact. No rezoning is used in the calculation.
- The forces acting on the disk perimeter due to stresses in the ring are computed and summed to give the resultant x and y forces and torque acting on the disk center

of mass. Frictionless contact is assumed between the disk and ring.

•Rigid body motion of the disk center of mass is computed and new positions for the disk perimeter points are determined. These new locations are then used as the fixed boundary for the next cycle of the computation.

Complete details of this numerical procedure are documented in [11].

DYNAMIC RESPONSE CALCULATIONS

Calculations were done in both plane stress and plane strain symmetries. The plane stress calculations were carried to 9.0 msec. The plane strain calculation was carried to 3.3 msec, the approximate time at which the hold-down bolts and plates were first observed to move in the experiment. Results were quite close for the two symmetries with the plane stress values being generally closer to the experimental data than the plane strain results. Unless otherwise noted, all results presented here are from plane stress calculations with a rate dependent yield model.

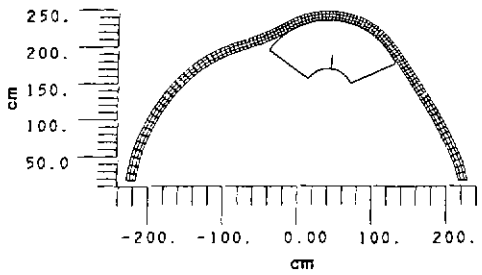

Fig. 4. Deformed stator ring and turbine missile at 3.3 msec.

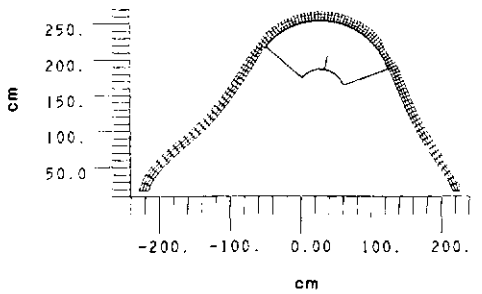

Fig. 5. Deformed stator ring and turbine missile position at 9.0 msec.

Figures 3–5 show mesh plots of the undeformed stator ring and turbine missile position at 0. msec (about 8 μsec prior to impact), and the deformed ring and missile position at 3.3 msec (time at which the hold-down bolts move) and 9.0 msec (time at which the hold-down bolts break), respectively. Figure 6 shows mesh plots comparing the deformed ring position at 9.0 msec with the undeformed position at 0. msec. Inspection of mesh plots between 3.0 and 9.0 msec (not shown here) indicates that bending of the ring begins to predominate over stretching after 3.3 msec. Missile c.g. position is indicated by the end point of the line perpendicular to the turbine disk's inner radius. Missile rotation is indicated by the orientation of this same line.

Figures 7 and 8 show mesh plots of the deformed stator ring and turbine missile position at 2 msec for strain-rate independent (static tensile data) and rate dependent yield models. The effect of rate dependency is particularly evident on the right side of the ring where less bending occurs with a rate dependent yield model.

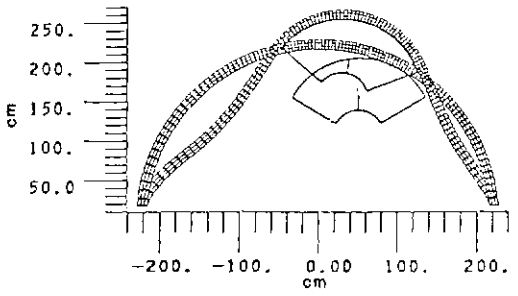

Fig. 6. Comparison of deformed stator ring and turbine missile position at 0.0 and 9.0 msec.

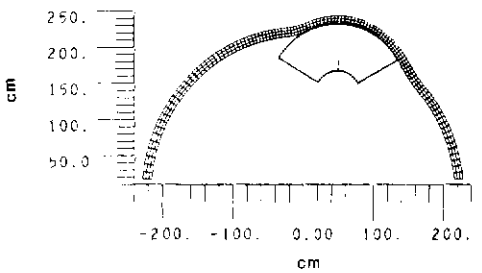

Fig. 7. Deformed stator ring and turbine missile position at 2 msec for rate independent yield model.

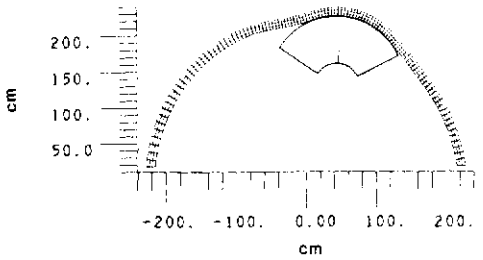

Fig. 8. Deformed stator ring and turbine missile position at 2 msec for rate dependent yield model.

The experimental deformed ring shape was very similar to that exhibited in the rate dependent calculation. Figure 9 shows a comparison of experimental and computed missile line-of-flight c.g. displacement histories. Both rate dependent and rate independent results are shown. The rate independent calculation was carried only to 2 msec. The rate independent displacements are seen to be greater than those observed in the experiment while the rate dependent displacements are lower than and closer to the experimental values. Thus, the slowing of the turbine missile is better simulated by the rate dependent calculation. The rate dependent displacements are seen to agree quite well with the experimental data up to about 3.3 msec (the time at which the hold-down bolts were first observed to move), the difference being 3.0% at 1.0 msec, 8.8% at 2.0 msec, and 9.0% at 3.3 msec. However, considerably better agreement could probably be obtained by using a dynamic effects factor with the rate independent model.

Figure 10 presents a comparison of computed (plane stress and plane strain) and experimental deformed shapes at 3.3 msec for the ring midsurface. The plane stress and plane strain results are seen to be quite close, particularly in the missile-ring contact region. The plane strain calculation shows a slightly greater bending of the ring near the right hand support and the upper left portion of the ring (-60 in. $< x < 0$) than for the plane stress cases.

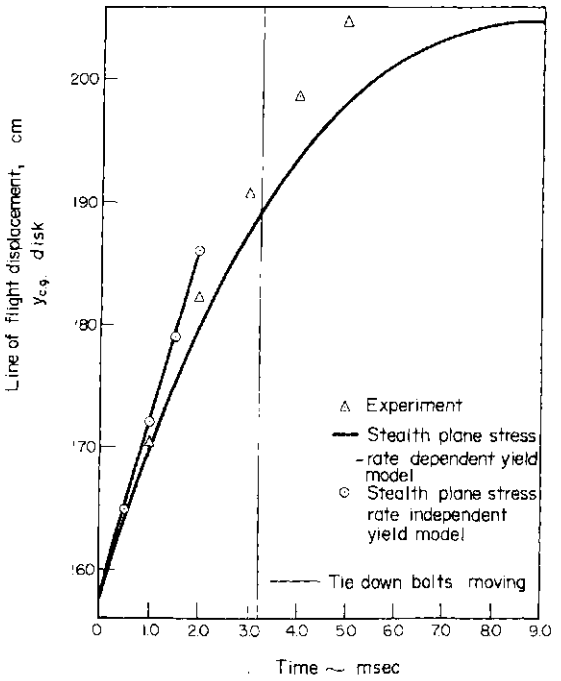

Fig. 9. Comparison of experimental and computed missile line-of-flight c.g. displacement histories.

Line-of-flight missile c.g. velocity vs time is presented in Fig. 11. The computed velocities are in good agreement with measured values at early times. At 1.0 msec, the computed velocity is less than 5% below that observed experimentally. At 2.0 msec, the difference is about 20% and at 3.3 msec about 24%. Thereafter, the calculated results show a steady drop in velocity, whereas in the experiment, missile velocity decreases at a much slower rate probably due to the hold-down bolts moving at 3.3 msec and finally failing at about 9.0 msec.

Figure 12 presents plots of missile kinetic energy (rotational plus translational), stator ring kinetic energy, ring internal (strain) energy and total energy as functions of time from the STEALTH calculations. The monitoring of these quantities provides a good means of assessing the reliability of the finite-difference solution as the calculation proceeds. In particular, the plots of total system energy show that the calculation is conserving energy (as the energy is transferred from the disk to the ring). For example, at 3.3 msec, the total ring energy is 123.9 in-lb and the change in kinetic energy of the disk is 123 in-lb, less than 1% difference. The greatest difference occurs at about 2 msec where the total system energy has dropped by about 10%. At 9.0 msec, the difference is only 4%. These differences in energy are well within the variation shown in most finite-difference impact calculations with similar grid zoning and would be reduced by using a finer grid with additional zones through the ring thickness.

Figures 13 and 14 show plots of STEALTH computed circumferential strains at the left support (80° left of the ring centerline) and at a position 10° left of the ring centerline, respectively. The strains are defined as $(l-l_0)/l_0$ where $(l-l_0)$ is the stretch of an element of original length l_0. The stretches are computed directly from the coordinates of the finite difference grid points. In Fig. 13, note the transition from small to large strains at about 5 msec. A similar change occurs in Fig. 14 at

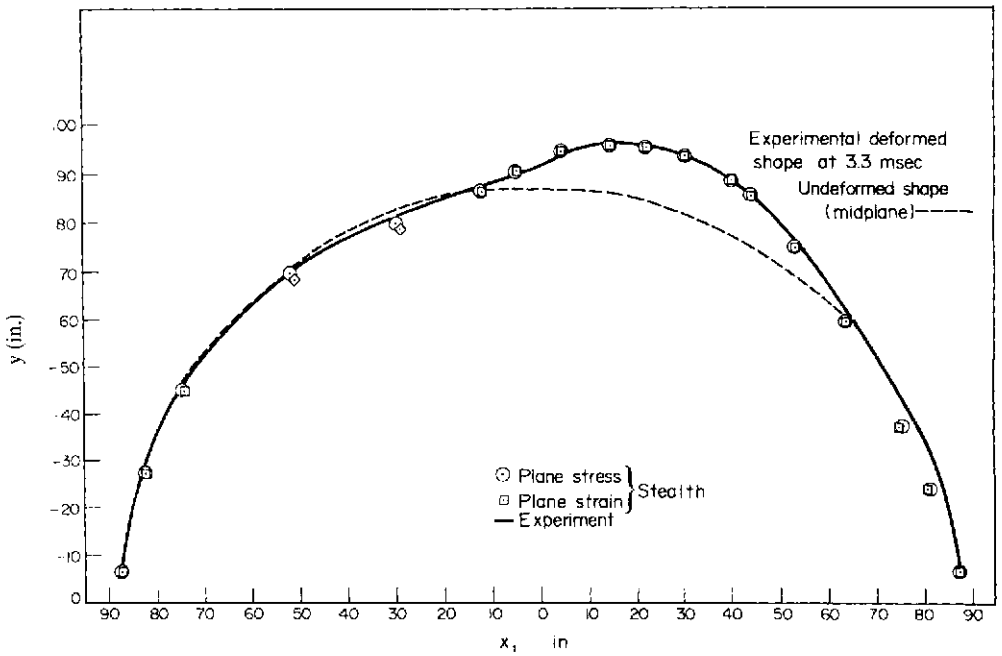

Fig. 10. Comparison of computed and experimental deformed shapes at 3.3 msec for ring midsurface.

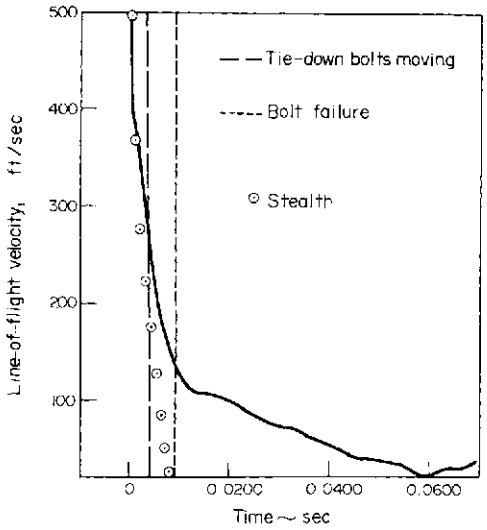

Fig. 11. Comparison of experimental and computed missile ling-of-flight c.g. velocity histories.

2 and 5 msec. Figures 15 and 16 present comparisons of experimental and computed strain histories on the inner and outer surfaces near the left support. For the outer surface, the agreement between experimental and STEALTH computed values is good to about 2.5 msec. For the inner surface, the peak computed strains up to about 5 msec are two to three times the experimental values.

Circumferential strain data was obtained at five additional radial locations and is given in [11]. Computed strains were generally higher than recorded in the experiment with characteristics similar to the results shown in Figs. 13–16. For the right support, however, the agreement between experimental and computed strains was much poorer, especially after 2 msec, and requires further study to resolve the discrepancy.

Comparisons of experimental and computed time histories of missile rotation angle and rotational velocity are given in [11]. The experimental values of rotation angle agree well with the computed values, particularly for times less than 4 msec. The experimental

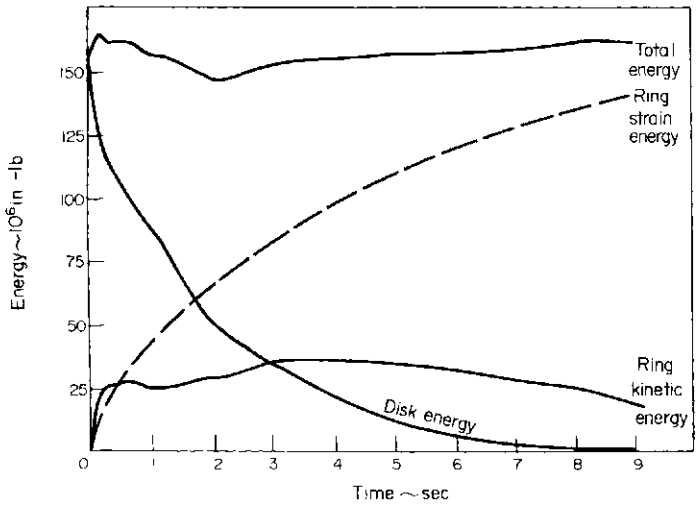

Fig. 12. Turbine missile energy histories—STEALTH plane stress.

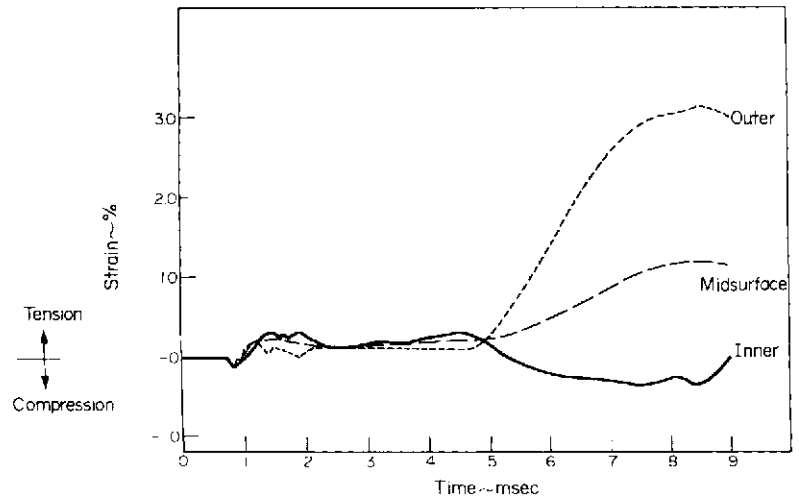

Fig. 13. Circumferential strains at left support (80° left of ring centerline) - STEALTH plane stress.

values of rotational velocity remain approximately constant rather than falling off as found in the STEALTH calculations. This discrepancy is perhaps due in part to the bolt motion and subsequent failure in the experiment, whereas the STEALTH calculation used fixed supports.

The computer time required for the entire plane stress calculation from 0. to 9.0 msec was 850 cp sec on a CDC 7600. This calculation time includes restart and archive tape writing.

employed represented the turbine missile as a rigid body which served as a kinematic boundary condition on the stator ring. A work hardening, strain-rate dependent material model was used to characterize the strength behavior of the stator ring. Friction effects were neglected. Tie-down bolt flexibility was not modeled and the stator ring ends were assumed fixed. Incorporation of a constraint model with a bolt-failure representation would undoubtedly bring the STEALTH results closer to the experimental data.

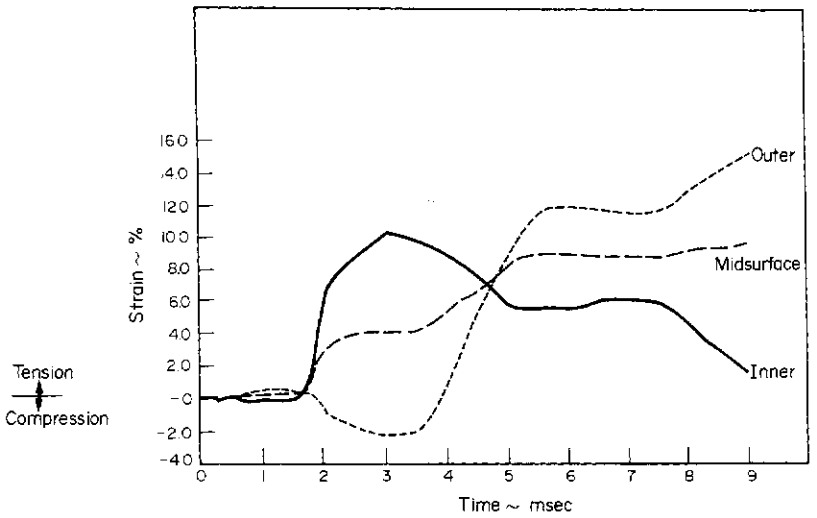

Fig. 14. Circumferential strains 10° left of ring centerline—STEALTH plane stress.

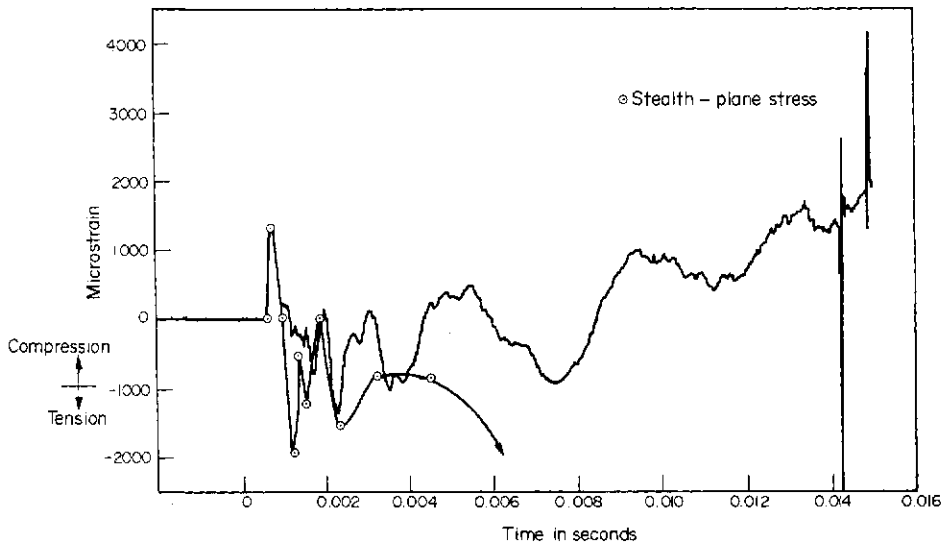

Fig. 15. Comparison of experimental and computed strains at left support outer surface.

CONCLUSION

Results from numerical simulation of the blunt impact of a 120° turbine disk fragment on the turbine internal stator blade ring have been presented. Comparison of these results with experimental data has successfully demonstrated the applicability of the nonlinear explicit finite-difference code STEALTH in determining the energy absorbtion of the stator blade ring. Calculations were performed in both plane stress and plane strain symmetries. The numerical model Predicted histories of line-of-flight missile c.g. displacement, missile rotation angle, rotational velocity and deformed shape of the stator ring agreed well with the experiment. Missile energy and line-of-flight velocity predictions were lower than observed experimentally but agreed reasonably well to about 3.3 msec. For times less than 3.0 msec, the predicted strains compared reasonably well with measured values.

In order to insure increased confidence in the prediction of turbine missile impact, several items merit

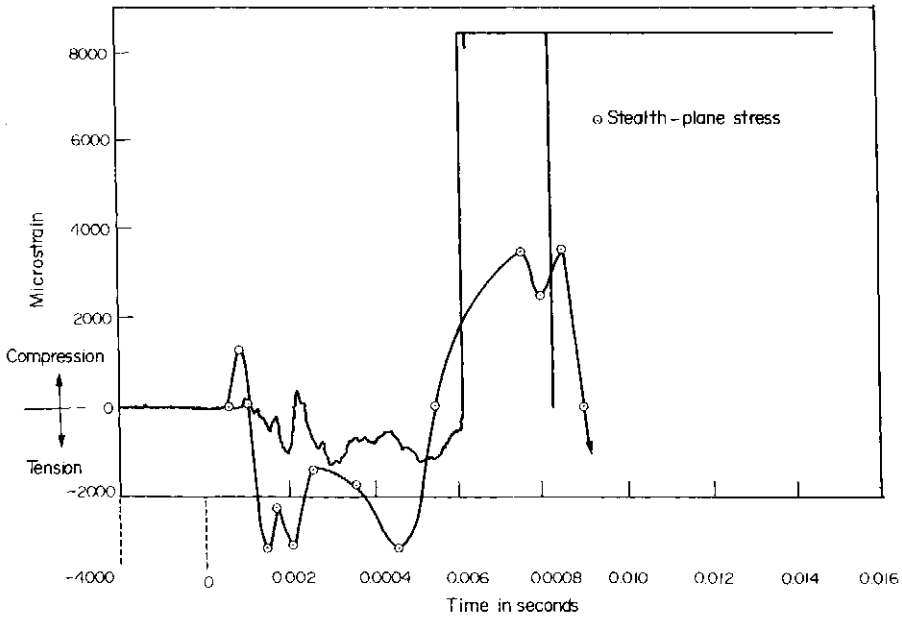

Fig. 16. Comparison of experimental and computed strains at left support inner surface.

continued investigation. Among these are:

- Inclusion of a hold-down bolt model.
- Numerical simulation of the piercing orientation impact and comparison with experimental data. This would require a dynamic fracture model.
- Simulation of three-dimensional effects in the piercing impact process, and the turbine model.
- Incorporation of stator blade models into the impact analysis. (The blades were assumed to be broken off in the current studies.)

Acknowledgement—This work was performed under the auspices of the EPRI, Palo Alto, Calif., Dr. George Sliter, Turbine Missile Research Program Manager.

REFERENCES

1. H. R. Yoshimura and J. T. Schamaun, Preliminary results of turbine missile casing tests. EPRI Research Project 399 Preliminary Report, EPRI, Palo Alto, Calif. (1978).
2. S. R. Bodner and P. S. Symonds, Experimental and theoretical investigation of the plastic deformation of cantilever beams subjected to impulsive loading. *J. Appl. Mech.* **29**, 719–728 (1962).
3. M. J. Manjoine, Influence of rate of strain and temperature on yield stress of mild steel. *J. Appl. Mech.* **66**, 211 218 (1944).
4. R. Hofmann, STEALTH, A lagrange explicit finite-difference code for solids, structural, and thermohydraulic analysis. EPRI NP-176, Summary, EPRI, Palo Alto, Calif. (1976).
5. R. Hofmann, STEALTH, A lagrange explicit finite-difference code for solids, structural and thermohydraulic analysis. EPRI NP-260, Vol. 1, *User's Manual*, Palo Alto, Calif. (1976).
6. R. Hofmann, STEALTH, A lagrange explicit finite-difference code for solids, structural and thermohydraulic analysis. EPRI NP-260, Vol. 2, *Sample and Verification Problems*. EPRI,
7. R. Hofmann, STEALTH, A lagrange explicit finite-difference code for solids, structural and thermohydraulic analysis. EPRI NP-260, Vol. 3, *Programmer's Manual*. EPRI, Palo Alto, Calif. (1976).
8. B. I. Gerber, STEALTH, A lagrange explicit finite-difference code for solids, structural and thermohydraulic analysis. EPRI NP-260, Vol. 4, *GRADIS Manual*. EPRI, Palo Alto, Calif. (1976).
9. J. Von Neumann and R. D. Richtmyer, A method for the numerical calculation of hydrodynamic shocks. *J. Appl. Phys.* **21**, 232 237 (1950).
10. M. L. Wilkins, The use of artificial viscosity in multidimensional fluid dynamic calculations. USRL-78348 (Preprint), Lawrence Livermore Laboratory, Livermore, Calif. (1976).
11. J. T. Gordon, Jr. and J. E. Reaugh, STEALTH Calculations of turbine missile casing impact. EPRI Project 399-4 Final Report. Science Applications, Inc., San Leandro, Calif. (1979).

Computers & Structures, Vol. 13, pp. 321–330, 1981
Printed in Great Britain.

0045-7949/81/010321-10$02.00/0

FINITE ELEMENT ANALYSIS OF ELASTIC–PLASTIC FIBROUS COMPOSITE STRUCTURES

YEHIA A. BAHEI-EL-DIN
Division of Structures, Department of Civil Engineering, Cairo University, Giza, Egypt

and

GEORGE J. DVORAK
Department of Civil Engineering, University of Utah, Salt Lake City, UT 84112, U. S. A.

and

SENOL UTKU
Department of Civil Engineering, Duke University, Durham, NC 27706, U.S.A.

(*Received* 25 *April* 1980)

Abstract—A three dimensional finite element code has been developed for the elastic–plastic analysis of fiber-reinforced composite materials and structures. The geometry, constitutive equations, and stiffness relations of the continuum element representing the composite are described. The finite element solution is obtained in the context of the displacement method of analysis. Solution of the nonlinear equilibrium equations is obtained with a Newton–Raphson type iteration technique. Results obtained using the finite element program for uniaxial loading of composite laminates show agreement with experiments. Other results for laminates describing development of plastic zones and overall stress-strain response are also shown for two problems; a plate with a hole and a notched plate.

INTRODUCTION

Since the early sixties the finite element method has been widely used as a reliable technique for the analysis of structures. In the early years of the finite element method most attention was focused on the linear elastic behavior of materials. However, due to its success in regard to linear analysis, the method in conjunction with iterative techniques has been used to analyze solids and structures in the elastic as well as the plastic range of their materials. In the present days many finite element codes exist for elastic-plastic analysis of structures with isotropic materials but not, to the authors' knowledge, for fiber-reinforced materials.

Nowadays, composite materials, in particular those reinforced by strong continuous fibers, have the attention of many researchers much like metals and other conventional materials had in the past. The increasing number of applications of fiber-reinforced composites in space, and recently, automobile industries demand an understanding of the material properties and its behavior. In most applications, structural elements made of composites are laminated plates. Thus, the analyst is faced with two problems in regard to composites; anisotropy and lamination. Real life applications also encounter complex geometries and loading regimes. Evaluation of stresses and deformation at edges, cut-outs, and joints is essential in understanding the strength and failure of composite structures. In addition, elastic–plastic analysis is crucial for metal-matrix composites since the onset of plastic yielding starts very early in the loading process as compared to the composite's ultimate strength. Indeed, such a comprehensive analysis can only be achieved by the finite element technique.

Application of the finite element method to fibrous composite structures exhibiting elastic–plastic deformation has been very limited. Adams and Miller [1], Adams [2], and Foye [3], employed the finite element method to unidirectional fiber-reinforced composites modelled on the microscale as arrays of brittle-elastic fibers embedded in an elastic–plastic matrix material. This microscopic analysis provides an understanding of the behavior of unidirectional composites, however, it cannot be extended to multidirectional laminates. Rather, we demand a finite element analysis which treats the fibrous composite as macroscopically homogeneous. This, however, has been hindered by the absence of continuum models which describe the elastic–plastic behavior of composites only in terms of the mechanical properties of the constituents and their volume fraction. Such models can be adopted in a numerical scheme only if they yield tractable constitutive equations.

A continuum material model for elastic–plastic composites has been recently developed by Bahei-El-Din and Dvorak [4–6]. The constitutive equations, which describe the behavior of the composite in a macroscopic sense, has been generated in matrix form, and therefore are tractable and can be readily incorporated in a numerical scheme. This paper describes a finite element code which employs the new constitutive theory. First, we describe the geometry, constitutive law, and stiffness relations of the three-dimensional element used in the present analysis. Next, the computational aspects of the computer program are described. Finally, we present finite element results for laminated metal-matrix composite plates.

†Formerly, graduate student and visiting assistant professor, Department of Civil Engineering, Duke University, Durham, NC 27706, U.S.A.

A CONTINUUM ELEMENT FOR FIBROUS MATERIALS

Geometry

Various one-, two- and three-dimensional elements have been used in finite element analyses to model various types of structures. Selection of a particular element is dictated by the nature of the structure and its response to loads. The laminated structure of most composites makes it necessary to conduct a three-dimensional analysis even for in-plane loads. This is due to the significance of the out-of-plane stresses, e.g. interlaminar shear and normal stresses, in evaluating the behavior of laminates. In the present finite element analysis the eight node hexahedral element has been used. The element represents a unidirectional composite material whose fiber is arbitrarily orientated in the structural coordinates.

Figure 1 shows the hexahedral element employed here, together with three coordinate systems. The axes X_j, $j=1, 2, 3$, are the structural overall axes. All structural type quantities, such as mesh point coordinates, stiffness matrix, etc., are described in the overall coordinates. The second coordinate system is the elemental local coordinate system x_j, $j=1, 2, 3$. The local axes are chosen as shown in Fig. 1 such that x_1-axis is along the vertex line 1-2 and x_2-axis lies in the plane containing the first four vertices of the element. These local axes serve as a mediator between the overall axes and the material axes $\bar{x}_j$, $j=1, 2, 3$. The latter are the principal material axes, where x_3-axis coincides with the fiber direction and x_1x_2-plane is the transverse plane of the composite material. In Fig. 1, $\bar{x}_2$-axis is drawn such that the fibers must be parallel to the plane containing the first four vertices of the element. Except for this requirement, the fiber orientation is arbitrary and the material axes can be identified with a single scalar quantity.

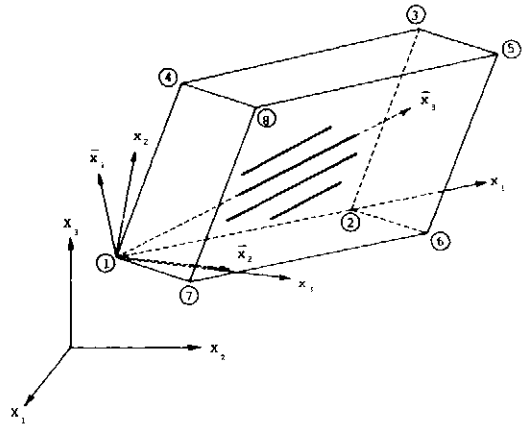

Fig. 1. A hexahedral element for unidirectional fibrous materials.

The orientation of the material axes, $\bar{x}_j$, $j=1, 2, 3$, can be fixed relative to the overall axes with the angle ϕ as shown in Fig. 2.

The positive direction of x_3-axis must be selected such that ϕ is never greater than 90°. The direction cosines of $\bar{x}_j$-axis, $j=1, 2, 3$, can be determined relative to the overall axes as follows: Let $\mathbf{t}_i$, $i=1, 2, 3$, denote a unit vector along the material x_i-axis described in the overall coordinate system. Vector $\mathbf{t}_2$ can be easily defined since $\bar{x}_2$-axis is coincident with the local x_3-axis and the direction cosines of the latter can be found from the overall coordinates of the element's vertices. Vector $\mathbf{t}_3$ can be found from the basic relations $\mathbf{t}_2^T\mathbf{t}_3=0$ and $\mathbf{t}_3^T\mathbf{t}_3=1$ which yield the following relations for t_{31} and t_{32} (see Fig. 2):

$$(1-t_{22}^2)t_{31}^2+(2t_{21}t_{22}\cos\phi)t_{31}+(t_{22}^2\cos^2\phi-t_{23}^2\sin^2\phi)=0, \quad (1)$$

and $t_{32}=\cos\phi$; if $|t_{21}|>0$,

$$(t_{23}^2)t_{31}^2+(\cos^2\phi-t_{23}^2)=0, \quad \text{and } t_{32}=\cos\phi; \quad (2)$$

if $t_{21}=0$, and $|t_{23}|>0$,

$$t_{31}=\sin\phi, \text{ and } t_{32}=0; \text{ if } t_{21}=t_{23}=0. \quad (3)$$

Equations (1) and (2) provide two values for t_{31} which require additional information to choose the proper value. Such information could be the sign of t_{31} in case 2 (Fig. 2), and the sign of t_{12} in case 1. Finally vector $\mathbf{t}_1$ can be easily found since the vectors $\mathbf{t}_j$, $j=1, 2, 3$, constitute an orthogonal basis.

Constitutive equations referred to material axes

Our objective is to describe the constitutive law of the composite material relative to the material axes $\bar{x}_j$, $j=1, 2, 3$, in a macroscopic sense. Here, we adopt a constitutive law which has been recently derived from a composite model by Bahei-El-Din and Dvorak [4–6]. The new model represents unidirectional composites by an elastic–plastic matrix material with a unidirectional constraint imposed by the elastic–brittle fibers. The matrix material is assumed to be of Mises-type and exhibiting kinematic hardening behavior. Thus, the inelastic strains of the composite lamina are caused by matrix deformation. The elastic constraint imposed on the matrix by the fiber affects the shape of the lamina yield surface, it leads to additional kinematic components in the hardening rule of the lamina, and it has an influence on the magnitude of overall plastic strains. Figure 3 shows a, schematic representation of the initial yield surface, hardening

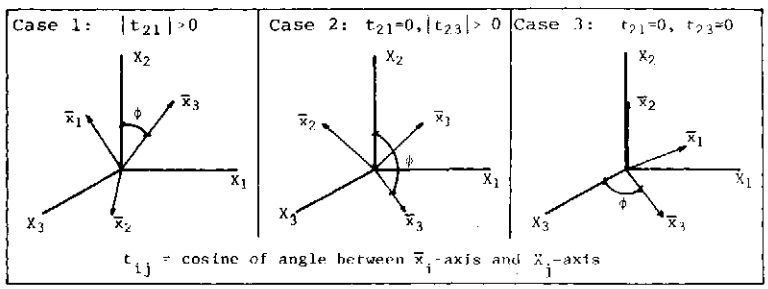

Fig. 2. Angle fixing material axes relative to overall axes.

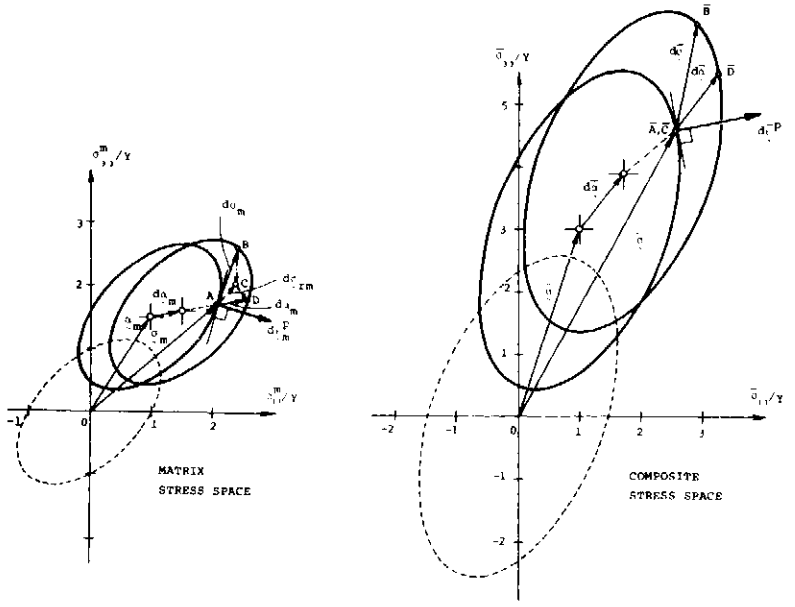

Fig. 3. Schematic representation of the constitutive equations of unidirectional composites.

rule, and normality rule in both matrix and composite stress space. We summarize here the constitutive equations which have been used in the present finite element analysis.

The overall, matrix and fiber stress increments are denoted $d\bar{\sigma}$, $d\sigma_m$ and $d\sigma_f$, respectively, while the respective strain increments are denoted $d\bar{\varepsilon}$, $d\varepsilon_m$ and $d\varepsilon_f$. Here, the stress and strain vectors are displayed as

$$d\sigma = [d\sigma_{11} d\sigma_{22} d\sigma_{33} d\sigma_{12} d\sigma_{13} d\sigma_{23}]^T$$

and

$$d\varepsilon = [d\varepsilon_{11} d\varepsilon_{22} d\varepsilon_{33} 2d\varepsilon_{12} 2d_{13} 2d\varepsilon_{13} 2d\varepsilon_{23}]^T.$$

Let $f(\bar{\sigma})$ denote the yield function of the composite lamina. Then, the flow rule for the lamina is

$$d\bar{\varepsilon} = \bar{\mathbf{M}}_e d\bar{\sigma},\ d\sigma_m = \mathbf{A}_{me} d\bar{\sigma},\ d\sigma_f = \mathbf{A}_{fe} d\bar{\sigma},$$
$$\text{if } f<0;\ \text{or } f=0,\quad \text{and}\quad df<0, \tag{4}$$

and

$$d\bar{\varepsilon} = \bar{\mathbf{M}}\, d\bar{\sigma},\ d\sigma = \mathbf{A}_m\, d\bar{\sigma},\ d\sigma_f = \mathbf{A}_f\, d\bar{\sigma},$$
$$\text{if } f=0,\quad \text{and}\quad df \geqslant 0. \tag{5}$$

Equation (4) specifies the flow rule for all elastic stress increments, where $\bar{\mathbf{M}}_e$ is the overall elastic compliance, and $\mathbf{A}_{re}$, $r=f, m$, is the elastic stress concentration factor. The flow rule for the elastic-plastic stress increments is represented by eqn (5), where $\bar{\mathbf{M}}$ is the overall instantaneous compliance, and $\mathbf{A}_r$, $r=f, m$, is the instantaneous stress concentration factor.

For a Mises-type matrix material, the yield function of the lamina is the quadratic form

$$f=(\bar{\sigma}-\bar{\alpha})^T \mathbf{A}_{me}^T \mathbf{C} \mathbf{A}_{me} (\bar{\sigma}-\bar{\alpha}) - Y^2 = 0,$$

where $\mathbf{C}=\begin{bmatrix} \mathbf{c} & \mathbf{0} \\ \mathbf{0} & 3\mathbf{I} \end{bmatrix}$, $\mathbf{c}=\begin{matrix} 1 & -1/2 & -1/2 \\ & 1 & -1/2 \\ \text{Sym.} & & 1 \end{matrix}$,

$\mathbf{I}$ is an identity matrix, and Y is the yield stress of the matrix material in simple tension. The overall translation $\bar{\alpha}$ of the yield surface is found by integrating the following equation along the loading path

$$d\bar{\alpha} = \dot{\mathbf{A}}_{me}^{-1} d\alpha_m - (\dot{\mathbf{A}}_{me}^{-1} \mathbf{A}_m - \mathbf{I}) d\bar{\sigma}, \tag{7}$$

where for a matrix material exhibiting kinematic hardening, $d\alpha_m$ denotes the incremental translation of the matrix yield surface (see Fig. 3). The translation $d\alpha_m$ can be obtained by adopting the kinematic hardening rule of Prager with Zigler's modification, namely

$$d\alpha_m = d\mu_m(\sigma_m - \alpha_m),\quad d\mu_m = \tfrac{1}{2}(\sigma_m - \alpha_m)^T \mathbf{C} d\sigma_m. \tag{8}$$

The constitutive equations are completed by giving expressions for the compliances $\bar{\mathbf{M}}_e$ and $\bar{\mathbf{M}}$, and for the stress concentration factors $\mathbf{A}_{me}$, $\mathbf{A}_{fe}$, $\mathbf{A}_m$ and $\mathbf{A}_f$. These are omitted here since the expressions are lengthy, and their interpretation is beyond the scope of this paper.

The formulation of the constitutive equations in a matrix form as described above simplifies their incorporation in a finite element calculation. A basic feature of these constitutive equations is the development of an elastic–plastic material matrix $\bar{\mathbf{L}}=\bar{\mathbf{M}}^{-1}$. During the course of the finite element calculations, matrix $\bar{\mathbf{L}}$ will simply replace the elastic material matrix $\bar{\mathbf{L}}_e=\bar{\mathbf{M}}_e^{-1}$, for every element which has yielded.

Coordinate transformation

The constitutive equations described earlier are referred to the material axes x_j, $j=1, 2, 3$ (Fig. 1). Since the fiber orientation may vary within a finite element mesh, e.g. for a laminated plate, the material axes are not universal per a composite structure. Therefore, the constitutive equations must be described in the overall axes, X_j, $j=1, 2, 3$ (Fig. 1). Namely, in the form

$$d\varepsilon = \mathbf{M}\, d\sigma,\ d\sigma = \mathbf{L}\, d\varepsilon;\ \mathbf{L}=\mathbf{M}^{-1},\ \mathbf{M}=\mathbf{M}^T, \tag{9}$$

where $d\sigma$ and $d\varepsilon$ are composite stress and strain vectors, respectively, and $\mathbf{M}$ and $\mathbf{L}$ are instantaneous compliance and material matrices, respectively, of the composite. Our objective is to determine eqn (9) when eqns (4) and (5) are known.

When the geometry of the hexahedral element is known as defined earlier, transformation of composite

stress and strain can be achieved in the form

$$d\bar{\sigma} = \mathbf{T}\, d\sigma,\ d\bar{\varepsilon} = \mathbf{N}\, d\varepsilon;\ \mathbf{N}^{-1} = \mathbf{T}^T. \tag{10}$$

The stress transformation matrix $\mathbf{T}$ is defined in terms of the direction cosines $\mathbf{t}_i$, $i = 1, 2, 3$, of the material axes as shown in the appendix. Substituting eqn (10) in the first of eqn (5), and comparing the result to eqn (9), we obtain

$$\mathbf{M} = \mathbf{T}^T \bar{\mathbf{M}} \mathbf{T},\quad \mathbf{L} = \mathbf{M}^{-1}. \tag{11}$$

Stiffness relations

Description of geometry and instantaneous material properties of the composite element suffices the definition of its stiffness relations. These, of course, should be defined in the overall coordinate system. Then, the overall stiffness relations of the composite structure are defined by assemblage of the elemental stiffness properties.

For a typical mth element, the total potential energy function π is written as

$$\pi^m = \tfrac{1}{2}\mathbf{w}^{mT}\mathbf{K}^m\mathbf{w}^m - \mathbf{w}^{mT}\mathbf{q}^m, \tag{12}$$

where $\mathbf{w}^m$ represents a listing of vertex displacements in overall coordinates. The stiffness matrix $\mathbf{K}$ and the load vector $\mathbf{q}$ are expressed for a continuum element as [7, 8]

$$\mathbf{K}^m = \int \mathbf{B}^T\mathbf{L}\mathbf{B}\, d(\text{vol}),$$

$$\mathbf{q}^m = \int \mathbf{B}^T\mathbf{p}\, d(\text{vol}) + \int \phi^T\mathbf{b}\, d(\text{vol}) \tag{13}$$

Here, $\mathbf{L}$ represents the instantaneous material matrix of the composite defined by eqn (11). The first term in the expression of $\mathbf{q}$ in eqn (13) represents vertex forces equilibrating the boundary stresses, and distributed loads $\mathbf{p}$, and the second term represents vertex forces equilibrating the body forces $\mathbf{b}$. Matrix ϕ represents the shape function of the continuum element and matrix $\mathbf{B}$ relates the strain vector ε^m to the vertex displacements $\mathbf{w}^m$, such that if $\mathbf{u}^m$ is an approximation of the displacements inside the element, then

$$\mathbf{u} = \phi\mathbf{w}^m,\ \varepsilon^m = \Lambda\mathbf{u} \Rightarrow \varepsilon^m = \mathbf{B}\mathbf{w}^m,\ \mathbf{B} = \Lambda\phi, \tag{14}$$

where Λ is a suitable linear differential operator.

In the present finite element analysis each hexahedral element is divided into five tetrahedrons. The stiffness and load matrices of the hexahedral element are obtained as the assemblage of the stiffness and load matrices of all five tetrahedrons. Since a hexahedron may be divided into five tetrahedrons in two ways, the stiffness and load matrices of a hexahedron are computed as the arithmetic average of two matrices, each generated from a set of five tetrahedrons. For each tetrahedron the stiffness and load matrices can be computed with eqn (13). We choose a linear shape function ϕ, in which case matrix $\mathbf{B}$ is constant and the integrals in eqn (13) can be easily evaluated.

In most applications of fiber-reinforced composites, one deals with laminates which consist of thin unidirectional composite laminae. In our finite element analysis, each lamina may be represented by at least one element in the thickness direction. Obviously, one cannot represent two or more consecutive laminae by one element since their material axes may not coincide. Thus, one will encounter elements of the type shown in Fig. 1 which have one dimension much smaller than the other two dimensions. In any case, the finite element mesh should be chosen such that the largest and smallest dimensions of an element do not differ by more than one order of magnitude. This will eliminate problems associated with numerical ill-conditioning of the element's stiffness matrix [9].

PAC78 COMPUTER PROGRAM

The three-dimensional composite element described in the previous article has been incorporated in a finite element code. The computer program, named PAC78, which was generated from an existing program for isotropic materials [10] conducts a finite element analysis using the displacement method. The nonlinearities caused by the elastic–plastic behavior of the material are handled by a modified Newton–Raphson iterative procedure. A brief description of the iterative solution is given next, and followed by a description of the PAC78 program.

Iterative solution of equilibrium equations

The equilibrium equations at the nodal points in the direction of unknown nodal displacements may be written in a general form as

$$\mathbf{q}(\mathbf{u}) = \mathbf{P} \tag{15}$$

where $\mathbf{q}$ and $\mathbf{P}$ represent internal and external nodal forces, respectively, and $\mathbf{u}$ represents independent nodal displacements. If the behavior of the structure is linear, then eqn (15) is linear in $\mathbf{u}$ and $\mathbf{q}$ is represented by $\mathbf{Ku}$, where $\mathbf{K}$ is the overall stiffness matrix of the structure. If, on the other hand, the behavior of the structure is nonlinear due to plastic deformation of its material, then eqn (15) represents a set of nonlinear algebraic equations. In this case, we can write eqn (15) in the form

$$\mathbf{r}(\mathbf{u}) = \mathbf{P} - \mathbf{q}(\mathbf{u}) = \mathbf{0}, \tag{16}$$

where $\mathbf{r}$ is the residual force vector which represents the unbalanced forces at the nodes. When $\mathbf{u}$ represents the true displacements for the equilibrium state corresponding to the load $\mathbf{P}$, then $\mathbf{r}$ is a null vector.

The solution of the nonlinear eqn (16) can be obtained to a desired accuracy by the modified Newton–Raphson iterative method [11]. Thus, successive approximations to the true displacements $\mathbf{u}$ can be obtained from the following recurrence formula,

$$\mathbf{u}^{(j+1)} = \mathbf{u}^{(j)} - \left[\mathbf{r}^{(0)}_{,\mathbf{u}}\right]^{-1}\mathbf{r}^{(j)},\quad j = 0, 1, \ldots, \tag{17}$$

where $\mathbf{u}^{(0)}$ is the displacement vector in a small neighborhood of the equilibrium state represented by eqn (16). The Jacobian matrix $\mathbf{r}^{(0)}_{,\mathbf{u}}$ is evaluated at the equilibrium state corresponding to $\mathbf{u}^{(0)}$. Thus, in view of eqn (16), we have

$$\mathbf{r}^{(0)}_{,\mathbf{u}} = -\mathbf{q}^{(0)}_{,\mathbf{u}} = -\mathbf{K}^{(0)}, \tag{18}$$

where $\mathbf{K}^{(0)}$ is the overall stiffness matrix evaluated at the equilibrium state corresponding to $\mathbf{u}^{(0)}$.

The recurrence formula 17 can be applied to a sequence of incremental loads to obtain the displacement vector for a particular loading level. If $\Delta\mathbf{P}^{(i)}$, $i = 1, 2, \ldots$, represents the load increment at the nodes, the cumulative displacements after application of the load increment can be obtained as

$$\mathbf{u}^{(i)}=\mathbf{u}^{(i-1)}+\{\Delta\mathbf{u}^{(i,j)}+\mathbf{K}^{(i,0)\ -1}\mathbf{r}^{(i,j)}\},$$
$$j=0, 1, \ldots \text{ until } \|\mathbf{r}^{(i,j)}\|<\varepsilon, \quad i=1, 2, \ldots, \tag{19}$$

where

$$\mathbf{r}^{(i,j)}=\Delta\mathbf{P}^{(i)}-\mathbf{q}(\Delta\mathbf{u}^{(i,j)}), \tag{20}$$

and

$$\mathbf{u}^{(0)}=\mathbf{0}, \quad \Delta\mathbf{u}^{(i,0)}=\mathbf{0}, \quad \mathbf{q}(\Delta\mathbf{u}^{(i,0)})=\mathbf{q}(\mathbf{0})=\mathbf{0}. \tag{21}$$

The residual vector $\mathbf{r}^{(i,j)}$ is computed with the conditions prevailing at the end of the jth iteration of the ith load step while $\mathbf{K}^{(i,0)}$ is computed from the geometry, material, and stresses at the beginning of the ith step. The iterative process enclosed in braces in eqn (19) is continued until the norm of $\mathbf{r}$ is smaller than a prescribed small positive number ε. A rapid change in the overall stiffness due to plastic yielding of a large number of elements within a load step may result in a slow convergence process since $\mathbf{K}$ is generated at the beginning of the step. In this case the stiffness matrix may be regenerated frequently during calculations for a particular load step.

Description of PAC78 program

The PAC78 program has been developed as a general purpose finite element program for an elastic plastic medium. The program may conduct a three-dimensional finite element analysis for two types of materials:

(1) Fiber-reinforced composite materials with a matrix material which could be nonhardening or exhibiting kinematic hardening behavior.

(2) Isotropic materials exhibiting kinematic hardening behavior. Thus, the PAC78 program can be used to conduct a three-dimensional elastic plastic analysis of composites both on the microscale, e.g. unidirectional composites with a periodic array of fibers, and on the macroscale, e.g. laminated structures.

The hexahedral element is the only type that PAC78 program uses to span the material volume. For fibrous materials, the special element described earlier has been used. By means of the displacement boundary conditions, any type of deformation may be simulated, e.g. beams, plates, plane strain, etc. Only mechanical loading is acceptable to PAC78, however, thermal loads may be added to the program pending development of a thermoplastic theory of composites.

The program consists of a main program and four major parts. A brief description of the program's four parts or links is given in Table 1. Shown in Fig. 4 is a flow diagram of the main program of PAC78. Each link of the program can be accessed by a main subroutine which is being called by the main program. In Fig. 5, the flow diagram of the main subroutine of the stress link which controls the iteration process, is shown. In this flow diagram, ITER and ITERS count the load steps and the number of iterations, respectively, PNORM and PNORMB represent the norm of the residual vector $\mathbf{r}$ and the norm of the load

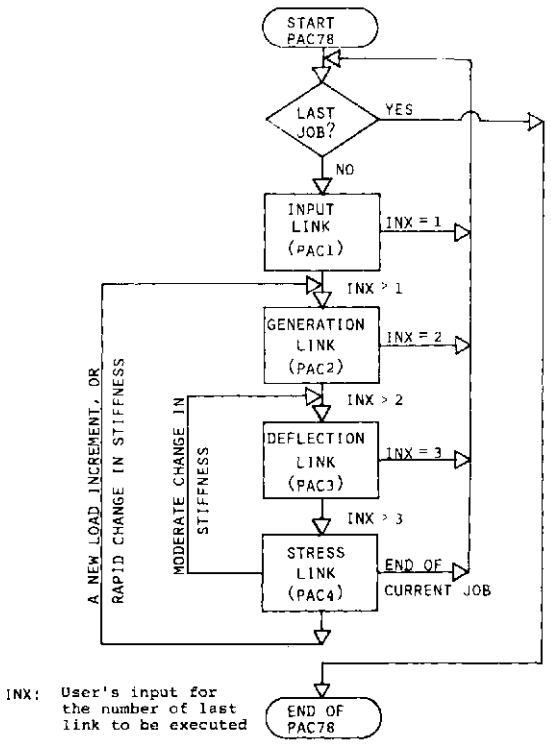

Fig. 4. Flow diagram of PAC78 computer program.

Table 1. Link numbers, names and functions for PAC78 program.

Link No.	Link Name	Function
1	INPUT	Input of the problem is obtained, checked, ordered, and printed out if requested. Relabeling of mesh points is performed upon request. Assembly constants are computed.
2	GENERATION	Governing equations for deflections are generated by generating and assembling overall stiffness matrix corresponding to instantaneous material properties, and generating and assembling overall load vector.
3	DEFLECTION	Governing Equations are solved for deflections and the complete list of nodal deflections is obtained and printed out in the overall coordinate system.
4	STRESS	Stresses and strains are computed for all elements and printed out. Nodal forces are computed and printed out. The iteration process is controlled by this link. Information is saved for post-processing.

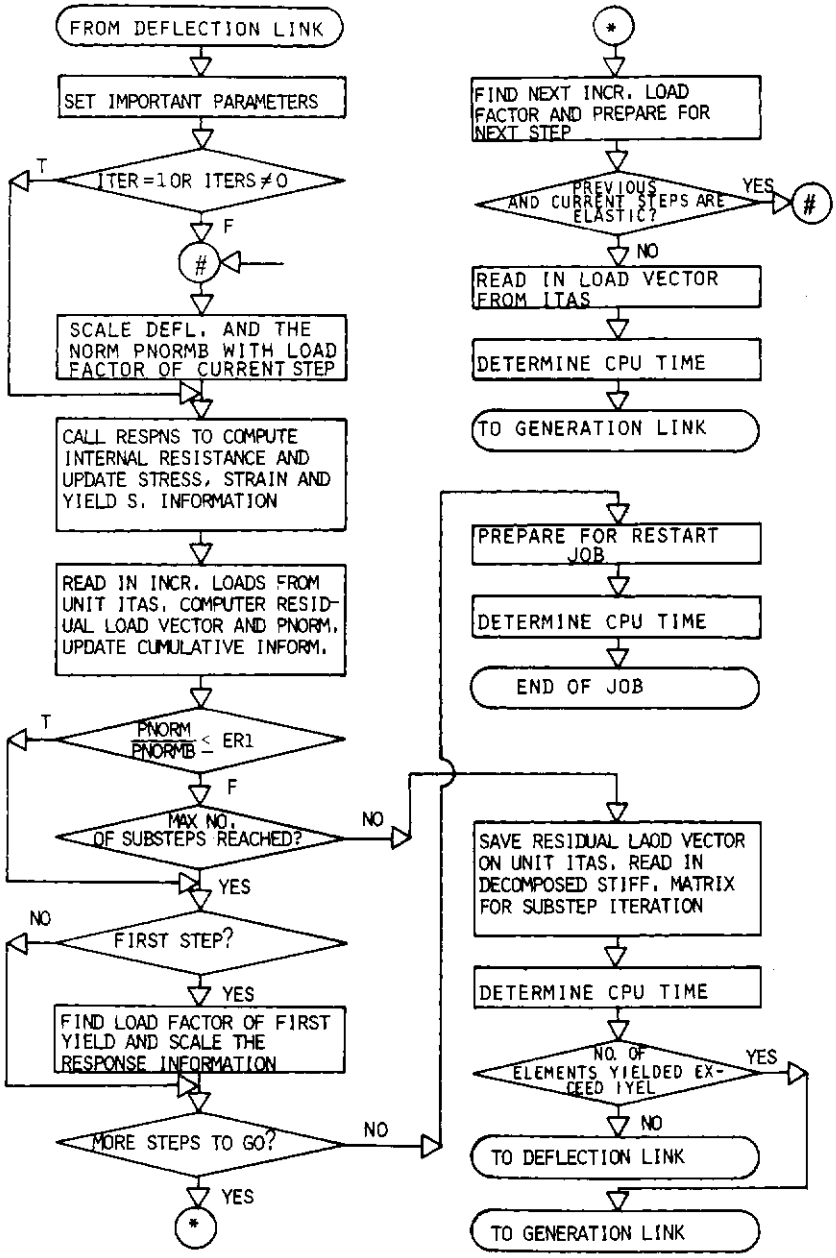

Fig. 5. Flow diagram of stress link of PAC78 program.

increment $\Delta\mathbf{P}$, respectively, ER1 is a measurement for convergence of the Newton–Raphson iteration, and IYEL is the user's indicator for generation of the stiffness matrix within a load step.

Because not all of the instructions of the program are required simultaneously, the PAC78 program is overlayed such that no more than one of the program's four links is stored in the memory during execution of a job. All data of the program are manipulated among the four links by means of a labelled common. To accommodate large loading regimes, the PAC78 program has a restart capability. If a restart job is to follow the current job being executed by the program, all necessary information is saved in an auxiliary storage file at the end of the job as shown in Fig. 5.

Assessment of accuracy

To assess the accuracy of the finite element analysis presented earlier, solutions for two problems were obtained using the PAC78 program. In the first problem we obtain finite element results for a thick-walled plane strain tube under internal pressure.

Figure 6 shows that the calculated pressure-expansion curve of the tube agrees closely with that obtained by Hodge and White [12] using finite differences and presented graphically in [13]. The curve is shown in a nondimensional form, where G is the shear modulus and k is the yield stress in simple shear. A collapse load has been also estimated by tracing the singularity ratio, which measures the positive definiteness of the overall stiffness matrix, as the pressure is increased. Fig. 6.

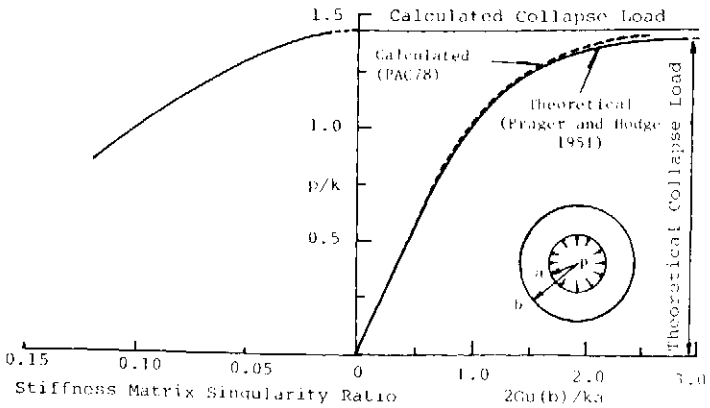

Fig. 6. Finite element results for a thick-walled cylinder under internal pressure.

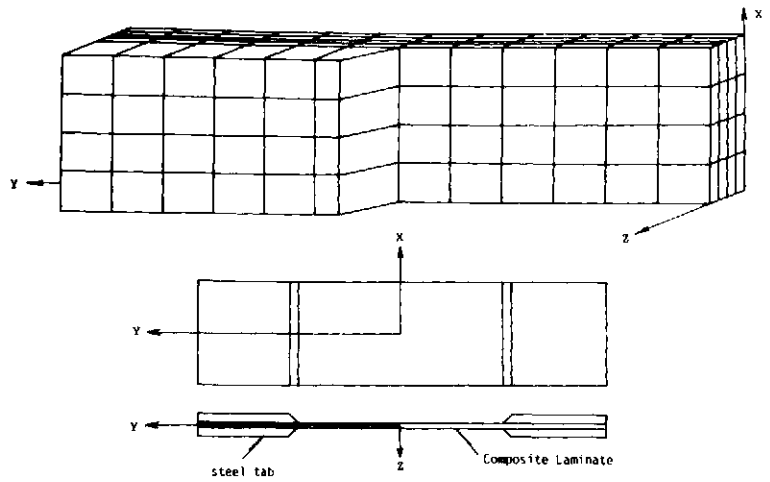

Fig. 7. Finite element mesh for uniaxial laminate specimens.

The calculated collapse load was found within a few per cent of that obtained with finite differences.

In the second problem, finite element results were obtained for a uniaxial composite laminate specimen under conditions which replicate experiments. The finite element mesh used for laminate specimens is shown in Fig. 7. Figures 8 and 9 indicate how the finite element calculations and the experimental results [14] compare for a $(0/\pm 45/90)$ symmetric laminate made of a 6061 aluminum matrix reinforced by 43 volume per cent of boron fibers. In these figures, n and κ denote the Ramberg–Osgood parameters used in the analysis to describe the stress–strain behavior of the aluminum matrix.

APPLICATION TO LAMINATED PLATES WITH DISCONTINUITIES

To demonstrate the capability of the PAC78 program in analyzing fibrous composite structures with complex geometries, we present results obtained for laminated plates with discontinuities. Two types of discontinuities are considered, a central circular hole and a single edge notch. The plates are loaded in uniaxial tension past their elastic limit. The elastic–plastic response of the plates is observed during the course of loading.

Plate with a circular hole

In this application a (0/90) symmetric laminated plate made of a 6061 aluminum matrix reinforced by 50 volume per cent of the FP fiber and containing a circular hole is loaded in simple tension. The geometry and finite element mesh are shown in Fig. 10. Since the laminate is symmetric, the finite element mesh consists of only two layers of unidirectional composite elements

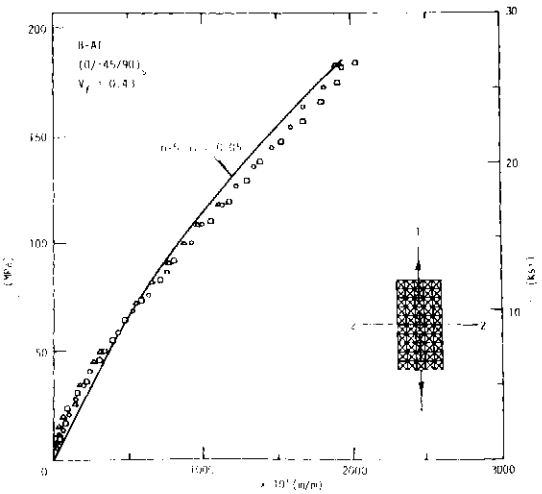

Fig. 8. Comparison of finite element calculations and experimental measurements of stress–strain curve for a $(0/\pm 45/90)_s$ B–Al plate.

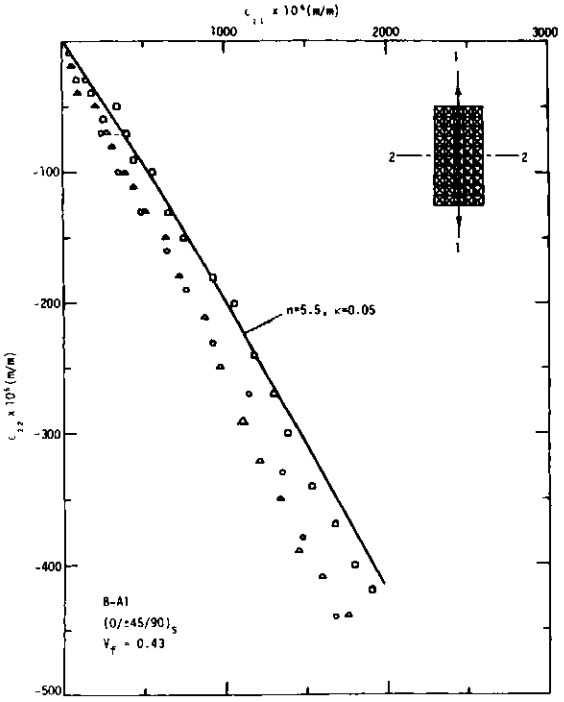

Fig. 9. Comparison of finite element calculations and experimental measurements of strains for a $(0/\pm 45/90)_s$ B-Al plate.

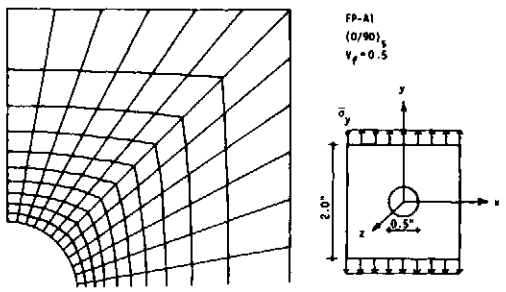

Fig. 10. Geometry of a $(0/90)_s$ FP–Al plate with a hole.

in the z-direction. The fiber direction for the outside layer of elements (0° layer) coincides with the loading direction, while the fiber direction for the inside layer of elements (90° layer) is perpendicular to the loading direction. The overall stress-strain response of the plate is shown in Fig. 11. Also shown in Fig. 11 is the stress–strain curve for an aluminum plate, which was obtained with the PAC78 program. Figures 12 and 13 show representative illustrations of the development of plastic zones in the layers of the composite plate. Other results and discussion of the behavior of the laminated plate with a hole are presented elsewhere [15].

Plate with an edge notch

The development of plastic zones at the tip of an edge notch in a $(0/\pm 45)$ symmetric plate is predicted using the finite element program. The plate, which is made of an aluminum matrix reinforced by 45 volume per cent of boron fibers, is loaded gradually past its elastic limit by a uniaxial tensile load. The load is applied uniformly to the ends of the plate which are also constrained against

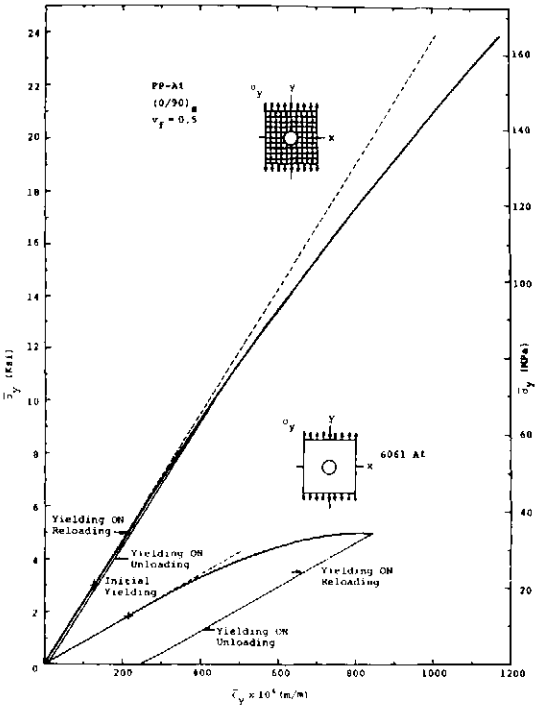

Fig. 11. Stress–strain curves of a $(0/90)_s$ FP–Al plate and an aluminum plate with holes.

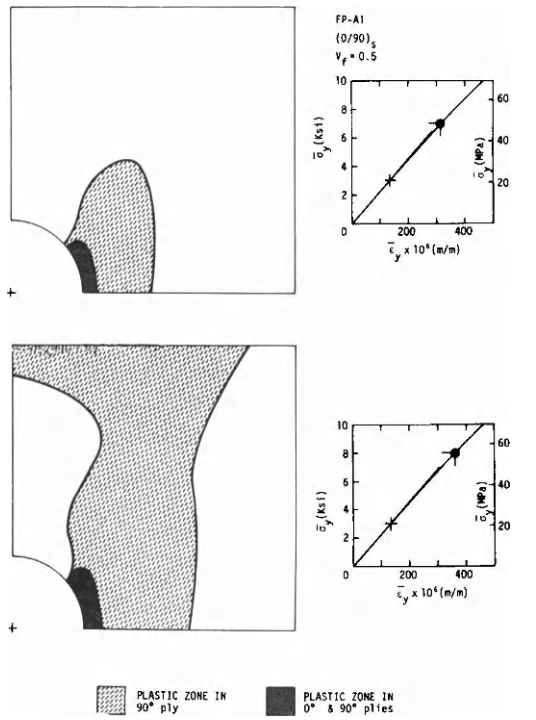

Fig. 12. Plastic zones in a $(0/90)_s$ FP–Al plate with a hole.

rotation. Figure 14 shows the geometry of the plate and the finite element mesh used in the analysis. First yielding starts at the tip of the notch in all off-axis layers ($\pm 45°$ layers) of the plate. Increasing the load beyond that for initial yield, plastic zones develop in the layers of the plate as shown in Fig. 15.

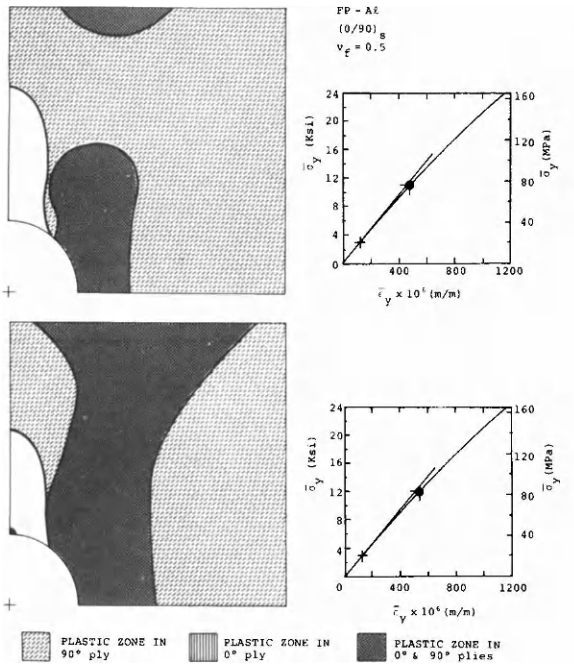

Fig. 13. Plastic zones in a $(0/90)_s$ FP-Al plate with a hole.

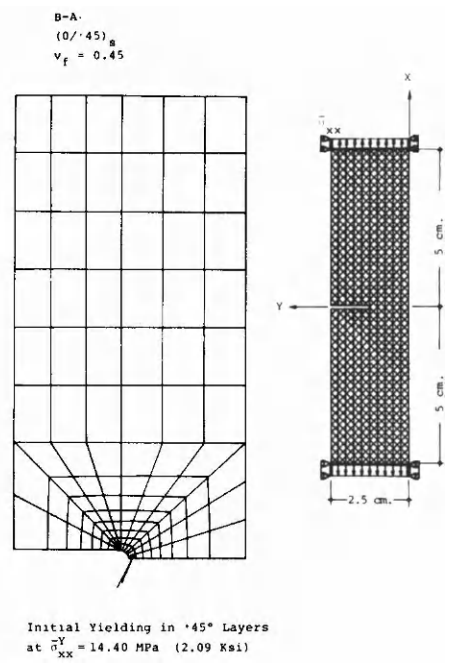

Fig. 14. Geometry of a notched $(0/\pm 45)_s$ B–Al plate.

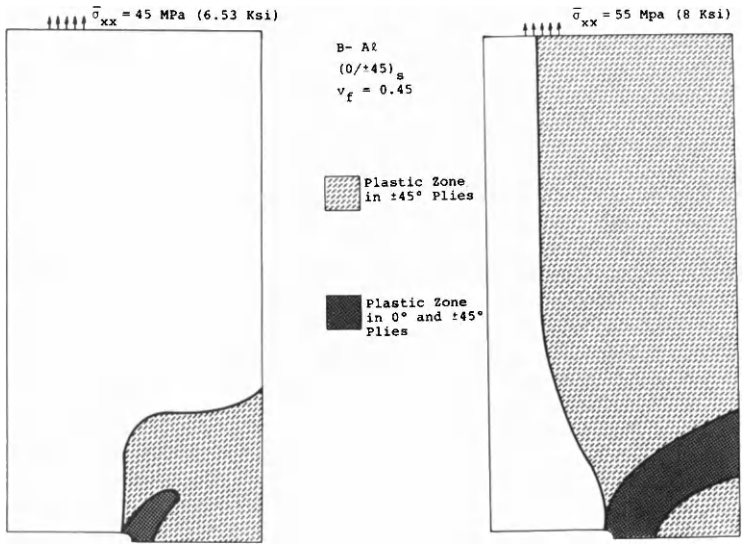

Fig. 15. Plastic zones in a notched $(0/\pm 45)_s$ B–Al plate.

CONCLUSIONS

A three-dimensional finite element analysis for elastic–plastic fiber-reinforced composite materials has been presented. The analysis, which treats unidirectional composite materials as macroscopically uniform, is suitable for fibrous composite structures such as laminated plates. As a byproduct, the analysis can be used for elastic plastic isotropic materials which permits study of microstructural models of unidirectional composites.

Results obtained with the finite element analysis for a composite laminate specimen have been shown to agree with experimental measurements. Agreement of finite element results with theoretical results for an isotropic thick-walled cylinder under internal pressure has been also shown. The capability of the finite element analysis in predicting the behavior of composite structures with complex geometry has been demonstrated for two laminated plates, one containing a hole, the other has an edge notch.

Of principal concern in the analysis of composite structures is the prediction of failure loads. An extension of the present finite element analysis to include failure analysis of composite structures may be achieved by adopting a failure criterion for unidirectional composites.

Acknowledgements—This work was supported by the U.S. Army Research Office. Computer time was supported by the Department of Civil Engineering, Duke University.

REFERENCES

1. D. F. Adams and A. K. Miller, Hygrothermal microstresses in a unidirectional composite exhibiting inelastic material behavior. *J. Composite Mater.* **11**, 285–299 (1977).
2. D. F. Adams, Inelastic analysis of a unidirectional composite subjected to transverse normal loading. *J. Composite Mater.* **4**, 310–328 (1970).
3. R. L. Foye, Theoretical post-yielding behavior of composite laminates. Part I—Inelastic micromechanics. *J. Composite Mater.* **7**, 178–193 (1973).
4. Y. A. Bahei-El-Din, Plastic analysis of metal–matrix composite laminates. Ph.D. Dissertation, Duke University (1979).
5. G. J. Dvorak and Y. A. Bahei-El-Din, Plasticity of composite laminates. *Proc. Research Workshop on Mechanics of Composite Materials* (Edited by G. J. Dvorak), pp. 32–54. Duke University (1978).
6. Y. A. Bahei-El-Din and G. J. Dvorak, Plastic yielding at a circular hole in a laminated FP-Al plate. *Modern Developments in Composite Materials and Structures*, (Edited by J. R. Vinson) pp. 123–147 (1979).
7. O. C. Zienkiewicz, *The Finite Element Method*, 3rd Edn. McGraw-Hill, New York (1977).
8. C. H. Norris, J. B. Wilbur and S. Utku, *Elementary Structural Analysis*, Part II, 3rd Edn. McGraw-Hill, New York (1976).
9. R. M. Barker, F. Lin and J. R. Dana, Three-dimensional finite-element analysis of laminated composites. *Comput. Structures* **2**, 1013–1029 (1972).
10. S. Utku, M. S. M. Rao and G. J. Dvorak, ELAS65 computer program for equilibrium problems of elastic–thermoplastic solids and structures. Structural Mechanics Series No. 15, Duke University (1973).
11. J. T. Oden, *Finite Elements of Nonlinear Continua*. McGraw-Hill, New York (1972).
12. P. G. Hodge, Jr. and G. N. White, Jr. A quantitative comparison of flow and deformation theories of plasticity. *J. Appl. Mech.* **17**, 180–184 (1950).
13. W. Prager and P. G. Hodge, Jr., *Theory of Perfectly Plastic Solids*. Wiley, New York (1951).
14. S. I. Shukow, Acoustic-mechanical characterization of boron-aluminum composite laminates. M. Sc. Thesis, The University of Delaware (1977).
15. Y. A. Bahei-El-Din and G. J. Dvorak, Plastic deformation of a laminated plate with a hole. *J. Appl. Mech.*, in press.

APPENDIX

Transformation of stress vectors

The transformation of the stress vector σ, described in the overall coordinates X_j, $j=1, 2, 3$, to the coordinate system $\bar{x}_j$, $j=1, 2, 3$ can be expressed as

$$\bar{\sigma}=\mathbf{T}\sigma, \tag{A1}$$

where $\bar{\sigma}$ is the description of the stress vector in the coordinates $\bar{x}_j$, $j=1, 2, 3$, and

$$\mathbf{T}=\begin{bmatrix} t_{11}^2 & t_{12}^2 & t_{13}^2 & 2t_{11}t_{12} & 2t_{11}t_{13} & 2t_{12}t_{13} \\ t_{21}^2 & t_{22}^2 & t_{23}^2 & 2t_{21}t_{22} & 2t_{21}t_{23} & 2t_{22}t_{23} \\ t_{31}^2 & t_{32}^2 & t_{33}^2 & 2t_{31}t_{32} & 2t_{31}t_{33} & 2t_{32}t_{33} \\ t_{11}t_{21} & t_{11}t_{22} & t_{13}t_{23} & t_{11}t_{22}+t_{12}t_{21} & t_{11}t_{23}+t_{13}t_{21} & t_{12}t_{23}+t_{13}t_{22} \\ t_{11}t_{31} & t_{12}t_{32} & t_{13}t_{33} & t_{11}t_{32}+t_{12}t_{31} & t_{11}t_{33}+t_{13}t_{31} & t_{21}t_{33}+t_{13}t_{32} \\ t_{21}t_{31} & t_{22}t_{32} & t_{23}t_{33} & t_{21}t_{32}+t_{22}t_{31} & t_{21}t_{33}+t_{23}t_{31} & t_{22}t_{33}+t_{23}t_{32} \end{bmatrix} \tag{A2}$$

Here, t_{ij} denotes the direction cosine of the angle between $\bar{x}_i$-axis and X_j-axis, $i, j=1, 2, 3$.

Computers & Structures, Vol. 13, pp. 331–340, 1981
Printed in Great Britain.

0045-7949/81/010331-10$02.00/0

LARGE DEFORMATION ANALYSIS OF LAMINATED SHELLS BY FINIFE ELEMENT METHOD

T. Y. CHANG and K. SAWAMIPHAKDI

Department of Civil Engineering, The University of Akron, Akron, OH 44325, U.S.A.

Received 11 *May* 1980)

Abstract—A finite element formulation is presented for conducting large deformation analysis of laminated anisotropic shells. The element adopted herein is a "degenerated" three-dimensional isoparametric element. Derivations of the nonlinear geometric element stiffness matrices were made on the basis of updated Lagrangian description. The numerical formulations of the shell element were implemented into a nonlinear finite program. Numerical characteristics of the element with respect to the mesh size and the use of integration orders were studied for a plate with simply supports and clamped supports. In addition, several examples are included to demonstrate the utility of the element.

INTRODUCTION

Finite element analysis of either thin or thick shells has been the subject of interest for many years and there is abundance of published work in the open literature. Most of the research effort was concentrated on the linear elastic materials or elastic–plastic material with the assumption of small deformation. In recent years, interest in this area has expanded to include the effect of geometric nonlinearity and post-buckling behavior of shells.

In the context of finite element analysis, numerous elements have been proposed for the analysis of shell-like structures. These range from the simple flat plate elements to more sophisticated doubly curved elements based on the thin shell theory. Comments on the merits and shortcomings of the various shell elements were given in a review article by Gallagher [1]. Among all the shell elements that have been investigated by previous researchers, it appears that the "degenerated" three dimensional (3-D) isoparametric solid element with independent rotational and translation degrees of freedom, originally proposed by Ahmad, Irons and Zienkiewicz [2] for linear analysis of thin shells, offers the best possibility for extension to nonlinear analysis. The basic idea of this element is to impose the constraint of the straight "normals" to its middle surface in order to overcome the numerical difficulty associated with the large stiffness ratio in the thickness direction of the 3-D solid element. With this constraint, the displacement field of the shell can be expressed in terms of the nodal degrees of freedom on the middle surface, i.e. 3—translations and 2—rotations at each node, and a maximum of 40 total degrees of freedom. It has been shown that this element produced good results for thick shells. However, for thin shells the element was found to be too stiff to represent the bending action of the structure due to the presence of shear stresses which do not exist in the structure. In this connection, some corrective steps have been proposed by various researchers. One method is the use of semi-Loof element by Iron [3], that a set of interpolation functions were derived by enforcing constraint conditions at discrete points on the element level. The simplest modification of the "degenerated" element is to use the reduced integration order in the evaluation of element stiffness which leads to satisfactory results in linear analysis [4]. Pawsey and Clough [5] applied the same reduced integration concept, called a selective integration procedure, in which the number of integration points varied with the strain energy terms associated with the specific strain components. Cook [6], Takemoto and Cook [7] introduced another improvement by adding a central node with 1–5 degrees of freedom. In the same context of reduced integration scheme, Hughes *et al.* [8] and Kanoknukulchai [9] separated the stiffness matrix of a 4-node plate/shell element into two parts: one related to the distortional energy and the other, volumetric energy. The part related to the distortional energy was evaluated numerically by the reduced integration and excellent responses were obtained. However, for problems involving geometric nonlinearity, separation of the stiffness matrix into distortional and volumetric parts would not be possible.

The "degenerated" 3-D solid element has recently been applied to the geometrically nonlinear static analysis of shells by Ramm [10]. In his work, the displacement field was approximated by use of quadratic and cubic Lagrangian interpolation functions and the equilibrium equations for large deformation analysis were derived on the basis of total Lagrangian formulation. Similar work was further extended by Bolouchi [11] including both the total and updated Lagrangian approaches for the shell element with variable nodes of 8–16 on the middle surface. Only isotropic materials were considered in his analysis. Large deformation analysis of shallow shells by use of the hydbrid elements was due to Pian and Boland [12]. Bergan and Clough [13] proposed a doubly curved quadrilateral element based on the von Karman strain expressions for plates in conjunction with the Marguerre shallow shell theory, and the element was applied to the large deflection analysis of shallow shells. A facet triangular shell element with a natural mode method was given by Argyris *et al.* [14] for the large deflection and post-buckling analysis of shells. Moreover, Horrigmoe and Bergan [15] presented a snap-through analysis of free-form shell by using the flat plate elements with an updated Lagrangian formulation. The only large deformation analysis of laminated composite shells that can be found from the literature is due to Noor and

Hartley [16], in which nonlinear triangular and quadrilateral elements were derived based on a shallow shell theory and the effect of shear deformation was included.

In the modelling of laminated anisotropic or orthotropic materials, Pryor and Barker [17] presented a linear finite element analysis of thin plate for which a 4-node plate element was used. The element stiffness was derived by assuming seven degrees of freedom at each node; 3 translations, 2 rotations and 2 for shear deformations. In the thickness direction, they assumed the rotations to be the same for all the constituent layers. Mawenya and Davies [18] used the "degenerated" 3-D solid elements with independent rotations for each layer. Consequently, the total number of degrees of freedom will increase proportionally with the number of layers of the plate. Panda and Natarajan [19] modified the work of Mawenya and Davies by assuming the same rotation throughout the thickness of the plate as in [18]. Additional work on the bending analysis of laminated anisotropic plate with small deformation was due to Noor and Mathers [20] using a cubic isoparametric element.

The objective of this paper is to extend the "degenerated" 3-D solid element to the large displacement analysis of shells with laminated anisotropic material construction. After some assessment of the previous work, the 8- node and 9- node elements are selected for the present work, although higher order elements may offer better accuracy, it nevertheless requires much more computational effort.

For large deformation analysis by finite element method, the equations of equilibrium of a structure may be derived from two alternative approaches: the total Lagrangian and the updated Lagrangian. From the theoretical standpoint, both approaches should lead to the same results for the same nonlinear problem. However, in practice the updated Lagrangian involves less amount of numerical effort for the problem considered herein and therefore it is more efficient in computation. In this paper, derivation of the element stiffness for the updated Lagrangian formulation is presented. In addition, the numerical characteristics in terms of the number of elements to be used, integration order with respect to the element aspect ratio, were investigated and the results are presented in the same format as the case of linear analysis of plates by Pugh *et al.* [21]. Finally, several numerical examples are given to demonstrate the applications of the shell element.

INCREMENTAL VIRTUAL WORK EQUATION

Following Hill's work [22, 23] consider the virtual work equation which is written with respect to a reference frame θ_i

$$\int_{v_\theta} (\tilde{S}_{ij}+\Delta\tilde{S}_{ij})\delta\left(\frac{\partial\Delta u_j}{\partial\theta_i}\right)\mathrm{d}v = \int_{v_\theta}(\bar{F}_i+\Delta\bar{F}_i)\delta\Delta u_i\,\mathrm{d}v+\int_{S_\theta}(\bar{T}_i+\Delta\bar{T}_i)\delta u_i\mathrm{d}S \qquad (1)$$

where $\tilde{S}_{ij}$ = Non-symmetric nominal stress tensor at time t with respect to the reference configuration θ_i, u_i = Displacement components at time t, $\bar{F}_i$ = Nominal body forces at time t per unit volume of the reference configuration θ_i, $\bar{T}_i$ = Nominal surface tractions at time t per unit surface of the reference configuration θ_i, $\Delta(\ )$ = Incremental value of $(\ )$ from time t to time $t+\Delta t$ and $\delta(\ )$ = Variational of $(\ )$.

By selecting the reference configuration at time t, we obtain the updated Lagrangian description of virtual work equation. Therefore, the reference coordinates θ_i are chosen to be the updated coordinates x_i at time t, eqn (1) thus becomes

$$\int_{V_t}(\sigma_{ij}+\Delta\tilde{S}_{ij})\delta\left(\frac{\partial\Delta u_j}{\partial x_i}\right)\mathrm{d}v = \int_{V_t}(F_i+\Delta F_i)\delta\Delta u_i\mathrm{d}v+\int_{S_t}(T_i+\Delta T_i)\delta\Delta u_i\mathrm{d}s \qquad (2)$$

where σ_{ij} = Cauchy stress tensor at time t, F = Body forces at time t per unit volume at time t and T_i = Surface traction at time t per unit surface at time t.

According to Hill [24], the constitutive relations of rate dependent materials may have the following general form

$$\Delta S^*_{ij}=C_{ijkl}D_{kl} \qquad (3)$$

where ΔS^*_{ij} = Jaumann (co-rotational) rate of the Kirchhoff stress, C_{ijkl} = A material stiffness matrix referred to the updated coordinates at time t. D_{kl} = Rate of deformation tensor

$$=\frac{1}{2}\left(\frac{\partial\Delta u_i}{\partial x_j}+\frac{\partial\Delta u_j}{\partial x_i}\right)$$

or in matrix notation, eqn (3) is rewritten as

$$\{\Delta S^*\}=[C]\{D\}. \qquad (4)$$

Moreover, the Jaumann rate of Kirchhoff stress tensor is related to the incremental nominal stress by

$$\Delta\tilde{S}_{ij}=\Delta S^*_{ij}+\sigma_{ik}\frac{\partial\Delta u_j}{\partial x_k}-(\sigma_{ik}D_{jk}+\sigma_{jk}D_{ik}). \qquad (5)$$

Finally, we obtain the virtual work equation for updated Lagrangian formulation as [25]

$$\int_{V_t}\left[C_{ijkl}\delta D_{kl}D_{ij}-\tfrac{1}{2}\sigma_{ij}\delta\left(2D_{ik}D_{kj}-\frac{\partial\Delta u_k}{\partial x_i}\frac{\partial\Delta u_k}{\partial x_j}\right)\right]\mathrm{d}v = R(t+\Delta t)-\int_{V_t}\sigma_{ij}\delta D_{ij}\,\mathrm{d}v \qquad (6)$$

where

$$R(t+\Delta t)=\int_{V_t}(F_i+\Delta\tilde{F}_i)\delta\Delta u_i\mathrm{d}v+\int_{S_t}(T_i+\Delta\tilde{T}_i)\delta\Delta u_i\,\mathrm{d}s.$$

Equation (5) represents a nonlinear equation concerning the unknown incremental displacements from time t to time $t+\Delta t$. We can derive the incremental finite element equations for the shell structure by using the "degenerated" 3-D solid element which are described in the next section.

DESCRIPTION OF THE ELEMENT

The geometry of shell can be represented by the coordinates and normal vectors of its middle surface as shown in Fig. 1. The middle surface is modeled by the so-called "degenerated" isoparametric element in three-dimensional space. Two different types of elements are considered: Serendipity element (8 node) and Lagrangian element (9 node). Each node has five degrees of freedom, i.e. three translations in the directions of the global axes and two rotations with respect to the

axes in the plane of the middle surface as shown in Fig. 2.

In reference to a set of rectangular Cartesian coordinates, let $x_i(t)$, $i=1, 2, 3$ be the components of the position vector of a generic point at time t, also let ξ, η and

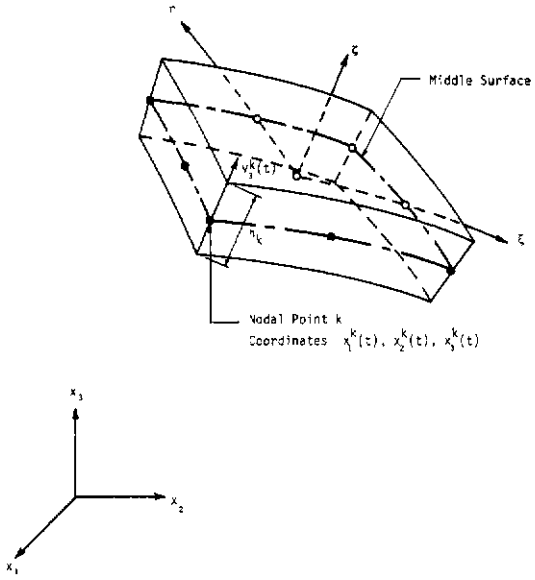

Fig. 1. Geometry of shell element at time t.

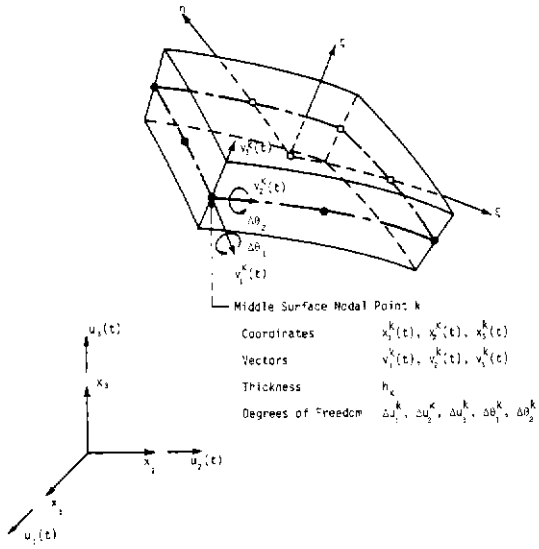

Fig. 2. Definition of "degenerated" 3-D isoparametric solid element at time t.

ζ be the natural coordinates of the shell element. Referring to Fig. 1, the Cartesian coordinates at any point of the shell at time t may be expressed by

$$x_i(t)=\sum_{k=1}^{m} N_k(\xi,\eta)x_i^k(t)+\frac{\zeta}{2}\sum_{k=1}^{m} N_k(\xi,\eta)h_k v_{3i}^k(t) \quad (7)$$

where $x_i(t)$ = Cartesian coordinate of any point on the shell at time t, $N_k(\xi,\eta)$ = Interpolation function associated with node k, $x_i^k(t)$ = Cartesian coordinate of nodal point k at time t, h_k = Thickness of shell in ζ direction at nodal point k, $v_{3i}^k(t)=i$th component of unit normal vector to the middle surface at nodal point k and time t and m = Number of nodes of the element.

The displacement vector of a generic point at time t and the incremental displacement vector can be written as

$$u_i=x_i(t)-x_i(0) \quad (8)$$

$$\Delta u_i=x_i(t+\Delta t)-x_i(t). \quad (9)$$

From eqns (7)–(9) the displacement vector at time t and the incremental displacement vector are given by

$$u_i=\sum_{k=1}^{m} N_k(\xi,\eta)u_i^k+\frac{\zeta}{2}\sum_{k=1}^{m} N_k(\xi,\eta)h_k(v_{3i}^k(t)-v_{3i}^k(0)) \quad (10)$$

$$\Delta u_i=\sum_{k=1}^{m} N_k(\xi,\eta)\Delta u_i^k+\frac{\zeta}{2}\sum_{k=1}^{m} N_k(\xi,\eta)h_k(v_{3i}^k(t+\Delta t)-v_{3i}^k(t), \quad (11)$$

where $u_i^k=x_i^k(t)-x_i^k(0)$ and $\Delta u_i^k=x_i^k(t+\Delta t)-x_i^k(t)$.

The unit normal vector, $\mathbf{v}_3$, and two unit tangential vectors $\mathbf{v}_1$ and $\mathbf{v}_2$, of the middle surface at node k for the time varying between 0 to t are evaluated from the Cartesian coordinates at that point by

$$\mathbf{v}_3=\left(\frac{\partial x_i}{\partial\xi}\right)\times\left(\frac{\partial x_i}{\partial\eta}\right)\left(\frac{\partial x_i}{\partial\xi}\right)\times\left(\frac{\partial x_i}{\partial\eta}\right) \quad (12)$$

$$\mathbf{v}_1=(\mathbf{e}_2\times\mathbf{v}_3)/|\mathbf{e}_2\times\mathbf{v}_3| \quad (13)$$

$$\mathbf{v}_2=\mathbf{v}_3\times\mathbf{v}_1 \quad (14)$$

where $\mathbf{e}_2$ is unit vector in x_2 direction.

To obtain the unit normal vector, $\mathbf{v}_3^k(t+\Delta t)$, we have to approximate in terms of $\mathbf{v}_1^k(t)$, $\mathbf{v}_2^k(t)$, $\mathbf{v}_3^k(t)$ and the incremental rotations from time t to time $t+\Delta t$ of vector $\mathbf{v}_1^k(t)$ and $\mathbf{v}_2^k(t)$. Let $\Delta\theta_1^k$ and $\Delta\theta_2^k$ be the incremental rotations about $\mathbf{v}_1^k(t)$ and $\mathbf{v}_2^k(t)$ respectively as shown in Fig. 2. By applying the Euler method [26] with the assumption $\Delta\theta_1^k$ and $\Delta\theta_2^k$ being small, the unit normal vector $\mathbf{v}_3^k(t+\Delta t)$ is expressed by

$$\mathbf{v}_3^k(t+\Delta t)=\mathbf{v}_3^k(t)-\mathbf{v}_2^k(t)\Delta\theta_1^k+\mathbf{v}_1^k(t)\Delta\theta_2^k. \quad (15)$$

Substituting the above equation into eqn (11), the incremental displacements can be written as

$$\Delta u_i=\sum_{k=1}^{m} N_k(\xi,\eta)\Delta u_i^k+\frac{\zeta}{2}\sum_{k=1}^{m} N_k(\xi,\eta)h_k(-v_{2i}^k(t)\Delta\theta_1^k+v_{1i}^k(t)\Delta\theta_2^k). \quad (16)$$

The unknown incremental displacements in the above equation are related to the quantities at time t which are already known. To obtain the displacement derivatives with respect to the global system $x_i(t)$, $i=1, 2, 3$, we employ the Jacobian transformation, $J(t)$, to relate the derivatives corresponding to the natural coordinates to the those of the Cartesian coordinates by

$$\begin{Bmatrix} \frac{\partial\Delta u_i}{\partial x_1(t)} \\ \frac{\partial\Delta u_i}{\partial x_2(t)} \\ \frac{\partial\Delta u_i}{\partial x_3(t)} \end{Bmatrix}=[J(t)]^{-1}\begin{Bmatrix} \frac{\partial\Delta u_i}{\partial\xi} \\ \frac{\partial\Delta u_i}{\partial\eta} \\ \frac{\partial\Delta u_i}{\partial\zeta} \end{Bmatrix} \quad (17)$$

where the Jacobian transformation matrix, $J(t)$, contains the derivatives of the coordinates, $x_i(t)$, with

respect to the natural coordinates ξ, η and ζ, i.e.

$$[J(t)]=\begin{bmatrix}\frac{\partial x_1(t)}{\partial\xi} & \frac{\partial x_2(t)}{\partial\xi} & \frac{\partial x_3(t)}{\partial\xi}\\ \frac{\partial x_1(t)}{\partial\eta} & \frac{\partial x_2(t)}{\partial\eta} & \frac{\partial x_3(t)}{\partial\eta}\\ \frac{\partial x_1(t)}{\partial\zeta} & \frac{\partial x_2(t)}{\partial\zeta} & \frac{\partial x_3(t)}{\partial\zeta}\end{bmatrix}. \tag{18}$$

From eqns (17) and (18) we find

$$\{\Delta u\}_{,j}=[B_1]\{\Delta u^k\} \tag{19}$$

where

$$\{\Delta u\}_{,j}$$

$$[\Delta u_{1,1}\Delta u_{1,2}\Delta u_{1,3}\Delta u_{2,1}\Delta u_{2,2}\Delta u_{2,3}\Delta u_{3,1}\Delta u_{3,2}\Delta u_{3,3}]^T \tag{20}$$

$$\{\Delta u^k\}$$

$$=[-\,-\,-\,-\,-\,\Delta u_1^k\Delta u_2^k\Delta u_3^k\Delta\theta_1^k\Delta\theta_2^k-\,-\,-\,-]^T \tag{21}$$

and

$$[B_1]=\begin{bmatrix}---a_k & 0 & 0 & -\frac{1}{2}d_kh_kv_{21}^k(t) & \frac{1}{2}d_kh_kv_{11}^k(t)----\\ ---b_k & 0 & 0 & -\frac{1}{2}e_kh_kv_{21}^k(t) & \frac{1}{2}e_kh_kv_{11}^k(t)----\\ ---c_k & 0 & 0 & -\frac{1}{2}f_kh_kv_{21}^k(t) & \frac{1}{2}f_kh_kv_{11}^k(t)----\\ ---0 & a_k & 0 & -\frac{1}{2}d_kh_kv_{22}^k(t) & \frac{1}{2}d_kh_kv_{12}^k(t)----\\ ---0 & b_k & 0 & -\frac{1}{2}e_kh_kv_{22}^k(t) & \frac{1}{2}e_kh_kv_{12}^k(t)----\\ ---0 & c_k & 0 & -\frac{1}{2}f_kh_kv_{22}^k(t) & \frac{1}{2}f_kh_kv_{12}^k(t)----\\ ---0 & 0 & a_k & -\frac{1}{2}d_kh_kv_{23}^k(t) & \frac{1}{2}d_kh_kv_{12}^k(t)----\\ ---0 & 0 & b_k & -\frac{1}{2}e_kh_kv_{23}^k(t) & \frac{1}{2}e_kh_kv_{13}^k(t)----\\ ---0 & 0 & c_k & -\frac{1}{2}f_kh_kv_{23}^k(t) & \frac{1}{2}f_kh_kv_{13}^k(t)----\end{bmatrix} \tag{22}$$

with

$$\begin{aligned}a_k&=J_{11}^{-1}N_{k,\xi}+J_{12}^{-1}N_{k,\eta}\\ b_k&=J_{21}^{-1}N_{k,\xi}+J_{22}N_{k,\eta}\\ c_k&=J_{31}^{-1}N_{k,\xi}+J_{32}^{-1}N_{k,\eta}\\ d_k&=a_k\zeta+J_{13}^{-1}N_k\\ e_k&=b_k\zeta+J_{23}^{-1}N_k\\ f_k&=c_k\zeta+J_{33}^{-1}N_k.\end{aligned}$$

In the analysis, the rate of deformation tensor is used and it has six components

$$D_{ij}=\tfrac{1}{2}(\Delta u_{i,j}+\Delta u_{j,i}). \tag{23}$$

After substituting the expressions of $\Delta u_{i,j}$ from eqn (19) the rate of deformation tensor will be in the form

$$\{D\}=[B_L]\{u^k\} \tag{24}$$

where

$$\{D\}=[D_{11}D_{22}D_{33}2D_{12}2D_{23}2D_{31}]^T \tag{25}$$

$$[B_L]=\begin{bmatrix}---a_k & 0 & 0 & -\frac{1}{2}d_kh_kv_{21}^k(t) & \frac{1}{2}d_kh_kv_{11}^k(t)---\\ ---0 & b_k & 0 & -\frac{1}{2}e_kh_kv_{22}^k(t) & \frac{1}{2}e_kh_kv_{12}^k(t)---\\ ---0 & 0 & c_k & -\frac{1}{2}f_kh_kv_{23}^k(t) & \frac{1}{2}f_kh_kv_{13}^k(t)---\\ ---b_k & a_k & 0 & -\frac{1}{2}h_k(e_kv_{21}^k(t)+d_kv_{22}^k(t)) & \\ & & & \frac{1}{2}h_k(e_kv_{11}^k(t)+d_kv_{12}^k(t))--- & \\ ---0 & c_k & b_k & -\frac{1}{2}h_k(f_kv_{22}^k(t)+e_kv_{23}^k(t)) & \\ & & & \frac{1}{2}h_k(f_kv_{12}^k(t)+e_kv_{13}^k(t))---- & \\ ---c_k & 0 & a_k & -\frac{1}{2}h_k(f_kv_{21}^k(t)+d_kv_{23}^k(t)) & \\ & & & \frac{1}{2}h_k(f_kv_{11}^k(t)+d_kv_{13}^k(t))---- & \end{bmatrix}. \tag{26}$$

Combining eqns (4), (5), (6), (19) and (24), the finite element matrices corresponding to the global coordinate system can be obtained with the following relationships

$$\int_{V_t}C_{ijkl}D_{kl}\delta D_{ij}\,dv \quad \text{equivalent to} \quad \left(\int_{V_t}[B_L]^T[C][B_L]\,dv\right)\{\Delta u^k\}$$

$$\int_{V_t}\sigma_{ij}\delta D_{ik}D_{kj}\,dv \quad \text{equivalent to} \quad \left(2\int_{V_t}[B_2]^T[\sigma][B_2]\,dv\right)\{\Delta u^k\}$$

$$\int_{V_t}\tfrac{1}{2}\sigma_{ij}\delta\Delta u_{k,i}\Delta u_{k,j}\,dv \quad \text{equivalent to} \quad \left(\int_{V_t}[B_1]^T[\sigma][B_1]\,dv\right)\{\Delta u^k\}$$

$$\int_{V_t}\sigma_{ij}\delta D_{ij}\,dv \quad \text{equivalent to} \quad \int_{V_t}[B_L]^T\{\sigma\}\,dv$$

where B_1 and B_L are already defined by eqns (22) and (26), and

$$[B_2]=\begin{bmatrix}---a^k & 0 & 0 & -\frac{1}{2}h_kd_kv_{21}^k(t) & \frac{1}{2}h_kd_kv_{11}^k(t)---\\ ---\frac{b_k}{2} & \frac{a_k}{2} & 0 & -\frac{1}{4}h_k(e_kv_{21}^k(t)+d_kv_{22}^k(t)) & \frac{1}{4}h_k(e_kv_{11}^k(t)+d_kv_{12}^k(t))---\\ ---\frac{c_k}{2} & 0 & \frac{a_k}{2} & -\frac{1}{4}h_k(f_kv_{21}^k(t)+d_kv_{23}^k(t)) & \frac{1}{4}h_k(f_kv_{11}^k(t)+d_kv_{13}^k(t))---\\ ---\frac{b_k}{2} & \frac{a_k}{2} & 0 & -\frac{1}{4}h_k(e_kv_{21}^k(t)+d_kv_{22}^k(t) & \frac{1}{4}h_k(e_kv_{11}^k(t)+d_kv_{12}^k(t))---\\ ---0 & b_k & 0 & -\frac{1}{2}h_ke_kv_{22}^k(t) & \frac{1}{2}h_ke_kv_{12}^k(t)\\ ---0 & \frac{c_k}{2} & \frac{b_k}{2} & -\frac{1}{4}h_k(f_kv_{22}^k(t)+e_kv_{23}^k(t)) & \frac{1}{4}h_k(f_kv_{12}^k(t)+e_kv_{13}^k(t))----\\ ---\frac{c_k}{2} & 0 & \frac{a_k}{2} & -\frac{1}{4}h_k(f_kv_{21}^k(t)+d_kv_{23}^k(t)) & \frac{1}{4}h_k(f_kv_{11}^k(t)+d_kv_{13}^k(t))----\\ ---0 & \frac{c_k}{2} & \frac{b_k}{2} & -\frac{1}{4}h_k(fv_{22}^k(t)+e_kv_{23}^k(t)) & \frac{1}{4}h_k(f_kv_{12}^k(t)+e_kv_{13}^k(t))---\\ ---0 & 0 & c_k & -\frac{1}{2}h_kf_kv_{23}^k(t) & \frac{1}{2}h_kf_kv_{13}^k(t)---\end{bmatrix} \tag{27}$$

$$[\sigma]=\begin{bmatrix}[\bar{\sigma}] & 0 & 0\\ 0 & [\bar{\sigma}] & 0\\ 0 & 0 & [\bar{\sigma}]\end{bmatrix} \tag{28}$$

$$[\bar{\sigma}]=\begin{bmatrix}\sigma_{11} & \sigma_{12} & \sigma_{31}\\ \sigma_{12} & \sigma_{22} & \sigma_{23}\\ \sigma_{31} & \sigma_{23} & \sigma_{33}\end{bmatrix} \tag{29}$$

$$\{\sigma\}=[\sigma_{11}\sigma_{22}\sigma_{33}\sigma_{12}\sigma_{23}\sigma_{31}]^T. \tag{30}$$

Then, the incremental equilibrium equation of the shell structure can be written as

$$([K_L]+[K_N])\{\Delta u^k\}=\{\Delta P\}. \tag{31}$$

In the above, the stiffness matrix of the structure consists of two major parts: K_L is the linear stiffness matrix as in the case of small deformation, and K_N, the nonlinear stiffness matrix due to large deformation and ΔP is the incremental load from time t to $t+\Delta t$. These matrices are given by

$$[K_L]=\int_{V_t}[B_L]^T[C][B_L]\,dv \tag{32}$$

$$[K_N]=\int_{V_t}([B_1]^T[\sigma][B_1]-2[B_2]^T[\sigma][B_2])\,dv \tag{33}$$

$$\{\Delta P\}=R(t+\Delta t)-\int_{V_t}[B_L]^T\{\sigma\}\,dv \tag{34}$$

where B_L = Linear strain displacement transformation matrix, B_1, B_2 = Geometric matrices due to large deformation and σ = Cauchy stress tensor.

MATERIAL MODELING

The shell structure considered in the present analysis may have laminated material construction, whereby each layer can be an orthotropic material with a given orientation as shown in Fig. 3. For the jth layer, the Jaumann rate of Kirchhoff stress is related to the deformation rate tensor by

$$\{\Delta S^*\}=[C']_j\{D\} \tag{35}$$

where C' is stiffness matrix referring to the material principal axes of the jth layer which may deform in conjunction with the material fibers. Since the shell is assumed to be relatively thin, the stress component normal to the middle surface can be ignored and the stiffness matrix C' has the following definition

$$[C']=\begin{bmatrix}c_{11} & c_{12} & 0 & 0 & 0 & 0\\ c_{12} & c_{22} & 0 & 0 & 0 & 0\\ 0 & 0 & 0 & 0 & 0 & 0\\ 0 & 0 & 0 & c_{44} & 0 & 0\\ 0 & 0 & 0 & 0 & c_{55} & 0\\ 0 & 0 & 0 & 0 & 0 & C_{66}\end{bmatrix} \tag{36}$$

where c'_{ij}s are the orthotropic constants.

For the evaluation of element stiffness, the material matrix referring to local coordinates must be transformed to the global system by using

$$[C]=[T]^T[C'][T] \tag{37}$$

where the transformation matrix T is defined, for example, in [27]. It is important to note that coordinate axes rotations in T include the initial orientation of the material axes and additional rotations resulting from deformations.

For the treatment of layering effect, two different schemes may be employed. One method is to perform numerical integration of the stiffness matrix for each layer to capture its material property. The other method is to derive an equivalent stiffness for the laminated shell by using a smearing process [28]. In this paper, the former method is adopted in the same manner as reference [19]. We define a variable ζ_j in the thickness direction for the jth layer; ζ_j varies from -1 to $+1$. Referring to Fig. 4 the stiffness matrices are then evaluated in accordance with

$$[K_L]=\sum_{j=1}^{P}\int_{V_t}[B_L]^T[C]_j[B_L]\frac{h_j}{h}\,dv \tag{38}$$

$$[K_N]=\sum_{j=1}^{P}\int_{V_t}([B_1]^T[\sigma]_j[B_i]-2[B_2]^T[\sigma]_j[B_2])\frac{h_j}{h}\,dv \tag{39}$$

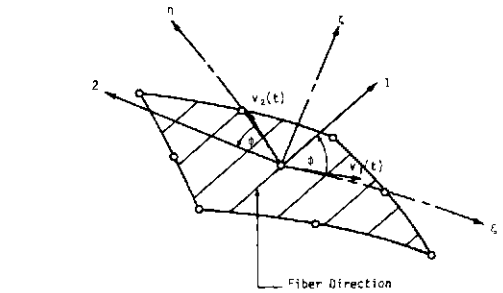

Fig. 3. Fiber direction with respect to natural (local) coordinate axes.

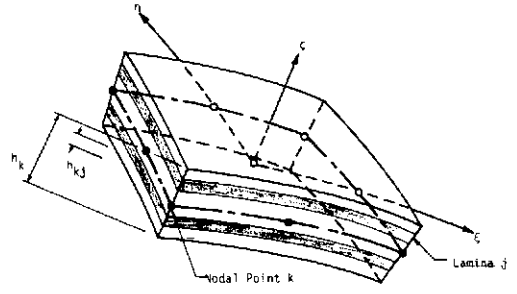

Fig. 4. Geometry of laminated shell element.

where

$$h_j = \sum_{k=1}^{m} N_k(\xi, \eta) h_{kj} \tag{40}$$

$$h = \sum_{k=1}^{m} N_k(\xi, \eta) h_k \tag{41}$$

$$\zeta = -1 + \frac{1}{h}\left[-h_j(1-\zeta_j) + 2\sum_{i=1}^{j} h_i\right] \tag{42}$$

p = total number of layers

NUMERICAL CHARACTERISTICS OF THE ELEMENT

In the finite element analysis of shell structures, two questions are often confronted by the analysts: selection of mesh size and use of integration order for the evaluation of element stiffness. The former factor is purely an economical consideration whereas the latter is associated with the generic nature of the element under consideration. As noted in the introduction, the "degenerated" 3-D solid element gives the right deformation behavior for linear thick shells. However, for thin shell structures, the element was found to be too stiff to represent the correct bending action due to the presence of unnecessary shear stresses. Then, reduced integration must be used to compensate such discrepancy. A systematic study on the small deformation plate bending was conducted by Pugh, Hinton and Zienkiewicz [21] by comparing the integration orders with respect to the aspect ratio of the plate (i.e. thickness/span of the plate). Such study for the case of nonlinear analysis has not yet been made.

In this section, we present a study on the convergence characteristics of both the 8-node and 9-node elements by varying

(i) Mesh size

(ii) Integration Order vs Aspect Ratio

Two integration orders are used: exact $(3\times3\times2)$ and reduced $(2\times2\times2)$ orders. Similar to [21], a simply supported plate and a clamped plate are considered. Linear isotropic material was assumed: $E = 30{,}000$ ksi and $\nu = 0.3$. Both plates are loaded into the large deformation range and the results are compared at a fixed load factor$(qa^4/Eh^4) = 200$ as seen in Fig. 5. Corresponding to this load factor, the maximum deflections obtained from the analytical solutions [29] are

	W_{max}/t
Simply supported plate:	1.66147
Clamped plate:	1.33676

t = thickness of the plate

At first, the effect of mesh size was studied for the plates with an aspect ratio chosen to be $= 0.005$, whereby the solution is relatively insensitive to the 8-node or 9-node elements or the integration order used. From symmetry, only one quarter of the plates were modeled by varying the element numbers from 1 to 25. The results are plotted in Figs. 6 and 7 for the simply supported and clamped plates, respectively. For the simply-supported plate, a minimum of 4 elements was necessary to obtain the convergent solution whereas the clamped plate requires 16 elements due to more complex deformation curvature. In either case, the 9-node element appears to give much better numerical response as compared to the 8-node element. In the second part of the study, the

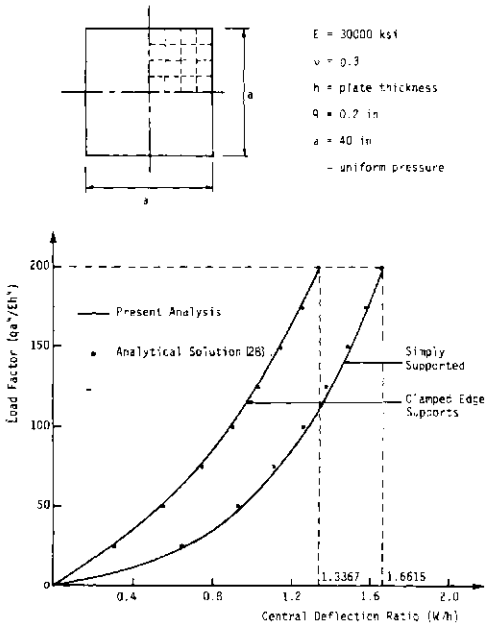

Fig. 5. Large deflection analysis of plate subjected to uniform pressure.

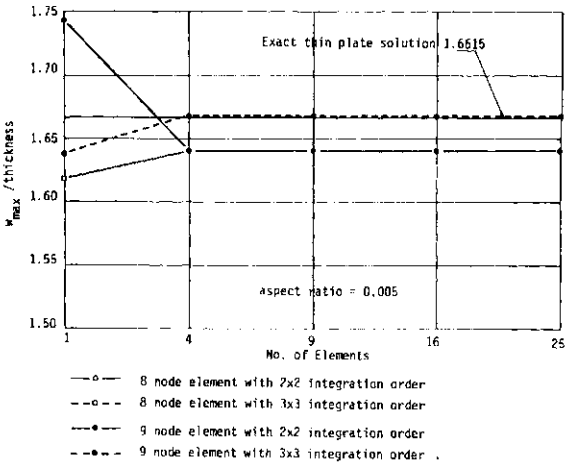

Fig. 6. Simply supported plate subjected to uniform load.

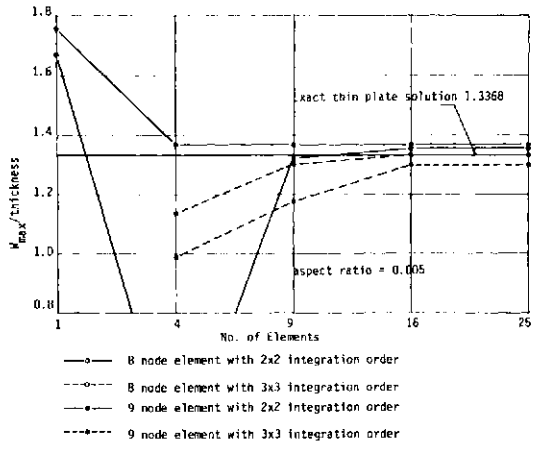

Fig. 7. Clamped edge supports plate subjected to uniform load.

mesh size was fixed with 4 elements for the simply supported plate and 16 elements for the clamped plate, and the thickness (aspect ratio) of the plate was varied from 10^{-1} to 10^{-4}. The plate was modeled by both 8-node and 9-node elements with the exact and reduced integration orders. The analysis results are plotted in Figs. 8 and 9. For the simply-supported plate in Fig. 8, the solution obtained from 8 node element with exact integration order deteriorates for the aspect ratio smaller than 0.005. In the case of clamped plate (Fig. 9), 8-node element with either the exact or reduced integration order gives very poor results for plate thickness smaller than 0.005. However, in all cases the 9-node element appears to yield satisfactory results whether the reduced integration order is used or not.

NUMERICAL EXAMPLES

The formulation of the shell element discussed in the previous section has been implemented into a nonlinear finite element program called NFAP [30]. Four sample problems were analyzed by use of the finite element program and the results are presented in this section.

(1) *Large deflection analysis of a hinged spherical shell*

The spherical shell is subjected to a concentrated central load at the crown. All edges are supported by hinges with no translations and the dimensions are given in Fig. 10. The material property is considered to be linearly elastic and isotropic. From double symmetry, only a quarter of the shell is modeled by a 2×2 mesh of 8 node elements. The reduced integration was used for evaluation of element stiffness. This problem was previously analyzed by Horrigmoe and Bergan [15] with a 5×5 mesh of triangular elements and closed form solution was obtained by Leicester [31]. In the present analysis a total of 16 loading steps were used. Since the structure exhibits softening behavior, the tangent modulus with equilibrium iterations (3 iterations per load step) gives convergent solution all the way to the buckling load (before snap-through) of 50 kN. Good agreement with the known results was obtained as seen in Fig. 10.

(2) *Large deflection of a circular cylindrical shell*

The circular cylindrical shell as shown in Fig. 11 is

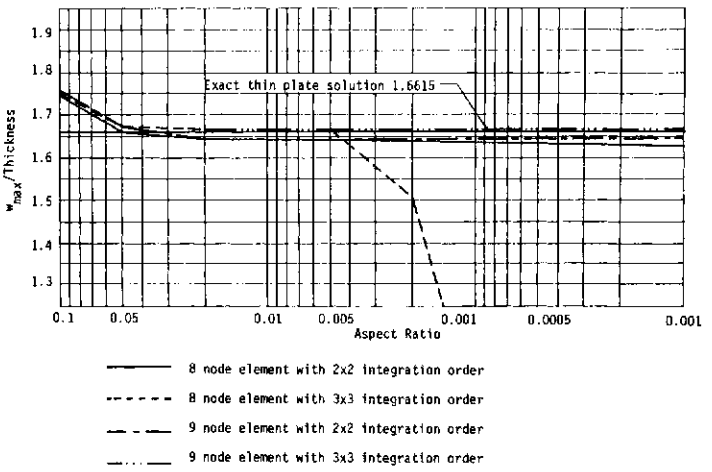

Fig. 8. Simply supported plate subjected to uniform load.

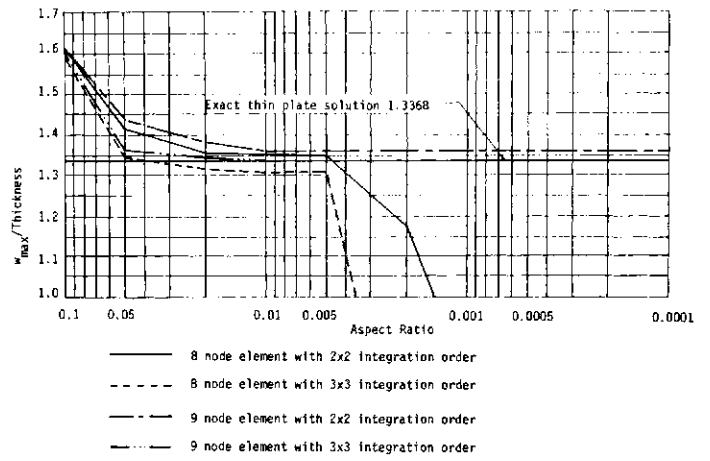

Fig. 9. Clamped edge supports plate subjected to uniform load.

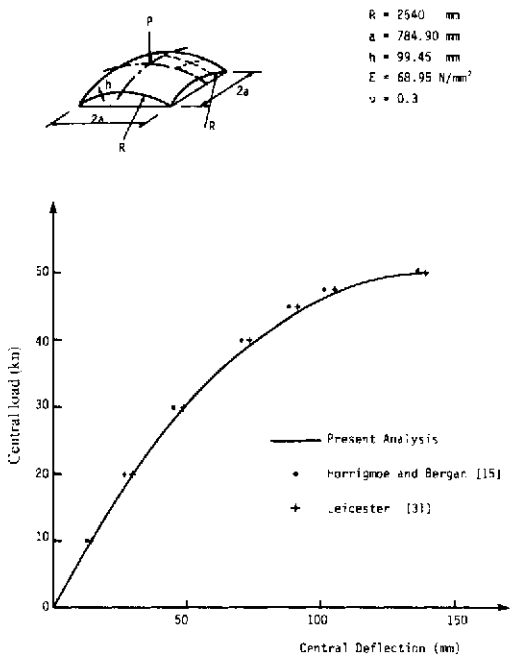

Fig. 10. Hinged spherical shell subjected to central concentrated load.

clamped along all four edges and subjected to a uniform normal load up to 3 kN/m^2. The material property is linearly elastic and isotropic. One quarter of the shell was modeled by sixteen 9-node elements with the exact integration order. In the analysis, the pressure load increment was varied at three stages: 0.25 kN/m^2 for the softening part, 0.0625 kN/m^2 near the snap-through deformation, and 0.25 kN/m^2 for the stiffening part. The incremental solution at the initial stage converges monotonically with an average of 3 iteration cycles. For the stiffening part, some oscillation of the iterative solution was observed and more iteration cycles (5–6) were necessary in order to obtain the convergent solution. The load-deformation response is compared with those obtained by Sabir and Lock [32] and Horrigmoe and Bergan [15]. Again, good agreement can be seen from Fig. 11.

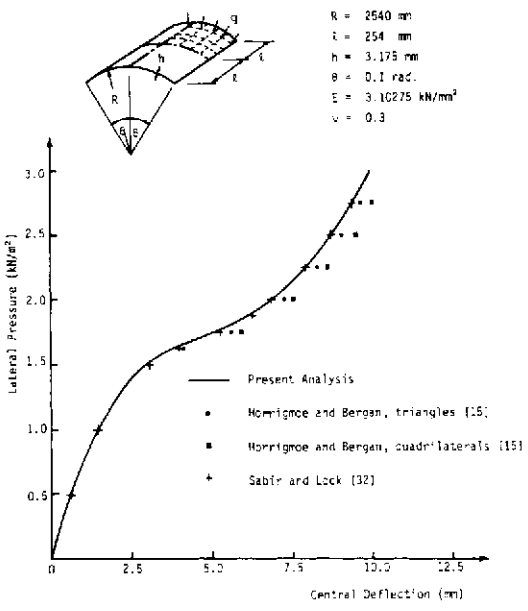

Fig. 11. A cylindrical shell subjected to uniform pressure.

(3) *A sandwich plate*

To verify the modeling of laminate material, a sandwich square plate, (50 in. × 50 in.) consists of two identical aluminum facings and an aluminum honeycomb core. The elastic constants and the thickness of the layers are:

Facing: $E = 10.5 \times 10^3$ ksi, $\nu = 0.3$, thickness = 0.015 in.
Core: $E = 0$, $G_{xz} = G_{yz} = 50$ ksi, thickness = 1 in.

The plate was represented by four 8-node elements with the reduced integraion order. The plate is subjected to a uniform load with clamped edges and the load was increased well into the nonlinear range (geometrically) of the plate. The same plate has also been analyzed by Schmit and Monforton [33]. The analysis results are plotted in Fig. 12 for the non-dimensionalized load vs deflection at the center of the plate. The present solution correlates quite well with those obtained by Schmit and Monforton for both linear and nonlinear response.

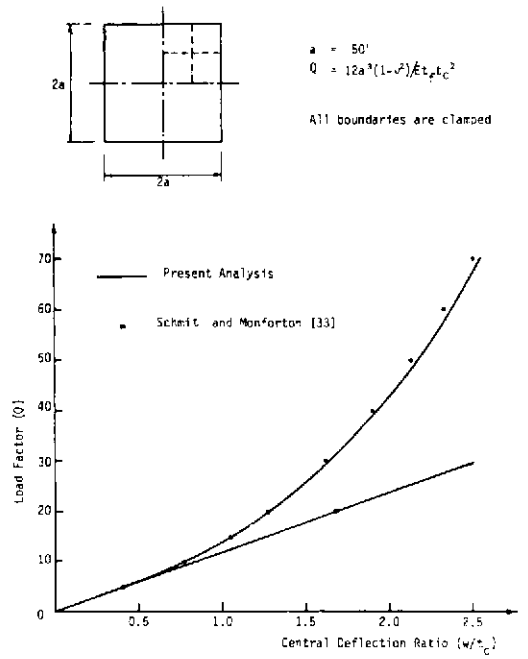

Fig. 12. Clamped sandwich plate subjected to uniform pressure.

(4) *A glass-epoxy thin-walled cylinder*

The last example considered herein is a glass-epoxy thin-walled cylinder clamped at both ends and subjected to internal pressure (Fig. 13). By use of symmetry, only one-eighth of the cylinder was modeled by a 5 × 5 mesh of 9-node elements with reduced integration order. The material is assumed to be linearly elastic and orthotropic and the elastic constants are given by

$$E_x = 2 \times 10^3 \text{ ksi}, \; E_y = 7.5 \times 10^3 \text{ ksi}, \; \nu_{yx} = 0.25$$

$$G_{xy} = 1.25 \times 10^3 \text{ ksi}, \; G_{yz} = G_{zx} = 0.625 \times 10^3 \text{ ksi}$$

For small deformation theory, the maximum radial displacement of the cylinder was found to be 7.177×10^{-4} in. at the pressure 4 ksi, which correlates with the result obtained by Rao [34]. The present analysis was also carried into the large deformation range of the cylinder. The load-deformation response is shown in Fig. 13. No comparison can be made since large deformation analysis of this problem was not found elsewhere.

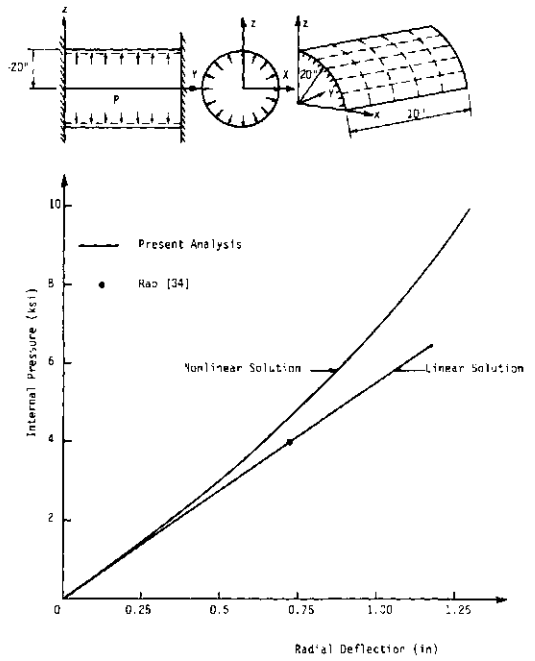

Fig. 13. Large deflection analysis of thin wall cylinder.

CONCLUSION

A large deformation analysis procedure for the laminated anisotropic shell is presented in this paper by use of a "degenerated" 3-D solid element with 8 or 9 nodes. The analysis approach is based on the updated Lagrangian formulation. From the study of numerical characteristics of the element, reduced integration order is necessary for the evaluation of stiffness matrix when the 8-node element is used. However, the 9-node element gives much better numerical behavior as compared to the 8-node element.

Future work will be extended to include nonlinear material models, post-buckling behavior of shells and more efficient numerical scheme for obtaining convergent solutions.

REFERENCES

1. R. H. Gallagher, Problems and progress in thin shell finite element analysis. In *Finite Element for Thin Shells* (Edited by D. G. Ashwell and R. H. Gallagher), pp. 1–14. Wiley, New York (1976).
2. S. Ahmad, B. M. Irons and O. C. Zienkiewicz, Analysis of thick and thin shell structures by curved finite elements. *Int. J. Numer. Meth. Engng* **2**, 419–451 (1970).
3. B. M. Irons, The semiloof shell element. In *Finite Element for Thin Shells* (Edited by D. G. Ashwell and R. H. Gallagher), pp. 197–222. Wiley, New York (1976).
4. O. C. Zienkiewicz, R. L. Taylor and J. M. Too, Reduced integration technique in general analysis of plates and shells. *Int. J. Numer. Meth. Engng* **3**, 275–290 (1971).
5. S. F. Pawsey and R. W. Clough, Improved numerical integration of thick shell finite elements. *Int. J. Numer. Meth. Engng* **3**, 575–586 (1971).
6. R. D. Cook, More on reduced integration and isoparametric elements. *Int. J. Numer. Meth. Engng* **5**, 141–142 (1972).
7. H. Takemoto and R. D. Cook, Some modifications of an isoparametric shell element. *Int. J. Numer. Meth. Engng* **7**, 401–405 (1973).
8. T. J. R. Hughes and W. Kanoknukulchai, A simple and efficient finite element for plate bending. *Int. J. Numer. Meth. Engng* **11**, 1529–1543 (1977).
9. W. Kanoknukulchai, A simple and efficient finite element for general shell analysis. *Int. J. Numer Meth. Engng* **14**, 179–200 (1979).
10. E. Ramm, A plate/shell element for large deflections and rotations. In *Formulations and Computational Algorithms in Finite Element Analysis* (Edited by K. J. Bathe, J. T. Oden and W. Wunderlick), pp. 264–293. M.I.T. Press, Cambridge, Mass. (1977).
11. S. Bolouchi, On finite element nonlinear analysis of general shell structures. Ph.D. Dissertation, Mechanical Engineering Department, M.I.T. 1979.
12. T. H. H. Pian and P. L. Boland, Formulation of large deflection shell analysis by assumed stress finite element method. In *Formulations and Computational Algorithms in Finite Element Analysis* (Edited by K. J. Bathe, J. T. Oden and W. Wunderlick), pp. 241–263. M.I.T. Press, Cambridge, Mass. (1977).
13. P. G. Bergan and P. W. Clough, Large deflection analysis of plates and shallow shells using the finite element method. *Int. J. Numer. Meth. Engng* **5**, 543–556 (1973).
14. J. H. Argyris, P. C. Dunne, G. A. Malejannakis and E. Schelkle, A simple triangular fact shell element with application linear and nonlinear equilibrium and elastic stability problems. *Comput. Meth. Appl. Mech. Engng* **10**, 371–403 (1977); **11**, 97–131 (1977).
15. G. Horrigmoe and P. G. Bergan, Nonlinear analysis of free form shells by flat finite elements. *Comput. Meth. Appl. Mech. Engng* **16**, 11–35 (1978).
16. A. K. Noor and S. J. Hartley, Nonlinear shell analysis via mixed isoparametric elements. *Comput. Structures* **7**, 615–626 (1977).
17. C. W. Pryor and R. M. Barker, A finite element analysis including transverse shear effects for application to laminated plates. *AIAA J.* **9**, 912–917 (1971).
18. A. S. Mawenya and J. D. Davies, Finite element bending analysis of multilayer plates. *Int. J. Numer. Meth. Engng* **8**, 215–225 (1974).
19. S. C. Panda and R. Natarajan, Finite element analysis of laminated composite plates. *Int. J. Numer. Meth. Engng* **14**, 69–79 (1979).
20. A. K. Noor and M. D. Mathers, Finite element analysis of anisotropic plates. *Int. J. Numer. Meth. Engng* **11**, 289–307 (1977).
21. E. D. L. Pugh, E. Hinton and O. C. Zienkiewicz, A study of quadrilateral plate bending elements with "reduced" integration. *Int. J. Numer. Meth. Engng* **12**, 1059–1079 (1978).
22. R. Hill, On uniqueness and stability in the theory of finite elastic strain. *J. Mech. Phys. Solids* **5**, 229–241 (1957).
23. R. Hill, Some basic principles in the mechanics of solids without a natural time. *J. Mech. Phys. Solids* **7**, 209–225 (1959).
24. R. Hill, On the classical constitutive relations for elastic/plastic solids. In *Recent Progress in Applied Mechanics* (Edited by B. Broberg, *et al.*). Wiley, New York (1967).
25. R. M. McMeeking and J. R. Rice, Finite element formulations for problem of large elastic/plastic deformation. *Int. J. Solids Structures* **11**, 601–616 (1975).

26. K. J. Bathe and E. L. Wilson, *Numerical Method in Finite Element Analysis*. Prentice-Hall, Englewood Cliffs, New Jersey (1976).
27. R. D. Cook, *Concept and Applications of Finite Element Analysis*. Wiley, New York (1974).
28. P. C. Chou, J. Carleon and C. M. Hsu, Elastic constants of layered media. *J. Composite Mater.* **6**, 89–93 (1972).
29. L. H. Donnell, *Beams, Plates and Shells*. McGraw-Hill, New York, (1976).
30. T. Y. Chang and S. Prachuktam, NFAP—a nonlinear finite element analysis program. *Rep. No. SE*76-3, The University of Akron, Oct. 1976.
31. R. H. Leicester, Finite deformations of shallow shells. *J. Engng Mech. Div., ASCE* **94**(EM-2)1409,1423 (1968).
32. A. B. Sabir and A. C. Lock, The application of finite elements to the large deflection geometrically nonlinear behavior of cylindrical shells. In *Variational Methods in Engineering* (Edited by C. A. Brebbia and H. Tottenham). Southampton University Press (1973).
33. L. A. Schmit and G. R. Monforton, Finite deflection discrete element analysis of sandwich plates and cylindrical shells with laminated faces. *AIAA J.* **8**, 1454–1461 (1970).
34. K. P. Rao, A rectangular laminated anisotropic shallow thin shell finite element. *Comput. Meth. Appl. Mech. Engng* **15**, 13–33 (1978).

Computers & Structures, Vol. 13, pp. 341–347, 1981
Printed in Great Britain.

0045-7949/81/010341-07$02.00/0

LARGE-DEFLECTION AND LARGE-AMPLITUDE FREE VIBRATIONS OF LAMINATED COMPOSITE-MATERIAL PLATES

J. N. REDDY† and W. C. CHAO*

Department of Engineering Science and Mechanics, Virginia Polytechnic Institute and State University, Blacksburg, VA 24061, U.S.A.

(Received April 1980)

Abstract—Finite-element analysis of the large-deflection theory (in von Karman's sense), including transverse shear, governing moderately thick, laminated anisotropic composite plates is presented. Linear and quadratic rectangular elements with five degrees of freedom (three displacements, and two shear rotations) per node are employed to analyze rectangular plates subjected to various loadings and edge conditions. Numerical results for bending deflections, stresses, and natural frequencies are presented showing the parametric effects of plate aspect ratio, side-to-thickness ratio, orientation of layers, and anisotropy.

The finite-element solutions are found to be in excellent agreement with the exact closed-form solutions in the linear analysis. In the nonlinear analysis, the finite-element solutions are in fair agreement with the perturbation solution. The load-deflection curve in the shear deformable theory does not deviate much from the linear theory, when compared to the load-deflection curve in the von Karman theory.

INTRODUCTION

In the finite-element analysis of nonlinear problems the geometric stiffness matrix is reformulated several times during each load step (also, during each time step in the transient analysis), consequently, the computational time involved is very large. Further, if the element used in the analysis has many degrees of freedom, storage considerations may preclude the use of such elements. These concerns are reflected in current research in computational mechanics, which is largely concerned with the development of numerical schemes that are computationally inexpensive but possess competitive accuracy when compared to traditional schemes.

Due to their high stiffness-to-weight ratio, and the flexible anisotropic property that can be tailored through variation of the fiber orientation and stacking sequence, fiber-reinforced laminated composites are finding increasing application in many engineering structures. Plates are common in many engineering structures, and therefore have received greater attention of the designer.

Much of the previous research in the analysis of composite plates is limited to linear problems (see, for example, [1–15]), and many of them were based on the classical thin-plate theory (see [1–3]), which neglects the transverse shear deformation effects. The transverse shear effects are more pronounced, due to their low transverse shear modulus relative to the in-plane Young's moduli, in filamentary composite plates than in isotropic plates. The shear deformable theory of Yang, Norris and Stavsky [16] (see also, Whitney and Pagano [17]), which is a generalization of Mindlin's theory for homogeneous, isotropic plates to arbitrarily laminated anisotropic plates, is now considered to be adequate for predicting the overall behavior such as transverse deflections and first few natural frequencies of layered composite plates. Finite-element analysis of rectangular plates based on the Yang–Norris–Stavsky (YNS) theory is due to Reddy [15, 18], who derived the YNS theory from the penalty function method of Courant [19]. A comparison of the closed-form solutions [17] with the finite-element solutions [14, 15] shows that the element predicts accurate solutions (see also [20]).

Approximate solutions to the large-deflection theory (in von Karman's sense) of laminated composite plates were attempted by Whitney and Leissa [21], Bennett [22], Bert [23], Chandra and Raju [24, 25], Zaghloul and Kennedy [26], Chia and Prabhakara [27, 28], and Noor and Hartley [29]. Chandra and Raju [24, 25], and Chia and Prabhakara [27, 28] employed the Galerkin method to reduce the governing nonlinear partial differential equations to an ordinary differential equation in time for the mode shape; the perturbation technique was used to solve the resulting equation. Zaghloul and Kennedy [26] used a finite difference successive iterative technique in their analysis. In all of these studies, the transverse shear effects were neglected. The finite element employed by Noor and Hartley [29] includes the effect of transverse shear strains; however, it is algebraically complex and involves eighty degrees of freedom per element. Use of such elements in the nonlinear analysis of composite plates inevitably leads to large storage requirements and computational costs.

The present paper is concerned with the large-deflection bending and large-amplitude free vibrations of laminated composite plates. The finite element used herein is a rectangular element based on the extended YNS theory (i.e. the transverse shear deformation is included) that includes the effect of large deflections (in the von Karman sense). The element has three displacements and two shear rotations per node and results in a 20×20 stiffness matrix for linear element and a 40×40 matrix for an eight-node quadratic element. Numerical results are presented for deflec-

†Professor.
*Graduate assistant.

tions, stresses and natural frequencies of rectangular plates for various edge conditions.

2. GOVERNING EQUATIONS OF MODERATELY THICK PLATES ACCOUNTING FOR LARGE DEFLECTIONS

Consider a plate laminated of thin anisotropic layers, oriented arbitrarily, and having a total thickness h. The origin of the coordinate system (x, y) is taken in the middle plane, denoted R, of the plate with the z-axis perpendicular to the plane of the plate. The thick plate theory of Whitney and Pagano [17] is modified here to include the non-linear terms of the von Karman theory. The displacement field is assumed to be of the form,

$$\begin{aligned} u_1(x, y, z, t) &= u(x, y, t) + z\psi_x(x, y, t), \\ u_2(x, y, z, t) &= v(x, y, t) + z\psi_y(x, y, t), \\ u_3(x, y, z, t) &= w(x, y, t). \end{aligned} \tag{2.1}$$

Here t is the time; u_1, u_2, u_3 are the displacements in x, y, z directions, respectively; u, v, w are the associated midplane displacements; and ψ_x and ψ_y are the slopes in the xz and yz planes due to bending only. Assuming that the plate is moderately thick and strains are much smaller than rotations, we write the nonlinear strain–displacement relations $2\varepsilon_{ij} = u_{i,j} + u_{j,i} + u_{m,i}u_{m,j}$,

$$\begin{aligned} \varepsilon_1 \equiv \varepsilon_{11} &= \frac{\partial u}{\partial x} + z\frac{\partial \psi_x}{\partial x} + \frac{1}{2}\left(\frac{\partial w}{\partial x}\right)^2 = \varepsilon_{11}^0 + z\mathscr{K}_1, \\ \varepsilon_2 \equiv \varepsilon_{22} &= \frac{\partial v}{\partial y} + z\frac{\partial \psi_y}{\partial y} + \frac{1}{2}\left(\frac{\partial w}{\partial y}\right)^2 = \varepsilon_{22}^0 + z\mathscr{K}_2, \\ \varepsilon_6 \equiv 2\varepsilon_{12} &= \frac{\partial u}{\partial y} + \frac{\partial v}{\partial x} + z\left(\frac{\partial \psi_x}{\partial y} + \frac{\partial \psi_y}{\partial x}\right) + \frac{\partial w}{\partial x}\frac{\partial w}{\partial y}, \\ &= \varepsilon_6^0 + z\mathscr{K}_6, \\ \varepsilon_3 \equiv \varepsilon_{33} &= \psi_x^2 + \psi_y^2, \quad \varepsilon_5 = \psi_x + \frac{\partial w}{\partial x}, \quad \varepsilon_4 = \psi_y + \frac{\partial w}{\partial y}. \end{aligned} \tag{2.2}$$

wherein the products of ψ_x and ψ_y with $\partial u_1/\partial x$ and $\partial u_2/\partial y$ are neglected. Since the constitutive relations are based on the plane-stress assumption, ε_3 does not enter the formulation.

Neglecting the body moments and surface shearing forces, one can write the equations of motion (in the absence of body forces) as

$$\begin{aligned} N_{1,x} + N_{6,y} &= Ru_{,tt} + S\psi_{x,tt} \\ N_{6,x} + N_{2,y} &= Rv_{,tt} + S\psi_{y,tt} \\ Q_{1,x} + Q_{2,y} &= P + Rw_{,tt} - \mathscr{N}(N_i, w) \\ M_{1,x} + M_{6,y} - Q_1 &= I\psi_{x,tt} + Su_{,tt} \\ M_{6,x} + M_{2,y} - Q_2 &= I\psi_{y,tt} + Sv_{,tt} \end{aligned} \tag{2.3}$$

where R, S, and I are the normal, coupled normal-rotary, and rotary inertia coefficients,

$$(R, S, I) = \int_{-h/2}^{h/2} (1, z, z^2)\rho \, dz = \sum_m \int_{z_m}^{z_{m+1}} (1, z, z^2)\rho^{(m)} \, dz \tag{2.4}$$

$\rho^{(m)}$ being the material density of the mth layer, P is the transversely distributed force, and N_i, Q_i and M_i are the stress and moment resultants defined by

$$(N_i, M_i) = \int_{-h/2}^{h/2} (1, z)\sigma_i \, dz, \quad (Q_1, Q_2) = \int_{-h/2}^{h/2} (\sigma_{xz}, \sigma_{yz}) \, dz \tag{2.5}$$

Here σ_i $(i = 1, 2, 6)$ denote the in-plane stress components ($\sigma_1 = \sigma_x$, $\sigma_2 = \sigma_y$, $\sigma_4 = \sigma_{yz}$, $\sigma_5 = \sigma_{xz}$ and $\sigma_6 = \sigma_{xy}$).

The nonlinear operator $\mathscr{N}(\cdot)$ in eqn (2.3) is given by,

$$\begin{aligned} \mathscr{N}(w, N_i) = &\frac{\partial}{\partial x}\left(N_1\frac{\partial w}{\partial x}\right) + \frac{\partial}{\partial y}\left(N_6\frac{\partial w}{\partial x}\right) \\ &+ \frac{\partial}{\partial x}\left(N_6\frac{\partial w}{\partial y}\right) + \frac{\partial}{\partial y}\left(N_2\frac{\partial w}{\partial y}\right) \end{aligned}$$

Assuming monoclinic behavior (i.e. existence of one plane of elastic symmetry parallel to the plane of the layer) for each layer, the constitutive equations for the mth layer (in the plate coordinates) are given by

$$\begin{Bmatrix} \sigma_1 \\ \delta_2 \\ \sigma_6 \end{Bmatrix} = [Q_{ij}^{(m)}]\begin{Bmatrix} \varepsilon_1 \\ \varepsilon_2 \\ \varepsilon_6 \end{Bmatrix}, \quad \begin{Bmatrix} \sigma_4 \\ \sigma_5 \end{Bmatrix} = \begin{bmatrix} Q_{44}^{(m)} & Q_{45}^{(m)} \\ Q_{45}^{(m)} & Q_{55}^{(m)} \end{bmatrix}\begin{Bmatrix} \varepsilon_4 \\ \varepsilon_5 \end{Bmatrix}, \tag{2.6}$$

where $Q_{ij}^{(m)}$ are the stiffness coefficients of the mth layer in the plate coordinates. Combining eqns (2.5) and (2.6), we obtain the plate constitutive equations,

$$\begin{Bmatrix} N_i \\ M_i \end{Bmatrix} = \begin{bmatrix} A_{ij} & B_{ij} \\ B_{ji} & D_{ij} \end{bmatrix}\begin{Bmatrix} \varepsilon_j^0 \\ \mathscr{K}_j \end{Bmatrix}, \quad \begin{Bmatrix} Q_1 \\ Q_2 \end{Bmatrix} = \begin{bmatrix} k_4^2\bar{A}_{44} & k_4k_5\bar{A}_{45} \\ k_4k_5\bar{A}_{45} & k_5^2\bar{A}_{55} \end{bmatrix}\begin{Bmatrix} \varepsilon_4 \\ \varepsilon_5 \end{Bmatrix}. \tag{2.7}$$

The A_{ij}, B_{ij}, D_{ij} $(i, j = 1, 2, 6)$, and $\bar{A}_{ij}$ $(i, j = 4, 5)$ are the respective inplane, bending-inplane coupling, bending or twisting, and thickness-shear stiffnesses, respectively:

$$(A_{ij}, B_{ij}, D_{ij}) = \sum_m \int_{z_m}^{z_{m+1}} Q_{ij}^{(m)}(1, z, z^2) \, dz,$$

$$\bar{A}_{ij} = \sum_m \int_{z_m}^{z_{m+1}}$$

Here z_m denotes the distance from the mid-plane to the lower surface of the mth layer.

Equations (2.3) and (2.7) must be adjoined by appropriate boundary conditions of the problem. The variational formulation of these equations indicate the following essential and natural boundary conditions:

$$\begin{aligned} &\textit{essential}: \text{ specify, } u_n, u_s, w, \psi_n, \\ &\textit{natural}: \text{ specify, } N_n, N_{ns}, q, M_n, M_{ns}. \end{aligned} \tag{2.9}$$

3. VARIATIONAL FORMULATION

Toward constructing a finite-element model of eqns (2.3), (2.7), and (2.9), we present a (quasi-) variational formulation of these equations. The total potential energy principle for the problem at hand takes the form,

$$\begin{aligned} 0 = \delta\pi(u, v, w, \psi_x, \psi_y) &= \int_R \{\delta u[Ru_{,tt} + S\psi_{x,tt} - N_{1,x} - N_{6,y}] \\ &+ \delta v[Rv_{,tt} + S\psi_{y,tt} - N_{6,x} - N_{2,y}] \\ &+ \delta w[P + Rw_{,tt} - Q_{1,x} - Q_{2,y} - \mathscr{N}(w, N_i)] \\ &+ \delta\psi_x[I\psi_{x,tt} + Su_{,tt} - M_{1,x} - M_{6,y} + Q_1] \\ &+ \delta\psi_y[I\psi_{y,tt} + Sv_{,tt} - M_{6,x} - M_{2,y} + Q_2]\} \, dx \, dy, \\ &= \int_R \{\delta u(Ru_{,tt} + S\psi_{x,tt}) + \delta u_{,x}N_1 + \delta u_{,y}N_6 \\ &+ \delta v(Rv_{,tt} + S\psi_{y,tt}) + \delta v_{,x}N_6 + \delta v_{,y}N_2 \\ &+ \delta w(P + Rw_{,tt}) + \delta w_{,x}Q_1 + \delta w_{,y}Q_2 \end{aligned}$$

$$+\frac{\partial\delta w}{\partial x}\frac{\partial w}{\partial x}N_1+\frac{\partial\delta w}{\partial y}\frac{\delta w}{\partial x}N_6+\frac{\partial\delta w}{\partial x}\frac{\partial w}{\partial y}N_6+\frac{\partial\delta w}{\partial y}\frac{\partial w}{\partial y}N_2$$
$$+\delta\psi_x(I\psi_{x,tt}+Su_{,tt})+\delta\psi_{x,x}M_1+\delta\psi_{x,y}M_6+\delta\psi_xQ_1$$
$$+\delta\psi_y(I\psi_{y,tt}+Sv_{,tt})+\delta\psi_{y,x}M_6+\delta\psi_{y,y}M_2+\delta\psi_yQ_2\}$$
$$\times\,\mathrm{d}x\,\mathrm{d}y+\int_{C_n}(\delta u_n\hat{N}_n+\delta u_s\hat{N}_{ns})\,\mathrm{d}s+\int_{C_q}\delta w\hat{q}\,\mathrm{d}s$$
$$+\int_{C_m}(\delta\psi_n\hat{M}_n+\delta\psi_s\hat{M}_{ns})\,\mathrm{d}s, \tag{3.1}$$

wherein quantities with "^" are specified on the respective portions of the boundary C, and C_n, C_q and C_m are respectively the (possibly overlapping) portions of the boundary on which $\hat{N}_n$ and $\hat{N}_{ns}$, $\hat{q}$, and $\hat{M}_n$ and $\hat{M}_{ns}$ are specified. It should be noted that on the complements of these portions (i.e. on C-C_n, C-C_q, and C-C_m) the in-plane displacements u_n and u_{ns}, transverse deflection w, and shear rotations ψ_n and ψ_{ns}, respectively, are specified.

4. FINITE ELEMENT MODEL

Now we present a finite-element model based on the variational form in eqn (3.1). Suppose that the region R is divided into a finite number of rectangular elements. Over each element the generalized displacements $(u, v, w, \psi_x, \psi_y)$ are interpolated by

$$u=\sum_i^r u_i\phi_i^1,\quad v=\sum_i^r v_i\phi_i^1,\quad w=\sum_i^s w_i\phi_i^2,$$
$$\psi_x=\sum_i^p \psi_{xi}\phi_i^3,\quad \psi_y=\sum_i^p \psi_{yi}\phi_i^3, \tag{4.1}$$

where ϕ_i^α ($\alpha=1, 2, 3$) is the interpolation function corresponding to the ith node in the element. Note that the in-plane displacements, the transverse displacement, and the slope functions are approximated by different sets of interpolation functions. While this generality is included in the formulation (to indicate the fact that such independent approximations are possible), we dispense with it in the interest of simplicity when the element is actually programmed and take $\phi_i^1=\phi_i^2=\phi_i^3$ ($r=s=p$). Here r, s and p denote the number of degrees of freedom per each variable. That is, the total number of degrees of freedom per element is $2r+s+2p$.

Substituting eqn (4.1) into eqn (3.1), we obtain

$$[K]\{\Delta\}=\omega^2[M]\{\Delta\}+\{F\} \tag{4.2}$$

For static bending, eqn (4.2) becomes

$$\begin{bmatrix}[K^{11}] & [K^{12}] & [0] & [K^{14}] & [K^{15}]\\ [K^{12}] & [K^{22}] & [0] & [K^{24}] & [K^{25}]\\ [0] & [0] & [K^{33}] & [K^{34}] & [K^{35}]\\ [K^{14}] & [K^{24}] & [K^{34}] & [K^{44}] & [K^{45}]\\ [K^{15}] & [K^{25}] & [K^{35}] & [K^{45}] & [K^{55}]\end{bmatrix}^e\begin{Bmatrix}\{u\}\\ \{v\}\\ \{w\}\\ \{\psi_x\}\\ \{\psi_y\}\end{Bmatrix}^e=\begin{Bmatrix}\{F^1\}\\ \{F^2\}\\ \{F^3\}\\ \{F^4\}\\ \{F^5\}\end{Bmatrix}^e \tag{4.3}$$

where the $\{u\}$, $\{v\}$, etc. denote the columns of the nodal values of u, v, etc. respectively, and the elements $K_{ij}^{\alpha\beta}(\alpha,\beta=1, 2, \ldots, 5)$ of the stiffness matrix and F_i^α of the force vector can be identified easily from eqn (3.1).

In the present study rectangular elements with four, eight, and nine nodes are employed with the same interpolation for all of the variables. The resulting stiffness matrices are 20×20 for the 4-node element and 40×40 for the 8-node element.

As pointed out in a recent study [15], the YNS theory can be derived from the corresponding classical thin-plate theory by treating the slope-displacement relations

$$\frac{\partial w}{\partial x}=-\theta_x,\quad \frac{\partial w}{\partial y}=-\theta_y, \tag{4.4}$$

as constraints. Indeed, when the constraints in eqn (4.4) are incorporated into the classical thin-plate theory by means of the penalty-function method, the resulting equations correspond to the YNS theory with the correspondence,

$$\theta_x\sim\psi_x,\quad \theta_y\sim\psi_y. \tag{4.5}$$

It is now well-known that whenever the penalty-function method is used, the so-called reduced integration (see Zienkiewicz *et al.* [30], and Reddy [20]) must be used to evaluate the matrix coefficients in eqn (4.3). That is, if the four-node rectangular element is used, the 1×1 Gauss rule must be used in place of the standard 2×2 Gauss rule to numerically evaluate the coefficients K_{ij}. The element equations in (4.2) are assembled in the usual manner, and the (essential) boundary conditions are imposed before solving either for generalized displacements, or for frequencies of natural vibration. It should be noted that, since the stiffness matrix $[K]$ depends on the solution $\{\Delta\}$, any one of the standard iterative procedures must be used.

5. NUMERICAL RESULTS AND DISCUSSION

The finite element presented herein was employed in the nonlinear analysis of rectangular plates. The following material properties typical of advanced fiber-reinforced composites were used in the present study:

Material I: $E_1/E_2=25$, $G_{12}/E_2=0.5$, $G_{23}/E_2=0.2$, $\nu_{12}=0.25$ (5.1)

Material II: $E_1/E_2=40$, $G_{12}/E_2=0.6$, $G_{23}/E_2=0.5$, $\nu_{12}=0.25$

It was assumed that $G_{13}=G_{23}$ and $\nu_{12}=\nu_{13}$. A value of 5/6 was used for the shear correction coefficients, $k_4^2=k_5^2$ (see Whitney [31]). All of the computations were carried on an IBM 370/158 computer.

To show the effect of the reduced integration, and to illustrate the accuracy of the present element, results of the linear analysis are presented for four-layer (equal thickness) cross-ply ($0°/90°/90°/0°$) square plate constructed of material I. The plate is subjected to sinusoidal distribution of transverse loading, and is assumed to be "simply-supported" in the following sense (SS−1):

$$\begin{aligned}&u_0(x,0)=u_0(x,b)=0,\ N_2(x,0)=N_2(x,b)=0,\\ &v_0(0,y)=v_0(a,y)=0,\ N_1(0,y)=N_1(a,y)=0,\\ &w(x,0)=w(x,b)=w(0,y)=w(a,y)=0,\\ &\psi_x(x,0)=\psi_x(x,b)=0,\ M_2(x,0)=M_2(x,b)=0,\\ &\psi_y(0,y)=\psi_y(a,y)=0,\ M_1(0,y)=M_1(a,y)=0.\end{aligned} \tag{5.2}$$

Of course, in the finite-element method only the essential boundary conditions (i.e. those on u, v, w, ψ_x and ψ_y) are imposed after the assembly of element equations. The finite-element solution is compared with the closed-form solution [20], and the 3-D elasticity solution of Pagano and Hatfield [5] in Fig. 1. It is clear from the figure that nondimensionalized deflection obtained

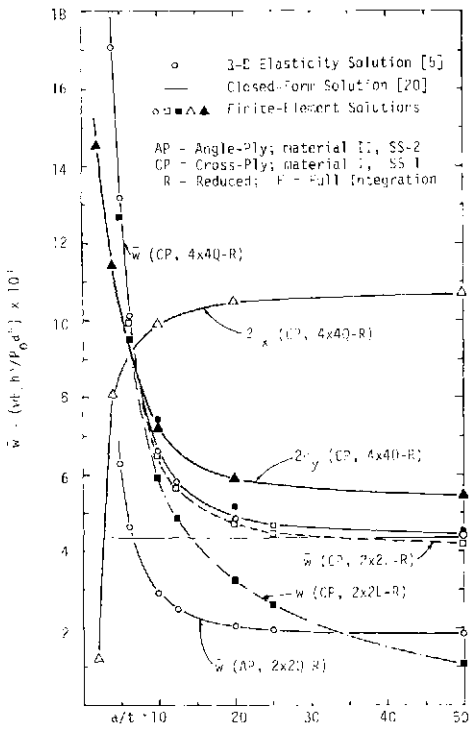

Fig. 1. Comparison of the exact closed-form solution and finite-element solution for four-layer ($0°/90°/90°/0°$), $45°/-45°/45°/45°$) square plates under sinusoidal loading.

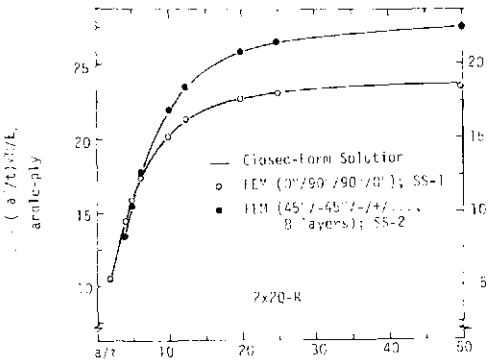

Fig. 2. Comparison of the closed-form and finite element solution for nondimensionalized fundamental frequencies square plates (material II).

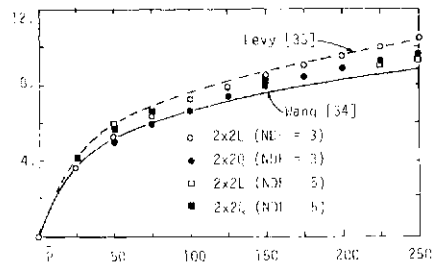

Fig. 3. Comparison of the nondimensionalized stress for simply supported (SS-3), isotropic ($\nu=0.3$) square plate under uniform loading.

by 2×2 mesh of linear elements is very sensitive to the integration (i.e. reduced and full integration) in the thin-plate range (i.e. $a/h>20$). However, the integration has virtually no noticeable effect in the thick-plate range, for quadratic elements. The solutions obtained using the quadratic elements (with reduced and full integration) are not plotted in Fig. 1 due to their closeness to the closed-form solution. The solutions (i.e. deflections and stresses) obtained by various elements, meshes, and integrations are reported in tabular form in [20]. The solution obtained by the 4×4 mesh of quadratic elements is in excellent agreement (indeed, to the third decimal point) with the closed-form solution. The stresses $\bar{\sigma}_x$ and $\bar{\sigma}_y$ were computed at the Gauss point $x=y=0.0625$ (close to the center of the plate) at $z=\pm h/2$, and $\pm h/4$, respectively.

Figure 1 also shows the nondimensionalized deflection for four-layer, angle-ply ($45°/-45°/45°/-45°$) square plate (material II) under sinusoidal loading. The boundary conditions used are of simply-supported (SS-2) type:

$$\begin{aligned} &u_0(0, y)=u_0(a, y)=0,\ N_6(0, y)=N_6(a, y)=0,\\ &v_0(x, 0)=v_0(x, b)=0,\ N_6(x, 0)=N_6(x, b)=0,\\ &w(x, 0=w(x, b)=w(0, y)=w(a, y)=0, \qquad (5.3)\\ &\psi_x(x, 0)=\psi_x(x, b)=0,\ M_2(x, 0)=M_2(x, b)=0,\\ &\psi_y(0, y)=\psi_y(a, y)=0,\ M_1(0, y)=M_1(a, y)=0. \end{aligned}$$

Again, the finite-element solution (obtained by using 2×2 mesh of eight-node quadratic elements with reduced integration: 2Q8-R) is in close agreement with the closed-form solution.

Figure 2 shows the nondimensionalized fundamental frequency for four-layer, cross-ply ($0°/90°/90°/0°$), and eight-layer, angle-ply ($45°/-45°/+/-\ldots$) square plates of material II. The support conditions for the cross-ply plate were assumed to be those in SS-1, and the support conditions used for angle-ply plate were those in SS-2. Results for both of the cases were obtained using mesh 2Q8-R. The finite-element solutions are gratifyingly close to the exact closed-form solutions.

Having established the credibility of the finite element developed herein for the linear analysis of layered composite plates, we now employ the element in the nonlinear analyses. First, results are presented for single-layer isotropic square plate under uniform loading. The essential boundary conditions used are:

simple-supported (SS-3): $u=v=u=0$ on all edges.

clamped (CC-1): $u=v=w=0$ on all edges,
$\psi_x=0$ along edges parallel to x-axis, (5.4)
$\psi_y=0$ along edges parallel to y-axis.

Figures 3–5 show the nondimensionalized deflection, $\bar{w}=w/h$, and non-dimensionalized stress, $\bar{\sigma}=\sigma a^2/Eh^2$, as a function of the load parameter, $\bar{P}=P_0a^4/Eh^4$ for clamped (CC-1) square plate, and simply-supported (SS-3) square plate, respectively. The results are compared with the Ritz solution of Way [32], double Fourier-series solution of Levy [33], the finite-difference solution of Wang [34], the Galerkin solution of Yamaki [35], and the displacement finite-element solution of Kawai and Yoshimura [36]. Finite-element solutions were computed for the five degrees of freedom (NDF = 5), and for three degrees of freedom (NDF = 3); in the latter case, the in-plane displacements were suppressed. The present solutions are in good agreement with the results of other investigators. Since

suppressing the in-plane displacements stiffen the plate, the deflections are smaller and stresses are larger than those obtained by including the in-plane displacements. Solutions of the other investigators were read from the graphs presented in their papers.

Next, results of the large-deflection bending analysis of layered composite, thin ($a/t=40$) plates are presented. Figure 6 shows the non-dimensionalized deflection versus the load parameter for two-, and six-layer, antisymmetric ($0°/90°/0°/\ldots$) cross-ply rectangular plates of material II, subjected to uniform loading. The plate is assumed to be clamped (CC-2) in the following sense:

$$w=\psi_x=0 \text{ along edges parallel to } y\text{-axis},$$
$$w=\psi_y=0 \text{ along edges parallel to } x\text{-axis}. \tag{5.5}$$

The present solution is in good agreement, for various aspect ratios, with the perturbation solution of Chia and Prabhakara [27]. Due to lack of tabulated results in [27], the relative differences in the two solutions cannot be discussed. It is clear that the nonlinear load-deflection curve is not deviated so much from the linear load-deflection line.

Figure 7 shows similar results for two-, and six-layer, angle-ply ($45°/-45°/-/+\ldots$), and clamped (CC-2) rectangular plate (material II) subjected to uniform loading. Again, the present result is in close agreement with that of Chia and Prabhakara [28]. The non-dimensionalized stress, $\bar{\sigma}_x$, for the cross-ply and angle-ply plates discussed above is plotted against the load parameter in Fig. 8.

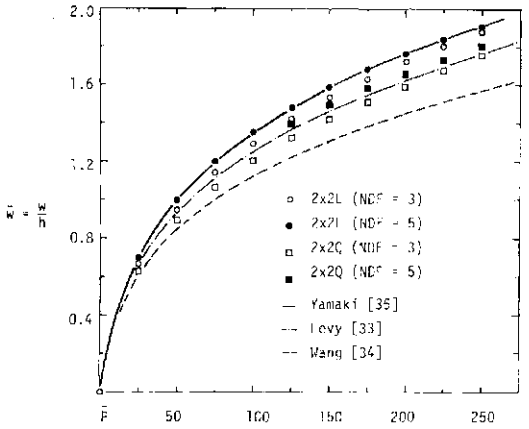

Fig. 4. Comparison of the nondimensionalized deflection for simply-supported (SS-3), isotropic ($\nu=0.3$) square plate under uniformly distributed pressure load.

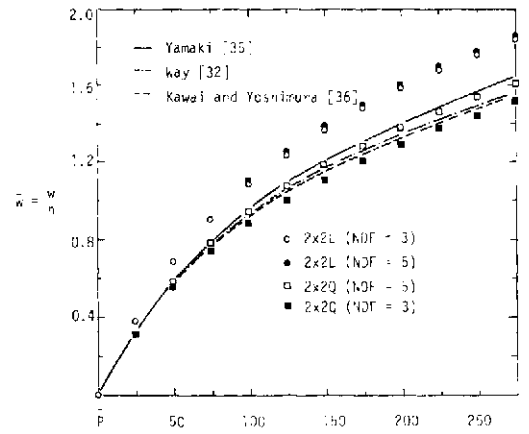

Fig. 5. Comparison of the nondimensionalized deflection for clamped (CC-1), isotropic ($\nu=0.3$) square plate under uniformly distributed pressure load.

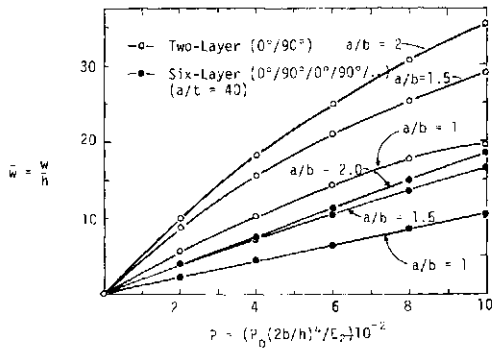

Fig. 6. Load deflection curves for antisymmetric cross-ply clamped (CC-2), rectangular plates (material II) under uniform loading.

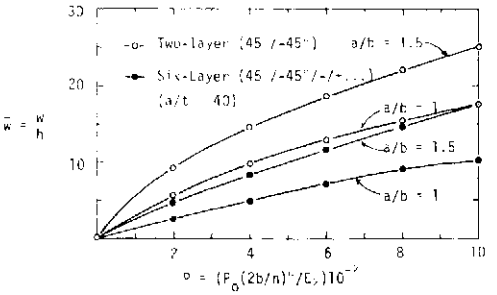

Fig. 7. Load–deflection curves for antisymmetric angle-ply clamped (CC-2), rectangular plates (material II) under uniform loading.

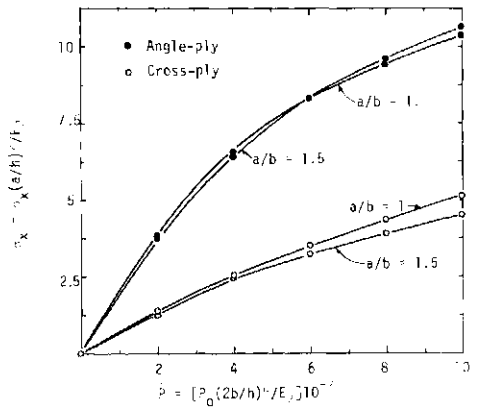

Fig. 8. Load-stress curves for two-layer clamped (CC-2), rectangular plates (material II) under uniform loading.

The effect of the transverse shear strain on the deflection and stresses on the load-deflection, and load-stress curves is shown in Fig. 9. Note that the deflection for $a/t=10$ is about 30% larger than that for $a/t=100$, at $\bar{P}=10$. That is, the deflections predicted by the classical thin-plate theory are lower than those predicted by the shear deformable theory.

Figure 10(a) shows the ratio of nonlinear to linear fundamental frequencies versus the amplitude-to-

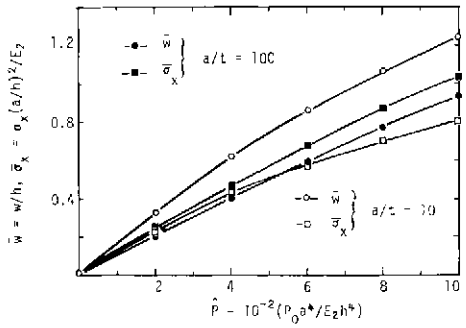

Fig. 9. Effect of the transverse shear on the load-deflection and load-stress curves for four-layer (0°/90°/90°/0°) simply-supported (SS-1) square plate (material I) under uniform loading.

turbation solution; of course, there is no proof that the perturbation solution is close to the exact. The load-deflection curve in the shear deformable theory does not deviate much from the linear theory, when compared to the load-deflection curve in the von Karman theory.

The finite-element developed herein is algebraically simple, and involves fewer degrees of freedom per element compared to traditional finite elements. Application of the present element (or an element based on the combined theory) to the following problem areas, at this writing, is either in development or awaiting:

—Transient analysis of layered composite plates (linear as well as nonlinear)

—Transient analysis of bimodulus (see [37–40]) composite plates (linear and nonlinear)

—Forced vibration of ordinary and bimodulus

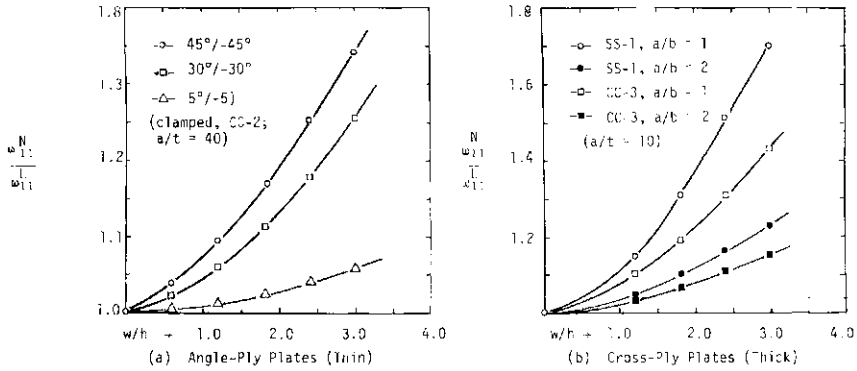

Fig. 10. Ratio of nonlinear frequency to linear frequency as a function of the ratio of amplitude to thickness for square plates (material II).

thickness ratio for two-layer angle-ply $(\theta/-\theta)$, clamped (CC-2) square plate of material II. The side-to-thickness ratio (a/t) was taken to be 40 (i.e. thin plate). Similar results are presented in Fig. 10b for two-layer, cross-ply (0°/90°), thick rectangular plates of material II. The boundary conditions used were simply-supported (SS-1), and clamped (CC-3):

$$\begin{aligned} &u = w = \psi_x = 0 \text{ along edges parallel to } y\text{-axis,} \\ &v = w = \psi_y = 0 \text{ along edges parallel to } x\text{-axis.} \end{aligned} \tag{5.6}$$

The side-to-thickness ratio used in this case was, $b/t = 10$ (i.e. thick plate). Since the present boundary conditions are somewhat different from those used by Chia and Prabhakara [28], the present solutions do not coincide with those in [28].

6. SUMMARY, CONCLUSIONS, AND SUGGESTIONS FOR FUTURE RESEARCH

A finite-element model is developed based on the combined theory of Yang, Norris, and Stavsky [16] and von Karman. That is, the model accounts for the transverse shear strain, and large rotations. Numerical results are presented for linear and nonlinear deflections, stresses, and natural frequencies of rectangular plates subjected to various edge conditions. The finite-element solutions are compared with the exact closed-form solutions in the linear case, and with the perturbation solution in the nonlinear case.

The finite-element solutions are found to be in excellent agreement with the exact closed-form solutions in the linear analysis. In the nonlinear analysis, the finite-element solutions are in fair agreement with the per-

composite plates.

—Static and transient (linear and nonlinear) analysis of plates with cut-outs.

—All of the above for cylindrical and doubly-curved thick shells [41].

Acknowledgements—The results reported herein were obtained during an investigation supported by the Structural mechanics Program, Office of Naval Research, Arlington, Virginia. The support is gratefully acknowledged.

REFERENCES

1. E. Reissner and Y. Stavsky, Bending and stretching of certain types of heterogeneous aeolotropic elastic plates. *J. Appl. Mech.* **28**, 402–408 (1961).
2. S. B. Dong, K. S. Pister and R. L. Taylor, On the theory of laminated anisotropic shells and plates. *J. Aerospace Sci.* **29**, 969–975 (1962).
3. C. W. Bert and B. L. Mayberry, Free vibrations of unsymmetrically laminated anisotropic plate with clamped edges. *J. Composite Mater.* **3**, 282–293 (1969).
4. N. J. Pagano, Exact solutions for composite laminates in cylindrical bending. *J. Composite Mater.* **3**(3), 398–411 (1969).
5. N. J. Pagano and S. J. Hatfield, Elastic behavior of multilayer bidirectional composites. *AIAA J.* **10**, 931–933 (1972).
6. S. Srinivas and A. K. Rao, Bending, vibration and buckling of simply supported thick orthotropic rectangular plates and laminates. *Int. J. Solids Structures* **6**, 1463–1481 (1970).
7. C. W. Pryor Jr. and R. M. Barker, A finite element analysis including transverse shear effects for applications to laminated plates. *AIAA J.* **9**, 912–917 (1971).

8. R. M. Barker, F. T. Lin, and J. R. Dara, Three-dimensional finite-element analysis of laminated composites. *National Symposium on Computerized Structural Analysis and Design*, George Washington University (1972).
9. P. K. Sinha and A. K. Rath, Vibration and buckling of cross-ply laminated circular cylindrical panels. *Aeronatutical Quart.* **26**, 211–218 (1975).
10. C. W. Bert and T. L. C. Chen, Effect of shear deformation on vibration of antisymmetric angle-ply laminated rectangular plates. *Int. J. Solids Structures* **14**, 465–473 (1978).
11. A. S. Mawenya and J. D. Davies, Finite element bending analysis of multilayer plates. *Int. J. Numer. Meth. Engng* **8**, 215–225 (1974).
12. S. C. Panda and R. Natarajan, Finite element analysis of laminated composite plates. *Int. J. Numer. Meth. Engng* **14**, 69–79 (1979).
13. R. L. Spilker, S. C. Chou and O. Orringer, Alternate hybrid stress elements for analysis of multilayer composite plates. *J. Composite Mater.* **11**, 51–70 (1977).
14. J. N. Reddy, Free vibration of antisymmetric, angle-ply laminated plates, including transverse shear deformation by the finite element method. *J. Sound Vib.* **66**(4), 565–576 (1979).
15. J. N. Reddy, A penalty plate-bending element for the analysis of laminated anisotropic composite plates. *Int. J. Numer. Meth. Engng 15*, 1187–1206 (1980).
16. P. C. Yang, C. H. Norris and Y. Stavsky, Elastic wave propagation in heterogeneous plates. *Int. J. Solids Structures* **2**, 665–684 (1966).
17. J. M. Whitney and N. J. Pagano, Shear deformation in heterogeneous anisotropic plates. *J. Appl. Mech.* **37**, 1031–1036 (1970).
18. J. N. Reddy, Simple finite elements with relaxed continuity for nonlinear analysis of plates. *Finite Element Methods in Engineering (Proc. 3rd Int. Conf. in Australia on Finite Element Methods)*, (Edited by A. P. Kabaila and V. A. Pulmano) pp. 265 281. The University of New South Wales, Sydney, Australia (1979).
19. R. Courant, *Calculus of Variations and Supplementary Notes and Exercises*, revised and amended by J. Moser, New York University (1956).
20. J. N. Reddy, A comparison of closed-form and finite element solutions of thick, laminated, anisotropic rectangular plates. *Res. Rep. No. OU-AMNE-79-19*, School of Aerospace, Mechanica. and Nuclear Engineering, University of Oklahoma, Norman (1979); also to appear in *J. Nuclear Engng and Design*
21. J. M. Whitney and A. W. Leissa, Analysis of heterogeneous anisotropic plates. *J. Appl. Mech.* **36**, 261–266 (1969).
22. J. A. Bennett, Nonlinear vibration of simply supported angle ply laminated plates. *AIAA J.* **9**, 1997–2003 (1971).
23. C. W. Bert, Nonlinear vibration of a rectangular plate arbitrarily laminated of anisotropic material. *J. Appl. Mech.* **40**, 452–458 (1973).
24. R. Chandra and B. B. Raju, Large amplitude flexural vibration of cross ply laminated composite plates. *Fibre Sci. Tech.* **8**, 243–263 (1975).
25. R. Chandra, Large deflection vibration of cross-ply laminated plates with certain edge conditions. *J. Sound Vib.* **47**(4), 509–514 (1976).
26. S. A. Zaghloul and J. B. Kennedy, Nonlinear analysis of unsymmetrically laminated plates. *J. Engng Mech. Div., ASCE* **101**(EM3), 169–185 (1975).
27. C. Y. Chia and M. K. Prabhakara, Large deflection of unsymmetric cross-ply and angle-ply plates. *J. Mech. Engng Sci.* **18**(4), 179–183 (1976).
28. C. Y. Chia and M. K. Prabhakara, A general mode approach to nonlinear flexural vibrations of laminated rectangular plates. *J. Appl. Mech.* **45**, 623–628 (1978).
29. A. K. Noor and S. J. Hartley, Effect of shear deformation and anisotropy on the non-linear response of composite plates. *Developments in Composite Materials-1* (Edited by G. Holister), pp. 55–65. Applied Science Publishers, Barking, Essex, England (1977).
30. O. C. Zienkiewicz, R. L. Taylor and J. M. Too, Reduced integration technique in general analysis of plates and shells. *Int. J. Numer. Meth. Engng* **3**, 575 586 (1971).
31. J. M. Whitney, Stress analysis of thick laminated composite and sandwich plates. *J. Composite Mater.* **6**, 426–440 (1972).
32. S. Way, Uniformly loaded, clamped, rectangular plates with large deformation. *Proc. 5th Int. Cong. Appl. Mech.*, pp. 123–128. (Cambridge, Mass., 1938). Wiley, New York (1939).
33. S. Levy, Bending of rectangular plates with large deflections. *Rep. No. 737, NACA* (1942).
34. C. T. Wang, Bending of rectangular plates with large deflections. *Rep. No. 1462, NACA* (1948).
35. N. Yamaki, Influence of large amplitudes on flexural vibrations of elastic plates. *ZAMM* **41**, 501 510 (1967).
36. T. Kawai and N. Yoshimura, Analysis of large deflection of plates by the finite element method. *Int. J. Numer. Meth. Engng* **1**, 123–133 (1969).
37. C. W. Bert, Recent advances in mathematical modeling of the mechanics of bimodulus, fiber-reinforced composite materials. *Recent Advances in Engineering Science (Proc. 15th Ann. Meeting of the Society of Engineering Science)* (Edited by R. L. Sierakowski), pp. 101–106. University of Florida, Gainesville, Florida (1978).
38. J. N. Reddy and C. W. Bert, Analysis of plates constructed of fiber-reinforced bimodulus composite material. *Mechanics of Bimodulus Materials* (Edited by C. W. Bert) AMD-Vol. 33, pp. 67 83. ASME, New York (1979).
39. J. N. Reddy and W. C. Chao, Finite-element analysis of laminated bimodulus composite-material plates. *Comput. Structures* **12**, 245 251 (1980).
40. C. W. Bert, J. N. Reddy, V. Sudhakar Reddy and W. C. Chao, Analysis of thick rectangular plates laminated of bimodulus composite materials. *AIAA/ASME/ASCE/AHS 21st Structures, Structural Dynamics and Materials Conf.*, Seattle, Washington. (12–14 May 1980).
41. C. W. Bert and V. Sudhakar Reddy, Cylindrical shells of bimodulus composite material. *ASCE National Convention*, Hollywood, Florida (27–31 Oct. 1980).

Computers & Structures, Vol. 13, pp. 349–355, 1981
Printed in Great Britain.

0045-7949/81/0103349-07$02.00/0

ON NUMERICAL NONLINEAR ANALYSIS OF HIGHLY FLEXIBLE SPINNING CANTILEVERS†

S. UTKU and M. EL-ESSAWI
Department of Civil Engineering, Duke University, Durham, NC 27706, U.S.A.

and

M. SALAMA
Jet Propulsion Laboratory, California Institute of Technology, Pasadena, CA 91103, U.S.A.

(*Received* 11 *May* 1980)

Abstract—The general nonlinear discretized equations of motion of spinning elastic solids and structures are derived as a set of nonlinear ordinary differential equations for the case when the strain–displacement and velocity-displacement relations are nonlinear up to the second order. It is shown that the cost of generation of such equations is proportional to the fourth power of the number of degrees of freedom. A computer program is written to automatically generate the equations for the case of spinning cantilevers with initial imperfections. The types and the number of the coordinate functions used in the trial solution are parameters of the program.

The linear equations of motion governing the dynamic behavior of rotating systems usually furnish a satisfactory mathematical model in the analysis and design of structural elements such as spinning satellites, linkages, helicopter blades, and appendages. However, when the spinning elements possess very small intrinsic structural stiffness, the linear equations of motion become inadequate [1]. A general formulation for the nonlinear equations of motion of spinning line-elements with little or no intrinsic structural stiffness is given in [2] considering the second order nonlinearities in the strain-displacement, and the velocity-displacement relationships. The formulation assumes that the material is linearly elastic. It includes the effects of a variety of initial geometric imperfections. The nonlinear equations given in [2] are four coupled quasi-linear integro-partial-differential equations of parabolic type, representing the dynamic force-equilibrium equations in axial displacement $u(x, t)$, transverse displacements $v(x, t)$, $w(x, t)$, and torsional rotation $\theta(x, t)$, where the independent variables x and t are the arclength along the perfect line-element axis and the time, respectively. The derivation of the equations is based on the Hamilton's variational principle for elastodynamics. Defining

$$\boldsymbol{\psi}^T = [u(x, t), v(x, t), w(x, t), \theta(x, t)] \tag{1}$$

These equations may be formally expressed as

$$\mathbf{N}[\boldsymbol{\psi}] = \mathbf{q} \quad \text{for } 0 \leqslant x \leqslant L \quad \text{and } t_0 \leqslant t \leqslant t_f \tag{2}$$

where $\mathbf{N}$ is the vector partial differential operator, $\mathbf{q}$ is the vector of known quantities, and L is the length of the perfect line–element. Associated with the governing eqns (2) are the boundary conditions

$$\mathbf{B}_\nu[\boldsymbol{\psi}] = \mathbf{g}_\nu, \quad \nu = 1, \ldots \text{ a T } x = 0 \quad \text{and } x = L \tag{3}$$

where $\mathbf{B}_\nu$, $\nu = 1, \ldots$, are the vector operators, and $\mathbf{g}_\nu$, $\nu = 1, \ldots$, are the vectors of known quantities at the boundary points. Reference [2] provides a variety of consistent boundary conditions.

The formulation given in [2] is highly nonlinear, and explicit solutions in terms of previously tabulated functions are most likely not possible. However, by suitably eliminating the spatial variable x, the quasi-linear parabolic partial differential equation problem may be transformed to a non-linear ordinary differential equation problem. The transient response or the stability problem of the spinning line element may then be studied through these nonlinear ordinary differential equations. This is the objective of the work described here.

At the beginning of this study the weighted residual methods were seriously considered for the reduction of the partial differential equations into the ordinary differential equations. In these methods, one proposes that the solution may be expressed as

$$\boldsymbol{\psi} = \boldsymbol{\phi}_0 + \text{diag } (c)_\mu \boldsymbol{\phi}_\mu \tag{4}$$

where the repeated indices indicate summation over their range. In (4), $\boldsymbol{\phi}_0$ and $\boldsymbol{\phi}_\mu$, $\mu = 1, \ldots, m$, are known coordinate functions of x, and $\mathbf{c}_\mu$, $\mu = 1, \ldots, m$ are the undetermined functions of t, diag $(c)_\mu$ is the diagonal matrix containing the components of $\mathbf{c}_\mu$ on its diagonal. The coordinate functions are such that (4) satisfies all of the boundary conditions given in (3) regardless of the values of $\mathbf{c}_\mu$. Defining the equation residue $\mathbf{e}$ of (2) as

$$\mathbf{e} = \mathbf{q} - \mathbf{N}[\boldsymbol{\phi}_0 + \text{diag } (c)_\mu \boldsymbol{\phi}_\mu] \tag{5}$$

and selecting linearly independent weighting functions ω_μ, $\mu = 1, \ldots, m$, of x, the ordinary differential equations for the undetermined functions of t may be obtained by requiring that $\mathbf{e}$ is a null vector in the vector space of ω_μ, i.e.

†This paper presents one phase of research carried out at the Jet Propulsion Laboratory, California Institute of Technology, under contract NAS 7-100 sponsored by the National Aeronautics and Space Administration. The effort was supported by Dr. A. Amos and Mr. R. Goetz, Materials and Structures Division, Office of Aeronautics and Space Technology, NASA.

$$\int_0^L \int_A \text{diag}(e)\,\omega_\mu \,dA\,dx = \mathbf{0} \quad \mu = 1, \ldots, m \qquad (6)$$

where A is the cross-section of the line element, and diag(e) is the diagonal matrix containing the components of $\mathbf{e}$ on its diagonal. The methods of collocation, subdomain, Galerkin, and the least squares would result, if one were to choose Dirac delta, generalized Heaviside, ϕ_μ, and $\mathbf{c}_\mu$ derivatives of $\mathbf{e}^T\mathbf{e}$, respectively, as the weighting functions. However, because of the following reasons the weighted residual methods were not used: (i) the partial differential operators are very complicated (see [2]). Although they possess some structure in their statement, it is very difficult to systematically generate from them the coefficient matrices involved in the nonlinear ordinary differential equations. (ii) The fact that the trial solutions in the weighted residual methods must satisfy all of the boundary conditions is a disadvantage relative to the methods where only the essential boundary conditions are satisfied by the trial solutions. (iii) When the ordinary differential equations are obtained in the form of $\dot{\mathbf{c}} = \mathbf{f}(\mathbf{c})$, presumably the equilibrium states and the stability characteristics of such states of the original system are reflected in $\mathbf{f}(\mathbf{c})$. Unfortunately, even in linear problems, unless the weighting functions are carefully selected, $\mathbf{f}(\mathbf{c})$ may be a very bad substitute for the original system (see [3]). For these reasons, the ordinary differential equations corresponding to the partial differential equations are obtained in this work by the Rayleigh–Ritz procedure, using the Hamilton's principle directly. As mentioned earlier, the formulation given in [2] is obtained from the principal functional of dynamics using the Hamilton's principle as

$$\delta \int_{t_0}^{t_f} \int_0^L \int_A (U + V - T)\,dA\,dx\,dt = 0 \qquad (7)$$

where U, V, and T are the densities of the strain energy, loss of potential energy of prescribed forces, and the kinetic energy, respectively, all expressed in terms of geometrically compatible deflection states which assume known values at times t_0 and t_f. In [2], the variational statement given in (7) is transformed into the partial differential equation formulation of (2) and (3), using the calculus of variations. Here, the variational statement given in (7) is transformed into a set of ordinary differential equations by means of the Rayleigh-Ritz procedure.

2. EXPRESSIONS FOR ENERGY DENSITIES

The spinning cantilever, and the way it is oriented in the inertially fixed cartesian coordinate system (X, Y, Z) is shown in Fig. 1. The figure also shows various other coordinate systems related with the line element. The constant spin Ω is about the Z-axis. The fixed point of the cantilever is point A in the figure, with coordinates (R_0, 0, 0) in the (X, Y, Z) system. The coordinate systems (x, y, z), (α_1, α_2, α_3) and (β_1, β_2, β_3) all belong to the line element, and are related with the perfect, imperfect but unstressed, and imperfect but stressed states of the line element. In all these coordinate systems, the first axis is tangent to the axis of the line element, the other two are coincident with the principal axes of the cross-sections. Their origins are all located at point A. Consider a coordinate system at point A and parallel to (X, Y, Z). This system may be made coincident with the (x, y, z) system with two successive rotations, first about Y with the cone angle c, and then about the rotated X with the pitch angle p. Quantities R_0, c, and p are used in specifying the orientation of the line element. The imperfect but unstressed state of the cantilever axis may be obtained by means of the known deflections u' (axial), v' (trans-

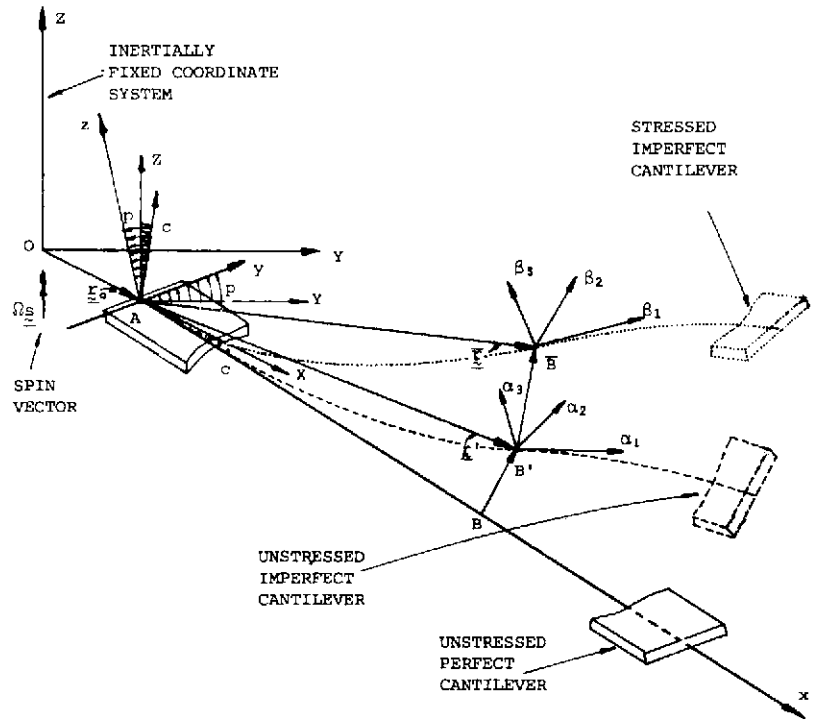

Fig. 1. The geometry of the spinning cantilever and the coordinate systems.

verse), w' (transverse), and θ' (rotational about the beam axis) from the perfect axis. The imperfect but stressed state of the cantilever axis is obtained by means of deflections $\bar{u}$ (axial), $\bar{v}$ (transverse), $\bar{w}$ (transverse), and $\bar{\theta}$ (rotational about the beam axis) from the perfect axis. Other points in the cross-sections can be located by means of the Bernoulli–Navier assumptions. The unknown deflections $u(x, t)$, $v(x, t)$, $w(x, t)$, and $\theta(x, t)$ define the system behavior, and may be expressed as $u=\bar{u}-u'$, $v=\bar{v}-v'$, $w=\bar{w}-w'$, and $\theta=\bar{\theta}-\theta'$. These are listed as ψ in (1). The energy densities appearing in (7) are expressed in terms of the components of ψ [2]. A short summary follows.

Strain energy density U

Consistent with the beam theory it may be assumed that only axial normal and transverse shear stresses can develop due to ψ. Then one may write

$$U=\tfrac{1}{2}\boldsymbol{\varepsilon}^T \operatorname{diag}(E, G, G)\boldsymbol{\varepsilon} \tag{8}$$

where E is the Young's Modulus, G is the Shear Modulus of the cantilever material, and

$$\boldsymbol{\varepsilon}^T=[\varepsilon_{11}, 2\varepsilon_{12}, 2\varepsilon_{13}] \tag{9}$$

where ε_{11}, ε_{12} and ε_{13} are the (1,1), (1,2), and (1, 3) components of the Green's strain tensor $\mathbf{E}$. Relative to point A (see Fig. 1), let $\mathbf{r}'$ and $\bar{\mathbf{r}}$ denote the position vectors of a material particle in the unstressed and the stressed states of the imperfect cantilever, respectively. Then

$$d\bar{\mathbf{r}}^T d\bar{\mathbf{r}}-d\mathbf{r}'^T d\mathbf{r}'=2\,d\boldsymbol{\alpha}^T\mathbf{E}\,d\boldsymbol{\alpha} \tag{10}$$

where $d\bar{\mathbf{r}}$ and $d\mathbf{r}'$ are the changes in the position vectors when the α-coordinates of the particle are changed with an infinitesimal amount $d\boldsymbol{\alpha}=[d\alpha_1, d\alpha_2, d\alpha_3]^T$ (see [4]). With the help of Fig. 1, position vector $\bar{\mathbf{r}}$ of the particle with coordinates (x, y, z) in the perfect state may be expressed in the (x, y, z) coordinate system as

$$\bar{\mathbf{r}}=\begin{Bmatrix} x \\ 0 \\ 0 \end{Bmatrix}+\begin{Bmatrix} \bar{u}-\bar{\Delta} \\ \bar{v} \\ \bar{w} \end{Bmatrix}+\mathbf{T}_{x\leftarrow\beta}\begin{Bmatrix} -\bar{\lambda} \\ \beta_2 \\ \beta_3 \end{Bmatrix} \tag{11}$$

where $\bar{\Delta}$ is the shortening of the beam axis due to transverse displacements $\bar{v}$ and $\bar{w}$, $\bar{\lambda}$ is the axial shortening due to warping of the cross-section, and $\mathbf{T}_{x\leftarrow\beta}$ is the coordinate transformation matrix from $(\beta_1, \beta_2, \beta_3)$ system into (x, y, z) system. Consistent with the second order approximation it can be shown that [2, 5]

$$\bar{\Delta}=\int_0^x \tfrac{1}{2}(\bar{v}_{,x}^2+\bar{w}_{,x}^2)\,dx \tag{12}$$

$$\bar{\lambda}=\chi\int_0^x \tfrac{1}{2}\bar{\theta}_{,x}^2\,dx \tag{13}$$

$$\mathbf{T}_{x\leftarrow\beta}=\begin{bmatrix} 1-\frac{1}{2}(\bar{v}_{,\beta_1}^2+\bar{w}_{,\beta_1}^2) & -\bar{w}_{,\beta_1}\bar{e}_3-\bar{v}_{,\beta_1} & \bar{v}_{,\beta_1}\bar{e}_3-\bar{w}_{,\beta_1} \\ \bar{v}_{,\beta_1} & 1-\frac{1}{2}\bar{v}_{,\beta_1}^2 & -\bar{e}_3-\bar{v}_{,\beta_1}\bar{w}_{,\beta_1} \\ \bar{w}_{,\beta_1} & \bar{e}_3 & 1-\frac{1}{2}\bar{w}_{,\beta_1}^2 \end{bmatrix} \tag{14}$$

where χ is the warping function of the cross-section, and $\bar{e}_3$ is the Euler angle defined as

$$\bar{e}_3=\bar{\theta}-\int_0^x \bar{v}_{,\tau}\bar{w}_{,\tau}\,d\tau. \tag{15}$$

In these expressions a comma in the subscript indicates differentiation with respect to the quantity(s) following the comma. Substituting from these equations and assuming that $\beta_2\cong\alpha_2$, $\beta_3\cong\alpha_3$, $\beta_{1,x}\cong 1+u_{,x}$, one may rewrite (11) as

$$\bar{\mathbf{r}}=\begin{Bmatrix} x \\ \alpha_2 \\ \alpha_3 \end{Bmatrix}+\begin{Bmatrix} \bar{u}-\alpha_2\bar{v}_{,x}-\alpha_3\bar{w}_{,x} \\ \bar{v}-\alpha_3\bar{e}_3 \\ \bar{w}+\alpha_2\bar{e}_3 \end{Bmatrix} - \begin{Bmatrix} \bar{\Lambda}+\bar{\lambda}+\alpha_2(\bar{w}_{,x}\bar{e}_3-\bar{u}_{,x}\bar{v}_{,x})-\alpha_3(\bar{v}_{,x}\bar{e}_3+\bar{u}_{,x}\bar{w}_{,x}) \\ \frac{1}{2}\alpha_2(\bar{v}_{,x}^2+\bar{e}_3^2)+\alpha_3\bar{v}_{,x}\bar{w}_{,x} \\ \frac{1}{2}\alpha_3(\bar{w}_{,x}^2+\bar{e}_3^2) \end{Bmatrix}. \tag{16}$$

By replacing bars above with primes, a similar expression may be obtained from (16) for $\mathbf{r}'$. Using these for $\bar{\mathbf{r}}$ and $\mathbf{r}'$ in (10) one may obtain expressions for the components of the strain tensor $\mathbf{E}$ in terms of the components of ψ, involving nonlinearities up to the second order. The expressions are given explicitly in [2]. The use of expressions for ε_{11}, ε_{12}, and ε_{13} in (9) and then $\boldsymbol{\varepsilon}$ from (9) into (8) would enable one to express the strain energy density in terms of the components of ψ, involving nonlinearities up to the fourth order. Observing that $G=E/[2(1+\nu)]$, one may rewrite (8) as

$$U=\tfrac{1}{2}E\mathbf{a}^T\mathbf{a} \tag{17}$$

where

$$\mathbf{a}=\left[\varepsilon_{11}, \frac{\sqrt{2}}{\sqrt{1+\nu}}\varepsilon_{12}, \frac{\sqrt{2}}{\sqrt{1+\nu}}\varepsilon_{13}\right]^T. \tag{18}$$

For the purposes of the developments presented here, it is sufficient to remember that $\mathbf{a}$ is nonlinear up to the second order in the components of ψ.

Kinetic energy density T

Let γ denote the unit mass of the material, and let $\mathbf{v}$ denote the description of the velocity vector in (x, y, z) coordinate system. Then, for the kinetic energy density T, one may write

$$T=\tfrac{1}{2}\gamma\mathbf{v}^T\mathbf{v}. \tag{19}$$

Let $\mathbf{r}_0$ denote the description of the position vector of point A (see Fig. 1) relative to a point 0 on the rotation axis [i.e., the origin of (X, Y, Z) system] in the (x, y, z) system, and let $\mathbf{r}$ denote the description of the position vector of the particle defined by $\bar{\mathbf{r}}$, relative to point 0 and in (x, y, z) system. Then

$$\mathbf{r}=\mathbf{r}_0+\bar{\mathbf{r}}. \tag{20}$$

Let $\boldsymbol{\Omega}\,\mathbf{s}$ denote the description of the spin vector in (x, y, z) system. Then the description of the velocity vector $\mathbf{v}$ in (x, y, z) system may be expressed as

$$\mathbf{v}=\dot{\mathbf{r}}+\boldsymbol{\Omega}\mathbf{s}\times\mathbf{r} \tag{21}$$

where a dot above indicates differentiation once with respect to time t. Noting that $\mathbf{r}_0$ is constant with respect to time, one may rewrite (21) as

$$\mathbf{v}=\dot{\bar{\mathbf{r}}}+\Omega\rho \tag{22}$$

where

$$\rho=\mathbf{s}\times(\mathbf{r}_0+\bar{\mathbf{r}}). \tag{23}$$

In (23) $\mathbf{s}$ is the description of the spin direction unit vector in (x, y, z) system. Clearly $\mathbf{v}$ is nonlinear to the second order in the components of ψ, since both $\dot{\bar{\mathbf{r}}}$ and $\bar{\mathbf{r}}$ are so. In terms of the rotation angles c and p mentioned earlier, the constant vectors $\mathbf{r}_0$ and $\mathbf{s}$ may be expressed in (x, y, z) system as

$$\mathbf{r}_0=R_0[\cos c, -\sin p\sin c, -\cos p\sin c]^T \tag{24}$$

and

$$\mathbf{s}=[\sin c,\ \cos c \sin p,\ \cos c \cos p]^T. \tag{25}$$

Density of loss of potential of prescribed forces V

Let the prescribed forces acting per unit length of the imperfect but unstressed cantilever be

$$\mathbf{q}=[F_1,\ F_2,\ F_3,\ F_4]^T \tag{26}$$

where F_1, F_2, F_3, and F_4 are in the directions of u', v', w', and e'_3, respectively. Then for V one may write

$$V=-\mathbf{d}^T\mathbf{q} \tag{27}$$

where

$$\mathbf{d}=(1/A)[(\bar{u}-\bar{\Delta})-(u'-\bar{\Delta}'),\ \bar{v}-v',\ \bar{w}-w',\ \bar{e}_3-e'_3]^T. \tag{28}$$

Note that $\mathbf{d}$ is nonlinear to the second order in the components of ψ, due to its first and the fourth components. In (28) A is the cross-sectional area of the cantilever.

3. TRIAL SOLUTIONS

The class of functions which may be used in conjunction with the variational statement (7) should be admissible, i.e. sufficiently smooth in the solution domain, and satisfy the essential boundary conditions. In the present problem, the essential boundary conditions exist only at $x=0$, and they may involve the components of ψ and their first spatial derivatives. Assuming that the essential boundary conditions are of homogeneous type, from the trial solution given in (4) one may write

$$\psi=\text{diag}\,(c)_\mu\phi_\mu \tag{29}$$

as a possible trial solution, provided that each coordinate function ϕ_μ satisfies the essential boundary conditions at $x=0$. Note that, so long as the essential boundary conditions are of homogeneous type, there is no need for coordinate function ϕ_0. As stated earlier the range of μ in (29) is m, therefore there are $4m$ undetermined functions $c(t)$ present in the trial solution.

The questions of what to select as coordinate functions, and how many to select are very important, since they determine not only the cost of the solution but also its accuracy. In the present formulation many diverse factors are included as problem parameters. Depending upon the values of the parameters, a certain number of coordinate functions of a certain type may provide a more accurate solution with less cost. For this reason, in the present work, the type and the number of the coordinate functions are taken as the parameters of the discretization.

The possible choices for the coordinate functions include the orthogonal functions, the generalized pyramid functions, and interpolating polynomials. In linear problems, the orthogonal functions yield diagonal matrices, the generalized pyramid functions yield banded matrices, and the interpolating polynomials provide a convenient means of truncation error estimation. The present work provides insight in these matters when the problems are nonlinear. This point is further discussed in the paper following the derivation of the nonlinear ordinary differential equations for the undetermined functions $c(t)$ in terms of the known yet unspecified type and number of coordinate functions $\phi(x)$.

Another very important aspect of numerical solutions is the way the discrete unknown quantities are ordered. Here, the way the undetermined functions $c(t)$ are ordered may become very crucial as a function of their total number. For example, when the problem is linear and the coordinate functions are selected as pyramid functions, the coefficient matrices in the ordinary differential equations become banded only if the undetermined functions are ordered as $\mathbf{c}^T=[\mathbf{c}_1^T, \mathbf{c}_2^T, \ldots, \mathbf{c}_m^T]$. In the present formulation the ordering of the undetermined functions is also taken as a parameter of the numerical solution. Therefore, the notation $\mathbf{c}$ will refer to the list of $4m$ number of undetermined functions $c(t)$ in some order. In fact, from now on, it will be assumed that the trial solution contains a total of n undetermined functions $c(t)$, i.e. the order of $\mathbf{c}$ is n, and instead of (29)

$$\psi=\begin{Bmatrix} u(x,t)\\ v(x,t)\\ w(x,t)\\ \theta(x,t)\end{Bmatrix}=\begin{Bmatrix} c_\alpha\phi^u_\alpha\\ c_\beta\phi^v_\beta\\ c_\gamma\phi^w_\gamma\\ c_\delta\phi^\theta_\delta\end{Bmatrix} \tag{30}$$

will be used. In (30), as usual, repeated indices indicate summation over the range. The ranges of α, β, γ, and δ are n_u, n_v, n_w, and n_θ, respectively, such that

$$n=n_u+n_v+n_w+n_\theta \tag{31}$$

and ϕ^u, ϕ^v, ϕ^w, and ϕ^θ are the coordinate functions $\phi(x)$ used in approximating the u, v, w, and θ components of ψ, respectively. The complete list of coordinate functions $\phi(x)$, ordered in the same manner as $\mathbf{c}$, will be shown by $\boldsymbol{\phi}$. The components of $\mathbf{c}$ and $\boldsymbol{\phi}$ will be referred to using latin indices, such as c_i and ϕ_i. Unless otherwise specified the ranges of latin indices will be taken as n.

4. FORMAL STATEMENT OF THE RESULTS OF RAYLEIGH–RITZ PROCEDURE

Let H denote the density of the Lagrangian function, i.e. the integrand of the variational statement in (7), so that one may write

$$H=U+V-T \tag{32}$$

Let $\bar{H}$ denote the Lagrangian function. By definition

$$\bar{H}=\int_0^L\int_A H\,\mathrm{d}A\,\mathrm{d}x. \tag{33}$$

From now on we will assume the notation that a bar above indicates integration in the spatial domain with respect to the spatial independent variables. Using (32) and (33), one may rewrite the variational statement in (7) as

$$\delta\int_{t_0}^{t_f}\bar{H}\,\mathrm{d}t=0. \tag{34}$$

If one uses ψ from (30) in (33), after the integration over the spatial variables $\bar{H}$ will become a function of $\mathbf{c}$ and $\dot{\mathbf{c}}$ only, i.e. formally

$$\bar{H}=\bar{H}(\mathbf{c},\dot{\mathbf{c}}). \tag{35}$$

With this, (34) becomes

$$\int_{t_0}^{t_f}(\delta\mathbf{c}^T\bar{H}_{,\mathbf{c}}+\delta\dot{\mathbf{c}}^T\bar{H}_{,\dot{\mathbf{c}}})\,\mathrm{d}t=0. \tag{36}$$

Since $\delta\mathbf{c}$ vanishes at $t=t_0$ and $t=t_f$ one has

$$\int_{t_0}^{t_f}\delta\dot{\mathbf{c}}^T\bar{H}_{,\dot{\mathbf{c}}}\,\mathrm{d}t=[\delta\mathbf{c}^T\bar{H}_{,\dot{\mathbf{c}}}]_{t_0}^{t_f}-\int_{t_0}^{t_f}\delta\mathbf{c}^T\frac{\mathrm{d}}{\mathrm{d}t}\bar{H}_{,\dot{\mathbf{c}}}\,\mathrm{d}t$$

$$=-\int_{t_0}^{t_f}\delta\mathbf{c}^T\frac{\mathrm{d}}{\mathrm{d}t}\bar{H}_{,\dot{\mathbf{c}}}\,\mathrm{d}t$$

and therefore (36) may be restated as

$$\int_{t_0}^{t_f} \delta \mathbf{c}^T \left(\overline{H}_{,\dot{\mathbf{c}}} - \frac{\mathrm{d}}{\mathrm{d}t} \overline{H}_{,\dot{\mathbf{c}}} \right) \mathrm{d}t = 0. \tag{37}$$

From the arbitrariness of $\delta \mathbf{c}$ in the open interval (t_0, t_f), (37) becomes

$$\overline{H}_{,\dot{\mathbf{c}}} - \frac{\mathrm{d}}{\mathrm{d}t} \overline{H}_{,\dot{\mathbf{c}}} = \mathbf{0}. \tag{38}$$

which is nothing but the Lagrange's equations. Substituting H from (32) into this equation one finally obtains

$$\overline{U}_{,\dot{\mathbf{c}}} - \frac{\mathrm{d}}{\mathrm{d}t} \overline{U}_{,\dot{\mathbf{c}}} + \overline{V}_{,\dot{\mathbf{c}}} - \frac{\mathrm{d}}{\mathrm{d}t} \overline{V}_{,\dot{\mathbf{c}}} - \overline{T}_{,\dot{\mathbf{c}}} + \frac{\mathrm{d}}{\mathrm{d}t} \overline{T}_{,\dot{\mathbf{c}}} = \mathbf{0} \tag{39}$$

which are the second order nonlinear ordinary differential equations in the n components of $\mathbf{c}$. These equations may be restated as

$$[\mathbf{M}(\mathbf{c})]\ddot{\mathbf{c}} + [\mathbf{C}(\mathbf{c}, \dot{\mathbf{c}})]\dot{\mathbf{c}} + [\mathbf{K}(\mathbf{c})]\mathbf{c} = \mathbf{p}. \tag{40}$$

Using the expressions developed earlier for the energy densities in (39), explicit expressions for $\mathbf{M}(\mathbf{c})$, $\mathbf{C}(\mathbf{c}, \dot{\mathbf{c}})$ and $\mathbf{K}(\mathbf{c})$ are given in the next section. Note that, when the coordinate functions $\phi(x)$ are of the type of generalized pyramid functions, the nth order matrices $\mathbf{M}(\mathbf{c})$, $\mathbf{C}(\mathbf{c}, \dot{\mathbf{c}})$, and $\mathbf{K}(\mathbf{c})$ represent the mass, the gyroscopic, and the stiffness matrix of the structure. The three terms on the left of (40) stand for the inertial, the gyroscopic and the restoring forces; the term of the right stands for the loading of the system.

5. EXPLICIT EXPRESSIONS FOR THE ORDINARY DIFFERENTIAL EQUATIONS OF MOTION

One may observe from (39) that the contributions to the ordinary differential equations of motion come from the strain energy [the first two terms in (39)], the kinetic energy [the last two terms in (39)], and the loss of potential of prescribed forces [the third and the fourth terms in (39)]. These contributions are expressed explicitly below.

Contributions from the strain energy $\overline{U}$

The strain energy density is given in (17) in terms of $\mathbf{a}$, and $\mathbf{a}$ is defined in (18) in terms of ε_{11}, ε_{12}, and ε_{13} which are given in [2]. Since the strain components ε_{11}, ε_{12}, and ε_{13} are second order nonlinear in the components of ψ, substitution of ψ from (30) yields

$$\mathbf{a} = \mathbf{a}_0 + \mathbf{A}_0\mathbf{c} + c_i\mathbf{A}_i\mathbf{c} \tag{41}$$

where $\mathbf{a}_0$, $\mathbf{A}_0$, and $\mathbf{A}_i$, $i = 1, \ldots, n$ are functions of spatial variables only. They are known when the initial imperfections, and the coordinate functions are known. Recalling that the strain energy $\overline{U}$ is the integral of U with respect to the spatial variables, and substituting $\mathbf{a}$ from (41) into (17) one obtains

$$\begin{aligned} \overline{U}/E = {} & \overline{\tfrac{1}{2}\mathbf{a}_0^T\mathbf{a}_0} + \mathbf{c}^T\overline{\mathbf{A}_0^T\mathbf{a}_0} + \tfrac{1}{2}\mathbf{c}^T\overline{\mathbf{A}_0^T\mathbf{A}_0}\mathbf{c} + \mathbf{c}^T c_i\overline{\mathbf{A}_i^T\mathbf{a}_0} \\ & + \mathbf{c}^T c_i\overline{\mathbf{A}_i^T\mathbf{A}_0}\mathbf{c} + \tfrac{1}{2}\mathbf{c}^T c_i c_j\overline{\mathbf{A}_i^T\mathbf{A}_j}\mathbf{c} \end{aligned} \tag{42}$$

where bars at the top indicate integration with respect to the spatial variables. Since $\overline{U}$ is not a function of $\dot{\mathbf{c}}$, then $\overline{U}_{,\dot{\mathbf{c}}} = \mathbf{0}$, which leads to

$$\frac{\mathrm{d}}{\mathrm{d}t} \overline{U}_{,\dot{\mathbf{c}}} = \mathbf{0}. \tag{43}$$

However, since $\overline{U}$ is a function of $\mathbf{c}$, from (42) one obtains

$$\begin{aligned} \overline{U}_{,\dot{\mathbf{c}}} = {} & E\overline{\mathbf{A}_0^T\mathbf{a}_0} + E[\overline{\mathbf{A}_0^T\mathbf{A}_0} + (\mathbf{i}_i\overline{\mathbf{a}_0^T\mathbf{A}_i}) + (\mathbf{i}_i\overline{\mathbf{a}_0^T\mathbf{A}_i})^T \\ & + (c_i\mathbf{I} + \tfrac{1}{2}\mathbf{i}_i\mathbf{c}^T)(\overline{\mathbf{A}_0^T\mathbf{A}_i}) + (\overline{\mathbf{A}_0^T\mathbf{A}_i})^T) \\ & + \tfrac{1}{2}(c_ic_j\mathbf{I} + c_j\mathbf{i}_i\mathbf{c}^T)(\overline{\mathbf{A}_i^T\mathbf{A}_j}) + (\overline{\mathbf{A}_i^T\mathbf{A}_j})^T)]\mathbf{c} \end{aligned} \tag{44}$$

where $\mathbf{I}$ is the nth order identity matrix, and $\mathbf{i}_i$ is its ith column.

Contributions from the kinetic energy $\overline{T}$

The kinetic energy density is given in (19) in terms of velocity vector $\mathbf{v}$ which is defined in (22) in terms of $\bar{\mathbf{r}}$, $\boldsymbol{\rho}$, and the spin rate $\boldsymbol{\Omega}$. Expressions for $\bar{\mathbf{r}}$ and $\boldsymbol{\rho}$ are given in (16) and (23), respectively. From these, it is seen that $\mathbf{v}$ is second order nonlinear in the components of ψ. Substitution of ψ from (30) into $\mathbf{v}$ yields

$$\mathbf{v} = (\mathbf{b}_0 + \mathbf{B}_0\dot{\mathbf{c}} + c_i\mathbf{B}_i\dot{\mathbf{c}}) + \boldsymbol{\Omega}(\mathbf{g}_0 + \mathbf{G}_0\mathbf{c} + c_i\mathbf{G}_i\mathbf{c}) \tag{45}$$

where $\mathbf{b}_0$, $\mathbf{g}_0$, $\mathbf{B}_0$, $\mathbf{G}_0$, and $\mathbf{B}_i$, $\mathbf{G}_i$, $i = 1, \ldots, n$, are functions of spatial variables only. They are known when the initial imperfections, and the coordinate functions are known. Recalling that the kinetic energy $\overline{T}$ is the integral of T with respect to the spatial variables, and substituting $\mathbf{v}$ from (45) into (19) one obtains

$$\begin{aligned} \overline{T}/\gamma = {} & \tfrac{1}{2}\overline{\mathbf{b}_0^T\mathbf{b}_0} + \dot{\mathbf{c}}^T\overline{\mathbf{B}_0^T\mathbf{b}_0} + \tfrac{1}{2}\dot{\mathbf{c}}^T\overline{\mathbf{B}_0^T\mathbf{B}_0}\dot{\mathbf{c}} + \dot{\mathbf{c}}^T c_i\overline{\mathbf{B}_i^T\mathbf{b}_0} \\ & + \dot{\mathbf{c}}^T c_i\overline{\mathbf{B}_i^T\mathbf{B}_0}\dot{\mathbf{c}} + \tfrac{1}{2}\dot{\mathbf{c}}^T c_ic_j\overline{\mathbf{B}_i^T\mathbf{B}_j}\dot{\mathbf{c}} \\ & + \boldsymbol{\Omega}^2(\tfrac{1}{2}\overline{\mathbf{g}_0^T\mathbf{g}_0} + \mathbf{c}^T\overline{\mathbf{G}_0^T\mathbf{g}_0} + \tfrac{1}{2}\mathbf{c}^T\overline{\mathbf{G}_0^T\mathbf{G}_0}\mathbf{c} + \mathbf{c}^T c_i\overline{\mathbf{G}_i^T\mathbf{g}_0} \\ & + \mathbf{c}^T c_i\overline{\mathbf{G}_i^T\mathbf{G}_0}\mathbf{c} + \tfrac{1}{2}\mathbf{c}^T c_ic_j\overline{\mathbf{G}_i^T\mathbf{G}_j}\mathbf{c}) \\ & + \boldsymbol{\Omega}(\overline{\mathbf{b}_0^T\mathbf{g}_0} + \mathbf{c}^T\overline{\mathbf{G}_0^T\mathbf{b}_0} + \dot{\mathbf{c}}^T\overline{\mathbf{B}_0^T\mathbf{g}_0} + \overline{\mathbf{c}^T c_i\mathbf{G}_i^T\mathbf{b}_0} \\ & + \dot{\mathbf{c}}^T\overline{\mathbf{B}_0^T\mathbf{G}_0}\mathbf{c} + \dot{\mathbf{c}}^T c_i\overline{\mathbf{B}_i^T\mathbf{g}_0} + \dot{\mathbf{c}}^T c_i\overline{\mathbf{B}_0^T\mathbf{G}_i}\mathbf{c} + \dot{\mathbf{c}}^T c_i\overline{\mathbf{B}_i^T\mathbf{G}_0}\mathbf{c} \\ & + \dot{\mathbf{c}}^T c_ic_j\overline{\mathbf{B}_i^T\mathbf{G}_j}\mathbf{c}) \end{aligned}$$

From this equation, by differentiation with respect to the components of $\mathbf{c}$, one may write

$$\begin{aligned} \overline{T}_{,\mathbf{c}} = {} & \boldsymbol{\Omega}^2\gamma\overline{\mathbf{G}_0^T\mathbf{g}_0} + \boldsymbol{\Omega}^2\gamma[\overline{\mathbf{G}_0^T\mathbf{G}_0} + (\overline{\mathbf{i}_i\mathbf{g}_0^T\mathbf{G}_i}) + (\overline{\mathbf{i}_i\mathbf{g}_0^T\mathbf{G}_i})^T \\ & + (c_i\mathbf{I} + \tfrac{1}{2}\mathbf{i}_i\mathbf{c}^T)((\overline{\mathbf{G}_0^T\mathbf{G}_i}) + (\overline{\mathbf{G}_0^T\mathbf{G}_i})^T) \\ & + \tfrac{1}{2}(c_ic_j\mathbf{I} + c_j\mathbf{i}_i\mathbf{c}^T)((\overline{\mathbf{G}_i^T\mathbf{G}_j}) + (\overline{\mathbf{G}_i^T\mathbf{G}_j})^T)]\mathbf{c} \\ & + \boldsymbol{\Omega}\gamma\overline{\mathbf{G}_0^T\mathbf{b}_0} + \boldsymbol{\Omega}\gamma[(\overline{\mathbf{i}_i\mathbf{b}_0^T\mathbf{G}_i}) + (\overline{\mathbf{i}_i\mathbf{b}_0^T\mathbf{G}_i})^T]\mathbf{c} \\ & + \boldsymbol{\Omega}\gamma[\overline{\mathbf{G}_0^T\mathbf{B}_0 + \mathbf{i}_i\mathbf{g}_0^T\mathbf{B}_i} + (c_i\mathbf{I} + \mathbf{i}_i\mathbf{c}^T)(\overline{\mathbf{G}_0^T\mathbf{B}_i} + \overline{\mathbf{G}_i^T\mathbf{B}_0}) \\ & + (c_ic_j\mathbf{I} + (c_i\mathbf{i}_j + c_j\mathbf{i}_i)\mathbf{c}^T)\overline{\mathbf{G}_j^T\mathbf{B}_i}]\dot{\mathbf{c}} \\ & + \gamma[\mathbf{i}_i\overline{\mathbf{b}_0^T\mathbf{B}_i} + \mathbf{i}_i\dot{\mathbf{c}}^T\overline{\mathbf{B}_i^T\mathbf{B}_0} + \tfrac{1}{2}(c_j\mathbf{i}_i + c_i\mathbf{i}_j)\dot{\mathbf{c}}^T\overline{\mathbf{B}_i^T\mathbf{B}_j}]\dot{\mathbf{c}} \end{aligned} \tag{47}$$

where the symbols are as defined earlier. Similarly, by differentiation with respect to the components of $\dot{\mathbf{c}}$ one may obtain

$$\begin{aligned} \overline{T}_{,\dot{\mathbf{c}}} = {} & \gamma\overline{\mathbf{B}_0^T\mathbf{b}_0} + \gamma\overline{\mathbf{B}_i^T\mathbf{b}_0}\mathbf{i}_i^T\mathbf{c} \\ & + \gamma[\overline{\mathbf{B}_0^T\mathbf{B}_0} + c_i((\overline{\mathbf{B}_0^T\mathbf{B}_i}) + (\overline{\mathbf{B}_0^T\mathbf{B}_i})^T) \\ & + \tfrac{1}{2}c_ic_j((\overline{\mathbf{B}_i^T\mathbf{B}_j}) + (\overline{\mathbf{B}_i^T\mathbf{B}_j})^T)]\dot{\mathbf{c}} + \boldsymbol{\Omega}\gamma\overline{\mathbf{B}_0^T\mathbf{g}_0} \\ & + \boldsymbol{\Omega}\gamma[\overline{\mathbf{B}_0^T\mathbf{G}_0} + \overline{\mathbf{B}_i^T\mathbf{g}_0}\mathbf{i}_i^T + c_i(\overline{\mathbf{B}_0^T\mathbf{G}_i} + \overline{\mathbf{B}_i^T\mathbf{G}_0}) \\ & + c_ic_j\overline{\mathbf{B}_i^T\mathbf{G}_j}]\mathbf{c}. \end{aligned} \tag{48}$$

From this, by differentiation with respect to time t, one gets

$$\overline{T}_{,\dot{c}} = \gamma[\overline{\mathbf{B}_0^T\mathbf{B}_0} + c_i(\overline{(\mathbf{B}_0^T\mathbf{B}_i)} + \overline{(\mathbf{B}_0^T\mathbf{B}_i)^T}) + \tfrac{1}{2}c_ic_j(\overline{(\mathbf{B}_i^T\mathbf{B}_j)} + \overline{(\mathbf{B}_i^T\mathbf{B}_j)^T})]\ddot{\mathbf{c}} + \gamma[\overline{\mathbf{B}_i^T\mathbf{b}_0}\mathbf{i}_i^T + \dot{c}_i(\overline{(\mathbf{B}_0^T\mathbf{B}_i)} + \overline{(\mathbf{B}_0^T\mathbf{B}_i)^T}) + \tfrac{1}{2}(\dot{c}_ic_j + c_i\dot{c}_j)(\overline{(\mathbf{B}_i^T\mathbf{B}_j)} + \overline{(\mathbf{B}_i^T\mathbf{B}_j)^T})]\dot{\mathbf{c}} + \Omega\gamma[\overline{\mathbf{B}_0^T\mathbf{G}_0} + \overline{\mathbf{B}_i^T\mathbf{g}_0}\mathbf{i}_i^T + (\overline{\mathbf{B}_0^T\mathbf{G}_i} + \overline{\mathbf{B}_i^T\mathbf{G}_0})(c_i\mathbf{I} + \mathbf{c}\mathbf{i}_i^T) + \overline{\mathbf{B}_i^T\mathbf{G}_j}(c_ic_j\mathbf{I} + \mathbf{c}(c_i\mathbf{i}_j^T + c_j\mathbf{i}_i^T))]\dot{\mathbf{c}} \quad (49)$$

where, as defined earlier, $\mathbf{I}$ is the nth order identity matrix, and $\mathbf{i}_i$ and $\mathbf{i}_j$ are its ith and jth columns, respectively.

Contributions from the potential loss of prescribed forces V

The density of potential energy loss of prescribed forces V is given in (27) in terms of $\mathbf{d}$ and $\mathbf{q}$ which are defined in (28) and (26), respectively. Vector $\mathbf{q}$ is a known quantity, and $\mathbf{d}$ involves only the components of ψ. The substitution of ψ from (30) in (28) yields

$$\mathbf{d} = \mathbf{d}_0 + \mathbf{D}_0\mathbf{c} + c_i\mathbf{D}_i\mathbf{c} \quad (50)$$

where $\mathbf{d}_0$, $\mathbf{D}_0$, and $\mathbf{D}_i$, $i = 1, \ldots, n$, are functions of spatial variables only, and they are known when the initial imperfections and the coordinate functions are known. Recalling that the loss of potential of prescribed forces, $\overline{V}$, is the integral of its density V, with respect to the spatial variables, and substituting $\mathbf{d}$ from (50) into (27), one may write

$$\overline{V} = -\overline{\mathbf{d}_0^T\mathbf{q}} - \mathbf{c}^T\overline{\mathbf{D}_0^T\mathbf{q}} - c_i\mathbf{c}^T\overline{\mathbf{D}_i^T\mathbf{q}}. \quad (51)$$

Since $\overline{V}$ is not a function of $\dot{\mathbf{c}}$, hence $\overline{V}_{,\dot{c}} = \mathbf{0}$, and therefore

$$\frac{\mathrm{d}}{\mathrm{d}t}\overline{V}_{,\dot{c}} = \mathbf{0}. \quad (52)$$

From (51), by differentiation with respect to the components of $\mathbf{c}$, one obtains

$$\overline{V}_{,c} = -\overline{\mathbf{D}_0^T\mathbf{q}} - [(\mathbf{i}_i\overline{\mathbf{q}^T\mathbf{D}_i}) + (\mathbf{i}_i\overline{\mathbf{q}^T\mathbf{D}_i})^T]\mathbf{c} \quad (53)$$

where $\mathbf{I}$ and $\mathbf{i}_i$ are the nth order identity matrix and its ith column, respectively.

Thus, having obtained explicit expressions for each of the terms of (39), one may obtain explicit expressions for $\mathbf{M}$, $\mathbf{C}$, and $\mathbf{K}$ matrices by rearranging (39) as in (40).

6. EXPRESSIONS FOR NONLINEAR MASS, GYROSCOPIC STIFFNESS AND LOAD MATRICES

Substituting the expressions given by (44), (43), (52), (53), (47) and (49) for the six terms of (39), one may obtain n number of coupled second order nonlinear ordinary differential equations for the n number of undetermined functions listed in $\mathbf{c}$. The rearrangement of these equations as in (40) leads to the following expressions for mass $\mathbf{M}$, gyroscopic $\mathbf{C}$, stiffness $\mathbf{K}$, and load $\mathbf{p}$ matrices appearing in (40).

$$\mathbf{M} = \gamma[\overline{\mathbf{B}_0^T\mathbf{B}_0} + c_i(\overline{(\mathbf{B}_0^T\mathbf{B}_i)} + \overline{(\mathbf{B}_0^T\mathbf{B}_i)^T}) + \tfrac{1}{2}c_ic_j(\overline{(\mathbf{B}_i^T\mathbf{B}_j)} + \overline{(\mathbf{B}_i^T\mathbf{B}_j)^T})] \quad (54)$$

$$\mathbf{C} = \gamma[-(\overline{(\mathbf{i}_i\mathbf{b}_0^T\mathbf{B}_i)} - \overline{(\mathbf{i}_i\mathbf{b}_0^T\mathbf{B}_i)^T}) + (\overline{(\mathbf{B}_0^T\mathbf{B}_i\dot{\mathbf{c}}\mathbf{i}_i^T)} - \overline{(\mathbf{B}_0^T\mathbf{B}_i\dot{\mathbf{c}}\mathbf{i}_i^T)^T}) + \tfrac{1}{2}(\overline{(\mathbf{B}_i^T\mathbf{B}_j)}^T\dot{\mathbf{c}}(c_j\mathbf{i}_i^T + c_i\mathbf{i}_j^T)) - \overline{((\mathbf{B}_i^T\mathbf{B}_j)^T\dot{\mathbf{c}}(c_j\mathbf{i}_i^T + c_i\mathbf{i}_j^T))^T}) + (\dot{\mathbf{c}}_i\overline{\mathbf{B}_i^T\mathbf{B}_0} + \tfrac{1}{2}(\dot{\mathbf{c}}_ic_j + c_i\dot{\mathbf{c}}_j)\overline{\mathbf{B}_i^T\mathbf{B}_j})] + \Omega\gamma[(\overline{(\mathbf{B}_0^T\mathbf{G}_0)} - \overline{(\mathbf{B}_0^T\mathbf{G}_0)^T}) + (\overline{(\mathbf{B}_i^T\mathbf{g}_0\mathbf{i}_i^T)} - \overline{(\mathbf{B}_i^T\mathbf{g}_0\mathbf{i}_i^T)^T}) + ((\overline{(\mathbf{B}_0^T\mathbf{G}_i + \mathbf{B}_i^T\mathbf{G}_0)}(c_i\mathbf{I} + \mathbf{c}\mathbf{i}_i^T)) - (\overline{(\mathbf{B}_0^T\mathbf{G}_i + \mathbf{B}_i^T\mathbf{G}_0)}(c_i\mathbf{I} + \mathbf{c}\mathbf{i}_i^T))^T) + (\overline{\mathbf{B}_i^T\mathbf{G}_j}(c_ic_j\mathbf{I} + \mathbf{c}(c_i\mathbf{i}_j^T + c_j\mathbf{i}_i^T))) - (\overline{(\mathbf{B}_i^T\mathbf{G}_j}(c_ic_j\mathbf{I} + \mathbf{c}(c_i\mathbf{i}_j^T + c_j\mathbf{i}_i^T)))^T)] \quad (55)$$

$$\mathbf{K} = E[\overline{\mathbf{A}_0^T\mathbf{A}_0} + (\overline{(\mathbf{i}_i\mathbf{a}_0^T\mathbf{A}_i)}^T + \overline{(\mathbf{i}_i\mathbf{a}_0^T\mathbf{A}_i)^T}) + \tfrac{1}{2}c_i(\overline{(\mathbf{A}_0^T\mathbf{A}_i)} + \overline{(\mathbf{A}_0^T\mathbf{A}_i)^T}) + \tfrac{1}{2}(((\overline{(\mathbf{A}_0^T\mathbf{A}_i)} + \overline{(\mathbf{A}_0^T\mathbf{A}_i)^T})\mathbf{c}\mathbf{i}_i^T) + ((\overline{(\mathbf{A}_0^T\mathbf{A}_i)} + \overline{(\mathbf{A}_0^T\mathbf{A}_i)^T})\mathbf{c}\mathbf{i}_i^T)^T) + \tfrac{1}{2}c_j(((\overline{(\mathbf{A}_i^T\mathbf{A}_j)} + \overline{(\mathbf{A}_i^T\mathbf{A}_j)^T})\mathbf{c}\mathbf{i}_i^T) + ((\overline{(\mathbf{A}_i^T\mathbf{A}_j)} + \overline{(\mathbf{A}_i^T\mathbf{A}_j)^T})\mathbf{c}\mathbf{i}_i^T)^T)] - \Omega\gamma[(\mathbf{i}_i\overline{\mathbf{b}_0^T\mathbf{G}_i}) + (\mathbf{i}_i\overline{\mathbf{b}_0^T\mathbf{G}_i})^T] - \Omega^2\gamma[\overline{\mathbf{G}_0^T\mathbf{G}_0} + (\overline{(\mathbf{i}_i\mathbf{g}_0^T\mathbf{G}_i)} + \overline{(\mathbf{i}_i\mathbf{g}_0^T\mathbf{G}_i)^T}) + \tfrac{1}{2}c_i(\overline{(\mathbf{G}_0^T\mathbf{G}_i)} + \overline{(\mathbf{G}_0^T\mathbf{G}_i)^T}) + \tfrac{1}{2}(((\overline{(\mathbf{G}_0^T\mathbf{G}_i)} + \overline{(\mathbf{G}_0^T\mathbf{G}_i)}\mathbf{c}\mathbf{i}_i^T)^T) + (((\overline{(\mathbf{G}_0^T\mathbf{G}_i)} + \overline{(\mathbf{G}_0^T\mathbf{G}_i)^T}\mathbf{c}\mathbf{i}_i^T) + \tfrac{1}{2}c_j(((\overline{(\mathbf{G}_i^T\mathbf{G}_j)} + \overline{(\mathbf{G}_i^T\mathbf{G}_j)^T}\mathbf{c}\mathbf{i}_i^T) + (((\overline{(\mathbf{G}_i^T\mathbf{G}_j)} + \overline{(\mathbf{G}_i^T\mathbf{G}_j)^T}\mathbf{c}\mathbf{i}_i^T)^T)] - [(\mathbf{i}_i\overline{\mathbf{q}^T\mathbf{D}_i}) + (\mathbf{i}_i\overline{\mathbf{q}^T\mathbf{D}_i})^T] \quad (56)$$

$$\mathbf{p} = \overline{\mathbf{D}_0^T\mathbf{q}} - E\overline{\mathbf{A}_0^T\mathbf{a}_0} + \Omega^2\gamma\overline{\mathbf{G}_0^T\mathbf{g}_0} + \Omega\gamma\overline{\mathbf{G}_0^T\mathbf{b}_0} \quad (57)$$

From (54) one may observe that the contributions to the mass matrix is purely due to the mass of the material (terms with γ factor). These contributions consist of 3 sets of real symmetric nth order matrices, which are constant, linear, and quadratic in $\mathbf{c}$.

From (55) it is seen that matrix $\mathbf{C}$ consists of the contributions from the mass of the material (terms with γ factor alone), and from the spin (terms with $\Omega\gamma$ factor). The non-spin contributions consist of 4 sets of nth order real matrices, the first 3 of which are skew-symmetric. The spin contributions consist of 4 sets of nth order real and skew-symmetric matrices, which are constant, linear, and quadratic in $\mathbf{c}$. The same pattern may be observed in non-spin contributions.

One may see from (56) that the contributions to the stiffness matrix are coming from the material stiffness (the terms with factor E), from Coriolis accelerations (terms with $\Omega\gamma$ factor), from centrifugal accelerations (terms with $\Omega^2\gamma$ factor), and from the loading (terms with $\mathbf{q}$). Note that the contributions consist of 12 sets of real nth order symmetric matrices which are constant, linear, and quadratic in $\mathbf{c}$.

It is seen from (57) that the contributions to the load vector come from the material stiffness, from the centrifugal and Coriolis accelerations, and from the loading itself. They are all nth order and constant.

7. GENERAL NATURE OF THE DISCRETIZATION AND ITS COST

The discrete equations given in (40) with $\mathbf{M}$, $\mathbf{C}$, $\mathbf{K}$, and $\mathbf{p}$ as in (54)–(57) respectively, for the spinning elastic systems, represent the general equations applicable not only to the line elements but also plates, shells, and solids, provided that the nonlinearities in strain-displacement, and velocity-displacement relations do not exceed the second order. Note that when the material is general anisotropic with positive definite real symmetric matrix $E\mathbf{D}$, the strain energy density U can still be expressed as in (17) provided that $\mathbf{a}$ in (17) is defined as

$$\mathbf{a} = \mathbf{D}^{1/2}\boldsymbol{\varepsilon}$$

where $\boldsymbol{\varepsilon}$ is the list of engineering strain components as $\boldsymbol{\varepsilon}^T = [\varepsilon_{11}, \varepsilon_{22}, \varepsilon_{33}, \gamma_{12}, \gamma_{13}, \gamma_{23}]$.

From the definitions of **M**, **C**, **K** and **p** in (54)–(57), one may observe that the following list of basic matrices are sufficient to define the discrete problem, in terms of **c** and $\dot{\mathbf{c}}$:

$$\overline{\mathbf{A}_0^T\mathbf{A}_0},\ \overline{\mathbf{B}_0^T\mathbf{B}_0},\ \overline{\mathbf{G}_0^T\mathbf{G}_0},\ \overline{\mathbf{B}_0^T\mathbf{G}_0},\ \overline{\mathbf{A}_0^T\mathbf{a}_0},\ \overline{\mathbf{G}_0^T\mathbf{g}_0},\ \overline{\mathbf{G}_0^T\mathbf{b}_0},\ \overline{\mathbf{D}_0^T\mathbf{q}} \tag{59}$$

$$\overline{\mathbf{A}_0^T\mathbf{A}_i},\ \overline{\mathbf{B}_0^T\mathbf{B}_i},\ \overline{\mathbf{G}_0^T\mathbf{G}_i},\ \overline{\mathbf{B}_0^T\mathbf{G}_i},\ \overline{\mathbf{B}_i^T\mathbf{G}_0}\ \overline{\mathbf{a}_0^T\mathbf{A}_i},\ \overline{\mathbf{b}_0^T\mathbf{B}_i},\ \overline{\mathbf{b}_0^T\mathbf{G}_i}$$
$$\overline{\mathbf{g}_0^T\mathbf{B}_i},\ \overline{\mathbf{g}_0^T\mathbf{G}_i},\ \overline{\mathbf{q}^T\mathbf{D}_i},\quad i=1,\ldots,n \tag{60}$$

and

$$\overline{\mathbf{A}_i^T\mathbf{A}_j},\ \overline{\mathbf{B}_i^T\mathbf{B}_j},\ \overline{\mathbf{G}_i^T\mathbf{G}_j},\ \overline{\mathbf{B}_i^T\mathbf{G}_j},\quad i=1,\ldots,n \text{ and } j=1,\ldots,n. \tag{61}$$

When the problem is linear, one has to compute only the matrices in (59). When the discrete problem (40) is to contain matrices which are at the most linear in $\dot{\mathbf{c}}$ and **c**, one should compute the matrices in (59) and (60). However, if the quadratic nonlinearities in the coefficient matrices are required, one has to compute all the matrices listed in (59)–(61). Note that $4\,n\times n$ and $4\,n\times 1$ matrices are listed in (59). In (60) there are $5n$ number of $n\times n$ matrices, and $6n$ number of $1\times n$ matrices, and in (61) there are $4n^2$ number of $n\times n$ matrices. Therefore, the total number of $n\times n$ matrices is $4+5n+4n^2$, and the number of nth order vectors is $4+6n$. If one assumes that the cost of generation of these matrices is proportional to the number of matrix elements, one observes that $n^2(4+5n+4n^2)+n(4+6n)=4n^4+5n^3+10n^2+4n$, therefore the cost of generation is proportional to the fourth power of the number of degrees of freedom. This should be compared to that of the linear analysis where the generation cost is proportional to the second power of the number of degrees of freedom or less.

In spite of its enormous cost, to obtain the nonlinear equations of motion of a multi-degree of freedom system is necessary because of the following reasons: (i) Reliable computation of the equilibrium states of motion by methods such as the one described in [6] requires the explicit expressions for the nonlinear equations. (ii) The study of the stability of these equilibrium states also requires the explicit expressions for the nonlinear equations [7].

The nonlinear discrete equations of motion for the cantilever in the form of (40) are given in [8] in a different format. A computer code is written to generate **M**, **C**, **K**, and **p** of (40) as in (54), (55), (56) and (57), respectively, for any selected type and number of coordinate functions, and in terms of **c** and $\dot{\mathbf{c}}$.

8. CONCLUSIONS

The general nonlinear discretized equations of motion of spinning elastic solids and structures are derived as a set of nonlinear ordinary differential equations for the case when the strain-displacement and velocity-displacement relations are nonlinear up to the second order. It is shown that the cost of generation of such equations is proportional to the fourth power of the number of degrees of freedom. A computer program is written to automatically generate the equations for the case of spinning cantilevers with initial imperfections. The types and the number of the coordinate functions used in the trial solution are parameters of the program.

REFERENCES

1. R. H. MacNeal, *Structural Dynamics of Heliogyro*. NASA CR-1745 (May 1971).
2. M. Salama and M. Trubert, Second order nonlinear equations of motion for spinning highly flexible line-elements. Paper No. 79-0736, 20th Structures, Structural Dynamics, and Materials Conference, St. Louis (Apr. 1979).
3. S. H. Crandall, *Engineering Analysis, A Survey of Numerical Procedures*. McGraw-Hill, New York (1956).
4. Y. C. Fung, *Foundations of Solid Mechanics*. Prentice-Hall, Englewood Cliffs, New Jersey (1965).
5. D. A. Peters and R. A. Ormiston, The effect of second order blade bending on the angle of attack of hingeless rotor blades. *J. Am. Helicopter Soc.* (Oct. 1973).
6. A. K. Noor and J. M. Peters, Reduced basis technique for nonlinear analysis of structures. AIAA/ASME/ASCE/AHS. 20th Structures, Structural Dynamics and Materials Conference, St. Louis (Apr. 1979).
7. Y. Ueda, Steady motions exhibited by Duffing's equation. Engineering Foundation Conference on New Approaches to Nonlinear Problems in Dynamics (Dec. 1979).
8. M. El-Essawi, *Discretization of Nonlinear Equations of Motion of Highly Flexible Spinning Cantilevers*, Structural Mechanics Series No. 22. School of Engineering, Duke University, Durham, NC (Mar. 1980).

Computers & Structures, Vol. 13, pp. 357–362, 1981
Printed in Great Britain.

0045-7949/81/010357-06$02.00/0

ELASTIC–PLASTIC ANALYSIS WITH NASTRAN USER ELEMENTS

L. A. LARKIN

A. O. Smith Corporation, Engineering Systems, 8797 North Port Washington Road, Milwaukee, WI 53217, U.S.A.

(*Received* 25 *April* 1980)

Abstract—Described herein are two user-developed elements that have been implemented in the elastic–plastic capability of NASTRAN. The first element is a thin-walled beam. The second is a flat, triangular shell element. The elements are shown to give good agreement with plastic limit analysis for five sample test problems. Application is made to static crush of auto frames. Both beam and shell models are investigated and good comparison is obtained with test data.

INTRODUCTION

Finite element analysis is now widely accepted by industry in the design phase of product development. Most often an elastic, static analysis is sufficient. Many times, some dynamic aspect of the problem is also considered. With increasing frequency, even the elastic–plastic characteristics must be considered. Because of the various analytical capabilities required, a large, general purpose finite element program is necessary. There are many candidates and no attempt will be made here to list or compare them. NASTRAN was selected because of its excellent overall capabilities and because of the availability of the source code without lease, licensing or other restrictions. NASTRAN Level 15.5 was the last "free" version of the code. Furthermore, since the elastic–plastic capability has remained virtually unchanged since the release of NASTRAN 15.5, this code may be linked with later versions. The writer has successfully linked this source code and the numerous changes described here into Version 50A of the MacNeal–Schwendler proprietary NASTRAN producing a version of MSC/NASTRAN that executes in approximately one-half the time required by NASTRAN 15.5.

The principal weakness in the NASTRAN elastic–plastic capability—Rigid Format 6—is the element library which is limited to only membrane behavior in shell elements and rod behavior in beam elements. This means present NASTRAN beam and shell elements will not yield in bending. Consequently, it was decided to develop and add to NASTRAN two new elements which will yield in bending: a beam element and a triangular flat shell element. These elements were added to NASTRAN as user developed dummy elements. Inclusion of these elements incorporate consideration of geometry changes. Details for adding elements to NASTRAN are documented in the *NASTRAN Programmer's Manual* [1].

DESCRIPTION AND VERIFICATION

The elastic–plastic beam element added to NASTRAN is the CDUM 3 element. It is an element which can be used to model thin-wall beam members. The input data includes the connecting grid points and an orientation vector. The input section property data is in the form of X, Y nodal coordinates and thickness data in sequential order around the thin-wall section. To describe abrupt thickness changes the nodal coordinates may be repeated and the new thickness given. Backtracking can be easily effected so that sections such as H or I shapes can be described.

The CDUM3 elastic–plastic beam does not use the hinge concept for plastic collapse. Instead, standard finite element formulations were used with numerical integration for calculating the stiffness matrix. Hinge formation and plastic collapse occur as a consequence of reaching the yield strain at sufficient integration points. To obtain a beam element capable of plastic collapse under these circumstances, the usual beam shape function had to be abandoned and a shape function with internal degrees of freedom and greater flexibility was used. The result is an element different from the usual Euler beam element. Comparisons thus far between CDUM3 models and Euler beam models in static analysis show displacements agree to three significant figures while the maximum stresses agree to within 1.5%. This is generally adequate for most engineering purposes.

Verification of the plastic collapse capability of the CDUM3 beam element will be demonstrated by correlation with limit analysis in two test problems. The first is a cantilever beam with an unequal-leg channel cross-section as shown in Fig. 1. The loading is a combined compression and bending. This simple example arose from an actual application to auto frame crush. This was a rear siderail section and the crush load was an eccentric compression through the rear bumper. The problem was converted here to one with compression and linear bending moment to more fully test the plastic collapse capability of the element. The theoretical limit analysis load was calculated from equilibrium after the plastic neutral axis was located by trial and error. The load–deflection curve calculated using NASTRAN Rigid Format 6 and the CDUM3 element is shown in Fig. 1. It is seen to give excellent agreement within 1% of the prediction of limit analysis.

The second example is shown in Fig. 2. It is a simple planar frame with a channel cross-section. This "building bent" problem is seen in many civil engineering texts on limit analysis. It is something of a classic because this deceivingly simple problem has an unusual

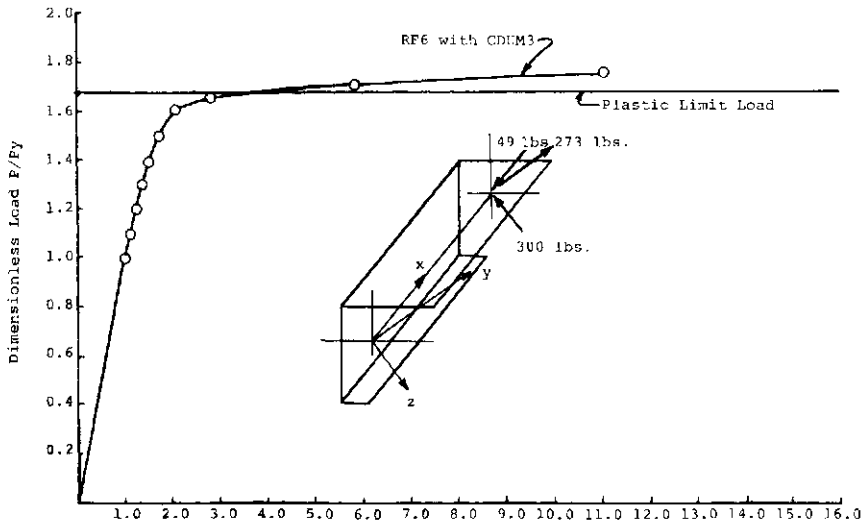

Fig. 1. Plastic collapse of thin-walled cantilever beam.

failure mechanism. There is no hinge at Grid 2 and segment 123 rotates clockwise about Grid 1 in the collapse mechanism. Segment 45 rotates clockwise about Grid 5 and segment 34 rotates counterclockwise. The plastic limit analysis curve was obtained from multiple NASTRAN static analyses using CBAR elements and inserting hinges at the CBAR ends as plastic hinges formed. NASTRAN Rigid Format 6 successfully solved this problem predicting collapse at a load 8% above the limit analysis as shown in Fig. 2.

The triangular, flat shell element added to NASTRAN is the CDUM4 element. This element was formed by combining the membrane behavior of the constant strain triangle with the bending element published by Bazeley, Cheung, Irons and Zienkiewicz [2]. Because plasticity is involved, the integration of the stiffness matrix is done numerically using a combination of Gauss and Newton–Cotes numerical integration schemes. The Prandtl–Reuss stress–strain law was implemented. Ideal, perfect plasticity may be used or the stress-strain curve may be table input.

Verification of the CDUM4 shell element will be shown by correlation with three sample problems for which both elastic solutions and plastic limit analysis solutions are known. The first, a rectangular cantilever beam loaded by in-plane forces, will test only the membrane properties of the element. The CDUM4 is a constant strain triangle in this situation and it behaved as expected, i.e. being on the stiff side of what beam theory, with shear deformations included, would predict.

Figure 3 shows the load-deflection curve from a NASTRAN Rigid Format 6 plastic collapse analysis of the model shown. From the elastic analysis, the load to

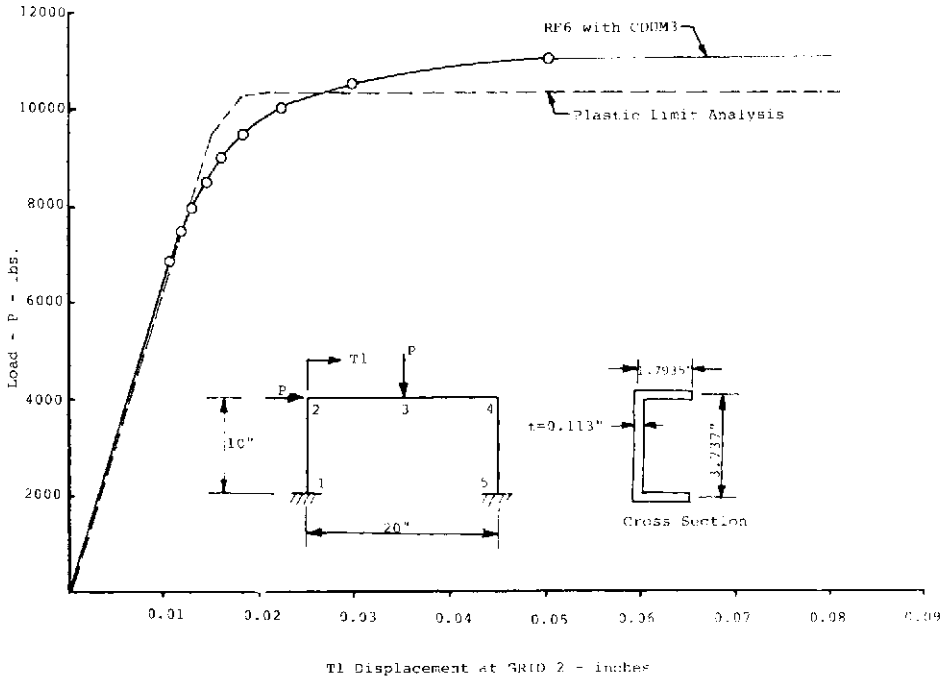

Fig. 2. Plastic collapse of planar frame.

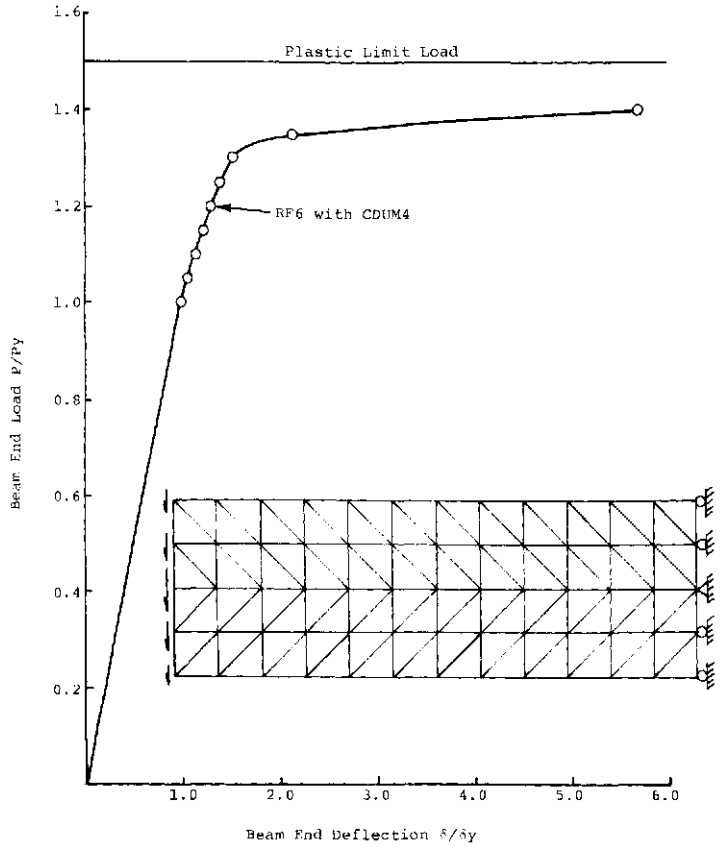

Fig. 3. Plastic collapse of cantilever beam of CDUM4 elements

initiate yield is determined. This is then applied and incremented to failure. It is seen the NASTRAN collapse load underestimates the limit analysis collapse load by about 7%. The yielded elements formed two symmetric fields at the wall support in a pattern exactly like that expected to form a plastic hinge.

The second test problem is a square, simply-supported, laterally loaded plate. This problem will test only the out-of-plane or bending properties of CDUM4. Studies for both uniform and concentrated loads

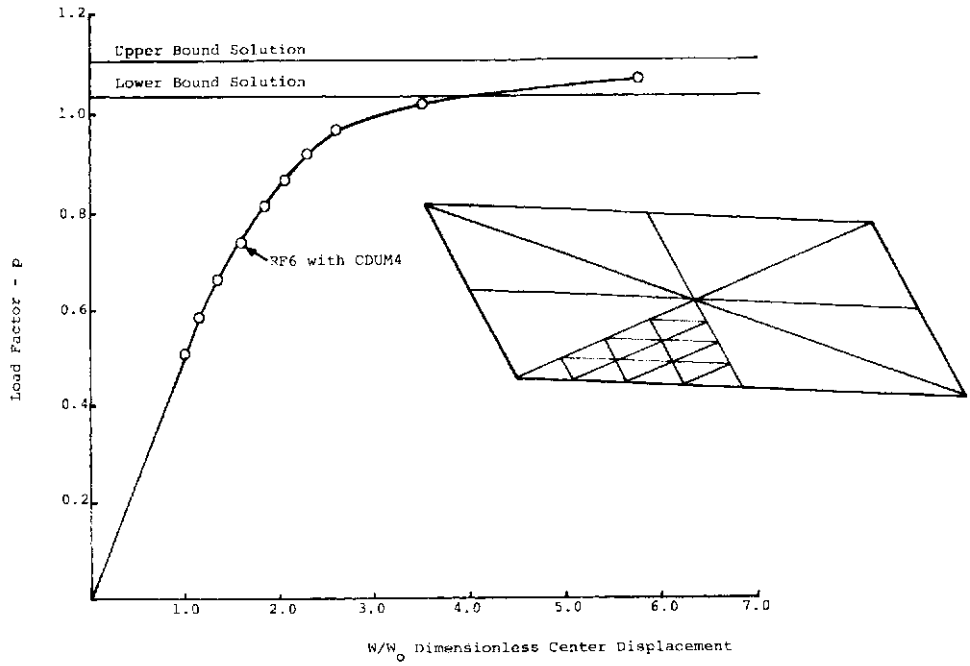

Fig. 4. Load-deflection for a square, uniformly loaded, simply supported plate.

showed good convergence to exact elastic values and agreed with the results obtained by the original investigators [2].

A NASTRAN Rigid Format 6 plastic collapse analysis was made for the case of a simply-supported, square plate under uniform load. Figure 4 shows the load deflection curve obtained. Although an exact limit analysis solution is not available, close upper and lower bounds have been obtained by Hodge and Belytschko [3]. Figure 4 shows close agreement between the NASTRAN collapse load and the bounds from limit analysis.

The third test problem is an infinite, circular, cylindrical shell with an axially symmetric ring load. There are both large hoop stresses and localized bending around the applied ring load, so this problem will test the combined bending and membrane capabilities of the CDUM4 element. Because displacements and stresses damp out rapidly, the infinite shell can be approximated by a long, finite shell. The radial displacements from an elastic analysis are plotted in Fig. 5 as a function of the distance from the load point. Good agreement is seen with elastic theory from Timoshenko [4].

The load–deflection curve at the applied load ring obtained from a NASTRAN Rigid Format 6 analysis is shown in Fig. 6. Again, good agreement is seen between the NASTRAN collapse load and the limit analysis collapse load obtained by Drucker [5].

APPLICATION TO AUTO FRAME CRUSH

Since the mass of the auto frame is a small fraction of the total vehicle mass, the crashworthiness of an auto can be studied from data extrapolated from quasi-static crush of the frame. Using this same argument,

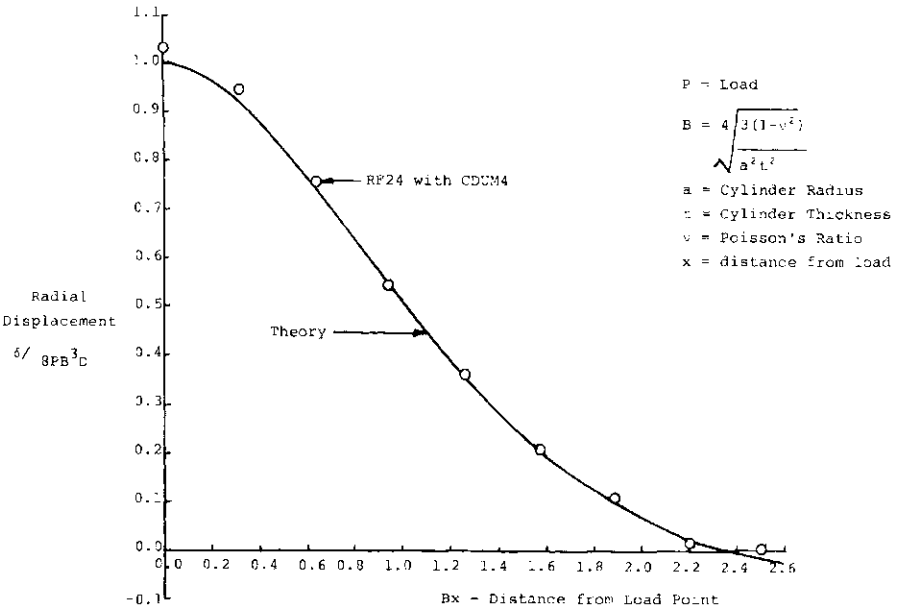

Fig. 5. Displacements from static analysis of ring loaded cylindrical shell.

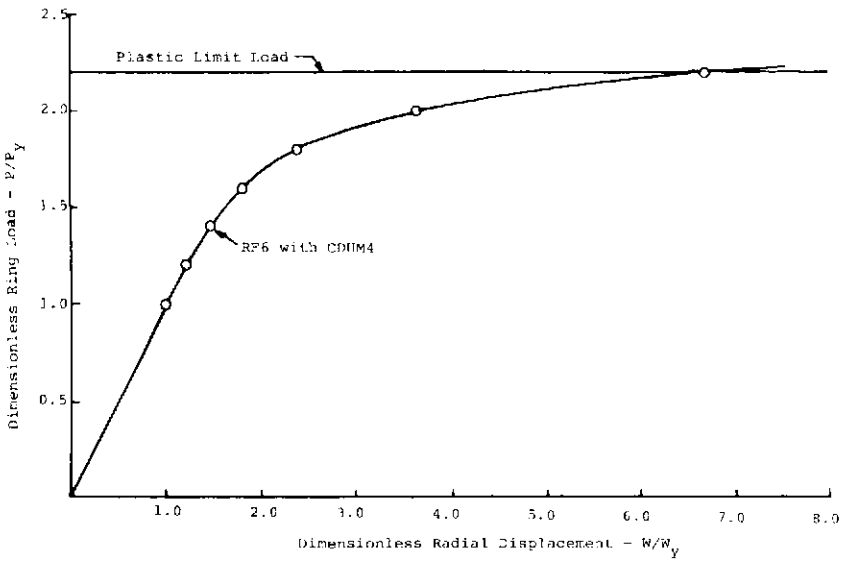

Fig. 6. Plastic collapse of ring loaded cylindrical shell.

these static crush tests can be made on isolated frame parts which is a convenient mode of testing in the laboratory.

The first example of static frame crush is on the front-most part of the frame known as the "front horn structure". A NASTRAN Rigid Format 6 plastic collapse analysis using CDUM3 beam elements and a one-half model of the structure is shown in Fig. 7. NASTRAN deformed plots have been superimposed to illustrate the progressive collapse under a longitudinal crush load. It is interesting to note from the deformed plots the obvious formation of plastic hinges. Plastic hinges are not used here as analysis tools but arise simply as a natural consequence of highly localized plastic flow.

The second example examines that part of an auto frame called the "torquebox". It is just behind the front horn structure. Figure 8 shows a detailed shell model of one-half the structure. That part assumed plastic is indicated in Fig. 8 and was modeled with 402 CDUM4 shell elements. The elastic part was modeled with 140 CQUAD2 elements and 48 CTRIA2 elements.

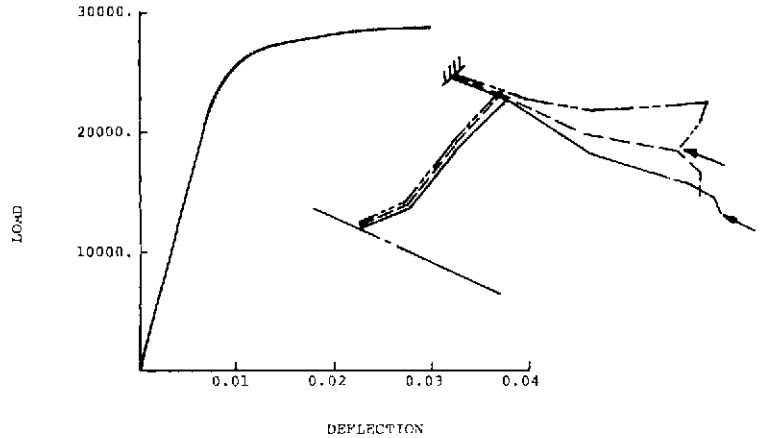

Fig. 7. Plastic collapse of auto frame front horn structure.

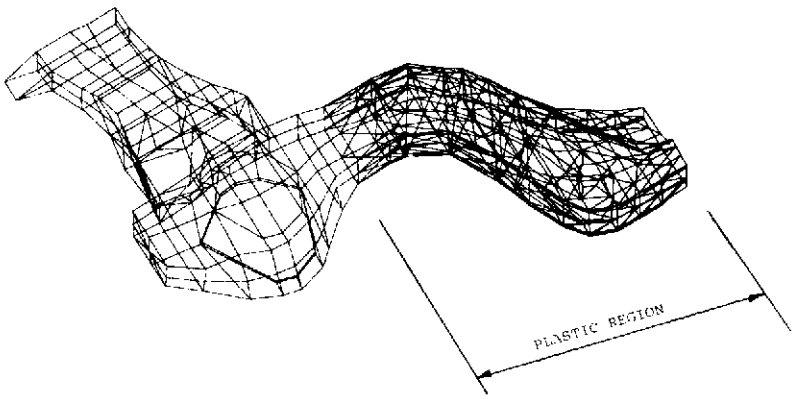

Fig. 8. Shell element model of auto frame torquebox.

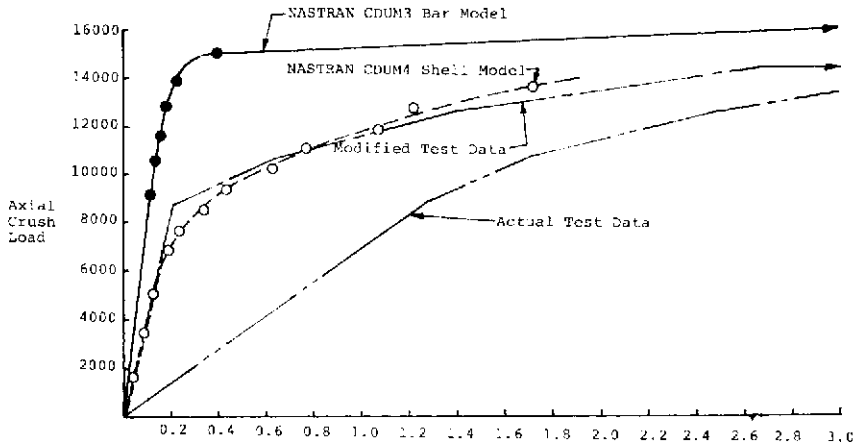

Fig. 9. Torquebox plastic collapse.

Figure 9 shows the load-deflection curve from a NASTRAN plastic collapse analysis of this shell model and compares it with test data. Also plotted in Fig. 9 is the NASTRAN collapse analysis of a CDUM3 beam model of this same structure. It is seen the test data indicates the actual structure is very flexible. This is due to the added deformation of the support and loading fixtures. Correcting this by shifting the test data to the left so the linear part matches the linear part of the calculated curve gives the "modified data" curve. Good agreement is seen between the shell model and the modified test data.

The load-deflection curve in Fig. 9 for the CDUM3 beam model shows a definite collapse load only 5% above test results. However, the overall structural behavior predicted by the CDUM3 model is much stiffer than test data. Understandably, the beam model seems less able to predict the details of the local deformation and yielding than the shell model.

In conclusion, thin-walled beam and triangular shell elements have been added to the elastic–plastic capability of NASTRAN. These have been verified by correlation with known solutions. Both new elements are seen to have useful roles in practical, industrial applications such as auto frame crush calculations. This work is viewed as a first major step in extending NASTRAN capability. Areas of interest for future work include the metal forming problem, development of solid elements and alternative forms for the stress-strain relationship.

REFERENCES

1. *The NASTRAN Programmer's Manual*, NASA SP-223. Scientific and Technical Information Office NASA, Washington, D.C. (1973).
2. G. P. Bazeley, Y. K. Cheung, B. M. Irons and O. C. Zienkiewicz, Triangular elements in plate bending-conforming and non-conforming solutions. *Proc. Air Force First Conf. Matrix Methods Structural Mech.*, AFFDL-TR-66-80, pp. 547-576. Wright-Patterson A. F. B., Ohio (1966).
3. P. G. Hodge, Jr. and T. Belytschko, Numerical methods for the limit analysis of plates. *J. Appl. Mech.* **35**, 796–802 (1968).
4. S. Timoshenko and S. Woinowsky-Krieger, *Theory of Plates and Shells*, 2nd Edn. McGraw-Hill, New York (1959).
5. D. C. Drucker, Limit analysis of cylindrical shells under axially-symmetric loading. *Proc. First Midwestern Conf. Solid Mech.* (1953).

Computers & Structures, Vol. 13, pp. 363–370, 1981
Printed in Great Britain.

0045-7949/81/010363-08$02.00/0

LARGE ELASTO–PLASTIC STRAIN ANALYSIS OF FLANGED HOLE FORMING

S. C. TANG
Engineering & Research Staff, Research, Ford Motor Company, Dearborn, MI 48121, U.S.A.

(*Received* 18 *April* 1980)

Abstract— This paper describes an analysis of stresses and deformation using the finite element method in a flanged hole produced by punch stretching during a sheet metal forming process. Due to the complexity of the finite strain theory for inelastic materials, the analysis is restricted to the membrane shell theory with axisymmetric deformation. The Lagrangian description of motion referred to a set of convected coordinates is used in the formulation. A computer program based upon the modified tangent stiffness method with an equilibrium check has been written. For the purpose of verification of the program, we applied it to compute the finite inelastic deformation of a circular sheet caused by stretch from a hemispherical punch. The present computer solution is in excellent agreement with those in the literature.

The program was applied to analyze flanged hole forming with four different punch shapes. The results reveal that the strain path during the forming process is not affected by the punch shape but the maximum punch load depends on the punch shape.

INTRODUCTION

An analysis of stresses and deformation using the finite element method in a flanged hole produced by punch stretching during a sheet metal forming process is proposed. Figure 1(a) shows a thin circular sheet, with a center hole, clamped along its periphery by a blank holder. A punch, of which the shape is a body of revolution, moves down to make contact with the circular sheet and to stretch this hole thereby forming the flange. For automobile components there are numerous flanged holes; for example, those holes used for inserting rubber bushings in the control arms of a suspension system. To be able to predict whether the flanged hole can be formed with a given sheet material and physical dimensions, such as the radius of the hole and the flange height, can save a lot of effort in contrast to the conventional trial-and-error approach. To analyze this process mathematically, we must use the finite inelastic strain theory (maximum strain usually larger than 30% in the flange) and solve a contact problem in order to get a reliable result. Due to such complexity, we restrict our analysis to the application of the membrane shell theory thereby neglecting the bending effect. This assumption is appropriate in the analysis of many automotive parts manufactured by sheet metal forming because of the thickness of a sheet (blank) is often small in comparison to the radius of either the punch or the die. We also assume in the analysis that the tools are rigid bodies.

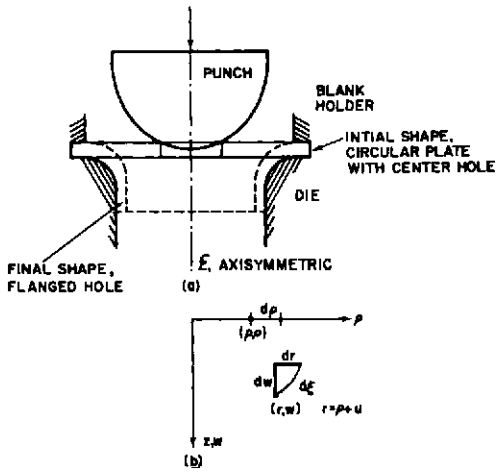

Fig. 1. Model for flanged hole forming and a material point on the meridional section.

We apply the Lagrangian description of motion to the finite deformation analysis of the thin sheet structure. Each material point on the middle-surface of the sheet is defined by a set of convected coordinates. The strain rate effect on the material properties is neglected. Due to a sheet formed by the cold roll process, the sheet material is only transversely isotropic and Hill's modification of Mises yield criterion for orthotropic material is adopted. Because unloading in the sheet could occur even during the process of punch stretching, the elastic strain is included in the formulation in addition to the plastic strain. To appreciate the physical nature of the constitutive equation, we derived it based on the relationship between physical components of stress and strain rates instead of tensor components. In the contact region, the relative motion between the sheet and the punch is governed by the frictional force. This frictional force is computed by application of the Coulomb friction law. A finite element method is used to solve this large elasto plastic deformation contact problem. A modified tangent stiffness method with the first order self-correction [1] of error due to piece-wise linearization is used in the solution procedure. The joint equilibrium check and contact condition verification are also made in the computation.

Applying the deformation theory of plasticity and neglecting the elastic strain and frictional force between the sheet and punch, Wang and Wenner [2] have analyzed stretch flanging by means of solving the equilibrium equation in the meridional direction.

Since they ignored the equilibrium condition in the direction normal to the sheet, their solution is only an approximation and the punch load cannot be computed from their analysis.

FORMULATION

Strain–displacement

We assume a circular membrane of which the middle-surface lies on the x-y plane initially in a stress-free state. A material point with a set of cylindrical coordinates $(\rho, \phi, 0)$ on the undeformed middle-surface moves to (r, ϕ, w) on the deformed middle-surface of the membrane. The deformation is axisymmetric. In other words, the motion is restricted such that the meridian angle ϕ does not change. We define the middle-surface by a set of convected coordinates (ρ, ϕ) and the metric tensors on the original and deformed surfaces are

$$a_{\alpha\beta}=\begin{bmatrix}1 & 0\\ 0 & \rho^2\end{bmatrix} \tag{2.1}$$

$$A_{\alpha\beta}=\begin{bmatrix}\lambda_1^2 & 0\\ 0 & \rho^2\lambda_2^2\end{bmatrix} \tag{2.2}$$

respectively, where λ_1 is the stretch ratio along the meridian and λ_2 the stretch ratio along the circumference. Because the deformation is axisymmetric, we only need to take a meridional section of both the original and the deformed surfaces for modelling. A material point with the original coordinates $(\rho, 0)$ moves to (r, w) with displacement components u and w in the horizontal and vertical directions, respectively, as shown in Fig. 1(b). We note that there is only one independent spatial variable, ρ. The stretch ratios can be expressed in terms of the displacement components and their partial derivatives with respect to ρ as follows:

$$\lambda_1^2=\left(\frac{\partial\xi}{\partial\rho}\right)^2=\left(1+\frac{\partial u}{\partial\rho}\right)^2+\left(\frac{\partial w}{\partial\rho}\right)^2 \tag{2.3}$$

$$\lambda_2^2=\left(\frac{r}{\rho}\right)^2=\left(1+\frac{u}{\rho}\right)^2. \tag{2.4}$$

The Lagrangian strain tensor $\gamma_{\alpha\beta}$ [3] is defined by

$$\gamma_{\alpha\beta}=\tfrac{1}{2}(A_{\alpha\beta}-a_{\alpha\beta}) \tag{2.5}$$

and in terms of the displacements, the non-zero components are

$$\gamma_{11}=\frac{\partial u}{\partial\rho}+\frac{1}{2}\left[\left(\frac{\partial u}{\partial\rho}\right)^2+\left(\frac{\partial w}{\partial\rho}\right)^2\right] \tag{2.6}$$

$$\rho^{-2}\gamma_{22}=\frac{u}{\rho}+\frac{1}{2}\left(\frac{u}{\rho}\right)^2. \tag{2.7}$$

Because the flow theory of plasticity is used in this study, we want the rate form. The rate forms of eqns (2.6) and (2.7) are

$$\dot\gamma_{11}=\frac{\partial\dot u}{\partial\rho}+\frac{\partial u}{\partial\rho}\frac{\partial\dot u}{\partial\rho}+\frac{\partial w}{\partial\rho}\frac{\partial\dot w}{\partial\rho} \tag{2.8}$$

$$\rho^{-2}\dot\gamma_{22}=\frac{\dot u}{\rho}\left(1+\frac{u}{\rho}\right). \tag{2.9}$$

Then, the physical components of the strain rate tensor become

$$\begin{Bmatrix}\dot\varepsilon_r\\ \dot\varepsilon_\phi\end{Bmatrix}=\lambda^{-1}\begin{Bmatrix}\dot\gamma_{11}\\ \rho^{-2}\dot\gamma_{22}\end{Bmatrix} \tag{2.10}$$

where

$$\underset{\approx}{\lambda}=\begin{bmatrix}\lambda_1^2 & 0\\ 0 & \lambda_2^2\end{bmatrix} \tag{2.11}$$

$\dot\varepsilon_r$ is the meridional strain rate and $\dot\varepsilon_\phi$ is the hoop strain rate. We note that $\dot\varepsilon_r$ and $\dot\varepsilon_\phi$ are identical to the rates of logarithmic strains.

Constitutive relationship

We extend the concept of the elasto–plastic strain theory for the infinitesimal strain to the finite strain. The total strain rate is assumed as the sum of the elastic and the plastic parts as

$$\dot\varepsilon=\dot\varepsilon^e+\dot\varepsilon^p. \tag{2.12}$$

For the membrane theory, the plane stress state is assumed and the elastic strain rates are expressed in terms of the rates of Cauchy stresses. In the matrix notation, they are expressed as

$$\begin{Bmatrix}\dot\varepsilon_r^e\\ \dot\varepsilon_\phi^e\end{Bmatrix}=\frac{1}{E}\begin{bmatrix}1 & -\nu\\ -\nu & 1\end{bmatrix}\begin{Bmatrix}\dot\sigma_r\\ \dot\sigma_\phi\end{Bmatrix} \tag{2.13}$$

in which E is Young's modulus, ν is Poisson's ratio, $\dot\sigma_r$ is the rate of meridian stress, and $\dot\sigma_\phi$ is the rate of hoop stress. Following Ref. [2], the equivalent stress for a transversely isotropic material during plastic deformation can be written in the following form:

$$\sigma_e=\left(\sigma_r^2+\sigma_\phi^2-\frac{2R}{1+R}\sigma_r\sigma_\phi\right)^{1/2} \tag{2.14}$$

in which R is the ratio of the plastic strain across the width to the plastic strain through the thickness of a specimen in the uniaxial tensile test. This is a special case of Hill's plastic anisotropic theory [4]. Then using the flow theory of plasticity, the plastic strain rates can be expressed as

$$\begin{Bmatrix}\dot\varepsilon_r^p\\ \dot\varepsilon_\phi^p\end{Bmatrix}=\frac{\alpha\dot\varepsilon_p}{\sigma_e}\begin{bmatrix}1 & -R/1+R\\ -R/1+R & 1\end{bmatrix}\begin{Bmatrix}\sigma_r\\ \sigma_\phi\end{Bmatrix} \tag{2.15}$$

where

$$\alpha=\begin{cases}1 & \text{for plastic loading}\\ 0 & \text{otherwise}\end{cases}$$

$\dot\varepsilon_p$ is the equivalent plastic strain rate defined as

$$\dot\varepsilon_p=\left(\frac{1}{E_t}-\frac{1}{E}\right)\dot\sigma_e \tag{2.16}$$

and E_t is the tangent modulus in the true-stress vs the natural-strain curve at the stress level σ_e. For a strain hardening material E_t is always greater than zero. Adding eqns (2.13) and (2.15) and using eqns (2.14) and (2.16), we have the constitutive equation in the rate form:

$$\begin{Bmatrix}\dot\varepsilon_r\\ \dot\varepsilon_\phi\end{Bmatrix}=\underset{\approx}{\Delta}\begin{Bmatrix}\dot\sigma_r\\ \dot\sigma_\phi\end{Bmatrix}$$

or

$$\begin{Bmatrix}\dot\sigma_r\\ \dot\sigma_\phi\end{Bmatrix}=\underset{\approx}{\Delta}^{-1}\begin{Bmatrix}\dot\varepsilon_r\\ \dot\varepsilon_\phi\end{Bmatrix} \tag{2.17}$$

where $\underset{\approx}{\Delta}$ is the material matrix of which its elements are shown in the appendix.

As mentioned previously, the Lagrangian formulation referred to the convected coordinates (ρ, ϕ) is used in this study so that the Kirchhoff stress tensor $\tau^{\alpha\beta}$ [3, 5] conjugate to the strain tensor $\gamma_{\alpha\beta}$ will be involved in the

virtual work equation. We should convert the Cauchy stress rate to the convected rate of the Kirchhoff stress tensor $\dot{\tau}^{\alpha\beta}$. The Cauchy stress tensor $\sigma^{\alpha\beta}$ is related to the Kirchhoff stress tensor $\tau^{\alpha\beta}$ by [5]

$$\sigma^{\alpha\beta}=\frac{dv}{d\bar{v}}\tau^{\alpha\beta} \tag{2.18}$$

where dv and $d\bar{v}$ are the volume element in the undeformed and deformed configuration, respectively. Due to small volume change during deformation,† we may set

$$\sigma^{\alpha\beta}\approx\tau^{\alpha\beta}. \tag{2.19}$$

We transform the tensor components of the Cauchy stress to the physical by multiplying the metric tensor as

$$\begin{Bmatrix}\sigma_r\\ \sigma_\phi\end{Bmatrix}=\underset{\sim}{\lambda}\begin{Bmatrix}\sigma^{11}\\ \rho^2\sigma^{22}\end{Bmatrix}. \tag{2.20}$$

Using eqn (2.19), eqns (2.20) and (2.14) can be written as

$$\begin{Bmatrix}\sigma_r\\ \sigma_\phi\end{Bmatrix}\approx\underset{\sim}{\lambda}\begin{Bmatrix}\tau^{11}\\ \rho^2\tau^{22}\end{Bmatrix} \tag{2.21}$$

$$\sigma_e=\left\{\lambda_1^4(\tau^{11})^2+\lambda_2^4(\rho^2\tau^{22})^2-\frac{2R}{1+R}\lambda_1^2\lambda_2^2\tau^{11}(\rho^2\tau^{22})\right\}^{1/2} \tag{2.22}$$

respectively. Differentiating eqn (2.21) with respect to t, we obtain the stress rate vector

$$\begin{Bmatrix}\dot{\sigma}_r\\ \dot{\sigma}_\phi\end{Bmatrix}\approx\dot{\underset{\sim}{\lambda}}\begin{Bmatrix}\tau^{11}\\ \rho^2\tau^{22}\end{Bmatrix}+2\begin{bmatrix}\tau^{11} & 0\\ 0 & \rho^2\tau^{22}\end{bmatrix}\begin{Bmatrix}\dot{\gamma}_{11}\\ \rho^{-2}\dot{\gamma}_{22}\end{Bmatrix} \tag{2.23}$$

it should be noted that $\dot{\gamma}_{11}=\lambda_1\dot{\lambda}_1$ and $\rho^{-2}\dot{\gamma}_{22}=\lambda_2\dot{\lambda}_2$ from eqns (2.5), (2.1) and (2.2) have been used in the derivation of the above equation. Substituting eqns (2.10) and (2.23) into eqn (2.17), we obtain the proper constitutive equation for the displacement method in the finite element solution:

$$\begin{Bmatrix}\dot{\tau}^{11}\\ \rho^2\dot{\tau}^{22}\end{Bmatrix}=\lambda^{-1}\left(\underset{\sim}{\Lambda}^{-1}\dot{\underset{\sim}{\lambda}}^{-1}-2\begin{bmatrix}\tau^{11} & 0\\ 0 & \rho^2\tau^{22}\end{bmatrix}\right)\begin{Bmatrix}\dot{\gamma}_{11}\\ \rho^{-2}\dot{\gamma}_{22}\end{Bmatrix}. \tag{2.24}$$

For an isotropic material in the plastic range $R=1$, it can be shown eqn (2.24) is a special case of the constitutive equation derived from a finite strain generalization of J_2 flow theory of plasticity by Hutchinson [6].

FINITE ELEMENT AND CONTACT CONDITIONS

Finite element application

Considering the axisymmetric deformation, we approximate the sheet geometry by a series of conical frustra; therefore, the meridional section is a series of line elements as shown in Fig. 2(a). There are two degrees of freedom at each node, i.e. the horizontal displacement component u and the vertical displacement component w. The linear interpolation function is used to determine the displacement field for an element. Using eqns (2.6) and (2.7), we obtain the strain vector in terms of nodal displacements for an element

$$\gamma=(\underset{\sim}{B}+\underset{\sim}{B}_n)u \tag{3.1}$$

†All volume change is due to only elastic deformation which is small for most metals.

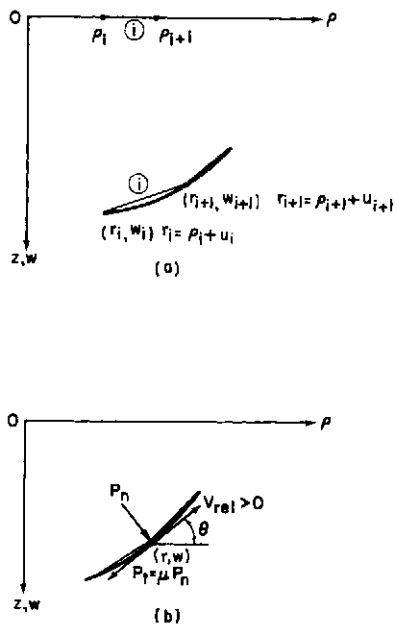

Fig. 2. A finite element on the meridional section and external force components at a contact point.

in which $\gamma^T=[\gamma_{11}\ \rho^{-2}\gamma_{22}]$, $u^T=[u_i\ w_i\ u_{i-1}\ w_{i-1}]$, $\underset{\sim}{B}$ contains constants and undeformed radial coordinates of the element, $\underset{\sim}{B}_n$ contains nodal displacement components, and the superscript T denotes the transpose of a matrix or vector. The elements of matrices B and $\underset{\sim}{B}_n$ are shown in the appendix. Differentiating eqn (3.1), we have the rate form

$$\dot{\gamma}=(\underset{\sim}{B}+2\underset{\sim}{B}_n)\dot{u}. \tag{3.2}$$

From the principle of virtual work, the element equilibrium equation becomes

$$\int_v(\underset{\sim}{B}+2\underset{\sim}{B}_n)^T\underset{\sim}{\tau}\,dv=\underset{\sim}{p} \tag{3.3}$$

where $\underset{\sim}{\tau}^T=[\tau^{11}\ \rho^2\tau^{22}]$, p is the nodal force vector, and v is the undeformed volume of an element. For a membrane

$$dv=|a_{\alpha\beta}|^{1/2}\,d\phi\,d\rho\,dz \tag{3.4}$$

where $|a_{\alpha\beta}|^{1/2}=\rho$. Taking a segment of 1 radian in the circumferential direction and invoking the assumption of plane stress, we can simplify eqn (3.3) for an element with the uniform initial thickness h_0 in the form

$$ho\int_{\rho_i}^{\rho_{i+1}}(\underset{\sim}{B}+2\underset{\sim}{B}_n)^T\underset{\sim}{\tau}\rho\,d\rho=p. \tag{3.5}$$

Following Ref. [7], the rate form of eqn (3.5) is

$$2ho\int_{\rho_i}^{\rho_{i+1}}\underset{\sim}{B}_n^T\underset{\sim}{\tau}\rho\,d\rho+ho\int_{\rho_i}^{\rho_{i+1}}(\underset{\sim}{B}+2\underset{\sim}{B}_n)^T\dot{\underset{\sim}{\tau}}\rho\,d\rho=\dot{\underset{\sim}{p}}. \tag{3.6}$$

If we rewrite eqn (2.24) in the form

$$\dot{\underset{\sim}{\tau}}=\underset{\sim}{D}\dot{\underset{\sim}{\gamma}} \tag{3.7}$$

and use eqn (3.2), the equilibrium condition in the rate form expressed by eqn (3.6) becomes

$$(\underset{\sim}{k}_0+\underset{\sim}{k}_s)\dot{\underset{\sim}{u}}=\dot{\underset{\sim}{p}}$$

where $\underline{k}_0$ is the tangent stiffness matrix including initial displacements and $\underline{k}_\sigma$ is due to initial stresses. These matrices are shown in the Appendix. The global tangent stiffness matrix is formed by assembling all element tangent stiffness matrices as

$$\underline{K}_T \dot{\underline{U}} = \dot{\underline{P}} \tag{3.9}$$

or in the incremental form

$$\underline{K}_T \Delta \underline{U} = \Delta \underline{P} - \underline{R}_s \tag{3.10}$$

where we have made the piece-wise linear approximation $\Delta U = \dot{U}\Delta t$, $\Delta P = \dot{P}\Delta t$, and $\underline{R}_s$ is the joint unbalanced force vector at the previous time step. At a node i, the unbalanced force vector is computed by

$$\underline{R}_{si} = \Sigma \left\{ \int_v (\underline{B} + 2B_n)^T \tau \, dv - \underline{p} \right\}_i \tag{3.11}$$

where the summation is taken over all the elements sharing the node i. In this study, we correct the joint unbalanced force computed from the above equation. Instead of Newton–Raphson type iteration, which might cause oscillation in the solution of the plasticity problem, to reduce the joint unbalanced force, we apply the first-order self-correction method [1] with sufficiently small time step (or external load increment).

Contact conditions

In this study, the punch as well as the die is considered as a body of revolution. The meridional section of the moving punch can be written in the general form

$$z = f(\rho) + t \tag{3.12}$$

where t is a time-like coordinate and we set the initial position of the punch (at $t = 0$) being point-contact with the sheet in the meridional section. When $t > 0$, i.e. after the punch moves, there are three different regions—a punch-contact region, a non-contact region where the joint force vector $\underline{P}$ zero, and a die contact region—in the sheet. We note that the equation of the die shape has the same form as that in eqn (3.12) except independence of t, since the die is stationary. If a material point with undeformed radial coordinate ρ is in contact, the deformed coordinates (r, w) must satisfy eqn (3.12), i.e.

$$w = f(r) + t \tag{3.13}$$

where $r = \rho + u$ and u is the horizontal displacement component. Two possible contact conditions can exist as follows:

(i) *Non-slip contact*. Applying Coulomb friction law, if

$$P_t < \mu P_n \tag{3.14}$$

where P_t = frictional force, μ = coefficient of friction and P_n = normal force at a contact node shown in Fig. 2(b), that point will move together with the punch without slipping or stand-still on the die. The deformed coordinates (r, w) not only satisfy eqn (3.13) but the velocity components must satisfy the equation

$$\begin{Bmatrix} \dot{u} \\ \dot{w} \end{Bmatrix} = \begin{Bmatrix} 0 \\ 1 \end{Bmatrix}. \tag{3.15}$$

For die contact, $\dot{w} = 0$ also, eqn (3.15) replaces the joint equilibrium condition. Actually it is written in the incremental form:

$$\begin{Bmatrix} \Delta u \\ \Delta w \end{Bmatrix} = \begin{Bmatrix} 0 \\ \Delta t \end{Bmatrix}. \tag{3.16}$$

(ii) *Slip condition*. The nodal point in contact is restricted to move along the punch or die surface; therefore, the kinematic condition may be obtained by taking the time derivative in eqn (3.13)

$$-\frac{df}{dr}\dot{u} + \dot{w} = 1$$

and the incremental form is

$$-\frac{df}{dr}\Delta u + \Delta w = \Delta t - R_{s2} \tag{3.17}$$

where R_{s2} is the residual correction due to numerical error in linearization and computed from $R_{s2} = w - f(r) - t$ at the previous time step.

Since the external joint force due to contact is governed by Coulomb friction law, $P_t = \mu P_n$ and P_t and P_n are not independent, only one independent equilibrium equation at the contact node can be established. The direction of the frictional force P_t is determined by the relative velocity between the punch and the sheet at the contact node

$$v_{rel} = \dot{u}\cos\theta + (1 - \dot{w})\sin\theta. \tag{3.18}$$

Figure 2(b) shows the positive direction of v_{rel}. The external joint force vector at the contact node is decomposed into the horizontal and vertical component

$$p = p_n \begin{Bmatrix} \sin\theta - \operatorname{sgn}(v_{rel})\mu\cos\theta \\ \cos\theta + \operatorname{sgn}(v_{rel})\mu\sin\theta \end{Bmatrix} \tag{3.19}$$

where $\theta = \tan^{-1}(-\partial w/\partial r) = g(r)$. Introducing H and V as the horizontal and vertical components, respectively, of the internal joint force at a contact node, the joint equilibrium equation can be written as

$$\begin{Bmatrix} H \\ V \end{Bmatrix} = P. \tag{3.20}$$

Using eqn (3.19), we may condense the above equations into one independent equation

$$H[\cos\theta + \operatorname{sgn}(v_{rel})\mu\sin\theta] - V[\sin\theta - \operatorname{sgn}(v_{rel})\mu\cos\theta] = 0. \tag{3.21}$$

Differentiating eqn (3.21) with respect to t and using eqns (3.20) and (3.19) gives the rate form

$$\dot{H}[\cos\theta + \operatorname{sgn}(v_{rel})\mu\sin\theta] - \dot{V}[\sin\theta - \operatorname{sgn}(v_{rel})\mu\cos\theta] - P_n(1+\mu^2)\dot{\theta} = 0. \tag{3.22}$$

We note that $\dot{\theta} = \dot{u}\,dg/dr$ and $\dot{P}_n$ is not involved in the above equation. In the actual solution, we adopt the incremental form

$$\Delta H[\cos\theta + \operatorname{sgn}(v_{rel})\mu\sin\theta] - V[\sin\theta - \operatorname{sgn}(v_{rel})\mu\cos\theta] - P_n(1+\mu^2)\Delta\theta = -R_{s1} \tag{3.23}$$

where the residual force is carried from the equilibrium check at the previous time step by means of eqn (3.21), i.e.

$$R_{s1} = H[\cos\theta + \operatorname{sgn}(v_{rel})\mu\sin\theta] - V[\sin\theta - \operatorname{sgn}(v_{rel})\mu\cos\theta]. \tag{3.24}$$

Equations (3.23) and (3.17) replace two equilibrium equations at a slipping contact node. We note that the

coefficient matrix of the linear simultaneous equations for the nodal displacement increment vector ΔU is no longer symmetric.

NUMERICAL EXAMPLES

Circular sheet by hemispherical punch stretching

As a verification of the present formulation and the computer program, we applied it to compute the finite inelastic deformation of a circular sheet stretched by a hemispherical punch. The problem has been solved numerically by Wang and Budiansky [8] and the actual experiments were performed by Ghosh and Hecker [9]. The dimensions of the sheet, punch and die used in the computation are shown in Fig. 3. The sheet was made of AK steel with $E=206.8$ G Pa, $\nu=0.30$, and the initial yield stretgth $\sigma_0=103.3$ M Pa. In the inelastic range, the stress–strain relationship is expressed by the power law

$$\sigma=K\varepsilon^n \tag{4.1}$$

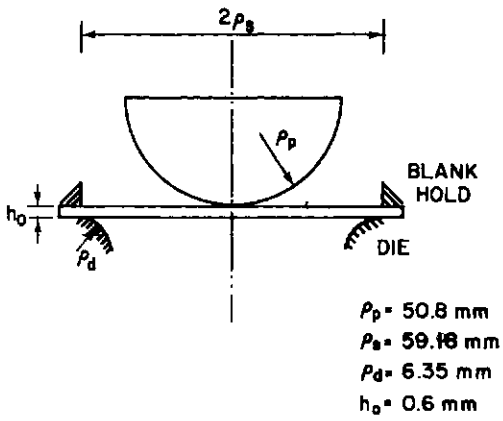

Fig. 3. Die and punch in hemispherical punch stretching.

where σ is the true stress, ε the natural strain, $K=510$ M Pa and $n=0.21$. The coefficient of friction μ between the punch and the sheet or the die and the sheet used in the computation was 0.17; the ratio of the width strain to the thickness strain in the plastic range during the uniaxial test was $R=1.8$. The equation of the punch is

$$z=(\rho_p^2-\rho^2)^{1/2}-\rho_p+t \tag{4.2}$$

where ρ_p is the punch radius. We note that the pole of the punch ($\rho=0$) contacts the center of the sheet at the time-like coordinate $t=0$. We modelled the sheet by using 10 and 20 equally spaced elements, respectively, and took $\Delta t=0.01$ mm in the first order self-correction method until punch reached the maximum displacement of 34.5 mm. The maximum residual error (unbalanced joint force) has an order of magnitude of 10^{-2} vs the maximum contact force of 10^3. Figures 4(a) and (b) show the meridional strain and circumferential strain versus the undeformed radial coordinate, respectively, as the punch moved by 34.5 mm. In these figures, we plotted the engineering strain measurement $e_r=\lambda_1-1$ and $e_\phi=\lambda_2-1$. We also showed the numerical solution of Ref. [8] and test results of Ref. [9] in the same figures for comparison. The present analysis

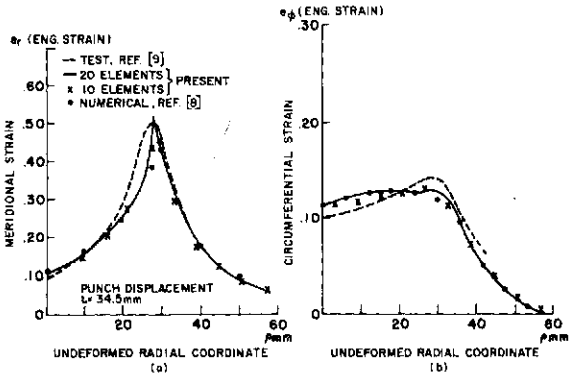

Fig. 4. Meridional and circumferential strain distribution for hemispherical punch stretching.

predicted the peak meridional strain occurred at point with the undeformed radial coordinate $\rho<\rho_s/2$ which was observed in the test; while Ref. [8] predicted at $\rho>\rho_s/2$. The maximum circumferential strain predicted by the present solution is closer to the test result.

Flanged hole by a spherical punch head

From the verification mentioned in the previous section, we realized the program was reliable so that we could apply it to predict stresses and deformation in a flanged hole produced by punch stretching during a sheet metal forming process. In the example, the sheet was clamped at a radius $\rho_s=16.54$ mm with a hole radius $\rho_h=10.16$ mm. The sheet was made of the low-carbon steel with $E=206.8$ G Pa, $\nu=0.30$, $\sigma_0=110.9$ M Pa, $K=500$ M Pa, $n=0.20$, $\mu=0.2$ and $R=1.0$. Figure 5(a) shows the initial position of the punch with a hemi-spherical head expressed by the equation

$$z=(\rho_p^2-\rho^2)^{1/2}-z_i+t \tag{4.3}$$

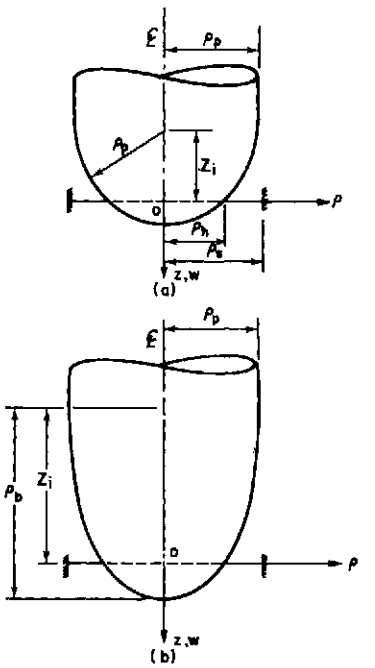

Fig. 5. Initial positions for a hemispherical and ellipsoid of revolution punch head in flanged hole forming.

where $\rho_p = 16.51$ mm is the radius of the spherical head and z_i the initial position of the center of the spherical head. We chose $z_i = 13.01$ mm so that only the edge of the hole touched the punch for the sheet at the stress-free state. We modelled the sheet by using 10 equally spaced elements and took $\Delta t = 0.0025$ mm until the punch moved by 19.05 mm when the flange was completely formed. The strain path [10] upon which the metal stamping engineers can predict whether the flanged hole will successfully be formed—the major principal strain $e_1 = e_\phi$ vs the minor principal strain $e_2 = e_r$ measured in the engineering sense—at the tip of the flange is plotted in Fig. 6. For the final configuration, the flange tip moved by $u = 6.35$ mm and $\bar{w} = 5.82$ mm which is the flange height. For $\rho_h/\rho_s = 0.6143$, Fig. 5 in Ref. [2] gives the flange height $\bar{w} = 0.346$

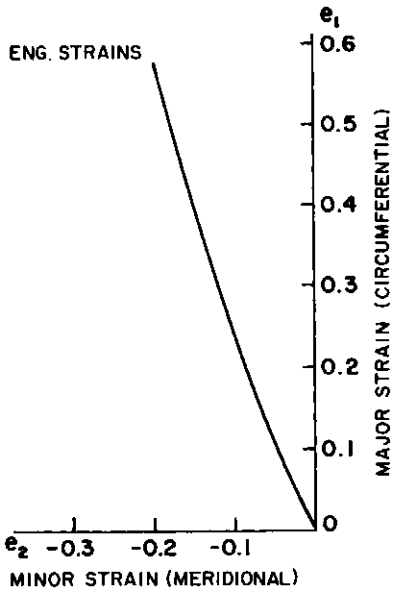

Fig. 6. Strain path in engineering measurement at the flange tip for flanged hole forming.

$\rho_s = 5.72$ mm which is very close to the present solution $w = 5.82$ mm. We also plotted the punch load vs the punch displacement during the stretching process in Fig. 7. The formulation in Ref. [2] cannot be used to compute the punch load.

Flanged hole by an ellipsoid of revolution punch head

We used the same steel sheet but the punch had a different head to form a flanged hole. The equation of the punch head is

$$z = \frac{\rho_b}{\rho_p}(\rho_p^2 - \rho^2)^{1/2} - z_i + t \tag{4.4}$$

where $\rho_p = 16.51$ mm, $\rho_b = 33.02$ mm, and $z_i = 26.03$ mm. Figure 5(b) shows the meanings of these parameters. The program predicted the strain path, e_1 vs e_2, for this head identical to that with the spherical head in Fig. 6. However, the punch load vs its displacement shown in Fig. 7 is entirely different. The peak load is lower; while the punch displacement is much more.

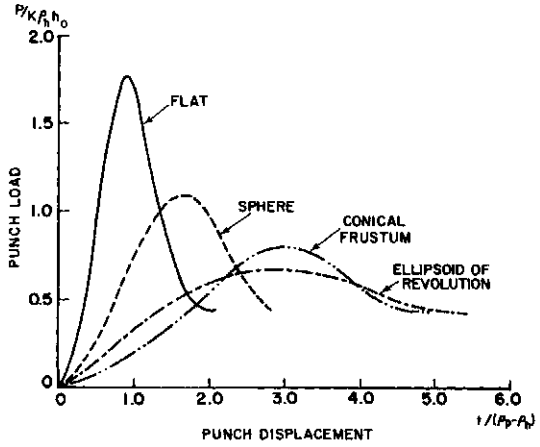

Fig. 7. Punch load vs displacement in flanged hole forming.

Flanged hole by a flat punch head

To avoid surface contact initially, we replaced the flat punch head by a sphere with a big radius as shown in Fig. 8(a). The program predicted the same strain path but the peak load was the highest and the punch moved the least distance as shown in Fig. 7 to form the hole.

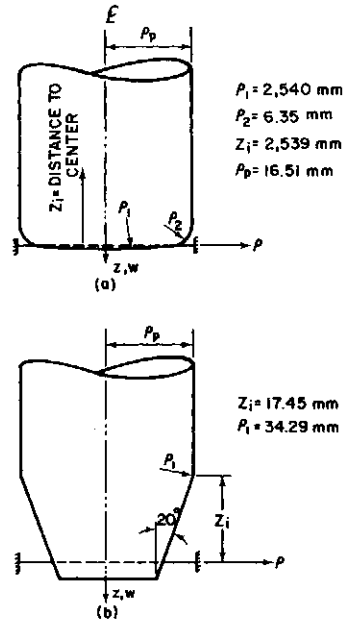

Fig. 8. Initial positions for an almost flat and conical frustum punch head.

Flanged hole by a conical frustum punch head

Figure 8(b) shows the dimensions of this head. The predicted strain path for this head still does not deviate from those for other punch shapes. The load versus punch displacement is closer to that for the ellipsoid of revolution punch head shown in Fig. 7.

SUMMARY AND DISCUSSION

In summary, the computer results reveal the following information for punch designs for flanged hole formation:

(1) The strain path—major vs minor principal strain component at the flange tip during the forming process—is independent of the punch shape for equal hole size and flange height.

(2) The maximum strain at the flange tip only depends upon the size of the hole and the flange height.

(3) The maximum punch loads depend upon the punch shape.

Preliminary test results seem to confirm the computer prediction qualitatively.

In this study, we assume that the sheet thickness is small in comparison to the tooling dimensions. Thus, the membrane theory of thin shells is applied. It, however, should be emphasized that for some chassis parts in an automobile structure, the above assumption does not hold. In those cases, a shell bending theory or even the three-dimensional continuum theory of solids with finite strains is required for more reliable prediction. In addition, the strain rate effect on the initial yield stress and subsequently hardening coefficients of the sheet material should be considered so that we can predict the influence of the punch velocity on the flanged hole forming for a strain-rate sensitive material.

Acknowledgements—The author wishes to thank Drs. S. K. Samanta and C. T. Chon for reading the manuscript and for making valuable suggestions concerning this work.

REFERENCES

1. J. R. Tillerson, J. A. Stricklin and W. C. Haisler, Numerical methods for solution of nonlinear problems in structural analysis. In *Numerical Solution of Nonlinear Structural Problems* (Edited by R. F. Hartung), AMD-6, pp. 67–101. ASME, New York (1973).
2. N. M. Wang and M. L. Wenner, An analytical and experimental study of stretch flanging. *Int. J. Mech. Sci.* **16**, 135–143 (1974).
3. A. E. Green and W. Zerna, *Theoretical Elasticity*. Oxford University Press, London (1960).
4. R. Hill, *Math. Theory of Plasticity*. Oxford University Press, London (1960).
5. A. E. Green and J. E. Adkins, *Large Elastic Deformation and Nonlinear Continuum Mechanics*. Oxford University Press, London (1960).
6. J. W. Hutchinson, Finite strain analysis of elastic-plastic solids and structure. In *Numerical Solution of Nonlinear Structural Problems* (Edited by R. F. Hartung), AMD-6, pp. 17–29. ASME, New York (1973).
7. O. C. Zienkiewicz, *The Finite Element Method in Engineering Science*, 2nd Edn. McGraw-Hill, London (1971).
8. N. M. Wang and B. Budiansky, Analysis of sheet metal stamping by a finite element method. *J. Appl. Mech., ASME* **45**, 73–82 (1978).
9. A. K. Ghosh and S. S. Hecker, Failure in thin sheets stretch over rigid punch. *Met. Trans.* **6A**, 1065–1074 (1975).
10. S. P. Keeler, Understanding sheet metal formability. *Machinery* **74** (Feb.–July 1968).

APPENDIX

Material matrix

The material matrix transforms the stress rate vector to the strain rate vector

$$\begin{Bmatrix} \dot{\varepsilon} \\ \dot{\varepsilon}_\phi \end{Bmatrix} = \underline{\underline{\Delta}} \begin{Bmatrix} \dot{\sigma}_r \\ \dot{\sigma}_\phi \end{Bmatrix} \tag{A1}$$

where

$$\underline{\underline{\Delta}} = \frac{1}{E}\begin{bmatrix} 1+\alpha(E/E_t-1)a^2/\sigma_e^2 & -\nu+\alpha(E/E_t-1)ab/\sigma_e^2 \\ -\nu+\alpha(E/E_t-1)ab/\sigma_e^2 & 1+\alpha(E/E_t-1)b^2/\sigma_e^2 \end{bmatrix} \tag{A2}$$

$$a=\sigma_r-\frac{R}{1+R}\sigma_\phi, \quad b=-\frac{R}{1+R}\sigma_r+\sigma_\phi$$

$$\alpha=\begin{cases}1 & \text{for plastic loading}\\ 0 & \text{otherwise}\end{cases}$$

Strain-nodal displacement matrix

Applying the linear interpolation functions to eqns (2.6) and (2.7), we obtain $\underline{\underline{B}}$ and $\underline{\underline{B}}_n$ in eqn (3.1) as follows:

$$\underline{\underline{B}}=\frac{1}{\rho_2-\rho_1}\begin{bmatrix} -1 & 0 & 1 & 0 \\ (\rho_2/\rho-1) & 0 & -(\rho_1/\rho-1) & 0 \end{bmatrix} \tag{A3}$$

$$\underline{\underline{B}}_n=\frac{1}{2(\rho_2-\rho_1)^2}\begin{bmatrix} -(u_2-u_1) & -(w_2-w_1) & (u_2-u_1) & (w_2-w_1) \\ (\rho_2/\rho-1)\{(\rho_2/\rho-1)u_1-(\rho_1/\rho-1)u_2\} & 0 & -(\rho_1/\rho-1)\{(\rho_2/\rho-1)u_1-(\rho_1/\rho-1)u_2\} & 0 \end{bmatrix} \tag{A4}$$

where the subscripts 1 and 2 mean the values at the end points, respectively, of a line element.

Element tangent stiffness matrix

In eqn (3.6), we denote the second term on the l.h.s. by

$$\underline{\underline{k}}_0\dot{\underline{u}}=h_0\int_{\rho_1}^{\rho_2}(\underline{\underline{B}}+2\underline{\underline{B}}_n)^T\dot{\tau}\rho\,\mathrm{d}\rho. \tag{A5}$$

Using eqns (3.7) and (3.2), we have

$$\underline{\underline{k}}_0\dot{\underline{u}}=\left\{h_0\int_{\rho_1}^{\rho_2}(\underline{\underline{B}}+2\underline{\underline{B}}_n)^T\underline{\underline{D}}(\underline{\underline{B}}+2\underline{\underline{B}}_n)\rho\,\mathrm{d}\rho\right\}\dot{\underline{u}}.$$

Since $\dot{u}$ is arbitrary, the tangent stiffness matrix including initial displacements can be set

$$\underline{\underline{k}}_0=h_0\int_{\rho_1}^{\rho_2}(\underline{\underline{B}}+2\underline{\underline{B}}_n)^T\underline{\underline{D}}(\underline{\underline{B}}+2\underline{\underline{B}}_n)\rho\,\mathrm{d}\rho$$

$$\approx\frac{h_k(\rho_2^2-\rho_1^2)}{2}\{(B+2B_n)^TD(B+2B_n)\}\Big|_{\rho=(\rho_1+\rho_2)/2}. \tag{A6}$$

We denote the first term on the l.h.s. of eqn (3.6) by

$$\underline{\underline{k}}_s\dot{\underline{u}}=2h_0\int_{\rho_1}^{\rho_2}\underline{\underline{B}}_n^T\underline{\tau}\rho\,\mathrm{d}\rho=\left\{h_0\int_{\rho_1}^{\rho_2}\underline{\underline{S}}\rho\,\mathrm{d}\rho\right\}\dot{u} \tag{A7}$$

where

$$\underline{\underline{S}}=\frac{1}{(\rho_2-\rho_1)^2}\begin{bmatrix} \tau^{11}+(\rho_2/\rho-1)^2\rho^2\tau^{22} & 0 & -\tau^{11}-(\rho_1/\rho-1)(\rho_2/\rho-1)\rho^2\tau^{22} & 0 \\ & \tau^{11} & 0 & -\tau^{11} \\ \text{sym} & & \tau^{11}+(\rho_1/\rho-1)^2\rho^2\tau^{22} & 0 \\ & & & \tau^{11} \end{bmatrix}. \tag{A8}$$

Since $\bar{u}$ is arbitrary, the tangent stiffness matrix due to initial stresses can be set

$$\underset{\sim}{k}_{\sigma} = h_0 \int_{\rho_1}^{\rho_2} \underset{\sim}{S} \rho \, \mathrm{d}\rho \approx \frac{h_0(\rho_2^2 - \rho_1^2)}{2} \underset{\sim}{S}\Big|_{\rho = (\rho_1 + \rho_2)/2} \tag{A9}$$

Computers & Structures, Vol. 13, pp. 371–376, 1981
Printed in Great Britain.

0045-7949/81/010371-06$02.00/0

MONTE CARLO SIMULATIONS OF RESPONSES OF NON-SYMMETRIC DYNAMIC SYSTEM TO RANDOM EXCITATIONS

P-T. D. SPANOS
Texas Institute of Computational Mechanics, University of Texas, Austin, TX 78712, U.S.A.

(*Received* 6 *May* 1980)

Abstract—Numerical simulation data regarding the statistics of the response of a non-symmetric dynamic system are presented.

A stationary and a modulated non-stationary white Gaussian process have been used as the excitations of the system. Non-stationary and stationary statistics of the system response are presented. The numerical data are used to extract information on the dependence of the response statistics on parameters such as the viscous damping and the magnitude of the nonlinearity of the dynamic system. Furthermore, they serve to examine the reliability of a random vibration analysis of the system, based on the technique of equivalent linearization.

1. INTRODUCTION

In recent years considerable interest has been shown in studying the response of dynamic systems to random excitations. From an engineering point of view this trend of scientific research can be justified by the fact that many natural excitations such as earthquakes, sea waves, and winds can be successfully described on a statistical basis. In addition, many of the physical systems dealt with in engineering applications exhibit nonlinear behavior attributed to geometrical considerations or to material properties.

Extensive research effort has been devoted to date to study the response of single-degree-of-freedom nonlinear systems to random excitation. Unfortunately, exact solutions have been obtained only for a limited class of problems. However, approximate solutions are obtainable for a large class of problems by means of well developed techniques. Pertinent information can be found in the review references [1, 2].

Undoubtedly, multi-degree-of-freedom nonlinear systems are more versatile than their single-degree-of-freedom counterparts in modeling physical problems realistically. Nonetheless, they are more difficult to treat analytically or numerically. To the author's knowledge no exact solutions have been presented for the non-stationary response of multi-degree-of-freedom nonlinear systems to random excitation. However, exact solutions for the stationary multi-dimensional probability density function of the response may be obtained for a certain class of problems. This can be achieved by solving the corresponding Fokker–Planck equation which governs the response probability density function. Unfortunately, for the application of this method several requirements rarely met in physical systems must be satisfied [3]. The scarcity or the non-existence of exact solutions has necessitated the development of methods of approximate random vibration analysis [3–14]. Typically, the reliability of an approximate method is examined by conducting Monte Carlo simulations using an analog or a digital computation system.

To date, most of the reported random vibration approximate analyses or simulations pertain to systems which exhibit symmetric nonlinearities with respect to the origin of the force versus displacement or velocity diagrams. A typical example of the symmetric nonlinearity is the cubic nonlinearity shown in Fig. 1. The assumption of symmetric nonlinearity is valid for a large class of interesting engineering problems. There are cases, however, where the nonlinear characteristics of the mechanical behavior of some component of the physical system considered are non-symmetric [15–17]. An example is the quadratic nonlinearity shown in Fig. 1. It should be noted that although the components of a system exhibit symmetric nonlinear behavior about some particular reference configuration, the mathematical model governing its dynamical response may be non-symmetric if the system is excited about some other configuration such as, for example, the position of static equilibrium [17]. It seems that there is a need for numerical simulations and approximate analyses of responses of non-symmetric dynamic systems under random excitations.

In this paper, first the most commonly used methods for approximate random vibration analyses are examined briefly, but critically. Then, a set of data obtained by digital simulations of the response statistics of a commonly encountered dynamic system are presented and discussed. Finally, the numerical data are used to assess the reliability of an approximate solution for the

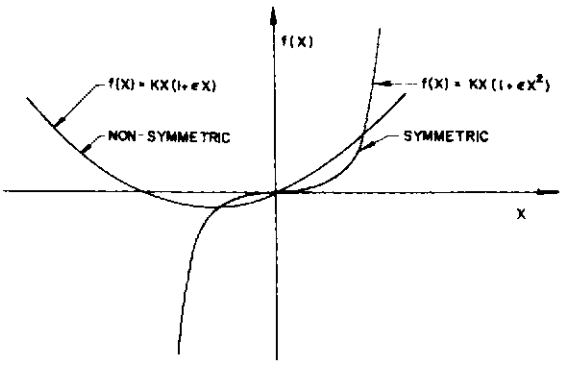

Fig. 1. Symmetric–nonsymmetric nonlinearity.

system response statistics obtained by using the technique of equivalent linearization. However, it is indicated that they could be used for accuracy studies of any other technique of approximate random vibration analysis.

2. METHODS FOR APPROXIMATE RANDOM VIBRATION ANALYSIS OF M–D–O–F SYSTEMS

Generally, there exist three techniques of approximate analysis of randomly excited nonlinear multi-degree-of-freedom systems. These are: the normal modes technique; the perturbation technique; and the equivalent linearization technique.

The normal modes technique is based on reducing the coupled equations of motion of the multi-degree-of-freedom system to a set of one-dimensional equations coupled only in the nonlinear terms and having statistically uncorrelated excitations [4]. Subsequently, solutions of the decoupled equations can be obtained by using any of the available methods of approximate analyses applicable for single-degree-of-freedom systems [1]. Unfortunately, the applicability of the normal modes approach is limited by the restrictive assumptions which must be made for the dynamical system and the random excitation [4].

The perturbation technique has been developed for weakly nonlinear systems as an adaptation of the classical asymptotic method for deterministic vibrations, to the field of random vibrations [5, 6]. In addition to the limitation of weak nonlinearity, considerable difficulties arise in the application of this technique in the absence of linear viscous damping from the oscillating system. This characteristic of the method is related to the more general problem of the lack of a rigorous foundation of the series expansion employed in the solution procedure.

Early discussions of the technique of equivalent linearization may be found in Refs. [4] and [7]. Subsequently, the method has been extended, used and discussed considerably. Typical examples of pertinent research effort may be found in Refs, [8–14]. Briefly, the concept of the method is to replace the nonlinear system by an equivalent linear system in such a manner that the ensemble average of the difference of the two systems is minimized, and to approximate the response of the nonlinear system by the response of the equivalent linear system. Numerical methods have been proposed in Ref. [8] for the determination of the elements of the equivalent linear system. This approach would require excessive computation time if it was to be applied to large systems. In addition, it could be hindered by the fact that the matrix which must be inverted for the determination of the equivalent linear system could be singular as it has been shown in Ref. [14]. Fortunately, direct formulae for the determination of the equivalent linear system have been obtained in Refs. [9, 10 and 13]. The existence and uniqueness of the equivalent linear system have been discussed in detail in Ref. [14].

The discussed methods have been primarily used for systems with symmetric nonlinearities. The response of such systems, initially at rest, to zero mean random excitations will be a zero mean process as well. For systems with nonsymmetric nonlinearities, it seems that the only additional parameter which must be introduced in analyzing the system dynamics by any of the approximate methods is a non-zero offset (mean) component for the response. Nevertheless, in view of the fact that appropriate theoretical bounds on the accuracy of the approximate methods are extremely limited the validity of such solution procedures must be investigated by using extensive simulation data.

3. SYSTEM DEFINITION

Consider the following nonlinear stochastic differential equation,

$$\ddot{x}+\beta\dot{x}+x[1+3\varepsilon+3\varepsilon x+\varepsilon x^2]=\lambda w(t)g(t); \qquad x(0)=\dot{x}(0)=0 \tag{1}$$

where $g(t)$ is a time dependent deterministic function and $w(t)$ is a stationary zero mean process with autocorrelation

$$\langle w(t)w(t+\tau)\rangle=\delta(\tau), \tag{2}$$

where $\delta(\tau)$ is the Dirac delta function.

The problem has been normalized so that, when $\varepsilon=0$ and $g(t)=1$, the stationary variance of x is equal to unity; that is,

$$\lambda^2=2\beta. \tag{3}$$

The parameter ε serves to indicate the severity of the nonlinearity.

Equation (1) has been derived by considering the time dependent deviation of a randomly excited Duffing oscillator from its position of static equilibrium under gravity. The usefulness and the popularity in engineering analyses of the Duffing oscillator may be attributed to the fact that its restoring force is the lowest degree polynomial nonlinear approximation of a symmetric nonlinearity.

No analytical methods are available for the determination of the exact non-stationary statistics of the response $x(t)$. However, if $g(t)=1$, the exact stationary probability density function $p_s(x)$ can be readily determined by using a general formula given in Ref. [1]. Specifically, it is found

$$p_s(x)=\exp\left[-(1+3\varepsilon)\frac{x^2}{2}-\varepsilon x^3-\varepsilon\frac{x^4}{4}\right] \Big/ \int_{-\infty}^{\infty}\exp\left[-(1+3\varepsilon)\frac{x^2}{2}-\varepsilon x^3-\varepsilon\frac{x^4}{4}\right]dx. \tag{4}$$

4. SYSTEM RESPONSE SIMULATIONS

4.1 *Procedure for generating response statistics data*

For the purpose of estimating both non-stationary and stationary statistics of the solution of eqn (1), a collection of three hundred (300) records of the white process $w(t)$ was simulated digitally in a CDC-6600 computation system. The dimensionless time scale

$$\tau=t/T \tag{5}$$

was used, where T is the period of oscillator (1), for $\varepsilon=0$. For the generation of a single record of the excitation $w(\tau)$, a sequence of n random numbers $N_1 \ldots N_n$ were sampled from a distribution with zero mean and standard deviation equal to one. A Gaussian distribution was used. There are several numerical schemes for generating numbers belonging to a Gaussian distribution with specified mean value and standard deviation. In the present study, the algorithm examined in Ref.

[20] was used. The numbers $N_1, \ldots N_n$ were assigned to n successive ordinates, $\tau_1 = 0$, $\tau_2 = \tau^*, \ldots$ spaced at equal intervals of length

$$\tau^* = 0.01. \tag{6}$$

Then, the values of $w(\tau)$ at τ_j were taken as

$$w(\tau_j) = cN_j/\sqrt{\tau^*},\ j = 1, 2, \ldots \tag{7}$$

where c is a normalization constant specified by the intensity of the autocorrelation function, eqn (2), of the simulated process. Linear variation of $w(\tau)$ over each and every interval τ^* was assumed. It can be proved that as the number of records tends to infinite (∞) and $\tau^* \to 0$ the family of the numerically generated records simulates a random process with uniform spectral density (white noise). Two different shapes of modulating functions $g(t)$ were used. Specifically,

$$g(t) = 1 \tag{8}$$

and

$$g(t) = \exp(-0.025t) - \exp(-0.25t). \tag{9}$$

The envelope defined by eqn (8) yields a white noise model for the excitation of system (1), while the envelope defined by eqn (9), Fig. 2, belongs to a general class of envelopes used in modeling seismic motion [18] and atmospheric turbulence [19].

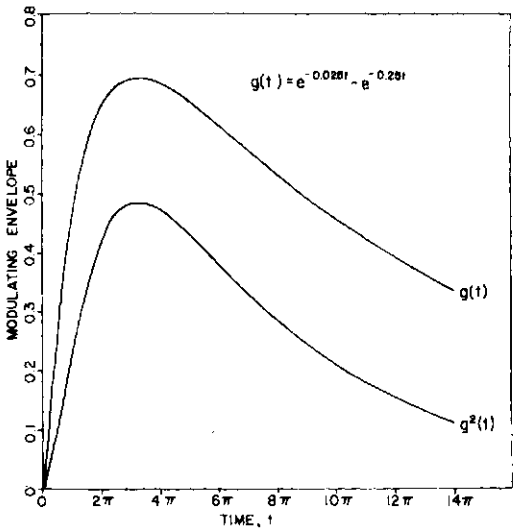

Fig. 2. Deterministic modulating envelope vs time.

The value

$$\varepsilon = 2.0$$

has been used for the nonlinearity parameter. Upon generating the first record $w_1(\tau)$ of the random excitation, the response of oscillator (1) was computed using a standard subroutine for ordinary differential equations. The values of $x(\tau)$ and $x^2(\tau)$ at $\tau_1 = 0$, $\tau_2 = \tau^*$, $\tau_3 = 2\tau^*, \ldots$ were stored in arrays of appropriate dimensions as the current values of $\langle x(\tau)\rangle$ and $\langle x^2(\tau)\rangle$. These values were subsequently continually updated by generating excitation records and computing the corresponding system response. In this manner, the storage capacity requirements of the computation system were kept minimal.

4.2 *Discussion of the data*

Numerical data obtained by the discussed procedure are shown in Figs. 3–10. Figures 3–8 show data regarding the non-stationary values of the offset (mean) and the standard deviation of $x(\tau)$, and the standard deviation of $\dot{x}(\tau)$.

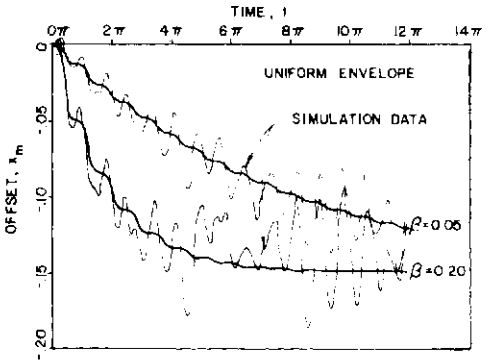

Fig. 3. Offset (mean) of the system displacement vs time; $\varepsilon = 2.0$, $g(t) = 1$.

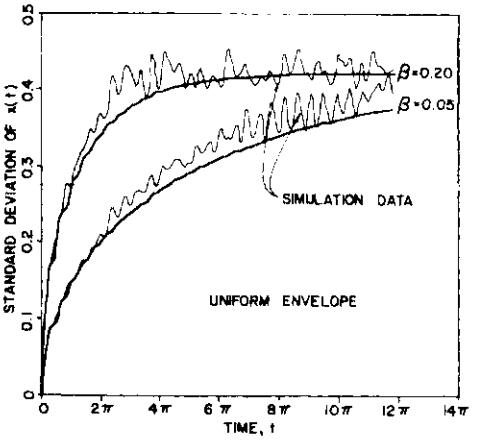

Fig. 4. Standard deviation of the system displacement vs time; $\varepsilon = 2.0$, $g(t) = 1$.

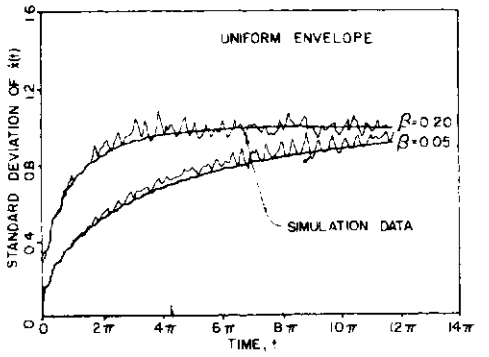

Fig. 5. Standard deviation of the system velocity vs time; $\varepsilon = 2.0$, $g(t) = 1$.

For the uniform envelope, eqn (8), Figs. 3–5 reveal a strong dependence of the rise time of the system on the damping coefficient β. Define the rise time T_f as the time required for the response statistics to reach a fraction f of their stationary values. Then it is noticed, for example, that the system response statistics reach

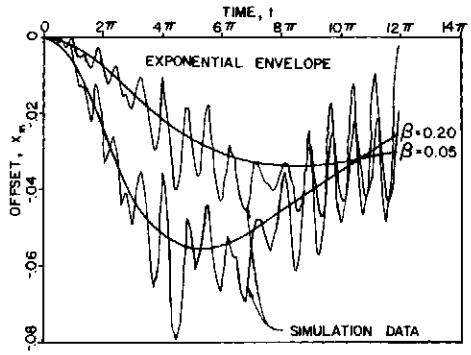

Fig. 6. Offset (mean) of the system displacement vs time; $\varepsilon = 2.0$, $g(t) = \exp(-0.025t) - \exp(-0.25t)$.

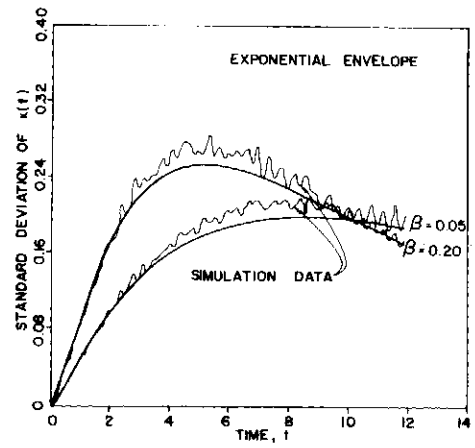

Fig. 7. Standard deviation of the system displacement versus time; $\varepsilon = 2.0$, $g(t) = \exp(-0.025t) - \exp(-0.25t)$.

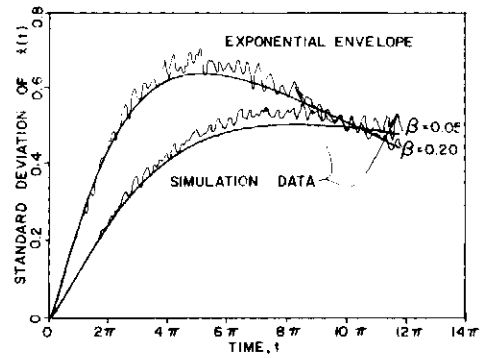

Fig. 8. Standard deviation of the system velocity vs time; $\varepsilon = 2.0$, $g(t) = \exp(-0.025t) - \exp(-0.25t)$.

approximately $f = 0.75$ of their stationary values in time equal to one (1) and four (4) cycles (T) of oscillation for $\beta = 0.20$ and $\beta = 0.05$, respectively. The equality of the ratio of the rise times to the inverse of the ratio of the damping coefficients seems to be valid for all the simulated response statistics and any percentage f. Therefore, it is postulated that T_f is inversely proportional to β, that is

$$T_f \sim \frac{1}{\beta}. \tag{10}$$

Regarding the dependence of T_f on f, it is noticed, for example, that for $\beta = 0.20$, the standard deviation of

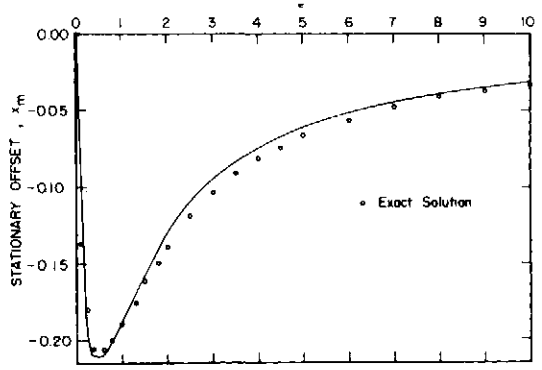

Fig. 9. Stationary offset (mean) of the system displacement versus the nonlinearity parameter ε; $g(t) = 1$.

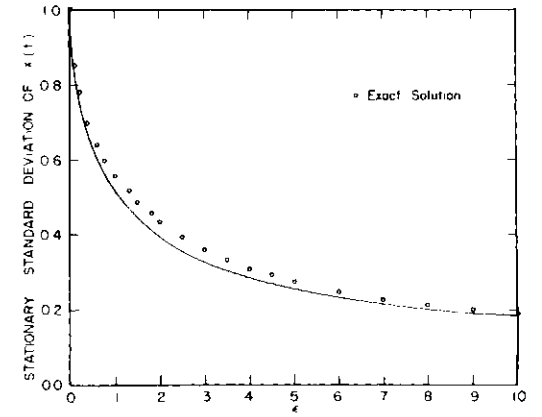

Fig. 10. Stationary standard deviation of the system displacement versus the nonlinearity parameter ε; $g(t) = 1$.

$x(t)$ reaches $f = 0.5, 0.75, 0.99$ at approx. $0.5T$, T, and $4T$ respectively. This trend seems to be consistent for all the response statistics and it is postulated that

$$T_f \sim \ln(1 - f) \tag{11}$$

where ln represents the natural logarithm of the number in the parenthesis. It is noted that due to the normalization used, eqn (3), the stationary values of the response statistics are identical for $\beta = 0.05$ and $\beta = 0.20$.

For the exponential envelope, eqn (9), Figs. 6–8 show again a strong dependence of the response statistics of the damping coefficient β. It is noted that due to the fact that $g(t)$ is non uniform in this case the maximum values of the response statistics are not identical for $\beta = 0.05$ and $\beta = 0.20$. Examining Fig. 2, it is observed that the maximum of $g(t)$ occurs at a time which is approximately equal to $1.5T$ and the maximum of $g^2(t)$ occurs at a slightly different time.

For $\beta = 0.05$, the maxima of the response statistics occur at times which are approximately equal to $4T$. At this time the value of $g^2(t)$ is only equal to approx. 3/5 of its maximum value. As soon as the response statistics reach their maximum values, they start decreasing with extremely low time rate, however.

For $\beta = 0.20$, the maxima of the response statistics are smaller than those corresponding to $\beta = 0.05$ and occur at times which are approximately equal to $2T$.

As soon as the response statistics reach their maximum values they start decreasing with a rate much lower than that corresponding to $\beta = 0.05$. Evidently,

these trends of the response statistics are compatible with the fact that the system with $\beta=0.05$ has a smaller energy dissipation capacity than the system with $\beta=0.20$. Unfortunately, the energy dissipation capacity of a specific system can be used for only qualitative or extremely unreliable quantitative predictions obtained mainly by extrapolations of trends detected by numerical studies similar to the present.

Concluding this section it is noted that the simulated numerical values $\bar{\hat{x}}(t)$ and $\hat{\bar{s}}(t)$ for the mean value $\mu(t)$ and the standard deviation $\sigma(t)$ respectively of the system response should be viewed as events of statistical experiments on the populations of the mean values and the standard deviations of samples of size $n=300$. Therefore, each datum point could be used only to determine the range of the theoretical mean value $\bar{x}(t)=\mu(t)$ and standard deviation $\bar{s}(t)=\sigma(t)$ of these populations with a certain level of confidence. For a specified confidence level, the relative ranges of $\bar{x}(t)$ and $\bar{s}(t)$ with respect to $\bar{\hat{x}}(t)$ and $\hat{\bar{s}}(t)$ and vice versa depend on the standard deviations $\sigma_2(t)$ of the populations of $\bar{\hat{x}}(t)$ and $\hat{\bar{s}}(t)$ respectively. For large values of n, these quantities can be approximated by $\sigma_1(t)\approx\sigma(t)/\sqrt{n}$ and $\sigma_2(t)\approx\sigma(t)/\sqrt{2n}$. Therefore, it should be expected that the fluctuation of the simulated from the theoretical values should be wider for the mean value than for the standard deviation of the system response. This theoretical prediction is verified by the numerical data shown in Figs. 3–8.

5. APPLICATION OF EQUIVALENT LINEARIZATION

An approximate solution for the statistics of system (1) can be obtained by using the technique of equivalent linearization [21]. In using this technique, an approximate solution of equation (1) is written in the form

$$x(t)=x_m(t)+\hat{x}(t), \tag{12}$$

where $x_m(t)$ is the deterministic offset (mean) of $x(t)$, and $\hat{x}(t)$ is a zero mean Gaussian random process. Then equation (1) is replaced by the two equations

$$\ddot{x}_m+\beta\dot{x}_m+x_m[1+3\varepsilon]+\varepsilon\langle x^2[x+3]\rangle=0 \tag{13}$$

and

$$\ddot{\hat{x}}+\beta\dot{\hat{x}}+\hat{x}[1+3\varepsilon+k_e]=\lambda w(t)g(t). \tag{14}$$

Equation (13) ensures that the solution defined by eqn (12) satisfies equation on the average. The symbol k_e appearing in equation represents the equivalent linear stiffness of the system and is determined so that the ensemble mean square error

$$\varepsilon^2\equiv\langle[\ddot{x}_m+\beta\dot{x}_m+x_m(1+3\varepsilon)+\varepsilon x^2(x+3)-k_e x]^2\rangle \tag{15}$$

is minimum. Using the analytical results of Ref. [21] it can be proved that this criterion is satisfied if and only if the equivalent linear stiffness is equal to

$$k_e=\varepsilon\frac{\partial}{\partial x}[3x^2+x^3]=6\varepsilon x_m+3\varepsilon[\langle\hat{x}^2\rangle+x_m^2]. \tag{16}$$

Equations (13) and (14) can be written as first order differential equations governing the vectors $(x_m, \dot{x}_m)^T$ and $(x,\dot{x})^T$. The reduction of the order, however, is associated with an increase of the dimension of the system. Therefore, from an equivalent linearization point of view the system described by eqn (1) must be treated as multi-dimensional. Using the equations for the vectors $(x_m, \dot{x}_m)^T$ and $(x, \dot{\hat{x}})^T$ and relying on standard methods of analysis of linear systems under random excitation, the following equation can be obtained

$$\begin{aligned}
&\dot{X}_1\equiv\dot{x}_m=X_2\\
&\dot{X}_2\equiv\ddot{x}_m=-\beta X_2-X_1[1+3\varepsilon+3\varepsilon X_1+\varepsilon X_1^2]-3\varepsilon X_3\\
&\dot{X}_3\equiv\frac{\mathrm{d}}{\mathrm{d}t}\langle\hat{x}^2\rangle=2X_4\\
&\dot{X}_4\equiv\frac{\mathrm{d}}{\mathrm{d}t}\langle\dot{\hat{x}}x\rangle=-(1+3\varepsilon+k_e)X_3-\beta X_4+X_5\\
&\dot{X}_5\equiv\frac{\mathrm{d}}{\mathrm{d}t}\langle\dot{x}^2\rangle=-2(1+3\varepsilon+k_e)X_4-2\beta X_5+2\beta g^2(t).
\end{aligned} \tag{17}$$

If $g(t)=1$, eqn (17) yields the following relationships for the stationary response statistics:

$$\begin{aligned}
&X_{2,s}=X_{4,s}=0\\
&X_{1,s}\cdot[1+3\varepsilon X_{3,s}+3\varepsilon X_{1,s}+\varepsilon X_{1,s}^2]+3\varepsilon X_{3,s}=0\\
&X_{3,s}=X_{5,s}/(1+3\varepsilon+k_e)\\
&X_{5,s}=1.
\end{aligned} \tag{18}$$

The set of eqns (17) was integrated numerically for identical ε and $g(t)$ to those used in the digital simulations. The numerical results for the offset (mean) X_1 and the standard deviation $\sqrt{X_3}$ of $x(t)$ and the standard deviation $\sqrt{X_5}$ of $\dot{x}(t)$ are shown in Figs. 3–8. as well. It should be mentioned that the computation time required to obtain the approximate analytical solution is of the order of 10^2–10^3 times smaller than the computation time required to generate one complete ensemble simulated solution.

Generally, good agreement between the simulated data and the analytical solution for all the response statistics for both envelopes and both values of the damping coefficient β can be claimed. Not only are the proper trends observed, such as shorter rise time of the system for larger damping, but the actual numerical values given by the two approaches are in fairly good agreement. and, in fact, the range of the relative error is approx. 0–10%. This agreement is extremely encouraging as the value of $\varepsilon=2.0$ represents a considerably nonlinear dynamic system. However, attention is called to the fact that the equivalent linearization repeatedly underestimates the values of the response statistics.

The set of eqns (18) has been solved numerically to determine the stationary values of $X_{1,s}$ and $X_{3,s}$. For the velocity, $\dot{x}(t)$, it is found that $\sqrt{X_{5,s}}$ is equal to unity. Identical value is given by the exact stationary probability density function of the velocity response of system (1). For the displacement $x(t)$, the obtained numerical values of $X_{1,s}$ and $\sqrt{X_{3,s}}$ are plotted in Figs. 9–10 vs the nonlinearity parameter ε. In the same figures the corresponding exact values of these statistics, determined by using eqn (4), are also shown. It is seen that fairly good agreement exists between the numerical values generated by the approximate and the exact solution even for extremely large values of the nonlinearity parameter ε. However, attention is called again to the fact that the equivalent linearization repeatedly underestimates the values of the response statistics.

6. SUMMARY

Numerical data obtained by digital simulations of the response statistics of a non-symmetric nonlinear dyn-

amic system under Gaussian excitations have been presented. The dynamic system has been obtained by considering the equation of motion of a Duffing oscillator with respect to the position of its static equilibrium under gravity. Two system excitations have been simulated. One has been a stationary white noise. The other has been obtained by modulating the white noise by an exponential deterministic envelope used in simulating seismic motions and atmospheric turbulence. The numerical data have revealed a significant decrease in the rise time of the system with increasing viscous damping.

An approximate solution for the system reponse statistics has been obtained by using the technique of equivalent linearization. Comparisons of the numerical data with the approximate solution have indicated that the latter is reliable within an approximate range of 0–10% relative error. However, the approximate solution consistently underestimates both the non-stationary and the stationary values of the system response statistics. It has also been found that the equivalent linearization technique is approximately five hundred (500) times more efficient computationally than the digital simulations in determining the system reponse statistics.

Acknowledgement—Partial support of this research by the grant NSF-PFR 7822868 from the National Science Foundation is gratefully acknowledged.

REFERENCES

1. T. K. Caughey, Non-linear theory of random vibrations. *Adv. Appl. Mech.* **11**, 209–253 (1971).
2. W. D. Iwan, Application of non-linear analysis techniques. In *Applied Mechanics in Earthquake Engineering* (Edited by W. D. Iwan) AMD8 ASME (1974).
3. T. K. Caughey, Derivation and application of the Fokker–Planck equation to discrete nonlinear dynamical systems subjected to white random excitation. *J. Accoust. Soc. Am.* **35**(11), 1683–1692 (1973).
4. T. K. Caughey, Equivalent linearization techniques. *J. Accoust. Soc. Am.* **35**(11), 1706–1711 (1963).
5. S. H. Crandall, Perturbation techniques for random vibration of non-linear systems. *J. Accoust. Soc. Am.* **35**(11), 1700–1705 (1963).
6. C. C. Tang, J. Penzien and R. Horonjeff, *The effects of runway uneveness on the dynamic responses of supersonic transports*, NASA CR-119, University of California, Berkeley, 1964.
7. R. C. Booton, The analysis of nonlinear control systems with randon inputs. *IRE Trans. Circuitry Theory* **1**, 32–34, (1954).
8. E. T. Foster, Semilinear random vibrations in discrete systems, *J. Appl. Mech., ASME* **35**, 560–564 (1968).
9. W. D. Iwan and I. Yang, Statistical linearization for nonlinear structures. *J. Engng Mech. Div., ASCE, EM6*, **97**, 1609–1623 (1971).
10. W. D. Iwan and I. Yang, Application of statistical linearization techniques to non-linear multi-degree-of-freedom systems. *J. Appl. Mech., ASME* **39**, 545–550 (1972).
11. W. D. Iwan, A generalization of the method of equivalent linearization. *Int. J. Non-Linear Mech.* **8**, 279–287 (1973).
12. K. M. Kaul and J. Penzien, Stochastic seismic analysis of yielding offhore towers. *J. Engng Mech. Div., ASCE* **EM6**, 1025–1028 (1974).
13. T. S. Atalik and S. Utku, Stochastic linearization of multi-degree-of-freedom non-linear systems. *Earthquake Engng Structural Dynamics* **4**, 411–420 (1976).
14. P-T. D. Spanos and W. D. Iwan, On the existence and uniqueness of solutions generated by equivalent linearization. *Int. J. Non-Linear Mech.* **13**, 71–78 (1978).
15. R. N. Burns, and H. K. Sachs, Ride comfort as influenced by asymmetric shock absorber characteristics. *Proc. 2nd Int. Conf. on Vehicle Mechanics*, Paris, 1973, pp. 89–106.
16. M. R. Whitehead, The optimization of undercarriage characteristics in transport aeroplanes using a hybrid computation technique. In *Stress, Vibration and Noise Analysis in Vehicles* (Edited by H. G. Gibbs and T. H. Richards, pp. 389–411. Wiley, New York (1975).
17. N. W. McLachlan, *Ordinary Non-Linear Differential Equations in Engineering and Physical Sciences*, Oxford, 1958.
18. Shinozuka, M. and Y. Sato, Simulation of nonstationary random process. *J. Engng Mech. Div., ASCE* **EM4**, 11–40 (1967).
19. J. Verdon and R. Steiner, Response of flight vehicles to nonstationary atmospheric turbulence. *AIAA J.* **11**, 1086–1089 (1973).
20. C. Knuth and E. Donald, *The Art of Computer Programming*, Vol. 2. Addison Wesley, Reading, Mass. (1969).
21. P-T. D. Spanos, Formulation of stochastic linearization for symmetric or asymmetric M.D.O.F. nonlinear systems. *J. Appl. Mech., ASME* **47**, 209–211 (1980).

Computers & Structures, Vol. 13, pp. 379–403, 1981
Printed in Great Britain.

0045-7949/81/010379-25/$02.00/0

COMPUTERIZED SYMBOLIC MANIPULATION IN NONLINEAR FINITE ELEMENT ANALYSIS

AHMED K. NOOR†
George Washington University Center, at NASA Langley Research Center, Hampton, VA 23665, U.S.A.

and

C. M. ANDERSEN‡
College of William and Mary in Virginia, Williamsburg, VA 23185, U.S.A.

Abstract—The potential of using computerized symbolic manipulation in the development of nonlinear finite elements is discussed. Three tasks which can be efficiently performed using computerized symbolic manipulation are identified: (1) generation of algebraic expressions for the stiffness coefficients of nonlinear finite elements, (2) generation of FORTRAN source code for numerical evaluation of stiffness coefficients, and (3) checking the correctness of the FORTRAN statements for the arrays of coefficients.

The symbolic and algebraic manipulation system MACSYMA is used in the present study. Two sample MACSYMA programs are presented for the development of the nonlinear stiffness coefficients of two-dimensional, shear-flexible, doubly-curved deep shell elements. The first program is for displacement models and the second program is for mixed models with discontinuous stress-resultant fields at interelement boundaries.

NOMENCLATURE

$A_{\alpha\beta\gamma\rho}, A_{\alpha 3\beta 3}$ shell compliance coefficients, inverse of shell stiffnesses
$B_{\alpha\beta\gamma\rho}, G_{\alpha\beta\gamma\rho}$
$C_{\alpha\beta\gamma\rho}$ extensional stiffnesses of the shell
$C_{\alpha 3\beta 3}$ transverse shear stiffnesses of the shell
$D_{\alpha\beta\gamma\rho}$ bending stiffnesses of the shell
$F_{\alpha\beta\gamma\rho}$ stiffness interaction coefficients of the shell
$H^i_{\mathcal{J}}$ stress-resultant parameters
K^{ij}_{IJ} linear stiffness coefficients of the shell element
$F^{ijk}_{IJK}, G^{ijkl}_{IJKL}$ nonlinear stiffness coefficients of the shell element
$M_{\alpha\beta}$ bending stress resultants
m number of nodes of the element
$\mathcal{N}^i$ shape or interpolation functions for generalized displacements
$\bar{\mathcal{N}}^i$ approximation functions for the stress resultants
$N_{\alpha\beta}$ extensional (in-plane) stress resultants
n number of approximation functions for each stress resultant
P_j^i consistent nodal force coefficients
p, p_α external load intensities in the coordinate directions
Q_α transverse shear stress resultants
$U^{(L)}, U^{(NL)}$ contributions of the linear and nonlinear terms to the total strain energy of the shell
u_α, w displacement components in coordinate directions
$V^{(L)}, V^{(NL)}$ contributions of the linear and nonlinear terms to the work done by internal forces
$U^{(c)}$ complementary energy of the shell
W work done by external forces
x_α, x_3 orthogonal curvilinear coordinate system
$\epsilon^{(L)}_{\alpha\beta}, \epsilon^{(NL)}_{\alpha\beta}$ linear and nonlinear parts of the extensional strains
$\tilde{\epsilon}^{(L)}_{\alpha\beta}$ and $\tilde{\epsilon}^{(NL)}_{\alpha\beta}$ approximate expressions for $\epsilon^{(L)}_{\alpha\beta}$ and $\epsilon^{(NL)}_{\alpha\beta}$ in terms of nodal displacement parameters ψ_j^i
$2\epsilon_{\alpha 3}, 2\tilde{\epsilon}_{\alpha 3}$ transverse shear strains and their approximate expressions in terms of ψ_j^i
$\kappa_{\alpha\beta}$ and $\tilde{\kappa}_{\alpha\beta}$ curvature changes and twist, and their approximate expressions in terms of ψ_j^i
$\bar{\pi}, \pi$ potential energy functional and its discretized form defined in eqns (1) and (8), respectively
$\bar{\Pi}, \Pi$ Hellinger–Reissner functional and its discretized form
$\tilde{\Pi}$ modified discretized functional defined in eqn (20)
ϕ_α rotation components
ψ_j^i nodal displacement parameters
$\Omega, \Omega^{(e)}$ domain of the shell and the finite element, respectively

Range of indices:
Lowercase Latin indices 1–m
Uppercase Latin Indices 1–5
Lowercase script indices 1–n
Uppercase script indices 1–8
Greek indices 1,2

1. INTRODUCTION

The idea of developing an algebraic package to simplify the generation of the characteristic arrays of finite elements (e.g. stiffness, geometric stiffness and mass coefficients) has been suggested and referred to by a number of investigators (e.g. Argyris, Zienkiewicz and Clough, among others) over the last fifteen years. Moreover, several publications have been devoted to the use of symbolic manipulation in the evaluation of stiffness coefficients for finite elements. The objectives of these studies included: (a) reducing the tedium of manual algebraic manipulations (b) eliminating the errors introduced by numerical quadrature and (c) improving the efficiency of element generation (e.g. reducing the number of floating-point arithmetic operations).

Most of the reported studies to-date have been limited to linear finite elements and can be grouped in two categories: (a) Algorithms which synthesize the characteristic arrays for *any* element from a given set of problem parameters (e.g. problem type, element shape and field variable approximation), and (b) algorithms which take advantage of the symmetry and/or other properties of a particular element (or set of elements) to efficiently generate the characteristic arrays.

Among the studies of the first category, mention may

†Professor of Engineering and Applied Science.
‡Senior Research Associate in Mathematics and Computer Science.

be made of the algebraic polynomial manipulator presented in Ref. [1], and the tensor generator of Ref. [2]. In Refs. [3, 4] symbolic processors (templates) were developed for generating the stiffness coefficients as a function of the problem parameters. The MACSYMA system was used in the latter two studies. In Ref. [5] a symbolic manipulation system INTER was presented for generating symbolic matrices, performing symbolic integration, differentiation, matrix multiplication and matrix inversion. The system is written partly in FORTRAN IV and partly in assembler language and is operational on IBM 370/168 computer.

Among the studies of the second category, mention may be made of Ref. [6], wherein the FORMAC system was used to generate the stiffness coefficients for triangular elements, with approximations of the field variable ranging from cubic to sextic polynomials. The FORMAC system was also used in Ref. [7] to generate analytic expressions of the stiffness coefficients of three-dimensional tetrahedral elements having 4 and 10 nodes (linear and quadratic elements). The similarities between the stiffness coefficients of the 4- and 10-node elements were used to reduce the computational effort in generating the stiffness coefficients of 10-node elements. In Ref. [8] an ALGOL program was used for the symbolic representation of the total strain energy in terms of displacement parameters for geometrically nonlinear plate and shallow shell elements. In a series of publications (Refs. [9–14]), the authors studied the use of group-theoretic methods (symmetry transformations) in conjunction with symbolic manipulation to reduce the computational effort required for element development.

Two of the aforementioned studies have addressed the question of simplifying the development of nonlinear finite elements (viz. Refs. [8, 9]), but the full potential of computerized symbolic manipulation has not yet been exploited. The present study focuses on some further aspects of this problem. Specifically, in addition to the analytic evaluation of integrals, the tasks which can be performed using computerized symbolic manipulation include: (1) generation of the algebraic expressions for the stiffness coefficients for nonlinear finite elements, (2) generation of FORTRAN source code for the numerical evaluation of stiffness coefficients and (3) checking the correctness of hand-coded FORTRAN expressions for these coefficients.

The present study is performed using the MACSYMA symbolic and algebraic manipulation system. A detailed discussion of the capabilities of the system is given in the MACSYMA manual (Ref. [15]) and a description of some of the available and anticipated aids to the MACSYMA user is given in Refs. [16, 17].

To fix ideas the discussion herein is focused on the development of the stiffness coefficients of two-dimensional shear-flexible, doubly-curved deep shell elements. Two sample MACSYMA programs are presented in Appendix A for the development of nonlinear stiffness coefficients of the elements. The first program is for displacement models and the second program is for mixed models with discontinuous stress-resultant fields at interelement boundaries.

The MACSYMA programs provide some insight into the selection of a hierarchy of appropriate intermediate variables that result in simplifying the algebraic expressions of the stiffness coefficients and improving the efficiency of their numerical evaluation. If intermediate variables are not used the expressions of the stiffness coefficients can become unwieldy and the the associated FORTRAN code will be quite inefficient.

2. FINITE ELEMENT FORMULATION

The analytical formulation is based on a modified form of the geometrically nonlinear Sanders–Budiansky type deep-shell theory with the effects of transverse shear deformation and bending-extensional coupling included (see Refs. [18, 19]). A total Lagrangian description of the shell deformation is used, and the shell configurations are referred to the lines of curvature coordinates of the undeformed shell. Two finite element formulations are considered. In the first formulation (displacement model) the fundamental unknowns consist of the displacement and rotation components of the shell middle surface and the element stiffness coefficients are obtained by using the principle of minimum potential energy. The fundamental unknowns in the second formulation (mixed model) consist of thirteen shell quantities: the generalized displacements u_α, w and ϕ_α and the stress resultants $N_{\alpha\beta}$, $M_{\alpha\beta}$ and Q_α ($\alpha, \beta = 1, 2$). The analysis is based on the Hellinger–Reissner mixed variational principle. No continuity requirements are imposed on the stress resultants at interelement boundaries and the stress resultants are eliminated at the element level.

Indicial notation is used throughout the development. A repeated index (subscript or superscript) in the same term denotes summation over the full range of the index. However, the rules of index notation are not applied to indices between parentheses.

2.1 *Displacement model*

The functional used in the development of the displacement model is given by:

$$\tilde{\pi}(u_\alpha, w, \phi_\alpha) = U^{(L)} + U^{(NL)} - W \tag{1}$$

where

$$U^{(L)} = \frac{1}{2}\int \{C_{\alpha\beta\gamma\rho}\epsilon^{(L)}_{\alpha\beta}\epsilon^{(L)}_{\gamma\rho} + 2F_{\alpha\beta\gamma\rho}\epsilon^{(L)}_{\alpha\beta}\kappa_{\gamma\rho} + D_{\alpha\beta\gamma\rho}\kappa_{\alpha\beta}\kappa_{\gamma\rho} + C_{\alpha 3\beta 3}(2\epsilon_{\alpha 3})(2\epsilon_{\beta 3})\}\,d\Omega \tag{2}$$

$$U^{(NL)} = \frac{1}{2}\int [C_{\alpha\beta\gamma\rho}(2\epsilon^{(L)}_{\alpha\beta}\epsilon^{(NL)}_{\gamma\rho} + \epsilon^{(NL)}_{\alpha\beta}\epsilon^{(NL)}_{\gamma\rho}) + 2F_{\alpha\beta\gamma\rho}\epsilon^{(NL)}_{\alpha\beta}\kappa_{\gamma\rho}]\,d\Omega \tag{3}$$

$$W = \int (p_\alpha u_\alpha + pw)\,d\Omega. \tag{4}$$

In eqns (2)–(4), $C_{\alpha\beta\gamma\rho}$, $D_{\alpha\beta\gamma\rho}$ and $F_{\alpha\beta\gamma\rho}$ are the extensional stiffnesses, the bending stiffnesses and the stiffness interaction coefficients of the shell; $C_{\alpha 3\beta 3}$ are transverse shear stiffnesses of the shell; $\epsilon^{(L)}_{\alpha\beta}$ and $\epsilon^{(NL)}_{\alpha\beta}$ are linear and nonlinear parts of the extensional strains; $\kappa_{\alpha\beta}$ are curvature changes and twist; $2\epsilon_{\alpha 3}$ are transverse shear strains; p_α and p are the external load components in the orthogonal coordinate directions x_α and x_3. The range of the subscripts α, β is 1, 2.

Finite Element Discretization. The shell region is decomposed into finite elements $\Omega^{(e)}$ connected at appropriate nodes, where superscript e refers to the element. A typical element is isolated from the model and

the fundamental unknowns are approximated by expressions of the form:

$$u_\alpha = \mathcal{N}^i \psi_\alpha{}^i \tag{5}$$

$$w = \mathcal{N}^i \psi_3{}^i \tag{6}$$

$$\phi_\alpha = \mathcal{N}^i \psi^i_{3+\alpha}. \tag{7}$$

In eqns (5)–(7) $\mathcal{N}^i$ are shape (or interpolation) functions; $\psi_J{}^i$ ($i = 1$–m, $J = 1$–5) are nodal displacement parameters; m equals the number of nodes of the element; the superscripts identify the node number; and subscripts refer to the ordering of nodal displacement parameters. For convenience, the same set of shape functions is used for approximating each of the fundamental unknowns.

Finite element equations. If the generalized displacements in the potential energy functional of eqn (1) are replaced by their expressions in terms of the shape functions, the resulting discretized functional can be expressed in the following form:

$$\pi(\psi_J{}^i) = \sum_{\text{elements}} \int_{\Omega^{(e)}} \left[\frac{1}{2} \bar{K}^{ij}_{IJ} \psi_I{}^i \psi_J{}^j + \frac{1}{6} \bar{F}^{ijk}_{IJK} \psi_I{}^i \psi_J{}^j \psi_K{}^k + \frac{1}{12} \bar{G}^{ijkl}_{IJKL} \psi_I{}^i \psi_J{}^j \psi_K{}^k \psi_L{}^l - \bar{P}_I{}^i \psi_I{}^i \right] \mathrm{d}\Omega. \tag{8}$$

In eqn (8) $\bar{K}^{ij}_{IJ}$, $\bar{F}^{ijk}_{IJK}$ and $\bar{G}^{ijkl}_{IJKL}$ are quadratic, cubic and quartic functions of $\mathcal{N}^i$ and their derivatives; and $\bar{P}_I{}^i$ represents the array of external forces. The range of the upper and lower-case Latin indices is 1–5 and 1–m, respectively. The $\bar{K}$, $\bar{F}$ and $\bar{G}$ are completely symmetric under the interchange of pairs of indices where each pair consists of a superscript and the subscript just beneath it.

The governing equations for each element are obtained by applying the stationary conditions of the discretized functional, eqn (8), and can be written in the following form:

$$K^{ij}_{IJ} \psi_i{}^j + \frac{1}{2} F^{ijk}_{IJK} \psi_I{}^j \psi_K{}^k + \frac{1}{3} G^{ijkl}_{IJKL} \psi_J{}^j \psi_k{}^k \psi_L{}^l = P_I{}^i \tag{9}$$

where K^{ij}_{IJ} are linear stiffness coefficients; F^{ijk}_{IJK} and G^{ijkl}_{IJKL} are nonlinear stiffness coefficients of the element and $P_I{}^i$ are nodal load coefficients of the element. The K, F, G and P arrays are the integrals, over the element domain, of the corresponding $\bar{K}$, $\bar{F}$, $\bar{G}$ and $\bar{P}$ arrays.

2.2 *Mixed model*

The form of the Hellinger–Reissner functional used in the development of mixed models is given by:

$$\bar{\Pi}(u_\alpha, w, \phi_\alpha, N_{\alpha\beta}, M_{\alpha\beta}, Q_\alpha) = V^{(L)} + V^{(NL)} - U^{(c)} - W \tag{10}$$

where

$$V^{(L)} = \int N_{\alpha\beta} \epsilon^{(L)}_{\alpha\beta} \, \mathrm{d}\Omega \tag{11}$$

$$V^{(NL)} = \int N_{\alpha\beta} \epsilon^{(NL)}_{\alpha\beta} \, \mathrm{d}\Omega \tag{12}$$

$$U^{(c)} = \frac{1}{2} \int \left[A_{\alpha\beta\gamma\rho} N_{\alpha\beta} N_{\gamma\rho} + 2B_{\alpha\beta\gamma\rho} N_{\alpha\beta} M_{\gamma\rho} + G_{\alpha\beta\gamma\rho} M_{\alpha\beta} M_{\gamma\rho} + A_{\alpha 3 \beta 3} Q_\alpha Q_\beta \right] \mathrm{d}\Omega \tag{13}$$

and the arrays A, B and G are shell compliance coefficients (inverse of the shell stiffnesses defined in eqns (2) and (3)).

Finite element discretization. In addition to the approximations of the generalized displacements, eqns (5)–(7), the stress resultants are approximated by:

$$N_{\alpha\beta} = \bar{\mathcal{N}}^i H^i_{\alpha+\beta-1} \tag{14}$$

$$M_{\alpha\beta} = \bar{\mathcal{N}}^i H^i_{\alpha+\beta+2} \tag{15}$$

$$Q_\alpha = \bar{\mathcal{N}}^i H^i_{\alpha+6} \tag{16}$$

where $\bar{\mathcal{N}}^i$ are approximation functions for the stress resultants; $H_\mathcal{J}{}^i$ ($i = 1$–n and $\mathcal{J} = 1$–8) are parameters used in the approximation; and n equals the number of shape functions used in the approximation. Note that the same set of functions is used for approximating each stress resultant and the approximation functions $\bar{\mathcal{N}}^i$ are different from the shape functions $\mathcal{N}^i$.

The discretized Hellinger–Reissner functional $\Pi(H_\mathcal{J}{}^i, \psi_I{}^i)$ is obtained by replacing both the generalized displacements and stress resultants in $\bar{\Pi}(u_\alpha, w, \phi_\alpha, N_{\alpha\beta}, M_{\alpha\beta}, Q_\alpha)$ by their expressions in terms of the shape and approximation functions, eqns (5)–(7) and (14)–(16). In the present study the shell compliance coefficients are assumed to be constant within each element and no continuity requirements were imposed on the stress resultants; therefore: (a) the $\bar{\mathcal{N}}^i$ are conveniently chosen to be orthonormal polynomials and the associated $H_\mathcal{J}{}^i$ are merely coefficients and not nodal stress-resultant parameters, (b) the coefficients $H_\mathcal{J}{}^i$ are eliminated on the element level. This is accomplished by taking the variation of $\Pi(H_\mathcal{J}{}^i, \psi_I{}^i)$ with respect to $H_\mathcal{J}{}^i$ and solving the resulting equations for $H_\mathcal{J}{}^i$. These equations can be written in the following form:

$$\int_{\Omega^{(e)}} \bar{\mathcal{N}}^i \bar{\epsilon}^{(L)}_{\alpha\beta} \, \mathrm{d}\Omega + \int_{\Omega^{(e)}} \bar{\mathcal{N}}^i \bar{\epsilon}^{(NL)}_{\alpha\beta} \, \mathrm{d}\Omega - A_{\alpha\beta\gamma\rho} H^i_{\gamma+\rho-1} - B_{\alpha\beta\gamma\rho} H^i_{\gamma+\rho+2} = 0 \tag{17}$$

$$\int_{\Omega^{(e)}} \bar{\mathcal{N}}^i \bar{\kappa}_{\alpha\beta} \, \mathrm{d}\Omega - B_{\alpha\beta\gamma\rho} H^i_{\gamma+\rho-1} - G_{\alpha\beta\gamma\rho} H^i_{\gamma+\rho+2} = 0 \tag{18}$$

$$\int_{\Omega^{(e)}} \bar{\mathcal{N}}^i (2\bar{\epsilon}_{\alpha 3}) \, \mathrm{d}\Omega - A_{\alpha 3 \beta 3} H^i_{\beta-6} = 0 \tag{19}$$

where $\bar{\epsilon}_{\alpha\beta}$, $\bar{\kappa}_{\alpha\beta}$ and $2\bar{\epsilon}_{\alpha 3}$ are the extensional, bending and transverse shear strain components expressed in terms of the nodal displacement parameters $\psi_I{}^i$.

If eqns (17)–(19) are used the functional $\Pi(H_\mathcal{J}{}^i, \psi_I{}^i)$ can be reduced to a quartic function of $\psi_I{}^i$ as follows:

$$\bar{\Pi}(\psi_I{}^i) = \sum_{\text{elements}} \int_{\Omega^{(e)}} (U_{\text{eff}} - W) \, \mathrm{d}\Omega \tag{20}$$

where U_{eff} = effective strain energy of the element

$$= \frac{1}{2} \left[C_{\alpha\beta\gamma\rho} \int_{\Omega^{(e)}} \bar{\mathcal{N}}^i (\bar{\epsilon}^{(L)}_{\alpha\beta} + \bar{\epsilon}^{(NL)}_{\alpha\beta}) \, \mathrm{d}\Omega \times \int_{\Omega^{(e)}} \bar{\mathcal{N}}^i (\bar{\epsilon}^{(L)}_{\gamma\rho} + \bar{\epsilon}^{(NL)}_{\gamma\rho}) \, \mathrm{d}\Omega \right]$$

$$\int_{\Omega^{(e)}} \bar{\mathcal{N}}^i(\bar{\epsilon}^{(L)}_{\alpha\beta} + \bar{\epsilon}^{(NL)}_{\alpha\beta})\,d\Omega \int_{\Omega^{(e)}} \bar{\mathcal{N}}^j \bar{\kappa}_{\gamma\rho}\,d\Omega \tag{21}$$

$$+ D_{\alpha\beta\gamma\rho} \int_{\Omega^{(e)}} \bar{\mathcal{N}}^i \bar{\kappa}_{\alpha\beta}\,d\Omega \int_{\Omega^{(e)}} \bar{\mathcal{N}}^j \bar{\kappa}_{\gamma\rho}\,d\Omega$$

$$+ C_{\alpha 3\beta 3} \int_{\Omega^{(e)}} \bar{\mathcal{N}}^i (2\bar{\epsilon}_{\alpha 3})\,d\Omega \int_{\Omega^{(e)}} \bar{\mathcal{N}}^j (2\bar{\epsilon}_{\beta 3})\,d\Omega \Big].$$

The effective stiffness coefficients are then obtained by taking the variation of the modified discretized functional $\bar{\Pi}$ with respect to ψ_I^i. The resulting nonlinear equations for each element have the same form as eqn (9).

It may be mentioned that by appropriate selection of the number of approximation functions, $\mathcal{N}^i$ and $\bar{\mathcal{N}}^i$, the mixed models with discontinuous stress fields at inter-element boundaries can have better performance than those with continuous stress fields (see Ref. [20]).

3. MACSYMA PROGRAMS

The MACSYMA programs used in generating the nonlinear stiffness coefficients for both the displacement and mixed models are listed in Appendix A. The programs are divided into functional parts to simplify their understanding. Appendix A also includes some programming comments and sample output from the displacement model program. A brief description of the input, intermediate variables used, and output from the program is given in this section.

3.1 *Input to the programs*

Generally, it is not beneficial in MACSYMA to separate the input data from the program commands in the same manner as in numerical programs. Nevertheless, certain statements need to be changed when developing different types of elements. For the displacement model program these statements can be identified as follows:

(a) Numerical values for

NDP = number of displacement parameters per node

NSC = number of strain components

NSCNL = number of strain components with nonlinear terms.

(b) The matrix LINEARSTRAINMATRIX, whose entries are the coefficients of the nodal displacement parameters in the expression for the linear strain vector.

(c) Expression of the nonlinear strain vector in terms of the nodal displacement parameters, along with a list of intermediate variable names used in this expression. A discussion of the use of the intermediate variables is given in the next section.

(d) A matrix CC of coefficients used in the constitutive relations of the shell.

The input to the mixed model program is similar to that of the displacement program except that there are also a set of substitution commands (lines 284–302 in the MACSYMA program) which serve to introduce some of the intermediate variables.

Neither the number of shape functions $\mathcal{N}^i$ and $\bar{\mathcal{N}}^i$ nor their definitions are specified and, therefore, the resulting algebraic expressions for the stiffness coefficients are not restricted to a particular element geometry. However, for the numerical evaluation of the stiffness coefficients, $\mathcal{N}^i$ and $\bar{\mathcal{N}}^i$ as well as the geometric characteristics of the shell reference surface must be specified.

3.2 *Intermediate variables and arrays used in the programs*

In order to reduce the complexity of the algebraic expressions for the stiffness coefficients, the following set of intermediate variables are used in the programs:

(a) *Basic strain functions.* These are defined by comment statements (lines 47–72 in the displacement model program). They are first used as entries in LINEARSTRAINMATRIX (lines 99–107) and as coefficients in the three quantities EPS1NL, EPS2NL and PHI (lines 118–120) constituting the NONLINEARSTRAIN vector (lines 121–125). The same functions are also used in the mixed model program.

(b) *Components S_I^{JK} of* LINEARSTRESSMATRIX *in the displacement model program.* This matrix is printed at line 175; the identification of the S_I^{JK} with components of LINEARSTRESSMATRIX is given in lines 181–186; and the names are generated in line 192. The components S_I^{JK} are first used as coefficients of the nodal displacement parameters in the definition of LINEARSTRESS (lines 188–192).

(c) *Coefficients of the nodal displacement parameters in* LINEARSTRAININTEGRAL *in the mixed model program.* Each of these coefficients represents an integral over the product of NB_{II} with a basic strain function. They are defined by comment statements (lines 245–250). Their names are generated by pattern matching statements (lines 256–260, 262) and they are first used in the definition of LINEARSTRAININTEGRAL (lines 261, 262).

(d) *Coefficients of the nodal displacement parameters in* NONLINEARSTRAININTEGRAL *in the mixed model program.* Each of these coefficients represents an integral over the product of NB_{II} times two basic strain functions. They are defined by comment statements (lines 268–281). Their names are introduced through a series of substitution commands (lines 284–302), and they are first used in the definition of NONLINEARSTRAININTEGRAL (line 303).

(e) *Coefficients $S_{II}^{\hat{A}\hat{A}}{}_I^B$ of the nodal displacement parameters in* LINEARSTRESSINTEGRAL *in the mixed model program.* The values of these coefficients are computed in lines 312–315 and their names are generated in line 325. They are first used in the definition of LINEARSTRESSINTEGRAL (lines 320–325).

3.3 *Output from the program*

The programs listed in the appendix display a number of intermediate results as well as expressions for the stiffness coefficients. Sample output from the displacement model program is also given in Appendix A and includes:

(a) The linear and nonlinear strain vectors expressed in terms of the nodal displacement parameters.

(b) The matrix LINEARSTRESSMATRIX whose entries are the coefficients of the nodal displacement parameters in the expressions for the stress resultants.

(c) Algebraic expressions for the *KK* arrays—the integrands of the linear stiffness coefficients.

(d) Algebraic expressions for the *FF* arrays—the integrands of the quadratic stiffness coefficients.

(e) MACSYMA-generated FORTRAN source statements for the *GG* arrays—the integrands of the cubic stiffness coefficients.

The algebraic expressions for the *KK* and *FF* arrays are in terms of intermediate variables representing components of LINEARSTRESSMATRIX. The *KK* arrays

not listed can be deduced from those listed by interchanging indices. The *FF* and *GG* coefficients listed are a subset of those actually produced by the MACSYMA program. However, the remaining *FF* and *GG* coefficients can be deduced from the ones listed by the use of permutational symmetry of indices as well as the symmetry under interchange of x_1- and x_2-coordinate directions. Both symmetries can be built into the FORTRAN code and, therefore, only the expressions for the *FF* and *GG* coefficients listed in the sample output need to be used.

The MACSYMA-generated FORTRAN source code can be simply embedded in a finite element system. Often, however, the efficiency of the code can be improved by manual modifications.

4. TASKS WHICH CAN BE EFFICIENTLY PERFORMED USING SYMBOLIC MANIPULATION

In addition to the analytic evaluation of integrals which is discussed in Refs. [9–14], the different tasks that can be efficiently performed using computerized symbolic manipulation include: (a) generation of analytic expressions for the linear and nonlinear stiffness coefficients, (b) generation of FORTRAN code for numerical evaluation of the stiffness coefficients, and (c) checking the correctness of hand-coded FORTRAN expressions. These tasks are discussed subsequently.

4.1 *Generation of analytic expressions for stiffness coefficients*

The use of computerized algebraic manipulation in generating the nonlinear stiffness coefficients can greatly reduce the tedium of the algebraic operations required and increase the reliability of the resulting expressions. As can be seen from the sample output of the MACSYMA programs presented in Appendix A, fairly concise expressions are obtained for the stiffness coefficients. Further optimization of the algebraic expressions can readily be achieved through the application of MACSYMA, preferably in an interactive manner.

It is important to emphasize the fact that without the introduction of a proper set of intermediate variables the expressions of the stiffness coefficients can become unwieldy and the associated FORTRAN code will be quite inefficient.

The sample MACSYMA programs provide some insight into the selection of appropriate intermediate variables. In particular, the following two guidelines are listed:

(a) Basic strain functions should be introduced to simplify the expressions of strains in terms of nodal displacement parameters. In the case of shell elements, the use of these functions allows the generalization of the formulation from lines of principal curvature coordinates to general curvilinear coordinates without appreciably complicating the mathematical structure of the stiffness coefficients or reducing the efficiency of the associated FORTRAN code. On the other hand, if the strains are expressed *directly* in terms of the shape functions and geometric characteristics of the surface rather than in terms of the basic strain functions, then the expressions of the stiffness coefficients become, in general, very lengthy.

(b) Subexpressions which occur repeatedly in the results should be defined as intermediate variables (e.g. components of the LINEARSTRESSMATRIX in the displacement model program).

In general, the coefficients of the unknown parameters in the expressions of the physical quantities appearing in the discretized functional are good candidates for intermediate variables (e.g. coefficients of the nodal displacement parameters in NONLINEARSTRAININTEGRAL and LINEARSTRESSINTEGRAL of the mixed model program).

4.2 *Automatic generation of FORTRAN code*

The sample output in Appendix A provides an example of FORTRAN source code automatically generated by the MACSYMA system.

If automatically generated FORTRAN code is desired, it can be copied on magnetic tape or cassette and transmitted to the computer of the analyst's home institution.

The MACSYMA generated FORTRAN code is, in general, not optimized for efficiency. Some improvements in efficiency can be made by using MACSYMA commands to identify common subexpressions and automatically assign intermediate variable names to them. However, in the case of multiply nested DO loops, minimizing the number of arithmetic operations can only be done by hand-coding of MACSYMA's algebraic output.

Through the use of computerized symbolic manipulation alternate programming strategies can be tried and the operation counts compared to identify the best strategy.

4.3 *Checking correctness of* FORTRAN *expressions*

The process of manually generating FORTRAN code, even when it is merely a restructuring of MACSYMA algebraic output, is prone to errors. Computerized symbolic and algebraic manipulation systems can be used for checking the correctness of the restructured (or modified) code by feeding the (edited) FORTRAN expressions of the code to the system, generating algebraic expressions from them and comparing these expressions with the original algebraic expressions of the stiffness coefficients. This process is best done interactively rather than in BATCH mode.

If the modifications in the automatically generated code affect the indices of the variables or the DO loop structure of the program, then a complete check requires comparing the original and modified symbolic expressions after performing the summation over the full range of the DO loops. In many cases, this process can be both time and core consuming and a partial check using a reduced range of the DO loops may be satisfactory.

It may be noted that manual optimization of the automatically generated FORTRAN code may become unnecessary in the future with the development of new compilers which can perform the optimization task.

5. PROBLEM AREAS IN THE APPLICATION OF SYMBOLIC COMPUTING TO NONLINEAR ANALYSIS

There are a number of problem areas which limit realization of the full potential of computerized symbolic manipulation in nonlinear analysis. Some of these problems are discussed in Ref. [21]. Herein two major problems are listed:

(a) *Inability to Optimize the* FORTRAN *code on* MACSYMA. At the present time computerized symbolic manipulation systems do not have the capability for the automatic generation of efficient code for the purpose of numerical computation (automatic programming). In the

production of such codes intermediate variables need to be automatically defined to minimize the arithmetic operation count.

(b) *Problems associated with interface between algebraic and numerical calculations.* These are mainly in the data transfer and occur because typically symbolic and numerical programs are executed on different computers.

CONCLUDING REMARKS

The potential of using computerized symbolic manipulation in the development of nonlinear finite elements is discussed. In addition to the analytic evaluation of integrals which has been discussed in previous publications, three tasks which can be efficiently performed using computerized symbolic manipulation are identified as: (a) generation of algebraic expressions for the stiffness coefficients of nonlinear finite elements (b) generation of FORTRAN source code for numerical evaluation of stiffness coefficients and (c) checking the correctness of the FORTRAN statements for the arrays of coefficients.

The symbolic and algebraic manipulation system MACSYMA is used in the present study. Two sample MACSYMA programs are presented for the development of the nonlinear stiffness coefficients of two-dimensional, shear flexible doubly-curved deep shell elements. The first program is for displacement models and the second program is for mixed models with discontinuous stress resultant fields at interelement boundaries. Fairly concise algebraic expressions for the stiffness coefficients are obtained through the use of a hierarchy of appropriate intermediate variables.

The sample MACSYMA programs provide some insight into the selection of appropriate intermediate variables that result in simplifying the algebraic expressions of the stiffness coefficients and improving the efficiency of their numerical evaluation.

Acknowledgements—This work was supported by the National Aeronautics and Space Administration, Langley Research Center. The MACSYMA symbolic manipulation system was developed by the Mathlab Group of the Laboratory for Computer Science, Massachusetts Institute of Technology. The Mathlab Group is supported, in part, by NASA under Grant. No. NSG 1323 and by the United States Department of Energy under Grant ET-78-C-02-4687.

REFERENCES

1. W. Luft, J. M. Roesset and J. J. Connor, Automatic generation of finite element matrices. *J. Structural Div. ASCE* **97**, 349–362 (1971).
2. R. H. Gunderson and A. Cetiner, Element stiffness matrix generator. *J. Structural Div. ASCE* **97**, 363–375 (1975).
3. A. R. Korncoff and S. J. Fenves, Symbolic generation of finite element stiffness matrices. *Comput. Structures* **10**, 119–124 (1979).
4. A. R. Korncoff and S. J. Fenves, Symbolic generation of finite element stiffness matrices. *Rep.* R-78-100. Department of Civil Engineering, Carnegie-Mellon University, Pittsburgh, Pennsylvania (1978).
5. M. M. Cecchi and C. Lami, Automatic generation of stiffness matrices for finite element analysis. *Int. J. Num. Meth. Engng* **11**, 396–400 (1977).
6. N. Chepurniy, Evaluation of high-order polynomial triangular finite elements using FORMAC. *Proc. Sec. Symp. Symbolic Algebraic Manipulation*, pp. 365–371 (1971).
7. P. Pedersen, On computer-aided analytic element analysis and the similarities of tetrahedron elements. *Int. J. Num. Meth. Engng* **11**, 611–622 (1977).
8. R. G. Vos, Generalization of plate finite elements to shells. *J. Engng Mech. Div. ASCE* **98**, 385–400 (Apr. 1972).
9. C. M. Andersen and A. K. Noor, Use of group-theoretic methods in the development of nonlinear shell finite elements. *Proc. Conf. Symmetry, Similarity and Group-Theoretic Methods in Mechanics*. University of Calgary, Canada (1974).
10. C. M. Andersen and A. K. Noor, A computerized symbolic integration technique for development of triangular and quadrilateral composite shallow-shell finite elements. *NASA TN D-8067* (1975).
11. C. M. Andersen and J. T. Bowen, A computer program for anisotropic shallow shell finite elements using symbolic integration. *NASA* TM-X-3325 (1976).
12. A. K. Noor and C. M. Andersen, Mixed isoparametric element for Saint Venant torsion. *Comput. Meth. Appl. Mech. Engng* **6**, 195–218 (1975).
13. A. K. Noor and C. M. Andersen, Mixed isoparametric finite element models of laminated composite shells. *Comput. Meth. Appl. Mech. Engng* **11**, 255–280 (1977).
14. C. M. Andersen, Evaluation of integrals for a ten-node isoparametric tetrahedral finite element. *Comput. Math. Applications* **5**, 297–320 (1978).
15. MACSYMA *Reference Manual*. The Mathlab Group, Laboratory for Computer Science, Massachusetts Institute of Technology, Version 9 (1977).
16. V. E. Lewis, User aids for MACSYMA. *Proc.* 1977 MACSYMA *Users' Conf.* NASA CP-2012, 277–290 (1977).
17. M. R. Gensereth, An automated consultant for MACSYMA. *Proc.* 1977 MACSYMA *Users' Conf.* NASA CP-2012, 309–313 (1977).
18. J. L. Sanders, Nonlinear theories for thin shells. *Quarterly of Appl. Math.* **21**, 21–36 (Apr. 1963).
19. B. Budiansky, Notes on nonlinear shell theory. *J. Appl. Mech. ASME* **35**, 393–401 (June 1968).
20. A. K. Noor and J. M. Peters, Mixed models and reduced/selective integration displacement models for nonlinear analysis of curved beams. *Int. J. Num. Meth. Engng* (to be published).
21. A. K. Noor and C. M. Andersen, Computerized symbolic Manipulation in structural mechanics—progress and potential. *Comput. Structures* **10**, 95–118 (1979).

APPENDIX A

MACSYMA *programs for generating stiffness coefficients of two-dimensional doubly-curved, deep shell elements*

This appendix includes (a) the MACSYMA displacement-model program, (b) the MACSYMA mixed model program, (c) programming comments and (d) sample output from the displacement-model program.

```
/*                                                                      1
* * * * * * * * * * * * * * * * * * * * * * * * * * * * * * * * * * *    2
*                                                                       *  3
*          PROGRAM FOR GENERATION OF STIFFNESS COEFFICIENTS             *  4
*              FOR TWO-DIMENSIONAL DEEP SHELL ELEMENTS                  *  5
*                      (DISPLACEMENT MODEL)                             *  6
*                                                                       *  7
* * * * * * * * * * * * * * * * * * * * * * * * * * * * * * * * * * *    8
*                                                                       *  9
*    PART 1:   Generation of Strain-Displacement Relations              * 10
*                                                                       * 11
*       The problem is formulated in terms of five fundamental          * 12
*    unknowns, the generalized displacements U1, U2, W, PHI1, and PHI2.* 13
*                                                                       * 14
*         NDP (Number of Displacement Parameters per node)  = 5         * 15
*                                                                       * 16
*    The eight strain components are EPS1, EPS2, 2*EPS12, KAPPA1,       * 17
*    KAPPA2, 2*KAPPA12, 2*EPS13, 2*EPS23;  but only the first three     * 18
*    contain nonlinear terms.                                           * 19
*                                                                       * 20
*         NSC (Number of Strain Components)                  = 8       * 21
*         NSCNL (Number of Strain Components with                      * 22
*            NonLinear terms)                                = 3       * 23
*                                                                       * 24
*    Discretization is achieved by approximating each fundamental       * 25
*    unknown within a given finite element as a linear combination of   * 26
*    shape functions N[I].  The same set of NNPE (number of nodes per   * 27
*    element) shape functions is used for each of the fundamental       * 28
*    unknowns.  The unknowns thereby introduced may be written as       * 29
*                                                                       * 30
*           A                                                           * 31
*         PSI      where A = 1,2,...,NDP  and I = 1,2,...,NNPE         * 32
*           I                                                           * 33
*                                                                       * 34
*       While superscripts will be used in the comment statements,      * 35
*    the programming commands will either use the superscript indices   * 36
*    as matrix indices or will incorporate them into variable names     * 37
*    through use of the concatenation (CONCAT) command.                 * 38
*                                                                       * 39
*       If lines of principal curvature coordinates are used, the       * 40
*    geometry of a shell is characterized by                            * 41
*                                                                       * 42
*         K1, K2  - the principal curvatures in the x- and y-directions* 43
*                                                                       * 44
*         A1, A2  - the coefficients of the first fundamental form      * 45
*                                                                       * 46
*    The strain-displacement relations are developed in terms of the    * 47
*    following basic strain functions:                                  * 48
*                                                                       * 49
*                    dN                                    dN           * 50
*              1     I                               1     I           * 51
*         NXA  = --  ---                     NYA  =  --  ---          * 52
*            I   A1 dX                          I    A2 dY            * 53
*                                                                       * 54
*                 N                                     N             * 55
*                  I   dA2                               I   dA1      * 56
*         NA1  = -----  ---                  NA2  = -----  ---        * 57
*            I   A1 A2 dX                       I   A1 A2 dY          * 58
*                                                                       * 59
*         NXM  = NXA  - NA1                  NYM  = NYA  - NA2        * 60
*            I      I      I                    I      I      I        * 61
*                                                                       * 62
*                 NXA  + NA1                            NYA  + NA2    * 63
*                    I      I                              I      I    * 64
*         NXP  = -----------                 NYP  = -----------       * 65
*            I       2                          I       2             * 66
```

```
*                                                                       *
*          NK1  = N  K1                    NK2  = N  K2                *
*             I    I                           I   I                  *
*                                                                       *
*          NXK  = NXP  (K2 - K1)           NYK  = NYP  (K1 - K2)       *
*             I      I                        I      I                 *
*                                                                       *
*     Since integration will be performed by means of numerical         *
*     quadrature, each basic strain function variable name will need a  *
*     second subscript IQ (herein suppressed) specifying the quadrature *
*     point at which the function is evaluated.                         *
*                                                                       *
* * * * * * * * * * * * * * * * * * * * * * * * * * * * * * * * * * * *
*                                                                      */$
 NDP : 5$
 NSC : 8$
 NSCNL : 3$
/*
 *     Generate the vector of nodal displacement parameters.           */$

 PSI[I] := TRANSPOSE(MATRIX([PSI1[I],PSI2[I],PSI3[I],PSI4[I],PSI5[I]]))$
/*
 *     Print the vector of nodal displacement parameters.              */$

 PSI[K];
/*
 *     Evaluate the portion of the strain vector which is linear in the  *
 *        displacements.  The row (strain component) index of            *
 *        LINEARSTRAINMATRIX  ranges from 1 to NSC .                     *
 *        The column (fundamental unknown) index ranges from 1 to NDP .  *
 *        The subscript is the nodal index.                              */$

 LINEARSTRAINMATRIX[I] := MATRIX(
    [ NXA[I], NA2[I], NK1[I],      0,      0],
    [ NA1[I], NYA[I], NK2[I],      0,      0],
    [ NYM[I], NXM[I],      0,      0,      0],
    [      0,      0,      0, NXA[I], NA2[I]],
    [      0,      0,      0, NA1[I], NYA[I]],
    [ NYK[I], NXK[I],      0, NYM[I], NXM[I]],
    [-NK1[I],      0, NXA[I],   N[I],      0],
    [      0,-NK2[I], NYA[I],      0,   N[I]]    )$

 LINEARSTRAIN[I] := LINEARSTRAINMATRIX[I] . PSI[I]$
/*
 *     Print the linear strain vector .                                */$

 LINEARSTRAIN[K];
/*
 *     Evaluate the portion of the strain vector which is nonlinear      *
 *        in the displacements.                                          */$

 EPS1NL[I] := NK1[I]*PSI1[I] - NXA[I]*PSI3[I];
 EPS2NL[I] := NK2[I]*PSI2[I] - NYA[I]*PSI3[I];
 PHI[I] := NXP[I]*PSI2[I] - NYP[I]*PSI1[I];
 NONLINEARSTRAIN[I,J] := [
    (EPS1NL[I]*EPS1NL[J] + PHI[I]*PHI[J])/2,
    (EPS2NL[I]*EPS2NL[J] + PHI[I]*PHI[J])/2,
    (EPS1NL[I]*EPS2NL[J] + EPS2NL[I]*EPS1NL[J])/2,
    0,0,0,0,0]$
/*
 *     Print the nonlinear strain vector .                             */$

 TRANSPOSE(NONLINEARSTRAIN[J,K]),EXPAND;
/*
```

```
*     Input a list of names of arrays of intermediate variables        *   131
*       which appear in the nonlinear strain-displacement parameter    *   132
*       relations.  Use this list to produce a RATVARS list which will *   133
*       govern the ordering of variables in the expressions for the    *   134
*       FF's and GG's to be developed subsequently.                    */$ 135
                                                                           136
 LISTOFARRAYNAMES : [NXA, NYA, NK1, NK2, NXP, NYP]$                        137
                                                                           138
 LISTOFINDICES : [[I], [J], [K], [L]]$                                     139
 RATVARSLIST : []$                                                         140
 FOR INDEX IN LISTOFINDICES DO                                             141
    FOR NAME IN LISTOFARRAYNAMES DO                                        142
       RATVARSLIST : APPEND(RATVARSLIST, [ARRAYMAKE(NAME,INDEX)])$         143
 APPLY('RATVARS,RATVARSLIST)$                                              144
/*                                                                         145
* * * * * * * * * * * * * * * * * * * * * * * * * * * * * * * * * * * *   146
*                                                                     *    147
*     PART 2:   Constitutive Relations                                *    148
*                                                                     *    149
*       The constitutive relations are assumed to be linear and to    *   150
*     have coefficients given by the matrix CC.                       *   151
*     The matrix CC has dimension NSC by NSC.                         *   152
*                                                                     *    153
*                                                                     *    154
* * * * * * * * * * * * * * * * * * * * * * * * * * * * * * * * * * * *   155
*                                                                     *    156
*     The portion of the stress vector which is linear in the         *   157
*     displacements is evaluated next.   Later S is to be identified *   158
*     with LINEARSTRESSMATRIX                                         */$ 159
                                                                           160
 CC : MATRIX(                                                              161
    [CC11, CC12, CC16, FF11, FF12, FF16,    0,    0],                     162
    [CC12, CC22, CC26, FF12, FF22, FF26,    0,    0],                     163
    [CC16, CC26, CC66, FF16, FF26, FF66,    0,    0],                     164
    [FF11, FF12, FF16, DD11, DD12, DD16,    0,    0],                     165
    [FF12, FF22, FF26, DD12, DD22, DD26,    0,    0],                     166
    [FF16, FF26, FF66, DD16, DD26, DD66,    0,    0],                     167
    [   0,    0,    0,    0,    0,    0, CC55, CC45],                     168
    [   0,    0,    0,    0,    0,    0, CC45, CC44]  )$                  169
                                                                           170
 LINEARSTRESSMATRIX[I] := CC . LINEARSTRAINMATRIX[I]$                      171
/*                                                                         172
*     Print the linear stress vector .                                 */$ 173
                                                                           174
 LINEARSTRESSMATRIX[K];                                                    175
/*                                                                         176
*     Evaluate the linear portion of the stress vector .               */$ 177
                                                                           178
 LINEARSTRESS[I] : LINEARSTRESSMATRIX[I] . PSI[I]$                         179
/*                                                                         180
*     Generate a new expression for the linear stress vector, this time *   181
*     in terms of intermediate variables given by  CONCAT(S,J,K)[I].  *   182
*     Here the CONCAT command creates a variable name by concatenation *   183
*     of the symbol  S  with the numerical values of  J  and K.       *   184
*     The new variable represents the  J,K  component of              *   185
*     LINEARSTRESSMATRIX with nodal index I .                          */$ 186
                                                                           187
 NULLLIST : []$                                                            188
 FOR II IN [I,J,K] DO (                                                    189
    LINEARSTRESS[II] : NULLLIST,                                           190
    FOR J THRU 8 DO LINEARSTRESS[II] : APPEND(LINEARSTRESS[II],            191
       [SUM(CONCAT(S,J,K)[II]*CONCAT(PSI,K)[II],K,1,NDP)])   )$            192
/*                                                                         193
```

```
 * * * * * * * * * * * * * * * * * * * * * * * * * * * * * * * * * * * * *
 *                                                                       *
 *     PART 3: Generation of the Elemental Stiffness Coefficients        *
 *                                                                       *
 *        The discretized functional (potential energy) is               *
 *                                                                       *
 *          PI(PSI) = Sumoverelements(U - W)                             *
 *                                                                       *
 *     where the strain energy U  has the form                           *
 *                                                                       *
 *               1                       A                 A    A B      *
 *          U  = - Integral[(LINEARSTRAIN + NONLINEARSTRAIN ) CC         *
 *               2                                                       *
 *                                 B                  B                  *
 *                  * (LINEARSTRAIN  + NONLINEARSTRAIN )] dAREA          *
 *                                                                       *
 *     and the external work has the form                                *
 *                                                                       *
 *          W = Integral[U1 p1 + U2 p2 + W p, dAREA]                     *
 *                                                                       *
 *     Since U is quartic in the displacements, it may be written in the *
 *     form                                                              *
 *                                                                       *
 *                   1   A B     A     B    1   A B C     A     B     C  *
 *      U = Integral[- KK     PSI   PSI   + - FF       PSI   PSI   PSI   *
 *                   2   I J     I     J    6   I J K     I     J     K  *
 *                                                                       *
 *                        1    A B C D     A     B     C     D           *
 *                      + -- GG         PSI   PSI   PSI   PSI ,  dAREA]  *
 *                        12   I J K L     I     J     K     L           *
 *                                                                       *
 *                                                                       *
 *     If  K, F  and  G  represent integrals of  KK, FF  and GG,         *
 *     respectively, over the element area, then the governing equations *
 *     for an individual shell element have the form                     *
 *                                                                       *
 *        A B    B   1  A B C    B    C   1  A B C D    B    C    D    A *
 *       K    PSI  + - F      PSI  PSI  + - G        PSI  PSI  PSI  = P  *
 *        I J    J   2  I J K    J    K   3  I J K L    J    K    L    I *
 *                                                                       *
 *     The numerical coefficients in the above two equations have been   *
 *     chosen such that the left hand side of the Newton-Raphson         *
 *     equation will have the simple form                                *
 *                                                                       *
 *           A B    A B C    C    A B C D    C    D          B           *
 *         (K    + F      PSI  + G        PSI  PSI ) DELTAPSI            *
 *           I J    I J K    K    I J K L    K    L          J           *
 *                                                                       *
 *                                                                       *
 * * * * * * * * * * * * * * * * * * * * * * * * * * * * * * * * * * * * *
 *                                                                       *
 *     Generate the integrands KK of the linear stiffness coefficients K *
 *        The multiplier (1/2) comes from the definition of the strain   *
 *        energy U .                                                     */$

  UK : (1/2)*
     LINEARSTRESS[I] . LINEARSTRAIN[J]$
/*
 *     The multiplier 2 comes from the relation between the KK's and U . */$

  FOR A THRU NDP DO (
     KKA:DIFF(UK,CONCAT(PSI,A)[I]),
     FOR B THRU A DO DISPLAY(
        ARRAYMAKE(CONCAT(KK,A,B),[I,J])
           :: 2*DIFF(KKA,CONCAT(PSI,B)[J]))    )$
/*
```

```
 *     Generate FORTRAN source code for evaluation of the KK's .          */$ 260
                                                                              261
  FOR A THRU NDP DO                                                           262
     FOR B THRU A DO                                                          263
        FORTRAN(CONCAT(KK,A,B,"(I,J)")                                        264
           = EV(ARRAYMAKE(CONCAT(KK,A,B),[I,J]),EVAL))$                       265
/*                                                                            266
 *     Generate the integrands FF and GG of the nonlinear stiffness       *   267
 *       coefficients F and G, respectively.  The multiplier (1/2)        *   268
 *       comes from the definition of the strain energy U .               *   269
 *       The multiplier 2 is due to having two cross terms.               *   270
 *       The multiplier (1/3) is due to averaging over three terms so     *   271
 *       as to make the FF's totally symmetric under the interchange of   *   272
 *       the indices I, J and K.                                          */$ 273
                                                                              274
  UF:(1/2)*2*(1/3)*                                                           275
     ( LINEARSTRESS[I] . NONLINEARSTRAIN[J,K]                                 276
     + LINEARSTRESS[J] . NONLINEARSTRAIN[K,I]                                 277
     + LINEARSTRESS[K] . NONLINEARSTRAIN[I,J])$                               278
/*                                                                            279
 *     The multiplier 6 is due to the relation between the FF's and U.    */$ 280
                                                                              281
  FOR A THRU NDP DO (                                                         282
     FFA:DIFF(UF,CONCAT(PSI,A)[I]),                                           283
     FOR B THRU A DO (                                                        284
        FFAB:DIFF(FFA,CONCAT(PSI,B)[J]),                                      285
        FOR C THRU B DO DISPLAY(                                              286
           ARRAYMAKE(CONCAT(FF,A,B,C),[I,J,K])                                287
               :: RAT(6*DIFF(FFAB,CONCAT(PSI,C)[K])))))$                      288
/*                                                                            289
 *     Generate FORTRAN source code for evaluation of the FF's.           */$ 290
                                                                              291
  FOR A THRU NDP DO                                                           292
     FOR B THRU A DO                                                          293
        FOR C THRU B DO                                                       294
           FORTRAN(CONCAT(FF,A,B,C,"(I,J,K)")                                 295
               = EV(ARRAYMAKE(CONCAT(FF,A,B,C),[I,J,K]),EVAL))$               296
/*                                                                            297
 *     The multiplier (1/2) comes from the definition of the strain       *   298
 *       energy U.  The multiplier (1/3) is due to averaging over three   *   299
 *       terms so as to make the expressions for the GG's totally         *   300
 *       symmetric under the interchange of the indices I, J, K and L .   */$ 301
                                                                              302
  UG:(1/2)*(1/3)*                                                             303
     ( NONLINEARSTRAIN[I,J] . CC . NONLINEARSTRAIN[K,L]                       304
     + NONLINEARSTRAIN[I,K] . CC . NONLINEARSTRAIN[J,L]                       305
     + NONLINEARSTRAIN[I,L] . CC . NONLINEARSTRAIN[J,K] )$                    306
/*                                                                            307
 *     The multiplier 12 is due to the relation between the GG's and U.   */$ 308
                                                                              309
  FOR A THRU NSCNL DO (                                                       310
     GGA:DIFF(UG,CONCAT(PSI,A)[I]),                                           311
     FOR B THRU A DO (                                                        312
        GGAB:DIFF(GGA,CONCAT(PSI,B)[J]),                                      313
        FOR C THRU B DO (                                                     314
           GGABC:DIFF(GGAB,CONCAT(PSI,C)[K]),                                 315
           FOR D THRU C DO DISPLAY(                                           316
              ARRAYMAKE(CONCAT(GG,A,B,C,D),[I,J,K,L])                         317
                 :: RAT(12*DIFF(GGABC,CONCAT(PSI,D)[L])))))))$                318
/*                                                                            319
 *     Generate FORTRAN source code for evaluation of the GG's.           */$ 320
                                                                              321
  FOR A THRU NSCNL DO                                                         322
     FOR B THRU A DO                                                          323
        FOR C THRU B DO                                                       324
           FOR D THRU C DO                                                    325
              FORTRAN(CONCAT(GG,A,B,C,D,"((I-1)*NNPE+J,K,L)") =               326
                 EV(ARRAYMAKE(CONCAT(GG,A,B,C,D),[I,J,K,L]),EVAL))$           327
```

```
/*                                                                      1
* * * * * * * * * * * * * * * * * * * * * * * * * * * * * * * * * * * *  2
*                                                                       *  3
*          PROGRAM FOR GENERATION OF STIFFNESS COEFFICIENTS             *  4
*              FOR TWO-DIMENSIONAL DEEP SHELL ELEMENTS                  *  5
*          (MIXED MODEL WITH DISCONTINUOUS STRESS RESULTANTS)           *  6
*                                                                       *  7
* * * * * * * * * * * * * * * * * * * * * * * * * * * * * * * * * * * *  8
*                                                                       *  9
*    PART 1:  Relations Between Strains and Displacement Parameters     * 10
*                                                                       * 11
*       The problem is formulated in terms of 13 fundamental unknowns   * 12
*    - the generalized displacements U1, U2, W, PHI1, and PHI2          * 13
*    and the stress resultants N1, N2, N12, M1, M2, M12, Q1, Q2 .       * 14
*    The generalized displacements are C0 continuous, but the stress    * 15
*    resultants have no continuity conditions imposed on them across    * 16
*    interelement boundaries.  The stress resultants are eliminated     * 17
*    on the element level.                                              * 18
*                                                                       * 19
*         NDP (Number of Displacement Parameters per node)  = 5         * 20
*         NSR (Number of Stress Resultants)                 = 8         * 21
*                                                                       * 22
*       Discretization is achieved by expanding each generalized        * 23
*    displacement within a given finite element as a linear combination * 24
*    of shape functions N[I], and each stress resultant as a linear     * 25
*    combination of approximation functions NB[II].  A set of NNPE      * 26
*    (Number of Nodes per Element) functions is used for the            * 27
*    generalized displacements, and a second set of NNBE (Number of     * 28
*    NB's per Element) functions is used for the stress resultants.     * 29
*    The unknowns thereby introduced may be written as                  * 30
*                                                                       * 31
*           A                                                           * 32
*         PSI      where A = 1,2,...,NDP  and I = 1,2,...,NNPE         * 33
*           I                                                           * 34
*                                                                       * 35
*          BB                                                           * 36
*         H         where BB = 1,2,...,NSR  and JJ = 1,2,...,NNBE     * 37
*          JJ                                                           * 38
*                                                                       * 39
*       While superscripts will be used in the comment statements,      * 40
*    the programming commands will either use the superscript indices   * 41
*    as matrix indices or will incorporate them into variable names     * 42
*    through use of the concatenation (CONCAT) command.                 * 43
*                                                                       * 44
*       If lines of principal curvature coordinates are used, the       * 45
*    geometry of a shell is characterized by                            * 46
*                                                                       * 47
*         K1, K2  - the principal curvatures in the x- and y-directions * 48
*                                                                       * 49
*         A1, A2  - the coefficients of the first fundamental form      * 50
*                                                                       * 51
*    The strain-displacement relations are developed in terms of the    * 52
*    following strain approximation functions:                          * 53
*                                                                       * 54
*                    dN                                    dN          * 55
*                  1   I                                 1   I         * 56
*         NXA  = ---- ---                       NYA  = ---- ---       * 57
*            I   A1 dX                             I    A2 dY         * 58
*                                                                       * 59
*                   N                                     N           * 60
*                    I   dA2                               I   dA1     * 61
*         NA1  = ----- ---                      NA2  = ----- ---      * 62
*            I   A1 A2 dX                          I   A1 A2 dY       * 63
*                                                                       * 64
*         NXM  = NXA  - NA1                     NYM  = NYA  - NA2     * 65
*            I       I      I                      I       I      I     * 66
*                                                                       * 67
```

```
*                  NXA  + NA1                              NYA  + NA2          *    68
*                     I      I                                I      I         *    69
*          NXP  = -----------                     NYP  = -----------          *    70
*             I        2                            I        2               *    71
*                                                                             *    72
*          NK1  = N  K1                           NK2  = N  K2                *    73
*             I     I                                     I   I               *    74
*                                                                             *    75
*          NXK  = NXP  (K2 - K1)                  NYK  = NYP  (K1 - K2)      *    76
*             I       I                              I       I               *    77
*                                                                             *    78
*     Since integration will be performed by means of numerical               *    79
*     quadrature, each strain approximation function name will need a         *    80
*     second subscript IQ (herein suppressed) specifying the quadrature       *    81
*     point at which the function is evaluated.                               *    82
*                                                                             *    83
* * * * * * * * * * * * * * * * * * * * * * * * * * * * * * * * * * * * * * *    84
*                                                                            */$   85
 NDP : 5$                                                                          86
 NSR : 8$                                                                          87
/*                                                                                 88
 *     Generate the vector of nodal displacement parameters.                 */$   89
                                                                                   90
 PSI[I] := TRANSPOSE(MATRIX([PSI1[I],PSI2[I],PSI3[I],PSI4[I],PSI5[I]]))$           91
/*                                                                                 92
 *     Print the vector of nodal displacement parameters.                    */$   93
                                                                                   94
 PSI[K];                                                                           95
/*                                                                                 96
 *     Evaluate the portion of the strain vector which is linear in the      *    97
 *        displacements.  The row (strain component) index of                *    98
 *        LINEARSTRAINMATRIX  ranges from 1 to NSR .                         *    99
 *        The column (fundamental unknown) index ranges from 1 to NFU .      *   100
 *        The subscript is the nodal index.                                  */$  101
                                                                                  102
 LINEARSTRAINMATRIX[I] := MATRIX(                                                 103
    [ NXA[I], NA2[I], NK1[I],      0,      0],                                    104
    [ NA1[I], NYA[I], NK2[I],      0,      0],                                    105
    [ NYM[I], NXM[I],      0,      0,      0],                                    106
    [      0,      0,      0, NXA[I], NA2[I]],                                    107
    [      0,      0,      0, NA1[I], NYA[I]],                                    108
    [ NYK[I], NXK[I],      0, NYM[I], NXM[I]],                                    109
    [-NK1[I],      0, NXA[I],   N[I],      0],                                    110
    [      0,-NK2[I], NYA[I],      0,   N[I]]    )$                               111
                                                                                  112
 LINEARSTRAIN[I] := LINEARSTRAINMATRIX[I] . PSI[I]$                               113
/*                                                                                114
 *     Print the linear strain vector .                                      */$  115
                                                                                  116
 LINEARSTRAIN[K];                                                                 117
/*                                                                                118
 *     Evaluate the portion of the strain vector which is nonlinear          *   119
 *        in the displacements.                                              */$  120
                                                                                  121
 EPS1NL[I] := NK1[I]*PSI1[I] - NXA[I]*PSI3[I];                                    122
 EPS2NL[I] := NK2[I]*PSI2[I] - NYA[I]*PSI3[I];                                    123
 PHI[I] := NXP[I]*PSI2[I] - NYP[I]*PSI1[I];                                       124
 NONLINEARSTRAIN[I,J] := [                                                        125
    (EPS1NL[I]*EPS1NL[J] + PHI[I]*PHI[J])/2,                                      126
    (EPS2NL[I]*EPS2NL[J] + PHI[I]*PHI[J])/2,                                      127
    (EPS1NL[I]*EPS2NL[J] + EPS2NL[I]*EPS1NL[J])/2,                                128
    0,0,0,0,0]$                                                                   129
/*                                                                                130
 *     Print the nonlinear strain vector .                                   */$  131
                                                                                  132
 TRANSPOSE(NONLINEARSTRAIN[J,K]),EXPAND;                                          133
                                                                                  134
```

```
/*                                                                          135
* * * * * * * * * * * * * * * * * * * * * * * * * * * * * * * * * * * * * * *  136
*                                                                           *  137
*     PART 2:   Constitutive Relations                                      *  138
*                                                                           *  139
*        The constitutive relations are assumed to be linear and to         *  140
*     have coefficients given by the matrix CC.                             *  141
*     The matrix CC has dimension NSR by NSR.                               *  142
*                                                                           *  143
*                                                                           *  144
* * * * * * * * * * * * * * * * * * * * * * * * * * * * * * * * * * * * * * *  145
*                                                                           *  146
*                                                                           */$ 147
                                                                               148
 CC : MATRIX(                                                                  149
    [CC11, CC12, CC16, FF11, FF12, FF16,    0,    0],                        150
    [CC12, CC22, CC26, FF12, FF22, FF26,    0,    0],                        151
    [CC16, CC26, CC66, FF16, FF26, FF66,    0,    0],                        152
    [FF11, FF12, FF16, DD11, DD12, DD16,    0,    0],                        153
    [FF12, FF22, FF26, DD12, DD22, DD26,    0,    0],                        154
    [FF16, FF26, FF66, DD16, DD26, DD66,    0,    0],                        155
    [   0,    0,    0,    0,    0,    0, CC55, CC45],                        156
    [   0,    0,    0,    0,    0,    0, CC45, CC44]  )$                     157
/*                                                                          158
* * * * * * * * * * * * * * * * * * * * * * * * * * * * * * * * * * * * * * *  159
*                                                                           *  160
*     PART 3: Introduction of Strain and Stress Integrals                   *  161
*                                                                           *  162
*        The discretized Hellinger-Reissner functional is                   *  163
*                                                                           *  164
*          PI(PSI,H) = Sumoverelements(V - UC - W)                          *  165
*                                                                           *  166
*     where                                                                 *  167
*                                                                           *  168
*                 AA                                AA                AA    *  169
*          V  = H    Integral[NB    (LINEARSTRAIN    + NONLINEARSTRAIN  ),  *  170
*                 II             II                                         *  171
*                                                                           *  172
*                                                             dAREA]        *  173
*                                                                           *  174
*                 AA                          AA                        AA  *  175
*             = H    (LINEARSTRAININTEGRAL    + NONLINEARSTRAININTEGRAL  )  *  176
*                 II                          II                        II  *  177
*                                                                           *  178
*                                                                           *  179
*                 1  AA                                  -1 AA BB   BB      *  180
*          UC = - H    Integral[NB    NB  , dAREA] (CC  )       H           *  181
*                 2  II             II   JJ                      JJ         *  182
*                                                                           *  183
*                 1  AA     -1 AA BB   BB                                  "*  184
*             = - H    (CC  )       H                                       *  185
*                 2  II               II                                  *  186
*                                                                           *  187
*     and the external work has the form                                    *  188
*                                                                           *  189
*          W = Integral[U1 p1 + U2 p2 + W p, dAREA]                         *  190
*                                                                           *  191
*     where the integrals are over the areas of the individual elements     *  192
*     and p1, p2 and p are the pressures in the x,y, and z-directions,      *  193
*     respectively.  The variables LINEARSTRAIN, NONLINEARSTRAIN,           *  194
*     LINEARSTRAININTEGRAL, and NONLINEARSTRAININTEGRAL appearing in V      *  195
*     are all functions of PSI.  The functions NB[II] are chosen to be      *  196
*     orthonormal with respect to integration over the element area.        *  197
*     Thus the integral in the definition of UC evaluates to a Kronecker    *  198
*     delta function on the indices II and JJ.                              *  199
*                                                                           *  200
```

```
*        Variation of PI with respect to the H's yields                  *   201
*                                                                        *   202
*                              AA                              AA        *   203
*          LINEARSTRAININTEGRAL    + NONLINEARSTRAININTEGRAL             *   204
*                              II                              II        *   205
*                                                                        *   206
*                                                 -1 AA BB   BB          *   207
*                                          - (CC  )       H     = 0      *   208
*                                                  II                    *   209
*                                                                        *   210
*        Because stress resultants are not required to be continuous     *   211
*     across element boundaries, a modified discretized functional PIBAR *   212
*     is formed by substituting the above equation into the function PI. *   213
*     The new function PIBAR,  which no longer depends on the H's,       *   214
*     has a quartic dependence on the PSI's.                             *   215
*                                                                        *   216
*          PIBAR(PSI) = Sumoverelements(U    - W)                        *   217
*                                        eff                             *   218
*                                                                        *   219
*     where the "effective" strain energy is                             *   220
*                                                                        *   221
*            1                          AA                         AA    *   222
*     U    = - (LINEARSTRAININTEGRAL    + NONLINEARSTRAININTEGRAL  )    *   223
*      eff   2                          II                         II    *   224
*                                                                        *   225
*            AA BB                          BB                      BB   *   226
*        * CC       (LINEARSTRAININTEGRAL    + NONLINEARSTRAININTEGRAL  ) *   227
*                                          II                      II    *   228
*                                                                        *   229
*     Let                                                                *   230
*                                                                        *   231
*                              AA       AA BB                     BB     *   232
*          LINEARSTRESSINTEGRAL     = CC       LINEARSTRAININTEGRAL     *   233
*                              II                                 II     *   234
*                                                                        *   235
*                AA B     B                                             *   236
*             = S      PSI                                              *   237
*                II J     J                                            *   238
*                                                                        *   239
* * * * * * * * * * * * * * * * * * * * * * * * * * * * * * * * * * * * *   240
*                                                                        *   241
*     Compute the vector LINEARSTRAININTEGRAL.                           *   242
*     The subscript is a nodal index (actually, a dummy index which is   *   243
*     summed over).  Integration is achieved by pattern matching.        *   244
*     A number of intermediate variables such as NNXA[I,II], NNYA[I,II], *   245
*     etc. are automatically introduced which represent integrals.       *   246
*     For example                                                        *   247
*                                                                        *   248
*          NNXA     = Integral[NXA  NB  , dAREA]                         *   249
*              I II               I   II                                *   250
*                                                                        *   251
*     The following list is the list of array names appearing in         *   252
*     LINEARSTRAINMATRIX.                                               */$ 253
                                                                             254
                                                                             255
 LISTOFARRAYNAMES : [N,NXA,NYA,NK1,NK2,NA1,NA2,NXM,NYM,NXK,NYK]$             256
 MEMBEROFLIST(XXX) := MEMBER(XXX,LISTOFARRAYNAMES)$                          257
 MATCHDECLARE(NNN,MEMBEROFLIST)$                                             258
 MATCHDECLARE(III,TRUE)$                                                     259
 DEFRULE(RULE1,NNN[III],CONCAT(N,NNN)[III,II]);                              260
 DEFINE(ARRAYMAKE(LINEARSTRAININTEGRAL,[I,II]),                              261
    APPLY1(LINEARSTRAIN[I],RULE1))$                                          262
/*                                                                           263
 *     Print the linear strain integral vector .                          */$ 264
                                                                             265
 LINEARSTRAININTEGRAL[K,LL];                                                 266
/*                                                                           267
```

```
*     Compute the vector NONLINEARSTRAININTEGRAL.  Examination of the   *   268
*     integrands suggests the introduction of a number of arrays of     *   269
*     intermediate variables to represent integrals over the product of *   270
*     NB[II] times two strain approximation functions.  For example     *   271
*                                                                       *   272
*          NNXPNXP       = Integral[NXP   NXP   NB   , dAREA]         *   273
*                I J II              I     J    II                     *   274
*                                                                       *   275
*     is an array which is symmetric in its first two indices, and      *   276
*                                                                       *   277
*          NXPYP       = Integral[NXP   NYP   NB   , dAREA]           *   278
*               I J II             I     J    II                      *   279
*                                                                       *   280
*     is an array without symmetry.                                     *$  281
                                                                            282
 NONLINEARSTRAIN[I,J]$                                                      283
 RATSUBST(NNXANXA[I,J,II],NXA[I]*NXA[J],%)$                                 284
 RATSUBST(NNYANYA[I,J,II],NYA[I]*NYA[J],%)$                                 285
 RATSUBST(NNXANYA[I,J,II]-NYA[I]*NXA[J],NXA[I]*NYA[J],%)$                   286
 RATSUBST(NNXPNXP[I,J,II],NXP[I]*NXP[J],%)$                                 287
 RATSUBST(NNYPNYP[I,J,II],NYP[I]*NYP[J],%)$                                 288
 RATSUBST(NNK1NK1[I,J,II],NK1[I]*NK1[J],%)$                                 289
 RATSUBST(NNK2NK2[I,J,II],NK2[I]*NK2[J],%)$                                 290
 RATSUBST(NXPYP[I,J,II],NXP[I]*NYP[J],%)$                                   291
 RATSUBST(NXPYP[J,I,II],NXP[J]*NYP[I],%)$                                   292
 RATSUBST(NK2K1[I,J,II],NK2[I]*NK1[J],%)$                                   293
 RATSUBST(NK2K1[J,I,II],NK2[J]*NK1[I],%)$                                   294
 RATSUBST(NXAK1[I,J,II],NXA[I]*NK1[J],%)$                                   295
 RATSUBST(NXAK1[J,I,II],NXA[J]*NK1[I],%)$                                   296
 RATSUBST(NXAK2[I,J,II],NXA[I]*NK2[J],%)$                                   297
 RATSUBST(NXAK2[J,I,II],NXA[J]*NK2[I],%)$                                   298
 RATSUBST(NYAK1[I,J,II],NYA[I]*NK1[J],%)$                                   299
 RATSUBST(NYAK1[J,I,II],NYA[J]*NK1[I],%)$                                   300
 RATSUBST(NYAK2[I,J,II],NYA[I]*NK2[J],%)$                                   301
 RATSUBST(NYAK2[J,I,II],NYA[J]*NK2[I],%)$                                   302
 DEFINE(ARRAYMAKE(NONLINEARSTRAININTEGRAL,[I,J,II]),RATSIMP(%))$            303
 TRANSPOSE(NONLINEARSTRAININTEGRAL[J,K,JJ]);                                304
/*                                                                          305
 *                                                              AA B*       306
 *     Compute the vector LINEARSTRESSINTEGRAL and its coefficients S    *   307
 *                                                              II J*/$ 308
                                                                            309
 LINEARSTRESSINTEGRAL[J,II] : CC . LINEARSTRAININTEGRAL[J,II]$              310
                                                                            311
 FOR AA THRU NSR DO                                                         312
    FOR B THRU NDP DO                                                       313
       S[AA,B] : DIFF(LINEARSTRESSINTEGRAL[J,II][AA,1],CONCAT(PSI,B)[J])$   314
 GENMATRIX(S,NSR,NDP);                                                      315
/*                                                                          316
 *     Express LINEARSTRESSINTEGRAL in terms of the intermediate         *   317
 *     variables SAAB[II,J]                                              */$ 318
                                                                            319
 NULLLIST:[]$                                                               320
 FOR IJK IN [I,J,K] DO (                                                    321
    LINEARSTRESSINTEGRAL[IJK,II]:NULLLIST,                                  322
    FOR AA THRU NSR DO                                                      323
       LINEARSTRESSINTEGRAL[IJK,II] : APPEND(LINEARSTRESSINTEGRAL[IJK,II],  324
          [SUM(CONCAT(S,AA,B)[IJK,II]*CONCAT(PSI,B)[IJK],B,1,NDP)])  )$     325
 TRANSPOSE(LINEARSTRESSINTEGRAL[J,II]);                                     326
/*                                                                          327
 * * * * * * * * * * * * * * * * * * * * * * * * * * * * * * * * * * * *  328
 *                                                                       *   329
 *     PART 4: Generation of the Linear and Nonlinear "Effective"        *   330
 *                       Stiffness Coefficients                          *   331
 *                                                                       *   332
 *       Let the effective strain energy be written as                   *   333
 *                                                                       *   334
```

```
*          U    = UK + UF + UG                                          *   335
*           eff                                                        *   336
*                                                                      *   337
*     where                                                            *   338
*                                                                      *   339
*                1                        AA                    AA     *   340
*          UK = - LINEARSTRESSINTEGRAL    LINEARSTRAININTEGRAL        *   341
*                2                       II                    II     *   342
*                                                                      *   343
*                1  A B     A     B                                   *   344
*             = - K     PSI   PSI                                      *   345
*                2  I J     I     J                                   *   346
*                                                                      *   347
*                                    AA                        AA      *   348
*          UF = LINEARSTRESSINTEGRAL    NONLINEARSTRAININTEGRAL       *   349
*                                    II                        II     *   350
*                                                                      *   351
*                1  A B C     A     B     C                           *   352
*             = - F       PSI   PSI   PSI                            *   353
*                6  I J K     I     J     K                           *   354
*                                                                      *   355
*                                                                      *   356
*                1                          AA    AA BB               *   357
*          UG = - NONLINEARSTRAININTEGRAL    CC                       *   358
*                2                          II                       *   359
*                                                                      *   360
*                                                                 BB   *   361
*                                     * NONLINEARSTRAININTEGRAL       *   362
*                                                                 II   *   363
*                                                                      *   364
*                1   A B C D     A     B     C     D                  *   365
*             = -- G         PSI   PSI   PSI   PSI                     *   366
*                12  I J K L     I     J     K     L                  *   367
*                                                                      *   368
*                                                                      *   369
*          A B   A B C   A B C D                                       *   370
*     and K    , F     , G          are completely symmetric under     *   371
*          I J   I J K   I J K L                                       *   372
*     interchange of pairs of indices, each pair consisting of a       *   373
*     superscript index and the subscript index directly beneath it.   *   374
*                                                                      *   375
*        Then the governing equations for an individual shell element  *   376
*     have the form                                                    *   377
*                                                                      *   378
*        A B    B   1  A B C    B    C   1  A B C D    B    C    D    A *   379
*       K    PSI  + - F      PSI  PSI  + - G        PSI  PSI  PSI  = P *   380
*        I J    J   2  I J K    J    K   3  I J K L    J    K    L    I *   381
*                                                                      *   382
*                                                                      *   383
* * * * * * * * * * * * * * * * * * * * * * * * * * * * * * * * * * * *   384
*                                                                      *   385
*     Compute the UK, UF and UG contributions to the effective strain  *   386
*     energy .                                                         */$  387
                                                                           388
 UK : (1/2)*LINEARSTRESSINTEGRAL[I,II] . LINEARSTRAININTEGRAL[J,II]$       389
                                                                           390
 UF : (1/2)*2*(1/3)*                                                       391
    ( LINEARSTRESSINTEGRAL[I,II] . NONLINEARSTRAININTEGRAL[J,K,II]         392
    + LINEARSTRESSINTEGRAL[J,II] . NONLINEARSTRAININTEGRAL[K,I,II]         393
    + LINEARSTRESSINTEGRAL[K,II] . NONLINEARSTRAININTEGRAL[I,J,II])$       394
                                                                           395
 UG : (1/2)*(1/3)*                                                         396
    ( NONLINEARSTRAININTEGRAL[I,J,II].CC.NONLINEARSTRAININTEGRAL[K,L,II]   397
    + NONLINEARSTRAININTEGRAL[I,K,II].CC.NONLINEARSTRAININTEGRAL[J,L,II]   398
    + NONLINEARSTRAININTEGRAL[I,L,II].CC.NONLINEARSTRAININTEGRAL[J,K,II])$ 399
                                                                           400
```

```
/*                                                                    401
 *     Generate the linear stiffness coefficients, the K's          */$ 402
                                                                      403
  FOR A THRU NDP DO (                                                 404
     CKA:DIFF(UK,CONCAT(PSI,A)[I]),                                   405
     FOR B THRU A DO                                                  406
        DISPLAY(ARRAYMAKE(CONCAT(K,A,B),[I,J])                        407
           :: RAT(2*DIFF(CKA,CONCAT(PSI,B)[J])))))$                   408
                                                                      409
/*                                                                    410
 *     Construct a list of variables.  This list will govern the     *  411
 *        ordering of variables in the expressions for the F's and G's. *  412
 *        The input needed is the following list of names of arrays of  *  413
 *        intermediate variables which represent integrals appearing in *  414
 *        NONLINEARSTRAININTEGRAL.                                  */$ 415
                                                                      416
  LISTOFARRAYNAMES:[NNK1NK1,NNK2NK2,NNXPNXP,NNYPNYP,NNXANXA,NNYANYA,NNXANYA, 417
     NXPYP,NNK2K1,NXAK1,NXAK2,NYAK1,NYAK2]$                           418
                                                                      419
  LISTOFINDICES : [[I,J],[J,I],[I,K],[K,I],[J,K],[K,J],               420
     [I,L],[L,I],[J,L],[L,J],[K,L],[L,K]]$                            421
  RATVARSLIST : []$                                                   422
  FOR INDICES IN LISTOFINDICES DO                                     423
     FOR NAME IN LISTOFARRAYNAMES DO                                  424
        RATVARSLIST : APPEND(RATVARSLIST,[ARRAYMAKE(NAME,INDICES)])$  425
  APPLY('RATVARS,RATVARSLIST)$                                        426
/*                                                                    427
 *     Generate the F's.                                            */$ 428
                                                                      429
  FOR A THRU NDP DO (                                                 430
     CFA : DIFF(UF,CONCAT(PSI,A)[I]),                                 431
     FOR B THRU A DO (                                                432
        CFAB : DIFF(CFA,CONCAT(PSI,B)[J]),                            433
        FOR C THRU B DO                                               434
           DISPLAY(ARRAYMAKE(CONCAT(F,A,B,C),[I,J,K])                 435
              ::RAT(6*DIFF(CFAB,CONCAT(PSI,C)[K])))))$                436
/*                                                                    437
 *     Generate the G's.                                            */$ 438
                                                                      439
  FOR A THRU NDP DO (                                                 440
     CGA : DIFF(UG,CONCAT(PSI,A)[I]),                                 441
     FOR B THRU A DO (                                                442
        CGAB : DIFF(CGA,CONCAT(PSI,B)[J]),                            443
        FOR C THRU B DO (                                             444
           CGABC : DIFF(CGAB,CONCAT(PSI,C)[K]),                       445
           FOR D THRU C DO                                            446
              DISPLAY(ARRAYMAKE(CONCAT(G,A,B,C,D),[I,J,K,L])          447
                 :: RAT(12*DIFF(CGABC,CONCAT(PSI,D)[L])) )))$         448
&
```

PROGRAMMING COMMENTS

Displacement Model Program:

Line No.	Comment
80	Dollar sign as terminator means not to display results.
82	Value assignments are indicated by :
87	Function assignments are indicated by :=
91	Semi-colon as terminator means to display results.
109	Dot indicates matrix multiplication.
141	FOR loops in MACSYMA are analogous to DO loops in FORTRAN.
144	APPLY('RATVARS, [A,B,C]) is equivalent to RATVARS(A,B,C). The effect of this command is to create a list of variable names which will govern the ordering of the variables in any subsequent expression which is in the internal representation known as the "canonical rational expression" form. It has no effect on expressions in "general" form.
192	CONCAT(S,5,8) (where S is undefined) creates the variable name S58.
192	SUM(EXP,K,1,5) evaluates to $\sum_{k=1}^{5} EXP$.
258	DIFF(EXP,X) evaluates the derivative of the expression EXP with respect to X.
256	DISPLAY command is used within FOR loops to display results.
264	FORTRAN(EXP) command is used to generate and display FORTRAN source code for EXP.
288	RAT(EXP) puts EXP into canonical rational expression form, a form which consists of a quotient of polynomials.

Line No.	Comment
296	EV(EXP,EVAL) is used to evaluate EXP using information from past assignment statements.

Mixed Model Program:

Line No.	Comment
257	MEMBER(VAR,LIST) returns TRUE or FALSE depending on whether the variable VAR is in LIST or not.
258	MATCHDECLARE is used in setting up a pattern match, a replacement of one expression by another when certain preset conditions are satisfied. In this case one condition is that MEMBEROFLIST(NNN) be TRUE.
260	Here DEFRULE defines a pattern matching rule called RULE1. The second argument of DEFRULE is to be replaced by the third argument in whatever expression the rule is applied to.
261	DEFINE(FUNCTION,EXP) evaluates its first argument and defines it according to the second argument.
262	APPLY1(EXP,RULE) applies the pattern matching rule RULE to the expression EXP.
284	RATSUBST(EXP1,EXP2,EXP3) replaces the subexpression EXP2 by the expression EXP1 wherever it occurs in EXP3.
303	RATSIMP is a simplifier command similar to RAT.
315	GENMATRIX(ARRAY,M,N) generates an M by N MATRIX from defined elements of ARRAY.

```
* * * * * * * * * * * * * * * * * * * *
*          SAMPLE OUTPUT              *
*  FROM DISPLACEMENT MODEL PROGRAM    *
* * * * * * * * * * * * * * * * * * * *
```

Linear strain (line 113)

```
[       NK1  PSI3  + NA2  PS12  + NXA  PSI1          ]
[          K     K      K     K      K     K         ]
[                                                    ]
[       NK2  PSI3  + NYA  PSI2  + NA1  PSI1          ]
[          K     K      K     K      K     K         ]
[                                                    ]
[            NXM  PSI2  + NYM  PSI1                  ]
[               K     K      K     K                 ]
[                                                    ]
[            NA2  PSI5  + NXA  PSI4                  ]
[               K     K      K     K                 ]
[                                                    ]
[            NYA  PS15  + NA1  PSI4                  ]
[               K     K      K     K                 ]
[                                                    ]
[ NXM  PSI5  + NYM  PSI4  + NXK  PSI2  + NYK  PSI1   ]
[    K     K      K     K      K     K      K     K  ]
[                                                    ]
[         N  PSI4  + NXA  PSI3  - NK1  PSI1          ]
[          K     K      K     K      K     K         ]
[                                                    ]
[         N  PSI5  + NYA  PSI3  - NK2  PSI2          ]
[          K     K      K     K      K     K         ]
```

Nonlinear strain (line 129)

```
                NXA  PSI3  NXA  PSI3    NK1  PSI1  NXA  PSI3    NXP  PSI2  NXP  PSI2    NYP  PSI1  NXP  PSI2
                  J     J    K     K      J     J    K     K      J     J    K     K      J     J    K     K
     MATRIX([-------------------- - -------------------- + -------------------- - --------------------
                         2                   2                   2                   2

   NXP  PSI2  NYP  PSI1    NYP  PSI1  NYP  PSI1    NXA  PSI3  NK1  PSI1    NK1  PSI1  NK1  PSI1
     J     J    K     K      J     J    K     K      J     J    K     K      J     J    K     K
 - -------------------- + -------------------- - -------------------- + --------------------],
            2                   2                   2                   2

 NYA  PSI3  NYA  PSI3    NK2  PSI2  NYA  PSI3    NXP  PSI2  NXP  PSI2    NYP  PSI1  NXP  PSI2    NYA  PSI3  NK2  PSI2
   J     J    K     K      J     J    K     K      J     J    K     K      J     J    K     K      J     J    K     K
[-------------------- - -------------------- + -------------------- - -------------------- - --------------------
          2                   2                   2                   2                   2

   NK2  PSI2  NK2  PSI2    NXP  PSI2  NYP  PSI1    NYP  PSI1  NYP  PSI1
     J     J    K     K      J     J    K     K      J     J    K     K
 + -------------------- - -------------------- + --------------------],
            2                   2                   2

 NXA  PSI3  NYA  PSI3    NK1  PSI1  NYA  PSI3    NYA  PSI3  NXA  PSI3    NK2  PSI2  NXA  PSI3    NXA  PSI3  NK2  PSI2
   J     J    K     K      J     J    K     K      J     J    K     K      J     J    K     K      J     J    K     K
[-------------------- - -------------------- + -------------------- - -------------------- - --------------------
          2                   2                   2                   2                   2

   NK1  PSI1  NK2  PSI2    NYA  PSI3  NK1  PSI1    NK2  PSI2  NK1  PSI1
     J     J    K     K      J     J    K     K      J     J    K     K
 + -------------------- - -------------------- + --------------------], [0], [0], [0], [0], [0])
            2                   2                   2
```

Linear stress matrix (line 175)

$$
\text{Col 1} = \begin{bmatrix}
CC16\,NYM/K + FF16\,NYK/K + CC11\,NXA/K + CC12\,NA1/K \\
CC26\,NYM/K + FF26\,NYK/K + CC12\,NXA/K + CC22\,NA1/K \\
CC66\,NYM/K + FF66\,NYK/K + CC16\,NXA/K + CC26\,NA1/K \\
FF16\,NYM/K + DD16\,NYK/K + FF11\,NXA/K + FF12\,NA1/K \\
FF26\,NYM/K + DD26\,NYK/K + FF12\,NXA/K + FF22\,NA1/K \\
FF66\,NYM/K + DD66\,NYK/K + FF16\,NXA/K + FF26\,NA1/K \\
-CC55\,NK1/K \\
-CC45\,NK1/K
\end{bmatrix}
$$

$$
\text{Col 2} = \begin{bmatrix}
CC12\,NYA/K + CC16\,NXM/K + FF16\,NXK/K + CC11\,NA2/K \\
CC22\,NYA/K + CC26\,NXM/K + FF26\,NXK/K + CC12\,NA2/K \\
CC26\,NYA/K + CC66\,NXM/K + FF66\,NXK/K + CC16\,NA2/K \\
FF12\,NYA/K + FF16\,NXM/K + DD16\,NXK/K + FF11\,NA2/K \\
FF22\,NYA/K + FF26\,NXM/K + DD26\,NXK/K + FF12\,NA2/K \\
FF26\,NYA/K + FF66\,NXM/K + DD66\,NXK/K + FF16\,NA2/K \\
-CC45\,NK2/K \\
-CC44\,NK2/K
\end{bmatrix}
$$

$$
\text{Col 3} = \begin{bmatrix}
CC12\,NK2/K + CC11\,NK1/K \\
CC22\,NK2/K + CC12\,NK1/K \\
CC26\,NK2/K + CC16\,NK1/K \\
FF12\,NK2/K + FF11\,NK1/K \\
FF22\,NK2/K + FF12\,NK1/K \\
FF26\,NK2/K + FF16\,NK1/K \\
CC45\,NYA/K + CC55\,NXA/K \\
CC44\,NYA/K + CC45\,NXA/K
\end{bmatrix}
$$

$$
\text{Col 4} = \begin{bmatrix}
FF16\,NYM/K + FF11\,NXA/K + FF12\,NA1/K \\
FF26\,NYM/K + FF12\,NXA/K + FF22\,NA1/K \\
FF66\,NYM/K + FF16\,NXA/K + FF26\,NA1/K \\
DD16\,NYM/K + DD11\,NXA/K + DD12\,NA1/K \\
DD26\,NYM/K + DD12\,NXA/K + DD22\,NA1/K \\
DD66\,NYM/K + DD16\,NXA/K + DD26\,NA1/K \\
CC55\,N/K \\
CC45\,N/K
\end{bmatrix}
$$

$$
\text{Col 5} = \begin{bmatrix}
FF12\,NYA/K + FF16\,NXM/K + FF11\,NA2/K \\
FF22\,NYA/K + FF26\,NXM/K + FF12\,NA2/K \\
FF26\,NYA/K + FF66\,NXM/K + FF16\,NA2/K \\
DD12\,NYA/K + DD16\,NXM/K + DD11\,NA2/K \\
DD22\,NYA/K + DD26\,NXM/K + DD12\,NA2/K \\
DD26\,NYA/K + DD66\,NXM/K + DD16\,NA2/K \\
CC45\,N/K \\
CC44\,N/K
\end{bmatrix}
$$

Linear stiffness coefficients - KK (lines 254-258)

```
KK11     = S31  NYM  + S61  NYK  + S11  NXA  - S71  NK1  + S21  NA1
   I, J      I    J      I    J      I    J      I    J      I    J

KK21     = S32  NYM  + S62  NYK  + S12  NXA  - S72  NK1  + S22  NA1
   I, J      I    J      I    J      I    J      I    J      I    J

KK22     = S22  NYA  + S32  NXM  + S62  NXK  - S82  NK2  + S12  NA2
   I, J      I    J      I    J      I    J      I    J      I    J

KK31     = S33  NYM  + S63  NYK  + S13  NXA  - S73  NK1  + S23  NA1
   I, J      I    J      I    J      I    J      I    J      I    J

KK32     = S23  NYA  + S33  NXM  + S63  NXK  - S83  NK2  + S13  NA2
   I, J      I    J      I    J      I    J      I    J      I    J

      KK33     = S83  NYA  + S73  NXA  + S23  NK2  + S13  NK1
         I, J      I    J      I    J      I    J      I    J

KK41     = S34  NYM  + S64  NYK  + S14  NXA  - S74  NK1  + S24  NA1
   I, J      I    J      I    J      I    J      I    J      I    J

KK42     = S24  NYA  + S34  NXM  + S64  NXK  - S84  NK2  + S14  NA2
   I, J      I    J      I    J      I    J      I    J      I    J

      KK43     = S84  NYA  + S74  NXA  + S24  NK2  + S14  NK1
         I, J      I    J      I    J      I    J      I    J

       KK44     = S64  NYM  + S44  NXA  + S54  NA1  + S74  N
          I, J      I    J      I    J      I    J      I  J

KK51     = S35  NYM  + S65  NYK  + S15  NXA  - S75  NK1  + S25  NA1
   I, J      I    J      I    J      I    J      I    J      I    J

KK52     = S25  NYA  + S35  NXM  + S65  NXK  - S85  NK2  + S15  NA2
   I, J      I    J      I    J      I    J      I    J      I    J

      KK53     = S85  NYA  + S75  NXA  + S25  NK2  + S15  NK1
         I, J      I    J      I    J      I    J      I    J

       KK54     = S65  NYM  + S45  NXA  + S55  NA1  + S75  N
          I, J      I    J      I    J      I    J      I  J

       KK55     = S55  NYA  + S65  NXM  + S45  NA2  + S85  N
          I, J      I    J      I    J      I    J      I  J
```

Nonlinear stiffness coefficients - FF (lines 282-288)

```
FF111      = ((S21  + S11 ) NYP  + (S21  + S11 ) NYP ) NYP
   I, J, K       K      K     J       J      J     K     I

     + (S11  NK1  + S11  NK1 ) NK1  + (S21  + S11 ) NYP  NYP  + S11  NK1  NK1
           K    J       J    K     I       I      I     K    J      I    K    J

FF333      = (S23  NYA  + S33  NXA  + S23  NYA  + S33  NXA ) NYA
   I, J, K       K    J      K    J      J    K      J    K     I

 + (S33  NYA  + S13  NXA  + S33  NYA  + S13  NXA ) NXA
       K    J      K    J      J    K      J    K     I

 + (S23  NYA  + S33  NXA ) NYA  + (S33  NYA  + S13  NXA ) NXA
       I    K      I    K     J       I    K      I    K     J

FF211      = ((- S21  - S11 ) NYP  + (- S21  - S11 ) NYP ) NXP
   I, J, K          K      K     J         J      J     K     I

     + (S31  NK1  + S31  NK1 ) NK2  + (S22  + S12 ) NYP  NYP  + S12  NK1  NK1
           K    J       J    K     I       I      I     K    J      I    K    J

FF311      = (- S31  NK1  - S31  NK1 ) NYA  + (- S11  NK1  - S11  NK1 ) NXA
   I, J, K        K    J       J    K     I         K    J       J    K     I

                                      + (S23  + S13 ) NYP  NYP  + S13  NK1  NK1
                                            I      I     K    J      I    K    J

FF133      = (- S33  NYA  - S13  NXA  - S33  NYA  - S13  NXA ) NK1
   I, J, K        K    J      K    J      J    K      J    K     I

                 + (S21  NYA  + S31  NXA ) NYA  + (S31  NYA  + S11  NXA ) NXA
                       I    K      I    K     J       I    K      I    K     J

          FF411      = (S24  + S14 ) NYP  NYP  + S14  NK1  NK1
               I, J, K       I      I     K    J      I    K    J

          FF422      = (S24  + S14 ) NXP  NXP  + S24  NK2  NK2
               I, J, K       I      I     K    J      I    K    J

  FF433      = (S24  NYA  + S34  NXA ) NYA  + (S34  NYA  + S14  NXA ) NXA
       I, J, K       I    K      I    K     J       I    K      I    K     J

FF321      = (- S21  NK2  - S32  NK1 ) NYA  + (- S31  NK2  - S12  NK1 ) NXA
   I, J, K        K    J       J    K     I         K    J       J    K     I

                                      + (- S23  - S13 ) NYP  NXP  + S33  NK1  NK2
                                            I      I     K    J      I    K    J

          FF421      = (- S24  - S14 ) NYP  NXP  + S34  NK1  NK2
               I, J, K       I      I     K    J      I    K    J

             FF431      = - S34  NK1  NYA  - S14  NK1  NXA
                  I, J, K       I    K    J      I    K    J

             FF432      = - S24  NK2  NYA  - S34  NK2  NXA
                  I, J, K       I    K    J      I    K    J
```

Nonlinear stiffness coefficients - GG (lines 322-327)

```
      GG1111((I-1)*NNPE+J,K,L) = (NYP(I)*(NYP(J)*((3*CC22+6*CC12+3*CC11)
     1   *NYP(K)*NYP(L)+(CC12+CC11)*NK1(K)*NK1(L))+NK1(J)*((CC12+CC11)*N
     2   K1(K)*NYP(L)+(CC12+CC11)*NYP(K)*NK1(L)))+NK1(I)*(NK1(J)*((CC12+
     3   CC11)*NYP(K)*NYP(L)+3*CC11*NK1(K)*NK1(L))+NYP(J)*((CC12+CC11)*N
     4   K1(K)*NYP(L)+(CC12+CC11)*NYP(K)*NK1(L))))/2.0
      GG3333((I-1)*NNPE+J,K,L) = (NXA(I)*(NXA(J)*(NYA(K)*((2*CC66+CC12)*
     1   NYA(L)+3*CC16*NXA(L))+NXA(K)*(3*CC16*NYA(L)+3*CC11*NXA(L)))+NYA
     2   (J)*(NXA(K)*((2*CC66+CC12)*NYA(L)+3*CC16*NXA(L))+NYA(K)*(3*CC26
     3   *NYA(L)+(2*CC66+CC12)*NXA(L))))+NYA(I)*(NXA(J)*(NXA(K)*((2*CC66
     4   +CC12)*NYA(L)+3*CC16*NXA(L))+NYA(K)*(3*CC26*NYA(L)+(2*CC66+CC12
     5   )*NXA(L)))+NYA(J)*(NXA(K)*(3*CC26*NYA(L)+(2*CC66+CC12)*NXA(L))+
     6   NYA(K)*(3*CC22*NYA(L)+3*CC26*NXA(L)))))/2.0
      GG2111((I-1)*NNPE+J,K,L) = -(NK2(I)*(NK1(J)*((-CC26-CC16)*NYP(K)*N
     1   YP(L)-3*CC16*NK1(K)*NK1(L))+NYP(J)*((-CC26-CC16)*NK1(K)*NYP(L)+
     2   (-CC26-CC16)*NYP(K)*NK1(L)))+NXP(I)*(NYP(J)*((3*CC22+6*CC12+3*C
     3   C11)*NYP(K)*NYP(L)+(CC12+CC11)*NK1(K)*NK1(L))+NK1(J)*((CC12+CC1
     4   1)*NK1(K)*NYP(L)+(CC12+CC11)*NYP(K)*NK1(L))))/2.0
      GG3111((I-1)*NNPE+J,K,L) = -(NYA(I)*(NK1(J)*((CC26+CC16)*NYP(K)*NY
     1   P(L)+3*CC16*NK1(K)*NK1(L))+NYP(J)*((CC26+CC16)*NK1(K)*NYP(L)+(C
     2   C26+CC16)*NYP(K)*NK1(L)))+NXA(I)*(NK1(J)*((CC12+CC11)*NYP(K)*NY
     3   P(L)+3*CC11*NK1(K)*NK1(L))+NYP(J)*((CC12+CC11)*NK1(K)*NYP(L)+(C
     4   C12+CC11)*NYP(K)*NK1(L))))/2.0
      GG1333((I-1)*NNPE+J,K,L) = -NK1(I)*(NXA(J)*(NYA(K)*((2*CC66+CC12)*
     1   NYA(L)+3*CC16*NXA(L))+NXA(K)*(3*CC16*NYA(L)+3*CC11*NXA(L)))+NYA
     2   (J)*(NXA(K)*((2*CC66+CC12)*NYA(L)+3*CC16*NXA(L))+NYA(K)*(3*CC26
     3   *NYA(L)+(2*CC66+CC12)*NXA(L))))/2.0
      GG2211((I-1)*NNPE+J,K,L) = (NXP(I)*(NXP(J)*((3*CC22+6*CC12+3*CC11)
     1   *NYP(K)*NYP(L)+(CC12+CC11)*NK1(K)*NK1(L))+NK2(J)*((-CC26-CC16)*
     2   NK1(K)*NYP(L)+(-CC26-CC16)*NYP(K)*NK1(L)))+NK2(I)*(NK2(J)*((CC2
     3   2+CC12)*NYP(K)*NYP(L)+(2*CC66+CC12)*NK1(K)*NK1(L))+NXP(J)*((-CC
     4   26-CC16)*NK1(K)*NYP(L)+(-CC26-CC16)*NYP(K)*NK1(L))))/2.0
      GG3311((I-1)*NNPE+J,K,L) = (NXA(I)*(NYA(J)*((CC26+CC16)*NYP(K)*NYP
     1   (L)+3*CC16*NK1(K)*NK1(L))+NXA(J)*((CC12+CC11)*NYP(K)*NYP(L)+3*C
     2   C11*NK1(K)*NK1(L)))+NYA(I)*(NXA(J)*((CC26+CC16)*NYP(K)*NYP(L)+3
     3   *CC16*NK1(K)*NK1(L))+NYA(J)*((CC22+CC12)*NYP(K)*NYP(L)+(2*CC66+
     4   CC12)*NK1(K)*NK1(L))))/2.0
      GG3211((I-1)*NNPE+J,K,L) = (NXA(I)*(NK2(J)*((-CC26-CC16)*NYP(K)*NY
     1   P(L)-3*CC16*NK1(K)*NK1(L))+NXP(J)*((CC12+CC11)*NK1(K)*NYP(L)+(C
     2   C12+CC11)*NYP(K)*NK1(L)))+NYA(I)*(NK2(J)*((-CC22-CC12)*NYP(K)*N
     3   YP(L)+(-2*CC66-CC12)*NK1(K)*NK1(L))+NXP(J)*((CC26+CC16)*NK1(K)*
     4   NYP(L)+(CC26+CC16)*NYP(K)*NK1(L))))/2.0
      GG2133((I-1)*NNPE+J,K,L) = -(NK2(I)*NK1(J)*(NXA(K)*((-2*CC66-CC12)
     1   *NYA(L)-3*CC16*NXA(L))+NYA(K)*((-2*CC66-CC12)*NXA(L)-3*CC26*NYA
     2   (L)))+NXP(I)*NYP(J)*(NXA(K)*((CC26+CC16)*NYA(L)+(CC12+CC11)*NXA
     3   (L))+NYA(K)*((CC22+CC12)*NYA(L)+(CC26+CC16)*NXA(L))))/2.0
```

Computers & Structures. Vol. 13, pp. 405–413. 1981
Printed in Great Britain.

0045-7949/81/010405-09$02.00/0

ARCHITECTURE OF A DISTRIBUTED ANALYSIS NETWORK FOR COMPUTATIONAL MECHANICS

CARLOS A. FELIPPA†

Applied Mechanics Laboratory, Lockheed Palo Alto Research Laboratory,
Lockheed Missiles & Space Co., Inc., Palo Alto, CA 94304, U.S.A.

(*Received* 9 *May* 1980)

Abstract—An integrated software system called NICE (Network of Interactive Computational Elements) is presently under development at the Applied Mechanics Laboratory. The overall purpose of this development is to further the formulation, implementation and application of advanced computational methods in fluid and solid mechanics. From a software engineering standpoint, system design stresses functional modularity, decentralization, adaptability to interactive computing environments, and ability to accommodate research, development, analysis and testing activities. A clear separation is established between architectural elements such as analysis control and data management, and result-productive computational components called processors. This paper gives a functional overview of the NICE architecture, for which the author is responsible. Control functions that shape the user's perception of the system are emphasized.

1. BACKGROUND

During the past decade, there has been steady demand for expanding capacity and improving throughput of engineering analysis software. This demand has been fueled by requests for more realistic modelling capabilities, growing interest in interdisciplinary problems, and pressure for the establishment of computer-based interaction among design, engineering, testing, and manufacturing organizations.

How have these requirements been met? Usually by patching up old software, or by developing new software based on unstructured, monolithic programming techniques. The predictable result has been software that is unreliable, difficult to use, costly to modify and maintain, overly dependent upon a small group of "insiders" who wrote it, and operable only on a specific computer system.

Why have users put up with such monstrosities? There has been little choice. Those responsible state that large, tightly-coupled centralized systems bring economies of scale. Computer time is a precious commodity, they argue, not to be wasted by lowly humans. (The Godzilla syndrome climaxed in the late 1960s, when it was seriously suggested that eventually one do-everything, gigantic computer program implemented on a pyramid of supercomputers would be sufficient to fulfill the needs of all engineering organizations in the U.S.A.).

Meanwhile, what has happened to computing? On the software side, technical breakthroughs in the early 1970s have by now crystallized into concepts and products such as structured programming, generalized database management, flexible control structures, and "friendly" operating systems. These tools have been sucessfully applied in fields as diverse as real-time simulation, information retrieval, business data processing, and manufacturing control. On the hardware side, impressive advances in microelectronics have led to the availability of vastly more powerful, yet low-cost hardware.

The impact of these advances on scientific computing, particularly engineering analysis, has not been impressive. This delay can be ascribed to a combination of reasons; among which overspecialization has certainly played a key role. Although scientific computing constitutes only a comparatively small portion of the overall data processing market, it is a portion that usually demands highly specialized skills. A closed-world atmosphere tends to foster the "software guru" problem. It is perhaps not surprising then that many organizations, through no obvious fault of their own, eventually become captive of highly complex systems that transcend the comprehension of developers and users alike.

Distributed processing

The first computer revolution was launched by the appearance of the stored-program digital computer on a commercial scale. There followed a period of rapid but centralized growth characterized by "the machine as wondrous object". The second computer revolution took shape by the mid-1970s, and was rooted in the appearance of LSI circuits. Resulting economic shock waves brought a decentralization trend in which more and more power is placed at the local level.

Computer hardware now extends over a fairly unbroken spectrum ranging from supercomputers to tiny microprocessors. Economies of scale have changed: no longer is the larger machine the most cost-effective. Realization of this fact initiated the boom of distributed processing, in which functionally specialized machines of varying power can talk to each other. The original concept was that of a tree of linked machines sprouting from a big mainframe and eventually ending at user terminals. This "pyramidal" view is now being superseded by more decentralized models. For example, a local computer network might consist of a high-performance minicomputer that communicates with

†Staff Scientist.

personal microcomputers on one side and with large "corporation database" machines on the other; in this model, number-crunching services are provided by specialized local machines, rather than a giant supercomputer.

Learning a lesson

It is natural to translate — with due caution — these decentralized hardware organization models into engineering analysis software. Many potentially useful concepts and tools are now here: top-down software design, structured implementation, interactive (and soon portable) operating systems, concurrent programming, database management technology.

The dominant theme of such an effort should be restoration of human pre-eminence through conceptual simplicity and functional modularization. Quoting Kernighan and Plauger ([1], p. 83): "we consistently take the view that people cost a lot more than machines, and that the disparity will increase in the future. Therefore the most important consideration is that people get their jobs done with a minimum of fuss and bother".

2. THE GENESIS OF NICE

The decision

After two decades of development of scientific and engineering software at the Applied Mechanics Laboratory (AML), a decision was made in 1979 to construct an integrated software system for computational mechanics. The decision was prompted by factors such as software development becoming a major component of in-house activities, many technology contracts calling for machine-transportable production level codes, and perception of a rapidly changing computational environment (Section 1).

A key challenge in building the integrated software system has been to accomodate the following conflicting usage requirements.

Research environment. Flexible and visible "white box" analysis flow; prompting conversational control; easy access to intermediate results; foolproof ways for branching "out of the system" into owncode and back again; human flow-time critical; computational efficiency, extensive error crosschecking and problem adaptivity unimportant.

Production environment. Ability to hide analysis details in "black box" fashion; aids for minimizing input preparation efforts; extensive data validity and consistency crosschecking; elaborate display facilities; ability to dispatch jobs to linked computers; reasonably efficient utilization of computer resources; problem adaptivity desirable.

Design guidelines

A real danger in trying to meet both extremes (with growth potential thrown in) is that another overcomplex monster may result. This would cripple it from birth. To forestall this danger, the following design guidelines were agreed upon.

(1) Clear-cut separation between computational and architecture components, with the latter being developed in advance.

(2) A network organization for independently executable computational elements called processors.

(3) Processors data-coupled through a common, online, global database.

(4) Multilevel control system based on a mnemonic command language.

(5) Modularity enforced by common architecture components and processor configuration standards.

Simple economics suggests that many processors will be prepared by the time-honored "divide and conquer" technique, i.e. cannibalization of useful portions of obsolescent monolithic codes. This heterogeneous provenance of processors dictates a database-coupled organization [2–4].

High operational flexibility calls for a system organization in which processor execution order is unconstrained, that is, a network. This "macro-flow" is generally unknown in advance, and may be changed by conversational users on the spur of the moment. A similar requirement dictates the use of a problem-oriented command language for micro-flow "white box" guidance within a processor.

Finally, adaptation to the production end as well as growth provisions strongly suggests a multilevel control structure. The underlying idea is that a user should not have to know more about software operations than that necessary for accomplishing his tasks. Inasmuch as one starts with a basic command language at the research end, a logical way to move toward the "smart black box" end relies on providing user-selectable procedural levels of increasing detail-concealing power.

NICE does it

Finding a happy name for the system turned out to be the toughest decision. After many proposals, it appears that NICE (Network of Interactive Computational Elements) has the inside track. It certainly lends itself to a bevy of puns, saws, and double entendres.

3. ARCHITECTURE AND PROCESSORS

Architecture

The first design guideline listed in Section 2 calls for clear separation between productive computational functions on the one hand, and overhead functions such as control and data management on the other. The latter constitute the system architecture. (The term is used here in the sense of "a style and method of design and construction".) Architectural software serves three major functions.

Control. General methods for guiding analysis flow among network processors (macro flow), and within each processor (micro flow).

Data management. General methods for creating and maintaining online databases for residence of volatile and permanent data structures.

Program library. General methods for developing and maintaining source code executable on a variety of machines and environments.

In this paper the control function will be emphasized on two accounts: it offers the most novel (unpublished) features, and it strongly shapes the user's perception of the system.

Processors

Within the context of a database-coupled program network, the term *processor* is used here to mean an executable software element that performs a distinct

productive function, and communicates with other processors only through the global database. (For more extensive nomenclature, see [3] or Appendix A.)

Figure 1 provides an overall view of the NICE system while an individual processor is under interactive control of a living user. The processor is shown as a "split coconut" to display its shell/kernel structure; further organizational details are provided in Appendix B.

First things first

Following modern programming methods [5–7], design of the architectural components proceeds first. Implementation preceeds that of any production-level processor by a reasonable lead time, estimated to be about a year in our case. This schedule does not imply isolated development, however; instead, production-level architecture software is first exercised on a pilot network of miniprocessors.

Why this separation? For most existing large-scale scientific codes, "architecture" developments have been *post-facto* reactions to crisis situations; e.g. moving to an interactive environment. Poorly planned development has led to some weird "spaghetti bowl" concoctions such as "data management systems" that do matrix calculations! Also, interwoven computational-architecture components die together when the program becomes obsolete. This wouldn't be so bad in itself, but cannibalization of potentially useful segments for building processor kernels (Appendix B) can then become excruciatingly painful.

Two NICE views

We may distinguish between two "dual" views of the NICE system as a network of connected processors. In the *processor-oriented* view sketched in Fig. 2(a), the processor is the fundamental entity. Think of the processor as a ship moving through a sea of data. The largely-volatile working data pictured as the ship's wake is the local database, which bears the brunt of processor activity. When the processor stops, the wake disappears. Beyond that extends the calmer sea of the global database.

In the *database-oriented* view sketched in Fig. 2(b), the global database is the fundamental entity, which effectively characterizes the network state over a timespan substantially exceeding that of individual processor executions. Processors may be abstractly viewed as auxiliary "data machines" (Fig. 3) through which global database contents are slowly modified.

The processor-oriented view is natural in research projects, which emphasize actions and algorithms. As one moves into production analysis and large engineering projects, the database-oriented view dominates. Readers familiar with computer science terminology may recognize similarities with action- and object-oriented conceptual views of modern programming languages [8].

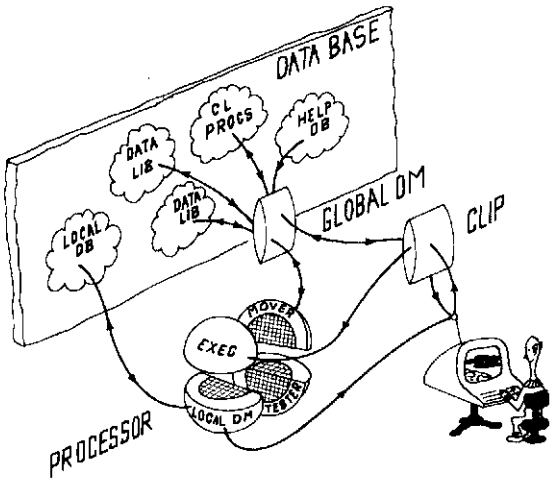

Fig. 1. NICE assembly schematics: Common architectural components (Global data manager, CLIP); "Split" running processor showing shell (executive, tester, local data manager and global–local mover) and kernel; database plane (data libraries, command language procedures, help database, local database); user.

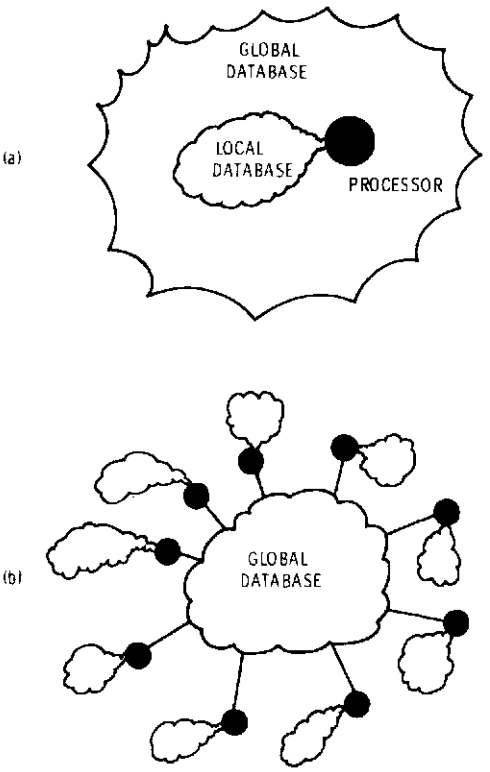

Fig. 2. Dual views of NICE system: (a) processor-oriented; (b) global-database-oriented.

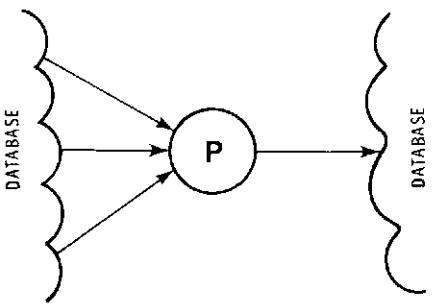

Fig. 3. Processor abstraction as "data machine".

4. PROCESSOR CONTROL

Let's examine the operation of a processor from the processor-oriented viewpoint. First we have to define some terms used in Fig. 1.

User. The beneficiary of the processor activity. A human user guiding the processor from an online terminal provides the simplest example. In more advanced situations, "surrogate users" in the form of smart non-human controllers and schedulers may assume the guidance role.

Running processor. The NICE processor under execution.

Global data manager. The software element through which the global database is accessed.

CLIP (*Command Language Interface Program*). A software element that works as a 3-way fixture for control and communication purposes. It is the only control system component that "accompanies" a running processor. Command language syntax details are covered in [9].

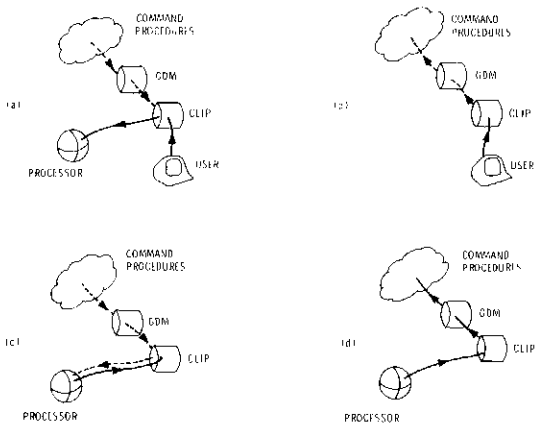

Fig. 4. User-processor-database operating modes: (a) Processor command; (b) User directive; (c) Processor directive; (d) Message.

Operating modes

The main function provided by CLIP is the support of various operation modes. These are briefly described below in increasing order of "whizziness".

The standard operating mode is the *processor-command mode*, depicted in Fig. 4(a). Commands may be either supplied directly by the user (solid line) or extracted from a command procedure residing on the global database (dashed line). These commands are interpreted by the processor executive.

The *user-directive mode* is illustrated in Fig. 4(b). Directives are special commands identified by a leading keyword whose first character is an asterisk. Directives are interpreted directly by CLIP while the processor stays "out of the loop".

Two especially important directives are: definition of a command procedure (headed by a *PROCEDURE keyword), and reference to an existent procedure (headed by a *CALL keyword). Processing of these directives travels the dashed-line path of Fig. 4(b). Transition from processor-command to user-directive mode is automatic. Once the directive is processed, CLIP returns to processor-command mode except while creating a procedure, in which case it waits for an *END directive (procedure definition being the only instance of a multi-command directive.)

Figure 4(c) depicts *processor-directive mode*. The processor supplies a directive or stream of directives to CLIP for immediate execution. A particularly important case, shown in dashed lines, is a *CALL directive that initiates reading of a command procedure. Transfer to processor-directive mode is effected via a processor reference to an "interrupt" entry point in CLIP. The processor-CLIP ensemble stays in this mode until the processor signals transfer to processor-command mode. The user remains "out of the loop" throughout.

Finally, the *message mode*, illustrated in Fig. 4(d), is an advanced variant of the processor-directive mode. The processor emits to CLIP a command procedure intended for downstream use by another processor. CLIP effectively functions as a "mailbox" through which the procedure is placed in the global database. Although the user is not directly involved in this action, he may access the message if desired.

To read the message, the target processor enters processor-directive mode and issues a *CALL [Fig. 4(c), dashed line]. The message mode forms the basis for synchronizing execution of NICE "mininetworks" to carry out complex computational processes such as coupled-system dynamics or optimization.

Data management

Only a brief picture of NICE data management will be given here, as the subject is treated in detail in Refs. [2–4]. Its key feature is distinction between two types of data management: local and global. Local management serves intra-processor operations, while global management serves inter-processor operations.

Local data management

A local database is an organized collection of working data used by a running processor. Although part of the data may survive program execution (e.g. for quick self-restarts), it is inaccessible outside of the processor.

In the construction of local database models, heavy emphasis is generally placed upon efficient utilization of scratch storage resources such as high-speed memory, extended core, drums, and paging disks. Consequently, local managers tend to be "made to order" to fit specific processors, and it is inappropriate to speak of *the* local database manager. Instead, a basic-level manager called VMSYST [10] is recommended for new processors. VMSYST is a virtual memory simulator based on a demand-paging scheme. There is also a basic utility called the "global-local mover", which effects transfers of data structures between the global database and a VMSYST-controlled local database. Both the local manager and mover are viewed as constituents of the processor "shell".

Based on these two utilities, high-level local managers can be built to support specific needs. An example of these is a "nested matrix manager" that handles multilevel matrix structures arising in substructuring and model-partitioning tasks.

Global data management

The global database serves as network skeleton and circulatory system. It implements facilities for medium- to long-term storage of processor-generated data structures, command procedures, and help documentation (see Fig. 1). It is partitioned into *data libraries*

residing on permanent disk files. A data library is an indexed file organization containing data sets identified by name. A library may be stored as data set of another, a "telescoping" operation useful for tape archival. There is a common global database manager called EZ-GAL [11], which provides two levels of service: processor support and stand-alone library access. The global manager shares the same I/O access method with VMSYST.

The global database is the architectural aspect that immediately impacts users "moving up the system" (Section 5). As such, its main attribute should be ease of use rather than computational efficiency. To accomplish this goal, global data structures should not only be readily identifiable, but subject to strict representation and self-description standards, and protected by various integrity checks.

5. WHAT THE USER SEES

It was noted in Section 2 that the architecture should be unobtrusive with regard to user tasks. In this section we examine the "incremental" aspect of the control functions in support of increasingly demanding usage levels.

Calculator level

A staff researcher is faced with the problem of performing some simple matrix calculations to complete a study contract. Just before leaving for a better-paying job in Silicon Valley, his programmer has kindly told him that processor MUP (Matrix Utility Processor) can do the job. So he swallows his pride, walks to a free CRT and logs in. Breezily following the NICE Primer, he starts MUP execution. On response to the first command prompt, he enters

DECLARE MATRIX ALFA (carriage return)

Too late, he suddenly remembers that the type and order of ALFA must be also given. However, MUP does not seem fazed; it prompts: TYPE? Taken by surprise, the user types WHAT? The processor responds

Type must be REAL, DOUBLE, INTEGER, CHAR
TYPE?

The user answers REAL. MUP now prompts: ORDER? And so it goes. After a while, the user gets in the "rythm" of MUPspeak. By trial and error, as well as occassional Manual consultations, he learns to load matrix values, print, edit, do operations. In a few hours the job is done and he triumfantly returns to his desk with a bunch of CRT hardcopies.

This example depicts the ultimate "white box": calculator level. A continuous dialogue is established between processor and user. The latter is aware of each calculation step, may check and recheck inputs, intermediate calculations, and final results. Most algorithmic decisions take place in the user's brain: the processor is just an arithmetic helper. At no time is the user aware of the existence of global or local databases, command interpreter, processor shell; all of this is irrelevant to the application.

True, use of a processor as a virtual hand-held calculator is extremely wasteful of machine time. (Such use should really be carried out on a personal microcomputer.) But it is very effective as far as human time is concerned, which is what matters. NICE users finish first.

The helping calculator

Next we find our programmerless hero working at home on a borrowed terminal, struggling to finish another project. He is again talking to friendly MUP. But amidst a complex calculation sequence, he suddenly can't recall the syntax of a critical command. Trial and error is out, saving run state is out (remember, he doesn't know about the global database), and, being absent-minded, has left the Manual at the office. Desperate, he tries HELP, and wonderful things happen: MUP informs him that a help library (whatever that is) has been attached; that "command help mode" has been entered; and finally displays a menu of help qualifiers. Yes, there is the one! He enters the appropriate qualifier and suddenly a condensed section of the MUP Manual is printed. To get out of help mode, he is told to type END HELP; MUP says that the help library has been released, and is ready to accept the next computational command.

The NICE architecture saved our hero when he didn't even know of its existence. On intercepting the cry for HELP, MUP entered processor-directive mode (Section 4), and issued a stream of directives to CLIP. The first directive resulted in the attachment of a global-database-resident help library for MUP. Condensed Manual sections pertaining to each MUP command were therein stored as command procedures, with their content "defused" as comments.

The "help menu" is merely a table of command procedure names. When the user requests concise help on command ADD, for example, he enters HELP ADD; this causes MUP to re-enter the processor-directive mode and emit an appropriate *CALL preceded and followed by directives controlling terminal display format. The end result is that help text appears magically on the terminal.

This help mechanism offers some nice features. Any help library can be accessed from any running processor (default being that processor's library) at any moment. There is no need to store help text in the processor itself. Accessing and display procedures are part of a uniform architecture external to the processor. Text centralization minimizes documentation lags. Interim changes or fixes can be rapidly posted as command procedure text to be *CALL-displayed at processor execution start.

The calcunet level

Our hero has done so well in the last project that he lands a juicy follow-on involving far more complex calculations. Preliminary study reveals that the project calls for

(1) Some matrices to be generated by NICE processors SH, RD and LU, before being presented to MUP;

(2) Some matrices to be generated by user-written code, because no NICE processor would make them;

(3) Results from MUP to be postprocessed by another user-written code before being sent to a NICE graphics processor.

From conversations with other NICE users, our researcher becomes aware of the existence of the global database, and its usefulness for moving data among NICE processors as well as between NICE processors and owncode. He quickly grasps that data structures such as matrices can be saved or retrieved from any NICE processor by learning a few commands. To do

this from owncode is a bit trickier, as more details about global database organization (e.g. data library creation and access, table-of-contents fields, data set storage) have to be mastered; but it is not a big deal.

We have just sketched the calculator-network level, or "calcunet" for short. A user working at this level is necessarily aware of the existence of multiple NICE processors and the global database; and of possible use of the latter for transmitting data between processors and owncode. He need not be aware of local databases or fancy command-driven control modes.

The procedure level

For most research work the computational facilities provided by the calcunet level are sufficient. But as one gets into real-world applications, the detailed, command-by-command guidance of processor activities soon becomes intolerable. (The same thing may be said for repetitive research tasks involving parameter studies.) It is then time to move to the command procedure level. This level provides:

(a) detail-hiding representation of tasks expressable as groups of commands;

(b) looping (DO WHILE) and branching (IF) conconstructs controlled by user-defined or processor-set PARAMETER-like variables;

(c) an "encapsulation" mechanism for entities such as processor-originated messages (Section 4) and help text;

(d) processor developers the ability to define macro-like extensions from basic commands right up to the "smart black box" level.

A NICE command procedure can have a very general structure. In essence it consists of a header identifier, an optional list of formal arguments, a "procedure template" body, and a terminator. A fairly trivial example:

```
*PROCEDURE ADD X TO Y (X; Y; Z)
.Z.=.X.+.Y.
*END ADD X TO Y
```

A possible reference:

```
*CALL ADD X TO Y (Z=RESULT; X=OP1;
Y=OP2)
```

Here OP1, OP2 and RESULT are local matrix names, which replace period-delimited matching text in the procedure body. Replacement takes place *before* the command is processed, so that the net effect of the *CALL is equivalent to issuing the command

```
RESULT=OP1+OP2
```

For this trivial example the use of a procedure is obviously not worth the trouble, but the situation is different when one confronts hundreds or thousands of commands.

The keyword-driven, call-by-name mechanism allows great freedom in designing high-level language constructs. For example, an actual argument may be a stream of commands or directives, a procedure name or even the text of another procedure! A procedure may call another procedure; the call tree may extend down to 12 levels. A procedure may call itself, which greatly facilitates production of recursive control systems for things such as nested generation of discrete models.

To make effective use of this level, the user's knowledge of the global database (in which procedures reside) has to be augmented by a fairly deep understanding of the command language. Armed with such knowledge, a programmer-user may be able to hook his own processors to CLIP. A detailed knowledge of local data management, however, is not yet required.

The macroprocessor level

We finally arrive at the operational level for which NICE was primarily designed: computational processes of interest in advanced nonlinear dynamics and optimization. Two examples:

(1) A coupled-field mechanical model is being numerically integrated by a partitioned solution procedure [12, 13]. This involves "almost cyclic" the execution of matrix processors. The execution flowpath may run sequentially or in parallel; some processors may be linear, others nonlinear. There may be irregularly spaced breakpoints corresponding, e.g., to step-size changes, automatic state save (for possible restarts), or user interrupts.

(2) A mechanical system is being optimized under the direction of a mathematical programming processor. This involves repeated execution of analysis processors such as structural stress, vibration and stability analyzers, in response to optimizer requests. Irregular references to other auxiliary processors (e.g. a full Hessian calculation) may occur.

We see that computer analysis of these problems leads naturally to "quasi-cyclic" processor execution streams. Hands-on guidance, even with the help of command procedures, may become tedious (impossible, of course, in batch operation). Two "processor ensemble" constructs, macroprocessors and mininet works (often abbreviated to mapros and mininets) cater to these applications. As mininets can contain macroprocessors, we deal with the latter first.

A macroprocessor is constructed by tightly bundling a set of processors so that their local databases coalesce. For this to be feasible, the same local data manager and global-local mover must be used. A master command procedure is written as control "wrapper". This procedure consists basically of one big loop; references to lower-level processor-driving procedures appear during loop traversal. In addition, the master procedure should take care of run contingencies via branchs and interrupts. A mapro online user effectively assumes the role of a spectator watching a "smart black box" perform like a trained seal, and intervenes only on breakpoint emergencies.

This tightly-coupled organization aims at high computational efficiency, as intermediate results can share scratch workspace instead of using up permanent online storage resources. Macroprocessors may be regarded as "problem customized" processors that are discarded once the problem is solved. (As they are not maintained, the question of monolithic code build-up does not arise.) Whoever puts a mapro together must have a deep knowledge of command procedures, command interpretation shells, and the use of local databases as communication media.

The mininet level

The most advanced usage level considered here is the mininetwork. This is a set of processors and/or macroprocessors that talk to each other via messages (Section 4). The master procedure of the mapro level is

impersonated here by a "go-between" controller called the *mininet scheduler* (MNS).

To illustrate the approach, consider an implicit time integration control processor that decides that a step-size change would be a good idea. To continue the integration process, the dynamic stiffness matrix has to be reformed and factored. But the time integrator does not contain matrix processing facilities; it is only an overseer. Also, a NICE processor is forbidden to execute another directly. So the integrator prepares a command procedure encoded in the language of the target matrix processor detailing "things to do", puts it into the global database, and goes into hibernation. The MNS, which regularly awakens, detects the message and calls the matrix processor into action. The latter enters processor-directive mode, reads the message, performs the operations, leaves the results in the global database, and writes a "job done" message. MNS then wakes up the integrator, which resumes activities.

Who writes MNS? Another program; in fact, an intelligent analysis controller [3]. But this would take us too far up the system.

The mininet mode offers some appealing features: it maximizes modularity, permits different local databases, easily adapts to parallel processor executions, and can be readily monitored by online users.

The message-driven coroutine mechanism just described in old hat in computer science. But at this level we may encounter a major stumbling block: the host operating system. It is very difficult, or even downright impossible, to implement satisfactorily such control sequences on the medieval operating systems of most large mainframes. But it is easy on modern operating systems such as VAX/VMS, UNIX or SOLO, which offer standard facilities for task synchronization (e.g. mailboxes, pipelines, semaphores). The fact that most of these "friendly" yet powerful operating systems are offered on minicomputers (and even microcomputers) tells us something about where the action is.

6. CENTRAL DIFFERENCE INTEGRATION

To illustrate the appearance of macroprocessors and mininetworks in nonlinear dynamics applications, let's consider the explicit time integration of an undamped mechanical model obeying the equations of motion

$$\mathbf{M}\ddot{\mathbf{x}} + \mathbf{F}_S(\mathbf{x}) = \mathbf{F}_A(t) \tag{1}$$

In eqn. (1), $\mathbf{x}$ is the state displacement vector, $\mathbf{M}$ the mass matrix, $\mathbf{F}_S(\mathbf{x})$ the internal stiffness force vector and $\mathbf{F}_A(t)$ the applied force vector. (More complex examples are discussed in [13, 14].) Now the variable step central difference algorithm of [15] for (1) is:

(a) Given: $\mathbf{x}_n$ and $\dot{\mathbf{x}}_{n-1/2}$ at time station $t = t_n$;
(b) evaluate force vectors $\mathbf{F}_{Sn}$ and $\mathbf{F}_{An}$;
(c) select next stepsize $h = t_{n+1} - t_n$;
(d) $\dot{\mathbf{x}}_{n+1/2} = \dot{\mathbf{x}}_{n-1/2} + h\mathbf{M}^{-1}(\mathbf{F}_{An} - \mathbf{F}_{Sn})$ (2)
(e) $\mathbf{x}_{n+1} = \mathbf{x}_n + h\dot{\mathbf{x}}_{n+1/2}$
(f) $n := n+1$; repeat.

For step (c), access to $\mathbf{x}_{n-1}$ and $\dot{\mathbf{x}}_{n-3/2}$ is required.

The algorithm (2) may be represented in the standard data flow diagram of structured design [5] as depicted in Fig. 5. The three main computational components, shown as "bubbles", are:

(I) Integrator: estimates stepsize, advances solution;
(A) Analyzer: calculates internal force vector;
(F) enForcer: obtains next applied force vector.

It is important to understand that in a data flow diagram, "bubbles" (I), (A) and (F) are not yet physical processors, but abstractions of processors as in Fig. 3. However, the data flow diagram does suggest ways in which processors can be written and connected.

There is much to be said for coding the integrator (I) as a separate processor, which can be checked and tuned-up once and for all. But the force evaluators (A) and (F) are more problem-dependent. In particular, the analyzer may be fairly complex if stiffness force calculations require access to a library of nonlinear finite elements. The applied forcer (F), on the other

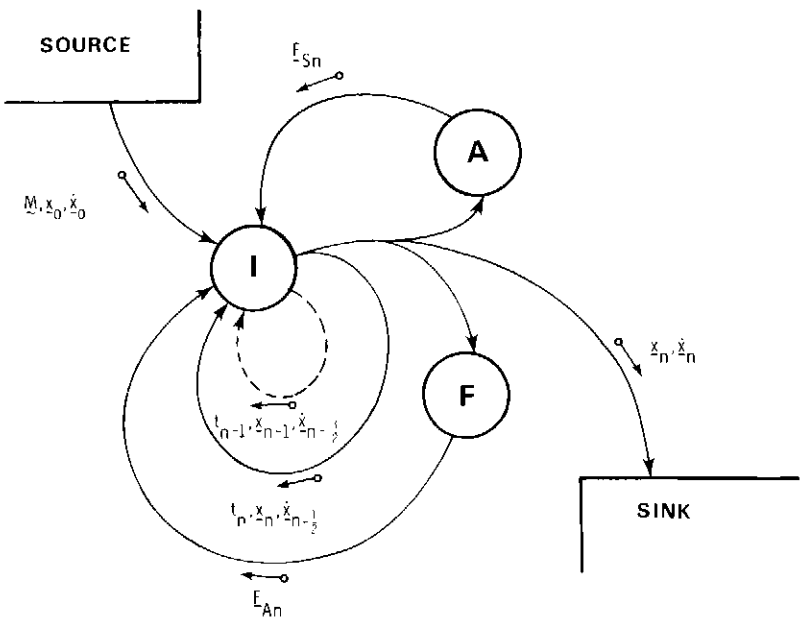

Fig. 5. Data flow diagram (after [5]) of central difference time integration for nonlinear structural dynamics.

hand, is usually simpler and can often be user-coded as needed (e.g. to access and digitize an explosion or earthquake record), and discarded when done.

The three processors may be linked in macroprocessor or mininetwork form. One virtue of the latter is that (F) and (A) may be executed in parallel (see. Fig. 5) should that prove useful. Now suppose that the mass matrix **M** varies with time; incorporation of such a feature in a mininet structure would be fairly trivial as it would not affect the internal logic of (A) and (F); or even that of (I) provided the stepsize control logic accounts for possible mass variations.

7. CONCLUDING REMARKS

There is a synergistic effect in program co-operation. Their combined power can be much greater than their aggregate power as isolated entities. A simple example: a structure and a fluid analyzer can, by themselves, solve certain problems in structural and fluid mechanics; if they can be made to work together, a "tensor product" domain of fluid-structure interaction problems can be handled. Through this approach, a vast range of problems in nonlinear mechanics can be attacked by an assorted combination of tools from a "computational benchmark" [16]. This viewpoint encourages growth in lieu of reinvention.

In view of obvious payoffs, why has program integration been so difficult? Because if an unstructured approach is followed, increases in application power are rapidly overwhelmed by the nonlinear growth in program complexity [17]. The whole thrust of modern software engineering is to devise techniques that abate or eliminate this growth. The architecture described herein is merely an expression of these techniques biased toward a particular application environment.

Acknowledgements—The author thanks his colleagues Thomas L. Geers and Philip Underwood for many productive comments. Implementation of the NICE pilot network has been partly supported by the Defense Nuclear Agency. The preparation of this paper was supported by the Independent Research Program of Lockheed Missiles and Space Co., Inc.

REFERENCES

1. B. W. Kernighan and P. J. Plauger, *Software Tools*. Addison-Wesley, Reading, Mass. (1976).
2. C. A. Felippa, Database management in scientific computing—I. General description, *Comput. Structures* **10**, 53–61 (1979).
3. C. A. Felippa, Database management in scientific computing—II. Data structures and program architecture, *Comput. Structures*, **12**, 1. 131–146 (1980).
4. C. A. Felippa, Database management in scientific computing—III. Implementation, in preparation.
5. E. Yourdon and L. L. Constantine, *Structured Design*. Prentice-Hall, Englewood Cliffs, New Jersey (1979).
6. R. C. Tausworthe, *Standardized Development of Computer Software*, (2 vols). Prentice-Hall, Englewood Cliffs, New Jersey (1977).
7. R. T. Yeh (Ed.), *Current Trends in Program Development*, Vol. II. Prentice-Hall, Englewood Cliffs, New Jersey (1978).
8. P. Wegner, Programming languages—concepts and research directions, in: *Research Directions in Software Technology* (Edited by P. Wegner). The MIT Press, Cambridge, Mass., 425–489 (1979).
9. C. A. Felippa, A command language for applied mechanics processors, LMSC-D633582. Lockheed Palo Alto Research Laboratory, Palo Alto, California (1980).
10. P. S. Jensen, A FORTRAN virtual storage simulator for non-virtual computers, LMSC-D676222. Lockheed Palo Alto Research Laboratory, California (1978).
11. C. A. Felippa, The global database manager EZ-GAL, Document LMSC-D678210. Lockheed Palo Alto Research Laboratory, Palo Alto, California (1980).
12. K. C. Park, Partitioned integration procedures for transient analysis of coupled field problems: stability analysis. *J. Appl. Mech.* **87**, 370–376 (1980).
13. C. A. Felippa and K. C. Park, Staggered transient analysis of coupled mechanical systems. *Comp. Meth. Appl. Mech. Engng* to appear (1980).
14. C. A. Felippa and K. C. Park, Direct time integration methods in nonlinear structural mechanics. *Comp. Meth. Appl. Mech. Engng.* **17/18**, 277–313 (1979).
15. K. C. Park and P. G. Underwood, A variable step central difference method for structural dynamics analysis I. Theoretical aspects, *Comp. Meth. Appl. Mech. Engng.* **22**, 241–258 (1980).
16. E. L. Ivie, The programmer's workbench—a machine for software development. *Comm. ACM*, **20**, 746–753 (1977).
17. J. D. Aron, *The Program Development Process*. Addison-Wesley, Reading, Mass. (1978).
18. D. M. Ritchie and K. Thompson, The UNIX time-sharing system. *Comm. ACM*. **17** (7), 365–375 (1974).

APPENDIX A

Glossary

CLIP—Command Language Interface Program. A communications controller described in Sec. 4.

Closed Interface- An interface in which communication is effected by supplying address/name pointers to data structures.

Command—A statement of a command language, translated as an individual action.

Command Language— An interpretable language used to guide processor execution in step-by-step fashion.

Controller—A software element whose primary function is to direct the activities of other software elements.

Converter— A kernel processor with single data structure input.

Database- In generic terms, a named collection of data organized according to a data model, and serving a specific purpose.

Data library—A named partition of a global database, which can be attached to a running processor as a physical, directly accessible entity.

Data set—A named sequence of logical records.

Distributed database—A global database partitioned over several computer systems.

Global database- A database residing on permanent online storage and accessible by a network of communicating programs.

Help database—A global database containing program documentation text for online examination by interactive users.

Interface –The point (or set of points) in a software element at which control or data is received or transmitted.

Kernel processor—A processor that generates only one data structure as its main product.

Local database—A database attached to, and accessible only by, a running program.

Logical module (also: *bubble*)—The conceptual visualization of a software element as a "data machine" that performs a specific function.

Macroprocessor (also: *mapro*) -An assembly of processors bundled by a master command procedure and communicating through a common local data manager.

Manager (Data)—A software element whose primary function is to store, maintain and retrieve data.

Mininetwork (also: *mininet*)- A subnetwork of processors and macroprocessors bundled by an message-handling controller and communicating only through the global database.
Mininet scheduler -A mininetwork task-synchronization controller.
Module (also: *box, physical module*)—The implementation of a logical module as a cohesive software element with closed and regular interfaces.
NICE Network of Interactive Computational Elements. The program network discussed in this paper.
NICE processor- A processor organized as a primary module, and which meets the guidelines stated in Appendix B.
Primary module A module implemented as an independently executable program.
Processor -A software element whose primary function is the production of data structures.
Processor kernel -The productive nucleus of a NICE processor.
Processor shell— A layer of software that interfaces a NICE processor kernel with external architectural components such as CLIP and the global manager. (Terminology suggested by the UNIX system [18].)
Program network (also: *network*)—A set of controllers and processors communicating through a common global database manager.
Regular interface -An interface organized so that the software element is minimally coupled with its environment, in the sense of Yourdon–Constantine [5].
Routine— A processor that does not meet NICE standards.
Software element—An aggregate of computer-processable statements identified by a name, and communicating with its access environment through well-defined interfaces.
Temporary database—The portion of a local database that disappears upon run termination.
Utility (also: *software tool*)- -A module that provides actual or potential support to several higher-order modules, but is not command executable. The main purpose of a utility program is to help develop other programs.
Working database -The database upon which a running program operates at a given moment. It embodies its local database as well as possibly segments of the global database.

APPENDIX B

Processor characteristics

Below is a summary of general characteristics of NICE processors, which may be of interest to software designers faced with a similar development. Although some requirements may be altered in light of pilot-network experiences, the overall design is expected to be stable.
Composition: shown in Fig. 6. A computational kernel is surrounded by a protective shell (a la UNIX). The shell contains four overhead components: executive, tester, local data manager, and global-local mover. The executive is a control interface that receives or submits commands via

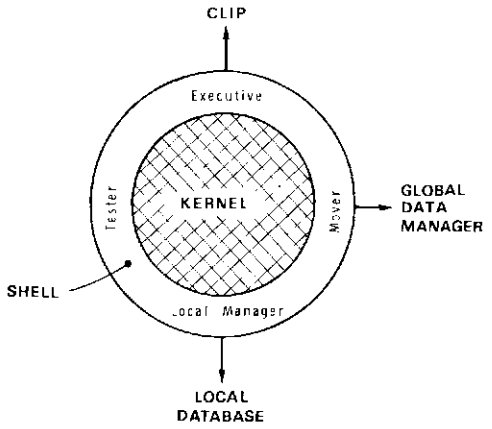

Fig. 6. Internal structure of a NICE processor.

CLIP (see Section 4). The tester is a self-contained command-driven checker that exercises kernel operations. The data management components are described in Section 4.
Development: there is only one processor developer, who remains responsible for maintenance. An "usage license fee" might be instituted to build maintenance funds. For new processors, top–down design and implementation as well as incremental testing are strongly recommended.
How big: we are talking about fairly small processors; typically having 500–10000 kernel statements. (Independently executable program modules of present large-scale analysis codes are an order of magnitude bigger: generally 10000–100000 statements.)
How many: probably 100–200 produced at a 20–50 yearly rate. Complemented by hundreds of user-written, not-so-NICE routines, which eventually are either discarded or enhanced into processors.
Control: a processor, including its tester, can only be executed through command statements. The choice of command interpretation and action translation is left at the developer's discretion.
Internal modularity: kernel should not talk directly to the global data manager. Communication with the local data manager and global-local mover is to be confined to high kernel levels.
Language: FORTRAN 77 recommended. Other languages such as PASCAL are acceptable if appropriate FORTRAN linkages are provided.
Local data management: processors potentially useful as macroprocessor components (Section 5) must use same local data manager and global-local mover utility.
Error checking and firewalls: in processors especially susceptible to erroneous or inconsistent inputs, 1/4 to 1/2 of kernel programming should be devoted to data validation and attendant protection mechanisms.

Computers & Structures, Vol. 13, pp. 415–423, 1981
Printed in Great Britain.

0045-7949/81/010415-09$02.00/0

MAGNA: A FINITE ELEMENT SYSTEM FOR THREE-DIMENSIONAL NONLINEAR STATIC AND DYNAMIC STRUCTURAL ANALYSIS

ROBERT A. BROCKMAN
University of Dayton Research Institute, Dayton, OH 45469, U.S.A.

(*Received* 9 *May* 1980)

Abstract—The finite element solution program MAGNA, developed for the nonlinear analysis of three-dimensional structures, is described. The program contains a fully compatible library of nonlinear elements, permitting shells, solids and other members to be joined in virtually any combination. Element-level computations, whose efficiency is critical in three-dimensional analysis, are discussed, and a method of implementation is described which eliminates a number of large matrix manipulations and produces highly vectorizable code. Applications are presented to demonstrate the capabilities and efficiency of the program. General areas of research which are necessary for the improvement of efficiency in three-dimensional nonlinear analysis are also discussed.

INTRODUCTION

Nonlinear finite element analysis experiencing a growing popularity in the aerospace, nuclear and automotive industries as a means of assessing structural integrity and safety under extreme service conditions. Structural problems involving large-displacements, plastic deformation or buckling instabilities can presently be analyzed with considerable confidence, to reduce the time and cost associated with preliminary design and design qualification.

Most practical problems, however, are truly three-dimensional, and the required nonlinear analysis so costly that undesirable simplifications are introduced in the finite element calculations. In this regard, it is generally stated that equation-solving represents the bulk of the computational effort in any finite element analysis. In three-dimensional nonlinear solutions, particularly with higher-order elements, this is often decidedly not the case: computations performed at the individual element level (nonlinear stiffness, force residuals) may in fact account for as much as 90% of the total computing cost. Relatively little research effort has been devoted to increasing the efficiency of these element-level algorithms, in spite of the fact that significant improvement in this area is necessary if three-dimensional nonlinear calculations are to be performed cost effectively.

Additional difficulties arise in many practical applications in which it becomes necessary to combine continuum finite elements (e.g. isoparametric solids) with other elements based upon specialized formulations (beams, plates or shells). The inherent incompatibility of these two classes of elements as implemented in most programs dictates the use of special constraints to enforce the desired displacement compatibility between elements. However, the need to consider rotational degrees of freedom which are not vector quantities makes the correct specification of these constraints particularly difficult. In nonlinear analysis, the precise interpretation of incremental rotations also becomes important, increasing the likelihood of errors in the model.

This paper describes the finite element solution program MAGNA (Materially And Geometrically Nonlinear Analysis), which has been developed specifically to treat practical problems in which general modeling capabilities and the consideration of three-dimensional nonlinear effects are required. Particular attention has been afforded the two problem areas mentioned above. The element-level computational procedures have been designed for efficiency in treating nonlinear elements with many degrees of freedom and relatively large bandwidth. For modeling flexibility, all of the finite elements in MAGNA are fully compatible, permitting plates, shells, solids and other components to be joined in virtually any combination.

The subsequent presentation includes a brief theoretical description, a summary of the MAGNA finite element library, and a discussion of some of the numerical procedures used for nonlinear element calculations. Some typical applications are discussed, and future areas of research and development are outlined. For additional description of the program, the interested reader should consult Ref. [1].

THEORETICAL CONSIDERATIONS

The nonlinear analysis performed by MAGNA is incremental in nature; a total Lagrangian description of motion is used, in which all kinematic and force quantities are referred to the initial configuration of the structure. The governing equations for a single increment between times t and $t+\Delta t$ derive from the principle of virtual work in the form [1, 2]:

$$\int_{{}_0V} [{}_tD_{ijkl}\,{}_te_{kl}\delta e_{ij} + {}_ts_{ij}\delta\eta_{ij} - {}_0\rho\ddot{u}_i\delta u_i]\,\mathrm{d}V - \int_{{}_0V} {}^{(t+\Delta t)}f_i\delta u_i\,\mathrm{d}V - \int_{{}_0A} {}^{(t+\Delta t)}t_i\delta u_i\,\mathrm{d}A + \int_{{}_0V} [{}_ts_{ij}\delta\,{}_te_{ij} + {}_0\rho\,{}_t\ddot{u}_i\delta u_i]\,\mathrm{d}V = 0. \quad (1)$$

Here a left subscript indicates the time at which a particular quantity is evaluated, and lack of a left subscript denotes an incremental value. In keeping with the

Lagrangian formulation, e_{ij} represents the (incremental) Green St. Venant strain tensor, which is divided into linear and nonlinear components

$$e_{ij}=\varepsilon_{ij}+\eta_{ij} \tag{2}$$

where

$$\varepsilon_{ij}=\tfrac{1}{2}(u_{i,j}+u_{j,i}+{}_tu_{k,i}u_{k,j}+{}_tu_{k,j}u_{k,i}) \tag{3}$$

$$\eta_{ij}=\tfrac{1}{2}u_{k,i}u_{k,j} \tag{4}$$

and s_{ij} are the increments of the symmetric Piola–Kirchhoff stress tensor [3]. The body forces ${}_{(t+\Delta t)}f_i$ and surface tractions ${}_{(t+\Delta t)}f_i$ are understood to be the forces acting on the body at time $t+\Delta t$, per unit initial volume and area, respectively. The instantaneous tangent modulus tensor ${}_tD_{ijkl}$ at small strains, is determined using the engineering stress–strain curve of a material.

Upon discretization by the finite element method, eqn (1) becomes

$$({}_t\mathbf{K}_T+{}_t\mathbf{K}_G)\dot{\mathbf{U}}+{}_0\mathbf{M}\ddot{\mathbf{U}}={}_{(t+\Delta t)}\mathbf{P}-{}_t\mathbf{R}-{}_0\mathbf{M}_t\dot{\mathbf{U}}. \tag{5}$$

Equation (5) is nonlinear and, after discretization with respect to time, can be solved iteratively for the nodal displacement increments $\mathbf{U}$. The major computational tasks in the nonlinear finite element solution are the formation of the tangent stiffness $\mathbf{K}_T$, the geometric stiffness $\mathbf{K}_G$ and the internal forces $\mathbf{R}$, the repeated solution of the resulting system, and updating of the state of stress and strain within individual finite elements.

The formulation leading to eqn (5) is sufficiently general to include large displacements, elastic–plastic deformations, and static or dynamic instability. All of the finite elements in MAGNA are based upon the governing equations outlined above, either directly or with slight modifications. Elastic–plastic calculations are performed directly in terms of the Piola stress and Green's strains for efficiency; this simplification involves the assumption of small strains and is generally not restrictive in practice. For the solution of dynamic response problems, eqn (5) is discretized in time using the generalized Newmark's method [4, 5], which leads to the simultaneous equations

$${}_t\mathbf{K}_{\text{eff}}\mathbf{U}={}_{(t-\Delta t)}\mathbf{P}_{\text{eff}}-{}_t\mathbf{R}-{}_0\mathbf{M}_t\dot{\mathbf{U}} \tag{6}$$

which must be solved at each increment. The matrix ${}_t\mathbf{K}_{\text{eff}}$ is the "effective stiffness matrix", a linear combination of the instantaneous stiffness, mass and damping matrices; ${}_{(t+\Delta t)}\mathbf{P}_{\text{eff}}$ represents the "effective load vector", which depends upon the current mechanical and inertial forces acting on the model. The choice of an implicit method of integration in time is appropriate for most problems involving three-dimensional continua, since critical time steps for explicit integration tend to become quite small when solid elements are are used.

FINITE ELEMENT LIBRARY

Perhaps the most unique feature of the MAGNA program is its fully compatible family of elements, which permits thin plates, shells, three-dimensional solids, membrane-type elements and truss members to be joined in virtually any combination. Compatibility of displacements on all interelement boundaries is automatically enforced, eliminating the need for the specification of constraints between dissimilar element types.

For the three-dimensional solid elements (Fig. 1), the element displacement shape functions are constructed using a variable-number-of-nodes scheme which permits the use of from 8 to 27 node points per element. The shape function algorithm is a generalization of the 8–21 node procedure due to Bathe and Wilson [6], and permits the definition of roughly one-half million different nodal patterns. This facility provides considerable flexibility in constructing transitions between coarse and fine regions of a finite element model. An additional useful feature of the solid element implementation is the ability to treat individual elements selectively, as "tangent-stiffness" elements (corresponding to eqn (5)), "pseudo-force" elements (in which nonlinear effects in eqn (5) are collected on the right-hand side of the equations), or "averaged-tangent-stiffness" elements (see the following section on element-level calculations). The option of specifying the method of accounting for nonlinear effects separately for each element can lead to considerable cost savings in many problems. In addition to the 8–27 variable-number-nodes element, the program contains separately programmed versions of the eight-, sixteen-, and twenty-node isoparametric solids, as well as a variable-node element based on a maximum of twenty nodes per element.

Shell analysis is performed using elements based upon the penalty function formulation of Refs. [7, 8]. Equation (1) is rewritten in terms of locally shallow shell coordinates, and penalty terms are appended which enforce the conditions of thin shell behavior in the limit of element size. The most important feature of the element, shown in Fig. 2, is its complete compatibility of displacements, on all external surfaces, with standard isoparametric solid elements; thus, shell-solid transitions or layered sandwich-type constructions can be modeled without difficulty. Arbitrarily large displacements and rotations can be considered, as well as shells with nonstandard edge conditions, and lateral boundaries which do not coincide with the direction normal to the shell midsurface. Higher-

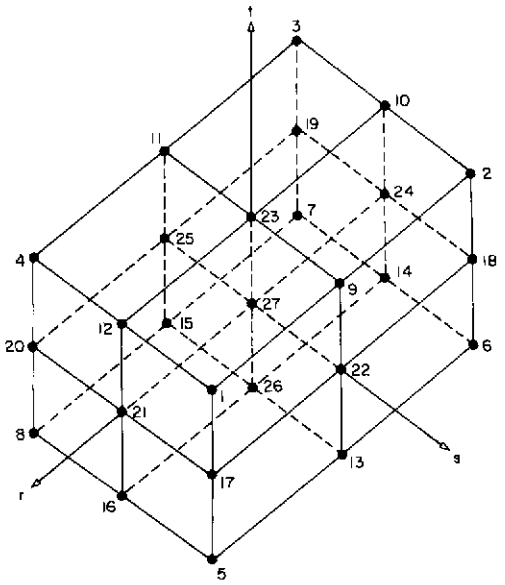

Fig. 1. Three-dimensional isoparametric solid element.

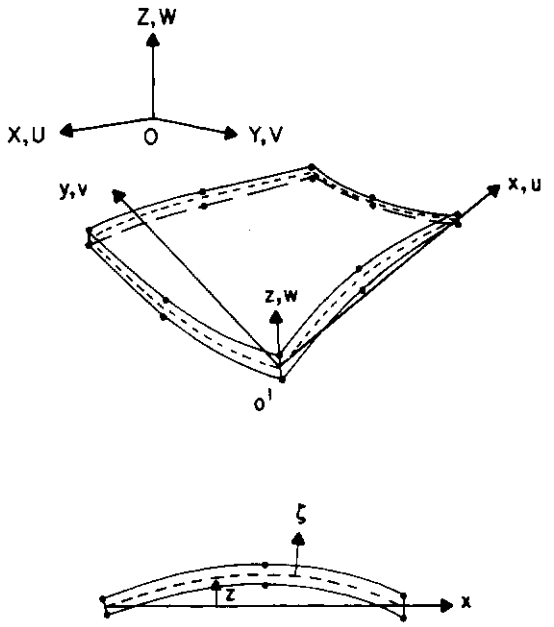

Fig. 2. Penalty function shell element.

order versions of this element and a compatible beam element formulation are under development.

ELEMENT LEVEL COMPUTATIONS

In three-dimensional, nonlinear elements, the choice of an algorithm for evaluation of the matrices of eqn (5) is crucial to overall analysis efficiency, since

(a) three-dimensional elements generally possess a relatively large number of degrees of freedom per element, and

(b) the operations generally must be performed numerous times during a nonlinear solution.

A breakdown of computing times for a typical nonlinear static solution using isoparametric solid elements is given in Table 1. The analysis consists of 16 loading increments, performed with a five-element model (20 nodes/element) having 147 degrees of freedom. Element and system stiffness matrices are recomputed at each increment. Table 1 shows that about ten times as much CPU time is spent on element-level calculations as on equation solving. Although this particular example is quite small, these proportions do not change significantly for problems an order of magnitude larger.

The basis of a number of algorithms for evaluating the element stiffness matrix is based upon the use of the incremental stress–strain and linearized strain–displacement relations in matrix form,

$$\mathbf{s} = \mathbf{D}\mathbf{e} \tag{7}$$

$$\mathbf{e} = {}_t\mathbf{B}\mathbf{u}, \tag{8}$$

along with the finite element approximation

$$\mathbf{u} = \mathbf{N}\mathbf{U} \tag{9}$$

where $\mathbf{U}$ are the nodal displacements. The tangent stiffness matrix for an element then becomes

$${}_t\mathbf{K}_T = \int_{{}_0V} \mathbf{N}^T {}_t\mathbf{B}^T {}_t\mathbf{D}\, {}_t\mathbf{B}\mathbf{N}\, \mathrm{d}V. \tag{10}$$

Equation (10) can be evaluated by numerical integration to form ${}_t\mathbf{K}_T$. The matrix multiplications can be performed directly, or a factored form employed,

$${}_t\mathbf{K}_T = \int_{{}_0V} {}_t\mathbf{F}^T {}_t\mathbf{F}\, \mathrm{d}V \tag{11}$$

where

$${}_t\mathbf{F} = {}_t\mathbf{D}^{1/2} {}_t\mathbf{B}\mathbf{N} \tag{12}$$

and ${}_t\mathbf{D}^{1/2}$ represents the Cholesky factor of ${}_t\mathbf{D}$. The required operations in either case are quite expensive, involving numerous inner products between relatively short vectors. In geometrically nonlinear analysis, ${}_t\mathbf{B}$ is a function of the deformation gradients, while in materially nonlinear problems, ${}_t\mathbf{D}$ may also vary within an element; thus, the integrand of eqn (10) must be completely reformed at each integration point. Even the use of sparse matrix algorithms does not improve efficiency to an acceptable level.

In the present development, a modification of the element stiffness algorithm proposed by Gupta and Mohraz [9] is used to improve the effectiveness of three-dimensional element calculations. Let Δ be a

Table 1. Distribution of computing time for a small 3-D nonlinear analysis

Function	Times Performed	Total CPU Sec+	Percentage
Input and File Initialization	1	0.254	0.5
Matrix Assembly	16	1.651	3.2
Equation Solution	16	4.336	8.5
Loads Processing	16	0.330	0.6
Element-Level Computations	17	43.342	84.8
Solution Recovery	16	1.214	2.4
TOTAL	-	51.127	100.0

+All computing times for the CYBER-175 computer (CPU speed approximately 2X CDC 6600)

vector of incremental displacement gradients,

$$\Delta^T = [u_{,x}\ u_{,y}\ u_{,z}\ v_{,x}\ v_{,y}\ v_{,z}\ w_{,x}\ w_{,y}\ w_{,z}]. \tag{13}$$

The linearized incremental strains are then written as

$$\mathbf{e} = {}_t\mathbf{C}\Delta, \tag{14}$$

and the tangent stiffness is defined by

$$\delta\mathbf{U}^T {}_t\mathbf{K}_T\mathbf{U} = \int_{{}_0V} \delta\Delta^T \mathbf{C}_t^T \mathbf{D}_t \mathbf{C}\Delta \, \mathrm{d}V. \tag{15}$$

If the vector of incremental nodal displacements is partitioned as

$$\mathbf{U}^T = [\mathbf{U}_1^T \mathbf{U}_2^T \mathbf{U}_3^T], \tag{16}$$

so that

$$u_i = \mathbf{N}\mathbf{U}_i, \tag{17}$$

then the element stiffness can be arranged in a similar fashion,

$${}_t\mathbf{K}_T = \begin{bmatrix} \mathbf{K}_{11} & \mathbf{K}_{12} & \mathbf{K}_{13} \\ \mathbf{K}_{12}^T & \mathbf{K}_{22} & \mathbf{K}_{23} \\ {}_t\mathbf{K}_{13}^T & \mathbf{K}_{23}^T & \mathbf{K}_{33} \end{bmatrix}. \tag{18}$$

Defining the symmetric matrix

$${}_t\mathbf{G} = {}_t\mathbf{C}_t^T \mathbf{D}_t \mathbf{C} \tag{19}$$

and denoting its entries by $g_{[i,j]}$, eqn (15) is rewritten using eqn (18),

$$\sum_{i=1}^{3}\sum_{j=1}^{3} \delta\mathbf{U}_i^T \mathbf{K}_{ij}\mathbf{U}_j = \int_{{}_0V} \sum_{i=1}^{3}\sum_{j=1}^{3}\sum_{k=1}^{3}\sum_{l=1}^{3} g_{[3i-3+k,3j-3+l]} u_{i,k} u_{j,l} \, \mathrm{d}V \tag{20}$$

or

$$\mathbf{K}_{ij} = \int_{{}_0V} \sum_{k=1}^{3}\sum_{l=1}^{3} g_{[3i-3+k,3j-3+l]} \mathbf{N}^T{}_{,k}\mathbf{N}_{,l} \, \mathrm{d}V. \tag{21}$$

Equation (21) can be used to advantage in forming the element tangent stiffness, as follows. Each of the six matrices $\mathbf{N}^T{}_{,k}\mathbf{N}^T{}_{,l}$ are computed and stored in the form of vectors. Each such vector is of length n^2, where n is the number of shape functions (i.e. nodes) for the element. Matrix ${}_t\mathbf{G}$ is also formed, and the individual matrix partitions, $\mathbf{K}_{ij}$ in eqn (18), are accumulated in vector form as indicated in eqn (21). Once the results for all integration points have been summed, the vectors containing the $\mathbf{K}_{ij}$ are distributed to the proper locations in ${}_t\mathbf{K}_T$. Thus, the primary operations to be performed at each integration point are simply summations of scalars times vectors. The length of the vectors involved in these operations are relatively large (400 for a 20-node element, 729 for a 27-node element, etc.), and at most 54 such products are needed at each sampling point for the entire matrix. If properly arranged, the accumulations of the $\mathbf{K}_{ij}$ vectors into ${}_t\mathbf{K}_T$ are also vector operations, although the vector length is only of order n.

The above computational strategy is also convenient for the calculation of the geometric stiffness matrix, since

$$\delta\mathbf{U}^T {}_t\mathbf{K}_G\mathbf{U} = \int_{{}_0V} \delta\Delta^T \mathbf{S}\Delta \, \mathrm{d}V \tag{22}$$

where

$$\mathbf{S} = \begin{bmatrix} \tau & 0 & 0 \\ 0 & \tau & 0 \\ 0 & 0 & \tau \end{bmatrix} \tag{23}$$

and τ is the stress tensor. A simple modification of ${}_t\mathbf{G}$ can be used to obtain ${}_t\mathbf{K}_G$ simultaneously with ${}_t\mathbf{K}_T$ at no additional cost.

It should be noted that, in eqn (21), considerable simplification is achieved if the factors $g_{[i,j]}$ are constant within an element. This is generally the case in linear analysis. For this special case, the products $\mathbf{N}^T{}_{,i}\mathbf{N}_{,j}$ can be integrated over the element once and for all, and reused to form each partition $\mathbf{K}_{ij}$. Thus, the needed scalar/vector multiplications are performed only once rather than at each integrating point. This simplification can also be profitably employed in nonlinear analysis; if the values of $g_{[i,j]}$ in eqn (21) are replaced by weighted average values, nonlinear element matrices can be evaluated, albeit approximately, for the same cost as their linear counterparts. If the element residual forces are computed exactly, this "averaged tangent stiffness" method provides an effective approximation for use within an iterative solution strategy. This variation, which can be selected element by element in MAGNA, tends to provide faster convergence than the commonly-used modified Newton ("constant stiffness") iteration in most cases.

NUMERICAL EXAMPLES

Four numerical solutions obtained using the MAGNA program are presented below, to demonstrate its capabilities and accuracy. Analyses including elastic-plastic deformation, large displacements and rotations, and the use of shell and solid elements in combination are discussed.

Thick circular plate

The simply-supported circular plate shown in Fig. 3 is subjected to a static load applied through a rigid punch. Dimensions of the plate are radius $R = 2.61$ in. and thickness $t = 0.2615$ in. The punch is 0.375 in. in diameter. Material properties of the plate, made of strain-hardening aluminum, are $E = 10^7$ psi, $\nu = 0.325$ and $\sigma_y = 10000$ psi is the initial yield stress. The uniaxial stress–strain curve is defined by the engineering stress-strain values shown in Table 2. Experimental load-deflection data for this example have been collected by Winter and Levine (Ref. [10], Plate 4A250), and analytical results presented by Hunsaker, Haisler and Stricklin [11].

A nonlinear analysis of the plate has been performed using MAGNA, with 14 solid elements used to rep-

Table 2. Engineering stress strain data for aluminum plate

ε	σ
0.	0.
0.00995	10000.
0.01310	20000.
0.04502	28000.
0.11800	36000.
0.36311	48000.

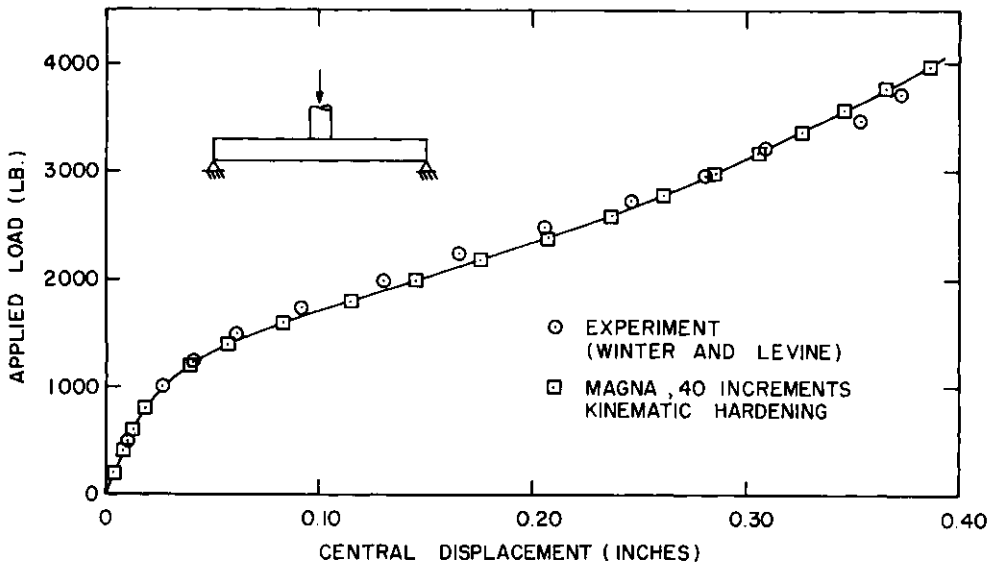

Fig. 3. Elastic–plastic analysis of center-punched circular plate.

resent one quadrant of the plate. The load-deflection solution given in Fig. 3 is obtained in 40 equal loading increments of 100 lb each, without iteration. The elastic–plastic analysis, performed using a subincremental algorithm and with kinematic hardening, shows excellent agreement with the experiment, despite the occurrence of relatively high strains (33%) at the maximum load.

Sandwich plate under pressure load

A square sandwich panel, 50 in. on each side, is subjected to uniform lateral pressure. The three-layer plate (Fig. 4) has aluminum face sheets ($E=10.5\times10^6$ psi; $\nu=0.3$), 0.015 in. thick, bonded to an aluminum honeycomb core one inch thick. The core is isotropic, with shear modulus $G=50{,}000$ psi. All lateral boundaries of the sandwich are fully clamped.

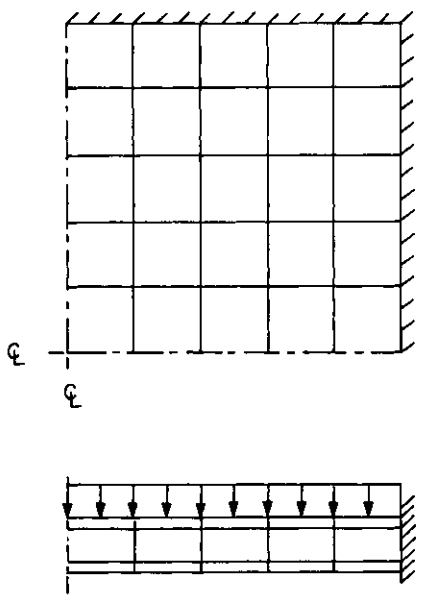

Fig. 4. Clamped sandwich panel under lateral pressure.

The finite element discretization of one quadrant of the panel consists of a total of 75 finite elements, 25 in each layer. The face sheets are modeled using eight-node, thin shell elements; three-dimensional eight-node solid elements, with a single integration point per element, are used for the sandwich core. Note that these element types are fully compatible, so that no special constraints are necessary for joining the shell and solid layers. The nonlinear solution has been obtained in load increments of one psi to a total pressure of 20 psi, followed by 2 psi increments to 30 psi.

The nonlinear central displacement of the sandwich is plotted versus load in Fig. 5. Nonlinear finite element results obtained by Monforton [12], using sixteen specially formulated bicubic sandwich elements, are shown for comparison. Agreement between the two finite element solutions is quite good. Figure 5 also shows the perturbation solution of Kan and Huang [13], which is valid for deflections smaller than the core thickness. Reasonable agreement with the two numerical solutions is observed in this region.

Clamped-hinged arch

A deep, clamped-hinged arch (Fig. 6) is subjected to a concentrated vertical load at the crown. Due to the asymmetry of the edge conditions, the arch is capable of executing extremely large, stable deflections prior to the onset of buckling. This behavior has been studied experimentally by Deutsch [14], and an analytical solution based upon Euler's inextensional theory is presented by DaDeppo and Schmidt [15]. The pre-buckling displacements, which exceed the radius of curvature, are accompanied by very large rotations; thus, the prediction of the arch response presents a demanding test of a finite element solution using thin shell elements.

The particular arch under consideration has radius of curvature $R=100$ in., thickness $t=1.0$ in., and a flexural rigidity of $EI=1.0\times10^6$ lb-in^2. The included angle is 215°. For this set of properties, the analysis of Ref. [15] indicates that stable behavior occurs up to a load of 897 lb, at which time the vertical displacement is

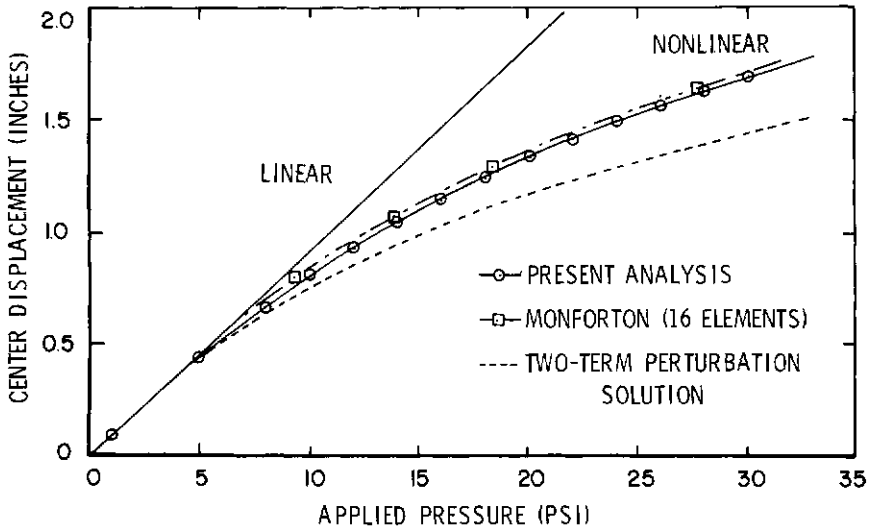

Fig. 5. Nonlinear load-deflection results for clamped sandwich plate.

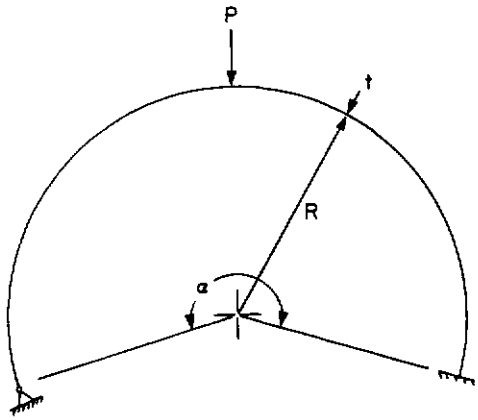

Fig. 6. Clamped-hinged arch under apex load.

113.7 in. Only prebuckling displacements are considered in the present analysis.

For the MAGNA finite element solution, the entire arch is represented by 43 thin shell elements. Displacements normal to the plane of the arch are suppressed to permit comparison with the analytical results, which do not account for finite width of the structure. The range of loading considered is 0–870 lb, applied in six equal increments. Full Newton–Raphson iterations are applied at each load step to maintain accuracy.

The deformed shape of the arch at maximum loading is shown in Fig. 7. The vertical displacement of the arch crown is slightly larger than the radius, and very large rotations are observed near the hinged support. Finite element results for the entire load-deflection history (obtained using 10-lb increments) are compared with the solution of DaDeppo and Schmidt in Fig. 8. Agree-

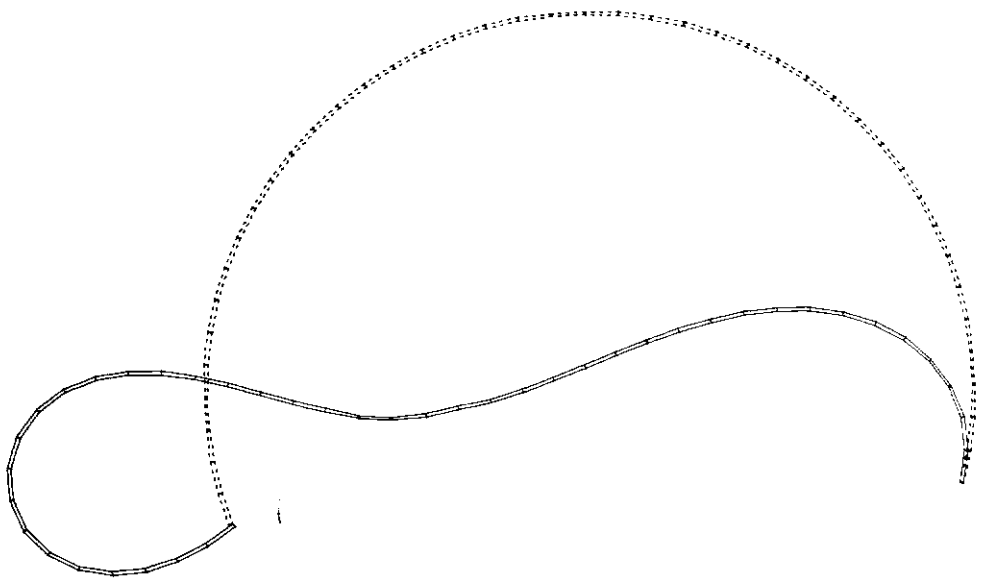

Fig. 7. Deformed arch geometry.

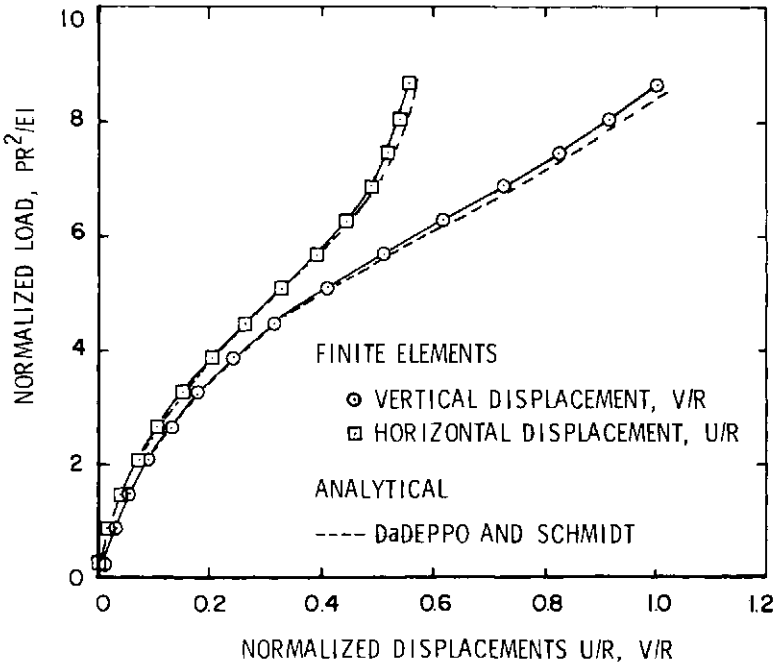

Fig. 8. Deflection history for clamped-hinged arch.

ment between the two predictions is quite good. The accuracy of the finite element solution in predicting rotations approximately eight times as large as those considered by most available thin shell theories is extremely good.

F-16 windshield canopy

The windshield transparency of the F-16 airplane is a monolithic, doubly-curved shell of polycarbonate material. Static tests of the windshield, performed as part of an impact study [16], have been reproduced numerically using MAGNA.

The undeformed geometry of one half of the canopy, modeled with 100 thin shell elements (613 degrees of freedom), is shown in Fig. 9. Line supports are assumed along the external boundaries, since the reaction forces are small for the range of loading considered. Material properties of the shell are taken to be $E=250{,}000$ psi, $\nu=0.325$. A load is applied to the windshield through a small circular pad, approximately two feet aft of the forward edge. Experimental values of the normal displacement have been obtained from deflectometer measurements on the inner surface [16].

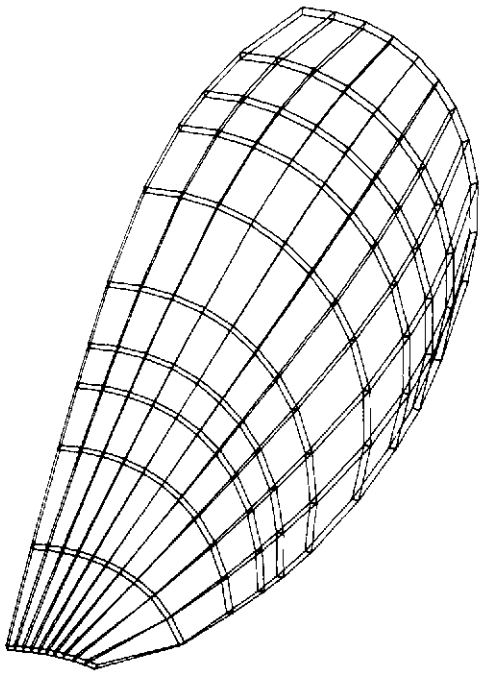

Fig. 9. Shell element model of F-16 windshield transparency.

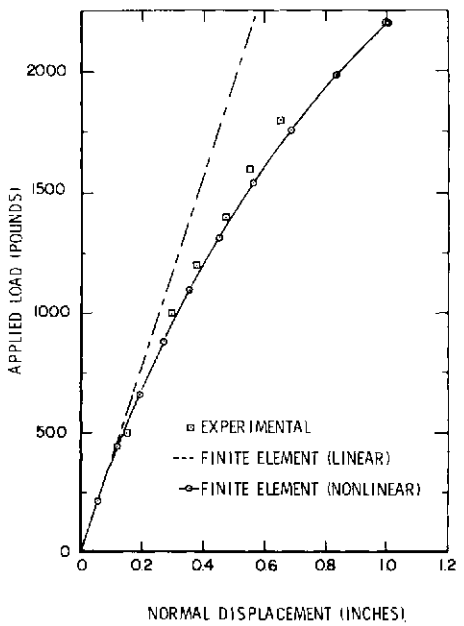

Fig. 10. Load vs deflection trace for F-16 windshield.

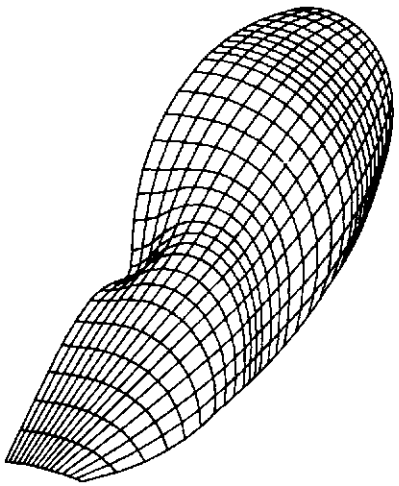

Fig. 11. Deformed F-16 canopy geometry.

Experimental and computed values of the canopy deflections, for the loading range 0–2200 lb, are compared in Fig. 10. In view of the uncertainties in material properties (about 20%), boundary conditions and local load distribution, the agreement between measured and calculated deflections is excellent. A plot of the deformed windshield geometry is shown in Fig. 11.

It is worthy of note that, though the nonlinear analysis consists of ten loading increments with all matrices recomputed at each increment, the total computing time is only 360 sec on the CDC CYBER-175. With full Newton–Raphson iterations, an almost identical solution is obtained in two increments in 250 CPU sec.

The above windshield problem has also been modeled using 3-D solid (20-node) elements, resulting in 1110 final degrees of freedom. Using a 27-point integration rule, the solid element solution yields results which are slightly stiffer than the shell analysis, but still in good agreement with the experiment. The CPU time for a ten-increment solution in this case is 920 sec on the CYBER-175. The results of nonlinear dynamic analyses performed for the F-16 using MAGNA are presented in Ref. [17].

FUTURE DEVELOPMENTS

Nonlinear analysis of three-dimensional problems presents some unique challenges to the developers and users of finite element technology. In contrast to linear analysis, and to nonlinear analysis using one- and two-dimensional elements, three-dimensional element computations are often so time-consuming that analysis cost constraints may preclude or discourage the use of an adequate model. Additional research in numerical methods for this aspect of the calculations is essential to improving the cost-effectiveness of nonlinear analysis in three dimensions. The element algorithms described here are presently being implemented on the CRAY-1 vector processor; it is hoped that the results will indicate possible directions for obtaining improved efficiency in element-level computations.

Further investigation is also required to develop methods of solution which optimize the use of element-level computations. These include adaptive methods for problems in which the character of the nonlinear response may vary throughout the analysis, as well as methods which rely on "reduced basis" approximations [18] to track the local behavior of primary solution parameters.

SUMMARY AND CONCLUSIONS

The MAGNA finite element program, developed for use in three-dimensional nonlinear analysis applications, has been described. Particular attention is given in the program to the problems of modeling flexibility and efficiency of element-level computations. Several applications have been presented to demonstrate the analysis capabilities of MAGNA; the results and computing times for these solutions indicate that the program is applicable to nonlinear problems of considerable size and complexity.

Acknowledgement—The author gratefully acknowledges the support provided by the Air Force Flight Dynamics Laboratory (AFFDL/FIER) in this work.

REFERENCES

1. R. A. Brockman, MAGNA: a finite element program for the materially and geometrically nonlinear analysis of three-dimensional structures subjected to static and transient loading. *UDR-TR-79-45*, University of Dayton Research Institute, Dayton, Ohio (1979).
2. P. Sharifi and D. N. Yates, Nonlinear thermo-elastic-plastic and creep analysis by the finite element method. *AIAA J.* **12**, 1210–1215 (1974).
3. J. T. Oden, *Finite Elements of Nonlinear Continua*. McGraw-Hill, New York (1972).
4. N. M. Newmark, A method of computation for structural dynamics. *Proc. ASCE. J. Engng Mech. Div.* **85**, 67–94 (1959).
5. D. P. Mondkar and G. H. Powell, Finite element analysis of nonlinear static and dynamic response. *Int. J. Numer. Meth. Engng* **11**, 449–520 (1977).
6. K. J. Bathe and E. L. Wilson, *Numerical Methods in Finite Element Analysis*. Prentice-Hall, Englewood Cliffs, New Jersey (1976).
7. R. A. Brockman, A penalty function approach for the nonlinear finite element analysis of thin shells. Ph.D. Thesis, University of Dayton (1979).
8. R. A. Brockman and F. K. Bogner, An efficient three-dimensional shell finite element for highly nonlinear problems. *ASME Century 2 Int. Computer Technology Conf.*, San Francisco, California (1980).
9. A. K. Gupta and B. Mohraz, A method of computing numerically integrated stiffness matrices. *Int. J. Numer. Meth. Engng* **5**, 83–89 (1972).
10. R. Winter and H. S. Levine, Experiments on large plastic deformations of circular plates with work hardening. Grumman Research Dept., *Rep. RE-502*, Grumman Aerospace Corp. (1975).
11. B. Hunsaker, W. E. Haisler and J. A. Stricklin, On the use of two hardening rules of plasticity in incremental and pseudo-force analysis. In *Constitutive Equations in Viscoplasticity: Computational and Engineering Aspects*, AMD Vol. 20, ASME (1976).
12. G. R. Monforton, Discrete element, finite displacement analysis of anisotropic sandwich shells. *Rep. No. 39*, Division of Solid Mechanics, Structures and Mechanics and Design, Case Western Reserve University (1970).
13. H. P. Kan and J. C. Huang, Large deflection of rectangular sandwich plates. *AIAA J.* **5**, 1706–1708 (1967).
14. E. Deutsch, Das Knicken von Bogenträgern bei Unsymmetrischer Belastung. *Der Bauingenieru* **21**, 353–360 (1940).
15. D. A. DaDeppo and R. Schmidt, Instability of clamped-

hinged circular arches subjected to a point load. *Trans. ASME, J. Appl. Mech.* **42**, 894–896 (1975).
16. R. M. Watt, AFFDL F-16 canopy bird impact test (final checked data). Data package. Project V415-18A, Vol. I, Von Karman Gas Dynamics Facility, Arnold Engineering Development Center, Arnold Air Force Station, Tennessee, June (1977).
17. R. E. McCarty, Finite element analysis of F-16 aircraft canopy dynamic response to Bird impact loading. *21st AIAA/ASME/ASCE/AHS Structures, Structural Dynamics and Materials Conf.*, Seattle, Washington, (May 1980).
18. A. K. Noor and J. M. Peters, Reduced basis technique for nonlinear analysis of structures, *AIAA J.* **18**, 455–462 (1980).

Computers & Structures, Vol. 13, pp. 425–465, 1981
Printed in Great Britain.

0045-7949/81/010425-41/$02.00/0

SURVEY OF COMPUTER PROGRAMS FOR SOLUTION OF NONLINEAR STRUCTURAL AND SOLID MECHANICS PROBLEMS

AHMED K. NOOR
George Washington University Center at NASA Langley Research Center, Hampton, VA 23665, U.S.A.

INTRODUCTION

The significant advances made in nonlinear finite element technology, coupled with the rapid developments in computer hardware and software provided the foundation from which general-purpose nonlinear finite element programs have evolved. After more than a decade of development, a wide variety of these programs are currently being used in government and industry for practical analysis and design of structures. Depending on the criteria for identifying general-purpose nonlinear finite element programs, estimates of their numbers vary between twenty and fifty. In addition, several hundred special-purpose and research-oriented nonlinear finite element programs are in existence. The potential user of a nonlinear finite element program is now faced with the problems of (1) getting information about, and sorting out, existing nonlinear finite element programs; and (2) identifying the program that is best suited for his particular needs.

Since early 1970 several bibliographies, data sheets and tables have been compiled about finite element software (e.g. Refs. [1–3] and the two recent surveys of nonlinear finite element programs given in Refs. [4 and 5]). Reference [4] outlines the capabilities of eleven general-purpose computer programs for nonlinear analysis, and Ref. [5] surveys the capabilities of twelve programs used for plastic analysis. The present paper aims at complementing these two surveys. Specifically, the objective of this paper is to give an overview of the current capabilities of thirty-six computer programs that can be used for solution of nonlinear structural and solid mechanics problems. These programs range from the large, general purpose codes with a broad spectrum of capabilities, rich variety of element types, large user community and comprehensive user support (e.g. ANSYS, ASAS-NL, ASKA, MARC, MSC/NASTRAN and SESAM-69) to the small, special purpose codes with limited user community such as BEAM, BRICK, PAC78 and WHAMS. The capabilities of the programs surveyed are listed in tabular form followed by a summary of the major features of each program. It is anticipated that this format will help in the initial selection of programs which are most suitable for a particular application. The final selection of the program to be used should, however, be based on a detailed examination of the documentation and the literature about the program.

Before listing the capabilities of the programs, some of the sources of information about computer programs and references on the background material needed for effectively using the programs are listed, and guidelines for selecting the code are discussed.

SOURCES OF INFORMATION ABOUT COMPUTER PROGRAMS

A partial list of users group and software dissemination services that provide information about finite element programs is given subsequently. A more complete list and a description of each group can be found in Ref. [6].

- ASIAC—Aerospace Structures Information and Analysis Center, AFFDL/FBR Wright-Patterson Air Force Base, Dayton, OH 45433.
- CEPA—Society for Computer Application in Engineering, Planning and Architecture, Inc., 358 Hungerford Drive, Rockville, MA 20850.
- COSMIC—Computer Software Management and Information Center, 112 Barrow Hall, University of Georgia, Athens, GA 30602.
- ICES—Users Group, Inc., P.O. Box 8243, Cranston, RI 02920.
- ICP—International Computer Programs, Inc., 9000 Keystone Crossing, Indianapolis, IN 46240.
- NISEE—National Information Service for Earthquake Engineering, 519 Davis Hall, University of California, Berkeley, CA 94720.
- NTIS—National Technical Information Service, U.S. Department of Commerce, 5285 Port Royal Road, Springfield, VA 22161.

These organizations publish catalogues and newsletters describing finite element programs.

BACKGROUND MATERIAL NEEDED FOR EFFECTIVE EVALUATION AND USE OF FINITE ELEMENT PROGRAMS

The user of a nonlinear finite element program is dependent on the detailed knowledge about theories, algorithms and assumptions behind the program features for the proper selection of models and algorithms as well as for monitoring the solution process. There are also many nonlinear problems whose solution may require modifying (slightly) the program. Therefore, the effective evaluation and use of nonlinear analysis programs requires, in addition to a basic knowledge of finite element discretization procedures, some knowledge about the following aspects of nonlinear analysis.

- Continuum mechanics basis and formulation aspects. This is particularly important when solving large strain problems. For background material see Refs. [7–9].
- Constitutive relations and material modeling (e.g. Refs. [10–12].
- Solution techniques for nonlinear static problems (e.g. Refs. [13–16]).
- Temporal integration and solution techniques for nonlinear dynamic problems (e.g. Refs. [17–20]).

● Considerations for the design of software systems for nonlinear analysis (e.g. Refs. [21, 22]).

GUIDELINES FOR SELECTION OF A COMPUTER PROGRAM

The analysis capabilities and user features vary considerably from one code to the other, and therefore, it is often difficult to identify the proper code that meets a specific need. A number of factors which affect the selection of a code are enumerated in the succeeding paragraphs. The order in which these factors are listed does not necessarily reflect the priority which should be given each factor; this remains the responsibility of the user of the code. (For a detailed discussion of the technical, operational and commercial criteria for selecting a code see Refs. [23, 24].)

1. *Analysis capabilities*

These include the range of applications and limitations of the code. The limitations include both those implied by the formulation aspects and numerical solution procedures adopted by the code as well as the element library available in the code.

2. *Adequacy of user-oriented features*

For nonlinear analysis the user's features such as automatic (or semi-automatic) mesh (or model) generation, error checks, displays of original model and of various intermediate results are essential for the effective use of the analysts' time.

3. *Maintainability*

Because of the rapid advances in computational methods, computer software and hardware technology, the maintenance of nonlinear analysis codes usually include updating the computational modules, extending the capabilities of the code and improving its performance. There exists well-established formal mechanisms for integration and quality assurance of software extensions. Maintenance of the code by personnel other than the developer (e.g. user's organization) can be quite expensive and time consuming.

4. *Adequacy of user support facilities*

In addition to the printed documentation (user manuals, training manuals, programming manuals, sample problems and test cases), the following services are desirable: training courses, users meetings, hotline consulting, assistance by data centers and consulting organizations.

5. *Portability*

Although most of the finite element codes are written in standard FORTRAN IV language, a code developed on one computer system may not be entirely compatible with another system due to differences in I/O facilities, operating system, precision of the machine (e.g. UNIVAC versus CDC), etc.

Once a code is acquired and implemented on to the user's computer system, it is important to establish its reliability by bench-mark problem runs. For a discussion on verification and qualification procedures (see Ref. [25]).

PROGRAM SURVEY AND DESCRIPTION

This section gives an overview of the capabilities of thirty-six computer programs for the solution of nonlinear structural and solid mechanics problems. Some of the programs have a much more limited scope than others. The information presented herein is based on a questionnaire sent to the developers of each program. The capabilities of the programs are listed in tabular form followed by a description of each program.

SUMMARY OF PROGRAM CAPABILITIES

In this section a brief description of each of the programs listed in the tables is given. These descriptions were supplied by the program developers.

ADINA

Descriptive Program Title: Automatic Dynamic Incremental Nonlinear Analysis.

Program Developer: K. J. Bathe, Department of Mechanical Engineering, Massachusetts Institute of Technology, Cambridge, MA 02139, U.S.A.

Date of First Release and Most Recent Update: 1975 and 1978.

General Information:
ADINA is a proprietary code. The code was developed on experiences obtained from codes SAP-IV and NONSAP. Development started in 1974. The program is fully operational but the analysis capabilities are continuously improved. Research and development efforts are being financed by a users group of ADINA. Members of the users group obtain the source codes of ADINA and ADINAT and all new developments as long as they remain members of the group. The source codes are transmitted with sample data cases and their solutions.

Program Capability:
ADINA is a general purpose linear and nonlinear static and dynamic three-dimensional finite element analysis program. The nonlinearities may be due to large displacements, large strains, and nonlinear material behavior. The material descriptions available are, depending on the element used, isotropic linear elastic, orthotropic linear elastic, isotropic thermo–elastic, curve description model, concrete model, Drucker–Prager-cap elastic–plastic model, isothermal von Mises plasticity model, thermo–elastic–plastic–creep model, and Mooney–Rivlin material. The program can be used to restart at preselected time steps. Vibration and dynamic analysis includes computation of eigenvalues and eigenmodes, and dynamic response. Dynamic spectral analysis capability is not included. Stability analysis includes: nonlinear collapse, dynamic and buckling. Multipoint constraint conditions and prescribed displacement conditions are available.
ADINAT has been employed for the solution of heat transfer and analogous field problems.

User Interface and Modeling Capabilities:
The ADINA and ADINAT programs do not include any pre- or post-processors. However, options are available to read program input from tape and to write program output to tape. Hence, the programs can directly be coupled to available pre- and post-processors. A number of pre- and post-processing programs are used in connection with ADINA and ADINAT, e.g. FEMGEN mesh generator. INGEN and GIFTS. A pre- and postprocessing program specifically designed for ADINA/ADINAT is currently under development.

Table 1.

I. FINITE ELEMENT SYSTEM FEATURES

		1. ADINA	2. ANSR-I	3. ANSR-II	4. ANSYS	5. ASAS-NL	6. ASKA	7. BEAM	8. BOSOR4	9. BOSOR5	10. BOVA	11. BOVAC	12. BRICK	13. DANUTA	14. DIAL	15. DRAIN-2D	16. DYCAST	17. ELAS55	18. HONDO-II
1.	Goal of Program System																		
	General purpose	●			●	●	●								●		●		
	Commercial	●	●	●	●	●	●		●	●						●	●		
	Research	●	●	●		●	●	●	●	●	●	●	●			●	●	●	
	Educational	●			●	●	●		●	●								●	
	Others (specify in Program Abstract)								●	●	●	●		●					●
2.	Types of Elements*																		
	Three-dimensional rod element	LGM	GM	GM	LGM	LGM	L, G,M							L, GM	L, GM	GM	L, GM		
	Three-dimensional beam element	LGM	GM	GM	L,G	LGM	L, G,M						L,M		L, GM	GM	L, GM		
	Plane stress	LGM	GM	GM	LGM	LM	L, G,M		L,G	L, GM	L,M	L,M		L, GM	L, GM	GM	L, GM		GM
	Plane strain	LGM	GM	GM	LGM	LM	L,M						L,M	L, GM	L, GM				GM
	Membranes in space	LGM			LGM	LGM	L, G,M								L, GM		L, GM		
	Shear panels	LGM			LGM	L	L												
	Plates	LGM		GM	LGM	LGM	L, G,M				L,M	L,M			L, GM				
	Thin shells	LGM		GM	LGM	LGM	L, G,M								L, GM				
	Thick shells	LGM			LGM	LGM	L, G,M								L, GM				
	Shells of revolution	LGM			L,G		L		L,G	L, GM					L, GM				
	Axisymmetric solids	LGM	GM	GM	LGM	LM	L,M							L, GM	L, GM				GM
	Three-dimensional solids	LGM		GM	LGM	LGM	L,M							L, GM	L, GM			L,M	
	Discrete stiffeners (for plates and shells)	LGM				LGM	L, G,M		L,G	L, GM	L,M	L,M			L, GM				
	Boundary element	LGM													L,G				
	Gap element	LGM		GM	G	G									L,G		L, GM		GM
	Others (specify in the Abstract)				●			L,M										●	

*L = linear analysis only, G = geometric nonlinearity only, M = material nonlinearity only,
GM = combined geometric and material nonlinearity, LGM = L, G, M, GM.

FINITE ELEMENT SYSTEM FEATURES (CONT'D.)

		19. JAC	20. LARSTRAN80	21. MARC	22. MSC/NASTRAN	23. NEPSAP	24. PAC78	25. PLANS	26. POLO-FINITE	27. SAMCEF	28. SAMSON	29. SESAM-69	30. SMART	31. STAGSC-1	32. STRAW	33. TEPSA	34. ULARC	35. WECAN	36. WHAMS
1.	Goal of Program System																		
	General purpose		●	●	●	●		●	●	●		●	●	●				●	
	Commercial		●	●	●	●		●	●	●		●					●	●	
	Research		●	●	●	●	●	●	●	●	●		●		●	●			●
	Educational		●		●				●							●			
	Others (See Program Abstract)	●									●								
2.	Types of Elements*																		
	Three-dimensional rod element		L, GM	L, GM	L, GM	L, GM		L, GM	L, GM	L,G		L,M	L,M	L, GM				L,M	
	Three-dimensional beam element		L, G,M	L, GM	L, GM	L, GM		L, GM	L	L		L, GM		L, GM				L, G,M	
	Plane stress		L, G,M	L, GM	L, GM	L, GM		L, GM	L,M	LGM		L,M	L,M	L, GM	GM	L, GM		L,M	GM
	Plane strain	GM	L,M	L, GM					L,M	LGM	M	L,M	L,M		GM	L, GM	L,M	L,M	GM
	Membranes in space		L, G,M	L, GM	L, GM	L, GM		L, GM		L,G		L,M	L,M	L, GM				L,M	
	Shear panels			L	L	L, GM				L				L, GM					
	Plates		L, G,M	L, GM	L, GM	L, GM		L,M	L	L		L, GM		L, GM				L,M	
	Thin shells		L, G,M	L, GM	L, GM	L, GM		L	L	L		L, GM		L, GM				L,M	
	Thick shells		L, G,M	L, GM	L, GM	L, GM		L,M	L	L		L, GM						L,G	
	Shells of revolution			L, GM	L	L, GM		L,M	L	LGM					GM			L	GM
	Axisymmetric solids	GM	L, G,M	L, GM	L	L, GM		L,M	L,M	LGM	M		L,M		GM	L, GM		L,M	GM
	Three-dimensional solids		L, G,M	L, GM	L	L, GM	L,M	L,M	L,M	L,M		L,M	L,M					L, G,M	
	Discrete stiffeners (for plates and shells)			L, GM	L, GM	L, GM		L,M	L	L		L, GM		L, GM				L,G	
	Boundary element					L,G			L,M	L			L,M						
	Gap element			L, GM	GM	L,G				L						L, GM		L,G	
	Others (See Program Abstract)			●	●								●			●	●	●	

*L = linear analysis only, G = geometric nonlinearity only, M = material nonlinearity only,
GM = combined geometric and material nonlinearity, LGM = L, G, M, GM.

FINITE ELEMENT SYSTEM FEATURES (CONT'D.)

			1. ADINA	2. ANSR-I	3. ANSR-II	4. ANSYS	5. ASAS-NL	6. ASKA	7. BEAM	8. BOSOR4	9. BOSOR5	10. BOVA	11. BOVAC	12. BRICK	13. DANUTA	14. DIAL	15. DRAIN-2D	16. DYCAST	17. ELAS55	18. HONDO-II
3.	Range of Applications and Phenomena																			
	Nonlinear Statics	Nonlinear response	●	●	●	●	●	●	●	●	●	●	●	●	●	●		●	●	
		Post-buckling and nonlinear collapse	●		●	●	●			●	●					●		●		
		Nonlinear contact problems				●	●	●							●	●		●		
		Cracking and fracture mechanics	●				●	●	●			●	●	●						
	Nonlinear Dynamics	Nonlinear vibrations	●			●														
		Transient response	●	●	●	●									●	●	●	●		●
		Wave propagation	●															●		●
	Nonlinear Interaction Problems	Fluid-structure interaction	●			●														
		Thermal-mechanical coupling	●			●	●													
		Combustion-mechanical coupling																		
	Large Strain Plasticity (or visco-plasticity) Problems	Static	●			●		●							●	●			●	
		Dynamic	●			●										●				●
4.	Formulation																			
	a) Fundamental unknowns																			
	Displacement method		●	●	●	●	●	●	●	●	●	●	●	●	●	●	●	●	●	●
	Force method																			
	Hybrid method						●									●				
	Mixed method															●				
	Others (See Program Abstract)																			
	b) Reference frame																			
	Total Lagrangian		●	●	●		●	●	●	●	●	●	●	●		●			●	
	Updated Lagrangian		●	●	●	●	●											●		●
	Eulerian														●					
	Others (See Program Abstract)																			

FINITE ELEMENT SYSTEM FEATURES (CONT'D.)

			19. JAC	20. LARSTRAN80	21. MARC	22. MSC/NASTRAN	23. NEPSAP	24. PAC78	25. PLANS	26. POLO-FINITE	27. SAMCEF	28. SAMSON	29. SESAM-69	30. SMART	31. STAGSC-1	32. STRAW	33. TEPSA	34. ULARC	35. WECAN	36. WHAMS
3.	Range of Applications and Phenomena																			
	Nonlinear Statics	Nonlinear response	•	•	•	•	•	•	•	•	•		•	•	•	•	•	•	•	
		Post-buckling and nonlinear collapse	•	•	•	•	•		•	•			•		•					
		Nonlinear contact problems	•	•	•	•	•		•					•			•		•	
		Cracking and fracture mechanics		•	•	•	•		•	•			•	•			•		•	
	Nonlinear Dynamics	Nonlinear vibrations		•	•	•	•				•	•	•			•				•
		Transient response		•	•	•	•				•	•	•		•	•			•	•
		Wave propagation										•				•			•	•
	Nonlinear Interaction Problems	Fluid-structure interaction			•	•								•	•	•				•
		Thermal-mechanical coupling	•		•	•	•				•		•	•		•	•			
		Combustion-mechanical coupling																		
	Large Strain Plasticity (or visco-plasticity) Problems	Static	•	•	•		•			•					•		•			
		Dynamic		•	•		•								•	•				•
4.	Formulation																			
	a) Fundamental unknowns																			
	Displacement method		•	•	•	•	•	•	•	•	•	•	•	•	•	•	•	•	•	•
	Force method										•									
	Hybrid method				•	•					•									
	Mixed method						•				•									
	Others (See Program Abstract)																			
	b) Reference frame																			
	Total Lagrangian			•	•		•	•		•	•			•	•				•	•
	Updated Lagrangian		•	•	•	•			•				•				•			
	Eulerian				•															
	Others (See Program Abstract)																	•		

FINITE ELEMENT SYSTEM FEATURES (CONT'D.)

				1. ADINA	2. ANSR-I	3. ANSR-II	4. ANSYS	5. ASAS-NL	6. ASKA	7. BEAM	8. BOSOR4	9. BOSOR5	10. BOVA	11. BOVAC	12. BRICK	13. DANUTA	14. DIAL	15. DRAIN-2D	16. DYCAST	17. ELAS55	18. HONDO-II
5.	Solution Techniques																				
	Nonlinear Statics	Incremental (moniterative)		●	●	●	●	●					●		●	●		●		●	
		Newton type methods		●	●	●		●	●	●	●	●	●	●			●		●	●	
		Others (See Program Abstract)		●				●												●	
	Nonlinear Dynamics	Modal superposition		●					●								●				
		Direct Integration	Explicit schemes	●					●								●		●		●
			Implicit schemes	●	●	●	●		●								●	●	●		
			Combined explicit/implicit														●				
		Others (See Program Abstract)																			
6.	Types of Loading																				
	Concentrated loads			●	●	●	●	●	●	●	●	●	●	●	●	●	●	●	●	●	●
	Line loads			●			●	●	●	●	●	●	●				●		●		●
	Axisymmetric loads			●			●	●	●		●	●				●	●		●		●
	Surface loads			●			●	●	●		●	●				●	●		●	●	●
	Volume loads			●			●	●	●	●			●				●				
	Gravity loads			●			●	●	●							●	●			●	
	Initial stresses, strains or velocities			●	●	●	●	●	●	●			●	●		●	●		●	●	●
	Thermal loading			●			●	●	●		●	●				●	●		●	●	
	Centrifugal loading						●	●								●	●				
	Deformation dependent loading (e.g., live load)							●	●		●	●									●
	Cyclic loading			●	●	●			●							●	●				●
	Random loading								●								●		●		
	Gyroscopic loading																				
	Nonproportional loading			●	●	●	●	●	●		●	●					●				●
	Contact loading			●			●	●	●							●	●		●		●
	Others (See Program Abstract)													●						●	

FINITE ELEMENT SYSTEM FEATURES (CONT'D.)

				19. JAC	20. LARSTRAN80	21. MARC	22. MSC/NASTRAN	23. NEPSAP	24. PAC78	25. PLANS	26. POLO-FINITE	27. SAMCEF	28. SAMSON	29. SESAM-69	30. SMART	31. STAGSC-1	32. STRAW	33. TEPSA	34. ULARC	35. WECAN	36. WHAMS
5.	Solution Techniques																				
	Nonlinear Statics	Incremental (noniterative)						●		●	●			●				●	●		
		Newton type methods			●	●	●	●	●		●	●		●	●	●					
		Others (See Program Abstract)		●			●			●					●		●			●	
	Nonlinear Dynamics	Modal superposition			●	●		●												●	
		Direct Integration	Explicit schemes		●	●						●	●	●		●	●				●
			Implicit schemes		●	●	●	●				●				●	●			●	●
			Combined explicit/implicit									●									●
		Others (See Program Abstract)																			
6.	Types of Loading																				
	Concentrated loads			●	●	●	●	●	●	●	●	●	●	●	●	●	●	●	●	●	●
	Line loads			●	●	●	●	●		●	●	●		●	●	●	●			●	●
	Axisymmetric loads			●	●	●	●	●		●	●	●	●		●		●	●		●	●
	Surface loads			●	●	●	●	●	●	●	●	●	●	●	●	●	●	●		●	●
	Volume loads			●	●	●		●			●	●		●	●	●		●		●	
	Gravity loads			●	●	●	●	●	●		●	●		●	●	●		●		●	
	Initial stresses, strains or velocities			●	●	●	●	●			●	●		●	●	●	●			●	●
	Thermal loading			●	●	●	●	●		●	●	●		●	●	●	●	●		●	
	Centrifugal loading			●		●	●	●		●		●		●				●		●	
	Deformation dependent loading (e.g., live load)			●	●	●	●	●				●		●	●	●					
	Cyclic loading			●	●	●	●	●		●	●				●	●		●		●	
	Random loading						●														
	Gyroscopic loading					●	●					●									
	Nonproportional loading			●	●	●	●	●	●	●	●	●		●		●			●		
	Contact loading			●	●	●	●	●				●			●			●		●	
	Others (See Program Abstract)																				

FINITE ELEMENT SYSTEM FEATURES (CONT'D.)

		1. ADINA	2. ANSR-I	3. ANSR-II	4. ANSYS	5. ASAS-NL	6. ASKA	7. BEAM	8. BOSOR4	9. BOSOR5	10. BOVA	11. BOVAC	12. BRICK	13. DANUTA	14. DIAL	15. DRAIN-2D	16. DYCAST	17. ELAS55	18. HONDO-II
7.	Support Conditions and Constraints																		
	Axisymmetric	●			●	●	●		●	●				●	●		●		●
	At boundaries	●	●	●	●	●	●	●	●	●	●	●	●	●	●	●	●	●	●
	At internal points	●			●	●	●	●	●	●	●			●	●		●	●	●
	Prescribed displacements	●		●	●	●	●							●	●		●	●	●
	Sliding interfaces				●	●	●							●	●				●
	Support at contact points	●			●	●	●							●	●				●
	Elastic foundation	●			●	●	●							●					●
	Frictional forces	●			●	●								●	●				●
	Multipoint constraints	●			●	●	●				●			●	●		●	●	
	Cyclic symmetry	●					●							●					
	Others (See Program Abstract)																	●	
8.	Material Properties, Material Models and Wall Construction																		
	Isotropic	●			●	●	●	●	●	●	●	●	●	●	●		●	●	●
	Anisotropic	●			●	●	●		●	●			●		●		●	●	
	Multilayered	●			●		●		●	●	●			●	●				
	Nonhomogeneous	●					●								●			●	●
	Temperature dependent elastic properties	●			●	●	●								●				●
	Temperature dependent plastic or viscoplastic properties	●			●	●	●								●			●	●
	Linear elastic	●			●	●	●	●	●	●	●	●	●	●	●		●	●	●
	Nonlinear elastic	●			●	●	●	●			●	●	●		●				●
	Elastic-perfectly plastic	●	●		●	●	●	●			●			●	●		●		●
	Elastic-plastic strain hardening	●		●	●	●	●	●		●	●				●		●	●	●
	Viscoelastic	●			●	●												●	●
	Viscoplastic	●			●													●	●
	High temperature creep	●			●	●	●			●					●			●	
	Others (See Program Abstract)																	●	

FINITE ELEMENT SYSTEM FEATURES (CONT'D.)

		19. JAC	20. LARSTRAN80	21. MARC	22. MSC/NASTRAN	23. NEPSAP	24. PAC78	25. PLANS	26. POLO-FINITE	27. SAMCEF	28. SAMSON	29. SESAM-69	30. SMART	31. STAGSC-1	32. STRAW	33. TEPSA	34. ULARC	35. WECAN	36. WHAMS
7.	Support Conditions and Constraints																		
	Axisymmetric	●	●	●	●	●		●	●	●	●		●		●	●		●	●
	At boundaries	●	●	●	●	●	●	●	●	●	●	●	●	●	●	●	●	●	●
	At internal points	●	●	●	●	●	●	●	●	●		●	●	●		●		●	
	Prescribed displacements	●	●	●	●	●	●	●	●	●		●	●	●		●		●	●
	Sliding interfaces	●		●	●	●			●	●	●		●	●	●			●	●
	Support at contact points	●		●	●	●				●			●			●		●	
	Elastic foundation			●	●	●			●	●			●	●				●	
	Frictional forces	●		●	●						●							●	
	Multipoint constraints			●	●	●	●	●	●	●		●		●		●		●	
	Cyclic symmetry				●														
	Others (See Program Abstract)				●														
8.	Material Properties, Material Models and Wall Construction																		
	Isotropic	●	●	●	●	●	●	●	●	●	●	●	●	●	●	●		●	●
	Anisotropic		●	●	●	●		●	●	●		●	●	●				●	
	Multilayered		●	●	●	●				●		●		●				●	
	Nonhomogeneous	●	●	●	●		●											●	
	Temperature dependent elastic properties	●	●	●	●	●				●			●		●	●		●	
	Temperature dependent plastic or viscoplastic properties	●	●	●		●				●			●		●	●		●	
	Linear elastic	●	●	●	●	●	●	●	●	●	●	●	●	●	●	●		●	●
	Nonlinear elastic	●	●	●	●				●	●			●	●		●			
	Elastic-perfectly plastic	●	●	●	●	●		●	●	●	●	●	●	●	●	●	●	●	●
	Elastic-plastic strain hardening	●	●	●	●	●	●	●	●	●	●	●	●	●	●	●		●	●
	Viscoelastic			●	●	●							●						
	Viscoplastic			●											●				
	High temperature creep	●	●	●		●		●					●			●		●	
	Others (See Program Abstract)						●									●		●	

FINITE ELEMENT SYSTEM FEATURES (CONT'D.)

			1. ADINA	2. ANSR-I	3. ANSR-II	4. ANSYS	5. ASAS-NL	6. ASKA	7. BEAM	8. BOSOR4	9. BOSOR5	10. BOVA	11. BOVAC	12. BRICK	13. DANUTA	14. DIAL	15. DRAIN-2D	16. DYCAST	17. ELAS55	18. HONDO-II
9.	Other Capabilities																			
	Substructuring	Repeated use of identical substructures	●			●	●	●								●				
		Mixing linear and nonlinear substructures	●				●	●							●					
		Mixing substructures with different types of nonlinearities	●			●														
	Restart capability		●		●	●	●	●			●	●			●	●		●	●	●
	Heat transfer capability		●			●	●	●							●					
	Others (See Program Abstract)									●	●				●					
10.	Program Operational on (model and operating system are specified in the Abstract)																			
	CDC		●	●	●	●		●	●	●	●	●	●	●	●	●	●	●		●
	IBM		●			●		●		●	●				●			●	●	
	UNIVAC		●			●	●	●		●	●				●	●		●		
	Honeywell									●	●									
	TELEFUNKEN		●																	
	ICL							●												
	Minicomputers		●			●	●	●												
	Supercomputers		●			●		●							●			●		
	Others (See Program Abstract)					●	●	●	●			●	●						●	
11.	Documentation																			
	Data preparation manual		●	●	●	●	●	●	●	●	●	●	●	●	●	●	●	●	●	●
	Programmer's manual		●	●	●		●	●	●			●	●	●					●	●
	Theoretical manual		●	●	●	●	●	●	●	●	●	●	●	●		●		●	●	●
	Sample problem output		●	●	●	●	●	●	●	●	●	●	●	●	●				●	
	Others (See Program Abstract)					●														

FINITE ELEMENT SYSTEM FEATURES (CONT'D.)

			19. JAC	20. LARSTRAN	21. MARC	22. MSC/NASTRAN	23. NEPSAP	24. PAC78	25. PLANS	26. POLO-FINITE	27. SAMCEF	28. SAMSON	29. SESAM-69	30. SMART	31. STAGSC-1	32. STRAW	33. TEPSA	34. ULARC	35. WECAN	36. WHAMS
9.	Other Capabilities																			
	Substructuring	Repeated use of identical substructures				●	●		●	●	●		●	●					●	
		Mixing linear and nonlinear substructures				●				●	●		●	●	●					
		Mixing substructures with different types of nonlinearities								●	●				●				●	
	Restart capability		●	●	●	●	●	●	●	●	●	●	●	●	●		●		●	●
	Heat transfer capability				●	●					●		●	●		●	●		●	
	Others (See Program Abstract)					●														
10.	Program Operational on (model and operating system are specified in the Abstract)																			
	CDC.		●	●	●	●	●		●	●	●	●	●	●	●		●	●	●	●
	IBM			●	●	●	●	●	●		●		●	●	●	●	●			
	UNIVAC			●	●	●	●		●		●		●	●	●					
	Honeywell									●										
	TELEFUNKEN										●									
	ICL																			
	Minicomputers				●	●	●		●	●	●		●		●				●	
	Supercomputers				●	●	●		●											
	Others (See Program Abstract)					●		●		●	●									
11.	Documentation																			
	Data preparation manual			●	●	●	●	●	●	●	●	●	●	●	●	●	●	●	●	●
	Programmer's manual			●	●	●		●					●		●		●			
	Theoretical manual			●	●	●	●	●	●		●	●	●	●	●	●	●			●
	Sample problem output			●	●	●	●	●	●	●	●		●	●	●		●		●	
	Others (See Program Abstract)		●			●														

II. USER INTERFACE AND MODELING CAPABILITIES

			1. ADINA	2. ANSR-I	3. ANSR-II	4. ANSYS	5. ASAS-NL	6. ASKA	7. BEAM	8. BOSOR4	9. BOSOR5	10. BOVA	11. BOVAC	12. BRICK	13. DANUTA	14. DIAL	15. DRAIN-2D	16. DYCAST	17. ELAS55	18. HONDO-II
1.	Input Form and Sequence																			
	Input Form	Fixed format	●	●	●	●	●		●		●	●	●	●			●	●	●	●
		Free form-list directed format				●	●	●		●					●	●				
		Problem oriented languages						●												
	Input Sequence	User directed	●			●		●		●	●					●		●		
		System directed		●	●				●			●	●	●	●		●		●	●
2.	Model Generation and Checking																			
	Automatic or Semi-Automatic Generator for	Nodal point coordinates	●	●	●	●	●	●	●	●	●	●	●	●	●	●			●	●
		Element connectivities	●	●	●	●	●	●	●	●	●	●	●	●	●	●			●	●
		Constraints, symmetry and boundary conditions	●	●	●	●		●	●	●	●	●			●	●			●	●
		Substructure connectivity	●			●		●								●				
		Repetition of identical segments	●			●	●	●					●		●	●				
		Loads	●	●	●	●		●		●	●				●	●				
		Others (See Program Abstract)				●												●		
	Automatic or Semi-Automatic Element Generators for	Triangular elements	●			●	●	●							●					
		Quadrilateral elements	●			●	●	●							●	●				●
		Body or shell of revolution elements	●			●	●	●		●	●					●				
		Three-dimensional solid elements	●			●		●							●	●				
		Two-dimensional shell elements	●			●	●	●								●				
		Intersections				●										●				
		Special types of structures					●	●		●	●	●	●	●	●					
	Data Checking Facilities	Line printer				●	●	●	●	●	●	●	●		●	●			●	●
		Plotter				●	●	●							●	●				
		Interactive graphics				●	●	●							●	●				

USER INTERFACE AND MODELING CAPABILITIES (CONT'D.)

			19. JAC	20. LARSTRAN 80	21. MARC	22. MSC/NASTRAN	23. NEPSAP	24. PAC 78	25. PLANS	26. POLO-FINITE	27. SAMCEF	28. SAMSON	29. SESAM-69	30. SMART	31. STAGSC-1	32. STRAW	33. TEPSA	34. ULARC	35. WECAN	36. WHAMS
1.	Input Form and Sequence																			
	Input Form	Fixed format	●		●	●		●	●		●	●	●	●	●	●	●	●	●	●
		Free form-list directed format		●	●	●	●				●				●					
		Problem oriented languages		●		●				●										
	Input Sequence	User directed		●	●	●	●		●	●	●		●	●			●		●	
		System directed	●				●	●				●			●	●		●	●	●
2.	Model Generation and Checking																			
	Automatic or Semi-Automatic Generator for	Nodal point coordinates		●	●	●	●	●		●	●	●	●	●	●	●	●		●	●
		Element connectivities		●	●	●	●	●		●	●	●	●	●	●	●	●		●	●
		Constraints, symmetry and boundary conditions		●	●	●	●	●		●	●		●	●	●				●	
		Substructure connectivity				●	●			●			●	●	●				●	
		Repetition of identical segments			●	●	●			●	●		●	●					●	
		Loads		●	●	●	●			●	●		●	●	●	●			●	●
		Others (See Program Abstract)	●			●		●												
	Automatic or Semi-Automatic Element Generators for	Triangular elements		●	●	●	●			●	●	●	●	●	●		●		●	●
		Quadrilateral elements		●	●	●	●			●	●	●	●	●	●		●		●	●
		Body or shell of revolution elements			●		●			●	●	●		●			●		●	●
		Three-dimensional solid elements		●	●	●	●	●	●	●	●		●	●					●	
		Two-dimensional shell elements		●	●	●	●			●	●		●	●	●				●	
		Intersections				●							●							
		Special types of structures			●															
	Data Checking Facilities	Line printer	●	●	●	●	●	●	●	●	●		●	●	●	●	●		●	●
		Plotter		●	●	●	●		●	●	●		●	●	●	●			●	●
		Interactive graphics		●	●	●	●			●	●		●	●	●				●	

USER INTERFACE AND MODELING CAPABILITIES (CONT'D.)

			1. ADINA	2. ANSR-I	3. ANSR-II	4. ANSYS	5. ASAS-NL	6. ASKA	7. BEAM	8. BOSOR4	9. BOSOR5	10. BOVA	11. BOVAC	12. BRICK	13. DANUTA	14. DIAL	15. DRAIN-2D	16. DYCAST	17. ELAS55	18. HONDO-II
	Plots and Graphics Display of Model	Complete undeformed structure				•	•	•		•	•				•	•		•		
		Part of structure				•	•	•							•	•		•		
		"Blow-up" option				•	•	•							•	•		•		
		Hidden-lines or surfaces				•														
		Orthographic views				•		•								•		•		
		Perspective and isometric views				•	•	•							•	•				
	Other Facilities	Digitizer input				•		•							•					
		Automatic renumbering of nodes, elements or equations				•	•	•							•	•		•	•	
		Table lookup of data				•		•				•	•		•					
		Others (See Program Abstract)																		
3.	Results Output Form																			
	Tabular Output	Fixed set	•	•	•	•	•		•			•	•	•			•	•	•	•
		User defined set and sequence				•	•	•					•		•	•		•		
		Maximum and minimum quantities		•	•	•	•	•		•	•	•				•				
		Stress exceedances				•	•	•								•				
		Others (See Program Abstract)							•			•	•	•					•	
	Plots	Deformed shape of structure				•	•	•		•	•				•	•		•		
		Contours				•	•	•	•						•	•				
		Surface functions						•							•	•				
		Selective output (e.g., by elements or regions)				•	•	•								•		•		
		Histories (e.g., time history)				•	•	•								•		•		
		Others (See Program Abstract)							•	•	•	•	•							
4.	Interactive Input and Control																			
		Parameter specification (e.g., load or time steps)				•	•	•								•		•		
		Singularity check				•	•	•								•		•		
		Error correction/recovery				•		•								•		•		

USER INTERFACE AND MODELING CAPABILITIES (CONT'D.)

			19. JAC	20. LARSTRAN80	21. MARC	22. MSC/NASTRAN	23. NEPSAP	24. PAC78	25. PLANS	26. POLO-FINITE	27. SAMCEF	28. SAMSON	29. SESAM-69	30. SMART	31. STAGSC-1	32. STRAW	33. TEPSA	34. ULARC	35. WECAN	36. WHAMS
	Plots and Graphics Display of Model	Complete undeformed structure		●	●	●	●		●	●	●		●	●	●	●			●	●
		Part of structure		●	●	●	●		●	●	●		●	●	●				●	
		"Blow-up" option		●	●	●	●		●	●	●		●	●	●				●	
		Hidden-lines or surfaces			●	●	●													
		Orthographic views		●	●	●	●		●	●	●		●	●	●				●	
		Perspective and isometric views		●	●	●	●			●	●		●	●	●				●	
	Other Facilities	Digitizer input		●									●	●	●					
		Automatic renumbering of nodes, elements or equations			●	●	●	●	●		●				●				●	
		Table lookup of data		●		●	●			●			●	●	●				●	
		Others (See Program Abstract)				●					●									
3.	Results Output Form																			
	Tabular Output	Fixed set	●		●		●	●	●		●	●			●	●	●	●	●	●
		User defined set and sequence		●	●	●	●		●	●	●		●	●	●	●	●			●
		Maximum and minimum quantities		●	●	●	●	●						●					●	
		Stress exceedances		●		●	●							●						
		Others (See Program Abstract)			●	●														
	Plots	Deformed shape of structure		●	●	●	●		●	●	●		●	●	●	●			●	●
		Contours		●	●	●	●		●		●		●	●	●				●	
		Surface functions		●			●				●		●	●						
		Selective output (e.g., by elements or regions)		●	●	●	●		●	●	●	●	●	●	●	●	●		●	●
		Histories (e.g., time history)		●	●	●	●				●	●		●	●	●	●		●	●
		Others (See Program Abstract)			●	●							●							
4.	Interactive Input and Control																			
	Parameter specification (e.g., load or time steps)			●	●	●	●		●	●	●			●	●					
	Singularity check			●	●	●	●		●	●	●		●	●	●					
	Error correction/recovery			●	●	●			●	●	●			●	●					

Element Library:
General truss, beam, two- and three-dimensional isoparametric (or subparametric) solid elements, a general thin shell, and fluid elements are available. Four different analysis procedures can be employed depending on the analysis to be performed: linear elastic analysis, materially nonlinear only analysis, total Lagrangian formulation, and updated Lagrangian formulation.

Solution Methods:
- Nonlinear dynamic response—Implicit time integration (Newmark or Wilson) with equilibrium iteration option, or explicit time integration (central difference method), modal superposition technique.
- Nonlinear static problems—Incremental solution, modified Newton–Raphson method with acceleration procedures, BFGS method.
- Equation solver for linear equations—compacted out-of-core solver.
- Substructuring capability.
- Extraction of frequencies and mode shapes—Determinant search or accelerated subspace iteration.

Notable Items:
- ADINA and ADINAT offer a very large range of applications in linear and nonlinear analysis with relatively few effective elements, a good library of material models and effective numerical methods. The programs contain state-of-the-art finite element procedures (e.g. in the element kinematic formulations, the formulation and implementation of the nonlinear material models, the iteration procedures in nonlinear static and dynamic analyses) with emphasis on reliability, accuracy and cost-effectiveness. The programs can be employed effectively in linear analysis, and then, with only a few input changes, in relatively simple and very complex nonlinear analyses.
- A companion general two-dimensional fluid dynamics code (ADINAF) is currently being developed.

Programming Language: FORTRAN IV.

Hardware/Operating System: CDC 6400/6600/7600, IBM and UNIVAC, BURROUGHS, CRAY and CYBER 203.

Program Size: Approximately 40,000 source statements in the core programs.

Documentation (Program description, sample analyses and user's manual—see Refs. [26–29].

Availability: Source programs of ADINA and ADINAT are available from the developer by joining the ADINA users group (for a fee). The program can be used on the CDC CYBERNET system.

ANSR-I AND ANSR-II

Descriptive Program Title: Analysis of Nonlinear Structural Response.

Program Developers: G. H. Powell and D. P. Mondkar, Department of Civil Engineering, University of California, Berkeley, CA 94720, U.S.A.

Date of First Release and Most Recent Update: ANSR-I-1973; ANSR-II-1980.

General Information:
- General purpose codes for static and dynamic response considering both large displacement and inelastic effects. ANSR-II is an extended version of ANSR-I. Intended primarily for research. Addition of new elements follows a standard procedure.
- ANSR-I allows nonlinear static analysis followed by nonlinear dynamic analysis. ANSR-II allows arbitrary sequences of static and dynamic analysis, and has the following features not contained in ANSR-I: restart from any earlier state; in-core and out-of-core equation solvers; unsymmetrical equation solvers; imposed static displacements; imposed dynamic displacements, including out-of-phase motions. Elements developed for ANSR-I require minor modifications for ANSR-II.

Program Capability:
Static load, dynamic load and dynamic ground motion analysis of two- or three-dimensional frame and finite element systems. No heat flow analysis. No creep analysis (although extension to consider creep is within the capability of the code).

Element Library:
- Truss, beam, two-dimensional isoparametric and three-dimensional isoparametric elements. Library of released elements currently limited. Many different elements under development.
- All nonlinearity is considered at the element level. Hence, the programmer may select the amount and type of nonlinearity to be considered. Elements with large deformations typically use total Lagrangian approach, but this is not essential. Elements with small and large displacements may be mixed in a single analysis if desired.

Solution Methods:
- Newton type iteration for static analysis (includes step-by-step constant stiffness and Newton–Raphson schemes).
- Step-by-step implicit integration (Newmark) for dynamic analysis, with iteration option within each step. Constant time step in each time segment, but time step may be changed between time segments.

Notable Items and Limitations:
No substructuring. Addition of new elements and materials relatively easy.

Programming Language: FORTRAN IV.

Hardware/Operating System: CDC 6400/6600/7600.

Program Size:
Approximately 5500 source statements for ANSR-I
7000 source statements for ANSR-II.

Documentation:
Theoretical manuals and user guides. See Ref. [30–36].

Program Availability: National Information Service for Earthquake Engineering, Computer Applications, 519 Davis Hall, University of California, Berkeley, CA 94720, U.S.A.

Cost approximately $400.

ANSYS

Descriptive Program Title: ANSYS Engineering Analysis System

Program Developer: J. A. Swanson and Staff, Swanson Analysis Systems, Inc., P.O. Box 65, Houston, PA 15342, U.S.A.

Date of First Release and Most Recent Update: 1970 and 1980.

General Information:
The ANSYS program is a proprietary general purpose program developed and maintained exclusively by Swanson Analysis Systems, Inc. The program is fully documented and kept under careful quality control. ANSYS is continuously being enhanced with the addition of state-of-the-art capability and improved modeling and problem solving techniques. Direct communication is available between the user and developer through hot-line telephone consulting and TELENET data transmission. User training seminars and workshop sessions are held periodically at various locations.

Program Capability:

- The ANSYS engineering analysis computer program is a large-scale general purpose computer program employing finite element technology for the solution of several classes of engineering analysis problems. The program capabilities include structural analyses (static and dynamic; elastic, plastic, creep and swelling; buckling; small and large deflections), and heat transfer analyses (steady-state and transient; conduction, convection and radiation). Structural and heat transfer analyses may be made in one, two or three dimensions, including axisymmetric and plane problems. Coupled thermal-fluid flow capability, coupled thermal–elastic capability and fluid–solid interaction capability are also available.
- A single model may be used for heat transfer, static structural, and dynamic structural analyses. Temperature output from the heat transfer analysis is in the form required for input to the structural analyses. Dynamic analyses may be made on structures that have been pre-stressed under static loading conditions.

User Interface and Modeling Capabilities:

- ANSYS may be run in either the interactive or the batch mode. Prompting commands are returned by the program in the interactive mode. Free-format data input is allowed in either mode. Plots may be formed "instantaneously" at graphics display terminals. Documentation and status information displays are available during interactive sessions.
- The ANSYS program includes a multiple region mesh generation capability within the main program as well as general two- or three-dimensional intersecting shell or solid mesh generating routines. The multiple region generation capability is used to fill in nodal points between two specified nodal points, to repeat specified sets of nodal points, to generate additional sets of elements from a specified set to form a group of elements, and to generate additional groups of elements.
- Nodes may be generated in any coordinate system. Symmetry reflections and coordinate system transfers are available. Nodes may be generated along a user-defined quadratic line. Digitizing via cross-hairs or tablet hardware may be used with the mesh generating routines.
- A postprocessing feature of the ANSYS program permits variables calculated from a solution run to be stored on a data file and included in a number of mathematical operations. The results may be printed and/or plotted. The variable operations include addition, subtraction, multiplication, division, square and square root operations, comparison and selection operations, and time derivative operations.
- Scanning is available during postprocessing to allow the user to find at which element or node a given threshold occurs. Values above, below, within, or without, a given range may be found.
- A postprocessing routine is available for combining the results of the seismic mode-frequency analysis. Root-sum-square combinations, absolute value combinations, comparison enveloping, and other operations may be performed.
- A postprocessing routine is available for generating a response spectrum based on a given (or ANSYS calculated) displacement versus time history.
- Results of various solutions involving axisymmetric elements with harmonic loadings may be scaled and summed to give solution to a non-axisymmetric loading.
- Postprocessing routines for stress evaluation in pressure vessels and piping networks (ASME, BPVC and ANSI codes) are available.

Element Library:
The library of finite elements available numbers more than forty for static and dynamic analyses, fifteen for heat transfer analyses, three for thermal–fluid analyses, three for thermal–electric analyses, and two for fluid–solid interaction analyses. The structural element types include spars, pipes and elbows, beams, fluid elements, plane and axisymmetric membranes, plates, shells and solids. Harmonically loaded axisymmetric elements are available for non-axisymmetric loadings. Most element types contain at least one element having complete plastic, creep and swelling capabilities. Plane and solid isoparametric elements are available. Additional structural elements include masses, springs, dampers, sliding interfaces, gap interfaces and cables. Arbitrary stiffness, mass and damping matrix elements are also available. Superelements may be formed from other ANSYS elements. The heat transfer element types include conducting bars, plates and solids, convection and radiation links. All heat transfer elements may be deleted or replaced by geometrically equivalent structural elements for thermal-stress evaluation. Nearly all elements are available with the large displacement option and many elements have additional large rotation and stress (geometric) stiffening capability.

Solution Methods for Nonlinear Problems:

- The ANSYS program uses the wave-front (or "frontal") direct solution method for solving the system of simultaneous linear equations developed by the matrix displacement method. The direct solution method does not place a "bandwidth" restriction on the problem definition.
- The "in-core wavefront" is limited by the amount of core storage required for a given problem. This tends to be restrictive only for analyses of arbitrary three-

dimensional structures on small computers. An out-of-core solution procedure is also available.

● The efficiency of the ANSYS program results from the selection of efficient solution techniques, such as the wavefront equation solver, Guyan reduction (dynamic matrix condensation) and Jacobi eigenvalue extraction, optimizing these techniques by elaborate programming, and tailoring the program to the type of computer system being used. An implicit numerical integration routine is used in each time step of transient analyses.

Notable Items and Limitations:
The ANSYS program contains versatile mesh generators and plot displays. This capability, together with the interactive mode of running, simplifies the modeling task. The ANSYS program is user oriented and self-contained. The user is guided through mesh generation, solution, postprocessing, and auxiliary operations within a single program. The wave-front solution procedure allows ease of modeling and remodeling without any restriction on node numbering. Element reordering is available within the program to minimize the wave front and the solution time. The ANSYS program also runs efficiently on linear problems. The program may be learned through self-education, interactive experimentation, or attending ANSYS seminars.

Programming Language: FORTRAN.

Hardware/Operating System: CDC 7600/6600/6500; CYBER 170 series, 70-series; IBM 360 series, 370 series, 3030 series; AMDAHL 470, CRAY-1, UNIVAC 1100 series, 1108, 1110; PRIME 400, 500 and 50 series; VAX 11/780; HARRIS 500 and 800 series.

Program Size: Over 100,000 source statements.

Documentation: See Refs. [37–41].

Program Availability: The ANSYS program is controlled exclusively by Swanson Analysis Systems, Inc., and is not available for sale or subject to user source modifications. The program may be used on a time-sharing basis through most major data centers throughout the world, e.g. Computer Sciences Corporation, Control Data Corporation, Structural Dynamics Research Corporation, United Computing Systems, Inc., and University Computing Company. Royalty charges for use of the program are included within the data center charges. Lease arrangements for installation on in-house computers are also available.

ASAS-NL

Descriptive Program Title: Atkins Structural Analysis System-Nonlinear.

Program Developer: Atkins Research and Development, Woodcote Grove, Ashley Road, Epsom, Surrey KT18 5BW, England.

Date of First Release and Most Recent Update: 1980.

General Information:
ASAS-NL is a proprietary code sponsored by a number of existing ASAS users and geared principally to the requirements of the nuclear industry. Development was started in 1978 and an active program of enhancement continues.

Program Capability:
● Although ASAS-NL can be viewed as a generic derivative of the general purpose linear elastic ASAS finite element code, it is a quite separate program designed *ab-initio* to solve nonlinear problems. Its architecture reflects the specific needs of nonlinear computations.

● Most nonlinear static problems due to material or geometric nonlinearity can be handled. Over twenty-five elements, ten solutions and ten material models are built in, thus providing wide ranging capabilities for plasticity, creep and swelling, large deflections and buckling. A number of novel techniques are available which provide cheap, albeit approximate solutions, for preliminary design purposes.

User Interface and Modeling Capabilities:
ASAS-NL interfaces with all relevant ASAS pre- and post-processors including ASASHEAT (transient heat flow calculations), COMPAS (superelement interface), ASBAND (bandwidth optimization), ASDIS (mesh display), ASPECT (stress contour plotting), MESH 3/4MESHMOD (mesh generations).

Element Library:
The range of elements available includes two and three dimensional isoparametric (serendipity) elements for continua, with truss, beam and an isoparametric family of shell elements for structures.

Solution Methods for Nonlinear Problems:
Any required combination of iterative/incremental procedures (i.e. Euler, Newton–Raphson), based on a frontal (out-of-core) linear equation solver.

Notable Items and Limitations:
ASAS-NL is designed to solve static (small strain) problems quickly and efficiently. Particular attention has been directed at the facilities for controlling and adjusting the computational sequences, either automatically, or at the behest of the analyst sensitive to the peculiarities of a given problem. Dynamics and large strain capabilities are not available, but their inclusion has been allowed for.

Programming Language: FORTRAN IV.

Hardware/Operating System: PRIME, UNIVAC.

Program Size: Core program—40,000.

Documentation: See Refs. [42, 43].

Program Availability: Atkins Research and Development, Woodcote Grove, Ashley Road, Epsom, Surrey KT18 5BW, England.

ASKA

Descriptive Program Title: Automatic System for Kinematic Analysis.

Program Developer: ASKA Group, Institute for Statics and Dynamics, University of Stuttgart, D-7000 Stuttgart 80, West Germany.

Date of First Release and Most Recent Update: 1970 and 1980.

General Information:
ASKA is a proprietary code. Development started in 1967 and is still continuing. Software maintenance and user support is provided on a long-term basis by the authors. There are more than seventy installations in eighteen countries.

Program Capability:
ASKA is a comprehensive software system mainly for linear static and dynamic analysis. However, some selected nonlinear applications are also covered, mainly elasto–plastic analysis and bifurcation buckling analysis. For elasto–plastic analysis the von Mises yield criterion and associated Prandtl–Reuss flow rule is adopted. Isotropic, kinematic and mixed hardening are included. Also, a Drucker–Prager generalization of the linear and the parabolic Mohr–Coulomb laws with non-associated flow is included.

User Interface and Modeling Capabilities:
Standard ASKA does not include pre- and post-processors. For this purpose there is a separate comprehensive interactive graphics package INGA that has been developed also at ISD together with ASKA. There is also a large number of pre- and postprocessors, e.g. FEMGEN and GIFTS, that are used in connection with ASKA.

Element Library:
At present more than seventy different element types are available, including thick shells, shell/continuum transition elements, harmonic ring elements, and crack tip elements.

Solution Methods for Nonlinear Problems: Newton-type methods.

Notable Items and Limitations:
ASKA has a very powerful multilevel substructure analysis capability based upon a central data base concept. It is capable of solving very large problems, even on minicomputers (VAX, PRIME).

Programming Language: Standard FORTRAN IV.

Hardware/Operating System: At present installed on eleven different computer systems including CDC, UNIVAC, IBM, ICL, HB, Burroughs, VAX, PRIME, CRAY.

Program Size: 600,000 FORTRAN statements in the core program; 60,000 FORTRAN statements in the pre/postprocessors.

Documentation: See Refs. [44–46].

Program Availability: Rent, purchase and support through:
Statik und Dynamik Forschungsgesellschaft mbH Postfach 80 10 44, D-7000 Stuttgart 80, West Germany.

BEAM

Descriptive Program Title: Inelastic Analysis of Reinforced and Prestressed Concrete Beams and Beam-Columns.

Program Developer: C. N. Kostem, Fritz Engineering Laboratory, 13, Lehigh University, Bethlehem, PA 18015, U.S.A. (also, J. M. Kulicki—c/o C. N. Kostem).

Date of First Release and Most Recent Update: 1973 and 1978.

General Information:
Program BEAM is designed to determine the elastic and inelastic response of beams and beam-columns. Structure and loading are assumed to be planar. For given loading, the incrementation is carried out until the collapse of the structure. All material nonlinearities have been incorporated through Ramberg–Osgood type stress–strain curve formulation. Cracking, crushing and yielding of the constituent materials are considered.

Program Capability:
The formulation is based on beam finite elements with axial distortion degree of freedom. FORTRAN EXTENDED coding permits the full transportability of the program. The program has been successfully implemented as a module in many other larger programs due to its modular design. BEAM has been developed for use as a research tool, and also for employment in the conduct of parametric studies on the inelastic analysis of beams. This necessitated an optimum code which could be easily modified by the user for different needs.

User Interface and Modeling Capabilities:
Program BEAM does not have a preprocessor. However, it includes a line printer graphics capability for the display of stress variation throughout the structure for any and every load increment. This permits the use of program BEAM with minimal engineering training, and no background in finite element method.

Element Library:
BEAM contains only one beam element, which has cubic flexural displacement and linear axial deformation displacement fields. Each element is layered through the depth to monitor the initiation and propagation of nonlinearities and damage through the loading history. Each layer is assumed to be in plane stress state.

Solution Methods for Nonlinear Problems:
Solution scheme is based on incremental/iterative tangent stiffness approach. Load steps, and number of iterations are defined by the user, depending upon the desired accuracy.

Notable Items and Limitations:
The main feature of the program is its self contained nature. The program was developed for one purpose, i.e. to simulate the inelastic response of reinforced and prestressed concrete beams. Other types of material could, and have been, considered; however, simulations as such can be better achieved by general purpose programs.

Programming Language: FORTRAN EXTENDED (Control Data Corporation).

Hardware/Operating System: CDC 6400 with SCOPE operating system (BEAM has also been successfully converted, and widely tested in Burroughs 5000 computers).

Program Size: Approximately 2000 cards.

Documentation: See Refs. [47, 48].

Program Availability: Dr. Celal N. Kostem, Fritz Engineering Laboratory, 13, Lehigh University, Bethlehem, PA 18015, U.S.A.

BOSOR4

Descriptive Program Title: Stress, Buckling, Vibration of Branched, Stiffened, Elastic Shells of Revolution.

Program Developer: David Bushnell, Department 52-33/205, Lockheed Palo Alto Research Laboratory, 3251 Hanover Street, Palo Alto, CA 94304, U.S.A.

Date of First Release and Most Recent Update: 1972 and 1979.

General Information:
BOSOR4 is used by more than 150 institutions all over the world and has received so much use that it is, for all practical purposes, bug free. The program is maintained by the developer who sends notices of any bugs found or other information of pertinence to all users. Several data service companies have BOSOR4, including United Computing Systems, Boeing Computer Service, McDonnell-Douglas Automation, CDC Cybernet (Rockville, Maryland), Information Systems Design, Westinghouse, Det Norske Veritas (Norway), CNES (France), CERN (Switzerland), FFA (Sweden), Matematischer Beratungs und Prog. (West Germany).

Program Capability:
BOSOR4 performs stress, buckling and modal vibration analyses of ring-stiffened, branched, segmented, shells of revolution with complex wall constructions, loaded either axisymmetrically or nonsymmetrically. Program branches include large-deflection axisymmetric stress analysis, small-deflection nonsymmetric stress analysis, modal vibration analysis with axisymmetric nonlinear prestress, and buckling analysis with axisymmetric or nonsymmetric prestress. Main advantage is the provision for realistic engineering details such as eccentric load paths, internal supports, arbitrary axisymmetric branching, and a "library" of wall constructions. A variety of loads can be applied simultaneously, loads that increase proportionally with each other, or combinations of loads, some of which are held constant and others of which vary (are eigenvalue parameters) during a case. Two unique features of BOSOR4 are that it is stable, and hence, reliable and it is *fast*. The program has been extensively used in the field for many years, essentially unchanged, so that bugs have been thoroughly shaken out. BOSOR4 has been thoroughly qualified by numerous comparisons with tests, most of which have been documented in the open literature.

User Interface and Modeling Capabilities:
User interface is via a free format preprocessor, B4PRE. Certain commonly occurring geometries, such as cylinders, spheres, cones, etc. are generated with use of integer pointers and user-provided end-point coordinates. BOSOR4 contains a Fourier series generator for automatically breaking down a nonsymmetric load into its Fourier harmonics. Also required from user for input are number of nodal points, discrete ring geometries, ranges and increments of circumferential wave numbers, load and temperature distributions, shell wall construction details, and constraint conditions. Output includes lists and plots of displacement distributions, stress resultants, stresses, vibration frequencies, buckling loads.

Element Library:
Discretization is by the finite difference energy method, which represents a kind of finite element that is extremely rapidly generated.

Solution Methods for Nonlinear Problems:
- Out-of-core Newton–Raphson solution solving technique.
- Eigenvalues extracted by inverse power method with spectral shifts and orthogonalization.
- Skyline method used for matrix factorization.

Limitations:
Fifteen-hundred degrees of freedom (d.o.f.) in nonaxisymmetric problems; 1000 d.o.f. in axisymmetric prebuckling stress analysis; maximum of 20 Fourier harmonics per case; knockdown factors for imperfection sensitivity not included; radius to thickness ratio should be greater than about 10.

Notable Items:
The program is *fast*. Complete (axisymmetric) structural systems can be analyzed in a few minutes. Program is reliable, since it has been exercised worldwide for many years essentially unchanged. Ideal for many preliminary design tasks.

Programming Language: FORTRAN IV.

Hardware/Operating System: UNIVAC 1110, CDC 6600 or 7600, IBM 360 or 370, VAX, SC4020 and CALCOMP plotters.

Program Size: About 14,000 statements.

Documentation: See Refs. [49–51].

Program Availability: BOSOR4 is available for use through data centers listed above. Also, the program may be purchased for $600 from the developer. Purchase includes source deck (tape), example cases and documentation.

BOSOR5

Descriptive Program Title: Buckling of Elastic-Plastic Complex Shells of Revolution Including Large Deflections and Creep.

Program Developer: David Bushnell, Dept. 52–53/205, Lockheed Palo Alto Research Laboratory, 3251 Hanover Street, Palo Alto, CA 94304, U.S.A.

Date of First Release and Most Recent Update: 1974 and 1979.

General Information:
BOSOR5 is used by more than seventy institutions all over the world. The program is maintained by the developer who sends notices of any bugs found or other

information of pertinence to all users. Several data service companies have BOSOR5 including United Computing Systems, Boeing Computer Service, McDonnell-Douglas Automation, CDC Cybernet (Rockville, Maryland), Information Systems Design, Westinghouse, Det Norske Veritas (Norway), CERN (Switzerland), FFA (Sweden). BOSOR5 does *not* supercede BOSOR4 as it does not perform modal vibration or linear nonsymmetric stress analysis. BOSOR5 has received extensive use for several years at organizations other than that of the developer and is reasonably bug-free.

Program Capability:
BOSOR5 can handle segmented and branched axisymmetric shells with discrete ring stiffeners, meridional discontinuities, and multi-material wall construction. The shell wall can be made up of as many as six layers, each of which is a different nonlinear material. In the prebuckling analysis, moderately large deflection axisymmetric behavior is presumed. Failure by axisymmetric collapse or by nonsymmetric bifurcation buckling from the axisymmetrically deformed prebuckling state are calculated. Main advantage is the provision for realistic engineering details such as eccentric load paths, internal supports, arbitrary axisymmetric branching, and flexibility of loading. A variety of loads can be applied simultaneously, loads that increase proportionally with each other, or loads that vary during the case in a nonproportional way. Two unique features of BOSOR5 are that it is stable (program not being changed except to eliminate bugs) and it is *fast*. Primary or secondary creep can be accounted for simultaneously with elastic–plastic behavior. Program has been thoroughly qualified by numerous comparisons with tests, most of which have been documented in the open literature.

User Interface and Modeling Capabilities:
BOSOR5 consists of three processors: pre, main and post. Input data is fixed format. Certain commonly occurring geometries such as cylinders, spheres, cones, etc. are generated with use of integer pointers and user-provided end-point coordinates. Also required from user for input are number and distribution of nodal points, discrete ring geometries, ranges and increments of circumferential wave numbers, load and temperature distributions, shell wall construction details, and constraint conditions. Output includes lists and plots of displacements, stress resultants, stresses and strains at several stations through the thickness, buckling loads. The main processor has a restart capability.

Element Library:
Discretization is by the finite difference energy method, which represents a kind of finite element that is extremely rapidly generated.

Solution Methods for Nonlinear Problems:
- Newton–Raphson, out-of-core solving.
- Very carefully designed strategy for combined large-deflection, material nonlinearity, involving a double iteration loop at each load level.
- Subincremental strategy for material nonlinearity (see Ref. [54]).
- Eigenvalues extracted by inverse power method with spectral shifts.
- Skyline method used for matrix factorization.

Notable Items and Limitations:
Fifteen-hundred degrees of freedom (d.o.f.) in nonaxisymmetric bifurcation buckling problem; 1000 d.o.f. in axisymmetric prebuckling stress analysis. Knockdown factors for imperfection sensitivity not included; radius to thickness ratio should be greater than about 10. Isotropic strain hardening with von Mises yield criterion and Norton creep law are included.

Programming Language: FORTRAN IV.

Hardware/Operating System: UNIVAC 1110, CDC 6600 or 7600, IBM 360 or 370, VAX, SC4020 and CALCOMP plotters.

Program Size: About 12,000 statements (core program, pre- and postprocessors).

Documentation: See Refs. [52–54].

Program Availability: BOSOR5 is available for use through the data centers listed above. BOSOR5 may be purchased for $500 from the developer. Purchase includes source deck (tape), example cases, and documentation.

BOVA

Descriptive Program Title: Bridge Overload Analysis.

Program Developer: C. N. Kostem, Fritz Engineering Laboratory, 13, Lehigh University, Bethlehem, PA 18015, U.S.A. (also, W. S. Peterson—c/o C. N. Kostem).

Date of First Release and Most Recent Update: 1975 and 1979.

General Information:
Program BOVA was developed to simulate the elastic and inelastic static response of simple span beam-slab bridges with reinforced concrete slab (or any isotropic or orthotropically reinforced plate) and reinforced or prestressed concrete beams. Beams are assumed to be solid, i.e. *I*-, *T*-beams, etc. The accuracy of the solutions deteriorate if applied to box-beam structures. The program has been extensively tested, and its accuracy has been demonstrated. Cracking, crushing, yielding and all other forms of material nonlinearities, including fully nonlinear stress–strain curves, have been incorporated into the program.

Program Capability:
The program is capable of providing the full simulation of bridge-like superstructures from zero load level up to the collapse of the structural system. Overzealous discretization of the structural system, and high degree of precision that may be described by the user, may require extensive central processor time. All practical and detailed research problems can be analyzed in an efficient manner. Program provides voluminous printout for all the stress, deformation and damage states for any given load level.

User Interface and Modeling Capabilities:
Program contains a minimal preprocessing capability, and printer plot post processing capability. Additional features have been added by other users. The accuracy of these modifications has not been fully demonstrated.

Element Library:
Program is built around ACM-plate bending element, and cubic beam finite element. Uniaxial deformation field for the beams and biaxial membrane displacement field for the plate bending elements have also been incorporated. Plate and beam elements are further discretized into layers to monitor the stress and damage variations through the depth of the members. Extremely sophisticated failure criteria have been developed and are for the first time incorporated into this program.

Solution Methods for Nonlinear Problems:
Solution is based on incremental or incremental iterative solution of the system tangent stiffness matrix. User has the option of defining the solution scheme, the accuracy checks and termination checks.

Notable Items and Limitations:
The program simulates the inelastic response of bridge superstructures. The program has been extensively tested, and it has been observed that even with "engineering" type rough discretization, the program can predict the stress and the damage to the structural system fairly accurately. The program has been available to the Departments of Transportation for wide scale deployment in the rating of bridge superstructures, and issuance of overload permits. This is the first time that bridge integrity is related to the load level in the definition of permits.

Programming Language: FORTRAN EXTENDED (Control Data Corporation).

Hardware/Operating System: CDC 6400 (SCOPE operating system; employs OVERLAYS) Burroughs 5000 series.

Program Size: Approximately 15,000 cards.

Documentation: See Refs. [55, 56].

Program Availability: Unsupported version of the program is available from Federal Highway Administration and Pennsylvania Department of Transportation. For supported version, contact: Dr. C. N. Kostem, Fritz Engineering Laboratory, 13, Lehigh University, Bethlehem, PA 18015, U.S.A.

BOVAC

Descriptive Program Title: Bridge Overload Analysis-Concrete Bridges.

Program Developer: C. N. Kostem, Fritz Engineering Laboratory, 13, Lehigh University, Bethlehem, PA 18015, U.S.A.

Date of First Release and Most Recent Update: 1979 and 1980.

General Information:
Program BOVAC is an enhanced version of program BOVA (Bridge Overload Analysis, by Dr. C. N. Kostem). Program was developed for average user without engineering background. The program is fully supported by the developer. All releases are made available, at no cost, to the users of the program. The main difference between BOVAC and BOVA is the addition of substantial preprocessing capability in BOVAC.

Program Capability:
Program is aimed at the analysis of beam-slab highway bridge superstructures. Extensive libraries have been built into the program to predefine the prestressed *I*-beam cross sections used in Pennsylvania. Similarly, the types of reinforcement detailing are automatically accomplished by the program. The program could be modified with great ease to enhance the library of bridge superstructure details.

User Interface and Modeling Capabilities:
Pre- and postprocessors have been built into the program. All pre- and postprocessing activities are carried out in core through the use of line printer graphics.

Element Library:
BOVAC employs ACM plate bending element with membrane degrees of freedom, and cubic beam element with axial deformation degree of freedom. For the types of applications other types of elements are found to be redundant.

Solution Methods for Nonlinear Problems:
BOVAC employs incremental iterative solution of system tangent stiffness equations. The user does not have control of the modifications of the solution technique via input data stream.

Notable Items and Limitations:
The program can be used by individuals without any finite element or even engineering background. It is intended for use for overload permit applications.

Programming Language: FORTRAN EXTENDED (Control Data Corporation).

Hardware/Operating System: CDC 6400 (SCOPE operating system; employs OVERLAYs) Burroughs 5000 computers.

Program Size: Approximately 17,000 cards.

Documentation: See Refs. [57, 58].

Program Availability: Unsupported version of the program is available through Federal Highway Administration and Pennsylvania Department of Transportation. For supported version contact the developer.

BRICK

Descriptive Program Title: Inelastic Analysis of Masonry Panel Wall-Beam Column Structures.

Program Developer: C. N. Kostem, Fritz Engineering Laboratory, 13, Lehigh University, Bethlehem, Pennsylvania 18015, U.S.A. (Also, P. Green—c/o C. N. Kostem).

Date of First Release: 1979.

General Information:
Program Brick is built around the appropriate portions of Program SOLID SAP. It is envisioned that the future developments of BRICK will be carried out for portions other than SOLID SAP. The listing of the current

version of the program has been provided in the user's manual. Future revisions will be related to this listed version.

Program Capability:
Program BRICK was developed to predict the elastic and inelastic response of wall panels consisting of two beams, two columns, and masonry wall. Prediscretization is provided to model the brick (or any other masonry blocks) and mortar. The aim of the program has been (1) the determination of the interaction between the masonry panel and the structural frame, and (2) to determine the damage initiation in wall panel and the propagation of the damage.

User Interface and Modeling Capabilities:
Program contains minimal amount of preprocessing capability in terms of automatic prediscretization. Output files have been defined for the prospective users to interface with appropriate post-processors.

Element Library:
Program employs high order plane stress elements to describe the behavior of bricks and masonry. Beam elements are used to define the beams and columns.

- ANALYTICAL CAPABILITIES
  - elastic and elasto-plastic calculations } STATIC AND
  - natural frequency and modal response to cyclic loading } DYNAMIC

element family	
one dimensional	(rod)
two dimensional	plane stress / plane strain / axisymmetric
three dimensional	(solid)

These elements have been described in the SOLID SAP manual.

Solution Methods for Nonlinear Problems:
Program employs incremental tangent stiffness method. The program could be considered as the core unit for future modifications by researchers.

Notable Items and Limitations:
Program has been developed as a research tool. It has been kept general and flexible enough for future modifications. The modifications can be tailored according to user needs.

Programming Language: FORTRAN IV.

Hardware/Operating System: CDC 6400 (SCOPE Operating System).

Program Size: Approximately 5000 cards.

Documentation: See Refs. [59, 60].

Program Availability: Refer to user's manual and/or developer.

DANUTA

Program Developer: S. A. Chacour, Advanced Technology Department, Allis-Chalmers Corporation, P.O. Box 712, York, PA 17405, U.S.A.

Date of First Release and Most Recent Update: 1971 and 1979.

General Information:
DANUTA is a highly automated computer program which uses the finite element technique for the static and dynamic analysis of structures encountered in the mechanical and civil engineering fields. The choice of elements and gridwork allow curved boundaries on surfaces, hence, the ease in simulating complicated structures such as pressure vessels, mechanical components, turbine blades, arched dams, shear walls, shells, etc.

Program Characteristics:
- ACCURACY

  Subparametric curvilinear elements whose shape functions and high precision enable accurate mathematical representation through relatively coarse modeling gridwork. Displacements and their first derivatives make up the degrees of freedom allowed at all corner nodes.

- OPTIMIZED SOLUTION TECHNIQUES

  Low cost results through the use of automated bandwidth minimizing procedure.

Note: The program accommodates models employing both plane stress and axisymmetric two-dimensional elements by imposing user selected constraints between the displacement components at the interface nodes.

- EASY MODELING
  - Choice of simple input formats based on single data type entries per record or free format.
  - A variety of preprocessors enabling automatic grid generation.
  - Input checking program plots geometry, node identification numbers, loading and constraints and provides complete echo of data deck in printed form each record having been checked for format as well as structural modeling errors.
  - A variety of flexible or rigid boundary conditions utilizing cyclic or reflection symmetry, and transformed local coordinates.
- WIDE VARIETY OF OUTPUT
  - Computer printed output in either condensed or full form.
  - Post-processor file for employing superposition of up to 32 separate loading cases. Nonlinear behavior as found in problems involving contact can thus be obtained.
  - Color coded plots depicting the deflected and undeflected structural model for static analysis or mode shape plots for dynamic analysis.

Programming Language: FORTRAN IV.

Hardware/Operating System: CDC 7600 (SCOPE), CDC CYBER 170 Series (NOS), CDC STAR, IBM, UNIVAC (EXEC8, Double Precision).

Program Size:

Core Program:	13300 records
Preprocessor:	3400 records
Post-Processor:	2250 records.

Availability: Program can be used on CDC CYBER 173 computer. Time sharing arrangements can be set up with the York plant.

DIAL

Descriptive Program Title: General Purpose Finite Element Code.

Program Developers: Gordon Ferguson and Norman A. Cyr, Lockheed Missiles and Space Company, Inc., 1111 Lockheed Way, Sunnyvale, CA 94086, U.S.A.

Date of First Release and Most Recent Update: 1975 and 1980.

General Information:
DIAL is a proprietary code which is undergoing continual development.

Program Capability:
DIAL is a general purpose finite element program with the ability to perform static and transient nonlinear analysis in addition to linear stress analysis, vibration and buckling. The element library consists of a full set of modern elements for two-dimensional (including Fourier modes) and three-dimensional analysis. The DIAL system consists of several independent processors which communicate via a generalized data base and file management system. Restart, analysis planning and branching, communication with other engineering programs and other logical user problems are easily performed within the architecture of the DIAL system.

User Interface and Modeling Capabilities:
User input may be any mixture of free field commands and FORTRAN subroutine calls, offering maximum flexibility. Full two- and three-dimensional automatic mesh generation capabilities are available. Post-processing functions include all standard printing and plotting features in addition to extensive data manipulation capabilities (e.g. stress rotation, extrapolation to nodes, etc.).

Element Library:
Complete sets of two- and three-dimensional isoparametric (linear parabolic, cubic, mixed order) solids and degenerate isoparametric thick shells and curved beams are available. Standard thin shell, truss and beam elements are also included. Special provisions are made for user defined stiffnesses and other elements.

Solution Methods for Nonlinear Problems:
Nonlinear static solution techniques include many variations of Newton type methods with automatic load step calculation. Nonlinear transient techniques include several implicit schemes using Newton methods and an explicit scheme, all with automatic time-step selection.

Notable Items and Limitations:
DIAL is a modern processor-oriented code with complete, up-to-date libraries of two- and three-dimensional elements capable of performing two-dimensional (plane stress, plane strain, axisymmetric with and without Fourier modes), and three-dimensional analysis. Due to the modular data base concept, user control is very versatile and economical. Large problems may be run in an interactive environment.

Programming Language: FORTRAN with selected machine coding in inner loops.

Hardware/Operating System: UNIVAC, CDC.

Program Size:

Analysis Processors:	50,000
Pre-processors:	15,000
Post-processors:	20,000.

Documentation: Program description, user's manual.

Program Availability: From code developers.

DRAIN-2D, DRAIN-TABS

Descriptive Program Title: Seismic Response Analysis of Inelastic Two-Dimensional Structures and Three-Dimensional Buildings.

Program Developer: G. H. Powell, Department of Civil Engineering, Division of Structural Engineering and Structural Mechanics, University of California, Berkeley, CA 94720, U.S.A.

Date of First Release: 1971.

General Information:
Developed as simple general purpose code for research in inelastic seismic response. Unsophisticated, but simple and efficient. Has received substantial use for both research and practical analysis. Designed to allow new elements to be added with relative ease.

Program Capability:
Static load analysis (for which behavior must be linear) followed by dynamic analysis under one- or two-dimensional ground motion. All support points must move in-phase. Calculates time histories of node and element response.
DRAIN-2D considers a single two-dimensional structure. DRAIN-TABS allows several two-dimensional structures to be linked together by rigid floor diaphragms, to allow modeling of three-dimensional buildings.

User Interface and Modeling Capabilities:
No pre-processors. Plotting routines have been developed but are not included in the basic package. Results may be saved on tape for post-processing.

Element Library:
A variety of bar, beam and panel elements are available. New elements can be added relatively easily.
Modeling typically assumes small displacements or second-order displacements (P-delta effect included). Since all nonlinearity is introduced at the element level,

large displacements could be considered, but because of the solution strategy this is not convenient.

Solution Methods:
Implicit step-by-step integration with constant time step. No iteration within step. Unbalances due to nonlinear behavior carried through to next step.

Programming Language: FORTRAN IV.

Hardware/Operating System: CDC 6400/6600/7600, DRAIN-2D: IBM 360 also.

Program Size:
Approximately 9000 cards for DRAIN-TABS
5000 cards for DRAIN-2D

Documentation: Theoretical manual and user guide. See Refs. [61–65].

Program Availability: National Information Service for Earthquake Engineering, Computer Applications, 519 Davis Hall, University of California, Berkely, CA 94720, U.S.A.
Cost approximately $300 each.

PLANS, DYCAST

Descriptive Program Title: *P*lastic and *L*arge Deflection *A*nalysis of *S*tructures, *D*ynamic *C*rash *A*nalysis of *S*tructures.

Program Developer: A. Pifko, A. Levy, H. Armen and H. Levine†, Research Department, Grumman Aerospace Corporation, Bethpage, NY 11714, U.S.A.

Date of First Release and Most Recent Update: PLANS—1972—Development Continuing; DYCAST—1976—Development Continuing.

General Information:
PLANS is a group of programs for the static nonlinear analysis of structures. PLANS programs consist of four programs for material nonlinearity: elastic–plastic analysis of three-dimensional built-up structures; elastic–plastic analysis of bodies of revolution; elastic–plastic creep analysis of three-dimensional solids; and the elastic–plastic fracture analysis of planar structures. Two programs were developed for combined material and geometric nonlinearity; one for three-dimensional built-up structures and the other for the nonlinear analysis and bifurcation buckling of folded plate structures. Initial version of PLANS was funded by NASA Langley Research Center and is available through COSMIC. Independent development is continuing at Grumman. DYCAST is a program for nonlinear dynamic analysis with particular emphasis on vehicle crashworthiness. Development of DYCAST is continuing under contract to NASA Langley Research Center.

†No longer at Grumman.

Program Capability:
PLANS/DYCAST as a group constitutes a general purpose finite element program for nonlinear analysis of structures. Having separated the programs by analysis class has enabled the implementation of solution algorithms most suitable for each type of analysis. The modules that analyze material nonlinearities alone employ the "pseudo-load or initial strain" concept within an incremental procedure to account for the effect of creep and plasticity and include the capability for cyclic plastic and creep analysis. The cyclic plastic behavior is accounted for by implementing the Prager–Ziegler kinematic hardening theory while cyclic creep behavior is treated according to the ORNL auxiliary rules for stress reversal. The "pseudoload" approach does not require that the stiffness matrix be updated at each step in the analysis but rather the effect of plasticity enters into the analysis as an effective load vector. Geometric nonlinearities are included by making use of an updated Lagrangian approach, which requires the reformation of the stiffness matrix due to changes in the geometry and stress field during an incremental/iterative procedure.

User Interface and Modeling Capabilities:
Current capability includes one common program for data checking, bandwidth optimization and plotting the undeformed structure. There are no general purpose mesh generators although a number of special programs have been written for particular mesh types as needed. Postprocessing programs are available for plotting the deformed structure and for time histories of displacement, velocity and acceleration. Limited capability exists for contour plotting.

Element Library:
The elements in PLANS that can be used for static plastic analysis are: three-dimensional thin-walled beam; two and three node axial force element; three to six node family of membrane triangles; higher order membrane and bending triangular element (strain and curvature degrees of freedom); eight to twenty node isoparametric solid; revolved triangle; revolved curved

Solution Methods for Nonlinear Problems:

- Nonlinear Dynamic Response —Choice of four time integrators; Implicit Newmark or Wilson and Explicit Central Difference or Variable Time-Step Modified Adams
- Nonlinear Static
  - Material and Geometric Nonlinearities —Incremental Solution, Modified Newton Iteration
  - Plastic Analysis —Incremental Solution with Equilibrium Correction
  - Elastic–Plastic-Creep —Incremental Predictor–Corrector Iterative (or Non-iterative) Method
- Equation Solver —Choice of two routines, in-core or out-of-core compacted solver
  —Diagonal matrix for explicit lumped mass
- Eigenvalue/Eigenvector Solver —Lanczos Method, Automatic Reduction of Matrix to Tridiagonal Form

shell and stiffener. Static material and geometric nonlinearity includes the first four element types mentioned above. DYCAST includes the first three element types mentioned above as well as a general nonlinear spring element.

Notable Items and Limitations:
PLANS and DYCAST have been written with a modular structure so that program size (number of nodes and elements and working core) can be easily changed. New elements can also be added in a straightforward manner. The programs can easily be converted for all existing computer hardware.
DYCAST has be written with vehicle crashworthiness as its principal application.
There are limitations in the element library particularly because of the absence of the isoparametric quadralateral and a simple plate bending element. Use of problem-adaptive controls for modeling nonlinearities should be added in order to enhance the "general purpose" capability of the program. These involve internal checks on the material constitutive equations, and time step/load step sizes.

Programming Language: FORTRAN IV.

Hardware/Operating System:
The programs were written for IBM or CDC computers and are fully portable among these. Currently operational on CDC CYBER 172–175 (NDS) and IBM 370/168 MVT (double precision). DYCAST and one of the PLANS programs is operational on CDC-STAR-100. PLANS is operational on DEC VAX/11/780.

Program Size:
PLANS—approximately 18,000 FORTRAN statements per program
DYCAST—approximately 25,000 FORTRAN statements
Pre-Post Processors—approximately 5000 FORTRAN statements.

Documentation:
A theoretical and user's manual is available for PLANS (see Refs. [66–68]). The DYCAST manual is under preparation.

Program Availability:
Versions of PLANS are available through COSMIC. Current versions are available from Grumman Aerospace Corporation for a fee (negotiable).

ELAS55

Descriptive Program Title: ELAS55 Computer Program for Equilibrium Problems of Thermo–Viscoelastic–Plastic Solids and Structures.

Program Developers: S. Utku, J. Q. Tarn† and G. J. Dvorak†, Civil Engineering Department, Duke University, Durham, NC 27706, U.S.A.

Date of First Release: April 1974.

General Information:
ELAS55 has been developed by the resources of the Computer Structural Analysis Fund of the School of Engineering of Duke University, Durham, North Carolina. It is based on the ELAS75 program (for the linear equilibrium problems of solids and structures) of the Fund. ELAS55 may be obtained from the Fund with a one-time nominal registration fee payable to the Fund. The cost of additional support and maintenance should be negotiated with the Fund; however, the basic support and maintenance are free. ELAS55 is a general purpose computer program for the nonlinear equilibrium problems of solids and structures, and it uses displacement finite element method for the solution.

Program Capability:
ELAS55 considers only the material nonlinearities. Geometry is defined by hexahedral elements only. Euler–Navier, Kirchhoff, axial symmetry, plane strain, etc. type assumptions may be imposed by means of the multi-point deflection boundary conditions. Through input parameters, various Newton–Raphson algorithms may be chosen. There can be up to 99 different materials. Each can be any combination of the following arranged in series: an anisotropic elastic solid (up to 21 elastic constants), an anistropic viscoelastic Kelvin solid (up to 21 Kelvin models with temperature dependent Kelvin Parameters which are not necessarily thermorheologically simple), and an isotropic elastic–plastic solid of the Mises type (the yield stress may be temperature dependent). Restart capability allows nonproportional loading.

User Interface and Modeling Capabilities:
There is no pre- or post-processor to go with the ELAS55 program. However, means of working with pre- and post-processors are already implemented in the program.

Element Library:
There is only hexahedral element in the program. All other elements can be simulated by means of the multi-point deflection boundary conditions.

Solution Methods for Nonlinear Problems:
Through input parameters various Newton–Raphson iterations can be chosen. With the input parameters, the user can control the frequency of generation of the instantaneous stiffness matrix (the Jacobian of residuals with respect to independent deflections), the number of subiterations using the same instantaneous stiffness matrix, and the number of finite elements which can yield for a given load increment.

Notable Items and Limitations:
In-core decomposition of the instantaneous stiffness matrix is a size limitation. Small deformations can also be a limitation for some problems. The possibility of multi-point deflection boundary conditions, and the variety of constitutive relations are strong points.

Programming Language:
FORTRAN IV (direct use for IBM 370/165 H compiler).

Hardware/Operating System:
Any middle to large size computer with FORTRAN IV compiler and a link-editor with overlaying feature.

Program Size: About 6500 source statements.

Documentation: See Refs.[69, 70].

†No longer at Duke University.

Program Availability:
One time registration fee payable to Duke University is $2000. For the source program, documentation, sample inputs and outputs, write to: Computer · Structural Analysis Fund, Department of Civil Engineering, Duke University, Durham, NC 27706 or call (919) 684-2434.

HONDO II

Descriptive Program Title: A Two-Dimensional Finite Element Program for the Solution of Large Deformation Finite Strain, Inelastic Transient Dynamic Response of Solids.

Program Developer: Samuel W. Key, Division 5531, Sandia National Laboratories, Albuquerque, NM 87185, U.S.A.

Date of First Release and Most Recent Update: First release 1974, second release 1978.

General Information:
HONDO II is a nonproprietary code. It was developed for use at Sandia National Laboratories on a variety of energetic problems including impact and blast loading. The program is currently in use at Sandia. Updates to correct errors as they become known are sent to the known users. No consulting or maintenance is provided except on a casual basis.

Program Capability:
The program is particularly useful in that it has a sliding interface capability which allows multiple independently meshed bodies to interact dynamically.

User Interface and Modeling Capabilities:
Pre- and post-processors are not included. The program accepts a binary file containing information from a mesh generator called QMESH. The program writes a binary output file which can be post-processed.

Element Library:
A four node quadrilateral with a choice of either constant stress assumption or variable stress with constant pressure.

Solution Methods for Nonlinear Problems:
Explicit central difference time integration including automatic selection and adjustment of time step to maintain numerical stability.

Notable Items and Limitations:
HONDO II is a special purpose program which for the intended applications works rapidly and reliably. The user should have an advanced education in solid mechanics covering stress wave propagation and large deformations.

Programming Language: FORTRAN IV.

Hardware/Operating System: CDC 7600.

Program Size: 3000 cards.

Documentation: See Ref. [71].

Program Availability: Upon request and submittal of a magnetic tape.

JAC

Descriptive Program Title: A Two-Dimensional Finite Element Program which Uses a Nonlinear Conjugate Gradient Technique for the Solution of the Nonlinear Quasi-Static Response of Solids.

Program Developer: J. H. Biffle, Division 5521, Sandia National Laboratories, Albuquerque, NM 87185, U.S.A.

Date of First Release and Most Recent Update: 1980.

General Information:
The code is a production version of a code used to research the use of explicit iterative techniques to solve highly nonlinear solid mechanics problems. Development started in 1978 and many iterative schemes were tried. The nonlinear conjugate gradient method appears to be the best of all explicit schemes considered.

Program Capability:
JAC is a finite element computer program for solving the large deformation, temperature dependent static problems for two-dimensional bodies. Either plane strain or axisymmetric geometry may be used. Material properties include isothermal and temperature dependent elastic–plastic, secondary creep and soil large strain models. Sliding interfaces can also be modeled. Solutions are obtained with the use of a nonlinear conjugate gradient technique. To accelerate convergence of the solution process during a load step, a fraction of the displacement increment of the previous load step may be used as an initial incremental displacement to start the solution. The formulation uses isoparametric nine-node Lagrangian elements which are integrated with a nine point rule evaluated at the nodes of the grid. To also accelerate convergence, a solution of a load increment can first be obtained with the use of four-node elements by using only the corner nodes of the nine-node elements. The four-node results are then used as a starting displacement vector to obtain the nine node element solution. When geometric nonlinearities are present, it is sometimes advantageous to calculate a geometrically linear solution and then restart the solution to obtain a geometrically nonlinear solution. Therefore, when obtaining the final nine node element solution, first a linear solution and then a geometrically nonlinear solution can be obtained. The program is recommended for use on highly nonlinear analyses and not for linear solutions. It is much more efficient to solve linear problems another way.

User Interface and Modeling Capabilities:
Pre- and post-processors are not included. The program accepts a binary file containing information from a mesh generator called QMESH. The program writes a binary output file which can be processed.

Element Library:
A nine-node Lagrangian element is used.

Solution Methods for Nonlinear Problems:
A nonlinear conjugate gradient method is used.

Notable Items and Limitations:
The program is a serious attempt to use an explicit solution technique for nonlinear static problems. It is hoped that the research will be most profitable with

three-dimensional problems. The convergence of the nonlinear problems is reliable, but for problems which exhibit a large spread in eigenvalues it can be slow.

Programming Language: FORTRAN IV.

Hardware/Operating System: CDC 7600.

Program Size: 2500 cards.

Documentation: User's manual is in preparation.

Program Availability: Upon request when release has been approved and manual has been written.

LARSTRAN 80

Descriptive Program Title: Large Strain Nonlinear Analysis.

Program Developer: Institute for Statics and Dynamics, University of Stuttgart, Pfaffenwaldring 27, 7000 Stuttgart 80, West Germany.

Date of First Release: 1981.

General Information:
Development from scratch since 1977. Software maintenance and user support will be provided on a long-term basis. Due to a rock bottom standardization in the FORTRAN IV coding, the system is machine-independent to the highest degree conceivable. An open concept allows user access in all levels of the program hierarchy.

Program Capability:
LARSTRAN 80 is a program system designed to provide a basis for nonlinear static and dynamic structural computations. Standard applications are the (modified) Newton–Raphson procedure, a third order Hermitian nonlinear dynamic algorithm, and an explicit nonlinear dynamic algorithm.
The finite element programs are easily attached to the system through a unified concept.

User Interface and Modeling Capabilities:
The user data input is facilitated by a simple but powerful data generation capability. There will exist a data compatibility path to and from the interactive graphics package INGA and to other software systems.

Element Library:
Currently about twenty different element types are included. The number of elements is continually increasing.

Solution Methods for Nonlinear Problems:
Newton-type iteration.
Implicit and explicit time integration.

Notable Items and Limitations:
The out-of-core logic is strictly maintained in all parts of the coding. Therefore, no limits are imposed in terms of some problem size. A central data base and neatly designed data structures (being transparent to the user) allows for user interaction and provides a stop/restart as a standard facility.

Programming Language: STANDARD FORTRAN IV.

Hardware/Operating System: CDC, UNIVAC, IBM.

Program Size: Approximately 30,000 lines of code/500 subroutines.

Documentation: See Ref. [72]. An updated users manual is in preparation.

Program Availability: Statik und Dynamik Forschungsgesellschaft mbH, Postfach 80 10 44, D-7000 Stuttgart 80, West Germany.

MARC

Descriptive Program Title: General Purpose Finite Element Program.

Program Developer: P. V. Marcal, President, MARC Analysis Research Corporation, 260 Sheridan Avenue, Suite 200, Palo Alto, CA 94306, U.S.A.

Date of First Release and Most Recent Update: 1970 and 1980.

General Information:
MARC is a proprietary code supported by MARC Analysis Research Corporation with offices in Palo Alto, California, Tokyo, Japan and The Hague, Holland. The current state-of-the-art of finite element technology is adapted and incorporated into the program. New releases of the program are generated at the rate of about one per year.

Program Capability:
MARC is designed for the linear and nonlinear analysis of structures in the static and dynamic regime. Its extensive element library makes it useful for elastic analysis and its broad coverage of structural mechanics makes it an invaluable nonlinear analysis tool. The following nonlinearities are handled by the program: elastic–plastic, large displacements, finite strain, creep, thermally dependent properties. An eigenvalue for buckling may be obtained after each load increment. Dynamic analysis can be carried out by the modal or the direct integration procedure. Anisotropic, elastomeric and incompressible material descriptions are available. Restart capability to restart analysis at any increment or time-step. A rigid-plastic flow capability and a fluid–solid modeling capability are available. The heat transfer uses element types of which a structural analog exists, making a decoupled thermo-mechanical model using the same mesh possible. Extensive constraint and servo link capabilities are available. Numerous user interfaces for specification of user selected parameters make the program extremely flexible.

User Interface and Modeling Capabilities:
Extensive pre- and postprocessing capabilities are built into the MARC program. They include mesh generation and plotting of deflected shapes and contours of element quantities. An interactive pre- and postprocessor, MENTAT, assists in the two- and three-dimensional mesh generation and other data preparation areas. Post-processing includes displaced geometries and contours of element quantities. MENTAT interfaces to MARC and NASTRAN.

Element Library:
Truss; beams; two-dimensional: triangle, linear and second order isoparametric; Axisymmetric: triangle, linear and second order isoparametric; eight-node quad for arbitrary loading; three-dimensional: eight-node, twenty-node brick, four-node, eight-node membrane; flat plate; generalized plane strain; two- and three-dimensional incompressible Hermann elements; doubly curved shells, axisymmetric shells; pipe bend, rebar; heat transfer; reduced integration elements; linear shear panel.

Solution Methods for Nonlinear Problems:
● Nonlinear static: Incremental solution, tangent modulus with modified Newton–Raphson iteration.
● Nonlinear dynamic response: Implicit time integration (Newmark or Houbolt) explicit (finite differences).
● Heat transfer: Backward differences (Crank–Nicholson).

Notable Items and Limitations:
Most of the different options can be used simultaneously to cover an extremely wide range of nonlinear applications.

Programming Language: FORTRAN IV.

Hardware/Operating System: CDC 6600, 7600, CYBER 175, 176, IBM, UNIVAC, PRIME, VAX.

Program Size:

Core Program:	60,000
Pre-processors:	5000
Post-processors:	10,000.

Documentation: See Refs. [73–74].

Program Availability: Data centers: CDC, McAuto, ISD, Boeing, USC, Babcock and Wilcox. Program is available for binary or binary and source leases from MARC Analysis Research Corporation.

MSC/NASTRAN

Descriptive Program Title: The *M*acNeal-*S*chwendler *C*orporation, "*NASA STR*uctural *AN*alysis"

Program Developer:
The initial release of NASTRAN was developed by a multicorporation team including MSC and funded by NASA; MSC/NASTRAN is a proprietary version of NASTRAN developed and maintained exclusively by MSC.

Date of First Release and Most Recent Update: 1969 and 1980.

General Information:
MSC/NASTRAN is an advanced version of the NASA-funded general purpose structural analysis program. All maintenance of the system and development of new capability is performed by the MSC staff. It is marketed and serviced from MSC's offices in Los Angeles, Munich and Tokyo, and is available at most major public data processing centers. Customer hotline service is available to assist users in critical situations. The user community is also aided by a wide variety of available courses and by the dissemination of known program errors and their avoidances.

Program Capability:
● MSC/NASTRAN is a large-scale general purpose digital computer program that solves a wide variety of engineering analysis problems by the finite element method. The program capabilities include static and dynamic structural analysis, heat transfer, aeroelasticity, acoustics, electromagnetism, and other types of field problems. It has been successfully used by large and small companies throughout the world engaged in such diverse fields as automotive, aerospace, civil engineering, shipbuilding, offshore oil, industrial equipment, chemical engineering, optics, and government research.
● The solution options available in MSC/NASTRAN go far beyond the scope of the questionnaire. In particular, the dynamics capabilities contain options for several types of dynamic reduction (modal synthesis, generalized dynamic reduction, and Guyan reduction), dynamic solutions (complex eigenvalues, random spectral analysis, enforced accelerations, and four real eigenvalue methods), and coupled nonstructural effects (aeroelastic flutter and gust response, hydroelastic effects and servomechanisms).

User Interface and Modeling Capabilities:
● Because of its wide dissemination, NASTRAN pre- and post-processors abound, particularly at the large data centers. MSC/NASTRAN includes batch mesh generation inside the system with its MSGMESH module, and interactive graphics postprocessing with its VIEW and GRASP programs.
● The basic program processes free and fixed field input data and has provisions for user-supplied unformatted data files. Output provisions exist for interfacing with most known plotter software. The specific outputs, controlled by the user, include displacements, velocities, accelerations, applied forces, constraint forces, internal element forces. Many diagnostic output options are also provided, such as timing factors, matrix characteristics and spill messages.

Element Library:
Large displacement updated Lagrangain formulation is available for rod, prismatic "bar", tapered "beam", general quadrilateral and triangular isoparametric plate and shells elements, "gap" element, shear panel and a family of isoparametric solid elements. In addition, plastic and nonlinear elastic properties, as well as the large displacement effects are now provided for the rod, beam, gap and plate elements.

Solution Methods for Nonlinear Problems:
● Nonlinear static solution sequences provide for user-selected combinations of incremental, initial stress, Newton–Raphson and modified Newton–Raphson methods.
● The current nonlinear transient procedure contains a limited capability for user-defined nonlinear load functions. The delivered Newmark–Beta method may also be used to calculate "static solutions" for problems with modest nonlinearities.

Notable Items and Limitations:
● In its initial design, the primary purpose of the NASTRAN program was the solution of linear elastic problems. Although limited capabilities were provided for differential stiffness, Euler buckling, and a piecewise linear plasticity analysis, most of the emphasis in the development was directed toward a comprehensive

dynamics capability and the processing of large order problems.

● Substantial new nonlinear capabilities have recently been incorporated into MSC/NASTRAN as part of a long range development plan. The large displacement analysis has been operational for two years. The newest system contains new, highly efficient solution code for both large displacement and nonlinear material analysis. Planned developments include full nonlinear transient analysis, more nonlinear element types, and Quasi-Newton options for the solution algorithms.

Programming Language: FORTRAN IV, with isolated machine-dependent assembly language routines.

Hardware/Operating System:
A single version is supplied for more than 200 computer installations, including the IBM 360/370, 3X00 and 4X00 series, the Amdahl series, the Itel A5, the Fujitsu M, all CDC systems, the UNIVAC 1100/EXEC 8 series, Digital's VAX 11/780, and the CRAY systems.

Program Size: Approximately 380,000 source statements for the delivered system.

Documentation: The original versions of the NASTRAN manuals were published by NASA (see Refs. [75–77]). In addition, the following manuals are available from MSC:

MSC/NASTRAN User's Manual (2 Volumes)
MSC/NASTRAN Programmer's Manual (4 Volumes)
MSC/NASTRAN Application Manual (2 Volumes)
MSC/NASTRAN Demonstration Problem Manual
MSC/NASTRAN Aeroelastic Supplement
MSC/NASTRAN Handbook for Linear Static Analysis
MSC/NASTRAN Primer (book by H. G. Schaeffer)
MSGMESH Analyst's Guide

Also, several NASTRAN user's conferences have been sponsored by MSC and NASA. Many papers have been published in these proceedings.

Program Availability:
MSC/NASTRAN is available on most large commercial data centers. An executable system, with test problems and DMAP files, is available for the computers listed above under a lease agreement.

NEPSAP

Descriptive Program Title: Nonlinear Elastic–Plastic Structural Analysis Program.

Program Developers: P. Sharifi† (original version), S. Nagarajan (modular, data base oriented system). Lockheed Missiles and Space Company, Inc., Department 81-12/Bldg. 154, 1111 Lockheed Way, Sunnyvale, CA 94086, U.S.A.

Date of First Release and Most Recent Update: 1972 and 1980.

General Information:
NEPSAP is an LMSC proprietary code. It is a fully productional system of modules linked together with a centralized data base system, and has been used by various divisions of Lockheed for several years. There is, however, a continuous development effort directed towards the inclusion of addition new capabilities. The NEPSAP system is available under licensing agreements for either a binary version alone or both binary and source code.

Program Capability:
NEPSAP is a general-purpose, three-dimensional, nonlinear finite element code capable of large displacement, thermo–elastic–plastic and creep analysis of arbitrary structures. The program can be used to model one-, two- and three-dimensional structural models composed of frame members, membranes, thick/thin plates and shells, isoparametric solids, or any combination of these. Although the code is formulated to account for both geometric and material nonlinearities, linear problems may be analyzed with no loss of efficiency. There is no inherent program limitation on the size of the models analyzed using NEPSAP. Analyses may be restarted at any load or time step. Finally, enhancements may be introduced rather easily due to the modular structure of the code.

User Interface and Modeling Capabilities:
Several pre- and post-processor modules are available as part of the NEPSAP system to enable the user to interface easily with the code. The model may be generated using either a user-written FORTRAN driver or by executing a very flexible preprocessor code which accepts keyword and list directed freefield data cards. A complete graphics package enables the user to debug and verify the model rapidly as well as to display the analysis results. Utility modules are also available to interrogate and/or modify the contents of the random access data base files and for selective review of output data.

Element Library: All of the element types available in NEPSAP may be used for nonlinear analyses.

Solution Methods for Nonlinear Problems:
A variety of incremental and iterative strategies may be selected by the user for both nonlinear static and dynamic problems, with the default method being the incremental method using a built-in load correction feature. For transient dynamics, implicit time integrators used are (a) generalized Newmark, (b) Houbolt, (c) Park and (d) user-defined single or multi-step methods.

Notable Items and Limitations:
NEPSAP offers a wide range of capabilities and proven utility over the last seven years for practical engineering problems. In addition, continued research and development efforts are undertaken in order to expand its capabilities. The modularity of the code enables enhancements to be introduced easily in a given module without affecting other modules. The centralized data base system also enables new modules to be created that can communicate easily with the rest of the NEPSAP system.

Programming Language: FORTRAN; a few selected routines are coded in assembly language.

Hardware/Operating System:
UNIVAC 1100/43, 1100/83 (EXEC 8); CDC CYBER 175 (Scope 3.4), CDC 7600 (Scope 2.1); CRAY-1 (CRAY OS); IBM 3033; TI/ASC; currently being adapted for VAX 11/780.

†Currently with: Merlin Technologies, Inc., 977 Town and Country Village, San Jose, CA 95128, U.S.A.

Program Size: Approximately 70,000–80,000 statements in the analysis modules and 5000–10,000 statements in pre- and post-processor modules.

Documentation: See Refs. [78–80].

Program Availability:
Program is currently not available on any service bureau network but may be made available in the future. Both the binary and the source codes may be obtained under licensing arrangements. Please contact: Dr. S. Nagarajan, Lockheed Missiles and Space Company, Inc., Department 81-12/Bldg. 154, 1111 Lockheed Way, Sunnyvale, CA 94086, U.S.A.

PAC78

Descriptive Program Title: Plastic Analysis of Composites.

Program Developer: Y. A. Bahei-El-Din, Department of Civil Engineering, Duke University, Durham, NC 27706, U.S.A. Permanent Address: Structural Division, Department of Civil Engineering, Faculty of Engineering, Cairo University, Giza, Egypt.

Date of First Release: 1980.

General Information:
Development of PAC78 started in 1978 on experiences obtained from ELAS65 code and composite research conducted by the developer at Duke University. Research and development efforts were financed by the U.S. Army Research Office and the Department of Civil Engineering at Duke University. Updates and further development efforts are financed by a user's group of PAC78 initiated at Duke University in 1980.

Program Capabilities:
PAC78 is a general purpose three-dimensional finite element analysis program. The program may be used for linear elastic analysis or nonlinear elastic–plastic analysis. Two material types are acceptable to the program, isotropic materials and fiber-reinforced composite materials. The composite material model is a three-dimensional continuum model with unidirectional elastic fibers and an elastic–plastic matrix. The matrix could be nonhardening or exhibiting kinematic hardening behavior. The isotropic material model is a three-dimensional continuum model exhibiting kinematic hardening behavior. For either of the material models, Mises yield criterion and the hardening rule of Prager with Ziegler's modification are employed. A restart capability is built in the program which allows analysis of problems with previous loading history. Loads handled by PAC78 are mechanical loads with any loading, unloading, and reloading, sequence.

User Interface and Modeling Capabilities:
PAC78 program does not include any pre- or post-processors. Users may prepare their own subroutines for automatic generation of nodal coordinates, element properties and connectivity, boundary conditions, and yield and hardening information of all material types.

Element Library:
The three-dimensional solid element (eight-node hexahedron) is the only type that the PAC78 program uses to span the material volume. By means of the deflection boundary conditions, any type of deformation may be simulated, e.g. beams, plates, plane strain, etc.

Solution Method:
Governing equations are generated in the context of the displacement method of analysis. Linear equilibrium equations are solved by Cholesky method. Nonlinearities are handled by a Newton–Raphson type iterative scheme.

Notable Items and Limitations:
PAC78 offers a means for predicting the elastic–plastic behavior of fiber-reinforced composite structures which could not be predicted otherwise, even for simple geometries. Since both isotropic and composite materials are handled by PAC78, users may use the program to analyze composites on both the microscale and the macroscale. New constitutive equations may be incorporated in the program with no major difficulties.

Programming Language: FORTRAN IV.

Hardware/Operating System: IBM 370/165 with H-compiler. Program operational on other hardware systems after minor changes in the source program and the overlaying instructions.

Program Size: 7150 statements

Documentation:
A user's manual which includes program description, input and output description, and sample analyses is in preparation.

Availability:
Program may be obtained through membership of PAC78 Users Group. Members of the group pay a one time membership initiation fee of $2000 and are entitled to receive a magnetic tape containing the source program and the overlaying instructions, a user's manual, and all updates of the program as they are available. Inquiries should be directed to Dr. S. Utku, Director, Computer Analysis of Composite Structures Fund, Department of Civil Engineering, Duke University, Durham, NC 27706, U.S.A.

POLO-FINITE

Descriptive Program Title: POLO-FINITE: A Structural Mechanics System for Linear and Nonlinear Static Analysis.

Developers: L. A. Lopez and D. R. Rehak, Department of Civil Engineering, University of Illinois-Urbana, Urbana, IL 61801, U.S.A., and R. H. Dodds, Department of Civil Engineering, University of Kansas, Lawrence, KS 66044, U.S.A.

Release Dates: First release 1975. Current release is Version 2.3, 31 January, 1980.

General Information:
POLO-FINITE is a comprehensive, integrated structural mechanics software system designed to meet the needs of three types of users: end users performing finite

element analysis; finite element and nonlinear material constitutive model researchers; and software engineers working in large systems design. POLO, an engineering supervisory system, was completed in 1974. Development of FINITE, a POLO subsystem, began afterwards and continues now at the Universities of Illinois–Urbana and Kansas. Major development efforts are directed at nonlinear dynamic analysis using substructured models, integrated graphics to support existing multi-level substructured analysis, and new nonlinear constitutive models.

System Capability:
POLO-FINITE is a general purpose finite element software system for the linear and nonlinear analysis of two and three-dimensional structures subjected to static loads. FINITE supports a user-defined multi-level substructuring annd static condensation capability. Mixed linear and nonlinear substructures are permitted. Nonlinear effects due to strain–displacement relations and material constitutive behavior may appear separately or combined on a substructure-by-substructure basis. FINITE automatically determines all operations necessary to fulfill linear and nonlinear computational requests. A completely automatic restart capability allows a user to modify any aspect of the problem specification. FINITE voids only the computed results dependent upon the modified data. Both interactive and batch processing modes are supported. Virtually any size-problem may be handled through the substructuring facilities. Specified boundary displacements and multipoint constraints may be imposed on both linear and nonlinear substructures. The system is designed on a virtual data base concept that greatly simplifies maintenance and expansion.

User Interface and Modeling Capabilities:
Users communicate with FINITE through a problem oriented language (POL) in both batch and interactive modes. The POL includes sophisticated coordinate and incidence data generation commands that minimize the need for "preprocessors". A separate, stand-alone graphics system currently exists to display the model and some analysis results.

Element Library:
General truss, beam, two- and three-dimensional isoparametric elements, including isoparametric transition elements, are currently available for nonlinear analysis. The extensive linear library (over 60 elements) of plate, curved shell, and shell-to-solid transition elements is being extended to incorporate nonlinear effects.

Solution Methods:
- Nonlinear static problems: All forms of the incremental Newton–Raphson method are supported. Users may specify multiple convergence tests and exercise complete control over the solution parameters in time-sharing or through restart in batch.
- Equation solver: Choleski hypermatrix for symmetric equations; Crout hypermatrix for nonsymmetric equations. Both are efficient out-of-core solvers implemented with the POLO virtual data base facilities.

Notable Items and Limitations:
The unique aspects of FINITE include the friendly user interface, the multilevel substructuring capability, and the extensive element library. No limitations are placed on the size of structure that may be analyzed. Specified displacements and multi-point constraints are especially convenient in nonlinear analysis for displacement control loading and modeling situations. A formal communication protocol allows researchers to readily add new nonlinear elements and material models without detail knowledge of the system organization. The lack of dynamic capability and more exotic material models are the major deficiencies.

Programming Language: ANSI 66 FORTRAN.

Hardware/Operating System:
- Burroughs—Large Systems (B6700, B6800, B7700, B7800)/MCP 2.8.1 and beyond.
- CDC CYBER/NOS 1.2 and beyond.
- Honeywell—HIS 6000, Series 60 Level 66/GCOS 4J and beyond.
- DEC-DEC10/TOPS.
- PRIME 400, 500 and 50 series.

Program Size:
- POLO—10,000 lines.
- FINITE—60,000 lines.
- Element and material libraries—80,000 lines.
- Associated graphics system—15,000 lines.

Documentation: See Refs. [81, 82].

Availability:
The system is normally distributed in object form and is made available to universities for no charge. Non-educational users should contact developers for details.

SAMCEF

Descriptive Program Title: Systeme d'Analyse des Milieux Continus par Elements Finis.

Program Developer: M. G. Sander, L.T.A.S., Aerospace Laboratory, University of Liege, Rue Ernest Solvay, 21, B-4000 Liege, Belgium.

Date of First Release and Most Recent Update: 1970 and 1980.

General Information:
SAMCEF is a university code. The package was first developed for research purposes. Progressively, further developments were financed by industries and since 1970, the program is fully operational. New developments are continuously added. It is being used in an industrial as well as research environment. The LTAS Group provides the users with the service they require for using the program, which is available for various computers. The price includes the source code, installation, documentation and training. A yearly contribution allows the users to obtain the updates.

Program Capability:
SAMCEF is a general purpose linear and nonlinear, static and dynamic, three-dimensional finite element analysis code. The program can perform a static analysis (linear and nonlinear) including the thermal effects, a dynamic analysis (linear and nonlinear) with computation of eigenvalues, eigenmodes and dynamic response, a

stability analysis including buckling and postbuckling and a weight optimization analysis of structures subjected to several static and dynamic constraints. The finite element library is very vast. In addition to the general elements (truss, beam, plate, shell), displacement and stress type elements allow a dual analysis of various problems. Hybrid and mixed shell elements are also available. A few scalar field elements provide a solution to some fluid mechanics problems. In most of the elements the material can be anisotropic. The thicknesses, cross-sections, moments of inertia may vary linearly inside the element. Shell elements can be made of sandwich material. The nonlinearities may be due to large displacements, large strains and nonlinear material behavior. Any analysis may be performed step by step: data preparation, element generation, structural assembly, and solution.

User Interface and Modeling Capabilities:
SAMCEF has pre- and postprocessors as well as graphics displays for the data and results.

Element Library:
General truss, beam, two-dimensional (plate and shell), three-dimensional (isoparametric) solid elements are available. For most of them the field is approximated by a variable degree polynomial. Therefore, it is easy to choose the degree of approximation which can vary from place to place in the same problem.

Solution Methods for Nonlinear Problems:
- Linear static analysis: Gauss elimination and substructuring.
- Linear dynamic analysis: Guyan condensation with either power or subspace iteration; Lanczos iteration.
- Nonlinear dynamic analysis: Newmark time integration (explicit and implicit) method with equilibrium iterations.
- Nonlinear static analysis: Incremental solution, Newton–Raphson method.

Notable Items and Limitations:
SAMCEF offers a very large range of applications. Specified displacement boundary conditions are included. The front width is limited to 1000 degrees of freedom. It is possible and easy to incorporate new element types.

Programming Language: FORTRAN IV.

Hardware/Operating System: IBM (OS, DOS, VS, CMS)—UNIVAC (double precision required)—CDC 6400/6600/7600—DEC 2040—VAX—SIEMENS.

Program Size:
Approximate number of source statements: 180,000.
Approximate number of subroutines: 2000.

Documentation: See Ref. [83].

Program Availability:
SAMCEF can be used on an IBM computer and a CDC computer. Source program is available from the developer for a fee.

SAMSON

Descriptive Program Title: A Computer Code for Dynamic Stress Analysis of Media Structure Problems with Nonlinearities.

Developers: R. L. Chiapetta, R. L. Chiapetta and Associates, 9748 Roberts Road, Palos Hills, IL 60465, U.S.A., T. Belytschko, Department of Civil Engineering, Northwestern University, Evanston, IL 60201, U.S.A.

Date of First Release: 1971.

General Information:
SAMSON was developed at IIT Research Institute under contract for the Air Force Weapons Laboratory, Kirtland Air Force Base, New Mexico. An update is planned for release in 1981. Government agencies or contractors can obtain the program from Kirtland Air Force Base.

Program Capability:
SAMSON was developed for determining the transient, nonlinear response of buried structures with a two-dimensional or axisymmetric three-dimensional geometry. Only material nonlinearities are included. The following material laws are available: elastic, elastic–plastic, and the cap model.

User Interface and Modeling Capability:
Rudimentary mesh generators are included. A versatile postprocessor is available from Kirtland Air Force Base.

Element Library:
Triangular and rectangular two-dimensional and three-dimensional axisymmetric element; springs; membrane elements.

Solution Methods:
Explicit time integration by Newmark β-method ($\beta = 0$).

Notable Items and Limitations:
The code has unlimited size capability and makes efficient use of extended core. However, only rectangular, not quadrilateral, elements are available.

Program Languages: FORTRAN IV.

Hardware/Operating Systems: CDC 6600/7600 (NOS).

Documentation: Program description, technical manual and user's manual—see Ref. [84].

SESAM-69

Descriptive Program Title: Super Element Structural Analysis Program Modulus.

Program Developer: A.S. Computas, Det Norske Veritas, P.O. Box 310, 1322 Høvik, Norway.

Date of First Release and Most Recent Update: 1969 and 1979.

General Information:
SESAM-69 is a proprietary code developed and maintained by A. S. Computas which is a subsidiary and the data division of the Norwegian classification society Det Norske Veritas. Development started in 1969 which is also the year for the release of the first program parts. All program developments are financed by Det Norske Veritas. The program is supported from the

headquarters in Oslo, Norway, and from four European branch offices (London, Paris, Rotterdam and Hamburg).

Program Capability:

● SESAM-69 is a general purpose program system for linear and nonlinear analysis. Both for static and dynamic analyses the solution algorithm is based on the multilevel superelement-technique. Considerable advantages are obtained with this technique both for linear and nonlinear problems.

● The total system is split into program modules of pipes, beams, membranes, shells and solids which may be executed autonomously or in combination with the superelement program. Nonlinearities include elasto–plasticity of three-dimensional membrane and solid structures, and combined large displacements and elasto–plasticity for shells. The program has complete saving-, restart-facilities. Vibration and dynamic analysis includes: computation of eigenvalues and eigenvectors, modal analysis and stepwise integration. Stability analysis includes: nonlinear collapse, and postbuckling analysis of shells.

User Interface and Modeling Capabilities:

● SESAM-69 utilizes highly efficient preprocessors both for the geometric modeling and specification of loads, boundary conditions, etc. Both interactive graphic and batch input specifications are available. The system also contains automatic coupling to programs for load calculation, thermal analysis, etc. A modulus in the program is available for calculation of three-dimensional added mass of submerged structures. The input data-generators have extensive checking and visualization facilities.

● The postprocessors perform print and plot of selected results (displacements, stresses, etc.) in the form of tables, isoplots, curveplot, etc.).

Element Library:
The nonlinear elements include: general truss, beam, membrane and three-dimensional isoparametric elements. Doubly curved thin/thick subparametric shell elements are available. The elements contain: linear elastic, elasto–plastic material formulations with different flow rules. Geometric nonlinearities are analyzed with the updated Lagrangian formulation.

Solution Methods for Nonlinear Problems:

● Nonlinear dynamic response: Implicit integration, Newmark's method. Nonlinear static response: Incremental solution, Newton–Raphson method.

● Equation solvers for linear equations: Compact out-of-core solver (skyline). Gauss elimination on submatrices.

Notable Items and Limitations:
Due to extensive use of superelements, SESAM-69 gives very few limitations with respect to problem size (number of elements, nodes, etc.). Relatively few nonlinear material models are available (only elasto–plasticity). Specified static boundary conditions are available. Dynamic loading from given displacements, velocities and accelerations are under development.

Programming Language: Simplified ANSI FORTRAN.

Hardware/Operating System: CDC 6600, 7600, CYBER 72, IBM 370 (OS/VS), UNIVAC 1100 series.

Program Size:

Preprocessors:	50,000 statements
Core Program:	100,000 statements
Postprocessors:	30,000 statements.

Documentation:
Extensive general descriptions, users manuals, maintenance manuals and example manuals are available from the developer (see Refs. [85–87]).

Program Availability:
The program is available at several European service-bureaus and computer installations. For further information the developer should be contacted. Normally absolute versions only are distributed, however, program sales will include also source code. Program fee to be negotiated with the developer.

SMART

Descriptive Program Title: *S*tructural *M*echanic *A*nalysis in the *R*eactor *T*echnology.

Program Developer: SMART-Group, Institute for Statics and Dynamics (ISD), University of Stuttgart, D-7000 Stuttgart 80, West Germany.

Date of First Release and Most Recent Update: 1976 and 1980.

General Information:
Development started in 1971 and is still continuing. Software maintenance and user support is provided on a long term basis by the authors. There are four installations in West Germany.

Program Capability:
SMART is a software system mainly for static (SMART I) and diffusion problems (SMART II). Both packages are fully compatible. Nonlinear applications are for SMART I: limit load analysis, viscoelastic creep problems and for SMART II: nonlinear, nonstationary coupled hygrothermal analysis.

User Interface and Modeling Capabilities:
There is a separate interactive graphics package INGA that has been developed also at ISD.

Element Library:
Fifteen different elements for static-nonlinear part (the same element types for nonlinear diffusion) including three-dimensional, two-dimensional, axisymmetric solids, flanges, cables, membranes, link-elements, and boundary-elements.

Solution Methods for Nonlinear Problems:
SMART I: iterative initial load solution.
SMART II: successive substitutions.

Notable Items and Limitations:
No limitation of problem size because of multilevel substructure technique, same as ASKA.

Programming Language: Standard FORTRAN IV.

Hardware/Operating System: At present installed on three different computer systems: CDC, UNIVAC, IBM.

Program Size:

Core program:	350,000
Pre/postprocessor (INGA):	60,000
Subroutines:	4000.

Program Availability: Rent and purchase through: Institut fur Statik und Dynamik der Luft-und Raumfahrtkonstruktionen, Universitat Stuttgart, Pfaffenwaldring 27, D-7000 Stuttgart 80, West Germany.

STAGSC-1

Descriptive Program Title: Structural Analysis of General Shells Version (-1).

Program Developer: B. O. Almroth, Dept. 52-53, Bldg. 205, Lockheed Palo Alto Research Laboratory, 3251 Hanover Street, Palo Alto, CA 94304, U.S.A.

Date of First Release and Most Recent Update: 1980.

General Information:
STAGSC-1 is available to the public at a nominal fee. Its development has been supported by NASA, Air Force and Lockheed. The program represents an extension of previous versions, STAGSA and STAGSC. Maintenance is funded by members in a users group. This includes updates and consultations. The version is "frozen" with respect to its scope but improvements in efficiency and ease of use may be included in updates.

Program Capability:
STAGSC-1 is a computer code for structural analysis of shell type structures. It contains options for static stress analysis, bifurcation buckling, vibrations and transient response. Geometric and material nonlinearities may be included. While primarily intended for shell analysis, STAGSC-1 includes spring and beam elements. A number of substructures can be defined separately. Input is particularly simple when these belong to a set of standard geometries. Shell wall may consist of orthotropic layers with different orientation. discrete stiffeners may be included. Thermal as well as mechanical loading may be considered. The latter case includes options to define forces or displacements. Initial shape imperfections and cutouts may be defined.

User Interface and Modeling Capabilities:
Although the currently available version of the code (STAGS-C1) is batch oriented with limited plotting capability, a new version of the code is being developed which has been integrated with the GIFTS package resulting in a totally interactive, graphics-oriented user interface. The integrated software system (GIFTS-STAGS or 'GIST') features GIFTS pre- and post-processing modules (plus bandwidth optimizer), STAGS analyses modules, corresponding "transformer" modules linking the two data bases and a conversational "control module" which guides the user through an analysis, employing automatic data-management and interactive "manipulation" of all participating program modules (which may perform in batch or interactive mode). The new system has been completed except for a finalization and verification stage currently in progress.

Element Library:
STAGSC-1 includes triangular and quadrilateral shell elements. Triangular elements are based on the Tocher triangle. Quadrilateral elements can be either based on combination of triangles or flat elements of a type developed especially for STAGS. Presently a curved AHMAD type element and a hybrid plate bending element are introduced as options. Linear springs and nonlinear beam elements are included.

Solution Methods for Nonlinear Problems:
For linear equations the skyline method (with Cholesky decomposition) is used. Eigenvalue problems are solved through the generation of invariant subspaces by simultaneous inverse power iteration. Nonlinear equations are solved by use of the modified Newton method with some automatic features for control of step size and relaxation factors. Time integration is done by explicit (central differences) or implicit (trapezoidal and stiffly stable) methods.

Notable items and Limitations:
STAGSC-1 does not include creep or visco-elasticity. It does not include three-dimensional elements. Boundary conditions are linear. Bifurcation buckling analysis does not include plasticity. Vibration analysis is linear. The nonlinear analysis is limited to "moderate rotations".

Programming Language: FORTRAN IV.

Hardware/Operating System: CDC 6600/7600 (Scope, NOS), UNIVAC (EXEC), IBM, VAX.

Program Size: 50,000.
Documentation: See Refs. [88, 89].

Program Availability: Program is available through COSMIC fees presently under negotiation. Tentatively: $2500 initial fee. $2500 a year membership fee in users group.

STRAW

Descriptive Program Title: Structural Transient Response of Assembly Wrappers.

Developer: J. M. Kennedy, Argonne National Laboratory, Reactor Analysis Safety Division, 9700 South Cass Avenue, Argonne, IL 60439, U.S.A.

Date of First Release and Most Recent Update: 1973 and 1980.

General Information:
STRAW was developed at Argonne National Laboratory using an early version of WHAMS as a starting point. The program is to be available from the Argonne Code Center.

Program Capability:
STRAW was developed initially for determining the short duration transient, nonlinear response of core subassemblies for safety analysis in the Liquid Metal Fast Breeder Reactor Program. The program has since been developed along a more general purpose nature with recent emphasis on inclusion of quasi-Eulerian-fluid elements and linear and nonlinear thermal stress capability in the implicit time integration version. Problems are limited to two-dimensional or three-dimensional axisymmetric geometry. The material models are elastic and elastic–plastic with isotropic hardening and temperature varying properties.

User Interface and Modeling Capabilities:
Simple mesh generator is a feature. Output includes user-selected time histories, pictures, printer plots, Calcomp plots of time histories and the deformed configuration.

Element Library:
Two dimensional beam, conical shell, a quadrilateral plane and axisymmetric continuum element, Lagrangian and quasi-Eulerian plane and axisymmetric fluid elements.

Solution Methods:
Explicit (Newmark β-method or central difference method) and implicit (Newmark β-method) time integration.

Notable Items and Limitations:
Employs dynamic allocation allowing one to use small or large core storage depending on type of problem being studied.

Programming Language: FORTRAN IV.

Hardware/Operating System: IBM.

Program Size: Explicit ~4000 cards, Implicit ~6000 cards.

Documentation: See Refs. [90–93].

Availability: Available from developer or in the near future from the Argonne Code Center.

TEPSA

Descriptive Program Title: Thermal Elastic–Plastic Stress Analysis.

Program Developer: Tai-Ran Hsu, Department of Mechanical Engineering, University of Manitoba, Winnipeg, Manitoba, Canada R3T 2N2.

Date of First Release and Most Recent Update: 1973 and 1980.

General Information:
TEPSA is a proprietary code. The use of this code can be arranged through the developer. The code was developed initially for the assessment of the multi-dimensional thermo–mechanical behavior of nuclear reactor fuel elements. The program is fully operational but new routines for many other applications are continuously developed. Comprehensive users manual is available at the cost of printing.

Program Capability:
TEPSA code is constructed on the basis of incremental variable stiffness finite element thermo–elasto–plasticity theory. Triangular and/or quadrilateral plates and torus elements are used for two-dimensional planar and three-dimensional axisymmetric structures. Both thermal and mechanical analyses are coupled; i.e. the thermal analysis is performed on the structural geometries at the immediate last load step. Code accepts temperature and strain-rate dependent material properties. Isotropic hardening rule is used for monotonic load increments and kinematic hardening rule for cyclic thermomechanical loadings. Special gap and crack elements are available for thermomechanical contacting surfaces and allow crack growth through elements. Code is constructed on the "modular" basis. Modules for special purposes such as finite strain plasticity, Fourier series coupling and thermomechanical creep can be readily adapted to the main program. The code can also handle solids involving phase change by special time-difference algorithm.

User Interface and Modeling Capabilities:
Mesh generator is available for the users.

Element Library:
Triangular/quadrilateral plate and torus (ring) elements are available for plane stress, plane strain and axisymmetric structures.

Solution Methods for Nonlinear Problems:
Incremental variable stiffness method is used for the nonlinear thermo–elastic–plastic analysis. Contact analysis is handled by the artificial noncompressive fluid concept. Successive reduction of stiffness is used for the crack propagation through elements.

Limitations:
Limited in the element library.

Programming Language: FORTRAN IV.

Hardware/Operating System: IBM, AMDAHL, CDC.

Program Size: Approximately 3000 statements.

Program Availability: Through the developer.

ULARC

Descriptive Program Title: Ultimate load Analysis of Small Plane Frames.

Program Developer: G. H. Powell, Department of Civil Engineering, Division of Structural Engineering and Structural Mechanics, University of California, Berkeley, CA 94720, U.S.A.

Date of First Release and Most Recent Update: 1970.

General Information:
A simple-minded code for calculation of collapse loads for small steel and reinforced concrete frames.

Program Capability:
Applicable to arbitrary plane frames in which plastic hinges may form. Calculates load–deflection relationship, sequence of hinge formation, rigid-plastic collapse load, and collapse mechanism. Also allows cyclic and non-proportional static loading, including allowance for unloading and reforming of hinges.

User Interface and Modeling Capabilities:
No pre- or post-processors. No mesh generation.

Element Library:
Two-dimensional beam elements with concentrated hinges at ends.

Solution Methods:
Piecewise linear analysis, with load forming each new hinge calculated automatically.

Programming Language: FORTRAN IV.

Hardware/Operating System: CDC 6400/6600/7600.

Program Size: Approximately 1100 cards.

Documentation: Users Guide.

Program Availability: National Information Service for Earthquake Engineering, Computer Applications, 519 Davis Hall, University of California, Berkeley, CA 94720, U.S.A.

Cost—approximately $100.

WECAN

Descriptive Program Title: Westinghouse Electric Computer ANalysis.

Program Developer: Analytical Mechanics, Westinghouse Research and Development Center, Pittsburgh, PA 15235, U.S.A.

Date of First Release and Most Recent Update: 1973 and 1980.

General Information:
WECAN is a proprietary code. It was and is developed jointly by Westinghouse Research and Development and other Westinghouse user divisions to be efficient, capable and easy to use. WECAN and its close relatives WAPPP (WECAN Auxiliary Pre- and Post-Processors) and FIGURES (Finite Element Interactive Graphics User RoutinES) were designed to provide a complementary system of computer programs for structural analysis. Maintenance is funded by a surcharge. New developments are funded by user organizations desiring new development.

Program Capability:
WECAN is a general purpose linear and nonlinear static and dynamic three-dimensional finite element analysis program. WECAN can solve static, modal, seismic response spectrum, harmonic response, linear and nonlinear dynamic transient, linear buckling, and heat transfer and analogous field problems. Isotropic, orthotropic, and anisotropic materials are permitted. Material properties are defined as a fifth order polynomial of temperature. WECAN can use the initial stress matrix to calculate static, modal or linear buckling problems. Substructures are linear but can be combined with nonlinear elements in the solution phase. Multilevel substructures are permitted. Substructures may be rotated, reflected or scaled. WECAN may be restarted at preselected time steps.

User Interface and Modeling Capabilities:
WAPPP is a collection of batch pre- and post-processors for WECAN. The pre-processors generate meshes and loads, check isoparametric elements shapes, reduce wave fronts, prepare input for general matrix input and for composite materials. The post-processors edit heat transfer results, edit mode shapes and frequencies, combine results, plot contours, deformed shapes, transients and general xy curves, process seismic data, calculate J-integrals and calculate Fourier coefficients.
FIGURES is a collection of interactive pre-processors that prepares input for WECAN. It can interactively plot what is being generated.

Element Library:
Spars, beams, straight pipes, elbows, thin shells, two- and three-dimensional isoparametric (with the capability to have different number of points on different edges of the same element), one-, and three-dimensional gap elements, a one-dimensional slider, a two-dimensional friction interface element and a three-dimensional isoparametric friction interface element are available for nonlinear analysis.

Solution Methods for Nonlinear Problems:
- Nonlinear dynamic response—Implicit time integration (Newmark or Houbolt) or modal superposition (three-dimensional gap element now permitted for modal superposition with plasticity and three-dimensional friction element to soon be added).
- Nonlinear static problems—Method of successive elastic approximations with extrapolation.
- Equation solver for linear equations—Wave front with as much in core as possible.

Notable Items and Limitations:
WECAN offers a very large range of applications but some features are lacking. Fluid-structure interaction is under development. Interactive post-processing of results is under development. Cyclic symmetry is under development. Basic workshops and advanced training sessions are offered periodically to train inexperienced and experienced WECAN users. An annual User's Colloquium is held each fall where users present papers in competition for prizes.

Programming Language: WECAN and WAPPP are over 99% FORTRAN IV, and less than 1% COMPASS. FIGURES—100% FORTRAN IV.

Hardware/Operating System: WECAN AND WAPPP—CDC 7600 (SCOPE). FIGURES—Data General Eclipse S230 (AOS).

Program Size:
- WECAN 110,000.
- WAPPP 50,000.
- FIGURES 10,000.

Documentation: See Refs. [94–96].

Program Availability:
Program can be used on Westinghouse PSCC Engineering Computer System for a surcharge on each run of WECAN, WAPPP or FIGURES.

WHAMS

Descriptive Program Title: Program for Transient Analysis of Two-Dimensional Structures and Continua.

Program Developer: T. Belytschko and R. Mullen, Department of Civil Engineering, Northwestern University, Evanston, IL 60201, U.S.A.

Date of First Release and Most Recent Update: 1973 and 1980.

General Information:
WHAMS is a research oriented program. The program has been used by about ten outside users but no formal mechanisms for updating the program or correction of bugs is available.

Program Capability:
WHAMS is primarily intended for transient problems of short duration with material and geometric nonlinearities. Large strains may be treated by some of the elements. Although implicit time integration is available, the emphasis in development has been on the explicit time integration. Problem geometry is limited to two-dimensional or three-dimensional, axisymmetric. The following material models are included: elastic, elastic–plastic with isotropic strain hardening, the cap model for soils. User supplied material laws can easily be added for explicitly integrated problems.

User Interface and Modeling Capabilities:
Simple mesh generators are included. Output includes user-selected time histories, pictures, printer plots, Calcomp plots of time histories and the deformed configuration.

Element Library:
Two-dimensional beam, conical shell, plane strain and axisymmetric elements with three to eight nodes, and Lagrangian fluid elements.

Solution Methods:
Explicit time integration with a maximum of two different time steps: explicit–implicit, and implicit time integration.

Programming Language: FORTRAN IV.

Hardware/Operating System: CDC 6400/6600 (NOS).

Program Size: 16,000 cards.

Documentation: See Refs. [97, 98].

Availability: Source is available from developer for $300 (1980).

REFERENCES

1. W. D. Pilkey, K. J. Saczalski and H. G. Schaeffer (Editors), *Structural Mechanics Computer Programs*. University Press of Virginia, Charlottesville, Virginia (1974).
2. B. Fredriksson and J. Mackerle, *Structural Mechanics Finite Element Computer Programs—Surveys and Availability*. Advanced Engineering Corporation, Box 3044, S-580 03, Linköping, Sweden.
3. B. Fredriksson and J. Mackerle, Overview and evaluation of some versatile general purpose finite element computer programs. In *Finite Element Methods in the Commercial Environment*, Vol. 2, pp. 390–419. Robinson and Associates (1978).
4. T. Y. Chang and J. Padovan, General purpose nonlinear finite element programs. *Structural Mechanics Software Series* 3, 79–101 (1980).
5. H. Armen and A. B. Pifko, Plastic analysis in general purpose programs. *Structural Mechanics Software Series* 3 (1980).
6. B. F. Pilkey, Computerized sources of abstracts of the engineering literature. In *Structural Mechanics Software Series*, Vol. 3, pp. 29–39. The University Press of Virgina, Charlottesville, Virginia (1980).
7. L. E. Malvern, Introduction to the Mechanics of a Continuous Medium. Prentice-Hall, New Jersey (1969).
8. O. C. Zienkiewicz and G. C. Nayak, A general approach to problems of large deformation and plasticity using isoparametric elements. In *Proc. 3rd Conf. Matrix Methods Structural Mech.* AFFDL-TR-71-160, pp. 881–928. Air Force Flight Dynamics Laboratory, Air Force Systems Commands and Air Force Institute of Technology (Dec. 1973).
9. S. Nemat-Nasser, Continuum bases for consistent numerical formulations of finite strains in elastic and inelastic structures. In *Finite Element Analysis of Transient Nonlinear Structural Behavior, AMD*, Vol. 14, pp. 85–97. American Society of Mechanical Engineers (1975).
10. G. C. Nayak and O. C. Zienkiewicz, Elasto-plastic stress analysis. A generalization for various constitutive relations including strain softening. *Int. J. Num. Meth. Engng* **5**, 113–135 (1972).
11. R. F. Jones, Jr., H. Armen and J. T. Fong (Editors), *Numerical Modeling of Manufacturing Processes*. ASME Special Publication PVB-PB-025 (1977).
12. H. Armen, Assumptions, models and computational methods for plasticity. *Comput. Structures* **10**, 161–174 (1979).
13. R. H. Hartung (Editor), *Numerical Solution of Nonlinear Structural Problems*, AMD, Vol. 6. American Society of Mechanical Engineers (1973).
14. C. A. Felippa, Procedures for computer analysis of large nonlinear structural systems. In *Large Engineering Systems*, pp. 60–101. Pergamon Press, Oxford (1976).
15. P. G. Bergan, G. Horrigmoe, B. Kräkeland and T. H. Soreide, Solution techniques for nonlinear finite element problems. *Int. J. Num. Meth. Engng* **12**, 1677–1696 (1978).
16. P. G. Bergan, Solution algorithms for nonlinear structural problems. *Proc. Int. Conf. Engng Application of the Finite Element Method*, pp. B.1–13.38. Computas, Oslo, Norway (1979).
17. T. Belytschko, J. R. Osias and P. V. Marcal (Editors), *Finite Element Analysis of Transient Nonlinear Structural Behavior*. AMD, Vol. 14. American Society of Mechanical Engineers (1975).
18. K. J. Bathe, E. Ramm and E. L. Wilson, Finite element formulations for large deformation dynamic analysis. *Int. J. Num. Meth. Engng* **9**, 353–386 (1975).
19. J. H. Argyris, J. St. Doltsinsis, W. C. Knudson, W. C. Laz and K. J. Willam, Numerical solution of transient nonlinear problems. *Comput. Meth. Appl Mech. Engng*, Vols. 17/18, pp. 341–309 (1979).
20. K. J. Bathe, Finite element formulation, modeling ans solution of nonlinear dynamic problems. In *Numerical Methods for Partial Differential Equations*. Academic Press, New York (1979).
21. E. Schrem, Structural aspects of software systems for nonlinear finite element analysis. In *Finite Elements in Nonlinear Mechanics*, TAPIR, pp. 621–645. Trondheim, Norway (1978).
22. P. Hermann, W. Knudson and S. Schneider, Considerations for the design of programs for nonlinear finite element analysis. In *Computational Aspects of the Finite Element Method*, pp. 177–178. Bundesanstalt fur Material prufug, Berlin (1979).
23. I. C. Taig, Selection criteria for structural analysis programs. AGARD Report No. 670, NATO-AGARD, pp. 11–20. Neuilly Sur Seine, France (Jan. 1979).
24. P. Sollogoob, L. Wahl and F. Dreyer, Main computer systems programs, presentation, criteria for selection, CNEXO/CTICM, 1978 (to be obtained from: CNEXO, B.P. 337, F-29273, Brest, or: CTICM, 20 Rue Jean Jaures, F-92807, Puteaux).
25. I. Berman (Editor), *Engineering Computer Software: Verification, Qualification and Certification*. ASME Publication (1971).
26. K. J. Bathe, ADINA—A finite element program for automatic dynamic incremental nonlinear analysis. *Rep.* 82448-1. Acoustics and Vibration Laboratory, Mechanical Engineering Department, Massachusetts Institute of Technology. Cambridge, Massachusetts (Sept. 1975), Revised (Dec. 1978).

27. K. J. Bathe, ADINAT—A finite element program for automatic dynamic incremental nonlinear analysis of temperatures. *Rep.* 82448-5. Acoustics and Vibration Laboratory, Mechanical Engineering Department, Massachusetts Institute of Technology, Cambridge, Massachusetts (May 1977), Revised (Dec. 1978).
28. K. J. Bathe, On the current state of finite element methods and our ADINA endeavors. *Advances in Engng Software* 2(2), 59–65 (1980).
29. K. J. Bathe (Editor), ADINA Conference Proceedings, August 1977 and August 1979, Mechanical Engineering Department, Massachusetts Institute of Technology, Cambridge, Massachusetts.
30. D. P. Mondkar and G. H. Powell, Static and dynamic analysis of nonlinear structures. *Rep. No.* EERC 75-10. Earthquake Engineering Research Center, University of California, Berkeley (March 1975).
31. D. P. Mondkar and G. H. Powell, ANSR-I—General purpose program for analysis of nonlinear structural response. *Rep. No.* EERC 75-37. Earthquake Engineering Research Center, University of California, Berkeley (Dec. 1975).
32. A. Riahi, D. G. Row and G. H. Powell, Three-dimensional inelastic frame elements for the ANSR-I program. *Rep.* EERC 78-6. Earthquake Engineering Research Center. University of California, Berkeley (Aug. 1978).
33. D. P. Mondkar and G. H. Powell, ANSR-II—Analysis of nonlinear structural response, user's manual. *Rep. No.* EERC 79-11. Earthquake Engineering Research Center, University of California, Berkeley (July 1979).
34. D. P. Mondkar and G. H. Powell, Three-dimensional truss bar element (Type 1) for the ANSR-II program. *Rep. No. No.* EERC 78-6. Earthquake Engineering Research Center, University of California, Berkeley (Aug. 1978).
35. D. G. Row, G. H. Powell and D. P. Mondkar, Two-dimensional beam-column element (Type 5—parallel element theory) for the ANSR-II Program. Rep. No. EERC 79-30. Earthquake Engineering Research Center, University of California, Berkeley (Dec. 1979).
36. A. Riahi, G. H. Powell and D. P. Mondkar, Three-dimensional beam-column element (Type 2—parallel element theory) for the ANSR-II program. *Rep. No.* EERC 79-31. Earthquake Engineering Research Center, University of California, Berkeley (Dec. 1979).
37. G. J. DeSalvo and J. A. Swanson, *ANSYS User's Manual.* Swanson Analysis Systems, Inc., Houston, Pennsylvania (July 1979).
38. P. Kohnke, *ANSYS Theoretical Manual.* Swanson Analysis Systems, Inc., Houston, Pennsylvania (1977).
39. P. Kohnke, *ANSYS Introductory Manual.* Swanson Analysis Systems, Inc., Houston, Pennsylvania (March 1979).
40. G. J. DeSalvo and J. A. Swanson, *Ansys Examples Manual.* Swanson Analysis Systems, Inc., Houston, Pennsylvania (July 1979).
41. G. J. DeSalvo, *ANSYS Verification Manual.* Swanson Analysis Systems, Inc., Houston, Pennsylvania (1979).
42. Engineering capabilities of ASAS-NL. *ARD Rep.* 30.5.78. Atkins Research and Development.
43. *ASAS-NL User Guide—Version A,* Atkins Research and Development (July 1979).
44. *ASKA Part III—1—Material Nonlinearities, User's Reference Manual,* ASKA UM 207. University of Stuttgart, West Germany (1972).
45. *ASKA Part III—2—Linear Buckling, User's Reference Manual,* ASKA UM 209. University of Stuttgart, West Germany (1973).
46. E. Schrem, *A Short Description of ASKA,* UM 215, Institute for Statics and Dynamics, University of Stuttgart, West Germany (1975) (includes bibliography).
47. J M. Kulicki and C. N. Kostem, The inelastic analysis of reinforced and prestressed concrete beam. *Fritz Engineering Laboratory Rep. No.* 378B.1. Lehigh University, Bethlehem, Pennsylvania (1972).
48. J. M. Kulicki and C. N. Kostem, User's guide to program BEAM. *Fritz Engineering Laboratory Rep. No.* 378B.2. Lehigh University, Bethlehem, Pennsylvania (1973).
49. D. Bushnell, Thin shells. *Structural Mechanics Computer Programs* (Edited by W. Pilkey, K. Saczalski and H. Schaeffer), pp. 277–358. University Press of Virginia, Charlottesville, Virginia (1974).
50. D. Bushnell, Stress, stability and vibration of complex, branched shells of revolution. *Comput. Structures* 4, 399–435 (1974).
51. D. Bushnell, BOSOR4-program for stress, buckling and vibration of complex shells of revolution. *Structural Mechanics Software Series* (Edited by N. Perrone and W. Pilkey), Vo. 1, pp. 11–143. University Press of Virginia, Charlottesville, Virginia (1977).
52. D. Bushnell, BOSOR5—A computer program for buckling of elastic-plastic complex shells of revolution including large deflections and creep. *User's Manual,* LMSC-D407166, Vol. I, *Test Cases* Vol. II; Theory and Comparisons with Test, LMSC-D407167, LMSC-D407168, respectively, Vol. III.
53. D. Bushnell, BOSOR5—Program for buckling of elastic-plastic complex shells of revolution including large deflections and creep. *Comp. Structures* 6, 221–239 (1976).
54. D. Bushnell, A strategy for the solution of problems involving large deflections, plasticity and creep. *Int. J. Num. Meth. Engng* 11, 683–708 (1977).
55. W. S. Peterson and C. N. Kostem, The inelastic analysis of beam-slab highway bridge superstructures. *Fritz Engineering Laboratory Rep. No.* 378B.5, Lehigh University, Bethlehem Pennsylvania (1975).
56. *W. S. Peterson and C. N. Kostem, User's Manual for program BOVA. Fritz Engng Lab. Rep No.* 378B.6A. Lehigh University, Bethlehem, Pennsylvania (1975).
57. W. S. Peterson and C. N. Kostem, The inelastic analysis of beam-slab highway bridge superstructures. *Fritz Engng Lab. Rep. No.* 378B.5. Lehigh University, Bethlehem, Pennsylvania (1975).
58. C. N. Kostem and G. Ruhl, User's Manual for Program BOVAC. *Fritz Engng Lab. Rep. No.* 433.1. Lehigh University, Bethlehem, Pennsylvania (1980).
59. C. N. Kostem and P. S. Green, Initiation and propagation of failure mechanism in masonry infill walls. *Fritz Engng Lab. Rep. No.* 433.5. Lehigh University, Bethlehem, Pennsylvania (1979).
60. C. N. Kostem and P. S. Green, A user's manual of a computer program for the analysis of reinforced concrete frames with masonry infilled walls. *Fritz Engng Lab. Rep. No.* 433.6. Lehigh University, Bethlehem, Pennsylvania (1979).
61. E. L. Wilson and H. H. Dovey, Three-dimensional analysis of building systems—TABS. *Rep. No.* EERC 72-8. Earthquake Engineering Research Center, University of California, Berkeley (Dec. 1972).
62. A. E. Kanaan and G. H. Powell, DRAIN-2D—A general purpose computer program for dynamic analysis of inelastic plane structures, *Rep. No.* 73-6. Earthquake Engineering Research Center, University of California, Berkeley (Apr. 1973), Revised (Sep. 1973).
63. G. H. Powell, DRAIN-2D User's Guide, *Rep. No.* 73-22. Earthquake Engineering Research Center, University of California, Berkeley, (Sep. 1973), Revised (Aug. 1975).
64. R. Guendelman, Inelastic Earthquake response of Three-Dimensional Buildings. Ph.D. Thesis, University of California, Berkeley (1976).
65. A. K. Jain and S. C. Goel, Hysteresis models for steel members subjected to cyclic buckling or cyclic end moments and buckling—user's guide for DRAIN-2D: EL9 and EL10. *Rep. No.* UMEE78R6. The University of Michigan, Ann Arbor, Michigan (Dec. 1978).
66. A. B. Pifko, H. S. Levine and H. Armen, PLANS—A finite element program for nonlinear analysis of structures, Vol. I—Theoretical Manual. NASA CR-2568 (Nov. 1975).
67. A. B. Pifko, H. Armen, A. Levy and H. S. Levine, PLANS—A finite element program for nonlinear analysis of structures, Vol. II—User's Manual. Grumman Research Department. *Rep.* RM-633; also NASA CR-145244 (May 1977).
68. R. Winter, A. B. Pifko and H. Armen, Crash simulation of

skin-frame structures using a finite element code. SAE Paper No. 770484 (Apr. 1977).
69. S. Utku, M. S. M. Rao and G. J. Dvorak, *ELAS65 Computer Program for Equilibrium Problems of Elastic–Thermoplastic Solids and Structures.* Structural Mechanics Series, No. 15, Department of Civil Engineering, Duke University, Durham, North Carolina (Aug. 1973).
70. S. Utku, J. Q. Tarn and G. J. Dvorak, *ELAS55 Computer Program for Equilibrium Problems of Thermo-Viscoelastic–Plastic Solids and Structures.* Structural Mechanics Series, No. 21, Department of Civil Engineering, Duke University, Durham, North Carolina (Sept. 1974).
71. S. W. Key, Z. E. Beisinger, R. D. Krieg, HONDO, A finite element computer program for the large deformation dynamic response of axisymmetric solids. SAND-78-0422, Sandia National Laboratories, Albuquerque, New Mexico (1978).
72. LARSTRAN User's Manual. University of Stuttgart, West Germany (Mar. 1978).
73. *MARC User Information Manuals: Vol. A—User Information Manual; Vol. B—MARC Element Library; Vol. C—Program Input Manual; Vol. D—User Subroutines and System Description; Vol. E—Demonstration Problems; Vol. F—Structural Analysis with MARC Course Notes; Vol. G—MARC Background Papers.* MARC Analysis Research Corporation, Palo Alto, California.
74. MENTAT, Interactive Graphics Finite Element Mesh Editor, Preprocessor and Postprocessor, MARC Analysis Research Corporation, Palo Alto, California (1980).
75. R. H. MacNeal (Editor), NASTRAN theoretical manual, NASA SP-221(01) (1972).
76. C. W. McCormick (Editor), NASTRAN user's manual. NASA SP-222(01) (1972).
77. C. W. Hennrich (Editor), NASTRAN programmer's manual. NASA SP-223(01) (1972).
78. User's manual for NEPSAP, Lockheed Missiles and Space Company Report LMSC-D556019 (July 1979 Revision).
79. User's guide for NEPSAP processors, Lockheed Missiles and Space Company Report LMSC-D556020 (Mar. 1980 Revision).
80. Theoretical manual for NEPSAP, Lockheed Missiles and Space Company Report LMSC-D556041 (Oct. 1976).
81. L. A. Lopez, R. H. Dodds and D. R. Rehak, *POLO-FINITE: A Structural Mechanics System User Manual.* Civil Engineering Department, University of Illinois-Urbana and University of Kansas (Sept. 1979).
82. L. A. Lopez, R. H. Dodds and D. R. Rehak, *POLO-FINITE Example Problems Manual.* Civil Engineering Department, University of Illinois-Urbana and University of Kansas.
83. S.A.M.C.E.F., Systeme d'Analyse des Milieux Continus par Elements Finis. Manuels d'Utilisation, Volume 1 et 2; Manuel Theorique, Volume 1. L.T.A.S. (Juin 1979).
84. R. L. Chiapetta, J. D. Rouse and T. Belytschko, A computer code for dynamic stress analysis of media—structure problems with nonlinearities (SAMSON), Vols. I–IV, Report AFFWL-TR-72-104. Air Force Weapons Laboratory, Kirtland Air Force Base (Feb. 1973).
85. N. Sandsmark and O. Egeland, Plastic and viscoelastic stress analysis of solids of revolution (SESAM-69). *User's Manual NV-334.* Det Norske Veritas, Oslo, Norway (1972).
86. O. Egeland and P. O. Araldsen, SESAM-69, A general purpose finite element method program. *Comput. Structures* 4, 41–68 (Jan. 1974).
87. SESAM-69, Superelement structural analysis program modules, general description. Computas A/S, Det Norske Veritas, Norway (Dec. 1976).
88. B. O. Almroth, F. A. Brogan and G. M. Stanley, Structural analysis of general shells. Vol. II, User Instruction for STAGSC-1, Lockheed Missiles and Space Company Report LMSC-D633873, Palo Alto, California (Jan. 1980).
89. B. O. Almroth and F. A. Brogan, The STAGS computer code NASA CR-2950 (Feb. 1978).
90. J. M. Kennedy, Nonlinear dynamic response of reactor-core subassemblies. ANL-8065 (Jan. 1974).
91. D. F. Schoeberle, J. M. Kennedy and T. B. Belytschko, Implicit temporal integration for long-duration accidents in a structural response—STRAW. ANL-8136 (Oct. 1974).
92. J. M. Kennedy and T. B. Belytschko, Energy Source and Fluid Representation in a Structural Response Code—STRAW. ANL-8140 (May 1975).
93. J. M. Kennedy and T. B. Belytschko, Theory and application of a quasi-Eulerian fluid element for the STRAW code. ANL-78-100 (Oct. 1978).
94. S. Gabrielse (Editor), *WECAN Verification Manual.* Westinghouse Research and Development Center and Nuclear Energy Systems, Pittsburgh, Pennsylvania (Aug. 1974).
95. J. W. Morris (Editor), *WAPPP User's Manual.* Vol. 1 and Vol. 2, Westinghouse Research and Development Center and Nuclear Energy Systems, 79-1E7-NESPD-R1 and -R2, Pittsburgh, Pennsylvania (last revised Jan. 1979).
96. A. W. Filstrup (Editor), *WECAN User's Manual, Vol. 1—Capabilities; Vol. 2—Element Library; Vol. 3—Usage; and Vol. 4—Input Summary, Glossary and References.* Westinghouse Research and Development Center and Nuclear Energy Systems, 79-1E7-NESPD-R5, -R6, -R7 and -R8, Pittsburgh, Pennsylvania (last revised Sept. 1979).
97. T. B. Belytschko and R. Mullen, WHAMS: A program for the transient analysis of structures and continua, *Structural Mechanics Software Series* (Edited by N. Peronne and W. Pilkey), Vol. II, pp. 213–230. University Press of Virginia, Charlottesville, Virginia (1978).
98. T. B. Belytschko and R. Mullen, WHAMS: A program for the transient analysis of structures and continua. *Technical Manual* in preparation.